

Springer Water

Anna Di Mauro
Andrea Scozzari
Francesco Soldovieri *Editors*

Instrumentation and Measurement Technologies for Water Cycle Management

 Springer

Springer Water

Series Editor

Andrey Kostianoy, Russian Academy of Sciences, P. P. Shirshov Institute of Oceanology, Moscow, Russia

Editorial Board

Angela Carpenter, School of Earth & Environment, University of Leeds, Leeds, West Yorkshire, UK

Tamim Younos, Green Water-Infrastructure Academy, Blacksburg, VA, USA

Andrea Scozzari, Institute of Information Science and Technologies (CNR-ISTI), National Research Council of Italy, Pisa, Italy

Stefano Vignudelli, CNR - Istituto di Biofisica, Pisa, Italy

Alexei Kouraev, LEGOS, Université de Toulouse, Toulouse Cedex 9, France

The book series Springer Water comprises a broad portfolio of multi- and interdisciplinary scientific books, aiming at researchers, students, and everyone interested in water-related science. The series includes peer-reviewed monographs, edited volumes, textbooks, and conference proceedings. Its volumes combine all kinds of water-related research areas, such as: the movement, distribution and quality of fresh-water; water resources; the quality and pollution of water and its influence on health; the water industry including drinking water, wastewater, and desalination services and technologies; water history; as well as water management and the governmental, political, developmental, and ethical aspects of water.

Anna Di Mauro · Andrea Scozzari ·
Francesco Soldovieri
Editors

Instrumentation and Measurement Technologies for Water Cycle Management

 Springer

Editors

Anna Di Mauro
Università degli Studi della Campania Luigi
Vanvitelli
Aversa, Caserta, Italy

Andrea Scozzari
Institute of Information Science
and Technologies (CNR-ISTI)
National Research Council of Italy
Pisa, Italy

Francesco Soldovieri
Institute for Electromagnetic Sensing
of the Environment
National Research Council of Italy
Naples, Italy

ISSN 2364-6934

ISSN 2364-8198 (electronic)

Springer Water

ISBN 978-3-031-08261-0

ISBN 978-3-031-08262-7 (eBook)

<https://doi.org/10.1007/978-3-031-08262-7>

© The Editor(s) (if applicable) and The Author(s), under exclusive license to Springer Nature Switzerland AG 2022

This work is subject to copyright. All rights are solely and exclusively licensed by the Publisher, whether the whole or part of the material is concerned, specifically the rights of translation, reprinting, reuse of illustrations, recitation, broadcasting, reproduction on microfilms or in any other physical way, and transmission or information storage and retrieval, electronic adaptation, computer software, or by similar or dissimilar methodology now known or hereafter developed.

The use of general descriptive names, registered names, trademarks, service marks, etc. in this publication does not imply, even in the absence of a specific statement, that such names are exempt from the relevant protective laws and regulations and therefore free for general use.

The publisher, the authors, and the editors are safe to assume that the advice and information in this book are believed to be true and accurate at the date of publication. Neither the publisher nor the authors or the editors give a warranty, expressed or implied, with respect to the material contained herein or for any errors or omissions that may have been made. The publisher remains neutral with regard to jurisdictional claims in published maps and institutional affiliations.

This Springer imprint is published by the registered company Springer Nature Switzerland AG
The registered company address is: Gewerbestrasse 11, 6330 Cham, Switzerland

Acknowledgements

Chapters of this book have been peer-reviewed by two reviewers per chapter. Reviewers have been selected partly internal and partly external to the book project. The editors are very indebted to the reviewers for their excellent and thorough contribution to the overall quality of the book.

Here, we acknowledge the reviewers of the whole book project:

Hickmat Hossen, Aswan University, Egypt

Sergey Stanichny, Marine Hydrophysical Institute—RAS, Russia

Gabriele Pieri, Institute of Information Science and Technologies (CNR—ISTI), Italy

Abdelazim Negm, Zagazig University, Egypt

Dmitry Glukhovets, Shirshov Institute of Oceanology—RAS, Russia

Xiaogang (Marshall) Ma, University of Idaho, USA

Paolo Cipollini, European Space Agency (ESA—ESTEC), The Netherlands

Stefano Vignudelli, Institute of Biophysics (CNR—IBF), Italy

Yuri Manstein, Immanuel Kant Baltic Federal University, Russia

Armando Di Nardo, University of Campania “Luigi Vanvitelli”, Italy

Katerina Mazi, Institute for Environmental Research & Sustainable Development, Greece

Andrea Rizzoli, University of Applied Sciences and Arts of Southern Switzerland, Switzerland

Carlo Giudicianni, University of Campania “Luigi Vanvitelli”, Italy

Manuel J. Rodriguez, Université Laval, Québec, Canada

Giovanni Francesco Santonastaso, University of Campania “Luigi Vanvitelli”, Italy

Michele Iervolino, University of Campania “Luigi Vanvitelli”, Italy

Maria Rosa Di Cicco, University of Campania “Luigi Vanvitelli”, Italy

Lev Eppelbaum, Tel Aviv University, Israel

Carlo Noviello, Institute for Electromagnetic Sensing of the Environment (CNR—IREA), Italy

Luigi Capozzoli, Institute of Methodologies for Environmental Analysis (CNR—IMAA), Italy

Enzo Rizzo, University of Ferrara, Italy

Ilaria Catapano, Institute for Electromagnetic Sensing of the Environment (CNR—IREA), Italy

Gianluca Gennarelli, Institute for Electromagnetic Sensing of the Environment (CNR—IREA), Italy

In addition, we are grateful to Prof. Andrey Kostianoy (Editor-in-Chief of the book series) for having stimulated and supported this project, and all the editorial staff within Springer, who have always been available and supportive at all times.

Finally, our sincere thanks go to the contributors of this volume, which have always shown a great enthusiasm and engagement, since the beginning of the book project.

Contents

1	Preface	1
	Anna Di Mauro, Andrea Scozzari, and Francesco Soldovieri	
2	Regional Adaptation of Water Quality Algorithms for Monitoring Inland Waters: Case Study from Irish Lakes	11
	Sita Karki, Kevin French, Valerie McCarthy, Conor Delaney, Jennifer Hanafin, Eleanor Jennings, Alastair McKinstry, and Aaron Golden	
3	Optical Remote Sensing in Lake Trasimeno: Understanding from Applications Across Diverse Temporal, Spectral and Spatial Scales	29
	Bresciani Mariano, Free Gary, Pinardi Monica, Laanen Marnix, Padula Rosalba, Fabbretto Alice, Mangano Salvatore, and Giardino Claudia	
4	Satellite Instrumentation and Technique for Oil Pollution Monitoring of the Seas	53
	Andrey G. Kostianoy and Olga Yu. Lavrova	
5	Satellite Instrumentation and Technique for Monitoring of Seawater Quality	79
	Andrey G. Kostianoy, Olga Yu. Lavrova, and Alexey Ya. Storchkov	
6	Inland Water Altimetry: Technological Progress and Applications	111
	Jean-François Cretaux	
7	Generic Strategy for Consistency Validation of the Satellite-, In-Situ-, and Reanalysis—Based Climate Data Records (CDRs) Essential Climate Variables (ECVs)	141
	Yijian Zeng, Wim Timmermans, and Zhongbo Su	

8	Optical Spectroscopy for on Line Water Monitoring	165
	Genni Testa, Gianluca Persichetti, and Romeo Bernini	
9	Fiber Optic Technology for Environmental Monitoring: State of the Art and Application in the Observatory of Transfers in the Vadose Zone-(O-ZNS)	189
	B. Abbar, A. Isch, K. Michel, M. Abbas, H. Vincent, P. Abbasimaedeh, and M. Azaroual	
10	Plants, Vital Players in the Terrestrial Water Cycle	223
	Tomas E. van den Berg, Satadal Dutta, Elias Kaiser, Silvere Vialet-Chabrand, Martine van der Ploeg, Tim van Emmerik, Miriam Coenders-Gerrits, and Marie-Claire ten Veldhuis	
11	Improving Water Quality and Security with Advanced Sensors and Indirect Water Sensing Methods	251
	Philippe Cousin, Anastasia Moutzidou, Anastasios Karakostas, Lefteris Gounaridis, Christos Kouloumentas, Mauro Fernandes Pereira, Apostolos Apostolakis, Paula Gorrochategui, Guillaume Aoust, and Bérengère Lebental	
12	Sensor Web and Internet of Things Technologies for Hydrological Measurement Data	279
	Sebastian Drost, Christian Malewski, and Simon Jirka	
13	Smart Sensors for Smart Waters	295
	Andreas Weingartner and Jordi Raich	
14	Catchment-Based Water Monitoring Using a Hierarchy of Sensor Types	341
	Joyce O'Grady, Ciprian Briciu Burghina, and Fiona Regan	
15	Spectral Induced Polarization (SIP) Imaging for the Characterization of Hydrocarbon Contaminant Plumes	363
	Adrián Flores-Orozco and Matthias Bücker	
16	Direct Current Electrical Methods for Hydrogeological Purposes	387
	Enzo Rizzo and Valeria Giampaolo	
17	Digital Soil Mapping Using Drone-Borne Ground-Penetrating Radar	417
	Kaijun Wu and Sébastien Lambot	
18	Seismic Methods for Aquifer Analysis: The Basso Livenza Case Study	437
	Umberta Tinivella, Michela Giustiniani, Stefano Picotti, and Flavio Accaino	

19 Multi-geophysical Field Measurements to Characterize Lithological and Hydraulic Properties of a Multi-scale Karstic and Fractured Limestone Vadose Zone: Beauce Aquifer (O-ZNS) 461
Céline Mallet, Clara Jodry, Arnaud Isch, Gautier Laurent, Jacques Deparis, and Mohamed Azaroual

20 Measuring the Dielectric Properties of Soil: A Review and Some Innovative Proposals 485
Iman Farhat, Lourdes Farrugia, Julian Bonello, Charles Sammut, and Raffaele Persico

21 GPR Water Pipe Monitoring and Leaks Characterization: A Differential Microwave Tomography Approach 511
Ilaria Catapano, Roberta Palmeri, Francesco Soldovieri, and Lorenzo Crocco

22 Hydrogeophysical Methods for Water Resources Protection and Management 529
Giorgio Cassiani, Matteo Censini, Ilaria Barone, Maria Teresa Perri, Jacopo Boaga, and Rita Deiana

23 Advanced Combined Geophysical-Geological Mapping of the Sea of Galilee and Its Vicinity 553
L. Eppelbaum, Y. Katz, and Z. Ben-Avraham

24 Modelling a Polluted Aquifer with Reconstructed Heterogeneity Using the Composite Medium Indicator Kriging 581
Francesco Chidichimo, Michele De Biase, and Salvatore Straface

Chapter 1

Preface



Anna Di Mauro, Andrea Scozzari, and Francesco Soldovieri

Instrumentation and measurement technologies are currently playing a key role in the monitoring, assessment and protection of water resources. The whole water sector involves multiple technological contexts for the monitoring of the resource, given the broad multidisciplinary context, which covers water from its natural domains up to the various man-made infrastructures.

The water cycle management refers to a very complex framework, which requires reliable technological responses to the questions raised in meteorology, hydrology, water resources management, hydraulic engineering and, more in general, environmental management, with the related societal implications. Measurement techniques and sensing methods for the observation of water systems are rapidly evolving, requiring a continuous update in the measurement technologies and methods.

It is now clear that an effective and sustainable planning of the water cycle management requires the design and implementation of a systematic monitoring approach. In particular, instrumentation and measurement technologies have a pervasive presence in all the necessary aspects about the assessment, monitoring and control of water systems. Thus, the assessment of the water resource and of its relationship with the various environmental stressors, including the anthropic pressures on it, requires adequate knowledge, technologies and infrastructures in order to deal with

A. Di Mauro (✉)

Università degli studi della Campania Luigi Vanvitelli, via Roma, 29, 81031 Aversa, Italy
e-mail: anna.dimauro@unicampania.it

A. Scozzari

CNR Istituto di Scienza e Tecnologie dell'Informazione, via Moruzzi, 1, 56124 Pisa, Italy
e-mail: andrea.scozzari@isti.cnr.it

F. Soldovieri

Istituto per il Rilevamento Elettromagnetico dell'Ambiente Consiglio Nazionale delle Ricerche,
via Diocleziano, 328, 80124 Napoli, Italy
e-mail: soldovieri.f@irea.cnr.it

© The Author(s), under exclusive license to Springer Nature Switzerland AG 2022

A. Di Mauro et al. (eds.), *Instrumentation and Measurement Technologies for Water Cycle Management*, Springer Water, https://doi.org/10.1007/978-3-031-08262-7_1

the challenges of today. It is also important to underline that this aspect applies to both quantitative and qualitative monitoring activities, being the threats to the quality of the resource also indirectly affecting its availability and quantity.

This book aims at providing an updated framework of observational techniques, sensing technologies and data processing approaches for water management and protection. In the frame of data analytics, attention is given to the synergy between different sensing systems and between measurements and modelling approaches. The coexistence in this book of measurement techniques, sensing methods and data science implications for the observation of water systems, emphasize the strong link between measurement aspects and computational and modelling aspects that characterises the whole water sector.

The present volume provides a portrait of current measurement technologies and data analysis approaches for water systems monitoring and management, also offering insights to the enabling technologies that are today fostering the concept of smart water systems.

The 23 chapters of this book are organised in order to give a survey of current technologies and available methods for the assessment and monitoring of the water resource in multiple domains. In particular, the selected contributions are intended to cover the following thematic areas: (i) remote sensing methods; (ii) instrumentation for direct water sensing; (iii) water sensor networks and ICT infrastructures; (iv) geophysical techniques; (v) synergy between measurements and modelling.

With the aim of assembling a useful scenario to the reader, this volume encompasses a number of applicative aspects that contribute to build a substantial overview of the field: (i) advancements in field-measurement approaches; (ii) development of new sensing techniques; (iii) innovative sensors and networking approaches enabling the IoT paradigm; (iv) remote sensing techniques for the monitoring of water resources and/or the related infrastructures; (v) data processing techniques and modelling approaches for water resources monitoring and assessment.

Within this framework, the contribution by Karki et al. [1] investigates the opportunities offered by the operational satellites belonging to the Copernicus programme. This chapter deals with inland water quality assessments based on Sentinel 2 imagery. Interestingly, the chapter introduces also validation activities through a case study regarding Irish lakes. Authors introduce different processors for the correction of atmospheric effects and experimental results obtained during their validation exercise. Finally, the authors illustrate their proprietary Earth Observation (EO) software for water quality assessment, in the form of a web platform that facilitates the data access to the various stakeholders.

The chapter by Bresciani et al. [2] analyses the observational potentiality of the synergy between satellite-born hyperspectral missions and in situ and proximal sensing measurements, focusing on a case study related to Lake Trasimeno in Italy. In particular, the chapter discusses the combined usage of the PRISMA satellite mission and the WISP station radiometer in order to provide accurate and high-resolution information for water monitoring. The availability of long time-series of satellite observations, provided by the ESA CCI Lakes initiative, enables a better

understanding of the dynamics and of the main drivers of complex phenomena like phytoplankton blooms, by studying the history of past bloom events.

The next two chapters move our attention from the inland water context to the seawater. The contribution by Kostianoy and Lavrova [3] provides an overview of the techniques based on satellite observations for the detection of oil spills on the sea surface. The development of methodologies for the quantitative assessment of the total amount of oil pollution in the oceans and in inland seas is particularly urgent. The chapter focuses on the usage of satellite-borne SAR (Synthetic Aperture Radar) systems, also providing a survey of past and existing missions based on SAR sensors. The possibility to get almost all-weather imaging, the independence from solar illumination and the high revisit frequency (with a global coverage) make the usage of SAR very attractive. At the end of the chapter, the authors make an interesting discussion of the benefits and drawbacks of SAR systems applied to the detection of oil spills.

Kostianoy et al. [4] address the wider context of seawater quality assessment and monitoring from satellite observations. The contribution focuses on oil pollution, suspended matter, and algae bloom. In addition to the SAR systems, mentioned for the monitoring of oil pollution in the previous chapter, authors here analyze the usage of multispectral ocean color scanners for all the three above mentioned applications. The chapter also discusses the relevance of natural and anthropogenic stressors to the quality of seawater in the coastal zone, which is indeed a hot topic in the current research and technological innovation framework.

Jean-Francois Cretaux [5] introduces the satellite radar altimetry as a fundamental sensing technique for the observational needs of today. In particular, the author deals with hydrological applications, which are of extreme importance in the frame of climate change studies, where quantitative assessments of lakes, rivers, and artificial reservoirs play a key role. The chapter presents the basics of satellite radar altimetry, the processing of the acquired data, and the possible synergy with other sensing techniques (e.g., optical). At the time of writing the chapter, there were about thirty years of data collected by using this technology, making such dataset a true asset for a variety of hydrological applications. In fact, the author reports that lakes have been identified by Global Climate Observing System (GCOS) and World Meteorological Organization (WMO) as proxies for climate change monitoring at global scale. Finally, the assimilation of altimetry data into models is a fundamental aspect for most hydrological applications.

Climate change has many implications with the wide range of phenomena observable by satellite remote sensing and in situ measurements. In fact, most parameters, data collections and time series are in some way connected with climate change processes. The great importance that today is attributed to long-term climate datasets requires consistent data architectures, which should be independent from the observational method that generated the data. In this frame, the chapter by Zeng et al. [6] focuses on the generation of consistent and fully characterised ECVs (Essential Climate Variables), both for what regards in-situ, satellite and reanalysis data products. This is an aspect of primary importance when dealing with CDRs (Climate Data Records) and their critical aspects, such as the gaps in the datasets and

the inter-calibration of different instruments. The chapter investigates and discusses the current practices of consistency validation and proposes a relevant example consisting in the hydrological cycle closure in a Chinese river basin, by identifying the needed observations to determine the natural system correctly and close its balance.

Therefore, the first six chapters of this book show a general portrait of the many implications of remote sensing technologies with the water sector, in particular for what regards specific monitoring demands. The impact of earth observation on water systems is highlighted by the variety of application contexts shown in these chapters.

The next four chapters introduce novel approaches for the direct sensing of water, also focusing on original and intriguing applications. In particular, the chapter by Testa et al. [7] addresses water quality measurements, focusing on on-line monitoring. It presents promising optical sensing approaches for the detection of chemical and biological water pollutants, including latest methods and instruments. More in detail, the application of optical spectroscopic techniques for on-line water monitoring as absorption spectroscopy, light scattering method, fluorescence spectroscopy and Raman spectroscopy are discussed, highlighting possible advantages and potentialities. The analysis emphasizes that the integration of numerous optical spectroscopic techniques capable of providing complementary information, as well as improved signal data processing, could result in a significant increase in detection selectivity, sensitivity, and accuracy.

Abbar et al. [8] present a review of Fiber Optic (FO) technologies applied to relevant environmental issues, focusing on groundwater management and protection. It reports the state of the art on the use of FO sensors for environmental monitoring and discusses the installation of these sensors at a specific site. In detail, a research project conducted in France (O-ZNZ project) that uses this type of technology is presented as an example of full-scale implementation for groundwater data generation. Through the monitoring boreholes, the multi FO sensors system successfully established at the O-ZNS site will aid the characterization of fluid flow and the imaging of the subsurface layers near the O-ZNS wells. The information provided by the application represents the starting point for future activities in the field.

The chapter by van den Berg et al. [9] goes further the mere sensing of water parameters. By focusing on the role played by terrestrial plants in the water cycle, this contribution places the main emphasis on the dynamics of water transport within plants, particularly trees, and offers a complete overview of all the main methodologies/technologies currently available for the effective monitoring of plant-water relations. Water transport in the frame of plant-water dynamics represents an unprecedented playground for experimenting a large variety of sensing techniques, e.g., gas exchange for stomatal conductance and transpiration monitoring, lysimetry, thermometry, radiometric measurements like reflectance monitoring, ultrasound spectroscopy, dendrometry, accelometry, scintillometry, stable water isotope analysis and eddy covariance. The contribution closes with an outlook of the monitoring possibilities and a discussion of the open problems like the combination of data taken at various different spatial scales.

A wide range of techniques is always involved when monitoring a combination of environmental variables. The overview of innovative techniques shows that the

current wide range of measurement possibilities continuously offers new opportunities for stakeholders to find the right answers to a variety of problems. Drinking water monitoring, agriculture and environmental sciences in general take benefit from technological advancements in terms of precision, cost, temporal and spatial scale of the measurements.

The chapter by Cousin et al. [10] describes the development of detection technologies for analysing drinking water and the interconnection of safety and security-related networks of sensors for water supply and distribution networks. Innovative technologies investigated and tested across several European projects are described, in order to show their applicability and potentialities. Sensing by traditional techniques, multiparameter water quality monitoring through nanomaterials and carbon nanotube-based multiparameter water quality sensing are discussed. The topic presented is relevant for the water community, due to the spread of smart metering systems that made available new sensing technologies. The continuous improvement of water safety plans requires the application and experimentation of such every technological development, in order to identify their most effective implementation.

The development of sensor networks and infrastructures for the monitoring of water systems is currently a hot topic in the research and innovation context in the water sector. The following three contributions give a worthwhile hint to the most recent implications between sensing systems and information management.

In their chapter, Drost et al. [11] provide guidelines on how to set up a measurement data infrastructure by using both standards from the Open Geospatial Consortium's (OGC) Sensor Web Enablement framework and the Internet of Things (IoT) technology. The authors present a brief review of relevant Sensor Web and IoT standards, analysing their capability to face various problems such as sensor data stream collection, measurement data harmonization, and deployment constraints. Then, a model for a modular water monitoring system integrating sensor data with spatial (research) data infrastructures by using Sensor Web and IoT technologies is described. The chapter shows how Sensor Web and IoT technologies can be used together to facilitate the publication of sensor data in Spatial Data Infrastructures and provides recommendations and open questions related to future development in the use of these technologies for hydrological measurement data.

The chapter by Weingartner and Raich [12] presents an overview of 20 years of water monitoring science and services by summarizing the achievements in the world of water monitoring, the still existing gaps and shortcomings, and identifying future trends. Several types of sensor technologies for water quality monitoring are described, emphasizing the data quality requirements and the need for innovative applications and tools. The analysis highlights that for valuable water quality monitoring, manufacturers should develop more efficient and intelligent self-cleaning systems, more robust electrodes, better installation infrastructures and longer-lasting quality. In addition, the authors also propose the adoption of smart corrective algorithms for improving data quality on board and without operator intervention.

The contribution by O'Grady et al. [13] proposes a systematic paradigm of hierarchically tested sensing technologies to be implemented for providing an effective monitoring at the catchment scale. Available in-situ sensor technologies and other

possible instrumentation for water quality monitoring are discussed, giving particular attention to sensor selection, deployment strategy, and cost. The literature review covers a wide ensemble of sources and provides an effective starting point for the reader who is interested in implementing a monitoring network.

Geophysical techniques are fundamental assets for the monitoring of water systems and are the foundation of most in situ (or proximal sensing) assessment and monitoring of the resource. The chapter by Flores-Orozco and Bucker [14] provides a very useful review about the capability of the Spectral Induced Polarization (SIP) imaging method to delineate the geometry of hydrocarbon contaminant plumes and monitor the effect of remediation measures. The first part of the chapter is devoted to provide a brief introduction into the SIP method, discusses the electrical properties of the rocks and soils and offers a detailed revision of the literature to illustrate the broad range of electrical properties of fresh and mature contaminant plumes. After, the challenges and good practices of collecting, processing and interpreting of SIP imaging data are highlighted for the characterization of a benzene plume on the field scale. Finally, a second case study is presented about the SIP monitoring results obtained along the injection of zero-valent iron particles for the remediation of a TCE (Trichloroethylene) plume.

In their chapter, Rizzo and Gianpaolo [15] deal with the direct current electrical methods, which are probably the most widely near surface geophysical techniques used for environmental investigations. The success of these methods is related to several factors such as; the theoretical concepts are relatively straightforward; field measurement techniques are highly scalable, allowing investigations to depths from tens of centimetres to hundreds of meters; instrumentation is relatively low cost and straightforward to operate. On the other hand, as clearly evident from the content of the chapter, significant efforts are still necessary about advanced data analysis in terms of 3D imaging and reliable and accurate tomographic approaches.

The contribution by Wu and Lambot [16] discusses the recent technological and scientific advances about the use of drone-based ground-penetrating radar (GPR) for digital soil mapping. In particular, a prototypical GPR system is described for the installation on a drone. Attention is provided to the scientific challenge of the full-wave inversion, which has the aim to retrieve the soil dielectric permittivity from the soil surface reflection. After, the retrieved dielectric permittivity is exploited to estimate volumetric soil water content through a petro-physical relation. As a final outcome of the approach introduced by the authors, soil moisture maps are presented with reference to agricultural fields in Belgium.

The chapter by Tinivella et al. [17] provides an interesting case study about the capability of the seismic method to study and monitor the aquifers. In particular, the case study has regarded an area in North East of Italy and all the phases of the experiment are provided in the chapter, from the choice of the acquisition parameters to the final interpretation. Both 2D and 3D data were acquired in different seasons in order to define any possible seasonal variation. In order to obtain detailed petro-physical information, amplitude preserving processing, advanced tomographic imaging and Amplitude Versus Offset procedures were exploited. In this way, the analysis permitted the estimation of the petro-physical properties of the subsoil and the detection and

localization of a deeper aquifer not yet identified, as confirmed by a subsequent new well. The discovered aquifer, at 480 m depth, has been proved suitable for extracting water for domestic purposes.

The chapter by Mallet et al. [18] is concerned with activities performed at the Observatory of transfers of the Vadose Zone (O-ZNS) implemented near Orléans (France). By combining multi-scales laboratory and field experiments using various monitoring techniques, this observatory is able to improve the knowledge about the processes regarding water flow and contaminants transport throughout a highly heterogeneous vadose zone. As specific case presented in the chapter, it is described a multi-geophysical monitoring strategy in order to overcome the limitations of each single geophysical methods. The presented analysis has permitted to highlight how coupling electrical and seismic methods improves drastically the lithological characterization of the facies. In addition, coupling electrical resistivity, ground penetrating radar and Nuclear Magnetic Resonance surveys has enhanced the estimation of the variations in water content within the vadose zone. Therefore, the whole set of results constitutes a first base to ongoing joint inversion that should lead to a refined characterization of the petro-physical and transport properties of the vadose zone.

In their chapter, Farhat et al. [19] deal with the indirect measurement of the water content in the soil by using Time Domain Reflectometry (TDR). TDR is able to measure the electromagnetic properties, namely, the complex dielectric permittivity, accounting in itself also for the electrical conductivity. After, semi semi-empirical relationships between dielectric permittivity and water content are used. In particular, the chapter deals with the features of TDR measurements, by focussing on the possibility of making use of multi-length TDR measurements where, at each frequency, information is gathered by means of TDR probes of different lengths. In this way, the dispersion law of the material can be retrieved and consequently improved information can be inferred about the water content, which for a given kind of soil should correspond to a specific dispersive behaviour.

The monitoring of water pipes and the detection of leaks represents a peculiar application of the Ground Penetrating Radar (GPR) for water distribution networks. The chapter by Catapano et al. [20] focuses on the usage of GPR enhanced by a novel data processing approach, providing a proof of concept of the reconstruction capability of the proposed technique. GPR represents a non invasive electromagnetic (EM) method for the direct measurement of underground features by exploiting scattering and reflection from EM discontinuities. Authors go through the explanation of the general working principle of GPR, the specific configuration for pipe monitoring and the tomographic imaging approach developed for water leaks monitoring. A useful validation exercise, built on a model based on a synthetic scenario, completes the chapter.

The next four chapters underline the importance of the synergy between measurement methods, data collection and modelling, both for what regards remotely-sensed data acquisition and for in-situ measurements.

The chapter by Cassiani et al. [21] presents a survey of hydro-geophysical methods and their application for water resources protection and management, making an excursus that covers the past twenty years. Hydro-geophysical techniques are

presented as a tool for long-term data acquisition for the monitoring of hydrological changes, and as an effective way for the calibration of subsurface hydrological models. The authors highlight how the physical processes underlying both disciplines must be taken into account when developing an observational approach based on geophysics, going further the mere “imaging” application. Moreover, the chapter also clarifies in a very effective way the usefulness of hydrogeophysics for the monitoring of hydrological processes over time, and, very interestingly, underlines the support of hydrogeophysical methods to data assimilation into numerical models.

Another interesting case-study regarding the integration of geophysical-geological methodologies is provided in the chapter by Eppelbaum et al. [22]. The case study regards the Sea of Galilee (Lake Kinneret), which is located in northern Israel, in an area of complex tectonic setting where the Dead Sea Transform crosscuts other fault systems. In the present study, gravitational, magnetic, paleomagnetic, radiometric and seismological data are analyzed together for the first time. This approach allowed a series of benefits: (i) to make significant changes in the structural plan and typology of geological units of various types and genesis; (ii) to identify a variety of sources, mechanisms and types of the geodynamic features (both deep and subsurface ones); (iii) to clarify the formation history of the region that is important from the standpoint of geo-ecology, assessment of the water resources, geodynamic forecast and monitoring of natural and engineering environmental factors.

Then, stochastic hydrology is the topic of the chapter by Chidichimo et al. [23], which closes this contributed volume. The identification of natural systems often deals with the intrinsic uncertainty in the determination of the geological structures that lie behind the development of numerical models. The authors of this contribution introduce an application of the composite media theory to a context with highly heterogeneous media. In particular, a case study is presented, dealing with the remediation of an industrial site in Naples (Italy). This chapter shows how a probabilistic reconstruction of geologic facies offers an effective alternative to the classical approach based on homogenization or averaging, and can support the optimization of modelling tools to describe the real behavior of the system, based on a better understanding of both the contamination process and its possible remediation.

This book is intended for a wide audience of readers, such as post-graduates, researchers and stakeholders at various levels. In addition, it may be useful for those experts who want to extend their field of view to adjacent fields of expertise.

The volume does not want to represent a mere container of the latest advances about specialist research activities. Instead, it wants to be a useful building block, providing a clear overview of current research and technological possibilities. Users and experts of diverse disciplines may find in this book an “entry point” to the large arena of the monitoring solutions that are available or under development today, with a hint to the related open issues and the future development possibilities. Moreover, our approach shall contribute to fill the gap between the stakeholders’ requirements and the available solutions.

References

1. Karki S, French K, McCarthy V, Delaney C, Hanafin J, Jennings E, McKinstry A, Golden A (2022) Regional adaptation of water quality algorithms for monitoring inland waters: case study from Irish lakes. In: Di Mauro A, Scozzari A, Soldovieri F (eds) *Instrumentation and measurement technologies for water cycle management, water*, Springer Nature Switzerland AG, pp 11–27. https://doi.org/10.1007/978-3-031-08262-7_2
2. Bresciani M, Free G, Pinardi M, Laanen M, Padula R, Fabbretto A, Mangano S, Giardino C (2022) Optical remote sensing in Lake Trasimeno: understanding from applications across diverse temporal, spectral and spatial scales. In: Di Mauro A, Scozzari A, Soldovieri F (eds) *Instrumentation and measurement technologies for water cycle management, water*. Springer Nature Switzerland AG, pp 29–52. https://doi.org/10.1007/978-3-031-08262-7_3
3. Kostianoy AG, Lavrova OYu (2022) Satellite instrumentation and technique for oil pollution monitoring of the seas. In: Di Mauro A, Scozzari A, Soldovieri F (eds) *Instrumentation and measurement technologies for water cycle management, water*. Springer Nature Switzerland AG, pp 53–77. https://doi.org/10.1007/978-3-031-08262-7_4
4. Kostianoy AG, Lavrova OY, Strochkov AY (2022) Satellite instrumentation and technique for the monitoring of seawater quality. In: Di Mauro A, Scozzari A, Soldovieri F (eds) *Instrumentation and measurement technologies for water cycle management, water*. Springer Nature Switzerland AG, pp 79–109. https://doi.org/10.1007/978-3-031-08262-7_5
5. Cretaux J-F (2022) Inland water altimetry: technological progress and applications. In: Di Mauro A, Scozzari A, Soldovieri F (eds) *Instrumentation and measurement technologies for water cycle management, water*. Springer Nature Switzerland AG, pp 111–139. https://doi.org/10.1007/978-3-031-08262-7_6
6. Zeng Y, Timmermans W, Su Z (2022) Generic strategy for consistency validation of the satellite-, In-situ-, and reanalysis-based climate data records (CDRs) essential climate variables (ECVs). In: Di Mauro A, Scozzari A, Soldovieri F (eds) *Instrumentation and measurement technologies for water cycle management, water*. Springer Nature Switzerland AG, pp 141–163. https://doi.org/10.1007/978-3-031-08262-7_7
7. Testa G, Persichetti G, Bernini R (2022) Optical spectroscopy for on line water monitoring. In: Di Mauro A, Scozzari A, Soldovieri F (eds) *Instrumentation and measurement technologies for water cycle management, water*. Springer Nature Switzerland AG, pp 165–188. https://doi.org/10.1007/978-3-031-08262-7_8
8. Abbar B, Isch A, Michel K, Abbes M, Vincent H, Abbasimaedeh P, Azaroual M (2022) Fiber optic technology for environmental monitoring: state of the art and application in the observatory of transfers in the Vadose Zone-(O-ZNS). In: Di Mauro A, Scozzari A, Soldovieri F (eds) *Instrumentation and measurement technologies for water cycle management, water*. Springer Nature Switzerland AG, pp 189–222. https://doi.org/10.1007/978-3-031-08262-7_9
9. van den Berg TE, Dutta S, Kaiser E, Vialet-Chabrand S, van der Ploeg M, van Emmerik T, Coenders-Gerrits M, ten Veldhuis M-C (2022) Plants, vital players in the terrestrial water cycle. In: Di Mauro A, Scozzari A, Soldovieri F (eds) *Instrumentation and measurement technologies for water cycle management, water*. Springer Nature Switzerland AG, pp 223–250. https://doi.org/10.1007/978-3-031-08262-7_10
10. Cousin P, Mouttzidou A, Karakostas A, Gounaridis L, Kouloumentas C, Fernandes Pereira M, Apostolakis A, Gorrochategui P, Aoust G, Lebalat B (2022) Improving water quality and security with advanced sensors and indirect water sensing methods. In: Di Mauro A, Scozzari A, Soldovieri F (eds) *Instrumentation and measurement technologies for water cycle management, water*. Springer Nature Switzerland AG, pp 251–277. https://doi.org/10.1007/978-3-031-08262-7_11
11. Drost S, Malewski C, Jirka S (2022) Sensor web and internet of things technologies for hydrological measurement data. In: Di Mauro A, Scozzari A, Soldovieri F (eds) *Instrumentation and measurement technologies for water cycle management, water*. Springer Nature Switzerland AG, pp 279–293. https://doi.org/10.1007/978-3-031-08262-7_12

12. Weingartner A, Raich J (2022) Smart sensors for smart waters. In: Di Mauro A, Scozzari A, Soldovieri F (eds) *Instrumentation and measurement technologies for water cycle management, water*. Springer Nature Switzerland AG, pp 295–340. https://doi.org/10.1007/978-3-031-08262-7_13
13. O'Grady J, Burghina CB, Regan F (2022) Catchment-based water monitoring using a hierarchy of sensor types. In: Di Mauro A, Scozzari A, Soldovieri F (eds) *Instrumentation and measurement technologies for water cycle management, water*. Springer Nature Switzerland AG, pp 341–362. https://doi.org/10.1007/978-3-031-08262-7_14
14. Flores-Orozco A, Bucker M (2022) Spectral induced polarization (SIP) imaging for the characterization of hydrocarbon contaminant plumes. In: Di Mauro A, Scozzari A, Soldovieri F (eds) *Instrumentation and measurement technologies for water cycle management, water*. Springer Nature Switzerland AG, pp 363–386. https://doi.org/10.1007/978-3-031-08262-7_15
15. Rizzo E, Giampaolo V (2022) Direct current electrical methods for hydrogeological purposes. In: Di Mauro A, Scozzari A, Soldovieri F (eds) *Instrumentation and measurement technologies for water cycle management, water*. Springer Nature Switzerland AG, pp 387–416. https://doi.org/10.1007/978-3-031-08262-7_16
16. Wu K, Lambot S (2022) Digital soil mapping using drone-borne ground-penetrating radar. In: Di Mauro A, Scozzari A, Soldovieri F (eds) *Instrumentation and measurement technologies for water cycle management, water*. Springer Nature Switzerland AG, pp 417–436. https://doi.org/10.1007/978-3-031-08262-7_17
17. Tinivella U, Giustiniani M, Picotti S, Accaino F (2022) Seismic methods for aquifer analysis: the Basso Livenza case study. In: Di Mauro A, Scozzari A, Soldovieri F (eds) *Instrumentation and measurement technologies for water cycle management, water*. Springer Nature Switzerland AG, pp 437–459. https://doi.org/10.1007/978-3-031-08262-7_18
18. Mallet C, Jodry C, Isch A, Laurent G, Deparis J, Azaroual M (2022) Multi-geophysical field measurements to characterize lithological and hydraulic properties of a multi-scale karstic and fractured limestone vadose zone: Beauce aquifer (O-ZNS). In: Di Mauro A, Scozzari A, Soldovieri F (eds) *Instrumentation and measurement technologies for water cycle management, water*. Springer Nature Switzerland AG, pp 461–484. https://doi.org/10.1007/978-3-031-08262-7_19
19. Farhat I, Farrugia L, Bonello J, Sammut C, Persico R (2022) Measuring the dielectric properties of soil: a review and some innovative proposals. In: Di Mauro A, Scozzari A, Soldovieri F (eds) *Instrumentation and measurement technologies for water cycle management, water*. Springer Nature Switzerland AG, pp 485–509. https://doi.org/10.1007/978-3-031-08262-7_20
20. Catapano I, Palmeri R, Soldovieri F, Crocco L (2022) GPR water pipe monitoring and leaks characterization: a differential microwave tomography approach. In: Di Mauro A, Scozzari A, Soldovieri F (eds) *Instrumentation and measurement technologies for water cycle management, water*. Springer Nature Switzerland AG, pp 511–527. https://doi.org/10.1007/978-3-031-08262-7_21
21. Cassiani G, Censini M, Barone I, Perri MT, Boaga J, Deiana R (2022) Hydrogeophysical methods for water resources protection and management. In: Di Mauro A, Scozzari A, Soldovieri F (eds) *Instrumentation and measurement technologies for water cycle management, water*. Springer Nature Switzerland AG, pp 529–552. https://doi.org/10.1007/978-3-031-08262-7_22
22. Eppelbaum L, Katz Y, Ben-Avraham Z (2022) Advanced combined geophysical-geological mapping of the Sea of Galilee and its vicinity. In: Di Mauro A, Scozzari A, Soldovieri F (eds) *Instrumentation and measurement technologies for water cycle management, water*. Springer Nature Switzerland AG, pp 553–579. https://doi.org/10.1007/978-3-031-08262-7_23
23. Chidichimo F, Biase MD, Straface S (2022) Modelling a polluted aquifer with reconstructed heterogeneity using the composite medium indicator Kriging. In: Di Mauro A, Scozzari A, Soldovieri F (eds) *Instrumentation and measurement technologies for water cycle management, water*. Springer Nature Switzerland AG, pp 581–599. https://doi.org/10.1007/978-3-031-08262-7_24

Chapter 2

Regional Adaptation of Water Quality Algorithms for Monitoring Inland Waters: Case Study from Irish Lakes



Sita Karki, Kevin French, Valerie McCarthy, Conor Delaney, Jennifer Hanafin, Eleanor Jennings, Alastair McKinstry, and Aaron Golden

Abstract The recent development of the Copernicus programme in Europe has ushered in a new generation of operational earth observing satellites. Field-based investigations and monitoring programmes are costly, time consuming and can be logistically challenging in remote or inaccessible locations. The advantages of in situ data monitoring are that they have very low uncertainties compared to satellite data, but they only provide readings at one location at one time. Satellite data are very complementary to field measurements for long-term and regional monitoring programmes. Through the Environmental Protection Agency (EPA)'s Remote Sensing of Irish Surface Water (INFER) project (2017-W-MS-30), we validated algorithms to infer lake water quality on the island of Ireland using Sentinel 2 imagery, which comprises two European Space Agency (ESA) terrestrial satellites with a combined temporal resolution of 5 days and spatial resolution of 10 m. The project is focused on the selection of optimal algorithms that will be applicable in a regional context in relation to the high cloud cover and relatively small sizes of the water bodies involved. C2RCC and Acolite processors were used to compute the chlorophyll-*a* and turbidity from identified lakes. Field radiometry was carried out using a TRIOS RAMSES radiometer at several sites to validate the algorithms. Standard field procedures were employed for acquiring glint-free reflectance from the water bodies. Based on the validation with field data, a coupled technique was developed to atmospherically correct and compute water quality parameters. The water quality products

S. Karki (✉) · J. Hanafin · A. McKinstry
Irish Centre for High-End Computing (ICHEC), IT302, National University of Ireland Galway,
University Rd, Galway, Ireland
e-mail: sita.karki@ichec.ie

K. French · V. McCarthy · E. Jennings
Centre for Freshwater and Environmental Studies, Dundalk Institute of Technology, Dundalk,
County Louth, Ireland

A. Golden
School of Mathematics, Statistics and Applied Mathematics, Ryan Institute, National University
of Ireland Galway, University Rd, Galway, Ireland

C. Delaney
National University of Ireland, Galway, University Rd, Galway, Ireland

generated using Sentinel-2 can be visualized via a web platform (<https://eoplatform.ichec.ie/infer>). Although the developed techniques offer many benefits for water quality monitoring, it is still challenging in the context of Ireland, where very few cloud-free scenes are available. In addition, the smaller sizes of lakes make it difficult to monitor them using the current resolution of Sentinel-2.

Keywords Sentinel-2 · Water quality · Chlorophyll-*a* · Turbidity · Total suspended matter · Lakes · Monitoring

2.1 Introduction

Aquatic ecosystems are crucial for human well-being and have important functions in the environment [33]. Lakes, for example, provide a source of drinking water, in addition to being important for irrigation [8, 14, 45]. Inland water bodies are important for fisheries and aquaculture activities, recreation, tourism, and they also provide vital habitats, supporting high levels of biodiversity [33]. The importance of these aquatic systems is well recognised through the implementation of numerous national and international regulations related to their protection, foremost being the EU Water Framework Directive (WFD) 2000/60/EC [18].

Many surface waterbodies are now under severe anthropogenic pressures from eutrophication, inorganic pollution, acidification, invasive species, high levels of drinking water extraction, and directional climate change [1, 7, 14, 15]. Management of these waterbodies needs an integrative and adaptive approach that can provide a comprehensive and reliable overview of their status, that in turn requires reliable and cost-effective monitoring programmes.

2.1.1 *Need for Remote Sensing Technologies*

Conventional monitoring of aquatic systems is often time consuming and labour intensive and consequently, in many cases, expanding current monitoring programmes both to improve spatial and temporal coverage is often considered prohibitively expensive [21, 41]. Additionally, even where a water body is monitored, these restrictions often mean that sampling is spatially limited and carried out at, for example, at a single monitoring point (e.g. the deepest point in the lake), which may not necessarily be representative of the entire water body. Moreover, sampling may often only be repeated over relatively long-time intervals (e.g. intervals of months or even years). Such low temporal resolution only provides a snapshot in time, and does not allow for detailed studies of changes and trends over time, and also cannot take short-term extreme or episodic changes into account [14, 21, 27, 39].

Monitoring programmes often do not operate at the frequency required to capture the dynamics of changes in lake chemistry and biota, particularly for processes

which occur over short periods of time such as those associated with planktonic and microbial communities [29]. In addition, increasing our understanding of lakes in a global context will require frequent and consistent long-term monitoring with a comprehensive spatial coverage [25].

The use of remote sensing is one of the options to address the spatial and temporal limitations of traditional monitoring programmes, while also increasing the number of surface waters that can be monitored [14, 36]. Recent and on-going research has identified a suite of water quality parameters that have the potential to be estimated using sensing technologies. These include chlorophyll-*a* (Chl-*a*), a common proxy for phytoplankton biomass, water colour, used as proxy for the concentration of colored dissolved organic matter (CDOM), and turbidity and related suspended sediment levels [36, 37]. Remote sensing has also been used to identify the occurrence of phytoplankton blooms and gain information on macrophyte composition [20].

The integration of remote satellite sensing into water quality research and monitoring has been proposed by many studies [5, 9, 39, 50]. Remote sensing techniques have already been successfully integrated in terrestrial ecosystem service assessments (e.g., Andrew et al. [3]; de Araujo Barbosa et al. [11]) for the assessment of indicators of terrestrial habitat quality (e.g., Spanhove et al. [42]). It, therefore, seems reasonable that the incorporation of remote sensing for monitoring of inland waterbodies is the next viable step to allow more detailed temporal and spatial studies of aquatic systems.

2.1.2 Water Quality Monitoring in Ireland

Rainfall is the key source of recharge for inland water in Ireland with eastern parts of the island receiving 750 to 1000 mm/year rainfall and the western part between 1000 and 1400 mm [31]. This difference in precipitation is also evident through the distribution of lakes on the island as shown in Fig. 2.1a, with the western half of the country showing a greater number of inland waterbodies being monitored. Unfortunately, the western regions are also more prone to cloud cover. Of these waterbodies, only a fraction is included in the national monitoring programme, which is carried out in order to fulfil requirements of the EU WFD [18]. The WFD requires member states to ensure all waterbodies in their jurisdiction reach at least ‘good’ water quality status and take a holistic approach to managing their waterbodies.

Chlorophyll-*a* concentration is a relatively easy and rapid analyses, which can be used as a proxy for phytoplankton biomass [19] and it is one of the biological quality elements (BQE) used to infer water quality status as part of Ireland’s monitoring strategy for the WFD [16]. Measurements are carried out through extraction of Chl-*a* pigment and subsequent quantification of the absorption of the extract using a spectrophotometer.

The total suspended matter (TSM) concentration and the related turbidity level are also key water quality parameters relevant for biological processes and water quality

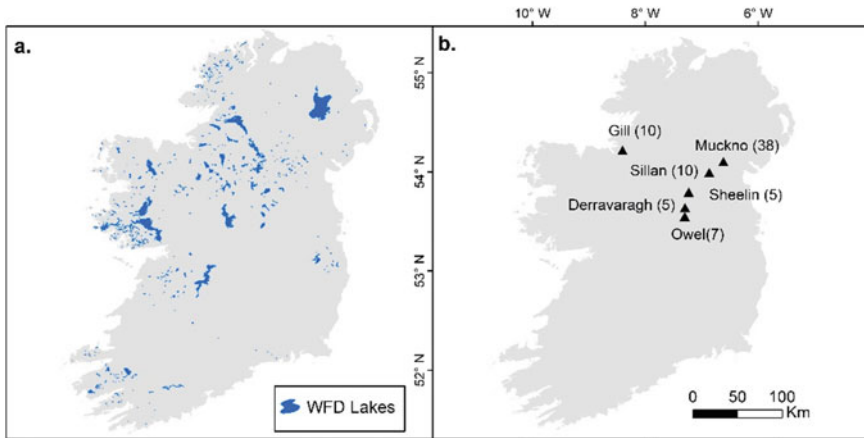


Fig. 2.1 Map of Ireland showing: **a** Lakes under WFD monitoring programme and **b** Lakes sampled in this project with the total number of samples collected for each lake

[26, 48, 49]. The concentration of particles can influence the transmission of light underwater and thus alter the productivity of water column phytoplankton and the living conditions of both vegetation and aquatic animals [24, 26, 32]. Furthermore, suspended sediments can impact quality by carrying pollutants and heavy metals of terrestrial origin [17, 32]. Knowledge of spatial and temporal patterns in the concentration of particles is, therefore, essential for the evaluation of water quality and associated environmental functions [26]. Total suspended sediment is measured gravimetrically by filtering a known volume of sample water through a glass fiber filter [2], which is then dried and weighed.

Turbidity is an expression of the optical property that causes light to be scattered and absorbed rather than transmitted, with no change in direction or flux level through the sample [2]. It is generally measured using commercial nephelometers, or portable turbidimeters and reported in nephelometric turbidity units (NTU) or in Formazin Nephelometric units (FNU). Correlations between turbidity and TSS can be difficult because the size, shape, and refractive index of the particles affect the light-scattering properties of the suspension [2].

Water clarity can also be estimated using a Secchi disk, an easy and inexpensive measure of turbidity for waterbodies [38]. A black and white disk is lowered into the area of interest until the disk is no longer visible and this depth recorded as a measure of transparency. One drawback to this method is it may not be useful in shallow waterbodies where the bottom of the waterbody can be seen from the surface. Although there can sometimes be issues related to systematic deployment [43], a Secchi disk measurement can be more precise than turbidity measurements [10].

Monitoring TSS and turbidity levels in larger waterbodies is generally challenging due to concentrations being heterogeneous in terms of space and time [26]. In addition, episodic weather events can trigger high inflows [12] or wind driven mass sediment re-suspension [4], leading to short-term reductions in water clarity.

Through the Environmental Protection Agency (EPA)'s Remote Sensing of Irish Surface Water (INFER) project (2017-W-MS-30), we focused on the application of earth observation data for computing water quality parameters and, therefore, provide a technique capable of addressing some of the spatial and temporal issues with traditional water monitoring programmes. The main objective of the study was to develop a processing chain that will help to establish remote sensing as a complimentary tool for monitoring lakes regionally by estimating chlorophyll-*a* and turbidity.

2.2 Methods

The study employed historical field samples to determine the best practices for sampling to optimize the temporal and spatial matchups between *in-situ* lake measurements and satellite imagery. Historical data together with bathymetry survey data were analysed to determine the influence of lake topographical conditions (e.g., bottom reflectance, adjacency) on the magnitude of reflectance. Based on the study, recommendations were made to collect samples 10 m away from the shorelines and at a depth of more than 6 m. Every lake has a unique topography and associated littoral zone, but these measures were followed to minimize the potential effect of bottom reflectance and signal mixing, which is common to small and shallow lakes.

2.2.1 Field Sampling

A site selection process was undertaken during the spring of 2019 to shortlist appropriate sites for field validation of satellite-derived products. A total of 6 lakes were sampled for field validation based on several criteria such as size, depth, trophic status and WFD status. In addition, a timetable for proposed sampling was established by drawing up a schedule of satellite overpasses starting from summer of 2019.

A GPS and a depth Sounder (Hondex PS-7) were used to locate sampling sites. Vertically integrated samples of the water column were taken using a plastic tube 5 cm in diameter and 6 m in length. Secchi depth transparency was measured by lowering a Secchi disk on the shaded side of the boat and recording the depth at which the disk was no longer visible to the nearest 0.1 m (d_1). The disk was then slowly hauled up and the depth at which the disk reappeared was again recorded to the nearest 0.1 m (d_2). The Secchi disk transparency was calculated by taking the arithmetic mean of these two measurements (d_1 and d_2).

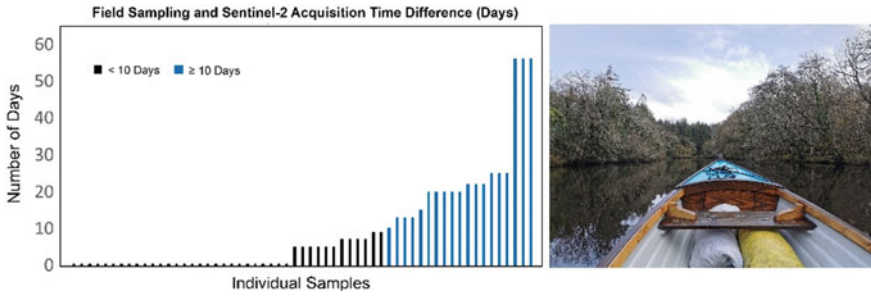


Fig. 2.2 Days delay between the field sampling and Sentinel-2 acquisitions for 59 field samples. Almost half of the data points had acquisition within the same day

Chlorophyll-*a* analyses were carried out on 1 L triplicate samples from each integrated water sample, filtered through Whatman® GF/C filters and extracted with methanol [44] with absorbance read in a spectrophotometer at 665 and 750 nm in a 5 cm cell.

Altogether 75 samples with Chl-*a* concentration and field transparency measurements were recorded as shown in Fig. 2.1b.

2.2.2 Sentinel-2 Imagery Collection

The Sentinel-2 archive was scanned for cloud-free views of the sampled locations. Sentinel-2 comprises the constellation of Sentinel 2A and 2B. Combined, they provide a revisit time of 5 days at the equator with a swath coverage of 290 km at 10 m spatial resolution for visible and near-infrared regions of the spectrum. Considering the fast-changing weather conditions of Ireland, it was difficult to obtain the exact overlap between the Sentinel-2 overpass and the field sampling. The target was to get the scene with a minimum number of days, but only 59 data points were useful, and the rest were discarded as no corresponding clear scenes (devoid of cloud or cloud shadow) were found. Figure 2.2 shows that almost half of the data had the same day acquisition whereas 75% of the data points had corresponding acquisition within two weeks.

2.2.3 Field Radiometry

Field radiometry was conducted using a TRIOS RAMSES radiometer from late 2019 to early 2020. The current procedure entails collection of reflectance data from the lakes during satellite overpass to minimize the potential error in the atmospheric correction. Altogether 6 data points from 4 different lakes were collected. The actual

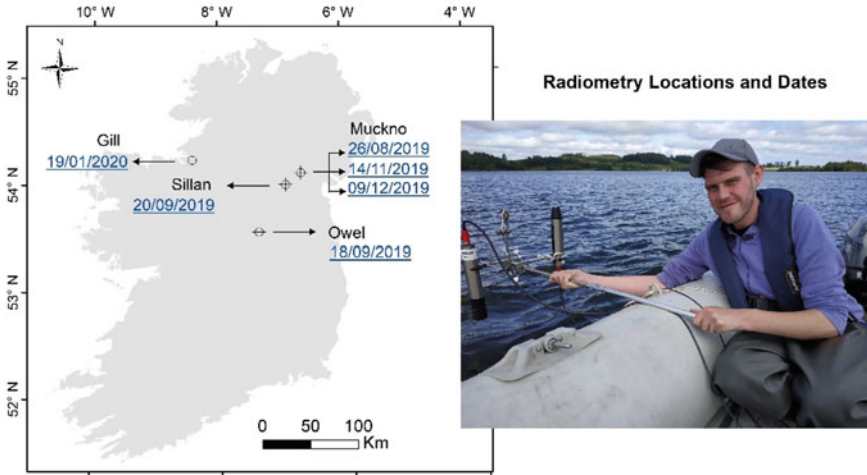


Fig. 2.3 Field radiometry locations and dates

number of field campaigns, date and location of radiometry are shown in Fig. 2.3. Glint free measurements were collected using the techniques described by Kutser et al. [28].

Acolite [40] and C2RCC [6, 13] processors were used to perform atmospheric correction and the computation of water quality parameters from the satellite data. The data collected from field sampling and radiometry were analyzed and compared with the results obtained using a water quality processor on the satellite data. Figure 2.4 shows the detailed break-down of the steps followed to identify the best workflow for the project. For atmospheric correction, a dark spectrum fitting technique [46, 47] was applied in Acolite whereas a neural network-based technique [6] was used in C2RCC processor to compute Chl-*a* and TSM. Within the Acolite processor, different algorithms were analyzed and finally the red edge algorithm by Gons et al. [23] was selected for processing Chl-*a* (mg/m^3). Similarly, the algorithm developed by Nechad et al. [34, 35] was used for turbidity (FNU) computation using Acolite.

2.3 Results and Discussions

Sentinel-2 derived results were compared with those measured from the field radiometry and sampling.

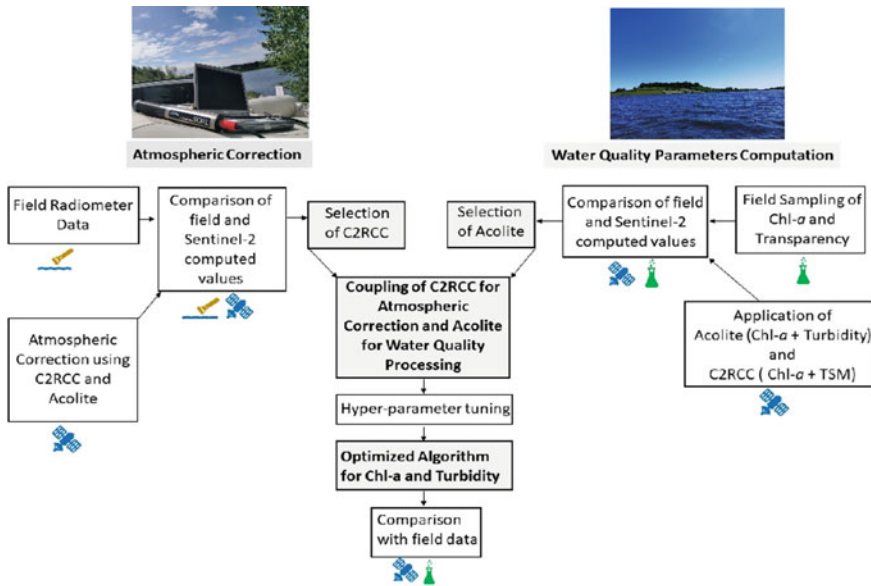


Fig. 2.4 Steps adopted to develop the optimized algorithm

2.3.1 Atmospheric Correction

The comparison of the field and satellite derived results showed that the C2RCC algorithm provided better estimates of atmospheric contribution compared to the Acolite processor. Figure 2.5 shows the measure of upwelling radiance (L_u) and downwelling irradiance (E_d) taken from the field radiometer at Lake Owel (Fig. 2.5a) and Lake Sillan (Fig. 2.5b) on 18th of September 2019. During the measurement, the downwelling irradiance was measured and the radiometer was turned upside down to measure the upwelling radiance. The remote-sensing reflectance was then computed, which is the ratio of downwelling irradiance that is incident on the surface of the water to the portion that is returned through the surface. The graphs also show the estimation after the glint had been removed. The top-of-atmosphere reflectance (R_{toa}) or the reflectance before the atmospheric correction and the surface reflectance for water pixels (R_{how}) derived from both C2RCC and Acolite are also shown on the graph. The surface reflectance after atmospheric correction from both processors were compared to the field radiometric measurements. The reflectance for water pixels from C2RCC (R_{how} , shown in brown) provides a better approximation of the glint-free (L_u/E_d) measurement from the radiometer compared to the one from Acolite (R_{how} , shown in black). Based on the similar comparison for all the locations of field radiometry, C2RCC was selected for the atmospheric correction of Sentinel-2 imagery.

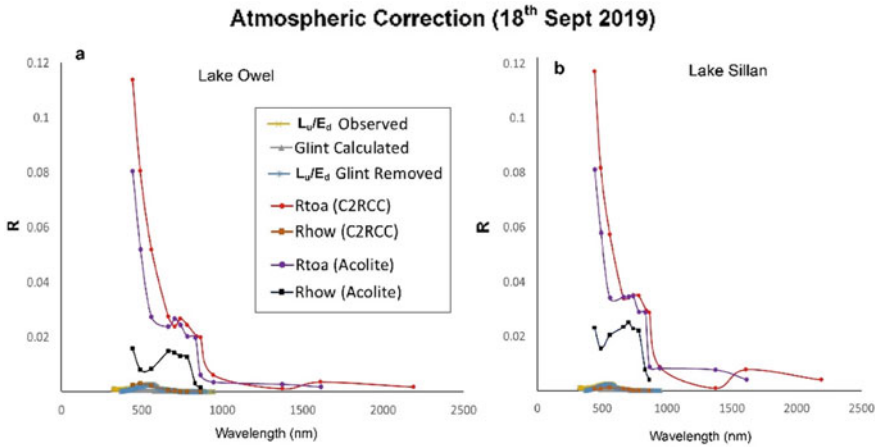


Fig. 2.5 Comparison of atmospheric correction results and field radiometer data for Lake Owel and Lake Sillan

2.3.2 Water Quality Parameters Validation

Sentinel-2 derived water quality results were compared with those measured from the field sampling. From each sampled location, chlorophyll-*a* (mg/m^3) and transparency (m) measurements were taken. C2RCC algorithm was used to compute chlorophyll-*a* and TSM, whereas the Acolite processor was able to compute chlorophyll-*a* and turbidity. Although not quite the same, as explained in the introduction section, turbidity, TSM and transparency are measures of the water clarity, and thus they were used for comparison in this study.

Comparing the results for turbidity, TSM and field transparency, the Acolite processor showed better approximation of the field condition than the C2RCC processor. Similarly, the chlorophyll-*a* estimation from the Acolite processor showed better approximation of the field measurements. For both, TSM and chlorophyll-*a* estimation, the results were concentrated around very low values compared to field measurement. This observation was not consistent with the behaviour of the C2RCC processor during atmospheric correction, where it performed better than Acolite. When comparing the surface reflectance for water pixels (Rhow) from C2RCC and Acolite, it is evident from Fig. 2.5 that the surface reflectance from C2RCC is closer to the radiometric measurements. This suggests that the sets of trained neural networks used in the model contribute to the better performance of C2RCC regarding atmospheric correction, but not for the water quality parameters as shown in Figs. 2.6 and 2.7.

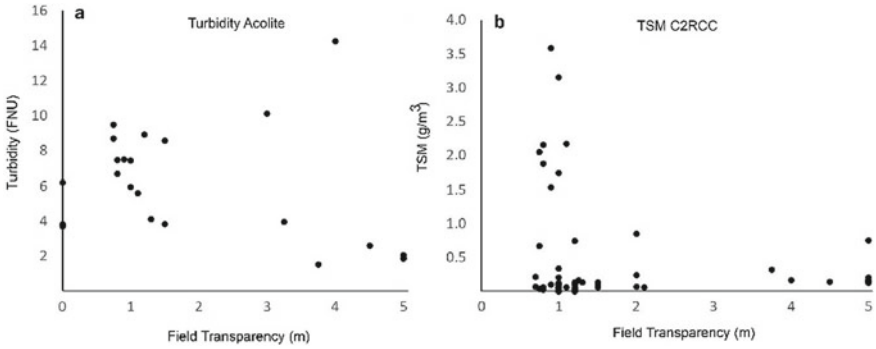


Fig. 2.6 Turbidity (FNU) and TSM (g/m^3) computation results from Acolite and C2RCC respectively. C2RCC shows the overall underestimation of values

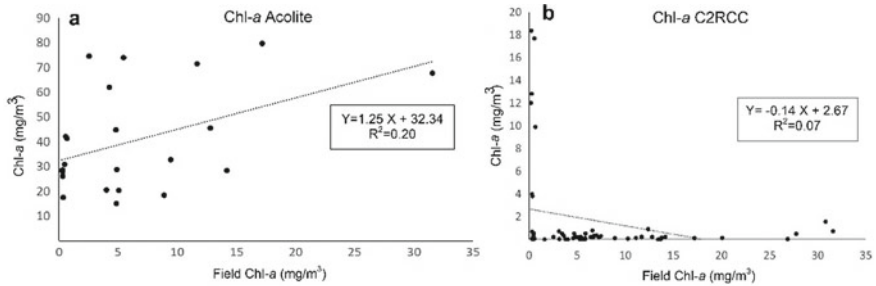


Fig. 2.7 Chlorophyll-*a* (mg/m^3) computation results from Acolite and C2RCC respectively. C2RCC shows the overall underestimation of values

2.3.3 Coupling of C2RCC and Acolite

Based on the overall results, the coupled approach was developed where the atmospheric correction was carried out using the C2RCC and the water quality parameters were computed using techniques adopted in the Acolite processor (Chl-*a*: [23], turbidity: [34, 35]). The parameters were tuned in the coupled algorithm to better reflect the field measured samples. The results from the final algorithm are presented in Fig. 2.8. The coupled technique showed better approximation of field measurements than each standalone processor.

The coupling of the atmospheric correction, water quality parameter processing, and subsequent hyperparameter tuning allowed the validation based on the regional water quality measurements in Ireland as demonstrated in Figs. 2.9 and 2.10. The figures show the chlorophyll-*a* and turbidity for Lake Egish with the area of around 1square kilometer located in the drumlin belt region close to the border with Northern Ireland. All the cloud-free scenes available for 2020 were used to monitor water quality for a total of six months (January, February, March, April, June and

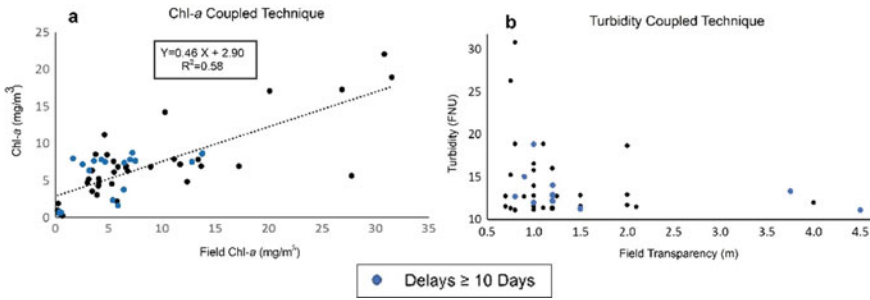


Fig. 2.8 Chlorophyll-*a* (mg/m^3) and Turbidity (FNU) computation results from coupled technique. Delays higher than 10 days are shown in blue

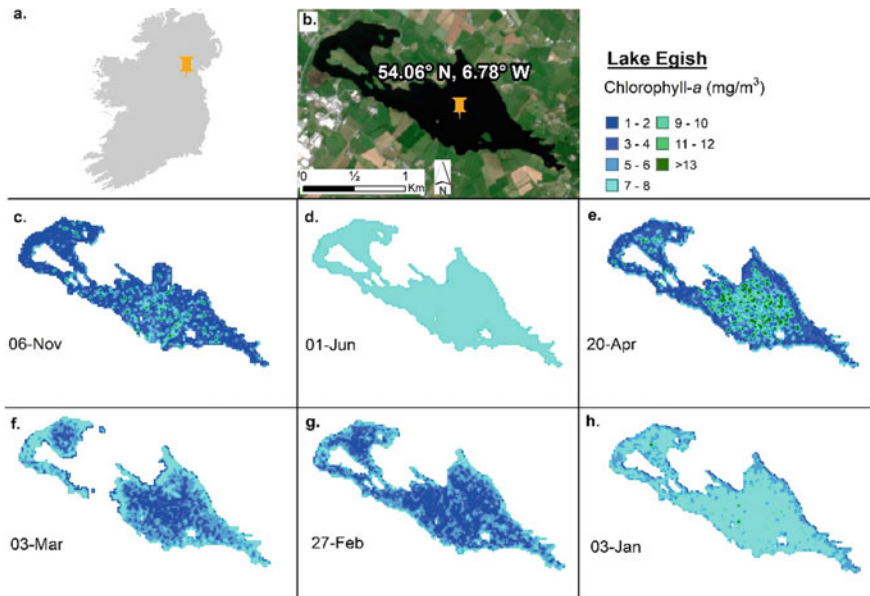


Fig. 2.9 Chlorophyll-*a* (mg/m^3) results from coupled technique for Lake Egish using the Sentinel-2 images acquired in 2020

November). Figure 2.9 shows the seasonal fluctuation of chlorophyll-*a* where it had lower magnitudes during the winter (January) and then slowly increased during the spring (April) and again decreased during the mid-summer (June). Figure 2.10 shows a similar trend for 2020 with the lake turbidity peaking during early spring and autumn (November). Both chlorophyll and turbidity show similar levels of seasonality probably because turbidity is affected by planktonic growth.

While remote sensing offers many benefits for water body monitoring, challenges and limitations still exist. The availability of cloud-free days at high latitudes is not

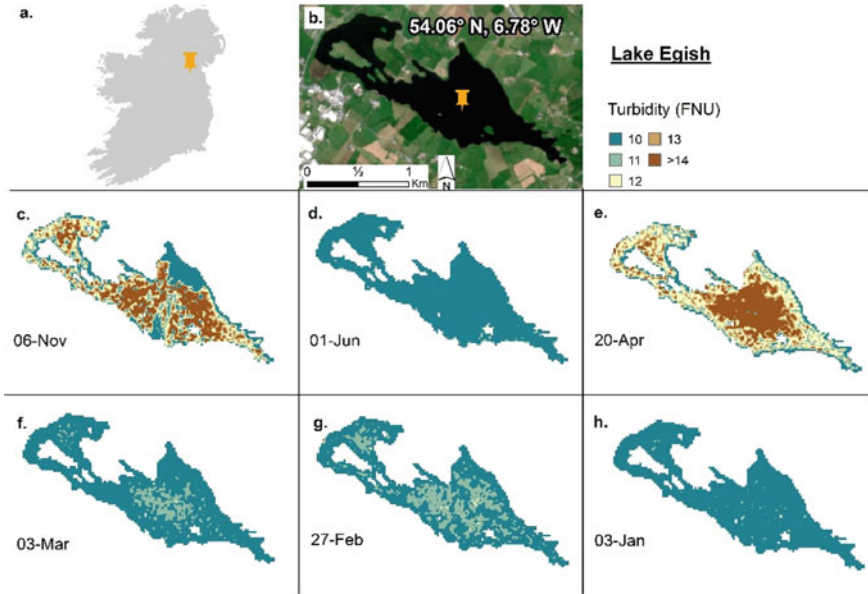


Fig. 2.10 Turbidity (FNU) results from coupled technique for Lake Egish using the Sentinel-2 images acquired in 2020

ideal for satellite coverage with an average of 216 rainy days in a year (59% of days in a year), based on 59 years of observation by Met [30], the Irish national meteorological service. The study also shows some parts of the country receiving disproportionately high amounts of rainfall causing further limitation for satellite monitoring. In this context, it is challenging to monitor lakes particularly during autumn and winter months when rainfall is usually at its highest. In addition, small and very shallow lakes can be quite challenging to monitor due to their topography at the current resolution of the Sentinel-2. The problem of frequent cloud cover and potential difficulties in satellite monitoring is not typical only to Ireland, but also common in other countries in the northern hemisphere [22].

2.3.4 EO Platform for Monitoring Water Quality

Based on the foundation of this coupled technique, a web-based platform was developed to allow users to visualize the water quality across Ireland as soon as the optimum (cloud- and shadow-free) Sentinel-2 scene becomes available. The platform automatically ingests most recent Sentinel-2 imagery and implements the coupled algorithm. The map of Chlorophyll-*a* and turbidity can be explored on the platform. The platform shows the recent water quality parameters across Ireland.

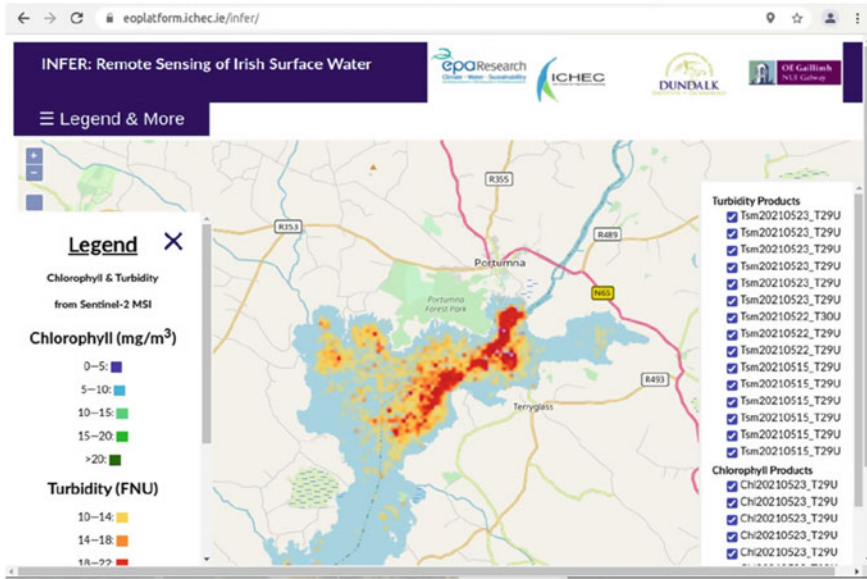


Fig. 2.11 Screen capture of the EO platform showing Chlorophyll-*a* (mg/m³) and Turbidity (FNU) products from Sentinel-2

The EO platform was developed using Python and JavaScript programming languages by utilizing open-source products such as QGIS, OpenLayers and GDAL libraries on a Linux based environment. The platform can be viewed using the website: <https://eoplatform.ichec.ie/infer> (Fig. 2.11).

2.4 Conclusions

We adapted and validated the atmospheric correction and water quality pro-cessor for fresh and inland fresh waters in Ireland applicable to Sentinel-2 imagery with the critical use field collected data, which provided essential water quality measurements and field radiometry. Field collected data sets were compared with those computed using the two most widely used algorithms for analyzing Sentinel-2 data, namely the C2RCC and Acolite processors. For atmospheric correction, the C2RCC based processor showed better performance whereas for chlorophyll-*a* and turbidity, the Acolite-based processor demonstrated enhanced efficacy. By coupling both C2RCC and Acolite-based processors, the advantages of both were combined, yielding an optimal means for inferring regional lake water quality monitoring in Ireland using Sentinel-2 data. The resulting workflow was integrated into a web platform facilitating third parties interested in monitoring lake water quality in the Republic of Ireland.

Although it is challenging to get long-time series of cloud-free scenes for Ireland due to its temperate maritime climate, we determined that satellite observations can be used to conduct regional monitoring of freshwater quality remotely. The addition of high-quality data from field measurements going forward can furthermore be used for continuous improvement of the model and subsequent validation. As such, we have been able to demonstrate that satellite observations can effectively complement traditional freshwater monitoring at regional scales in an essentially automatic and cost-effective manner, permitting the optimal use of in situ monitoring logistics to identify and investigate specific sites in a more controlled and evidence-based fashion.

Acknowledgements Remote Sensing of Irish Surface Waters (2017-W-MS-30) project is funded under the EPA Research Programme 2014-2020. The EPA Research Programme is a Government of Ireland initiative funded by the Department of Environment, Climate and Communications. It is administered by the EPA, which has the statutory function of coordinating and promoting environmental research. Authors would like to thank Martin Holland from Dundalk Institute of Technology who assisted with field sampling.

References

1. Adrian R, O'Reilly CM, Zagarese H, Baines SB, Hessen DO, Keller W, Livingstone DM, Sommaruga R, Straile D, Van Donk E, Weyhenmeyer GA (2009) Lakes as sentinels of climate change. *Limnol Oceanogr* 54(6, part 2):2283–2297. https://doi.org/10.4319/lo.2009.54.6_part_2.2283
2. American Public Health Association (APHA) (1999) Standard methods for the examination of water and wastewater, 20th edn. APHA, Washington DC, p 1268
3. Andrew ME, Wulder MA, Nelson TA (2014) Potential contributions of remote sensing to ecosystem service assessments. *Prog Phys Geogr* 38(3):328–353. <https://doi.org/10.1177/0309133314528942>
4. Birch G, O'Hea L (2007) The chemistry of suspended particulate material in a highly contaminated embayment of Port Jackson (Australia) under quiescent, high-wind and heavy-rainfall conditions. *Environ Geol* 53:501–516. <https://doi.org/10.1007/s00254-007-0662-5>
5. Birk S, Ecke F (2014) The potential of remote sensing in ecological status assessment of coloured lakes using aquatic plants. *Ecol Ind* 46:398–406. <https://doi.org/10.1016/j.ecolind.2014.06.035>
6. Brockmann C, Doerffer R, Peters M, Stelzer K, Embacher S, Ruescas A (2016) Evolution of the C2RCC neural network for Sentinel 2 and 3 for the retrieval of ocean colour products in normal and extreme optically complex waters. In: Proceedings of the ESA living planet. Prague, Czech Republic 9–13 May
7. Brönmark C, Hansson LA (2002) Environmental issues in lakes and ponds: current state and perspectives. *Environ Conserv* 29(3):290–307. www.jstor.org/stable/44520612
8. Carvalho L, McDonald C, de Hoyos C, Mischke U, Phillips G, Borics G, Poikane S, Skjelbred B, Solheim AL, Van Wichelen J, Cardoso AC (2013) Sustaining recreational quality of 44 European lakes: minimizing the health risks from algal blooms through phosphorus control. *J Appl Ecol* 50(2):315–323. <https://doi.org/10.1111/1365-2664.12059>
9. Chen J, Jönsson P, Tamura M, Gu Z, Matsushita B, Eklundh L (2004) A simple method for reconstructing a high-quality NDVI time-series data set based on the Savitzky-Golay filter. *Remote Sens Environ* 91(3–4):332–344. <https://doi.org/10.1016/j.rse.2004.03.014>

10. Davies-Colley RJ, Smith DG (2001) Turbidity, suspended sediment, and water clarity: a review. *J Am Water Resour Assoc* 37(5):1085–1101. <https://doi.org/10.1111/j.1752-1688.2001.tb03624.x>
11. de Araujo Barbosa CC, Atkinson PM, Dearing JA (2015) Remote sensing of ecosystem services: a systematic review. *Ecol Ind* 52:430–443. <https://doi.org/10.1016/j.ecolind.2015.01.007>
12. de Eyto E, Jennings E, Ryder E, Sparber K, Dillane M, Dalton C, Poole R (2016) The response of a humic lake ecosystem to an extreme precipitation event: physical, chemical and biological implications. *Inland Waters* 6:483–498. <https://doi.org/10.1080/IW-6.4.875>
13. Doerffer R, Schiller H (2007) The MERIS case 2 water algorithm. *Int J Remote Sens* 28(3–4):517–535. <https://doi.org/10.1080/01431160600821127>
14. Dörnhöfer K, Oppelt N (2016) Remote sensing for lake research and monitoring—recent advances. *Ecol Ind* 64:105–122. <https://doi.org/10.1016/j.ecolind.2015.12.009>
15. Dudgeon D, Arthington AH, Gessner MO, Kawabata ZI, Knowler DJ, Lévêque C, Naiman RJ, Prieur-Richard AH, Soto D, Stiassny ML, Sullivan CA (2006) Freshwater biodiversity: importance, threats, status and conservation challenges. *Biol Rev* 81(2):163–182. <https://doi.org/10.1017/S1464793105006950>
16. Environmental Protection Agency (EPA) (2017) Water quality in Ireland 2010–2015. Environmental Protection Agency
17. Erftemeijer PL, Lewis RRR III (2006) Environmental impacts of dredging on seagrasses: a review. *Mar Pollut Bull* 52(12):1553–1572. <https://doi.org/10.1016/j.marpolbul.2006.09.006>
18. European Commission (2000) Directive 2000/60/EC of the European Parliament and of the Council of 23 October 2000 establishing a framework for community action in the field of water policy. *Off J Euro Communities* 5(327):1–72
19. Felip M, Catalan J (2000) The relationship between phytoplankton biovolume and chlorophyll in a deep oligotrophic lake: decoupling in their spatial and temporal maxima. *J Plankton Res* 22(1):91–106. <https://doi.org/10.1093/plankt/22.1.91>
20. Free G, Little R, Tierney D, Donnelly K, Caroni R (2006) Environmental protection agency, environmental research technological development and innovation programme. A reference-based typology and ecological assessment system for Irish lakes. In: Preliminary investigations (2002-W-FS-1-M1): Final Report, Environmental Protection Agency, Wexford, Ireland
21. Giardino C, Pepe M, Brivio PA, Ghezzi P, Zilioli E (2001) Detecting chlorophyll, Secchi disk depth and surface temperature in a sub-alpine lake using Landsat imagery. *Sci Total Environ* 268(1–3):19–29. [https://doi.org/10.1016/S0048-9697\(00\)00692-6](https://doi.org/10.1016/S0048-9697(00)00692-6)
22. GLaSS (2016) Global Lakes Sentinel Services. Final Report Available at: <https://cordis.europa.eu/docs/results/313/313256/final1-glass-final-report.pdf>. Accessed 20 November 2020
23. Gons HJ, Rijkeboer M, Ruddick KG (2002) A chlorophyll-retrieval algorithm for satellite imagery (medium resolution imaging spectrometer) of inland and coastal waters. *J Plankton Res* 24(9):947–951. <https://doi.org/10.1093/plankt/24.9.947>
24. Havens KE, James RT, East TL, Smith VH (2003) N: P ratios, light limitation, and cyanobacterial dominance in a subtropical lake impacted by nonpoint source nutrient pollution. *Environ Pollut* 122(3):379–390. [https://doi.org/10.1016/s0269-7491\(02\)00304-4](https://doi.org/10.1016/s0269-7491(02)00304-4)
25. Hestir EL, Brando VE, Bresciani M, Giardino C, Matta E, Villa P, Dekker AG (2015) Measuring freshwater aquatic ecosystems: the need for a hyperspectral global mapping satellite mission. *Remote Sens Environ* 167:181–195. <https://doi.org/10.1016/j.rse.2015.05.023>
26. Hou X, Feng L, Duan H, Chen X, Sun D, Shi K (2017) Fifteen-year monitoring of the turbidity dynamics in large lakes and reservoirs in the middle and lower basin of the Yangtze River, China. *Remote Sens Environ* 190:107–121. <https://doi.org/10.1016/j.rse.2016.12.006>
27. Jennings E, Jones S, Arvola L, Staehr PA, Gaiser E, Jones ID, Weathers KC, Weyhenmeyer GA, Chiu CY, de Eyto E (2012) Effects of weather-related episodic events in lakes: an analysis based on high-frequency data. *Freshw Biol* 57(3):589–601. <https://doi.org/10.1111/j.1365-2427.2011.02729.x>
28. Kutser T, Vahtmäe E, Paavel B, Kauer T (2013) Removing glint effects from field radiometry data measured in optically complex coastal and inland waters. *Remote Sens of Environment* 133:85–89. <https://doi.org/10.1016/j.rse.2013.02.011>

29. Marcé R, George G, Buscarinu P, Deidda M, Dunalska J, de Eyto E, Flaim G, Grossart HP, Ivanovic V, Lenhardt M, Moreno-Ostos E (2016) Automatic high frequency monitoring for improved lake and reservoir management. *Environ Sci Technol* 50(20):10780–10794. <https://doi.org/10.1021/acs.est.6b01604>
30. Met Éireann (2001) Analysis of trends at some Irish rainfall stations. In: Technical report 59, The Irish Meteorological Service. Available at: <http://edepositireland.ie/bitstream/handle/2262/22820/TN59.pdf?sequence=1>. Accessed 1 Oct 2020
31. Met Éireann (2018) Rainfall climate of Ireland. Available at: <https://www.met.ie/climate/what-we-measure/rainfall>. Accessed 2 Oct 2020
32. Moore KA, Wetzel RL, Orth RJ (1997) Seasonal pulses of turbidity and their relations to eelgrass (*Zostera marina* L) survival in an estuary. *J Exp Marine Bio Ecol* 215(1):115–134. [https://doi.org/10.1016/S0022-0981\(96\)02774-8](https://doi.org/10.1016/S0022-0981(96)02774-8)
33. Moss B, Hering D, Green AJ, Aidoud A, Becares E, Beklioglu M, Bennion H, Boix D, Brucet S, Carvalho L, Clement B, Davidson T, Declerck S, Dobson M, Donk E, Dudley B, Feuchtmayr H, Friberg N, Grenouillet G, Hillebrand H, Hobaek A, Irvine K, Jeppesen E, Johnson R, Jones I, Kernan M, Lauridsen TL, Manca M, Meerhoff M, Olafsson J, Ormerod S, Papastergiadou E, Penning WE, Ptacnik R, Quintana X, Sandin L, Seferlis M, Simpson G, Triga C, Verdonschot P, Verschoor AM, Weyhenmeyer GA (2009) Climate change and the future of freshwater biodiversity in Europe: a primer for policy-makers. *Freshwater Rev* 2(2):103–130. <https://doi.org/10.1608/FRJ-2.2.1>
34. Nechad B, Ruddick K, Neukermans G (2009) Calibration and validation of a generic multi-sensor algorithm for mapping of turbidity in coastal waters. In: SPIE Europe remote sensing. International society for optics and photonics 7473(74730H–74730H). <https://doi.org/10.1117/12.830700>
35. Nechad B, Ruddick K, Park Y (2010) Calibration and validation of a generic multisensor algorithm for mapping of total suspended matter in turbid waters. *Remote Sens Environ* 114(4):854–866. <https://doi.org/10.1016/j.rse.2009.11.022>
36. Palmer SC, Kutser T, Hunter PD (2015) Remote sensing of inland waters: challenges, progress and future directions. *Remote Sens Environ* 157:1–8. <https://doi.org/10.1016/j.rse.2014.09.021>
37. Pinaridi M, Fenocchi A, Giardino C, Sibilla S, Bartoli M, Bresciani M (2015) Assessing potential algal blooms in a shallow fluvial lake by combining hydrodynamic modelling and remote-sensed images. *Water* 7(5):1921–1942
38. Preisendorfer RW (1976) *Hydrologic optics*, vol 6. U.S Dept. of Commerce, Washington
39. Reyjol Y, Argillier C, Bonne W, Borja A, Buijse AD, Cardoso AC, Daufresne M, Kernan M, Ferreira MT, Poikane S, Prat N (2014) Assessing the ecological status in the context of the European water framework directive: where do we go now? *Sci Total Environ* 497:332–344. <https://doi.org/10.1016/j.scitotenv.2014.07.119>
40. Royal Belgian Institute of Natural Sciences (RBINS) (2018) Acolite atmospheric correction processor. Available at: <https://odnature.naturalsciences.be/remsem/software-and-data/acolite>. Accessed 10 October 2018
41. Schaeffer BA, Schaeffer KG, Keith D, Lunetta RS, Conmy R, Gould RW (2013) Barriers to adopting satellite remote sensing for water quality management. *Int J Remote Sens* 34(21):7534–7544. <https://doi.org/10.1080/01431161.2013.823524>
42. Spanhove T, Borre JV, Delalieux S, Haest B, Paelinckx D (2012) Can remote sensing estimate fine-scale quality indicators of natural habitats? *Ecol Ind* 18:403–412. <https://doi.org/10.1016/j.ecolind.2012.01.025>
43. Steel EA, Neuhausser S (2002) Comparison of methods for measuring visual water clarity. *J North Am Benthological Soc* 21(2):326–335. <https://doi.org/10.2307/1468419>
44. Standing Committee of Analysts (1980) The determination of chlorophyll a in aquatic environments. Her Majesty's Stationary Office, London, UK
45. Stendera S, Adrian R, Bonada N, Cañedo-Argüelles M, Hugueny B, Januschke K, Pletterbauer F, Hering D (2012) Drivers and stressors of freshwater biodiversity patterns across different ecosystems and scales: a review. *Hydrobiologia* 696(1):1–28. <https://doi.org/10.1007/s10750-012-1183-0>

46. Vanhellemont Q (2019) Adaptation of the dark spectrum fitting atmospheric correction for aquatic applications of the landsat and sentinel-2 archives. *Remote Sens Environ* 225:175–192. <https://doi.org/10.1016/j.rse.2019.03.010>
47. Vanhellemont Q, Ruddick K (2018) Atmospheric correction of metre-scale optical satellite data for inland and coastal water applications. *Remote Sens Environ* 216:586–597. <https://doi.org/10.1016/j.rse.2018.07.015>
48. Vollenweider RA, Giovanardi F, Montanari G, Rinaldi A (1998) Characterization of the trophic conditions of marine coastal waters with special reference to the NW Adriatic Sea: proposal for a trophic scale, turbidity and generalized water quality index. *Environ: Off J Int Environ Soc* 9(3):329–357. [https://doi.org/10.1002/\(SICI\)1099-095X\(199805/06\)9:3<329::AID-ENV308>3.0.CO;2-9](https://doi.org/10.1002/(SICI)1099-095X(199805/06)9:3<329::AID-ENV308>3.0.CO;2-9)
49. Wetzel RG (2001) *Limnology: lake and river ecosystems*. Gulf professional publishing
50. Williamson CE, Saros JE, Vincent WF, Smol JP (2009) Lakes and reservoirs as sentinels, integrators, and regulators of climate change. *Limnol Oceanogr* 54(6):2273–2282. https://doi.org/10.4319/lo.2009.54.6_part_2.2273

Chapter 3

Optical Remote Sensing in Lake Trasimeno: Understanding from Applications Across Diverse Temporal, Spectral and Spatial Scales



Bresciani Mariano, Free Gary, Pinardi Monica, Laanen Marnix, Padula Rosalba, Fabbretto Alice, Mangano Salvatore, and Giardino Claudia

Abstract Under the current Anthropocene Epoch there is an urgent need to deliver high-quality data, information and knowledge to the decision-making process for a sustainable management of environmental concerns, in particular for inland water. Most literature address the advantages brought by remote sensing (RS) techniques in operational monitoring and management of lakes. In the present work, optical RS is applied to a complex ecosystem, the turbid eutrophic shallow Lake Trasimeno (Italy). A first example of RS application addresses the use of high frequency spectroradiometric measurements collected by a WISPstation to retrieve intra-inter daily and seasonal dynamics of chlorophyll-a and phycocyanin. A second section focuses on long term trends of water quality by means of satellite data time series for the whole lake surface. Then we exploit the latest generation of hyperspectral satellite images (PRISMA and DESIS) utilizing the high spectral resolution and improving the accuracy of estimated lake water quality. Finally, high spatial resolution satellite data is used for a finer scale mapping of bottom substrates. Application of these techniques improved scientific understanding on the timing, composition and distribution of phytoplankton blooms, the role of nutrients and climate drivers as well as changes in the extent and composition of aquatic plants.

B. Mariano (✉) · F. Gary · P. Monica · F. Alice · M. Salvatore · G. Claudia
Institute for Electromagnetic Sensing of the Environment, National Research Council, Via Bassini
15, 20133 Milan, Italy
e-mail: bresciani.m@irea.cnr.it

L. Marnix
Water Insight, Marijkeweg 22, 6709 PG Wageningen, The Netherlands

P. Rosalba
ARPA UMBRIA, Via Pievaiola, 207/B-3 Loc. S. Sisto, 06132 Perugia, Italy

3.1 Introduction

A key message of the Organization for Economic Cooperation and Development's (OECD) Environmental Strategy for the first decade of the twenty-first century to address environmental sustainability was to improve information available for decision making by measuring progress using quality indicators; for water quality of lakes and rivers, in particular, the progress made is still insufficient [1]. Reasonable management of some of the world's most serious environmental problems depends on the delivery of high-quality data, information and knowledge to the decision-making process [2]. Data quality comprises components of relevance, reliability, accuracy, accessibility, timeliness, interpretability and coherence [3]. For the freshwater ecosystems in Europe, the EU Water Framework Directive (WFD) is an ambitious legislation framework, which collects all information on the state of water in order to verify the commitment of the different countries to preserve water resources and to achieve a good state of water quality [4]. Substantial progress has been made in the past 30 years in understanding the causes of both water scarcity and water quality degradation, as well as in developing effective strategies to prevent or mitigate its adverse effects [5–7]. However, this is still not enough, especially if we consider emerging pressures such as global warming and climate change, which alter ecosystems dynamics and makes understanding and modelling more challenging.

In particular, many studies have highlighted how lakes are ecosystems of particular importance for the assessment of already ongoing climate change [8, 9] and the need of large data-sets to provide more information that can lead to a capacity for understanding and the management of current and future issues.

Since 1991, Bukata et al. [10] suggested that satellite monitoring of optically-active components of inland water is an essential input to studies addressing the impact of climate change; since this first contribution, several other scientific articles pointed out the importance of satellite data for monitoring water quality of lakes with particular focus on the relationship with climate change (e.g., Yang et al. [11]). In fact, satellite remote sensing can provide near-real time, synoptic, and repeated data for monitoring physical and biogeochemical parameters of water status that avoids interpretive problems associated with spatial and temporal under sampling of traditional limnological field campaigns. Indeed, over the last three decades, there has been a significant advancement in the development of both technology and algorithms that allow the monitoring via satellite of ocean color to be used for studying coastal and ocean water quality [12]. Earth observation (EO) data acquired by satellites is increasingly used for providing information on a suite of functionally relevant indicators of water quality and ecosystem conditions from a local to global scale [13]. In the most recent review articles [14–18], robustness and maturity of remotely sensed based monitoring of the lakes have been addressed in terms of sensors availability, data quality, variability and consistency of processing algorithms, validation and accuracy assessment of the output products and advantages brought by satellite remote sensing to operational monitoring and the management of lake systems.

In this chapter, we present the application of EO techniques to the case study of Lake Trasimeno (Italy), a turbid eutrophic shallow lake. In order to provide an exhaustive description of the potential of EO data for monitoring aquatic environments, we divided the chapter into four sections. Section 3.3 First, we present the use of data acquired by a WISPstation, an in situ fixed spectroradiometer, for continuous point monitoring with high temporal frequency that can depict sub-hourly, daily and seasonal dynamics of lake water quality; these reflectance measurements can also be exploited for the validation of satellite data processing. Section 3.4 focuses on the relevance of time series of satellite data for the analysis of long term trends and inter-annual dynamics of the status of lake water with a synoptic view over the whole lake surface based on data produced by the Lakes Climate Change Initiative (CCI) project. Section 3.5, we present the characteristics of the latest generation of hyperspectral satellite images as exploited for deriving high accuracy and up-to-date information on lake water status that can be achieved as a result of the high spectral resolution offered by these sensors. Section 3.6 focuses on the opportunities offered by satellite and/or airborne sensors that acquire data with very high spatial resolution for a finer spatial analysis of water surface optical properties. Based on the applications presented in this chapter, we can draw the conclusion that synoptic view, high temporal frequency of observation, high spatial and spectral resolution offered by RS techniques constitute a unique source of information for monitoring complex ecosystem such as Lake Trasimeno.

3.2 Study Area

This study focuses on Lake Trasimeno, a post-tectonic, shallow (maximum depth 6.3 m), located in central Italy (43°08'N; 12°06'E; Fig. 3.1). It is the fourth largest lake of the country (average surface area 120.5 km² with a circular shape) with three small islands (Polvese, Maggiore and Minore islands) and has an extensive bay—Oasi la Valle that is colonized by aquatic vegetation in the south-east [19]. Nearly all the littoral zones of Trasimeno are colonized by aquatic vegetation mainly composed by helophytes (e.g. *Phragmites australis*, *Typha angustifolia*), and hydrophytes (e.g. *Potamogeton pectinatus*, *Chara globularis*, *Myriophyllum spicatum*) [20].

Lake Trasimeno is of significant conservation importance and is part of a Natural Regional Park, Site of Community Interest, Special Protection Zone and of two Natura 2000 sites (IT5210018 and IT5210070) [21].

The catchment of Lake Trasimeno lies over a substratum of low permeability (turbidite), covered by Plio-Pleistocene and Holocene deposits, with a variable content of silicatic and of carbonatic minerals [22, 23]. However, despite their low permeability, these formations host small aquifers [22] where all the infiltrating water radially flows towards the lake [24]. Because of the small area of the catchment relative to the lake area, the annual water inflows are frequently lower than evaporation losses and the water balance of the lake is therefore strongly affected by the pluviometric regime [23] and by the extreme variability of the climate that

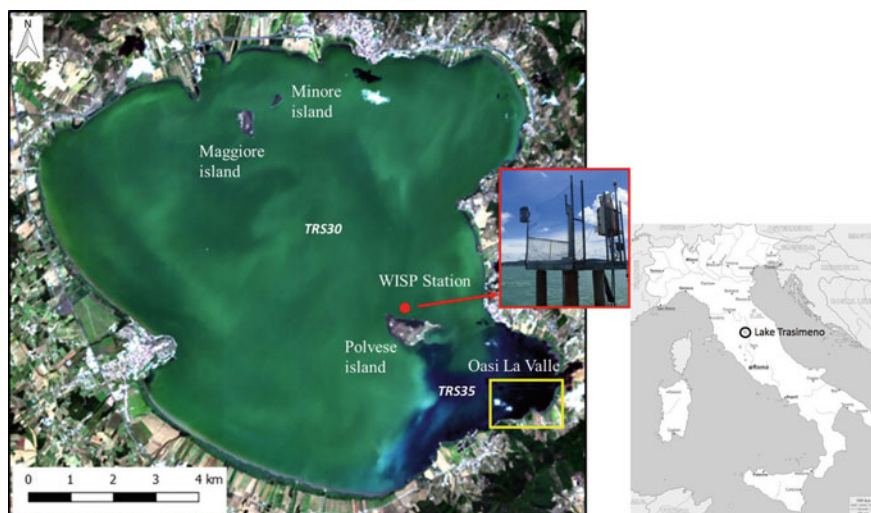


Fig. 3.1 True color composition of Lake Trasimeno from satellite (PRISMA data acquired on 25 July 2020) and its location in Italy. The image shows the WISPstation position (red dot) and the Oasi La Valle bay colonized by macrophytes (yellow box). Inset (red box) is a picture of the platform supporting the WISPstation. The ARPA Umbria stations (TRS30 and TRS35) used for WFD monitoring are also indicated

characterizes the Mediterranean area. In the past, the lake was subject to human interventions on inflows and outflows in order to regulate the lake level since Etruscan or Roman times [21, 23]. A dramatic hydrological crisis occurred in the 1950s due to the artificial outflow threshold being displaced after its restructuring at the end of the nineteenth century [25]. Following the enlargement of the catchment area the lake level increased from 1960 to 1965, followed by an alternation of wet and drought periods. In order to prevent flooding of the coastal area, on one occasion in 2015, the artificial outlet was opened for some days after being closed for about 30 years [24]. Under the current climate change scenario, the lake level is in a low phase and the rules restricting abstraction together with the maintenance works on the inflowing rivers seem to be insufficient to avoid the significant reduction in water availability [25]. During drought periods, higher concentrations of suspended solids, an accumulation of dissolved salts and an increase of the total alkalinity can occur [26].

The consequences of the periodically low water levels have had a negative effect on the entire ecosystem, in terms of impoverishment of native biodiversity and reduced fishing yield; these effects are exacerbated by water abstractions for irrigation purposes and by the presence of civil and agricultural discharges [21]. Tourism, fisheries and agriculture (cultivated lands cover about 70% of the catchment) are the most important activities in the Trasimeno area.

Lake Trasimeno is generally turbid (average Secchi disk depth 1.1 m and the average total suspended matter was 10.4 gm^{-3} for the period 2002–2008) and in

meso-eutrophic conditions with chlorophyll-a (Chl-a) concentration up to 90 mg m^{-3} [21, 27]. The water column is unstratified, with recurring sediment resuspension as a result of wind action. According to the WFD, the lake is currently classified at moderate ecological status [28].

Lake Trasimeno has a phytoplankton community dominated by chlorophytes and dinoflagellates. Cryptophytes also comprised a relatively large portion of the biomass, whereas euglenophytes and diatoms are relatively scarce [29]. The high nutrient concentrations favor the occurrence of phytoplankton blooms, including cyanobacteria species (e.g. *Cylindrospermopsis raciborskii*, *Planctothrix agardhii*) [26, 30]. The zooplankton is dominated by cyclopoids tending to have the greatest relative biomass in autumn, and Cladocera with peaks in winter or spring [29].

The fish community of Lake Trasimeno comprises 19 species and is dominated by cyprinids [31]. The most important commercial native fish species in the lake are tench (*Tinca tinca*), southern pike and eel (*Anguilla Anguilla*). The remarkable decline of tench, and other native species, coincided with a substantial expansion of the alien goldfish (*Carassius auratus*) [31].

3.3 High Frequency Spectroradiometric Measurements

Phytoplankton responds to changes in environmental conditions very quickly [32], and phytoplankton growth in Lake Trasimeno is also influenced by both phytoplankton physiology and external factors, including light, temperature, and nutrients. Drivers affecting short-term dynamics in populations and communities are complex and may consist of several factors acting in parallel. Sometimes environmental drivers induce rhythmic oscillations, which are easily linked to recognized important factors such as diurnal shifts in temperature and light [33, 34]. In addition to the high dynamics of phytoplankton, the low lake depth influences the resuspension of the bottom sediments due to wind action. These resuspensions determine the typical turbid water conditions for Lake Trasimeno. Diurnal and seasonal variation affect the physicochemical variables thereby causing variation in the abundance and diversity of plankton [35] and suspended sediments.

Bresciani et al. [19] recently evaluated the dynamics of the Chl-a concentrations of Lake Trasimeno for six months in 2018, using data gathered from the fixed position autonomous radiometer WISPstation (located 400 m north from the Polvese island as in Fig. 3.1). Briefly, the WISPstation allows continuous measurements with two radiance sensors that look downward to the water surface at an angle of 40° from the vertical (L_{up}) and a sky looking radiance sensor looking upward at an angle of 40° from the vertical (L_{sky}) in the NNW direction and two radiance channels collecting L_{up} and L_{sky} in the NNE direction and two irradiance channels in a wavelength range of 350 to 1100 nm. Data are transmitted to the database (“WISPcloud”) automatically through a cellular connection.

In this work, we develop the analysis of Bresciani et al. [19] by extending the temporal range for Chl-a analysis as well as by adding the analysis of phycocyanin

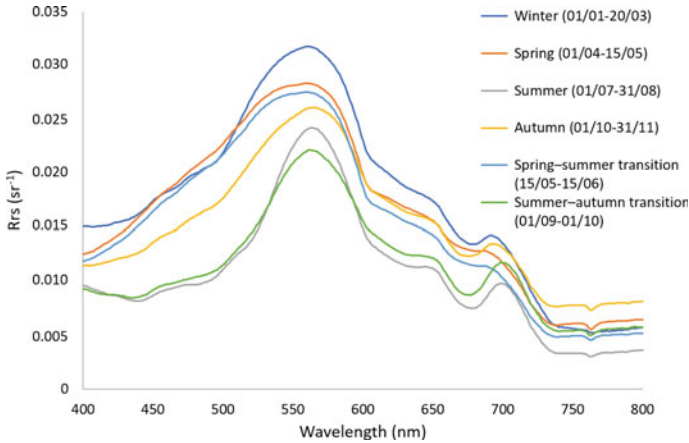


Fig. 3.2 Average Water spectral signatures (remote sensing reflectance, Rrs) from WISPstation data on the six different time intervals for the WFD classification [40]

(PC) derived, as for Chl-a, from the conversion of Remote Sensing Reflectance (Rrs) measured by the WISPstation [36]. Moreover, the hyperspectral Rrs data from the WISPstation enable us to also simulate the band setting of satellite data providing valuable reference data to be compared to satellite observations [37]; an example of using the WISPstation data for this is presented in Sect. 3.5.

The WISPstation Rrs data used in this section were collected continuously from 24th April 2018 to 30th November 2020 every 15 min. Over 30,000 acquisitions of Rrs data with corresponding values of Chl-a and phycocyanin (PC) for water quality monitoring purposes were available for the analysis. The Chl-a was derived through a standard water quality algorithm [38] and for PC retrieval the algorithms of Simis [39].

Figure 3.2 shows average values of Rrs in different periods of the year, selected based on the time interval for the WFD classification [40]. In summer and in summer-to-autumn the effect of phytoplankton on Rrs is evident in the lower values of the blue wavelengths and generates the typical feature of absorbance/reflectance in the region between 665 and 705 nm. In both cases it is also evident the contribution of cyanobacteria pigments in between 625 and 650 nm. In the winter and spring the higher values of Rrs were attributed to both a lower presence of phytoplankton and higher concentrations of Total Suspended Matter (TSM).

Examining the WISPstation data for Chl-a it is interesting that the start and rate of increase of the summer bloom was remarkably similarly in the three investigated years (Fig. 3.3). The increase always began in the first week of July and peaked in September. The rate of increase was linear up until early September (with an $R^2 > 0.8$). In particular, considering the Day of Year (DOY) 180 to 250 (29th June–7th September) the slopes of the increase were 0.54, 0.50 and 0.59 for 2018, 2019 and 2020 respectively and were not significantly different in a linear model (testing year for interaction with DOY or between individual years ($p > 0.05$) [41–43].

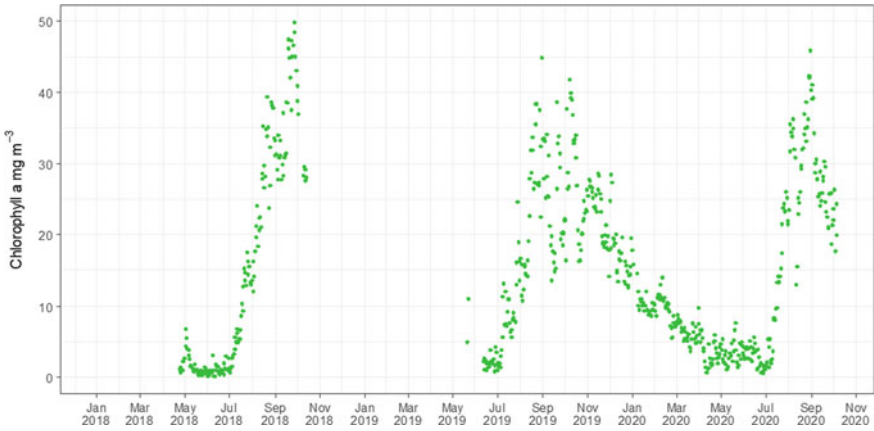


Fig. 3.3 Chlorophyll-a concentration averaged at daily level from the WISPstation data

The WISPstation also produces estimates of the pigment phycocyanin useful for estimating the seasonal dynamics of cyanobacteria. Figure 3.4 shows a plot of Chl-a and phycocyanin concentrations for 2020. It can be seen that sudden increases in Chl-a correspond to sudden increases in phycocyanin. For example from the 1st of August, a rapid increase in Chl-a from 22 to 35 mg m⁻³ over a period of four days corresponds to a period of rapid increase in phycocyanin. Conversely the rapid decline in phycocyanin on the 11th of August is matched by a decline in Chl-a. A similar pattern occurs at the beginning of September where an increase in cyanobacteria drives the Chl-a to its annual maximum level. Utilizing the phycocyanin results from the WISPstation showed how cyanobacteria played a key role in the sudden increases and declines in Chl-a in mid to late summer. Combining Chl-a and phycocyanin data allows managers to see when the composition of blooms is driven by potentially

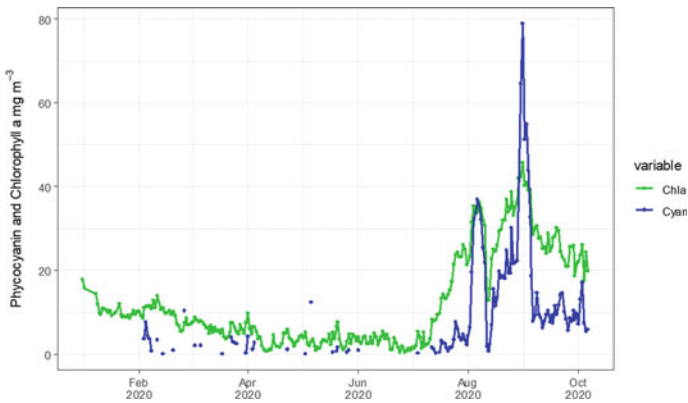


Fig. 3.4 Chlorophyll-a (green) and phycocyanin (blue) pigment concentration averaged at daily level from the WISPstation data

toxic cyanobacteria in almost real time. However, despite the presence of potentially harmful algae, toxicity tests carried out for bathing water purposes have been reported as negative for Trasimeno lake [44].

The high frequency measurements provided by the WISPstation have unique value in improving scientific knowledge and in providing opportunities for improved management for high value recreational lakes like Trasimeno. Examining the timing and rate of bloom development using high frequency data revealed that it was consistent among the three years examined. This predictability provides an opportunity to understand and model the timing and size of blooms for management purposes.

In Italy there are three phases of monitoring in lakes at risk of cyanobacteria blooms: routine, alert and emergency which are differentiated by response (sampling intensity and parameters measured) and management action (ranging from none to risk-communication, scum removal and a bathing ban) in response to increasing health risk [45]. One of the main challenges in the current guidelines is the provision of adequate temporal and spatial monitoring of cyanobacteria. Daily sampling is unfeasible and wind-driven accumulations of cyanobacteria can present dangerous concentrations of toxins within a period of hours [46]. One of the benefits of the WISPstation is that it couples Chl-a and phycocyanin data allowing managers to see when the composition of blooms is driven by potentially toxic cyanobacteria in almost real time and would improve all monitoring phases if incorporated. The drawback is that the WISPstation is limited to a fixed position on the lake.

The mechanisms driving the sudden increase in cyanobacteria detected by the WISPstation are likely to include nutrient inputs, mixing, wind driven accumulations or surface accumulation given their buoyancy and previous work has indicated that these factors are linked to variation in Chl-a [19, 46]. In addition, the drivers in the observed pattern of Chl-a and PC are also likely to be highly dependent on species succession in response to and alongside changing physical and chemical drivers. The rapid changes in Chl-a and PC during the August–September period are typically reflected in highly dynamic changes in the phytoplankton community. For example in 2018, cyanobacteria dominance shifted from *Snowella lacustris* (8th July–5th August) to *Cylindrospermopsis raciborskii* (12th August–10th September) and finally to *Planktothrix agardhii* (16th–24th September) [47]. Such changes in seasonal composition were also indicated by the different spectral signatures over time in Fig. 3.2.

3.4 Long Term EO Data-Set

The European Space Agency's (ESA) climate change initiative (CCI) aims to exploit the long term global earth observation record to produce essential climate variables (ECVs) supporting the United Nations Framework Convention on Climate Change (UNFCCC). The objective of the CCI dataset for the ECV Lakes is to use satellite data to create the largest and longest possible consistent, open global record of five lake

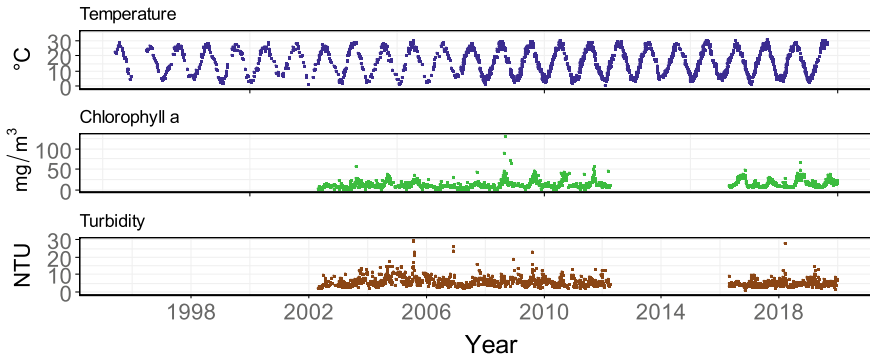


Fig. 3.5 Climate Change Initiative (CCI) results for Lake Trasimeno for LSWT, Chl-a and turbidity from 1996 to 2019

thematic variables: lake water level, extent, temperature, water-leaving reflectance, and ice cover. The main characteristics of this data set [48] are:

- Spatial coverage: 250 globally distributed lakes, set to expand to around 2,000 in the second phase.
- Spatial resolution: 1/120 degree global grid.
- Temporal resolution: daily netCDF files containing all variables and associated uncertainty.
- Temporal coverage: from 1992 up to 2019.

For Lake Trasimeno, lake surface water temperature (LSWT), Chl-a and turbidity (the latter two derived from water-leaving reflectance) were available in the CCI Lakes database version 1.0 (Fig. 3.5). The dataset for LSWT dates from 1993 while that for the other parameters starts in 2002. The increased intensity of satellite monitoring is visible comparing LSWT recorded in the 1990s with that currently. There is a significant data gap in Chl-a and turbidity from 2012 to 2015 due to the failure of the MERIS satellite. One of the current management issues facing Trasimeno lake is eutrophication. The lake can be classified as eutrophic based on Chl-a with seasonal blooms hindering the recreational use of the lake. The peak height of the blooms can be seen to increase from 2008 onwards in Fig. 3.5. The variation in bloom incidence between years can also be seen by plotting the distribution for each year. Figure 3.6 shows a ridge plot for the data where several years are noted to have concentrations above 30 mg m^{-3} . Such blooms typically occur in early to mid-September, only 2003 and 2005 had blooms centered in August in the data analyzed (Fig. 3.5).

The CCI data set presents an opportunity to examine what parameters are important in controlling the size of blooms and their inter-annual variation. In order to do this the Chl-a data were linearly interpolated to daily resolution. The most continuous period 2003–2011 was included for analysis. Few in situ environmental data sets are available to match this temporal resolution so daily climatic data were obtained from ERA5, the fifth generation ECMWF reanalysis for the global climate and

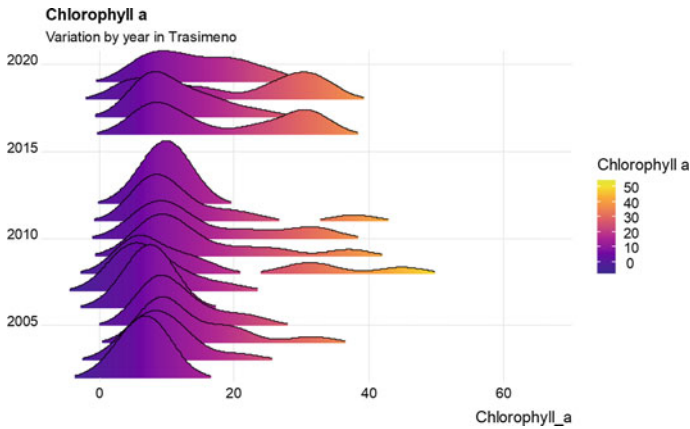


Fig. 3.6 Ridge plot showing distribution of Chl-a concentration mg m^{-3} from 2002 to 2019 for Lake Trasimeno

weather (<https://cds.climate.copernicus.eu/cdsapp#!/home>). Data used in the analysis included: wind direction and speed, 2 m temperature (the air temperature at 2 m above surface), total precipitation and the sum of rainfall for the previous seven days. Several studies have detected changes in Italian lakes linked to long term climate change and fluctuations in large scale regional climate drivers such as the North Atlantic Oscillation (NAO) and the East Atlantic pattern (EA) during winter [49, 50]. Daily values of the NAO (North Atlantic Oscillation) were taken from NOAA-CPC (<https://www.cpc.ncep.noaa.gov/products/precip/CWlink/pna/nao.shtml>).

For the analysis two approaches were trialed—Google AI (Auto ML) and Nonparametric Multiplicative Regression (NPMR). NPMR [51] was used to estimate the response of average daily Chl-a to climate and environmental parameters listed above. NPMR describes response surfaces using variables in a multiplicative instead of an additive way. This method is advanced and can better defining unimodal responses compared to methods such as multiple regression [51]. It has previously been applied to model tree species distribution [52], the response of lichens to climate change [53] and in time-series analysis [54]. NPMR was implemented with the software HyperNiche version 2.3 [55]. The Chl-a response was estimated with a local mean multiplicative smoothing function with Gaussian weighting. NPMR models were created by the stepwise adding of predictors with fit represented by a cross-validated R^2 (xR^2) which can be considered as a measure of fit similar to a traditional R^2 . The sensitivity, which is an indicator of the influence of each parameter included in the NPMR, was estimated by altering the range of predictors by $\pm 5\%$, with resulting deviations expressed as a proportion of the observed range of the response variable. Sensitivity can aid in comparing the importance of variables included in models because NPMR models are unlike standard linear regression having no fixed coefficients or slopes. Google AI (Auto ML) is a service that applies machine learning

models to diverse data types such as images, text, or numeric data aiming to automate the selection and application of models to data. Google AI (Auto ML) was also applied to produce a model for Chl-a as a designated feature. The supervised learning model followed a regression approach with chronological assignment using the first 80% of the timeseries for model training with each subsequent 10% used for validation (a fine-tuning of the models hyper parameters) and testing (with independent data deriving the model's performance statistics) (<https://cloud.google.com/automl-tables>). Both modeling approaches included the time component as the most important accounting for 87.3% as feature importance in Google AI and a combined (year and day of year) percentage sensitive value of 66.7% in NPMR. The next most important parameter was the NAO in both modelling approaches with a 3.9% feature importance in Google AI and 0.6% sensitivity in NPMR. No other parameters were included in the NPMR model while the Google AI approach estimated the seven day antecedent sum of rainfall as having a feature importance of 3.1% with no other variables accounting for more than 3%.

While a precise comparison is not possible between the two approaches owing to different model design and performance statistics they could be considered as broadly similar comparing the Google AI R^2 of 0.65 with that of the NPMR xR^2 of 0.54. A NPMR plot of Chl-a (as contour lines in Fig. 3.7) with NAO and the day of year (DOY) indicates that NAO appears to be most relevant to Chl-a concentration in the weeks around DOY 250 (7th September). More positive values of the NAO in early to mid-September were associated with higher Chl-a (Fig. 3.7). The importance of time in the models is likely linked to the consistency in timing of large September blooms over the years that dominate the seasonal pattern (Fig. 3.5). The size of these blooms is likely to be mostly determined by nutrients such as phosphorus given its key role in controlling algal populations [56]. Total phosphorus (TP) was not available at daily frequency for the lake but we can compare Chl-a concentration in early to mid-September with annual TP concentrations sourced from local authorities (<https://apps.arpa.umbria.it/acqua/Home>) and published values [26] (Fig. 3.8). The R^2 of the relationship was 0.65 indicating the strong influence of annual TP in determining

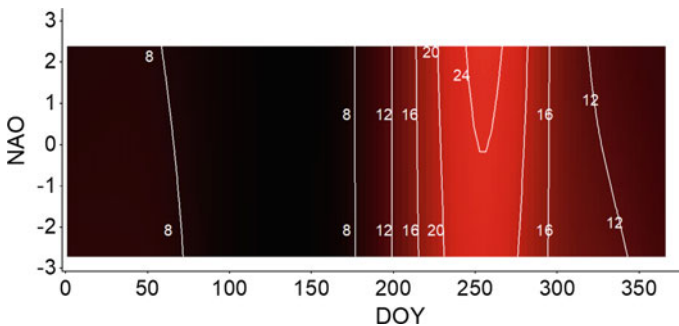
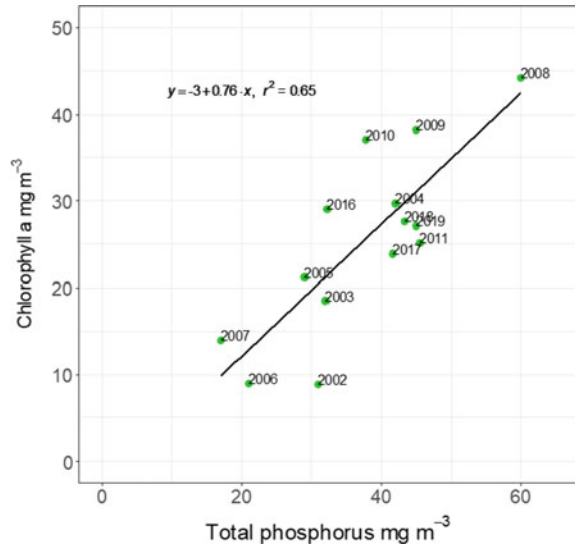


Fig. 3.7 Model estimates for Chl-a mg m^{-3} (contour lines) against DOY (Day of Year) and NAO (North Atlantic Oscillation)

Fig. 3.8 Chlorophyll-a (average of a two week period around day 250—7th September) and annual average total phosphorus



the size of the September phytoplankton bloom. In summary the analysis indicates that years with high TP concentrations and high NAO in early to mid-September, indicative of high pressure with warm sunny weather [57], will tend to lead to the largest phytoplankton blooms. The high temporal resolution of the CCI satellite data coupled with the ERA5 climatic data proved crucial to understanding the inter-annual dynamics driving phytoplankton blooms. It would not be possible to match the temporal and spatial coverage afforded by satellite monitoring with boat based sampling and laboratory analysis. However, such traditional methods are key to understanding providing TP and other nutrient concentrations and Chl-a data for validating satellite estimates.

The examination of the CCI timeseries for Chl-a indicated the importance of the temporal component and NAO for both AI and NPMR. While the importance of the temporal component reflects the regularity of the large blooms that dominate the annual pattern the influence of NAO was interesting. Previous work has identified the importance of winter values of teleconnection indices like the NAO and the EA where, for example, in deep sub-alpine lakes higher values lead to warmer winters preventing mixing and reducing nutrient supply from the hypolimnion [49, 50]. It has also been associated with controlling the onset of spring blooms and zooplankton abundance in some lakes [58]. In this study a higher NAO value in September was related to higher Chl-a and this may have resulted from higher temperatures and sunnier weather increasing cyanobacteria growth during this period. A meta-analysis of European lakes previously found summer cyanobacteria biomass to be associated with winter NAO which was attributed to a direct physiological influence of higher temperatures on growth or an increased period of stratification, although the latter would be irrelevant in the case of shallow Trasimeno likely to be more influenced by prevailing weather conditions [59]. As several species of cyanobacteria change

dominance during summer, the NAO may also influence the timing of the seasonal succession but this would require further analysis for confirmation.

The AI analysis also found the antecedent 7-day rain to be significant and this is likely to be indicative of the supply of nutrients to the lake. Examination of satellite images has previously identified phytoplankton blooms in the vicinity of an inflow to Trasimeno lake during summer that was followed by a widespread increase in Chl-a in the lake [19]. The good relationship between TP measured by local authorities and the average concentration of the September bloom, shows both how Chl-a is constrained by nutrients and also demonstrates the benefits of using satellite data to obtain a better temporal and spatial resolution.

3.5 Spaceborne Imaging Spectrometry

In recent years new spaceborne missions dedicated to hyperspectral measurements have been developed [60] and in this section imagery data acquired from PRISMA (Hyperspectral Precursor of the Application Mission) and DESIS (DLR Earth Sensing Imaging Spectrometer) are presented for assessing water quality in Lake Trasimeno.

PRISMA, a fully funded mission by the Italian Space Agency (ASI), is an EO system with innovative, electro-optical instrumentation that combines a hyperspectral sensor with a medium-resolution panchromatic camera. The PRISMA orbit is characterized by a revisit time in a nadir-looking configuration of 29 days, the system is capable of acquiring images distant 1000 km in a single pass (with a total rotation left to right side looking and vice versa) so that the temporal resolution can be improved significantly. The PRISMA Payload is composed of an Imaging Spectrometer, able to take images at 30 m resolution in a continuum of spectral bands ranging from 400 to 2500 nm, and a 5 m resolution Panchromatic Camera [61]. DESIS is a hyperspectral instrument integrated in the Multi-User-System for Earth Sensing (MUSES) platform installed on the International Space Station (ISS). The mission is operated by Teledyne Brown Engineering (TBE), Alabama, USA, and the German Aerospace Center (DLR), Germany. DESIS is realized as a pushbroom imaging spectrometer spectrally sensitive over the VNIR range from 400 to 1000 nm with a spectral sampling distance of 2.55 nm [62].

Within this study imagery data from PRISMA and DESIS of Lake Trasimeno acquired on the 25th July 2020 and on the 26th May 2020, respectively are used for water quality mapping. PRISMA data were downloaded as Level 1 (L1) products (top-of-atmosphere calibrated radiance), then imported and converted to ENVI format (L3Harris Technologies, Inc., Melbourne, FL, USA), re-projected with a geographic lookup table (GLT) Bowtie correction and re-scaled to physical units of $\text{mWcm}^{-2}\text{sr}^{-1} \mu\text{m}^{-1}$, in the case of DESIS the geocoded L1C products in ENVI format were simply re-scaled to physical units of $\text{mWcm}^{-2}\text{sr}^{-1} \mu\text{m}^{-1}$.

To map water quality, L1 PRISMA and DESIS imagery were firstly corrected for atmospheric effects in order to compute remote sensing reflectance R_{rs} . To this

aim, the ATCOR code (version 9.3.0, ATCOR-2 module) [63] was used as in Pepe et al. [64]. The code was pre-configured in order to handle data acquired from both sensors (e.g. spectral setting, swath) and then the correction was performed with varying visibility and water vapor, the related viewing and solar angles, a rural model for aerosols and by setting to 258 m above-sea-level the altitude of the target. The ATCOR-derived atmospherically corrected reflectance was then converted into remote sensing reflectance R_{rs} dividing by π . The ATCOR-derived R_{rs} values were compared to the WISPstation synchronous measurements (cf. Section 1). In particular, WISPstation data overlapping the sensing time of PRISMA within 15 min were averaged while, R_{rs} spectra of PRISMA and DESIS, were extracted from imagery data corresponding to a 3×3 pixel Region of Interest (ROI) centering the WISPstation position (cf. Figure 3.1). The comparison between spaceborne data and field measurements is shown in Fig. 3.9, that also includes the results of common descriptive statistical metrics (e.g., Bracaglia et al. [65]): root mean square difference (RMSD), spectral angle (SA), and the square of the coefficient of correlation (R^2) defined in the Table 3.1. The comparison of ATCOR-derived R_{rs} values with in situ measurements proved overall a very good agreement at all wavelengths. The magnitude and shape of PRISMA and DESIS are comparable to in situ data even if a more detailed examination of the peaks/dips seems to indicate a minor spectral shift of PRISMA.

In order to convert the R_{rs} data into biophysical water parameters such as Chl-a, Total Suspended Matter (TSM) and Colored Dissolved Organic Matter (CDOM) we

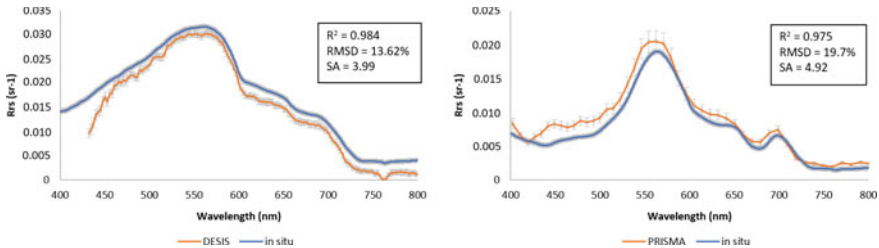


Fig. 3.9 Comparison between spectral signatures acquired by the WISPstation and obtained after atmospheric correction of DESIS (on the left) and PRISMA (on the right). The boxes contain the values of statistical metrics R^2 , RMSD and SA

Table 3.1 Statistical metrics used to assess the agreement of R_{rs} between spaceborne data and field measurements

Root mean square difference (RMSD)	$\sqrt{\frac{\sum_{i=1}^n (y_i - x_i)^2}{n}}$
Spectral angle (SA)	$\cos^{-1} \frac{\sum_{i=1}^n y_i x_i}{\sqrt{\sum_{i=1}^n y_i^2} \sqrt{\sum_{i=1}^n x_i^2}}$
Square of the coefficient of correlation (R^2)	$\frac{\sum_{i=1}^n (x_i - \bar{x})(y_i - \bar{y})}{\sqrt{\sum_{i=1}^n (x_i - \bar{x})^2} \sqrt{\sum_{i=1}^n (y_i - \bar{y})^2}}$

The values of statistical metrics RMSD, SA and R^2 are reported

used the BOMBER tool [66], which implements a non-linear optimisation procedure to derive water parameters from a four-component bio-optical model. To this aim the bio-optical model was parameterized with the specific inherent optical properties of Lake Trasimeno as described in Giardino et al. [67].

For Chl-a we can compare the image products from PRISMA and DESIS with in situ data collected by ARPA Umbria on the 25th May 2020 and 20th July 2020. The Chl-a concentrations were measured from samples collected from the euphotic zone at two WFD stations named Center and San Feliciano (Fig. 3.1). Chl-a concentration was then determined in the laboratory spectrophotometrically (using acetone 90% for the extraction) and calculated following Lorenzen [68]. The results of the comparison show a good agreement between hyperspectral-derived products (for which the standard deviation can be also computed over the 3×3 ROI) and laboratory measurements. In particular, on the 26th May 2020: in situ data were 2.8 and 4 mg m^{-3} (respectively for stations TRS30 and TRS35) with corresponding values from DESIS of 2.9 ± 0.3 and 3.8 ± 0.5 mg m^{-3} . On the 25th July 2020, in situ data were 18.7 and 13.2 mg m^{-3} (respectively for stations TRS30 and TRS35), with corresponding values from PRISMA of 19.7 ± 0.6 mg m^{-3} (st.dev 0.6) and 12.5 ± 1.7 mg m^{-3} .

Figures 3.10 and 3.11 show the true-color composite and products obtained from DESIS and PRISMA, nicely depicting the ranges of concentrations and spatial patterns in Lake Trasimeno. Overall the DESIS map of spring 2020 shows rather turbid conditions, with TSM concentration reaching 20 g m^{-3} . In contrast, Chl-a concentrations remain rather low (maximum of 8 mg m^{-3}), while the absorption due to CDOM is between 0 and 1 m^{-1} . In the case of the PRISMA image, the mapping indicates more productive waters typical of the summer season, with Chl-a concentrations reaching 30 mg m^{-3} . In this case TSM and CDOM are lower than 10 g m^{-3} and 0.5 m^{-1} respectively, indicating a dominance of phytoplankton with respect to the other water components. By comparing DESIS and PRISMA products, as well as the true-color composite, it is also evident how the region characterised by the presence of aquatic vegetation in the south-east bay of Lake Trasimeno, covers a greater area in the PRISMA scene compared to the DESIS. This localized feature is consistent with the seasonal changes in macrophyte abundance. In late May, at the time of DESIS image acquisition, the aquatic plants have just started their phenological cycle; compared to late July, at the time of the PRISMA image when all plants are much more developed. In addition, this will influence water conditions, since the macrophyte community tends to keep the water clearer, therefore the TSM concentrations from DESIS are higher than those observed by PRISMA.

3.6 High Spatial Resolution Products

High spatial resolution images (<5 m pixel resolution from e.g. WorldView, Rapid-Eye, PlanetScope) are typically designed for terrestrial applications, nevertheless these sensors can have aquatic applications whenever finer scale mapping is needed

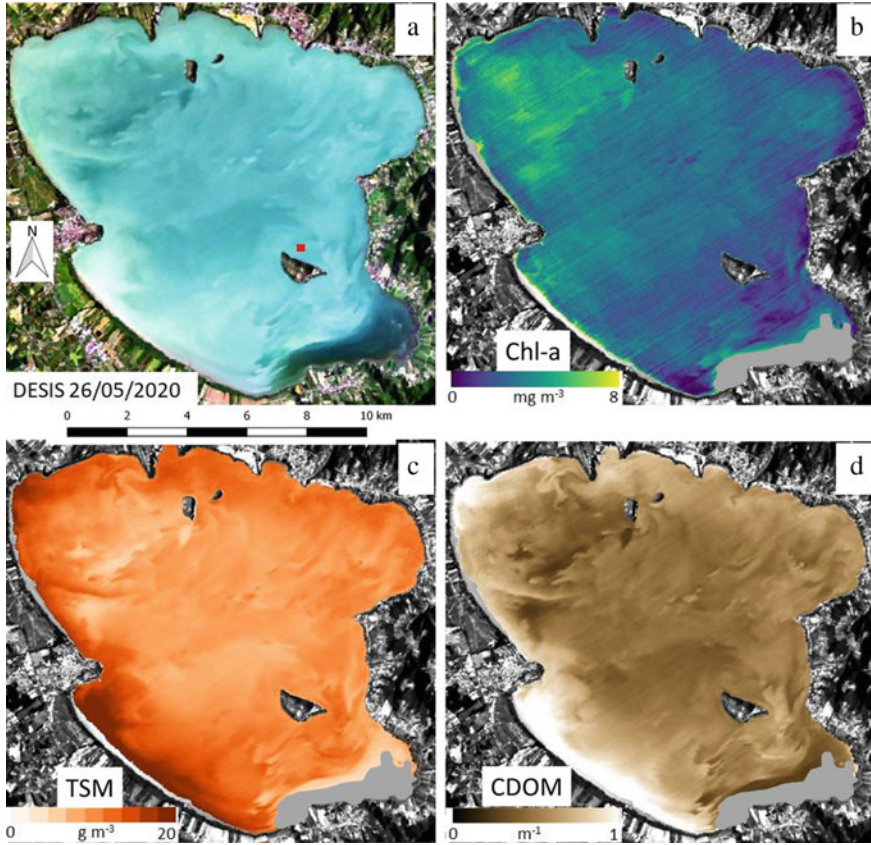


Fig. 3.10 The pseudo true colour DESIS image acquired on 26th May 2020 and the three BOMBER-retrieved products. The lake area with substrates colonized by aquatic vegetation (in grey) in the Oasi la Valle bay (cf. Fig. 3.1) are masked as BOMBER was run for optically deep waters only

(e.g., Giardino et al. [69], Niroumand-Jadidi [70] for water constituents; and e.g. Doxani et al. [71], Arsen [72], Halls and Costin [73] for macrophyte mapping and coastal bathymetry). High spatial resolution satellite data is often preferable to medium-to-low spatial resolution data, for example, when the ecosystems include small macrophyte stands, when macrophyte community expansion or recession occurs over a few square meters, or whenever fine-scale mapping is required to support proper management decisions. In such situations, it is important to remember that high spatial resolution images are usually acquired on demand by commercial entities and it will be necessary to obtain a quote in advance for the service. Moreover the data may be challenging due to a high variation of sensor angles and a signal to noise ratio not optimised for aquatic applications [74].

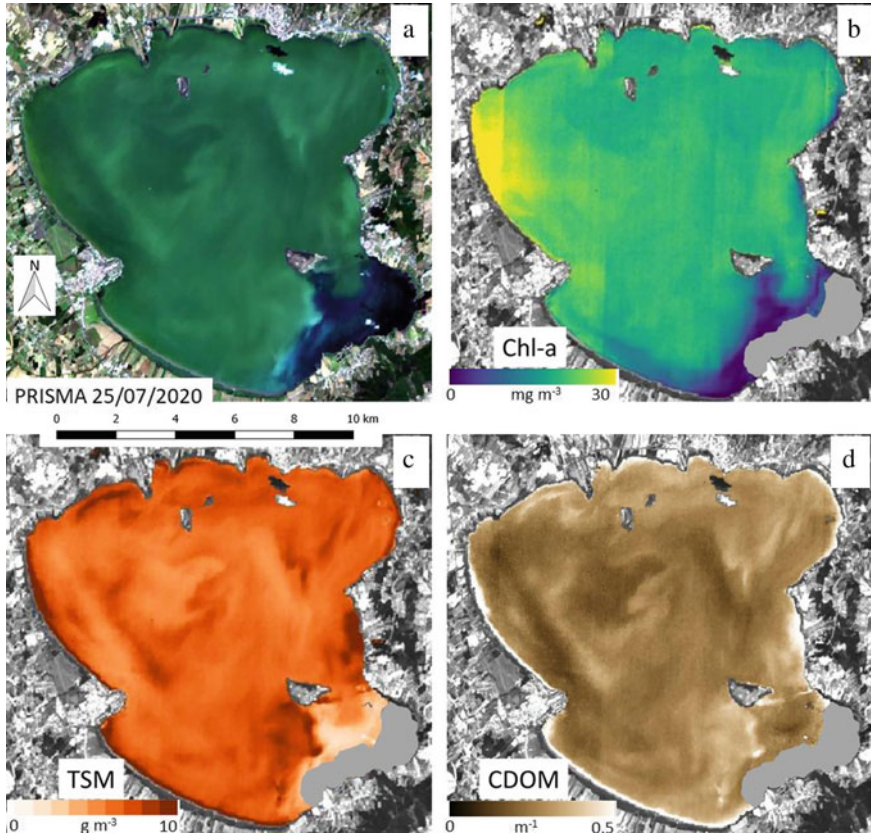


Fig. 3.11 The pseudo true colour PRISMA image acquired on 25th July 2020 and the three BOMBER-retrieved products. The lake area with substrates colonized by aquatic vegetation (in grey) in the Oasi la Valle bay (cf. Fig. 3.1) are masked as BOMBER was run for optically deep waters only

In the case of Lake Trasimeno, the use of high spatial resolution satellite images was previously investigated to obtain information on the status and changes of macrophyte communities, that are unfortunately showing a slight deterioration. In particular, *Potamogeton* associations declined by about 20% from 2003 to 2008 [27]. Moreover, the progressive dieback of the common reed [75] on the lake littoral occurred with a loss of about 66% of its total surface area in the period between 1988 and 2005 [75, 76]. The macrophyte decrease is mostly attributable to an increase of water turbidity, even if some fish species (such as goldfish, common carp and grass carp) that are prospering in the lake, can eat significant quantities of vegetation [77]. The invasive red swamp crayfish (*Procambarus clarkia*) and coypu (*Myocastor coypus*) might have also contributed to the macrophyte decline in Lake Trasimeno, due to their feeding habits [78, 79]. Previous work tracing a period of decline in

common reed health has used different high spatial resolution images (QuickBird, ASTER and ALOS-AVNIR/2) by Bresciani et al. [80].

In this study, an example of the use of high spatial resolution satellite data is shown to estimate the portion of Lake Trasimeno covered by submerged macrophytes (with also a subdivision of the type of association of macrophytes present) and to assess whether there have been changes over time. To the aim, data have been gathered from the WorldView-3 multispectral satellite sensor, launched in 2014, with a spatial resolution at nadir at 1.24 m having 8 bands in the region from 400 to 1040 nm. The WordView-3 image of Lake Trasimeno was acquired on the 4th August 2019 and it was atmospherically corrected with Simulation of the Satellite Signal in the Solar Spectrum vector code (6SV) [81, 82]. Then, the bio-optical model BOMBER [66] parametrized with specific inherent optical properties of Lake Trasimeno [67] was used to estimate bottom types from imagery data. Before to run the bio-optical model we applied a Normalized Difference Water Index (NDWI) to maps the presence of common reed and emergent macrophytes area according to Lantz and Wang [83]. The bottom type map (Fig. 3.12) shows the main association of submerged macrophytes growing in the Oasi La Valle, in the southern-east part of Lake Trasimeno (cf. Fig. 3.1). The map in red and green tones shows areas dominated by dense submerged macrophyte stands. Although this area is still rather extended, a decrease of about 100 hectares of submerged macrophytes is observed when compared to the same period of 2014 [67].

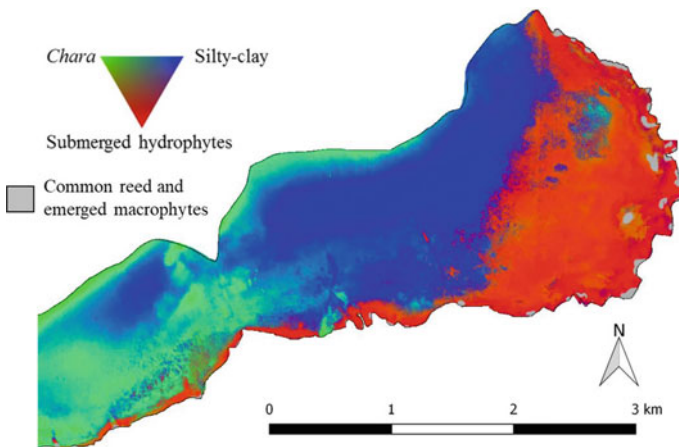


Fig. 3.12 Map of the benthic substrate and submerged macrophytes in the southern eastern portion of the Lake Trasimeno (Oasi La Valle site) retrieved by WordView-3 image acquired on the 4th August 2019. In grey the common reed and emergent macrophytes

3.7 Conclusions

This work demonstrates that remote and proximal sensing data can provide accurate and high-resolution information for water monitoring and management and extend the scientific understanding of Lake Trasimeno. The integrated and multi-scale approach (combining sources from field, fixed station and multiple satellites) to assessing Chl-a and other water quality parameters has the benefit of improving confidence, knowledge and substantially increases the potential for research, monitoring and model development.

High temporal and spectral resolution spectroradiometric data, such as those obtained by WISPstation in Lake Trasimeno, allows the estimation of phytoplankton pigment concentration and in particular to identify the start and rate of increase of the summer bloom. The phenology was found to be consistent in the three years investigated (2018–2020), with a bloom typically increasing between the 29th June–7th September and a slope ranging from 0.50 to 0.59. Moreover, PC retrieval demonstrated that cyanobacteria played a pivotal role in the sudden increases and declines in Chl-a in mid to late summer. For water managers, one of the benefits of the use of the WISPstation data is the coupling of the retrieval of different pigments that allows the identification of different phytoplankton functional groups and the detection, in almost real time, of potentially toxic cyanobacteria. Coupling high frequency (hourly) and temporal (daily, seasonal) data helped to develop understanding, giving clear benefits for water management in detecting and predicting bloom event dynamics and manifestation. A drawback is that the WISPstation is limited to a fixed position and describes a point-like portion of the lake; a gap that can be successfully filled with the satellite technology.

The availability of long time-series of satellite observations for different parameters, such as LSWT, Chl-a and turbidity from the recent ESA CCI Lakes database [48] allowed a clear view over time showing that the peak height of the algal blooms increased from 2008 onwards. Moreover, the performed analysis suggested that years with high TP concentrations and high NAO in early to mid-September, indicative of high nutrient availability with warm sunny weather, will tend to lead to the largest phytoplankton blooms. Currently the lake is classified as eutrophic and periodic blooms can interfere with the recreational use and tourism in the lake area. Therefore, long-time series of satellite-derived maps allow the examination of the phenology and intensity of phytoplankton bloom history, an opportunity to identify drivers of the long-term dynamics in communities which is a complex subject as it may consist of several factors acting in parallel and it is also an opportunity for managers to identify hotspot zones that tend to show higher bloom events.

With the CCI dataset set to expand to 2000 lakes in the second phase of the project it will represent an important resource for the scientific community and water quality managers.

The new generation of satellite hyperspectral data (i.e., PRISMA, DESIS) among other things, offers the opportunity for high quality spatial data on water quality.

The comparison between spaceborne Rrs data and field measurements (by WISP-station) shown a good agreement ($R^2 = 0.98$) as did the comparison between Chl-a hyperspectral-derived products and Chl-a laboratory measurements. DESIS derived maps of spring 2020 shown that Lake Trasimeno was characterized by high turbidity ($TSM > 20 \text{ gm}^{-3}$) and low Chl-a concentration (up to 8 mg m^{-3}) and low presence of aquatic vegetation. Instead, in summer the PRISMA-derived maps indicated more productive waters ($\text{Chl-a} > 30 \text{ mg m}^{-3}$), and low turbidity ($TSM < 10 \text{ g m}^{-3}$) influenced by the presence of submerged vegetation in the southern-east part of the lake which favors increased water transparency.

Another important aspect to be considered is the availability of high resolution spatial data in supporting specific analysis on primary producers, such as hotspots of algal blooms and submerged macrophytes cover and abundance. On this last issue, in this study an example of the use of high spatial resolution satellite data (WorldView-3 with 1.2 m pixel resolution) was shown to estimate the portion of Lake Trasimeno covered by submerged macrophytes (with also a subdivision of the type of association of macrophytes) and to assess whether there have been changes over time. In fact, the bottom type map produced (2019) shown a decrease of submerged macrophytes compared to the same period of 2014.

The different approach applied in this work may be transferred to other water bodies to analyze specific features of phytoplankton species, which can threaten the conservation of aquatic habitats and interfere with human recreational activities (e.g. touristic navigation, fishing), thus heavily impacting on the ecosystem and socio-economics.

Overall, this study confirms how advanced remote sensing technology is continuously providing enhanced opportunities to monitor changes in space and time and to perform retrospective analysis of water quality status. Integrated data from different optical sensors are also a key element because such an approach allows, upon verification of the methods and accuracies, the continuity of consistent analysis of water quality, and guarantees a support to decision-makers involved in monitoring, management and conservation of aquatic ecosystems.

Acknowledgements This research is co-funded by ESA CCI LAKES project (GA n. 40000125030/18/I-NB) and by the Italian Space Agency with PRISCAV project (grant nr. 2019-5-HH.0) and by the H2020 EOMORES project (GA n. 730066) for the WISPstation. We would like to thank the “Cooperativa dei Pescatori del Trasimeno” for the support in field campaigns. Many thanks to Alessandra Cingolani, Fedra Charavgis and Valentina DellaBella from ARPA Umbria for useful discussions on research results. We are grateful to Luca Nicoletti and Luca Galli from ARPA Umbria for collecting water samples. We also thank the Province of Perugia for the availability to use the platform in Polvese Island used for the WISPstation. We are very grateful to Ettore Lopinto from ASI and to Uta Heiden and Nicole Pinnel from DLR for valuable discussions on PRISMA and DESIS products respectively.

References

1. Organisation for Economic Co-operation and Development (2001) OECD environmental strategy for the first decade of the 21st Century: adopted by OECD environmental ministers. OECD
2. Giovannini E (2008) Understanding economic statistics: an OECD perspective. OECD, Paris
3. Coicaud JM, Zhang J (2011) The OECD as a global data collection and policy analysis organization: some strengths and weaknesses. *Global Pol* 2(3):312–317
4. Directive (2000) Directive 2000/60/EC of the European Parliament and of the council of 23 October 2000 establishing a framework for community action in the field of water policy. *Off J Europ Commun* L327:1–72
5. Garrote L (2017) Managing water resources to adapt to climate change: facing uncertainty and scarcity in a changing context. *Water Resour Manage* 31(10):2951–2963
6. Carvalho L, Mackay EB, Cardoso AC, Baattrup-Pedersen A, Birk S, Blackstock KL, Borics G, Borja A, Feld CK, Ferreira MT, Globevnik L (2019) Protecting and restoring Europe's waters: an analysis of the future development needs of the water framework directive. *Sci Total Environ* 658:1228–1238
7. Woolway RI, Kraemer BM, Lenters JD, Merchant CJ, O'Reilly CM, Sharma S (2020) Global lake responses to climate change. *Nat Rev Earth Environ* 1(8):388–403
8. Williamson CE, Saros JE, Vincent WF, Smol JP (2009) Lakes and reservoirs as sentinels, integrators, and regulators of climate change. *Limnol Oceanogr* 54:2273–2282
9. Adrian R, O'Reilly CM, Zagarese H, Baines SB, Hessen DO, Keller W, Livingstone DM, Sommaruga R, Straile D, Van Donk E, Weyhenmeyer GA (2009) Lakes as sentinels of climate change. *Limnol Oceanogr* 54(6):2283–2297
10. Bukata RP, Jerome JH, Kondratyev KY, Pozdnyakov DV (1991) Satellite monitoring of optically-active components of inland waters: an essential input to regional climate change impact studies. *J Great Lakes Res* 17(4):470–478
11. Yang J, Gong P, Fu R, Zhang M, Chen J, Liang S, Xu B, Shi J, Dickinson R (2013) The role of satellite remote sensing in climate change studies. *Nat Clim Chang* 3(10):875–883
12. Hu C, Lee Z, Ma R, Yu K, Li D, Shang S (2010) Moderate resolution imaging spectroradiometer (MODIS) observations of cyanobacteria blooms in Taihu Lake, China. *J Geophys Res: Oceans* 115(C4)
13. Tyler AN, Hunter PD, Spyrakos E, Groom S, Constantinescu AM, Kitchen J (2016) Developments in Earth observation for the assessment and monitoring of inland, transitional, coastal and shelf-sea waters. *Sci Total Environ* 572:1307–1321
14. Odermatt D, Gitelson A, Brando VE, Schaepman M (2012) Review of constituent retrieval in optically deep and complex waters from satellite imagery. *Remote Sens Environ* 118:116–126
15. Ogashawara I, Mishra DR, Mishra S, Curtarelli MP, Stech JL (2013) A performance review of reflectance based algorithms for predicting phycocyanin concentrations in inland waters. *Remote Sens* 5(10):4774–4798
16. Gholizadeh MH, Melesse AM, Reddi LA (2016) Comprehensive review on water quality parameters estimation using remote sensing techniques. *Sensors* 16:1298
17. Greb S, Dekker AG, Binding C, Bernard S, Brockmann C, DiGiacomo P, Griffith D, Groom S, Hestir E, Hunter P, Kutser T (2018) Earth observations in support of global water quality monitoring. International Ocean-Colour Coordinating Group
18. Kutser T, Hedley J, Giardino C, Roelfsema C, Brando VE (2020) Remote sensing of shallow waters—a 50 year retrospective and future directions. *Remote Sens Environ* 240:111619
19. Bresciani M, Pinaridi M, Free G, Luciani G, Ghebrehiwot S, Laanen M, Giardino C et al (2020) The use of multisource optical sensors to study phytoplankton spatio-temporal variation in a Shallow Turbid Lake. *Water* 12(1):284
20. Taticchi MI (1992) Studies on Lake Trasimeno and other water bodies in Umbria Region (Central Italy). In: Guilizzoni P, Tartari G, Giussani G (eds) *Limnology in Italy*. Tipografia Griggi, Baveno, Italy, pp 295–317

21. Carosi A, Ghetti L, Padula R, Lorenzoni M (2019) Potential effects of global climate change on fisheries in the Trasimeno Lake (Italy), with special reference to the goldfish *Carassius auratus* invasion and the endemic southern pike *Esox cisalpinus* decline. *Fish Manage Ecol* 26(6):500–511
22. Deffenu L, Dragoni W (1978) Idrogeologia del Lago Trasimeno. *Geologia Applicata e Idrogeologia* 13:11–67
23. Dragoni W (2004) Il Lago Trasimeno e le variazioni climatiche (in Italian with English transl.) Provincia di Perugia, 60 pp
24. Frondini F, Dragoni W, Morgantini N, Donnini M, Cardellini C, Caliro S, Chiodini G et al (2019) An Endorheic Lake in a changing climate: geochemical investigations at Lake Trasimeno (Italy). *Water* 11(7):1319
25. Ludovisi A, Gaino E, Bellezza M, Casadei S (2013) Impact of climate change on the hydrology of shallow Lake Trasimeno (Umbria, Italy): history, forecasting and management. *Aquat Ecosyst Health Manage* 16(2):190–197
26. Ludovisi A, Gaino E (2010) Meteorological and water quality changes in Lake Trasimeno (Umbria, Italy) during the last fifty years. *J Limnol* 69(1):174–188
27. Giardino C, Bresciani M, Villa P, Martinelli A (2010) Application of remote sensing in water resource management: the case study of Lake Trasimeno, Italy. *Water Res manag* 24(14):3885–3899
28. Cingolani A, Charavgis F (2017) Valutazione dello stato ecologico e chimico dei corpi idrici lacustri (2013–2015). ARPA Umbria Technical report, 25 pp
29. Havens KE, Elia AC, Taticchi MI, Fulton RS (2009) Zooplankton–phytoplankton relationships in shallow subtropical versus temperate lakes Apopka (Florida, USA) and Trasimeno (Umbria, Italy). *Hydrobiologia* 628(1):165–175
30. Salmaso N (2010) Long-term phytoplankton community changes in a deep subalpine lake: responses to nutrient availability and climatic fluctuations. *Freshw Biol* 55:825–846
31. Lorenzoni M, Dolciami R, Ghetti L, Pedicillo G, Carosi A (2010) Fishery biology of the goldfish *Carassius auratus* (Linnaeus, 1758) in Lake Trasimeno (Umbria, Italy). *Knowl Manag Aquat Ecosyst* 396:01
32. Coesel PFM, Kwakkestein R, Verschoor A (1978) Oligotrophication and eutrophication tendencies in some Dutch moorland pools, as reflected in their desmid flora. *Hydrobiologia* 61:21–31
33. Pernthaler A, Pernthaler J (2005) Diurnal variation of cell proliferation in three bacterial taxa from coastal North Sea waters. *Appl Environ Microbiol* 71:4638–4644
34. Ruiz-González C, Lefort T, Massana R, Simó R, Gasol JM (2012) Diel changes in bulk and single-cell bacterial heterotrophic activity in winter surface waters of the northwestern Mediterranean Sea. *Limnol Oceanogr* 57:29–42
35. Ezra AG, Nwankwo DI (2001) Composition of phytoplankton algae in Gubi Reservoir, Bauchi, Nigeria. *J Aquat Sci* 16(2):115–118
36. Peters S, Laanen M, Groetsch P, Ghezehegn S, Poser K, Hommersom A, De Reus E, Spaais L (2018) WISP station: a new autonomous above water radiometer system. In: Proceedings of the ocean optics XXIV conference. Dubrovnik, Croatia, 7–12 October 2018
37. Giardino C, Bresciani M, Braga F, Fabbretto A, Ghirardi N, Pepe M, Brando VE et al (2020) First evaluation of PRISMA level 1 data for water applications. *Sensors* 20(16):4553
38. Gons HJ (1999) Optical teledetection of chlorophyll a in turbid inland waters. *Environ Sci Technol* 33:1127–1132
39. Simis S (2006) Blue-green catastrophe: remote sensing of mass viral lysis of cyanobacteria. Ph.D. Thesis, Vrije University, Amsterdam
40. Wolfram G, Argillier C, de Bortoli J, Buzzi F, Dalmiglio A, Dokulil MT et al (2009) Reference conditions and WFD compliant class boundaries for phytoplankton biomass and chlorophyll-a in Alpine lakes. *Hydrobiologia* 633:45–58
41. Pinheiro J, Bates D, DebRoy S, Sarkar D, Team RC (2013) nlme: Linear and nonlinear mixed effects models. *R Package Version* 3(1):111
42. Lenth RV (2016) Least-squares means: the R package lsmeans. *J Stat Softw* 69:1–33

43. R Core Team (2019) R: a language and environment for statistical computing. Vienna. R Foundation for Statistical Computing, Austria. <https://www.R-project.org/>
44. Charavgis F, Cingolani A, Di Brizio M, Tozzi G, Rinaldi E, Stranieri P (2018) Qualita' delle acque di balneazione dei laghi Umbri. ARPA, Umbria
45. Funari E, Manganelli M, Buratti FM, Testai E (2017) Cyanobacteria blooms in water: Italian guidelines to assess and manage the risk associated to bathing and recreational activities. *Sci Total Environ* 598:867–880
46. Hamilton DP, Carey CC, Arvola L, Arzberger P, Brewer C, Cole JJ, Gaiser E, Hanson PC, Ibelings BW, Jennings E (2015) A Global lake ecological observatory network (GLEON) for synthesising high-frequency sensor data for validation of deterministic ecological models. *Inland Waters* 5:49–56
47. Charavgis F, Cingolani A, Di Brizio M, Rinaldi E, Tozzi G, Stranieri P (2020) Qualita' delle acque di balneazione dei laghi Umbri, stagione balneare 2019. ARPA, Umbria
48. Crétaux J-F, Merchant CJ, Duguay C, Simis S, Calmettes B, Bergé-Nguyen M, Wu Y, Zhang D, Carrea L, Liu X, Selmes N, Warren M (2020) ESA Lakes climate change initiative (Lakes_cci): Lake products, Version 1.0. centre for environmental data analysis, 08 June 2020
49. Rogora M, Buzzi F, Dresti C, Leoni B, Lepori F, Mosello R et al (2018) Climatic effects on vertical mixing and deep-water oxygen content in the subalpine lakes in Italy. *Hydrobiologia* 824(1):33–50
50. Salmaso N, Boscaini A, Capelli C, Cerasino L (2018) Ongoing ecological shifts in a large lake are driven by climate change and eutrophication: evidences from a three-decade study in Lake Garda. *Hydrobiologia* 824(1):177–195
51. McCune B (2006) Nonparametric multiplicative regression for habitat modeling. Oregon State University, Oregon
52. Yost AC (2008) Probabilistic modeling and mapping of plant indicator species in a Northeast Oregon industrial forest, USA. *Ecol Ind* 8(1):46–56
53. Ellis CJ, Coppins BJ, Dawson TP, Seaward MR (2007) Response of British lichens to climate change scenarios: trends and uncertainties in the projected impact for contrasting biogeographic groups. *Biol Cons* 140(3–4):217–235
54. Nicolaou N, Constantinou TG (2016) a nonlinear causality estimator based on non-parametric multiplicative regression. *Front Neuroinf* 10
55. McCune B, Mefford MJ (2009) HyperNiche. In: Nonparametric multiplicative habitat modeling. MjM Software, Oregon, USA
56. Sakamoto M (1966) Primary production by phytoplankton community in some Japanese lakes and its dependence on lake depth. *Arch Hydrobiol* 62:1–28
57. Criado-Aldeanueva F, Soto-Navarro J (2020) Climatic Indices over the Mediterranean Sea: a review. *Appl Sci* 10(17):5790
58. Gerten D, Adrian R (2000) Climate-driven changes in spring plankton dynamics and the sensitivity of shallow polymictic lakes to the North Atlantic Oscillation. *Limnol Oceanogr* 45(5):1058–1066
59. Blenckner T, Adrian R, Livingstone DM, Jennings E, Weyhenmeyer GA, George DG et al (2007) Large-scale climatic signatures in lakes across Europe: a meta-analysis. *Glob Change Biol* 13(7):1314–1326
60. Rast M, Painter TH (2019) Earth observation imaging spectroscopy for terrestrial systems: An overview of its history, techniques, and applications of its missions. *Surv Geophys* 40:303–331
61. Loizzo R, Guarini R, Longo F, Scopa T, Formaro R, Facchinetti C, Varacalli G (2018) PRISMA: the Italian hyperspectral mission. In: Proceedings of the international geoscience and remote sensing symposium on observing, understanding and forecasting the dynamics of our planet (IGARSS). Valencia, Spain, 22–27 July 2018
62. Alonso K, Bachmann M, Burch K, Carmona E, Cerra D, de los Reyes R, Dietrich D, Heiden U, Holderlin A, Ickes J et al (2019) Data products, quality and validation of the DLR Earth sensing imaging spectrometer (DESI). *Sensors* 19:4471
63. Richter R, Schläpfer D (2018) Atmospheric/topographic correction for satellite imagery (ATCOR-2/3 User Guide, Version 9.3. ReSe Applications Schläpfer, Langeggweg, 3

64. Pepe M, Pompilio L, Gioli B, Busetto L, Boschetti M (2020) Detection and classification of non-photosynthetic vegetation from PRISMA hyperspectral data in croplands. *Remote Sensing* 12:3903
65. Bracaglia M, Santoleri R, Volpe G, Colella S, Benincasa M, Brando VE (2020) A virtual geostationary ocean color sensor to analyze the coastal optical variability. *Remote Sensing* 12:1539
66. Giardino C, Candiani G, Bresciani M, Lee Z, Gagliano S, Pepe M (2012) BOMBER: a tool for estimating water quality and bottom properties from remote sensing images. *Comput Geosci* 45:313–318
67. Giardino C, Bresciani M, Valentini E, Gasperini L, Bolpagni R, Brando VE (2015) Airborne hyperspectral data to assess suspended particulate matter and aquatic vegetation in a shallow and turbid lake. *Remote Sens Environ* 157:48–57
68. Lorenzen CJ (1967) Determination of chlorophyll and phaeo-pigments: spectrophotometric equations. *Limnol Oceanogr* 12:343–346
69. Giardino C, Bresciani M, Cazzaniga I, Schenk K, Rieger P, Braga F, Matta E, Brando VE (2014) Evaluation of multi-resolution satellite sensors for assessing water quality and bottom depth of Lake Garda. *Sensors* 14(12):24116–24131
70. Niroumand-Jadidi M, Bovolo F, Bruzzone L, Gege P (2020) Physics-based bathymetry and water quality retrieval using planetscope imagery: Impacts of 2020 Covid-19 lockdown and 2019 extreme flood in the Venice Lagoon. *Remote Sens* 12(15):2381
71. Doxani G, Papadopoulou M, Lafazani P, Pikridas C, Tsakiri-Strati M (2012) Shallow-water bathymetry over variable bottom types using multispectral Worldview-2 image. *Int Archives Photogrammetry, Remote Sens Spatial Inf Sci* 39(8):159–164
72. Arsen A, Crétau JF, Berge-Nguyen M, Del Rio RA (2014) Remote sensing-derived bathymetry of lake Poopó. *Remote Sensing* 6(1):407–420
73. Halls J, Costin K (2016) Submerged and emergent land cover and bathymetric mapping of estuarine habitats using worldView-2 and LiDAR imagery. *Remote Sensing* 8(9):718
74. Fisher JR, Acosta EA, Dennedy-Frank PJ, Kroeger T, Boucher TM (2018) Impact of satellite imagery spatial resolution on land use classification accuracy and modeled water quality. *Remote Sens Ecol Conserv* 4(2):137–149
75. Gigante D, Landucci F, Truffini A, Venanzoni R (2013) Phytosociological and ecological features of a dying-back reed bed at the Lake Trasimeno (central Italy). *Archives Geobotany* 14(1–2):81–89
76. Gigante D, Venanzoni R, Zuccarello V (2011) Reed die-back in southern Europe? a case study from Central Italy. *CR Biol* 334(4):327–336
77. Sheffer M (1998) Ecology of shallow lakes. Chapman & Hall, London, UK
78. Prigioni C, Balestrieri A, Remonti L (2005) Food habits of the coypu, *Myocastor coypus*, and its impact on aquatic vegetation in a freshwater habitat of NW Italy. *Folia Zool* 54(3):269–277
79. Souty-Grosset C, Anastácio PM, Aquiloni L, Banha F, Choquer J, Chucholl C, Tricarico E (2016) The red swamp crayfish *Procambarus clarkii* in Europe: impacts on aquatic ecosystems and human well-being. *Limnologica* 58:78–93
80. Bresciani M, Stroppiana D, Fila G, Montagna M, Giardino C (2009) Monitoring reed vegetation in environmentally sensitive areas in Italy. *Italian J Remote Sens* 41(2):125–137
81. Vermote EF, Tanré D, Deuze JL, Herman M, Morcette JJ (1997) Second simulation of the satellite signal in the solar spectrum, 6S: an overview. *IEEE Trans Geosci Remote Sens* 35(3):675–686
82. Kotchenova SY, Vermote EF, Matarrese R, Klemm FJ Jr (2006) Validation of a vector version of the 6S radiative transfer code for atmospheric correction of satellite data. Part I: path radiance. *Appl Opt* 45(26):6762–6774
83. Lantz NJ, Wang J (2013) Object-based classification of Worldview-2 imagery for mapping invasive common reed, *Phragmites australis*. *Can J Remote Sens* 39(4):328–340

Chapter 4

Satellite Instrumentation and Technique for Oil Pollution Monitoring of the Seas



Andrey G. Kostianoy and Olga Yu. Lavrova

Abstract The chapter provides a brief overview of satellite instrumentation, techniques and methods for oil spill detection on the sea surface. Monitoring of oil pollution from space is usually carried out using the synthetic aperture radars (SAR) and advanced synthetic aperture radars (ASAR) installed on satellites launched in different years by USA, ESA, USSR, Japan, Canada, Germany, and Italy. The first SAR system was installed on the SEASAT satellite launched on 27 June 1978, and since that time SAR systems showed their efficiency in oil spill detection on the sea surface. As any remote, in-situ or laboratory method, SAR remote sensing has a set of advantages (wide swath, all weather, day/night, daily periodicity, etc.) as well as disadvantages which include look-alikes caused by natural oceanic and atmospheric phenomena and processes, which need to be discriminated from oil pollution. Application of the SAR systems is illustrated by several examples of oil spill detection in different parts of the World Ocean and inland seas. Discussion of the assessment of total volume of oil pollution for the Baltic and Mediterranean seas shows that this is a difficult task and we still do not know real values of oil pollution of the marine environment. Development of scientific foundations and methodology for the quantitative assessment of environmental state of marine areas and of total amount of oil pollution of the World Ocean and inland seas is extremely urgent. Excessive human activity on the sea, including shipping, exploration and development of off-shore oil and gas reserves, construction and operation of underwater pipelines, platforms, terminals, storage facilities, ports, etc., entail very high risk of oil pollution in many sea areas.

A. G. Kostianoy (✉)

P.P. Shirshov Institute of Oceanology, Russian Academy of Sciences, 36, Nakhimovsky Pr,
Moscow 117997, Russian Federation
e-mail: kostianoy@gmail.com

S.Yu. Witte Moscow University, 12, 2nd Kozhukhovskiy Per., Bldg. 1, Moscow 115432, Russian
Federation

A. G. Kostianoy · O. Yu. Lavrova

Space Research Institute, Russian Academy of Sciences, 84/32, Profsoyuznaya Str, Moscow
117997, Russia
e-mail: olavrova@iki.rssi.ru

Keywords Satellite instrumentation · Techniques · Monitoring · World Ocean · Seas · Oil pollution · Oil spills · SAR · Aerial surveillance

4.1 Introduction

In recent years, remote sensing of the Earth from space has undergone rapid development, which is associated with the following three factors: firstly, this field of space technologies is the second after space communications, where significant commercial potential is seen; secondly, the problem of anthropogenic impact on the World Ocean requires a global network for monitoring the ocean surface and the near-surface layer of the atmosphere, a key element of which is space surveillance; and in the third, various satellite information about the state of the World Ocean, the atmosphere and land is the most important source of data for global and regional climate research. In many cases, remote sensing data on water pollution and quality is a single source of valuable information even if this is not a direct in-situ method of measurements. Direct and indirect (remote sensing) methods of measurements of water quality have their own instrumentation and techniques, as well as advantages and disadvantages characteristic for them.

It is of urgent necessity to develop the science basis and techniques for quantitative estimation of the state of marine environment. Here, the crucial point is evaluating pollution and metocean dynamics through a comprehensive analysis of satellite data. Certain inland (Mediterranean, Red, Baltic, Black, Caspian) and marginal (North, Barents, Kara) seas and large gulfs (Persian, Mexico, Guinea, Oman) are strongly affected by excessive human activity with a high risk of oil pollution, including shipping, exploration and development of off-shore oil and gas reserves, construction and operation of underwater pipelines, platforms, terminals, storage facilities, ports, etc. Shipping activities certainly causes serious harm to the marine environment, but in the case of discharge of oil-contaminated waters in the coastal zone. We consider such cases in this chapter. In the open ocean, such discharges usually do not take place. But the listed other sources of pollution have been causing more significant harm lately, which is demonstrated, in particular, by satellite monitoring.

First of all, we discuss sea surface oil pollution of anthropogenic origin. Satellite instrumentation and technique for oil pollution monitoring of the seas, as well as examples of oil pollution in different parts of the World Ocean will be presented in this chapter. Satellite instrumentation and technique for evaluation of water quality (suspended matter, algae, wastewater) in lakes and seas are presented in other chapters of this book.

Pollution of marine surfaces with oil-containing films is the main parameter of water pollution which is under satellite monitoring and attention of researchers during four decades starting from the launch of the SEASAT satellite on 27 June 1978 [4, 28, 31, 51, 56, 61, 70, 72, 73, 76]. Methods and technologies developed by scientists for satellite detection of oil pollution at the sea surface began to be applied in the practical monitoring systems [12, 13, 14, 35, 37, 40, 45–46, 50, 52]. For example, in

the Baltic Sea, HELCOM (Helsinki Commission) monitors and annually publishes summary maps of spatial distribution oil spills, but only those that were detected by aerial surveillance, and this is only a few dozen per year [40]. Much more oil spills are detected using satellite methods, for example, in the CleanSeaNet Project of the European Maritime Safety Agency (EMSA) or in the framework of daily operational satellite monitoring of oil pollution in the Southeastern Baltic Sea related to beginning of oil production at the Lukoil D-6 offshore oil platform in 2004 [11, 35, 45–47]. A significant difference between the EMSA cumulative maps of oil pollution and those produced for the Southeastern Baltic Sea is in the algorithms for automatic detection of oil pollution (derived from radar data only) used in EMSA and expert-based approach based on the integrated analysis of SAR (Synthetic Aperture Radar), IR (infrared), optical satellite imagery, meteorological and oceanographic data, as well as numerical modelling of oil spill drift and transformation (Seatrack Web) used for the Lukoil D-6 offshore oil platform monitoring. Our integrated approach to the oil spill monitoring allows significantly reduce the probability of false alarms which is a typical problem for automatic detection systems [40, 46, 50, 52].

Accurate detection of oil slicks in radar images is still an important issue. Quite a number of natural phenomena hamper reliable identification of oil on the sea surface because they produce similar signatures in radar images, especially at low wind. Such “look-alikes” include organic films, algal bloom, some types of ice and snow, water areas shaded by land features, rain cells, upwelling zones, internal waves, and calm water [50, 52]. According to EMSA, false oil spill alarm rate reaches 60% in the coastal zone. This can be clearly seen on the maps of identified oil pollution, which are formed annually by EMSA and are posted on their website. Figure 4.1 shows such a map for 2018. Red circles correspond to higher detection confidence level (Class A), green—a lower detection confidence level (Class B). As can be seen from the figure, the number of green circles prevails, especially in areas where regular observations from aircraft are not carried out.

Monitoring of oil pollution from space is usually carried out using the synthetic aperture radars (SAR) and advanced synthetic aperture radars (ASAR) installed on different satellites. A correct detection of oil spills requires a number of additional information on wind speed and direction, wave height and direction, water and air temperature, ice cover, algal bloom, structure and dynamics of surface mesoscale and sub-mesoscale currents and phenomena, atmospheric fronts to describe the manifestation, transformation and distribution of oil films [46, 50, 52]. Long-term monitoring of ecological state and oil pollution around the Lukoil D-6 offshore oil platform in the Southeastern Baltic Sea has shown that real-time numerical modelling of oil spill drift and transformation is of vital importance for such kind of monitoring systems in any part of the World Ocean [1, 16–20, 23, 33, 69, 81]. In case of the Lukoil D-6 monitoring we successfully used the Seatrack Web model of the Swedish Meteorological and Hydrological Institute (SMHI), which today has a spatial resolution of 2 nautical miles (n m) and a time step of 15 min [6, 36]. Seventeen-year long satellite monitoring of the Southeastern Baltic Sea has shown that mesoscale and sub-mesoscale vortical structures and water dynamics play a crucial role in the transport of the pollutants, thus even much more high spatial resolution is required in



Fig. 4.1 CleanSeaNet oil spill detection statistics for 2018: dots on the map represent the spills in the European seas which have a higher detection confidence level (in red) and a lower detection confidence level (in green) (<http://www.emsa.europa.eu/csn-menu/csn-service.html>)

numerical models. Recently, an ultra-high resolution circulation model (0.125 n grid) of the Southeastern Baltic Sea was compiled from the General Estuarine Transport Model (GETM) in order to simulate the mesoscale and sub-mesoscale eddy field in the area. The model results showed almost the digital twins of eddies revealed with daily optical and infrared satellite imagery available for the period of May–August 2015 [80]. Such kind of ultra-high resolution circulation models could significantly improve a forecast of the oil spill drift.

4.2 Physical Principles and Methods of Oil Spill Detection

Currently, radar (SAR) sounding in the microwave range is one of the main methods of remote study of both oceanic processes and processes of interaction between the ocean and the atmosphere. During the past four decades it showed effectiveness in oil spill detection on the sea surface. Radar survey technique is unique in that it obtains high resolution (up to several meters) images in a wide swath, day and night in any season and under any weather/cloud conditions. Active remote sensing of the ocean

surface is based on measuring variation of scattered radar signal. In case of a satellite-based synthetic aperture (SAR) or side-looking radar on the airplane the information about the parameters of the underlying surface is contained in the reflection function, which is observed in the form of an electromagnetic wave backscattered from the sea surface. The reflection function is determined both by the properties of the surface itself, and by the conditions of its formation, i.e., by the system emitted and received signals. The radar image of the sea surface depends on sensing electromagnetic range, polarization and angle of incidence of the radar signal [26, 50].

A radar emits an electromagnetic wave with a length λ , frequency $f = C/\lambda$, where C is speed of propagation of electromagnetic waves in the medium (in vacuum $3 \cdot 10^8$ m/s), the wave vector indicates the direction of propagation of the wave, as well as the polarization (horizontal or vertical) of the wave. The last property is very important, since the orientation the polarization plane relative to the reflecting surface depends on the wave reflection coefficient. The radar systems are designed to operate in horizontal (H) and vertical (V) planes. As a transmitted signal depolarizes when reaching the Earth surface, a specific SAR can operate in four different polarization combinations: HH, HV, VH, and VV. The first letter refers to the transmitted signal while the second letter refers to the backscattered signal. HH and VV signals are known as co-polarized signals, while HV and VH signals are known as cross-polarized signals [71].

Vertical polarization is used to study a wide class of processes and phenomena that manifest on the sea surface by modulating the gravitational-capillary component of the surface wave spectrum. Horizontal polarization, being less sensitive to variations in the small-scale roughness of the sea surface, is widely used for observing sea ice, and separating areas with ice cover from open water. Since the intensity of scattering by the sea surface is significantly reduced when using radiation and reception at cross polarizations (VH and HV), such modes are used to highlight objects on the sea surface that cause multiple scattering, such as ships and ice cover deformations (hummocks, cracks, cracked ice) [50].

Satellite radars of the first generation had the ability to monitor the Earth on one fixed polarization of the probing signal, the horizontal (HH), for example, the SAR on the Almaz-1, RADARSAT-1, Seasat, JERS-1 satellites, or the vertical (VV)—the SAR on ERS 1/2 satellites. The new generation of satellite radars installed on Envisat, RADARSAT-2 and TerraSAR-X have the ability to survey in various modes: VV, HH, VV/HH, VV/VH, HH/HV [50].

The spectral bands of SAR systems are specified by the following codes: K (0.8–2.5 cm); X (2.5–3.8 cm); C (3.8–7.5 cm); S (7.5–15 cm); L (15–60 cm); and P (60–120 cm). The SARs with wavelengths from 1.11 cm ($f = 27$ GHz) up to 30 cm ($f = 1$ GHz) are used for the ocean studies. Usually radars operate in a pulse mode, although continuous radiation is sometimes used.

The general principle for oil spills detection on the sea surface is known since ancient times when sailors used olive oil or other oily substances to spill over the sea surface to reduce waves around ships. We don't know how really effective was this method during storm conditions, but this physical mechanism works well in damping the gravity-capillary waves (with a characteristic wavelength of several centimeters)

which are always present on the sea surface. Different types of oil products can damp the gravity-capillary waves 10–30 times, and radars working on the same wavelength can easily discriminate water areas with developed from damped gravity-capillary waves. On SAR images water areas with damped gravity-capillary waves look like black zones because the emitted radar signal does not return back to the antenna. Grey areas on SAR images show zones from which the scattered (by gravity-capillary waves) radar signal partially returns back to the radar [3, 7, 21, 25, 31, 58, 74, 79]. Discharges which contain any kind of oil products will result in a formation of an oil slick. This is proved by numerous in-situ measurements done by the Baltic Sea countries and regularly published by HELCOM (<https://helcom.fi/wp-content/uploads/2020/01/HELCOM-Aerial-Surveillance-Report-20XX.pdf>), as well as by measurements in the North Sea [12], Mediterranean Sea [13, 14], and other regions of the World Ocean. Discharges which does not contain oil products will not result in slicks on the sea surface detected by SAR with the exception of, for example, palm or vegetable oils, but these are very rare cases, especially in large quantities.

There are two obstacles in correct detection of oil spills at the sea surface by this method. The first one is related to the fact that the damping of gravity-capillary waves works well at winds of about 3–8 m/s [50], because light winds do not generate capillary waves, and the sea surface is quasi-calm and smooth enough to reflect the radar signal without scattering back to the radar. This is the reason why calm water looks like an oil spill on the sea surface, as well as a real oil spill can be hidden when released on calm water. Wind force over about 8 m/s leads to wind-wave breaking, mixing in the upper layer, and formation of foam. All this destroys gravity-capillary waves on the sea surface and even an oil spill cannot smooth the sea surface enough to be detected by the radar. Thus, in stormy conditions the whole water area has a grey color where all peculiarities at the sea surface are hidden. The second issue is related to the natural look-alikes in the ocean and atmosphere mentioned above, which can also damp gravity-capillary waves and smooth the sea surface. Thus, radar will not be able to discriminate between an oil spill and a look-alike. Both issues are serious obstacles for a progress in automatic detection of oil spills in SAR images [4, 10, 22, 24, 27, 77]. To overcome this problem we use an expert-based approach which includes integrated analysis of SAR, as well as all available satellite, meteorological and oceanographic data for the area under investigation [46, 50]. Our long-standing experience shows that this integrated approach can significantly reduce the level of false alarms.

4.3 Satellites and Sensors

Different SAR systems have been installed on the following satellites [2, 29, 50, 52, 71]: the USA SEASAT with the first spaceborne SAR (27 June–10 October 1978), the USSR Kosmos-1980 (1988) and Almaz-1 (1991–1992), the ESA ERS-1 (1991–2000), the Japanese JERS-1 (1992–2008), the ESA ERS-2 (1995–2011), the Canadian Radarsat-1 (1995–2013), the ESA Envisat (2002–2012), the Japanese ALOS

(2006–2011), the Canadian Radarsat-2 (2007–present), the German TerraSAR-X (2007–present), the Italian COSMO SkyMed (2007–present), the Indian RISAT-2 (2009–present), the German TanDEM-X (2010–present), the Indian RISAT-1 (2012–2017), the Chinese Huanjing-1C (2012–present), the ESA Sentinel-1A (2014–present), the Japanese ALOS-2 (2014–present), the ESA Sentinel-1B (2016–present), the Argentina SAOCOM (2018–present), and the Canadian Radarsat Constellation Mission with three identical spacecrafts (2019–present). Sentinel-1A and Sentinel-1B SAR data are the only ones that are freely available on the internet. SAR imagery can be downloaded from the ESA Copernicus Open Access Hub platform (<https://www.sentinel-hub.com/>). Spatial resolution of the modern SAR systems installed on the satellites is of 1–5 m [71]. Table 4.1 shows the main characteristics of SAR systems installed on different satellites.

For a brief example let us take the ASAR that was once mounted on the Envisat satellite and widely used for oil pollution monitoring in oceans and seas. It had a phased array antenna with an incidence angle from 15° to 45° and operated in C-band (5.7 cm) in five polarization modes (VV, HH, VV/HH, HV/HH, VH/VV). The obtained data were used in many applications beside oil spill monitoring, such as determining ice cover and ship location and studying some oceanic (currents, fronts, eddies, internal waves) and atmospheric (internal gravity waves, convection, atmospheric fronts and vortices) phenomena and processes. The ASAR design allowed adapting the survey configuration (polarization, resolution, swath width) to the specifics of the object of observation.

The ASAR Wide Swath Mode (WSM) surveying provided the ability to survey in a 400 km swath with a spatial resolution of 150 m × 150 m at one of the selected polarizations of the signal (VV or HH) and allowed obtaining radar images of the same area with a period of repeated observations from 1 day in the polar regions to 1 week at the Equator. Alternating Polarization Mode (APM) allowed receiving simultaneous image pairs of the underlying surface formed at different combinations of polarizations of the radiated and received radar signals, namely VV/HH, HH/HV and VV/VH in a 100 km wide swath and with a spatial resolution of up to 30 m. When working in a narrow swath (Image Mode), the phased antenna array by changing the angle of radiation of the signal allowed to select any of 7 bands and obtain an image with a high spatial resolution (30 m × 30 m) at one of the selected polarizations VV or HH ranging in size from 56 km (7th band) to 100 km (1st band). Envisat completed its work in orbit on April 8, 2012. Since 2014, Sentinel –1A/–1B data, which is freely available from ESA, have become the most widespread.

4.4 Examples of Oil Spill Pollution

In this Section we present examples of oil pollution of the ocean surface acquired by different satellites. From April 20 to May 28, 2010 we daily followed the evolution of oil pollution in the Gulf of Mexico which resulted from the accident on the *BP Deepwater Horizon* oil platform that occurred on April 20, 2010 [49, 50]. The

Table 4.1 The main characteristics of SAR systems on satellites (based on data presented in [29, 50, 52, 71])

	SEASAT	ERS-1/2	Almaz-1	JERS-1	Radarsat-1	Envisat	Radarsat-2	Terra-SAR-X	Sentinel-1 A/B
Country/agency	USA	ESA	USSR	Japan	Canada	ESA	Canada	Germany	ESA
Year of launch	1978	1991/1995	1991	1992	1995	2002	2007	2008	2014/2016
Range	L	C	S	L	C	C	C	X	C
Frequency, GHz	1.275	5.25	3.1	1.275	5.3	5.7	5.3	9.65	5.405
Wavelength, cm	23.5	5.66	9.6	23.5	5.66	5.66	5.66	3.13	5.55
Polarization	HH	VV	HH	HH	HH	HH, VV, VH, HV	HH, VV, VH, HV	HH, VV, VH, HV	HH/HV, VV/VH
Incidence angle, °	20	23	17–62	39	20–50	15–45	20–60	20–55	18.3–47
Swath width, km	100	100	30–60	75	50–500	56–400	18–500	10/30/100	80/250/400
Spatial resolution, m	25	25	25	18	8–100	25–150	3–100	1/3/16	3.5–40

development of the situation was traced on the basis of a joint analysis of optical (MODIS-Aqua, MODIS-Terra) and radar images (ASAR Envisat), which proved to be very effective since the optical images made it possible to exclude from consideration the areas of calm water on the ASAR images (Fig. 4.2). Also, the radar images gave more complete information about dimensions of the areas covered with oil films indiscernible on optical images. The uniqueness of this accident was in a very large oil spill (up to 23,000 km²) which was continuously fed during several months by

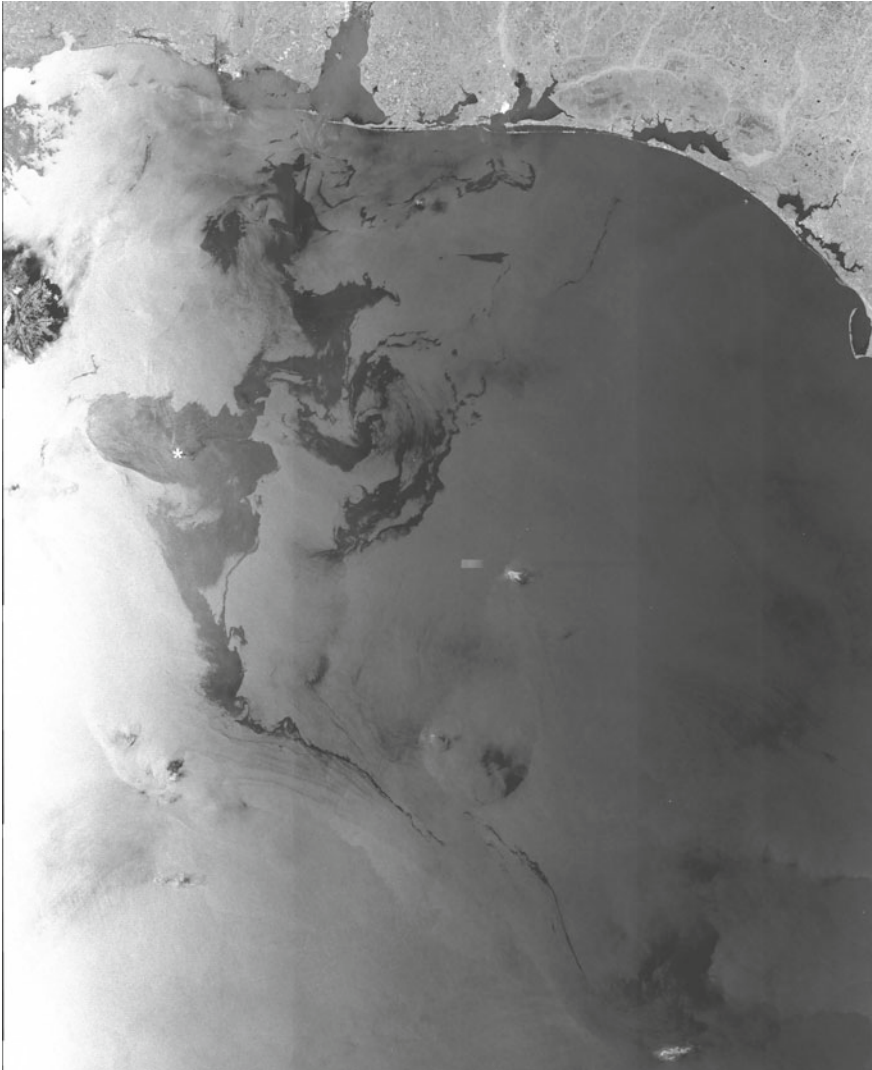


Fig. 4.2 Oil spills (black patches) in the northern part of the Gulf of Mexico on the ASAR Envisat image obtained on June 3, 2010 (03:44 UTC). The accident area is asterisked. (© ESA, 2010)

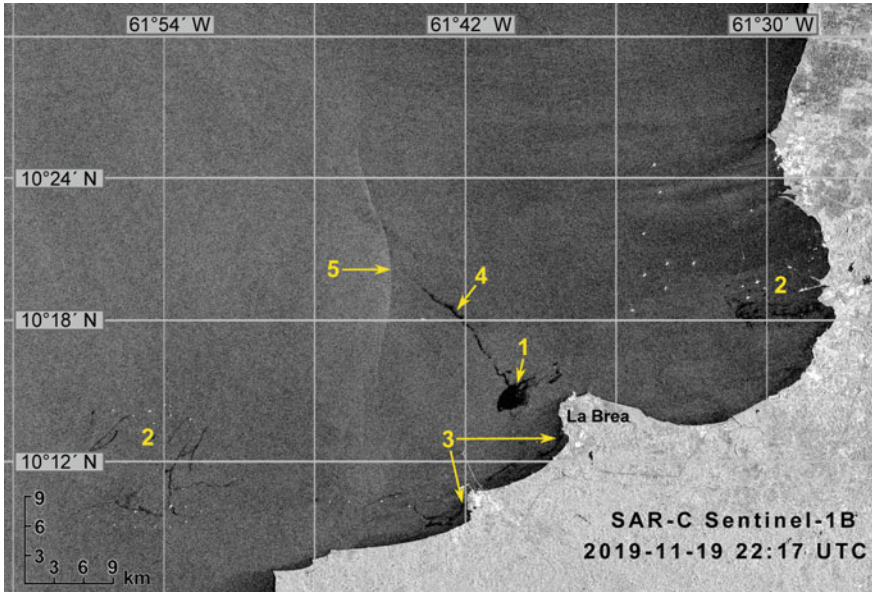


Fig. 4.3 Oil spills off Point Fortin, southwestern Trinidad, the Caribbean (SAR C Sentinel-1B, 19 November 2019, 22:17 UTC). See text for explanation of numbers

oil flux from a well with a discharge of about 800 ton per day at a depth of 1500 m on the seafloor [49]. This ecological catastrophe was one of the largest in the US history.

Figure 4.3 shows western coast of Trinidad and Tobago, the Caribbean on 19 November 2019. Several oil spills were observed in the coastal zone off Point Fortin: (1) oil spill from the anchored ship, oil spill area is of 3.5 km²; (2) oil pollution at anchorage of ships; (3) wastewater discharges from coasts; (4) discharge from a moving vessel, length of oil spill is of 6.5 km; (5) surface manifestation of internal wave train. Point Fortin, officially the Republic Borough of Point Fortin, the smallest Borough in Trinidad and Tobago, is located in southwestern Trinidad. After the discovery of oil reserves in the area in 1906, the town grew into a major oil-producing center with an economic culmination between the 1940s and 1980s. A construction of a liquefied natural gas plant by Atlantic LNG in late 1990s revived the economy. The LNG terminal is located in the Port of Point Fortin.

Another area of regular oil pollution is in the eastern part of the Gulf of Guinea at the confluence of the three branches of the Niger River, as shown by long-term satellite observations (Fig. 4.4). The largest area of marine surface pollution was caused by an accidental discharge. On 20 December 2011, the Shell's Bonga offshore oil spill of 40,000 barrels resulted from the routine transfer of crude oil from the *Bonga* floating production, storage and offloading vessel (FPSO) to a waiting oil tanker in the Gulf of Guinea [44]. An export line linking the FPSO and the tanker was identified as the likely source of leakage. It was likely the largest oil spill which

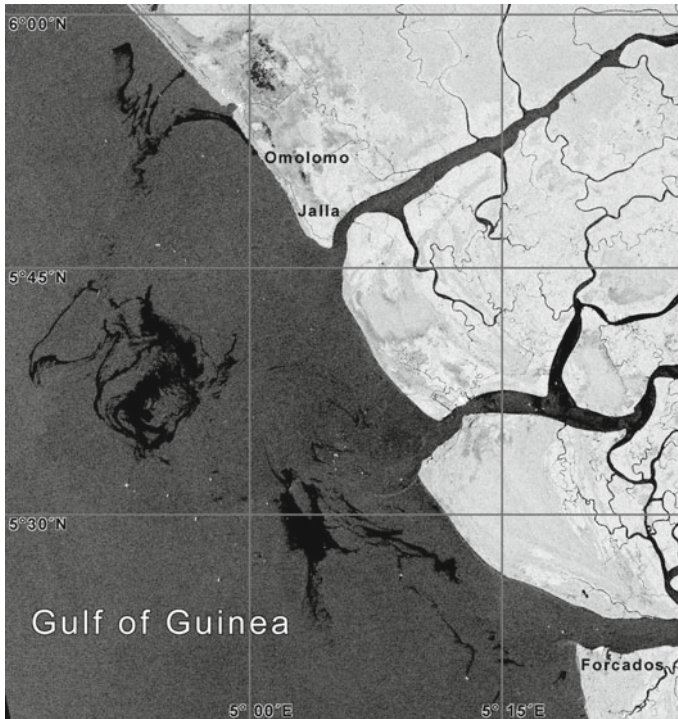


Fig. 4.4 Oil pollution in the Gulf of Guinea. (SAR C Sentinel-1A, 08 February 2022, 17:53 UTC) (©ESA 2022). Ships in the sea are visible as bright white dots

had occurred offshore Nigeria since 1998. The spill was clearly detected on the ASAR Envisat image acquired on 21 December 2011, 09:30 UTC, as well as quite well visible on the MODIS-Terra optical image. At the acquisition time, the spill was 80 km long, 15 km wide, and had a total area of 923 km². Beside this huge oil spill in the region of the *Bonga* FPSO vessel, a number of other cases of oil pollution of coastal waters were identified in the same ASAR image of 21 December 2011 [44]. The total area of 11 large spills, excluding the *Bonga* one, was over 100 km². Moreover, three river plumes from the Niger River arms polluted with oil products were also detected with a total area of 78 km² [44]. Terleeva et al. [75], based on the analysis of ASAR Envisat medium resolution imagery taken off western coast of Central Africa for 2003–2009, showed that the largest number of oil spills was observed along the coast of Nigeria (148), Cameroon and Equatorial Guinea (98), Ghana (49), Cote d’Ivoire (31), and Togo/Benin (9). Individual oil spill area varied from 0.5 to 80 km². These case studies, based on irregular satellite information, confirm that coastal waters of Nigeria are highly polluted.

Figure 4.5 shows numerous ships visible as bright white dots and oil spills in the Hormuz Strait, the Persian Gulf, in front of Port of Bandar Abbas on 4 April 2020. Bandar Abbas is a port city and capital of Hormozgān Province on the southern coast

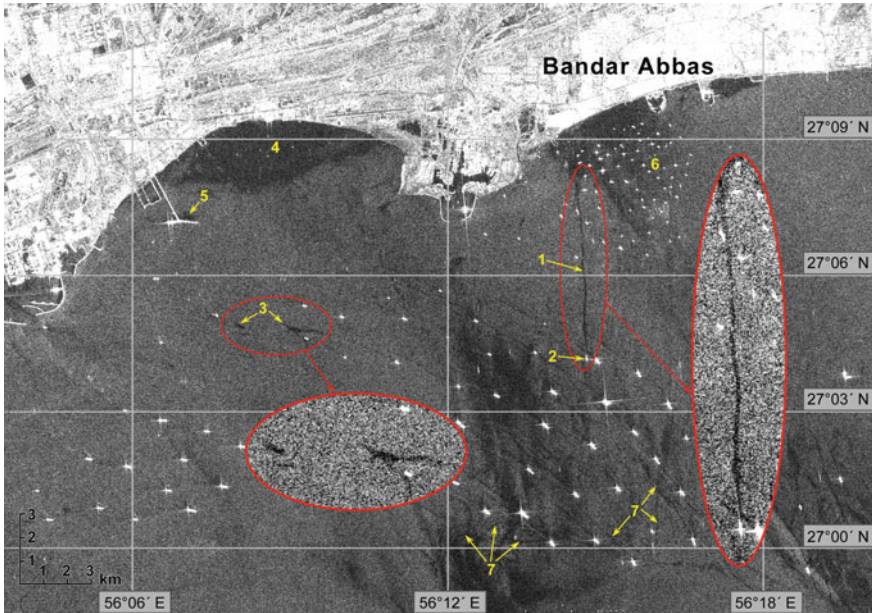


Fig. 4.5 Oil spills off Bandar Abbas in the Hormuz Strait, the Persian Gulf (SAR C Sentinel-1A, 4 April 2020, 14:17 UTC). See text for explanation of numbers

of Iran on the Persian Gulf. The port occupies a strategic position in the narrow Strait of Hormuz, and it is the location of the main Iranian Navy base. A significant part of the trade between Iran and other countries of the world is carried out through this port. Numbers on the Fig. 4.5 show: (1) discharge from a moving vessel, length of oil spill is of 5 km; (2) ship from which polluted water was discharged; (3) oil spill from the anchored ship; (4) near-shore area of turbid water; (5) wastewater discharges from a pier; (6) ships; (7) accumulation of films of surface-active substances (biogenic films) in convergent zones of currents.

Sentinel-1A and Sentinel-1B SAR imagery for 2018 and 2019 clearly reveal cases of oil pollution in the Port of Suez (Gulf of Suez, the northern part of the Red Sea) (Fig. 4.6), as well in the areas of major tourist resorts of Egypt on the Red Sea [34]. We found that the dirtiest area in the Northern Red Sea is the Port of Suez area where ships are waiting for the passage through the Suez Canal. A series of SAR images for different dates of 2018–2019 showed that almost in every satellite image there is one or several oil spills, as well as films of surface active substances (oily and waste waters). The coastal zones around Hurgada and Sharm el-Sheikh resorts looks quite clean, but even here small-size oil spills occur as well [34]. Egypt seems to be at risks of oil pollution impacts because it has a series of largest tourist resorts stretched for dozens of km along the coast, and the extensive shipping traffic which goes to the Gulf of Suez and further via the Suez Canal to the Mediterranean Sea, as well as

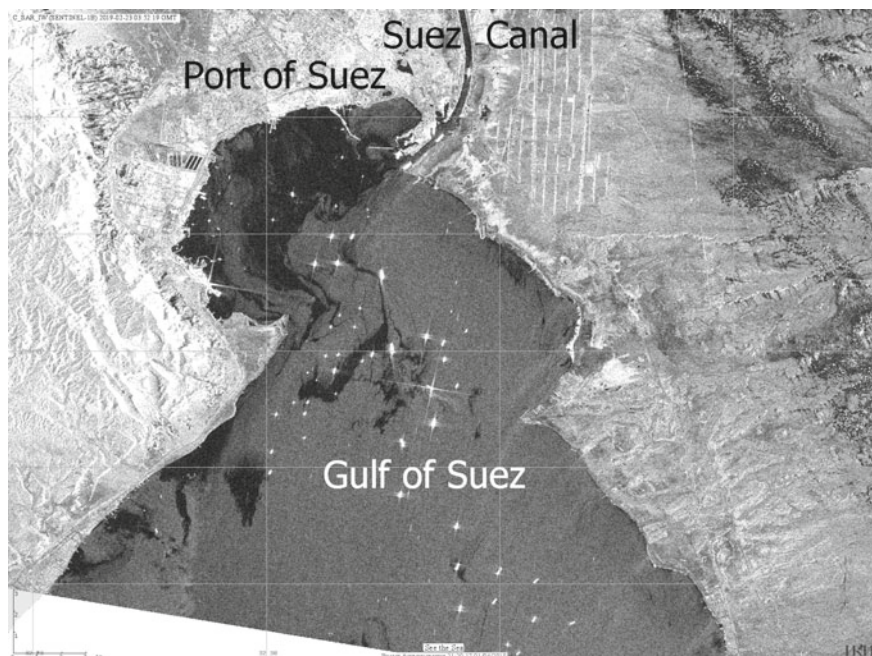


Fig. 4.6 SAR-C Sentinel-1B image of Port Suez in the Gulf of Suez on 23 February 2019, 03:52:19 GMT. Black patches are oil spills and white dots are ships

to the Gulf of Aqaba. This ship traffic carries about 15% of all global maritime trade and 10% of global seaborne oil passing through the Red Sea and the Suez Canal.

It is evident that the above mentioned ship traffic should have the same oil pollution effect on the other side of the Suez Canal in the Southeastern Mediterranean Sea. About 17,550 ships passed through the Suez Canal in 2017. Beside the very busy ship traffic in the Mediterranean waters of Egypt, in the last decade, there has been a substantial development of offshore gas and oil fields along the Mediterranean coasts of Egypt, where the most active companies are BP, BG, Eni, IEOC, EGAS, Total, RWE Dea and Dana Gas [39]. Indeed, our preliminary research for oil pollution in coastal waters of Egypt based on the analysis of the Sentinel-1A and Sentinel-1B SAR imagery for 2017–2019 showed large concentration of oil spills in the offshore area between Damietta and Port Said, which coincides both with maritime traffic related to the Suez Canal and offshore activities related to gas exploration and production (Fig. 4.7). Two dozen SAR images showed that almost in every satellite image there is one or several oil spills, as well as films of surface-active substances (oily and waste waters) in the coastal waters of Egypt [39].

The port of Kaliningrad is situated on the southeastern coast of the Baltic Sea. The only Russia's ice-free port on the sea, it comprises a commercial sea port, a river port, a sea fishing port and Kaliningrad Sea Canal. Container lines connect to the Netherlands, UK, Germany, Poland and Lithuania. In 2010–2020, Kaliningrad port

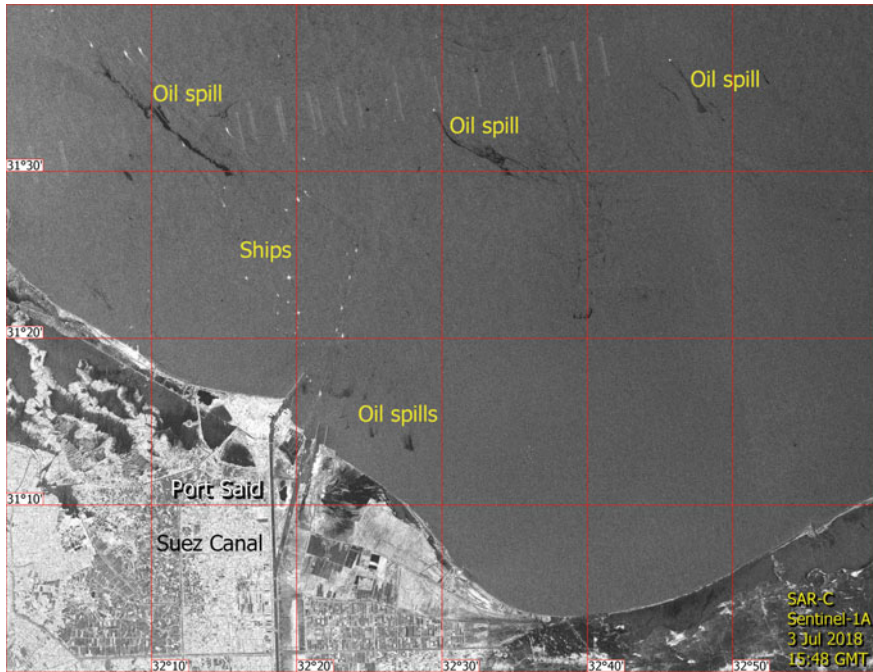


Fig. 4.7 SAR-C Sentinel-1A image of oil pollution offshore of Port Said, the Southeastern Mediterranean Sea on 3 July 2018, 15:48 GMT. Black patches are oil spills and white dots are ships and offshore platforms

turnover ranged 2–4 million tons. Vessels are awaiting pilotage to the port anchor at the entrance to Kaliningrad Sea Canal, near the town of Baltiysk. In the Russian Baltic, the risk of oil pollution is mostly associated with tanker and ship traffic to and from the port of Kaliningrad.

In 2004, a complex environmental monitoring project was launched by LUKOIL-Kaliningradmorneft in connection to offshore oil production at Kravtsovskoye (D-6) field. The platform is mounted on the sea bottom at a depth of 30 m, at a distance of 22.5 km from the Curonian Spit and 8 km from the Lithuanian sea border. The monitoring routine included satellite remote sensing of oil pollution in the vicinity of the platform and in a larger adjacent area of about 60,000 km² in the southeastern Baltic, i.e. nearly 1/6 of the total Baltic Sea area. Operational receiving, processing and analysis of various data from ENVISAT ASAR, RADARSAT SAR, NOAA AVHRR, Terra/Aqua MODIS, TOPEX/Poseidon, and Jason-1 instruments was organized on a daily basis in order to accurately detect oil spills and effectively reduce false alarms from look-alikes [11, 35, 43, 45–48]. It is noteworthy that this near-real time monitoring system, that we organized in 2004, was the first one in Russia and up to date remains the only such system still in operation.

Since 2003, satellite monitoring of oil pollution in the Baltic, Black and Caspian Seas has been regularly performed by Space Research Institute of Russian Academy

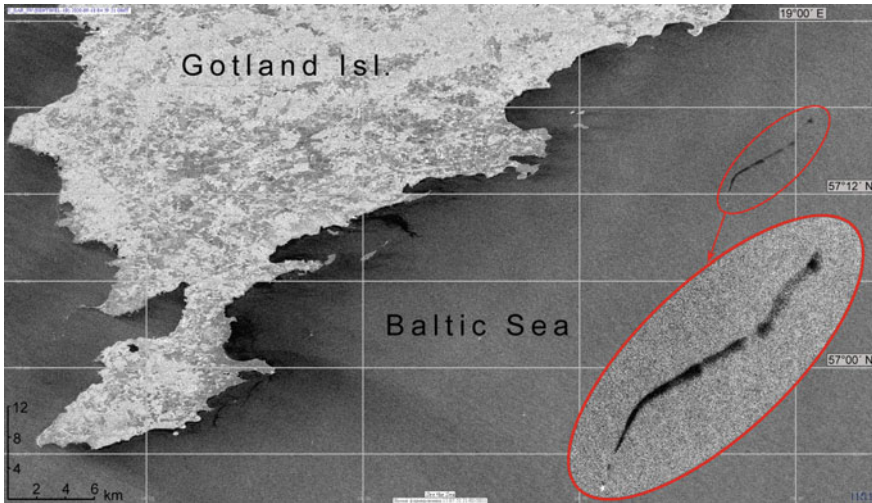


Fig. 4.8 Oil spill detected near Gotland Island in the Baltic Sea on SAR-C Sentinel-1B, 18 September 2020, 04:59 UTC

of Sciences in the framework of national and international research projects. This unique monitoring with an analysis of several thousands of SAR images gave detailed statistical information on the spatial and temporal distribution of oil spills as well as individual characteristics of oil spills detected.

For example the monitoring of the Southeastern part of the Baltic Sea [44, 52] showed that the individual oil spill area varied from 0.1 to 105 km², and yearly total surface of oil pollution varied from 150 to 830 km² [11, 47]. The largest number of oil spills is regularly found along the main shipping routes. Figure 4.8 shows one of the recent examples of oil spills detected along the shipping route east of Gotland Island. Length of oil spill is of 11.5 km.

Satellite monitoring for the Black Sea showed that similar to the Baltic, North and Mediterranean seas, the detected oil spills are accumulated along the main shipping routes coming to the main ports and sea terminals. For the Black Sea, these are routes from the Bosphorus Strait to Odessa (Ukraine), Kerch Strait between the Black Sea and the Sea of Azov, Novorossiysk (Russia), and ports of Georgia [8, 9, 50, 52, 59, 62, 72]. Figure 4.9 shows one of the recent examples of oil spills detected in the Black Sea. Numbers 1 and 2 indicate discharges of water containing oil products from standing ships. The area of spot 1 was 1.5 km², and spot 2 was 1.6 km². The length of oil slick 3 caused by a discharge from a moving vessel was 21.4 km.

Satellite monitoring of oil pollution in the Caspian Sea [50, 52, 53, 60, 63, 64] allowed to show that the most polluted area of the Caspian Sea is located around Neftyanje Kamni (Oily Rocks), one of the oldest oil production area located eastward of Absheron Peninsula, Azerbaijan [52, 64]. Figure 4.10 shows one of the recent examples of oil spills detected around Neftyanje Kamni and other offshore

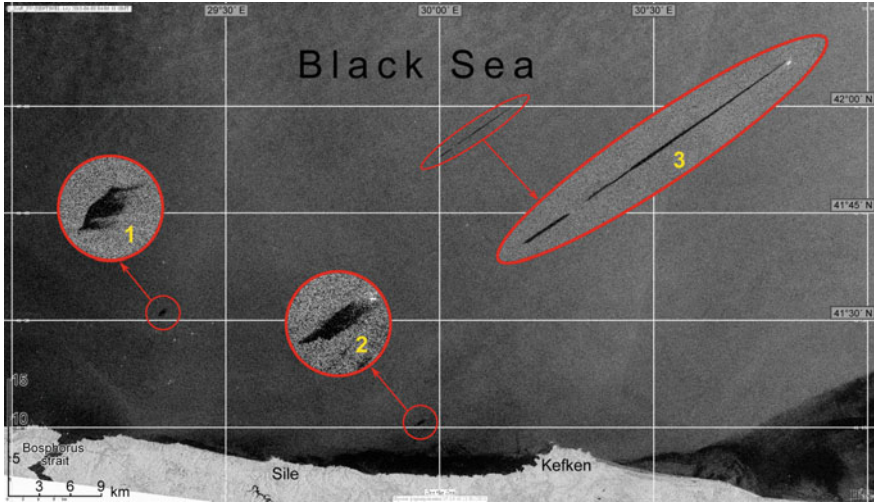


Fig. 4.9 Oil spills detected in the Black Sea eastward of the Bosphorus Strait on SAR-C Sentinel-1A, 08 June 2018, 04:06 UTC. See text for explanation of numbers

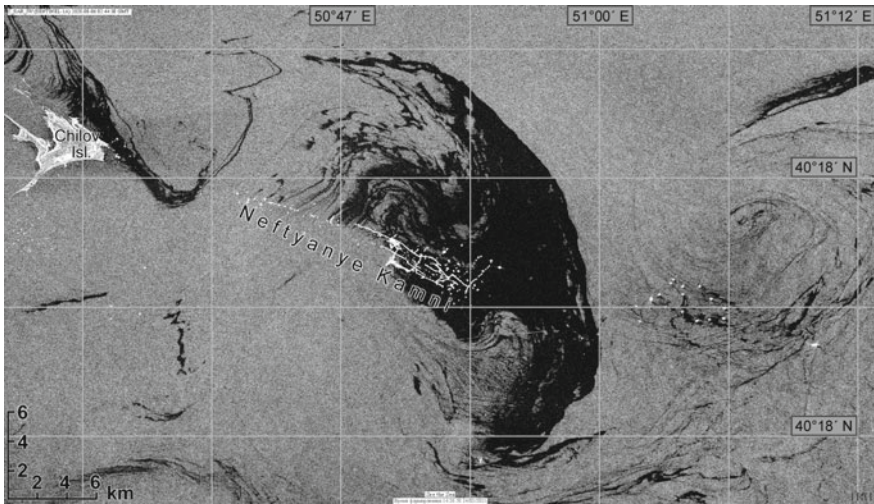


Fig. 4.10 Oil spill detected around Neftyaneye Kamni in the Caspian Sea on SAR-C Sentinel-1A, 06 August 2020, 02:44 UTC

oil platforms in the Caspian Sea. The area of oil spill around Neftyaneye Kamni is 251 km².

Discharges from ships in the Caspian Sea are identified in SAR images much less frequently than oil pollution around offshore oil platforms or petroleum hydrocarbons emission from the seabed [64], and they are usually observed along shipping routes.

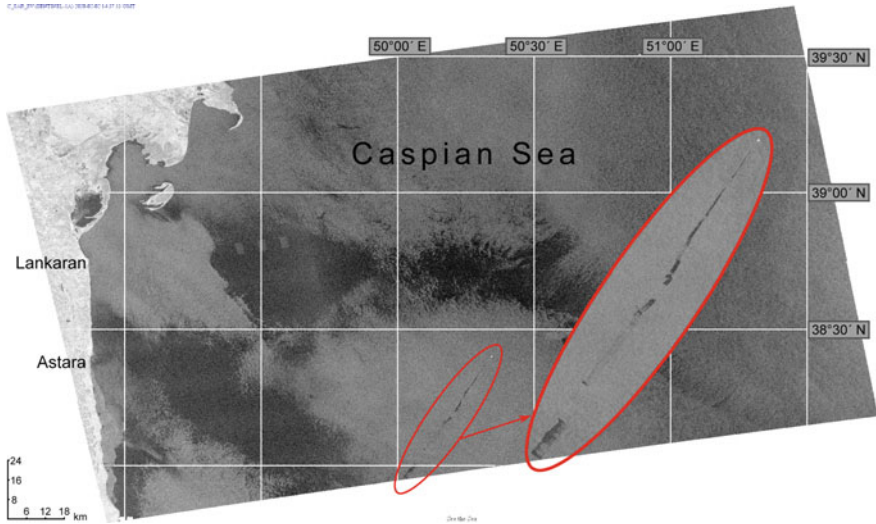


Fig. 4.11 Oil spill detected in the south-eastern part of the Caspian Sea on SAR-C Sentinel-1A, 02 February 2020, 14:37 UTC

Figure 4.11 shows just such a case. The length of the oil slick caused by a discharge from a moving vessel is 56 km.

4.5 Discussion

Forty-year-long history of SAR application in satellite monitoring of oil pollution has proved the efficiency of this kind of instruments and methods for reliable detection of oil spills on the sea surface. Of course, there are some weather restrictions for use of SAR systems as well as natural look-alikes caused by different ocean and atmosphere features and processes, but they do not outweigh the benefits of this remote sensing method. We can list the following advantages of SAR systems in oil spill detection:

1. Round-the-clock work due to the use of active sensing, and the image characteristics do not depend on the time of the day and solar illumination (night, Polar night);
2. Imaging is almost independent of the weather because microwave radiation freely penetrates the atmosphere and clouds;
3. The uniformity of water microwave dielectric properties implies that backscatter variations originate only from the geometry of the disturbances, which makes satellite data interpretation far less complicated;;
4. High spatial resolution (several meters) in a wide swath (300–400 km);
5. Regular monitoring (up to daily, and even several times per day) of any water areas of the World Ocean remotely;

6. Possibility to organize near-real-time monitoring, a SAR image can be received 30–60 min after a satellite passage over the monitoring area;
7. Low cost of satellite monitoring in comparison with aerial surveillance and ship patrolling.

Concerning the drawbacks of this method, we can list the following issues:

1. Presence of look-alikes on the sea surface (see Table 4.2).
2. Restrictions related to wind speed of 3–8 m/s, when this method works well. Big problems in identification of oil spills arise in calm water and storm conditions.
3. Difficulties in oil spill detection in presence of sea ice.
4. Relatively high cost of one SAR image, which is a problem for scientific research, which sometimes requires hundreds of images. The cost of SAR

Table 4.2 The main types of the oil spill “look-alikes” and their radar manifestations on the sea surface

Hydrophysical process	The shape of the manifestation on the radar image	Areas of origins	Hydrometeorological conditions
Biogenic surface films	Display the structure of surface currents	Coastal zones	Destroyed when wind speed >7 m/s
Local wind weakening areas	Extensive areas of reduced backscattering	Everywhere	Wind speed <2 m/s
Areas of wind shadows	Areas of reduced backscattering oriented along the wind direction	In the vicinity of the mountainous terrain shoreline	Even with strong winds up to 15 m/s
Rain cells	Light-colored cellular structures with a dark center	Everywhere	Intense rains and strong winds
Boundary of the hydrological or atmospheric front	Wide dark band with irregular edges, which are caused by unsteadiness of the frontal zone	Everywhere	Presence of a hydrological or atmospheric front
Ocean internal waves	Thin quasi-periodic bands of radar signal amplification and attenuation	Continental slope	Wind speed <8 m/s
Atmospheric internal gravity waves	Wide quasi-periodic bands of radar signal amplification and attenuation	Everywhere	Stable stratification of the near-water atmospheric layer, shear currents in atmosphere
Young ice	Extensive areas of reduced radar scattering	Usually near shoreline, at the edge of the ice sheet	Cold season
Areas with algal bloom	Low backscatter levels	Everywhere	Warm season

imagery significantly increases in the direction of the near- and real-time monitoring, when satellite data are delivered in one or several hours. Sentinel-1A and Sentinel-1B SAR data are the only ones that are freely available on the internet now, but with a delay of about a day.

Automatic identification of oil pollution leads to a large false alarm in the case of oil look-alike on the sea surface. It is especially difficult to distinguish between anthropogenic and biogenic films. For confident detection of exactly oil pollutions an expert analysis is required. The expert takes into account all local peculiarities, hydrometeorological factors like wind speed, atmospheric fronts, rain, ice cover, upwelling, water dynamics, as well as algal bloom, and previous SAR images. When possible, satellite optical data are used as additional information on the sea surface.

We have to note also, that oil pollution monitoring in the Mediterranean, North, Baltic Seas, as well as in USA and Canada is normally carried out by special patrol aircrafts and ships. Different countries have different number of patrol aircrafts which are equipped by different sets of the monitoring instruments from simple visual observations to a complete set of the following sophisticated sensors, which should be regarded as remote sensing instruments as well [5, 30]:

- Side-Looking Airborne Radar (SLAR);
- Infrared/Ultraviolet (IR/UV) sensor which is a passive sensor using reflected sunlight in the ultraviolet region (0.32–0.38 micron) for detecting oil spills;
- Microwave radiometer (MWR) which is a passive sensor and is used for oil spill detection and oil thickness measurements. Oil emits stronger microwave radiation than water and appears brighter than the water (which is dark in the background);
- Laser FluoroSensors (LFS) and Scanning Laser Environmental Airborne Fluorosensor (SLEAF) sensors were found to be the best available sensors for oil spill detection since they both detect and classify oil on all surfaces and also operate in the day or night conditions;
- Forward-Looking InfraRed (FLIR) camera provides longwave infrared imaging for oil spill detection in field conditions;
- Laser-Ultrasonic Remote Sensing of Oil Thickness (LURSOT) sensor which detects the oil based on its acoustic or mechanical properties rather than its optical and electromagnetic properties. Absolute oil thickness can be measured using this technique. The laser-acoustic sensor is an active sensor and can operate day and night;
- Video camera for recording visual observations of oil pollution.

Aerial surveillance has its own advantages and disadvantages in comparison with satellite remote sensing. The surveys are expensive and depend on the availability of multiple instruments, weather conditions and time of the day. As a rule, they are conducted in daylight in good weather. Very often sea areas under monitoring are located far from the base airports for patrol aircrafts, and it takes time to go to the oil spill location and back. Usually, aircrafts cannot perform transboundary monitoring flights over water area of the neighboring country. Aerial survey theoretically requires

about 10 flight hours to monitor the area of $300 \text{ km} \times 300 \text{ km}$ which is a typical frame for one Radarsat SAR image taken instantly.

To rise the efficiency of the aerial surveillance authorities have to improve the tactics of aerial observations, which has to take into account the real traffic along the main ship routes, operational information from the AIS and port authorities, to increase the number of night flights, and probably to use unmanned aerial vehicles (UAV), which have now a wide range of research and civilian applications, as well as more than 12 h endurance and range more than 200 km [41].

Satellite remote sensing of oil pollution allows to build accumulative maps of oil spills detected in different seas during years (see Fig. 4.1 as an example). These maps can be found in the following publications: for the Baltic Sea [11, 47, 48], the Mediterranean Sea [13, 14], the Black Sea [52] and the Caspian Sea [52, 63]. Having such a huge statistics on oil spills and general information on oil pollution it is interesting to get an answer to the question—what is the level of oil pollution of the World Ocean and inland seas?

Kostianoy and Lavrova [42] and Carpenter and Kostianoy [15] summarized the following information on the oil pollution in different seas:

1. Total yearly oil pollution of the World Ocean from all sources is estimated at 1.7 to 8.8 million tons (the more realistic value was about 3.2 million tons) in 1970s [32, 65], 0.47–8.3 (1.3) million tons in 1990s [68], and 2.6–4.8 million tons in 2000s [57], which is about 0.05–0.1% from the world oil production (4.76 billion tons in 2011).
2. Oil pollution of the Baltic Sea is estimated at 20–60,000 tons per year. The realistic value seems to be between 1000 and 5000 tons [42].
3. Oil pollution of the North Sea is estimated at 15,000–60,000 tons per year plus the authorized dumping of 10,000–20,000 tons [66, 67].
4. In the Mediterranean Sea it has been estimated at 1600–1,000,000 tons per year. The realistic value seems to be between 50,000 and 100,000 tons per year [15, 38, 78].

4.6 Conclusions

In summary, we have to admit that the real amount of oil pollution in the World Ocean and inland seas is still unknown. According to various sources, both the number of observed spills and total volume of spilt oil differ dramatically, sometimes a thousand times. An obvious explanation lies with the differences in the observation techniques, i.e. aerial surveillance, satellite monitoring, and in-situ measurements with varying instruments. Oil spill statistics obtained by different techniques are incomplete and incomparable even within one sea. There is a variety of factors that matter: the number of patrol ships, aircrafts and helicopters per country and per unit of the sea area; the number of flight hours per country and per unit of the sea area; the number of night flight hours; availability of different sensors on the aircrafts; usage of the satellites, etc.

As long-term experience shows, the satellite-based synthetic aperture radar remains the principal instrument for oil pollution monitoring. In spite of the known disadvantages mentioned above (dependence on wind speed, oil look-alikes, etc.), it allows receiving high spatial resolution data on an operational basis. In order to reduce the percentage of false alarms, it is reasonable to use an integrated approach to monitoring that combines multisensor and multiplatform satellite survey with analysis of metocean data and local water area features with the help of qualified and experienced operators. For operational monitoring of large water areas, e.g. the entire Mediterranean Sea, it is necessary to develop methods of automatic detection of oil pollution.

Acknowledgements The research was partially funded in the framework of the Russian Science Foundation no. 19-77-20060 Project «Assessing ecological variability of the Caspian Sea in the current century using satellite remote sensing data» (2019–2022). This publication was prepared in the framework of the scientific activities related to “The Caspian Sea Digital Twin” Programme performed in the framework of the UN Decade on Ocean Science for Sustainable Development (2021–2030).

References

1. Ainsworth CH, Chassignet EP, French-McCay D, Beegle-Krause CJ, Berenshtein I, Englehardt J, Fiddaman T, Huang H, Huettel M, Justic D, Kourafalou VH, Liu Y, Mauritzen C, Murawski S, Morey S, Özgökmen T, Paris CB, Ruzicka J, Saul S, Shepherd J, Socolofsky S, Solo Gabriele H, Sutton T, Weisberg RH, Wilson C, Zheng L, Zheng Y (2021) Ten years of modeling the Deepwater Horizon oil spill. *Environ Model Softw* 142:105070, <https://doi.org/10.1016/j.envsoft.2021.105070>
2. Alpers W (2014) Remote sensing of African coastal waters using active microwaves instrument. In: Barale V, Gade M (eds) *Remote sensing of the African Seas*. Springer, Netherlands, pp 75–94
3. Alpers W, Hühnerfuss H (1989) The damping of ocean waves by surface films: a new look at an old problem. *J Geophys Res* 94:6251–6265
4. Alpers W, Holt B, Zeng K (2017) Oil spill detection by imaging radars: challenges and pitfalls. *Rem Sens Environ* 201:133–147. <https://doi.org/10.1016/j.rse.2017.09.002>
5. Al Shammari A (2018) Oil spills detection by means of UAS and inexpensive airborne thermal sensors. Open Access Master's Thesis, Michigan Technological University, p 70. <https://doi.org/10.37099/mtu.edu/dc.etr/607>
6. Ambjörn C, Liungman O, Mattsson J, Håkansson B (2014) Seatrack web: the HELCOM tool for oil spill prediction and identification of illegal polluters. In: Kostianoy A, Lavrova O (Eds.) *Oil pollution in the Baltic sea. The handbook of environmental chemistry*, vol 27. Springer, Berlin, Heidelberg. https://doi.org/10.1007/978-3-642-21112-0_120
7. Bass FG, Puzenko SA (1994) Detection of oil spills on the sea using radar measurements. *J Electromagn Waves Appl* 8(7):859–870. <https://doi.org/10.1163/156939394X00623>
8. Bedritskii AI, Asmus VV, Krovotyntsev VA, Lavrova OYu, Ostrovskii AG (2007) Satellite monitoring of pollution in the Russian sector of the Azov and Black Seas in 2003–2007. *Russ Meteorol Hydrol* 32(11):669–674
9. Bedritskii AI, Asmus VV, Krovotyntsev VA, Lavrova OYu, Ostrovskii AG (2009) Space monitoring of pollution of the Russian sector of the Azov-Black Sea basin in 2008. *Russ Meteorol Hydrol* 34(3):137–147

10. Brekke C, Solberg A (2005) Oil spill detection by satellite remote sensing. *Rem Sens Environ* 95:1–13
11. Bulycheva EV, Krek AV, Kostianoy AG, Semenov AV, Joksimovich A (2016) Oil pollution in the Southeastern Baltic Sea by satellite remote sensing data in 2004–2015. *Transp Telecommun* 17(2):155–163
12. Carpenter A (ed) (2016) Oil pollution in the North Sea. Springer International Publishing AG, Cham, Switzerland, p 312. <https://doi.org/10.1007/978-3-319-23901-9>
13. Carpenter A, Kostianoy AG (eds) (2018a) Oil pollution in the Mediterranean sea: Part I—the international context. Springer International Publishing AG, Cham, Switzerland, p 350. <https://doi.org/10.1007/978-3-030-12236-2>
14. Carpenter A, Kostianoy AG (eds) (2018b) Oil pollution in the Mediterranean sea: Part II—national case studies. Springer International Publishing AG, Cham, Switzerland, p 291. <https://doi.org/10.1007/978-3-030-11138-0>
15. Carpenter A, Kostianoy AG (2018c) Conclusions for Part I: the international context. In: Carpenter A, Kostianoy AG (eds) Oil pollution in the Mediterranean sea: Part I—the international context. Springer International Publishing AG, Cham, Switzerland, pp 325–344
16. Cheng Y, Li X, Xu Q, Garcia-Pineda O, Andersen OB, Pichel WG (2011) SAR observation and model tracking of an oil spill event in coastal waters. *Mar Pollut Bull* 62(2):350–363. <https://doi.org/10.1016/j.marpolbul.2010.10.005>
17. Cucco A, Daniel P (2018) Numerical modeling of oil pollution in the Western Mediterranean sea. In: Carpenter A, Kostianoy A (eds) Oil pollution in the Mediterranean sea: Part I. The handbook of environmental chemistry, vol 83. Springer, Cham. https://doi.org/10.1007/698_2016_99
18. De Dominicis M, Pinardi N, Zodiatis G, Archetti R (2013) MEDSLIK-II, a Lagrangian marine surface oil spill model for short-term forecasting—Part 2: numerical simulations and validations. *Geosci Model Dev* 6:1871–1888. <https://doi.org/10.5194/gmd-6-1871-2013>
19. De Padova D, Mossa M, Adamo M et al (2017) Synergistic use of an oil drift model and remote sensing observations for oil spill monitoring. *Environ Sci Pollut Res* 24:5530–5543. <https://doi.org/10.1007/s11356-016-8214-8>
20. Dietrich JC, Trahan CJ, Howard MT, Fleming JG, Weaver RJ, Tanaka S, Luettich L, Yu RA, Dawson CN, Westerink JJ, Wells G, Lu A, Vega K, Kubach A, Dresback KM, Kolar RL, Kaiser C, Twilley RR (2012) Surface trajectories of oil transport along the Northern Coastline of the Gulf of Mexico. *Cont Shelf Res* 41:17–47. <https://doi.org/10.1016/j.csr.2012.03.015>
21. Espedal H, Wahl T (1999) Satellite SAR oil spill detection using wind history information. *Int J Rem Sens* 20(1):49–65
22. Fiscella B, Giancaspro A, Nirchio F, Pavese P, Trivero P (2000) Oil spill detection using marine SAR images. *Int J Rem Sens* 21(18):3561–3566. <https://doi.org/10.1080/014311600750037589>
23. French-McCay DP, Spaulding ML, Crowley D, Mendelsohn D, Fontenault J, Horn M (2021) Validation of oil trajectory and fate modeling of the Deepwater horizon oil spill. *Front Mar Sci* 8:618463. <https://doi.org/10.3389/fmars.2021.618463>
24. Gade M (2006) On the imaging of biogenic and anthropogenic surface films on the sea by radar sensors. In: Gade M, Hühnerfuss H, Korenowski GM (eds) Marine surface films: chemical characteristics, influence on air-sea interactions, and remote sensing. Springer, Heidelberg, pp 189–204
25. Gade M, Alpers W (1999) Using ERS-2 SAR images for routine observation of marine pollution in European coastal waters. *Sci Total Environ* 237–238(441–448):3
26. Gade M, Alpers W, Bao M (1996) Measurements of the radar backscattering over different oceanic surface films during the SIR-C/XSAR campaigns. In: Proceedings of international geoscience and remote sensing symposium (IGARSS'96), vol 2, pp 860–862
27. Holt B, Zeng K (2017) Oil spill detection by imaging radars: challenges and pitfalls. *Rem Sens Environ* 201:133–147. <https://doi.org/10.1016/j.rse.2017.09.002>
28. Ivanov AYU (1998) Assessment of marine oil pollution using KOSMOS-1870 and ALMAZ-1 radar images. *Mapp Sci Rem Sens* 35(3):202–217. <https://doi.org/10.1080/07493878.1998.10642092>

29. Jackson CR, Apel JR (2004) Synthetic aperture radar marine user's manual. US Department of Commerce, National Oceanic and Atmospheric Administration, Washington, USA. <http://www.sarusersmanual.com>. Accessed on 15 February 2021
30. Jha MN, Levy J, Gao Y (2008) Advances in remote sensing for oil spill disaster management: state-of-the-art sensors technology for oil spill surveillance. *Sensors* 8(1):236–255. <https://doi.org/10.3390/s8010236>
31. Hovland HA, Johannessen JA, Digranes J (1994) Slick detection in SAR images. In: *Proceedings of IGARSS'94*, pp 2038–2040
32. Izrael YuA, Tsyban AV (2009) Anthropogenic ecology of the ocean. Nauka, Moscow, p 532 (in Russian)
33. Klemas V (2010) Tracking oil slicks and predicting their trajectories using remote sensors and models: case studies of the Sea Princess and Deepwater Horizon oil spills. *J Coastal Res* 26(5):789–797. West Palm Beach (Florida), ISSN 0749-0208
34. Kostianaia EA, Kostianoy AG, Lavrova OYu, Soloviev DM (2020) Oil pollution in the Northern Red Sea: a threat to the marine environment and tourism development. In: Elbeih SF, Negm AM, Kostianoy A (eds) *Environmental remote sensing in Egypt*. Springer Nature Switzerland AG, Cham, pp 329–362
35. Kostianoy AG (2021) Oil pollution: the Baltic sea. In: Fath BD, Jorgensen SE (eds) *Environmental management handbook*, 2nd ed. Managing water resources and hydrological systems vol 4. Taylor and Francis, CRC Press, pp 349–368. <https://doi.org/10.1201/9781003045045-37>
36. Kostianoy AG, Ambjörn C, Solovyov DM (2014a) Seatrack web—a numerical tool for environmental risk assessment in the Baltic sea. In: Kostianoy AG, Lavrova OYu (eds) *Oil pollution in the Baltic sea*, vol 27. Springer, Berlin, Heidelberg, New York, pp 185–220
37. Kostianoy AG, Bulycheva EV, Semenov AV, Krainyukov AV (2015) Satellite monitoring systems for shipping, and offshore oil and gas industry in the Baltic Sea. *Transp Telecommun* 16(2):117–126
38. Kostianoy AG, Carpenter A (2018) History, sources and volumes of oil pollution in the Mediterranean sea. In: Carpenter A, Kostianoy AG (eds) *Oil pollution in the Mediterranean sea: Part I—the international context*. Springer International Publishing AG, Cham, Switzerland, pp 9–31
39. Kostianoy AG, Kostianaia EA, Soloviev DM (2020) Oil pollution in the Mediterranean waters of Egypt. In: Elbeih SF, Negm AM, Kostianoy A (eds) *Environmental remote sensing in Egypt*. Springer Nature Switzerland AG, Cham, pp 305–328
40. Kostianoy AG, Lavrova OYu (eds) (2014a) Oil pollution in the Baltic sea. In: *The handbook of environmental chemistry*, vol 27. Springer, Berlin, Heidelberg, New York, p 268
41. Kostianoy AG, Lavrova OYu (2014b) Conclusions. In: Kostianoy AG, Lavrova OYu (eds) *Oil pollution in the Baltic sea*, vol 27. Springer, Berlin, Heidelberg, New York, pp 249–264
42. Kostianoy AG, Lavrova OYu (2014c) Introduction. In: Kostianoy AG, Lavrova OYu (eds) *Oil pollution in the Baltic sea*, vol 27. Springer, Berlin, Heidelberg, New York, pp 1–14
43. Kostianoy AG, Lavrova OYu, Mityagina MI, Solovyov DM, Lebedev SA (2014b) Satellite monitoring of oil pollution in the Southeastern Baltic sea. In: Kostianoy AG, Lavrova OYu (eds) *Oil pollution in the Baltic sea*. Springer, Berlin, Heidelberg, New York, vol 27, pp 125–154
44. Kostianoy AG, Lavrova OYu, Solovyov DM (2014) Oil pollution in coastal waters of Nigeria. In: Barale V, Gade M (eds) *Remote sensing of the African Seas*. Springer, New York, Heidelberg, Dordrecht, London, pp 149–165
45. Kostianoy AG, Lebedev SA, Litovchenko KT, Stanichny SV, Pichuzhkina OE (2004) Satellite remote sensing of oil spill pollution in the southeastern Baltic Sea. *Gayana* 68(2), Part 2:327–332
46. Kostianoy AG, Litovchenko KT, Lavrova OYu, Mityagina MI, Bocharova TYu, Lebedev SA, Stanichny SV, Soloviev DM, Sirota AM, Pichuzhkina OE (2006) Operational satellite monitoring of oil spill pollution in the southeastern Baltic Sea: 18 months experience. *Environm Res Eng Manage* N4(38):70–77
47. Krek E, Kostianoy A, Krek A, Semenov AV (2018) Spatial distribution of oil spills at the sea surface in the Southeastern Baltic Sea according to satellite SAR data. *Transp Telecommun* 19(4):294–300

48. Krek EV, Krek AV, Kostianoy AG (2021) Chronic oil pollution from vessels and its role in background pollution in the Southeastern Baltic Sea. *Rem Sens* 13:4307. <https://doi.org/10.3390/rs13214307>
49. Lavrova OYu, Kostianoy AG (2011) A catastrophic oil spill in the Gulf of Mexico in April–May 2010. In: *Izvestiya, atmospheric and oceanic physics*, vol 47(9). Pleiades Publishing, Ltd, pp 1114–1118
50. Lavrova OYu, Kostianoy AG, Lebedev SA, Mityagina MI, Ginzburg AI, Sheremet NA (2011) Complex satellite monitoring of the Russian seas. IKI RAN, Moscow, p 470 (in Russian)
51. Lavrova OY, Mityagina MI (2013) Satellite monitoring of oil slicks on the Black Sea surface. In: *Izvestiya—Atmospheric and Ocean Physics*, vol 49(9), pp 897–912
52. Lavrova OYu, Mityagina MI, Kostianoy AG (2016) Satellite methods of detection and monitoring of marine zones of ecological risks. Space Research Institute, Moscow, p 336 (in Russian)
53. Lavrova OYu, Mityagina MI, Kostianoy AG (2019) Online database “See The Sea” for the Caspian Sea. *Ecologica Montenegrina* 25:79–90
54. Lavrova OYu, Mityagina MI, Kostianoy AG, Semenov AV (2014) Oil pollution in the southeastern Baltic Sea in 2009–2011. *Transp Telecommun* 15(4):322–331
55. Lavrova OYu, Mityagina MI, Kostianoy AG, Stochkov M (2017) Satellite monitoring of the Black sea ecological risk areas. *Ecologica Montenegrina* 14:1–13
56. Lu J (2003) Marine oil spill detection, statistics and mapping with ERS SAR imagery in south-east Asia. *Int J Rem Sens* 24(15):3013–3032
57. Migliaccio M, Gambardella A, Tranfaglia M (2006) Oil spill observation by means of polarimetric SAR data. In: *Proceedings of SEASAR 2006*, Frascati, Italy, January 23–26 2006, ESA SP-613, April 2006
58. Mityagina M, Churumov A (2006) Radar backscattering at sea surface covered with oil films. *Global Developments in Environmental Earth*, pp 783–790
59. Mityagina M, Lavrova O (2015) Satellite monitoring of the Black Sea surface pollution. In: *2015 IEEE international geoscience and remote sensing symposium (IGARSS)*, Milan, Italy, pp 2291–2294. <https://doi.org/10.1109/IGARSS.2015.7326265>
60. Mityagina MI, Lavrova OYu (2015) Multi-sensor satellite survey of surface oil pollution in the Caspian Sea. In: *Proceedings of SPIE 9638*, remote sensing of the ocean, sea ice, coastal waters, and large water regions, p 96380Q. <https://doi.org/10.1117/12.2194511>
61. Mityagina M, Lavrova O (2016) Satellite survey of inner seas: oil pollution in the Black and Caspian Seas. *Rem Sens* 8:875. <https://doi.org/10.3390/rs8100875>
62. Mityagina MI (2019) Assessment of surface oil pollution risks of the southeastern Black Sea based on long-term satellite data. In: *Proceedings of SPIE 11150*, remote sensing of the ocean, sea ice, coastal waters, and large water regions, p 111501C. <https://doi.org/10.1117/12.2532867>
63. Mityagina MI, Lavrova OYu, Kostianoy AG (2019) Main pattern of the Caspian Sea surface oil pollution revealed by satellite data. *Ecologica Montenegrina* 25:91–105
64. Mityagina MI, Lavrova OYu (2020) Oil pollution hotspots on the Caspian Sea surface identified using satellite remote sensing. In: *Proceedings of SPIE 11529*, remote sensing of the ocean, sea ice, coastal waters, and large water regions, p 115290L. <https://doi.org/10.1117/12.2573501>
65. Monin AS, Voitov VI (1984) Black tides. Moscow, “Molodaya Gvardiya”, p 160 (in Russian)
66. Oceana (2003) The other side of oil slicks. In: *The dumping of hydrocarbons from ships into the seas and oceans of Europe*, p 31. <http://www.oceana.org/north-america/publications/reports/the-other-side-of-oil-slicks>. Accessed 22 May 2012
67. Oceana (2004) The EU fleet and chronic hydrocarbon contamination of the oceans, p 58. <http://www.oceana.org/north-america/publications/reports/the-eu-fleet-and-chronic-hydrocarbon-contamination>. Accessed 22 May 2012
68. Patin SA (2008) Oil spills and their impact on the marine environment and living resources. VNIRO Publishing, Moscow, p 508 (in Russian)
69. Periañez R (2020) A Lagrangian oil spill transport model for the Red Sea. *Ocean Eng* 217:107953. <https://doi.org/10.1016/j.oceaneng.2020.107953>

70. Redondo JM, Platonov A, Tarquis A (2008) Detection and prediction from SAR multiscale analysis. In: The 2nd international workshop on advances in SAR oceanography from Envisat and ERS missions, SeaSAR 2008, 21–25 January 2008, Rome, Italy
71. Sano EE, Matricardi EAT, Camargo FF (2020) State-of-the-art of radar remote sensing: fundamentals, sensors, image processing, and applications. *Revista Brasileira de Cartografia* 72:1484–1508. <https://doi.org/10.14393/rbcv72nespecial50anos-56568>
72. Shcherbak SS, Lavrova OY, Mityagina MI, Bocharova TY, Krovotyntsev VA, Ostrovskii AG (2008) Multisensor satellite monitoring of seawater state and oil pollution in the northeastern coastal zone of the Black Sea. *Int J Rem Sens* 29(21):6331–6345. <https://doi.org/10.1080/01431160802175470>
73. Shi L, Ivanov AY, He M-X, Zhao C (2008) Oil spill mapping in the western part of the East China Sea using synthetic aperture radar imagery. *Int J Rem Sens* 29(21):6315–6329
74. Solberg A, Schistad H, Storvik G, Solberg R, Volden E (1999) Automatic detection of oil spills in ERS SAR images. *IEEE Trans Geosci Rem Sens* GE-37:1916–1924.4
75. Terleeva NV, Kamagate SA, Ivanov AY (2012) Oil pollution in the Gulf of Guinea based on satellite radar data. *Earth from Space* 13:51–56 (in Russian)
76. Topouzelis K, Bernardini A, Ferraro G, Meier-Roux S, Tarchi D (2006) Satellite mapping of oil spills in the Mediterranean Sea. *Fresenius Environ Bulletin* 15(9A):1009–1014
77. Topouzelis K, Karathanassi V, Pavlakis P, Rokos D (2007) Detection and discrimination between oil spills and look-alike phenomena through neural networks. *ISPRS J Photogramm Rem Sens* 62(4):264–270. <https://doi.org/10.1016/j.isprsjprs.2007.05.003>
78. UNESCO (2003) The integrated, strategic design plan for the coastal ocean observations module of the Global Ocean Observing System. GOOS Report n° 125, IOC Information Documents Series N 1183, UNESCO, Paris, p 190
79. Valenzuela GR (1978) Theories for interaction of electromagnetic and oceanic waves—a review. *Boundary Layer Meteorol* 13:61–75
80. Zhurbas V, Välib G, Kostianoy A, Lavrova O (2019) Hindcast of mesoscale eddy field in the Southeastern Baltic Sea: model data vs satellite imagery. *Russ J Earth Sci* 19:ES4006. <https://doi.org/10.2205/2019ES000672>
81. Zodiatis G et al (2018) Numerical modeling of oil pollution in the Eastern Mediterranean Sea. In: Carpenter A, Kostianoy A (eds) *Oil pollution in the Mediterranean Sea: Part I. The handbook of environmental chemistry*, vol 83. Springer, Cham. https://doi.org/10.1007/698_2017_131

Chapter 5

Satellite Instrumentation and Technique for Monitoring of Seawater Quality



Andrey G. Kostianoy, Olga Yu. Lavrova, and Alexey Ya. Storchkov

Abstract The chapter provides a brief overview of satellite instrumentation, techniques and methods for monitoring of seawater quality (oil pollution, suspended matter, and algae bloom). Monitoring of oil pollution from space is usually carried out using the Synthetic Aperture Radar remote sensing systems, but under certain conditions, for example, in the zone of the sunglint, optical imagery is also very effective. Ocean color scanners are unique instrumentation for detection and monitoring of suspended matter (turbid waters) and chlorophyll-a (algae bloom) concentrations in the surface layer of the ocean. As any remote, in-situ or laboratory method, the ocean color scanners have a set of advantages (multispectral approach, high spectral resolution, high spatial resolution, etc.) as well as disadvantages which include dependence on the sunlight (there are no optical imagery during the night and Polar night) and clouds, dependence of the swath and repetition period on the spatial resolution of the sensor, etc. Application of the optical satellite remote sensing systems is illustrated by several examples of oil spill detection, turbid waters, and algal bloom in different seas of the World Ocean, and inland seas. Natural processes like wind-wave mixing in the coastal zone, river runoff, runoff from shallow lagoons, and algae bloom, as well as anthropogenic impact related to offshore and coastal mining, construction of ports and fairways, laying of underwater pipelines and cables, significantly impact seawater quality in the coastal zone of the World Ocean, and inland seas.

Keywords Satellite instrumentation · Techniques · Monitoring · World Ocean · Seas · Seawater quality · Oil pollution · Suspended matter · Algae bloom

A. G. Kostianoy (✉)

P.P. Shirshov Institute of Oceanology, Russian Academy of Sciences, 36, Nakhimovsky Pr.,
Moscow 117997, Russian Federation
e-mail: kostianoy@gmail.com

S.Yu. Witte Moscow University, 12, 2nd Kozhukhovskiy Per., Bldg. 1, Moscow 115432, Russian
Federation

A. G. Kostianoy · O. Yu. Lavrova · A. Ya. Storchkov
Space Research Institute, Russian Academy of Sciences, 84/32, Profsoyuznaya Str., Moscow
117997, Russia
e-mail: olavrova@iki.rssi.ru

5.1 Introduction

The main pollutants of the aquatic environment include petroleum hydrocarbons and petroleum products, organochlorine phosphorus-containing compounds, heavy metals, technogenic radionuclides, suspended matter at high concentrations and chemical toxic substances [73]. Marine pollution is the result of pollution of the hydrosphere, atmosphere, surface parts of the lithosphere and soils. Pollutant transfer occurs not only as a result of river, underground, and surface runoff, but also as a result of transboundary atmospheric and water transport, currents and ice transport. The overwhelming part of pollutants enters the coastal waters, which are the most polluted in the marine environment.

Sources of oil and oil supply to the sea are sewage, shipping, hydrocarbon production in water areas, drilling platforms, emergency spills, hydrocarbon lenses in the soil, oil refineries, dumping, and natural seepages. They lead to the formation of an oil film, pollution of coasts, seabirds, deterioration of fisheries for fish, mollusks and crustaceans, a decrease in moisture and gas exchange, provoke the accumulation of metals and toxic organic compounds, and increase secondary pollution [73].

Suspended substances come as a result of economic activities in the coastal zone—laying of pipelines and cables, explosions at the bottom and dumping. Discharge of rivers, water exchange with shallow lagoons, wind-wave mixing in the coastal zones are natural factors which increase water turbidity. Anthropogenic and natural factors cause an increase in water turbidity, secondary pollution, a decrease in photoactive radiation (PAR), bioproductivity, changes in the structure of biological populations, and the death of benthos [51, 52, 73].

Eutrophication of surface waters caused by an excess of nutrients (mainly of phosphorus and nitrogen), is an acute environmental issue for many inland seas, which is becoming more acute every year. In the Baltic Sea, eutrophication of waters results in a violent bloom of blue-green algae, which every year covers more and more areas [22, 25].

International maritime trade is steadily rising since 1985, and by 2018 the total transport by containers, dry cargo, main bulks and tankers has increased by three times and reached 11 billion tons, from which 3.2 billion tons are transported by tankers (crude oil, liquefied natural gas, liquefied petroleum gas) [76]. Over the past twenty years, in the Baltic, North, Barents, Mediterranean, Red, Caspian, Black, and other seas, the offshore oil and gas industry has increased its activities for exploration, production and transportation of hydrocarbons through oil and gas terminals, offshore pipelines, and ports. This was accompanied by the construction of new offshore oil and gas pipelines, oil and gas terminals, and by an increase in the shipping intensity. This leads to increasing environmental risks of pollution by the petroleum products as a result of accidents with all kind of ships and chronic pollution of the sea surface. Shipping activities, including trade, transportation of oil, fishery, tourism and military actions have major negative impacts on the offshore marine environment and the coastal zone. This is the cause of around 45% of the total oil pollution in the World Ocean [5–9, 27, 42–44, 69, 70].

An enrichment of the seawater with nutrients (eutrophication of waters) and warming of the seas lead to anomalous water bloom even in the areas where this process was not previously been observed. Eutrophication of the marginal and inland seas, coastal lagoons, lakes and water reservoirs, as well as rivers, mainly due to an excess of phosphorus and nitrogen is an important issue that became more acute every year. Silica, iron, and carbon can also cause algal bloom formation. For example, dust storms, reach in iron and silica, from deserts (for example, Sahara) can cause an algal bloom in the neighboring water areas. Satellite imagery shows that an intense bloom of the blue-green algae (mainly Cyanobacteria, many of these algae are toxic) every year lasts longer and covers larger areas of the seas. Harmful Algal Bloom (HAB) is a bloom of algae that causes negative impacts on the marine environment, and other biological organisms by a production of natural toxins. The diversity of the HABs threatens coastal areas and causes large-scale marine mortality events, including the shellfish poisonings.

Satellite monitoring of the marine environment in the open ocean, coastal and inland seas is one of the most important instrument for monitoring the seawater quality. This method is based on receiving data from various sensors: radiometers, spectrometers, scanners, scatterometers, radars and altimeters, installed on the satellites (for example, Terra, Aqua, NOAA, GFO, TOPEX/Poseidon, Envisat, Jason 1/2/3, RADARSAT 1/2, ERS-2, TerraSAR-X, Landsat, QuikSCAT, IRS, KOMPSAT-2, IKONOS, EROS A, SPOT, FORMOSAT-2, QuickBird, "Meteor-M", Sentinel-1/2/3 and many others). These sensors allows to receive information on sea surface temperature, concentration of suspended matter and chlorophyll, other optical characteristics of the seawater, oil pollution, sea level anomalies, water dynamics, ice cover, wind speed, wave height and other parameters with high temporal and spatial resolution.

For instance, Synthetic Aperture Radars (SARs) which were installed on the Envisat, ERS-2, RADARSAT 1/2, TerraSAR-X, Sentinel-1A/1B, and other satellites are unique tools for detection of oil pollution of the sea surface [45, 51, 52]. SAR data allows to quickly observe the environmental conditions in the water area subjected to effluents of various nature, define the area of pollution, and study physical processes which determine the advection of pollution across the water areas. In some cases it is possible to identify the ships responsible in oil pollution. The possibility of surveying very large water areas in a short time, repeated observations of the same area with a short time interval in almost any weather conditions, make the use of satellite information the cheapest, most efficient and objective method for monitoring oil pollution. Satellite instrumentation and technique for oil pollution detection in the seas are discussed in the accompanying chapter in this book [45].

As concerns high concentration of suspended matter (due to river discharges, water exchange with lagoons and estuaries, wind-wave mixing in the coastal zones) and intense algal bloom (due to discharges from industrial enterprises, and fertilizers from agricultural fields), the most effective method of monitoring is satellite observations, for example, with help of spectroradiometers MERIS on the Envisat, MODIS on the Aqua and Terra, MSI on the Sentinel-2A/2B, and OLCI/SLSTR on

the Sentinel-3A/3B. These satellite observations have a number of evident advantages for environmental monitoring of the seawater quality compared to ship in-situ observations.

In this chapter we briefly discuss satellite instrumentation and technique for the analysis of seawater quality related to oil pollution, high concentration of suspended matter (turbid waters) and high concentration of chlorophyll-a (algal bloom events), and we show examples of application of satellite remote sensing to detection of these events in different coastal and inland seas.

5.2 Physical Principles and Methods of Remote Sensing of Seawater Quality

Ocean color scanners detect the spectral properties of water leaving radiation, which carries information on various optical characteristics of the ocean surface layer—concentration of suspended matter and chlorophyll, water bloom, transparency of water, etc. The optical spectral range allows observation of ice fields, icebergs, as well as oil pollution but under certain conditions. In remote sensing methods, the optical wavelength range is considered to be in the range from 0.1 μm to 1000 μm . This optical range of electromagnetic waves includes the ultraviolet (UV) part of the spectrum (0.1–0.38 microns), the visible band—the blue band (B) (0.38–0.5 microns), green (G) (0.5–0.6 microns), red (R) (0.6–0.78 microns), and infrared (IR), which includes near-IR (0.78–3.0 microns), medium-IR (3–50 microns), and far-IR (50–1000 microns).

Visible radiation represents electromagnetic waves which are perceived by the human eye. It occupies a part of the spectrum with a wavelength from around 0.38 μm (violet) to 0.78 μm (red). Visible remote sensing is based on the ability to observe the brightness of the scattered and reflected sunlight by the sea surface. Incident solar radiation is partially reflected by the sea surface, the upper layer of the sea, suspended matter, and by the seabed in the shallow water. Reflective properties of the sea surface are determined by several optical characteristics, including spectral and integral reflectance, spectral and integral albedo, and contrast.

The brightness of the optical radiation of the sea is the sum of the brightness of sunlight reflected from the sea surface (B_s), from the subsurface layer (B_u) and from the seabed (B_b). All components of the brightness of optical radiation significantly depend on the lighting conditions.

The brightness coefficient of solar radiation reflected from the sea surface (B_s) depends on the illumination, direction of the sea surface observation, and the sea surface state. Reflected radiation is formed by the direct and scattered solar radiation. Reflected direct sunlight is called sunglint when sunlight reflects from the sea surface at the same angle to the normal that an optical sensor is viewing the sea surface. The brightness of radiation from the sea surface is equal to the incident radiance multiplied by the reflection coefficient, and is several times higher than the brightness of the sea

radiation outside the sunglint area. The brightness of the sea surface that does not glint in the direction of observation from the satellite is determined by the reflection of solar radiation from the sea surface scattered by the atmosphere and clouds (sky radiation). When direct solar radiation is reflected by an unperturbed (mirror) sea surface, there is one glint direction. The presence of roughness inhomogeneities at the sea surface, such as wind waves, leads to appearance of a family of glint directions, and leads to peculiarities in the interpretation of satellite images. In the sunglint area, less rough zones will have a higher brightness caused by the presence of a large number of local elements at the sea surface reflecting direct solar radiation. Outside the sunglint at the sea surface, the opposite picture is observed - the areas with reduced roughness correspond to a lower brightness due to the presence of a smaller number of local inclined areas reflecting solar radiation [28, 51, 60]. It should be noted that the presence of oil or surfactant films at the sea surface can have a significant effect on the intensity of optical radiation reflected by the sea surface. Figure 5.1 shows a color-synthesized satellite image obtained using the Multispectral Instrument (MSI) onboard Sentinel-2 in the sunglint area in the Northeastern Black Sea. The image clearly shows films of natural origin involved in the dynamics of vortices and accumulated in the appropriate convergence zones, as well as numerous traces after the ships. An elongated spot marked with an oval on the left corresponds to the manifestation of the oily waters discharged from the ship. The oil slick has a typical “comb” structure which forms under the influence of the wind, when oil accumulates on the leeward side of the slick. In addition, the near-surface wind may cause small-scale dynamic processes in the upper layer of the sea. The most known of them is the Langmuir circulation, which represents vertical vortices of alternating

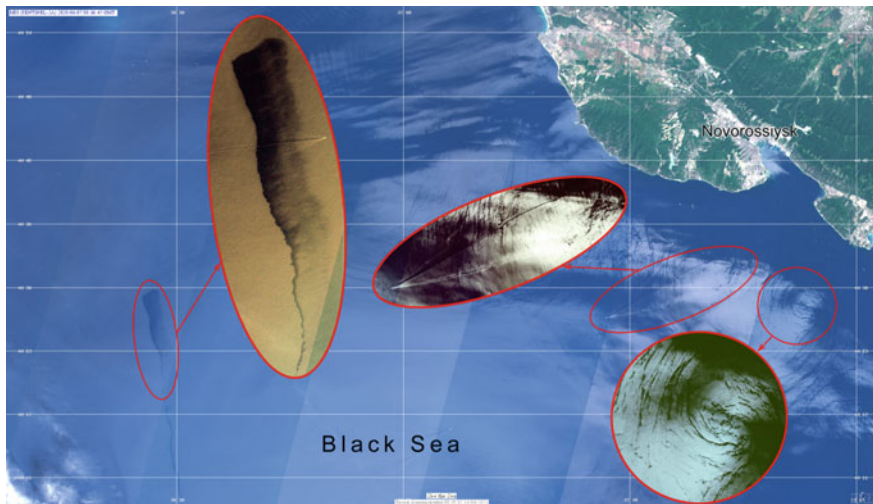


Fig. 5.1 Fragment of the true color MSI Sentinel-2A image (composite of 4, 3 and 2 spectral channels) obtained on June 07, 2020 in the north-eastern part of the Black Sea in the sunglint zone. Ovals mark oil pollution, wake trails and vortex, manifested by biogenic films

directions elongated in the wind direction [15, 57, 59]. The area of the oil spill in Fig. 5.1 is of 27 km².

The intensity of radiation from the subsurface layer of the sea (B_u) is in direct proportion to the intensity of sunlight penetrating into the surface layer of water, which is a function of the height of the sun above the horizon. The depth from which the radiation scattered in the surface layer is received is determined by the value of the vertical attenuation coefficient of optical radiation. The blue color characteristic for deep transparent waters results from strong scattering by water molecules in the short-wavelength part of the light spectrum. Ocean waters have a blue color both due to scattering in the blue region of the spectrum and due to absorption in its red part. Since seawater contains organic and inorganic impurities, additional optical processes occur. Thus, suspended particles strongly affect the optical characteristics of seawater [36, 51].

The brightness of the radiation reflected by the seabed (B_b) is determined by the lighting conditions, the depth and transparency of the water, and the reflectivity of the seabed.

Admixtures that affect the upward radiation flux can be collected into three main groups [36, 50, 51]:

Colored dissolved organic matter (“yellow substance”) is the main substance which determines the absorption of the sun light by seawater in the short-wavelength part of the spectrum. This group of admixtures includes all organic compounds dissolved in water, which strongly absorb ultraviolet and blue rays, and therefore the seawater acquires a yellow–brown color. The absorption index of the yellow substance is used as a characteristic of the content of colored organics in seawater. This is one of the main characteristics of coastal seawater quality [11].

Suspended matter is understood as all particles present in water. This group of admixtures includes sand, clay minerals, grains and fragments of quartz and other minerals, detritus, skeletons of plankton and other organisms. Suspended matter cause very strong light scattering in water, which is dependent on the radiation wavelength. Spectral dependency of light scattering varies from the suspended matter composition. For example, according to [33] low-parametric model, spectra of the scattering coefficients and volume scattering functions follow a power law with exponents 1.7 and 0.3 for the fine and coarse fractions, respectively. The particle backscattering coefficient is calculated from the data of satellite ocean color scanners, but with some errors. It characterizes the concentration of suspended matter in water, determines the albedo of the water column, and is a convenient parameter for satellite monitoring.

A special group of admixtures is formed by **phytoplankton**. Due to chlorophyll content it gives strong absorption bands in the blue (0.44 μm) and red (0.675 μm) parts of the radiation spectrum. Chlorophyll concentration is the only characteristic of marine ecosystems, the spatial and temporal variability of which can be studied with the help of satellite observations [12]. Chlorophyll concentration is the most important parameter for characterizing phytoplankton biomass, and calculating the primary production of the oceans.

Thus, the signal received by the sensors in the optical range is determined by scattering on phytoplankton, detritus and suspended mineral particles, and by solar radiation reflected from the sea surface. It should be noted that optical sensors register solar radiation reflected from the sea surface and transmitted through the atmosphere. The “true” color of the ocean is formed by the spectral composition of the radiation emerging from the water column, while the ocean color “seen” by the satellite sensor on the orbit is due in large part to the influence of the atmosphere. A large number of studies are devoted to calculation of the characteristics of the upward radiation from the sea surface, in which various methods of atmospheric correction, taking into account the influence of the atmosphere, are used [32, 77].

5.3 Satellites and Sensors

A fairly large number of remote sensing satellites are in operation now with instruments that provide observations of the Earth in the optical range. The number of these operating satellites and instruments is increasing. There is a large number of information resources that store, update and provide information about various sensors and satellites for Earth observation. Today, the following resources are the most complete and convenient to get technical information on sensors and specification of instruments installed at these satellites:

ESA—<https://earth.esa.int/web/eoportal/satellite-missions>

NASA—<https://www.nasa.gov/missions>

NASA, JPL—https://www.jpl.nasa.gov/missions?mission_status=current

NOAA—<https://www.nesdis.noaa.gov/content/satellite-missions>

USGS—https://www.usgs.gov/core-science-systems/nli/landsat/landsat-satellite-missions?qt-science_support_page_related_con=0#qt-science_support_page_related_con

IOCCG—<https://ioccg.org/resources/missions-instruments/current-ocean-color-sensors/>

CEOS—<http://database.eohandbook.com/>

The study of various optical characteristics of seawater, areas of distribution of suspended matter, the determination of zones of intense bloom of phytoplankton is carried out by multichannel spectroradiometers, such as CZCS, MODIS-Aqua/Terra, MERIS Envisat, MSS and TM Landsat-5, ETM + Landsat-7, OLI/TIRS Landsat-8, MSI Sentinel-2A/B, OLCI/SLSTR Sentinel-3 A/B, hyperspectral sensors Hyperion, HICO, and others [26, 36, 51, 52].

There are currently 14 ocean color scanners in orbit that meet the basic requirements for determining different parameters related to the ocean color and water quality with global coverage of the oceans. The characteristics of these scanners are presented in Table 5.1. They all have polar orbits, but the table also includes two geostationary instruments GOCI and GOCI-II, which, although it does not have a global coverage, but covers an area of more than 6 mln km² and takes measurements every hour during daylight hours [26, 36]. The past SeaWiFS and MERIS scanners

Table 5.1 Current ocean color scanners which can be used for monitoring the seawater quality (modified from [26])

Scanner	Agency/Country	Satellite	Launch date	Swath, km	Spatial resolution, m	Bands	Spectral coverage, nm
MODIS	NASA/USA	Terra (EOS-AM1)	18.12.1999	2330	250/500/1000	36	405–14,385
MODIS	NASA/USA	Aqua (EOS-PM1)	04.05.2002	2330	250/500/1000	36	405–14,385
OCM-2	ISRO/India	Oceansat-2 (India)	23.09.2009	1420	360/4000	8	400–900
GOCI Geostationary	KARI/KIOST/South Korea	COMS	26.06.2010	2500	500	8	400–865
VIIRS	NOAA/USA	Suomi NPP	28.10.2011	3000	375/750	22	402–11,800
MSI	ESA	Sentinel-2A	23.06.2015	290	10/20/60	13	442–2202
OLCI	ESA/ EUMETSAT	Sentinel-3A	16.02.2016	1270	300/1200	21	400–1020
MSI	ESA	Sentinel-2B	07.03.2017	290	10/20/60	13	442–2186
VIIRS	NOAA/NASA/USA	JPSS-1/NOAA-20	18.11.2017	3000	370/740	22	402–11,800
SGLI	JAXA/Japan	GCOM-C	23.12.2017	1150–1400	250/1000	19	375–12,500
OLCI	ESA/ EUMETSAT	Sentinel-3B	25.04.2018	1270	300/1200	21	400–1020
COCTS CZI	NSOAS/CAST/China	HY-1C	07.09.2018	3000 950	1100 50	10 4	402–12,500 433–885
GOCI-II Geostationary	KARI/KIOST/South Korea	Geo-Kompsat-2B	18.02.2020	2500 × 2500	250	13	380–900
COCTS CZI	NSOAS/CAST/China	HY-1D	11.06.2020	3000 950	1100 50	10 4	402–12,500 433–885

should also be added to the list of available datasets of satellite ocean color scanners. On the International Ocean Color Coordinating Group (IOCCG) website, we can find all the necessary information about the above mentioned sensors and satellites [26].

In the near future, it is planned to launch new satellite ocean color scanners [5]. First of all, this is the launch every 5 years (2021, 2026 and 2031) of JPSS satellites with VIIRS (Joint Polar Satellite System—a satellite system developed by US NASA for obtaining data required for weather forecasting and scientific observations of climate). In 2022, NASA plans to launch the PACE satellite observatory (Plankton, Aerosol, Cloud, ocean Ecosystem) with the OCI instrument (Ocean Color Instrument). In 2023, OLCI is slated to be launched on the Sentinel-3C satellite.

The popularity of satellite ocean color scanners is associated, first of all, with the fact that radiation in the visible range of the spectrum is the only type of radiation that can pass (and exit back) through the sea surface with low losses, accordingly, only ocean color scanners can provide information about the characteristics of the ocean subsurface layer and the processes taking place in this layer. “Passive” satellite ocean color scanners using solar radiation have an advantage over “active” radars, which requires a radiation source on board the satellite, also from an economic point of view.

The following characteristics of the ocean surface layer, determined from the data of satellite ocean color scanners, are included in the standard products for processing data from the MODIS and VIIRS satellite color scanners related to the ocean [1, 36] (Table 5.2). A similar set is provided by the OLCI [74], the table has appropriate comments.

For practical use, the most informative and widely used parameters are Chlorophyll-a and TSM concentrations. Both can be regarded as the main characteristics of the seawater quality because larger concentrations of Chlorophyll-a and TSM (turbid waters) mean worse seawater quality and vice-versa.

5.4 Examples of Oil Spill Pollution, Turbid Waters and Algae Bloom

5.4.1 Oil Pollution

In this Section we present examples of application of the ocean color scanners for detection and monitoring of oil pollution, turbid waters and algae bloom in different regions of the World Ocean and inland seas. In the companion chapter [45] in this book we already mentioned that from April 20 to May 28, 2010 we daily followed the evolution of the huge oil spill in the Gulf of Mexico which resulted from the accident on the BP *Deepwater Horizon* oil platform that occurred on April 20, 2010 [51, 58]. The development of the situation with time was traced on the basis of a joint analysis of radar images (ASAR Envisat), as well as with the use of optical (MODIS-Aqua,

Table 5.2 Standard products for processing data from the MODIS and VIIRS satellite color scanners related to the ocean (modified from [1, 36])

Parameter	Comment
Remote sensing reflectance, R_{rs} , sr^{-1}	It is calculated for spectral channels for: MODIS—412, 443, 469, 488, 531, 547, 555, 645, 667, 678 nm; VIIRS—410, 443, 486, 551, 671 nm; OLCI—400, 412, 443, 490, 510, 560, 620, 665, 674, 681, 709 nm
Chlorophyll-a concentration, chl_{or_a} , $mg\ m^{-3}$	$Chlor_a$ is calculated by the MODIS and VIIRS data using values of R_{rs} for 2–4 wavelengths from the 440–670 nm range [1] $Chlor_a$ is calculated by the OLCI data using two-four wavelengths 443, 490, 510 and 560 nm, and by neural network method
Diffuse attenuation coefficient at 490 nm, Kd_{490} , m^{-1}	It is calculated for downwelling irradiance for the layer 0-z1, where z1—«first optical depth» equal to $\sim 1/Kd_{490}$. For MODIS data, it is calculated via the R_{rs} values at 488 and 547 nm, for VIIRS data—490 and 550 nm, for OLCI data—490 and 560 nm
Inherent optical properties, IOPs, m^{-1}	To calculate the IOPs based on the MODIS and VIIRS data, a special software GIOP (Generalized IOP) [1, 80, 81] was developed which allows calculation the spectral characteristics of marine absorption and backscattering coefficients for water column constituents (e.g., colored dissolved organic material (CDOM) and algal and non-algal particles) for 443 nm wavelength. It seems that the GIOP is also applicable to the OLCI data C2RCC (Case 2 Regional Coast Colour, https://www.brockmann-consult.de/portfolio/water-quality-from-space/) algorithm is also used to calculate the IOPs. The latest development of C2RCC neural networks and the algorithm for optically complex waters are described in [3]
Particulate organic Carbon, POC, $mg\ m^{-3}$	The POC is calculated via the relationship of R_{rs} for 443 and 547–560 nm wavelengths using an empirical relationship derived from in-situ measurements of POC for the Atlantic and Pacific oceans. It is likely applicable for the OLCI data also

(continued)

Table 5.2 (continued)

Parameter	Comment
Particulate inorganic Carbon, PIC, mol m^{-3}	This algorithm derives the concentration of PIC, calculated using observed in situ relationships between water-leaving radiances, spectral backscattering coefficients, and concentrations of PIC (i.e., calcium carbonate or calcite). The PIC algorithm is a hybrid of two independent approaches, defined as the 2-band approach (normalized water-leaving radiances in two bands near 443 and 555 nm) and the 3-band approach (spectral top-of-atmosphere reflectances at three wavelengths near 670, 750, and 870 nm). The algorithm is applicable to all current ocean color scanners. The PIC product is included as part of the standard Level-2 OC product suite and the Level-3 PIC product suite [1]
Photosynthetically available radiation, PAR, $\text{Einstein m}^{-2} \text{d}^{-1}$	This algorithm estimates daily average photosynthetically available radiation (PAR) at the ocean surface in $\text{Einstein m}^{-2}\text{d}^{-1}$. PAR is defined as the quantum energy flux from the Sun in the 400–700 nm range. For ocean color applications, PAR is a common input used in modeling marine primary productivity. The algorithm is applicable to MODIS, MERIS, SeaWiFS, and VIIRS, but it can be operated on all ocean color scanners. The PAR product is included as part of the standard Level-2 OC product suite and the Level-3 PAR product suite [1, 16]
Instantaneous PAR, iPAR, $\text{Einstein m}^{-2} \text{s}^{-1}$	This algorithm returns instantaneous photosynthetically active radiation (iPAR) in $\text{Einstein m}^{-2} \text{s}^{-1}$. The iPAR product represents the total PAR incident on the ocean surface in the 400–700 nm range at the time of the satellite observation (the PAR product, in contrast, provides a daily average). This is a companion product to the normalized fluorescence line height algorithm, the combination of which can be used to estimate fluorescence quantum yield. It works for the MODIS and OLCI data ([1, 74])
Total suspended matter concentration, TSM, g m^{-3}	It is a part of the standard OLCI products (including errors of calculation). It is calculated via the Rrs values for 15 spectral channels (400–753.5 nm, 779, 865 and 1020 nm) by neural network method

MODIS-Terra) imagery thanks to the effect of the oil spill displaying in the sunglint, which was very often for this location in the Gulf of Mexico (Fig. 5.2). Figure 5.2 shows this oil spill reflected on the sea surface on 17 May 2010. The spill is well visible and for this case study the analysis of optical imagery was as effective as oil spill detection on SAR imagery (see Fig. 5.2 in [45] for comparison).

Another example concerns the Shell's *Bonga* offshore oil spill of 40,000 barrels resulted from the transfer of crude oil from the *Bonga* Floating Production, Storage and Offloading vessel (FPSO) to oil tanker in the Gulf of Guinea on December 20, 2011 [48]. This case study was also mentioned in the companion chapter by [45] as an example of SAR application for detection of oil pollution. The spill was 80 km long, 15 km wide, and had a total area of 923 km². The spill was quite well visible also on the MODIS-Terra true color optical image (Fig. 5.3), but we have to note that other 11 smaller oil spills in the coastal zone and in the mouth of the arms of the Niger River Delta detected on the ASAR image of 21 December 2011 (see Fig. 5.4 in [45]) are not visible in the true color optical image because they were hidden by clouds and river plumes with high concentration of suspended matter.

In the Caspian Sea, the most oily polluted area is located eastward of Absheron Peninsula in Azerbaijan where Neftyanje Kamni (Oily Rocks), one of the oldest offshore oil production area is located. As it was shown in the companion chapter by

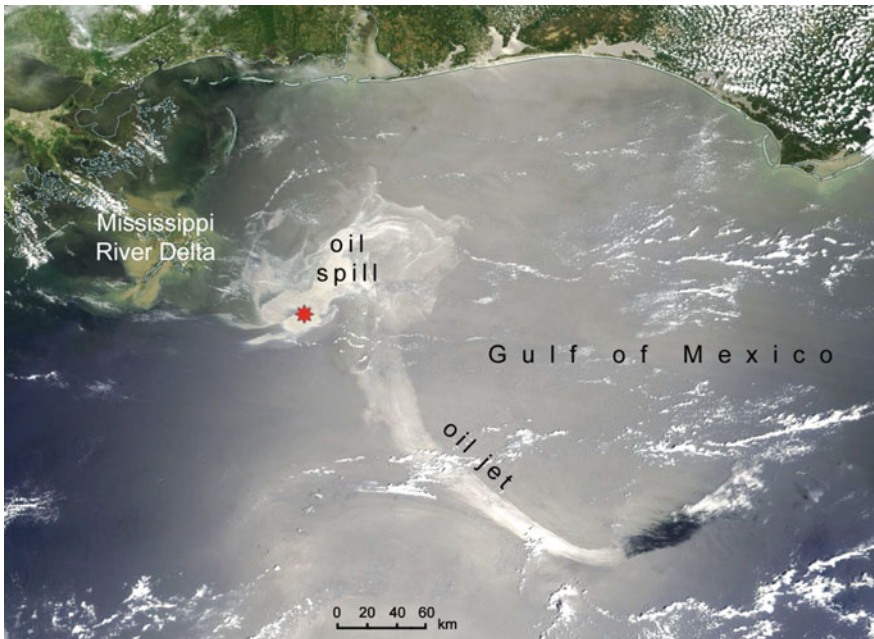


Fig. 5.2 Satellite image of oil pollution with an oil jet propagating to southeastward according to MODIS-Terra true color image on May 17, 2010, 16:40 UTC (MODIS Rapid Response Team). Star shows location of the BP *Deepwater Horizon* oil platform

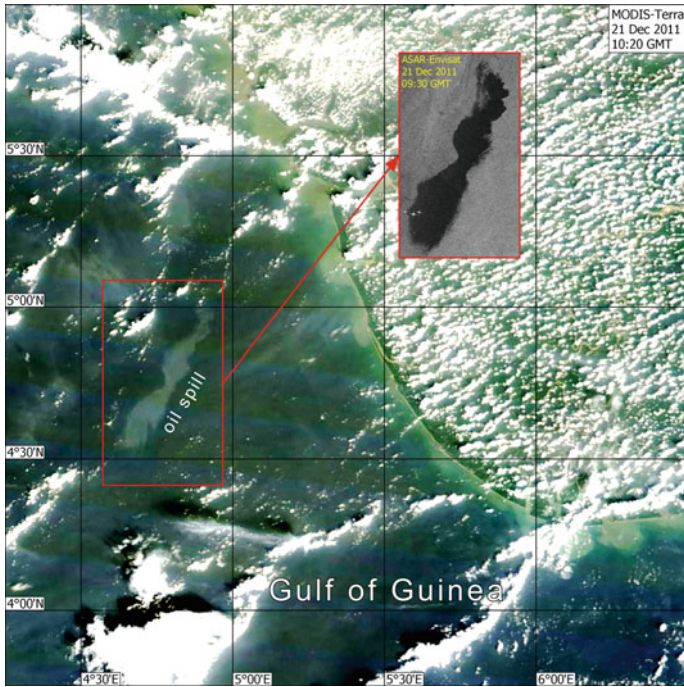


Fig. 5.3 The Shell's *Bonga* oil spill displayed on MODIS-Terra true color image on December 21, 2011, 10:20 GMT. For comparison, the ASAR Envisat image of the same oil spill is presented in the red frame for the same date—December 21, 2011, but 50 min earlier (09:30 GMT)

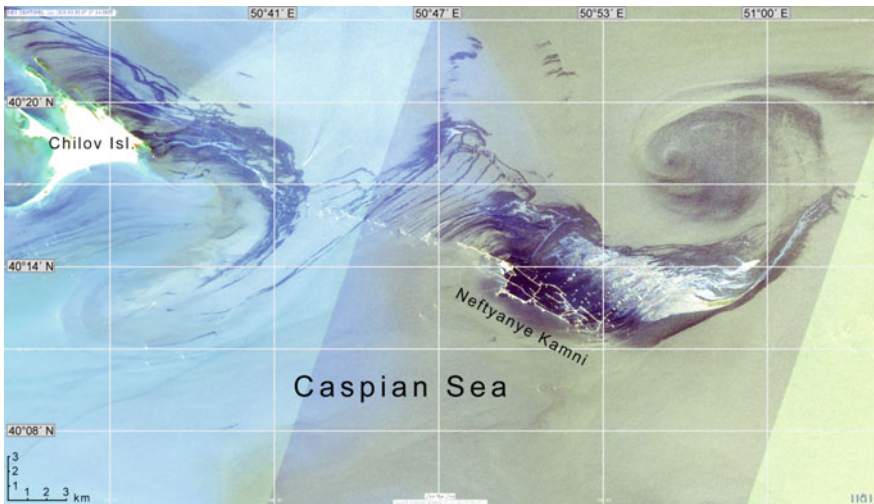


Fig. 5.4 Oil spills in the Neftyanje Kamni area displayed on MSI Sentinel-2A image (composite of 8, 4 and 2 spectral channels) on August 8, 2020, 07:37 GMT

[45], very large oil spills are detected on every SAR image of this area (see Fig. 5.10 in [45]). Despite serious limitations for monitoring oil pollution using optical data, associated primarily with cloudiness, there are significant advantages. In the VIS image obtained in the sunglint area, oil-containing films increase brightness and appear as light structures with characteristic iris, surrounded by a dark halo. Our experience shows that the oil film in the VIS images could be visible even better than in the radar images. The reason is that observed contrasts are caused not only by smoothing surface waves by the oil slick, but also by the differences in the optical characteristics of clean water and the oil film. Optical data, especially images with sunglint effect, often help to interpret radar data and decide on the origin of a slick film: whether it is an oil or biogenic film because oil and biogenic films are manifested differently in optical data. Oil films are brighter and have shiny signatures in color composites [62]. Identification of pollution of the marine environment and studying the oceanic dynamic processes occurring in this environment must be done in close interrelation, since, getting into the marine environment, pollution becomes part of this environment and develops along with it under the influence of meteorological and hydrological factors. The factors that have the greatest impact on the size, shape and direction of propagation of oil spills in the vicinity of offshore oil platforms are the near-surface wind and surface currents. The area of the Absheron Peninsula is the most windy region in the entire water area of the Caspian Sea. Here, the orographic and cape effects create favorable conditions for the development of frequent storm winds. The system of surface currents in the oil production area of Neftyanje Kamni is complex and unstable [52].

Based on the analysis of a large number of satellite images, it was found that surface currents have a significantly greater effect on the spread of surface oil pollution than the near-surface wind. As a rule, at the first stage of its evolution after surfacing, oil pollution spreads and propagates mainly under the impact of the near-surface wind. At the second stage of its propagation, oil pollution can be captured by surface currents, and spread by these currents over sufficiently large distances, or become involved in vortex movements [61]. Examples of the influence of vortex processes on the spread of oil pollution are shown in Figs. 5.4 and 5.5. In Fig. 5.4, which is a fragment of the MSI Sentinel-2A color-synthesized image from August 8, 2020, the rainbow film is clearly visible at the platforms located in the eastern part of Chilov Island and in the area of the eastern part of the Neftyanje Kamni. Under the influence of the cyclonic vortex, the oil slick spreads over a distance of more than 45 km, including being involved in a cyclonic vortex with a diameter of 10 km. The total area of oil pollution exceeded 100 km².

A similar situation was observed on May 15, 2020 (Fig. 5.5), the oil slick was also involved in the vortex flow. Taking into account the involvement in the vortex, the oil pollution spread over a distance of more than 50 km. Since the iridescent oil film is almost completely absent, apart from individual spots in the Chilov Island and at the western end of the Neftyanje Kamni area, it can be assumed that significantly less amount of oil products appeared on the sea surface.

Another source of oil pollution in the Caspian Sea is caused by mud volcanism on the seabed. Two main areas of seep sources can be distinguished westward of

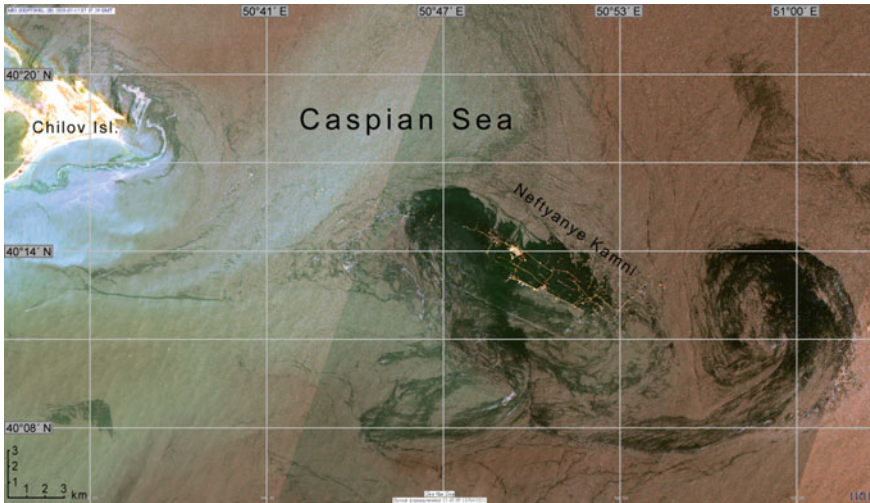


Fig. 5.5 Oil spills in the Neftyanje Kamni area displayed on MSI Sentinel-2B image (composite of 4, 3 and 2 spectral channels) on May 15, 2020, 07:37 GMT

Cheleken Peninsula which belongs to Turkmenistan, and in the northwestern part of the Southern Caspian [63, 64]. Oil films with natural hydrocarbon seeps appear on the sea surface in the form of well-recognizable numerous circles, sickle-shaped, horseshoe-shaped and spiral-shaped structures of relatively small size (Fig. 5.6). Such film contamination is regularly detected on satellite images of these areas and is concentrated on the sea surface in approximately the same places.

5.4.2 Turbid Waters

Suspended matter is included in almost all currently existing water quality classifications, because this is one of the main elements in the cycle of matter in natural water bodies. Suspended matter plays a significant role in water bodies. In particular, in the relatively shallow seas like the Baltic Sea, the Sea of Azov, the Northern Caspian Sea, other coastal zones of the World Ocean and inland seas a large amount of suspended matter is formed as a result of vertical mixing during wind wave impact. The other sources of turbid waters in the coastal zone are river runoff and runoff from shallow semi-isolated bays and lagoons which form river and lagoon plumes with high concentration of suspended matter. For example, the transparency of the Baltic Sea waters is decreasing during decades. According to [25], in the Northern Baltic Sea, water transparency has decreased from around 9 m in 1914–1939 to 6 m by the end of the twentieth century. The same trend is observed in the Southern Baltic and in a number of coastal zones [22]. Currently, the monitoring of suspended matter concentration in the Baltic Sea waters is carried out by the adjacent countries

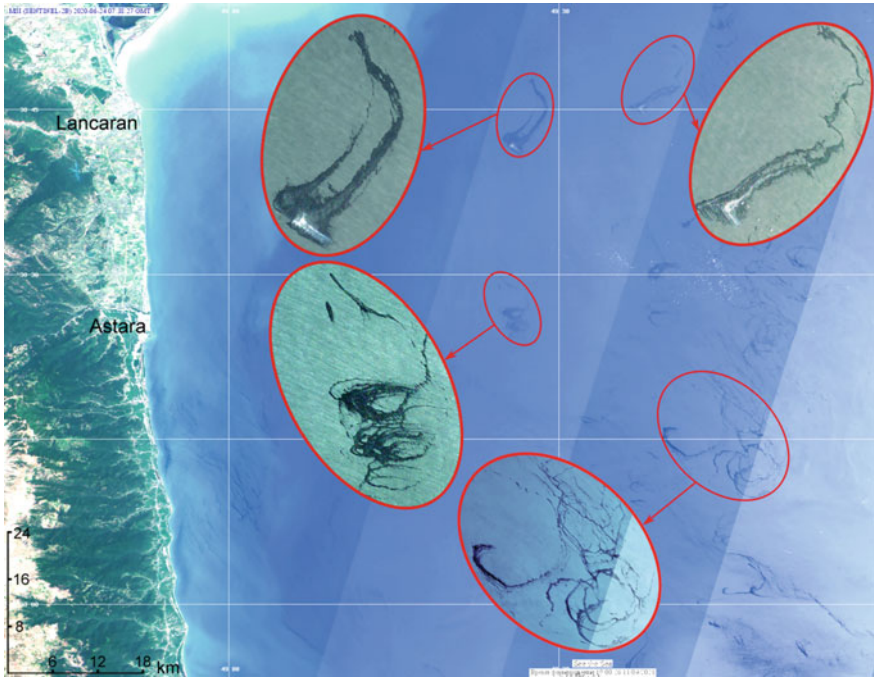


Fig. 5.6 Example of the manifestations of oil slicks from a natural seep on the seafloor in the western part of the Southern Caspian Sea in MSI Sentinel-2B image (composite of 4, 3 and 2 spectral channels) on June 24, 2020, 07:38 GMT

and international organizations. For example, the maps of the spatial distribution of turbidity and water bloom are regularly produced by the Finnish Environment Institute (SYKE).

Quantitative estimates of turbidity and suspended particulate matter (SPM) can be obtained from satellite remote sensing data using various algorithms that, strictly speaking, should take into account numerous factors, including varying chemical compositions of ocean water, coastal shelf waters, water of estuaries and fresh water bodies, geometrical parameters of satellite sounding at a given moment, intrinsic properties of orbital equipment, and current weather conditions in the study area and other factors [2, 21, 53, 79]. After numerous comparisons and simultaneous measurements, it was found impossible to develop an universal algorithm for evaluating the standard characteristics of seawater color based only on available data from satellite optical sensors because of very diverse set of characteristics and ambiguity in their interpretation under certain observation conditions. As noted in [68], there are three main types of algorithms commonly used to derive SPM from water reflectance: (1) empirical, (2) semi-analytical and (3) analytical algorithms. Empirical single-band and band-ratio models have been commonly used in coastal and estuarine areas [14, 71]. These types of models are dependent on SPM and water reflectance ranges, and

require calibration with regional measurements [68]. Semi-analytical and analytical models are based on the inherent optical properties and provide a more global application [10, 66].

To date, scientists from different countries have developed a number of specialized algorithms to evaluate characteristics of coastal marine and lake waters [23, 31, 75]. Originally, some of the standard algorithms were developed for the SeaWiFS instrument, then for MODIS on Aqua and Terra, and MERIS on the Envisat satellite [13].

Regional algorithms for determination the TSM concentration from satellite data in the Gulf of Finland and the Southeastern Baltic Sea [39, 78] as well as for the Black, Caspian and Barents Seas [33–35] have been developed at the P.P. Shirshov Institute of Oceanology, Russian Academy of Sciences (Moscow). They are successfully used to study the seasonal and long-term variability of suspended matter in these regions [4, 33–35, 39].

The Ocean and Land Colour Instrument (OLCI) instrument on Sentinel-3 (launched in 2016) was developed in part to provide continuity with measurements made previously by MERIS till April 2012. The algorithms developed for MERIS were adapted for OLCI [82]. Some of them were automated and made available in the specialized BEAM-VISAT software used by a great number of researchers.

Examples of such algorithms are: Case 2 Regional (C2R), FUB/WeW, Eutrophic Lake (EUL) and Boreal Lake (BL) [13], as well as the Maximum Chlorophyll Index (MCI) and Fluorescence Line Height (FLH). It was expected that some of these algorithms could be compatible with currently used sensors on the Sentinel and Landsat satellites [65].

For atmospheric correction, turbidity and SPM estimation the following standard algorithms were used: C2RCC (Case 2 Regional Coast Colour, <https://www.brockmann-consult.de/portfolio/water-quality-from-space/>) and algorithms provided by the ACOLITE (<http://odnature.naturalsciences.be/remsem/software-and-data/acolite>) software are often used. The C2RCC processor was originally developed by Doerffer and Schiller [13] and now is implemented in the ESA Sentinel Toolbox SNAP software (<https://step.esa.int/main/toolboxes/snap/>). The latest development of C2RCC neural networks and the algorithm for optically complex waters are described in [3]. The software calculates marine environment characteristics based on multispectral sensor data from satellites of the latest generation (SeaWiFS, MERIS, MODIS, VIIRS, OLCI, OLI, and MSI). It is also applicable to historical data from sensors that finished their operation long ago. Thus, it allows “recalculating”, for certain purposes, previously calculated parameters to meet current requirements.

Another group of algorithms that are used now is implemented in the ACOLITE processor and intended for calculating the main optical parameters. ACOLITE, developed at the Royal Belgian Institute of Natural Sciences (RBINS), is based on the works of a team of researchers led by Dr. Bouchra Nechad and described in detail in [66, 67]. ACOLITE is specifically developed for marine, coastal, and inland waters and supports free processing of Landsat-8 and Sentinel-2 data.

In the framework of a set of Russian Science Foundation projects, the maps of the TSM concentration were built and analyzed for different areas in the Gulf of

Finland (the Baltic Sea), the northeastern and eastern parts of the Black Sea, and in the Caspian Sea [51–54, 65].

Additional regular satellite information on the spatial distribution and temporal variability of turbid waters in the Southeastern Baltic Sea was collected during the integrated monitoring of the Lukoil D-6 offshore oil platform in 2004–2016 (Fig. 5.7) [47], in the Gulf of Finland during satellite monitoring of the Nord Stream 1 offshore gas pipeline construction in 2010–2013 (Fig. 5.8) [18–20, 46], and in the eastern part of the Black Sea during satellite monitoring of the Dzhubga-Lazarevskoye-Sochi offshore gas pipeline construction in 2010 (Fig. 5.9) [41]. Figure 5.8 is very spectacular because simultaneously it shows a very large area covered by turbid waters resulted from natural wind-wave mixing along the coast of Finland (number 1), the Narva River plume with high concentration of suspended matter (number 2), and an evident anthropogenic impact on the marine environment caused by the coastal dredging and fairway construction related to construction of Ust-Luga Port (number 3). It is interesting to mention that daily satellite monitoring of the Nord Stream 1 offshore gas pipeline construction could prove that sometimes naturally caused water areas of high concentration of suspended matter could be as large as a thousand of kilometers square while the anthropogenic impact from the pipeline construction was of the order of 1 km² only [18–20, 46].

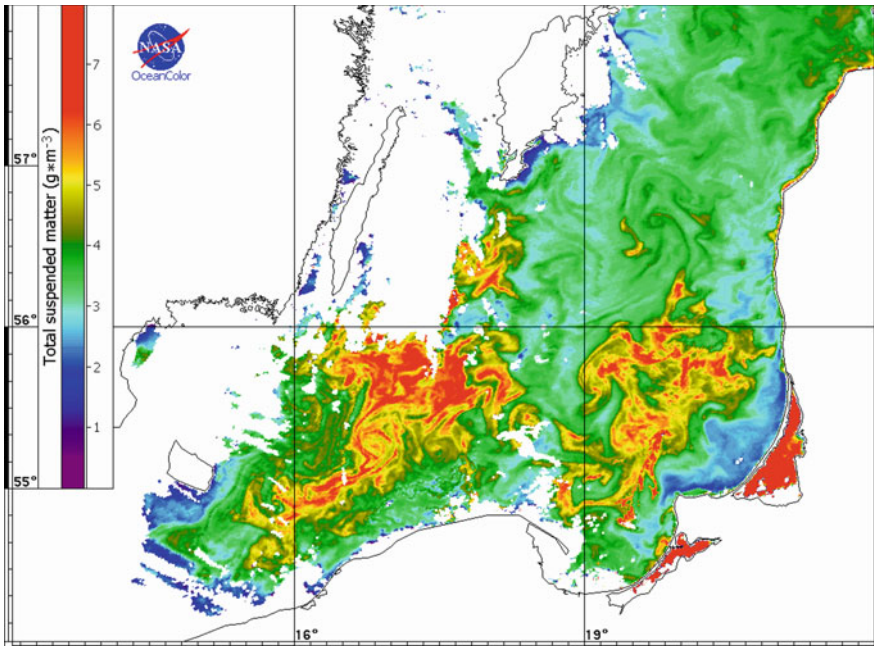


Fig. 5.7 Total suspended matter (g/m^3) in the Baltic Sea derived from MODIS-Terra on July 1, 2016

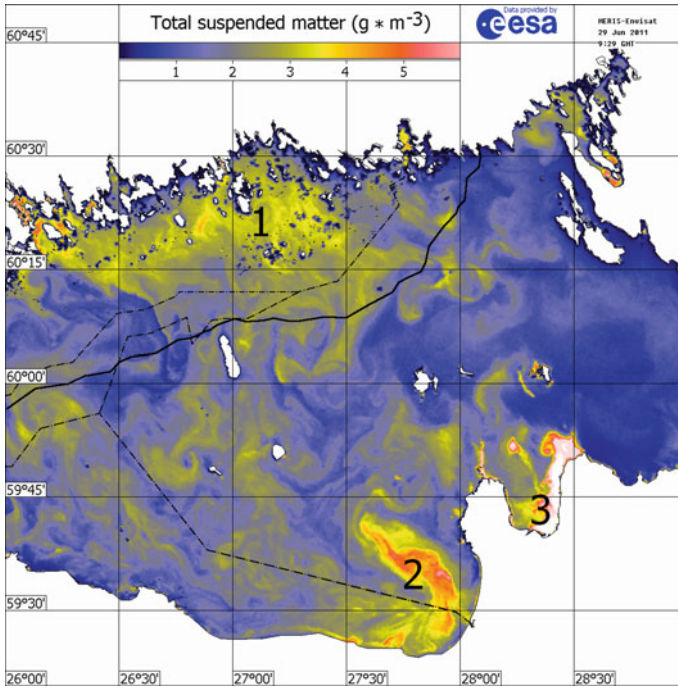


Fig. 5.8 Total suspended matter (g/m^3) in the Gulf of Finland derived from MERIS-Envisat on June 29, 2011. Numbered areas show: (1) natural wind-wave mixing in the coastal zone of Finland; (2) river plume of Narva River at the border between Estonia and Russia; (3) construction of Ust-Luga Port in Russia. Dashed lines are EEZ borders between Estonia, Russia and Finland. Solid black line shows location of the Nord Stream 1 offshore pipeline

Figure 5.9 shows spatial distribution of the TSM concentration in the surface layer of the eastern part of the Black Sea, in the area of construction of the Dzhubga-Lazarevskoye-Sochi offshore gas pipeline on July 8, 2010. The MERIS-Envisat data made it possible to determine the absolute TSM concentration in the study area, which was within $0.25\text{--}1.0 \text{ g}/\text{m}^3$. The obtained picture of the TSM spatial distribution clearly shows that in the central part of the zone, waters with an increased content of TSM are involved in a dipole structure with a larger anticyclonic part, which carries them 70 km perpendicularly from the coast. The structure of the turbid water in the river plume near the mouth of the Bzyp River is clearly visible. The TSM concentration at the river mouth reaches $10 \text{ g}/\text{m}^3$. There are no sources of suspended matter along the gas pipeline [41].

The latest generation optical data with high spatial resolution, as well as the algorithms for recovering quantitative values of the TSM developed for them, make it possible to determine with high accuracy the values of this important parameter in various parts of river plumes. This is confirmed by in-situ measurements, which were repeatedly carried out synchronously with satellite imagery, in particular, by

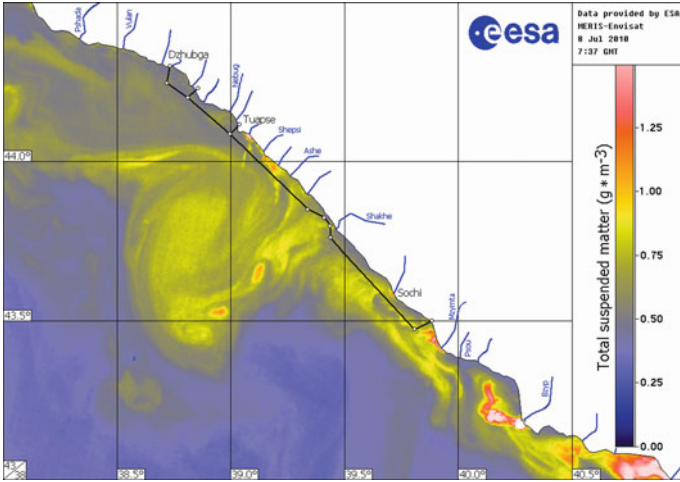


Fig. 5.9 Total suspended matter (g/m^3) in the coastal zone of the eastern part of the Black Sea derived from MERIS-Envisat on July 8, 2010. Blue lines show small rivers running to the Black Sea. Black line shows the location of the Dzhubga-Lazarevskoye-Sochi offshore gas pipeline

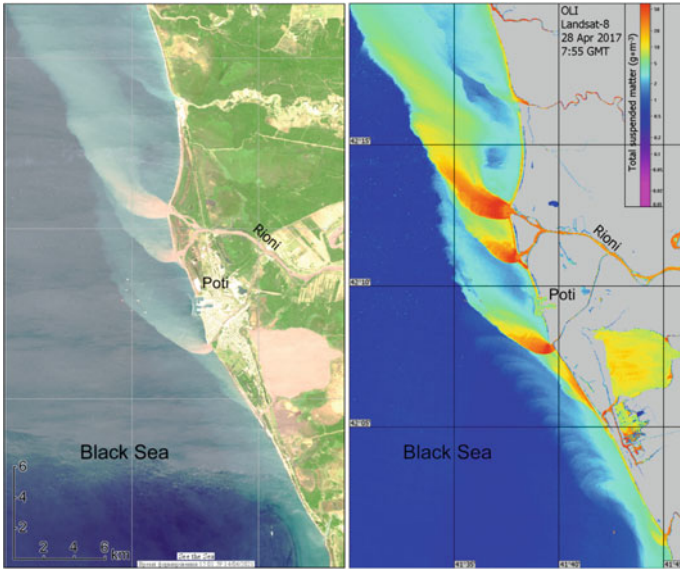


Fig. 5.10 Rivers plumes in the Eastern Black Sea in OLI Landsat-8 on April 28, 2017, 07:55 GMT: left—true color image (composite of 4, 3 and 2 spectral channels); right—TSM (g/m^3)

Space Research Institute of Russian Academy of Sciences [65] for the Black and Baltic Seas.

The highest TSM values are typical for estuarine zones of plumes of mountain rivers during the flood period. Over ten big mountain rivers flow into the Eastern Black Sea. On all cloudless satellite images of the optical range, without exception, the plumes of these rivers are well identified. During the period of glacier melting, TSM reaches values of over 60 g/m^3 (Fig. 5.10). The maximal area of highest TSM concentration (closest to the mouth,) is 175 km^2 . Such size is typical for March–April and some days in November featuring peak values of sediment load carried to the sea by all the rivers [52–54]. Figure 5.10 shows a fragment of the true color image of OLI Landsat-8 (Fig. 5.10 left) obtained during the flood on April 28, 2017 over the water area of the eastern part of the Black Sea and TSM derived from the OLI Landsat data (Fig. 5.10 right). The plumes of the three branches of Rioni River clearly depicts in this image. Even higher TSM values are typical for mountain rivers flowing into the western part of the Caspian Sea, such as Terek and Sulak Rivers (Fig. 5.11). In the mouth of the Sulak River, TSM in late May–early June exceeds 150 g/m^3 , which is confirmed, in particular, by MSI Sentinel-2 data from May 11, 2020 (Fig. 5.11).

Turbid waters containing a large amount of suspended matter are carried out into the sea not only by rivers. They can also enter the sea when water is carried out from closed lagoons through natural straits or artificial canals. The study of turbid waters from Vistula Lagoon into Gdansk Bay (the Baltic Sea) is of great theoretical and practical importance (Fig. 5.12). Depending on the wind and coastal currents, turbid lagoon waters can spread over long distances, both northeast and southwest [55].

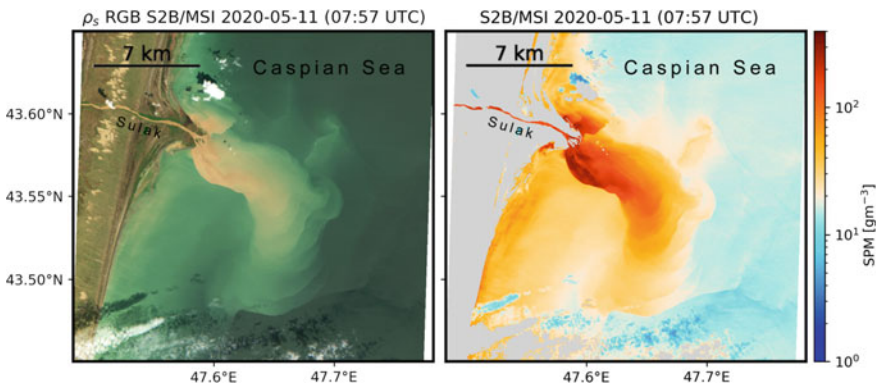


Fig. 5.11 The Sulak River plume in the Western Caspian Sea in MSI Sentinel-2B on May 11, 2020, 07:57 GMT: left—true color image (composite of 4, 3 and 2 spectral channels); right—TSM (g/m^3)

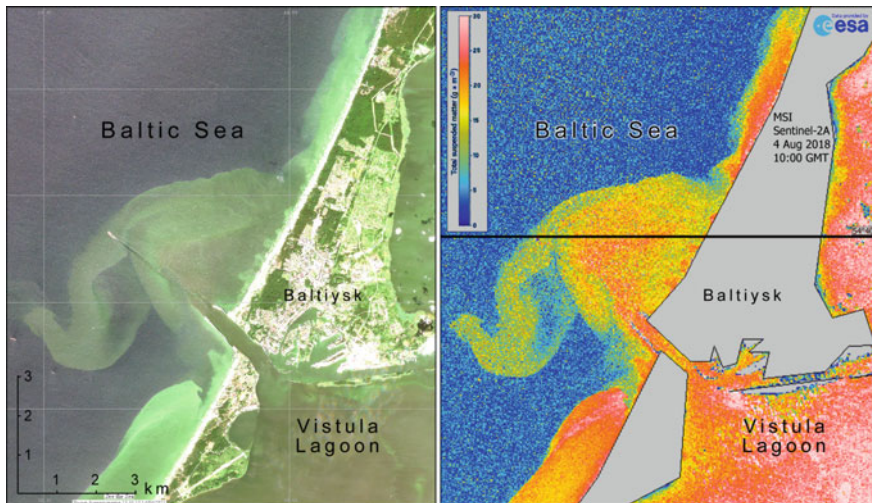


Fig. 5.12 Plume from the Vistula Lagoon in the Gdansk Bay (the Baltic Sea) in MSI Sentinel-2A on August 4, 2018, 10:00 GMT: left—true color image (composite of 4, 3 and 2 spectral channels); right—TSM (g/m^3)

5.4.3 Algae Bloom

For example, in the Baltic Sea, annually in July–August, a huge area of water is covered by cyanobacterial blooms. These water blooms are mainly caused by two types of cyanobacteria: *Nodularia spumigena* and *Aphanizomenon flosaquae*. Reinart and Kutser [72] showed that since the accumulations of cyanobacteria are located either on the sea surface or just below the surface, this causes increased values of the normalized brightness of the upward radiance in comparison with waters free of cyanobacteria. Analysis of temporal variability of cyanobacterial bloom intensity in the Baltic Sea based on the CZCS (1979–1984), SeaWiFS and MODIS (1998–2006) ocean color scanners were carried out by Kahru et al. [30, 29]. Based on the analysis of this date set, in addition to constructing annual cumulative maps for each pixel of the bloom area of 1×1 km in size, the frequency of cyanobacteria bloom events was calculated. In 2002, the Swedish Meteorological and Hydrological Institute (SMHI) has developed the Baltic Algae Watch System for monitoring the cyanobacterial bloom in the Baltic Sea, based on the AVHRR data processing [24]. As a result of the conducted for the period 1997–2009 study, maps of the number of days with bloom of cyanobacteria, maps of bloom areas were obtained and the intensity of bloom was calculated.

A decade ago, the spatial characteristics of the formation and distribution of seawater bloom were reconstructed using data from satellite spectroradiometers (MODIS Aqua/Terra, MERIS Envisat). The technique for detecting areas of intense phytoplankton bloom is based on the use of various combinations of spectral channels in the visible range of the spectrum. In particular, the detection of blooms of

(partially toxic) blue-green algae using the data of the MODIS and MERIS spectroradiometers is based on the use of data from the green and red channels. The signal of the first of them is formed as a result of reflection by particles suspended in water, including subsurface clusters of cyanobacteria. The signal of the red part of the spectrum is absorbed to a greater extent by water, therefore its intensity is determined by reflectors located in the immediate vicinity to the surface. Thus, the combination of these channels makes it possible to distinguish between surface and subsurface cyanobacterial clusters. For the MODIS sensor, these two channels are 551 and 670 nm, for MERIS—560 and 665 nm [17]. An integral assessment of biogenic pollution consists, first of all, in determining the spatial localization of biogenic films (identified by radar data and data in the visible range) and areas of intense algae bloom (identified by color-synthesized images in the visible range) and calculating the area occupied by this biological pollution. Today, the algorithms elaborated for MERIS are used for VIIRS-NPP, OLI Landsat-8, MSI Sentinel-2, OLCI Sentinel-3, and other sensors.

Regional algorithms elaborated at P.P. Shirshov Institute of Oceanology, Russian Academy of Sciences (Moscow) for determining the Chlorophyll-a concentration from satellite data in the Gulf of Finland and the Southeastern Baltic Sea [78] made it possible to monitor the effects of eutrophication in these regions.

Several examples of the algae bloom events in the Baltic Sea are presented in Figures 5.13, 5.14 and 5.15. Figure 5.13 shows chlorophyll-a concentration in the Baltic Proper, where maximum concentrations are observed along the shallow coasts where sea surface layer is much warmer than surrounding waters in summer. Figure 5.14 shows the algae bloom event in the Southeastern Baltic Sea in the true colors. A light green color indicates a higher concentration of algae on the sea surface, while dark green color corresponds to relatively clean waters. At the same time concentration of algae represent a very good tracer which clearly shows signatures of mesoscale and sub-mesoscale water dynamics like eddies, jets, filaments, and currents (Fig. 5.14). These processes are well displayed in the Chlorophyll-a concentration (mg/m^3) derived from OLCI Sentinel-3A on August 8, 2018 (Fig. 5.15). Also, Chlorophyll-a concentration maps well depicts sources of high concentration of Chlorophyll-a. In the Southeastern Baltic Sea these are discharges from the Vistula River and the Vistula Lagoon.

An example of an anomalous algal bloom of cyanobacteria *Nodularia* off the Iranian coast in the Southern Caspian in 2005 is shown in Fig. 5.16. It began to develop in the second decade of August and continued until the end of September and covered an area of 20,000 km^2 . An abnormal algal bloom was recorded according to the MODIS spectroradiometer of the Aqua satellite on August 12 and peaked on September 1, 2005 [35].

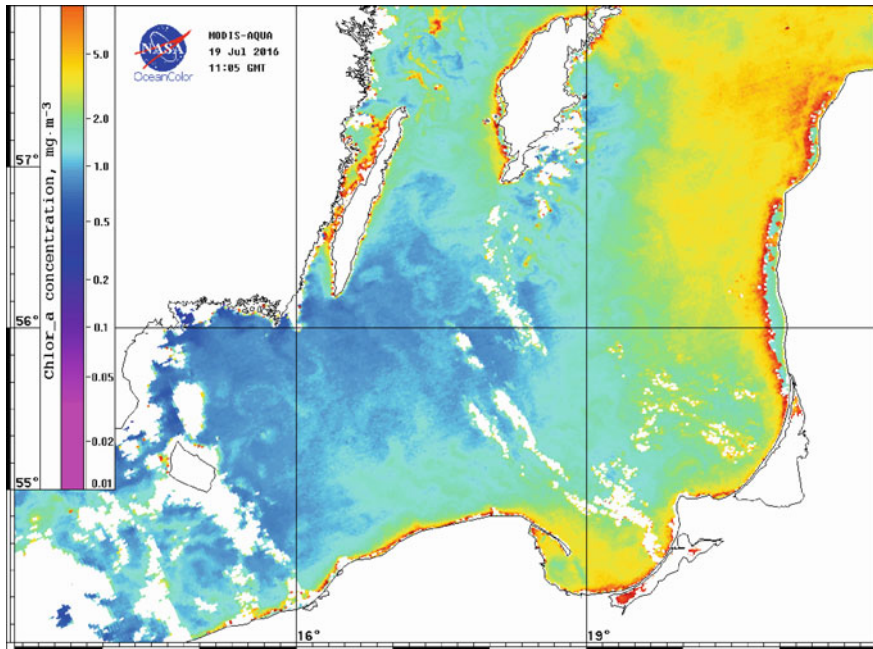


Fig. 5.13 Chlorophyll-a concentration (mg/m^3) in the Southeastern Baltic Sea derived from the MODIS-Aqua on 19 July 2016

5.5 Conclusions

Satellite-based ocean color scanners determine the spectral properties of radiation rising from the sea surface, which carries information on various optical characteristics of the sea surface layer: suspended matter and chlorophyll concentration, water transparency, water bloom, etc. The absorption index of yellow matter is used as a characteristic of the content of colored organic matter in sea water. This is one of the main characteristics of coastal water quality. The particle backscattering coefficient is calculated from the data of satellite ocean color scanners, but with some errors. It characterizes the concentration of suspended matter in seawater, determines the albedo of the surface layer, and is one of the convenient monitoring parameters. Chlorophyll concentration is the only one characteristic of marine ecosystems whose spatial and temporal variability can be studied with the help of satellite observations. This is the key parameter for characterizing phytoplankton biomass and calculation the amount of primary production of the oceans [34–38, 51, 52].

Also, the bio-optical Essential Climate Variables (ECVs), which include the “color of the ocean” and “phytoplankton”, are extremely important for the Earth’s climate, since they directly or indirectly affect the albedo and temperature of the ocean surface, heat-mass and gas exchange between the atmosphere and the ocean. as well as some ocean surface ECVs (e.g. waves, ice, partial pressure of carbon dioxide,

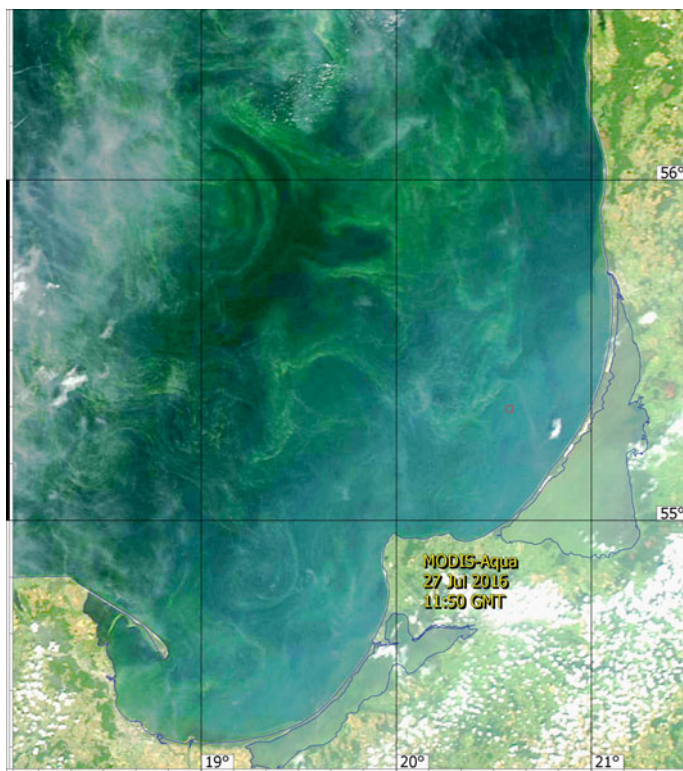


Fig. 5.14 True color image of the Southeastern Baltic Sea acquired from MODIS-Aqua on July 27, 2016. Light green colors on the sea surface show areas with high concentration of chlorophyll-a

ocean acidity). Thus, satellite-based ocean color scanners plays a very important role in the monitoring both the seawater quality and several ECVs [36].

As any remote, in-situ or laboratory method, the ocean color scanners have a set of advantages (multispectral approach, high spectral resolution, high spatial resolution, etc.) as well as disadvantages which include dependence on the sunlight (there are no optical imagery during the night and Polar night) and clouds, dependence of the swath and repetition period on the spatial resolution of the sensor, etc. Nevertheless, an integrated approach which combines different satellite remote sensing systems, for instance, SAR and ocean color scanners, gives the best result in the marine environment monitoring.

Our experience in the two decade long monitoring of the Baltic, Black, and Caspian seas led to the determination of zones of ecological risks in these seas related to both oil pollution and high concentration of suspended matter and chlorophyll-a. For the Black Sea, we identified 15 zones of ecological risk located along the main shipping routes, ports and oil terminals, mouths of rivers, and 8 such zones in the Caspian Sea [40, 49, 52, 56].

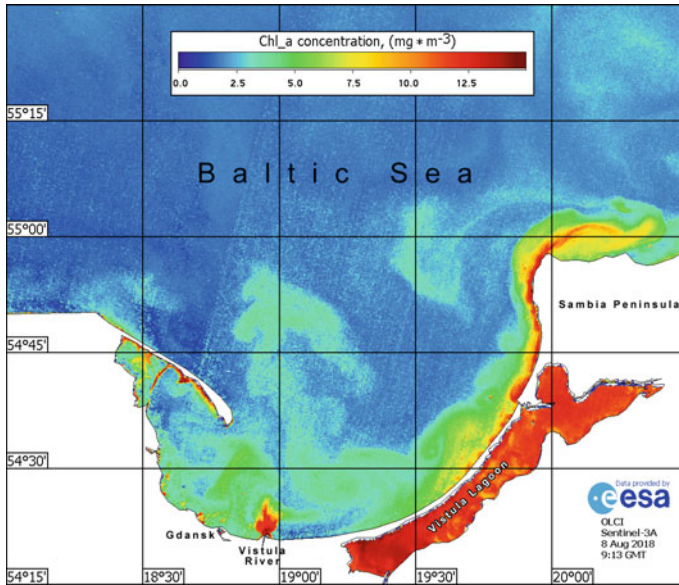


Fig. 5.15 Chlorophyll-a concentration (mg/m^3) in Gdansk Bay derived from OLCI Sentinel-3A on August 8, 2018



Fig. 5.16 True color image of the Southern Caspian Sea acquired from MODIS-Aqua on August 19, 2005. Light green colors on the sea surface in the middle of the sea show areas with high concentration of chlorophyll-a

Acknowledgements The authors are thankful to D.M. Soloviev (Marine Hydrophysical Institute of RAS) for preparation of a set of satellite imagery. The research was partially funded in the framework of the Russian Science Foundation no. 19-77-20060 Project «Assessing ecological variability of the Caspian Sea in the current century using satellite remote sensing data» (2019–2022). This publication was prepared in the framework of the scientific activities related to “The Caspian Sea Digital Twin” Programme performed in the framework of the UN Decade on Ocean Science for Sustainable Development (2021–2030).

References

1. Algorithm Descriptions (2021). <https://oceancolor.gsfc.nasa.gov/atbd/>. Accessed on 09.03.2021.
2. Berdeal I, Hickey B, Kawase M (2002) Influence of wind stress and ambient flow on high discharge river plume. *J Geophys Res* 107(C9):3130. <https://doi.org/10.1029/2001JC000932>
3. Brockmann C, Doerffer R, Peters M, Kerstin S, Embacher S, Ruescas A (2016) Evolution of the C2RCC neural network for sentinel 2 and 3 for the retrieval of ocean colour products in normal and extreme optically complex waters. In: Living planet symposium, proceedings of the esa living planet symposium. 740. ISBN 978-92-9221-305-3
4. Bukanova T, Kopelevich O, Vazyulya S, Bubnova E, Sahling I (2018) Suspended matter distribution in the south-eastern Baltic Sea from satellite and in situ data. *Int J Remote Sensing*. <https://doi.org/10.1080/01431161.2018.1519290>
5. CEOS (2021) The CEOS database: mission, instruments and measurements. <http://database.eohandbook.com>. Accessed on 09.03.2021
6. Carpenter A (ed) (2016) Oil pollution in the North Sea. Springer International Publishing AG, Cham, Switzerland, 312 p. <https://doi.org/10.1007/978-3-319-23901-9>
7. Carpenter A, Kostianoy AG (eds) (2018a) Oil pollution in the Mediterranean Sea: Part I—the international context. Springer International Publishing AG, Cham, Switzerland, 350 pp. <https://doi.org/10.1007/978-3-030-12236-2>
8. Carpenter A, Kostianoy AG (eds) (2018b) Oil pollution in the Mediterranean Sea: Part II—national case studies. Springer International Publishing AG, Cham, Switzerland, 291p. <https://doi.org/10.1007/978-3-030-11138-0>
9. Carpenter A, Kostianoy AG (2018c) Conclusions for Part I: the international context. In: Carpenter A, Kostianoy AG (eds) Oil pollution in the Mediterranean Sea: Part I—the international context. Springer International Publishing AG, Cham, Switzerland, pp 325–344
10. Chen J, D’Sa E, Cui T, Zhang X (2013) A semi-analytical total suspended sediment retrieval model in turbid coastal waters: a case study in Changjiang river estuary. *Opt Express* 21:13018–13031. <https://doi.org/10.1364/oe.21.013018>
11. Coble PG (2007) Marine optical biogeochemistry: the chemistry of ocean color. *Chem Rev* 107:402–418. <https://doi.org/10.1021/cr050350>
12. Doerffer R, Fiseher J (1994) Concentration of chlorophyll, suspended matter, and gelbstoff case II water derived from satellite coastal zone color scanner data with inverse modeling methods. *J Geophys Res* 99(C4):7457–7466
13. Doerffer R, Schiller H (2007) The MERIS Case 2 water algorithm. *Int J Remote Sens* 28(3–4):517–535. <https://doi.org/10.1080/01431160600821127>
14. Doxaran D, Froidefond JM, Castaing P (2002) A reflectance band ratio used to estimate suspended matter concentrations in sediment-dominated coastal waters. *Int J Remote Sens* 23:5079–5085. <https://doi.org/10.1080/0143116021000009912>
15. Ermakov S, Kapustin I, Molkov A, Leshev G, Danilicheva O, Sergievskaya I (2018) Remote sensing of evolution of oil spills on the water surface. In: Proceedings of SPIE 10784, Remote sensing of the ocean, sea ice, coastal waters, and large water regions. 107840L. <https://doi.org/10.1117/12.2325745>

16. Frouin RR, McPherson J, Ueyoshi K, Franz BA (2012) A time series of photosynthetically available radiation at the ocean surface from SeaWiFS and MODIS data. In: Proceedings of SPIE, vol 8525. 852519 (December 11, 2012). <https://doi.org/10.1117/12.9812642012>
17. Gower J, Doerffer R, Borstad GA (1999) Interpretation of the 685 nm peak in water-leaving radiance spectra in terms of fluorescence, absorption and scattering, and its observation by MERIS. *Int J Remote Sens* 20(9):1771–1786. <https://doi.org/10.1080/014311699212470>
18. Grishin N, Kostianoy A (2012a) Satellite monitoring of suspended matter pollution resulted from the Nord Stream gas pipeline construction in Russian waters of the Baltic Sea in 2010–2011. *Int Water Technol J* 2(1):80–89
19. Grishin NN, Kostianoy AG (2012b) On satellite monitoring of suspended matter transport during the construction of an offshore gas pipeline Nord Stream in Russian waters of the Baltic Sea in 2010. *Current problems in remote sensing of the Earth from space*, vol 9, no 1, pp 167–175 (in Russian)
20. Grishin NN, Kostianoy AG (2013) The use of satellite monitoring of suspended matter transport for the assessment of transboundary environmental impact of construction the Russian section of the offshore gas pipeline Nord Stream. *Current problems in remote sensing of the Earth from space*, vol 10, no 1, pp 303–319 (in Russian)
21. Güttler FN, Niculescu S, Gohin F (2013) Turbidity retrieval and monitoring of Danube Delta waters using multi-sensor optical remote sensing data: an integrated view from the delta plain lakes to the western–northwestern Black Sea coastal zone. *Remote Sens Environ* 132:86–101. <https://doi.org/10.1016/j.rse.2013.01.009>
22. HELCOM (2018) State of the Baltic Sea—Second HELCOM holistic assessment 2011–2016. In: *Baltic Sea Environment Proceedings* 155. ISSN 0357–2994 Available at: www.helcom.fi/baltic-sea-trends/holistic-assessments/state-of-the-baltic-sea-2018/reports-and-materials/. Accessed on 28 Mar 2021
23. Han B, Loisel H, Vantrepotte V, Mériaux X, Bryère P, Ouillon S, Dessailly D, Xing Q, Zhu J (2016) Development of a semi-analytical algorithm for the retrieval of suspended particulate matter from remote sensing over clear to very turbid waters. *Remote Sens* 8:211. <https://doi.org/10.3390/rs8030211>
24. Hansson M, Hakansson B (2007) The Baltic algae watch system—a remote sensing application for monitoring cyanobacterial blooms in the Baltic sea. *J Appl Remote Sens* 1(1):011507, 10pp
25. Hopkins CCE. (2000) Overview of monitoring in the Baltic Sea: Report to the Global Environment Facility/Baltic Sea Regional Project. AquaMarine Advisers, 39pp
26. IOCCG (2021) <http://ioccg.org/resources/missions-instruments/current-ocean-colour-sensors>. Accessed on 7 Mar 2021
27. Izrael YuA, Tsyban AV (2009) *Anthropogenic ecology of the ocean*. Nauka, Moscow 529p (in Russian)
28. Jackson CR, Alpers W (2010) The role of the critical angle in brightness reversals on sunglint images of the sea surface. *J Geophys Res* 115(9)
29. Kahru M, Savchuk OP, Elmgren R (2007) Satellite measurements of cyanobacterial bloom frequency in the Baltic Sea: interannual and spatial variability. *Mar Ecol Prog Ser* 343:15–23
30. Kahru M, Elmgren R (2014) Multidecadal time series of satellite-detected accumulations of cyanobacteria in the Baltic Sea. *Biogeosciences* 11:3619–3633
31. Knaeps E, Ruddick KG, Doxaran D, Dogliotti AI, Nechad B, Raymaekers D, Sterckx SA (2015) SWIR based algorithm to retrieve total suspended matter in extremely turbid waters. *Remote Sens Environ* 168:66–79. <https://doi.org/10.1016/j.rse.2015.06.022>
32. Kopelevich OV, Burenkov VI, Sheberstov SV (2006) Development and use of regional algorithms for calculating the bio-optical characteristics of the seas of Russia from the data of satellite color scanners. *Curr Problems Remote Sensing Earth Space* 3(2):99–105
33. Kopelevich OV (2012) Application of data on seawater light scattering for the study of marine particles: a selective review focusing on Russian literature. *Geo-Marine Lett* 32(2):183–93
34. Kopelevich OV, Burenkov VI, Ershova SV, Sheberstov SV, Evdoshenko MA (2004) Application of SeaWiFS data for studying variability of bio-optical characteristics in the Barents, Black and Caspian Seas. *Deep Sea Res Part II: Topical Stud Oceanogr* 51(10–11):1063–1091

35. Kopelevich OV, Burenkov VI, Sheberstov SV (2008) Case studies of optical remote sensing in the Barents Sea, Black Sea, and Caspian Sea. In: Remote sensing of the European seas. Springer, Berlin, pp 53–66. https://doi.org/10.1007/978-1-4020-6772-3_4
36. Kopelevich OV, Kostianoy AG (2018) Use of bio-optical parameters of the ocean, derived from satellite data, as essential climate variables. *Fundamental Appl Climatol* 3:8–29. <https://doi.org/10.21513/2410-8758-2018-3-8-29> (in Russian)
37. Kopelevich OV, Sheberstov SV, Burenkov VI, Vazyulya SV, Likhacheva MV (2007) Assessment of underwater irradiance and absorption of solar radiation at water column from satellite data. In: Proceedings of SPIE, 6615, 661507
38. Kopelevich OV, Vazyulya SV, Saling IV, Sheberstov SV, Burenkov VI (2015). Electronic atlas “Bio-optical characteristics of the seas of Russia according to the data of satellite color scanners 1998–2014”. In: Current problems in remote sensing of the Earth from space, vol 12, no 6, pp 99–110
39. Kopelevich O, Vazyulya S, Sheberstov S, Bukanova T (2016) Suspended matter in the surface layer of the South-Eastern Baltic from satellite data. *Oceanology* 56(1): 46–54. <https://doi.org/10.1134/S0001437016010069>
40. Kosarev AN, Kostianoy AG, Zonn IS (2009) Kara-Bogaz-Gol Bay: physical and chemical evolution. *Aquatic Geochem* 15(1–2): 223–236 (Special Issue: Saline Lakes and Global Change). <https://doi.org/10.1007/s10498-008-9054-z>
41. Kostianoy AG, Kostianaia EA, Soloviev DM (2016) Satellite monitoring of Dzhubga-Lazarevskoye-Sochi offshore gas pipeline construction. In: Zhiltsov SS, Zonn IS, Kostianoy AG (eds) Oil and gas pipelines in the Black-Caspian Seas Region. Springer International Publishing AG, Switzerland, pp 225–260. https://doi.org/10.1007/698_2016_465
42. Kostianoy AG, Lavrova OYu (2014a) Oil pollution in the Baltic Sea. The handbook of environmental chemistry, vol 27. Springer, Berlin, 268pp
43. Kostianoy AG, Lavrova OYu (2014b) Conclusions. In: Kostianoy AG, Lavrova OYu (eds) Oil pollution in the Baltic Sea, vol 27. Springer, Berlin, pp 249–264
44. Kostianoy AG, Lavrova OYu (2014c) Introduction. In: Kostianoy AG, Lavrova OYu (eds) Oil pollution in the Baltic Sea, vol 27. Springer, Berlin, pp 1–14
45. Kostianoy AG, Lavrova OYu (2022) Satellite instrumentation and technique for oil pollution monitoring of the seas. In: Di Mauro A, Scozzari A, Soldovieri F (eds) Instrumentation and measurement technologies for water cycle management, Springer Nature Switzerland AG, pp 53–77. https://doi.org/10.1007/978-3-031-08262-7_4
46. Kostianoy AG, Lavrova OYu, Mityagina MI, Solovyov DM (2014a) Satellite monitoring of the Nord Stream gas pipeline construction in the Gulf of Finland. In: Kostianoy AG, Lavrova OYu (eds) Oil pollution in the Baltic Sea, vol 27. Springer, Berlin, pp 221–248
47. Kostianoy AG, Lavrova OYu, Mityagina MI, Solovyov DM, Lebedev SA (2014b) Satellite monitoring of oil pollution in the Southeastern Baltic Sea. In: Kostianoy AG, Lavrova OYu (eds) Oil pollution in the Baltic Sea, vol 27. Springer, Berlin, pp 125–154
48. Kostianoy AG, OYu, Lavrova, Solovyov DM (2014) Oil pollution in coastal waters of Nigeria. In: Barale V, Gade M (eds) Remote sensing of the African Seas. Springer, Berlin, pp 149–165
49. Kostianoy AG, Lebedev SA, Solovyov DM (2013) Satellite monitoring of the Caspian Sea, Kara-Bogaz-Gol Bay, Sarykamys and Altyn Asyr Lakes, and Amu Darya River. In: Zonn IS, Kostianoy AG (eds) The Turkmen Lake Altyn Asyr and water resources in Turkmenistan, vol 28. Springer, Berlin, pp 197–232
50. Kronberg P (1988) Remote sensing of the Earth. Mir, Moscow, p 350
51. Lavrova OYu, Kostianoy AG, Lebedev SA, Mityagina MI, Ginzburg AI, Sheremet NA (2011) Complex satellite monitoring of the Russian seas. IKI RAN, Moscow, 470pp (in Russian)
52. Lavrova OYu, Mityagina MI, Kostianoy AG (2016a) Satellite methods of detection and monitoring of marine zones of ecological risks. Space Research Institute, Moscow, 336p (in Russian)
53. Lavrova OYu, Soloviev DM, Mityagina MI, Stochkov AYa, Bocharova TYu (2015) Revealing the influence of various factors on concentration and spatial distribution of suspended matter based on remote sensing data—remote sensing of the ocean, sea ice, coastal waters, and large

- water regions 2015. In: Bostater CR, Mertikas SP, Neyt X (eds) Proceedings of SPIE, vol 9638. <https://doi.org/10.1117/12.2193905>
54. Lavrova OYu, Soloviev DM, Strochkov MA, Bocharova TYu, Kashnitsky AV (2016b) River plumes investigation using Sentinel-2A MSI and Landsat-8 OLI data. Remote sensing of the ocean, sea ice, coastal waters, and large water regions 2016. In: Bostater CR, Neyt X, Nichol C, Aldred O (eds) Proceedings of SPIE, vol 9999, 99990G. <https://doi.org/10.1117/12.2241312>
 55. Lavrova O, Krayushkin E, Golenko M, Golenko N (2016c) Effect of wind and hydrographic conditions on the transport of Vistula Lagoon waters into the Baltic Sea: Results of a combined experiment. IEEE J Selected Topics Appl Earth Observations Remote Sens 9(9):5193–5201. <https://doi.org/10.1109/JSTARS.2016.2580602>
 56. Lavrova OYu, Mityagina MI, Kostianoy AG, Strochkov M (2017) Satellite monitoring of the Black Sea ecological risk areas. *Ecologica Montenegrina* 14:1–13
 57. Lavrova OYu, Mityagina MI (2013) Satellite monitoring of oil slicks on the Black Sea surface. *Izv Atmos Ocean Phy* 49(29):897–912. <https://doi.org/10.1134/S0001433813090107>
 58. Lavrova OYu, Kostianoy AG (2011) A catastrophic oil spill in the Gulf of Mexico in April–May 2010. In: *Izvestiya, atmospheric and oceanic physics*, vol 47(9). Pleiades Publishing, Ltd, pp 1114–1118
 59. Marmorino G, Smith GB, Toporkov JV, Sletten MA, Perkovich D, Frasier SJ (2008) Evolution of ocean slicks under a rising wind. *J Geophys Res-OCEANS* 115:C04030
 60. Mironenko VA, Stanichny SV (1999) Possibilities of ecological monitoring of the shelf by satellite and polygon means. Environmental control systems. Collected papers, Marine Hydrophysical Institute, 303p
 61. Mityagina M, Lavrova O (2016) Satellite survey of inner seas: oil pollution in the Black and Caspian Seas. *Remote Sens* 8:875. <https://doi.org/10.3390/rs8100875>
 62. Mityagina MI, Lavrova OYu, Kostianoy AG (2019) Main pattern of the Caspian Sea surface oil pollution revealed by satellite data. *Ecologica Montenegrina* 25:91–105
 63. Mityagina MI, Lavrova OYu (2020) Oil pollution hotspots on the Caspian Sea surface identified using satellite remote sensing. In: Proceedings of SPIE 11529, Remote sensing of the ocean, sea ice, coastal waters, and large water regions 2020, 115290L. <https://doi.org/10.1117/12.2573501>
 64. Mityagina M, Lavrova O (2022) Satellite survey of offshore oil seep sites in the Caspian Sea. *Remote Sens* 14:525. <https://doi.org/10.3390/rs14030525>
 65. Nazirova K, Alferyeva Y, Lavrova O, Shur Y, Soloviev D, Bocharova T, Strochkov A (2021) Comparison of in situ and remote-sensing methods to determine turbidity and concentration of suspended matter in the estuary zone of the Mzymta River, Black Sea. *Remote Sens* 13:143. <https://doi.org/10.3390/rs13010143>
 66. Nechad B, Ruddick KG, Park Y (2010) Calibration and validation of a generic multisensor algorithm for mapping of total suspended matter in turbid waters. *Remote Sens Environ* 114:854–866. <https://doi.org/10.1016/j.rse.2009.11.022>
 67. Nechad B, Ruddick K, Schroeder T, Oubelkheir K, Blondeau-Patissier D, Cherukuru N, Brando V, Dekker A, Clementson L, Banks AC, Maritorena S, Werdell PJ, Sá C, Brotas V, Caballero de Frutos I, Ahn Y-H, Salama S, Tilstone G, Martinez-Vicente V, Foley D, McKibben M, Nahorniak J, Peterson T, Siliò-Calzada A, Röttgers R, Lee Z, Peters M, C (2015) CoastColour Round Robin data sets: a database to evaluate the performance of algorithms for the retrieval of water quality parameters in coastal waters. *Earth Syst Sci Data* 7:319–348. <https://doi.org/10.5194/essd-7-319-2015>
 68. Novoa S, Doxaran D, Ody A, Vanhellemont Q, Lafon V, Lubac B (2017) Atmospheric corrections and multi-conditional algorithm for multi-sensor remote sensing of suspended particulate matter in low-to-high turbidity levels Coastal Waters. *Remote Sens* 9:61. <https://doi.org/10.3390/rs9010061>
 69. Patin S (1999) Environmental impact of the offshore oil and gas industry. *Ecomonitor Pub* 425p
 70. Patin SA (2008) Oil spills and their impact on the marine environment and living resources. Moscow, VNIRO Publishing, 508pp (in Russian)

71. Petus C, Chust G, Gohin F, Doxaran D, Froidefond J-M, Sagarminaga Y (2010) Estimating turbidity and total suspended matter in the Adour River plume (South Bay of Biscay) using MODIS 250-m imagery. *Shelf Res* 30(5):379–339. <https://doi.org/10.1016/j.csr.2009.12.007>
72. Reinart A, Kutser T (2006) Comparison of different satellite sensors in detecting cyanobacterial bloom events in the Baltic Sea. *Remote Sens Environ* 102(1–2):74–85
73. Romankevich EA, Aibulatov NA (2004) Geochemical state of the seas of Russia and human health. *Vestnik of the Earth Sciences Branch of RAS* 1(22)
74. Sentinel-3 OLCI (2021) <https://sentinel.esa.int/web/sentinel/user-guides/sentinel-3-olci/product-types/level-2-water>. Accessed on 09.03.2021
75. Tavora J, Boss E, Doxaran D, Hill P (2020) An algorithm to estimate suspended particulate matter concentrations and associated uncertainties from remote sensing reflectance in coastal environments. *Remote Sens* 12:2172. <https://doi.org/10.3390/rs12132172>
76. UNCTAD (2020) United Nations conference on trade and development. Review of maritime transport 2019. United Nations, Geneva, 31 Jan 2020, 132p
77. Urdenko VA, Zimmerman G (eds) (1987) Remote sensing of the sea taking into account the atmosphere (1987) V.2. Part 2. Publishing house of the Institute of Space Research of the Academy of Sciences of GDR, Moscow, Berlin, Sevastopol, 197pp
78. Vazyulya S, Khrapko A, Kopelevich O, Burenkov V, Eremina T, Isaev A (2014) Regional algorithms for the estimation of chlorophyll and suspended matter concentration in the Gulf of Finland from MODIS-Aqua satellite data. *Oceanologia* 56(4):1–19. <https://doi.org/10.5697/oc.56-4.737>
79. Warrick JA, DiGiacomo PM, Weisberg SB, Nezlin NP, Mengel M, Jones BH, Ohlmann JC, Washburn L, Terrill EJ, Farnsworth KL (2007) River plume patterns and dynamics within the Southern California. *Bight Cont Shelf Res* 27:2427–3244. <https://doi.org/10.1016/j.csr.2007.06.015>
80. Werdell PJ, Franz BA, Bailey SW et al (2013) Generalized ocean color inversion model for retrieving marine inherent optical properties. *Appl Opt* 52:2019–2037
81. Werdell PJ, Lachlan IW, McKinna et al (2018) An overview of approaches and challenges for retrieving marine inherent optical properties from ocean color remote sensing. *Progr Oceanogr* 160:186–212
82. Xue K, Ma R, Shen M, Li Y, Duan H, Cao Z, Wang D, Xiong J (2020) Variations of suspended particulate concentration and composition in Chinese lakes observed from Sentinel-3A OLCI images. *Sci Total Environ* 721:137774. <https://doi.org/10.1016/j.scitotenv.2020.137774>

Chapter 6

Inland Water Altimetry: Technological Progress and Applications



Jean-François Cretaux

Abstract Hydrology, which is one of the oldest scientific disciplines, has experienced multiple technological and methodological breakthroughs over the last three decades. The advent of satellite radar altimetry have participated to a new range of applications in the monitoring of the continental water heights (on lakes, rivers, floodplains), in the study of global water cycle, and with a high range of scientific and societal applications. Satellite altimetry which was initially designed for oceanography has been widely used since the launch of Topex / Poseidon in 1992 in Hydrology because and it has allowed to calculate water height over the continental water bodies without restrictions, continuously, globally, regularly, and accurately. We present in this chapter the basics of the technics and how the data are processed, its forces and limitations, how it can be used together with other technics, how it can be assimilated into models, and what are the main outcomes over the last thirty years. Among hundreds of papers that are presenting applications of satellite altimetry in hydrology, we have done the choice to strengthen, what we believe are key studies that have left their mark on this discipline: Studies all centered on the use of satellite altimetry, for lakes, for rivers, for monitoring of artificial reservoirs, and how these measurements can be used in hydrological model in particular for studying ungauged basins.

Keywords Radar and laser satellite altimetry · Lakes · Rivers · Floodplains · Hydrological models

6.1 Introduction

Over the last decades, the questions of water availability, water uses, water sharing and supplying fresh water for basic human and economic needs became central in hydrology science. With the increasing of water scarcity in several regions, increasing of frequency of extreme floods in other regions, short, mid and long-term evolutions

J.-F. Cretaux (✉)

CNES/Legos, UMR 5566, Université de Toulouse, 14 Av Edouard Belin, 31400 Toulouse, France
e-mail: jean-francois.cretaux@legos.obs-mip.fr

of water stocks and discharge, there is a need for capacity of predictions, data assimilation in models, and basin scale data collection of essential variables used in the models. Lakes rivers and wetlands are moreover also highly linked to the continental water cycle. The major part of the world's demand on water relies on continental surface waters (rivers, lakes, wetlands and artificial reservoirs) and less by underground aquifer and sea water desalinization. However, ground hydrological survey's networks have regularly and drastically declined worldwide. In this context, current remote sensing techniques have been widely deployed by several countries for land surface monitoring purposes, including the survey of water over the oceans and the continents. It is therefore essential to quantify changes of the continental water cycle and to describe in an accurate manner the quantity of fresh water available on the Earth as well as its variability on time scales ranging from sub-seasonal to inter-decadal. Water is moreover not homogeneously distributed on Earth and does not coincide with the domestic, industry and agriculture needs. At global scale, river discharge is predominant in equatorial and temperate climate regions. Lakes are also irregularly distributed across continents with high concentration in the northern hemisphere and in boreal regions [29, 79, 89]. In any case, the fraction of water available for human use -agriculture, domestic use, industry, hydroelectricity, recreational activities, etc.- is negligible, being few thousandths of the total quantity of water on Earth. Monitoring this available quantity is therefore a major issue for humanity. For rivers, the key variable is the discharge. In the case of lakes and reservoirs, the key variable is the volume of water stored. These two variables depend on the level of water, which is a single parameter that can be directly measured. For what regards lakes and reservoirs, the relationship between volume and level is direct. For rivers, where the measurement of the discharge is often complex and expensive, empirical laws have made it possible to establish relatively simple relations between the water level in a reach and the flow that crosses it [64]. In a world where anthropogenic pressure on water is threatening the sustainability of the resource, the dramatic decrease of in situ (and freely available) data about the water levels in lakes and rivers, makes satellite radar altimetry an attractive source of information, which is fundamental for the monitoring of surface water bodies. In particular, satellite altimetry offers a straightforward view on the spatial and temporal distribution of surface water stocks. Currently, this technology permits the monitoring of several thousand sites on the largest hydrological basins and lakes, natural or artificial of the planet. The accuracy of the measurements ranges from a few centimeters on large lakes to a few decimeters on rivers. The temporal resolution varies from almost daily on the largest lakes to monthly on most of the reaches. In this chapter, we will describe how the satellite altimetry has been used since the mid-nineties in order to contribute addressing many of the issues related above. We'll rely on some key papers published last thirty years, focusing on for lakes, artificial reservoir, rivers and wetlands, and considering different applications: prediction, assimilation into models, water budget estimation, linkage to climate change, and role in the water cycle.

6.2 Radar and Laser Altimetry

6.2.1 Altimetry, the Principle and the Missions

There are several modes of operation for radar altimeters, LRM (Low Resolution Mode), SAR (Synthetic Aperture Radar) and INSAR (Interferometric SAR). The principle of radar altimetry is to send an electromagnetic pulse towards the nadir of the satellite and measure the round-trip time of the emitted wave and its echo travelling back from the illuminated surface (Fig. 6.1). The distance R between the satellite and the reflecting surface (called “range”) is calculated by multiplying half time of this round trip by the speed of light.

The ellipsoidal height H of the reflecting surface is given by the following relation:

$$H = Alt - R + \sum C_p + \sum C_g + B \quad (6.1)$$

where Alt is the altitude of the satellite above the ellipsoid of reference.

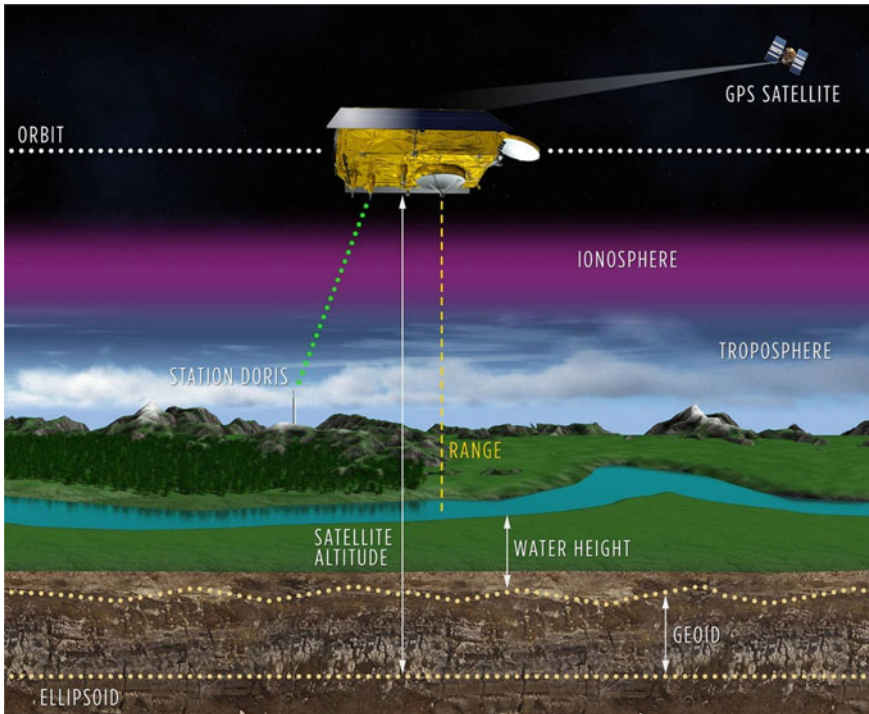


Fig. 6.1 principle of the satellite altimetry technique over continental waters

The ellipsoid height is then converted to altitude by taking into account the local undulation of the geoid N :

$$h = H - N \quad (6.2)$$

The terms C_p and C_g consist essentially of two types: propagation corrections (C_p) and geophysical corrections (C_g). Propagation corrections are related to the prevailing radiative transfer effects introduced by the atmosphere, essentially consisting in a delay (i.e., the fact that radar pulses travel through the atmosphere at a lower speed than the speed of light). Geophysical corrections are connected with vertical movements of the Earth's surface (e.g., tides) for which it is desirable to correct the measurement to a fixed reference in the Earth's reference frame. An electromagnetic instrumental bias (B) must also be considered when several satellites are used for the calculation of a mean lake or river height [27].

The methodology to calculate water height over continental water (lakes, rivers, wetlands), with description of each of the term of Eqs. 6.1 and 6.2 has been published in dozens of papers, so we'll not describe it in details. In the following we will assume that the reader has some basic knowledge or practice in pulse-limited radar altimetry. Some of technical terms and concepts were already introduced in [90]. For an in-depth presentation of technical aspects of satellite altimetry, the reader is invited to refer to [20, 21, 37] and for specific application to inland water we invite the readers to refer to [10, 28].

Altimetry was initially designed in the 1970s for oceanography. It was then used for the study of continental surfaces that lent themselves to it, notably in hydrology and glaciology, two application contexts where the observation of the height of water or ice surfaces is imperative. The principle of the instrument does not change, but the heterogeneity of the targets or the presence of slopes complicates the interpretation of the measurements. Moreover, we speak of altimetry missions, because all the sensors on-board the satellites contribute to the quality of the measurement. Positioning sensors for the orbit, but also radiometers for sensitivity to atmospheric humidity or dual-frequency altimetry systems to correct ionospheric delay are all onboard the same platform, in order to improve the accuracy of height measurements. However, not all these auxiliary sensors work on continental surfaces as well as on ocean surfaces.

The first altimetry missions date back to the 1970s. More than 30 years passed since the GEOdetic SATellite (GEOSAT) satellite mission was launched and the radar altimetry performances were progressively increasing, allowing using them over continental waters, reaching today few centimeters precision in range estimation over big lakes [27, 30, 38, 73, 74]. The radar altimetry progress is due on one hand to precise orbit determination with the new DORIS (Doppler Orbitography and Radiopositioning Integrated by Satellite) positioning system [18] and on the other hand to the evolution of radar altimeters and their performances.

But the first one that was really used over continents was the Franco-American oceanographic mission Topex/Poseidon (T/P), launched on 10 August 1992 by CNES (French Space Agency) and NASA (US Space Agency). T/P collected measurements

for 13 years, and it's been followed by two other satellites: Jason-1, launched on 7 December 2001, and Jason-2, launched on 20 June 2008. Jason-1, optimized for the oceans, has collected almost no measurements on continental surfaces, except on a few large lakes. Jason-2, more flexible, still collects measurements on large rivers and hundreds of lakes. It has shifted in 2016 onto a geodetic orbit, which is much less useful than repeat orbit, but its successor, Jason-3, launched in 2016, now ensures the continuity of the measurements along the same original orbit of Jason-2. Indeed, all of these satellites are in the same orbit, which allows the creation of long time series of measurements. The other important satellite family for continental water altimetry is the ERS-2, Envisat, and SARAL family. ERS-2 and Envisat were ESA (European Space Agency) missions. They were launched respectively on April 21, 1995 and March 1, 2002. ERS-2 operated until early 2003 and Envisat until the end of 2012. Envisat was replaced on the same orbit by the SARAL satellite, which was launched jointly by CNES and ISRO (Indian Space Agency) on February 25, 2013. One important objective of the mission was to extend the time series started in 1995 with ERS-2.

For many years, considerable efforts have been made towards enhancing the capabilities of radar altimetry. SAR-Interferometric mode (SARIn) tracker on-board Cryosat-2 mission came with several major improvements.

Instead of transmitting—as in LRM mode—the radar pulses sufficiently “slowly” (1 to 2 kHz) so that the individual echoes are well decorrelated from each other by the natural roughness of the water surface and a “Brownian” waveform can be obtained by adding the received powers, in SAR mode, pulses are transmitted at a high rate, of the order of 10 kHz, making use of the fact that these echoes will be highly correlated with each other. In practical terms, the SAR mode allows the disc illuminated by the radar to be “sliced”, i.e. waveforms are much less spread out, giving a much improved ground resolution (of the order of 300 m).

Cryosat-2, launched in April, 8, 2010, is equipped with the SIRAL instrument having two antennas, mounted about 1.1 m apart, which receive the same signal almost simultaneously. SIRAL operates in Ku-band, SAR mode, and thanks to its dual antenna configuration it also offers a SARIn (interferometric) mode. This SARIn mode of Cryosat-2 allows determining the precise position of the reflecting point in the radar footprint. This is particularly useful since in many cases over continental waters, the measurements are not taken directly at the nadir, which means that, SIRAL can solve the signal location along-track and across-track giving possibility to locate the echo source in 3-dimensional space. The range extension due to the tilt of the measurement can be easily corrected in the particular case of SARIn operation, since the relative position of the reflector with respect to the satellite is known exactly. The big disadvantage of Cryosat-2 for hydrology is that we cannot keep the idea of measuring water level of lakes and reservoir at high temporal frequency, since the repeat cycle is 369 days. However, it has the advantage of very short inter-track distance (7.5 km at the equator) which allows monitoring a large number of small lakes not visible with other altimeters. With now more than 10 years of data, with very high-density coverage of the measurements, this would be possible to determine decadal water level changes on thousands of small lakes worldwide. Nielsen et al.

[68] and Jiang et al. [48] among other authors have shown the great interest of using this mission over small lakes and along rivers.

In 2016 and in 2018, ESA has launched two satellites carrying among other instruments radar altimeters, the SENTINEL-3A and 3B satellites. These satellites are planned to last a dozen years each, which guarantees the continuity of the time series of measurements over nearly a quarter of a century since it will be followed by a series of two other ones, Sentinel-3C and 3D. Each satellite in a pair is placed in an orbit with 27 days of repeatability, the two orbits being interleaved. These satellites operate in SAR mode, in Ku band. This program is the first operational altimetry program for monitoring continental water levels. With the increased accuracy using the SAR mode compared to the LRM mode, in addition to the OLTC onboard, there are actually thousands of virtual stations and lakes that are potentially tracked, with a very high accuracy.

A second major step will be achieved by the Franco-American CNES/NASA SWOT mission, which is scheduled to be launched in end of 2022 and will operate for 3 years. With SWOT, there will be no longer only measurements along the ground tracks of the orbits, but a quasi-total coverage of the globe (with the notable exception of the poles) thanks to its wide swath radar interferometer (Fig. 6.2). The orbit has

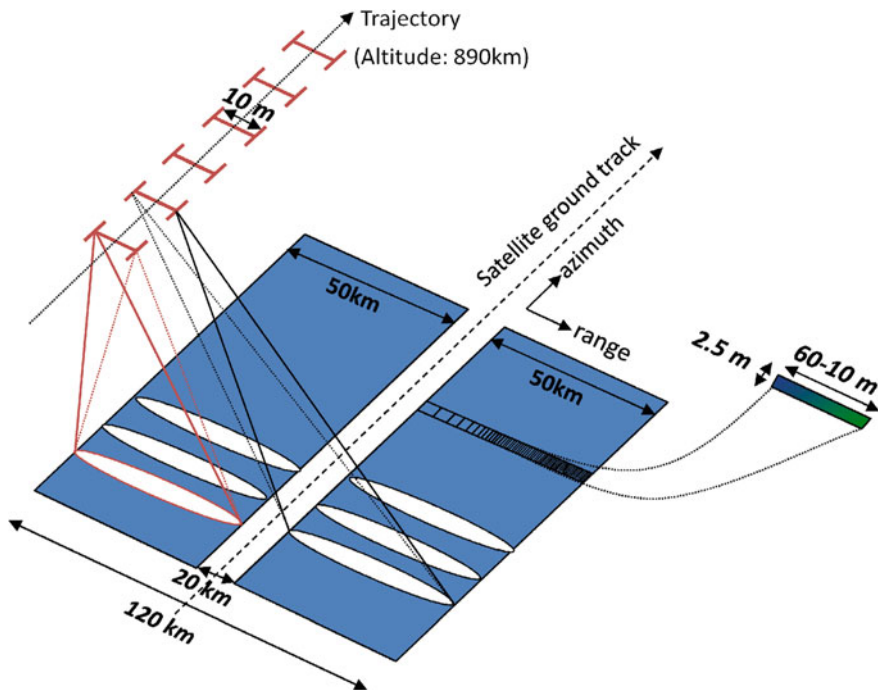


Fig. 6.2 SWOT principle. The cross-track resolution range is lost near range (60 m compared to 10 m far range). Along track the resolution is 2.5 m. A ± 10 km is blinded near the Nadir. The two swaths (left and right) have a 50 km width

been chosen in such a way that the swaths are contiguous when crossing the equator. This mission will be characterised by at least 2 measurements per 21 day cycle. The expected accuracy should be comparable to that of the SENTINEL-3 missions, i.e. a decimeter accuracy at a spatial resolution of the order of 1 km^2 . Such a complete coverage will impact positively the study and usage of long time series. Since the lifetime of a satellite mission does not exceed ten years, producing series of several tens of years necessarily requires the concatenation of series produced by successive missions. Since the SWOT swaths will overlap the ground tracks of all other missions, they will allow an accurate calculation of biases with all missions still flying, such as the SENTINEL-3 and Jason missions, and of all missions between them. Extending into the past with the archives of previous missions the time series collected from 2022 onwards will allow a much finer study of the long-term evolution of the global hydrological cycle. In particular, it will be possible to study the impact of human activities from global to local scales, down to the watershed level. The SENTINEL-6/MF mission launched in November 2020, with its follow-on scheduled for the year 2026, already ensures the continuity of the Jason missions in terms of coverage, but with the strong technical advantage given by the availability of the SAR operational mode.

One of the challenges for the future will be to maintain a constellation of satellites in orbit, in order to ensure the continuity of services, both in hydrology and oceanography. Nevertheless, projects are emerging in space agencies to strengthen the use of this technique, especially for hydrology at high temporal resolution. CNES is working on a new altimetric concept to observe rivers, no longer with weekly or monthly cycles, but daily. This is to meet operational needs for monitoring floods that may occur in very short time. The principle is based on the orbiting of a constellation of small satellites (SMall Altimetry Satellites for Hydrology^{SMASH}), in formation, so that the temporal resolution at a given point will be one day, even if the spatial coverage will be less dense than with classical altimeters or with SWOT. The constellation is formed by ten satellite of small size and weight carrying a nadir altimeter, put on a sun synchronous orbit. It will allow monitoring small width's rivers (50 m) and lakes (10 ha), with a very short latency of few hours.

To ensure continuity of swath altimetry measurements, a concept is under study (phase A) at CNES and will be proposed to ESA in the framework of the "Copernicus—New Generation" program, concerning a part of the new generation Sentinel-3 (after 2030). This concept, called Wide Swath Altimetry (WiSA), corresponds to a constellation of probably 2 wide swath altimeters, quite similar to SWOT. However, the specifications of this mission are relaxed compared to SWOT, but with a much longer design lifetime of about 10 years.

It seems very promising for the future to imagine, with these new missions in preparation (SMASH, WISA) or about to be operational (SWOT), allowing to obtain in quasi real time and on a long period of time, measurements with high spatial and temporal resolution. This will probably open new perspectives of applications for the monitoring of continental waters.

In addition to radar altimeters, the NASA has launched two satellites (ICESat and ICESat-2) carrying each a laser altimeter. The ICESat was launch on January 12, 2003

on a near polar (94° of inclination) at 90 days repeat and near circular orbit with an altitude of 590 km [76]. It operates the first Lidar onboard a satellite, namely a dual beam laser (GLAS) emitting at wavelength of 1064 and 532 nm [98]. Altimetry is derived of the 1064 nm beam measurement. The laser footprint is ~ 70 m and the data spacing is ~ 170 m. Because the laser beam suffers technical problems, it is turned on only for short periods (typically 2-month windows twice a year). However, thanks to its high orbital coverage of the Earth surface, many studies have been published using this mission, in particular for the monitoring and the understanding of the lake water level changes over the Tibetan Plateau [96]. This mission has ended in 2009.

In September 15, 2018 the ICESat-2 satellite was launched, carrying the Advanced Topographic Laser Altimeter System (ATLAS). This laser splits a single laser pulse into beams, by three pairs, providing a very dense coverage of the Earth Surface. It has a very high vertical accuracy with a small footprint (~ 17 m of diameter, compared to several km for radar altimeters) which allows measuring water height on very small lakes [11]. There is no doubts that after few years of operation of this mission, this will provide us with a completely original and hitherto unequalled view of continental surface waters.

6.2.2 Limitations, Accuracy, and Current Improved Algorithms

The classical nadir altimetry has still many disadvantages among others: echo source localization ambiguities and off-nadir target tracking abilities which means that there is no guarantee that the range measurements are taken directly at nadir and their precise localization cannot be calculated. However, this can be turned into advantage in some situations when river sections for example are so small that no nadir measurements are collected just right over the target but could be seen in obliquity few kilometers aside of the river: this is called the hooking effect allowing measuring very small river sections or very narrow reservoirs [80]. In addition to that, waveforms received during continental overflight have huge variety of shapes and noise artifacts which can mislead classical tracking and retracking algorithms.

6.2.2.1 Retracking of the Waveforms

Satellite altimeters are active radars (or lidar) designed to measure the two-way travel time of short radar pulses reflected from the Earth's surface. The shape of the reflected signal, known as the "waveform", represents the time evolution of the reflected power as the radar pulse hits the surface. Waveforms are acquired thanks to a tracking system placed on-board the satellite known as "trackers". Almost all oceanic waveforms have standard "ocean-like" or "Brown-like" shapes, where initial

thermal noise is followed by a sharp rise called leading edge, and a gently end sloping plateau mixed with noise known as the trailing edge.

The purpose of the on-board tracker is to interpret received waveforms, adapt to changes in the pulse shape, and adjust the reception window and gain attenuation for next incoming echoes. The tracker predicts the likely position of next echoes based on information derived from the echoes recorded previously to ensure fine adjusting of the reception window. This computation is performed autonomously on-board the satellite, and most recent nadir altimeters, uses a second order filter closed loop (called the α - β tracker) which uses the error signal and interpolates the position and gain of the range window for next 100 Pulse Repetition Intervals (PRIs).

In order to obtain the highest possible accuracy on range measurements, waveforms are down linked to the Earth and the interpretation of these data is done on the ground. This process is called the waveform retracking. This approach grants flexibility in data reprocessing with new better adapted algorithms. Indeed, over continents, a huge diversity of waveforms exists. Many of them are strongly contaminated by noise from multiple land returns especially in rapidly changing topography. Over continents the echo received is very different from the Brown-like shape presented above. It becomes extremely variable, depending on the greater or lesser contamination produced by the backscattering of the surrounding environment of the water body, especially in the case of rivers or small lakes. It is therefore no longer possible to find a single analytical expression for the determination of an accurate A/R time for all waveforms. However, waveforms useful for continental hydrology (lakes, rivers, reservoirs) are expected to possess generally at least one distinctive leading edge from radar beam interaction with water surface. Even oceanic class waveforms can be encountered in the middle of very large lakes, while specular waveform can be observed closer to the shore lake, where generally wave are very small.

In order to solve this problem, and to measure lakes and river water height with high accuracy, dedicated algorithms have been developed over the last two decades. This specific data processing is called waveform retracking.

An essential step was taken with the Envisat mission launched in 2001 by ESA. For this mission, ESA decided to break with the principle of a single range estimate and to propose in its GDRs (Geophysical Data Records), for each measurement, several range estimates made by algorithms that are very different in principle. Frappart et al. [33] then showed that the quality of the estimates varied significantly according to the algorithm used and that, among the four possibilities proposed in the Envisat GDRs, the so called OCOG retracker [3] allows obtaining the most accurate results. Since then, in order to promote the use of satellite altimetry in hydrology, the Jason-2, Jason-3 and Saral-AltiKa also contains ranges retracked with the OCOG retracker. For some historical missions (Topex/Poseidon, ERS1, ERS2) the wave forms have been retracked too, while at the same time other initiatives applied different retracking algorithms and provided dedicated processing for hydrology products. A full description with many details on the retrackers is given in Cretaux et al. [28].

6.2.2.2 Open Loop Tracking Command (OLTC)

Since JASON-2, a new concept is the combination of Digital Elevation Model (DEM) with DORIS on-board navigator (DIODE [47]) also called the an Open-Poop Tracking Command (OLTC, [15, 85]) This experimental mode has the ability to replace the standard tracking closed-loop. The planned reception window position is calculated directly by the altimeter, by combining the altitude information provided by DORIS/DIODE on one hand, and on the other one, the altitude derived from the DEM recorded in the on-board memory. Depending on the quality and the sampling of this fragmentary DEM, reception window position can be estimated with a precision of few meters. The combined use of DIODE data and the pseudo DEM altitude ensures target tracking abilities independent of the return echo shape. This mode can be extremely useful for tracking upcoming areas of special strengths, such as rivers and lakes. It also guarantees no tracking anomalies dues to unexpected echo formation or target topographic position and can be used in areas where conventional trackers fail. DIODE/DEM mode was tested on the SENTINEL-3A and SENTINEL-3B during the tandem phase, in order to compare performance of close and open loops. It has shown that open loop presents almost no missing data which was not the case with close loop and that accuracy with open loop has also been improved [85]. From previous studies the OLTC was also implemented on Jason-2 and Jason-3 and it has been shown that the number of target has been increased by more than 40% in open loop [5, 65]. Currently the OLTC is onboard Jason-3, sentinel-3A and sentinel-3B and last version includes more than 33,000 targets.

6.2.2.3 Full Focus SAR

In SAR altimetry, in contrast to LRM, the radar pulses are emitted at much higher rate (18,000 per second instead of 2000), which allows the phase of the signal remaining constant from one pulse to another one. Based on this characteristic, the SAR altimetry is based on the doppler effect. The data processing is therefore different than the one used for LRM. Interpreting this doppler effect, it allows discriminating the radar wave form footprint in small slices of 300 m along the track of the satellite (Fig. 6.3). It is classically named unfocused SAR processing and it is applied to burst of 64 pulses. This technique has the advantage over the LRM to allow a greater fineness of measurement for coastal areas, deltas, lakes, rivers or narrow reservoirs. Since unfocused SAR is design only for bursts that are coherently processed together, a new method, called unfocused SAR has been recently developed following the paper of [31]. In this method, the SAR integration time has been increased. Since the resolution is inversely related to the integration time, in fully focus SAR altimetry, it allows to improve drastically the along-track resolution: from 300 m to 50 cm allowing for a better noise reduction and consequently increasing accuracy for small water bodies. Cross-track resolution remains unchanged.

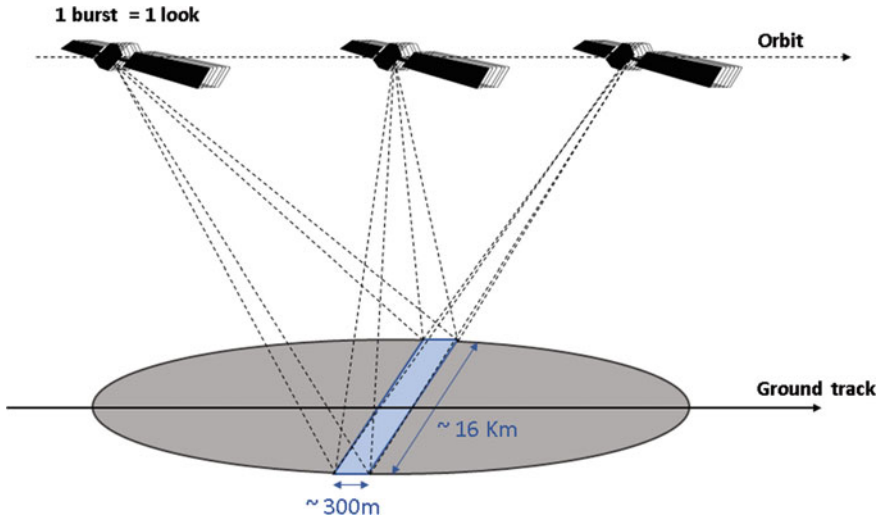


Fig. 6.3 Principle of the SAR altimetry. It uses the doppler effect to determine where the beam reflected, between reflections from behind and in front of the transmitted beam, allowing to split the beam in small width slices of 300 m along the track over the footprint

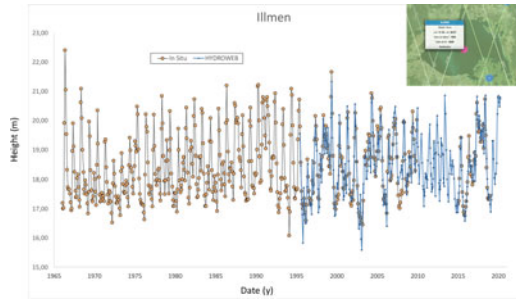
The application of this algorithmic technique on SAR measurements from past (Cryosat-2), current (Sentinel-3A/B) and future (Sentinel-C/D) missions could represent a tremendous advance in the monitoring of small lake or river structures.

6.2.2.4 Assessment of Altimetry Accuracy on Lakes and Rivers

Since the first altimetry missions in the 90s until today, the technique has largely evolved as indicated above, dedicated algorithms for continental surfaces have been developed to improve performance, and finally many studies have been conducted to evaluate performance in different terrain configurations: large/small lakes, wide or narrow rivers ([6, 67] and many others). It would be tedious to quote all these studies, and probably we would forget some, however we can mention some synthetic results on the subject.

Logically, successive improvements in altimeters have led to increasingly higher performance for continental waters. With older altimeters it was shown that water levels could be determined in large lakes better than decimeter [46, 77, 78] and decimeter on large rivers such as the Amazon [33] if OCOG-type retracking algorithms were used. Then, many studies focused on the Ka-band altimeter (Saral/AltiKa) showing a clear improvement for smaller targets [1, 34, 63] it is with the advent of SAR altimetry that the performances have crossed a threshold with more often centimetric accuracies [25, 38, 49, 52, 68, 91]. In the framework of the CCI project on lakes, the quality of successive altimeters is evaluated, and confirms very amply the clear improvement with SAR altimeters (Fig. 6.4).

Fig. 6.4 Comparison of water height of lake Illmen (Russia) measured with in situ and with satellite altimetry. Until 2016, the standard deviation of the difference is 33 cm, then 15 cm once SAR altimetry on Sentinel-3A was used



It is therefore remarkable that altimetry has now made it possible to measure water levels in lakes and rivers with unprecedented accuracy, opening the door to numerous applications, notably for long-term monitoring of the water cycle, or the impact of climate change. New applications in the field of accurate discharge determination on rivers [5, 7, 13, 39, 40, 44, 70, 74, 75] or flood monitoring in large flood plains [35] are also now within reach.

6.3 Applications of Satellite Altimetry

Historically, researchers have principally tried to quantify the accuracy of satellite altimetry products for lakes and rivers first, considering in situ datasets available. The idea of many papers was to simply demonstrate that satellite altimetry allows measuring water height with a high accuracy aiming to deliver some valuable products for hydrologists. However, the quality was somehow not always at the required level for improving the models or the predictions or the water resources monitoring. This was, what we can call, the primitive era of hydrology from altimetry, in another words, an attempt to modestly contribute to hydrology, and to promote the use of this technic in a context of in situ data scarcity.

Thanks to improvements in the instruments in orbit, thanks to increasing involvement of researchers, and thanks to improvement in the altimetry level 1 and level 2 data processing, gradually, this technique has taken off towards multiple applications with more and more efficient results. This has resulted in several innovations in the field of assimilation of altimetric data in runoff/rainfall models, for the quantification of water balance on a basin or large lake scale, for monitoring water stock variations in large floodplains, and finally for flood prediction models in particular. This has also led, as indicated in the introduction, to the major space agencies explicitly including water cycle objectives in the new instruments designed by these agencies. None of these advances were made in isolation, that is, little by little, satellite altimetry has been used in conjunction with other satellite techniques: optical and radar imagery, gravimetry, active and passive microwave, etc. Today, the constellation of instruments in orbit is very favorable and allows us to consider that satellite altimetry has

entered a new era, an adulthood that makes it essential for many applications. We will show some concrete examples illustrated by leading publications in the field.

Continental waters are an integral part of the global climate system with important links and feedbacks generated through influence on surface energy and moisture fluxes between continental water, atmosphere and oceans. Because of their response to regional and global variations in the climate system, lakes, are not only an integrator of climate processes, but also strong indicator of existing or potential change. It is important to well understand what are temporal and spatial scales of variability of natural parameters of lakes, what are teleconnections, feedbacks and mechanisms responsible for the changes, what are natural and anthropogenic causes of recent and historical changes in the hydrophysical and meteorological parameters. This lack of comprehensive and multidisciplinary assessment of environmental changes in hydrometeorological and limnological conditions, that have been taking place for the last 20–30 years, stresses the need for a dedicated effort aimed at filling this important information gap. Significant improvement may be made using satellite observations that for three last decades provide low-cost, regular and reliable data over vast regions. Since the launch of Topex/Poseidon, one of the most discussed topics with altimetry was to measure lake levels, and to demonstrate the high quality of these measurements and to think about various applications. Over the last ten years, a very high numbers of papers have been published for the survey of the Tibetan lakes. More recently, in 2019, the ESA has opened a new phase of the CCI (Climate Change Initiative) for the measurements and production of Lake water level fully based on satellite altimetry. Since, hundreds of studies have shown that this technic is mature enough for such purpose; it was also decided to develop a fully operational monitoring of lake level through the C3S and Copernicus European programs based on Hydroweb database developed at Legos, Toulouse, France (<http://hydroweb.theia-land.fr>). The United States Department of Agriculture has also developed an operational monitoring of lakes and reservoirs (G-REALM (www.pecad.fas.usda.gov/cropexplorer)) fully based on satellite altimetry. Other groups, De Monfort University, (Leicester, RU¹), DFG (Deutsches Geodätisches Forschungsinstitut) of Munich University (TUM, Germany²), ANA (Agencia Nacional de Aguas, Brasilia, Brasil³) and DTU (Space, National Space Institute, in Denmark⁴) have also developed their own database of lakes (and rivers) using satellite altimetry.

6.3.1 Lake Studies Using Satellite Altimetry

In order to illustrate the large interest of satellite altimetry for lakes, the example of the Tibetan lakes is particularly compelling. The Tibetan Plateau (TP) is the highest

¹ **River & Lake** (tethys.eaprs.cse.dmu.ac.uk/RiverLake).

² **DAHITI** (dahiti.dgfi.tum.de).

³ **Hidrosat** (hidrosat.ana.gov.br).

⁴ **AltWater** (<http://altwater.dtu.space/>).

and most extensive upland in the world and is generally considered as the Third Pole. It is one of the most sensitive regions of the Earth to climate changes [45] and many others). The climate system of the TP is characterized by climate high spatio-temporal variability of rainfalls with very dry conditions in the northwest (50 mm/year of rainfalls in average) to more humid conditions in the Southeast (700 mm/year in average).

In mountain regions the water storage in lakes are indicators of many changes at regional and global scales. They are also essential as a source of fresh water for population and for ecology of the surrounding terrestrial areas that are highly dependent on the water cycle and inter-annual variability of water storage of the lakes themselves. Radar altimetry data over mountain lakes is a very suitable because they are often the only one source of information for surface water level monitoring, and the strength of the radar altimetry is enhanced when associated with other remote sensing data. For the TP, the advantages of using radar altimetry for the lakes are that these lakes are fully natural, and moreover the region is still poorly instrumented. Therefore, Radar (and laser) altimetry presents a unique opportunity to study the impact of climate change on the TP from the prism of lakes (Fig. 6.5), and it has been intensively utilized last years [54, 60, 84, 93, 96], Cretaux et al. [24].

Several studies have now already been published to investigate the impact of climate change on the TP, particularly in term of water resources. It has been widely

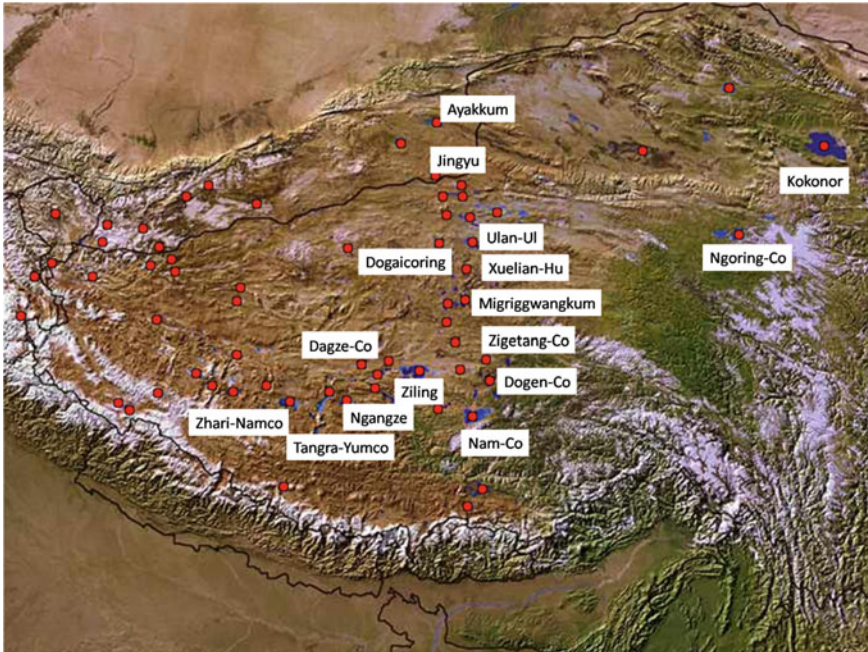


Fig. 6.5 Map of the TP with the location of the largest lakes with potential water height using satellite radar altimetry

recognized and admitted that the TP heated over the last decades in a higher degree ($0.36^{\circ}/\text{decade}$ from 1964 to 2007: [92], and of $0.16^{\circ}\text{C}/\text{decade}$ from 1955 to 1996: [62] than over the rest of the Earth. In contrast to the homogeneous air temperature increases over the TP, precipitation long term changes present regional patterns and large inter-annual variability. It became dryer in its northeastern and western parts [50] with acceleration of this tendency over the last 30 years [45], while it tends to become much wetter in the eastern and central parts of the TP [50]. Significant warming over the last 30 years has been observed over the TP with pronounced effects in winter [45, 50, 62].

Climate change on the Tibetan Plateau has also been extensively studied over the past 10 years in terms of impacts on water level and stocks changes in lakes [58, 61, 97]. Generally, the studies were aiming to understand the observed lake level changes in terms of glacier mass balance and precipitation changes over the TP. Over the last four decades, it has been shown by Zhang et al. [97] that the lake level increased were principally observed on endorheic lakes indistinctly for glacier-fed and non-glacier-fed lakes. Several studies have concluded that the major driver of the observed lake level changes over the TP is the increased rainfall since glacier mass loss represents additional water supply leading to additional lakes expansion [97]. In order to determine the lake level change over the TP, covered, we recall, by hundreds of lakes in nearly fully remote areas, the altimetry mission like ICESat (1&2) or Cryosat-2 were suitable due to their very dense coverage (Table 6.1). A recent paper, [60], has highlighted the interest of Cryosat-2. The water level changes of more than 260 lakes were measured over a period of 10 years, from 2010 until 2019. Among many other studies, this paper illustrates with great relevance the incomparable capacity of altimeters to meet this challenge. These authors have shown that over the last decade, 76% of the lakes presented a positive trend of water level changes, with higher amplitude in the north TP than in the South. Thanks to the Cryosat-2 data they therefore did an interannual mapping of lake level changes, that they have completed with analysis of GRACE data allowing them to determine Total Water Storage (TWS) changes over this region. They observed three different phases, during the period 2010–2019: a quick increase until 2013, followed by a period of stable (or decline) water level until 2016 and for the last period, until now, they found a second fast rising of the lake levels. Geographically they observed that the lakes in the inner TP gained approximately 90% of the TWS gain during the decade 2010–2019. Many other studies have shown similar results, particularly during the period 2002–2009, using ICESat-1 data, or using satellite imagery on hundreds of lakes over the TP, but we wished to emphasized that a mission like Cryosat-2, which moreover operated in SARin mode over the TP, was not so much used in literature for lakes and river survey (mainly because of the very long period of repeat cycle), but that after a decade, this satellite can reveal all its interest and quality for such purposes.

Table 6.1 Summary of past and current satellite altimetry missions

Satellite (mode)	Agency	Frequency	Equatorial inter-track (km)	Period	Cycle (d)
T/P (LRM)	NASA/CNES	Ku	315	1992–2005	10
Jason-1 (LMR)	NASA/CNES	Ku	315	2002–2011	10
Jason-2 (LRM)	NASA/CNES/EUMETSAT/NOAA	Ku	315	2008–	10
Jason-3 (LRM)	NASA/CNES/EUMETSAT/NOAA	Ku	315	2016–	10
Sentinel-6-Jason-Cs (SAR)	NASA/CNES/EUMETSAT/NOAA/ESA	Ku	315	2020–	10
GFO (LRM)	NRL	Ku	165	2002–2008	17
ERS-1 (LRM)	ESA	Ku	80	1991–2000	35
ERS-2 (LRM)	ESA	Ku	80	1995–2002	35
Envisat (LRM)	ESA	Ku	80	2002–2011	35
SARAL (LRM)	CNES/ISRO	Ka	80	2013–	35
Sentinel-3A (SAR)	ESA	Ku	104	2015–	27
Sentinel-3B (SAR)	ESA	Ku	104	2016–	27
CryoSat-2 (LRM/SAR/SarIn)	ESA	Ku	7.5	2010–	369
ICESat-1 (LRM)	NASA	Laser	28.8	2003–2010 ara>	91
ICESat-2 (LRM)	NASA	Laser	28.8	2018–	91

6.3.2 *Reservoir and Transboundary Water Monitoring Using Satellite Altimetry*

Over the twentieth century, after a stable situation until the 1950s, the number of dams and reservoirs has increased continuously and drastically [19]. They are among the most widespread manmade infrastructure in global watersheds, are an important component of water resources management and, due to the international nature of many river basins, can play a role in regional politics. Their role is essential in many regions where water resources are sparse since they allow mitigation of negative impact of inter-annual flooding. They allow producing electricity, or supplying water for irrigation and cities.

In arid and semiarid regions, the management of reservoir is crucial since the availability of water for irrigation or human consumption fully depends on upstream reservoir release. Despite their social and environmental significance, our spatial inventories of dams and reservoirs, even for the large ones, have been insufficient, and we are lacking a thorough and accurate dataset documenting and quantifying the water storage temporal changes at regional to global scale. Moreover, more than 260 rivers worldwide are currently transboundary (crossing one or more international boundaries) and drain a total of 145 countries [94]. This means that a large number of countries are dependent on water originating from one or several upstream countries, and the water released from reservoirs. Any new construction of dams along a river, potentially can create a source of conflict between riparian countries, since it exacerbates the impacts of upstream hydraulic infrastructure and water use on downstream countries, as it is the case in different part of the world. For example, along the Tigris Euphrates, along the Nile, or in Central Asia [26]. Gleditsch and Hegre [41] show that the potential for conflict over transboundary river basins due to water sharing will increase over time. River basin commissions have been established a number of transboundary river basins to solve these issues and facilitate sustainable basin-scale water management. However, such initiatives have, in some cases, been limited by a lack of data sharing among countries or lack of in situ observing systems.

Although information system like ICOLD gives metadata on a very huge number of reservoirs on all continents, the water level, and storage variations in time are well known on only a very few regions while it is hardly or impossible to measure on the majority of the river basins. Based on model it however has been shown by Biemans et al. [8] that water supply by reservoirs worldwide for irrigation purposes has increased from $18 \text{ km}^3 \text{ year}^{-1}$ at the beginning of the XXth century to $460 \text{ km}^3 \text{ year}^{-1}$ to the end of the century. They have also highlighted a high disparity between different regions of the world. They have found that the impact of reservoirs is more pronounced in Asia, Europe and Africa. They also have shown time dependencies with for example amplitude of discharge variations of $\pm 10\%$ between May and February in Europe. However it is needed that results of models could be validated through measurements. Historically, the knowledge of reservoir storage change and discharge has been controlled by nations in which the reservoir and river reaches are located. Water management for such river, therefore, rely on international

treaties for transboundary cooperation. Without such treaties, basic and essential information such as water level changes on reservoir and discharge along the river, or water withdrawal for irrigation, are not disseminated between countries and can provoke inefficient water management and water use [43]. In such cases, remote sensing data, particularly altimetry data, have the potential to complement scarce in situ measurements. Several studies have demonstrated the benefits of satellite altimetry for improved forecast systems or for the calibration/validation of hydrological models in the specific context of transboundary basins [7, 26, 71], Hossain et al. [44].

On the Ganges and Brahmaputra rivers, the floods spread from upstream to downstream towards Bangladesh in several days. Nadir altimetry, which also allows to measure water levels in different places of the rivers, has in this case the ability to predict with a few days in advance the intensity of streamflow downstream during the floods. This was demonstrated by Biancamaria et al. [7]. The authors of this study have shown that the amount of water that propagates from upstream to downstream is predictable thanks to altimetry. For example, with the Topex/Poseidon mission, water level anomalies are predicted with a delay of about 5–10 days and an accuracy of about 40–60 cm. Coupled with hydro-meteorological information, this system based on satellite altimetry has been extended in another study [44] which relied on Jason-2 data on the Ganges and Brahmaputra rivers. Thanks to this, predictions could be made in the framework of an operational system, managed by the government of Bangladesh, with 3-day forecasts on several sites. Again, this system was based on a hydrodynamic model to improve the predictions. The forecasts were compared with downstream flow measurements and proved to be highly accurate up to 5 days. The great interest of these studies is that for the first time, at the turn of the 2010s, satellite altimetry was seen as a system with very important societal applications. Historically, we can say that it is at this time that altimetry has really moved from its infancy for hydrology, to a maturity that has come to light and allowed to imagine many new applications. We will see it later with studies on hydrodynamic models on large rivers and the assimilation of altimetric data in poorly gauged river basins.

If we now consider reservoirs along rivers at global scale, it appears that altimetry can also be of great interest. Indeed, in the global water cycle balance, and the understanding of the Global Sea Level Rise (GSLR) the artificial reservoirs play a role which is still not well assessed. It has been established that, the cumulative impoundment water on land due to reservoirs has rose from 0 in 1900 up to 11,000 km³ in 2007, which corresponds to a global sea level drop of about 3 cm and an average rate of -0.55 mm/year over the last 50 years [19].

It is considered that every new dam built, immediately causes a sea level drop. Chao et al. [19] based their study on the International Commission on Large Dams (ICOLD) database, which includes 29,484 reservoirs when they wrote their article. This is, as far as we know, the only attempt to use global in-situ data on dams and reservoirs to estimate their impact on the global sea level rise (GSLR). Among the different contributors to the GSLR, nowadays, reservoirs impact is still the object of the most uncertain quantification [42]. Gregory et al. [42] have shown that for reservoirs contribution, between the estimation given by Chao et al. [19] and another

one from Lettenmaier and Milly [59] many uncertainties remain. Moreover, inter-decadal variability is also likely significant with exponential increase of dams built between 1950 and 1980 followed by a decrease of new constructions over the last 40 years.

Since impact of reservoirs still remains a source of uncertainty on the GLSR attribution, inter-decadal and inter-annual changes of reservoirs water storage at global scale is also poorly known, if not completely unknown. Figure 6.6 shows for four reservoirs in North and South America, Africa, and Asia (Mead, Sobradino Cahora Bassa, and Kapchagay) that the water level changes over decades are on the order of several meters or dozens of meters. A global assessment of reservoirs intern-annual level variations worldwide was until recently impossible due to, first, lack of in situ data available, and secondly because of potential remote sensing data, like radar altimetry, covers a small proportion of reservoirs worldwide. Things have changed recently, mainly with the new ICESat-2 satellite, and it has been shown in a paper written by Cooley et al. [11].

This study has allowed us to foresee that within a few years we will be able to quantify perfectly the impact of artificial reservoirs on the water cycle, and in particular on sea level variations. Although [19] were able to show that this impact should be considered in the global budget, the estimates were still based on metadata that did not provide precise figures of these impacts. The study by Cooley et al. [23] is based on laser altimetry with the ICESat-2 mission over about a year and a half

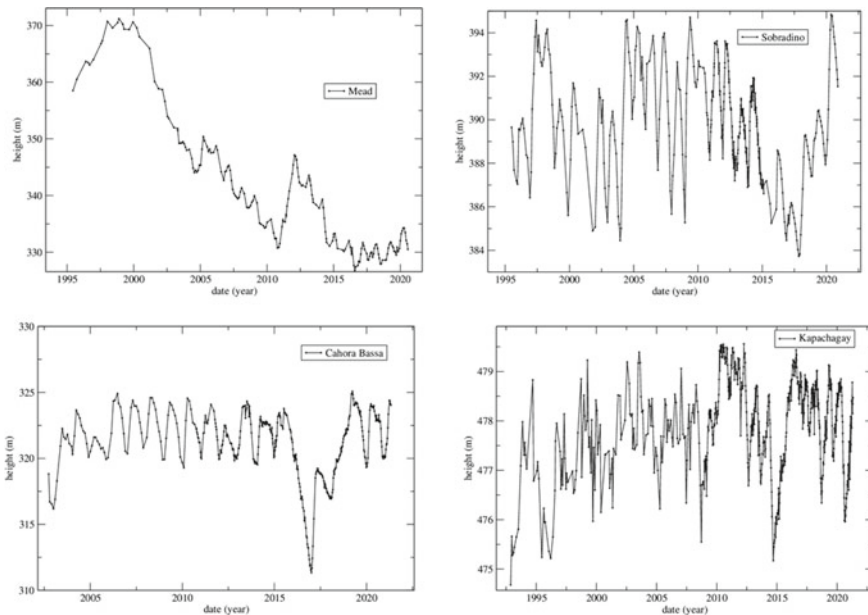


Fig. 6.6 Water level changes on artificial reservoirs, calculated using satellite altimeters: Envisat, Saral/AltiKa, Cryosat-2, sentinel-3A and sentinel-3B. *Source* Hydroweb data base

of measurements. This is of course insufficient to estimate multi-annual trends, but this study has shown that this mission can monitor a considerably large number of artificial reservoirs, and for the first time has quantified the seasonal variations of these artificial reservoirs over the globe. In this study, for the first time, almost 9000 reservoirs or lakes on which a dam has been built could be measured. A map of seasonal water level variations was even proposed. It could be shown that the highest variations are found in the Middle East and South America. For the watersheds where these values are high, such as the Brahmaputra or the Amazon, the variations are significantly higher than those of natural lakes in these same regions. Cooley et al. [11] have shown that artificial reservoirs present a major contribution to the surface water storage variability (57% was measured) although it represents a very small portion (4%) of the lakes and reservoirs at the Earth's surface. This study lays the foundations for what can be measured in the future, while waiting for the ICESat-2 mission to accumulate more data, but also in the perspective of SWOT.

6.3.3 Water Level Over Rivers and Applications for Ungauged Basin

Rapidly after the launch of Topex / Poseidon in 1992, first studies were performed in order to use the altimetry data for river level determination [9, 55]. The complexity to measure accurate water level along rivers was quite limiting and thus, in a first step, it was done only over the biggest rivers in the world like the Amazon, which was probably the most studied so far [2, 12, 35, 39, 40, 69, 70, 73, 80, 81, 83, 95]. Then, many other rivers were studied using satellite altimetry: the Congo [4, 57], the Ganga-Brahmapoutra [32, 34, 66, 71, 72, 94], the Mekong [13, 16], the Rio Negro [36] (Léon et al. 2006), the Sao Fransisco [63], the Zambèze (Michailovski et al. 2012, 2014; Kittel et al. 2021) the Ob [56], the Garonna [6] the Chinese river [49]. We probably miss many others. Large scale global monitoring was also done [82, 88].

However, in comparison to use of altimetry over lakes, some difficulties are more pronounced over rivers. The concept of a “virtual station” (VS) was developed by Seyler et al. (2005) to define a site for satellite altimetry measurement of water level over a river reach. Many efforts have been made to improve range determination from radar waveforms. However, having a good range estimate is not enough, because it is also necessary to identify the measurements related to the morphology of the surroundings of the water body, i.e. the banks of a reach or a lake, which should be discriminated from those measurements actually associated with the water surface of the object studied.

The ground footprint of the radar beam covers several tens of km². A reflecting surface on the ground like a water body, can appear in this footprint well before the satellite is exactly at the zenith of the water body. If the reflecting surface is homogeneous, the energy received decreases with the angle of incidence and the distance to

the center of the footprint. But it frequently happens that the energy reflected by an off-center object in the footprint is higher than the energy reflected by the objects in the center of the disk. The on-board tracking system will then progressively center the reception window on this dominant power peak, which position in the time domain is used for range estimation. This results in a parabolic shape of the reflected energy and of the range. Over rivers in general, it is therefore crucial to correctly select the measurements depending on their position. It may be challenging over rivers with moving river banks, or with high water extent variability in very flat areas. Moreover, in the case of oblique targets, the collection of consecutive measurements over several kilometers and on both sides of a river bed may be necessary. The tilted measurements might at first appear to be an annoying artifact. They have been actually proven to be extremely useful. On very small lakes and narrow rivers that can be considered as such bright spots, fitting these parabolas to the set of measurements concerned allows to estimate heights in a much more accurate way than if one were to use the only measurement (if it exists) at the nadir of the object [17]. Taking this artifact into account allows to calculate thousands of time series on small rivers, especially when they flow in dense forest, as in the Amazon or the Congo basin.

All the studies mentioned above have progressively demonstrated that it is possible to obtain very precise time series of water levels on rivers. However, these estimates cannot be an end in itself, and since the late 2000s, early 2010s some studies have shown that we can, and must, go well beyond. If for lakes, the water stock variable is essential, for rivers it is the discharge variable. The question then became: can we deduce from these measurements of water height by satellite at virtual stations, the discharge of rivers.

The river discharge informs on the evolution of the water stock in the watershed upstream of the measurement point. Its knowledge is therefore essential, both for scientific studies and for the evaluation of the impact of human activities on the hydrological cycle or simply for the management of these activities, from the watershed scale to the global Earth scale. In practice, it is not possible to directly measure the amount of water passing through the cross section of a river bed. The flow rate, which is the amount of water per unit of time, is estimated indirectly by measuring the velocity of the flow, integrated over the cross section of the river. These measurements are costly and time consuming. It is therefore not feasible to repeat them every day. In order to have a daily estimate of the discharge, the operators establish empirical relations between the discharge and the height of water in the reach, the measurement of the height of water being much easier to carry out at lower cost, even to automate. These head-flow relationships (called rating curves) are calculated from a few discharge measurements, taken at the most varied states of the hydrological cycle, from low water to high water. One can easily imagine calculating these rating curves from altimeter measurements. Several methods have been developed for this purpose. The first method consisted in taking discharge measurements from the in-situ station closest to the Virtual Altimeter Station considered, and fitting an empirical curve. This method has been used by Zhakarova et al. (2006) on the Amazon, [71] on the Ganges, [14] on the Mekong, and [56] on the Ob, among others.

The second approach was to calculate discharge from a model, essentially a rainfall-runoff model. These models estimate the fraction of rainfall which is captured by the vegetation, which is evaporated, which penetrates the soil and which will reach the river by runoff or subsurface discharge. The first study of this type was that of Guetirana et al. (2009) on sub-basins of the Amazon. The methodology was later extended to the entire Amazon basin by Guetirana and Peters-Lidard (2012). The work of [74] is very similar to that of Guetirana et al. (2009) in the data used, both for the discharge model (HPI MGB model, [22]) and for the virtual station database [81]. The advantage of the methodology proposed by Paris et al. [74] is that it provides, in addition to the discharge itself, uncertainty in the value, which is related to the uncertainties in the elevation data, in the model discharges, and in the goodness of fit of the rating curve to the height-discharge pairs. This uncertainty information is far from negligible. The discharge from the rating curves can be very different from those measured. It is therefore important that users of these discharge estimates have this information in some way, and propagation of uncertainties is the common way to inform about the accuracy of the estimate. Other authors developed original methods based on combination of several sensors (radar altimetry and optical imagery) to determine the discharge of rivers at virtual stations [75, 86, 87].

Further work was done at the same time by Paiva et al. [69, 70], this time not determining flows from elevation data coupled with rating curves or by combining different spatial sensors, but by directly assimilating the height measurements on the virtual stations into the MGB model, which was applied to the Amazon basin. The Amazon basin is the largest hydrological system in the world which is drastically driving the carbon cycle and consequently the global climate. The importance to monitor the hydrological cycle over the Amazon basin is moreover essential for navigation purpose, or understanding the extreme flood and drought. This understanding necessarily requires a fine modeling of physical phenomena and a massive use of in situ and satellite data.

In the studies of Paiva et al., [69, 70], the large-scale hydrological-hydrodynamic model MGB-IPH [22] was used to simulate the basin, with precipitation forcing provided by in situ data. Their analyses showed the preponderant role of the initial conditions, in particular the surface water, for the predictability of the large Amazonian rivers and the knowledge of the large-scale hydrodynamics. But the real novelty of this study was that for the first time, satellite altimetry water height over a high number of virtual stations (calculated over the whole Amazon basin, including the main river channels) were assimilated into a rainfall/discharge model, leading to an improvement of the prediction of the model. The results were promising, as the model was able to predict the discharge in the main Amazonian rivers with a significant antecedence (between 1 and 3 months). They demonstrated that not only did satellite altimetry allow to obtain high accuracy water levels on rivers, but also that the main benefit was to improve model outputs by assimilation. In the same way as it has been demonstrated for lakes, for transboundary basins, for reservoir monitoring, we can say that from then on, altimetry was no longer the main subject of study, but the tool allowing an improved knowledge of the hydrodynamics of large rivers. This is a great difference, and a great advance.

A similar approach was implemented in Kittel et al. [51, 53]. They used altimetry data from several missions (sentinel-3A and sentinel-3B, Cryosat-2) that were more recent and more accurate especially for Sentinel than the data used in, [69, 70]. They have moreover demonstrated the capabilities of satellite altimetry to improve hydraulic models' parameter calibration and used them on African ungauged basins.

6.4 Conclusion

With the increasing of water scarcity, particularly marked in arid and semi-arid regions, and in the frame of global climate change and demographic pressure, monitoring systems of climate related parameters provide essential information for decision makers, water resources management activities, and hydrology science. However, over the last decades, ground hydrological survey's networks have drastically declined worldwide. In this context, current remote sensing techniques have been widely deployed by several countries for land surface monitoring purposes, including the survey of water over the oceans and the continents. Lakes have been identified by Global Climate Observing System (GCOS) and World Meteorological Organization (WMO) as proxies for climate change monitoring over continents. Indeed, large inland lakes receive, transform and intensify climatic signal, and meanwhile they are very sensitive to climate change and human water uses.

In the 30 years since the launch of Topex/Poseidon, satellite altimetry has quickly established itself as a very useful system for oceanography. For continental surfaces, the path has been more tortuous and it took much more time to be adopted by a large number of researchers, but also for applications in different fields (flood prediction, reservoir monitoring, water cycle studies, climate change impact studies). The road has been longer but it would be impossible or very tedious to list all the studies that have demonstrated it over the years. For this reason, we have selected some studies that we believe have marked a breakthrough and have led to new applications.

For the monitoring of natural lakes in relation to climate change, the production of articles has grown exponentially over the years, with a great deal of attention paid to the lakes of the Tibetan plateau. The number of published studies on this subject is considerable over the last 10 years, and it was difficult to choose one to illustrate it. However, the paper published by Liguang et al. [60] seems to have demonstrated the power of altimetry for this type of research, with results that are both recent and very interesting. S. Cooley and co-authors have shown on their side in a recent paper in *Nature* journal that using the Lidar data on ICESat-2 mission allows the monitoring thousands of artificial reservoirs in order to quantify their role in the total water storage change at seasonal to inter-annual scale.

Similarly, it seems to us that in the early 2010s, a number of studies have emerged around the applications of altimetry on flood prediction, and the implementation of operational systems. The paper by Biancamaria et al. [7], unless we are mistaken, prefigured the many subsequent studies on the subject, and the great expectations raised by the SWOT mission. Around the same time, after many papers demonstrating

that altimetry could accurately measure water levels on rivers, researchers focused on the assimilation of these altimetry data in rainfall / flow models at the scale of large basins. This is why we have chosen to illustrate this work through the work of Paiva et al. [69, 70] on the Amazon basin. These were the first studies on the subject that showed that we could use these data to improve the models over the biggest river basin in the world.

After almost 30 years of application of satellite altimetry in hydrology, a new era is already underway with the advent of new missions carrying much more accurate instruments, and is progressively leading to placing this technique at the heart of strategies for monitoring large basins, lakes and reservoirs, in a framework of research but also operational applications of multiple interests. The coming years will see the emergence of new instruments such as the Ka-band interferometer that will be launched in 2022 on the SWOT satellite. The gain in terms of spatial coverage and measurement density will be considerable, as well as the gain in terms of products that can be delivered: instantaneous, height, slope, width and discharge of all the rivers in the world, water stocks variations of millions of lakes, and monitoring of large flood plains.

References

1. Arsen A, Cretaux JF, Abarca-Del-Rio R (2015) Use of SARAL/ALtiKa over mountainous lakes, intercomparison with Envisat mission *J Adv Space Res. The Saral/ALtiKa satellite Altimetry Mission*, 38:534–548. <https://doi.org/10.1080/01490419.2014.1002590>
2. Azarderakhsh M, Rossow WB, Papa F, Norouzi H, Khanbilvardi R (2011) Diagnosing water variations within the Amazon basin using satellite data. *J Geophys Res* 116:D24107. <https://doi.org/10.1029/2011JD015997>
3. Bamber JL (1994) Ice sheet altimeter processing scheme. *Int J Remote Sens* 15(4):925–938
4. Becker M, Silva JS, Calmant S, Robinet V, Seyler F (2014) Water level fluctuations in the Congo Basin derived from Envisat satellite altimetry. *Remote Sens* 6(10):9340–9358
5. Biancamaria S, Schaedele T, Blumstein D, Frappart F, Boy F, Desjonquieres J-D, Pottier C, Blarel F, Fernando N (2018) Validation of jason-3 tracking modes over French rivers. *Remote Sens Environ* 209:77–89
6. Biancamaria S, Frappart F, Leleu A-S et al (in revision) (2017) Satellite altimetry water elevations performance over a 200 m wide river: evaluation over the Garonne River. *Adv Space Res.* <https://doi.org/10.1016/j.asr.2016.10.008>
7. Biancamaria S, Hossain F, Lettenmaier DP (2011) Forecasting transboundary river water elevations from space. *Geophys Res Lett* 38(L11401). <https://doi.org/10.1029/2011GL047290>
8. Biemans H, Haddeland I, Kabat P, Ludwig F, Hutjes RWA, Heinke IJ, Von Bloh W, Gerten D (2011) Impact of reservoirs on river discharge and irrigation water supply during the 20th century. *Water Resour Res* 47:W03509. <https://doi.org/10.1029/2009WR008929>
9. Birkett CM (1998) Contribution of the TOPEX NASA Radar Altimeter to the global monitoring of large rivers and wetlands. *Water Resour Res* 34(5):1223–1239. <https://doi.org/10.1029/98WR00124>
10. Birkett CM, Beckley B (2010) Investigating the performance of the JASON-2/OSTM radar altimeter over lakes and reservoirs. *Mar Geodesy* 33(1):204–238
11. Birkett CM (1995) The contribution of TOPEX/POSEIDON to the global monitoring of climatically sensitive lakes. *J Geophys Res [Oceans]* 100(C12):25179–25204

12. Birkett CM et al (2002) Surface water dynamics in the Amazon Basin: application of satellite radar altimetry. *J Geophys Res* 107: D20, 8059. <https://doi.org/10.1029/2001JD000609>
13. Birkinshaw SJ, O'Donneell GM, Moore P, Kilsby CG, Fowler HJ, Berry PAM (2010) Using satellite altimetry data to augment flow estimation techniques on the Mekong River. *Hydrol Process* 24:3811–3825. <https://doi.org/10.1002/hyp.7811>
14. Birkinshaw SJ, Moore P, Kilsby CG, O Donnell GM, Hardy AJ, Berry P (2014) Daily discharge estimation at ungauged river sites using remote sensing. *Hydrol Proc* 28:1043–1054
15. Blumstein D, Lasson L, Le Gac S et al (2019) Major upgrade of OLTC on sentinel-3A and 3B in 2018: benefits for inland waters users. *ESA Living Planet Symposium*, Milan, Italy
16. Boergens E, Buhl S, Dettmering D, Klüppelberg C, Seitz F (2016) Combination of multi-mission altimetry data along the Mekong River with spatio-temporal kriging. *J Geod*
17. Calmant S, Seyler F, Cretaux JF (2008) Monitoring continental surface waters by satellite altimetry, survey in geophysics, special issue on 'Hydrology from Space' 29(4–5):247–269. <https://doi.org/10.1007/s10712-008-9051-1>
18. Cerri L, Berthias J-P, Bertiger WI, Haines BH, Lemoine FG, Mercier F, Ries JC, Willis P, Zelensky NP, Ziebart M (2010) Precision orbit determination standards for the Jason series of altimeter missions. *Mar Geodesy* 33(S1):379–418
19. Chao BF, Wu Y, Hand Li YS (2008) Impact of artificial reservoir water impoundment on global sea level. *Science* 320:212–4
20. Chelton DB, Walsh E, MacArthur J (1989) Pulse compression and sea level tracking in satellite altimetry. *J Atmos Ocean Technol* 6:407–438
21. Chelton DB, Ries JC, Haines BJ, Fu LL, Callahan PS (2000) Satellite altimetry. In: Fu LL, Cazenave A (eds) *Satellite altimetry and Earth sciences: a handbook of techniques and applications*. Academic Press, San Diego, USA, pp 1–132
22. Collischonn W, Allasia D, Silva BC, Tucci CEM (2007) The MGB-IPH model for large-scale rainfall-runoff modelling. *Hydrol Sci J* 52(5):878–895
23. Cooley SW, Ryan JC, Smith L (2021) Human alteration of global surface water storage variability. *Nature* 591:78–81. <https://doi.org/10.1038/s41586-021-03262-3>
24. Cretaux J-F, Abarca Del Rio R, Berge-Nguyen M et al (2016) Lake volume monitoring from space, survey in geophysics. 37:269–305. <https://doi.org/10.1007/s10712-016-9362-6>
25. Cretaux J-F, Bergé-Nguyen M, Calmant S, Jamangulova N, Satylkanov R, Lyard F, Perosanz F, Verron J, Montazem AS, Leguilcher G, Leroux D, Barrie J, Maisongrande P, Bonnefond P (2018) Absolute calibration/validation of the altimeters on Sentinel-3A and Jason-3 over the lake Issykkul. *Remote Sens* 10:1679. <https://doi.org/10.3390/rs10111679>
26. Cretaux J-F, Biancamaria S, Arsen A, Bergé-Nguyen M, Becker M (2015) Global surveys of reservoirs and lakes from satellites and regional application to the Syrdarya river basin. *Environ Res Lett* 10(1):015002. <https://doi.org/10.1088/1748-9326/10/1/015002>
27. Crétaux J-F, Calmant S, Romanovski V, Perosanz F, Tashbaeva S, Bonnefond P, Moreira D, Shum CK, Nino F, Bergé-Nguyen M, Fleury S, Gegout P, Abarca Del Rio R, Maisongrande P (2011) Absolute calibration of Jason radar altimeters from GPS kinematic campaigns over Lake Issykkul. *Mar Geodesy* 34(3–4):291–318. <https://doi.org/10.1080/01490419.2011.585110>
28. Crétaux J-F, Nielsen K, Frappart F, Papa F, Calmant S, Benveniste J (2017) *Hydrological applications of satellite altimetry: rivers, lakes, man-made reservoirs, inundated areas* (CRC Press, 2017), earth obs edn
29. Downing JA, Prairie YT, Cole JJ et al (2006) The global abundance and size distribution of lakes, ponds, and impoundments. *Limnol Oceanogr* 51:2388–2397. <https://doi.org/10.4319/lo.2006.51.5.2388>
30. Duan Z, Bastiaanssen WGM (2013) Estimating water volume variations in lakes and reservoirs from four operational satellite altimetry databases and satellite imagery data. *Remote Sens Environ* 134:403–416. <https://doi.org/10.1016/j.rse.2013.03.010>
31. Ejido A, Smith W (2017) Fully focus SAR altimetry: theory and applications. *IEEE trans Geosci Remote Sens* 55:1
32. Finsen F, Milzow C, Smith R, Berry P, Bauer-Gottwein P (2014) Using radar altimetry to update a large-scale hydrological model of the Brahmaputra river basin. *Hydrol Res* 45(1):148–164. <https://doi.org/10.2166/nh.2013.191>

33. Frappart F, Calmant S, Cauhopé M, Seyler F, Cazenave A (2006) Preliminary results of ENVISAT RA-2 derived water levels validation over the Amazon basin. *Remote Sens Env* 100(2):252–264. <https://doi.org/10.1016/j.rse.2005.10.02>
34. Frappart F, Papa F, Mariou V et al (2015) Preliminary assessment of SARAL/AltiKa observations over the Ganges-Brahmaputra and Irrawaddy Rivers. *Mar Geodesy* 38(Sup1):568–580. <https://doi.org/10.1080/01490419.2014.990591>
35. Frappart F, Papa F, Santos da Silva J et al (2012) Surface freshwater storage and dynamics in the Amazon basin during the 2005 exceptional drought. *Env Res Lett* 7:044010 (7pp). <https://doi.org/10.1088/1748-9326/7/4/044010>
36. Frappart F, Papa F, Famiglietti JS, Prigent C, Rossow WB, Seyler F (2008) Interannual variations of river water storage from a multiple satellite approach: a case study for the Rio Negro River basin. *J Geophys Res* 113:D21104. <https://doi.org/10.1029/2007JD009438>
37. Fu LL, Cazenave A (2001) *Satellite altimetry and Earth Science, a hand book of techniques and applications*. Int Geophys Ser 69. Academic Press
38. Gao Q, Makhoul E, Escorihuela MJ, Zribi M, Segui PQ, Garcia P, Roca M (2019) Analysis of Retracker's performances and water level retrieval over the Ebro River basin using sentinel-3. *Remote Sens* 11(6):25. <https://doi.org/10.3390/rs11060718>
39. Getirana ACV, Peters-Lidard C (2013) Water discharge estimates from large radar altimetry datasets in the Amazon basin. *Hydrol Earth Syst Sci* 17:923–933. <https://doi.org/10.5194/hess-17-923-2013>
40. Getirana ACV, Peters-Lidard C (2012) Water discharge estimates from large radar altimetry datasets in the Amazon basin. *Hydrol Earth Syst Sci Discuss* 9:7591–7611. <https://doi.org/10.5194/hessd-9-7591-2012>
41. Gleditsch NP, Hegre H (2000) Shared rivers and interstate conflict. *Polit Geogr* 19(8):971–996
42. Gregory JM, White NJ, Church JA, Bierkens MFP, Box JE, Van Der Broeke MR, Cogley JG, Fettweis X, Hanna E, Huybrechts P, Konikow LF, Leclercq PW, Marzeion B, Oerlemans J, Tamisiea ME, Wada Y, Wake LM, Van de Wal RSW (2013) Twentieth-century global-mean sea level rise: is the whole greater than the sum of the parts? *J Clim* 26:4476–4498
43. Hossain F, Katiyar N (2006) Improving flood forecasting in international river basins. *EOS (AGU)* 87(5):49–50
44. Hossain F, Siddique-E-Akbor AH, Mazumdar LC, ShahNewaz SM, Biancamaria S, Lee H, Shum CK (2013) Proof of concept of an altimeter-based river forecasting system for trans-boundary flow inside Bangladesh. *IEEE J Sel Topics in Appl Earth Observ PP*(99):1–15. <https://doi.org/10.1109/JSTARS.2013.2283402>
45. Huang L, Liu J, Shao Q, Liu R (2011) Changing inland lakes responding to climate warming in northern Tibetan Plateau. *Clim Change* 24:479–502. <https://doi.org/10.1007/s10584-011-0032-x>
46. Hwang C, Peng M-F, Ning J, Luo J, Sui C-H (2005) Lake level variations in China from TOPEX/Poseidon altimetry: data quality assessment and links to precipitation and ENSO. *Geophys J Int* 161:1–11. <https://doi.org/10.1111/j.1365-246X.2005.02518.x>
47. Jayles C, Chauveau JP, Rozo F (2010) DORIS/JASON-2: Better than 10 cm on-board orbits available for near-real-time altimetry. *Adv Space Res* 46(12):1497–1512
48. Jiang L, Schneider R, Andersen OB, Bauer-Gottwein P (2017) Cryosat-2 altimetry applications over rivers and lakes. *Water* 9:211. <https://doi.org/10.3390/w9030211>
49. Jiang L, Nielsen K, Dinardo S, Andersen OB, Bauer-Gottwein P (2020) Evaluation of sentinel-3 SRAL SAR altimetry over Chinese rivers. *Remote Sens Environ* 237:111546. <https://doi.org/10.1016/j.rse.2019.111546>
50. Kang S, Xu Y, You Q, Flügel W, Pepin N, Yao T (2010) Review of climate and cryospheric change in the Tibetan Plateau. *Environ. Res Lett* 5:8pp. <https://doi.org/10.1088/1748-9326/5/1/015101>
51. Kittel CMM, Nielsen K, Tøttrup C, Bauer-Gottwein P (2018) Informing a hydrological model of the Ogooué with multi-mission remote sensing data. *Hydrol Earth Syst Sci* 22:1453–1472. <https://doi.org/10.5194/hess-22-1453-2018>

52. Kittel CMM, Jiang LG, Tottrup C, Bauer-Gottwein P (2021) Sentinel3 radar altimetry for river monitoring—a catchment-scale evaluation of satellite water surface elevation from sentinel-3A and sentinel-3B. *HESS*, 25:333–357. <https://doi.org/10.5194/hess-25-333-2021>
53. Kittel CMM (2020) Satellite radar observations for hydrologic and hydrodynamic modelling, PhD thesis, DTU, dept of environmental engineering, technical university of Denmark
54. Kleinhohenbrink M, Lindenbergh RC, Ditmar PG (2015) Monitoring of lake level changes on the Tibetan Plateau and Tian Shan by retracking Cryosat SARIn waveforms. *J Hydrol* 521:119–131
55. Koblinsky CJ, Clarke RT, Brenner AC, Frey H (1993) Measurement of river level variations with satellite altimetry. *Water Resour Res* 29(6):1839–1848. <https://doi.org/10.1029/93WR00542>
56. Kouraev A, Zakharov EA, Samain O, Mognard-Campbell NM, Cazenave A (2004) Ob' river discharge from Topex/Poseidon satellite altimetry. *Remote Sens Environ* 93:238–245. <https://doi.org/10.1016/j.rse.2004.07.007>
57. Lee H, Beighley RE, Alsdorf D, Jung HC, Shum CK, Duan J, Guo J, Yamasaki D, Andreadis K (2011) Characterization of terrestrial water dynamics in the Congo Basin using GRACE and satellite radar altimetry. *Remote Sens Env* 115:3530–3538
58. Lei Y, Yang K, Wang B, Sheng Y, Bird BW, Zhang G, Tian L (2014) Response of inland lake dynamics over the Tibetan Plateau to climate change. *Climate Change*, 125(2):281–290. <https://doi.org/10.1007/s10584-014-1175-3>
59. Lettenmaier DP, Milly PCD (2009) Land waters and sea level. *Nat Geosci* 2:452–454. <https://doi.org/10.1038/ngeo567>
60. Liguang J, Nielsen K, Andersen OB, Bauer-Gottwein P (2020) A bigger picture of how the Tibetan lakes change over the past decade revealed by Cryosat-2 altimetry. *J Geophys Res Atmos*. <https://doi.org/10.1029/2020JD033161>
61. Liu J, Wang S, Yu S, Yang D, Zhang L (2009) Climate warming and growth of high-elevation inland lakes on the Tibetan Plateau. *Global Planet Change* 67:209–217
62. Liu XD, Chen BD (2000) Climatic warming in the Tibetan Plateau during recent decades. *Int J Climatol* 20(14):1729–1742
63. Maillard P, Bercher N, Calmant S (2015) New processing approaches on the retrieval of water levels in Envisat and SARAL radar altimetry over rivers: a case study of the São Francisco River Brazil. *Remote Sens Environ* 156:226–241
64. Manning R (1891) On the flow of water in open channels and pipes. *Trans Civil Eng Ireland* 20:161–207
65. Martin-Puig C, Leuliette E, Lillibrige J, Roca M (2016) Evaluating the performance of Jason-2 open-loop and closed-loop tracker modes. *J Atmos Oceanic Technol* 33:2277–2288. <https://doi.org/10.1175/JTECH-D-16-0011.1>
66. Michailovsky CI, Milzow C, Bauer-Gottwein P (2013) Assimilation of radar altimetry to a routing model of the Brahmaputra River. *Water Resour Res* 49:4807–4816
67. Morris CS, Gill SK (1994) Evaluation of the TOPEX/POSEIDON altimeter system over the Great Lakes. *J Geophys Res* 99(C12):24527–24539. <https://doi.org/10.1029/94JC01642>
68. Nielsen K, Stenseng L, Andersen OB, Villadsen H, Knudsen P (2015) Validation of CryoSat-2 SAR mode based lake levels. *Remote Sens Environ* 171:162–170
69. Paiva RCD, Buarque DC, Colischonn W et al (2013) Large-scale hydrologic and hydrodynamic modelling of the Amazon River basin. *Water Resour Res* 49(3):1216–1243. <https://doi.org/10.1002/wrcr.20067>
70. Paiva RCD, Collischonn W, Bonnet M-P, de Gonçalves LGG, Calmant S, Getirana A, da Santos Silva J (2013b) Assimilating in situ and radar altimetry data into a large-scale hydrologic-hydrodynamic model for streamflow forecast in the Amazon. *Hydrol Earth Syst Sci* 10:2879–2925
71. Papa F, Durand F, Rossow WB, Rahman A, Bala SK (2010) Seasonal and interannual variations of the ganges-Brahmaputra River discharge, 1993–2008 from satellite altimeters. *J Geophys Res* 115:C12013. <https://doi.org/10.1029/2009JC006075>

72. Papa F, Bala SK, Pandey RK, Durand F, Rahman A, Rossow WB (2012) Ganga-Brahmaputra river discharge from Jason-2 radar altimetry: an update to the long-term satellite-derived estimates of continental freshwater forcing flux into the Bay of Bengal. *J Geophys Res* 117:C11021. <https://doi.org/10.1029/2012JC008158>
73. Paris A, de Paiva RD, da Silva JS, Moreira DM, Calmant S, Garambois P-A, Collischonn W, Bonnet M-P, Seyler F (2016) Stage-discharge rating curves based on satellite altimetry and modeled discharge in the Amazon basin. *Water Resour Res* 52:3787–3814
74. Ričko M, Birkett CM, Carton JA, Cretaux J-F (2012) Intercomparison and validation of continental water level products derived from satellite radar altimetry. *J Appl Rem Sens* 6. <https://doi.org/10.1117/1.JRS.6.061710>
75. Scherer D, Schwatke C, Dettmering D, Seitz F (2020) Long-term discharge estimation for the lower Mississippi River using satellite altimetry and remote sensing images. *Remote Sens* 12:2693. <https://doi.org/10.3390/rs12172693>
76. Schutz B (2004) ICESat laser altimetry, EGU, 25–30 April, Nice, France. *Geophys Res Abstracts* 6:05333
77. Schwatke C, Dettmering D, Bosch W, Seitz F (2015) DAHITI—an innovative approach for estimating water level time series over inland waters using multi-mission satellite altimetry. *Hydrol Earth Syst Sci Copernicus GmbH* 19:4345–4364. <https://doi.org/10.5194/hess-19-4345-2015>
78. Seyler F, Bonnet M-P, Calmant S, Cauhopé M, Cazenave A, Cochonneau G, Divol J, Do-Minh K, Frappart F, Gennero M-C, Guyenne-Blin K, Huynh F, Leon J-G, Lille D, Maheu C, Mangeas M, Martiny M, Mercier F, Rocquelain G, Tocqueville L, Touraivane L, Zanifé O-Z (2005) CASH « Contribution de l'Altimétrie Spatiale à l'hydrologie » Rapport intermédiaire d'opération d'une recherche financée par le Ministère de la Recherche, Octobre 2005, Décision d'aide n° : 04 T 131.
79. Sheng YW, Song CQ, Wang JD, Lyons EA, Knox BR, Cox JS, Gao F (2016) Representative lake water extent mapping at continental scales using multi-temporal Landsat-8 imagery. *Remote Sens Environ* 185:129–141
80. Silva J, Calmant S, Seyler F, Filho O, Cochonneau G, Mansur WJ (2010) Water levels in the Amazon basin derived from the ERS 2 and ENVISAT radar altimetry missions. *Remote Sens Environ* 114(10):2160–2181
81. Silva JS, Calmant S, Seyler F, Lee H, Shum CK (2012) Mapping of the extreme stage variations using Envisat altimetry in the Amazon basin rivers. *Int Water Technol J* 2(1):14–25
82. Silva J, Calmant S, Seyler F, Moreira DM, Oliveira D, Monteiro A (2014) Radar altimetry aids managing gauge networks. *Water Resour Manag* 28:587–603. <https://doi.org/10.1007/s11269-013-0484-z>
83. Silva JS, Seyler F, Calmant S, Rotunno Filho OC, Roux E, Araujo AAM, Goyot J-L (2012b) Water level dynamics of Amazon wetlands at the watershed scale by satellite altimetry. *Int J Remote Sens* 33(11):3323–3353. <https://doi.org/10.1080/01431161.2010.531914>
84. Song C, Huang B, Ke L, Richards KS (2014) Seasonal and abrupt changes in the water level of closed lakes on the Tibetan Plateau and implications for climate impacts. *J Hydrol* 514:131–144
85. Taburet N, Zawadzki, Vayre M, Blumstein D, LE Gac S, Boy F, Raynal M, Labroue S, Cretaux J-F, Femenias P (2020) S3MPC: improvement on inland water tracking and water level monitoring from the OLC onboard Sentinel-3 altimeters. *Remote Sens* 12(18):AN 3055. <https://doi.org/10.3390/rs12183055>
86. Tarpanelli A, Santi E, Tiurian MJ, Filippucci P, Amarnath G, Brocca L (2019) Daily river discharge estimates by merging satellite optical sensors and radar altimetry through artificial neural network. *IEEE* 57(1):329–341. <https://doi.org/10.1109/TGRS.2018.2854625>
87. Tarpanelli A, Brocca L, Barbetta S, Faruolo M, Lacava T, Moramarco T (2015) Coupling MODIS and radar altimetry data for discharge estimation in Poorly Gauged River Basins. *IEEE Trans Geosciences Remote Sens* 8(1):141–149. <https://doi.org/10.1109/JSTARS.2014.2320582>
88. Tourian MJ, Tarpanelli A, Elmi O, Qin T, Brocca L, Moramarco T, Sneeuw N (2016) Spatiotemporal densification of river water level time series by multimission satellite altimetry. *Water Resour Res* 52:1140–1159

89. Verpoorter C, Kutser T, Seekell DA, Tranvik LJ (2014) A global inventory of lakes based on high-resolution satellite imagery. *Geophys Res Lett* 41:6396–6402. <https://doi.org/10.1002/2014GL060641>
90. Vignudelli S, Kostianoy AG, Cipollini P, Benveniste J (eds) (2011) *Coastal altimetry*. Springer, Berlin Heidelberg
91. Villadsen H, Andersen OB, Stenseng L, Nielsen K, Knudsen P (2015) CryoSat-2 altimetry for river level monitoring—evaluation in the Ganges-Brahmaputra River basin. *Remote Sens Environ* 168:80–89
92. Wang B, Bao Q, Hoskins B, Wu G, Liu Y (2008) Tibetan Plateau warming and precipitation change in East Asia. *Geophys Res Lett* 35:L14702. <https://doi.org/10.1029/2008GL034330>
93. Wang X, Gong P, Zhao Y et al (2013) Water-level changes in China's large lakes determined from ICESat/GLAS data. *Remote Sens Environ* 132:131–144
94. Wolf A, Nathrius J, Danielson J, Ward B, Pender J (1999) International river basins of the world. *Int J Water Res Devel* 15(4):387–427
95. Zakharova E, Kouraev A, Cazenave A, Seyler F (2006) Amazon River discharge estimated from T/P altimetry. *Compte Rendus Géosc* 338(3):188–196. <https://doi.org/10.1016/j.crte.2005.10.003>
96. Zhang G, Xie H, Kang S, Yi D, Ackley S (2011) Monitoring lake level changes on the Tibetan Plateau using ICESat altimetry. *RSE* 115:1733–1742. <https://doi.org/10.1016/j.rse.2011.03.005>
97. Zhang G, Bolch T, Chen W, Cretaux J-F (2021) Comprehensive estimation of lake volume changes on the Tibetan Plateau during 1976–2019 and basinwide glacier contribution. *Sci Total Environ*. <https://doi.org/10.1016/j.scitotenv.2021.145463>
98. Zwally HJ, Abdalati W, Abshire J, Bentley C, Blair J, Bryan A, Brenner J, Bufton J, Dezio S, Ekholm D, Hancock D, Harding T, Herring B, Minster S, Palm K, Quinn B, Schutz J, Spinehirne RT (2002) ICESat's laser measurements of polar ice, atmosphere, ocean and land. *J Geodynamics* 34:3–4

Chapter 7

Generic Strategy for Consistency Validation of the Satellite-, In-Situ-, and Reanalysis—Based Climate Data Records (CDRs) Essential Climate Variables (ECVs)



Yijian Zeng, Wim Timmermans, and Zhongbo Su

Abstract The Climate Data Record (CDR) is a time series of measurements of sufficient length, consistency and continuity to determine climate variability and change. The generation of ECVs (Essential Climate Variables)/CDRs needs to put strong emphasis on the generation of fully described, error-characterized and consistent satellite-based ECV products (Zeng et al. in *Remote Sensing* 11:1–28, 2019). For example, generation of many ECVs, such as in the ESA (European Space Agency) CCI (Climate Change Initiative) projects (Plummer et al. in *Remote Sens Environ* 203:2–8, 2017), requires ancillary information about the state of the atmosphere, e.g., cloud screening for SST (sea surface temperature) and atmospheric correction for space-borne altimeters. As such, the consistency between the various ECV products (e.g. cloud flagged in one ECV and non-flagged in another one) extends to ensuring consistency in the approaches of CDR generation. The in-situ datasets also need to be continuously characterized in terms of their long-term accuracy, stability and homogeneity. Reanalysis results, as an alternative source of ECV, requires similar endeavors to investigate its consistency (Zeng et al. in *Int J Appl Earth Obs Geoinf* 42:150–161, 2015).

In this Chapter, the current practices on consistency validation will be analyzed, based on the consistency validation requirements, the validation capacities, and the current practice examples. The essentials of consistency validation will be summarized. Based on the essentials, the generic strategy for consistency validation will be proposed and discussed.

Y. Zeng (✉) · W. Timmermans · Z. Su
Department of Water Resources, ITC Faculty of Geo-Information Science and Earth Observation,
University of Twente, Enschede, Netherlands
e-mail: y.zeng@utwente.nl

7.1 Consistency Validation Requirements and Capacities

7.1.1 Consistency Validation Requirements

7.1.1.1 In-situ Products

For in-situ products, the scope of quality control may include [47]: (a) data validation, (b) data cleaning or remedial actions and (c) quality control monitoring. How all these aspects are in consistency shall be checked to ensure the climate quality of in-situ products.

Based on the in-situ network observations, the gridded datasets can be produced with the internationally accepted estimation methods, which include: (a) mathematical estimation methods (e.g. inverse distance weighting, spline functions); (b) estimation based on physical relationships (e.g. regression, discriminant and principal component analysis); (c) spatial estimation methods (e.g. Kriging). The combination of different methods (e.g. the use of a regression model and interpolation of residuals) is a common practice. Often, the production of gridded datasets follows a step-wise approach incorporating different estimation procedures.

The estimation method for producing gridded datasets may contain errors. This is because the spatial interpolation assumed that the climatological patterns between widely spaced stations are known and can be modeled, while in reality many factors (e.g. topography, local peculiarities or the existence of water bodies) influence the climate of a region. It is therefore essential to validate the gridded datasets to estimate such errors. The validation of gridded datasets may include: (a) split validation (testing the methodology using a smaller subset excluded in the estimation procedure); and (b) cross-validation (repeated removals of observations from the sample and analysis of residuals between observed and estimated values) [3, 4].

7.1.1.2 Satellite Products

The major challenge for climate observation is to have a consistent architecture for observations that is independent of a climate variable's origin and observing method and principles. This requires that each key climate variable shall be measured using independent observations and examined with independent analysis. This highlights the continuing importance of single-source long-term climate datasets for climate variability and trend analysis, the uncertainty of which shall be quantified by (inter) comparing with other independent datasets [50].

The independent analysis is to verify algorithms that are used for generating climate data (e.g. intercomparison between different retrieval algorithms). It is especially crucial for satellite-based observation data where analysis systems may involve different sets of combination between algorithm theoretical basis documents (ATBDs) and instruments. For example, the independent product can be generated with 3 scenarios by: (1) using the same instrument with different sets of ATBDs; (2)

using the same ATBDs on different instruments; or (3) using different ATBDs and different instruments. It is therefore important to verify the accuracy and stability of various outputs for specific variables by thorough inter-comparison, providing insights into errors and help product users to be aware of product differences.

In addition to single-source independent datasets, integrated products are needed as well to ensure reliable conclusions on the detected variability and trends. The integrated data is produced by blending data from different sources [52, 53], or by integrating observations of variables related to one another, e.g., using data from different instruments or using other data or products to warn of potential issues [19]. For example, the estimation of soil moisture from microwave emission can benefit from analyses of precipitation (e.g. either from in-situ or satellite observation). This requires endeavor to check the physical consistency among different physical variables, apart from the inter-comparison among different independent integrated products.

Although the satellite observations play a vital role in monitoring global climate, to contribute fully and effectively to the detection of climate variability and change (thus long-term consistent climate records), the satellite observing system shall be implemented and operated in a manner to ensure that these data are sufficiently homogeneous, stable and accurate for climate purposes. To address these technical and resource challenges, the GCOS (Global Climate Observing System) Climate Monitoring Principles (GCMPs) were proposed to and extended to assist space agencies in addressing the key operational issues: (1) Continuity, consistency and overlap; (2) Orbit stability; (3) Sensor calibration; and (4) Data interpretation, sustained data products and archiving.

To follow the GCMPs and be able to address the consistency requirement, there are a few key issues that need to be reckoned: (1) Gaps in FCDRs (Fundamental Climate Data Record) must be avoided; (2) Different instruments should be well (inter) calibrated; (3) The generation of long-term ECV products shall be sustained including regular reprocessing; and (4) The optimum use of satellite data (e.g. integrated with in-situ data and model results) requires the organization of data service systems that ensure an on-going accessibility to the data in the future.

7.1.1.3 Reanalysis Products

Within the current WMO Global Framework for Climate Services (GFCS), reanalysis contributes to both components of “observation and Monitoring” and “Research, Modelling and Applications”. The reanalysis can be referred to “reanalysis products” or “reanalysis process”.

The reanalysis products (datasets) contain possibly the gridded fields of physical variables from NWP (Numerical Weather Prediction) model (e.g. including land surface and sea-state components), ocean model (e.g. including dynamic sea ice and biogeochemistry components), or atmospheric composition model (e.g. GEMS and MACC). The reanalysis products can be considered as a scientific and numerical blending of model data and observational data.

The reanalysis process refers to the activities in integrating an invariant, modern version of a data assimilation system and numerical weather prediction model, over a long time period, by assimilating a selection of observations. The reanalysis process shall also include evaluation, monitoring and quality control of reanalysis products and of observations [42, 49].

It is well acknowledged that the reanalysis products are consistent with the meteorological parameters, in the sense that they are constrained by the coupled model. On the other hand, in general, there are still significant disconnections between the various Earth system elements in the assimilation, although the models of the various elements can be as far as coupled or fully integrated.

For example, analysis updates from observations (so-called increments) are typically computed separately for each Earth system element's data assimilation, and it is only during the model integration that all states are made physically consistent between one another. This point indicates that such reanalysis results is produced by a weakly coupled data assimilation scheme, because it uses the coupled model only for generating background estimates for each analysis cycle while the analysis itself is uncoupled [11, 34]. This has consequences for the consistency validation of reanalysis production, which entails considering not only validation of the overall system/process but also the validation of the individual ECV datasets. For the consistency validation of ECV datasets, the inter-comparison of reanalysis products or with other independent datasets will be sufficient. As for the validation of reanalysis systems, it requires information for the components listed as below [49, 51]: (1) the observations input; (2) the forcing or boundary datasets input; (3) the model configuration (for the various Earth system elements); (4) the data assimilation system (in the various Earth system elements).

7.1.2 Consistency Validation Capacities

The vision of GCOS is to enable all users having access to the climate observations, data records and information that they require to address climate variability and change. GCOS strives to provide sustainably reliable physical, chemical and biological observations and data records for the total climate system—across the atmospheric, oceanic and terrestrial domains, including hydrological and carbon cycles and the cryosphere [48]. Another very important remit of GCOS is to provide the climate monitoring requirements for the observations, which can then be implemented by contributions coming from different programmes [5, 17]. To achieve this vision, both the in-situ and satellite observing systems are indispensable components for GCOS, to provide observations over the breadth of environments from ocean bottom to the upper atmosphere. The existing in-situ and satellite observing systems represent the validation capacities, which will enable the inter-comparison among independent observations and the independent analysis.

7.1.2.1 In situ-based Capacities

GCOS has coordinated three types of in-situ networks for different purposes [48]:

- To produce stable long-term series and for calibration/validation purpose, the Global Reference observing networks were built/coordinated to provide highly-detailed and accurate observations at a few locations. This includes the most advanced of the Reference networks, the GCOS Reference Upper Air Network (GRUAN). It is to note that GRUAN is not a set of identical stations, but all stations will make a core set of first priority observations. There are guidelines for setting up sites, characterizing instrument error, data quality control, and manual for the data management [37].
- The Global Baseline observing networks were built/coordinated to provide long-term high-quality data records of key global climate variables and enable calibration for the comprehensive and designated networks. It involves a limited number of selected locations that are globally distributed. For example, the GCOS Surface Network (GSN), the GCOS Upper Air Network (GUAN), the WMO Global Atmosphere Watch (GAW) and the Baseline Surface Radiation Network (BSRN) [19, 22].
- The Comprehensive Observing networks were built/coordinated to provide observations at the detailed space and time scales required to fully capture the nature, variability and change of a specific climate variable. It includes regional and national networks, for example, the GCOS-affiliated WMO GAW global Atmospheric CO₂ and CH₄ Monitoring Networks. These networks are operated primarily for non-climate monitoring but also provide important observations for climate purposes [19, 22].

The above mentioned networks are used to produce reference data for different purposes, the detailed procedures/guidelines/manuals are documented to make such selection of networks as transparent as possible [17, 18]. It serves for documenting a traceable validation process.

The difference among these three types of in-situ networks can be demonstrated by using GUAN and GRUAN. The GUAN is designed to provide evenly distributed radiosonde network over the globe, measuring temperature, pressure (geopotential height), wind, and humidity (at least to the troposphere) at least 25 days each month, although the target is the collection of twice daily radiosonde observations at the 0000 and 1200 UTC synoptic hours. The lowered observation requirement can be attributed to [37]: (1) instrumentations used in GUAN varies from country to country; (2) data collection rate is better in some areas than others; (3) lapse/inability in the acquisition of replacement radiosondes at some locations may lead to temporal gaps in the climate record; and (4) lack of sustaining resources to support existing networks, which leads to the change of instrumentation and the change in location, which will affect homogeneity of GUAN stations. It is clear that these shortfalls of GUAN can also cause inconsistency in the climate record. It is therefore needed for upper air observations meeting reference standards, which led to the establishment of GRUAN in 2004 [26].

GURAN network served as reference standards for the larger GUAN network, aiming to quantify and reduce measurement uncertainties and to make measurements in a stable way over multi-decadal time scales to achieve data homogeneity in time and spatially between measurement sites. In addition, GRUAN will provide a traceable reference standard for global satellite-based measurements of atmospheric essential climate variables and will ensure that potential gaps in satellite measurements programs do not invalidate the long-term climate record. However, it is to note that GRUAN network has its own limitations to measure all parameters with minimum systematic error [26].

Thematically, the in-situ network support different domains of ECVs, which includes 5 categories: atmosphere surface, atmosphere upper-air, atmosphere composition, oceans, and terrestrial. It is noticed that except for Terrestrial and Atmosphere-Composition categories, the observing network in the rest of domains contains both routine/baseline networks and reference networks, which indicate the relatively high capacity of the in-situ observing system for doing consistency validation. On the other hand, this indicates the relatively low capacity of the in-situ observing networks of Terrestrial and Atmosphere-Composition domains, to do consistency validation for the domain-relevant ECVs (See Table 7.1), which requires the reference in-situ observations.

7.1.2.2 Space-Based Capacities

There are 54 GCOS Essential Climate Variables (ECVs) [5, 36] required to support the work of the UNFCCC (United Nations Framework Convention on Climate Change) and the IPCC (Intergovernmental Panel on Climate Change). Table 7.2 indicates 29 of the 54 ECVs can be observed from space (noticed that the observing principles for carbon dioxide, methane and other GHGs are similar and considered as one ECV product) [20]. The space-observable ECVs are in **bold**.

To meet the requirements indicated in 1.1.2, space agencies working through the CEOS and the Coordination Group on Meteorological Satellites (CGMS) have established mechanisms to ensure coordination in agencies' operation and exploitation, for the optimum use of satellite data, by establishing Virtual Constellations on Atmospheric Composition, Precipitation, Land Surface Imaging, Ocean Surface Topography, Ocean Colour Radiometry, and Ocean Surface Vector Winds. The similar coordination mechanism was taken to avoid gaps in FCDRs, which due to missing observations or instrument changes can introduce errors in trend analyses.

The potential future gaps in the satellite ECVs have been conducted through WMO and CEOS, which has been regarded necessary to be routinely updated and acted upon [7, 46]. Developed by WMO in support of Earth Observation applications, studies and global coordination, OSCAR (Observing System Capability Analysis and Review Tool) is an online resource tool that provides the status and the planning of global observing systems as well as instrument specifications at platform level (<http://www.wmo-sat.info/oscar/>).

Table 7.1 Overview of all GCOS-relevant network components and systems

Atmosphere			Oceans	Terrestrial
Surface	Upper-air	Composition		
GCOS surface network (GSN)	GCOS reference upper-air network (GRUAN)	GCOS-affiliated WMO/GAW global atmospheric N ₂ O, CO ₂ and CH ₄ monitoring networks	Global surface drifting buoy array on 5*5 degree resolution	GCOS/GTOS baseline global terrestrial network rivers (GTN-R)
Baseline surface radiation network (BSRN)	GCOS upper-air network (GUAN)	WMO/GAW GCOS global baseline total ozone network	Global tropical moored buoy network	GCOS/GTOS baseline global lake network
Full WWW & GSN	full WWW & GUAN	WMO/GAW GCOS global baseline profile ozone network	Voluntary observing ships	WWW/GOS synoptic network
Global tropical moored buoy network	Aircraft (ASDAR etc.)	WMO/GAW aerosol network	Global reference mooring network	GCOS/GTOS baseline global terrestrial network-glaciers (GTN-G)
Voluntary observing ships	Profiler (radar) network		GLOSS core sea-level network	GCOS/GTOS baseline global terrestrial network-permafrost (GTN-P)
Global reference mooring network	Ground-based GPS receiver network		Argo network	global terrestrial network hydrology (GTN-H)
GLOSS core sea-level network				
Argo network				

The inter-comparison of sensors and the (inter)calibration of instruments between satellites has received more and more attentions, which leads to the development of the Global Space-based Inter-calibration System (GSICS) jointly between the WMO Space programme, CGMS and the CEOS Working Group on Calibration and Validation (WGCV). GSICS is to ensure the generation of well-calibrated FCDRs. To focus on the sustained generation of long-term ECV products, the SCOPE-CM (The sustained coordinated processing of environmental satellite data for climate monitoring) initiative has been established with contribution from various space agencies.

The above indicates the current efforts to address the requirements for generating ECV CDR from space, and more or less represent the current capacity of satellite

Table 7.2 Overview of ECVs capable of being monitored from space grouped by measurement domain and area covered

	Atmosphere	Terrestrial	Ocean
Energy & Temperature	Surface Radiation Budget, Earth Radiation Budget, Surface Temperature, Upper Air Temperature, Surface and Upper Air Wind Speed	Albedo, Latent and Sensible Heat fluxes, Land Surface Temperature	Ocean Surface Heat Flux, Sea Surface Temperature, Subsurface Temperature
Other Physical Properties	Surface Wind, Upper Air Wind, Pressure, Lightning, Aerosol Properties		Surface Currents, Subsurface Currents, Ocean Surface Stress, Sea State, Transient Traces
Carbon Cycle and other GHGs	Carbon Dioxide, Methane, Other long-lived GHG, Ozone, Precursors for Aerosol and Ozone	Soil Carbon, Above-ground Biomass	Inorganic Carbon, Nitrous Oxide
Hydrosphere	Precipitation, Cloud Properties, Water Vapour (Surface), Water Vapour (Upper Air), Surface Temperature,	Soil Moisture, River Discharge, Lakes, Groundwater,	Sea Surface Salinity, Subsurface Salinity, Sea Level, Sea Surface Temperature
Snow & Ice		Glaciers, Ice Sheets and ice shelves, Permafrost, Snow	Sea Ice
Biosphere		Land Cover, Leaf Area Index (LAI), Fraction of Absorbed Photosynthetically Active Radiation (FAPAR), Fire	Plankton, Oxygen, Nutrients, Ocean Colour, Marine Habitat Properties
Human Use of Natural Resources		Water Use, Greenhouse Gases (GHG) Fluxes	Marine Habitat Properties

The highlighted ECVs are (will be) available via the Copernicus Climate Change Services (C3S) Climate Data Store (CDS) (Adopted from Table 7.2, GCOS 2016 Implementation Plan, GCOS-200)

remote sensing in contributing to GCOS ECVs. There are specific gap analysis implemented by JRC [46] and UKEOF [30], to identify how better to coordinate among the existing players to the maximum use of current resources for space-based ECVs, for Europe and UK, respectively.

The generation of many ECVs requires ancillary information about the state of the atmosphere and others. The various ECV products may use different sets of ancillary information (e.g. cloud flagged in one ECV and non-flagged in another one). This will certainly cause inconsistency among different ECV products. On the other hand, for the generation of a certain ECV, it needs different sources of data. For example, for sea surface temperature, there are different sensors observing the temperature of different “surfaces” [19, 29]: the traditional in-situ SST is taking measurement from well underneath the sea surface (e.g. near-surface and mixed-layer “bulk temperatures”); the infrared (IR) radiometer measures the ‘skin’ SST;

and, the passive microwave (MW) radiometer measures the ‘sub-skin’ SST. How to harmonize these three different observations of SST is complicated, due to different measurement depths and diurnal thermal stratification.

The similar inconsistency issue may exist in other ECV products. On the other hand, to be able to identify such inconsistency, the satellite observing system for certain ECV and the corresponding in-situ observing networks shall be maintained and collocated temporally and spatially. Nevertheless, these datasets (both satellite and in-situ) may be affected by the changes in demands on the data, observing practices and technologies. These changes can alter the characteristics of observational records (e.g. change in mean and/or variability). It is, therefore, required to follow a certain procedure to process the raw measurements before they can be used to detect climate variability and climate change. In this sense, for satellite observing systems, the mentioned GSICS and SCOPE-CM can be helpful in establishing an unbroken chain for the satellite measurements to be used/produced in a way to meet internationally recognized measurement standards, which consequently means consistent, homogeneous observational records.

7.1.2.3 Reanalysis-Based Capacities

With a sufficiently realistic global circulation model, by assimilating observational data from multiple sources into a dynamically coherent dataset, reanalysis can produce multi-decadal, gridded datasets that estimate a large variety of atmospheric, sea-state, and land surface parameters, including many that are not directly observed [13, 34, 35]. Reanalysis data can help improve the medium-range forecasts, by using them to assess the performance of operational forecast system and to evaluate the effect of new model developments and other changes [38]. This is actually corresponding to a strong feedback loop between improvements in the global observing system, advances in data assimilation methodology, and development of better forecast models through analysis [11].

The currently well-recognized need for the development of reanalysis is a more explicit representation of atmosphere–ocean interaction, which will improve surface fluxes of heat and momentum, tropical precipitation, and surface wave fields. The current reanalysis estimate of these parameters suffers from bias and drifts, due to the lack of model feedback between ocean and atmosphere and therefore the poor representation of processes that govern the near surface temperature and wind conditions [6, 11].

A similar concern holds for the representation for land surface. For example, in the current configuration of ECMWF, the 4D-Var analysis of upper-air prognostic variables is performed separately from simpler analyses of screen-level parameters (temperature, humidity) and land surface parameters (soil moisture, soil temperature, snow depth). Consequently, there is a lack of dynamic feedback in the analysis between the land surface and the atmospheric boundary layer [11, 40].

For atmospheric composition, the coupled modelling of meteorological, chemical, and aerosol variables and combined use of observations of trace species and

meteorology in the 4D-Var analysis is desired. It is because these are the basic elements needed for a fully coupled data assimilation system, in which observations of atmospheric constituents lead to physically consistent adjustments to the meteorological variables, and conversely, meteorological observations can have an immediate impact on estimates of the constituent concentrations [11]. However, due to the not-yet-adequate observations (e.g. the model background is not well constrained by observations), there are large and unrealistic changes in the upper-stratospheric circulation. As a result, the current practice for atmospheric composition reanalysis does not yet allow direct adjustments to the meteorological parameters based on trace-gas observations. Instead, the observations of atmospheric constituents need to be bias-corrected (via variational bias corrections) before being assimilated into the data assimilation system for generating the coupled 4D-Var analysis of meteorological variables.

From the above, on one hand there are limits in the current reanalysis in achieving consistency among different physical parameters across domains. On the other hand, the analysis provides complete description of physically plausible atmosphere, ocean and land parameters consistent with instrumental observations. The reanalysis adds value to the instrumental record [49].

For example, by constraining the model background with the observations, reanalysis produces useful estimates for model variables that are not well observed, such as stratospheric winds, radiative fluxes, root-zone soil moisture, etc. However, due to the absence of direct observations, it is difficult to quantify the uncertainty of those model-generated variables, which depend on errors in the model as well as on the observations. Nevertheless, the reanalysis permits the budget diagnostics [2, 27, 28, 43], which are useful for demonstrating shortcomings and progress in climate reanalysis, and the examination of increments can be highly informative about shortcomings in the assimilating model [11]. It is to note that, depending on the diagnostic, the results can be different due to differences either in the observation data, the assimilation scheme or forecast model, or any combination of these.

Uncertainty characterization and consistency validation are therefore required for reanalysis (e.g. including both products and processes), to understand uncertainty that may come from insufficient observation coverage, insufficient data quality, unknown observation uncertainties or assimilating model deficiencies [21, 49].

There are currently international efforts to tackle this issue through inter-comparing reanalysis, for example: the SPARC reanalysis inter-comparison project was proposed in 2012 [15], and the Reanalysis.org portal was established to provide researchers with help to obtain, read and analyze reanalysis datasets created by different organizations. The CORE-CLIMAX project has also proposed a procedure for comparing reanalysis [41], and comparing reanalysis to assimilated observations and CDRs, through inter-comparing reanalysis results. Furthermore, there are recently emerging many reanalysis inter-comparison tools [16], for example: web-based reanalysis inter-comparison tools (<https://reanalyses.org/atmosphere/writ>), KNMI Climate Explorer (<http://climexp.knmi.nl/start.cgi?someone@somewhere>), MERRA Atlas (<http://gmao.gsfc.nasa.gov/ref/merra/atlas/>), and the Climate Reanalyzer (<http://cci-reanalyzer.org/>).

7.2 Case Study: Consistency Among Hydrological Cycle Variables

Based on observation data (e.g. both in-situ and satellite), we can quantify the water cycle components in river basins and compare these to the results obtained by using reanalysis data. TWS (terrestrial water storage) are obtained by balancing precipitation, evaporation and river runoff from satellite observations and in-situ observations. The same is also obtained from Interim Reanalysis data (ERA-Interim). Upon comparing these TWS data to the GRACE (Gravity Recovery and Climate Experiment) observations of storage changes, we conclude that a method can be devised to separate the impacts on the water cycle components by climatic and human factors. Demonstration cases are presented for the Yangtze river basin (Fig. 7.1).

We start with the mass conservation equation for water, which takes the form of:

$$\frac{\partial S}{\partial t} = P_{GPCP} - E_{SEBS} - R_{Obs} \cdot f(P_{i,j}, E_{i,j}) \tag{7.1}$$

where S is the amount of water stored at surface and subsurface per unit of land surface; P_{GPCP} uses the GPCP (Global Precipitation Climatology Project) data is used; E_{SEBS} uses the SEBS (Surface Energy Balance System) [39] derived land evapotranspiration; R_{Obs} is the in-situ observed river discharge; $f(P_{i,j}, E_{i,j}) = (P_{i,j} - E_{i,j}) / (P - E)$ is a scaling factor to distribute the observed discharge to each pixel, $P_{i,j}, E_{i,j}$ are GPCP precipitation and SEBS ET for pixel (i, j) and P, E are the mean GPCP precipitation and SEBS ET for the catchment area of interest, all expressed in cm of water depth.

The TWS anomaly and cumulative TWS anomaly are estimated from GPCP precipitation, SEBS estimated evapotranspiration [8, 9], observed discharge as well

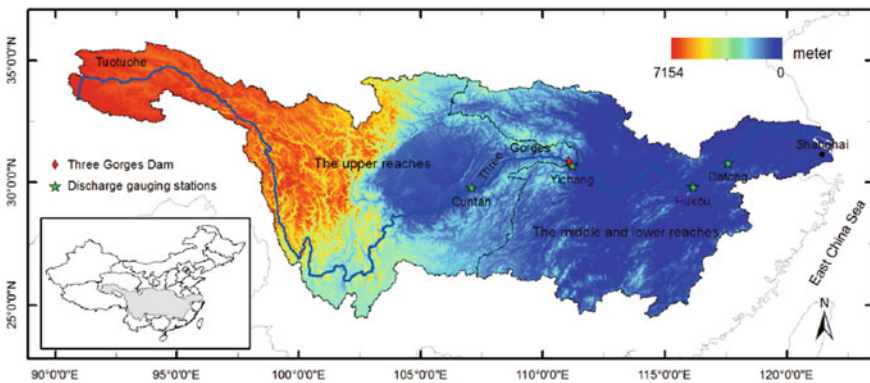


Fig. 7.1 Yangtze river basin (Upper Yangtze reach, from Tuotuohe, to Yichang; Middle reach from Yichang to Hankou; Lower reach from Hankou to the river mouth near Shanghai; Cuntan, Yichang, Hankou, and Datong are four gauging stations located along the mainstream of the Yangtze)

as from ERA-interim data, which are compared with GRACE TWS for the Upper Yangtze reach and the whole Yangtze river basin. The river discharge measurements from Yichang station for the period 2001–2010 are used for the Upper reach study. The discharge measurements from Datong for the period of 2005–2010 are used for the whole Yangtze River basin study. The GPCP precipitation data (precipitation in cm/month) was obtained at <http://jisao.washington.edu/data/gpcp/>; GRACE data was obtained at: <http://grace.jpl.nasa.gov/> (data version: RL05.DSTvSCS1401). The GRACE monthly grid data represents the equivalent water height deviation from its average value over Jan 2004 to Dec 2009).

From the results shown in Figs. 7.2 and 7.3, it can be seen that the TWS derived from the observation data and from ERA reanalysis data are consistent with each other, indicating that both datasets capture the surface dynamics of the water cycle fluxes. However, the TWS derived from GRACE has somewhat larger amplitudes than those from observation data and reanalysis data, indicating deep groundwater contributions. From Fig. 7.3, it may be concluded that after the filling of the Three Gorges Dam reservoir (Yichang station, upper panel in Fig. 7.3) started in 2004, the storage of the upper reach increased in the following years in 2005–2007 period, but

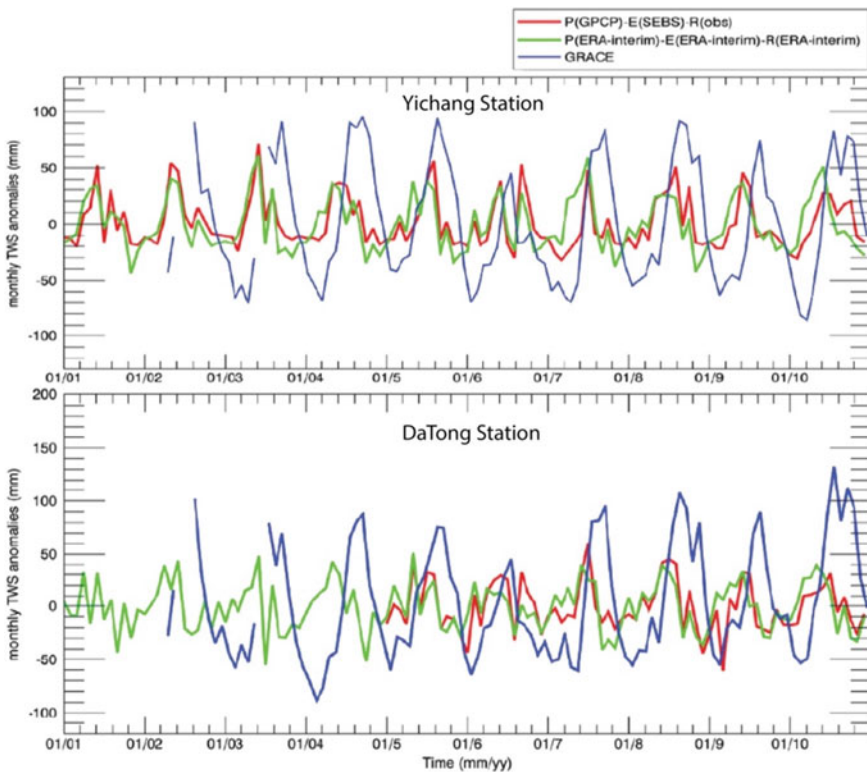


Fig. 7.2 Terrestrial water storage anomaly over (Top) Yichang Station and (bottom) Datong Station

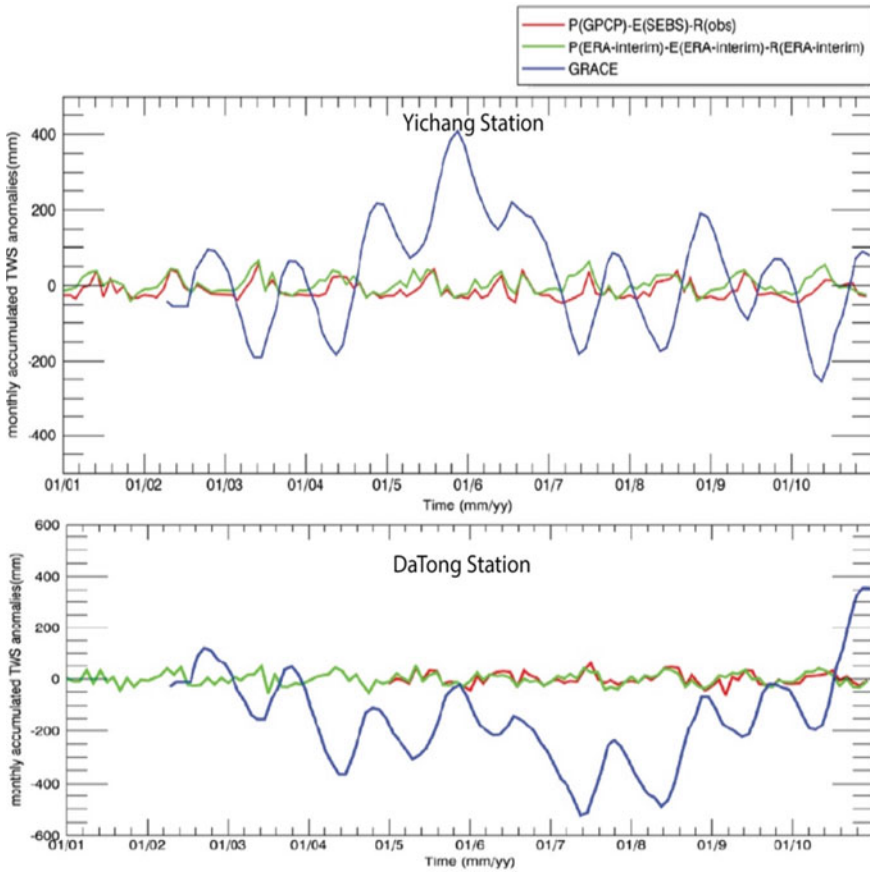


Fig. 7.3 Cumulative terrestrial water storage anomaly over (Top) Yichang Station and (bottom) Datong Station

returned to the average gradually afterwards. This indicates the dominant climatic control of the Yangtze River system in the upper reach. For the lower reach, it can be seen that there was a reduced storage from 2004–2008 but it gradually returned to its pre-Three Gorges stage afterwards.

It is noted that the monthly TWS anomaly and cumulative anomaly over Yichang Station (i.e. the upper reach), calculated using an earlier version of GRACE data (RL04 ssv201008), are completely different from the results shown in Figs. 7.2 and 7.3. For the TWS anomaly, the earlier version of GRACE data has a phase difference of about 10 days, when compared to the current version (results not shown). For the cumulative TWS anomaly, the earlier version does not show the increase of monthly accumulative TWS anomaly after 2004 (results not shown), which was expected due to the filling of the Three Gorges Dam reservoir (upper panel in Fig. 7.3).

The reason for the difference between the two versions of GRACE data can be very complex. Many parameter choices and solution strategies are possible for the complex inversion of relative ranging observations between the two formation-flying GRACE spacecraft, the precise orbit determination via GPS and various corrections for spacecraft accelerations not related to gravity changes. One of the most important parameters for the post-processing of GRACE observations is the land grid scaling coefficients, the use of which enables the representation of surface mass variations at small spatial scales. Without the scaling coefficients, the mass variations at small spatial scales tend to be attenuated. On the other hand, the scaling coefficients are computed by applying the same filters (e.g. de-striping, Gaussian, and degree 60 filters) applied to the GRACE data to a land-hydrology model (i.e. NCAR's CLM4), through which the gain factor is derived by minimizing the difference between the model's smoothed and unfiltered monthly water storage variations at any geographic location. With its origin, the gain factors tend to be dominated by the annual cycles of water storage variations. Meanwhile, the inter-annual trends in particular in hydrology models are very uncertain, it is therefore suggested that it may not be suitable to quantify trends. Nevertheless, within the accepted error ranges, GRACE data is still useful for detecting trends [44, 45].

From the above, it is obvious that the exact explanation for the different results over the upper Yangtze reach, calculated from the two data versions, needs intensive dedicated research. Nevertheless, it is also possible to have a quick check on the meta-information about each change made for the production of GRACE data [41]. Such meta-information can help explain if the difference between Figs. 7.2 and 7.3 could be attributed to what has been changed during the production of new version dataset. It was found that in the new version of GRACE data, July-2004, October-2004, March-2005 and February-2006 were replaced/updated, which corresponds to the dates in which the differences between the two versions of GRACE data were identified (see Figs. 7.2 and 7.3).

7.3 Essentials of Current Practices and Strategy for Future Work

7.3.1 Essentials of Consistency Validation for Current Practice Examples

According to the above, the climate monitoring needs to ensure consistency and quality of the products, the realization of which requires thorough inter-comparison on two aspects:

- a. Thorough (inter)comparison among multiple independent datasets/products for a specific climate variable;

- b. Thorough (inter)comparison among different climate variables, which are physically interlinked.

The first type of inter-comparison can be implemented at point or grid scales to check the product differences of a specific climate variable and the reasons for such differences, while the second type of inter-comparison will check the physical consistency from the functional point of view of different climate variables. In addition, the cross-cutting validation using data assimilating system is an alternative way to check physical consistency of ECVs across domains:

- c. Cross-cutting consistency validation among different climate variables across domains, using data assimilating system.

The above three types of validation activities can be regarded as *the quality consistency check* on climate data products.

At the same time, it is important to recognize that different methodologies and verification approaches used for inter-comparison may lead to the same conclusion, but with different reasons behind. Other than this, the generation processes (/production chain) of different datasets and products differing from each other can complicate the analysis of the (inter)comparison results, if all the necessary information are not provided.

To facilitate the assessment on this kind (e.g. production chain), the CORE-CLIMAX project [41] proposed a System Maturity Matrix (SMM), which is adapted from Bates and Privette [1, 14]. The SMM is a tool to assess the system maturity of a CDR. SMM basically assesses whether CDR generation procedures have been compliant with best practices developed and accumulated by the scientific and engineering communities. This can be regarded as *the process consistency check*.

It is to note that the Climate Change Initiative (CCI) of the European Space Agency (ESA) has defined three consistency levels of satellite CDRs for Earth system monitoring [36]: “(1) consistency in format and metadata to facilitate their synergistic use (technical level), (2) consistency in assumptions and auxiliary datasets to minimize incompatibilities among datasets (retrieval level); and (3) consistency between combined or multiple CDRs within their estimated uncertainties or physical constraints (scientific level).” As such, the ‘process consistency check’ can be mapped to the ESA-CCI’s ‘technical level’, while the ‘quality consistency check’ mapped to both the ‘retrieval level’ and ‘scientific level’.

According to ESA-CCI [36], the assessment methods for consistency on the ‘retrieval level’ include: visual (combined images, or homogeneity), contingency matrix, class combination maps, difference maps, and statistical comparison, the ‘scientific level’ includes: visual (features as expected), quantitative variability, trend analysis, difference maps, trend comparisons, and correlations & other measures of co-variability. These assessment methods are applicable to either one single ECV product (self-consistency) or those ECVs consisting of several quantities (multi-product, and mutual consistency) (e.g., the glacier ECV in ESA-CCI consists of the three products: glacier outlines, elevation change, and velocity).

Based on the definition of ‘single/multi-product’, [49] described an overarching structure for the assessment of quality and usability (AQUE) of ECV products,

considering ‘single product assessment’, ‘multi-product intercomparison’, ‘thematic assessment’, and ‘usability assessment’. The AQUE aims to support a traceable climate service, where the uncertainty from the upstream of climate service (i.e., technical and scientific quality of ECV products) propagates into the resulting benefit (utility) for the end users.

7.3.2 *Generic Strategy of Consistency Validation*

For the quality consistency check, one of the first step is to understand the validation requirements (see Sect. 7.1.1). It shall be realized that for different users (therefore about different applications) the requirements will be different.

For example, there are two kinds of reanalysis (e.g. NWP-like reanalysis or reanalysis for climate change assessment), having different requirements in terms of data usage. A traditional NWP-like reanalysis (e.g. for the past 30yrs) tends to assimilate all available observations unless they are known to be unusable for certain reasons. The climate reanalysis, going further back in time (e.g. for the past 100 yrs), on the other hand, only assimilates those observations that are known to be suitable for climate applications. It implies that a climate reanalysis requires extra efforts in validating the input data than the NWP-like reanalysis.

With that in mind, it is important to implement a *user (validation) requirement review* as the first step, which includes (but is not limited to):

- definition of user requirements on products (e.g. coverage, vertical resolution, spatial and temporal resolution, data length etc.);
- consistency validation requirements (e.g. only inter-comparison required or the ECV consistency across domains required);
- service specification (e.g. near-real-time monitoring/forecast at European/Global Scale, value added products, satellite retrievals etc.);
- requirements for measures and metrics (e.g. root mean square error, relative frequency histograms, Pearson’s correlation coefficient etc.);
- requirements for independent reference observation data (e.g. is it traceable to in-situ measurements?);
- requirements for equivalent products (e.g. is the heuristic reference needed?).

Based on the requirement review, the dedicated *validation plan* can be made and may include (not limited to):

- definition of terminology (e.g. consistency, accuracy, stability etc.);
- description of data under evaluation (data processing and archiving center, model/data processor version, instrument, calibration version, log-file, input and initialization data, measured parameter, native data format, file name convention);
- reference data selection (e.g. the same as the above item, plus the information error budget of data comparison, characterization of sensitivity and information content);

- range of comparison;
- co-location criteria, conversion of units, temporal/spatial re-sampling and smoothing;
- performance and validation statistics (e.g. error budget analysis);
- description of the validation protocol;
- description of the validation process (e.g. both internal and external) [50].

It is noted that, for the description of data under evaluation and the selection of reference data, the known and relevant uncertainties shall be detailed. This will facilitate proper interpretation of the validation results and traceability of the validation process.

After implementing the validation plan, all results of validation measures shall be integrated and published as a *validation report*. This third step needs to coordinate and harmonize all validation activities/results, available quality information, and the service endorsement information. It implies that the validation results from geophysical product and algorithm validation, through validation against service specifications and requirements, to the service endorsement by core/key users (e.g. external review) shall all be collected. Endorsement by core/key users facilitates the feedback loops of the validation process, which is the most important element of the whole validation processes. This external review element provides feedbacks from the end-users to the developers, producers and providers, i.e. the new information for improving the quality of current products.

Arguably, the three steps identified above: (1) User (Validation) Requirement Review; (2) Validation Plan; and (3) Validation Report, are general in a way to validate products corresponding to user requirements, and cannot be referred to consistency validation. On the other hand, it is needed to understand how the consistency is defined before implementing consistency validation, which can be reflected/specified in the user (validation) requirement review. And then, in the validation plan, especially for the description of the data under evaluation and the reference data selection the detailed information shall be investigated, which will help to identify the causes when inconsistency being identified. The case study shows that the cause of inconsistency can be identified from the log-files of the data production. In addition, in the validation plan, the practical aspects of consistency validation can be identified, for example: co-location criteria, conversion of units, temporal/spatial re-sampling and smoothing.

7.4 Discussion and Conclusions

The Climate Data Store (CDS) of the Copernicus Climate Change Services (C3S) envisions that it shall include essential climate variables (ECVs), uncertainty estimates, reanalysis, multi-model data (e.g. seasonal forecasts and up-to-date climate projections), and in-situ and satellite data. Furthermore, CDS should contain only 'climate compliant' data, as defined by Evaluation and Quality Control working group of C3S. This implicates that one may find certain ECV variable from different

sources, and there is a need to do consistency check to determine which dataset are fit for certain particular purpose. On the other side, when there is a certain ECV variable under evaluation, one would like to collect as many as possible independent datasets, under the constraints that they are measuring the same thing, to do (inter)comparison, in order to understand comprehensively the associated uncertainty.

For the in-situ datasets, the homogeneity adjustment plays a critical role in producing long-term climate data. There are direct and indirect methodologies to do homogeneity detection and adjustment [32]. However, it is still difficult to avoid all the inhomogeneities caused by, for example, changes in instrumentation, station moves, changes in the local environment (e.g. building construction), or the introduction of different observing practices like a new formula for calculating mean daily temperature or different observation times. The existence of independent datasets and data assimilation technique provide unprecedented opportunities to spot “bugs” in the in-situ datasets [23]. The use of satellite data can also help monitoring in-situ observations, for example, by using AATSR SST data, the error characteristics of the ‘bad’ buoy for measuring SST can be identified [10].

For the satellite, reanalysis, and multi-model datasets, the same principle of consistency validation as discussed above (e.g. collect as many as possible available independent datasets) is applicable. On the other hand, this principle needs to be constrained with the reference data selection procedure as mentioned in Sect. 7.3. It is to note that based on the discussion in Sect. 7.3 the collection of all kinds of validation information is to identify the missing validation information and processes (e.g. validation gaps), which are necessary to set priorities for future validation reports. And, consistency validation is a key for identifying such gaps.

Through consistency validation, it is also helpful to identify gaps for the current capacities of existing networks (see Sect. 7.1.2). For example, taking water cycle closure as an example, we can thematically identify what needs to be measured. When the needed variable was compared to a dataset, one may find out that in the dataset only land fluxes were observed while soil moisture and soil temperature, or water vapor, or relative humidity were not. From this sense, one may identify the gap, the filling of which requires measurements of other relevant physical variables. This can be useful to help bring different observation networks together, which may be established from different initiatives/projects/programs. In this way, one can suggest a way to gain added-value to current existing observation entities.

In the hydrological cycle closure example implemented over Yangtze River Basin, it is assumed that the total water storage change at a scale of river basin equals to the input minus output. In this sense, the basic water balance equation (i.e. total water storage change = Precipitation—Evaporation—Runoff) can be used to identify what observations are still lacking. However, for the current case, only runoff data can be collected from in-situ observations. The precipitation data was from GPCP, the evaporation was calculated by using SEBS model. Apart from the difficulty of defining runoff data at grid scale, a harmonized approach is needed to bring different sources of data together to do consistency check. The harmonized approach can include two parts: (a) how to adjust different physical metrics to a common benchmark that enables them to be used to do consistency check; (2) the definition

of a physically thematic framework to do consistency check (e.g. in this case, the water balance equation).

Nevertheless, from the Yangtze river case, the TWS anomaly signal calculated from different sources of data (e.g. GPCP precipitation, SEBS evaporation and In-situ runoff) are consistent with that calculated from reanalysis data. It seems that GPCP, SEBS evaporation, and in-situ runoff data are consistent with each other, since they are compared with model results (ERA-Interim), which can be regarded being a physically consistent system that is physically constrained by the coupled model. On the other hand, the analysis schemes for the different components are separate and use different methodologies. For example, for the atmosphere-land domains, the screen-level parameter analysis is the first to be completed and is used as input for the soil moisture and snow analysis. The analyzed surface variables generate feedback for the upper-air analysis for the next assimilation window, through their influence on the first-guess forecast that propagates information from one cycle to the next. In this sense, this can be identified as weakly coupled system. The similar weakly coupled system exists for the atmosphere-ocean domains though.

The weakly coupled data assimilation scheme is widely used in reanalysis centers. One advantage of this weakly coupled approach is that, for example, the ocean initialization, obtained by running an ocean model with surface boundary conditions from an atmospheric (re)analysis, can benefit from the wealth of atmospheric observations and sophisticated atmospheric data assimilation methods. And, such uncoupled approach also permits modularity and easy implementation. The disadvantage is that the surface properties of both atmosphere (e.g. wind conditions and near surface temperature) and oceans (e.g. sea surface temperature) cannot be consistently assimilated within the separate assimilation systems.

The efforts in developing coupled data assimilation for atmosphere and ocean have been intensively undertaking at ECMWF, e.g. with ERA-CLIM2 project, which aimed to develop a first coupled ocean-atmosphere reanalysis of the twentieth century, together with consistent estimates of carbon fluxes and stocks [6, 11]. The new data assimilation scheme has been designed in a way to allow dynamic two-way exchange of information between ocean and atmosphere within a single analysis cycle, which can accommodate observations that are sensitive to both oceanic and atmospheric variables [6, 11]. This ‘strongly coupled data assimilation’ technique allows feedbacks between the ocean and atmosphere models [24, 25], which facilitate the direct correction of the ocean modeling by the atmosphere observations, and vice versa.

Nevertheless, it is recognized that both the observational record and the model have inherent uncertainties that are not always quantifiable [31]. Therefore, it is important to expose all available information pertaining to these uncertainties, and make them accessible to the scientific community. It is also important to enable users to assess the observational information content of specific reanalyzed parameters as a function of space and time, depending on whether those parameters have been directly observed or indirectly constrained by observations of other parameters. All these information will allow end-users to draw meaningful inferences about

the uncertainties in their own estimates, meeting the requirements for their specific applications [6, 12].

So far, there are many programmes/initiatives dedicated to the quality assurance of satellite-based ECV CDRs [49]. However, a consistent, international coordination mechanism for in-situ observations and reanalysis for climate services is not yet existing, which should be further pursued, taking the momentum generated by the Copernicus Climate Change Services. It is well recognized that understanding climate change is fully relied on the observation capacity (i.e., global satellite and conventional observational data in the atmosphere, the land, and the ocean), the development of fully coupled Earth system models, as well as data assimilation systems that can ingest these observation data. It highlights a continuous cycle of research and development in all these key activities: from in-situ data collection/rescue, satellite observation reprocessing, Earth system model advancement, to data assimilation methods for reanalysis (including its production and evaluation). Such a research cycle can, therefore, provide a continuously improving interpretation of the evolution of the Earth system.

References

1. Bates JJ, Privette JL (2012) A maturity model for assessing the completeness of climate data records. *EOS Trans Am Geophys Union* 93:441–441
2. Berrisford P, Kållberg P, Kobayashi S, Dee D, Uppala S, Simmons AJ, Poli P, Sato H (2011) Atmospheric conservation properties in ERA-Interim. *Quarterly J Royal Meteorol Soc* 137:1381–1399
3. Blatchford M, Mannaerts MC, Zeng Y, Nouri H, Karimi P (2020a) Influence of spatial resolution on remote sensing-based irrigation performance assessment using WaPOR data. *Remote Sensing* 12:2949
4. Blatchford ML, Mannaerts CM, Njuki SM, Nouri H, Zeng YJ, Pelgrum H, Wonink S, Karimi P (2020) Evaluation of WaPOR V2 evapotranspiration products across Africa. *Hydrol Process* 34:3200–3221
5. Bojinski S, Verstraete M, Peterson TC, Richter C, Simmons A, Zemp M (2014) The concept of essential climate variables in support of climate research, applications, and policy. *Bull Am Meteor Soc* 95:1431–1443
6. Buizza R, Brönnimann S, Haimberger L, Laloyaux P, Martin MJ, Fuentes M, Alonso-Balmaseda M, Becker A, Blaschek M, Dahlgren P, de Boisseson E, Dee D, Doutriaux-Boucher M, Feng X, John VO, Haines K, Jourdain S, Kosaka Y, Lea D, Lemarié F, Mayer M, Messina P, Perruche C, Peylin P, Pullainen J, Rayner N, Rustemeier E, Schepers D, Saunders R, Schulz J, Sterin A, Stichelberger S, Storto A, Testut C-E, Valente M-A, Vidard A, Vuichard N, Weaver A, While J, Ziese M (2017) The EU-FP7 ERA-CLIM2 project contribution to advancing science and production of earth system climate reanalyses. *Bull Am Meteor Soc* 99:1003–1014
7. CEOS (2012) The Response of the Committee on Earth Observation Satellites (CEOS) to the Global Climate Observing System Implementation Plan 2010 (GCOS IP–10), pp 111. http://www.ceos.org/images/WGClimate/ceos_response_to_gcoss_ip-10_24_september_2012_formatted.pdf
8. Chen X, Su Z, Ma Y, Liu S, Yu Q, Xu Z (2014) Development of a 10-year (2001–2010) 0.1° data set of land-surface energy balance for mainland China. *Atmos Chem Phys* 14:13097–13117
9. Chen X, Su Z, Ma Y, Middleton EM (2019) Optimization of a remote sensing energy balance method over different canopy applied at global scale. *Agric For Meteorol* 279:107633

10. CMUG (2013) Deliverable 4.1 Scientific Exploitation Plan. CMUG Deliverables, pp 23
11. Dee DP, Balmaseda M, Balsamo G, Engelen R, Simmons AJ, Thépaut JN (2013) Toward a consistent reanalysis of the climate system. *Bull Am Meteor Soc* 95:1235–1248
12. Dee DP, Kallen E, Simmons A, Haimberger L (2011a) Comments on “reanalyses suitable for characterizing long-term trends”. *BAMS*. <https://doi.org/10.1175/2010bams3070.1>
13. Dee DP, Uppala SM, Simmons AJ, Berrisford P, Poli P, Kobayashi S, Andrae U, Balmaseda MA, Balsamo G, Bauer P, Bechtold P, Beljaars ACM, van de Berg L, Bidlot J, Bormann N, Delsol C, Dragani R, Fuentes M, Geer AJ, Haimberger L, Healy SB, Hersbach H, Hólm EV, Isaksen L, Kållberg P, Köhler M, Matricardi M, McNally AP, Monge-Sanz BM, Morcrette JJ, Park BK, Peubey C, de Rosnay P, Tavolato C, Thépaut JN, Vitart F (2011) The ERA-Interim reanalysis: configuration and performance of the data assimilation system. *Quarterly J Royal Meteorol Soc* 137:553–597
14. EUMETSAT (2014) CORE-CLIMAX system maturity matrix instruction manual. Deliverable D222, CC/EUM/MAN/13/002, pp 41. <http://www.coreclimax.eu/?q=Reports>
15. Fujiwara M, Polavarapu S, Jackson D (2013) A proposal of the SPARC reanalysis/analysis intercomparison project. *SPARC Newsletter* 38:14–17
16. Fujiwara M, Wright JS, Manney GL, Gray LJ, Anstey J, Birner T, Davis S, Gerber EP, Harvey VL, Hegglin MI, Homeyer CR, Knox JA, Krüger K, Lambert A, Long CS, Martineau P, Molod A, Monge-Sanz BM, Santee ML, Tegtmeier S, Chabrilat S, Tan DGH, Jackson DR, Polavarapu S, Compo GP, Dragani R, Ebisuzaki W, Harada Y, Kobayashi C, McCarty W, Onogi K, Pawson S, Simmons A, Wargan K, Whitaker JS, Zou CZ (2017) Introduction to the SPARC reanalysis intercomparison project (S-RIP) and overview of the reanalysis systems. *Atmos Chem Phys* 17:1417–1452
17. GCOS (2003) GCOS Climate Monitoring Principles. <http://www.wmo.int/pages/prog/gcos/index.php?name=ClimateMonitoringPrinciples>
18. GCOS (2010a). Guideline for the generation of datasets and products meeting GCOS requirements. GCOS-143, Geneva, Switzerland, pp 12
19. GCOS (2010b) Implementation plan for the global observing system for climate in support of the UNFCCC (2010 UPDATE). GCOS-138, Geneva, Switzerland, pp 180
20. GCOS (2011) Systematic observation requirements for satellite-based data products for climate, 2011 Update, Supplemental details to the satellite-based component of the “Implementation Plan for the Global Observing System for Climate in Support of the UNFCCC (2010 Update)”. GCOS-154, Geneva, Switzerland, pp 139
21. Gregow HWL, Makela H, Jylha K, Kaiser-weiss A, Obregon A, Kaspar K, Poli P, Tan D, Kekki S, Arslan A-N, Eichler K (2014) Deliverable D5.52 Reanalysis and user needs with respect to climate change services. CORE-CLIMAX Deliverables, pp 78
22. Houghton J, Townshend J, Dawson K, Mason P, Zillman J, Simmons A (2012) The GCOS at 20 years: the origin, achievement and future development of the global climate observing system. *Weather* 67:227–235
23. Kaiser-Weiss AK, Kaspar F, Heene V, Borsche M, Tan DGH, Poli P, Obregon A, Gregow H (2015) Comparison of regional and global reanalysis near-surface winds with station observations over Germany. *Adv Sci Res* 12:187–198
24. Laloyaux P, Balmaseda M, Dee D, Mogensen K, Janssen P (2016) A coupled data assimilation system for climate reanalysis. *Q J R Meteorol Soc* 142:65–78
25. Laloyaux P, de Boisseson E, Balmaseda M, Bidlot J-R, Broennimann S, Buizza R, Dalhgren P, Dee D, Haimberger L, Hersbach H, Kosaka Y, Martin M, Poli P, Rayner N, Rustemeier E, Schepers D (2018) CERA-20C: a coupled reanalysis of the twentieth century. *J Adv Model Earth Syst* 10:1172–1195
26. Lawrimore J (2014) Review of specific observing system activities related to observing system design (GCOS). CBS/OPAG-IO/OSDW1/Doc 5.4, pp 19
27. Lorenz C, Kunstmann H (2012) The hydrological cycle in three state-of-the-art reanalyses: intercomparison and performance analysis. *J Hydrometeorol* 13:1397–1420
28. Mapes BE, Bacmeister JT (2012) Diagnosis of tropical biases and the MJO from patterns in the MERRA analysis tendency fields. *J Clim* 25:6202–6214

29. Merchant CJ, Paul F, Popp T, Ablain M, Bontemps S, Defourny P, Hollmann R, Lavergne T, Laeng A, de Leeuw G, Mittaz J, Poulsen C, Povey AC, Reuter M, Sathyendranath S, Sandven S, Sofieva VF, Wagner W (2017) Uncertainty information in climate data records from Earth observation. *Earth Syst Sci Data* 9:511–527
30. Parker J, Stott Z (2013) Coordinating Climate Science Observations (final report), pp 104. <http://www.ukeof.org.uk/documents/CCOP2014FINALreport1.pdf>
31. Penny SG, Hamill TM (2017) Coupled data assimilation for integrated earth system analysis and prediction. *Bulletin of the American Meteorol Soc* 98:ES169–ES172
32. Peterson TC, Easterling DR, Karl TR, Groisman P, Nicholls N, Plummer N, Torok S, Auer I, Boehm R, Gullett D, Vincent L, Heino R, Tuomenvirta H, Mestre O, Szentimrey T, Salinger J, Førland EJ, Hanssen-Bauer I, Alexandersson H, Jones P, Parker D (1998) Homogeneity adjustments of in situ atmospheric climate data: a review. *Int J Climatol* 18:1493–1517
33. Plummer S, Lecomte P, Doherty M (2017) The ESA climate change initiative (CCI): a European contribution to the generation of the global climate observing system. *Remote Sens Environ* 203:2–8
34. Poli P, Brunel P (2018) Assessing reanalysis quality with early sounders Nimbus-4 IRIS (1970) and Nimbus-6 HIRS (1975). *Adv Space Res* 62:245–264
35. Poli P, Hersbach H, Dee DP, Berrisford P, Simmons AJ, Vitart F, Lalouaux P, Tan DGH, Peubey C, Thépaut J-N, Trémolet Y, Hólm EV, Bonavita M, Isaksen L, Fisher M (2016) ERA-20C: an atmospheric reanalysis of the twentieth century. *J Clim* 29:4083–4097
36. Popp T, Hegglin MI, Hollmann R, Ardhuin F, Bartsch A, Bastos A, Bennett V, Boutin J, Brockmann C, Buchwitz M, Chuvieco E, Ciais P, Dorigo W, Ghent D, Jones R, Lavergne T, Merchant CJ, Meysygnac B, Paul F, Quegan S, Sathyendranath S, Scanlon T, Schröder M, Simis SGH, Willén U (2020) Consistency of satellite climate data records for earth system monitoring. *Bull Am Meteor Soc* 101:E1948–E1971
37. Seidel DJ, Berger FH, Immler F, Sommer M, Vömel H, Diamond HJ, Dykema J, Goodrich D, Murray W, Peterson T, Sisterson D, Thorne P, Wang J (2009) Reference upper-air observations for climate: rationale, progress, and plans. *Bull Am Meteor Soc* 90:361–369
38. Simmons AJ, Hollingsworth A (2002) Some aspects of the improvement in skill of numerical weather prediction. *Q J R Meteorol Soc* 128:647–677
39. Su Z (2002) The surface energy balance system (SEBS) for estimation of turbulent heat fluxes. *Hydrol Earth Syst Sci* 85–99
40. Su Z, de Rosnay P, Wen J, Wang L, Zeng Y (2013) Evaluation of ECMWF’s soil moisture analyses using observations on the Tibetan Plateau. *J Geophys Res: Atmospheres* 118:5304–5318
41. Su Z, Timmermans W, Zeng Y, Schulz J, John VO, Roebeling RA, Poli P, Tan D, Kaspar F, Kaiser-Weiss AK, Swinnen E, Toté C, Gregow H, Manninen T, Riihelä A, Calvet JC, Ma Y, Wen J (2018) An overview of european efforts in generating climate data records. *Bull Am Meteor Soc* 99:349–359
42. Su Z, Zeng Y, Others (2020) An integrative information aqueduct to close the gaps between global satellite observation of water cycle and local sustainable management of water resources (iAqueduct). *Water*, Accepted
43. Trenberth KE, Fasullo JT, Mackaro J (2011) Atmospheric moisture transports from Ocean to land and global energy flows in reanalyses. *J Clim* 24:4907–4924
44. Wang H, Jia L, Steffen H, Wu P, Jiang L, Hsu H, Xiang L, Wang Z, Hu B (2013) Increased water storage in North America and Scandinavia from GRACE gravity data. *Nature Geosci* 6:38–42
45. Wang X, de Linage C, Famiglietti J, Zender CS (2011) Gravity recovery and climate experiment (GRACE) detection of water storage changes in the Three Gorges Reservoir of China and comparison with in situ measurements. *Water Resour Res* 47:W12502
46. Wilson J, Dowell M, Belward A (2010) European capacity for monitoring and assimilating space based climate change observations—status and prospects. *JRC Scientific and Technical Reports (EUR 24273 EN)*, European Commission, Joint Research Center, Institute for Environment and Sustainability, pp 47

47. WMO (2013) Guide to the global observing system. WMO-488, Geneva, Switzerland, pp 174
48. WMO (2016) The global observing system for climate: implementation needs GCOS 200 (GOOS-214)
49. Zeng Y, Su Z, Barmpadimos I, Perrels A, Poli P, Boersma KF, Frey A, Ma X, de Bruin K, Goosen H, John VO, Roebeling R, Schulz J, Timmermans W (2019) Towards a traceable climate service: assessment of quality and usability of essential climate variables. *Remote Sensing* 11:1–28
50. Zeng Y, Su Z, Calvet JC, Manninen T, Swinnen E, Schulz J, Roebeling R, Poli P, Tan D, Riihelä A, Tanis CM, Arslan AN, Obregon A, Kaiser-Weiss A, John VO, Timmermans W, Timmermans J, Kaspar F, Gregow H, Barbu AL, Fairbairn D, Gelati E, Meurey C (2015) Analysis of current validation practices in Europe for space-based climate data records of essential climate variables. *Int J Appl Earth Obs Geoinf* 42:150–161
51. Zeng Y, Su Z, Schulz J, Calvet J-C, Poli P, Tang D, Manninen T, Riihelä A, Tanis C-M, Arslan A-N, Swinnen E, Tote C, Obregon A, Andre K-W, Roebeling R, John V, Kaspar K, Timmermans WJ, Timmermans J (2014) Generic validation strategy for CDRs/ECVs. CORE-CLIMAX Deliverables, pp 1–31
52. Zeng YJ, Su ZB, Van der velde R, Wang LC, Xu K, Wang X, Wen J (2016) Blending satellite observed, model simulated, and in situ measured soil moisture over tibetan plateau. *Remote Sensing* 8
53. Zhuang R, Zeng Y, Manfreda S, Su Z (2020) Quantifying long-term land surface and root zone soil moisture over tibetan plateau. *Remote Sensing* 12:509–509

Chapter 8

Optical Spectroscopy for on Line Water Monitoring



Genni Testa, Gianluca Persichetti, and Romeo Bernini

Abstract The occurrence of different contaminants in drinking water, surface water, domestic wastewater, and other water sources has led to increased interest in developing new methods and instruments for water quality monitoring able to provide adequate and rapid management interventions. A critical analysis of the main optical spectroscopy techniques for online water monitoring and their recent progress are presented. Not all spectroscopic techniques have yet reached a degree of maturity adequate for the purpose, however, even in these cases, their potentialities in this field are shown.

Keywords On-line Monitoring · Spectroscopic Methods · Absorption Spectroscopy · Fluorescence Spectroscopy · Raman Spectroscopy · Light Scattering Methods

8.1 Introduction

The occurrence of different contaminants in drinking water, surface water, domestic wastewater, and other water sources has led to increased interest in developing new methods and instruments for water quality monitoring able to provide adequate and rapid management interventions.

In this context, on-line monitoring techniques are of great interest not only as a valid alternative to conventional laboratory analyses, but it can also be of fundamental importance for monitoring rapid phenomena, for example in storm-driven spikes of pollutants that would otherwise not be detected, or where automation is required such as in water treatment plants.

Recent developments in spectroscopic techniques have improved the detection sensitivities, quantitatively and qualitatively. Among them, techniques based on optical methods often do not require sample pretreatment and allow their immediate application in on-line monitoring. A critical analysis of the main optical spectroscopy

G. Testa (✉) · G. Persichetti · R. Bernini
Institute for Electromagnetic Sensing of the Environment (IREA), National Research Council of Italy (CNR), Via Diocleziano 328, 80124 Naples, Italy
e-mail: testa.g@irea.cnr.it

techniques for on-line water monitoring and their recent progress are presented. Not all spectroscopic techniques have yet reached a degree of maturity adequate for the purpose, however, even in these cases, their potentialities in this field are shown.

8.1.1 Absorption Spectroscopy

Absorption spectroscopy represents one of the most common approach for on-line and in-situ water monitoring since it offers the potential to permit a label-free spectral detection and identification of specific analytes in an easy way.

This approach is based on the fact that when the light passes through a medium, part of the light energy is absorbed due to the interaction between the light and pollutant molecules. The absorbance is directly proportional to the medium thickness according the Lambert-Beer law:

$$A = \log\left(\frac{I_0}{I}\right) = K(\lambda)C \quad (8.1)$$

A is the absorbance; I_0 and I are the intensities of the incident and outgoing light; K is the molar absorption coefficient of the absorbing substance and the wavelength λ of the incident light; C is the concentration of the absorbing substance in mol/L; and L is the thickness of the absorbing layer in cm. The length L is an important measurement parameter as it fixes the path length that the light travels through the sample. It must be suitably selected in order to optimize the data, a too short path length results in weak signals, whereas long path length could cause data saturation.

UV–VIS Spectroscopy

Currently, absorption spectroscopy for water monitoring is mainly based on UV (180–400 nm) and visible (400–800 nm) spectrum because several pollutants absorb in these spectral regions [1, 2]. Therefore, based on the Lambert–Beer law it is possible to detect the concentration of pollutants in water.

Initially, the research has been focused on single wavelength spectroscopy techniques, e.g. the wavelength of 210 nm is employed for nitrate determination [3]. Absorbance at 254 nm, also referred to as SAC (Spectral Absorption Coefficient), is typically used to measure the organic loading of water and could be related to the total organic carbon (TOC) [4] and chemical oxygen demand (COD) [5]. The wavelength of 280 nm is chosen for the estimation of the biochemical oxygen demand (BOD) [6].

These approaches are very simple and reliable for on-line analysis; however, they could be applied only when samples are transparent and very few and well-known substances are presents. In fact, the simple occurrence of turbidity can strongly influence absorption measurements due to the light scattering attenuation. This problem could be avoided by adopting filtration stages that remove the suspended particles in the sample; however, this is a complex task to be implemented for on-line monitoring.

Alternatively, compensation/subtraction techniques that remove the scattering interference by an additional wavelength have been introduced. These approaches are based on the fact that turbidity can cause light scattering over the whole UV–VIS spectrum range, and additional measurements in the spectral region, where pollutants do not absorb, can be used to evaluate the scattering influence [7].

When the number of contaminants increases and the sample constituents are complex, it is very difficult to obtain reliable and accurate measurements using single/dual wavelength techniques, because water pollutants typically exhibit broad-band absorption and overlapping spectra, and the Lambert-Beer law may be not valid [8]. In order to overcome these limitations, multi-wavelengths or full spectrum UV–Visible spectroscopy techniques have been developed [1, 9] in recent years. These approaches permit the simultaneous detection of multiple contaminants, but typically require more complex data analysis in order to find a correlation between the indicator values (COD, BOD, total suspended solids (TSS), ...) and the absorption spectra in the measured range of wavelengths.

Dimensionality-reduction methods such as principal components analysis (PCA), partial least squares (PLS) and multiple stepwise regression (MSR) have been widely applied for multi-parameter detection [10]. A comparison of these methods has been carried out by Avagyan et al. [11] for high accuracy detection of dissolved organic carbon (DOC) from absorbance measurements in the entire UV–Vis range (200–750 nm). Multi-sensor data fusion approach merging temperature, pH, conductivity and UV–Vis absorption spectrum, by means of an artificial neural network (ANN), has been used to estimate the COD pollution in real wastewater samples [12]. Neural Network could enable the simultaneous measurements of total nitrogen (TN), total phosphate (TP) as well as TSS from on-line UV absorbance measurement [13]. Alternative approaches like evolutionary algorithm method (EVO) and support vector machine (SVM) have been applied in different scenarios (sewers, rivers, wastewater treatment plants (WWTPs)) for the estimation of three water quality parameters (TSS, COD total and dissolved) [14]. Machine learning techniques have been employed to develop a water quality monitoring system able to evaluate COD, TSS and Oil & Grease (O&G) concentrations [15].

Typically, UV–Vis spectroscopic measurements are performed with a single fixed pathlength L . However, alternative approaches based on dual or variable pathlength have been proposed in order to improve both the accuracy and the dynamic measurement range [16, 17].

NIR Spectroscopy

More recently, absorption spectroscopy has been extended to include near-infrared (NIR; 750–2500 nm) and mid-infrared (MIR; 2500–16,000 nm) wavelength regions in order to improve the performances of on-line water quality monitoring [18–20]. In fact, the infrared region provides important information about the chemical nature and molecular structure of the sample under analysis.

In the context of water monitoring, the absorption bands of interest in the NIR spectrum are those related to the overtones and combinations of the oxygen-hydrogen (O–H), nitrogen-hydrogen (N–H) and carbon-hydrogen (C–H) group vibrations.

However, because NIR spectra exhibit usually broad and weak absorption bands, they are more complicated to interpret as compared with that of the fundamental frequency in the MIR region. Hence, multivariate techniques like PCA are required to extract useful information [21]. For these reasons, the power of optical spectroscopy in NIR region has been sometimes underestimated. NIR absorption spectroscopy has been successfully applied to on-line measurement of the chemical oxygen demand and TSS in wastewater [22, 23]. The combination of visible and short wave near infrared wavelengths (Vis/SW-NIR 400–1000 nm) has been employed to quantify the 5-day biochemical oxygen demand (BOD₅), COD and TSS for urban wastewaters monitoring [24].

An alternative approach to traditional NIR spectroscopic techniques has been proposed by aquaphotomics [25], which is based on the monitoring of the water absorbance bands modifications due to the interaction with the molecules of solute. Since the NIR water spectrum related to covalent OH and hydrogen bonds is greatly influenced by contaminant molecules, this approach allows the detection of pollutants also at trace levels. Gowen et al. [26] demonstrated the detection and quantification of the pesticides Alachlor and Atrazine in aqueous solution at ppm levels. Recently, aquaphotomics has been applied for the detection of several substances like salts, sugars, acids, metals in water as well as for monitoring different steps of purification process in water treatment systems [27]. An interesting feature of this approach is the ability to detect specific substances, like salts and metals that do not absorb in the NIR, due to their interaction with OH bonds in water.

MIR Spectroscopy

Optical spectroscopy in the MIR range provides more specific information about the chemical composition of the sample compared to UV–VIS and NIR, because most of the fundamental frequencies for molecular vibrations (e.g., stretching, bending, scissoring) occur in these regions. However, the analysis of water samples, due to the high absorption coefficient of water in the MIR, require the adoption of very thin path length, in the micron range, to avoid strong signal attenuation. In order to overcome this problem, the attenuated total reflection (ATR) spectroscopy approach has been developed. In this approach, the light is directed onto a high-refractive-index crystal prism and is reflected at the sample-prism interface due the total internal reflection. This internal reflection produces an evanescent wave that extends beyond the surface of the crystal and interacts with the sample. Hence, in this case the absorption spectroscopy is enabled, via the evanescent field, and for this reason it is also called evanescent wave spectroscopy (EWS). MIR spectroscopy has been exploited in several water monitoring applications, typically by Fourier-transform infrared (FTIR) spectrometers.

FTIR spectroscopy has been used for on-line measurement of COD, TOC, Volatile Fatty Acids (VFA), and Partial and Total Alkalinity (PA and TA) in anaerobic digestion processes for the treatment of industrial wastewaters [28]. The same approach has been employed for the on-line monitoring of VFA, COD, alkalinity, sulfate, total nitrogen, ammonia and nitrate at a full-scale plant [29]. The FTIR technology has

been also successfully applied for the quantification of pharmaceuticals and other emerging pollutants in wastewater [20, 30].

However, despite these results, FTIR based spectroscopy for on-line and in-situ monitoring remain an unsuitable approach, due to the cost and complexity of the instrumentation. FTIR spectrometers are based on a Michelson interferometer, and are typically benchtop, bulky equipment with free-space optics based on thermal source (globars), which emit a low overall spectral power density in the MIR wavelength range and could require liquid nitrogen cooled detector to achieve high sensitivities. Furthermore, they require complex sampling systems that make the instrument quite unsuitable to be handled during in-situ measurements.

In order to overcome these problems, alternative approaches based on IR chalcogenide glasses fibers transmitting from 2 to about 12 μm have been proposed. The adoption of optical fibers permits to realise an ATR optical probe that could be coupled to FTIR spectrometer and, differently from conventional ATR crystal, could be directly immersed in the sample under analysis avoiding the sampling procedure [31]. Alternatively, the fiber itself could be used for ATR measurements. In this configuration an optical fiber without cladding allows the interaction of the evanescent field with the sample, implementing the so-called fiber evanescent wave spectroscopy (FEWS). [32, 33]. This approach has been extended to other waveguides structures (e.g., planar structures, hollow waveguides, etc.) [34] that, with a suitable design of the waveguide geometry, could also enable a signal enhancement and an increase of the sensitivity. A further improvement of the performances has been obtained by coating the sensor surface with selective membranes or films that allow an enrichment of analyte molecules [35].

A great breakthrough in MIR spectroscopy toward on-line sensing applications has been the introduction of the quantum cascade lasers (QCLs). Compared to the thermal sources typically used in FTIR spectrometers, QCLs exhibit high optical power in both continuous and pulsed mode. Furthermore, they are small and could be made broadly tunable with very high spectral resolution over a wide wavelength range in the mid-infrared spectrum. These features make QCLs sources the best choice for MIR spectroscopy sensors. Using a QCL as tunable laser spectrometer, a sensing platform for toluene trace detection at ppm levels in aqueous solutions has been demonstrated based on a Germanium-on-silicon waveguide [36]. Thin-film gallium arsenide/aluminium gallium arsenide (GaAs/AlGaAs) waveguide, coupled to a broadly tunable quantum cascade laser (QCL), has been integrated into a miniaturized liquid flow cell for continuous trace analysis of chlorinated hydrocarbons (CHCs) in water at low ppm concentration levels [37].

8.1.2 Light Scattering Methods

Light scattering methods are considered to be powerful tools for water quality monitoring [38]. The analysis of the light scattered by a solution containing particulate matter can provide useful information for assessing water quality condition.

The presence of particle matters hinders the transmittance of light through a water sample due to light scattering and confer a qualitative characteristic, known as turbidity, to water. Suspended sediment in water can cause a range of environmental risks; the analysis of the turbidity can give a first, rapid and qualitative assessment of water quality.

Turbidity

Turbidity is a measure of the relative clarity of water and it is considered an important water quality indicator.

Turbidimetric analysis consists of the measurement of the attenuation of incident light due to scattering and it is analogous to absorption measurements, although the reason for the decrease in intensity is different. As a consequence, the presence of turbidity in water sample can cause measurement deviations in absorption measurements, limiting the applicability of the Beer Lambert Law. Thus, it is very important to compensate for the impact of turbidity in spectroscopic analysis [39, 40].

The instrument that measures turbidity is commonly called a turbidimeter. A typical general optical system for turbidity measurements is shown in Fig. 8.1; basically, the system includes a light source, 90° degree-, back- and forward-scattering light detector.

When a beam of radiation of intensity I_0 passes through a nonabsorbing liquid sample containing suspended particles homogeneous in size, shape and composition, the transmitted intensity I is given by

$$I = I_0 e^{(-\tau L)} \quad (8.2)$$

where τ is the turbidity coefficient, and L is the optical pathlength in the sample.

Suspended solids in water, primarily settleable solids larger than $2 \mu\text{m}$, contribute to increase turbidity and constitute the part of total solids floating in a water body (TSS). If required, this contribution to the light scattering can be rejected by manually filtering TSS from water sample. Moreover, the measured scattered signal can arise

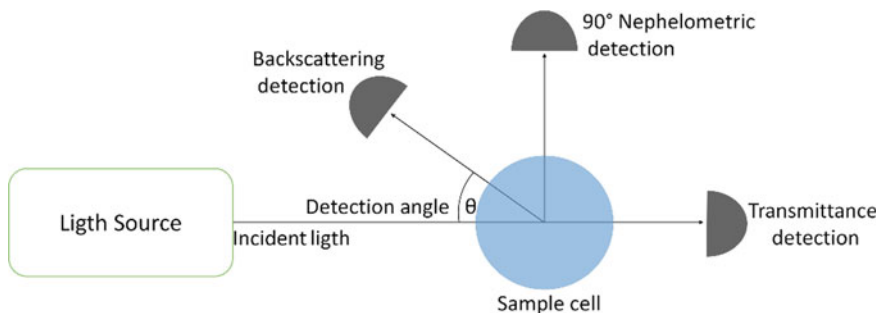


Fig. 8.1 Schematic design of a simple turbidimeter

from the particles of interest, but, if present, also from dust and other background scatterers. To reduce unwanted scattering signal, diluted solutions can be used.

At low particle concentration C , the turbidity τ is linearly related to the concentration C of the scattering particles,

$$-\log\left(\frac{I_0}{I}\right) = PLC \quad (8.3)$$

where $P = 2.303 \tau/C$.

As the particle concentrations increases, scattering becomes more intense, but if the concentration exceeds a certain level, the intensity of scattered light drops rapidly due to multiple scattering.

Turbidimeter instrument based on multiple detection at different angles can be used to reduce noise in the low turbidity signal using the ratio of the light measured by the different detectors [41–43].

Turbidity is usually measured in nephelometric turbidity units (NTU). Nephelometry refers to the procedure of measuring the intensity of light scattered at 90° to the beam (Fig. 8.1).

The presence of dispersed, suspended solids particles such as silt, clay, algae and other microorganisms, organic matter and other small particles affect the water quality for potable water systems, as well as for wastewater and natural aquatic systems. A sudden change in turbidity can be linked, e.g., to an uncontrolled pollution source (biological, organic or inorganic) or caused by a problem in the water treatment process.

Turbidity can be somewhat correlated with microbial contamination of water, but, given that turbidity is a nonspecific indicator of particulates, the relationship is highly dependent on the scenario and therefore of limited value. Although turbidity is not a direct measure of microbial content, the presence of suspended solids in water provides protection to microorganisms, supporting the regrowth of a variety of hazardous pathogens [44]. Moreover, high level of turbidity can affect chlorination and UV disinfection efficacy in water distribution systems, increasing the chance of possible recontamination [45, 46]. For these reasons, excessive turbidity in potable water can be harmful to human health. According to the World Health Organization, the turbidity of drinking water should not exceed 5 NTU, and be preferably much lower than 1 NTU when measured after disinfection treatment [47].

Nutrients, algae, suspended sediments and heavy metal contaminants impact the aquatic environment and influence the survival of aquatic organisms (flora and fauna) [48, 49]. As a matter of fact, the turbidity is imposed as a mandatory parameter to be measured by EU member states in the Marine Strategy Framework.

Nowadays relatively inexpensive instruments are commercially available that allow for in-situ, yet accurate measurements of turbidity level of water.

Turbidity is intrinsically a nonspecific optical method for measuring the amount of minute solid materials in water. Correlation of turbidity with particle type and

concentration is difficult because the shape, size and composition of particles influence the optical properties of the scattered light (scattered direction, intensity, spectral content) from suspension. However, the concentration of a variety of inorganic ions can be measured by adding suitable precipitation reagents to the sample to form suspensions. The most popular method for sulfate determination in water is based on turbidimetric analysis after the precipitation of sulfate as barium sulfate to form a stable monodisperse suspension [50, 51]. Other inorganic ions, like phosphate, nitrogen and potassium have been successfully determined using turbidimetric methods [52–54]. The content of chloride ions in waters, which is commonly determined using spectrophotometric techniques involving highly toxic reagents, can also be monitored using turbidimetry with safer conditions [55, 56].

Turbidimetric instruments based on the use of precipitation reagents and employing flow injection analysis (FIA) system have been demonstrated [57, 58]. In a turbidimetric FIA system the sample preparation is automated by a continuous piping network. Nowadays, such automated benchtop turbidimetric instruments are commercially available; despite having limited deployment capabilities, they can be highly accurate and sensitive.

Benchtop turbidimeter instruments, often required to meet the needs of high sensitivity measurements, are off-line instruments requiring sample collection and consequent transport to the laboratory for analysis, which can be expensive, time and sample consuming and does not offer the opportunity to catch real-time change of water condition. A real-time turbidity monitoring system can lead to smart water management and fast decision making, by acting as a type of “early warning system” for possible water contamination. For these reasons, recently, intense research has been devoted to the development of novel turbidimeter designs for continuous on-line monitoring of water quality conditions [59–64]. Measuring mandated low levels of turbidity can represent a significant cost challenge, especially in the context of low-resource communities in developing regions. Thus, the availability of cheaper sensors is extremely relevant, and novel design to reduce the cost of turbidimetric devices have been proposed [59, 61, 65].

In conclusion, turbidimetric method is a simple and rapid test, widely used as a qualitative indicator of environmental water condition.

Flow Cytometry

A valuable approach to investigate the microbiological quality of water is flow cytometry (FCM) [66]. FCM is based on analysis of the scattered and/or fluorescent light emitted by the suspended cells when passing through a laser beam. One of the most relevant features of a FCM is that it allows the analysis of a microbial community on a single-cell level.

In a FCM system, cells suspended in water sample are arranged in a single file via hydrodynamic focusing effect. The focused cell stream passes through the optical interrogation system as shown in Fig. 8.2. A laser beam strikes each cell one-by-one when they pass through the interrogation point. A series of high sensitivity photodetector are arranged in order to collect both side- and forward-light scattered from each particle and eventually, other emitted signals, e.g. fluorescence.

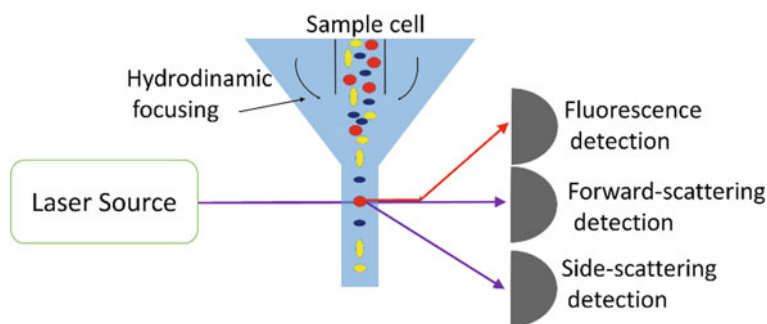


Fig. 8.2 Schematic of a flow cytometer

The most straightforward and common uses of FCM is based on measuring each scattering events for counting total cell content, although it is difficult to obtain reliable counts for environmental samples containing large amounts of non-specific microorganisms. Basically, forward scatter signals can be related to cell size, while side scatter signals are related to cell complexity. By exploiting natural autofluorescence of some cells, or with the use of appropriate dyes, fluorescent signals can also be detected to add useful information about the cells populations under analysis. Simultaneous analysis of scatter and fluorescence data can provide characteristics such as the enumeration, relative size, viability and nucleic-acid content of the microbial content in a water sample [67].

FCM is a high throughput, fast and robust method and it is now generally recognized as a valuable tool for the characterization of waterborne bacteria populations [66]. Although, to our knowledge, FCM has not yet been formally endorsed for water quality assessment, an increasing number of regulatory bodies are exploring the benefits of the methodology [68, 69].

FCM has been widely demonstrated for microbial monitoring in wastewater plants, which are the first stage of water reuse. FCM has been, e.g., applied for studying the effectiveness of the enhanced biological phosphorus removal process [70, 71], to quantify viruses in activated sludge [72] and to investigate the role of sludge-reduction processes on bacterial viability [73, 74].

In the context of drinking water quality monitoring, FCM has been, e.g., applied to assess the removal of waterborne pathogens in wastewater plants achievable by filtration [75–77] and disinfection [78–81]. In the context of aquatic ecosystem monitoring, FCM have been successfully used for analyzing, e.g., phytoplankton distributions [44, 82], and some field-portable devices have also been demonstrated [83, 84].

Typically, environmental bacteria need to be labelled with a fluorescent dye before measurement, in order to distinguish them from the background. Only rarely can direct measurements be performed, e.g. phytoplankton analysis can be conducted by exploiting their auto-fluorescence [85]. Today, microbial water quality is principally

monitored either by periodic sampling and time-consuming laboratory methodologies or by indirect on-line measurements. Since these approaches are inadequate to support fast microbial risk assessment and management, it becomes necessary to implement the on-line monitoring approach, especially for drinking water treatment plants and distribution system [86]. The automation of sample preparation and dilution is a fundamental requisite to apply FCM for on-line monitoring. Several examples of automated systems have been developed in recent years for environmental research applications [87–89].

Full-scale application of automated FCM system has been recently demonstrated for on-line monitoring of drinking water [86, 90, 91] and aquatic ecosystem [92, 93].

Although significant progress has been made in FCM-based monitoring of water samples, there are still certain points that should be addressed in order to better exploit the potential of FCM for microbial water quality assessment, like a faster and low-cost automation of sample preparation, the detection of waterborne viruses, the establishment of universal protocols for the detection of specific pathogens.

8.1.3 Fluorescence Spectroscopy

Fluorescence spectroscopy is a technique effectively and frequently employed in medicine, material sciences, chemistry and biology.

The extreme success of this technique is due to the numerous advantages it offers over other spectroscopic techniques. In particular, since autofluorescence (or natural fluorescence) does not require a pretreatment of the sample, it is easy to apply. Its high sensitivity also allows a rapid detection of substances and finally a fair selectivity completes the characteristics that make this technique particularly advantageous.

All these positive characteristics make the use of this technique in on-line water monitoring significantly attractive and justify the continuous interest in this approach. However, the application of this technique to water monitoring was very early. According to Smart et al. [94] the first mention of the fluorescence of natural waters is attributed to Dienert in 1910 [95]. Then, the development of modern spectrofluorometers (equipped with diffraction gratings capable of adequate resolution of wavelength), the introduction of high-energy excitation sources and the use of modern photomultipliers, has allowed in the late 1980s some high resolution characterizations of the fluorescent substances present in the water.

Depending on the type of application, different device configurations have been proposed. The most common configurations in such sensors make use of open-path (right angle detection or intersecting cones—optical window exposed to the environment) or closed-path (flow-through).

The technology is now mature enough that several commercial devices are currently available for on-line monitoring [96–98]. Many of them are submersible, as this configuration is particularly suitable for prolonged use in the field.

Even though a few decades ago light sources such as Xenon flash lamps were more common, today light emitting diodes (LEDs) or lasers are replacing them due

to their compactness, cost effectiveness and efficiency. Photomultipliers, photodiodes or charge-coupled devices (CCDs) are common detectors, especially in commercial devices, whereas spectrophotometers are less used due to their lower quantum efficiency, but they represent a useful choice when a fast sensor in a wide wavelength range is required.

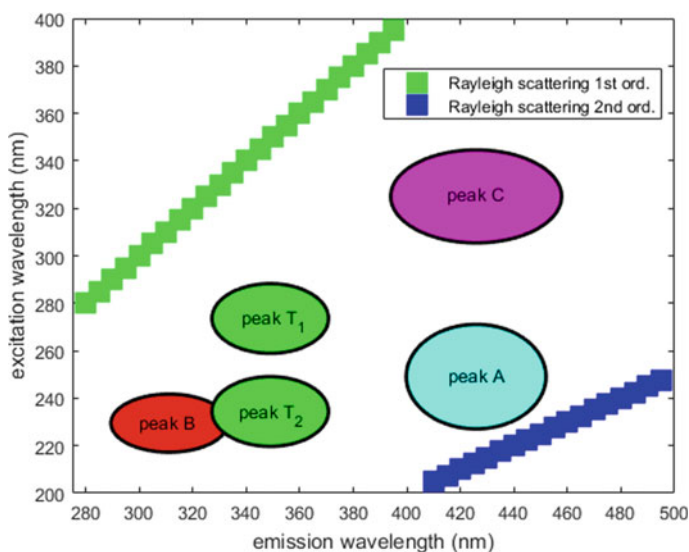
From its beginnings, fluorescence spectroscopy has seen increasing use as a suitable analytical method to identify dissolved organic matter (DOM), organic traces and pollutants in different types of water environments such as, for example, in marine, surface and groundwater. The DOM is made up of decaying matter of animal or plant origin. It is a heterogeneous mixture of different constituents: fatty acids, phenolic compounds, humic substances, amino acids, nucleic acids and also carbohydrates, hydrocarbons and other compounds. This mixture is widespread on the planet and constitutes one of the largest carbon reservoirs on the planet [99]. In many cases the DOM in a water body could also be associated with an active community of microbes. It is this microbial community that, by consuming oxygen, leads to high levels of BOD and therefore to the subsequent collapses of oxygen levels that can be particularly devastating for aquatic ecosystems. Proteins found in the cell walls of these microorganisms have been shown to fluoresce in the same region as the amino acid tryptophan. Tryptophan-like fluorescence (TLF) can therefore be used as a measure of microbial activity within a water body and therefore as an indicator of BOD [100].

For the description of the most often observed fluorescence peaks we will use one of the first and most common nomenclatures, that is the one adopted by Coble et al. [101]. The humic-like fluorophores, derived from the decomposition of plant material, have peaks named as C and A. Peak C shows fluorescence at the excitation—emission wavelengths $\lambda_{\text{ex}} = 300\text{--}350$ nm, $\lambda_{\text{em}} = 400\text{--}500$ nm while peak A is related to $\lambda_{\text{ex}} = 220\text{--}260$ nm, $\lambda_{\text{em}} = 400\text{--}450$ nm. In marine water, humic-like peak appears blue-shifted and labelled as M peak. In addition to humic-like matter, other fluorescence peaks are due to the aforementioned material similar to tryptophan and tyrosine (“tyrosine-like”), as free or bound molecules in amino acids and proteins. Their peaks are commonly labelled as T and B peaks, respectively, and show fluorescence at distinctive wavelengths in natural waters. Tryptophan-like fluorescence (peak T₁) occurs at $\lambda_{\text{ex}} = 265\text{--}300$ nm, $\lambda_{\text{em}} = 300\text{--}350$ nm whereas tyrosine-like fluorescence (peak B) is less commonly observed and occurs at $\lambda_{\text{ex}} = 230\text{--}280$ nm, $\lambda_{\text{em}} = 300\text{--}320$ nm. Peak T also has a shorter wavelength excitation/emission pair (called T₂) with excitation in the range $\lambda_{\text{ex}} = 210\text{--}240$ nm and emission $\lambda_{\text{em}} = 300\text{--}350$ nm. These data, averaged by different literature sources [101–103], are summarized in Table 8.1.

An experimental approach to provide an overview of the phenomenon is offered by the so-called emission excitation matrix (EEM). In this method, first proposed by Coble [102], the recordings of the different fluorescence emissions are obtained from an excitation scan at different wavelengths. A very schematic representation of an EEM is illustrated in Fig. 8.3, where the typical spectral ranges relative to the DOM peaks are reproduced. The unwanted signals due to the excitation source also appear in the same figure. These signals are due to Rayleigh scattering which is

Table 8.1 Excitation/emission fluorescence peaks and attribution

Name of fluorescence peak	Wavelength range of fluorescence excitation (nm)	Wavelength range of fluorescence emission (nm)	Attribution
Peak A Peak C	~220–260 ~300–350	400–450 400–500	Humic-like materials of terrestrial origin. Dissolved organic carbon
Peak B	~230–280	~300–320	Tyrosine-like material
Peak T ₁	~265–300	300–350	Tryptophan-like material
Peak T ₂	~210–240	300–350	Tryptophan-like material
Peak M	350	380–420	Humic-like materials of marine origin

**Fig. 8.3** Schematic representation of the typical ranges of the emission excitation matrices in water samples. The diagonal line represents the elastic scattering (Rayleigh) of the excitation light

generated by particles and molecules smaller than the excitation wavelength. Due to the diffraction grating used as a dispersive element, sometimes a second order effect is also observed in some instruments (an extra band of Rayleigh scatter).

Different studies on the correlation between fluorescence and standard parameters of water revealed that peaks T and C relate not only to BOD but also to chemical oxygen demand (COD) and total organic carbon (TOC) [104–107].

In addition to humic and protein substances, other contaminants in water can be detected by means of fluorescence spectroscopy. These pollutants include aromatic hydrocarbons and pesticides. Gas and liquid chromatography are frequently used techniques for pesticides and hydrocarbons detection. Both of them require expensive equipment and time-consuming extraction or separations procedures. For this reason, fluorescence spectroscopy is a convenient alternative to those techniques. However, it must be said that, only aromatic hydrocarbons exhibit fluorescence whereas aliphatic hydrocarbons are traditionally considered non-fluorescent (with the main exception of some synthetic compounds [108]).

Monoaromatic compounds, as benzene, toluene, xylene (collectively known as BTX) and phenols, emit fluorescence in the wavelength range 250–290 nm.

When two or more aromatic rings are present, i.e. for polycyclic aromatic hydrocarbons (PAHs), a redshift is observed. For instance, compounds with two aromatic ring-like naphthalene, exhibit a fluorescence peak at 310–330 nm, whereas phenanthrenes owning three aromatic rings show a fluorescence peak in the wavelength range 345–355 nm [109, 110].

Another possibility of on-line monitoring offered by fluorescence spectroscopy is that related to the detection of microplankton, in which particular interest concerns cyanobacteria [111]. Compared to other approaches, fluorescence also allows *in vivo* detection [112], and commercial devices, commonly based on the detection of chlorophyll-*a* and phycocyanin (an accessory pigment characteristic of cyanobacteria) are currently available [113].

Obviously, in addition to aspects that make fluorescence particularly attractive as a technique for on-line water monitoring, it is also necessary to underline possible problems in its practical use. For example, particular attention must be paid to factors influencing the fluorescence intensity, as this aspect could affect the measurements reproducibility, or, in the worst case, their reliability.

The fluorescence emission phenomenon is highly affected by the water temperature, the sample composition, the concentration as well as salinity or the pH.

In general, temperature is considered the most relevant fluorescence quencher in water [114]. This effect is enhanced with increasing temperature as non-radiative processes related to thermal agitation are more efficient at high temperature [115].

According to Baker, by reducing the temperature from 45 to 10 °C the DOM fluorescence intensity increased by about 48% while the fluorophore most susceptible to this phenomenon was tryptophan [116]. Hence, a temperature correction of the data is therefore necessary, at least in environments where a large shift of this variable is expected.

However, this phenomenon can be neglected when the temperature variation is minimal. According to Carstea et al. [117] the DOM fluorescence intensity would increase by 0.3% for a decrease in temperature of 0.5 °C and by 2.6% for a 3 °C temperature change. For instance, Carstea et al. demonstrated the first on-line monitoring of effluent wastewater using fluorescence spectroscopy, without temperature compensation of the data, establishing that wastewater diurnal variation was depending on the flow rate and on antecedent rainfall [118].

A well-known fluorescence quencher for several fluorophores is oxygen [119], but some metal ions also play a detrimental role in fluorescence emission. Iron, aluminium and copper can form complexes with DOM that absorb light more strongly than un-complexed DOM while fluorescing less.

This metal quenching seems to affect mostly the humic substances and less the amino acids [114]. The quenching of fluorescent DOM by trace metals has been examined in wastewaters [120] and in natural aquatic systems [121, 122].

Nevertheless, it is quite doubtful that this phenomenon can play a prominent role in other environments where concentrations of DOM and metals are expected to be both low such as, for instance, in water distribution systems [123].

Another issue affecting the fluorescence of water is the inner filter effect (IFE). This effect consists in an apparent decrease in the intensity of the fluorescence phenomenon, or even in a distortion of the detected spectrum as a result of absorption of exciting or emitted light. For this reason, a correction of the spectra with an absorbance-based approach [124] is sometimes necessary, depending on the sample to be analyzed. According to Kothawala et al. [125], this correction approach can be applied to samples with absorbance values of up to 1.5 cm^{-1} , whereas for higher values a dilution of the samples is recommended (thus disadvantaging this solution for on-line monitoring).

Water pH can affect the fluorescence intensity as also the shapes of the detected spectra. Regarding the fluorescence of the DOM, different studies report that the pH has a particular influence on fulvic- and humic-like matters and to a lesser extent on tryptophan-like matters [120, 126, 127]. The possible mechanisms justifying the experimental observations were examined by Patel-Sorrentino et al. [128].

Finally, the salinity of the sample also affects the fluorescence. Salinity can generate conformational changes of the molecule or a charge transfer resulting, for specific molecules, in an increased photoreactivity and fluorescence loss [129, 130].

It can therefore be concluded that, whenever possible, it would be advisable to measure parameters such as temperature, pH and salinity of the samples, and therefore, if these parameters have values capable of influencing the fluorescence of the water, it will be necessary to correct the acquired spectra. However, no correction is required if the pH is between 6 and 8 and the sample temperature is between 20 and 25 °C [114], or in case of qualitative monitoring. For instance, Carstea et al. [118] demonstrated the ability to detect minor changes in on-line monitoring of wastewater using fluorescence spectroscopy without correction for IFE or extensive calibration. All on-line fluorescence sensors for water monitoring, if left long enough in their measurement environment, will experience biofouling buildup. One of the first approaches to prevent biofouling has been the use of substances containing tributyl tin (TBT), no longer in use today because of the known negative environmental impact [131]. Latest anti-biofouling methods include pressurised air cleaning or recent anti-biofouling nanocoating technologies. A list of promising techniques used to protect against biofouling in marine environment are reviewed by Delauney et al. [132].

In conclusion, on-line fluorescence spectroscopy is useful not only for detecting protein-like and humic-like fractions, but also in monitoring algal blooms and pesticide and petroleum pollution. Its main strength is to allow a rapid qualitative analysis to be followed by standard investigations, or, with due attention, a quantitative analysis of the water.

8.1.4 Raman Spectroscopy

At present, the possibility of on-line monitoring of waters based on Raman spectroscopy (RS) and related techniques is still challenging. However, it seemed appropriate to include in this context a brief excursus on the potentiality for on-line monitoring offered by this technique, even if not yet fully mature for the purpose. Raman spectroscopy is based on the well-known inelastic scattering phenomenon discovered in 1928 by C. V. Raman and K. S. Krishnan and independently a few months later by G. Landsberg and L. Mandelstam.

A Raman scattering cross section is very small: the ratio of the Raman scattered intensity to that of Rayleigh scattering is typically 10^{-6} for pure liquids, whereas for samples made up of particles of micrometric size this value may be as low as 10^{-12} . However, recent advances in electronics, lasers, optics, and nanotechnology have made Raman spectroscopy suitably sensitive for many areas of application.

In addition to technological improvements, the advent of advanced Raman techniques has further contributed to lowering the achievable detection limits. Those techniques include surface enhanced Raman spectroscopy (SERS), resonance Raman scattering (RRS) and Fourier transform-Raman spectroscopy (FT-RS). For on-line monitoring, these techniques appear potentially more interesting than an unpractical sample pre-concentration.

In SERS, metallic nanostructures of the substrate are exploited to concentrate electromagnetic energy via optical modes called surface plasmons (SPs), allowing enhancement factors up to 14 orders of magnitude relative to normal RS [133].

In RRS the energy of the incoming photons coincides with an electronic transition of the molecule, thus producing an intensification of the Raman signal that can be even several orders of magnitude compared to normal Raman spectroscopy. In FT-RS, a Michelson interferometer is used to detect a signal unaffected by fluorescence, which is the main issue in RS. The detailed description of the individual techniques is well described in many textbooks [134, 135] and is beyond the scope of the present chapter.

RS has been used for the detection of organic contaminants in water since the 1970s [136, 137]. By means of Raman spectroscopy techniques, it is possible to detect several inorganic substances of interest in water monitoring: cyanide, nitrate, nitrite, chlorate, hypochlorite and perchlorates, asbestos, sulfate and heavy metals, and some examples are given in the following.

RS was employed for detection of several nitrates, nitrites and sulfates by Lombardi et al. [138]. Lombardi et al. observed a shift in concentration of the position

of the major nitrate peak at approximately 1050 cm^{-1} . In the same study, Lombardi et al. also demonstrated that the detection of the Raman characteristic peak shift rather than peak intensity could be used for quantitative detection of nitrates in aqueous solution.

Kauffmann et al. [139] described a general methodology for quantitative detection of inorganic salts in water. The procedure was applied to determine the concentration of sodium nitrate (NaNO_3) solutions, with a range of 0–100 mM, achieving a limit of detection of 0.9 mM. Persichetti et al. [140] achieved a limit of detection of nitrate around 20 mM, i.e. below the maximum contaminant level of 50 mg/L for nitrate that is recommended for public drinking water by the World Health Organization (WHO) guideline.

RRS was used by Furuya et al. [141] for nitrite detection in waste and treated waters after transforming NO_2 into a colored product (azo dye) by means of a chemical reaction. This approach achieved a detection limit of 0.5 ppb, which is approximately an order of magnitude lower than that of the usual colorimetric methods. UV excitation wavelengths at 204 and 230 nm were used for RRS coupled with an intensified CCD detector for detection of nitrate and nitrite in wastewater by Ianoul et al. [142], allowing limits of detection for nitrate and nitrite $<14\text{ mM}$ ($<200\text{ ppb}$).

Zhang et al. adopted shell-isolated nanoparticle enhanced Raman spectroscopy (SHINERS) to detect nitrite traces (indirectly from azo dye) in complex samples such as tap water and lake water [143]. SHINERS is a SERS technique in which plasmonic nanoparticles are enclosed within a shell composed of an insulating material (specifically Zhang et al. used a substrate composed of Au/SiO_2 nanoparticles). With this approach the authors demonstrated limits of detection of 0.07, 0.08, and 0.10 ppm by considering modes observed at 1137, 1395, and 1432 cm^{-1} , respectively.

Wang et al. applied droplet microfluidic chip combined with SERS technology for trace detection of mercury (II) ions in water environment [144]. In this approach, the strong affinity between Au nanoparticles of the SERS substrate with Hg^{2+} ions is able to produce changes in the SERS signal of rhodamine B molecules that is monitored. Wang et al. determined a limit of detection approximately between 100 and 500 ppb in the concentration range of 0.1–2.0 $\mu\text{g/L}$.

By using ink-jet printing of Ag nanoparticles on a Si wafer, Eshkeiti et al. [145] found novel SERS substrates for detection of toxic heavy metals such as CdS, HgS, and ZnO.

Also, organic pollutants such as PAHs, dioxin, herbicides and insecticides are effectively detected by means of RS techniques. Non-specific co-adsorption on metal nanostructures of other species in the matrix solution often reduce the sensitivity of detection in SERS and compromise direct analysis in natural and polluted waters [146]. To circumvent this issue, Marino-Lopez et al. developed a SERS substrate based on a microporous silica capsule with gold nanoparticles [147]. With this sensing platform, Marino-Lopez et al. achieved a detection limit of 1.77 $\mu\text{g/L}$ for dichlorodiphenyltrichloroethane (DDT).

Although single-molecule detection is certainly one of the main potentialities offered by SERS, the quantification at ultralow concentrations remains a major obstacle in pollutant analysis. This is due to the strong signal fluctuations at ultralow

concentration regimes that limit SERS expectations as a quantitative analytical approach. For this reason, de Albuquerque et al. [148] developed a statistical procedure based on single-molecule SERS for the quantification at ultralow concentration without requiring preconcentration of the sample.

Regarding PAHs detection, Xie et al. [149] adopted SERS substrates made of per-6-deoxy-(6-thio)- β -cyclodextrin (CD-SH) modified gold nanoparticles to qualitatively and quantitatively identify a mixture of five dissolved PAHs (anthracene, pyrene, chrysene, triphenylene and coronene). The limits of detection for pyrene, anthracene, chrysene and triphenylene were found to be 10, 100, 100, and 1000 nM, respectively.

In summary, the possible advantages and potentialities of RS-based techniques are manifold. However, even if those techniques could facilitate miniaturization and on-site analysis, there is still a great deal of effort to be made towards on-line monitoring. In particular, the use of SERS for quantitative analysis is still challenging due to the complex interactions between target molecules, light, nanostructure of the substrate and plasmon, as well as the creation of suitable platforms allowing reuse or continuous operations.

8.2 Conclusions

This chapter discusses the application of optical spectroscopy techniques for on-line water monitoring. As it has been reported, a variety of optical spectroscopy techniques have been developed and applied to detect organic and inorganic pollutants in different water environments. Although the results are very promising, the practical application to on-line monitoring still remains limited to specific situations. Further efforts are needed in order to develop multi-contaminant sensing systems that are effective, reliable and low-cost and could be applied for on-line monitoring purposes at full-scale systems. From this point of view, the technology evolution of optical and optico-electronic components (light sources, detectors, spectrometers, ...) in the last years could lead to great improvements of the sensor miniaturization, with a simultaneous decrease of the costs. Finally, in perspective, a strong enhancement in terms of detection selectivity, sensitivity and accuracy could be achieved with the integration of multiple optical spectroscopic techniques able to provide complementary information, together with advanced signal data processing.

References

1. Thomas O, Burgess C (eds) (2017) UV-visible spectrophotometry of water and wastewater, 2nd edn. Elsevier Science, Amsterdam
2. van den Broeke J, Langergraber G, Weingartner A (2006) On-line and in-situ UV/vis spectroscopy for multi-parameter measurements: a brief review. *Spectrosc Eur* 18(4):15–18

3. Singh P, Singh MK, Beg YR, Nishad GR (2019) A review on spectroscopic methods for determination of nitrite and nitrate in environmental samples. *Talanta* 191:364–381
4. Dobbs RA, Wise RH, Dean RB (1972) The use of ultra-violet absorbance for monitoring the total organic carbon content of water and wastewater. *Water Res* 6(10):1173–1180
5. Mrkva M (1975) Automatic U.V. control system for relative evaluation of organic water pollution. *Water Res* 9 (5-6):587–589
6. Brookman SKE (1997) Estimation of biochemical oxygen demand in slurry and effluents using ultra-violet spectrophotometry. *Water Res* 31(2):372–374
7. Shi Z, Chow CWK, Fabris R et al (2021) Evaluation of the impact of suspended particles on the UV absorbance at 254 nm (UV₂₅₄) measurements using a submersible UV-Vis spectrophotometer. *Environ Sci Pollut Res* 28:12576–12586
8. Langergraber G, Fleischmann N, Hofstaedter F (2003) A multivariate calibration procedure for UV/VIS spectrometric quantification of organic matter and nitrate in wastewater. *Water Sci Technol* 47(2):63–71
9. Thomas O, Théraulaz F, Cerdà V, Constant D et al (1996) Wastewater quality monitoring. *Trends Anal Chem* 16:419–424
10. Pacheco Fernández M, Knutz T, Barjenbruch M (2020) Multi-parameter calibration of a UV/vis spectrometer for online monitoring of sewer systems. *Water Sci Technol* 82(5):927–939
11. Avagyan A, Runkle BRK, Kutzbach L (2014) Application of high-resolution spectral absorbance measurements to determine dissolved organic carbon concentration in remote areas. *J Hydrol* 517:435–446
12. Charef A, Ghauch A, Baussand P, Martin-Bouyer M (2000) Water quality monitoring using a smart sensing system. *Measurement* 28(3):219–224
13. Jeong HS, Lee SH, Shin HS (2007) Feasibility of on-line measurement of sewage components using the UV absorbance and the neural network. *Environ Monit Assess* 133:15–24
14. Lepot M, Torres A, Hofer T et al (2016) Calibration of UV/vis spectrophotometers: a review and comparison of different methods to estimate TSS and total and dissolved COD concentrations in sewers, WWTPs and rivers. *Water Res* 101:519–534
15. Qin X, Gao F, Chen G (2012) Wastewater quality monitoring system using sensor fusion and machine learning techniques. *Water Res* 46:1133–1144
16. Chen B, Wu H, Li SFY (2014) Development of variable pathlength UV–vis spectroscopy combined with partial-least-squares regression for wastewater chemical oxygen demand (COD) monitoring. *Talanta* 120:325–330
17. Causse J, Thomas O, Jung AV, Thomas MF (2017) Direct DOC and nitrate determination in water using dual pathlength and second derivative UV spectrophotometry. *Water Res* 108:312–319
18. Mizaikoff B (2003) Infrared optical sensors for water quality monitoring. *Water Sci Technol* 47(2):35–42
19. Gowen AA, Tsenkova R, Bruen M, O'Donnell C (2012) Vibrational spectroscopy for analysis of water for human use and in aquatic ecosystems. *Crit Rev Environ Sci Technol* 42(23):2546–2573
20. Quintelas C, Melo A, Costa M et al (2020) Environmentally-friendly technology for rapid identification and quantification of emerging pollutants from wastewater using infrared spectroscopy. *Environ Toxicol Pharmacol* 80:103458
21. Pasquini C (2018) Near infrared spectroscopy: a mature analytical technique with new perspectives—a review. *Anal Chim Acta* 1026:8–36
22. Dahlbacka J, Nyström J, Mossing T et al (2014) On-line measurement of the chemical oxygen demand in wastewater in a pulp and paper mill using near infrared spectroscopy. *Spectr Anal Rev* 2:19–25
23. Pascoa RNM, Lopes JA, Lima JLFC (2008) In situ near infrared monitoring of activated dairy sludge wastewater treatment processes. *J Near Infrared Spectrosc* 16:409–419
24. Melendez-Pastor I, Almendro-Candel MB, Navarro-Pedreño J et al (2013) Monitoring urban wastewaters' characteristics by visible and short wave near-infrared spectroscopy. *Water* 5(4):2026–2036

25. Tsenkova R (2009) Aquaphotomics: dynamic spectroscopy of aqueous and biological systems describes peculiarities of water. *J Near Infrared Spectrosc* 17:303–313
26. Gowen A, Tsuchisaka Y, O'Donnell C, Tsenkova R (2011) Investigation of the potential of near infrared spectroscopy for the detection and quantification of pesticides in aqueous solution. *Am J Anal Chem* 2(8):53–62
27. Muncan J, Matovic V, Nikolic S et al (2020) Aquaphotomics approach for monitoring different steps of purification process in water treatment systems. *Talanta* 206:120253
28. Steyer P, Bouvier JC, Conte T et al (2002) On-line measurements of COD, TOC, VFA, total and partial alkalinity in anaerobic digestion processes using infra-red ectrometry. *Water Sci Technol* 45(10):133–138
29. Spanjers H, Bouvier JC, Steenweg P et al (2006) Implementation of in-line infrared monitor in full-scale anaerobic digestion process. *Water Sci Technol* 53(4–5):55–61
30. Quintelas C, Mesquita DP, Ferreira EC, Amaral AL (2019) Quantification of pharmaceutical compounds in wastewater samples by near infrared spectroscopy (NIR). *Talanta* 194:507–513
31. Eccleston R, Wolf C, Balsam M et al (2016) Mid-infrared spectroscopy for monitoring of anaerobic digestion processes—prospects and challenges. *Chem Eng Technol* 39:627–636
32. Michel K, Bureau B, Boussard-Plédel C et al (2004) Monitoring of pollutant in waste water by infrared spectroscopy using chalcogenide glass optical fibers. *Sensor Actuators B-Chem* 101(1–2):252–259
33. Lu R, Li W, Mizaikoff B, Katzir A et al (2016) High-sensitivity infrared attenuated total reflectance sensors for in situ multicomponent detection of volatile organic compounds in water. *Nat Protoc* 11:377–386
34. Mizaikoff B (2013) Waveguide-enhanced mid-infrared chem/bio sensors. *Chem Soc Rev* 42(22):8683–8699
35. Karlowatz M, Kraft M, Mizaikoff B (2004) Simultaneous quantitative determination of benzene, toluene, and xylenes in water using mid-infrared evanescent field spectroscopy. *Anal Chem* 76(9):2643–2648
36. Benítez N, Baumgartner B, Missinne J et al (2020) Mid-IR sensing platform for trace analysis in aqueous solutions based on a germanium-on-silicon waveguide chip with a mesoporous silica coating for analyte enrichment. *Opt Express* 28:27013–27027
37. Haas J, Stach R, Sieger M et al (2016) Sensing chlorinated hydrocarbons via miniaturized GaAs/AlGaAs thin-film waveguide flow cells coupled to quantum cascade lasers. *Anal Methods* 8:6602
38. Banna MH, Imran S, Francisque A, Najjaran H, Sadiq R, Rodriguez M, Hoorfar M (2014) Online drinking water quality monitoring: review on available and emerging technologies. *Crit Rev Environ Sci Technol* 44(12):1370–1421
39. Li J, Tong Y, Guan L, Wu S, Li D (2019) A turbidity compensation method for COD measurements by UV–vis spectroscopy. *Optik* 186:129–136
40. Hu Y, Wen Y, Wang X (2016) Novel method of turbidity compensation for chemical oxygen demand measurements by using UV–vis spectrometry. *Sensor Actuators B-Chem* 227:393–398
41. Lihua Z, Haijiang T, Jiaran Z, Daoliang L, Shuangyin L (2014) A novel measurement principle and basic performance of turbidimeter based on dual detection intensity ratio. *Sens Lett* 12:710–714
42. Zhu Y, Cao P, Liu S, Zheng Y, Huang C (2020) Development of a new method for turbidity measurement using two NIR digital cameras. *ACS Omega* 5(10): 5421–5428
43. Ji Y, Chen F (2014) The research and design of intelligent photoelectric turbidity sensor. *Appl Mech Mater* 602–605:2531–2534
44. De Roos AJ, Gurian PL, Robinson LF, Rai A, Zakeri I, Kondo MC (2017) Review of epidemiological studies of drinking-water turbidity in relation to acute gastrointestinal illness. *Environ Health Perspect* 125(8):086003
45. Léziart T, Duthel de la Rochere PM et al (2019) Effect of turbidity on water disinfection by chlorination with the emphasis on humic acids and chalk. *Environ Technol* 40(13):1734–1743

46. LeChevallier MW, Evans TM, Seidler RJ (1981) Effect of turbidity on chlorination efficiency and bacterial persistence in drinking water. *J Appl Environ Micro-biol* 42:159–167
47. World Health Organization (2017) Guidelines for drinking-water quality: fourth edition incorporating first addendum, 4th edn + 1st add. World Health Organization, 2017. <https://apps.who.int/iris/handle/10665/254637>
48. Austin AN, Hansen JP, Donadi S, Eklöf JS (2017) Relationships between aquatic vegetation and water turbidity: a field survey across seasons and spatial scales. *PLoS ONE* 12(8):e0181419
49. Bilotta GS, Brazier RE (2008) Understanding the influence of suspended solids on water quality and aquatic biota. *Water Res* 42(12):2849–2861
50. Ayala A, Leal LO, Ferrer L et al (2012) Multiparametric automated system for sulfate, nitrite and nitrate monitoring in drinking water and wastewater based on sequential injection analysis. *Microchem J* 100:55–60
51. Kortazar L, Sáez J, Agirre J et al (2014) Application of multivariate analysis to the turbidimetric determination of sulphate in seawater. *Anal Methods* 6:3510–3514
52. Lima JLFC, Rangel AOSS, Souto MRS et al (1997) Turbidimetric flow-injection determination of total nitrogen and potassium in vegetables. *Anal Chim Acta* 356:259–265
53. Torres JRO, Tubino M (1994) Turbidimetric determination of potassium by flow injection analysis. *Anal Lett* 27:1625–1636
54. Simonet BM, Grases F, March JG (2001) Determination of phosphate in urine by sequential injection analysis. *Fresen J Anal Chem* 369:96–102
55. Zenki M, Iwadou Y (2002) Repetitive determination of chloride using the circulation of the reagent solution in closed flow-through system. *Talanta* 58(6):1055–1061
56. Mesquita RBR, Fernandes SMV, Rangel AOSS (2002) Turbidimetric determination of chloride in different types of water using a single sequential injection analysis system. *J Environ Monit* 4:458–461
57. Vieira JA, Raimundo IM, Reis BF (2001) Turbidimetric determination of sulphate employing gravity flow-based systems. *Anal Chim Acta* 438:75–81
58. Turkey NS, Jeber JN (2021) A flow analysis system integrating an optoelectronic detector for the quantitative determination of active ingredients in pharmaceutical formulations. *Microchem J* 160:105710
59. Lambrou TP, Panayiotou CG, Anastasiou CC (2012) A low-cost system for real time monitoring and assessment of potable water quality at consumer sites. In: Proceedings of the sensors IEEE, Taipei, Taiwan, pp 1–4, 28 Oct 2012
60. Matos T, Faria CL, Martins MS et al (2020) Design of a multipoint cost-effective optical instrument for continuous in-situ monitoring of turbidity and sediment. *Sensors* 20:3194
61. Gillett D, Marchiori A (2019) A low-cost continuous turbidity monitor. *Sensors* 19(14):3039
62. Kelley CD, Krolick A, Brunner L et al (2014) An affordable open-source turbidimeter. *Sensors* 14(4):7142–7155
63. Bilro L, Alberto N, Pinto JL, Nogueira R (2012) Optical sensors based on plastic fibers. *Sensors (Basel)* 12(9):12184–12207
64. Yeoh S, Matjafri MZ, Mutter KM, Oglat AA (2019) Plastic fiber evanescent sensor in measurement of turbidity. *Sens Actuators A* 285:1–7
65. Murphy K, Heery B, Sullivan T et al (2015) A low-cost autonomous optical sensor for water quality monitoring. *Talanta* 132:520–527
66. Safford HR, Bischel HN (2019) Flow cytometry applications in water treatment, distribution, and reuse: a review. *Water Res* 151:10–133
67. Koch C, Harnisch F, Schröder U, Müller S (2014) Cytometric fingerprints: evaluation of new tools for analyzing microbial community dynamics. *Front Microbiol* 5:273
68. Olivier A, Crook J, Anderson M et al (2016). Expert panel final report: evaluation of the feasibility of developing uniform water recycling criteria for direct potable reuse. California State Water Resources Control Board
69. Scottish Water (2014) Business plan 2015 to 2021 appendices

70. Günther S, Trutnau M, Kleinstaub S et al (2009) Dynamics of polyphosphate-accumulating bacteria in wastewater treatment plant microbial communities detected via DAPI (4',6'-diamidino-2-phenylindole) and tetracycline labeling. *Appl Environ Microbiol* 75(7):2111–2121
71. Mehlig L, Petzold M, Heder C et al (2013) Biodiversity of polyphosphate accumulating bacteria in eight WWTPs with different modes of operation. *J Environ Eng* 139(8):1089–1098
72. Brown MR, Camezuli S, Davenport RJ et al (2014) Flow cytometric quantification of viruses in activated sludge. *Water Res* 68:414–422
73. Foladori P, Laura B, Gianni A, Giuliano Z (2007) Effects of sonication on bacteria viability in wastewater treatment plants evaluated by flow cytometry–fecal indicators, wastewater and activated sludge. *Water Res* 41(1):235–243
74. Foladori P, Tamburini S, Bruni L (2010) Bacteria permeabilization and disruption caused by sludge reduction technologies evaluated by flow cytometry. *Water Res* 44(17):4888–4899
75. Magic-Knezev A, Zandvliet L, Oorthuizen WA et al (2014). In: Nakamoto N, Graham N, Collins MR, Gimbel R (eds) *Progress in slow sand and alternative biofiltration processes*, p 51e58
76. Wang Y, Hammes F, Boon N, Egli T (2007) Quantification of the filterability of freshwater bacteria through 0.45, 0.22, and 0.1 mm pore size filters and shape dependent enrichment of filterable bacterial communities. *Environ Sci Technol* 41:7080–7086
77. Vignola M, Werner D, Wade MJ et al (2018) Medium shapes the microbial community of water filters with implications for effluent quality. *Water Res* 129:499–508
78. Nie X, Liu W, Chen M et al (2016) Flow cytometric assessment of the effects of chlorine, chloramine, and UV on bacteria by using nucleic acid stain and 5-cyano-2,3-ditolyltetrazolium chloride. *Front Environ Sci Eng* 10(6):1–9
79. Kong X, Ma J, Wen G, Wei Y (2016) Considerable discrepancies among HPC, ATP, and FCM detection methods in evaluating the disinfection efficiency of gram-positive and -negative bacterium by ultraviolet radiation and chlorination. *Desalin Water Treat* 57(37):17537–17546
80. Cheswick R, Moore G, Nocker A et al (2020) Chlorine disinfection of drinking water assessed by flow cytometry: new in-sights. *Environ Technol Innov* 19:101032
81. Trask BJ, van den Engh GJ, Elgershuizen JHBW (1982) Analysis of phytoplankton by flow cytometry. *Cytometry* 2:258–264
82. Vives-Rego J, Lebaron P, Nebe-von Caron G (2000) Current and future applications of flow cytometry in aquatic microbiology. *FEMS Microbiol Rev* 24:429–444
83. Olson RJ, Shalapyonok A, Sosik HM (2003) An automated submersible flow cytometer for analyzing pico- and nanophytoplankton: FlowCytobot. *Deep Sea Res Part I Oceanogr Res Pap* 50:301–315
84. Gériques Ribeiro C, Marie D, Lopes dos Santos A et al (2016) Estimating microbial populations by flow cytometry: comparison between instruments. *Limnol Oceanogr Methods* 14:750–758
85. Pomati F, Kraft NJ, Posch T et al (2013) Individual cell based traits obtained by scanning flow-cytometry show selection by biotic and abiotic environmental factors during a phytoplankton spring bloom. *PLoS ONE* 8(8):e71677
86. Favere J, Buysschaert B, Boon N, De Gussem B (2020) Online microbial fingerprinting for quality management of drinking water: full-scale event detection. *Water Res* 170:115353
87. Dubelaar GBJ, Gerritzen PL (2000) CytoBuoy: a step forward towards using flow cytometry in operational oceanography. *Sci Mar* 64:255–265
88. Broger T, Odermatt RP, Huber P, Sonnleitner B (2011) Real-time on-line flow cytometry for bioprocess monitoring. *J Biotechnol* 154:240–247
89. Hammes F, Broger T, Weilenmann HU et al (2012) Development and laboratory-scale testing of a fully automated online flow cytometer for drinking water analysis. *Cytometry A* 81(6):508–516
90. Farhat N, Kim LH, Vrouwenvelder JS (2020) Online characterization of bacterial processes in drinking water systems. *npj Clean Water* 3(16)
91. Buysschaert B, Vermijs L, Naka A et al (2018) Online flow cytometric monitoring of microbial water quality in a full-scale water treatment plant. *npj Clean Water* 1

92. Besmer MD, Weissbrodt DG, Kratochvil BE et al (2014) The feasibility of automated online flow cytometry for in-situ monitoring of microbial dynamics in aquatic ecosystems. *Front Microbiol* 5:265
93. Göröcs Z, Tamamitsu M, Bianco V et al (2018) A deep learning-enabled portable imaging flow cytometer for cost-effective, high-throughput, and label-free analysis of natural water samples. *Light Sci Appl* 7:66
94. Smart PL, Finlayson BL, Rylands WD, Ball CM (1976) The relation of fluorescence to dissolved organic carbon in surface waters. *Water Res* 10:805–811
95. Dienert F (1910) De la recherche des substances fluorescentes dans le controle de la sterilisation des eaux. *C R Hehd Seances Acad Sci Paris* 150(8):487–488
96. Chelsea Instruments (2021) <https://chelsea.co.uk/product-category/fluorometers/>. Accessed 25 Feb 2021
97. Modern Water (2021) BODCheck modern water. http://www.modernwater.com/assets/downloads/Factsheets/MW_Factsheet_BODChek_highres.pdf. Accessed 25 Feb 2021
98. TriOS (2021) <https://www.trios.de/en/matrixflu-vis.html>. Accessed 25 Feb 2021
99. Moran MA, Kujawinski EB, Stubbins A et al (2016) Deciphering ocean carbon in a changing world. *PNAS* 113(12):3143–3151. <https://doi.org/10.1073/pnas.1514645113>
100. Hudson N, Baker A, Ward D et al (2008) Can fluorescence spectrometry be used as a surrogate for the biochemical oxygen demand (BOD) test in water quality assessment? An example from South West England. *Sci Total Environ* 391:149–158
101. Coble PC, Green S, Blough NV et al (1990) Characterization of dissolved organic matter in the Black Sea by fluorescence spectroscopy. *Nature* 348:432–435
102. Coble PC (1996) Characterization of marine and terrestrial DOM in seawater using excitation-emission matrix spectroscopy. *Mar Chem* 51(4):325–346. [https://doi.org/10.1016/0304-4203\(95\)00062-3](https://doi.org/10.1016/0304-4203(95)00062-3)
103. Carstea E, Bridgeman J, Baker A et al (2016) Fluorescence spectroscopy for wastewater monitoring: a review. *Water Res* 95:205–219
104. Henderson RK, Baker A, Murphy KR et al (2009) Fluorescence as a potential monitoring tool for recycled water systems: a review. *Water Res* 43(4):863–881
105. Baker A, Andersen MS, Marjo CE et al (2014) Investigation of pollution in rivers and groundwater by fluorescence. pp 1–14
106. Sorensen JP, Lapworth DJ, Marchant BP et al (2015) In-situ tryptophan-like fluorescence: a real-time indicator of faecal contamination in drinking water supplies. *Water Res* 81:38–46
107. Sorensen JPR, Sadhu A, Sampath G et al (2016) Are sanitation interventions a threat to drinking water supplies in rural India? An application of tryptophan-like fluorescence. *Water Res* 88:923–932
108. Guan R, Dong B, Xu C et al (2020) A strategy to construct fluorescent non-aromatic small-molecules: hydrogen bonds contributing to the unexpected fluorescence. *Chem Commun* 56:4424
109. Abbas O, Rebufa C, Dupuya N et al (2006) Assessing petroleum oils biodegradation by chemometric analysis of spectroscopic data. *Talanta* 75(4):857–871
110. Pharr DY, McKenzie JK, Hickman AB (1992) Fingerprinting petroleum contamination using synchronous scanning fluorescence spectroscopy. *Groundwater* 30(4):484–489
111. Persichetti G, Viaggiu E, Testa G et al (2019) Spectral discrimination of planktonic cyanobacteria and microalgae based on deep UV fluorescence. *Sens Actuators B-Chem* 284:228–235. <https://doi.org/10.1016/j.snb.2018.12.111>
112. Gregor J, Maršálek BA (2005) Simple in vivo fluorescence method for the selective detection and quantification of freshwater cyanobacteria and eukaryotic algae. *Acta Hydro-Chim Hydrobiol* 33:142–148
113. Choo F, Zamyadi A, Newton K, Newcombe G et al (2018) Performance evaluation of in situ fluorometers for real-time cyanobacterial monitoring. *H2Open J* 1(1):26–46. <https://doi.org/10.2166/h2oj.2018.009>
114. Carstea EM (2012) Fluorescence spectroscopy as a potential tool for in-situ monitoring of dissolved organic matter in surface water systems. *Water Pollut (Nuray Balkis IntechOpen)*. <https://doi.org/10.5772/28979>

115. Valeur B, Berberan-Santos MN (2012) *Molecular fluorescence: principles and applications*, 2nd edn. Wiley-VCH. <https://doi.org/10.1002/9783527650002>
116. Baker A (2005) Thermal fluorescence quenching properties of dissolved organic matter. *Water Res* 39(18):4405–4412
117. Carstea EM, Baker A, Bieroza M et al (2014) Characterisation of dissolved organic matter fluorescence properties by PARAFAC analysis and thermal quenching. *Water Res* 61:152–161
118. Carstea EM, Zakharova YS, Bridgeman J (2018) Online fluorescence monitoring of effluent organic matter in wastewater treatment plants. *J Environ Eng* 144:1–9. [https://doi.org/10.1061/\(ASCE\)EE.1943-7870.0001360](https://doi.org/10.1061/(ASCE)EE.1943-7870.0001360)
119. Lakowicz JR, Weber G (1973) Quenching of fluorescence by oxygen. A probe for structural fluctuations in macromolecules. *Biochemistry* 12(21):4161–4170. <https://doi.org/10.1021/bi00745a020>
120. Reynolds DM, Ahmad SR (1995) The effect of metal-ions on the fluorescence of sewage waste-water. *Water Res* 29(9):2214–2216
121. Yamashita Y, Jaffe R (2008) Characterizing the interactions between trace metals and dissolved organic matter using excitation-emission matrix and parallel factor analysis. *Environ Sci Technol* 42(19):7374–7379
122. Ryan DK, Weber JH (1982) Copper(II) complexing capacities of natural waters by fluorescence quenching. *Environ Sci Technol* 16:866–872
123. Heibati M, Stedmon CA, Stenroth K et al (2017) Assessment of drinking water quality at the tap using fluorescence spectroscopy. *Water Res* 125:1–10. <https://doi.org/10.1016/j.watres.2017.08.020>
124. Lakowicz J (2006) *Principles of fluorescence spectroscopy*. Springer, US, NY, USA
125. Kothawala DN, Murphy KR, Stedmon CA et al (2013) Inner filter correction of dissolved organic matter fluorescence. *Limnol Oceanogr Methods* 11(12):616–630
126. Vodacek A, Philpot WD (1987) Environmental effects on laser induced fluorescence spectra of natural waters. *Remote Sens Environ* 21(1):83–95
127. Baker A, Elliott S, Lead JR (2007) Effects of filtration and pH perturbation on organic matter fluorescence. *Chemosphere* 67(10):2035–2043
128. Patel-Sorrentino N, Mounier S, Benaim JY (2002) Excitation-emission fluorescence matrix to study pH influence on organic matter fluorescence in the Amazon basin rivers. *Water Res* 36(10):2571–2581
129. Osburn CL, Morris DP, Thorn KA et al (2001) Chemical and optical changes in freshwater dissolved organic matter exposed to solar radiation. *Biogeochemistry* 54:251–278
130. Chen J, Gu BH, LeBoeuf EJ et al (2002) Spectroscopic characterization of the structural and functional properties of natural organic matter fractions. *Chemosphere* 48(1):59–68
131. Conny RN, Del Castillo CE, Downing BD et al (2014) Experimental design and quality assurance: in situ fluorescence instrumentation. In: Coble PG, Lead JR, Baker A, Reynolds DM, Spencer RGM (eds) *Aquatic organic matter fluorescence*. Cambridge University Press, New York, pp 190–230
132. Delauney L, Compère C (2010) Biofouling protection for marine environmental sensors. *Ocean Sci* 6:503–511
133. Kneipp K, Kneipp H, Itzkan I et al (2002) Ultrasensitive chemical analysis by Raman spectroscopy. *J Phys Cond Matt* 14:R597–R624
134. McCreery RL (2005) *Raman spectroscopy for chemical analysis*, vol 225. John Wiley & Sons
135. Ferraro JR, Nakamoto K, Brown CW (2003) Chapter 3—Special techniques, introductory Raman spectroscopy, 2nd edn. Academic Press, pp 147–206. <https://doi.org/10.1016/B978-012254105-6/50006-8>
136. Bradley EB, Frenzel CA (1970) On the exploitation of laser Raman spectroscopy for detection and identification of molecular water pollutants. *J Water Res* 4:125–128
137. Baldwin SF, Brown CW (1972) Detection of ionic water pollutants by laser excited Raman spectroscopy. *Water Res* 6:1601–1604
138. Lombardi DR, Wang C, Sun B et al (1994) Quantitative and qualitative analysis of some inorganic compounds by Raman spectroscopy. *J Appl Spectrosc* 48(7):875–883(9)

139. Kauffmann TH, Fontana MD (2015) Inorganic salts diluted in water probed by Raman spectrometry: data processing and performance evaluation. *J Sens Actuators B-Chem* 209:154–161
140. Persichetti G, Bernini R (2016) Water monitoring by optofluidic Raman spectroscopy for in situ applications. *Talanta* 155:145–152. <https://doi.org/10.1016/j.talanta.2016.03.102>
141. Furuya N, Matsuyuki A, Higuchi S et al (1980) Determination of nitrite ion in waste and treated waters by resonance Raman spectrometry. *J Water Res* 14(7):747–752
142. Ianoul A, Coleman T, Asher SA (2002) UV resonance Raman spectroscopic detection of nitrate and nitrite in wastewater treatment processes. *J Anal Chem* 74(6):1458–1461
143. Zhang KG, Hu YL, Li GK (2013) Diazotization-coupling reaction-based selective determination of nitrite in complex samples using shell-isolated nanoparticle-enhanced Raman spectroscopy. *J Talanta* 116(22):712–718
144. Wang G, Lim C, Chen L et al (2009) Surface enhanced Raman scattering in nanoliter droplets: towards high-sensitivity detection of mercury(ii) ions. *J Anal Bioanal Chem* 394(7):1827–1832
145. Eshkeiti A, Narakathu BB, Reddy ASG et al (2011) A novel inkjet printed surface enhanced Raman spectroscopy (SERS) substrate for the detection of toxic heavy metals. *J Procedia Eng* 25(35):338–341
146. Bodelón G, Pastoriza-Santos I (2020) Recent progress in surface-enhanced Raman scattering for the detection of chemical contaminants in water. *Front Chem* 478(8):1–8. <https://doi.org/10.3389/fchem.2020.00478>
147. Marino-Lopez A, Sousa-Castillo A, Blanco-Formoso M et al (2019) Microporous plasmonic capsules as stable molecular sieves for direct SERS quantification of small pollutants in natural waters. *Chemnanomat* 5:46–50. <https://doi.org/10.1002/cnma.201800355>
148. de Albuquerque CDL, Sobral-Filho RG, Poppi RJ et al (2018) Digital protocol for chemical analysis at ultralow concentrations by surface-enhanced Raman scattering. *Anal Chem* 90:1248–1254. <https://doi.org/10.1021/acs.analchem.7b03968>
149. Xie YF, Wang X, Han XX et al (2011) Selective SERS detection of each polycyclic aromatic hydrocarbon (PAH) in a mixture of five kinds of PAHs. *J Raman Spectrosc* 42(5):945–950

Chapter 9

Fiber Optic Technology for Environmental Monitoring: State of the Art and Application in the Observatory of Transfers in the Vadose Zone-(O-ZNS)



**B. Abbar, A. Isch, K. Michel, M. Abbas, H. Vincent, P. Abbasimaedeh,
and M. Azaroual**

Abstract The structure and dynamics of the Vadose Zone (VZ) play a major role in the groundwater recharge process and in the transport of contaminants. By monitoring the mass and heat transfer processes within the VZ, it will be possible to predict the contaminants travel time and implement suitable solutions to preserve the groundwater resources. Several environmental monitoring solutions have been developed in recent years to better understand the complex hydrogeological processes that occur along the VZ. The use of Fiber Optic (FO) sensors is a promising technology for environmental monitoring. Compared to conventional sensors, the FO sensors allow measuring and monitoring different parameters, while offering interesting specificities. To improve our knowledge on the reactive processes occurring during mass and heat transfers within the VZ of the Beauce aquifer, the Observatory of transfers in the VZ is being developed near Orléans (France). Three types of distributed FO

B. Abbar (✉) · A. Isch · M. Abbas · M. Azaroual
University of Orléans, CNRS, BRGM, ISTO, UMR 7327, 45071 Orléans, France
e-mail: bouamama.abbar@cnrs-orleans.fr

A. Isch
e-mail: arnaud.isch@terrainnova.fr

M. Abbas
e-mail: mohamad.abbas@cnrs-orleans.fr

M. Azaroual
e-mail: m.azaroual@brgm.fr

K. Michel · M. Azaroual
BRGM, French Geological Survey, 45060 Orléans, France
e-mail: k.michel@brgm.fr

H. Vincent · P. Abbasimaedeh
CEMENTYS, 9 Rue Léon Blum, 91120 Palaiseau, France
e-mail: huguesvincent@cementys.com

P. Abbasimaedeh
e-mail: pouyanabbasi@cementys.com

sensors (DTS, DSS and DAS) have been installed at the O-ZNS experimental site in July 2020. This chapter presents the state of the art on the use of FO sensors for environmental monitoring. The installation of these sensors at the O-ZNS site is then discussed along with the future developments and targeted results.

Keywords Fiber optics · Monitoring · Vadose zone · Groundwater · Contaminant transfer

9.1 Introduction

The Vadose Zone (VZ) is a three-phase (water–air–solid) medium spanning from the surface of the soil down to the aquifer, and is considered as a place of intense and complex exchange and transfer of mass and heat [1, 2]. The vadose zone structure plays an important role in the groundwater recharge process, as well as in the transport of contaminants through the potential development of preferential flow paths and storage reservoirs. Monitoring and understanding the VZ dynamics and physicochemical processes is of utmost importance in predicting the fate of contaminants, and in implementing suitable solutions that can help protect groundwater resources and tackle environmental concerns.

Since the 1950s, contaminations related to intensive agricultural activities have been highlighted in different hydrosystems around the world [3]. Since this period, the nitrate and pesticides contents in groundwater have increased linearly and drastically [4]. Due to growing concern among local communities about the need to protect groundwater resources for drinking and agricultural purposes, a growing body of work has focused on the identification and direct characterization of flow processes within the VZ. However, these processes are still unclear today because of the difficulties implemented in acquiring direct measurements of such phenomena. In this context, the Observatory of transfers in the Vadose Zone (O-ZNS) is being implemented in an agricultural field in Villamblain (near Orléans in France). The O-ZNS project aims to understand and quantify mass and heat transfers over the long term (several decades) thanks to a large access well instrumented with coupled and multi-method environmental monitoring techniques, and surrounded by several monitoring boreholes.

Remarkable progress has been made in recent years concerning the development of new and innovative technologies for environmental monitoring. The use of Fiber Optic (FO) technologies is a promising solution for monitoring the VZ. Indeed, FO sensors provide similar functions to conventional sensors (monitoring, control, or measurement), while offering interesting specificities and potentially added value. The advantages of these sensors include the immunity to electromagnetic interferences, the measurement of several parameters, and the capabilities of remote feeding or interrogation [5]. Additionally, thanks to their high flexibility, FO sensors can provide spatial and temporal information through directly burying them in geological formations or attaching them to subsurface structures. FO sensors are capable

of recording continuously, over large distances and at a higher frequency range than traditional sensors. Or et al. [6] indicated that conventional monitoring sensors have certain limitations mainly related to their low sensitivity to low frequencies signals and require regular maintenance. These sensors are generally designed for near-surface applications and require significant additional developments or adaptations before being able to monitor the shallow subsoil (hard geological facies) over the long term. The FO technology has led to the observation of previously unobserved low frequency signals [7, 8] which can provide valuable information related to complex and highly coupled hydrogeological and geochemical processes. Some FO sensors including Fiber Bragg Sensors (FBG) and Distributed Temperature Sensors (DTS) are currently used for the monitoring of fluids flow [9, 10], hydrogeological processes [11, 12], water content, and energy exchanges along the VZ [13–15]. Infrared optical fibers based on chalcogenide glass are used as sensors for the determination of volatile organic pollutants in groundwater. The system works following the fiber evanescent wave spectroscopy (FEWS) principle. It was tested in situ, in real time, and under real field conditions [16, 17]. Distributed Acoustic Sensors (DAS) are used to monitor micro-seismic activity, record Vertical Seismic Profiles (VSP) and detect fractures [18–20]. Many studies have also highlighted the potential of the Distributed Strain Sensor (DSS) for the monitoring of mechanical deformations linked to land subsidence or landslide [21, 22], and of deformations related to swelling and erosion of VZ material [23–25]. Lu et al. [26] and Zhong et al. [27] highlighted the potential of FO sensors in the development of industrial artificial intelligence systems. Wen et al. [28], have proposed a target recognition technique based on DAS measurements with machine learning. Many researchers have used the data obtained by FO sensors in the development of predictive models dedicated to deciphering complex hydrogeological processes [29, 30]. In recent years, several FO prototypes sensors have also been developed to measure other parameters which do not directly affect the FO such as the pH [31], metallic ion concentrations of chromium [32], salinity [33], relative humidity [34, 35], and hydrogen concentration [36]. The BRGM (French Geological Survey) have developed two optical sensors prototypes dedicated to CO₂ gas measurements in collaboration with the CNRS, University of Caen, University of Rennes and the IDIL company [37, 38].

This chapter presents a state of the art of FO sensors for environmental monitoring and their installation along three boreholes at the O-ZNS experimental site. First, the fundamentals of FO technology with a brief review of the detection systems currently used in environmental monitoring are presented. In particular, the two FO sensors types: Bragg grating sensors and distributed sensors (DTS, DAS, DSS) are treated separately, where their respective advantages and limitations are discussed. We then discuss the context and the instrumentation strategy of the O-ZNS project and present the installation of the distributed FO sensors at the O-ZNS experimental site.

9.2 Fiber Optic Technology: State of the Art and Environmental Applications

Fiber optic technology remains one of the greatest technological advances for the permanent monitoring design in recent years [39–41]. It doesn't have the disadvantages of conventional detection methods (power, impedance, sensitivity to electromagnetic fields), while allowing access to long distance measurements. FO technology offers very high bandwidth with high transmission speed.

FO is a glass cylinder that guides the light in its core (optical waveguide), by the principle of total internal reflection [39, 42]. In some cases, the core of the fiber is made of silicon oxide (SiO_2), surrounded by an optical cladding ($125\ \mu\text{m}$) that is made of lower quality silica (Fig. 9.1a). The whole is protected by a third layer composed of a polymer coating ($250\ \mu\text{m}$, cf. Fig. 9.1a).

There are different types of FO, including Multi-Mode (MM) and Single-Mode (SM). These different typologies make it possible to obtain different characteristics in terms of bandwidth, signal dispersion (influencing the quality of signal reception) or amplification of the optical signal. The core of the MM fiber is larger with a diameter of 50 or $62.5\ \mu\text{m}$ and light signals can follow different paths depending on the angle of refraction (Fig. 9.1b) [43]. The light signals arrive at the end of the cable at different times, inducing some dispersion of the signal. In most cases, the MM fiber is reserved for smaller distance measurements (less than $10\ \text{km}$) compared to the SM fiber. The latter is characterized by a small diameter core ($9\ \mu\text{m}$), and its light signal follows a single mode of propagation unlike the MM fiber. Consequently, the light propagation path is direct and the signal is less disturbed (Fig. 9.1c). The small diameter of the fiber core requires a significant luminous intensity, therefore expensive laser diodes, which makes the use of SM fiber more expensive compared to the MM fiber.

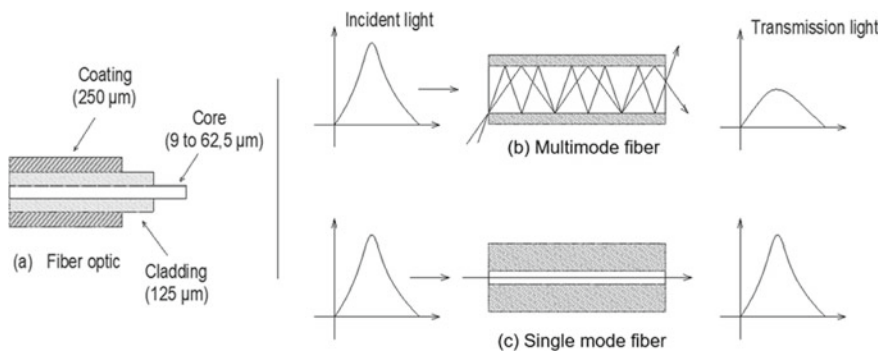


Fig. 9.1 a FO composition, b multi-mode FO: the light signals follow different paths depending on the angle of refraction, c single-mode FO: the light propagation path is direct without signal dispersion. Adapted from: [43–46]

The FO sensors are able of covering the functions of traditional sensors: monitoring, detection, and localization. Their measurement principle is based on the detection of changes in the transmitted light signal in an optical fiber. Changes in the environment around the fiber (stress, temperature or pressure) can cause variations in the transmitted signal. Different physical phenomena are used to modulate the transmitted light, which gives each sensor its characteristic performance. There are two main families of FO sensors: Fiber Bragg Grating (FBG) sensors (point measurements) and distributed sensors (continuous measurements).

9.2.1 Fiber Bragg Grating Sensors: Point Measurements

FBG sensors represent short sections of the FO that contains a modulation or a periodic variation of the refractive index (Fig. 9.2). When these sensors are lit by a coherent light, each FBG reflects a precise wavelength [47]. The reflected wavelength is measured by an optical interrogator and is sensitive to temperature and deformations variations of the FBG sensor. According to Bragg’s law, established by Nobel Prize winner Sir William Lawrence Bragg in 1915, the reflected wavelength of light from the grating is defined by Lecoy [48]:

$$\lambda_B = 2 \Lambda_B n_{eff} \text{ (nm)} \tag{9.1}$$

where λ_B is the reflected Bragg wavelength (nm), n_{eff} is the effective refractive index of the fiber core and Λ_B is the period of the Bragg grating. n_{eff} and Λ_B both vary with the temperature and the strain of the fiber. When the fiber undergoes deformation or when its temperature changes, a variation in the reflected wavelength λ_B can be observed:

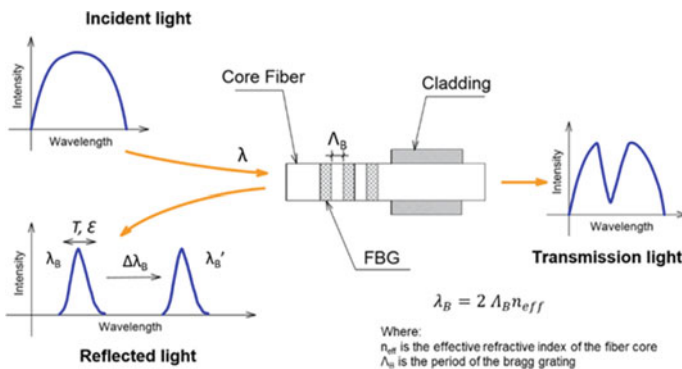


Fig. 9.2 Schematic representation of the Fiber Bragg Grating (FBG) principle. Adapted from [45, 49]

Table 9.1 Characteristics of Bragg grating FO sensor

Parameters	Value
Spatial resolution	A few millimeters ~2 mm (length of the Bragg grating)
Spatial range (L)	Up to 10 km typical (depends on link losses)
Temperature resolution	0.01 °C
Temperature range	–150 °C to up to 1000 °C
Strain resolution	0.1 μm/m
Strain range	1–4%
Number of measurement lines analyzed in parallel	10
Typical number of Bragg gratings analyzed at the measurement rate	300
Cable price ^a (from Solifos company)	5–10 €/m
FBG sensors (T/ε) price (from FTMesures and CEMENTYS company)	~375 €/sensor
FBG interrogator price (from FTMesures company)	~11 k€

Compiled from scientific publications, quotes, and data sheets

^aAverage price in Europe in 2020

$$\frac{\Delta\lambda_B}{\lambda_B} = K\varepsilon + \alpha\Delta T \quad (9.2)$$

where the coefficient K is due to photo-elasticity (around 0.8), ε (–) is the deformation of the fiber, and ΔT (°C) is the temperature variation which expands the glass (hence the coefficient α of the order of $6 \cdot 10^{-6} \text{ }^\circ\text{C}^{-1}$).

The appearance of point sensors with Bragg gratings dates back to the 1990s [49]. These sensors allow the detection of pressures, deformations and temperature (Table 9.1) and the monitoring of parameters that do not directly affect the fiber (humidity, pH, salinity, etc.) [50]. These sensors can be installed directly on the soil surface to monitor deformation caused by the extraction of groundwater from an aquifer [11, 12, 51]. Alemohammad et al. [52] developed a FBG temperature and pressure sensor for soil and groundwater monitoring. This sensor was successfully tested in-situ during the thermal remediation of brownfields and the results obtained were comparable to those recorded by conventional sensors. FBG multi-parameters sensors (temperature, pressure and deformation) have been developed by Drusová et al. [51] for monitoring groundwater flow velocity. During the in-situ experiments [51], the FBG deformation sensors were installed in a field near a drinking water extraction well in Hengelo (Gelderland, Netherlands). The obtained results showed that the FBG deformation sensors were able to detect the consolidation of the VZ material caused by the extraction of groundwater in the well within a radius of 250 m. FBG sensors can also be used as extensometers to monitor natural subsidence of

soils or subsidence induced by mining. Wang et al. [53] designed micro-seismic and displacement sensors based on FBG technology. These prototypes were used in a surface subsidence monitoring system in an iron mine. According to an in-situ experiment, Huang et al. [12] have shown the feasibility of monitoring the pore water pressure profile in a borehole using FBG pressure sensors. In recent years several prototypes based on the FBG technique have been developed to detect other parameters which do not directly affect the FO such as pH, gases concentrations, heavy metals or salinity. A pH sensor based on the FBG technique in all-polymer FO was proposed by Janting et al. [31]. The sensor was coated with a layer ranging from 5 to 10 μm of pH-sensitive hydrogel. The hydrogel contracts or expands depending on the change in the pH value. The variations in pH were controlled by following the changes induced by the deformation of the fiber in the reflected Bragg wavelength λ_B . Several prototypes have been developed by adding a sensitive polymer to the FBG sensor to detect other parameters such as metallic ions of chromium [32], salinity [33, 54], relative humidity [34, 35]. Alexandre et al. [55] proposed an FBG sensor to detect hydrogen. The FBG sensor was coated with a 5 nm layer of palladium to improve the sensitivity of silica to hydrogen. Encouraging results have been observed with a sensor response time of 10 min. The results of these studies highlight that FBG sensors provide efficient and precise measurements. Table 9.1 shows some characteristics of Bragg gratings systems.

9.2.2 *Distributed FO Sensors: Continuously Sensitive*

In the distributed FO sensors, the FO itself becomes the detection element and the measurement is possible at each point of the fiber. The measurement range of the distributed sensors goes from a few meters to several tens of kilometers with a metric, decametric or even centimetric resolution. Continuous, real-time measurement is nowadays a real advantage in the field of monitoring. Distributed FO sensors are used in several fields such as pipelines and wells monitoring [40, 56, 57], the oil and gas industry [58], and for monitoring several environmental parameters such as the stress, deformation, temperature, pressure, and gases concentrations [36].

Distributed FO sensors are currently attracting great interest in various fields, particularly in environmental monitoring, due to the low cost of the sensor and its fully distributed detection. However, interrogators (data analyzers) are relatively expensive compared to point sensor systems (see Tables 9.1 and 9.2). The operating principle of these sensors is based on the analysis of the light signal transmitted through the fiber: a laser sends a coherent light into the fiber of given wavelength λ_0 . At all points of the fiber, the heterogeneities and the molecular vibrations of the silica will backscatter a small part of this light (Fig. 9.3a). Part of the light is returned with the same wavelength λ_0 as the incident light (Rayleigh peak). Secondary light peaks (Brillouin and Raman) are also created on both sides of the incident wavelength λ_0 . Distributed FO sensors are based on three types of light-matter interactions, namely the *Rayleigh*, *Raman* and *Brillouin* backscatter phenomena. Several spectral

Table 9.2 Characteristics of distributed FO sensors

Parameters	DTS (<i>Raman</i>)	DAS (<i>Rayleigh</i>)	DSS (<i>Brillouin</i>)
Scattering mode	Raman	Rayleigh	Brillouin
Scattering categories	Inelastic	Elastic	Inelastic
Detect parameters	Temperature	Temperature/Strain (strain rates) caused by acoustic waves	Temperature/Strain
FO Requirement	Multi-mode (MM)	Single mode (SM)	Single mode (SM)
Cable recommended	Loose tube cable	Loose tube cable	Loose tube cable/Tight buffered cable
Maximal range	10 km	50 km	30 km
Spatial resolution	1 m	1–2 m	1 m
Precision	0.1 °C	0.1 °C	1 °C / 20 $\mu\epsilon$
Maximal detection frequency	–	1–50 kHz <0.1 Hz (micro-seismic)	–
Advantage	Precise measurements	Precise measurements	Stable measurements based on Brillouin frequency measurement
Disadvantage	Based on the measurement of the power amplitude, which can be disturbed in certain places of the fiber (curvature, connectors, splices)	High cost of interrogators systems generates a large volume of data (about 1 teraocet/day of measurement)	High cost of interrogators systems
Functions	Ground water flow monitoring Thermal conductivity soil water content estimation (ADTS method)	Surfaces and crossholes seismic measurements Subsoils fracture detection (passive seismic)	Soil movement monitoring
Cable price ^a (Solifos company)	5–10 €/m	5–10 €/m	5–10 €/m
FBG interrogator price ^a (CEMENTYS company)	~50 k€	~145 k€	~80 k€

Compiled from scientific publications, quotes, and data sheets

^aAverage price in Europe in 2020

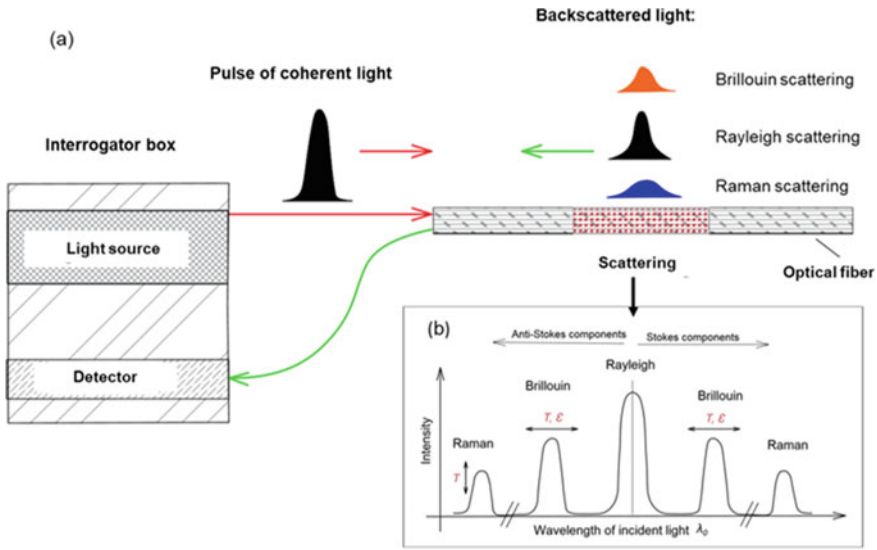


Fig. 9.3 a Schematic diagram of distributed FO sensors, b backscatter spectrum with Rayleigh, Brillouin, and Raman bands as well as the Stokes and anti-Stokes bands. Adapted from [56, 59]

components are observed in backscattering of light by silica, corresponding to these three scattering phenomena (see Fig. 9.3b).

Backscattering phenomena are classified in two categories [40]:

- (i) Elastic scattering: the scattered photons keep their energy and therefore have the same frequency as the incident wave, this is the case with Rayleigh backscattering (sensitive to temperature and acoustic waves).
- (ii) Inelastic scattering: photons lose (Stokes components) or gain (anti-Stokes components) energy and presents therefore a frequency (or wavelength) offset from that of the incident wave. Raman backscatter (temperature sensitive) and Brillouin backscatter (temperature and strain sensitive) are inelastic diffusions. The Raman frequency offset is around 13 THz while the Brillouin frequency offset is around 10 GHz.

These three types of scattering (*Raman*, *Brillouin* and *Rayleigh*) are shown in Fig. 9.3 and are detailed below.

Raman scattering is caused by the interaction of photons from a monochromatic light source with the molecules of the material. This results in the emission and absorption of optical phonons, with frequencies equal to the vibration frequencies of molecules in the material, of the order of ten THz. The backscattered wave then undergoes either an energy loss (Stokes wave) or an energy gain (anti-Stokes wave). Raman-based distributed temperature sensing (DTS) systems operate on the basis of the intensity ratio of the anti-Stokes component on the Stokes component of the spectrum [59, 60]:

$$R(T) = \frac{I_{a-s}}{I_s} = \left(\frac{\lambda_s}{\lambda_{a-s}} \right)^4 \exp\left(-\frac{hcv_{vib}}{kT}\right) \exp(-\Delta\alpha z) \quad (9.3)$$

where $R(T)$ is the resulting temperature, I_{a-s} is the intensity of the component of the anti-Stokes spectrum, I_s is the intensity of the component of the Stokes spectrum, λ_s is the wavelength of the component of Stokes spectrum, λ_{a-s} is the wavelength of the component of the anti-Stokes spectrum, h is the Planck constant, c is the speed of light in a vacuum, v_{vib} is the vibration frequency, $\Delta\alpha$ is the optical attenuation between the components of the Stokes and anti-Stokes spectrum, k is the Boltzmann constant, T is the temperature and z is the head position of the FO.

Raman scattering is used to measure the temperature of the FO because the latter varies with changes in temperature. DTS uses MM fibers to measure Raman scattering and thus monitor fiber temperature (Table 9.2). Temperature sensors (DTS Raman) are used in several applications such as measuring the temperature profile in a borehole, and detecting leaks or fire events [46]. However, for Raman DTS it is necessary to use MM fibers, which represents a limit for the industry, since the measurement range is greater in SM than in MM fiber. This is the main disadvantage for these sensors in the case of long-range applications such as temperature monitoring of railways or pipelines. The Raman DTS is based on the measurement of the power amplitude and can be disturbed in certain places of the fiber (curvature, connectors, splices). DTS can also be used to monitor the thermal response of the material to the active heating of the sensing fiber [Active Heated Fiber Optics method (A-DTS)] [14, 15]. This method represents an interesting alternative to traditional sensors to monitor the variations of the water content within the VZ. The principle of A-DTS consists of heating the sensing cable with an electrically generated heat pulse and monitoring the thermal response of the VZ materials before and after the heat pulse. The resulting temperature variations can be linked to the water content of the materials [15].

Brillouin scattering comes from the interaction of light with acoustic waves (or acoustic phonons) which propagate in the fiber. It causes a frequency shift of the backscattered spectrum according to the Stokes and anti-Stokes components (Fig. 9.3). The Brillouin shift frequency depends linearly on the deformation and the temperature of the material [56]. This offset varies with the temperature changes ΔT and deformation ε of the FO according to the following equation:

$$\Delta\nu_B = C_T \Delta T + C_\varepsilon \varepsilon \quad (9.4)$$

where $\Delta\nu_B$ (Hz) is the Brillouin offset frequency, and C_T and C_ε are respectively the temperature sensitivity and deformation coefficients. They both depend on the type of FO used.

The Brillouin scattering is used to measure the temperature and the deformation of the FO. Brillouin Distributed Strain Sensing (DSS) is based on frequency measurement and uses SM fiber. Thus, the Brillouin DSS measurement is independent of the

optical loss in the fiber unlike the Raman-based DTS. However, since Brillouin scattering is both sensitive to deformation and temperature, some measurement errors can appear in one of the two parameters when the other varies.

Rayleigh scattering is caused by the interaction between an electromagnetic field which propagates in the fiber and the impurities present in the silica which modulate the refractive index [56]. This type of scattering is mainly used to assess optical losses but it has also proven its sensitivity to acoustic vibrations. Rayleigh scattering is used in Distributed Acoustic Sensing (DAS) to measure each acoustic wave surrounding a SM fiber. DAS is used in several applications such as seismic acquisition and to monitor the health of structures [18, 19, 50, 61–64].

9.2.3 Distributed Sensors Performance in the Environmental Application

Distributed detection represents a suitable solution for environmental monitoring, in particular for the detection of fractures in geological formations and for groundwater monitoring. The distributed FO sensors allow measuring the temperature and deformation over several kilometers. In recent years, a growing body of work has focused on the development of distributed FO sensors suited for environmental monitoring purposes. A multitude of researchers have studied the application and performance of these sensors [19, 56, 63, 65–67].

a. Distributed temperature sensing (DTS)

DTS Raman technology has been widely used in environmental monitoring [56, 58], particularly in boreholes for estimating the thermal conductivity of the VZ [68]. Unlike conventional temperature sensors, the DTS system allows continuous measurements over ranges of up to 30 km and a spatial resolution of around one meter (Table 9.3). Thanks to their low thermal mass, the sensing fibers quickly equilibrate (<1 min) to the temperature of their environment and provide measurements of the most ambient temperatures [57]. The first uses of this technique date back to the 1990s, when DTS were used to monitor geothermal energy in Mexico, Indonesia and the USA [69]. Temperature sensing for hydrogeology purposes using the DTS system dates back to the late 1990s. Hurtig et al. [70] used the DTS system to detect flow in a fractured rock along a borehole after performing hot and cold-water injections. Majorowicz and Smith [71] were among the first researchers to use the DTS technology in order to track temperature variations in the VZ when drilling a new oil well. Selker et al. [65] studied the possibility of using this technology in hydrological applications. They have shown that the DTS system can be useful for observing hydrogeological processes, including evaporation and infiltration Freifeld et al. [68] also used DTS technology in boreholes to measure the thermal conductivity of the VZ. Several studies have been carried out to better understand the capacities and limits of the DTS system [65, 72], and the validation of measurements and their

Table 9.3 An overview of recent applications of the DTS system for environmental monitoring

References	Measurements	DTS instrument	FO cable	Data collecting
[79]	Soil/rock thermal properties (surface and boreholes installation)	Ultima™ XT DTS (Silixa Ltd., UK)	FO cable (Brugg Kabel AG, Switzerland)	Sampling res.: 25 cm Temporal res.: 10–30 s Temperature res.: 0.02 °C
[64]	Soil/Rock thermal properties (boreholes installation)	DTS	MM fiber optic cable: BRUsens DTS 4.0 mm non-metallic, from Solifos—Switzerland	Installation/Calibration
[80]	Groundwater flow quantification in fractured rock boreholes	Ultima™ DTS (Silixa Ltd., UK) with a 1.8 km maximum length	A-DTS cable with diameter of 6.3 mm: from AFL FO (USA)	Sampling res.: 29 cm Temporal res.: 1 s Temperature res.: 0.01 °C
[76]	Spatial variation of the water content of sandy soil	Ultima™ DTS (Silixa Ltd., UK)	A-DTS cable: from Brug—Switzerland	Sampling res.: 0.125 m Temporal res.: 1 s
[75]	Soil water content in the surface soil	Linear Pro series DTS (AP Sensing, Böblingen, Germany) maximum measurement range of 4 km	A-DTS cable: (BRUsteel, Brugg Cable AG, Brugg, Switzerland)	Sampling res.: 0.5 m Temporal res.: 30 s
[81]	Spatio-temporal variability of groundwater discharge	Oryx DTS—Sensomet, UK	BruSteel MM cables (from Brug—Switzerland)	Sampling res.: 1 m Temporal res.: 20 min
[15]	Soil water content	Oryx DTS—Sensomet, UK	A-DTS cable: BruSteel (from Brug—Switzerland)	Heating time: 120 s
[14]	Soil water content	SensorTran DTS System	A-DTS cable: BruSteel (from Brug—Switzerland)	Sampling res.: 0.5 m
[68]	Thermal conductivity/Temperature in VZ	Agilent DTS N4385A	A-DTS cable with MM fiber	Thermal measurement interval: 15 min. 64 h heating/58 h cooling
[13]	Soil moisture	DTS (maximum measurement range of 4 km)	A-DTS cable: 50/120 MM fiber	Sampling res.: 1 m Temporal res.: 40 s

calibration [73, 74]. These studies contributed to the validation of this technology and to the take-off of its use in environmental applications.

As discussed above, many researchers have investigated the potential of DTS to measure water content in the soil using A-DTS [14, 75]. The objective was to quantify the thermal response of the soil to a heat pulse over time in the form of a cumulative increase in temperature [14]:

$$T_{cum} = \int_0^{t_0} \Delta T dt \quad (9.5)$$

where T_{cum} is the cumulative temperature increase ($^{\circ}\text{C}$) during the total integration time t_0 (s), and ΔT is the temperature change recorded by DTS compared to the ambient temperature of the materials [pre-pulse temperature ($^{\circ}\text{C}$)].

The cumulative temperature increase (T_{cum}) during a heat pulse is a function of the thermal properties of the soil such as thermal conductivity (W/mK). The soil water content was deduced from T_{cum} using a calibration equation [14]. For a homogeneous soil, a high thermal conductivity can result in a higher water content. To relate the cumulative temperature T_{cum} and the water content, different adjustment curves were used [76]. Benítez-Buelga et al. [77] adjusted a polynomial curve connecting T_{cum} with the soil water content using the results obtained experimentally. The resulting equation is presented in Eq. (9.6):

$$T_{cum} = \frac{1}{a + bSWC + \frac{c}{SWC}} \quad (9.6)$$

where a , b and c are numerical parameters. The R^2 of the fit curve was 0.99. Then the water content of the soil was expressed by the following relation (named SWCpoly) (Eq. 9.7):

$$\text{Soil water content (SWC)} = \frac{\left(\frac{1}{T_{cum}} - a\right) + \sqrt{\left(\frac{1}{T_{cum}} - a\right)^2 - 4bc}}{2b} \quad (9.7)$$

The values of the numerical parameters are $a = 8.4 \times 10^{-5}$, $b = 2.6 \times 10^{-5}$ and $c = 1.6 \times 10^{-5}$.

The resulting temperature variations are related to the water content of the soil [14, 15]. This method has been used in recent years to monitor the groundwater flow and to measure soil water content [13]. Liu et al. [78] have used the A-DTS to detect groundwater flow in boreholes. They showed that the temperature of a heating sensor cable installed in a borehole was sensitive to the horizontal flow of groundwater through the surrounding material. Read et al. [10] also proposed a technique based on A-DTS to follow the vertical speed of fluid in boreholes using a heating sensing cable. Zubezcu et al. [76] have estimated the spatial variation of the water content of

a sandy soil in an agricultural field. The temperature data recorded by the DTS over a length of 133 m were correlated to the water content of the sandy soil using the equations described above (Eqs. 9.6 and 9.7).

All these studies have contributed to the maturation of this technology and the development of DTS systems is in constant evolution. It is now possible to measure variations of temperatures of 0.01 °C with spatial resolutions at the centimetric scale and with high frequencies. Table 9.3 summarizes recent studies made with the use of DTS sensors for environmental monitoring purposes.

b. Distributed acoustic sensing sensors (DAS)

The DAS technology has evolved rapidly in recent years. This new system uses a FO cable to detect acoustic frequency signals over large distances [18, 19, 61, 63, 64, 75]. The use of this technology in boreholes applications provides key information on the characteristics and geometry of fractures by monitoring variations in seismic velocity. James et al. [19] used the DAS system to detect and characterize fractures along the VZ without an active source and at a high temporal and spatial resolution. This study was conducted in a field at the Blue Canyon Dome (New Mexico). Fractures were generated by two stimulations in wells placed at the center of four monitoring wells. The FO cables were installed behind the PVC casing of the boreholes and used to record the ambient noise before and after each stimulation. The results showed a reduction of speed in the near-well area (center of the test area) and suggested the creation of fractures. This hypothesis was confirmed by tomographic images. Mellors et al. [8] conducted an exhaustive review of previous work on the use of DAS sensors in boreholes and in harsh environments. According to its synthesis, the DAS fiber sensors should be effective in boreholes applications and able to withstand high temperatures. The DAS technology has also been used for several years to carry out surface and crosshole seismic measurements. The DAS technology is increasingly used in boreholes as seismic sensors and can replace geophones. As a matter of fact, many experiments carried out at the soil surface and in boreholes have shown that this technique can be used as a good seismic sensor [20, 82–84]. Bakulin et al. [85] used the DAS system as a surface seismic sensor to carry out seismic surveys. The obtained results showed the possibility of using the DAS system as a seismic surface sensor instead of conventional accelerometers or geophones. Harris et al. [86] used the DAS system as part of the Aquistore carbon storage project (Canada) to monitor CO₂ injection into underground reservoirs (between 3.10 and 3.35 m deep). Many Vertical Seismic Profiles (VSP) were carried out with DAS and geophones to monitor the geological structure of reservoirs on the Aquistore site over time. The results obtained showed that DAS systems can provide results comparable to geophones and represents an effective alternative to traditional seismic acquisition methods.

Furthermore, the DAS technique presents many advantages over geophones because it can be carried out on the entire borehole at the same time and over several kilometers, unlike geophones which are generally deployed in short networks [82]. FO cables are easier to install temporarily or permanently in boreholes for the monitoring of the VZ. Additionally, measurements can be carried out simultaneously in

several boreholes by using a single DAS interrogator and a single FO cable. The same application with the use of geophones would require many equipment (network of geophones, recording instruments) and would also be difficult to install. However, despite these advantages, DAS technology is still under development and requires a validation of the interpretations of the measured signals and a characterization of its degree of complementarity with respect to traditional seismic measurements. Indeed, the spatial resolution issues (currently varies between 1 and 10 m) and sensitivity to environmental factors (temperature, pH, Eh, etc.) are not yet precisely determined, in particular in limestone rocks. Table 9.4 summarizes recent studies conducted with the use of DAS system for seismic measurements and fracture detection in the VZ.

c. Distributed Strain Sensing (DSS)

The Distributed Strain Sensing technology has emerged in recent years as a promising solution for monitoring deformations in the subsoil [91]. Displacements or deformations created in subsoil materials are transferred to a sensitive cable (sensor) through a trench or a borehole, causing changes in the light signal to be sent through the cable. By comparing the signals before and after deformation, it is possible to precisely determine the deformation amount of the surrounding materials. DSS systems are available on the market with a high measurement sensitivity of up to $0.5 \mu\epsilon$ [23]. Monitoring deformation by FO sensors has several advantages over conventional methods (conventional electrical strain gauge [92]), which are limited by the sensitivity to electromechanical interference and sensor corrosion.

DSS sensors have been used primarily for monitoring land subsidence and landslides [21, 22]. Liu et al. [25] adopted the DSS system in an in-situ experiment to monitor land subsidence in a borehole located in Tianjin (China). The authors have shown that DSS technology is effective for monitoring land subsidence in coastal areas. CEMENTYS (French company specializing in FO technology) have been using a DSS system (Brillouin-BOTDA (Optical Time Domain Analyzer)) for monitoring a buried pipeline with a length of 300 m in the French Alps since 2013. The area is subject to ground motion and CEMENTYS company is ensuring the pipeline integrity. To study strains on the pipeline body, three *Sensolux TM*[®] FO cables were glued directly on the surface of the pipeline. This 120° straight shape is needed to detect and measure strains in any flexural direction. This layout is also necessary to study its 3-dimensions behavior in time. The installed DSS system allows to follow the displacement and the stress in three dimensions (X, Y and Z) around the pipeline in real time and in the long term as presented in Fig. 9.4.

Recent studies have also used the DSS technology to improve the knowledge about hydrogeological processes occurring along the VZ (Table 9.5). Zhang et al. [93] used the DSS system to monitor micro-deformations associated with digging a new well in a rural area of the city of Mobarra (Chiba, Japan). The FO cable was installed behind the PVC casing and cemented in two observation boreholes located at different distances from the new well (3 and 9 m). Small changes in deformation were observed in both boreholes while drilling the wells. The authors suggest that these changes were related to the hydrodynamic deformations (between fluid and solid) and the permeability variations of VZ materials. The injection of fluids into the VZ during

Table 9.4 An overview of recent applications of the DAS system for environmental monitoring

References	Measurements	DAS instrument	FO cable	Data collecting
[84]	Seismic monitoring Reservoirs imaging	DAS	SM FO cable (length: 977 m)	Gauge length: 10 m Spatial res.: 1 m Duration of acquisitions: 4.5 days Frequency sampling: 1-kHz
[20]	Fracture monitoring in fractured Bedrock	iDAS (Silixa Ltd., UK)	Tight buffered cable 9/125 μ m, SM fiber	Temporal sampling: 1 kHz Spatial sampling: 0.25 m
[64]	Soil/rock thermal properties (boreholes installation)	DAS A1-R (FEBUS, Fr)	SM FO cable: BRUens DAS 6.0 mm non-metallic, from Solifos—Switzerland	Installation/Calibration
[87]	Monitoring of groundwater flow Ambient seismic noise measurements	iDAS (Silixa Ltd., UK)	SM FO cable of 1280 m length	Gauge length: 10 m Spatial res.: 0.25–1.0 m Frequency sampling: 5–50 kHz
[88]	Surface imaging using ambient noise	iDAS (Silixa Ltd., UK)	SM telecommunication fibers	Gauge length: 10 m Spatial res.: 2 m Frequency sampling: 500 Hz Generated data: 8 TB
[19]	Fracture detection and imaging through relative seismic velocity changes using DAS and ambient seismic noise	iDAS (Silixa Ltd., UK)	Tactical SM	Gauge length: 10 m Duration of acquisitions: 13 h Frequency sampling: 30 s
[89]	Seismic monitoring of the near surface	iDAS (Silixa Ltd., UK)	Comparison of 4 cables: (1) a gel-filled polyethylene cable; (2) a tight-buffered, tactical cable; (3) a gel-filled, steel-armored cable; (4) a tight-buffered, steel-tubing cable	Gauge length: 10 m Duration of acquisitions: 3 weeks Spatial res.: 1 m Frequency sampling: 1-kHz Generated data: 2.7 TB
[90]	Seismic monitoring Geophone and DAS comparison VSP data acquisition	DAS	SM FO cable	Gauge length: 10 m Spatial resolution: 1.0 m
[87]	Geophone and DAS system comparison VSP data acquisition	iDAS (Silixa Ltd., UK)	SM FO cable	Gauge length: 10 m Spatial resolution: 2.0 m

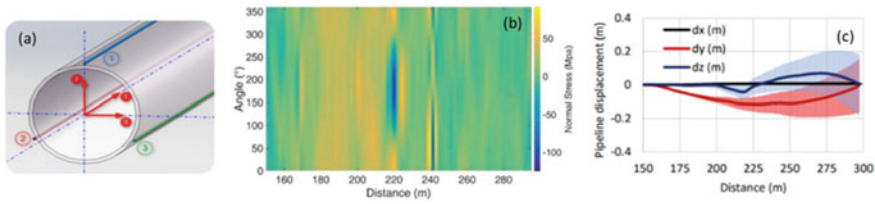


Fig. 9.4 **a** The disposition of FO (sensors) on the surface of the pipeline, **b** the stress and **c** displacement variations in three dimensions (X, Y and Z) observed around the pipeline

drilling causes changes in fluid pressure, and can induce change in the properties of the VZ geological facies (mainly in heterogeneous and permeable materials). A similar study was carried out by Lei et al. [24] in the same city, during a pumping experiment. A vertical well located between two pumping wells was equipped with a DSS cable sensitive to micro-deformation down to a depth of 300 m. The results obtained showed that compressive deformation was observed in the VZ materials after several hours of pumping. The authors also underlined the direct link between the observed deformations and the properties (permeability, heterogeneity) of the VZ materials. The highest deformations were observed in the more permeable and heterogeneous layers (sandy sediments) during the pumping period. In a laboratory study, Zhang et al. [23] observed deformations (dilatation) using a DSS system on a sample of sandstone rock (high clay content and low permeability) during its saturation processes. The authors suggested that this deformation is related to two factors: (i) the change in pore pressure due to the accumulation of water in the pores of the sample; (ii) and the swelling effect of the clay. This works has highlighted that the DSS system not only has the potential to provide geomechanical information on the VZ materials, which can play an important role in preventing landslide hazards and land subsidence, but can also give valuable information on the link between the deformation of materials and the fluids flow in the VZ. This set of findings improve our understanding of the role of fluid flow in rock deformation within the VZ.

9.2.4 Chalcogenide FO Sensors

Fiber Evanescent Wave Spectroscopy (FEWS) simply requires dipping the fiber into a liquid under analysis or putting it in direct contact with the analyte. FEWS using chalcogenide glass fibers is an efficient tool land. The chalcogenide fibers can be specifically shaped for head sensing thanks to the fibers' thermo-forming capability [94]. It also allows investigation in different fields; e.g. the detection of contaminants in waste water [16, 95], the monitoring of chemical or industrial processes [96, 97], the detection of bacterial contamination in food [98, 99], and applications in the medical field [100]. Consequently, these materials can contribute to the development

Table 9.5 Examples of recent applications of the DSS system for environmental monitoring

References	Measurements	DSS instrument	FO cable	Data collecting
[21]	Measurements of distributed deformations related to water pumping in an aquifer in Shengze, southern Yangtze Delta, China	Advantest N8511 BOTDR analyzer (Tokyo, Japan)	Tight-buffed strain cables, 2 mm diameter (Nanzee Sensing, Suzhou, China) FO cable installed in a vertical borehole 150 m deep	Spatial res.: 1 m Noise level of $40 \mu\epsilon$ Duration of acquisitions: from 2014 to 2016
[23]	Measure rock deformation while injecting water into low-permeability dry sandstone. Laboratory study	(NBX-7020; Neubrex Co., Ltd., Kobe, Japan) Maximum measurement range of 20 km	Strain FO cable, the FO cable was wound helically around the rock sample	Measurement accuracy: $0.5 \mu\epsilon$ Spatial res.: 2 cm Material: sandstone sample (from Gunma, Japan)
[24]	Geomechanical monitoring Distributed strain measurements at a pumping test (Mobara, Japan)	Neubrescope NBX-8000 device	A strain FO cable was custom-made for this study FO cable was installed behind the PVC casing in an observation well located between three pumping wells	Spatial res.: 1 cm Temporal res.: 5 min
[25]	Land subsidence monitoring in Tianjin, China	AV6419 optical fiber temperature/strain analyzer produced by the 41st Research Institute of China Electronics Technology Group Corporation, China	FO cable 2 mm diameter produced by Suzhou NanZee Sensing Ltd., China FO cable installed in a vertical borehole 100 m deep	Spatial res.: 1 m Resolution accuracy: 10 cm Strain measurement accuracy is $\pm 50 \mu\epsilon$
[93]	Strain monitoring in two observations wells (where FO cables were installed) while drilling a new well. Mobara city (Chiba, Japan)	NBX-SR7000 (Neubrex Co., Ltd., Japan) Maximum measurement range of 25 km	Stainless-steel wire reinforced cable (strain cable with rectangular shape, 2.0×3.8 mm) FO cable installed behind the PVC casing in tow observations wells 144 m deep	Measurement accuracy: $0.5 \mu\epsilon$ Spatial res.: 5 cm

of pioneering glass technologies in IR spectral windows to design innovative optical sensors [101].

An optical sensor based on mid-IR fluorescence to probe gas molecules has already been developed using a transmission configuration instead of FEWS for the detection of carbon dioxide by means of the 4.3 μm emission of a Dy^{3+} doped chalcogenide fiber [37]. Due to their high degree of mechanical integration and reliability (connectors, fiber coating techniques), optical fiber-based sensors are designed for commercial purposes. Compared to FEWS using undoped chalcogenide fibers as the sensitive media, this sensor has been developed in order to produce its own mid-IR fluorescence source. The resolution of real time detection could be enhanced and the overall compactness and complexity of the optical system can be efficiently reduced. FEWS relies on the optical absorption of the surrounding environment of the optical fiber, with a typical penetration depth of a few micrometers for the evanescent waves. The degree of integration of such devices is potentially high thanks to the rare earth doped chalcogenide fiber converting the pump signal from a visible or near infrared laser diode to mid-IR. By means of frequency conversion, the sensor could allow remote monitoring using silica fibers considering that the inverse photon conversion from mid-IR to visible or near-IR can be used based on a rare earth up-conversion phenomenon [101]. An all-optical IR fiber sensor for in-situ carbon dioxide monitoring was developed by BRGM, University of Caen, University of Rennes and IDIL [38]. This sensor can be typically deployed over the kilometer range with a sensitivity of few hundreds of ppm, making it suitable for field operations. The sensors prototypes were tested in a 100 m deep dry pit at the LSBB facility (Low-Noise Underground Laboratory) in Rustrel, France (Fig. 9.5).

The results led to the development of a carbon dioxide prototype for field experiments comprising a Dy^{3+} : GaGeSbS MWIR emitting fiber and an Er^{3+} : GaGeSbS conversion fiber. Carbon dioxide sensing experiments were performed using this all-optical sensor for various CO_2 concentrations ranging from 0.2% (2000 ppm) to 100% [38].

The All-optical CO_2 detection system present key advantages over electronic devices, especially for high pressure working conditions and electromagnetic compatibilities, since there are no electronic parts within an all-optical CO_2 detection head. The originality of this approach lies in the development of an all-optical method allowing real time in-situ analysis combined with a remote, direct and continuous monitoring in a wide range of concentrations.

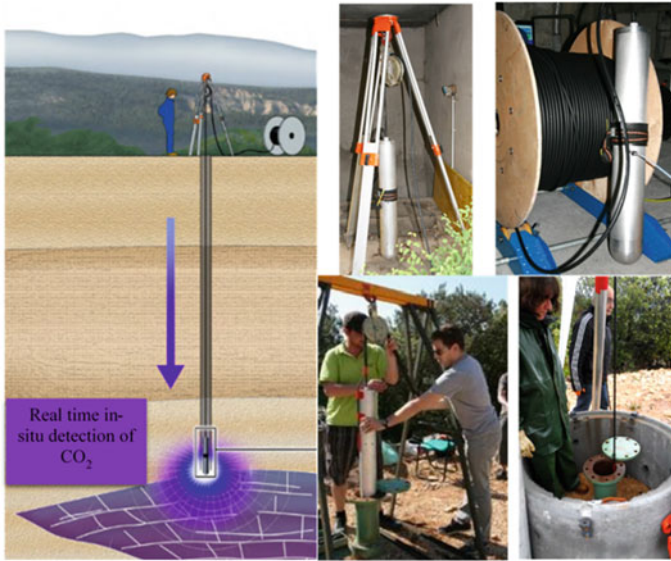


Fig. 9.5 All-optical IR FO sensor deployed in an experimental site located in Rustrel, France (Low-Noise Underground Laboratory (LSBB))

9.3 O-ZNS Project: Main Objectives, First Results and Instrumentation Strategy

9.3.1 *The Beauce Limestone Aquifer*

The Beauce limestone aquifer is located in the Centre-Val de Loire Region (France) and extends over 9700 km² [102] between the Seine river (northeastern part) and the Loire river (southwestern part). This mostly unconfined aquifer constitutes one of the largest groundwater reservoirs in France with an average stock of water of 20 billion m³ [103], and is mainly composed of Cenozoic limestone from upper Oligocene to lower Miocene whose origin is mostly lacustrine [104]. The thickness and the topography of the Beauce limestone aquifer ranges from 10 to 200 m and from 70 m up to 190 m [105]. The Beauce represents the main cereal-producing region in Europe [106] and its land use consists essentially in agriculture (74%), 50% of which is irrigated [107]. Over the past decades, this intensive agricultural activity have led to the implementation of governmental policies and regulatory measures whose actions aim at controlling water withdrawals [108, 109] and preserving groundwater quality, particularly towards pesticides and nitrates contaminations [110, 111].

9.3.2 The Objectives of the O-ZNS Project

The VZ, which is identified as a key component of the Critical Zone (CZ), represents a cornerstone in assessing water balance, understanding groundwater recharge and managing contamination problems for the protection of groundwater resources. To this aim, a growing body of studies focused on deciphering the complex and coupled physical, geochemical, and microbiological processes which govern the mass and heat transfers within the VZ [2, 112].

In this context, the main target of the O-ZNS is to acquire original and unique long-term data on the reactive transfer processes of mass and heat in the VZ. The project aims to follow in-situ and in real time the highly coupled physical, chemical, and biological processes that might influence the water flow and solutes transport in the VZ. The O-ZNS project also aims at assessing the performance of all types of instrumentation dedicated to non-destructive measurements or local sampling of fluids, geological facies, and microbial communities in the VZ.

The O-ZNS experimental site is under development in an agricultural field located in the heart of the Beauce Region, at Villamblain, about 30 km northwest of Orléans (DMS coordinates: $X = 48^{\circ} 1' 5.131''$; $Y = 1^{\circ} 34' 55.333''$) (Fig. 9.6). It consists of the installation of an exceptional access well (diameter ~ 4 m and depth ~ 20 m) surrounded by several boreholes. This allows the instrumentation of the entire VZ column, from the soil surface down to the aquifer (saturated zone fluctuating between -15 and -23 m deep).

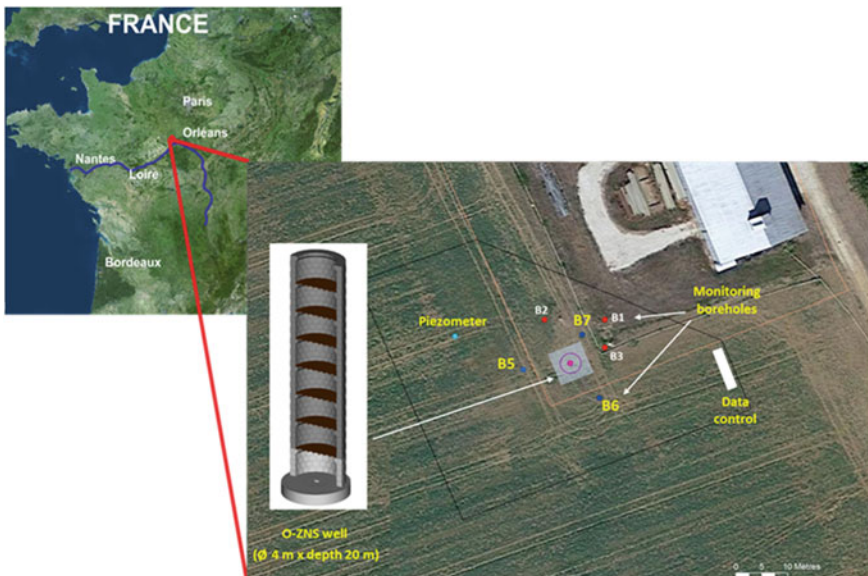


Fig. 9.6 O-ZNS experimental site located in Villamblain (30 km northwest of Orléans, France) at the heart of the Beauce Region

9.3.3 Preliminary Investigations Made Within the Framework of O-ZNS Project

The first geotechnical investigations were made at the O-ZNS experimental site in the spring of 2017. Three cored boreholes (B1, B2, B3, cf. Fig. 9.7) have been drilled on March 2017 from 0 to 20 m deep. The description made by visual examination of undisturbed cores showed that the VZ profile presents both high vertical and lateral lithological heterogeneities [113, 114].

Three main lithological units were identified along the VZ profiles from the soil surface down to 20 m deep (Fig. 9.7):

- 0.0–1.5 m: silt loam soil typical of the Beauce region and referred to as a Hypereutric Cambisol according the World Reference Base for Soils [115],
- 1.5–8.0 m: fragmented powdery limestone facies that was cryoturbated in its upper part and which also contains calcareous sand interbeds,
- 8.0–20 m: massive, fractured or altered/karstified hard limestone rock.

Many authors stressed that the determination of the hydraulic properties, i.e. water retention and hydraulic conductivity, of the VZ materials is critical for a precise assessment of water flow, and mass and heat transfers from the soil surface down to the aquifer [116–120]. The first study conducted within the framework of the O-ZNS project was dedicated to the determination of hydraulic properties of soft and hard representative samples selected along the whole VZ profile and taken from three cored boreholes drilled in spring 2017 (B1, B2, B3 on Fig. 9.6). The hydraulic properties of the samples were determined in the ISTO vadose zone laboratory using the multistep outflow method applied by a triaxial system and related to physical, mineralogical and chemical analysis made on the same samples in order to investigate water flow pathways [113, 114]. The results of this work highlighted the high heterogeneity of the properties of both soft and hard VZ materials and provided valuable information on the influence of the presence or absence of different types of secondary minerals and the impact of alteration processes on water flow within the VZ.

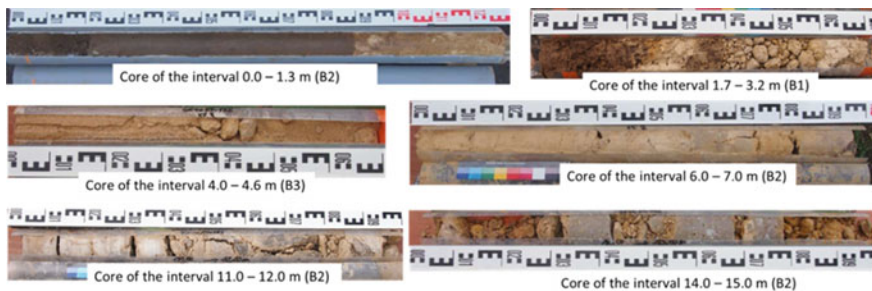


Fig. 9.7 Lithological description of the materials encountered throughout the VZ column of the O-ZNS experimental site

Based on these laboratory hydraulic properties measurements, a second on-going study is focused on the simulation of water flow and the estimation of water travel time through the VZ performed by a virtual tracing experiment simulated over a period of more than 50 years using HYDRUS-1D software [121] and meteorological and water table level data as input. The primary results showed a mean water travel time of 18.7 and 29.0 years for the initial (1 mg/L) and the peak concentration of bromide to reach the maximum water table level (−14.84 m), respectively [114, 122]. The variability in the water travel time within the VZ was mainly induced by two key factors: the meteorological data and the high heterogeneity in the properties of the VZ materials, especially through the weak permeability of the massive limestone rock facies which could lead to the occurrence of perched water tables in the VZ profile.

9.3.4 Instrumentation Strategy of the O-ZNS Project

The O-ZNS project aims to monitoring the mass and heat transfer processes within the VZ of the Beauce aquifer. This broad objective will be addressed thanks to the instrumentation of (i) the vadose zone laboratory based in Orléans (ISTO); (ii) the large VZ access well that will be drilled in 2021; (iii) the surrounding boreholes, including those drilled in 2017 and 2020, three of which are currently instrumented with FO cables (Sect. 9.4). The results obtained through the first multidisciplinary studies made within the framework of the O-ZNS project focused on properties obtained at the laboratory scale and within the matrix component of the VZ of the Beauce limestone aquifer. However, optical imaging made on the boreholes and lithological description made on the core samples [113, 122] showed that natural (macro-) fractures with possible karstification were observed at the field scale and have been episodically subjected to intense leaching of water under or close to fully saturated conditions. The water flow and solute transport observed at the field scale could consequently be significantly faster and influenced by preferential flow paths through interconnected fracture networks, notably after exceptional heavy rainfall [123, 124].

The identification and characterization of these open fractures networks and the understanding of the location of these preferential flow pathways is thus essential. This represents one of the key objectives of the O-ZNS project towards deciphering the complex processes which govern the mass and heat transfers within this highly heterogeneous VZ. To this end, a wide variety of environmental monitoring solutions are actually being explored using coupled geological, hydrogeological and geophysical monitoring techniques for the in-situ monitoring of water flow and solute transport within the whole VZ column and some of the key compartments of the CZ (rhizosphere-soil-VZ-aquifer) (Fig. 9.8). This includes, inter alia, hydrogeological monitoring solutions, some of which are considered innovative [125–132].

A second objective of the O-ZNS project is to support the development of innovative methods and sensors (geophysical imagery, microchips, coupling between

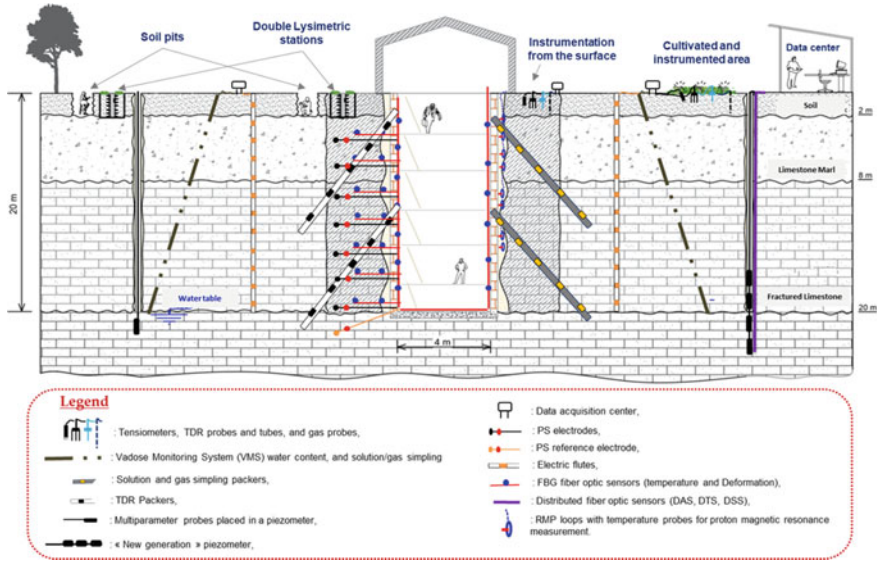


Fig. 9.8 Schematic sketch representing the spatial deployment of the environmental monitoring instrumentations at the O-ZNS observatory site (Villamblain, Orléans, France)

knowledge of “disciplines” and joint interpretations, etc.) for a fine characterization of the dynamics of the VZ. Among these methods is the FO technology, which is increasingly used for environmental monitoring applications.

9.4 Installation of FO Sensors on the O-ZNS Experimental Site

As part of O-ZNS instrumentation, three types of distributed FO sensors (flexible sensing cables cf. Table 9.6) were installed in a continuous loop along three boreholes (with a depth varying from 21 to 23 m) surrounding the future large observatory well and were connected to a data center (Fig. 9.9a). These sensors will allow the monitoring of fluid flow, the characterization of rock fractures, and the micro-movements detection in the VZ of the Beauce limestone aquifer. The FO cables were supplied by the Solifos company (Switzerland) and installed by the CEMENTYS company (France) in July 2020. The disposal of the cables is shown in Fig. 9.9. As these cables are flexible, they were installed in a continuous loop along three boreholes (B5, B6, B7) without splicing. The ends of the cables are located inside the data control. They will soon be connected with the interrogators respectively to each technology.

Table 9.6 summarizes the main characteristics of the three cables used. Considering that the DTS cable consists of four MM fibers (two 50 μm and two 62.5 μm), the DSS and DAS cables are made up of one and four SM fibers, respectively.

Table 9.6 Main characteristics of FO cables installed on the O-ZNS experimental site

Characteristics	DTS cable	DAS cable	DSS cable
Color	Black	Green	Blue
Diameter (mm)	4.0	6.5	2.8
Cable type	Loose	Loose	Tight
FO	2 MM-FO (62.5/125)	4 SM-FO	1 SM-FO
Sensitivity	Temperature	Acoustic noise/Temperature	Strain/Deformation
Interrogation system	Raman	Rayleigh	Brillouin, FBG
Other information	Non-metallic cable, compact design, flexibility	Non-metallic cable, good acoustic response, high tensile strength, high chemical resistance	Non-metallic cable, protective and stress transfer layer, strain range up to 1% (10,000 μ strain)

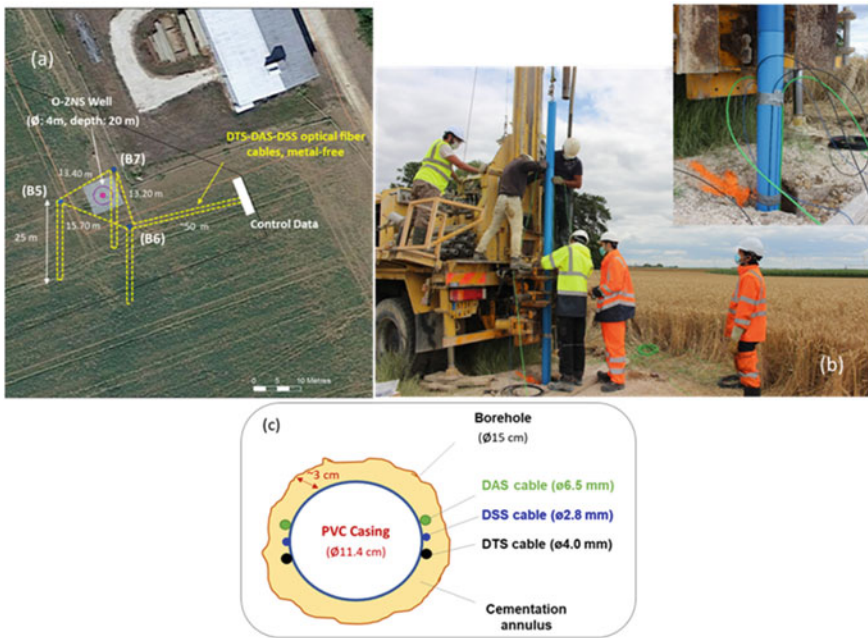


Fig. 9.9 **a** Aerial photography of the O-ZNS experimental site showing the position of the main well and the three surrounding monitoring boreholes (B5, B6, B7). The FO cables were installed in loops covering the three boreholes (drawn in yellow). **b** The installation of FO cables (DTS: black, DAS: green, DSS: blue) in the three boreholes made with CEMENTYIS in July 2020. **c** Axial cross section of the borehole showing the area behind casing installation of FO cables

These cables were chosen based on their flexibilities, their resistances in a harsh environment and their compositions. To avoid any disruption of future geophysical measurements on the O-ZNS site, the cables were installed in the boreholes without metal reinforcements or protections. Illustrations of the installation are shown in Fig. 9.9. The cables were installed behind the PVC casing and sealing with a mixture of 60% of sand (0/4 mm), 40% of limestone filler and 20% of water to ensure a good coupling between the FO cables and the materials of the VZ. The use of cement was indeed excluded because of the geochemical perturbations (pH) induced by the reaction between cement and the limestone rocks of the VZ.

After their installation in the boreholes, all fibers were checked with an OTDR (Optical Time Domain Reflectometer). The purpose of the OTDR measurements was to verify that the fibers have not been damaged during the installation operations along the boreholes. It is a method which makes it possible to characterize the FO from only one of its ends, and leads to the precise localization of the faults, to the measurement of the attenuation of the fiber and to the differential losses between two chosen points of the fiber. Thanks to the OTDR measurements we have confirmed that the FO installed on the O-ZNS site are intact and present no faults over its entire linear.

The multi FO sensors system installed at the O-ZNS site will help in the fine characterization of the subsoil structure in the near O-ZNS well zone through the three boreholes B5, B6 and B7. The DTS system will provide continuous and real-time temperature profile information at resolutions up to 0.01 °C with a spatial resolution down to centimeter scale. This information will be very useful for the identification of active fractures in the VZ of the O-ZNS site under ambient flow conditions or following a rapid heating episode (using heat as a tracer for fracture detection [9, 80]). The DTS will also be used to monitor heat movements throughout the depth of the VZ to estimate the flow rates of fluids in boreholes [68, 70]. Monitoring of the natural fluid flow system in the VZ is important for accurate predictions of the fate and transfer of contaminants. The DSS systems will be used for the monitoring of consolidation and geomechanical deformations of VZ materials with a high sensitivity. Recent studies have shown that it can also be used to understand the deformations (or micro-deformations) associated with the fluids flow in the VZ through hydromechanical coupling [23]. In our case, the DSS system will be very useful for the detection of micro-movements linked to the digging of the O-ZNS well, to fluid infiltration and to measure the deformations in the capillary fringe area linked to the recharge/discharge of the aquifer. DAS technology also shows promise for the detection and monitoring of cracks and fractures throughout the VZ [19]. The use of this technology for the O-ZNS project will provide key information on the characteristics and geometry of fractures by monitoring changes in seismic velocity. However, this technology is, to date, at an early stage of maturity and it is necessary to characterize their degree of complementarity/coupling with traditional seismic measurements. Comparative seismic measurements (DAS and conventional seismic methods) on the surface and in boreholes are planned in the O-ZNS site to assess the potential of this technology in environmental monitoring. Detailed research is also needed to study the sensitivity of DAS measurements to variations in environmental factors (temperature, pH, Eh,

micro-movements, etc.). The information which will be re-purified (or confirmed) by this multi-sensors FO device will constitute an interoperable database which can improve the understanding of coupled and complex processes governing water flow and solute (including contaminants) and heat transfers in the VZ of the Beauce limestone aquifer.

9.5 Conclusion

This chapter provides a comprehensive overview of fiber optic sensors (distributed and point sensors) and contains numerous results and references from recent scientific publications and industrial technical papers on the principles, types and recent environmental monitoring applications of FO sensors. The deployment of distributed fiber optic sensors at the O-ZNS site was also presented. Thanks to their intrinsic characteristics and flexibility, fiber optic sensors are increasingly used in environmental monitoring applications, especially for monitoring the vadose zone. They are insensitive to electromagnetic fields and can provide information in real time and continuously over several kilometers (in the case of distributed sensors). However, there are still some limitations that prevent the generalization of this technology in monitoring designs. The high cost of interrogators remains the major constraint hindering the adoption of fiber optic systems in environmental monitoring applications. Many technological innovations have been made in recent years to improve the performance of interrogator systems and increase their value for money. Further improvements are still needed to further reduce costs and make them more affordable. For a successful installation, good coupling between the sensors and the materials (or the structure to be monitored) is also essential. The installation of the sensors and the cementing operations must be carried out with sufficient care to ensure good sensor-material contact and to avoid the development of a vacuum which disturbs the measurements. Improvements in spatial resolution and measurement range are also required to make it a promising method in environmental applications. Additional in-situ studies, including comparisons with results obtained with traditional sensors, are also essential to validate the prototypes under development for monitoring physicochemical parameters (pH, Eh, salinity, metal ions, etc.) and gases concentrations. The multi-FO sensor system (DTS, DSS and DAS) which were successfully installed at the O-ZNS site will help characterize the temperature, deformations and micro-movements near the O-ZNS main well and will improve our understanding of mass and heat transfers within the highly heterogeneous VZ of the Beauce aquifer.

Acknowledgements This research work was conducted within the framework of the O-ZNS project which is part of PIVOTS project. We gratefully acknowledge the financial support provided by the Région Centre-Val de Loire (ARD 2020 program and CPER 2015–2020) and the French Ministry of Higher Education and Research (CPER 2015–2020 and public service to BRGM). This operation is also co-funded by European Union with the European Regional Development Fund. This research work is co-funded by the Labex VOLTAIRE (ANR-10-LABX-100-01).

Authors are also thankful for the help of Dominique Goncalves, Nicolas Bensaou, Quentin Pochez, and Emile Klotz (CEMENTYS engineers), Farid Laachir (ISTO), Clara Jodry (EOST), Anthony Bonjour (ATTIS Environment), Luigi Ardito and Olivier Serrano (BRGM) during the drilling of the boreholes and the installation of the fiber optic sensors.

References

1. Nimmo JR (2005) Unsaturated zone flow processes. In: Anderson MG, Bear J (eds) *Encyclopedia of hydrological sciences*. Wiley, Chichester, pp 2299–2322
2. Arora B, Dwivedi D, Faybishenko B, Jana RB, Wainwright HM (2019) Understanding and predicting vadose zone processes. *Rev Mineral Geochem* 85(1):303–328
3. Stephens DB (2018) *Vadose zone hydrology*. CRC Press
4. Philippe É, Habets F, Ledoux E, Goblet P, Viennot P, Mary B (2011) Improvement of the solute transfer in a conceptual unsaturated zone scheme: a case study of the Seine River basin. *Hydrol Process* 25(5):752–765
5. Grattan KT, Meggitt BT (eds) (1995) *Optical fiber sensor technology*, vol 1. Chapman & Hall, London
6. Or D, Tuller M, Stothoff S (2006) Review of vadose zone measurement and monitoring tools for Yucca Mountain performance confirmation program. US Nuclear Regulatory Commission report under contract NRC-02-02-012
7. Jin G, Roy B (2017) Hydraulic-fracture geometry characterization using low-frequency DAS signal. *Lead Edge* 36(12):975–980. <https://doi.org/10.1190/tle36120975.1>
8. Mellors RJ, Messerly M, Morris J, Ryerson R, Sherman C, Yu C, Allen G (2018) Modeling potential EGS signals from a distributed fiber optic sensor deployed in a borehole (No. LLNL-PROC-745469). Lawrence Livermore National Lab. (LLNL), Livermore, CA, United States
9. Read T, Bour O, Bense V, Le Borgne T, Goderniaux P, Klepikova MV et al (2013) Characterizing groundwater flow and heat transport in fractured rock using fiber-optic distributed temperature sensing. *Geophys Res Lett* 40(10):2055–2059
10. Read T, Bour O, Selker JS, Bense VF, Le Borgne T, Hochreutener R, Lavenant N (2014) Active-distributed temperature sensing to continuously quantify vertical flow in boreholes. *Water Resour Res* 50(5):3706–3713
11. Gambolati G, Teatini P (2015) Geomechanics of subsurface water withdrawal and injection. *Water Resour Res* 51:3922–3955
12. Huang AB, Wang CC, Lee JT, Ho YT (2016) Applications of FBG-based sensors to ground stability monitoring. *J Rock Mech Geotech Eng* 2016(8):513–520
13. Weiss JD (2003) U.S. patent no. 6,581,445. U.S. Patent and Trademark, Washington, DC
14. Sayde C, Gregory C, Gil-Rodriguez M, Tuffillaro N, Tyler S, van de Giesen N, English M, Cuenca R, Selker JS (2010) Feasibility of soil moisture monitoring with heated fiber optics. *Water Resour Res* 46:W06201. <https://doi.org/10.1029/2009WR007846>
15. Ciocca F, Lunati I, Van de Giesen N, Parlange MB (2012) Heated optical fiber for distributed soil-moisture measurements: a lysimeter experiment. *Vadose Zone J*
16. Michel K, Bureau B, Boussard-Plédel C, Jouan T, Adam JL, Staubmann K, Baumann T (2004) Monitoring of pollutant in waste water by infrared spectroscopy using chalcogenide glass optical fibers. *Sens Actuators B Chem* 101(1–2):252–259. <https://doi.org/10.1016/j.snb.2004.03.014>
17. Michel K, Bureau B, Boussard-Plédel C, Adam J-L (2015) Réalisation d'un capteur à fibre optique infrarouge pour la détection des polluants dans les eaux usées. *Déchets sciences et techniques [En ligne]*, N°34, mis à jour le: 04/03/2015. <http://odel.irevues.inist.fr/dechets-sciences-techniques/index.php?id=2102>. <https://doi.org/10.4267/dechets-sciences-techniques.2012>

18. Parker T, Shatalin S, Farhadiroushan M (2014) Distributed acoustic sensing—a new tool for seismic applications. *First Break* 32(2):61–69. <https://doi.org/10.3997/1365-2397.2013034>
19. James SR, Knox HA, Preston L, Knox JM, Grubelich MC, King DK et al (2017) Fracture detection and imaging through relative seismic velocity changes using distributed acoustic sensing and ambient seismic noise. *Lead Edge* 36(12):1009–1017
20. Becker MW, Coleman TI, Ciervo CC (2020) Distributed acoustic sensing (DAS) as a distributed hydraulic sensor in fractured bedrock. *Water Resour Res.* e2020WR028140
21. Zhang C, Shi B, Gu K, Liu S, Wu J, Zhang S, Zhang L, Jiang H, Wei G (2018) Vertically distributed sensing of deformation using fiber optic sensing. *Geophys Res Lett* 45(21):11–732
22. Murdoch LC, Germanovich LN, DeWolf SJ, Moysey SMJ, Hanna AC, Kim S, Duncan RG (2020) Feasibility of using in situ deformation to monitor CO₂ storage. *Int J Greenhouse Gas Control* 93:102853. <https://doi.org/10.1016/j.ijggc.2019.102853>
23. Zhang Y, Xue Z (2019) Deformation-based monitoring of water migration in rocks using distributed fiber optic strain sensing: a laboratory study. *Water Resour Res* 55(11):8368–8383
24. Lei X, Xue Z, Hashimoto T (2019) Fiber optic sensing for geomechanical monitoring: (2)-distributed strain measurements at a pumping test and geomechanical modeling of deformation of reservoir rocks. *Appl Sci* 9(3):417
25. Liu SP, Shi B, Gu K, Zhang CC, Yang JL, Zhang S, Yang P (2020) Land subsidence monitoring in sinking coastal areas using distributed fiber optic sensing: a case study. *Nat Hazards* 103(3):3043–3061
26. Lu P, Lalam N, Badar M, Liu B, Chorpeneing BT, Buric MP, Ohodnicki PR (2019) Distributed optical fiber sensing: review and perspective. *Appl Phys Rev* 6(4):041302
27. Zhicheng Z, Liu K, Han X, Lin J (2019) Review of fiber-optic distributed acoustic sensing technology. *Instrumentation* 6(4)
28. Wen H, Peng Z, Jian J, Wang M, Liu H, Mao ZH et al (2018) Artificial intelligent pattern recognition for optical fiber distributed acoustic sensing systems based on phase-OTDR. In: 2018 Asia communications and photonics conference (ACP). IEEE, pp 1–4
29. Wang X, Lee J, Thigpen B, Vachon GP, Poland SH, Norton D (2008) Modeling flow profile using distributed temperature sensor (DTS) system. In: Intelligent energy conference and exhibition. Society of Petroleum Engineers
30. Sherman C, Mellors R, Morris J, Ryerson F (2019) Geomechanical modeling of distributed fiber-optic sensor measurements. *Interpretation* 7(1):SA21–SA27
31. Janting J, Pedersen JK, Woyessa G, Nielsen K, Bang O (2019) Small and robust all-polymer fiber Bragg grating based pH sensor. *J Lightwave Technol* 37(18):4480–4486
32. Kishore PVN, Madhavarasu SS, Putha K, Moru S, Gobi KV (2016) Hydrogel coated fiber Bragg grating based chromium sensor. In: Optical sensing and detection IV, vol 9899. International Society for Optics and Photonics, p 98991B
33. Guzman-Sepulveda JR, Ruiz-Perez VI, Torres-Cisneros M, Sanchez-Mondragon JJ, May-Arrijoja DA (2013) Fiber optic sensor for high-sensitivity salinity measurement. *IEEE Photonics Technol Lett* 25(23):2323–2326
34. Yeo TL, Sun T, Grattan KT, Parry D, Lade R, Powell BD (2005) Polymer-coated fiber Bragg grating for relative humidity sensing. *IEEE Sens J* 5(5):1082–1089
35. Elsherif M, Moreddu R, Hassan MU, Yetisen AK, Butt H (2019) Real-time optical fiber sensors based on light diffusing microlens arrays. *Lab Chip* 19(12):2060–2070
36. Delepine-Lesoille S, Bertrand J, Lablonde L, Phéron X (2012) Distributed hydrogen sensing with Brillouin scattering in optical fibers. *Photonics Technol Lett* 24(17)
37. Starecki F, Charpentier F, Doualan JL, Quétel L, Michel K, Chahal R et al (2015) Mid-IR optical sensor for CO₂ detection based on fluorescence absorbance of Dy³⁺: Ga₅Ge₂₀Sb₁₀S₆₅ fibers. *Sens Actuators B Chem* 207:518–525
38. Starecki F, Braud A, Doualan J-L, Ari J, Boussard-Plédel C, Michel K, Nazabal V, Camy P (2019) All-optical carbon dioxide remote sensing using rare earth doped chalcogenide fibers. *Opt Lasers Eng* 122:328–334. <https://doi.org/10.1016/j.optlaseng.2019.06.018>
39. Barrias A, Casas JR, Villalba S (2016) A review of distributed optical fiber sensors for civil engineering applications. *Sensors* 16(5):748

40. Hartog A (2017) An introduction to distributed optical fibre sensors. CRC Press, 442pp
41. Schenato L (2017) A review of distributed fiber optic sensors for geo-hydrological applications. *Appl Sci* 7(9):896. <https://doi.org/10.3390/app7090896>
42. Di Sante R (2015) Fibre optic sensors for structural health monitoring of aircraft composite structures. *Recent advances and applications. Sensors* 15(8):18666–8713
43. Annamdas KKK, Annamdas VGM (2010) Review on developments in fiber optical sensors and applications. In: *Fiber optic sensors and applications VII*, vol 7677. International Society for Optics and Photonics, p 76770R
44. Mihailov SJ (2012) Fiber Bragg grating sensors for harsh environments. *Sensors* 12(2):1898–1918
45. Miah K, Potter DK (2017) A review of hybrid fiber-optic distributed simultaneous vibration and temperature sensing technology and its geophysical applications. *Sensors* 17(11):2511
46. Bao Y, Huang Y, Hoehler MS, Chen G (2019) Review of fiber optic sensors for structural fire engineering. *Sensors* 19(4):877
47. Ferraro P, de Natale G (2002) On the possible use of optical fiber Bragg gratings as strain sensors for geodynamical monitoring. *Opt Laser Eng* 37:115–130
48. Lecoy P (2016) Les fibres optiques en capteurs et en instrumentation. *La Revue 3 E. I* 85
49. Hill K, Meltz G (1997) Fiber Bragg grating technology fundamentals and overview. *J Lightwave Technol* 15(8):1263–1276
50. Kashyap R (2009) *Fiber Bragg gratings*. Academic Press, Cambridge
51. Drusová S, Wagterveld RM, Wexler AD, Offerhaus HL (2019) Dynamic consolidation measurements in a well field using fiber Bragg grating sensors. *Sensors* 19(20):4403
52. Alemohammad H, Azhari A, Liang R (2017) Fiber optic sensors for distributed monitoring of soil and groundwater during in-situ thermal remediation. In: *Fiber optic sensors and applications XIV*, vol 10208. International Society for Optics and Photonics, p 102080I
53. Wang J, Jiang L, Sun Z, Hu B, Zhang F, Song G, et al (2017) Research on the surface subsidence monitoring technology based on fiber Bragg grating sensing. *Photonic Sens* 7(1):20–26
54. Cong J, Zhang X, Chen K, Xu J (2002) Fiber optic Bragg grating sensor based on hydrogels for measuring salinity. *Sens Actuators B Chem* 87(3):487–490
55. Aleixandrea M, Corredera P, Hernandez ML, Sayago I, Horrillo MC, Gutierrez-Monreal J (2007) Study of a palladium coated Bragg grating sensor to detect and measure low hydrogen concentrations. In: *Proceedings of the 2007 Spanish conference on electron devices*, 31 Jan–2 Feb 2007, Madrid, Spain, pp 223–225
56. Selker JS et al (2006) Distributed fiber-optic temperature sensing for hydrologic systems. *Water Resour Res* 42
57. Tyler SW, Selker JS, Hausner MB (2009) Environmental temperature sensing using Raman spectra DTS fiber-optic methods. *Water Resour Res* 45(4)
58. Baldwin CS (2014) Brief history of fiber optic sensing in the oil field industry. In: *Fiber optic sensors and applications XI*, vol 9098. International Society for Optics and Photonics, p 909803
59. Koudelka P, Petrujova B, Latal J, Hanacek F, Siska P, Skapa J, Vasinek V (2010) Optical fiber distributed sensing system applied in cement concrete commixture research. *Radio Eng* 19(1):172–177
60. Brown G (2008) Downhole temperatures from optical fiber. *Oilfield Rev* 20(4):34–39
61. Molenaar MM, Hill D, Webster P, Fidan E, Birch B (2012) First downhole application of distributed acoustic sensing for hydraulic-fracturing monitoring and diagnostics. *SPE Drill Completion* 27(01):32–38. <https://doi.org/10.2118/140561-PA>
62. Daley TM, Freifeld BM, Ajo-Franklin J, Dou S, Pevzner R, Shulakova V, Kashikar S, Miller DE, Goetz J, Hennings J, Lueth S (2013) Field testing of fiber-optic distributed acoustic sensing (DAS) for subsurface seismic monitoring. *Lead Edge* 32(6):699–706. <https://doi.org/10.1190/le32060699.1>
63. Kasahara J, Hasada Y, Kuzume H, Fujise Y, Yamaguchi T (2019) Seismic feasibility study to identify supercritical geothermal reservoirs in a geothermal borehole using DTS and DAS. In: *81st EAGE conference and exhibition 2019*, vol 2019, no 1. European Association of Geoscientists & Engineers, pp 1–5

64. Ringstad C, Røed MH, Jestin C, Calbris G, Eliasson P, Jordan M, Wüstefeld A (2020) A multi-fibre optic sensing system for cross-well monitoring at the Svelvik CO₂ field lab. In: First EAGE workshop on fibre optic sensing, vol 2020, no 1. European Association of Geoscientists & Engineers, pp 1–5
65. Selker J, Van de Giesen N, Westhoff M, Luxemburg W, Parlange MB (2006) Fiber optics opens window on stream dynamics. *Geophys Res Lett* 33(24):24401. <https://doi.org/10.1029/2006GL027979>
66. Westhoff MC, Savenije HHG, Luxemburg WJ, Stelling GS, Van de Giesen NC, Selker JS et al (2007) A distributed stream temperature model using high resolution temperature observations. *Hydrol Earth Syst Sci* 11(4):1469–1480
67. Keller CA, Huwald H, Vollmer MK, Wenger A, Hill M, Parlange MB, Reimann S (2011) Fiber optic distributed temperature sensing for the determination of the nocturnal atmospheric boundary layer height. *Atmos Meas Tech* 143–149
68. Freifeld BM, Finsterle S, Onstott TC, Toole P, Pratt LM (2008) Ground surface temperature reconstructions: using in-situ estimates for thermal conductivity acquired with a fiber-optic distributed thermal perturbation sensor. *Geophys Res Lett* 35:L14309. <https://doi.org/10.1029/2008GL034762>
69. Siska P, Latal J, Bujok P, Vanderka A, Klempa M, Koudelka P et al (2016) Optical fiber based distributed temperature systems deployment for measurement of boreholes temperature profiles in the rock massif. *Opt Quant Electron* 48(2):108
70. Hurltig E, Großwig S, Jobmann M, Kühn K, Marschall P (1994) Fibre-optic temperature measurements in shallow boreholes: experimental application for fluid logging. *Geothermics* 23(4):355–364
71. Majorowicz JA, Smith SL (1999) Review of the ground temperatures in the Mallik field area: a constraint to the methane hydrate stability. *Bull Geol Surv Can* 544:45–56. ISSN 0068-7626
72. Roshan H, Young M, Andersen M, Acworth R (2014) Limitations of fibre optic distributed temperature sensing for quantifying surface water groundwater interactions. *Hydrol Earth Syst Sci Discuss* 11(7):8167–8190. <https://doi.org/10.5194/hessd-118167-2014>
73. Hausner MB, Suárez F, Glander KE, Giesen NVD, Selker JS, Tyler SW (2011) Calibrating single-ended fiber-optic Raman spectra distributed temperature sensing data. *Sensors* 11(11):10859–10879. <https://doi.org/10.3390/s111110859>
74. Van De Giesen N, Steele-Dunne SC, Jansen J, Hoes O, Hausner MB, Tyler S, Selker J (2012) Double-ended calibration of fiber-optic Raman spectra distributed temperature sensing data. *Sensors* 12(5):5471–5485. <https://doi.org/10.3390/s120505471>
75. Gamage DNV, Biswas A, Strachan IB, Adamchuk VI (2018) Soil water measurement using actively heated fiber optics at field scale. *Sensors* 18:1116. <https://doi.org/10.3390/s18041116>
76. Zubelzu S, Rodríguez-Sinobas L, Saa-Requejo A, Benitez J, Tarquis AM (2019) Assessing soil water content variability through active heat distributed fiber optic temperature sensing. *Agric Water Manag* 212:193–202
77. Benítez-Buelga J, Rodríguez-Sinobas L, Sánchez Calvo R, Gil-Rodríguez M, Sayde C, Selker JS (2016) Calibration of soil moisture sensing with subsurface heated fiber optics using numerical simulation. *Water Resour Res* 52(4):2985–2995
78. Liu G, Knobbe S, Butler J (2013) Resolving centimeter-scale flows in aquifers and their hydrostratigraphic controls. *Geophys Res Lett* 40:1098–1103. <https://doi.org/10.1002/grl.50282>
79. Folch A, del Val L, Luquot L, Martínez-Pérez L, Bellmunt F, Le Lay H et al (2020) Combining fiber optic DTS, cross-hole ERT and time-lapse induction logging to characterize and monitor a coastal aquifer. *J Hydrol* 588:125050
80. Maldaner CH, Munn JD, Coleman TI, Molson JW, Parker BL (2019) Groundwater flow quantification in fractured rock boreholes using active distributed temperature sensing under natural gradient conditions. *Water Resour Res* 55(4):3285–3306
81. Sebok CH, Munn JD, Coleman TI, Molson JW, Parker BL (2019) Groundwater flow quantification in fractured rock boreholes using active distributed temperature sensing under natural gradient conditions. *Water Resour Res* 55(4):3285–3306

82. Mateeva A, Lopez J, Potters H, Andrey J, Cox B, Kiyashchenko D et al (2014) Distributed acoustic sensing for reservoir monitoring with vertical seismic profiling. *Geophys Prospect* 62(VERTICAL seismic profiling and microseismicity frontiers):679–692
83. Dean T, Cuny T, Hartog A (2017) The effect of gauge length on axially incident P-waves measured using fibre optic distributed vibration sensing. *Geophys Prospect* 65:184–193
84. Kasahara J, Hasada Y, Kuzume H, Fujise Y, Mikada H, Yamamoto K (2020) Seismic feasibility study to identify and characterize supercritical geothermal reservoirs using DTS, DAS, and surface seismic array. In: *Proceedings World geothermal congress*
85. Bakulin A, Hemyari E, Silvestrov I (2019) Acquisition trial of DrillCAM: real-time seismic with wireless geophones, instrumented top drive and near-bit accelerometer. In: *SEG Technical program expanded abstracts 2019*. Society of Exploration Geophysicists, pp 157–161
86. Harris K, White D, Melanson D, Samson C, Daley TM (2016) Feasibility of time-lapse VSP monitoring at the Aquistore CO₂ storage site using a distributed acoustic sensing system. *Int J Greenhouse Gas Control* 50:248–260
87. Kruiver P, Obando-Hernández E, Pefkos M, Karaoulis M, Bakx W, Doornenbal P et al (2020) Fibre optic monitoring of groundwater flow in a drinking water extraction well field. In: *First EAGE workshop on fibre optic sensing*, vol 2020, no 1. European Association of Geoscientists & Engineers, pp 1–5
88. Ajo-Franklin JB, Dou S, Lindsey NJ, Monga I, Tracy C, Robertson M et al (2019) Distributed acoustic sensing using dark fiber for near-surface characterization and broadband seismic event detection. *Sci Rep* 9(1):1–14
89. Dou S, Lindsey N, Wagner AM, Daley TM, Freifeld B, Robertson M, Peterson J, Ulrich C, Martin ER, Ajo-Franklin JB (2017) Distributed acoustic sensing for seismic monitoring of the near surface: a traffic-noise interferometry case study. *Sci Rep* 7(1):1–12
90. Willis ME, Barfoot D, Ellmauthaler A, Wu X, Barrios O, Erdemir C et al (2016) Quantitative quality of distributed acoustic sensing vertical seismic profile data. *Lead Edge* 35(7):605–609
91. Shi B, Zhang D, Zhu H-H (2019) *Distributed fiber optic sensing for geoengineering monitoring*, 1st edn. Science Press, Beijing (in Chinese)
92. Murdoch LC, Freeman CE, Germanovich LN, Thrash C, DeWolf S (2015) Using in situ vertical displacements to characterize changes in moisture load. *Water Resour Res* 51(8):5998–6016
93. Zhang Y, Lei X, Hashimoto T, Xue Z (2020) In situ hydromechanical responses during well drilling recorded by fiber-optic distributed strain sensing. *Solid Earth* 11(6):2487–2497
94. Houizot P, Anne ML, Boussard-Pledel C, Loreal O, Tariel H, Lucas J (2014) Shaping of looped miniaturized chalcogenide fiber sensing heads for mid-infrared sensing. *Sensors* 14:17905–17914
95. Sanghera JS, Kung FH, Busse LE, Pureza PC, Aggarwal ID (1995) Infrared evanescent absorption-spectroscopy of toxic-chemicals using chalcogenide class fibers. *J Am Ceram Soc* 78:2198–2202
96. Le Coq D, Michel K, Keirsse J, Boussard-Pledel C, Fonteneau G, Bureau B (2002) Infrared glass fibers for in-situ sensing, chemical and biochemical reactions. *C R Chim* 5:907–913
97. Anne ML, La Salle ELG, Bureau B, Tristant J, Brochot F, Boussard-Pledel C (2009) Polymerisation of an industrial resin monitored by infrared fiber evanescent wave spectroscopy. *Sens Actuators B Chem* 137:687–691
98. Brandily ML, Monbet V, Bureau B, Boussard-Pledel C, Loreal O, Adam JL (2011) Identification of foodborne pathogens within food matrices by IR spectroscopy. *Sens Actuators B Chem* 160:202–206
99. Jiang X, Jha A (2015) Engineering of a Ge-Te-Se glass fibre evanescent wave spectroscopic (FEWS) mid-IR chemical sensor for the analysis of food and pharmaceutical products. *Sens Actuators B Chem* 206:159–169
100. Anne ML, Le Lan C, Monbet V, Boussard-Pledel C, Ropert M, Sire O (2009) Fiber evanescent wave spectroscopy using the mid-infrared provides useful fingerprints for metabolic profiling in humans. *J Biomed Opt* 14

101. Chahal R, Starecki F, Boussard-Plédel C, Doualan JL, Michel K, Brilland L et al (2016) Fiber evanescent wave spectroscopy based on IR fluorescent chalcogenide fibers. *Sens Actuators B Chem* 229:209–216. <https://doi.org/10.1016/j.snb.2016.01.091>
102. de Frutos Cachorro J, Erdlenbruch K, Tidball M (2017) A dynamic model of irrigation and land-use choice: application to the Beauce aquifer in France. *Eur Rev Agric Econ* 44(1):99–120. <https://doi.org/10.1093/erae/jbw005>
103. Le Coz D (2000) Gestion durable d'une ressource en eaux souterraines Cas de la nappe de Beauce. *La Houille Blanche* 7–8:116–121. <https://doi.org/10.1051/lhb/2000085>
104. Ménillet F, Edwards N (200) The Oligocene–Miocene Calcaires de Beauce (Beauce limestones), Paris Basin, France. <https://doi.org/10.1306/St46706C38>
105. Flipo N, Monteil C, Poulin M, de Fouquet C, Krimissa M (2012) Hybrid fitting of a hydrosystem model: long-term insight into the Beauce aquifer functioning (France). *Water Resour Res* 48(5):W05509. <https://doi.org/10.1029/2011WR011092>
106. Graveline N (2020) Combining flexible regulatory and economic instruments for agriculture water demand control under climate change in Beauce. *Water Resour Econ* 29:100143. <https://doi.org/10.1016/j.wre.2019.100143>
107. Lejars C, Fusillier JL, Bouarfa S, Coutant C, Brunel L (2012) Limitation of agricultural groundwater uses in Beauce (France): what are the impacts on farms and on the food-processing sector? *Irrig Drain* 61:54–64. <https://doi.org/10.1002/ird.1659>
108. Légifrance (1992) LOI n° 92-3 du 3 janvier 1992 sur l'eau (1)
109. European Commission (2000) Directive 2000/60/EC of the European Parliament and of the council of 23 October 2000 establishing a framework for community action in the field of water policy
110. European Commission (1991) Council directive of 12 December 1991 concerning the protection of waters against pollution caused by nitrates from agricultural sources (91/676/EEC)
111. European Commission (2009) Directive 2009/128/EC of the European Parliament and of the council of 21 October 2009 establishing a framework for community action to achieve the sustainable use of pesticides
112. Vereecken H, Schepf A, Hopmans JW, Javaux M, Or D (2016) Modeling Soil processes: review, key challenges, and new perspectives. *Vadose Zone J* 15(5). <https://doi.org/10.2136/vzj2015.09.0131>
113. Aldana C, Isch A, Bruand A, Azaroual M, Coquet Y (2021) Relationship between hydraulic properties and material features in a heterogeneous vadose zone of a vulnerable limestone aquifer. *Vadose Zone J* 20(4):e20127. <https://doi.org/10.1002/vzj2.20127>
114. Isch A, Aldana C, Coquet Y, Azaroual M (2020) Material characteristics, hydraulic properties, and water travel time through the heterogeneous vadose zone of a Cenozoic limestone aquifer (Beauce, France). *EGU* 2020. <https://doi.org/10.5194/egusphere-egu2020-5862>
115. IUSS Working Group WRB (2015) World reference base for soil resources 2014, update 2015. In: International soil classification system for naming soils and creating legends for soil maps. *World Soil Resources Reports No. 106*. FAO, Rome
116. Vereecken H, Huisman JA, Bogaen H, Vanderborght J, Vrugt JA (2008) On the value of soil moisture measurements in vadose zone hydrology: a review. *Water Resour Res* 44(4):W00D06. <https://doi.org/10.1029/2008WR006829>
117. Whalley WR, Ober ES, Jenkins M (2013) Measurement of the matric potential of soil water in the rhizosphere. *J Exp Bot* 64(13):3951–3963. <https://doi.org/10.1093/jxb/ert044>
118. Lekshmi SUS, Singh DN, Baghini MS (2014) A critical review of soil moisture measurement. *Measurement* 54:92–105. <https://doi.org/10.1016/j.measurement.2014.04.007>
119. Nolz R (2016) A review on the quantification of soil water balance components as a basis for agricultural water management with a focus on weighing lysimeters and soil water sensors. *J Land Manag Food Environ* 67(3). <https://doi.org/10.1515/boku-2016-0012>
120. Singh G, Kaur G, Williard K, Schoonover J, Kang J (2018) Monitoring of water and solute transport in the vadose zone: a review. *Vadose Zone J* 17(1):23. <https://doi.org/10.2136/vzj2016.07.0058>

121. Šimůnek J, van Genuchten MTh, Šejna M (2016) Recent developments and applications of the HYDRUS computer software packages. *Vadose Zone J* 15(7):25. <https://doi.org/10.2136/vzj2016.04.0033>
122. Isch A, Coquet Y, Aldana C, Bruand A, Azaroual M (2021) Simulation of water flow and estimation of travel time through the heterogeneous vadose zone of a vulnerable limestone aquifer based on laboratory hydraulic properties measurements. Manuscript submitted for publication in *J Hydrol* (under review)
123. Wellings SR, Bell JP (1980) Movement of water and nitrate in the unsaturated zone of Upper Chalk near Winchester, Hants., England. *J Hydrol* 48(1):119–136. [https://doi.org/10.1016/0022-1694\(80\)90070-0](https://doi.org/10.1016/0022-1694(80)90070-0)
124. McLing TL, Brandon W, Zavata B, Smith RW, Smith C (2017) The application of radon for mapping open fracture networks in a thin vadose zone. *Vadose Zone J* 16(7). <https://doi.org/10.2136/vzj2016.11.0116>
125. Isch A, Azaroual M (2019) Fluids transfers and hydrodynamics of the Vadose Zone of the O-ZNS platform site. In: Knowledge's frontiers in water unsaturated hydrogeosystems: interface dynamics, heterogeneities & couplings, Orléans
126. Abbar B, Isch A, Azaroual MM (2020) Fiber optic and hydrogeological sensors for the monitoring of mass and heat transfers through the vadose zone of a Cenozoic limestone aquifer (Beauce, Orléans, France). In: AGU Fall meeting
127. Abbar B, Jodry C, Isch A, Laurent G, Azaroual M (2020) Monitoring of the mass and heat transfers through a heterogeneous karstic limestone vadose zone of an agricultural field (Beauce aquifer, Orleans, France), EGU 2020-5294. Virtual, 3–8 May 2020. <https://doi.org/10.5194/egusphere-egu2020-5294>
128. Pütz T, Fank J, Flury M (2018) Lysimeters in vadose zone research. *Vadose Zone J* 17(1):180035. <https://doi.org/10.2136/vzj2018.02.0035>
129. Isch A, Montenach D, Hammel F, Ackerer P, Coquet Y (2019) A comparative study of water and bromide transport in a bare loam soil using lysimeters and field plots. *Water* 11(6):1199. <https://doi.org/10.3390/w11061199>
130. Weihermüller L, Siemens J, Deurer M, Knoblauch S, Rupp H (2007) In situ soil water extraction: a review. *J Environ Qual* 36(6):1735–1748. <https://doi.org/10.2134/jeq2007.0218>
131. Dahan O, Talby R, Yechieli Y, Adar E, Lazarovitch N (2009) In situ monitoring of water percolation and solute transport using a vadose zone monitoring system. *Vadose Zone J* 8(4):916. <https://doi.org/10.2136/vzj2008.0134>
132. Quinn P, Parker BL, Cherry JA (2015) Blended head analyses to reduce uncertainty in packer testing in fractured-rock boreholes. *Hydrogeol J* 24(1):59–77. <https://doi.org/10.1007/s10040-015-1326-2>

Chapter 10

Plants, Vital Players in the Terrestrial Water Cycle



Tomas E. van den Berg, Satadal Dutta, Elias Kaiser, Silvere Vialet-Chabrand, Martine van der Ploeg, Tim van Emmerik, Miriam Coenders-Gerrits, and Marie-Claire ten Veldhuis

Abstract Plant transpiration accounts for about half of all terrestrial evaporation. Plants need water for many vital functions including nutrient uptake, growth and leaf cooling. The regulation of plant water transport by stomata in the leaves leads to the loss of 97% of the water that is taken up via their roots, to the atmosphere. Measuring plant-water dynamics is essential to gain better insight into its roles in the terrestrial water cycle and plant productivity. It can be measured at different levels of integration, from the single cell micro-scale to the ecosystem macro-scale, on time scales from minutes to months. In this contribution, we give an overview of state-of-the-art techniques for plant-water dynamics measurement and highlight several promising innovations for future monitoring. Some of the techniques we will cover include: gas exchange for stomatal conductance and transpiration monitoring, lysimetry, thermometry, heat-based sap flow monitoring, reflectance monitoring including satellite remote sensing, ultrasound spectroscopy, dendrometry, accelometry, scintillometry, stable water isotope analysis and eddy covariance. To fully assess water transport within the soil-plant-atmosphere continuum, a variety of techniques are required to monitor environmental variables in combination with biological responses at different scales. Yet this is not sufficient: to truly account for spatial heterogeneity, a dense network sampling is needed.

T. E. van den Berg
Integrated Devices and Systems, University of Twente, Enschede, The Netherlands

S. Dutta
Dynamics of Micro and Nanosystems, Delft University of Technology, Delft, The Netherlands

E. Kaiser · S. Vialet-Chabrand
Horticulture and Product Physiology, Wageningen University and Research, Wageningen, The Netherlands

M. van der Ploeg · T. van Emmerik
Hydrology and Quantitative Water Management, Wageningen University and Research, Wageningen, The Netherlands

M. Coenders-Gerrits · M.-C. ten Veldhuis (✉)
Water Resources, Delft University of Technology, Delft, The Netherlands
e-mail: J.A.E.tenVeldhuis@tudelft.nl

10.1 Introduction

10.1.1 *Terrestrial Water Cycle and the Role of Transpiration*

Fresh water is a scarce resource in many regions of the world, and around 70% is used by agriculture [1]. It is the most important factor determining crop yields in countries with less industrialized agricultural practices, where the greatest share of agriculture depends on rainfall for its water supply [2]. Global environmental change will likely change the evaporative demand and rainfall in these regions, intensifying the competition between water use for agriculture and human consumption [3]. Plants, and especially irrigated crop plants, require large amounts of fresh water for growth. For example, producing 1 kg of cereal requires 1–3 tonnes of fresh water, putting a high price on food security and water availability [3]. Plants use water in their circulatory system (e.g., to move nutrients), and transpiration of water vapor from the plant to the atmosphere drives exchange from the roots to the rest of the plant. Leaf transpiration provides a cooling mechanism and is a prerequisite for CO₂ uptake and plant growth. Thus, plants have an intimate relationship with water: they need it for their basic functions, growth and reproduction, but 97% of water taken up by plants is lost to the atmosphere as water vapor, accounting for more than 95% of evapotranspiration in certain ecosystems [4]. Future population growth and its increased food demand are likely to exacerbate current scarcities of fresh water [5], as is the increasing salinization of agricultural areas, which itself is caused to a large extent by the soil water flows triggered by transpiration [6]. Therefore, we are in dire need of crops with better water use efficiency and sensors that allow agricultural water users to adjust water supply better to the exact needs of plants.

10.1.2 *Water Movement in the Plant*

Water and nutrient uptake by the roots, and upwards movement through the plants' vasculature, are driven by a negative hydrostatic pressure in the leaves, which builds up by water lost through transpiration. Water is moved upwards through the plant, if the hydrostatic pressure potential in the leaves is more negative than the combination of matrix potential (e.g., capillary action), soil osmotic potential (i.e., movement of water across a semipermeable membrane) and gravitational potential in the canopy (i.e., force exerted by gravity due to the height of the water column in the plant). Redwoods (*Sequoia sempervirens*), the tallest trees on earth (up to 120 m long) can build up a hydrostatic pressure potential of up to -1.9 MPa in their uppermost leaves, making it possible to move water against gravity to such heights [7]. Long-distance transport of water in the plant is facilitated by the xylem, a specialized vascular system consisting of long, connected cells that function similarly to pipes. Mature xylem vessel cells are dead and empty by design and have a small resistivity to water

movement. The xylem vascular system starts in the root, extends throughout the stem and branches, and delivers water and solutes directly to the leaves, which are the main sites of transpiration.

10.1.3 Root-Soil Water Exchange

The roots are the plant organ for water uptake from the soil and thus the first location where changes in water supply are perceived. The root system consists of a complex architecture of primary and lateral roots which vary in length, number and diameter. Together with cell size and the capillary forces in the plant and soil, they determine root water uptake ability. Coarse roots, the first roots to emerge from the seed, determine the depth of rooting and thereby the uptake of water from deeper soil layers. Root morphological plasticity enables plants to maintain water uptake from deeper layers when drought occurs [8, 9]. In addition, their traits determine the ability to grow in compact soil. The lateral roots that branch from other roots form a dense network of fine roots with root hairs that directly interact with soil particles and extract water and nutrients from them. Water absorption in the roots takes place through active and passive processes. Root cells require energy (ATP) to absorb minerals from the soil; the increased concentration of minerals in the roots generated by this process reduces root water potential relative to its surroundings, thus driving water absorption through endosmosis. Most water absorption through the roots is passive and directly driven by the negative water potential, which is created by the transpiration of water from the air-exposed parts of the plants, mainly through the stomata.

10.1.4 Stomata

Diffusion, the movement of molecules from high to low concentration areas, is the main mechanism of transpiration. Gas diffusion mainly happens through stomata, tiny adjustable pores surrounded by a pair of guard cells and embedded mainly in the leaf surface, but also present in a smaller numbers in other plant organs (e.g., stem). Apart from the stomata, the leaf surface is covered by a waxy layer called the cuticle, which is largely impenetrable to water. Stomata constantly adjust a trade-off between the diffusion of CO₂ into the leaf and the diffusion of water vapor out of the leaf, by opening and closing in response to numerous internal and external cues. For example, high light intensity, low atmospheric CO₂ concentration ([CO₂]), and high air humidity all lead to stomatal opening, whereas the opposite situation (low light intensity, high [CO₂], low air humidity) leads to stomatal closure. Further, several stresses, such as drought, soil salinity, heatwaves, ozone and several pathogens trigger stomatal closure, greatly reducing the rate of transpiration as well as photosynthesis and growth. Stomata open when guard cells swell upon active water

uptake (following ion up-take, which increases their osmotic potential), leading to a widening of the stomatal pore. There is a large diversity in the shape of stomata that influences their functionality [10], and their number and pattern across the leaf surface vary depending on plant growth conditions [11]. Up to 900 stomata can cover every mm^2 of leaf surface, and although this is only 0.3–5% of the surface of the leaf, they are responsible for 95% of terrestrial transpiration. The concentration gradient of water vapor inside and outside the leaf is strongly dependent on temperature and air humidity but is generally several orders of magnitude larger than the corresponding $[\text{CO}_2]$ gradient. Therefore, to fix 1 mol of CO_2 , leaves must transpire approximately 400 mols of water. The current increase in atmospheric $[\text{CO}_2]$ may reduce plant transpiration, as elevated $[\text{CO}_2]$ leads to a higher water use efficiency of CO_2 uptake, but this effect may be counteracted by a simultaneous increase in leaf and air temperature [12].

10.1.5 Atmosphere and Soil Effects on Transpiration

Even though stomata can control transpiration, different meteorological processes influence the concentration gradient of water between leaf and atmosphere [13]. Changes in net radiation received, air relative humidity, air temperature and wind speed influence transpiration independently of stomatal control. Therefore, the role of stomatal conductance also depends on environmental variables that need to be assessed at different scales [14]. An example is boundary layer conductance, representing a resistance to diffusion at the surface of the leaf that is influenced by leaf geometry and wind speed. Within the canopy, boundary layer conductance (g_b) acts in series with stomatal conductance (g_s) and can represent a substantial limitation of transpiration under certain circumstances (e.g., large leaf, low wind speed). Boundary layer conductance also occurs at the scale of the canopy and limits the rate of water vapor exchange between the canopy and atmosphere. Water availability in the soil, and resistance to water transport within the plant, represent additional factors that can limit transpiration and force stomata to close to maintain the plant's water status. Under drought, if stomatal closure is not sufficient to maintain plant water status, plants can alter their osmotic potential and cell turgor (force of the liquid in a plant cell exerted on its own cell wall), to limit water loss by transpiration. In this case, humidity within the leaf can decrease below the saturation point of water vapor, an essential assumption for most techniques used to measure stomatal conductance.

10.1.6 Measuring Plant Water Relations: Where and How

To fully assess water transport within the soil-plant-atmosphere continuum, a variety of techniques is required to monitor environmental variables and biological responses at different scales (Fig. 10.1). Plant water relations can be monitored at many levels

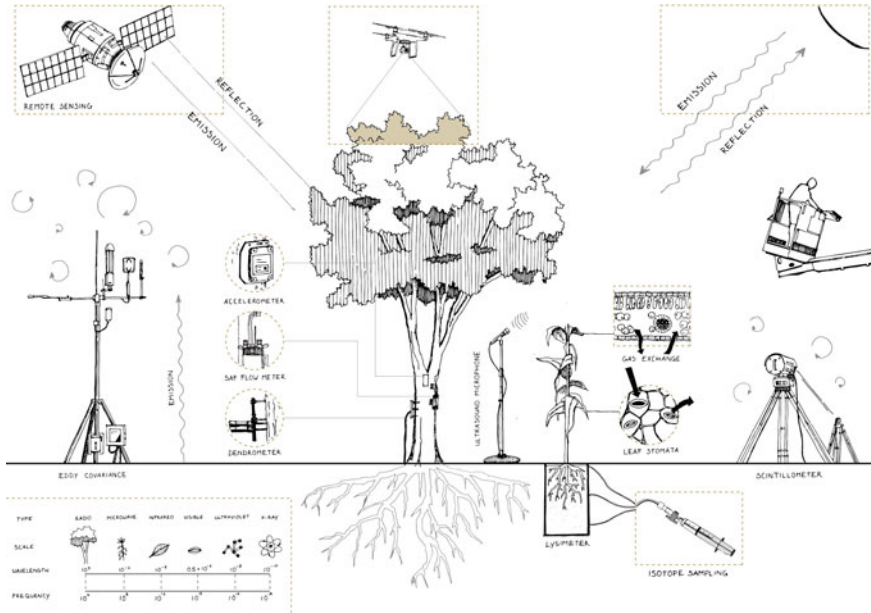


Fig. 10.1 Graphical impression of the different techniques to measure Plant water status and dynamics (by Cher van den Eng)

of integration, from single cells to hectares of canopy, and from minutes to months. In the following sections, we aim to give an overview of the various techniques for monitoring such relations, which are briefly summarized in (Table 10.1).

10.2 Measuring Techniques for Stomatal Conductance and Water-Vapor Exchange at the Leaf Atmosphere Interface

10.2.1 Microscopy

Stomatal conductance to water vapor (g_s), the rate of passage of gasses through the stomatal pore, is defined mainly by the number and pore size of stomata. A diffusion-based equation allows for calculation of g_s from leaf anatomical traits and to estimate the theoretical maximum gas diffusion rate [15–17]:

$$g_s = \frac{\frac{d}{v} Da}{(l + \frac{\pi}{2} \sqrt{\frac{a}{\pi}})} \tag{10.1}$$

Table 10.1 Overview of available methods and their respective areal scale, temporal scale, measuring principle and sample

Technology	Areal scale	Temporal scale	Measuring principle	Sample
Microscopy	$\mu\text{m}^2\text{-cm}^2$	min	VIS-NIR imaging (nm)	Leaf surface (stomata)
Gas Exchange	cm^2	s-min	IR spectroscopy (μm)	Water vapor
Thermometry	$\text{cm}^2\text{-km}^2$	s-min	Thermal IR imaging (μm)	Leaf surface
Scintillometry	$\text{m}^2\text{-km}^2$	hour-day	Refractive index NIR spectroscopy (nm- μm)	Air above canopy
Eddy Covariance	km^2	hours	IR spectroscopy (μm) Temperature (T) and velocity (m s^{-1})	Water vapor Air
Dielectric Constant	cm^2	min	Microwave scatter (mm)	Plant tissues
Hyperspectral Imaging	$\text{cm}^2\text{-km}^2$	min	Reflectance Imaging (nm-mm)	Plant tissues
Ultrasound spectroscopy	cm^2	s	MegaHz spectroscopy	Plant tissues
Ultrasound xylem cavitations	μm	s	Ultrasound spectroscopy	Air bubble cavitations
Accelerometry	cm^2	s-min	Sway (m s^{-2})	Trees
Field Radar	$\text{m}^2\text{-km}^2$	min-hours	Microwave scatter (mm)	Plant tissues
Lysimetry	cm^2	hours	Weighting (g-kg)	Water reservoir
Sap Flow Measurements	cm^2	s	Heat balance	Plant stem
Dendrometry	cm^2	hours	Diameter (mm-m)	Plant stem
Stable water isotopes	cm^2	hours-weeks	Fractionation	Water or water vapor

where d is the diffusivity of water vapor in air ($\text{m}^2 \text{s}^{-1}$), v is the molar volume of air ($\text{m}^3 \text{mol}^{-1}$), D the stomatal density (nr m^{-2}), a is the stomatal pore area (m^2) and l its depth (m); note that d and v are both temperature and air pressure dependent. $\frac{\pi}{2} \sqrt{\frac{a}{\pi}}$ represents an “end correction”, an additional diffusive resistance that is related to converging and diverging concentration shells at both ends of the stomatal pore. Different corrections are possible, depending on stomatal architecture and distribution over the leaf (clustering), which are important to produce accurate g_s estimates [18].

The stomatal pore is often assumed to be elliptical, and the area is estimated from the width and length of the aperture. D is estimated using a microscope by counting the number of stomata per unit area (e.g., field of view) over different areas and each side of the leaf. This takes into consideration the heterogeneous stomatal distribution across the leaf surface. Steady-state stomatal aperture is measured on many stomata acclimated to one condition (combination of temperature, humidity, $[\text{CO}_2]$, etc.). In contrast, kinetics of stomatal movement are measured by continuous observation of a limited number of stomata during a change in conditions. Individual, neighboring stomata can show a large variety of responses despite being subjected to the same stimuli, and several stomata need to be measured to represent the overall response at leaf level. Microscopy is useful to obtain a better understanding of plant water relations at the level of single stomata, but currently of limited use for plant monitoring in the field, due to its high cost and labor-intensive employment. However, with more autonomous systems, microscopy could provide solutions for g_s monitoring in uniform and stable environments, such as vertical farms or greenhouses.

10.2.2 Gas Exchange Measurements

Gas exchange is measured by enclosing a part or a complete plant inside a chamber where the environment is controlled. Water vapor concentration can be measured using an infrared gas analyzer (IRGA) or a capacitive humidity sensor. In the case of an IRGA, the concentration of water vapor in an air sample is proportional to the radiation absorbed by water molecules at specific sub-millimeter infrared wavebands, giving a characteristic absorption spectrum [19]. The absorption follows the Beer-Lambert Law and is therefore dependent on the radiation pathway and the concentration of water vapor. A capacitive humidity sensor consists of a hygroscopic dielectric material (i.e., a very poor conductor of electric current that tends to absorb water) placed between a pair of electrodes. Absorption of moisture by the dielectric material results in an increase in sensor capacitance, resulting in an increase in circuit current. At equilibrium conditions, the current is proportional to the amount of moisture present in a hygroscopic material and depends on both ambient temperature and ambient water vapor pressure. There are mainly two types of gas exchange chamber, “closed” and “open”, depending on the air flow renewal within the chamber. In a “closed” system, the plant sample is placed within a chamber where the air is recycled, and air water vapor concentration increases due to transpiration. The slope of the increase in water vapor concentration over time is measured over a short period and used to estimate the transpiration rate. A major limitation of this system is that the plant may respond to the changing relative humidity within the chamber during the measurement, which means that the air needs to be dried or renewed for the following measurement. This problem is solved in an “open” system by using a constantly renewed incoming air flow that is altered by the sample when passing through the chamber. The difference in water vapor concentration before and after the chamber is proportional to the transpiration rate. Such a system generally requires two IRGA

to measure the chamber input and output, and requires regular intercalibration of the IRGA, due to possible drift of the signal over time. Based on transpiration, leaf temperature, and the microclimate within the chamber, g_s can be derived, representing the average response of stomata over the leaf surface. To estimate g_s , one needs to assume that the air within the leaf is saturated with water vapor, which is true for well-watered conditions. The water vapor gradient can therefore be calculated based on leaf temperature and surrounding conditions. A constant mixing of air in the chamber enables a large boundary layer conductance to be maintained, thus allowing derivation of g_s from transpiration. Gas exchange measurements are vital for crop science and plant physiology, because of their direct measurements and good temporal as well as areal resolution for individual plants. Examples of field-based measurements exist [20], but these are not wide-spread for general monitoring.

10.2.3 Scintillometry and Eddy Covariance

Turbulent movements of air above a canopy (in the surface boundary layer), called eddies, transport gases including water vapor, and can be used to detect evaporation over a fixed optical path length (scintillometry) or over a variable area (eddy covariance). Scintillation describes changes in the brightness of an object when viewed through a medium [21]. A well-known and readily observable example for scintillations is a twinkling of the air just above roads on hot summer days. Scintillometers use this optical phenomenon by measuring fluctuations in NIR radiation (e.g., at $0.94 \mu\text{m}$) transmitted over a defined path (100 m–4.5 km). These fluctuations within the canopy air boundary layer are used to measure the turbulence structure of the air refractive index (caused especially by fluctuations in temperature and humidity). The derived turbulence structure parameter is used with Monin-Oblukhov similarity theory to estimate sensible heat flux, which, with information on available energy, allows estimation of area-averaged water vapour fluxes (see e.g., [22–24]). While scintillometers are most often used to estimate heat fluxes, they have been found to provide accurate estimations of evaporation at longer time scales (days-months; [21, 25]). Eddy covariance functions as a combination of several measuring techniques of the air above the canopy, combined in a single measuring spot: A sonic anemometer measures direction and velocity of air, an IRGA measures water vapor concentration, and a thermistor measures air temperature. Estimation of net exchange between the canopy and the atmosphere uses the sum of the vertical components of fluxes in the passing eddies at a single sensor position (see [26, 27]). Together, these measurements allow calculation of the fluxes of heat and water vapor exchanged between the canopy and the atmosphere. The measurement footprint of this technique varies depending on the direction and force of the wind. Eddy covariance produces the most reliable results over flat terrain with homogenous vegetation and at steady environmental conditions [28]. Data can be logged at 30–60 min time steps during the day, which is faster than e.g. scintillometry. Several hundred sites around the globe continuously log data, and over 2000 annual datasets have been gathered. Eddy covariance

is most often used to estimate carbon flows (with water vapor concentration as a by-product), and results of evaporation are not published as often. Nevertheless, more than 1500 site-years of evaporation have been published [29], enabling one to draw conclusions on plant-climate interactions.

10.3 Measuring Techniques of Water Status and Transpiration from Leaf to Canopy Scale

10.3.1 Thermometry

Measuring leaf temperature is essential to determine the vapor pressure gradient between leaf and atmosphere but can also be used to measure leaf transpiration. Within the leaf, the transition from liquid to gas at the sites of evaporation results in energy loss and leaf cooling. By calculating the leaf energy balance (the sum of incoming and outgoing energies), it is possible to quantify the energy loss due to transpiration [30] via

$$R_n - C - \lambda E = S, \quad (10.2)$$

with R_n the net radiation (W m^{-2}), C the sensible heat transfer (W m^{-2}), λ the latent heat of evaporation of water (J kg^{-1}), E the evaporative flux ($\text{kg m}^{-2}\text{s}^{-1}$) and S the net physical storage (W m^{-2}) causing the change in leaf temperature [31]. This requires quantification of all incoming radiation (R_n), which can be difficult to estimate over large areas, especially within the canopy, where leaves can have different heights and orientations. Simultaneous measurement of reference materials with known optical and thermal properties can help reduce the complexity of the energy balance equations, by accounting for part of the effects due to the surrounding environment. Contrary to a gas exchange chamber, the plant is undisturbed, enabling the study of transpiration under natural conditions. Estimating g_s from the rate of water loss requires an estimate of the boundary layer conductance g_b , which mainly depends on wind speed and leaf anatomy, and therefore can vary within the canopy. Methods to estimate g_b rely on energy balance to determine the resistance to heat transfer ($=1/g_b$) between an object and the surrounding environment. For example, a heated aluminum plate can be used to estimate g_b , by monitoring the time required for the plate temperature to reach a new equilibrium with the ambient conditions. A large g_b results in rapid equilibration of plate and air temperature. Temperature can be measured using contact and non-contact methods, which differ in terms of precision and accuracy. Contact measurements using thermocouples, thermistors and resistance temperature detectors (RTD) give relatively accurate and precise point estimates of leaf surface temperature. Heat conduction along the cable, surrounding air conditions on the side of the sensor exposed to the air, and temperature gradients within the leaf, can influence the measurements, as the sensor only touches the leaf surface. Non-contact measurements use infrared radiation (IR) emitted by the leaf in the

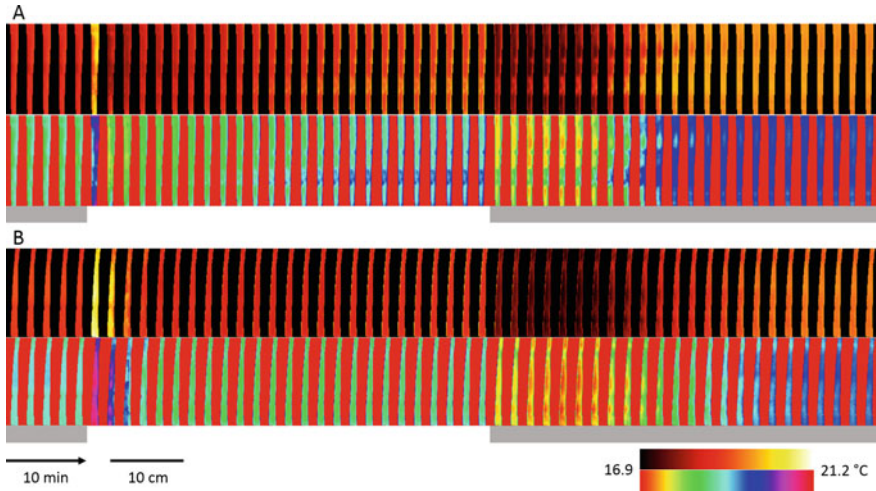


Fig. 10.2 Time series of thermal images displaying leaf temperature spatiotemporal differences for two leaves (A and B) subjected to changes in light intensities (grey background: $0 \mu\text{mol m}^{-2} \text{s}^{-1}$, white background: $430 \mu\text{mol m}^{-2} \text{s}^{-1}$). Two different colour scales are used to highlight either temperature kinetics or heterogeneity over the leaf surface. (taken from [31] under CC BY 4.0 License)

$0.7\text{--}14 \mu\text{m}$ range to estimate the temperature (T) of any object in the field of view using the Stefan-Boltzmann law

$$\text{IR} = \epsilon\theta T^4, \theta = 5.67 \times 10^{-8} \text{Wm}^{-2}\text{K}^{-4} \quad (10.3)$$

and are generally less precise. Infrared thermocouples and thermal imaging (Fig. 10.1) use this principle and provide estimates that account (to an extent) for the temperature gradient within the leaf. Thermometry using infrared requires knowledge of the emissivity of the object measured (leaf: $0.94\text{--}0.96$) and is influenced by the infrared radiation emitted by the surrounding objects and their reflection by the sample. The emissivity represents the capacity of the surface of an object to emit energy as infrared radiation and is determined as the ratio (between 0 and 1) of the infrared radiation emitted by the surface of the object and that of the surface of a perfect black body at the same temperature. The higher the emissivity, the stronger will be the signal received from the object by the camera sensor, relatively lowering the effects from the reflected signal due to the surrounding environment. Thermal imaging is a promising technique for transpiration measurements, because it is non-invasive, high-throughput and can cover relatively larger fields of view. Also, as any imaging technique, it provides information on the spatial heterogeneity of the process measured.

Future developments in camera technology and machine vision could enable UAVs to do large scale measurements of not only canopy temperature but also tran-

spiration for more relevant biological interpretation. Satellite thermal imaging uses a coarser methodology compared to thermometry, as reference structures with known optical and thermal parameters are unavailable. Instead, hot and cold pixels are selected; cold pixels represent well-watered plants under non-stress condition with full ground cover, while hot pixels represent bare agricultural land or water-stressed crops with close to zero evaporation [32, 33]. Evaporation is then calculated via the surface energy balance equation, modified as the METRIC Algorithm [34]. The temperature change in the cold pixels is a direct result of stomatal adjustments, which is one of the faster responses to changing water availability. A frequently used measure of water stress is the Crop Water Stress Index (CWSI):

$$CWSI = \frac{T_{\text{canopy}} - T_{\text{wet}}}{T_{\text{dry}} - T_{\text{wet}}} \quad (10.4)$$

With measured canopy temperature T_{canopy} , and upper and lower boundaries for canopy temperature T_{dry} and T_{wet} , respectively. The boundaries correspond to the canopy transpiring equally to the potential evaporation, and the lowest transpiration occurring at high water stress. These can be determined empirically or theoretically. The *CWSI* is nonlinearly related to canopy transpiration and can change depending on the wind speed conditions (influencing g_b). The actual canopy temperature can be measured from remote sensing imagery, such as from Landsat-8 and Sentinel-2. Examples of applications include water stress monitoring of citrus trees [33]. The main advantage of using thermal methods is that canopy temperature is a faster response to water stress than water potential, vegetation water content, or dielectric properties. However, also thermal reflectance is obstructed by cloud cover, and the revisit time of most available remote sensing missions is not suitable for day-to-day monitoring.

10.3.2 Optical Measurements

The solar radiation that reaches the Earth's surface has its intensity mostly distributed in the wavelength range of 250 nm till 2000 nm. Different bands of the spectrum interact with the leaf and its tissues in different ways. From the viewpoint of a plant's physiology, the spectrum of radiation can be categorized into three functionally relevant groups: (a) ultraviolet UV-B (250–350 nm), (b) Photosynthetically active radiation (PAR) from 380 nm till 750 nm, and (c) near-infrared (NIR) of wavelengths exceeding 750 nm. When light is incident on a leaf surface, it undergoes primarily four kinds of interaction with the cells/tissues. These are (a) Specular reflection, that occurs at the outermost smooth cuticular surface due to a difference in the optical refractive indices at the air-cuticle interface. Specular reflection ($\sim 3\%$) is significant at shorter wavelengths of light (250–400 nm) which have a shorter penetration depth; (b) Diffuse reflection [35–38], that occurs at the interfaces of the plant cell walls with the air-spaces deep inside the leaf. This phenomenon is significant for light of wave-

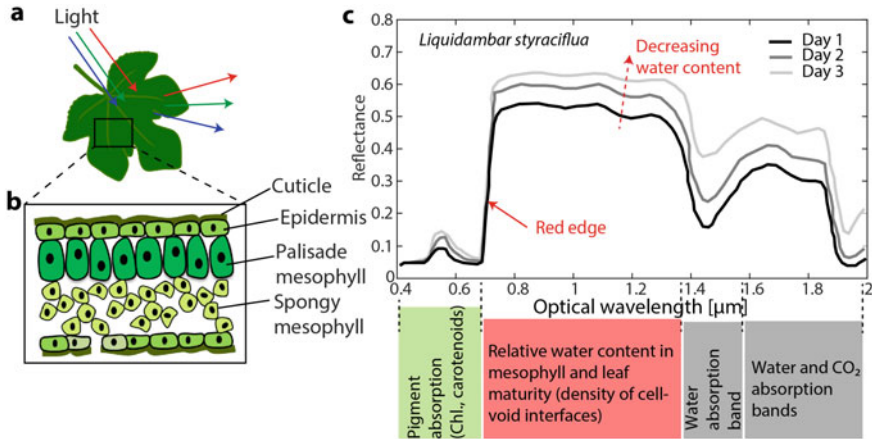


Fig. 10.3 **a** Incident solar radiation undergoes both specular and diffuse reflection from the leaf surface. **b** Schematic cross-section of a typical dicot leaf showing the cuticle, epidermis and the mesophyll tissues. The photosynthetically active radiation gets absorbed mostly in the chloroplasts of the upper palisade cells (having a higher chlorophyll concentration). The NIR components in the light scatters at the cell-air boundaries of the deeper spongy mesophyll leading to diffuse reflection. **c** Spectral reflectance of a single leaf of *Liquidambar styraciflua* [41], measured on indicated days of drought-stress ("Reprinted from Remote sensing of environment, Vol. 30, Hunt Jr, E. R., and Rock, B. N., Detection of changes in leaf water content using Near- and Middle-Infrared reflectances, 43–54, 1989, with permission from Elsevier"). Reflectance increases with decreasing water content. The reflection minima at wavelengths of 420 nm and 650 nm are due to light absorption by chlorophyll. The minima at wavelengths around 1450 nm and 1900 nm are due to absorption by water and carbon dioxide respectively

lengths longer than 400 nm, since the light needs to penetrate to a depth of at least ~ 100 nm before it can interact with different plant cell types; (c) Scattering, that occurs when the size of a particle is similar to the wavelength of the light. Typically, plant cells are larger than 10 μm , and thus do not contribute much to scattering. However, Mie scattering can occur due to the sub-micron sized organelles within the cells [39]; (d) Resonant absorption, that occurs when light of specific wavelengths causes electronic or molecular transitions to excited energy levels. Both photosynthetic pigments, chlorophyll *a,b* and carotenoids exhibit absorption bands between 350 and 500 nm, while chlorophyll *a,b* has an additional absorption band between 600 and 700 nm [40]. Water molecules exhibit absorption bands in the NIR spectrum e.g., between 1400 and 1500 nm and between 1900 and 2000 nm. The absorbed light energy either is converted to chemical energy during photosynthesis (PAR) or transformed to vibrational energy (heat), leading to a rise in the leaf temperature.

The reflectance spectrum of leaves as shown in Fig. 10.3 is heavily used in remote sensing to monitor the relative water content (RWC). Among the most successful methods to detect water stress are the ones that use reflectance data at two different NIR wavelengths: at 0.76–0.90 μm and at 1.55–1.65 μm as done by Hunt et al. [41, 42]. The ratio of reflectances $R_{1.6}/R_{0.82}$ is often termed as the Moisture Stress

Index (MSI). The underlying physics behind these techniques is that water absorbs strongly in the band 5 and is quite transparent to band 4, while both wavelengths having a similar reflection coefficient. Another example is the Normalized Difference Infrared Index using the NIR and MIR bands [$NDII = (NIR - MIR)/(NIR + MIR)$], which correlated highly with canopy water content [43]. Hunt et al. developed an optically derived parameter called as the Leaf Water Content Index (LWCI), defined as:

$$LWCI = \frac{-\log[1 - (R_{0.82} - R_{1.6})]}{-\log[1 - (R_{0.82} - R_{1.6}^{FT})]} \quad (10.5)$$

where $R_{0.82}$, and $R_{1.6}$ are respectively the reflectance factors measured for the test leaf at 0.82 μm , and 1.6 μm . $R_{1.6}^{FT}$ is the reflectance factor of a reference leaf at full turgor with known RWC. The RWC of a test leaf of weight W can be calculated from the measured dry weight (W^D) and weight at full turgor (W^{FT}) as:

$$RWC = \frac{(W - W^D)}{(W^{FT} - W^D)} \quad (10.6)$$

Additionally, optical remote sensing can estimate the vegetation greenness or vegetation cover. The reflectance spectrum of leaves exhibits a steep edge in the 680–780 nm wavelength interval, coinciding with the sharp transition in the chlorophyll a absorption window. This band is often termed the “red edge” and the first order derivative of reflectance in the red edge is very sensitive to variations in chlorophyll concentration and decreases are a common symptom of nutrient deficiencies (e.g., water). Rather than analyzing the reflectance of a single band, multispectral data is used to calculate indices. The most frequently used index is the Normalized Difference Vegetation Index (NDVI) [44]. NDVI is related to many relevant vegetation properties, such as leaf area index, biomass, chlorophyll concentration, and vegetation cover, and can be calculated using:

$$NDVI = \frac{NIR - Red}{NIR + Red} \quad (10.7)$$

With the reflectance in the near infrared (NIR) and for the red band (Red). NDVI is used to estimate transpiration. Although this is mainly based on empirical relations. For example, through multiplying reference evaporation by NDVI-based crop coefficients. A recent study [45] used NDVI derived from Landsat-7 and Landsat-8 imagery to explore the relation with sap flow and transpiration in a temperate forest. A positive correlation was found between the spatial variability in sap flow and NDVI. It was also shown that NDVI follows the sap flow during the beginning of a new cycle of plant growth, demonstrating the potential for plant monitoring. NDVI can also be used to monitor the impact of droughts on vegetation. For example, NDVI derived from the SPOT-Vegetation mission was used to calculate water stress coefficients for croplands and mixed-vegetation areas [46]. Main drawbacks of optical techniques, such as the NDVI, include signal saturation for surfaces with high

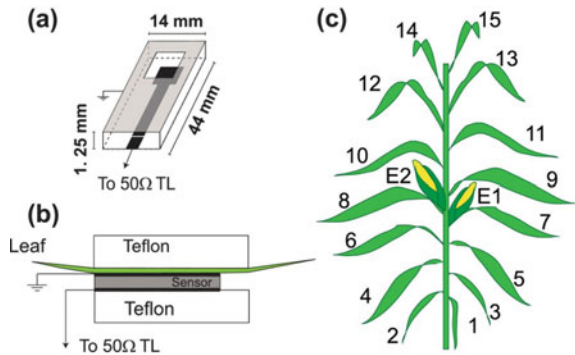
biomass, and blocking by cloud cover. Especially the latter makes optical techniques not always suitable for monitoring vegetation dynamics at shorter time scales.

10.3.3 Microwave Measurements

Plant water status has a direct influence on its dielectric properties, which are a measure of its interaction with microwaves. Microwaves are sensitive to vegetation, because of scattering and attenuation as the signal travels through the vegetation layer. The degree of scattering and attenuation depends on vegetation properties (dielectric constant, geometry, architecture), and microwave characteristics (frequency, incidence angle, polarization). For example, higher frequencies (shorter wavelengths) are more likely to be directly reflected by the canopy, and lower frequencies (longer wavelengths) penetrate further through the vegetation layer. In remote sensing, microwaves are used in either passive or active methods. Active methods (radar) emit microwaves and measure the reflected backscatter. Passive methods (radiometry) only measure the naturally emitted, and attenuated, microwaves. Initially, understanding the variation in vegetation dielectric properties were mainly interesting for (space-borne) radar and radiometer applications. The dielectric constant is an important parameter in several models that relate plant water status to microwave backscatter. However, the emergence of in-vivo dielectric measurement methods also offers the possibility to directly monitor plant water status non-destructively. Examples include the use of a microstrip line resonator, coupled to a vector network analyzer (VNA) (Fig. 10.4). Per measurement, the reflection coefficient of the emitted signal is measured, which depends on the dielectric constant of the sample. So far it has been shown, in corn and tomato leaves, that dielectric responses are directly coupled to leaf gravimetric leaf water content (Fig. 10.5) [47, 48].

Field-based radars can be used to monitor vegetation water status with high spatial and temporal frequency. Both soil moisture and plant water content affect the total backscatter. Higher soil moisture result in higher direct scatter from the soil.

Fig. 10.4 **a** Microstrip line resonator used for in-vivo dielectric measurements. **b** Illustration of leaf sample placement. **c** Schematic of a corn plant including leaf and ear numbering (taken from [48] under CC BY 4.0 License)



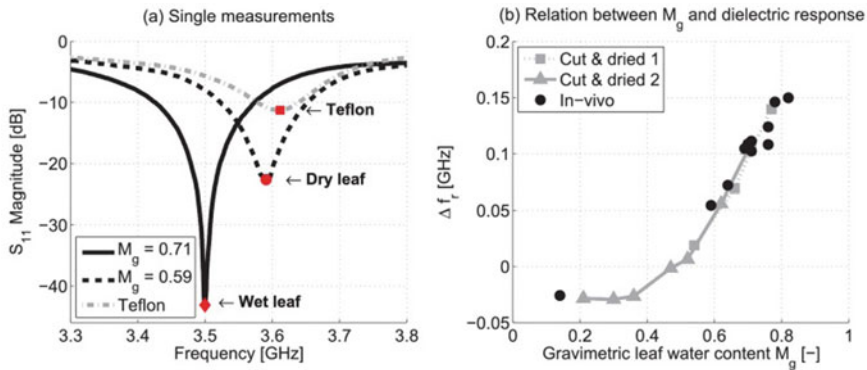


Fig. 10.5 **a** Comparison of dielectric response for dry and wet leaves, and **b** for leaves with varying gravimetric leaf water content (taken from [48] under CC BY 4.0 License)

Increased plant water content increases the direct backscatter from vegetation but can also increase the attenuation of the soil backscatter component. During periods of decreased soil moisture availability, the backscatter is mainly determined by the plant water dynamics. Although to date such setups have mainly been used for fundamental experiments to explore the potential for water status monitoring using remote sensing radar, future developments may result in more cost-effective and practical field-radar systems.

Changes in plant water status in the short (water stress, harvest) or long term (growth, leaf senescence or fall) on large scales are often measured by active and passive microwave methods via satellites. The benefit of using microwave-based methods is the independence of sunlight and cloud cover. For example, RapidScat Ku-band radar aboard the International Space Station was sensitive to vegetation water stress in the Amazon rainforest. Due to its orbit, diurnal cycles of backscatter could be reconstructed monthly. The observed changes in diurnal variability in radar backscatter were associated with changes in water status of the canopy measured on the ground [49]. This demonstrated the potential use of such missions for drought detection and monitoring, using radar remote sensing. Radar remote sensing also offers the possibility to use vegetation dynamics as a measure of root zone water availability [8]. Under water-limited conditions, surface and root zone soil moisture dynamics are decoupled. Yet, Sentinel-1 radar backscatter (C-band) was shown to be dominated by vegetation dynamics of the corn canopy, which was directly related to root zone soil moisture [50]. When using radiometry, the Vegetation Optical Depth (VOD) is a good measure of plant-water dynamics, as VOD is determined by canopy biomass and its water content (VWC). There is a linear relation between VOD and VWC, the latter can in turn be linearly or exponentially related to leaf water potential. The correlation of VOD with leaf water potential has been used to determine the isohydricity of vegetation at global scales. Isohydricity is an important factor that determines the response to vegetation water stress [51, 52].

10.4 Measuring Techniques of Plant Water Dynamics

10.4.1 Transpiration Measurements via Sap Flow Dynamics

Measurements of sap flow in plants provide a direct estimate of transpiration, at the whole plant level or for individual branches [53]. Sap flow measurements provide high time resolution and can be automated which makes them particularly useful for in-field studies [54]. Most techniques are based on the application of heat as a tracer for sap movement [55]. Techniques that directly measure sap flow rate (g h^{-1}) are based on external application of heat to the stem and derive flow rate by solving the stem heat balance. Other techniques apply heat pulses or continuous heating through probes inserted into the stem and derive a stem-average heat flux density ($\text{cm}^3 \text{cm}^{-2} \text{h}^{-1}$) [56].

Measurement of sap flow rate by the stem heat balance method is non-invasive, a heater is wrapped around the stem and enclosed in a layer of cork or similar material, which in turn is isolated by layers of foam and a weather shield to protect from solar radiation. The method can be applied to both woody and herbaceous stems, for stem diameters as small as 2 mm up to 125 mm. Sap flow is derived from the heat balance of the heated stem segment, by applying pairs of thermocouples that measure heat loss in radial and axial (along the stem, in the direction of the sap flow) direction.

$$P = q_v + q_r + q_f \quad (10.8)$$

where P is the applied heating power (in W), q_v , q_r are the rates of vertical and radial heat loss and q_f heat uptake by the moving sap stream (W). The sap mass flow rate (F_m , kg s^{-1}) is derived from

$$F_m = \frac{2q_f}{c_s(\Delta T_a + \Delta T_b)} \quad (10.9)$$

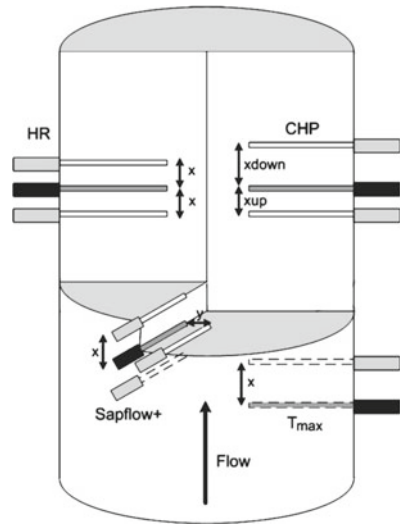
where c_s is the specific heat capacity of the sap and ΔT_a and ΔT_b are temperature differentials across the heated zone.

The main weakness of this method is that it requires in-situ calibration of the effective thermal conductance of the materials surrounding the heater. This is typically done for periods of zero sap flow, which can be difficult to achieve under field conditions.

Heat pulse methods are based on measurement of the velocity of a heat pulse as it is carried by the sap flow. Temperature is measured upstream and downstream of a heat probe that is inserted into the stem. Several approaches have been developed; an example is the Compensation Heat-Pulse velocity method (CHP, illustrated in Fig. 10.6). Here, the velocity of the heat pulse v_h is derived from

$$v_h = \frac{x_d - x_u}{2t_e} \quad (10.10)$$

Fig. 10.6 Schematic overview of methods for sap flow measurement based on heat pulse velocity, including CHP, T_{max}, Heat ratio and Sapflow+



where x_u and x_d are the distances between the heater and the upstream and downstream temperature sensors and t_e is the time after release of the heat pulse at which the upstream and downstream temperatures are equal. The upstream sensor being closer to the heater than the downstream sensor (Fig. 10.6), t_e equals the time needed for convection in the moving sap stream to move the peak of the heat pulse from the heater to the midway point between the upstream and downstream temperature sensors. The sap flow velocity is derived from the heat pulse velocity by

$$av_s = \frac{\rho_s m c_s m}{\rho_s c_s} \tag{10.11}$$

where a is the fraction of conducting sap wood over the total stem cross-section, ρ and c are density and specific heat capacity of the sap and sap-and-wood-matrix.

Heat pulse methods are based on the assumption that wood is thermally homogeneous, and that equilibration of sap and surrounding wood occurs near-instantaneously. Temperature probes are inserted into the sapwood, at one or more locations downstream and upstream of a heating probe. Several heat pulse methods have been developed apart from CHP, including the T_{max} method, Heat Ratio method, calibrated average gradient method and Sapflow+, as illustrated in Fig. 10.6 (see [57] for a complete review). In all heat pulse-based methods, heat pulse velocity is derived from differential temperatures along the axial direction of the stem, in some methods a tangential measurement is added. Heat pulse velocity is converted to flux density by accounting for sapwood water content and sapwood and dry wood density and specific heat capacities. Most heat pulse-based methods, except CHP, require an estimate of sapwood diffusivity which needs to be determined during zero flow conditions or can be determined empirically. Since all sap flux density methods rely on inserting probes into the sapwood, development of wound tissue occurs that locally

alters sapwood properties and heat dissipation. This effect can be limited by regularly relocating the probes. Wound correction equations have been developed for some of the heat-pulse systems. Reliability of the heat-pulse systems is strongly influenced by correct spacing of the temperature probes and by the assumption of thermal homogeneity of the sapwood. Especially for hardwood species non-uniform distribution of sap-conducting tissue this cause deviations in the sap flux density estimates [58].

10.4.2 Dendrometry

Dendrometers can be used to measure the changes in total stem, bark, xylem and phloem width individually. Changes in water content leads to cell shrinking and swelling. In turn the tissue of the stem can vary in size [59]. Dendrometers are placed on the stem or stalk and measure stem diameter variations. Stem variations follow diurnal variations. Depending on the isohydricity of the plant, these diurnal variations are affected by changing water availability. Besides short-term changes in stem width, dendrometers can also be used to monitor longer-term changes in stem radius. These changes can be related to plant growth and can give additional insight in the extent to which optimal crop growth is obtained [59].

10.4.3 Lysimetry

Lysimeters are often used to study the relation between the water cycle and vegetation, for example to quantify seasonal changes. Weighable lysimeters allow for precise quantification of the water balance terms at the soil plant atmosphere interface. Weighable lysimeters are often equipped with soil sensors, to follow processes in the soil which may change over time (e.g. [60]) or have a direct relation with plant physiology [61]. For monitoring soil water processes two often employed techniques are sensors for water content and for the water potential (e.g. [62]). Together these sensors can be used to determine the water retention characteristic of a soil, and the soil hydraulic conductivity. Lysimeters typically range from pot experiments (see above) to 12 m³ [63]. For determining the water balance at larger scales, radar interferometry has been identified as a potential technique for soils with swelling and shrinking properties [64]. In addition lysimeter results can be spatially extrapolated using thermal imaging [65].

10.4.4 Stable Water Isotopes Measurements

The use of stable water isotopes to study water behavior and flow paths has become more common in the last decades (e.g., [66, 67]). Stable water isotopes are considered

an ideal tracer, as the oxygen (^{18}O and ^{16}O) and hydrogen (^2H and H) atoms of water molecules are stable and naturally present in water.

Stable water isotopes are particular of interest to partition total evaporation (E_{tot}) into transpiration (E_t) and soil evaporation (E_s) (e.g., [68–70]). The fact that during evaporation, the light isotopes (^{16}O and H) are preferred to evaporate, results in an enrichment of heavy isotopes (^{18}O and ^2H in the remaining residue, e.g., the soil [71]). This process is called fractionation. For root water uptake (transpiration) fractionation does not occur: the plant just takes the available water without changing the isotopic ratio [72]. This distinct difference allow to partition total evaporation.

The isotopic ratio of heavy over light isotopes (R) is often expressed in comparison to the Vienna Standard Mean Ocean Water (VSMOW):

$$\delta_{\text{sample}} = \left(\frac{R_{\text{sample}}}{R_{\text{VSMOW}}} - 1 \right) \times 1000\text{‰} \quad (10.12)$$

By means of a simple isotopic mixing mass balance ($\delta_{E_{tot}} \cdot E_{tot} = \delta_{E_t} \cdot E_t + \delta_{E_s} \cdot E_s$), the transpiration ratio can be calculated via the 'isotopic-two-source-model' [73]:

$$\frac{E_t}{E_{tot}} = \frac{\delta_{E_{tot}} - \delta_{E_s}}{\delta_{E_t} - \delta_{E_s}} \quad (10.13)$$

The main challenge of this approach is the correct sampling of the isotopic ratios, where minor errors can easily propagate into large uncertainties [74–76]. To estimate $\delta_{E_{tot}}$ and δ_{E_s} , often the Craig-Gordon model is applied that uses as input water vapor samplings and soil water samplings, respectively [77]. While for δ_{E_t} the water vapor directly originating from the leaves is collected via special chambers [78]. Traditionally, 'cold traps' are used to condensate this water vapor (from the air or leaves) into liquid, so that the sample can be injected into an isotopic ratio mass spectrometer [79, 80]. However, obtaining full condensation without fractionation remains challenging, often leading to erroneous evaporation ratio estimates [81]. Fortunately, recent advances in laser-based instruments allow the direct analysis of water vapor [82–84]. These developments also enabled improved use of the Keeling-plot method [73, 85]. This method assumes that the isotopic concentration in the atmosphere (C_a) is the sum of some background concentration (C_{bg}) plus the concentration from the total evaporation $C_{E_{tot}}$:

$$C_a = C_{bg} + C_{E_{tot}} \quad (10.14)$$

Combining this via a simple mass balance ($\delta_a C_a = \delta_{bg} C_{bg} + \delta_{E_{tot}} C_{E_{tot}}$) the following linear relationship is obtained:

$$\delta_a = C_{bg} (\delta_{bg} - \delta_{E_{tot}}) \frac{1}{C_a} + \delta_{E_{tot}} \quad (10.15)$$

Thus by plotting $1/C_a$ versus δ_a for different heights (or times), the intercept provides the isotopic ratio of the transpiration ($\delta_{E_{tot}}$). The Keeling plot method works for stable water isotopes as well as for carbon isotopes to estimate e.g., the water use efficiency.

10.5 Novel Approaches to Plant Water Status Measurements

10.5.1 *Acoustic Measurements of Leaf and Plant Water Status*

10.5.1.1 Multiple Resonant Ultrasound Spectroscopy of Leaves

Unlike light, sound energy does not interfere directly with the physiological activity of plants and can thus be used to monitor the physical state of plant organs non-invasively. Exciting a plant part with acoustic waves at ultrasonic frequencies enables one to probe its inner structure. Leaves, being a few hundred microns thick, are suitable targets for studying their inner structure and water-content via a technique known as non-contact resonant ultrasound spectroscopy (NC-RUS) [86]. When excited with ultrasound (Fig. 10.7a), the transmitted acoustic signal exhibits multiple orders of vibration resonances (Fig. 10.7b) of the leaf and its inner cell structure; the fundamental frequency varies inversely with leaf thickness. The resonant frequency of a vibrating element is a strong function of its elastic modulus (stiffness) and mass density. Both parameters are sensitive to the turgor pressure determined by its water potential. NC-RUS, therefore, provides a way to monitor the in-vivo response of leaf anatomy to drought stress.

A recent study [86, 87] showed how analyzing the higher order acoustic resonances with a metaheuristic two-layered algorithm can lead us to extract the structural and viscoelastic properties of the constituent layers of leaf tissues. These distinguishing traits show up in the extracted acoustic impedances and elastic moduli using NC-RUS and are related to its water status [86].

10.5.1.2 Acoustic Emission from Xylem Vessels

During heavy drought stress, when soil water potential falls below -0.5 MPa, air bubbles may form within xylem vessels as a result of cavitation [89, 90]. Post formation, these bubbles can expand and block the vessels (embolism), thereby hindering water-transport. Vulnerability to cavitation is a popular method to quantify plant drought resistance. Bubble formation in xylem vessels is accompanied by the emission of low intensity sound bursts (see Fig. 10.7c), typically in the far audible and ultrasonic range (frequencies > 10 kHz). Some attempts have been made to understand the underlying characteristics of the emitted sound pulses, although they are

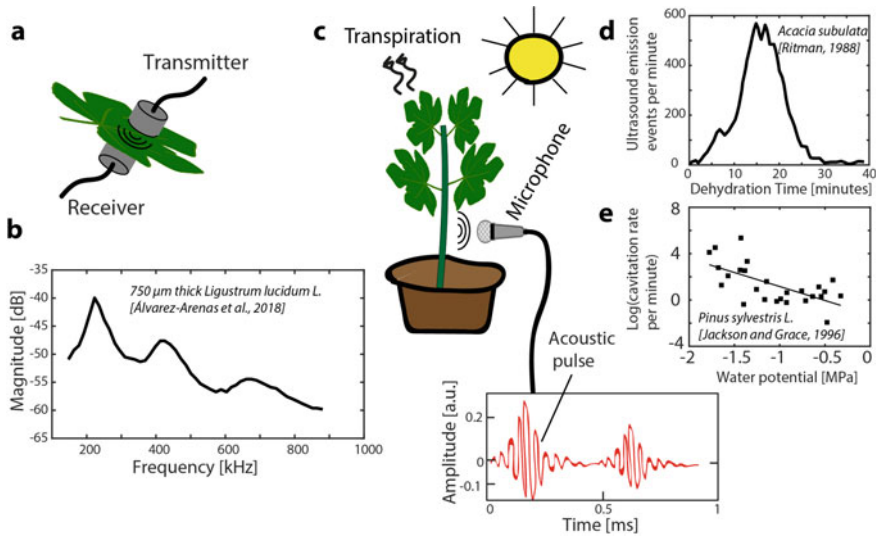


Fig. 10.7 **a** Schematic showing an ultrasound transceiver set-up to perform multiple resonant spectroscopy of a leaf. **b** A typical frequency response of a *Ligustrum lucidum* leaf when ultrasound is transmitted through it [86]. The characteristic peak frequencies represent acoustic resonances in the layered mesophyll tissue of the leaf (“Reprinted from [Álvarez-Arenas, T. E. G., Sancho-Knapik, D., Peguero-Pina, J. J., Gómez-Arroyo, A., & Gil-Pelegrín, E. (2018). Non-contact ultrasonic resonant spectroscopy resolves the elastic properties of layered plant tissues. *Applied Physics Letters*, 113(25), 253704, with the permission of AIP Publishing]”). **c** Plants undergo cavitation in its xylem vessels and emit ultrasound bursts under drought-stress coupled with rapid transpiration. The sound bursts are weak in intensity and resemble damped sinusoidal oscillations containing multiple frequencies; these can be recorded non-invasively with a microphone. **d** A typical evolution of ultrasound emission rate (events per minute) of a drought-stressed *Acacia* tree, as a function of the time of dehydration [88]. **e** The rate of sound emission (events per minute) versus the water potential in *Pinus sylvestris* trees [89]

still at a speculative stage. Ritman and Milburn [88] suggested that the length of the vessels has an influence on the cut-off frequency of the sound: ranging 500 Hz to beyond 100 kHz.

The sum of emission events over time during drought is a good measure of the loss in stem hydraulic conductivity [91–94] and can be used as an indirect and non-destructive marker for drought-stress resistance of a plant. The rate of sound emission events has been observed [89] to roughly follow an exponential dependence on the negative water potential. The emission rate of the sound bursts at first tends to increase with time (as water potential becomes more negative), and eventually decreases and ceases to occur when all vulnerable vessels are embolized [95] (see Fig. 10.7d, e). Further, vessels of larger diameter are more prone to cavitation. In the seminal work by Jackson and Grace [89], a high correlation was observed between acoustic emission rate per minute and the diurnal cycles of PAR and Vapor Pressure Deficit in Scotts Pine trees.

Advances in microelectronics technology have boosted the performance of acoustic sensors. State-of-the-art acquisition systems [96, 97] are able to record and store waveforms from multiple channels at high sampling rates. A popular application of acoustic monitoring is to determine the endpoint of a plant's vulnerability curve (VC), which is a curve of the % loss in hydraulic conductivity versus xylem water potential. The endpoint physiologically corresponds with complete cavitation of the xylem vessels, and thus the full breakdown of the plant's hydraulic pathway. Vergeynst et al. [98] developed a mathematical procedure to determine the endpoint by finding the local maximum of the 3rd derivative of the curve of cumulative acoustic emissions versus time. In another work [99], hydraulic measurements on 16 plant species showed that the highest acoustic activity occurred near the 50 % point of the VC, which is the inflection point.

A plant's response to drought-stress depends on both its physiological and anatomical characteristics [100] and *in vivo* measurements are necessary to map it completely. Conventional methods to determine a plant's vulnerability to cavitation are destructive, and labor-intensive, which hampers their field-applicability. Acoustic (ultrasound) monitoring has the potential to measure non-destructively, enabling automated and continuous measurements in the field.

10.5.2 Accelerometry

Accelerometers can be used to monitor the sway of plants and trees. Sway is determined by physical properties such as biomass and elasticity [101], which in turn are related to water content. Plant mass is directly influenced by the plant water content and the elasticity depends on the stiffness and the density, which are also both affected by water content. Also, plant geometry (size, shape, distribution, orientation of leaves, branches stalks, fruits) influences the sway response to wind forcing [102]. Sway can be used to monitor plant response to water availability, by looking at the change in either their natural frequency or the slope of the power spectrum of sway [103, 104]. Under increased water stress, changes in water content can lead to direct changes in the sway characteristics, offering a direct method to detect and monitor vegetation water stress in the field [105]. Also, accelerometers are relatively inexpensive, allowing for large-scale implementation in-situ.

10.6 Outlook

Plant-based measurement techniques provide direct estimates of leaf and plant water status that are useful to analyze and diagnose behavior of individual plants. For many applications, including those in hydrology, information at higher aggregation levels is required, typically from plot (~100–1000 m) to ecosystem (~1–100 km) scale. Depending on the type and scale of the problem at hand, combining in-situ and remote

sensing observations provides a way of bridging the scale gap. However, variability within the grid cell measurement, provided by remote sensing observations, needs to be accounted for. A strategy needs to be adopted that combines in-situ observations at representative locations to cover spatial variability with remote sensing observations that capture spatial average conditions. Especially in areas with complex vegetation and terrain, this can be challenging. Even in managed crop fields, heterogeneities of soil and atmosphere conditions as well as natural phenotype variability cause plants to interact differently with their environment. Sparse single measurements nor remote sensing observations can adequately resolve such variability. Solutions are needed that enable ubiquitous in-situ sensing of plant water relations, robustly, autonomously and at limited cost. Current techniques to study plant-water relations strongly rely on measurements at the leaf or plant scale. Upscaling to plant, plot or ecosystem scales requires representative sampling of a sufficient number of specimens to account for vegetation heterogeneity and environmental variability (soil, topography, atmosphere). Remote sensing offers larger-scale observations that help to compare between individual samples and large scale mean behavior, yet they are inevitably indirect observations subject to uncertainties associated with signal conversion. Moreover, satellite or UAV-based remote sensing platforms suffer from low temporal resolution. To truly account for spatial heterogeneity, a dense network sampling is needed. With the advent of low-cost data computing and communication technologies, the only remaining limitation is sensor cost, power, autonomy and robustness. Such multisensory networks with autonomous smart analytics could provide stakeholders with input on transpiration, water content and early stress detection at unprecedented temporal and areal scales. Sensor nodes that combine available (temperature, humidity, wind speed, dendrometry, sap flow) with new sensing methods (RF, hyperspectral, ultrasound, accelerometry) will benefit from more robust data and better stressor identification. Developments in the field of autonomous data acquisition and analysis will largely help to make such sensor networks reality. An example of such a real time, large scale, high frequency and long-term monitoring network is the TREETALKER NETWORK [106], where tree physiological parameters from 600 trees are monitored to determine the impact of climate changes on forests ecosystem services and forest dieback. In addition, the decreasing cost and improvements in the field of thermal and hyperspectral cameras as well as the upgrade of models dealing with such data will boost their use in the monitoring of plant water relations. The use of power generated by the plants rhizosphere itself could even be used to measure autonomously and robustly at remote locations [107]. Together the broad scale of measuring techniques provide an ever-growing choice to fit the stakeholders with the right solution in terms of accuracy, cost, temporal and areal scale to the wide variety of challenges in agriculture and environmental sciences.

References

1. Falkenmark M, Rockstrom J, Rockström J (2004) Balancing water for humans and nature: the new approach in ecohydrology. *Earthscan*
2. Rosa L, Rulli MC, Davis KF, Chiarelli DD, Passera C, D'Odorico P (2018) Closing the yield gap while ensuring water sustainability. *Environ Res Lett* 13(10):104002
3. Patrick E (2017) Drought characterization and management in central Asia region and turkey. Technical report
4. Stoy PC, El-Madany TS, Fisher JB, Gentine P, Gerken T, Good SP, Klosterhalfen A, Liu S, Miralles DG, Perez-Priego O et al (2019) Reviews and syntheses: turning the challenges of partitioning ecosystem evaporation and transpiration into opportunities. *Biogeosciences* 16(19):3747–3775
5. Alexandratos N, Bruinsma J (2012) World agriculture towards 2030/2050: the 2012 revision
6. Rana M, Mark T (2008) Mechanisms of salinity tolerance. *Annu Rev Plant Biol* 59:651–681
7. Koch GW, Sillett SC, Jennings GM, Davis SD (2004) The limits to tree height. *Nature* 428(6985):851–854
8. Buitink J, Swank AM, van der Ploeg M, Smith NE, Benninga HJF, van der Bolt F, Carranza CDU, Koren G, van der Velde R, Teuling AJ (2020) Anatomy of the 2018 agricultural drought in the Netherlands using in situ soil moisture and satellite vegetation indices. *Hydrol Earth Syst Sci* 24(12):6021–6031
9. van der Ploeg MJ, Gooren HPA, Bakker G, de Rooij GH (2008) Matric potential measurements by polymer tensiometers in cropped lysimeters under water-stressed conditions. *Vadose Zone J* 7(3):1048–1054
10. Tracy L, Jack M (2020) Guard cell metabolism and stomatal function. *Ann Rev Plant Biol* 71:273–302
11. Hetherington AM, Woodward FI (2003) The role of stomata in sensing and driving environmental change. *Nature* 424(6951):901–908
12. Ainsworth EA, Long SP (2021) 30 years of free-air carbon dioxide enrichment (face): what have we learned about future crop productivity and its potential for adaptation? *Global Change Biol* 27(1):27–49
13. Jarvis PG, McNaughton KG (1986) Stomatal control of transpiration scaling up from leaf to region. *Adv Ecol Res* 15:1–49
14. Jarvis PG (1995) Scaling processes and problems. *Plant Cell Environ* 18(10):1079–1089
15. Brown HT, Escombe F (1900) VIII. static diffusion of gases and liquids in relation to the assimilation of carbon and translocation in plants. *Philos Trans Royal Soc Londn Ser B, Containing Pap Biol Character* 193(185–193):223–291
16. Franks PJ, Beerling DJ (2009) Maximum leaf conductance driven by CO₂ effects on stomatal size and density over geologic time. *Proc Natl Acad Sci* 106(25):10343–10347
17. Franks PJ, Farquhar GD (2001) The effect of exogenous abscisic acid on stomatal development, stomatal mechanics, and leaf gas exchange in *Tradescantia virginiana*. *Plant Physiol* 125(2):935–942
18. Peter L, Dani O (2015) Effects of stomata clustering on leaf gas exchange. *New Phytologist* 207(4):1015–1025
19. Long SP, Farage PK, Garcia RL (1996) Measurement of leaf and canopy photosynthetic CO₂ exchange in the field. *J Experimental Botany* 47(11):1629–1642
20. Song Q, Xiao H, Xiao X, Zhu X-G (2016) A new canopy photosynthesis and transpiration measurement system (capts) for canopy gas exchange research. *Agric Forest Meteorol* 217:101–107
21. Hemakumara HM, Chandrapala L, Moene AF (2003) Evapotranspiration fluxes over mixed vegetation areas measured from large aperture scintillometer. *Agric Water Manage* 58(2):109–122
22. Meijninger WML, De Bruin HAR (2000) The sensible heat fluxes over irrigated areas in western turkey determined with a large aperture scintillometer. *J Hydrol* 229(1–2):42–49

23. Thiermann V, Grassl H (1992) The measurement of turbulent surface-layer fluxes by use of bichromatic scintillation. *Boundary-Layer Meteorol* 58(4):367–389
24. Van Kesteren B, Hartogensis OK, Van Dinther D, Moene AF, De Bruin HAR (2013) Measuring H₂O and CO₂ fluxes at field scales with scintillometry: part i-introduction and validation of four methods. *Agric Forest Meteorol* 178:75–87
25. Moorhead JE, Marek GW, Colaizzi PD, Gowda PH, Evett SR, Brauer DK, Marek TH, Porter DO (2017) Evaluation of sensible heat flux and evapotranspiration estimates using a surface layer scintillometer and a large weighing lysimeter. *Sensors* 17(10):2350
26. Aubinet M, Vesala T, Papale D (2012) Eddy covariance: a practical guide to measurement and data analysis. Springer Science & Business Media
27. Whitehead JD, Twigg M, Famulari D, Nemitz E, Sutton MA, Gallagher MW, Fowler D (2008) Evaluation of laser absorption spectroscopic techniques for eddy covariance flux measurements of ammonia. *Environ Sci Technol* 42(6):2041–2046
28. Baldocchi DD (2003) Assessing the eddy covariance technique for evaluating carbon dioxide exchange rates of ecosystems: past, present and future. *Global Change Biol* 9(4):479–492
29. Gilberto P, Carlo T, Eleonora C, Housen C, Danielle C, You-Wei C, Cristina P, Jiquan C, Abdelrahman E, Marty H et al (2020) The fluxnet2015 dataset and the oneflux processing pipeline for eddy covariance data. *Sci Data* 7(1):1–27
30. Prashar A, Jones HG (2014) Infra-red thermography as a high-throughput tool for field phenotyping. *Agronomy* 4(3):397–417
31. Silvere V-C, Tracy L (2019) Dynamic leaf energy balance: deriving stomatal conductance from thermal imaging in a dynamic environment. *J Experimental Botany* 70(10):2839–2855
32. Bastiaanssen WGM, Menenti M, Feddes RA, Holtslag AAM (1998) A remote sensing surface energy balance algorithm for land (sebal). 1. formulation. *J Hydrol* 212:198–212
33. Sajad J, Shahrokh Z-P, Dev N (2021) Assessing crop water stress index of citrus using in-situ measurements, landsat, and sentinel-2 data. *Int J Remote Sensing* 42(5):1893–1916
34. Jamshidi S, Zand-Parsa S, Jahromi MN, Niyogi D (2019) Application of a simple landsat-modis fusion model to estimate evapotranspiration over a heterogeneous sparse vegetation region. *Remote Sensing* 11(7):741
35. Gausman HW, Allen WA, Cardenas R, Richardson AJ (1970) Relation of light reflectance to histological and physical evaluations of cotton leaf maturity. *Appl Optics* 9(3):545–552
36. Lois G (1987) Diffuse and specular characteristics of leaf reflectance. *Remote Sensing Environ* 22(2):309–322
37. Knippling EB (1970) Physical and physiological basis for the reflectance of visible and near-infrared radiation from vegetation. *Remote Sensing Environ* 1(3):155–159
38. Slaton MR, Hunt Jr ER, Smith WK (2001) Estimating near-infrared leaf reflectance from leaf structural characteristics. *Am J Botany* 88(2):278–284
39. Gates DM, Keegan HJ, Schleiter JC, Weidner VR (1965) Spectral properties of plants. *Appl Optics* 4(1):11–20
40. Croft H, Chen JM (2017) Leaf pigment content. In: Reference module in earth systems and environmental sciences. Elsevier Inc, Oxford, pp 1–22
41. Hunt Jr ER, Rock BN (1989) Detection of changes in leaf water content using near-and middle-infrared reflectances. *Remote Sensing Environ* 30(1):43–54
42. Hunt Jr ER, Rock BN, Nobel PS (1987) Measurement of leaf relative water content by infrared reflectance. *Remote Sensing Environ* 22(3):429–435
43. Hardisky MA, Klemas V, Smart M (1983) The influence of soil salinity, growth form, and leaf moisture on the spectral radiance of spartina alterniflora canopies. *Photogramm Eng Remote Sensing* 49:77–83
44. Yilmaz MT, Hunt Jr ER, Goins LD, Ustin SL, Vanderbilt VC, Jackson TJ (2008) Vegetation water content during smex04 from ground data and landsat 5 thematic mapper imagery. *Remote Sensing Environ* 112(2):350–362
45. van Dijke AJH, Mallick K, Teuling AJ, Schlerf M, Machwitz M, Hassler SK, Blume T, Herold M (2019) Does the normalized difference vegetation index explain spatial and temporal variability in sap velocity in temperate forest ecosystems? *Hydrol Earth Syst Sci* 23:2077–2091

46. Abid N, Bargaoui Z, Mannaerts CM (2018) Remote-sensing estimation of the water stress coefficient and comparison with drought evidence. *Int J Remote Sensing* 39(14):4616–4639
47. van Emmerik T, Steele-Dunne S, Judge J, van de Giesen N (2015) A comparison between leaf dielectric properties of stressed and unstressed tomato plants. In: 2015 IEEE International Geoscience and Remote Sensing Symposium (IGARSS). IEEE, pp 275–278
48. Van Emmerik T, Steele-Dunne SC, Judge J, Van De Giesen N (2016) Dielectric response of corn leaves to water stress. *IEEE Geosci Remote Sensing Lett* 14(1):8–12
49. van Emmerik T, Steele-Dunne S, Paget A, Oliveira RS, Bittencourt PRL, de Barros FV, van de Giesen N (2017) Water stress detection in the amazon using radar. *Geophys Res Lett* 44(13):6841–6849
50. Benninga HJF, van der Velde Coleen Carranza R, van Emmerik T, van der Ploeg M. Exploring the sensitivity of vegetation radar backscatter to rootzone soil moisture. *Biogeosciences*, submitted
51. Frappart F, Wigneron J-P, Li X, Liu X, Al-Yaari A, Fan L, Wang M, Moisy C, Le Masson E, Laffkih ZA et al (2020) Global monitoring of the vegetation dynamics from the vegetation optical depth (vod): a review. *Remote Sensing* 12(18):2915
52. Konings AG, Gentine P (2017) Global variations in ecosystem-scale isohydricity. *Global Change Biol* 23(2):891–905
53. Čermák J, Kučera J, Nadezhdina N (2004) Sap flow measurements with some thermodynamic methods, flow integration within trees and scaling up from sample trees to entire forest stands. *Trees* 18(5):529–546
54. Clearwater MJ, Luo Z, Mazzeo M, Dichio B (2009) An external heat pulse method for measurement of sap flow through fruit pedicels, leaf petioles and other small-diameter stems. *Plant Cell Environ* 32(12):1652–1663
55. Poyatos R, Granda V, Flo V, Adams MA, Adorján B, Aguadé D, Aidar MPM, Allen S, Alvarado-Barrientos MS, Anderson-Teixeira KJ et al (2021) Global transpiration data from sap flow measurements: the sapfluxnet database. *Earth Syst Sci Data* 13(6):2607–2649
56. Smith DM, Allen SJ (1996) Measurement of sap flow in plant stems. *J Experimental Botany* 47(12):1833–1844
57. Vandegehuchte MW, Steppe K et al (2013) Sap-flux density measurement methods: working principles and applicability. *Functional Plant Biol* 40(3):213–223
58. Víctor F, Jordi M-V, Kathy S, Bernhard S, Rafael P (2019) A synthesis of bias and uncertainty in sap flow methods. *Agric Forest Meteorol* 271:362–374
59. Zweifel R, Zimmermann L, Newbery DM (2005) Modeling tree water deficit from microclimate: an approach to quantifying drought stress. *Tree Physiol* 25(2):147–156
60. Robinson DA, Hopmans JW, Filipovic V, van der Ploeg M, Lebron I, Jones SB, Reinsch S, Jarvis N, Tuller M (2019) Global environmental changes impact soil hydraulic functions through biophysical feedbacks. *Global Change Biol* 25(6):1895–1904
61. van der Ploeg MJ, Teuling AJ (2013) Going back to the roots: the need to link plant functional biology with vadose zone processes. *Proc Environ Sci* 19:379–383
62. van Der Ploeg MJ, Gooren HPA, Bakker G, Hoogendam CW, Huiskes C, Koopal LK, Kruidhof H, De Rooij GH (2010) Polymer tensiometers with ceramic cones: direct observations of matric pressures in drying soils. *Hydrol Earth Syst Sci* 14(10):1787–1799
63. Dijkema J, Koonce JE, Shillito RM, Ghezzehei TA, Berli M, Van Der Ploeg MJ, Van Genuchten MTh (2018) Water distribution in an arid zone soil: numerical analysis of data from a large weighing lysimeter. *Vadose Zone J* 17(1):1–17
64. te Brake B, Hanssen RF, van der Ploeg MJ, de Rooij GH (2013) Satellite-based radar interferometry to estimate large-scale soil water depletion from clay shrinkage: possibilities and limitations. *Vadose Zone J* 12(3):1–13
65. Voortman BR, Bosveld FC, Bartholomeus RP, Witte JPM (2016) Spatial extrapolation of lysimeter results using thermal infrared imaging. *J Hydrol* 543:230–241
66. Gat JR (1996) Oxygen and hydrogen isotopes in the hydrologic cycle. *Ann Rev Earth Planetary Sci* 24(1):225–262
67. Kendall C, McDonnell JJ (2012) *Isotope tracers in catchment hydrology*. Elsevier

68. Good SP, Soderberg K, Guan K, King EG, Scanlon TD, Caylor KK (2014) $\delta^{21}\text{O}$ isotopic flux partitioning of evapotranspiration over a grass field following a water pulse and subsequent dry down. *Water Resources Res* 50(2):1410–1432
69. Jimenez-Rodriguez CD, Coenders-Gerrits M, Wenninger J, Gonzalez-Angarita A, Savenije H. Contribution of understory evaporation in a tropical wet forest. *Hydrol Earth Syst Sci* 24:2179–2206
70. Youri R, Philippe B, Isabelle B, Laurent C, Jean-Louis D, Jean-Paul G, Patricia R, Michel V, Thierry B (2010) Partitioning evapotranspiration fluxes into soil evaporation and plant transpiration using water stable isotopes under controlled conditions. *Hydrol Process* 24(22):3177–3194
71. Allison GB, Barnes CJ (1983) Estimation of evaporation from non-vegetated surfaces using natural deuterium. *Nature* 301(5896):143–145
72. Ehleringer JR, Dawson TE (1992) Water uptake by plants: perspectives from stable isotope composition. *Plant Cell Environ* 15(9):1073–1082
73. Yakir D, da SL Sternberg L (2000) The use of stable isotopes to study ecosystem gas exchange. *Oecologia* 123(3):297–311
74. Coenders-Gerrits AMJ, Van der Ent RJ, Bogaard TA, Wang-Erlandsson L, Hrachowitz M, Savenije HHG (2014) Uncertainties in transpiration estimates. *Nature* 506(7487):E1–E2
75. Phillips DL, Gregg JW (2001) Uncertainty in source partitioning using stable isotopes. *Oecologia* 127(2):171–179
76. Wei Z, Yoshimura K, Okazaki A, Kim W, Liu Z, Yokoi M (2015) Partitioning of evapotranspiration using high-frequency water vapor isotopic measurement over a rice paddy field. *Water Resources Res* 51(5):3716–3729
77. Craig H, Gordon LI (1965) Deuterium and oxygen 18 variations in the ocean and marine atmosphere (consiglio nazionale delle ricerche laboratorio di geologia nucleare, Pisa, Italy)
78. Wang L, Good SP, Caylor KK, Cernusak LA (2012) Direct quantification of leaf transpiration isotopic composition. *Agric Forest Meteorol* 154:127–135
79. Sheppard PA (1958) Transfer across the earth's surface and through the air above. *Quarterly J Royal Meteorol Soc* 84(361):205–224
80. Wen X, Yang B, Sun X, Lee X (2016) Evapotranspiration partitioning through in-situ oxygen isotope measurements in an oasis cropland. *Agric Forest Meteorol* 230:89–96
81. Griffis TJ (2013) Tracing the flow of carbon dioxide and water vapor between the biosphere and atmosphere: a review of optical isotope techniques and their application. *Agric Forest Meteorol* 174:85–109
82. Marcel G, Matthias B, Paul K, Heike W, Josefina H, Thomas H (2016) In situ unsaturated zone water stable isotope (2 h and 18 o) measurements in semi-arid environments: a soil water balance. *Hydrol Earth Syst Sci* 20(2):715–731
83. Rodriguez CDJ (2020) Evaporation partitioning of forest stands: the role of forest structure
84. Patrizia N, Alexander G (2018) High-resolution vertical profile measurements for carbon dioxide and water vapour concentrations within and above crop canopies. *Boundary-Layer Meteorol* 166(3):449–473
85. Keeling CD (1958) The concentration and isotopic abundances of atmospheric carbon dioxide in rural areas. *Geochimica et cosmochimica acta* 13(4):322–334
86. Álvarez-Arenas TEG, Sancho-Knapik D, Peguero-Pina JJ, Gómez-Arroyo A, Gil-Peagrín E (2018) Non-contact ultrasonic resonant spectroscopy resolves the elastic properties of layered plant tissues. *Appl Phys Lett* 113(25):253704
87. Fariñas MD, Jimenez-Carretero D, Sancho-Knapik D, Peguero-Pina JJ, Gil-Peagrín E, Álvarez-Arenas TG (2019) Instantaneous and non-destructive relative water content estimation from deep learning applied to resonant ultrasonic spectra of plant leaves. *Plant Methods* 15(1):1–10
88. Ritman KT, Milburn JA (1988) Acoustic emissions from plants: ultrasonic and audible compared. *J Experimental Botany* 39(9):1237–1248
89. Jackson GE, Grace J (1996) Field measurements of xylem cavitation: are acoustic emissions useful? *J Experimental Botany* 47(11):1643–1650

90. Zimmermann U, Haase A, Langbein D, Meinzer F (1993) Mechanisms of long-distance water transport in plants: a re-examination of some paradigms in the light of new evidence. *Philos Trans Royal Soc Londn Ser B: Biol Sci* 341(1295):19–31
91. Hervé C, Eric B, Stéphane H, Sylvain D, Brendan C, Steven J (2013) Methods for measuring plant vulnerability to cavitation: a critical review. *J Experimental Botany* 64(15):4779–4791
92. Lo Gullo MA, Salleo S (1993) Different vulnerabilities of quercus ilex L. to freeze- and summer drought-induced xylem embolism: an ecological interpretation. *Plant Cell Environ* 16(5):511–519
93. Sabine R (2015) A new type of vulnerability curve: is there truth in vine? *Tree Physiol* 35(4):410–414
94. Vergeynst LL, Dierick M, Bogaerts JAN, Cnudde V, Steppe K (2015) Cavitation: a blessing in disguise? New method to establish vulnerability curves and assess hydraulic capacitance of woody tissues. *Tree Physiol* 35(4):400–409
95. De Roo L, Vergeynst LL, De Baerdemaeker NJF, Steppe K (2016) Acoustic emissions to measure drought-induced cavitation in plants. *Appl Sci* 6(3):71
96. Gernot M, Denis C, Dani O (2012) Sources and characteristics of acoustic emissions from mechanically stressed geologic granular media—a review. *Earth-Sci Rev* 112(3–4):97–114
97. Wolkerstorfer SV, Rosner S, Hietz P (2012) An improved method and data analysis for ultrasound acoustic emissions and xylem vulnerability in conifer wood. *Physiologia Plantarum* 146(2):184–191
98. Vergeynst LL, Sause MGR, De Baerdemaeker NJF, De Roo L, Steppe K (2016) Clustering reveals cavitation-related acoustic emission signals from dehydrating branches. *Tree Physiol* 36(6):786–796
99. Markus N, Barbara B, Sabine R, Anton N, Stefan M (2015) Xylem cavitation resistance can be estimated based on time-dependent rate of acoustic emissions. *New Phytologist* 208(2):625–632
100. McDowell N, Pockman WT, Allen CD, Breshears DD, Cobb N, Kolb T, Plaut J, Sperry J, West A, Williams DG et al (2008) Mechanisms of plant survival and mortality during drought: why do some plants survive while others succumb to drought? *New Phytologist* 178(4):719–739
101. Van Emmerik T, Steele-Dunne S, Hut R, Gentine P, Guerin M, Oliveira RS, Wagner J, Selker J, Van de Giesen N (2017) Measuring tree properties and responses using low-cost accelerometers. *Sensors* 17(5):1098
102. Jackson T, Shenkin A, Moore J, Bunce A, Van Emmerik T, Kane B, Burcham D, James K, Selker J, Calders K et al (2019) An architectural understanding of natural sway frequencies in trees. *J Royal Soc Interface* 16(155):20190116
103. Sethi S, Dellwik E, Angelou N, Bunce A, van Emmerik T, Duperat M, Ruel J-C, Wellpott A, Van Bloem S, Achim A, Kane B, Ciruzzi DM, Loheide II SP, James K, Burcham D, Moore J, Schindler D, Kolbe S, Wiegmann K, Rudnicki M, Lieffers VJ, Selker J, Gougherty AV, Newson T, Koester A, Miesbauer J, Samelson R, Wagner J, Coomes D, Jackson TD, Gardiner B (2020) The motion of trees in the wind: a data synthesis. *Biogeosciences Discuss*
104. van Emmerik T, Steele-Dunne S, Gentine P, Oliveira RS, Bittencourt P, Barros F, van de Giesen N (2018) Ideas and perspectives: tree–atmosphere interaction responds to water-related stem variations. *Biogeosciences* 15(21):6439
105. Ciruzzi DM, Loheide SP (2019) Monitoring tree sway as an indicator of water stress. *Geophys Res Lett* 46(21):12021–12029
106. Castaldi S, Antonucci S, Asgharina S, Battipaglia G, Marchesini LB, Cavagna M, Chini I, Cocozza C, Gianelle D, La Mantia T et al (2020) The Italian treetalker network (itt-net): continuous large scale monitoring of tree functional traits and vulnerabilities to climate change. In: EGU general assembly conference abstracts, p 20591
107. Sudirjo E (2020) Plant microbial fuel cell in paddy field: a power source for rural area. PhD thesis, Wageningen University

Chapter 11

Improving Water Quality and Security with Advanced Sensors and Indirect Water Sensing Methods



Philippe Cousin, Anastasia Moutzidou, Anastasios Karakostas, Lefteris Gounaridis, Christos Kouloumentas, Mauro Fernandes Pereira, Apostolos Apostolakis, Paula Gorrochategui, Guillaume Aoust, and Bérengère Lebental

P. Cousin (✉)
EGM, 06560 Valbonne, France
e-mail: philippe.cousin@egm.io

A. Moutzidou · A. Karakostas
ITI-CERTH, 6th km Harilaou - Thermi, 57001 Thermi, Thessaloniki, Greece
e-mail: moutzid@iti.gr

A. Karakostas
e-mail: akarakos@iti.gr

L. Gounaridis · C. Kouloumentas
National Technical University of Athens, Athens 15573, Greece
e-mail: lgou@mail.ntua.gr

C. Kouloumentas
e-mail: ckou@mail.ntua.gr; christos.kouloumentas@optagon-photonics.eu

C. Kouloumentas
Optagon Photonics, Athens 15341, Greece

M. F. Pereira
Department of Physics, Khalifa University of Science and Technology, Abu Dhabi, UAE
e-mail: mauro.pereira@ku.ac.ae; pereira@fzu.cz

M. F. Pereira · A. Apostolakis
Institute of Physics, Czech Academy of Sciences, Prague, Czech Republic
e-mail: apostolakis@fzu.cz

P. Gorrochategui · G. Aoust
mirSense, Centre d'intégration NanoINNOV, 91120 Palaiseau, France
e-mail: paula.gorrochategui@mirsense.com

G. Aoust
e-mail: Guillaume.Aoust@mirsense.com

B. Lebental
Université Gustave Eiffel, COSYS, Marne-La-Vallée, France
e-mail: berengere.lebental@univ-eiffel.fr

Laboratoire de Physique des interfaces et Couches Minces, UMR 7647, Ecole Polytechnique-CNRS, Institut Polytechnique Paris, Palaiseau, France

Abstract As far as Water is concerned, a lot of new directives and world concerns highlight among others the need for using ICT technologies, the global healthcare issues, the demand for fresh water, the food/beverage quality and safety, the environmental protection and the security strategies to reduce intentional contamination, all of the above having worldwide massive economic, natural and social impacts. However, despite an increasing demand for adaptability, compacity and performances at ever decreasing costs, the vast majority of water network monitoring systems remains based on sensor nodes with predefined and vertical applicative goals hindering interoperability and increasing costs (OPEX and CAPEX) for deploying new and added value services. Innovative technological products could answer the following acute needs in the field. This chapter introduce advance research works in sensing within two H2020 EU projects: the aqua3S project addressing sensors for Water Security purposes and LOTUS addressing low-cost multiparameter sensors for water quality.

11.1 Issues and Challenges on Water Sensing

Water is vital to all forms of life on Earth (human, animal and plant) and its quality is essential for health. It is also an unavoidable component in a wide range of industrial processes, from energy production to construction activities or food production. In spite of this, at least 11% of the European population and 17% of EU territory to date have experienced water scarcity-related problems. Millions of people are killed each year world-wide as a direct consequence of waterborne infectious diseases.¹

Water supplies are generally spread between surface and groundwater, while usages are highly differentiated between industrial, agricultural and domestic use. Pollution of water supplies is an ever-present risk while drink water losses in the supply network are massive (up to 50% in some cities). Continued management of increasing volumes of waste water, and of evermore frequent exceptional rain events requires increasing investments from water companies and cities.

Therefore, the protection of water quantity and quality is one the cornerstones of environmental protection schemes worldwide. The World Health Organization has placed drinking water quality on top of its priorities list, strongly advocating for the implementation of water safety plans.² Strong regulatory norms are being imposed for water quality at the European level,³ with an ever-increasing number of pollutants of different natures (chemical, biological, agricultural, industrial, pharmaceutical, cosmetic, radioactive, warfare agents) ideally requiring active monitoring.

¹ WHO assembly notes: <http://www.who.int/mediacentre/events/2011/wha64/journal/en/index5.html>, http://www.who.int/water_sanitation_health/en/.

² World Health Organization and International Water Association brochure: "A Roadmap to Support Country-Level Implementation of Water Safety Plans" (2010).

³ European Water Directive, http://ec.europa.eu/environment/water/index_en.htm.

11.1.1 Guaranteeing the Sustainability of Its Water Cycle Is Essential to European Resilience

Long-term management of such an extended, complex, demanding and strategic aspect of European resources requires widespread, low-cost monitoring means [1] with highly differentiated requirements (from drink water to waste water) and adaptive capabilities (from draught to flood events, from low to high demand levels). Monitoring is needed all along the water distribution cycle, from the water collection points like lakes, rivers and groundwater aquifers, to the reservoir and water pipes that transport it to the consumer. This also applies to the sewage system that takes the used water back to the treatment plants or collecting points.

In addition to the important EU Water Directives, water quality monitoring is also a target of several global challenges reported in the EU Digital Single Market for water services⁴ calling to use more ICT and Digital service for Water or the recent EU green deal policies⁵ published in 2020 where water will play a pivotal role, particularly for the Clean Energy, Sustainable Industry, Biodiversity, From Farm to Fork and Eliminating Pollution thus heading to the realisation a Water Smart Society according to Water Europe.⁶ These documents highlight among others the need for using ICT technologies, the global healthcare issues, the demand for fresh water, the food/beverage quality and safety, the environmental protection and the security strategies to reduce intentional contamination, all of the above having worldwide massive economic, natural and social impacts. However, despite an increasing demand for adaptability, compacity and performances at ever decreasing costs, the vast majority of water network monitoring systems remains based on sensor nodes with predefined and vertical applicative goals hindering interoperability and increasing costs (OPEX and CAPEX) for deploying new and added value services. Innovative technological products could answer the following acute needs in the field:

- **Need for multifunctional probes at low cost:** Typically, 10 different kinds of sensors, each with a unit price in the order of € 300 to € 1000, are required to monitor points of interest in a network, which is not economically viable for large scale deployment. Some multiparameter probes exist on the market but their cost, ranging from € 3.000 to € 25.000, remains a bottleneck towards their widespread use. The issue is further emphasized by the decrease in water consumption, observed notably in Germany, which lowers the turnover for operators of water networks and thus pushes them to limit their investment in monitoring solutions.
- **Need for compactness:** Existing solutions for drinking water monitoring do not fit in the 100mm pipes constituting most of the networks. Their large size often results from lack of integration and non-optimized design, and is in part responsible for the high cost.

⁴ Digital Single Market for Water Services Action Plan, <https://ec.europa.eu/futurium/en/system/files/ged/ict4wateractionplan2018.pdf>.

⁵ https://ec.europa.eu/info/strategy/priorities-2019-2024/european-green-deal_en.

⁶ <https://watereurope.eu/>.

- **Need for enhanced energy autonomy and resilience:** Permanent power supply isn't always available and there is a need for energy autonomous probe. However, probes could require frequent offline calibrations and maintenance (from 1 to 12 months depending on the product; especially for battery replacement) which is incompatible with permanent monitoring and massive deployment.
- **Need for developing innovative detectors of very high sensitivity:** There is a need to develop a new generation of detectors, whose sensitivity matches the requirements of the end users. In the case of NH₃, the existing sensors do not deliver the required accuracy, hence our proposal of a QCL-based detector. Note further that the system developed for aqua3S, combining a vaporizer and a QCL+photoacoustic detector is unique and can be adapted for other substances for which either there are currently no sensors or for which the existing commercial sensors can't meet the requirements of the end users.
- **Need for easy and plug&play deployment:** Still a lot of probes are wired and connected to proprietary data systems. Such approaches lead to complex and expensive deployment when there is need for a significant number of probes deployed. With the availability of new long-distance, low energy radio technologies such as Lora, Sigfox, NB-IoT and the coming 5G associated to standardised water data models and brokers (e.g., Fiware4water project⁷) can facilitate the deployment of probes and data exploitation.
- **Need for combining all sources of information to maximize the information alert for security:** There exist several sources that can be used for monitoring the water quality including sensors, satellite data, social media, and drones. Each one of these sources has distinct features that add value to alert raising. Specifically, sensors provide reliable real-time measurements on a local level; satellite provide pollutant identification on a greater scale but in more infrequent intervals; social media introduce the end user's aspect in a direct and prompt way on specific on local level and finally, drones can monitor on-demand and from close distance the area of interest and capture events that may affect water quality. Therefore combining data from the aforementioned sources is a way to balance the advantages and disadvantages of each source and eventually offer a more complete and reliable solution towards alert raising.

11.2 New Sensing Techniques Developed for Water Security

In order to address the aforementioned challenges, several direct and indirect sensing technologies are under development by the aqua3S project. In the next sections, a general overview of the aqua3S project including all the technologies included, its objective and its impact is provided. Next, the direct and indirect sensing technologies for monitoring water quality are described in detail.

⁷ <https://www.fiware4water.eu/>.

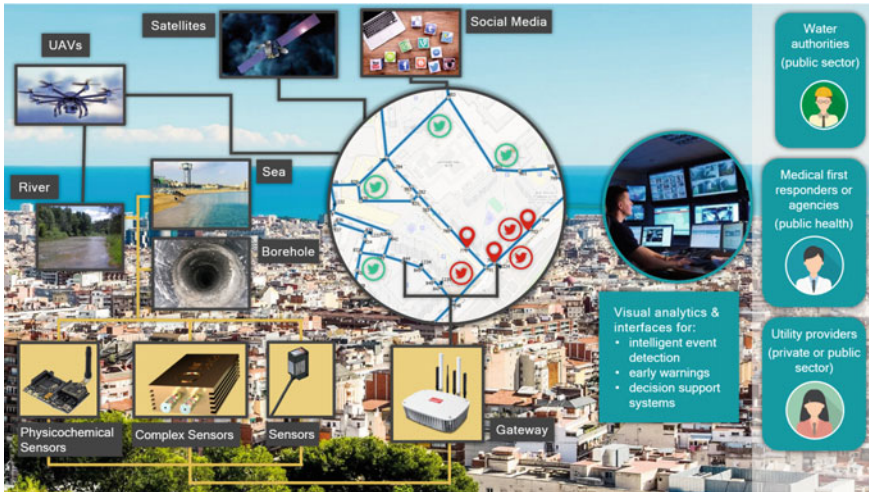


Fig. 11.1 Overview of the aqua3S project concept

11.2.1 Introduction of Aqua3S

aqua3S⁸ is a Horizon 2020 funded project that aims at bridging the gap between the technologies related to the analysis of drinking water and their integration to existing water networks towards reducing the exposure of citizens to potential risks. In order to feel this gap aqua3S combines novel technologies in water safety and security into a framework that integrates data from the operators' legacy systems as well. Furthermore, it creates standardized methods and strategies for water safety and security for all involved stakeholders (Fig. 11.1).

Towards this goal, aqua3S integrates a series of state-of-the-art technological achievements from multidisciplinary fields. Specifically, a combination of high precision key point spectroscopic sensors and widely spread refractive index sensors are deployed at fixed points throughout existing water distribution network; on the other hand, sensor measurements are supported by videos from Unmanned Aerial Vehicles, satellite images and social media observations from the citizens that report low-quality water in their area, promoting social interaction with the citizens by: creating social awareness, deploying public warnings and alerts to the public and deploying first responder's mitigation actions and solutions. Furthermore, aqua3S semantically enriches incoming information from multiple sources, capitalising on advanced knowledge representation and intelligent context-based reasoning solutions. Also, in order to aid organizations identify their level of preparedness and resilience in case of a threat crisis, management modeling is realized covering vulnerability of water and water systems from infrastructure attacks, chemical and biological attacks. Moreover, the outcome of the optimised and parallelized algorithms

⁸ <https://aqua3s.eu/>.

for threat detection and localization, as well as that of the early warning and decision support systems are visualized in a bespoke visual analytics tool. It includes a 3D representation map to offer a highly scalable solution to the potential stakeholders, which supports them during crisis management, delivering full awareness. In order to support decision support, a tool for localised intervention suggestions and a crisis classification module that assesses the severity threat levels are developed. The goal is to provide to the practitioners seamless and valid assessments of the crisis causing by hazardous natural or manmade malicious emergencies. The development of the aforementioned technologies are guided by the user needs and the gaps recognized in the legacy systems. Security requirements are also considered since this objective serves the demands of the water practitioners to safe and secure existing water networks and protects them from natural or malicious hazardous circumstances. The aqua3S platform is evaluated and tested within the operational environment and thus, driven by end-users and experts from the water domain specific pilots design and implement in the field. aqua3S is demonstrated in real use case scenarios in a number of locations, including four large metropolitan cities, Brussels, Paris, Sofia, Thessaloniki, and smaller rural municipalities in Bulgaria, Cyprus and Italy. Last, but certainly not least, aqua3S works towards the standardization and demonstration of strategies and polices to water facilities for the purpose of both safety and security of water. This involves exploring the current and proposed European legal framework regulating water security to understand the current policy requirements and make policy recommendations. Furthermore, current standards and practices being used by water security authorities, industry, policy makers, health care and civil protection across the European Union are identified and assessed to determine standardization gaps, needs and opportunities. Eventually, aqua3S aims at standardizing all the innovative and validated proposed solutions in order to be used by other water authorities beyond the project lifetime.

To sum up, the core objective of aqua3S is to support all the phases in a water related crisis management sequence. Thus, aqua3S aims at improving the awareness of water authorities and companies in relation to a problem by helping the crisis managers to better observe and control their regions, and by improving the collaboration among the involved stakeholders due to reliable and functional connections between the platform end-users. The facilitation of innovative technical solutions also allows water authorities and companies to do more focused and productive crisis management by providing information emerging from various sources to the authorities and by providing a common picture of the situation to all stakeholders and an environment that can be used during preparedness and response for reinforcing communication and information sharing. Finally, aqua3S facilitates the information flow to the water authorities, by considering other communication channels apart from sensors, making possible to inform about an emergency across different devices or services.

11.2.2 *Sensor-Based Techniques*

The aqua3S project is engaged in developing and implementing different sensor technologies to strengthen water quality monitoring networks in different European countries. The current challenge here arises from the lack of cost-effective, sensitive and reliable sensors in aquatic systems. On the one hand, the security of supplied water quality commonly requires specific and expensive analysis devices and sensors, whose costs involve greater amounts of financial investment [2]. On the other hand, the use of commercially available sensors for online water analysis is limited by their working range with respect to temperature and humidity and response delays caused by abrupt changes in ambient parameters [3, 4].

aqua3S integrates a series of state-of-the-art technological achievements from multidisciplinary fields, namely of the area of sensors technology, IoT semantic reasoning, high-level analytics, decision support systems, crisis management and situational awareness focusing on water sector. The sensing aqua3S system will consist of a combination of high precision key point spectroscopic sensor and refractive index sensor deployed at fixed points throughout existing water distribution network of a district of interest. The two main types of sensors will be developed and integrated into the security platform of the water utility partners, delivering real time alerts and quantitative information about the presence of water contaminants:

1. A refractive index (RI) sensor, which consists of a single mode, single polarization vertical cavity surface emitting laser (VCSEL) which feeds through a fiber array unit (FAU) a TriPleX chip with 6 parallel sensing asymmetric Mach Zehnder interferometers (aMZIs). The light collected from the aMZIs is guided with single mode fibers to photodiodes (PDs) and the detected signals are amplified and sampled. The electronic boards that control the VCSEL and the sampling of the detected signals are synchronized. The samples are transferred to the sensing window of the chip via a microfluidic system that comprises a peristaltic pump and proper tubing the interconnects the sample with the photonic chip.
2. A mid-infrared (MIR) spectroscopic sensor which consists of a gas sensing platform named multiSense [5, 6], integrated with a vaporizer and a microfluid device. The multiSense platform combines an optimized infrared quantum cascade laser (QCL) and a heated photoacoustic cell, permitting the accurate detection of the spectral signature of the vaporized gases of a water sample.

In the following subsections we will provide additional details for the development of the sensors and their properties.

11.2.2.1 **Refractive Index Sensor**

The refractive index (RI) sensor aims to monitor the evaluation of the refractive index of the water samples with remarkably high accuracy and provide early warning signals in case any of the water substances' concentration will increase above the

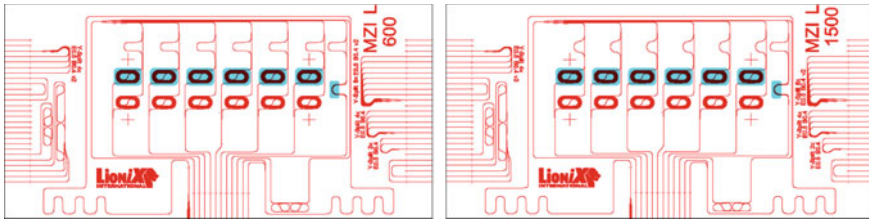


Fig. 11.2 The layout of the photonic circuit. It consists of an asymmetric Mach Zehnder interferometer (aMZI) for calibration purposes, an aMZI with very low sensitivity, and a 6-fold array of sensing aMZIs with a common sensing window. Left: sensing aMZIs with 600 pm and Right: sensing aMZIs with 1500 pm FSR, respectively

safe value. The core of the RI sensor is a photonic structure based on asymmetric Mach Zehnder interferometers (aMZIs) that will be integrated onto the photonic integrated circuit (PIC). The vertical external cavity laser (VCSEL) that will be used as light source, the photodiodes (PDs) that will translate the optical signal to a photocurrent, the corresponding electronic controllers and the microfluidic system are equally important components of the RI sensor which were optimized in terms of the water composition changing detection. Therefore, a compact, low-cost device will be prepared together with the high-level digital signal processing (DSP) algorithms will make the RI sensor capable to detect events happening to the water composition with high precision.

Photonic chip

Passive photonic chips based on a TriPleX platform [7] and having aMZIs as sensing structures, will be used with tapered in- and output that are suited for butt-end coupling to a fiber array unit (FAU), for the detection of the water composition change. The detection mechanism is based on the change of the refractive index in the top-cladding of the aMZIs when different samples are present in this area. This change can be sensed by the evanescent tail of the propagating optical mode, adding a phase delay and afterwards be translated into a wavelength shift of the transfer function (TF) of the aMZIs. (Figure 11.2).

Figure 11.2 presents the layout of the photonic integrated circuit (PIC) in a waveguide structure for single-mode operation at 850 nm. It comprises an asymmetric Mach-Zehnder interferometer (aMZI) for calibration purposes, a reference aMZI with sensing window that has been engineered by locally removing the top-cladding silicon oxide layer above the silicon nitride strip and low (9.4 nm/RIU) in order to be able to follow the very large shift in bulk refractive index changes, and a 6-fold array of sensing aMZIs with a common sensing window. Two different aMZI structures will be used, with two different sensitivities. The structures with 600 pm FSR have 2000 nm/RIU and the structures with 1500 pm FSR have 5000 nm/RIU sensitivity, respectively. Both aMZI types, incorporate spiral structures with a sensing pathlength of 12.5 mm. A multimode interference (MMI) coupler [8, 9], or a Y-junction splits on-chip the input light into eight parts in order to feed all the aMZIs. After these

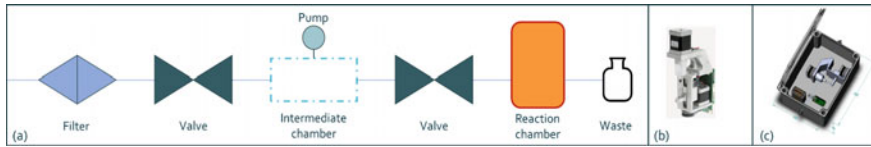


Fig. 11.3 Fluidic cartridge (a), microfluidic pump (b) and waterproof packaging (c)

elements, the signals are forwarded to the output waveguides that form, together with the input waveguide a 9-fold array with $127\ \mu\text{m}$ pitch.

Microfluidic system

The RI sensor should be placed in a lake or a piping system where the refractive index of water is constantly monitored, and an immediate flag is risen at a change of it. In order for the RI sensor to have this capability, a microfluidic system is necessary, where the photonic chip can be easily be exchanged and be auto aligned with the fiber array unit embedded in the cartridge. Within the device, the water will be filtered and actively pumped through the cartridge, over the photonic chip, back into the fluidic system or waste (Figure 11.3).

Part of the microfluidic system will be the fluidic cartridge, as it can be seen in Fig. 11.3a. The latter will be non-disposable and 3D printed with seat for the photonic chip and an alignment structure towards embedded fiber array unit. Furthermore, the fluidic cartridge will contain a filter unit with a pore size that will isolate any extensive water substances (e.g., little pebbles and stones, soil) that would be harmful for the sensing photonic chip. Before and after the microfluidic pump (Fig. 11.3b), which will control the flow rate and the volume of the introducing water sample to the sensing area, two valves will be placed for establishing operating water pressure conditions. The photonic chip will be placed in the reaction chamber, followed by an intermediate reservoir which will act as a pre-waste canopy. The final waterproof, 3D printed packaging (Fig. 11.3c), will include the microfluidic system, the control electronics and the battery pack, providing a few hours of autonomous operation.

Control electronics

The RI sensor will consist of a set of electronic devices and other subsystems, which will be interconnected, enabling the sensor to perform the required individual functions. The operation of all these subsystems will be controlled by an advanced micro-computer with sufficient computing power, memory capacity, number of interface ports and the ability to support different communication protocols with the peripheral elements (Fig. 11.4).

Raspberry Pi4 was selected as the microcontroller and the micro-computer of RI sensor (Fig. 11.4a). It has a powerful processor as well as high memory capacity. Moreover, the board has a built-in Wi-Fi and Bluetooth transceivers which enhance the microcontroller, with the ability to connect to the internet. With the use of the Wi-Fi, the measurement data will be sent to the internet platform and could be collected by a higher-level server for further processing. RPi4 will be responsible for operating

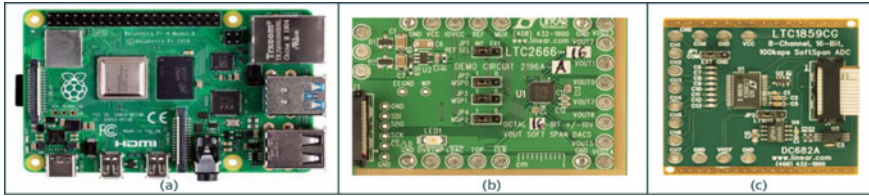


Fig. 11.4 Micro-controller/microcomputer based on RPi4 (a), DAC evaluation board (b) and ADC evaluation board (c)

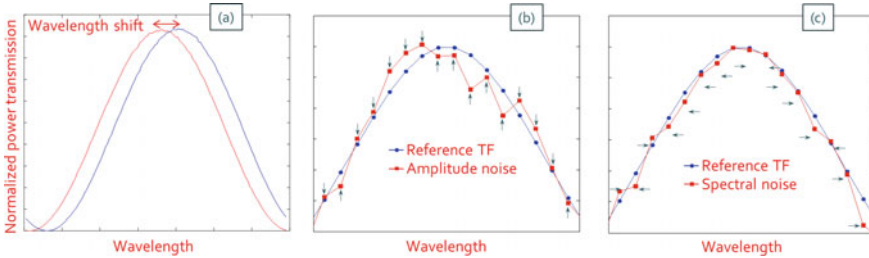


Fig. 11.5 Example of wavelength shift (a), representation of amplitude and spectral noise in the TF (b) and (c) respectively

the RI sensor, providing the driving signal to the VCSEL source, collecting and processing the data from the aMZI on-chip sensors and controlling the fluidic system. The Digital to Analog Converter (DAC) evaluation board, presented in Fig. 11.4b, will be responsible for generating the analog input signal of the VCSEL. The Analog to Digital Converter (ADC), shown in Fig. 11.4c, will be responsible for digitizing the output signal photocurrent that will be generated by the photodiodes and will be amplified by a transimpedance amplifier (TIA), at an appropriate sampling rate so the digital samples can be further processed by the RPi4 microcontroller.

Digital Signal Processing (DSP)

The RI sensor will employ a new generation of DSP algorithms that substantially improve the limit of detection of the refractive index change and a new generation of smart algorithms that classify these changes into suspicious ones or not. This powerful method for the processing of the measurement data, the estimation and calculation of the phase delay that these RI changes add on the aMZI transfer functions (TFs), and the corresponding translation into wavelength shift, is based on the fundamental properties of the well-known Fast Fourier Transform (FFT) (Fig. 11.5).

This measurement data processing method has been evaluated under different levels and types of measurement noise (thermal, spectral, amplitude noise), has taken into account the physical characteristics of the aMZI photonic structures and real system parameters, relevant to the light source, to the photodetectors and to the electronic boards [10, 11]. The RI changes that could be detected, cover the range of Limit of Detection (LoD) from 10^{-2} to 10^{-7} Refractive Index Units (RIU), with ultra-high accuracy (<0.5 pm) describing the efficient nature of the FFT-based algorithm.

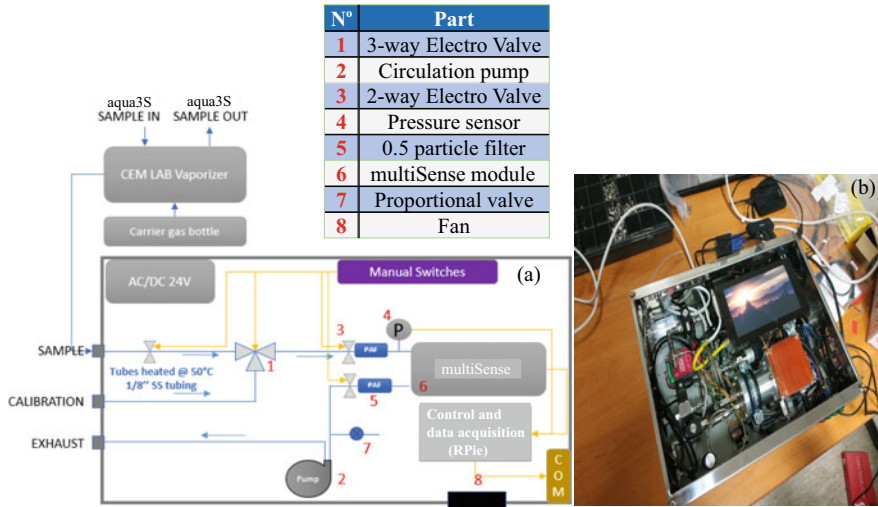


Fig. 11.6 **a** Schematic of the whole gas analyzer to be developed in the aqua3S project. **b** The analyzer, including a multiSense OEM sensor

11.2.2.2 Quantum Cascade Laser Based Sensor

In this section we present the on-going design and development of a Quantum Cascade Laser (QCL) based sensor for real-time detection of contaminants in water. In this study, we focus on investigating the levels of ammonia in water samples which are commonly monitored by water utility companies that participate in the aqua3S project. In principle, ammonia in water is an indicator of possible bacterial, sewage and animal waste pollution resulting in deterioration of the disinfection efficiency as well as taste and odour problems in drinking water [12]. In order to monitor the changes in ammonia (NH_3) levels we will compare the measured spectral signatures and absorption lines of evaporated water taken from the water distribution system to the absorption lines of NH_3 . Thus, our detection scheme relies on a sensor that consists of a gas sensing platform named multiSense [6] which has to be integrated in a gas analyzer developed for contaminant sensing in a water sample. We note that analyzer depicted in Fig. 11.6a, b is a prototype specifically built for the aqua3S project and not a regular product of mirSense. The idea is to vaporize the water sample to obtain a gas sample, the only state of matter suitable for detection within multiSense. The vaporizer is particularly suited for precise vapour flow delivery from the water sample allowing the multiSense gas unit to detect the chemical substances (see Fig. 11.6a). Furthermore, ammonia molecules in vapor state are compatible with laser photoacoustic spectroscopy in the Mid-Infrared (MIR) region (absorbing light with a wavelength between 3 and 12 μm), in which multiSense technology operates [6]. Although THz spectroscopic systems based on semiconductor superlattices have been made or proposed [13–18], trace gas sensing in the mid-infrared using

QCLs still promises higher specificity, sensitivity and extended detection limits (Gas dependent, from a few 10s *ppb* to *ppm* level) [5, 6, 19]. These measurement specifications should comfortably fit with the requirements for an ambient NH_3 sensor. In fact, the advantages of the proposed approach should result in measurements with enhanced accuracy complemented with long-term, unattended and continuous operation in comparison with the existing solutions [3, 4].

The key steps followed for developing the ammonia sensor with enhanced sensitivity can be summarized as follows: (i) Spectroscopy study of the detection of NH_3 in a humidified gas matrix to identify the laser optimum characteristics, (ii) optimization of the QCL design, in particular tuned for the right wavelength and the minimum amount of power necessary to reach the specification limit of detection, (iii) Fabrication and tests of the optimized QCL, (iv) Design and fabrication of the prototype, combining the multiSense unit, the vaporizer and the necessary gas management surroundings.

QCL wavelength selection

We will now describe in detail the wavelength selection process followed for the detection of ammonia in a vaporized water sample. The gas mix will be considered as air, with a temperature between -10 and 50°C and a typical pressure of 1 bar. The measurement gas cell within multiSense will hence be regulated at 60, 10°C above the given limit to ensure that the cell temperature will not drift in case of an external temperature of 50°C . The target molecule will be NH_3 , with a range of detection of 0–100 ppm. The limits of detection in the gas phase have been calculated as 15 ppb based on the liquid evaporative method. The allowed measurement time will be considered as 1 s. The wavelength selection process aims to identify the best spectral range to detect target species with multiSense. In order to cover any case, we study the detection of each gas in the most unfavorable gas matrix: (a) The gas of interest is present at its limit of detection, (b) The other interfering species are present at their maximum potential concentration. The first step is to identify the most intense absorption feature, expressed in the unit $\text{cm}^{-1} \text{ppm}^{-1}$. In a second step, the most favorable lines are compared with multiSense performances to evaluate the corresponding limit of detection. The performance of mirSense photoacoustic detection system is given by its normalized noise equivalent absorption (NNEA) defined at 3σ . The minimum detectable absorption is by definition [20]

$$\alpha_{G,min}(3\sigma) = \frac{\text{NNEA}}{P_L} \sqrt{\Delta f}, \quad (11.1)$$

where P_L is the minimum required power and Δf is the detection bandwidth in Hz. Here the NNEA values are given by the multiSense datasheet as well as the correspondence between the available acquisition frequency and Δf (equivalent noise detection bandwidth). The strongest absorption lines for NH_3 are found between 900 and 1200cm^{-1} . In ambient air, the choice of the wavelength is not only limited to the choice of a strong line, but rather to a choice of interference-free absorption line. Figure 11.7 demonstrates the strongest absorption lines of NH_3 in the MIR region.

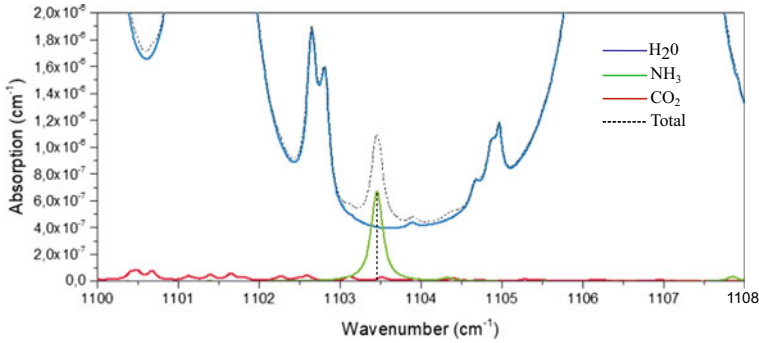


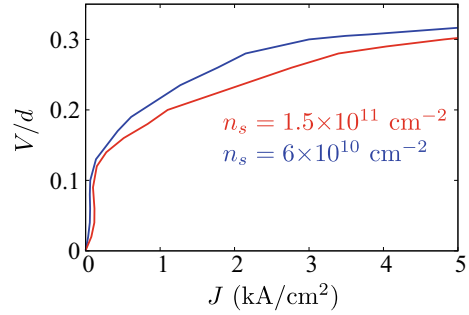
Fig. 11.7 NH_3 absorption at $T = 60^\circ\text{C}$, among the other species of the gas matrix. The vertical dashed line is described in the text

One can notice that the main interfering specie is H_2O (blue line, Fig. 11.7). In order to calculate the minimum required power, we use the detection duration T_d corresponding to detection bandwidth $\Delta f = \sqrt{0.3/T_d} = 7 \times 10^{-2}$ Hz and the NNEA of the multiSense unit $\text{NNEA} = 2 \times 10^{-8} \text{ W cm}^{-1} \text{ Hz}^{-1/2}$. Thus, we estimated a minimum average power, $P_L = 16.4$ mW, by using for the targeted wavelength indicated by the vertical line in Fig. 11.7.

Optimization of the QCL structures

To push QCL based spectroscopy systems to their maximum capabilities, optimization of the QCL structures is needed in combination with accurate simulations. Here, we will perform simulations for QCL structures similar to Ref. [21] designed for light emission near $9 \mu\text{m}$ which desirable wavelength for the detection. Our methodology can be summarized by the following self-consistent procedure [22, 23]: (a) Solution of the band structure problem including mean field effects due to ionized doping regions to be used as input for the quantum transport and many body solvers, (b) Solution of the Dyson equations describing carrier-phonon, potential fluctuation, impurity scattering and interface roughness mechanisms leading to realistic steady state nonequilibrium distributions. (c) Solution of the nonequilibrium Green's functions equations to determine the current voltage characteristic of the QCLs and (d) Solution of the nonequilibrium Green's functions (NEGF) equations for the optical polarization including many body effects. Absorption/gain spectra are obtained in linear response in the field, but they are arbitrarily nonlinear in the carrier density. Conventionally the operation of QCLs is modeled by rate equations between the levels of the active regions, while the current flow through the injector is taken into account phenomenologically. The transition rates can be evaluated microscopically within Fermi's golden rule for electron-electron scattering and phonon scattering. On the other hand, NEGF approach is a more sophisticated approach which allows consistent treatment of the quantum evolution and the scattering processes. To determine now the transport properties of QCL structure under bias, we need the information contained in the following NEGF: the retarded Green's function \mathbf{G}^{ret} and the corre-

Fig. 11.8 Current-voltage characteristics at room temperature for two different doping concentrations



lation function $\mathbf{G}^<$. These functions obey the quantum transport equations that can be delivered from the Hamiltonian $\hat{H} = \hat{H}_0 + \hat{H}_{scatt} + \hat{H}_{MF}$, where \hat{H}_0 contains the kinetic energy, the superlattice potential, the electric potential due the applied voltage. \hat{H}_{scatt} describes the different interaction mechanism leading to electron scattering and which are treated in form of self-energies. Finally \hat{H}_{MF} is the mean field due the charge distribution in the heterostructure which is obtained by solving Poisson's equation. We evaluate the current density using the rate of change of the position operator [24]

$$J(t) = \frac{e}{V_s} \frac{i}{\hbar} \langle [\hat{H}, \hat{z}] \rangle, \quad (11.2)$$

where $J(t)$ is the average current density flowing in the system volume V_s and it has two contributions

$$J_0(t) = \frac{e}{\hbar V_s} \text{Tr}\{[\hat{H}_0, \hat{z}] \mathbf{G}^<(t, t')\} \quad \text{and} \quad J'(t) = \frac{e}{V_s} \frac{i}{\hbar} \langle [\hat{H}_{scatt} + \hat{H}_{MF}, \hat{z}] \rangle. \quad (11.3)$$

Numerical applications of our theory for a structure similar to [21] were performed at a room temperature. Figure 11.8 shows the current-voltage characteristics for different sheet densities n_s . Once the Green's functions are found and current-voltage relations calculated, we will re-diagonalise the problem in the Wannier Stark basis, leading to the actual energy states needed for optical processes. The polarization function is calculated leading to the optical susceptibility from which absorption/gain and refractive index changes can be obtained. The calculation of absorption/gain spectra will be compared with transmission spectroscopy measurements of QCLs operating in the mid-infrared.

Currently, we are completing the development activities of the MIR-sensor involving carefully arranged processes of selection, customization and integration of the sensor units to meet the technical requirements determined by the end users of the aqua3S project. Details will be published elsewhere. The new sensor will be integrated into the security platform of water utility partners and tested in field conditions.

11.2.3 Complementing Direct Sensing by Indirect Techniques

This section presents the indirect techniques developed within aqua3S for monitoring water quality. The sources that considered are satellite data retrieved from the Copernicus Open Access Hub and data from social media platforms and specifically from Twitter. These data complement the data from sensors in the task of water monitoring by identifying tweets related to water quality and the existence of pollutants on water surface using satellite data.

11.2.3.1 Area Monitoring Using Satellite Data

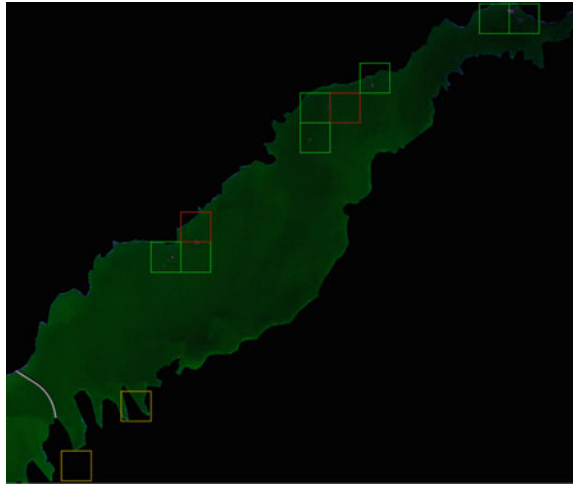
In the recent years, the advent of remote sensing technologies provided an abundance of satellite data covering areas all over the world. These collections of information over large spatial areas, are systematically renewed, allowing in a timely manner the characterization of the natural features on the ground or water and observe surface areas. As a result, monitoring how they change over time, helps us determine potential hazards and schedule future action steps.

For the discovery and downloading of satellite images, the Copernicus Open Access Hub has been proved a solid choice. The European Space Agency (ESA)'s platform provides open and immediate accessibility to recent Sentinel products with the possibility to also request and download older archived products that helped with the observation of past incidents. The high availability of the service guarantees a constant source of products with a systematic coverage over most of the continental land surfaces and coastal waters. The supported API allowed to programmatically set the criteria for fetching the required data and feed them to the analysis process. The supported filters include among others the definition of the mission's name, the sensing time, the bounding box of the underlying area of interest, and the product type. The process is executed multiple times within the day in order to timely retrieve the newest products that meet the set requirements.

After a new Copernicus product has been collected, it is passed to either the flood monitoring or oil spill detection analysis algorithms in order to generate the corresponding information maps, depending on the satellite mission name. As far as the *flood monitoring* is concerned, it uses Synthetic Aperture Radar (SAR) data that are captured by the Sentinel-1 constellation. SAR data ignore weather and illumination condition allowing it to penetrate clouds and operate during even nighttime. The aforementioned properties make this satellite type ideal to track flood outbreaks. On the other hand, the *oil spill detection* is based on Sentinel-2 optical data, that provide a more vivid delineation of the captured area and attempts to detect pollutants oil spills on surface water like lakes that pose a threat to the water supply network.

For the flood monitoring algorithm, we applied a change detection technique on a time series of processed Sentinel-1 products. We followed some pre-processing steps that are required in order to transform the Sentinel-1 GRD-IW product to a format that is suitable for further analysis. We applied the orbit file that provides an accurate position of SAR image and performed thermal noise removal, radiometric

Fig. 11.9 Oil spill map of a Balkan lake. With green the successfully identified oil spills. In red the missed oil spills. With yellow the false positives



calibration, speckle noise removal, terrain correction and eventually converted the backscatter intensity values from linear scale to logarithmic. To detect the changes relative to flood, we take into account a time series of the previous 30 satellite images, in order to detect fluctuations when comparing to a normal state of an area. Outlier detection was applied comparing the target image against the time series. For the outlier detection (i.e., the flood areas) [25] we used the formula:

$$\frac{(X - T S_{mean})}{T S_{std}} > \alpha \quad (11.4)$$

The oil spill detection algorithm takes as input a Sentinel-2 image and splits it into smaller patches. Then it attempts to tackle the hazard as a binary classification problem by predicting the presence of oil spill within each patch of the initial image. The VGG16 (Visual Geometric Group 16) [26] convolutional neural network architecture was selected. We re-trained the four top layers of the VGG16 to fine-tune the network. Eventually the last layer that uses a SoftMax activation was modified in order to support the two output classes of oil and water respectively. For the dataset due to shortage of past incidents and annotated data we created an augmented dataset based on patches of a previous clean image where we artificially added some randomly shaped and colored oil spills. We combined Nir, Green & Swir Sentinel-2 bands to form the composite images, with water appearing transparent, in contrary to oil, shores and other objects that are highlighted in a red color (Figure 11.9).

In essence, the vast number of sources of satellite imagery allowed the predicting and monitoring over a variety of incidents that occur on earth's surface. With the small interval of the new data on the Copernicus platform makes possible the timely and precise identification of the flooded areas and outbreaks of oil spill events playing a key role in the insurance of public safety against natural phenomena or deliberate actions.



Fig. 11.10 Example of a collected tweet, enriched with a reliability score and detected location

11.2.3.2 Social Media Sensing

The wide adoption of social media in the daily life of billions of people results to large and continuous streams of online content generated by users that can timely reflect what is happening around the globe. Since any topic can be covered nowadays by social media posts, water quality and security is another subject that is expected to concern online users. Thus, we argue that the acquisition of such social media data can serve as an alternative source of information and support the creation of social awareness in a water distribution network.

We have selected to use the social media platform of Twitter for two reasons. First, the platform’s high popularity promises prolific and real-time crowd-sourced information. Secondly, Twitter offers various free API endpoints for retrieving tweets, amongst which Twitter Streaming API that allows access to Twitter’s public stream of data and retrieves tweets almost at the moment that they are published. Using the filtering option “Track” provided by Streaming API, we are able to retrieve posts whose text contains one or more keywords. Considering that the topic to be monitored on social media is water quality and security, we have specified a set of related keywords to track (e.g., “muddy water”, “water odour”, “dam pollution”, etc.) and each time a newly published tweet matches these criteria, it is instantly retrieved.

After a new tweet has been collected, two analysis techniques are performed to extract further knowledge from the social media data, each one for a different purpose. The *reliability estimation* aims to tackle the growing problem of fake news distributed through social media, by filtering out suspicious posts, while the *automatic geotagging* targets to supplement tweets with geographical information, based on the locations that are mentioned in their text. Both analysis results are appended to the information originally provided by Twitter in order to enrich the tweet (Fig. 11.10).

The reliability is estimated by an automatic verification technique [27, 28] that is able to predict whether a given tweet is real or fake, together with a confidence value. It relies on two independent classification models that are built on the same training data, but use different sets of features: tweet-based (e.g., text characteristics, existence of emoticons, number of hashtags, etc.) and user-based (e.g., number of followers, existence of profile image, etc.). After feature extraction is completed, model bagging is applied to obtain more reliable results, based on the predictions of the two classification models, i.e., one from each feature set. The classification

algorithm is Logistic Regression, while an agreement-based retraining strategy is performed at prediction time to combine the two bags of models in a semi-supervised learning manner.

The automatic geotagging methodology is motivated by the limited geographical information that Twitter provides and is able to turn tweets into geo-referenced data based on their textual content. In particular, each tweet text is properly preprocessed and is fed to a Bidirectional Long Short-Term Memory model [29] that assigns Named Entity Recognition labels to every qualified word of the text. Single words (e.g., “Rome”) or sets of words (e.g., “River Tiber”) that are recognised as locations are given as query to the OpenStreetMap API,⁹ which connects them with open geo-data and responds with the exact WGS84 coordinates. However, it should be noted that this methodology is language-specific.

To sum up, the real-time collection of citizen observations on Twitter based on water-related keywords and their automatic geotagging can serve in the detection and localization of potential incidents of water pollution, either by accident or malevolent acts. In addition, the estimation of the posts’ reliability can improve the quality of incoming information and protect end users from hoax news.

11.3 Low-Cost Multiparameter Water Quality Monitoring Through Nanomaterials

Current sensors cost, represents a major blocking factor to largely deploy sensors which are needed to monitor various water quality parameters (usual and new ones) within various water contexts. To address this issues, the H2020 research project PROTEUS(10) followed by LOTUS(11) conduct advanced research which are detailed here after.

11.3.1 Monitoring Matrix Composition: A Challenge of In-situ Water Quality Monitoring

The 2000 EU Water Framework directive includes no less than 12 classes of pollutants and 45 priority substances relevant to water policy in its 2014 consolidated version [30]. This list of priority pollutants and their regulatory thresholds vary across the globe [31]. Even across a reduced spatial perimeter, such as a single lake or river basin or urban water body, the composition of a water matrix, and consequently of water quality, varies strongly spatially and temporally [32–34].

As a consequence, assessing accurately water quality requires the capability to measure accurately extremely wide range of chemicals in concentrations ranging

⁹ <https://wiki.openstreetmap.org/wiki/API>.

from sub-ppb to ppm, as well as biological materials. The complexity of the analytical requirements naturally favors the use of off-site laboratory tools, such as those described in [35]. They need to be coupled with on site sampling strategies, which remain to this day economically, practically and scientifically challenging [36].

Naturally, water quality stakeholders would like to bring laboratory methods directly to the field, while bringing down their costs. In practice, the monitoring systems widely available today for real-time water quality are single parameter sensors for temperature, pH, turbidity, (free and total) chlorine, dissolved oxygen, total organic carbon, specific conductance, oxidation reduction potential, fluoride, nitrate, arsenic... This panel of relatively affordable and more or less reliable single parameter sensors (typically from 300 to 3000€ field-installation-costs not included) is usually used to indicate water contamination but is seldom capable of pointing out the cause of a contamination. Henceforth, it is being progressively complemented by expensive (typically from 3000 to 15,000€, field-installation-costs not included) and bulky commercial multiparameter probes integrating in a single package several single parameter probes [37].

While these multiparameter probes theoretically satisfy the need for in-situ water composition monitoring, in practice they remain considerably less deployed than monoparameter probes because of their high costs, large size, low versatility, heavy calibration requirement and lack of reliability. The future of in-situ water quality monitoring lies in the capability to offer multiparameter probes with the cost, size, sensing quality, reliability, maintenance requirements of single-parameter sensor probes. This has precisely been the goal of the 2015–2018 H2020 project Proteus,¹⁰ followed by still ongoing H2020 projects LOTUS¹¹ and Fiware4Water,¹² as well as the SATT Paris Saclay project Micad'O,¹³ four projects whose outcomes and status we report in the following sections.

11.3.2 Carbon Nanotube-Based Multiparameter Water Quality Sensing: A Solution?

Nanomaterials are highly promising to enable high sensitivity and low cost water quality monitoring [38]. Among nanomaterials, carbon nanotubes (CNTs) have been heavily studied for environmental monitoring due to their excellent chemical stability, their large specific surface area, as well as their commercial availability in bulk at reasonable cost [39]. Notably, CNTs have been reported for electrical sensing in water of pH, micronutrients and metal ions, nitrogen under its different forms, hardness, dissolved oxygen, disinfectants, sulfur under its different forms. However, this remains mostly monoparameter sensing, except for some heavy metals moni-

¹⁰ <http://www.proteus-sensor.eu/>.

¹¹ <https://www.lotus-india.eu/>.

¹² <https://www.fiware4water.eu/>.

¹³ <https://satt-paris-saclay.fr/vitrine-technologique/micado/>.

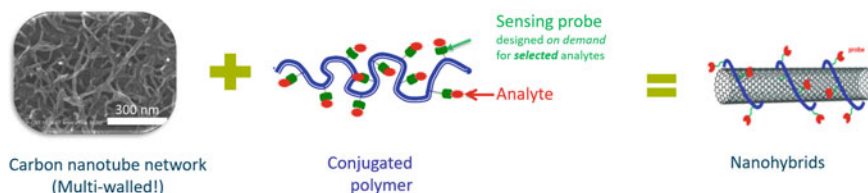


Fig. 11.11 Functionalization of carbon nanotubes by conjugated polymers to create nanohybrids capable to detect selectively predefined analytes

tored jointly via stripping voltammetry (for example [40] for metals Cadmium, Zinc and Lead). There are also frequent reports on the monitoring of pH jointly with a secondary species [41].

However, beyond these two specific scenarios, there are no report on true multi-parameter sensing for water quality monitoring with CNTs. This is surprising because sensor array based on CNTs are regularly reported regarding air quality monitoring [42] or biosensors [43]. The principle of operation of CNT sensor array is as follows: while pristine (e.g., without additives) CNTs have high sensitivity to most analytes, they also have low selectivity between different analytes [44]. To enhance their selectivity, CNTs are functionalized with materials featuring known sensitivity to the target analyte. To enable the detection of several species at the same time, devices incorporating CNT with different functionalizations are located next to each other and their data are correlated to enable accurate derivation of the concentration of target species [45].

During Proteus project, we endeavored to demonstrate at prototype scale the viability of this approach for multiparameter water quality monitoring, as in reported in Sect. 11.3.3. Following the success of Proteus, ongoing projects aim at bringing the technology at pre-industrial level for field deployment and subsequent commercialization, as is detailed in Sect. 11.3.4.

11.3.3 Success at Prototype Level

During Proteus, we first designed, patented and synthesized a set of polymers [46] suitable to enhance via functionalization the selectivity of CNTs, as shown in Fig. 11.11. CNTs carrying different polymers were integrated into a matrix of chemistors (e.g., resistive devices whose resistance changes with the concentration of the target analyte), as shown in Fig. 11.12. The matrix of chemistors was then co-integrated with microelectronics-based physical sensors (temperature, conductivity, flow rate, pressure). The resulting sensor chip was then co-integrated, jointly with a CMOS-chip-based analog front end, into a sensor head mounted into a waterproof sensor node (Fig. 11.13).

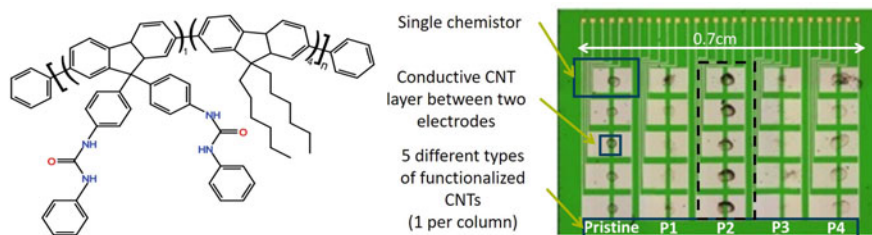


Fig. 11.12 Left: Formula of the FF-UR polymer, one of the conjugated polymers used for CNT functionalization. Right: Image of a 5×5 CNT chemistor array with 5 different types of functionalized CNTs

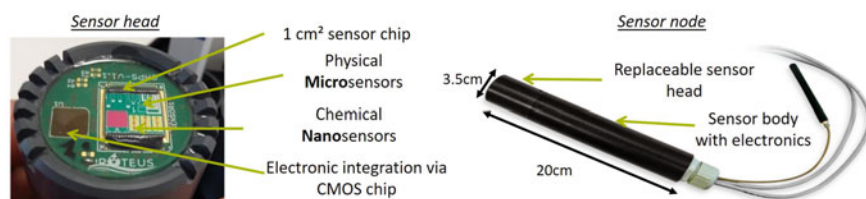


Fig. 11.13 Images of (left) a sensor head and (right) a sensor node

The sensor node had the capability, validated at lab level and partially in Sense-City¹⁴ 40m long water loop, to monitor the nine following quantities: temperature, conductivity, pressure, flow rate, pH, Chlorine, Chloride, Nitrate and Calcium. With its size (3.5cm in diameter by 20 cm in length), the sensor node had a volume over ten times smaller in volume than competing commercial solutions, e.g., was close in size with existing single-parameter sensing solutions. In small series production (5–10 units), the unit fabrication cost was evaluated at around 550€ only, which made the product already widely competitive with its commercial counterparts. Moreover, numbers clearly showed the capability to reach sales price lower than 1000€ (calibration included) for production volume in the 10000 units per year.

As synthesized in Fig. 11.14, the sensor node was able to interface with a production SCADA (Supervisory Control and Data Acquisition) system using the MODBUS protocol¹⁵ over a RS485 (wired) or over a LORA (Long Range) (wireless) connection. Alternately, using an event-based architecture inspired from Internet of Things, it could send data to a dedicated cloud using the MQTT (Message Queuing Telemetry Transport) protocol over LORA. It enabled the connection of the system to advanced visualization tools and with machine-learning-based predictive software. The sensor node could also operate completely autonomously in energy via the coupled use of a piezoelectric vortex generator (installed in the drink water pipe), a solar panel, a CMOS-integrated power management unit, an low-power

¹⁴ <https://sense-city.ifttar.fr/>.

¹⁵ MODBUS is a de facto market standard on communication bus, and it the word originates historically from "modicum communication bus".

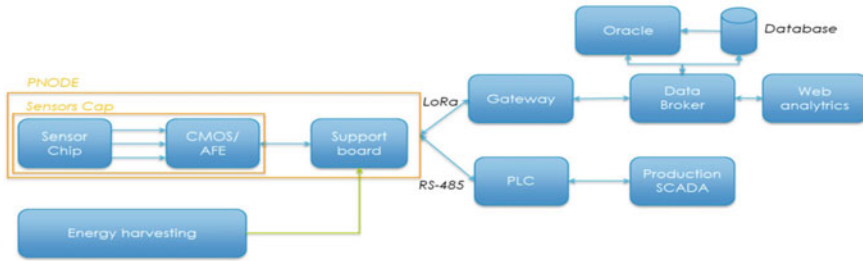


Fig. 11.14 IT architecture of Proteus sensor node deployment. AFE: analog front end. PLC: programmable logic controller. SCADA: Supervisory control and data acquisition. Oracle: Proteus-developed IA-based predictive module

CMOS (complementary metal-oxide semiconductor) analog front end, and finally an adaptive software (state machine) optimizing power consumption based on sensor measurements and energy availability.

Beside demonstrating the viability of multiparameter water quality monitoring with functionalized carbon nanotube-based chemistor array, the project also showed determining progress beyond state of the art in various fields of science:

- The cointegration of CNT sensors with microelectronic sensors on a single monolithic 1cm^2 silicon chip was at the state of the art regarding both the high number of parameters monitored (9 proved so far) and the high number of sensing elements in a single chip (32 at most).
- Some of the sensing elements inside the chip were completely novel: the flowrate sensor on a silicon chip on the one hand, the CNT-based nitrates, calcium and chloride sensors on the other hand.
- The use of functionalized CNT-based chemistor array for water quality monitoring was novel as well, not to mention that it was the first time such level of integration, with CMOS, MEMS, packaging, energy harvesting and cloud-based data gathering was achieved for CNT-based water quality sensors.
- Regarding the CMOS chip, the ADC design was state of the art, while a completely new design for filtering was implemented. The inductor-free DC-DC converter based in a switched-capacitor topology was also beyond SOTA.
- On the piezoelectric vortex generator for energy harvesting, the results yielded a new understanding of the physics of this type of harvesters. Moreover, field trials prove that energy harvesting is definitely possible from an actual drink water pipe with intermittent flow.
- At software level, Proteus sensor node cognitive capabilities, notably enabling optimized management of energy supply, surpassed the SOTA for commercial devices.

11.3.4 Reaching Pre-industrial Series for Field Deployments

Despite its success, Proteus outcomes did not allow for direct commercialization of the technology because of three main factors: high device-to-device performance variability of the chemical sensors, no field validation of system reliability (not permitted within the project time frame) and ownership of the technology building blocks split by different stakeholders (a natural drawback of collaborative projects). Since the conclusion of Proteus, NACRE research team, the joint research team between Université Gustave Eiffel, CNRS and Ecole Polytechnique in France which already coordinated Proteus, has been tackling these challenges through various projects. In short, LOTUS focuses on reproducibility and field deployments of the technology, Fiware4water on its reliability through hardware and software means and Micad'O on its commercial launch through the startup Soterias.¹⁶ The three projects include field testing of the solution to demonstrate its real life suitability.

The first scheduled product monitors temperature, conductivity, chlorine and pH in a single package. It targets 3 months under flow without calibration, for a sales price in the 3,500 € range. Though the selected design—improved from Proteus—allows to target up to 20 different analytes on the same chip in addition to temperature and conductivity, it was elected to reduce the scope of the product for the short term to a limited number of parameters in order to focus more intensively on reproducibility, reliability and industrialization. This first panel of parameters was determined to be the best common denominator between the requirements of the different investigated use cases. Parameters such as hardness, dissolved oxygen, nitrate, fluoride, arsenic and iron are already under investigation for the following versions.

A process to achieve pre-industrial series is now available: sensor chips can be produced with perfect yield and sufficient reproducibility at a rhythm of about 30 chips per week. A process for full sensor node assembly is subsequently available. It could easily reach 100 sensor nodes per month of production capability. While the packaging of the sensor node has remained similar in shape and size to Proteus, the solution is now plug-and-play to any micro computer (RaspberryPi for instance) via a standard USB port. Data is displayed in real-time through Grafana-enabled dashboards. As an option, the sensor can be operated through a connector box specially developed by the company EGM to enable wireless communication (via LORA) and energy autonomy (via solar panel).

Performances and reliability testing started during the last quarter of 2020 and results are preliminary only. Sensing performances are promising: average error on active chlorine, pH and conductivity are around respectively 0.05 mg/L, 0.2 pH units and 20 μ S/cm, while limits of detection lie around 0.02 mg/L, 0.07 pH units and 16 μ S/cm. Longest lifetime is one month and counting of continuous operation in static water, while tests under flow are pending.

The outcomes of these tests are eagerly awaited to launch field deployments during second quarter of 2021. Two deployments in drink water networks are planned, one in Cannes, France, the other in Guwahati, India. A use case enabled by its small

¹⁶ <https://www.soterias.solutions/>.

size, the solution will also be integrated in a mobile chlorination station outfitting a drink water distribution tanker in Bengaluru, India. It will be also be adapted into a portable solution to diagnose drink water well quality in Guwahati and into a boat-mounted solution to diagnose river quality in Varanasi, India. In parallel, it will be used to optimize irrigation efficiency in Jalgaon, India, and to optimize operations in innovative waste water treatment plants in Warangal and Chennai, India.

These demonstrations will introduce Soterias multiparameter sensor probe to a wide panel of scenarios of water quality monitoring in Europe and India. This is essential to launch commercialization, then to later reach large volume of sales, which in turn will allow to decrease costs and further expand sales. A cost reduction by a factor of 10 is hoped for by stakeholders, which roughly would require sales beyond the 10,000 units range. While this price reduction will be in part achieved through economy of scale, there will be technological challenges to meet for the large volume manufacturing and calibration of CNT-enabled chips.

11.4 Conclusions and Future Work

Water is vital for all life and thus its protection is of great importance. Unfortunately, water quality and quantity is under threat due both to natural or man-made disasters. The World Health Organization and the EU have taken several measures towards its protection, such as strong regulatory norms and implementation of water safety plans. Along with the water directives, several European projects revolve around water safeguarding by developing innovative technological products. As far as the outcome of such research actions are concerned, they involve the development of detection technologies to analyse drinking water and the interconnection of safety- and security-related networks of sensors that are deployed among water supply and distribution networks. The aim of such actions is to check how the use of current sensor technologies, including methods to monitor reservoirs, and sea or river levels for early warning, could support water safety and security.

Regarding the technologies presented in this chapter, they involve the development of new low-cost sensors with high sensitivity that can be installed in several places of the water distribution network and measure single or multiple substances. As far as the aqua3S project is concerned, apart from the direct sensing methods that involve the use of sensors, other innovative indirect sensing methods are presented that involve the use of satellite imagery and social media. These methods although don't have the accuracy of sensors, they offer real-time assessments (social media) or cover larger areas (satellite imagery). The project has also proven that new technologies can help detecting new pollutants. The LOTUS project has also made evidence that advance chip approach (e.g., with MEMS and CNT) can be the solution to produce mass market sensor and thus drastically decreased the cost (i.e., X10 less)

Thus, all together, by exploiting and combining the information offered by all the aforementioned techniques, we are moving towards better monitoring of larger parts of the networks including the water sources and water distribution network

and eventually, we are making a step towards ensuring water safety and security. What is of utmost importance to stress is that water safety and security are part of the “crisis management and civil protection” field, which is prioritized by the European Committee for Standardization and it involves establishing security-related standards that aim at facilitating response, effectiveness, efficiency and cooperation during hazardous events. Thus, with the proposed technologies we are also addressing some of the challenges defined by Mandate M/487 to Establish Security Standards. In complement water quality can be more largely monitored ensuring also water safety for the citizens.

Acknowledgements This work was supported by the EC-funded projects H2020-644852-Proteus, H2020-832876-aqua3S, H2020-820881-LOTUS and H2020-821036-Fiware4Water and by the SATT Paris Saclay project Micad’O.

References

1. Quevauviller P (2005) Emerging tools for monitoring water quality. *J Environ Monit* 7:545
2. Raich J (213) Review of sensors to monitor water quality. European reference network for critical infrastructure protection (ERNICIP) project
3. Cämmerer M, Mayer T, Penzel S, Rudolph M, Borsdorf H (2020) Application of low-cost electrochemical sensors to aqueous systems to allow automated determination of nh_3 and h_2s in water. *Sensors* 20(10):2814
4. Yaroshenko I, Kirsanov D, Marjanovic M, Lieberzeit PA, Korostynska O, Mason A, Frau I, Legin A (2020) Real-time water quality monitoring with chemical sensors. *Sensors* 20(12):3432
5. Carras M, Aoust G, Maisons G, Brun M, Spitz O, Grillot F (2019) Quantum cascade laser technology and applications at mirsense, from spectroscopy to chaotic communication
6. Gorrochategui P, Aoust G (2020) MultiSense OEM gas analyzer demo kit general user’s guide. mirSense
7. Wörhoff K, Heideman RG, Leinse A, Hoekman M (2015) Triplex: a versatile dielectric photonic platform. *Adv Opt Technol* 4(2):189–207
8. Gounaridis L, Groumas P, Schreuder E, Heideman R, Katopodis V, Kouloumentas C, Avramopoulos H (2015) Design of grating couplers and mmi couplers on the triplex platform enabling ultra-compact photonic-based biosensors. *Sens Actuators B: Chem* 209:1057–1063
9. Gounaridis L, Groumas P, Schreuder E, Tsokos C, Mylonas E, Raptakis A, Heideman R, Avramopoulos H, Kouloumentas C (2019) Design of ultra-compact multimode interference (mmi) couplers and high efficiency grating couplers in triplex platform as part of a photonic-based sensor. In: *Integrated optics: devices, materials, and technologies XXIII*. vol 10921. International Society for Optics and Photonics, p 1092127
10. Gounaridis L, Groumas P, Schreuder E, Heideman R, Avramopoulos H, Kouloumentas C (2016) New set of design rules for resonant refractive index sensors enabled by FFT based processing of the measurement data. *Optics Exp* 24(7):7611–7632
11. Gounaridis L, Groumas P, Schreuder E, Tsekenis G, Marousis A, Heideman R, Avramopoulos H, Kouloumentas C (2017) High performance refractive index sensor based on low q-factor ring resonators and FFT processing of wavelength scanning data. *Opt Exp* 25(7):7483–7495
12. Organization WH et al (2017) Guidelines for drinking-water quality: incorporating first addendum (2017)
13. Apostolakis A, Pereira MF (2019) Controlling the harmonic conversion efficiency in semiconductor superlattices by interface roughness design. *AIP Adv* 9(1):015022

14. Apostolakis A, Pereira MF (2019) Potential and limits of superlattice multipliers coupled to different input power sources. *J Nanophoton* 13(3):1–11. <https://doi.org/10.1117/1.JNP.13.036017>
15. Apostolakis A, Pereira MF (2020) Superlattice nonlinearities for gigahertz-terahertz generation in harmonic multipliers. *Nanophotonics* 9(12):3941–3952
16. Pereira MF, Zubelli JP, Winge D, Wacker A, Rodrigues AS, Anfertev V, Vaks V (2017) Theory and measurements of harmonic generation in semiconductor superlattices with applications in the 100 ghz to 1 thz range. *Phys Rev B* 96. <https://doi.org/10.1103/PhysRevB.96.045306>
17. Pereira MF, Anfertev VA, Zubelli JP, Vaks VL (2017) Terahertz generation by gigahertz multiplication in superlattices. *J Nanophoton* 11(4):1–6
18. Pereira M, Anfertev V, Shevchenko Y, Vaks V (2020) Giant controllable gigahertz to terahertz nonlinearities in superlattices. *Sci Rep* 10(1):1–9
19. Dhillon S, Vitiello M, Linfield E, Davies A, Hoffmann MC, Booske J, Paoloni C, Gensch M, Weightman P, Williams G et al (2017) The 2017 terahertz science and technology roadmap. *J Phys D: Appl Phys* 50(4):043001
20. Kosterev AA, Tittel FK, Serebryakov DV, Malinovsky AL, Morozov IV (2005) Applications of quartz tuning forks in spectroscopic gas sensing. *Rev Sci Instr* 76(4):043105
21. Lyakh A, Maulini R, Tsekoun A, Go R, Patel CKN (2012) Multiwatt long wavelength quantum cascade lasers based on high strain composition with 70% injection efficiency. *Opt Exp* 20(22):24272–24279
22. Pereira M Jr, Lee SC, Wacker A (2004) Controlling many-body effects in the midinfrared gain and terahertz absorption of quantum cascade laser structures. *Phys Rev B* 69(20):205310
23. Schmielau T, Pereira M Jr (2009) Nonequilibrium many body theory for quantum transport in terahertz quantum cascade lasers. *Appl Phys Lett* 95(23):231111
24. Lee SC, Wacker A (2002) Nonequilibrium green's function theory for transport and gain properties of quantum cascade structures. *Phys Rev B* 66(24):245314
25. Iglewicz B, Hoaglin DC (1993) How to detect and handle outliers, vol 16. *Asq Press*
26. Simonyan K, Zisserman A (2014) Very deep convolutional networks for large-scale image recognition. *arXiv preprint arXiv:1409.1556*
27. Boididou C, Papadopoulos S, Apostolidis L, Kompatsiaris Y (2017) Learning to detect misleading content on twitter. In: *Proceedings of the 2017 ACM on international conference on multimedia retrieval*, pp 278–286
28. Boididou C, Papadopoulos S, Zampoglou M, Apostolidis L, Papadopoulou O, Kompatsiaris Y (2018) Detection and visualization of misleading content on twitter. *Int J Multimedia Inf Retr* 7(1):71–86
29. Lample G, Ballesteros M, Subramanian S, Kawakami K, Dyer C (2016) Neural architectures for named entity recognition. *ArXiv preprint arXiv:1603.01360*
30. Directive 2000/60/ec of the european parliament and of the council establishing a framework for community action in the field of water policy (Oct 2000). <http://data.europa.eu/eli/dir/2000/60/2014-11-20>
31. Kruse P (2018) Review on water quality sensors. *J Phys D: Appl Phys* 51(20):203002
32. Kuo YM, Liu W, Zhao E, Li R, Muñoz-Carpena R (2019) Water quality variability in the middle and down streams of Han river under the influence of the middle route of south-north water diversion project, China. *J Hydrol* 569:218–229. <https://doi.org/10.1016/j.jhydrol.2018.12.001>. <http://www.sciencedirect.com/science/article/pii/S0022169418309296>
33. Shi B, Bach PM, Lintern A, Zhang K, Coleman RA, Metzeling L, McCarthy DT, Deletic A (2019) Understanding spatiotemporal variability of in-stream water quality in urban environments—a case study of Melbourne, Australia. *J Environ Manage* 246:203–213. <https://doi.org/10.1016/j.jenvman.2019.06.006>
34. Singh KR, Dutta R, Kalamdhad AS, Kumar B (2019) An investigation on water quality variability and identification of ideal monitoring locations by using entropy based disorder indices. *Sci Total Environ* 647:1444–1455. <https://doi.org/10.1016/j.scitotenv.2018.07.463>
35. Coquery M, Morin A, Bécue A, Lepot B (2005) Priority substances of the European water framework directive: analytical challenges in monitoring water quality. *TrAC Trends Anal*

- Chem 24(2):117–127. <https://doi.org/10.1016/j.trac.2004.11.004>, <http://www.sciencedirect.com/science/article/pii/S0165993604030894>
36. Thompson J, Pelc C, Jordan T (2020) Water quality sampling methods may bias evaluations of watershed management practices. *Sci Total Environ* 142739. <https://doi.org/10.1016/j.scitotenv.2020.142739>, <http://www.sciencedirect.com/science/article/pii/S0048969720362689>
 37. Adu-Manu KS, Tapparello C, Heinzelman W, Katsriku FA, Abdulai JD (2017) Water quality monitoring using wireless sensor networks: current trends and future research directions. *ACM Trans Sens Netw (TOSN)* 13(1):1–41
 38. Vikesland PJ (2018) Nanosensors for water quality monitoring. *Nat Nanotechnol* 13(8):651–660
 39. Schroeder V, Savagatrup S, He M, Lin S, Swager TM (2019) Carbon nanotube chemical sensors. *Chem Rev* 119(1):599–663. <https://doi.org/10.1021/acs.chemrev.8b00340>
 40. Hwang GH, Han WK, Park JS, Kang SG (2008) Determination of trace metals by anodic stripping voltammetry using a bismuth-modified carbon nanotube electrode. *Talanta* 76(2):301–308. <https://doi.org/10.1016/j.talanta.2008.02.039>
 41. Saetia K, Schnorr JM, Mannarino MM, Kim SY, Rutledge GC, Swager TM, Hammond PT (2014) Spray-layer-by-layer carbon nanotube/Electrospun fiber electrodes for flexible Chemiresistive sensor applications. *Adv Funct Mater* 24(4):492–502
 42. Wang T, Guo Y, Wan P, Zhang H, Chen X, Sun X (2016) Flexible transparent electronic gas sensors. *Small* 12(28):3748–3756
 43. Abbott J, Ye T, Qin L, Jorgolli M, Gertner RS, Ham D, Park H (2017) Cmos nanoelectrode array for all-electrical intracellular electrophysiological imaging. *Nature Nanotechnol* 12(5):460–466
 44. Zhang T, Mubeen S, Myung NV, Deshusses MA (2008) Recent progress in carbon nanotube-based gas sensors. *Nanotechnology* 19(33):332001. <https://doi.org/10.1088/0957-4484/19/33/332001>
 45. Jurs PC, Bakken G, McClelland H (2000) Computational methods for the analysis of chemical sensor array data from volatile analytes. *Chem Rev* 100(7):2649–2678
 46. Zucchi G, Lebental B, Loisel L, Ramachandran S, Gutiérrez AF, Wang X, Godumala M, Bodelot L (2018) Chemical sensors based on carbon nanotubes functionalised by conjugated polymers for analysis in aqueous medium

Chapter 12

Sensor Web and Internet of Things Technologies for Hydrological Measurement Data



Sebastian Drost, Christian Malewski, and Simon Jirka

Abstract Water management associations are responsible for monitoring large catchments and water bodies and thus have a great need for various hydrological measurement data. Most often, this comprises meteorological parameters as well as physical and chemical observations of water reservoirs, rivers and dams. In this context, low-cost sensors provide a great potential for densifying comprehensive monitoring systems. Typically, such a system requires the interoperable sharing of hydrological observation data as well as an efficient communication between the sensor devices. To establish smart water monitoring solutions, a sensor network infrastructure is needed that facilitates the management of a large amount of observation data and applies modern Internet of Things (IoT) communication approaches. This chapter aims to provide guidance in setting up a measurement data infrastructure that relies on both, standards of the well-established Sensor Web Enablement framework of the Open Geospatial Consortium (OGC) and IoT technologies. We introduce a concept for a modular water monitoring system that combines Sensor Web and IoT technologies to integrate sensor data in Spatial (Research) Data Infrastructures. Furthermore, the feasibility of this approach will be demonstrated with the presentation of an operational deployment at a German water management association.

S. Drost (✉) · S. Jirka
52°North GmbH, Münster, Germany
e-mail: s.drost@52north.org

S. Jirka
e-mail: jirka@52north.org

C. Malewski
Wupperverband, Wuppertal, Germany
e-mail: cmi@wupperverband.de

12.1 Introduction

Water monitoring is a crucial task within hydrology. Especially, water management associations have a great need for a vast amount of hydrological measurement data which gives important insights into different hydrological and meteorological processes within large catchment areas. Meteorological parameters, data about water levels and discharge of rivers as well as different chemical and physical parameters of large water bodies are of great importance [1]. Consequently, water management associations often operate large sensor networks that comprise different types of sensor devices for measuring these various hydrological parameters. This may include for example water gauges, sensors detecting physical parameters or even optical sensors for determining certain chemical concentrations. In order to make the collected data usable, such networks require an infrastructure that facilitates the management of measurement data. E.g., measurement data must be continuously collected from sensor devices and datasets must be disseminated in an interoperable way to be accessible for a broad range of users [2]. Furthermore, different types of observations must be harmonized within a standardized model, which contributes to a consistent understanding of measurement parameters [3]. Almost all these challenges have been addressed by an international standardization organization, the Open Geospatial Consortium (OGC). Central element of the OGC's standardization activities towards sensor data interoperability is the Sensor Web Enablement (SWE) initiative. The SWE framework comprises various standards that aim to make sensor devices and observation data accessible via the web in an interoperable way [4].

Beside the efforts of SWE new technologies, standards and communication patterns have been established in the last decade, which are related to the Internet of Things (IoT). Especially the expansion of low-cost sensor systems as well as the growing number of smart everyday objects have stimulated a multitude of IoT solutions. The vision of a network of physical objects in the IoT has advanced sensor technology to a whole new level, since the number of everyday objects, that have the ability to monitor their environment, increased enormously [5]. This led to new technical developments, aiming to suffice the requirements of building broad networks including a large number of physical objects that collect a variety of information and communicate with each other or interact with people. Aside from the classical fields of application (e.g., smart home, industrial automation, smart cities and intelligent transport system), IoT also provides a great potential for environmental monitoring [6]. Since sensor devices with embedded processing units are becoming smaller and cheaper, existing sensor networks can be expanded with ease, which contributes to a higher spatial coverage of in-situ measurements. In addition, by exploiting wireless communication protocols that are suitable for constrained environments, sensor devices are directly enabled for data dissemination via the web. This facilitates the analysis and processing of observation data by users or computing devices, which also contributes to the establishment of near real-time water monitoring [7].

The OGC has already addressed the changing demands on operating broad sensor networks and consuming large sensor data streams with the release of the OGC

SensorThings API in 2016 [8]. The goal of the SensorThings API is to transfer standardization efforts into the world of IoT, which also aims to bridge the gap between the Sensor Web environment and the IoT world [9]. However, setting up approaches and patterns from the IoT on existing sensor networks that rely on SWE technologies still requires some additional efforts.

This chapter offers guidance in building an architecture for collecting and managing hydrological measurement data, that relies on different standards and technologies of both worlds. The first part covers different encoding standards, interoperable interfaces and communication protocols from SWE and IoT with relevance for the proposed use case as well as technical challenges that are related to the implementation of an efficient water monitoring. In the middle part of the chapter, we propose a concept for an innovative water monitoring system that relies on SWE and IoT technologies by utilizing the OGC SensorThings API. In addition, we demonstrate the suitability of the proposed concept for handling a high number of sensor devices with the presentation of a pre-operational deployment at a German water management association. Finally, the last part discusses the approach with respect to challenges and future developments in the fields of SWE and IoT regarding real-time sensing requirements and measurement data harmonization.

12.2 Relevant Standards and Technologies

12.2.1 Sensor Web Standards

The Open Geospatial Consortium's (OGC) Sensor Web Enablement (SWE) initiative provides a well-established framework for managing heterogeneous sensor networks. The SWE architecture includes a comprehensive set of models, encodings and services which contribute to the implementation of interoperable and service-oriented networks of heterogeneous sensor systems and clients [4]. To address different challenges regarding the description and discovery of sensors and measurement data as well as its standardized accessibility via the web, several OGC standards have been developed. This includes:

- *Observations and Measurements (O&M)* [10, 11]: A model as well as an (XML) encoding for observation data
- *Sensor Model Language (SensorML)* [12]: A model as well as an XML encoding for metadata describing the processes and sensors through which observation data was generated
- *Sensor Observation Service (SOS)* [13]: A web service interface standard defining how sensor data and metadata can be queried from a server using various types of filters
- *OGC SensorThings API (STA)* [8]: A complementary standard based on REST and JSON that defines approaches on how to encode and access sensor data in a

more lightweight manner; this standard also includes an approach on how to use MQTT based data streams for data publication and delivery.

In addition to these standards, it is important to mention that there are further standards and best practices available, which aim to customize and optimize the previously mentioned specifications to the needs of hydrological applications. This comprises especially the OGC WaterML 2.0.1 standard [14] which defines how to encode hydrological time series data based on O&M. Furthermore, the OGC SOS 2.0 Hydrology Profile Best Practice gives guidance on how to apply and enhance the SOS 2.0 interface for the specific requirements of hydrology [15].

In the past, SWE architecture implementations have been successfully utilized for various use cases from the hydrological domain. Within the field of oceanography, Sensor Web infrastructures facilitated the sharing of heterogeneous observation data for oceanographic research and ocean observing [16, 17]. In addition, the suitability of Sensor Web technologies for time critical applications was demonstrated with the combined usage of a Sensor Observation Service and Web Processing Service as part of a water dam monitoring system [18] as well as with the implementation of a Sensor Web based flood monitoring system [19].

12.2.2 *Internet of Things Technologies*

The Internet of Things (IoT) comprises a broad range of technologies for enabling the networking of physical objects and includes a variety of architectural patterns for building smart sensor networks. In IoT each physical object is seamlessly embedded within its environment and acts as a sensor that collects and shares information via the internet. Thus, IoT has a great ability for implementing smart applications with a focus on device monitoring or machine-to-machine (M2M) communication. In recent years, IoT technologies especially contributed to the progress in automation systems for the industrial sectors as well as to the widespread use of smart home solutions. In addition, within the public sector, emerging smart city concepts benefit from IoT since smart technical solutions are adopted for optimizing public services [20].

Common architectures in IoT consist of different layers, each one addressing certain aspects regarding information collection, networking, data transmission and information sharing. Different internet technologies serve as essential building blocks for each layer. Due to the vast number of standards and protocols that are related to IoT, a technical survey of these would be out of the scope of this chapter. A comprehensive overview is given for example in [21].

Within the field of IoT, a variety of message protocols exists that are responsible for data exchange at the application level, i.e., AMQP, MQTT, XMPP, DDS and COAP [22]. However, with respect to our proposed concept, we focus on the Message Queuing Telemetry Transport (MQTT) protocol, which serves as a key technology for

push-based delivery of sensor data streams. MQTT is an open protocol for message-based communication. Message transmission follows the publish/subscribe pattern which enables a loose coupling and message broadcasting between multiple clients [23].

Within the field of water monitoring IoT technologies are a promising approach for building smart sensor networks. Wireless networking technologies in combination with event-driven communication patterns provide the basis for a decentralized water monitoring with multiple low-cost sensors devices [24]. This enables a cost-effective observation of a broad range of hydrologic observation parameters for large areas. Not surprisingly, the number IoT solutions within the field of hydrology consistently increases and the applicability of wireless sensor networks for water monitoring have been demonstrated in various use cases, such as in [25].

12.3 Technical Challenges for Efficient Water Monitoring

Hydrological near real-time applications benefit from the exploitation of recent IoT technologies within well-established sensor networks. IoT application protocols such as MQTT, COAP or AMQP enable push-based data delivery within resource constrained environments, which is a building block for realizing smart water monitoring applications. It enables seamless integration of a large number of sensor devices in a plug-and-play manner as well as lightweight data collection flows. However, the integration of IoT technologies into existing Sensor Web architectures comes with different challenges regarding the connection of disparate sensor devices as well as the harmonization of different protocols and data formats [26–28]. Following, the key challenges for constructing a sensor system that enables efficient water monitoring by combining Sensor Web standards with state-of-the-art IoT technologies are addressed.

12.3.1 *Collecting Sensor Data Streams*

Sensor networks often comprise a variety of sensors from different vendors which differ in output formats and communication protocols. Thus, custom sensor connectors and drivers must be developed to integrate and harmonize heterogeneous sensor data streams within a common SWE-based platform. Since building those interconnecting drivers often become a time consuming and expensive task, it is essential to implement the transmission of measurement data from the sensor devices to the SWE observation data store in an interoperable and reusable way. In fact, this requirement becomes more critical with an increasing number of sensor devices, which is common as part of IoT architectures. Hence, a standardized connection strategy to IoT data streams is needed to ensure a seamless plug-and-play integration of a huge amount of unknown IoT devices.

12.3.2 Data Management

Collecting observation data from a variety of IoT sensor devices for analysis purposes becomes a challenging task because researchers have to deal with a vast amount of mostly unstructured datasets. A common management server that stores collected observation data in a well-defined schema and provides interoperable access to it, accelerates the post-processing and analysis of measurement data. Such a server requires connectors to various sensor devices as well interoperable interfaces for sharing measurement data, which contributes to the interconnection between IoT sensor devices and users via the web.

12.3.3 Lightweight Deployment

Coupling IoT standards with existing sensor hardware provides a great potential within resource constrained environments. In particular, IoT application protocols such as MQTT are optimized to reduce communication overheads to be viable via resource constrained communication links. However, consuming measurement data streams from sensor devices often suffers from the non-standardized vendor specific communication protocols, which in many cases do not meet the technical requirements of practical applications. Thus, implementing IoT communication patterns such as M2M or data stream broadcasting becomes impractical relying on a variety of legacy device interfaces and protocols. For this reason, it is required to enhance existing sensor hardware by implementing an interconnection solution that enables the transmitting of raw sensor data streams to service endpoints via IoT application protocols.

12.3.4 Data Harmonization

IoT application protocols often lack interoperability of the transmitted payload, since protocols such as MQTT and AMQP solely define standards for message transporting but do not address payload encodings. Thus, a common payload encoding and application schema is required that is geospatially enabled and suffices the time-series character of observation data. In addition, the encoding must be viable for constrained communication links. E.g., XML encoding would not be appropriate since it produces heavy communication overheads. Data harmonization using a streamlined payload encoding therefore contributes to an interoperable observation data consumption.

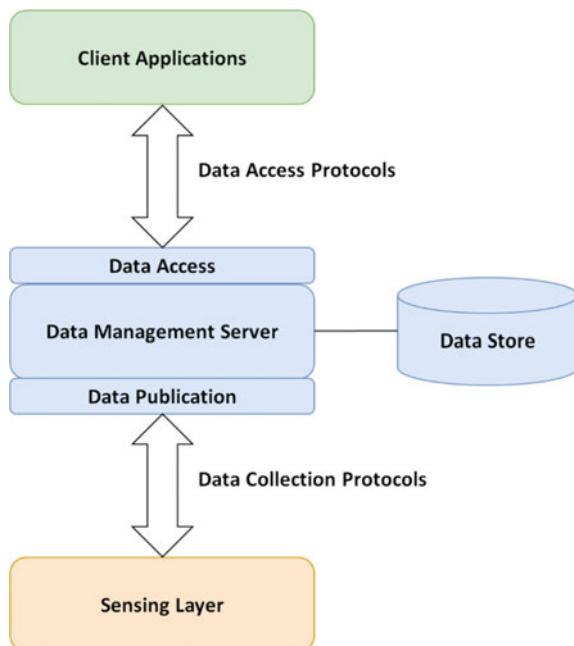
12.3.5 Semantic Interoperability

Implementing plug-and-play mechanisms for sensor devices requires connectors to the sensor data streams that are aware of device interfaces and observed properties. Interoperable metadata descriptions facilitate the access of sensor descriptions and measured observation data. SensorML provides a great potential for modeling and encoding such metadata in a flexible manner [12]. However, to be aware of domain specific requirements related to water monitoring, metadata descriptions must also consider semantic interoperability, which contributes to the interpretation of hydrological measurement data. Hence, a thematic vocabulary for sensor specifications and observed parameters is needed, which may be covered by a specific SensorML application profile.

12.4 Concept for a Sensor Web Based Water Monitoring System

This section describes the developed concept for a modular water monitoring system that relies on interoperable Sensor Web technologies for enabling different data flows. In order to build such a distributed system, several functional aspects need to be considered. Figure 12.1 provides an overview of these fundamental building

Fig. 12.1 Base architecture overview for a water monitoring system



blocks. Subsequently, we will discuss how these building blocks can be realized in practice relying on different Internet of Things and Sensor Web technologies.

As shown in Fig. 12.1, it is necessary to consider the following building blocks for building a distributed water monitoring system:

- *Sensing Layer*: This layer comprises all the sensor hardware and data loggers that are used for gathering hydrological measurements.
- *Data Collection Protocols*: In order to transport the collected measurement data from the sensor layer into a common data store, dedicated protocols are needed. It is important to take into account that these protocols have to be implemented in the Sensing Layer as well as on any data management server that shall be used within the system.
- *Data Management Server*: The Data Management Server is a core element of the whole system. On the one hand it is responsible for accepting the incoming data streams (potentially in combination with further processing steps such as quality control). On the other hand, it provides interfaces to all data consumers (Client Applications) to access the available measurement data.
- *Data Store*: In order to store the collected measurement data, the Data Management Server requires functionality for data persistence. Typically, this can be realized through a database (e.g., relational database management systems or specialized data stores such as time series databases).
- *Client Applications*: This layer comprises all tools that help to visualize and work with the available data. It may comprise tools such as data analysis (e.g., with the statistical programming language R), data viewers (e.g., web applications), geographic information systems or hydrological expert applications. In order to access the available measurement data, these applications need to handle at least one of the Data Access Protocols offered by the Data Management Server.

For implementing this system architecture, it is necessary to map the different building blocks to specific technologies and protocol standards. Such a mapping is illustrated in Fig. 12.2 and described below. It is important to note, that for the described architecture open-source implementations are already available. Thus, the cost for implementing such a system will be mainly influenced by the sensing technology, the hardware for data transmission and the server infrastructure.

The sensor layer consists of the specific sensing hardware that is used for monitoring different hydrological parameters. This hardware strongly depends on the domain specific needs so that the developed architecture has to support a broad range of different devices. Thus, to integrate the different sensors into the system, different (potentially sensor-specific) Sensor Connectors are needed. These connectors are responsible for reading the sensor outputs and forwarding them into the system. Here, different strategies are feasible:

- Reading textual sensor output, such as CSV files and inserting them into a Sensor Web server
- Data loggers that connect to the sensor ports and forward the data into the system

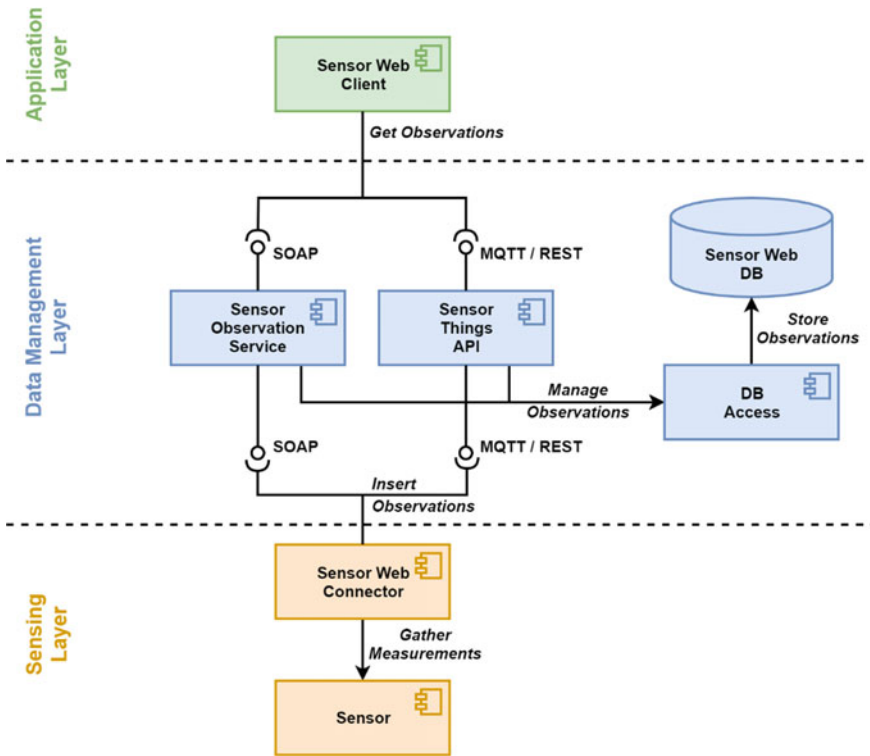


Fig. 12.2 Technologies for implementing a sensor web system for water monitoring

- Manufacturer-specific software packages, that provide well-defined access to acquired sensor data
- Internet of Things protocols.

In the following, this paper will focus on a specific Internet of Things protocol: MQTT. Thus, our connector needs the capability to read the sensor outputs and to forward them to an MQTT broker.

On the data Management Layer we have already mentioned the OGC SOS and SensorThings API standards. While the publication via the OGC SOS standard would require the execution of XML-based operation calls, the OGC SensorThings API offers additional options. Besides a REST-based approach, it also has the ability to accept incoming data streams via MQTT. For this purpose, the SensorThings API comes with an integrated MQTT Broker, any client can connect to for publishing or consuming observation messages. As MQTT offers a lightweight push-based data delivery approach that helps to reduce latencies in data publication, the following sections will focus on the combination of the SensorThings API and MQTT.

It is important to mention that both standards, SOS and SensorThings API share common foundations as defined by the OGC Observations and Measurements data

model. Thus, it is possible to operate both interfaces on top of a common data store (in this case a relational database), so that both interfaces can be used for feeding the same database. At the same time, this database can also be used for sharing the same data via both interfaces to different types of applications.

In addition, these standards can also be used to fulfill reporting or data publication obligations such as those defined by the European INSPIRE Directive [29]. Both mentioned services have the potential to match the corresponding requirements. For the SOS specification this has been documented in a dedicated Technical Guidance Document [30]. In the case of the SensorThings API a corresponding approach has been published by [9].

Finally, the Application Layer can comprise many different types of applications. In our application scenario we focus primarily on the web-based visualization of sensor data. In the presented case, the SensorThings API standard is used as a data source for the web application as it offers a more lightweight REST/JSON interface for accessing and exploring sensor data and metadata.

Besides the web-based visualization of sensor data, another common scenario in hydrologic research would be the discovery and retrieval of big time-series datasets for analysis purposes. Therefore, the SOS interface defines dedicated operations for querying and filtering measurement data. However, with an embedded MQTT broker, the SensorThings API enables a publish/subscribe pattern for near real-time data delivery which is even more applicable for time-critical use cases such as water monitoring.

12.5 Deployment and Evaluation at the Wupperverband

The Wupperverband is a water management association in Germany. The association manages the water quantity and quality within the catchment area of the Wupper river, a tributary to the Rhine River. The Wupperverband runs 14 water reservoir facilities and 11 sewage-treatment facilities. In order to fulfill its responsibilities, the safety and performance of both, the water bodies and water facilities, are continuously monitored through automatic and manual measurements. The responsibility for the management of these measurements is partitioned among specialist departments. Thus, the measurements are structured by their varying context e.g., water dam safety measurements, hydrological measurements, or deformation measurements. The result is a set of isolated expert systems within which data exchange is hard to achieve. To overcome this situation and ease the data exchange, the Wupperverband introduced a Sensor Web infrastructure as an intermediate layer, that integrates the measurement data from the variety of expert systems in a central system.

The existing Sensor Web infrastructure is realized as a three-layer architecture. The core of that infrastructure is a harmonized database schema for handling observation data and time series metadata. On top of the database a web service layer provides the data as both, a non-standardized REST/JSON format, and an OGC standardized SOAP/XML format (SOS). Web clients, as the consumer layer, adopt

the former one to allow for data exploration, analysis and monitoring. The database is fed by a set of heterogeneous import scripts automatically by parsing exported data documents from expert systems. The latencies of these pull-based workflows range from hourly to monthly imports. The dam systems remain secure though, because the data is present in expert systems, namely process control systems, dedicated to a water facility.

During the last years, parts of the sensor network of the discussed river dam have been renewed. Since the effort for connecting these new sensing devices to the corresponding process control system is still ongoing, a lightweight solution was needed to reconcile the gap of data transmission. Thus, a data stream workflow that builds upon the SensorThings API has been evaluated. The SensorThings API provides multiple enhancements for the Sensor Web infrastructure regarding requirements of nowadays water resource management:

1. A state-of-the-art interface definition is provided which allows for serving observations and their metadata in a standardized manner.
2. The SensorThings API provides a robust way for feeding data via the service layer, allowing for iterative replacement of former database import scripts.
3. It enables stream-based data processing and production, which is especially required for near real-time water monitoring as well as in a data science context.
4. The SensorThings HTTP API is very generic. HTTP requests can be tailored to be optimized according to the varying needs of web clients.

Besides these enhancements, however, the focus is on the minimization of data communication latency among the three layers that were described ahead, starting with the importing workflow.

In what follows, the setup of the sensor web infrastructure at a river dam facility is described. The stationary sensors are connected to a central controlling unit (Simatic S7-300) measuring and delivering data in a fixed interval. To map incoming sensing data given in a vendor specific protocol to the SensorThings API specific format, the controlling unit hosts a NodeRED server (Fig. 12.3). NodeRED is an open data flow manager queuing a set of data processing nodes to a data flow pipeline. For convenience, NodeRED provides a graphical user interface that serves as a documentation of implemented data flows. In the present use case, a data mapping logic is realized in NodeRED (Fig. 12.4):

1. The data source is the data logger which receives raw measurement data from the sensor systems.
2. Measurement data streams are stored via the SensorThings MQTT API which serves as a data sink within the data flow pipeline.
3. The nodes in between map the raw sensor data format to the SensorThings API encoding format and assign the SensorThings observations to a certain topic.

The raw database is equipped with database triggers. Once a new value is stored within the database, the raw value is distributed to the harmonized database schema, where database triggers share the data to subordinated databases. This push-based

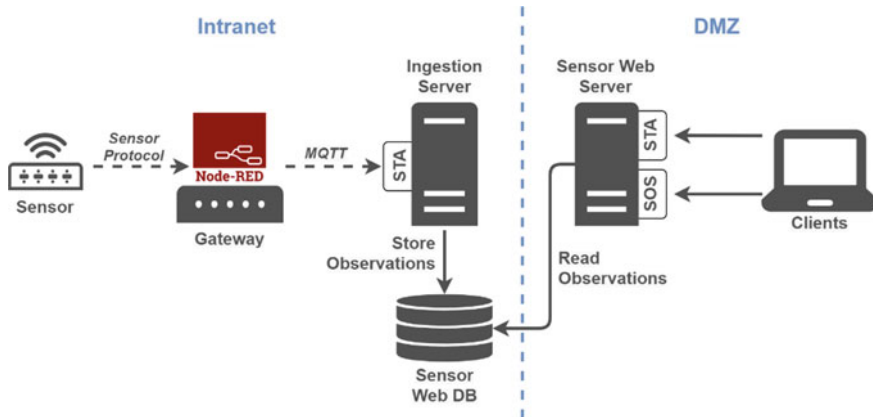


Fig. 12.3 IoT enabled sensor web infrastructure at the Wuppervverband

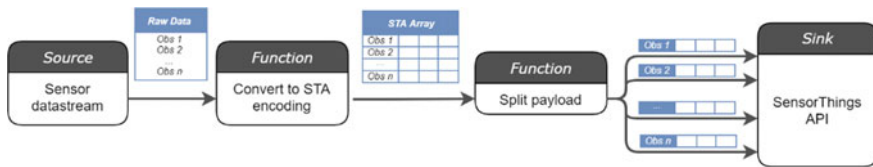


Fig. 12.4 NodeRED data flow pipeline for mapping raw sensor data streams to the SensorThings API encodings

workflow ensures that the raw value is communicated in near real time, so that the sensors' measuring interval is the only delay in data processing.

The described setup has been deployed for over a year and up to now with more than 100 sensing devices measuring a variety of parameters hourly. During this time, the data flow worked as expected. Due to the small number of devices, the scalability of a single SensorThings API instance can rarely be assessed. In accordance with the cloud computing based approach, however, horizontal scaling is possible by deploying additional database and SensorThings API instances.

12.6 Future Challenges

Within this chapter we have shown how Sensor Web and Internet of Things technologies can be used together to facilitate the publication of sensor data in Spatial Data Infrastructures. However, despite the feasibility demonstrated during our evaluation, there are future challenges that need to be addressed to increase the applicability of our approach.

Within our proposed concept, we have focused in the first step on measurements collected by stationary in-situ sensors. However, besides this, there are further relevant types of measurement data. This comprises for example measurements along the z-axis (profiles) or data collected along the trajectory of a mobile sensor platform. While the SensorThings API generally also supports these types of data, it does offer several options for encoding such observations. Thus, we see a need for further work to develop a dedicated profile of the OGC SensorThings API standard that provides further guidance on how to encode additional, potentially more complex types of data.

One important question concerns the organization of potentially large numbers of sensor data streams. Protocols such as MQTT allow organizing data streams in a hierarchical structure. However, depending on the specific use cases, different types of the hierarchy are needed to support users in discovering and consuming the data they need. In the case of hydrological data, typical views towards the data are centered around geographic (e.g., all sensors at a location, along a river, within a catchment area), thematic (e.g., all sensors measuring a specific parameter), or qualitative (e.g., raw vs. quality assured data) criteria. Consequently, further best practice guidance would be desirable on how to organize sensor data streams in hydrological applications.

As part of our evaluation, we have shown the suitability of our proposed architecture within a pre-operational deployment for water monitoring tasks of a water management association. However, for the future, we expect further increasing amounts of sensors and measurement data that need to be handled. While our solution, based on a relational database, was already tested with hundreds of sensors, we expect that challenges will arise if this number increases by magnitudes. Thus, to ensure scalability, we plan to investigate alternative approaches for data persistency to complement the relational database model approach. While the metadata about sensors might still be efficiently managed via relational models, dedicated time series databases promise a more efficient handling of the actual measurement data.

Another challenge concerns the semantics of the collected data. While the general structure of the measurement data is already well defined through the OGC SensorThings API specification, the content of the data underlies not further semantic regulations. For example, the parameters observed by a sensor (e.g., water level) might be provided in many different spellings and notations. This may cause difficulties when integrating different data streams from multiple sources. Thus, we recommend to further investigate the use of vocabularies as demonstrated within other scientific domains [31]. This allows recommendations on hydrological vocabularies that provide the necessary foundation for using them in IoT applications.

Furthermore, the OGC SensorThings API standard used in our architecture for sharing observation data does not yet include a standardized approach for controlling the access to observation data. However, as many data streams deliver non-public data that shall only be shared with specific user groups (e.g., raw data which is only available for internal use while quality-controlled data might be published for a broader audience), it will be necessary to further investigate how access control functionality could be established.

Finally, we recommend establishing a link to further protocols that go beyond the Internet of Things community. For example, the OPC Unified Architecture (OPC UA) is a commonly used industry standard applied in many operational systems [32]. As these systems deliver a multitude of observation data, it should be investigated how a connection to OPC UA can be established, so that the OGC SensorThings API can serve as an interoperability layer that abstracts from the underlying data acquisition systems, independently if they are based on industry or Internet of Things protocols.

Acknowledgements This work has been co-funded as part of the WaCoDiS project by the Federal Ministry of Transport and Digital Infrastructure (Germany), BMVI, as part of the mFund program.

References

1. World Health Organization (2017) Guidelines for drinking-water quality
2. Bröring A, Echterhoff J, Jirka S, Simonis I, Everding T, Stasch C, Liang S, Lemmens R (2011) New generation sensor web enablement. *Sensors* 11(3):2652–2699
3. Wang C, Chen Z, Chen N, Wang W (2017) A Hydrological sensor web ontology based on the SSN ontology: a case study for a flood. *ISPRS Int J Geo Inf* 7(1):2
4. Reed C, Botts M, Percivall G, Davidson J (2013) OGC® sensor web enablement: overview and high level architecture. Document Reference Number: OGC 07-165r1
5. Mattern F, Floerkemeier C (2010) From the internet of computers to the internet of things. In: Sachs K, Petrov I, Guerrero P (eds) *From active data management to event-based systems and more*, vol 6462. Springer, Berlin, Heidelberg, Germany, pp 242–259
6. Ahmed U, Mumtaz R, Anwar H, Mumtaz S, Qamar AM (2020) Water quality monitoring: From conventional to emerging technologies. *Water Supply* 20(1):28–45
7. Geetha S, Gouthami S (2016) Internet of things enabled real time water quality monitoring system. *Smart Water* 2(1):1
8. Liang S, Huang C-Y, Khalafbeigi T (2016) OGC SensorThings API part 1: sensing. Document reference number: OGC 15-078r6
9. Kotsev A, Schleidt K, Liang S, van der Schaaf H, Khalafbeigi T, Grellet S, Lutz M, Jirka S, Beauflis M (2018) Extending INSPIRE to the internet of things through SensorThings API. *Geosciences* 8(6):221
10. Cox S (2011) OGC implementation specification: observations and measurements (O&M) - XML implementation 2.0 (10-025r1). Open Geospatial Consortium Inc, Wayland, MA, USA
11. ISO TC 211 (2011). ISO 19156:2011—Geographic information—observations and measurements—international Standard. International Organization for Standardization, Geneva, Switzerland
12. Botts M, Robin A (2014) OGC implementation specification: sensor model language (SensorML) 2.0.0 (12-000). Open Geospatial Consortium Inc, Wayland, MA, USA
13. Bröring A, Stasch C, Echterhoff J (2012) OGC implementation specification: sensor observation service (SOS) 2.0 (12-006). Open Geospatial Consortium Inc, Wayland, MA, USA
14. Taylor P (2014) OGC implementation specification: waterML 2.0.1: Part 1—Timeseries (10-126r4). Open Geospatial Consortium Inc, Wayland, MA, USA
15. Andres V, Jirka S, Utech M (2014) OGC best practice: OGC sensor observation service 2.0 hydrology profile (OGC 14-004r1). Open Geospatial Consortium Inc, Wayland, MA, USA
16. Jiang Y, Li J, Guo Z (2010) Design and implementation of a prototype system of ocean sensor web. In: *IET International conference on wireless sensor network 2010 (IET-WSN 2010)*, Beijing, China, 15–17 Nov. 2010, pp 21–26

17. Jirka S, Toma DM, del Rio J, Delory E (2014) A sensor web architecture for sharing oceanographic sensor data. In: 2014 IEEE sensor systems for a changing ocean (SSCO), Brest, France, 13–17 Oct. 2014, pp 1–4
18. Stasch C, Pross B, Gräler B, Malewski C, Förster C, Jirka S (2018) Coupling sensor observation services and web processing services for online geoprocessing in water dam monitoring. *Int J Digital Earth* 11(1):64–78
19. Kussul N, Mandl D, Moe K, Mund J-P, Post J, Shelestov A, Skakun S, Szarzynski J, Van Langenhove G, Handy M (2012) Interoperable infrastructure for flood monitoring: SensorWeb, grid and cloud. *IEEE J Selected Top Appl Earth Observat Remote Sens* 5(6):1740–1745
20. Zanella A, Bui N, Castellani A, Vangelista L, Zorzi M (2014) Internet of things for smart cities. *IEEE Internet Things J* 1(1):22–32
21. Al-Fuqaha A, Guizani M, Mohammadi M, Aledhari M, Ayyash M (2015) Internet of things: a survey on enabling technologies, protocols, and applications. *IEEE Commun Surveys Tutor* 17(4):2347–2376
22. Yassein MB, Shatnawi MQ, Al-zoubi D (2016) Application layer protocols for the internet of things: a survey. In: 2016 International conference on engineering & MIS (ICEMIS), Agadir, Morocco, 22–24 Sept. 2016, pp 1–4
23. OASIS (2015) MQTT version 3.1.1 Plus Errata 01. Edited by Andrew Banks and Rahul Gupta. 10 December 2015. OASIS Standard Incorporating Approved Errata 01. <http://docs.oasis-open.org/mqtt/mqtt/v3.1.1/errata01/os/mqtt-v3.1.1-errata01-os-complete.html>. Latest version: <http://docs.oasis-open.org/mqtt/mqtt/v3.1.1/mqtt-v3.1.1.html>
24. Adu-Manu KS, Tapparelo C, Heinzelman W, Katsriku FA, Abdulai J-D (2017) Water quality monitoring using wireless sensor networks: current trends and future research directions. *ACM Trans Sens Netw* 13(1):1–41
25. Martínez R, Vela N, el Aatik A, Murray E, Roche P, Navarro JM (2020) On the use of an IoT integrated system for water quality monitoring and management in wastewater treatment plants. *Water* 12(4):1096
26. del Rio J, Toma DM, Martinez E, O'Reilly TC, Delory E, Pearlman JS, Waldmann C, Jirka S (2018) A sensor web architecture for integrating smart oceanographic sensors into the semantic sensor web. *IEEE J Oceanic Eng* 43(4):830–842
27. Martínez E, Toma DM, Jirka S, Del Rio J (2017) Middleware for plug and play integration of heterogeneous sensor resources into the sensor web. *Sensors* 17(12):2923
28. Pearlman J, Jirka S, del Rio J, Delory E, Frommhold L, Martinez S, O'Reilly T (2016) Oceans of tomorrow sensor interoperability for in-situ ocean monitoring. In: OCEANS 2016 MTS/IEEE Monterey, Monterey, CA, USA, 19–23 Sept. 2016, pp 1–8
29. European Parliament & European Council (2007) Directive 2007/2/EC of the European parliament and of the council of 14 March 2007 establishing an Infrastructure for Spatial Information in the European Community (INSPIRE). Strasbourg, France
30. INSPIRE MIG sub-group MIWP-7a (2016) Technical Guidance for implementing download services using the OGC Sensor Observation Service and ISO 19143 Filter Encoding - Version 1.0. Ispra, Italy
31. Kokkinaki A, Darroch L, Buck J, Jirka S (2016) Semantically enhancing SensorML with controlled vocabularies in the marine domain. In: Proceedings of the geospatial sensor webs conference (GSW 2016), Münster, Germany, 29–31 Aug 2016
32. OPC Foundation (2017) OPC 10000–1: OPC unified architecture—Part 1: overview and concepts release 1.04. Scottsdale, AZ, USA: OPC Foundation

Chapter 13

Smart Sensors for Smart Waters



Andreas Weingartner and Jordi Raich

Abstract This chapter is looking back on 20 years of online water quality monitoring, focussing on important achievements during that period, describe the current state of research and technology, and will take the oracle’s perspective at current and future trends. An overview of water monitoring topics is given, by method, measured substance, instrument, and by their applications. Focus is on substances of special environmental or health concern that can be detected by “solid state” sensors, and on applications that are a bit off the beaten monitoring track, to get a feeling for the always widening domain of on-line and real-time water quality monitoring.

Keywords Online sensors · Water quality monitoring · Smart sensors · Data quality · Internet of things · Soft Sensors · Digital twin · Indirect measurements · UV–Vis Spectrometry

13.1 Introduction

We are writing this chapter about water quality monitoring almost simultaneously with the handing over of one of the leading companies in water quality monitoring, s-can Messtechnik GmbH, to new ownership. This is an opportunity to look back on 20 years of water monitoring science and services through now “neutralized” glasses, to summarize the amazing achievements in the world of water monitoring during that period, not shy about mistakes and still existing gaps and shortcomings.

We are presenting here our subjective and anecdotal view about water monitoring topics, by method, measured substance, instrument, and by their applications; and not an encyclopaedic technology overview. Focus is on substances of special environmental or health concern that can be detected by “solid state” sensors, and on

A. Weingartner (✉)
casAgua GmbH, Klosterplatz 8, 4801 Traunkirchen, Austria
e-mail: andreas.weingartner@casagua.at

J. Raich
s::can Messtechnik GmbH, Brigittagasse 22-24, 1200 Vienna, Austria

applications that are a bit off the beaten monitoring track, to get a feeling for the always widening domain of on-line and real-time water quality monitoring.

13.1.1 The Historical View

The last 20 years can be seen as a blooming period of online water quality monitoring. Around the year 2000, about 20 relevant manufacturers offered solutions for about 50 online parameters. Today, instruments are available for more than 100 physical, chemical, biological, and radiological online parameters, from more than 300 manufacturers globally, with many new companies preparing their launches. The increase of the number of monitoring-related scientific publications has been exponential (to be observed i.e. via researchgate.net, or by the number of articles and adverts in scientific and commercial magazines), as well as the number of start-up companies and mergers and acquisitions, reflecting the business relevance [1, 2].

Cost-efficient, reagent-free, continuous, low-maintenance, low power, intelligent and networking devices—summarised under the term “smart”—became a common vision. Water infrastructure and water projects cannot be planned without water quality sensors anymore; but when money gets tight during realisation, the monitoring budget is often the first one to be cut.

Also, water quality monitoring still remains at the larger utility or institutional level, and did not yet find its way down to smaller units or even into the capillaries of the water system: the building level, or even the consumer level. However, extrapolating the very recent trend to “smart” and “managed” buildings, combined with ongoing innovation at the sensor—and data management side, it is without risk to predict that water quality sensors will be “ubiquitous” in 10–20 years.

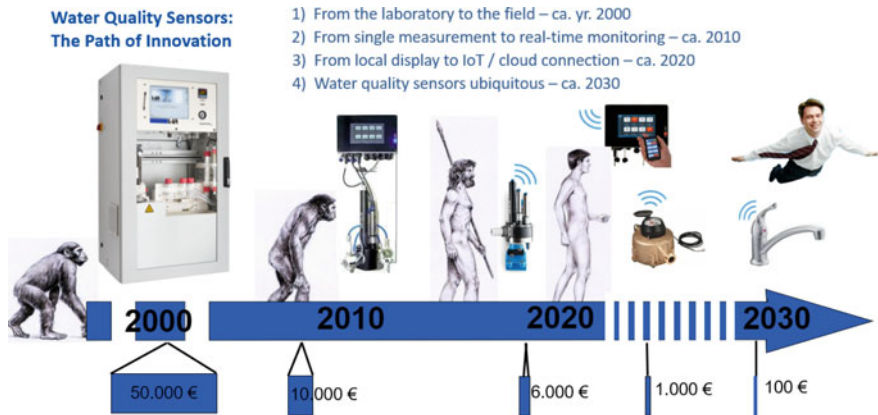


Fig. 13.1 Technology trends of the last 20 years

So, the question arises: compared to other fields of technology (such as cars, houses, medical, etc.), why do we still use so few sensors in water, i.e. to monitor and control water quality in distribution systems? Shouldn't every drop of water be controlled before consumption? Why is it that consumers accept such an evident and transparent deficit? To answer this and other questions, have a look at the wonderful Smart-Water book by Gustaf Olsson and Pernille Ingildsen [3] where they state: *“Even if sensors are not new to water utilities, it is important to recognise that transforming a water utility to a “Smart Water Utility” is a fundamental cultural change of the organisation.”*

13.1.2 Why Measure Water Quality Online—The Drivers

As a general rule, the more dynamic a water system, the more important is the real-time monitoring and control, as opposed to taking grab samples and conducting lab analysis in less dynamic systems. Besides dynamicity of the system, other drivers for online monitoring are: consumer's health and safety (drinking water monitoring including security aspects [8], with special fragility in intermittently pressurized systems); system efficiency and cost reduction potential which includes automation and control applications; environmental impact of dynamic water systems, including plant emission monitoring or sewer management systems; research interests, which can be of scientific, investigative or documentary nature; and, last not least: digitalization of the water sector, which is driven by apparent buzzwords such as “smart water”, “big data”, “digital transformation”, “digital twin”, etc. The success of SWAN (Smart Water Networks Forum, www.swan-forum.com), representing a relevant cross-section through the global water industry, indicates that these actually are not only buzzwords anymore but time has come for “data-driven solutions in the water and wastewater industry”.

Water quality sensors are the eyes into water bodies and water infrastructure, often connected via communication networks, streaming their measured data and other information into central data platforms. However, different types of sensors will be needed in the world of large and dense sensor networks; how will they distinguish from today's state of technology?

For a general overview of water quality topics, we recommend to consult [4]. For a more comprehensive overview on sensor technologies we recommend these three compilations: [5] gives a practical overview of technologies, applications and case studies, and the connected data base allows to search related information. Orellana et al. [6] is a bit older but still a valid and comprehensive overview of online sensors and their applications, and its validity proves how conservative the world of water is. The more recent [7] provides a comprehensive and complete overview with a focus on new technologies and gives a picture of how water quality monitoring could develop in the (near) future.

13.1.3 Why Norms and Standards Are so Important for Operators

Limits and standards for water quality are provided by international norms and standards, such as by the WHO [14]. However, this is one of the dilemmas of online water quality sensors: the specification of their “real” performance. Generally, sensors are specified by the manufacturer under narrow laboratory conditions and standards. Easily reproducible parameters such as signal-noise, signal linearity, signal-response, or measuring range can be promised by such specification; however, they have almost nothing to do with the application in a real-water environment, such as i.e. in raw waste water, where adverse conditions have bigger impact on the performance of sensors than most operators and even manufacturers are aware of.

For higher acceptance by water operators and managers, the evaluation of the performance of sensors under standardized real-world conditions has been an important task over the years. Several norms, standards and procedures were developed, such as ISO 15839:2003 [9], or UK-MCERT [10] or the US-EPA ETV [11] (unfortunately ended 2014). National standards can be found in many countries globally.

Still, in reality, waters can change concentration and composition quickly, and resulting signal-concentration-ratios or matrix-related cross-sensitivities are almost impossible to mimic in a laboratory environment. From a manufacturer’s perspective, the effort of testing a sensor against these national and international norms is a risky challenge, as any certificate would only open one market, but the cost of such testing often outweighs the triggered commercial advantage. Especially for small manufacturers, the hurdle of national certification is disruptive.

The acceptance of online methods for regulatory and compliance purpose is a slow process, which has not greatly advanced during the last 20 years, with exceptions such as amperometric free chlorine measurement by the US-EPA [20], and turbidity standards by ISO [22] and by US-EPA [23].

13.2 Water Quality Needs Data Quality

An overview of the terminology used in the following chapter gives the ISO 15839 [9] norm. Percentage numbers indicated here are based on experience and application data collected over the years by the authors and co-workers; evidence can be provided upon specific request.

13.2.1 Reproducibility and Precision

When repeating a measurement with the same instrument in the same medium under same conditions, the result should always be the same—then we can call the instrument precise. Typical sources of “noise” are volumetric addition of reagents, oxidation/reduction steps, pumping, timing, cross-talking, fouling, etc. Therefore, in order to achieve highest reproducibility, any instrument-internal sources of noise should be eliminated at first.

Only simple, solid state instruments can perform at highest precision: Precision can be achieved at $\pm 1\%$ over long periods of time with a solid state, self-referencing, self-cleaning optical sensor. One special example is [25], Krycklan Research Catchment portal <https://data.krycklan.se/>. A UV–Vis spectrometer was left in surface water over the winter. When taken out and its baseline checked, the baseline was perfectly at zero. After one year continuous operation without any intervention, the Total Organic Carbon (TOC_eq) was $\pm 1\%$ of the lab. Such level of stability is reserved to solid state optical measurements. Figure 13.2 quite drastically confirms the superiority of a solid state optical sensor in terms of precision, compared to a “classical” oxidizing process analyzer.

Both analyzers were installed in a groundwater well near the Danube river, under changing hydraulic conditions: The “noise” of the classic analyzer (green dots) is about 8 times higher than of the spectrometric sensor (red line). The spectrometric sensor can detect relevant micro-fluctuations where the analyzer can only see major trends, and some fluctuations after data filtering (if the noise is “white”).

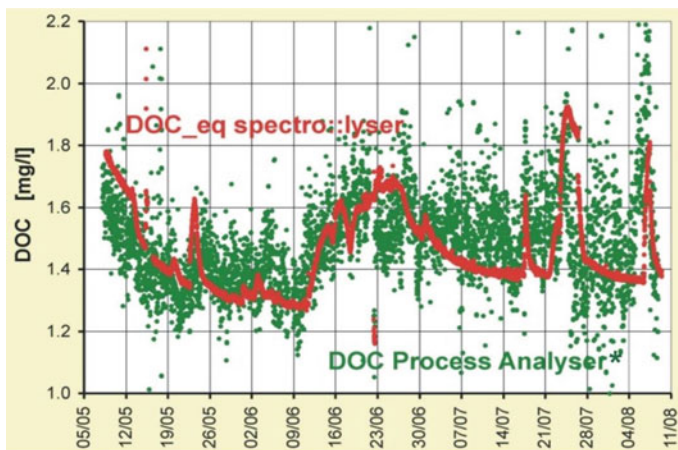


Fig. 13.2 Comparison of a UV–Vis spectrometer with process analyzer. LIFE99 ENV/A/403, Univ.f. Life Science, Vienna, AT [26]

13.2.2 Accuracy and Error—Who Is Right, Who Is Wrong?

“Accuracy” is a parameter that can be resolved by agreement: Every norm is an agreement and can be replaced by another, more efficient one, if all involved parties agree.

Error is defined as the deviation of a “surrogate” measurement, i.e. of a sensor installed in the field, from a reference measurement following a norm. A small error indicates good accuracy.

But is it so simple to tell who is right and who is wrong?

In any accuracy/error analysis, the accumulated Total Error of the two compared Measurements (TEM) must be considered. Major error contributors are: Representativity of sample; sampling synchronization; transport and storage incl. stabilization; error of the reference measurement; calculation errors. All these errors accumulate in the reference measurement chain, while the online method is free of most of them. Typically, depending on measurand and conditions, 70–90% of the TEM derives from errors outside the laboratory. For organic carbon parameters such as TOC, an average error of $\pm 5\%$ of the measured value in a defined range can be achieved by a well trained team under good conditions, at one location over a controlled period of time, i.e. during a specific campaign (Fig. 13.3).

Correlation between lab and online measurements was extremely good. The errors of both methods behaved very much like “white noise”, meaning that by doing more measurements, the correlation would always get tighter tangentially, as there is minimal systematic residual error on both methods respectively. The internal error of each method is expressed by the standard deviation, and the online method is 2.5 times better than the reference method. The combined error can not be smaller than that of one method, therefore the combined standard deviation cannot be lower than

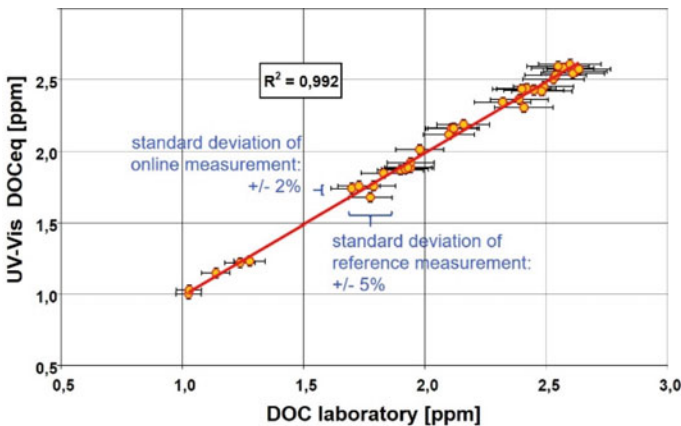


Fig. 13.3 Danube river monitoring, from LIFE99 ENV/A/403, Univ.f. Life Science, Vienna, AT [26]

of the reference method. Often, the reference measurement's TEM limits the quality of the correlation.

Such great performance can be celebrated in the scientific literature; but will cause frustration if established as the yardstick for "real-world" monitoring, after the campaign is over and the scientists have left the plant or project. Under real-world conditions, an error of $\pm 10\%$ should be considered very satisfying for totalizing organic carbon measurements. However, for parameters that i.e. involve solids, such as Total Suspended Solids TSS, or bio-oxidation, such as Biological Oxygen Demand (BOD_x), even such performance is hard to achieve under real-world conditions.

13.2.3 The "Smart Water" Paradigm—A Plea for Comparability

Parameters such as precision, accuracy, stability, linearity, etc., have established to qualify the performance of stand-alone probes in applications such as discharges into receiving water bodies.

As one example, the corresponding author has developed an evaluation method and chart [27] in close vicinity to ISO 15839 [9], in co-operation with Conagua, the Mexican water authority. The evaluation chart contains a "Sensor Performance" score based on (a) Accuracy, (b) Drift/Bias, (c) Stability, (d) Response time, and (e) Availability; and an "Applicability" score describing fitness of a parameter for (a) compliance reporting, (b) pollution load invoicing, (c) spill detection; all this for evaluation of industrial emission monitoring systems. More information is available upon request.

However, when operating many sensors in a network, "comparability" becomes the critical performance indicator. In a network of complex process analyzers, good comparability will hardly be achievable. To make such a network comparable, a substantial training- and quality assurance system needs to be established, which often goes beyond a reasonable cost-effect ratio.

We need to re-think sensor qualification when we think "smart water". But also for compliance monitoring and reporting, trend analysis, scientific research, and last not least, any fees upon discharge, comparability is even more essential than extreme local accuracy—which traditionally has been promoted by laboratories. Good comparability allows to set measurement values from several sensors on the same scale (a) over time and (b) over location, if all sensors are applying the same "precise"—but not necessarily "accurate"—measurement method.

So, how can comparability be reached in sensor network applications? Only the most simple, reliable, precise and with that comparable sensors should be used. Solid-state sensors might not be super accurate in a sense as described above; but they are comparable—because they all behave the same way in the same medium. And only after comparability comes interpretability.

13.2.4 Real-Time Data Validation

Never enough effort can be invested into real-time validation of measured data; which is considered one of the major bottlenecks with broader implementation of water quality sensors.

Over the last two decades, quite some research has been invested into tools for time series analysis. Examples are [28] who published a manual for—off-line—time series analysis. Horsburgh et al. [29] provides a functional introduction into the topic before inviting to use their open source software base <https://github.com/ODM2/ODMToolsPython> as a starting point for off-line analysis and data validation.

A well proven commercial product is the real-time data validation tool “vali::tool”, from s::can Messtechnik GmbH, Vienna, AT (www.s-can.at). It is a self-learning software that runs on their local controller, analysing data streams from any connected sensors, predicting the most probable next value, detecting and even correcting anomalies such as inconsistent noise levels, outliers, sudden jumps, data gaps, and others. Figures 13.4 and 13.5 give examples of raw data time series together with validation results [30].

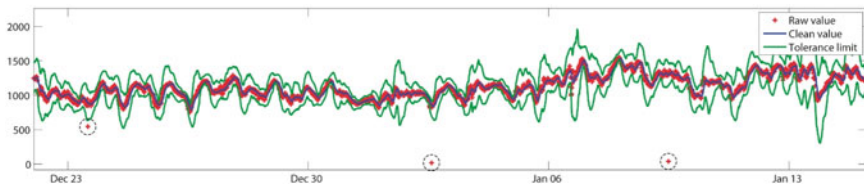


Fig. 13.4 Outlier detection: The algorithm estimates an upper and lower tolerance limit around the prediction for the next parameter value. Values outside the tolerance are outliers (marked with dashed circles, and ignored). The tolerance limits are automatically adapted to prediction errors

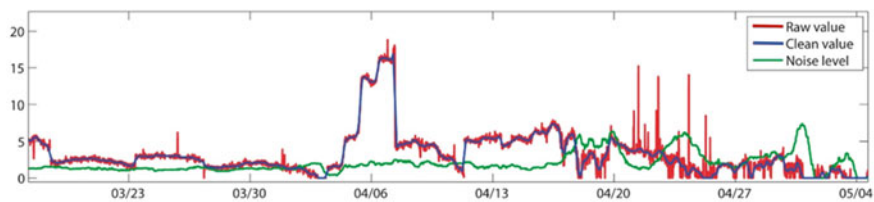


Fig. 13.5 Noise detection: The algorithm measures deviations of the parameter values from a smoothed time series to estimate and predict the noise level. Deviations from typical noise levels are often an indicator of installation problems such as in this figure, where the elevated noise level after 04/18 was the result of the monitoring station partly falling dry

13.3 Substances, Tools and Applications

Investment into R&D of new sensing devices has exponentially grown over the last two decades, nevertheless, the way how we are monitoring water quality has not (yet) changed dramatically. Maybe with the two exceptions that (a) optical oxygen sensors took over the market (which didn't very much change the reach of application of oxygen sensors), and (b) that real-time UV–Vis spectrometry became a broadly accepted method and tool. Some 20.000 UV–Vis sensors opened new sectors of water monitoring. Generally, field instruments became digital, (slightly) more intelligent, more practical to use, and more communicative.

The organic carbon group still is the number one pollutant in many countries globally; in other countries, nutrients (nitrogen- and phosphorus-based) have taken the number one position; once this problem is more or less under control, concerns are focussing on micropollutants such as pesticides, and “emerging contaminants”, such as pharmaceutical residuals, hormonally active substances, microplastics, etc.

Summarizing the most popular parameters, UV-spectrometry has established for turbidity, TSS, colour, organics, nitrate/nitrite, hydrogen sulphide, and event detection; fluorescence for algae (species), oil in water, and organics fractionation; fluorescence and luminescence for dissolved oxygen; electrochemical sensors for pH, redox, ammonia, nitrate, and chloride; for total phosphorus/phosphate, as well as for organic nitrogen, we are missing real-world solid-state sensors. In the reminder of this chapter, we had to remove with regret parameters that should have been included, mainly pH and disinfectants such as chlorine, simply because of lack of space.

13.3.1 UV–Vis Spectral Sensors

We can group optical instruments by measuring principle: Light absorption (UV, Vis, NIR), emittance (fluorescence, luminescence), scattering (turbidity, TSS, flow cytometry), and vibrational scattering (Raman [108], MIR, IR).

13.3.1.1 Instrumental Principles

Many articles have been published about technology and applications of probe-type UV–Vis spectrometers. The related instruments and methods have established quite well, and found some acceptance in international and national norms. A comprehensive overview of the technology, methods, and potentials can be found in [31, 32], more in [33–36].

Figure 13.6 illustrates the most popular substance groups that can be detected in the UV spectrum: Organic carbon compounds, single aromatic contaminants BTEX and phenols; ions (NO_3/NO_2 , Cr^{VI} , HS^-), and in the visible spectrum turbidity, TSS, and colour. An important feature is that due to the simultaneous measurement

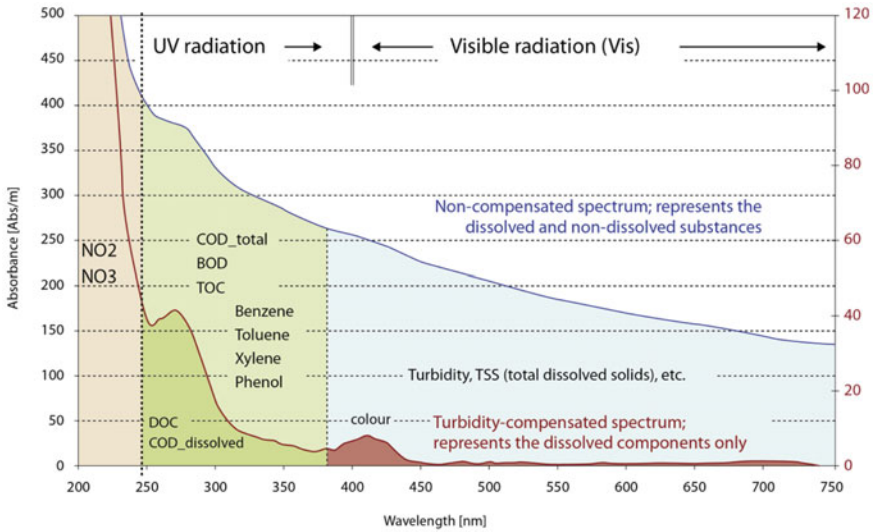


Fig. 13.6 Substance/groups in the UV–Vis spectrum

of solids (and fractions thereof), a UV–Vis spectrometer can reliably distinguish between the particulate and the dissolved fractions of organics.

A practical hint goes to operators of spectrometer probes: There is an established attitude with operators to immediately calibrate a sensor when the displayed value deviates from expectation. This approach originates from the use of pH sensors, which need to be calibrated regularly due to aging of sensor components (membrane, electrolyte). If applied to a 2-beam submersible spectrometer, we would call this “emotional calibration” as it does not need to be calibrated due to its non-drifting measurement system, as illustrated in Fig. 13.7.

Whenever a deviation from the expected value is being observed, calibration is not the right answer but will only overpaint a deviating status. The one important check with a spectrometer is to verify whether the measured UV–Vis spectrum is correct and linear, using distilled water or a zero filter, and a standard filter/liquid standard. If this is provided, the following points need to be checked in order of importance:

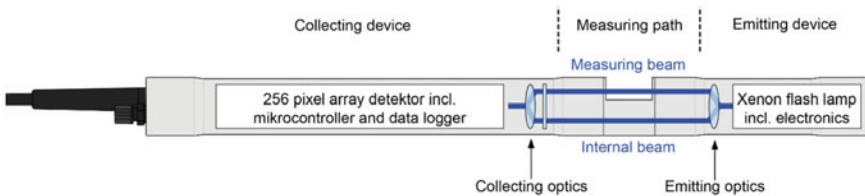


Fig. 13.7 Wear in the optical measuring path is being compensated by the internal beam

1. Fouling on the optical windows (precipitation of minerals, attaching of oil and grease)
2. Problem with installation (i.e. gas bubbles at windows)
3. Problem with reference measurement (laboratory or quick test)
4. Use of wrong calibration algorithm, “global calibration” algorithm not fit to describe the medium
5. Substantial change of water composition, so the used calibration algorithm fell out of its validity
6. Instrument malfunction

“Classical” UV–Vis probes with high-resolution detectors and broad band UV light sources have found their niche and will remain useful for at least another two decades. The next generation, however, based on LED-array light sources, is going to open a bigger volume market. Prices will drop dramatically with volume, and UV-LED technology will revolutionize the low-cost “smart water” market in the near future (Table 13.1).

The first probe of the LED generation came from s::can Messtechnik GmbH. It was the only instrument on the market that combined 180° spectral absorption

Table 13.1 Comparing the main differences between two spectrometer-types

	High-resolution spectrometer	LED-based spectrometer
Dynamic range, abs	ca. 2,5	ca. 1,8
Resolution	254 pixel, fixed	<10 pixel, variable
Range, ca	200–800 nm	245–900 nm (≥230 nm)
Light source	Xenon	LED-Array
Detector	fibre-optic high res. spectrometer (180°)	Two integrating photodiodes (180°/90°)
COD, TOC, DOC	Yes	Yes
Nitrate, Nitrite	Yes	No
Colour	Yes	Yes
Single substance detection	Yes	No
90° turbidity	No	Yes
Anomaly and event detection	Yes	No
Weight	ca. 1100 g	ca. 400 g
Size (length)	ca. 45 cm	25 cm
Energy consumption	Low	Very low
Market price, ca. €	7.000–12.000	3.000–6.000

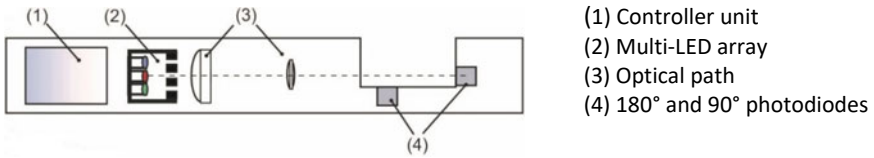


Fig. 13.8 An LED based spectrometer probe

measurement with 90° scattering to comply to DIN 38404-3 [21] for UV (SAC) measurement as well as ISO7027 [22] and EPA180.1 [23] for turbidity (Fig. 13.8).

13.3.1.2 Organic Carbon Matters

“(Natural) organic matter”, “Dissolved Organic Matter”, “Total/Dissolved Organic Carbon”—all attempts to summarize a group of substances that have in common to be the source of all life on earth, but also can be a threat. They cover a wide range of substances and can be naturally water-born, naturally terrestrial born, or anthropogenic.

The COD (chemical oxygen demand) is the most regulated pollution parameter globally, and limited in almost every effluent discharge norm. No direct toxicological effect can be attributed to COD, as it summarizes a broad diversity of substances from harmless carbohydrates to i.e. highly toxic pesticides. The reason to limit organic loads is to not overstress the sequential ecological or technical water systems. EU 2000/60/EC [16] indicates in Annex VIII: [49] “Substances which have an unfavourable influence on the oxygen balance (and can be measured using parameters such as BOD, COD, etc.)” Eventual toxic effects, however, might rather occur

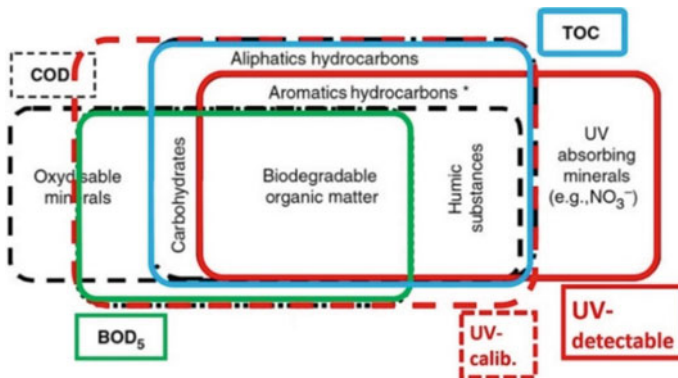


Fig. 13.9 Organic and inorganic matter by detectability, and principle of “matrix adaptation” (Weingartner based on [31])

in the same matrix with organic carbon peaks, and therefore COD peaks should also be responded to due to toxicity suspect.

COD, Total Organic Carbon (TOC) or Biological Oxygen Demand (BOD) are the traditional totalizing parameters to measure—a certain portion of—the substance group, each of them with their advantages, limitations, and applications. There are several sensors for online and in-situ monitoring of those parameters. Amongst them, UV–Vis spectrometry can either be co-related to those traditional parameters, but also be applied for further fractionation of organics, and with that, goes far beyond the classical totalizing analysis. Due to the diversity of molecular structures of organic and mineral compounds detectable in the UV–Vis, this is a broad and quickly evolving field (Fig. 13.9).

By what we commonly call “calibration”, we expand the domain of UV visible compounds into the domain of compounds that actually do not absorb light. This procedure expands the solid red frame “UV” to the dotted red frame “UV-calib.”, by just applying a factor. Actually, the term “calibration” is not correct here because “calibration” compensates the aging of sensors over time; instead we should use the term “matrix adaptation”. Substantial fluctuation of the organic matrix will have an influence on accuracy, and matrix adaptation will be needed in case of high accuracy expectation (Table 13.2).

Table 13.2 General overview of organic groups by detectability (Weingartner based on [31])

Substance group	COD	BOD	TOC	UV	ALL
Saturated compounds	1	1	2	0	2
Aliphatic unsaturated hydrocarbons	2	2	2	1	2
Aromatic compounds	1	0	2	2	2
Acids	2	1	2	1	2
Aldehydes, ketones	1	1	2	1	2
Alcohols	2	1	2	0	2
Phenolic compounds	2	1	2	2	2
Aliphatic amines	1	1	1	0	2
Aromatic amines	1	1	2	2	2
N unsaturated heterocycles	0	0	2	2	2
S unsaturated heterocycles	1	0	1	2	2
Humic-like substances	1	1	1	2	2
Total conversion	63%	42%	88%	63%	100%

2: 90–100% conversion or high UV absorption, or UV absorption after photo-oxidation

1: Partial conversion or partial UV absorbing compounds

0: Non-detectable (no conversion or no UV absorption)

Measurement of TOC using strong chemical or photocatalytic oxidation is the most complete converter. However, UV-spectrometry is the only realistic method to be used on-line and unattended in the field at reasonable cost. It gives a comprehensive and stable approximation if operated properly, to monitor most municipal and industrial effluents, and provides good agreement with TOC in surface-, ground-, and drinking waters—but sure has its limitation at largely fluctuating matrices.

It might be time to accept online “surrogate” methods as independent standards, and not just in reference to normed methods. All normative detection methods to monitor organic carbon have their limitations, do not reflect 100% of the organic carbon, and are not suitable for broad field use. The introduction of a “UV-spectral COD” standard would be just another convention, a useful, simple and comparable standard for “smart water” applications, always taking into account the limitations.

As an alternative to detect abnormal organic composition and with that, potentially toxic spills, the use of the UV-spectrum as a “fingerprint” of the water matrix in a generic way is receiving more and more acceptance, such as in the India guidelines for industrial effluents [19]. Anomalies in the UV-spectrum compared to a trained baseline can serve as an alarm that can escalate immediate action, and/or trigger automatic samplers, in all kinds of waters [37–42, 99, 100].

13.3.1.3 Phenols, Phenolic Compounds, Phenol Index

Due to the strong chromaticity of the aromatic ring, specific phenolic compounds can be individually assessed by UV-spectrometry, such as Alkylphenols, Chlorophenols, Nitrophenols, or Polyphenols. The total concentration can be used to characterise industrial wastewater discharges, expressed by the popular “phenol index”, as in ISO 6439:1990. However this analytical procedure is complex and not quantitative, as some phenolic compounds do not fully react. A simpler alternative for the rapid estimation of the “phenol index” is the UVSD method based on UV-spectrometry, as described in [32].

13.3.1.4 BTEX—Benzene, Toluene, Ethylbenzene, Xylene

The expression BTEX is summarizing benzene and its alkyl derivatives toluene, ethylbenzene, and xylenes. Due to their aromatic structure and chromaticity, they can be directly detected and quantified by UV-spectrometry. Their UV-spectra are finely resolved and relatively expressive, so detection is possible even against a strong matrix (Fig. 13.10).

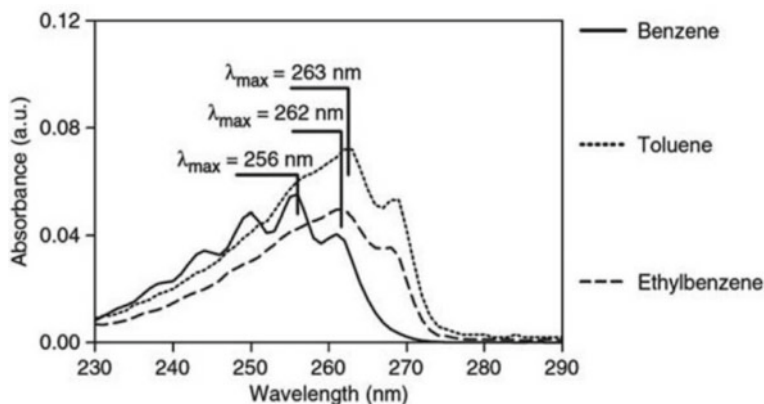


Fig. 13.10 UV spectra of benzene, toluene, and ethylbenzene [from 31]

13.3.1.5 Oil-In-Water, Hydrocarbons

Oil, in all its forms and occurrences, is one of the globally most feared types of water pollution. It can result in harm to the aquatic environment, be toxic to water treatment plants, can cause health issues to humans, and will generate bad publicity. Therefore, in most countries of the world, the discharge of water contaminated with oil and all types of hydrocarbons to natural waters as well as to sewer systems is forbidden, or at least regulated. Thus, there is a need to monitor—and detect—the (absence of) oil in water, or specific fractions of it.

In the EU, the dangerous substances directive 2006/11/EC [17] defined: “Persistent mineral oils and hydrocarbons of petroleum origin”—which is redundant with the now in force EU 2000/60/EC [16] Framework Directive and 2013/39 [15] as amendment. A direct toxicological effect cannot be attributed to Oil-in-Water, as it summarizes a broad diversity of substances from rather harmless (but un-aesthetic) fat-and-grease compounds to highly toxic PAHs, MTBE, etc. The toxicity profiles of several petroleum products are i.e. discussed in “Petroleum Products in Drinking-water” in WHO [12].

The detection and quantification of Oil-in-Water can be expressed i.e. as “Total Hydrocarbons”, “Oil-in-Water”, “Oil-and-Grease”, “Petroleum derived Hydrocarbons”, “Total Petroleum Hydrocarbons” (TPH), BTEX, PAHs, or others. The detection is normally defined by the method such as ASTM D3921-96(2011) [18], and/or by reference standards. A large portion of oil is contained in droplets and must be dissolved before analysis, thus is not directly accessible to in-situ sensors. Floating oil can be detected by relatively simple floating devices, looking at distinct differences of physical properties between oil and water such as the dielectric constant; conductivity; capacitance; multi-frequency acoustic properties, and others.

Only the very small dissolved portion can be detected by in-situ optical sensors. It includes compounds such as BTEX, NPDs, organic acids and phenolics, often detectable both by UV–Vis spectrometry and fluorescence. An important limitation for both methods is that most aliphatic compounds are not detectable (see Fig. 13.9) because of a lack of chromophores. The more refined an oil, the less detectable it will be by direct optical methods.

Quantification of Oil-in-Water by simple optical sensors would only be possible in a stable matrix, which is never the case in industrial, municipal or receiving waters. Therefore the given concentration values are to be considered indicative, confined to detect events and to alarm on high concentration of Oil in Water—at ppm, but not ppb level—and i.e. trigger the taking of a sample. Reliable real-time alarming on oil spills by simple optical methods, however, is an important contribution to pollution control, and should be implemented in all industries that have the potential of releasing oil/hydrocarbons with their effluents, and at all surface water intake infrastructure.

13.3.1.6 Hydrogen Sulphide

(Hydrogen) sulphide occurs both naturally and from human-made processes. It is associated with sewers and waste water treatment plants, manure-handling operations, pulp and paper operations, etc. Apart from toxic and smelling fumes, sulphide in aqueous form is corrosive and destroys water infrastructure.

Only the HS- species can be detected by UV spectrometry, but not the H₂S, which is the reason why at pH lower than 9, combined with fluctuating pH, the pH must be measured and results adjusted [95]. If pH is lower than 6 and/or constant, the standard calibration will be sufficient. UV-spectral monitoring became a standard in sewer projects to control chemical dosage for sulphide control [94].

13.3.1.7 Chromium VI

Chromium is associated with negative effects for the environment and human health, sadly reflected i.e. in the horrible poisoning of ten-thousands of people around the India leather capital of Kanpur. Cr(VI) is a suspected carcinogen and causes allergic contact dermatitis at low concentrations. Acute and chronic damage to the aquatic environment, as well as to soils, plants, plant-eating animals and humans is observed, by further accumulation consequential to re-use of contaminated water in agriculture. The ratio of chromium(III) to chromium(VI) varies widely, and relatively high concentrations of the dangerous (VI) species can be found locally in ground waters.

For online field measurement, there is no reliable quantification down to the limit relevant for human health ($50 \mu\text{g/l}$) [13]. However, Cr(VI) can be detected by spectral sensors by its absorption peaks at ca. 270 nm and 370 nm. The distinguishing of Cr(VI) from overlapping compounds is not a simple task, which is why Cr(VI) must be considered a research parameter, but useful after individual local evaluation and calibration; and for alarming and triggering an auto-sampler.

13.3.1.8 UV-Spectral Fractionation of Organics

A very promising field of research is the correlation of UV-spectral features to organic fractions, classes or species and their characteristics such as chemical composition, molecular size, geo-origin, source discrimination, oxidation state, reactivity and biological degradability, but also their technological behaviour, i.e. during treatment and distribution. An advantage of in-situ UV-Vis spectrometry is that the technology is affordable, reliable and well proven, so the progress mainly depends on reliable reference analysis of organic fractions, and on intelligent algorithms to distil the information from UV spectra. For further reading we recommend [44–49, 53]. [50] builds a bridge between UV-spectral and fluorescence fractionation of organics, and [66] give an overview of organic fractions as observed in diverse effluents (Fig. 13.11).

Fig. 13.11 Clusters of organics defined by their DOC concentration versus UV-spectral slopes, which allows allocation of their origin [66]

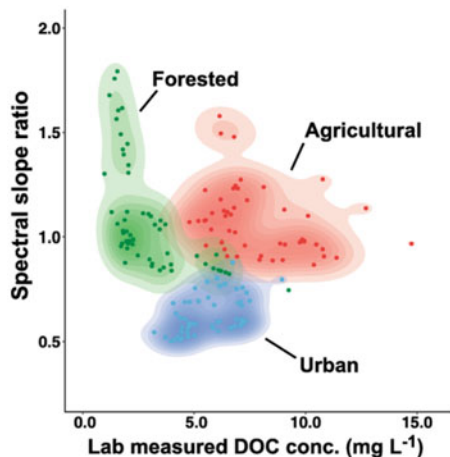


Table 13.3 Spectral gradients for “technological fractionation”, SA Water [107]

Parameter	Interpretation
A_{254}	Standard UV absorbance parameter
A_{254}/A_{202}	Ratio of absorbencies at 254 and 202 nm, a measure of activation of NOM (can be affected by the presence of nitrate)
$\frac{dA_{290}}{d\lambda}$	First derivative of absorbance at 290 nm, sensitive to the concentration of chlorine and NOM properties
$\frac{d^2 \ln A_{290}}{d\lambda^2}$	Second derivative of the logarithm at 290 nm; sensitive to chlorine concentration
$\frac{d^2 A_{310}}{d\lambda^2}$	Second derivative of absorbance at 310 nm, a potential measure of chlorine concentration
$\ln A_{350}$	Logarithm of absorbance at 350 nm, sensitive to NOM concentration and activity
$\frac{d \ln A_{330-370}}{d\lambda}$	Slope of logarithms of absorbance in the 330–370 nm region, expected to be a measure of the molecular weight of NOM and its activity
ASI $ASI = 0.56 \frac{(A_{254} - A_{272})}{(A_{220} - A_{230})}$	Absorbance slope index, expected to be a measure of the molecular weight of NOM and its activity

13.3.1.9 Technological Fractionation

For describing technical water applications, we suggest the term “technological fractionation”, which allocates properties to identify and quantify organic’s technologically relevant behaviour, such as: Biodegradability, (filter) adsorbability, coagulability, reactivity with chlorine to form disinfection-by-products, and others (Table 13.3).

Like for SA Water, such indicators can be extremely helpful for operators who try to optimize the design and operation of treatment plants and distribution systems. Further investigation and comparison to findings of other researchers at different water sources is encouraged, to evaluate and probably standardize some of these indicators to make them accessible and useful for water operators and managers. Concrete applications of technological fractionation are described in Sect. 13.4.

13.3.2 “Indirect” Spectral Measurement

13.3.2.1 Disinfection-By-Products (DBPs) and Their Precursors

DBPs are a complex group of substances, with the group of Trihalomethanes (THMs) as the most regulated. They occur when a disinfectant reacts with organic matter,

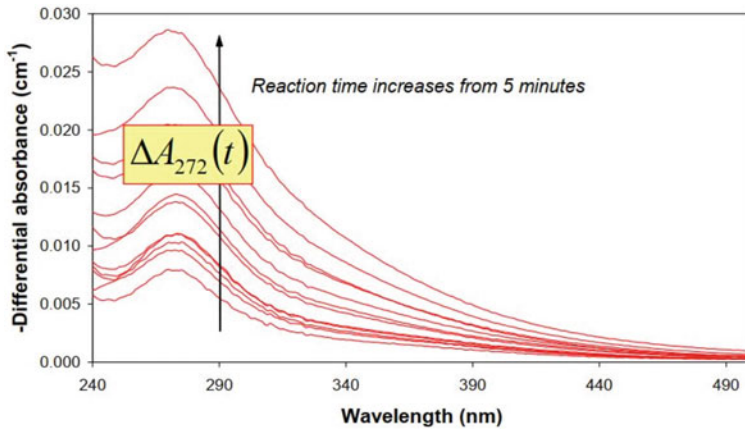


Fig. 13.12 Lake water “delta spectra” with increasing negative (!) absorption, starting after 5 min. reaction time [74]

building “halogenated” organic molecules. Long term toxic (cancerogenic and mutagenic) potential is attributed to this group, which is why the accepted limits are quite strict between 50 and 100 ppb globally. For operators with high and/or reactive TOC in their source water, it can be headache to maintain this level, and to keep a balance between hygienic safety and toxic risk. The dosage of disinfectant is normally kept high as a first priority to maintain hygienic safety, meaning that there can be phases of over-dose during periods of low TOC. During such phases, levels of DBPs can and often do go beyond allowed limits.

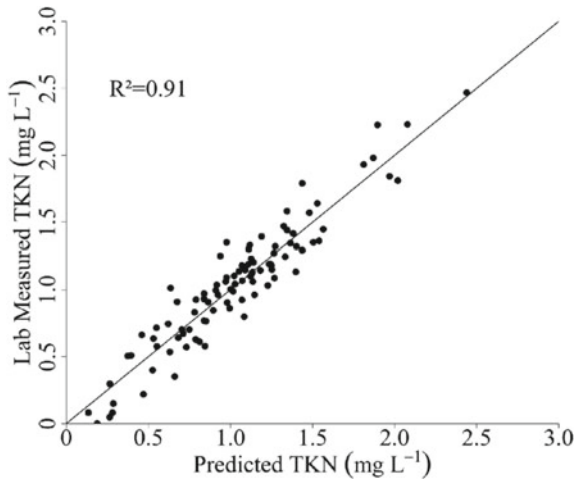
The exact quantification of DBPs is reserved to the laboratory. Delta UV-spectrometry can be an alternative for field monitoring: DBPs are not directly detectable in the UV spectrum, but the change of the organic matrix during oxidation is reflected by a reduced signal, which can be used by comparing spectra before and after oxidation (Fig. 13.12).

Korshin [73] discovered this interesting phenomenon, and continued to develop methods for identification [74], while [71, 72] investigated the suitability of the parameter in full scale. Stéphanie and Caetano et al. [75] report of correlations better than 90% for THMs and haloacetic acids (HAAs), by using the established parameter of delta 272 nm.

13.3.2.2 Phosphorus and Total Nitrogen

Even if a method is “blind” for a target parameter, information could be implicit or hidden. That could be a “pattern” or “fingerprint” of measurable parameters of the catchment area that are correlated to the target parameter. Such extrapolation we would call indirect or implicit measurement.

Fig. 13.13 Total nitrogen predicted by UV-spectrometry [76]

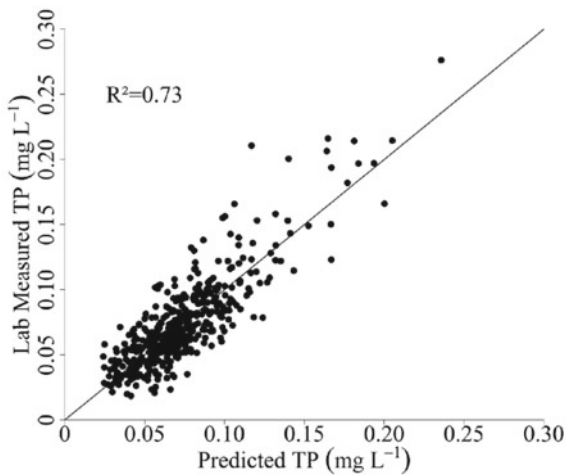


Nitrogen-, carbon-, and phosphorus-compounds and suspended solids were target substances in long-term observations at the University of North Carolina [76]. Spectrometric sensors were operated in the river/marine/brackish environment, and samples taken, via an innovative sampling platform.

DOC and NO₃ always correlate well to lab measurements. The achieved correlations indicate diligent work of all involved actors, and their use of optimized algorithms. This is not unexpected because these parameters exhibit strong enough signal for differentiation against a fluctuating background matrix.

Surprising is the correlation to total phosphorus and total nitrogen by spectrometry as shown in Figs. 13.13 and 13.14.

Fig. 13.14 Total phosphorus predicted by UV-spectrometry [76]



Phosphorus is not visible in any part of the UV–Vis spectrum, neither is the organic part of total nitrogen. But how could the researchers establish reasonable models for these parameters, considering the extremely dynamic measuring situation influenced by a tidal and seasonal mix of river, brackish and marine waters? In case of nitrogen (TKN), it can be assumed that the concentration of organic nitrogen is relatively small in such application compared to the mineral nitrogen fraction (which is detected by spectrometry), so the introduced noise is not getting dominant. In case of phosphorus (TP), the relationship is more delicate, because it seems that phosphorus comes synchronized with substances that produce a distinct absorption signal in the UV–Vis spectrum, and with that, reflect the characteristics of the dynamic catchment. It is established that much of the total phosphorus TP will come attached to small particles and colloids and therefore will correlate to the visible part of the spectrum, which can at least partly explain the r^2 of 73%. One could then argue that this relationship is accidental and not functional, just learning behaviour of the past while predictive quality remains fragile. However considering that the data spread over all seasons, it can be assumed that for this specific catchment, the correlation might be quite robust. For sure, the found algorithms will not be transferable to other catchments, but will require at least to be evaluated and validated, however, could be useful indeed.

These results receive further support by researchers working with real-time monitoring of solid-surface stormwater run-off, who also were able to establish prediction of substances that are invisible in the UV–Vis spectrum, such as phosphate or total nitrogen [67]. Carreres-Prieto et al. [43] established models based on data from 43 WWTPs using genetic algorithms and found correlation of 74% for total nitrogen TN and 71% for TP (total phosphorus), using a cost efficient low resolution VIS spectrometer (380–700 nm).

13.3.3 Light Scattering Technologies

13.3.3.1 Turbidity and Particle Speciation

The interest behind measuring turbidity is to know the concentration and weight of particles; after that, learn about the size of the particles and its distribution, and finally, about their form and shape. A detailed overview of the physical foundation provides [64].

ISO7027 [22] and EPA180.1 [23] are the standard methods to measure turbidity in drinking water in Europe and USA, respectively. The methods differ in several important details, which is why the results of both measurements are never 100% similar. Generally, EPA180.1 is a robust method but as it uses broad band white light, is prone to cross-sensitivity to colour; while ISO7027 uses a narrow band light

source at 880 nm and therefore is robust against colour, but less sensitive to the smaller fraction of solids.

The main problem with 90° scatter turbidity is that it is not linear to solids concentration (TSS), and smaller particles are causing more 90° scatter per mass than big ones. The potential of 180° spectral scatter turbidity is in its linearity over a much wider range, because the turbidity spectrum—a 3rd order polynomial—adapts to concentration and particle size [68].

In Germany, the parameter AFS63 (particles between 0.45 and than 63 μm size) has established through DWA-A102/BWK-A3, for evaluation of stormwater discharges, based on the finding that most of the contaminating pollution into a receiving water is attached or adsorbed to this fraction [69]. Recently, this parameter received particular attention due to its correlation to microplastics concentration [70]. However, there is no established method yet to determine AFS63 online; UV-Vis spectrometry is a candidate offering features that can be compared to particle size distribution [68].

Turbidity sensors can be made extremely cost efficient and are already installed in every day appliances such as intelligent washing machines, and thus are candidates for “smart water” applications. Interesting is the overlap of turbidity with organic colloids in the range of 350 nm, which still uses affordable LEDs but provides more information than the isolated turbidity signal at 880 nm [43].

13.3.3.2 Refractive Index

A microfluidic sensor by Optiqua <https://optiqua.com/> uses refractive index spectra detected on a MEMS chip. It detects comparative deviations from a baseline and is can be inserted into water pipelines.

13.3.3.3 Flow Cytometry

Flow cytometry (FCM) is an important optical method to check the microbiological composition of water, by counting, sorting, and characterizing the single cells; basically by shooting laser light onto a sample, and detecting light scatter and fluorescence. Applications are in water treatment, distribution, and reuse. Nearly 300 studies between 2000 and 2018 applied FCM to water quality assessment [109]. Automated and standardized FCM data collection and analysis methods are still missing, as well as standard methods and resources to support comparability of results.

13.3.4 Fluorescence Spectroscopy

Over the last decade, fluorescence spectroscopy received a lot of attention in the scientific world [56]. Focus has been on identification and classification of pollution, microbial/hygienic investigation, emerging contaminants detection, oil in water, algae, and some more, all of them related to fractionation/speciation. A technology trend has been 3D EEM (Excitation-Emission-Intensity) (Figs. 13.15 and 13.16).

Fig. 13.15 Left: 3-D EEM graphs plot excitation spectra against emission spectra, with the third axis representing Raman scatter intensity (in RU Raman Units) represented by colour [53]

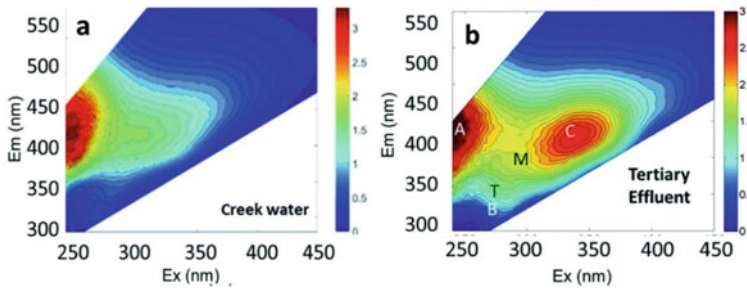
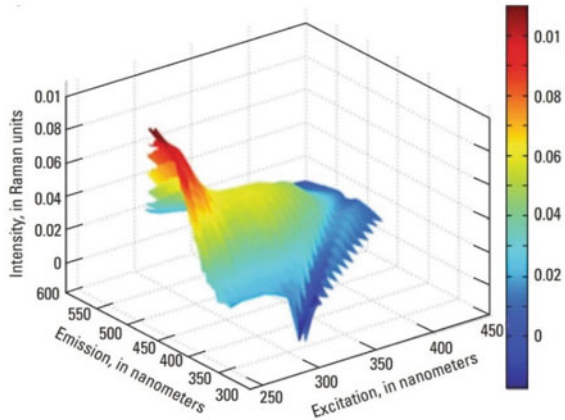


Fig. 13.16 Exemplary comparison of two different water types: Creek water and WWTP effluent [62]

Table 13.4 Adapted from [62]: Overview of substance groups distinguishable by fluorescence indices

Peak	Wavelength nm	Description
A	Ex260 Em 380:460	Terrestrial humic-like, high molecular weight, aromatic humic, hydrophobic acid fraction (HPOA); always high in wetlands and forested environments
B	Ex275 Em310	Tyrosine-like organic compounds, associated with amino acids and hydrophobic neutral fraction (HPON); indicates more degraded peptide material
T	Ex275 Em340	Tryptophan-like organic compounds, associated with amino acids, hydrophobic base fraction (HPOB), and hydrophilic acid fraction (HPIA); indicates less degraded peptide material
C	Ex350 / Em420:480	High molecular weight, humic-like compounds; high in terrestrial environments
M	Ex312 / Em380:420	Low molecular weight, marine humic-like compounds
Chla	Ex265 / Em696	Chlorophyll A
I	Ex 260 / Em 290	Due to Ibuprofen

Peaks A, C and M represent humic-like, natural origin peaks which are known to be associated with aromatic C bonded structures in humic and fulvic acids, while peaks B and T are associated with microbial sources of organic matter, aromatic amino acids and other fluorescent compounds, and can be of natural or anthropogenic origin. Such “heat-curves” provide interesting images of organics composition and fractionation, and allow to visualise a complex matter. The coloured peaks represent classes of organics, and often co-relate with the fluorescence pairs of Table 13.4.

Current topics in fluorescence research are:

- Characterisation of natural organics [55, 63]
- Characterisation, discrimination, speciation, and origin of waste water into receiving waters [54, 57]
- Detection of microbial and faecal contamination including *E. coli* [60, 61]
- Correlation of 3D-EMM to “emerging contaminants” and micropollutants [52, 58, 59]
- Detection of oil in surface waters, and its fractionation
- Transfer of 3D-EEM fluorescence data to portable fluorimeters [62] and to UV–Vis spectral sensors [50]. These optical methods are based on the same opto-chemical principles, so the results of the more complex laboratory method might be useful to “calibrate” the more cost efficient field instruments.

Some research needs are:

- For field fluorescence probes, researchers use different wavelength pairs for the same claimed index/substance class, so a good starting point would be to standardize, to make results comparable.

- One should be careful with the transfer of encouraging results from lab spiking experiments to field fluorimeters for determination of demanding parameters such as faecal contamination or “emerging substances”, often in the ng/l range. Background fluorescence in real waters fluctuates at a much higher level than the signal from the target parameter, preventing detection of those parameters.
- UV spectra contain information similar to excitation-emission pairs, or in other words, what absorbs, also fluoresces. UV spectrometry is less selective but more stable against changes of the background matrix due to a broad coverage of the optical spectrum for compensation. UV spectrometers should be deployed side by side to fluorimeters, to assess which of the technologies is more suitable in which type of application.
- Standards for quantitative interpretation of visually identified 3D-EMM classes are still missing, even if there are many attempts to standardise by characteristics such as organic chemistry (fulvic, humic, hydrophilic, hydrophobic), aromaticity, biochemical class (carbohydrates, proteins, lipids, thiols), age and oxidation status, origin, some physical properties, and others.
- Quantitative interpretation would make 3D-EMM really useful for water managers and operators, but until then, they would rather consider 3D-EMM a qualitative or comparative method.

13.3.4.1 Optical Oxygen Based on Fluorescence/Luminescence

Fluorescence based optical DO (dissolved oxygen) sensors have taken over the market, in process control as well as in environmental applications. Reason is their long-term stability and minimal maintenance needs. The traditional Clark-type electrochemical sensor will survive only in niche segments.

Although it could be expected that optical DO probes will be comparable in their performance, stability, and cost, there are quite remarkable differences:

- (1) Zero oxygen measurement: Shortcut nitrogen elimination processes are becoming more and more popular in waste water treatment, and DO probes are crucial for process control close to the zero oxygen level. These processes are more likely to produce NO (nitric oxide) and N₂O (nitrous oxide) than conventional processes. Researchers found that some optical DO probes suffer dramatically from cross-sensitivity to the produced NO, displaying a strong offset—in the ppm range—when there actually was zero oxygen in the medium [89]. The suffering probes were based on the luminescence principle, measuring the excited state lifetime, such as the Hach LDO (Loveland, CO), and are not recommendable for the low oxygen range in the presence of NO. Probes that are using the fluorescence (absolute intensity) principle, such as the INSITE (Slidell, LA, USA) Model 10 did not suffer from this cross-sensitivity, and were accurate down to zero DO concentration.

- (2) Maintenance: The luminescence probes need to have their membrane caps replaced bi-annually, and are not to be exposed to direct sunlight; routine calibration is not foreseen between membrane cap changes. For the fluorescence-intensity type of probes, there is no replacement parts at all, and they appear to be maintenance free for several years; routine calibration is not foreseen at all.

13.3.5 *Electrical Conductivity*

Conductivity is only being mentioned here because it is maybe the only one widespread sensor today that can be considered established, accurate, comparable, long term reliable, almost maintenance free, and affordable, both by investment and by operation costs. It can be useful in many applications, and can even be correlated to other, more expensive parameters such as salinity, or sometimes even COD.

Electrical conductivity reflects the ability of a liquid to conduct electricity, and is displayed in Siemens/cm. It is a measure for the total ions in the medium, but it has little significance for detection of pollution or toxicity, therefore must be considered an indicative parameter. However, it can show general trends and deviations of water quality, and can, especially if combined with other simple parameters such as pH and temperature, indicate problems with processes or water treatment steps. In some industries such as metal, plating, leather, and mining, it can be a good indicator for problems in case of high peaks, and it can support other sensor's results in case of such high deviations.

Even if probably the reach of interpretation is not very far, we always prefer to work with a solid set of reliable conductivity data over time than doing retrospective guesswork on a fragile set of i.e. ISE data.

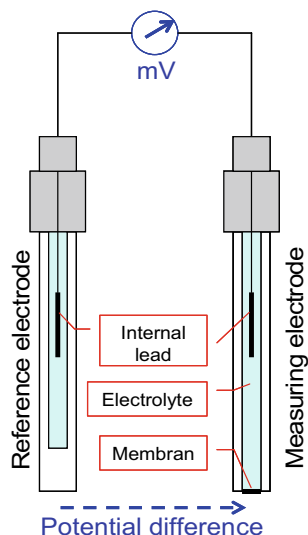
13.3.6 *Ion Selective Electrodes (ISE), Sensors and Probes*

Due to the importance of ISE probes for the control of wastewater plants and environmental applications, we give it more space here. To start with a concluding remark: The potential of the technology still has not been fully appreciated and developed until today, although a lot of research has been invested during the last two decades.

The range of substances detectable by ISE spans from the nitrogen species NH_4 (ammonia), NH_3 (free ammonia) and NO_3 (nitrate) over chloride, iodide, fluoride, potassium, sodium, up to some heavy metals. While NO_3 and NO_2 can be measured by UV-spectrometry, NH_4 and NH_3 do not absorb UV light, and thus can only be detected by ISE.

During the 1980s and 1990s, the reputation of ion selective ammonium sensors had suffered as not being reliable enough for control applications. After encouraging publications by some researchers [85–87] indicating satisfaction with ISE ammonia

Fig. 13.17 Schematic of the ISE measurement



sensors, the manufacturers jumped on and started to design and market a new generation of those probes around this publicity; which remained, however, technically quite similar as before, mainly adding some improvements for better handling, and creating consumables business. The selectivity of the membranes as a critical factor improved only by a small margin, and is still overpainted by the noise of batch-to-batch manufacturing quality and applicational challenges, thus was not a game changer.

The principle is an amperometric measurement of the potential created by the target ion across a ion-specific solid or liquid membrane (the ionophore), against the potential on the reference electrode (Fig. 13.17). The electrical potential (in mV) depends on the ion's concentration, according to the NERNST equation; on digital sensors, the non-linear signal-concentration equation ($\text{mV} \geq \text{mg/L}$) is calibrated and stored on board of the probe.

Of several, the two main methodical limitations are pH-dependency of the measured species, and cross interference from other ions, or specificity. The measurement itself is quite reliable today, the membranes are selective and rather robust, and interferences from other ions are not a big problem in "normal" waters [88]. However, to widen the range of applications, some manufacturers added a second ion-selective sensor to compensate for the main interfering ion (potassium for ammonium cations, or chloride for nitrate anions), plus a pH sensor. With introduction of additional sensors, also sources of error including the "human factor" were introduced. Those high-end systems now need to be kept clean, checked and calibrated for two ISE electrodes, one pH sensor, and one reference electrode. Not a trivial task that can only be recommended in specific applications, such as at the lowest end of the concentration range (<1 ppm); and/or where pH is relatively high AND fluctuating; and/or

where the ionic composition is fluctuating. Due to the additional maintenance effort, it became a common practise to deactivate compensating electrodes.

Also the detection of free ammonia (NH_3), the fish-toxic species in environmental applications, is possible, but a pH sensor must be added to distinct the species. Combining a UV-spectral sensor with an ISE probe, Total Inorganic Nitrogen ($\text{NO}_3 + \text{NO}_2 + \text{NH}_4$; in Germany: N_gesamt) can be indicated.

13.3.6.1 Practical Experience with ISE Probes

In general, ISE sensors are less robust than optical sensors. They need regular “ccc” (cleaning, calibration, consumables). When combining ISEs with optical sensors in monitoring stations, maintenance of the ISE probe will define the frequency of service visits, and with that, the cost of operation. When used for plant control, the satisfaction level is often higher, because maintenance is a must otherwise control will run out of control [5].

The ISE probes as offered by the major manufacturers today are fit for reliable measurement, even if still rather complex and delicate. There is a wide range of experiences in the records of the scan GmbH service department, from one large US WWTP where NH_4 measurement was accurate over 3 years without the sensor ever leaving the water; to the influent of some smaller WWTPs in Italy that never could leave the NH_4 sensor alone longer than one week during the summer period. The finding there: While flow in the sewer system was minimal during summer draught, local industries cleaned their infrastructure, using highly concentrated detergents and solvents—which, when arriving at the plant in almost undiluted concentration, quickly damaged the membranes and poisoned the electrolyte. In small systems, such events can become dominant. Also, some plants struggled during these toxic periods. In that way, sensor malfunctions can even be used to catch spills, not only to achieve longer service times, but to protect the plant.

Calibration: Whenever unexpected deviation from a reference value is observed with an ISE probe, calibration should be done as the very last step, only after all other sources of malfunction have been checked according to a Standard Maintenance Procedure (SMP).

We disclose here a “secret table” of potential malfunctions to be checked, an empirical ranking after 15 years of designing, manufacturing and servicing ISE probes:

1. Conditioning / adaptation of electrodes to the ionic matrix done sufficiently (12 h)?
2. Fluctuating ionic matrix and interferences / stable calibration will be difficult
3. Mechanical stress to membranes / avoid pressure air cleaning if you can, it can be very abrasive
4. Chemical stress to membranes by solvents or detergents / check occurrence in small sewer systems

5. Rhythmically “jumping” values / electrical noise, “wandering currents” from nearby machines / check electrical connections and grounding
6. Reference electrode drifting – often ignored / check, calibrate, use non-salt-bridge variant
7. Quick aging and/or poisoning of electrolyte / demanding application, very high or very low mineralised media
8. Problem with reference lab measurement or quick test
9. Electrode storage conditions unfit, or shelf life exceeded

Another practical observation: The highest cost (risk) is unplanned maintenance, and with that, the time consumed for investigation of error causes. The highest satisfaction with ISE probes is with operators who are able to minimize unplanned maintenance by designing, establishing and training SMPs, to lead service staff through a step-by-step procedure to eliminate or reduce the “guessing-time”.

Companies such as *s::can Messtechnik GmbH* provide (graphical) representation of those deviations, also offering simple tests, to help the operator to identify the problem. Next logical step would be to convert these tools into self-detecting algorithms, and let the probe itself find out (a) whether there is a problem (b) what might cause the problem (c) how it can be cured. And with this, finally be “intelligent”.

Table 13.5 Simple cost comparison between optical and ISE nitrate measurement

	ISE NO ₃			Optical NO ₃		
		Cost/year			Cost/year	
CAPEX incl. accessories, installation and start-up		€ 600	6.000 €		€ 1100	11.000 €
Consumables		€ 700	1 NH4 + 1/3 reference elec.		€ 50	Cleaning system parts
Check and clean		€ 720	Weekly 15 min		€ 180	Monthly 15 min
Calibrate		€ 120	3-monthly 30 min		€ 0	Never
Exchange and deep check		€ 120	yearly 1 h		€ 120	Yearly 1 h
Total h/yr			Total 16 h/yr			Total 4 h/yr
Labour cost 60 €/h						
Purchase, over 10 yrs	27%	€ 600		76%	€ 1100	
Labour cost	42%	€ 960		21%	€ 300	
Consumables	31%	€ 700		3%	€ 50	
		€ 2260 Total cost/yr			€ 1450 Total cost/yr	

A simple cost comparison between optical and ISE nitrate measurement in Table 13.5 unveils a surprising economic advantage for the optical measurement. Surprising because the initial purchase price is substantially higher, but along 10 years of ownership, the cost is almost 40% lower. While purchase is the main cost portion for optical probes, labour is the main cost for ISEs, however will depend on the application, and on competence of staff.

13.4 Turning Data into Information—Some Monitoring and Control Applications

13.4.1 Control of Waste Water Processes

The very first commercial applications of online water quality sensors were control applications at wastewater treatment plants (WWTPs), as the efficient control of treatment processes without having “eyes” in the process is difficult. Blower control by oxygen concentration was the pioneer application, starting at German treatment plants in the 70ies of the past century. Advanced or short-cut nitrogen removal processes today aim at minimizing energy consumption, without external carbon source, and minimizing the greenhouse gas production [84]. Examples are ammonia feed-back control [82, 83], control of sequencing batch reactors SBRs [81, 93], control of Anammox/Demon processes [77–80, 82, 83], nitrogen species incl. nitrate for effluent control [85, 90, 91], and nitrogen species, COD, TSS and sulphide for sewer control and management [92, 94, 95].

One important difference to other sensor applications is that the proper functioning is mission critical once the sensor is integrated into process control: A drifting sensor will cause a drifting process, loss of efficiency, or even compliance failure. In other applications, such sensor will not cause immediate problems and a malfunction might only be noted retrospectively. Consequentially, sensors for real-time control are generally more appreciated than those that are used i.e. for compliance monitoring [5]. With such lack of incentive, maintenance receives lower priority, and sensors are more prone to malfunction.

On the other hand, perfect accuracy is not a must for control applications, but stable, drift free measurements that well reflect the dynamics of the process in real-time are.

Even if sensors are getting more and more stable and reliable, they will never be perfect. Therefore, for control applications, research has to focus on real-time detection of any malfunctions by smart algorithms (with drift detection being still the main challenge), corrective algorithms, preventive maintenance, and efficient operator communication.

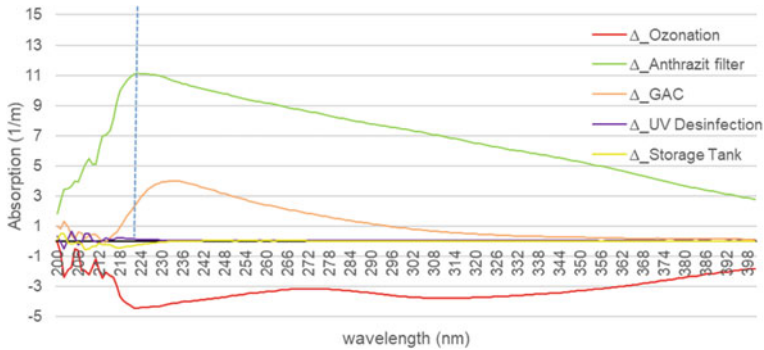


Fig. 13.18 Delta spectro-metry for profiling UV-spectral changes along a surface water treatment plant [51]

13.4.2 *Delta Spectrometry for Process Control*

Two on-line spectrometers are placed before and after a treatment step; the difference (delta) spectrum [37] opens a new perspective, as it allows to closely track minimal changes of water composition along the treatment step, and gives a more comprehensive picture than “classical” single parameters (Fig. 13.18).

Without deep diving into analysis here, the delta spectra along the treatment profile illustrate the effect of each treatment step respectively. Delta spectra can be used directly to standardize the treatment target for each step, and control the process by tracking deviations from it. A special spectrum is the negative one (red), post-ozonation, which is explained by the reduction of chromophores when oxidizing the larger organic molecules, which helps to predict Disinfection-Byproduct precursors [73].

13.4.3 *Prediction of Assimilable Organic Carbon (AOC) by Delta Spectrometry*

AOC is a term to assess the biostability of waters, and it is closely related to the organic composition. Standard Method 9217 [24] is used for AOC determination. UV-Vis spectrometry has been tested to extract information related to biostability [49–51]. AOC is related to small molecular weight compounds with strong representation of the proteins class. It has been estimated in drinking water as a small fraction of 0.1–9% of the TOC [96]. Regarding limitations for growth of microorganism, heterotrophic bacteria did not increase when AOC was $<10 \mu\text{g/L}$, and water is considered biologically stable when AOC is $<50 \mu\text{g/L}$ [96], referring to Kaplan and v.d. Kooji.

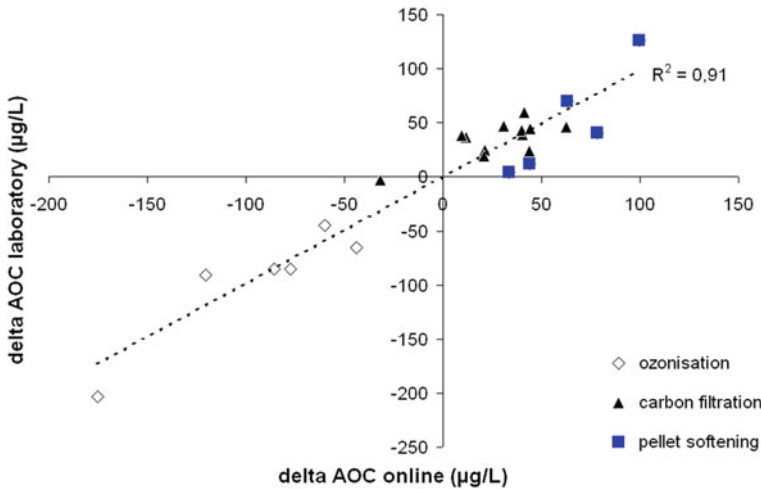


Fig. 13.19 Correlation between predicted AOC based on delta spectra, and laboratory AOC [96]

During oxidation/ozonation, the NOM macromolecules such as humic and fulvic acids are being cracked into smaller ones, and the availability of AOC and with that reactivity increases. This is especially important in drinking water networks that are operated without residual disinfectant. The resulting changes are visible in the UV-spectrum and allow the estimation of changes in AOC concentration along ozonation, pellet softening, and GAC filtration, at Amsterdam Waterworks [96] (Fig. 13.19).

Laboratory analyses of AOC concentration and UV–Vis delta spectra were correlated to develop algorithms that predict the change of AOC from the delta spectra along the treatment process. The relation could be established for the entire treatment process, and less strongly, for individual treatment steps.

13.4.4 Predictive or Feed-Forward Control (FFC)

Predictive control systems are of great advantage when the raw water quality fluctuates strongly. Based on historical data and experiments, a starting model is being established to predict the optimum amount of chemical to be added or other treatment options to achieve the treatment target. A sensor array provides real-time information about the actual water matrix, and the model predicts the optimum dosage or treatment. The dosing pump or actuators are triggered by this information. Ideally, there is a feed-back loop from product water sensors. This way, over- as well as under-treatment is avoided, and the use of chemicals, energy and other operating materials are optimized. The model can be self-learning and constantly improving, to avoid drift and erratic behaviour—a “digital twin” of the process (Table 13.6).

Table 13.6 An overview of FFC applications along a surface water treatment plant, see also Fig. 13.18

Source water blending	Prediction, control and neutralization
Coagulation control	Selection of best fitting coagulant and flocculant chemicals and combinations
	Prediction of chemicals demand
	Optimized dosage
	Feed-back control for backup strategy
	Documentation of finished water quality
Oxidation (Ozone, AO, etc.)	Predict, optimize and control dosage
Filter	Monitoring and control
GAC	Prediction of breakthrough
	Optimization of reactivation
Membrane filters	Prediction and reduction of membrane fouling [105]
	Selection of best membranes
	Monitoring and prediction of break-through
	Optimization of cleaning process and used chemicals
Disinfection	Chlorine demand prediction and control
	Disinfection By-products prediction and minimization
	Safeguard and prove hygienic control

13.4.5 Feed Forward Coagulation Control (FFCC)

A good overview on coagulation control basics and applications is given by US-EPA [102]. Typically, operators are used to adjust the coagulant dose once per day, sometimes based on manual jar tests, and thus accept periods of overdose; underdose is rare in the real world as operators tend to adjust at the “safe side”. Main classical parameters are turbidity (NTU) and organics (T/DOC). Reduction of DOC is a bottleneck to reduce disinfection by-product (DBP) formation potential, often difficult because the dissolved organics need to be motivated to form flocs before they can be settled or filtered. Reductions of 30–50% would be satisfying, while turbidity should be reduced almost completely [103].

FFCC would be the “golden standard” in dynamic systems (river intakes) but still is rarely implemented. The advantages are: Better and more regular water quality; less chemical consumption because there is no overdosing; less residuals, e.g. less residual aluminium (Alzheimer-suspect) in product water; reduced organic substances; less energy for mixing, pumping, aeration, backwash; less sludge; OPEX reduction.

The UV–Vis spectrum provides a comprehensive picture of water quality, and, together with innovative algorithms, can be used in a non-correlated fashion, as a whole “fingerprint” of the medium. FFCC based on UV–Vis-spectra has established in some countries such as Australia [101], New Zealand [104] and UK.

13.4.6 Prediction of Chlorine Demand and Feed Forward Chlorine Control

Prediction of chlorine demand is an extremely valuable parameter and part of any feed-forward control strategy. It has been investigated for several years at the Australian Water Quality Centre in South Australia, with interesting results [5, 106, 107]. Chlorine demand is predicted based on spectral gradients (and with that, organic composition) as suggested in chapter “Technological fractionation”. Figure 13.20 shows a good fit between laboratory und prediction. The online measurement indicates micro-fluctuations that cannot be seen by manual sampling and lab analysis.

In Fig. 13.21, a sudden drop of chlorine demand was registered at around 2am, and it was noted that the water flow was reduced during that period. Slower plant flow resulted in better water quality by reduction of organic carbon content, and with that, less chlorine demand. In a conventional system, the dosing system would adjust the dose via a feed-back control loop based on chlorine residual at the outlet (red line), which would come 20 min. later than when using the chlorine demand predictor which detects the drop in demand in real-time and adjusts dosage immediately. Chlorine overdosing is prevented.

Fig. 13.20 Chlorine demand predicted (pink) versus laboratory [106]

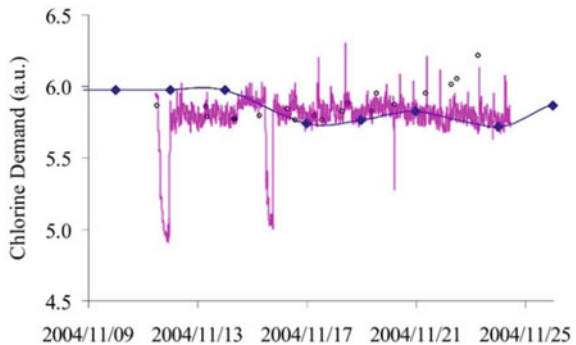
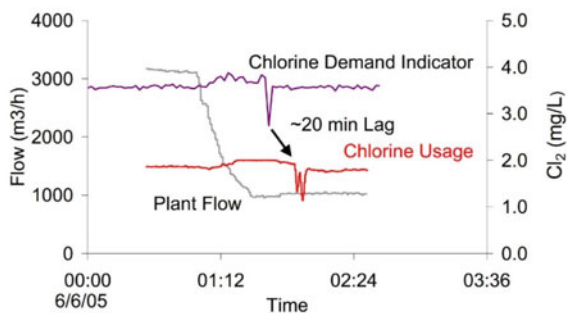


Fig. 13.21 Chlorine dosing [107]



13.4.7 Industrial Emissions Monitoring

Today, only a small proportion of industrial pollution events globally are being detected in real-time. Reason is that real-time monitoring—i.e. of organics—is a rare exception in industrial discharges, and if installed, equipment is rarely maintained properly, and if maintained properly, it is often not streaming data into a living real-time alarm system.

Manual sampling procedures are not suitable to detect such events because it is very unlikely that an official person will be at site taking a sample right when such event is happening. Because of being blind during the event, no counter-measures can be taken in real-time to minimize the consequences. Therefore, the often catastrophic impact for human health and environment resulting from a toxic spill can only be documented in retrospective, if at all. In addition, the regular discharge of polluting and toxic loads into water bodies is a constantly growing stress to the environment, especially because permits are typically given case by case, neglecting the accumulative nature of discharges along a water body. The accumulative nature of non degradable substances such as heavy metals in water-related compartments such as sediment, soil—via irrigation—and plants is often not well understood and not regulated, and, right in this moment, is building up at a fatal speed in “quickly developing (and not well controlled) economies”. In order to overcome the massive impact of industrial discharges into the environment, some countries have started implementation of ambitious industrial monitoring programs, with India monitoring about 10,000 industrial effluents for water quality. An overview gives <https://www.cpcb.nic.in/ocems6/>, the categorization of industries in [97].

The basics of these programs are at the sensor and parameter level. The (non-published but available upon request) study [98] is meant to give some answers to the question: Which parameters/pollutants should be measured in which industries, how can they be measured, and where to set realistic limits. The focus is set on online, solid-state, heavy-duty, optical or electrochemical sensors, because only such sensors will work in industrial applications, surviving aggressive media and negligence by operators.

With regard to “monetary reflection” of the polluting discharge, there are typically two components: Regular billing of discharged load, typically in kg or tons per time period, such as in many European countries; and fines for violation or substantial exceed of compliance limits, such as in Korea or India. An innovative approach, i.e. in Germany and France, is to translate substance concentrations into “pollution-units” (“Schadeinheiten” SE), so substances can be compared on the same scale regarding their polluting impact. In such a system, i.e. 20 mg/l COD polluting impact would equal to 0,001 mg/l Mercury, or 0.01% The polluter-pays-principle is being requested by the EU and international authorities.

13.5 Trends

13.5.1 *IO(W)T—The Internet of (Water) Things*

Innovation in the water industry seems to be driven by buzz words such as “smart water”, “big data”, “digital transformation”, “IoT—internet of things”, etc. The integration of water quality sensors into the IoT is one mega trend happening right now. After about 15 years of “smart water” discussion, this trend might still be more industry-pushed than customer-demand-pulled, but, following ongoing market research [1], there is enough indicators that customer demand is taking over.

It is not hard to predict that every sensor will have an I.P. address, will be connected to the “cloud”, and will talk to many other devices via the same interface. It seems a clear track, with advantages for operators and consumers, but it is still a long way to go, because in an industrial environment, conditions are demanding, from security questions over energy consumption to protocol standardization.

13.5.2 *Digital Twin (DT)*

The DT working group <https://www.swan-forum.com/digital-twin-h2o-work-group/> inside the SWAN forum defines DT as follows: “*A DT can be defined as an actively integrated, accurate digital representation of our physical assets, systems, and treatment processes with a constant stream of data pairing from the physical twin for continuous calibration More concretely, a DT for a water utility is a combination of modelling software that utilizes data from multiple sources and usually across multiple departments and expertise.*”

13.5.3 *Sensors for the People*

Water of safe quality should be provided in a controlled manner to each citizen of the world. There is no justification that even today, millions of people drink water of doubtful quality. Technology is needed to monitor water quality in an extremely cost efficient and reliable manner. Optical sensors, especially if based on LED technology, have the potential to be integrated into any devices that are near to the point of use, such as valves, pumps, water meters, even faucets, and with this become ubiquitous.

13.5.4 Soft Sensors—Mining the Wealth of Water Data

Today's sensors and sensors packages produce huge amounts of data, such as highly resolved UV–Vis or fluorescence spectra, fingerprinting water quality at high temporal and spatial density. To condense this information into single parameters to be able to compare with “classical” laboratory parameters is an unnecessary waste. Why TOC, when fractionation of organics is possible with the same instrument? Why TSS, when classification of particle size is possible?

There is a huge potential in re-directing research towards better exploitation of data, mining of so far hidden information, use of redundancy of information for quality assurance, use of swarm intelligence in sensor networks to predict system performance and reaction, focus on baseline training and event detection, on technological fractionation for process control optimization, on better understanding of historical data, changes and trends in watersheds, to prepare our water system for the impacts of climate change, and more efficient management and maintenance of an expensive infrastructure.

The data are already being produced every day, all around the world, and are waiting to be mined. Owners and operators of sensors could take more advantage of their investment, get more insight into their water processes, and use that insight to more efficiently manage a most valuable resource—if scientists and manufacturers only provided them suitable algorithms and tools.

On the business side, there is a lot of room for start-ups to develop (self-learning) algorithms, tools, and apps to validate sensor health in real-time, detect anomalies, and even take corrective action.

13.6 Practical Deficits—The Urgent Wish List

- Make existing sensors better

We can claim that we do not need novel sensing technologies at the time being, but we need the existing sensors to become easier to use, more reliable, better integrated, and more affordable. Amongst others, we need more efficient and intelligent self-cleaning systems, and more robust electrodes.

But compared to modern consumer electronics such as smart phones, water quality sensors appear to be old-fashioned and laid back. This is to be explained with the generally conservative character of the water industry, managing a fragile medium that needs to be accomplished without taking a risk, but also with the relatively small R&D budgets of the manufacturers. However, there will be a massive cross-diffusion of hard and soft technologies from the consumer market into the water sensor market (cheap LEDs as just one example), so that modern sensors will be much more powerful, especially on the software side. Young operators are living in a digital world today and are used to simple and comfortable user interfaces and powerful communication; they are tired to accept a world of analogue (or baroque-style-digital) tools

in their professional environment. They want to have simple to use apps, powerful controllers and interfaces, huge data storage, web servers on board, I.P. address and the internet protocol, Bluetooth for smartphone-to-sensor communication, local data evaluation and training options, and features implemented that make sensors and data more reliable—and their life easier.

- Make sensor infrastructure better

Maybe we should go back to what we had expected when we planned a sensor purchase, and actually make them do what we had expected, by improving the installation and integration infrastructure. In that context, the (hard and soft) environment and infrastructure accommodating sensors deserves more focus and better design, which is a shared task for manufacturers, system integrators, consultants, and operators.

- Standard Maintenance Procedure (SMP) Apps

Standards for quality control and quality assurance (QA/QC) of sensors should be condensed into standardized maintenance procedures (SMPs), ideally synchronized across the industry. The lack of SMPs is considered a main bottleneck with broader acceptance and wider use of water quality sensors. They should be simple to follow and self-explaining, so they can survive in the rough world of water operators. Ideally, SMPs would be implemented into Apps that actively guide the operator through all procedures, and with this also can become a part of an asset management and QA/QC systems.

- A SIMPLE solid state online phosphate sensor
- Reliable online sensors for microbiological parameters.

13.7 Conclusions

The authors assume that today, the purchase price of sensors is not anymore preventing their broad deployment. However preventive is indeed the wide spread opinion that (a) the cost (and effort) of sensor operation is too high, and (b) measured data are not reliable enough. Some say, sensors should be more intelligent, self-monitoring and error-detecting, and communicate all information about their well-being to the operator via a digital interface. Even if this contains some truth, we think it is not ideal to accept all today's shortcomings of sensors and their infrastructure and communicate all this to the control room. This would only further overload the already stressed operators, and make sensors even less interesting for them. Instead, manufacturers should eliminate the shortcomings at the root, by designing more reliable sensors, more enduring quality, better installation infrastructure, but also

intelligent, corrective algorithms that improve data quality on-board without operator intervention. By solving these tasks on the sensor level, the task of integration into any network can be more easily accomplished via conventional digital interfaces.

Then, consumables do not have to be as expensive as they often are today, and the attempt to apply the “printer-cartridge” model to the water sensor market increases the cost of operation to such level that a broader implementation is not feasible. Also, the idea to make users dependent of highly specialised experts and “service contracts” caused mistrust (“doesn’t this work without service contract?”), and prevented from enthusiasm.

In the end, only such sensors will be fit for “smart water” applications that are intelligent, extremely reliable, and self-sufficient, allow to be operated and maintained in a planned routine mode at minimum maintenance intervals and with minimum operator communication, so that corrective interventions would be a rare exception, and cost of operation would be minimized.

The best sensor is the one that the operator forgets, but enjoys a rich and reliable data stream, just as rich and reliable as the water stream from her tap.

References

Compilations

1. Frost Radar (2020) Global smart online water sensor solution market. Benchmarking Future Growth Potential
2. Raymond James Water Quarterly <https://www.raymondjames.com/>
3. Ingildsen P, Olsson G (eds) (2016) Smart water utilities—complexity made simple. IWA Publishing 2016, Open Access Book 2020
4. Boyd CE (2015) Water quality. In: An introduction, 2nd edn. Springer
5. van den Broeke J et al (2014) Compendium of sensors and monitors and their use in the global water industry. WERF Water Environment Research Foundation & IWA International Water Association
6. Orellana G, Cano-Raya C, López-Gejo J, Santos AR (2011) Online monitoring sensors. In: Wilderer P (ed) Treatise on water science, vol 3. Academic Press, Elsevier, Oxford, pp 221–262
7. Kruse P (2018) Review on water quality sensors. J Phys D: Appl Phys 51:203002

Norms and Methods

8. Hohenblum P, Pitchers R, Raich J, van der Valérie Tanchou B, Gaag AW (2016) Proposal for a guidance related to a water security plan to protect drinking water. Publications Office of the European Union, ERNCIP Thematic Group Chemical and Biological (CB) Risks to Drinking Water, p 2016
9. ISO 15839/2003 Water quality—on-line sensors/analysing equipment for water—specifications and performance tests, ISO copyright office, 2003, confirmed 2019

10. The UK Environment Agency Monitoring Certification Scheme (MCERTS): Performance standards and test procedures for continuous water monitoring equipment Part 2—Performance standards and test procedures for on-line monitors. Environment Agency Version 3.1, Aug 2010, revision 2014
11. US-EPA Environmental Technology Verification (ETV) Program (2000). <https://semspub.epa.gov/work/HQ/189908.pdf>
12. The World Health Organization (2008) Petroleum products in drinking-water—background document for development of WHO Guidelines for Drinking-water Quality. WHO/SDE/WSH/05.08/123, World Health Organization
13. The World Health Organization (2003) Chromium in drinking-water—background document for development of WHO guidelines for drinking-water quality. World Health Organization, WHO/SDE/WSH, p 2003
14. The World Health Organization (2011) Guidelines for drinking-water quality, 4th (edn)
15. DIRECTIVE 2013/39/EU of the European Parliament and of the Council of 12 August 2013 amending Directives 2000/60/EC and 2008/105/EC as regards priority substances in the field of water policy (Emerging Substances)
16. DIRECTIVE 2000-60-EC—23 Oct 2000—establishing a framework for community action in the field of water policy
17. DIRECTIVE 2006/11/EC—15 Feb 2006—on pollution caused by certain dangerous substances discharged into the aquatic environment of the community
18. ASTM D3921-96 (2011) Standard test method for oil and grease and petroleum hydrocarbons in water
19. The Central Pollution Control Board CPCB, Delhi, India (2014) Guidelines for online continuous monitoring system for effluents
20. US-EPA Method 334.0 (2009) Determination of residual chlorine in drinking Water using an on-line chlorine analyzer, EPA 815-B-09-013, Sept 2009
21. DIN 38404-3: German standard methods for the examination of water, waste water and sludge—physical and physical-chemical parameters (group C)—Part 3: determination of absorption in the range of the ultraviolet radiation. Spectral absorptions coefficient (C 3)
22. ISO 7027-1:2016 Water quality—determination of turbidity—Part 1: quantitative methods
23. US-EPA Method 180.1 (1993) Determination of turbidity by Nephelometry
24. 9217 Assimilable Organic Carbon AOC, Standard method for the examination of water and wastewater. American Public Health Association. American Water Works Association. Water Environment Federation <https://www.standardmethods.org/doi/abs/https://doi.org/10.2105/SMWW.2882.190>

Precision, Accuracy, Time Series

25. Weingartner A (2015) Using s::can spectro::lyser™ with ruck::sack in the Krycklan Research Catchment, customer communication of s::can Messtechnik GmbH, Vienna. Details at: <https://www.slu.se/en/departments/field-based-forest-research/experimental-forests/vindeln-experimental-forests/krycklan/>
26. LIFE99 ENV/A/403—Technischer Schlussbericht (2002) Management of sensible water uses with the help of innovative sensor technology
27. Weingartner A (2019) Parameter evaluation method and chart for industrial effluent monitoring (not published, available on specific request)
28. US-EPA Office of Water (2016) Exploratory analysis of time-series data to prepare for real-time online water quality monitoring. US-EPA 817-B-16-004
29. Horsburgh JS, Reeder SL, Spackman Jones A, Meline J (2015) Open source software for visualization and quality control of continuous hydrologic and water quality sensor data. Environ Model Softw 70:32–44

30. Raich-Montiu J, Edthofer F, Wurm R, Weingartner A (2016) Real-time monitoring of Ganges River basin during Kumbh Mela ceremony. In: Smart water utilities by Pernille Ingildsen and Gustaf Olsson, IWA

Spectrometry

31. Thomas O, Burgess C (eds) (2017) UV-Visible spectrophotometry of water and wastewater, 2nd edn. Elsevier Science
32. Thomas O, Theraulaz F, Domeizel M, Massiani C (1993) UV spectral deconvolution: a valuable tool for waste water quality determination. *Environ Technol* 14(12):1187–1192
33. van den Broeke J, Langergraber G, Weingartner A (2006) On-line and in-situ UV/Vis spectroscopy for multi-parameter measurements. *Spectrosc Eur* 8(4):2006
34. van den Broeke J, Koster T (2019) Spectroscopic methods for online water quality monitoring. In: ICT for smart water systems, measurements and data science. The Handbook of Environmental Chemistry, Springer
35. van den Broeke J, Ross PS, Edthofer F, van der Helm AWC, Weingartner A, Rietveld LC (2009) The versatility of Online UV/Vis spectroscopy—an overview. In: van den Hoven, Kazner (eds) *Technau 2009 proceedings* chapter 14. IWA Publishing, London, UK
36. van den Broeke J, Brandt A, Hofstädter F, Weingartner A (2006) Monitoring of organic micro-contaminants in drinking water using a submersible UV/Vis spectrophotometer. In: Pollert J, Dedus B (eds) *Security of water supply systems: from source to tap*. Springer

Delta Spectrometry, Event Detection

37. Langergraber G, Weingartner A, Fleischmann N (2004) Time-resolved delta spectrometry: a method to define alarm parameters from spectral data. *Water Sci Technol* 50(11):2004
38. Weingartner A, Ruzicka M (2003) Sensors for water security and alarm systems. In: *Proceedings of the conference “Dodavka vody v krizovych situaciach”*, Bratislava, Slovak Republic., 11 Sept 2003
39. van den Broeke J, Edthofer F, Weingartner A (2011) Clean data and reliable event detection—turning results from online sensors into information. In: Borchers U, Thompson KC (eds) *Water contamination emergencies: monitoring, understanding and acting*. RSC Publishing
40. Thompson KA, Scott RA, Kadiyala R, Weingartner A, van den Broeke J (2009) Advances in data validation, event detection, and communications structures for a CWS—case study: Glendale, Arizona. In: *Proceedings of the American Water Works Association—2009 Water Security Congress*, Washington DC, USA
41. Chandrasekaran S, Rebolledo M, Bartz-Beielstein T (2020) EventDetectR—an open-source event detection system. Institute for Data Science, Engineering, and Analytics, TH Koeln
42. Russo S, Luerig M, Hao W, Matthews B, Villez K (2020) Active learning for anomaly detection in environmental data. *Environ Model Softw* 134(104869):2020
43. Carreres-Prieto D, García JT, Cerdan-Cartagena F, Suardiaz-Muro J, Lardín C (2022) Implementing early warning systems in WWTP. An investigation with cost-effective LED-VIS spectroscopy-based genetic algorithms. *Chemosphere* 293

UV-Spectral Fractionation of Organics

44. Weishaar JL, Aiken GR, Bergamaschi BA, Fram MS, Fujii R, Mopper K (2003) Evaluation of specific ultraviolet absorbance as an indicator of the chemical composition and reactivity of dissolved organic carbon. *Environ Sci Technol* 37(20):4702–4708
45. Erlandsson M, Futter MN, Kothawala DN, Köhler SJ (2012) Variability in spectral absorbance metrics across boreal lake waters. *J Environ Chem* 14(10):2643–2652
46. Ruhala SS, Zarnetske JP (2017) Using in-situ optical sensors to study dissolved organic carbon dynamics of streams and watersheds: a review. *Sci Total Environ* 575:713–723
47. Lee MH, Osburn CL, Shin KH, Hur J (2018) New insight into the applicability of spectroscopic indices for dissolved organic matter (DOM) source discrimination in aquatic systems affected by biogeochemical processes. *Water Res* 147:2018
48. Müller RA, Kothawala DN, Podgrajsek E, Sahlée E, Koehler B, Tranvik LJ, Weyhenmeyer GA (2014) Hourly, daily, and seasonal variability in the absorption spectra of chromophoric dissolved organic matter in a eutrophic, humic lake. *J Geophys Res Biogeosci* 119:2014
49. Jacobs SR, Weeser B, Rufino MC, Breuer L (2020) Diurnal patterns in solute concentrations measured with in situ UV-Vis sensors: natural fluctuations or artefacts? *Sensors* 20(859):2020
50. Hansen AM, Kraus TEC, Pellerin BA, Fleck JA, Downing BD, Bergamaschi BA (2016) Optical properties of dissolved organic matter (DOM): effects of biological and photolytic degradation. *Limnol Oceanogr* 61:1015–1032
51. Alferes J, Kornfeind L, Ingildsen P, Hjorth L, Weingartner A (2019) Use of UV-Vis spectrometry for innovative online monitoring of the biostability and organic composition in a drinking water plant. In: 10th IWA symposium on modelling and integrated assessment watermatex

Fluorescence Fractionation of Organics

52. Sharikova AV (2009) UV laser and LED induced fluorescence spectroscopy for detection of trace amounts of organics in drinking water and water sources. University of South Florida, Thesis, p 2009
53. Hansen AM, Fleck JA, Kraus TEC, Downing BD, Dessonneck TV, Bergamaschi BA (2018) Procedures for using the Horiba Scientific Aqualog Fluorometer to measure absorbance and fluorescence from dissolved organic matter. Open File Report 2018–1096, U.S. Geological Survey
54. Mendoza LM, Mladenov N, Kinoshita AM, Pinongcos F, Verbyla ME, Gersberg R (2020) Fluorescence-based monitoring of anthropogenic pollutant inputs to an urban stream in Southern California, USA. *Sci Total Environ* 718:2020
55. Jaffé R, Cawley KM, Yamashita Y (2014) Applications of excitation emission matrix fluorescence with parallel factor analysis (EEM-PARAFAC) in assessing environmental dynamics of natural dissolved organic matter (DOM) in aquatic environments: a review. In: Rosario-Ortiz F (ed) *Advances in the physicochemical characterization of dissolved organic matter: impact on natural and engineered systems*, vol 1160. American Chemical Society, Washington, DC, pp 27–73
56. Carstea EM, Bridgeman J, Baker A, Reynolds DM (2016) Fluorescence spectroscopy for wastewater monitoring: a review. *Water Res* 95(C):205–219
57. Carstea EM, Baker A, Savastru R (2014) Comparison of river and canal water dissolved organic matter fluorescence within an urbanised catchment. *Water Environ J* 28(1):11–22
58. Sgroi M, Roccaro P, Korshin GV, Vagliasindi FGA (2017) Monitoring the behavior of emerging contaminants in wastewater-impacted rivers based on the use of fluorescence excitation emission matrixes (EEM). *Environ Sci Technol* 51(8):4306–431

59. Sgroi M, Roccaro P, Korshin GV, Greco V, Sciuto S, Anumold T, Snyder SA, Vagliasindia FGA (2017) Use of fluorescence EEM to monitor the removal of emerging contaminants in full scale wastewater treatment plants. *J Hazardous Mater* 323(Part A):367–376
60. Sorensen JPR, Vivanco A, Ascott MJ, Gooddy DC, Lapworth DJ, Read DS et al (2018) Online fluorescence spectroscopy for the real-time evaluation of the microbial quality of drinking water. *Water Res* 137:301–309
61. Sorensen JPR, Baker A, Cumberland SA, Lapworth DJ, MacDonald AM, Pedley S et al (2018) Real-time detection of faecally contaminated drinking water with tryptophan-like fluorescence: defining threshold values. *Sci Total Environ* 622–623:1250–1257
62. Wasswa J, Mladenov N, Pearce W (2019) Assessing the potential of fluorescence spectroscopy to monitor contaminants in source waters and water reuse systems. *Environ Sci: Water Res Technol* 5(2):370–382
63. Osburn CL, Mikan MP, Etheridge JR, Burchell MR, Birgand F (2015) Seasonal variation in the quality of dissolved and particulate organic matter exchanged between a salt marsh and its adjacent estuary. *J Geophys Res Biogeosci* 120(1430–1449):2015
64. Jonasz M, Fournier GR (2007) Light scattering by particles in water—theoretical and experimental foundations. Elsevier

Stormwater

65. Cizek AR, Johnson JP, Birgand F, Hunt WF, McLaughlin RA (2019) Insights from using in-situ ultraviolet-visible spectroscopy to assess nitrogen treatment and subsurface dynamics in a regenerative stormwater conveyance (RSC) system. *J Environ Manage* 252(109656):2019
66. Vaughan MCH, Bowden WB, Shanley JB, Vermilyea A, Sleeper R, Gold AJ, Pradhanang SM, Inamdar SP, Levia DF, Andres AS, Birgand F, Schroth AW (2017) High-frequency dissolved organic carbon and nitrate measurements reveal differences in storm hysteresis and loading in relation to land cover and seasonality. *Water Resour Res* 53(7):2017
67. Houle J (2018) Utilizing in-situ ultraviolet-visual spectroscopy to measure nutrients and sediment concentrations in stormwater runoff. US-EPA project RFQ-RT-16-00065, oral presentation at WEFTEC 2018
68. Weingartner A (2019) Potential und Ansätze zur selektiven Online Überwachung des AFS63 mittels UV-Vis-Spektrometrie, 9. Kommunalen Erfahrungsaustausch: Regenwassermanagement in der Praxis, Gelsenkirchen
69. Welker A, Dierschke M, Gelhardt L (2019) Methodische Untersuchungen zur Bestimmung von AFS63 (Feine Abfiltrierbare Stoffe) in Verkehrsflächenabflüssen. *Gwf Wasser+Abwasser*, Apr 2019
70. Broß L, Badenberg SC, Krause S, Schaum C (2020) Abfiltrierbare Stoffe als Begleitparameter. *KA Korrespondenz Abwasser, Abfall* –(69) Nr.1, 2020

DBPS

71. Beauchamp N, Dorea C, Bouchard C, Rodriguez M (2018) Use of differential absorbance to estimate concentrations of chlorinated disinfection by-product in drinking water: critical review and research needs. *Critical Rev Environ Sci Technol* 48(2):210–241
72. Beauchamp N, Laflamme O, Simard S, Dorea C, Pelletier G, Bouchard C, Rodriguez M (2018) Relationships between DBP concentrations and differential UV absorbance in full-scale conditions. *Water Res* 131:110–121

73. Korshin GV, Li CW, Benjamin MM (1997) (1997) The decrease of UV-absorbance as an indicator of TOX formation. *Water Res* 31(4):946–949
74. Yan M, Korshin GV, Chang H-S (2014) Examination of disinfection by-product (DBP) formation in source waters: a study using log-transformed differential spectra. *Water Res* 50:179–188
75. Stéphanie G, Caetano D (2020) Real-time estimation of disinfection by-products through differential UV absorbance. *Water* 12:2536

Indirect Measurements

76. Etheridge JR, Birgand F, Osborne JA, Osburn CL, Burchell II MR, Irving J (2014) Using in situ ultraviolet-visual spectroscopy to measure nitrogen, carbon, phosphorus, and suspended solids concentrations at a high frequency in a brackish tidal marsh. *Limnol Oceanogr: Methods* 12:10–22

WWTP and Sewer Control

77. Weingartner A (2014) Nitrite measurement in waste water treatment - summary sheet for s::can Messtechnik GmbH
78. Lackner S, Gilbert EM, Vlaeminck SE, Joss A, Horn H, van Loosdrecht MCM (2014) Full-scale partial nitrification/anammox experiences—an application survey. *Water Res* 55:2014
79. Regmi P, Holgate B, Fredericks D, Miller MW, Wett B, Murthy S, Bott CB (2015) Optimization of a mainstream nitrification-denitrification process and anammox polishing. *Water Sci Technol* 72(4):2015
80. Pedrousoa A, Val del Rioa A, Morales N, Vazquez-Padin JR, Campos JL, Mosquera-Corralla A (2021) Mainstream anammox reactor performance treating municipal wastewater and batch study of temperature, pH and organic matter concentration cross-effects. *Process Saf Environ Prot* 145:2021
81. Lemaire R, Chauzy J, Veuillet F, DiMassimo R, Sorensen K, Deleris S (2011) Advanced control system to reduce N₂O emission and improve performance of an SBR treating N-Rich effluent via nitrite pathway. *Water Environ Fed, WEFTEC* 6480–6493
82. Åmand L, Laurell C, Stark-Fujii K, Thunberg A, Carlsson B (2014) Lessons learnt from evaluating full-scale ammonium feedback control in three large wastewater treatment plants. *Water Sci Technol* 69(7):2014
83. Åmand L (2014) Ammonium feedback control in wastewater treatment plants. Uppsala Dissertations from the Faculty of Science and Technology 104. Uppsala: Acta Universitatis Upsaliensis, p 256
84. Ahn J-H, Kim S, Park H, Pagilla K, Chandran K (2010) N₂O emissions from activated sludge 2008–2009: results of a nationwide monitoring survey in the United States
85. Rieger L, Langergraber G, Thomann M, Fleischmann N, Siegrist H (2004) Spectral in-situ analysis of NO₂, NO₃, COD, DOC and TSS in the effluent of a WWTP. *Water Sci Technol, IWA Publishing* 50:143–152
86. Rieger L, Siegrist H, Winkler S, Saracevic E, Votava R, Nadler J (2001) In-situ measurement of ammonium and nitrate in the activated sludge process. *Water Sci Technol* 45(4–5):93–100
87. Winkler S, Saracevic E, Rieger L, Siegrist H, Nadler J (2001) Kostengünstige und wartungsarme in-situ Ammonium- und Nitratmessung. *VDI-Berichte* 1619:2001
88. Rieger L, Vanrolleghem PA, Langergraber G, Kaelin D, Siegrist H (2008) Long-term evaluation of a spectral sensor for nitrite and nitrate. *Water Sci Technol* 57(10):1563–1569

89. Klaus S, Sadowski M, Jimenez J, Wett B, Chandran K, Murthy S, Bott CB (2007) Nitric oxide production interferes with aqueous dissolved oxygen sensors. *Environ Eng Sci* 34(9):2017
90. Langergraber G, Fleischmann N, Hofstädter F (2003) A multivariate calibration procedure for UV/VIS spectrometric quantification of organic matter and nitrate in wastewater. *Water Sci Technol* 47(63–71):2003
91. Egerland B, Weingartner A (2017) Online-Messtechnik steuert vierte Reinigungsstufe. *WWT Wasserwirtschaft Wassertechnik*, Frankfurt am Main, Germany, Apr 2017
92. Hofstaedter F, Ertl T, Langergraber G, Lettl W (2003) A. Weingartner (2003) On-line nitrate monitoring in sewers using UV/VIS spectroscopy. In: Wanner J, Sykora V (eds) *Proceedings 5th International Conference of AČE ČR “Odpadní vody—Wastewater 2003”*, 13–15 May 2003. Czech Republic, Olomouc, pp 341–344
93. Langergraber G, Gupta JK, Pressl A, Hofstaedter F, Lettl W, Weingartner A, Fleischmann N (2004) On-line monitoring for control of a pilot-scale sequencing batch reactor using a submersible UV/VIS spectrometer. *Water Sci Technol* 50(10):73–80
94. Auguet O, Pijuan M, Guasch-Balcells H, Borrego CM, Gutierrez O (2015) Implications of downstream nitrate dosage in anaerobic sewers to control sulfide and methane emissions. *Water Res* 68:2015
95. Sutherland-Stacey L, Corrie S, Neethling A, Johnson I, Gutierrez O, Dexter R, Yuan Z, Keller J, Hamilton G (2008) Continuous measurement of dissolved sulfide in sewer systems. *Water Sci Technol* 57(3):375–381

AOC

96. van den Broeke J, Ross PS, van der Helm AWC, Baars ET, Rietveld LC (2008) Use of on-line UV/Vis-spectrometry in the measurement of dissolved ozone and AOC concentrations in drinking water treatment. *Water Sci Technol—WST* 57(8)

Industrial Effluent Monitoring

97. CPCB (2016) Final document on revised classification of industrial sectors under red, orange, green and white categories. Central Pollution Control Board, Feb 29 2016, New Delhi, India
98. Weingartner A (2020) Industrial effluent monitoring—a basis for decision making. CasAgua Consulting GmbH, Mexico City (upon request)
99. Weingartner A (2018) Identification and management of industrial wastewater emissions by smart sensing and real-time communication. *Sensors for Smart Wastewater Management*, Singapore International Water Week
100. Langergraber G, Fleischmann N, Hofstaedter F, Weingartner A, Lettl W (2003) Detection of (unusual) changes in wastewater composition using UV/VIS spectroscopy 2003). In: Ruzickova I, Wanner J (eds) *Proceedings of the 9th IWA conference on “Design, operation and costs of large wastewater treatment plants”*—Poster papers, Prague, Czech Republic, 1–4 Sept 2003, pp 135–138

Feed-Forward

101. Fabris R, Chow C, Dexter R, Colton J, Knoblauch J, Drikas M (2013) Feed-forward coagulant control using online UV/Vis monitoring. *Water Sci Technol Water Supply* 13(2):420–426

102. US-EPA Drinking Water Advice Note No. 15 (2014) Optimisation of chemical coagulant dosing at water treatment works
103. Eikebrokk B, Juhna T, Østerhus SW (2006) Water treatment by enhanced coagulation—operational status and optimization issues. TECHNEAU EU project final report
104. Laidlow C (2007) Greater Wellington Water (2007) Feed Forward—the holy grail of coagulation control. NZWWA J
105. Alresheedi M (2019) Fouling indices for quantification of natural organic matter fouling and cleaning in ceramic and polymeric membrane systems. PhD Thesis, University of Ottawa, Ottawa-Carleton Institute for Environmental Engineering
106. Fitzgerald F, Chow CWK, Holmes M (2006) Disinfectant demand prediction using surrogate parameters—a tool to improve disinfection control. J Water Supply Res Technol AQUA 55(6):2006
107. Chow C, Fabris R, Dixon M (2008) Case studies using s::can on-line monitoring systems. Australian Water Quality Centre, South Australia, Research Report 75

Novel Methods

108. Zhiyun L, Deen MJ, Selvaganapathy PR (2014) Raman spectroscopy for in-line water quality monitoring—instrumentation and potential. Sensors
109. Safford H, Bischel HN (2018) Flow cytometry applications in water treatment, distribution, and reuse: a review. Water Res 151(15):2018

Chapter 14

Catchment-Based Water Monitoring Using a Hierarchy of Sensor Types



Joyce O'Grady, Ciprian Briciu Burghina, and Fiona Regan

Abstract The design of optimal monitoring networks at catchment level is both a challenge and an opportunity in the smart city era. New knowledge, information and services can be built by integrating diverse multimodal data streams, at scales appropriate to inform effective decision making. To this end a comprehensive, integrated hierarchical platform is ultimately required for fusing, gathering and analysing large volumes of data. Such workflows could include hydrological and geospatial data, land-use and activity data, remote data from aerial and space-borne platforms and *in-situ* data from both fixed and mobile platforms. In this context, this chapter aims to provide insight into how the future catchment monitoring platforms might look like and to synthesize and review recent technological progress. Emphasis is placed on the realisation of fit-for-purpose cost effective catchment monitoring programmes with immediate opportunity for implementation and state-of-the art emerging technologies are discussed in this context. In the first part, commercially available *in-situ* sensor technologies are reviewed to provide a starting point for users in the critical sensor selection process. A classification is provided based on operation principle while drawbacks and benefits are presented. Practical considerations, relating to monitoring requirements, deployment strategy, and cost are discussed to aid practitioners in the design of water quality monitoring networks. In the second part, aerial and satellite remote sensing platform are reviewed and constrains and technological limitations are presented. Examples of successful use of combined monitoring approaches are discussed with an emphasis on early warning and forecasting of pollution events. Technological gaps that should be filled to achieve an ideal catchment observation system are identified.

Keywords Catchment · Aerial images · Satellite · Hyperspectral · Sensor sonde · Grab sample · Water quality

J. O'Grady · C. B. Burghina · F. Regan (✉)
School of Chemical Sciences, Dublin City University, Dublin, Ireland
e-mail: fiona.regan@dcu.ie

DCU Water Institute, Dublin City University, Dublin 9, Ireland

14.1 Introduction

Catchments can be extremely complex systems, where the quality and quantity of the water is influenced by biological, chemical, physical, ecological and environmental factors [1]. A catchment area for water is usually defined as the area of land around a lake, river or some form of water body [2, 3]. Catchment monitoring is important as it facilitates sustainable management of the area. It also highlights problems or threats concerned with the area [4]. Monitoring systems are put in place to better understand the key drivers influencing the quality of the water bodies and land surrounding the catchment and help develop best management practices.

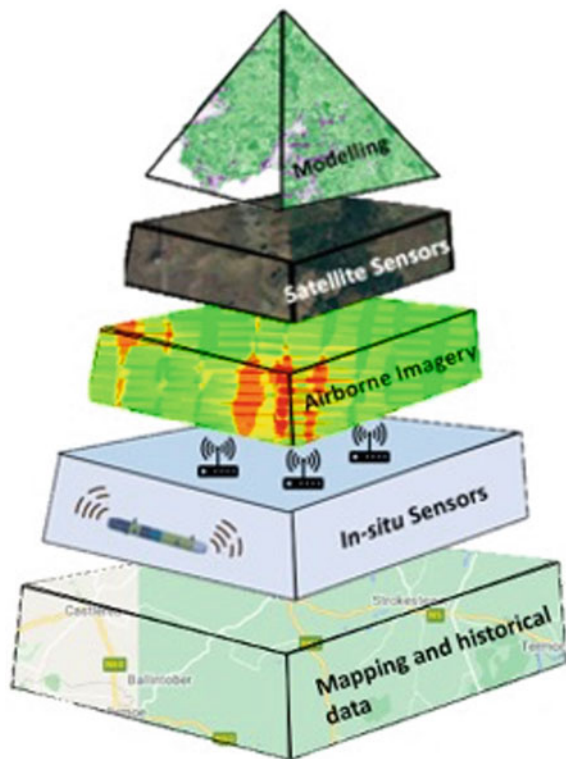
Monitoring water quality is of local and global interest and is driven by legislation such as the Water Framework Directive (WFD) [5] in Europe, the Clean Water Act [6] in Canada, the Australian Water Act [7] and the US Clean Water Act [8] in the United States. In order to obtain more information about a catchment, monitoring and sampling must be carried out as frequently as possible. *In-situ* instrumentation overcomes the problem of frequency by providing long-term intensive observation, sampling and collection of data. The effective monitoring of water quality parameters has a profound impact on the overall quality of a catchment area [9]. A number of aquatic systems and organisms are dependent on the quality of the water for survival [10, 11].

The design of water quality monitoring networks (WQMN) comprises scientific, economic, legal and technical considerations and remains a critical challenge in both developed and developing countries. WQMN can be classified in three administrative types: driven by legislation and regulation (routine monitoring), decision support (early warning and forecast) and pollution source identification [12]. In terms of limitations, WQMN are constrained by financial resources (for implementation and operation), instrumentation and technology, accessibility to site and administrative and legal considerations [13]. Critical design parameters for WQMN include the monitoring locations, monitoring frequency and the water quality indicators and these key parameters are often optimised to address network drivers and constrains [14]. Long term *in-situ* sensing platforms have been used for water quality monitoring over the past two decades [15, 16] and the technology has been in a 'growing stage' since 2013 [13]. The instruments employed provide real-time, periodic and for the most part reliable data. Through *in-situ* sensor monitoring, out-of-specification (OOS) parameters can be instantly identified and managed [17, 18]. The design of WQMN is closely related to the modelling approaches and an effective water quality modelling platform needs a well deployed WQMN. Recent developments combine data-driven models and physical process based models with network design models to improve performance [13]. In addition, recent years have seen the rapid development of aerial and satellite remote sensing [19] and Geographic Information System (GIS) techniques. Remote sensing techniques allow uniform data collection across large areas and the datasets are often times open source. In catchment monitoring, remote sensing is mainly used for capturing land use and land change over time and combined with *in-situ* WQMN provide a cost effective solution. Although remote

sensing contributes promising outputs and offers a replacement to traditional field sampling [20], limitations concerning the accuracy of the products obtained exist, with ground truth data often required to validate observations [21]. Therefore, there is added value in combining remote sensing with other monitoring technologies to provide more accurate and reliable data. Hierarchical sensor networks, combining multiple data streams could potentially disrupt the barrier for comprehensive catchment monitoring. To this end, a hierarchal framework for comprehensive monitoring at catchment scale is proposed (Fig. 14.1), and includes hydrogeological and geospatial data, *in-situ* data from both fixed and mobile platforms, remote data from aerial and space-borne platforms and modelling. *In-situ* instrumentation and remote monitoring platforms stand out due to the rapid technological developments taking place and provide an immediate opportunity for implementation and the realisation of fit-for-purpose cost effective catchment monitoring programmes.

In this context, this chapter aims to provide a review of commercially available *in-situ* sensor technologies for water quality monitoring with an emphasis on state-of-the art emerging sensors. Practical considerations, relating to sensor selection process, deployment strategy and cost are discussed to aid practitioners in WQMN design. In the second part, aerial and satellite remote sensing platform are discussed

Fig. 14.1 A hierarchy of sensing approaches can provide a complete and reliable monitoring system for a catchment



and a review of hierarchical approaches combining multimodal data sets at catchment level is provided.

14.2 *In-situ* and Remote Instrumentation

14.2.1 *In-situ* Instrumentation

A wide range of sensors exist for water monitoring which allow both *in-situ* and *on-site* operation. Portable test kits or instruments often complement or validate data for *in-situ* sensors or are used to provide spatial resolution. Such instruments aid in pollution source tracking and quick screening of water samples, and are more available for bio-chemical parameters which are inherently challenging to monitor using *in-situ* sensors [20, 21]. However, they cannot provide data in real-time and at sufficient temporal frequency. Coupled with the need for personnel to carry out the work, they are less desirable than the *in-situ* sensors and won't be covered in this chapter. Autonomous sensors on the other hand provide real-time or near-real-time information at high frequency, which in turn facilitates decision support in real-time. In addition, they provide extensive baseline data and an improved understanding of water quality changes and trends. From an application point of view sensors can be classified as hyperspectral and multispectral radiometers, acoustic sensors (velocity and sound), hydrometric sensors (gauge, water level, flow) and water quality sensors. This section aims to summarise only the main commercially available water quality sensors and provide a list of available technologies which is by no means exhaustive.

Based on the sample measurement principle, *in-situ* water monitoring instrumentation can be broadly classified in two main categories: sample-draw and interface (Table 14.1). Sample-draw sensors rely on transfer of the sample from the outside environment into the sensor. Sample processing steps, including filtration, mixing with on-board stored reagents or incubation to pre-defined temperatures are carried out prior to the detection step or during detection. The analyte detection and quantification is achieved in strictly controlled conditions to achieve good analytical performance. Such systems widely known as wet-chemistry based sensors or analysers are particularly successful for species and analytes that are challenging or impossible to measure using interface based sensors. They are commonly used for nutrients [24] including nutrient speciation, faecal indicator bacteria [25] and algal toxins [26] (Table 14.1). Wet-chemistry based sensors are in general more expensive and bulkier than their interface based counterparts (ie. ion selective and optical) but they provide better accuracy, precision and resolution [27]. With recent advancements in microfluidics and integrated optoelectronics they are becoming smaller and more power efficient for dissolved nutrient species [28] although systems capable of sample digestion (i.e. for phosphorus fractionation) still require high power and extensive maintenance.

Table 14.1 Commercially available water quality sensors and instrumentation for *in-situ* application

	Sensor	Parameter	Analysis time	Manufacturer	Reference
<i>Sample draw sensors</i>					
Nutrients	HydroCycle-PO ⁴	SRP	RT	Sea-Bird Scientific	https://www.sea-bird.com/
	PHOSPAX Sigma	SRP, TRP	10 min	Hack Lange GmbH	https://de.hach.com/
	Alyza IQ	NH ₄ ⁺	RT	WTW a Xylem brand	https://www.xylemanalytics.com/en
	Amtax SC	NH ₄ ⁺	0–15 min	Hack Lange GmbH	https://de.hach.com/
Faecal indicators	AlertSystem	<i>E. coli</i> , coliforms <i>or</i> enterococci	1–12 h	Fluidion SAS	http://fluidion.com/en/products/alert-system-2
	ColiFast Alarm	coliforms, <i>E. coli</i>	2.5–15 h	ColiFast AS	https://www.colifast.no/products/
	ColiMinder® CMI-02	GUS activity	15	VWMS GmbH	https://www.coliminder.com/
	BactControl	GUS, GAL activity	75	MicroLAN B.V	http://www.microlan.nl
Toxicity	iTOXcontrol	Toxicity monitoring- <i>Vibrio fischeri</i> light emission	NS	MicroLAN B.V	http://www.microlan.nl
	Algae Toximeter II	Toxicity monitoring using green algae	NS	Bbe Moldaenke GmbH	https://www.bbe-moldaenke.de/en/
Algae	ALGcontrol	Algae speciation	NS	MicroLAN B.V	http://www.microlan.nl

(continued)

Table 14.1 (continued)

	Sensor	Parameter	Analysis time	Manufacturer	Reference
	PhycoSens	<i>Chl a</i> , BGA, GA, Diatoms, cryptophyceae	NS	Bbe Moldaenke GmbH	https://www.bbe-moldaenke.de/en/
<i>Interface sensors</i>					
Multiparameter sondes	YSI EXO-series	C, T, D, pH, ORP, fDOM, BGA, Rho, NO ₃ ⁻ (optical), <i>Chl a</i> , DO, Turb, NH ₄ ⁺	RT	YSI, a Xylem brand	https://www.ysi.com/exo
	Sea-Bird HydroCAT-EP	C, T, D, pH, Turb, <i>Chl a</i> , DO	RT	Sea-Bird Scientific	https://www.sea-bird.com/
	DS5X, HL7	C, T, D, pH, ORP, BGA, Rho, NO ₃ ⁻ (ISE), <i>Chl a</i> , DO, Turb	RT	Hydrolabs	https://www.hydrolab.com/
	Eureka Trimeter™	C, T, D, pH, OPR, DO, <i>Chl a</i> , BGA, Rho, Crude & refined oil	RT	Eureka	http://rshydro.ie/eureka-m-20.html
	Proteus	C, T, D, pH, OPR, DO, Crude & refined oil, Try, CDOM	RT	Proteus Instruments Ltd	https://www.proteus-instruments.com/
	MIDAS CDT+	C, T, D, pH, OPR, DO, <i>Chl a</i>	RT	Valeport	https://www.valeport.co.uk/
Single/multi wavelength absorption, scatter and fluorescence probes	Spectro::lyser V3	Turbidity, <i>Chl a</i> , TOC, DOC, BOD, Temp	RT	S::can GmbH	https://www.s-can.at/products
	Nitratax Plus SC	NO ₃ ⁻	RT	Hack Lange GmbH	https://de.hack.com/
	SUNA V2	NO ₃ ⁻	RT	Sea-Bird Scientific	https://www.sea-bird.com/
	ECO-FLNTU-RT	Turb, <i>Chl a</i>	RT		
	SeaOWL UV-A	Crude oil, <i>Chl a</i>	RT		

(continued)

Table 14.1 (continued)

	Sensor	Parameter	Analysis time	Manufacturer	Reference
	VLux series	BGA (PC/PE), Try, <i>Chl a, b, c</i> , Turb, CDOM, BTEX, PAH,	RT	Chelsea Technologies	https://chelsea.co.uk/
	EnviroFLU, matrixFlu VIS, nanoFLU	<i>Chl a</i> , PC, Rho, CDOM, PAH	RT	TriOS Mess- und Datentechnik GmbH	https://www.trios.de/en/index.php
	TTurb, TpH	Turb, pH	RT		
	NICO, LISA, OPUS	NO ₃ ⁻ , NO ₂ ⁻ , SAC254, TOC etc	RT		
	OBS501	Turb	RT	Campbell Scientific	https://www.campbellsci.com/
	C3, CP6	T, D, Try, Rho, fDOM, crude and fine oil, PC, PE, <i>Chl a</i> ,	RT	Turner Designs	https://www.turnerdesigns.com/
	PhytoFind	Algae speciation	RT		
	Hyperion series	Turb, <i>Chl a</i> , PC, Rho	RT	Valeport	https://www.valeport.co.uk/
	Algal Torch	BGA, <i>Chl a</i>	RT	Bbe Moldaenke GmbH	https://www.bbe-moldaenke.de/en/
	FluorProbe	Algae speciation, <i>Chl a</i>			

NS-not specified, RT-real-time, SRP-soluble reactive phosphorus, TRP-total reactive phosphorus; GUS-β Glucuronidase, *E. coli* marker enzyme; GAL- β Galactosidase (total coliforms marker enzyme); BGA-blue green algae; GA-green algae; *Chl a,b,c*- Chlorophyll a,a,b,c; C-conductivity, T-temperature, D-depth (derived from pressure); ORP-oxidation reduction potential; DO—dissolved oxygen, Try—tryptophan, Rho-Rhodamine; NO₃⁻—nitrate; CDOM-chromophoric dissolved organic matter; Turb—turbidity; PC—phycocyanin; PE- phycoerythrin; TOC-total organic carbon; BOD—biological oxygen demand; PAH-polycyclic aromatic hydrocarbons; BTEX-benzene, toluene, ethylbenzene and xylene, Fdom—fluorescent dissolved organic matter

A second category of sensors rely on measurements carried out at the interface with the environment and they are available for an extensive range of parameters. From a measuring principle perspective, they can be grouped in electronic sensors (i.e. temperature, conductivity and pressure), optical sensors (measuring scatter, absorption and fluorescence) and hybrid sensors. In addition to the electronic or optical detection, hybrid sensors leverage gas diffusion membranes or selective analyte recognition membranes to achieve selectivity. Common examples

include the membrane-based optical dissolved oxygen sensors and the ion selective electrode sensors. To date, the power horse of environmental monitoring has been the multiparameter sonde (Table 14.1). These sensors bring together a multitude of probes in a modular plug and play design, where in addition to the conductivity, temperature and depth (CTD) probes (provided as fixed in the configuration), users can select a wide range of hybrid or optical probes to suit their application. Among the most widely used parameters are turbidity, DO and *Chl a*, although with recent advancements, NO_3^- optical probes are now available (see YSI EXO series, Table 14.1).

The plug & play design offered by these sensors suits a wide range of monitoring needs, the same sonde can be used to address different monitoring requirements by simply replacing the probes. An added advantage of measuring multiples parameters in the same unit is that for example temperature compensation is directly applied to fluorescent signal, producing more accurate measurements. High-end sondes have now up to 7 available ports which allows monitoring of a wide range of parameters simultaneously. The main draw-back of multiparameter sondes is the higher capital cost and the overall ownership cost required to keep them operational which limits the spatial distribution often times needed in monitoring programmes. Hybrid probes that rely on membranes tend to have a lifetime of up to 2 years and incur additional costs for replacement and service [29].

Another class of environmental sensors that are recently getting traction are the optical sensors. The main advantage of these sensors is the simple measurement principle, which relies on the interaction of ultra violet (UV), (visible) VIS an infrared (IR) radiation with matter. These sensors use absorption, fluorescence or scatter to detect a wide range of parameters (see Table 14.1). Progress in this field has been mainly catalysed by light emitting diodes (LEDs) becoming increasingly available in the UV region, cheaper, more reliable and powerful and by new smaller, more performant and cheaper photodetectors. Optical sensors are slowly replacing their ISE counterparts mainly due to stability over time, robustness, longer lifetime, and lower costs but also due to the wide range of parameters that are optically active. By far the most employed optical parameter in environmental monitoring is turbidity. The measurement of turbidity is split into two basic methodologies: turbidimetry, in which the degree of transmission of light is determined, and nephelometry, in which the degree of light-scattering is determined [30, 31]. Both principles are derived from mathematical models for real world observations. In case of turbidimetry, the principles reply on Beer-Lambert laws while for nephelometry many theories and models have been developed to describe a range of scattering processes, and these models are mostly derived from Mie theory [30]. Most turbidity probes rely on light scatter, although some use light transmission. Another category of frequently used optical probes are the fluorometers, which are now commercially available for a range of parameters (see Table 14.1). Fluorometers have been traditionally used for *Chl a* measurement but are now available for a range of other pigments like PC, PE and for algal speciation. Fluorescence signals are known to be affected by temperature, turbidity, pH, quenchers and ionic strength and interpretation of such data has to be carried out with caution. If for *Chl a* probes, most manufacturers

recommend site calibration (i.e. validation with *Chl a* extracts) for other parameters is inherently more difficult and often times not possible. Fluorometers operating in the UV region are even more susceptible to errors particularly due to overlapping absorption and emission bands from multiple dissolved and particulate components. Example of species absorbing in the UV region and emitting in the UV–VIS include marine and terrestrial humic like material, crude oil (PAHs), refined oil (BTEX), a range of amino acids like tryptophan (Try) often linked to bacterial contamination and biological oxygen demand (BOD) and CDOM (chromophoric dissolved organic matter)/fDOM (fluorescent dissolved organic matter). To differentiate between the different species, fluorometers use multiple excitation/emission wavelengths finely tuned for the analyte of interest and some apply signal correction algorithms for interferences like background fluorescence or turbidity. In general measurements based on fluorescence where the emission of light is measured at a wavelength different than the excitation wavelength, are sensitive and specific. The last measurement principle used by the optical probes relies on absorption derived from light attenuation. Such probes perform single- or multi- wavelength sensing in the UV to IR spectral regions and rely on data processing via wavelengths based algorithms and partial-least-square regressions to calculate nutrient concentrations for example [32]. Example of such sensors include, Spectro::lyser or nitro/multi::lyser (Scan:: Messtechnik GmbH, Austria), TriOS NICO, (TriOS Mess- und Datentechnik GmbH, Germany), SUNA V2 Nitrate Sensor (SeaBird Scientific) or Nitratax Plus SC (Hack Lange GmbH), Table 14.1.

14.2.2 Practical Consideration for In-situ Sensing

14.2.2.1 Sensor Deployment Infrastructure and Platforms

Multiple deployment platforms exist for *in-situ* instrumentation and are classified in fixed and mobile. Fixed platforms include buoys and mini buoys (for lakes, coastal and transitional water bodies applications), floating pontoons, bridges, subsea moorings and purposely build structures to anchor or fix the instrumentation on the river/lake/sea floor or banks. Such platform provides monitoring at fixed location and can be accompanied by untended vertical profilers for water column profiling. One limitation of such platforms is the power demand as most rely on on-board power or solar panels, hence the instrumentation selection process is constrained by power requirements. Another option is the use of water monitoring stations, traditionally used for rivers and lake monitoring. Such stations are connected to the power grid and the water sample is pumped and circulated through a measurement tank within the station. The instrumentation is either submersed in the tank or samples from the tank (for example, wet chemical analyser). Main advantages of such monitoring stations are that they can accommodate many sensors and instrumentation that are otherwise not rated for outdoor operation and provide better security and access to site. A comparable approach is the development of mobile monitoring stations which offer

the best of both worlds. Such an example is provided in Germany, where fully equipped mobile trailers are used to monitor agricultural catchments and provide both spatial flexibility and a tool for rapid deployment in emergency situations [33]. Overall, fixed monitoring platforms offer excellent temporal resolution, but the spatial resolution is limited by the number of sensors or sensor nodes. Mobile platforms on the other hand provide good spatial resolution and allow mapping of water bodies with high accuracy. Mobile platforms can be classified in surface vehicles, buoyancy engine vehicles and thruster-driven subsurface vehicles [34]. Autonomous surface vehicles can support small to medium payloads and use wind, solar and wave-power to extend endurance. Buoyancy engine platforms include drifters and gliders. These platforms have very low power requirements due to their small size, and use low power payloads and instrumentation but provide long endurance missions and are heavily employed in ocean observations [34]. The last category is thruster-driven subsurface vehicles, which are typically propeller driven.

14.2.2.2 Monetary Cost

Water managers are concerned with the quantity and quality of water and how policies and infrastructure can be implemented to improve or maintain ecosystem health and protect human wellbeing. A key component of managing water resources is monitoring and reporting in which case sensors and instrumentation play a critical role. The design of any monitoring network is driven by the monitoring objectives (present and future) and available resources (human and monetary). The cost of WQMN infrastructure using *in-situ* sensor largely remains high and is often times prohibitive. Critical design parameters for WQMN include the monitoring locations, monitoring frequency and the water quality indicators. Limited financial resources require a small number of monitoring stations but on the other hand the WQMN must cover large enough areas. From the design point of view, four main methods exist for WQMN including: topological, multivariate statistics, geostatistical, information entropy and were recently reviewed [13]. Optimisation methods using multiple criteria can be employed to minimise network cost and maximise reliability, coverage and detection probability [13]. In terms of the water quality indicators, monitoring stations or nodes can include multiple parameter instrumentation which tends to be higher cost, or lower cost single parameter sensors. The nodes in the network that measure simple parameters like turbidity provide the analytical data but are also used as proxies or surrogates for water quality changes and provide management support at a reduced cost. Such monitoring networks adopt a more complex hierarchical architecture, and nodes are assigned different priority levels [35].

With a growing environmental sensor market and new state of the art optical sensor available for a wide range of parameters, sensor performance is a critical in the selection process. Emerging sensors which have not been fully validated and tested in environmental applications rely on verification by third parties. This includes mainly published peer-reviewed scientific literature coming from academia but also from independent organisations. The Alliance for Coastal Technologies (ACT) for

example provides verification reports on performance testing of emerging technologies in operational environments [36]. Another limitation of water monitoring sensors to date is biofouling, which in turn affects the integrity of the data and increases operational costs [37]. Biofouling is the build-up of any unwanted biological matter on a surface, biofilms are created by micro and macro-organisms [38]. The ACT has estimated that up to 50% of operational budgets are attributed to biofouling, depending on location and season. Established and emerging antifouling strategies have been reviewed recently and it was concluded that there is no ideal solution available, but rather a combination of multiple approaches driven by monitoring application [37]. To minimise WQMN operational cost the selection of sensors with robust proven antifouling protection is critical.

14.2.3 Remote Instrumentation

In recent years the application of using remotely sensed data for environmental water quality monitoring has increased [39]. Remote sensing can be defined simply as a sophisticated method of gathering, detecting, and monitoring the physical characteristics of an area without coming into contact with it. It enables detailed information of the monitored area to be collected at a distance. Remote sensing facilitates the measurement of the reflected and emitted radiation of the area using cameras that can collect the remotely sensed images [40]. Remote sensing data is generally used to monitor water qualitative parameters such as secchi disk depth, *Chl a*, temperature, TOC, total suspended matter (TSM), turbidity, conductivity, CDOM, suspended solids (SS) and sea surface salinity [41] (see Table. 14.2). The increase in spatial resolution has coincided with spectral resolution producing high quality images providing information from 10 to 100 square meters [42]. This range in resolution is suitable for a number of applications and studies, such as land-cover classification, water quality monitoring and species assemblages, conservation and planning management. Remote sensing applications are capable of capturing data by means of multispectral and hyperspectral images. Multispectral imaging enables the capture of light from a narrow range of wavelengths in the electromagnetic spectrum. These wavelengths are generally separated out using filters on the multispectral instrument. Hyperspectral imaging is similar to multispectral in a way that it is able to collect and analyse information from wavelengths within the electromagnetic spectrum, it can produce a spectrum for every pixel in a collected image. Multispectral and hyperspectral imaging differ in the number of bands they have and the narrowness of the bands. To produce high resolution images provide the user to “see the unseen” [43] hyperspectral imaging is used. Hyperspectral imaging is generally used for agricultural, ecological, atmospheric and oceanography applications.

Although remote sensing contributes promising outputs and offers a replacement to traditional field sampling enabling, fast, temporal, spatial and frequent observations [20], it still deals with some limitations concerning the accuracy of the products

Table 14.2 List of common water quality parameters and their remotely sensed method of monitoring. Adapted from [44]

Sensor	Parameter	Spatial resolution	Units	References
<i>Satellite</i>				
MODIS	Dissolved oxygen	1 km	mg/L	[45, 46]
Landsat MODIS	Total organic carbon	Landsat 30 m MODIS 250–500 m	mg/L	[47]
Landsat SPOT	Total suspended matter	Landsat 30 m SPOT 20 m	mg/L	[48]
Landsat MERIS	Turbidity	Landsat 30 m MERIS 300 m	NTU	[49, 50]
CHRIS Proba satellite	Conductivity	17 m	μs/cm	[51, 52]
Landsat	Colour dissolved organic matter	30 m	mg/L	[53]
<i>Aerial</i>				
Airborne imaging spectrometer for applications (AISA)	Chlorophyll-a	2 m	mg/L	[40]
Airborne scanning low frequency microwave radiometers (SLFMRs)	Sea surface salinity	100 m	PSU	[54, 55]

obtained, data continuity, excess tools and software for atmospheric correction (scattering and absorption effects, cloud cover etc.) and the precision of the results [20, 21]. Therefore, there is added value in combining remote sensing with other monitoring technologies to provide more accurate and reliable data.

14.3 Hierarchical Approach to Monitoring Catchment-Based Problems

To successfully carry out water monitoring in catchments a hierarchy of sensing approaches should be employed to overcome the main challenges associated with water monitoring [56]. The use of an hierarchical monitoring system will help bridge the gaps of certain monitoring platforms. Enabling real-time, high resolution data, maintaining the quality of the water and prediction of threats. To do this, different monitoring technologies can be integrated and combined with information and communications technology (ICT) and advanced data analysis and machine learning (ML), to provide long term datasets to help manage, protect and facilitate smart decision-making processes required to effectively monitor a catchment area [57]. *In-situ* sensing platforms provide rapid, robust and reliable environmental monitoring. They provide near real or real-time analysis of environmental water pollution parameters, allowing many data points to be gathered at high temporal frequency.

Common commercial sensors for water monitoring measurements include temperature, pH, turbidity, dissolved oxygen, *Chl a*, and salinity are frequently deployed in catchments. Many studies incorporate these devices to ground truth data obtained from remote sensing applications. Remote sensing facilitates the measuring of the reflected and emitted radiation of the area using cameras that can collect remotely sensed images without coming into contact with the observed area [58]. The combination of using different types of sensing technologies for catchment monitoring has been reviewed in the literature within the last decade. The most common catchment-based water monitoring reviews are concerned with applications including harmful algal blooms, nutrient fluxes, sediment and erosion, flooding and changes in water level.

14.3.1 Combinations of Sensor Types to Monitor Pollution Events

Harmful algal blooms (HABs) are a major concern in both coastal and inland water catchments [59–61]. The monitoring HABs has been carried out by a vast number of sensing systems [62–64]. A number of studies have demonstrated the use of remote sensing platforms as well as *in-situ* sensors to detect, measure and characterise different algae populations, basing their measurements on *Chl-a* levels. Most *in-situ* sensors are used to measure chlorophyll levels by means of autonomous platforms, whereas remote sensing applications such as airborne and satellite sensors typically use ocean colour and hyperspectral imagery to determine and measure bloom biomass [65, 66]. The use of remote sensing applications using satellite sensors such as MODIS-MERIS facilitate the capture of high resolution hyperspectral imagery of areas where *Chl-a* is highly concentrated [67]. The use of *in-situ* sensing platforms can often include detection of certain parameters such as temperature which can highlight an onset effect in the level of *Chl-a* and therefore emphasizing the need for some water parameters to be measured in real-time [68]. The need for higher resolution imagery for monitoring of smaller inland lakes, estuaries, rivers and bays is essential. This is where satellite sensors such as the Landsat series can offer solutions. The Landsat series is equipped with an onboard thematic mapper (ETM) that facilitates a spatial resolution of 30 m. Demonstrating the need for a hierarchical approach to catchment based monitoring where more than one monitoring technology can be used in a study to improve data collection and information obtained [69] (see Table 14.3).

In terms of an hierarchical approach to monitoring, there has been surge towards remote sensing applications for rural catchment areas. Technology such as satellite (Landsat, Sentinel, MERIS and MODIS) and airborne imagery sensors (drones with red, green and blue (RGB) cameras, LiDAR and CASI) provide information from 10 to 100 square meters [42]. These show advantages for catchment monitoring because of the level of information and data that can be obtained that would be impossible

Table 14.3 Summary of catchments studies using a combined approach to water quality monitoring

Site	Waterbody	Catchment pollution event	Sensor		Parameter of interest	References
			Remote sensing	<i>In-situ</i> sensing		
Lake Chivero, Zimbabwe	Lake	HABs	MODIS	Field monitoring—multiparameter probe	<i>Chl a</i>	[86]
Lake Chivero and Manyema	Lake	HABs	Landsat 5–7 (TM and ETM +)	Field monitoring—multiparameter probe	TURB, TP, Chl-a and TSM	[87]
Poyang River, China	River	HABs	MERIS	WETLabs Environmental Characterization Optics ECO-FL sensor—fluorometer	<i>Chl a</i>	[88]
Lake Erie	Lake	HABs	Resonon Pika II hyperspectral imager and	Xylem EXO2 sonde—multiparameter	Cyanobacteria	[89]
Norway, Norwegian fjord	Fish farm	Nutrient pollution	CWolf—remotely operated vehicle	<i>In-situ</i> Ultraviolet Spectrometer (ISUS) and Submersible Ultraviolet Nitrate Analyzer (SUNA)	NO ₃ ⁻ discharge	[17]

Adapted from [44]

to capture from another platform. However, constraints regarding data availability, accuracy of obtained products, software, tools, leave gaps where other technologies from different tiers in the hierarchical approach can be used to complete the data set. Producing a monitoring system that can provide temporal, spatial and frequent data collection [20, 21]. Stauffer et al. [70] demonstrated a combined approach to monitoring which includes different hierarchical levels of technology [70]. The study was carried out Lake Erie, USA and investigated the spatial and temporal variability of HAB's using airborne hyperspectral imagery incorporation with an autonomous sensing device (Xylem EXO2 sonde) and periodic sampling, highlighting the impact that incorporating a hierarchical approach can have on the collection of validated data (Table. 14.3). An overabundance of nutrient levels has been shown to negatively impact catchments and the aquatic ecosystem present in that body of water [71]. Typically for many case studies examining nutrient fluxes in rural catchments the two main methods of monitoring are *in-situ* sensing and traditional sampling. An emergence of autonomous underwater vehicles (AUV) for nutrient monitoring has shown promise (Table 14.3). This has been demonstrated by Eichhorn et al. [17] as a tool to detect NO_3^- discharge in Norwegian fjords near fish farms [17]. The study used AUVs to measure nutrient levels and discovered a high level of NO_3^- in the surface waters, resulting from the likely discharge from fish farms and in flow from other surrounding rivers. The incorporation of satellite and *in-situ* sensing platforms would have provided more evidence based results on pollution sources and other contaminants, as highlighted in a study carried out by Japitana et al. [20]. The latter study by Japitana et al. used remote sensing combined with GIS technology to extract the physical and spectral characterised essential in water quality catchment monitoring [20]. The study used different monitoring techniques to obtain hyperspectral images (satellite sensing), *on-site* measurements (WSN-based sensors) and the development of digital elevation modelling dataset (GIS).

The transport of sediment into different waterways can have a major influence on the quality of water within a catchment [72]. This is mainly due to the build-up of suspended solids in the bed of a lake/river which can have an overwhelming effect on the on the quality of the water and inhabitants of that waterbody [73]. Many agricultural catchments are impacted by SS and pollutants entering the water [74]. A hierarchical approach to monitoring can be used in the reduction or in some cases the mitigation of water bodies that exceed the normal levels of SS.

Climate related extreme weather event frequencies, intensity, and geographic distribution is considered a major driving force behind flooding rains, coastal flooding, storm surges, and hurricanes [75, 76]. Research into the prediction and monitoring of flooding events has escalated in recent years. Early warning forecasting for extreme weather events are emerging, which provide catchment managers with information to help manage a catchment area. Traditional rain gauges are no longer fit for purpose in a monitoring scenario where the need for more data is critical again illustrating the opportunity to implement a hierarchical sensing approach [77]. In recent years the research into flood risk assessment models have shown the need for other monitoring systems to validate the findings [78–80]. Two meso-scale catchment areas (Gard and Ardèche) in the South-East of France were used

to determine the causes of flash flooding over a four year period [81]. This case study demonstrated the combined use of both continuous and adaptive monitoring techniques to capture enough data to support the findings of the model. The incorporation of drone technology into catchment monitoring applications facilitates rapid and repeated sampling of inland waters that may be difficult to access by personnel or by boat, it also reduces the cost involved with the deployment of boats [82, 83]. A study in central Italy used drone technologies to measure water level and the datasets obtained were validated using standard values and employed Ground Control Points (GCP) as references [39]. The drones were used to obtain hyperspectral images to measure the water level, in addition to *in-situ* sensing platforms such as water level loggers as reliable for data comparison. The need to ground truth the data from hyperspectral imagers on drones is important, therefore the requirement of another type of monitoring technology is advantageous. The limitations surrounding the operation of drone systems are concerned with flight path access and permission (shared with manual manned aircrafts), flight range (limited acreage), climate conditions, regulations in different countries and the cost [84].

A good verification of a hierarchical monitoring framework was illustrated by McGrane et al. 2017 on the River Ray, UK [85]. This work combined the use of *in-situ* and spatial land monitoring for the development of a hydrological model (TETIS). The model was used to determine different water sources in sub catchments and investigate the differences in hydrological elements across contrasting land-use during extreme storm events.

14.4 Conclusions

With increasing environmental pressure due to global climate change, increases in global population and the need for sustainable obtained resources, water resources management is critical. Water monitoring networks and their designs are fundamental to the management of catchments and the first step steps in providing early warning, forecasting and baseline data to stakeholders.

This chapter summarises the principles, methods and technologies that have been applied to measure water quality, observation of land use/land change and environmental impacts on catchments. To be fit-for-purpose, monitoring has to be carried out in a cost effective way and allow implementation at larger spatial scales. Rapid developments of *in-situ* water quality monitoring instrumentation and remote sensing (aerial and satellite) have the immediate potential to catalyse progress towards cost effective sensor networks at catchment scales. Hierarchical monitoring approaches using sensor networks from different layers, combining multiple data streams could potentially disrupt the barrier for comprehensive catchment monitoring. In the era of data driven models, increased data collection and its availability from *in-situ* and remote sensors is critical for the development of novel artificial intelligence (AI) and ML methods which in turn will provide more effective models and data treatment algorithms.

In-situ sensing instrumentations plays a central role and is becoming increasingly used and implemented. Technological development in the field is progressing rapidly and a shift towards optical sensors is clearly noticed. The main advantages of these type of sensors that fundamentally work on simple principles like fluorescence, scatter and absorption are the capital and operational costs, life-time, availability for a wide range of parameters and fouling protection. Wet-chemistry based sensors are used traditionally where analytical precision and accuracy is required and where no alternative sensors exist (i.e. nutrients speciation, faecal indicator bacteria) while multiparameter sondes still remain the powerhouse for environmental applications. It is likely, the future will see lower cost sensors, increasingly specialised and easier to integrate and maintain. To date however, optical sensors have the highest potential for immediate uptake and integration into new WTQNs or scale-up of existing ones. The use of proxy and surrogate parameters for water quality changes is projected to increase as they can offer real-time management support at a reduced cost. Combined with new data analytics platforms and historical data this type of sensors can provide the spatial resolution needed at catchment scale.

The use of a combined approach to water quality monitoring for different pollution events has been demonstrated in this chapter. It highlights how using more than one sensor type can be used to better understand the needs of the catchment and to prevent further deterioration of a catchment area, by investigating indicators or point sources causing pollution events. It also discussed the different combinations commonly used to monitor specific water quality parameters. While the use of remote data presents significant new opportunities, it is not without challenges; namely, array, volume and complexity of data, requirement for *in-situ* and other data to inform interpretation, availability of suitable workflows and access to computational resources.

In summary this chapter investigates the advantages and limitations of associated with the development of tiered monitoring hierarchical systems and how they can be employed to catchment monitoring programmes. A key scientific question remains and centres on how to gather, fuse and subsequently analyse large volumes of multi-dimensional data from conventional earth observations sources as well as emerging sensor platforms to generate new insights and information.

Acknowledgements The Authors acknowledge funding by the Irish Marine Institute as part of the Burrishoole Ecosystem Observatory Network 2020: BEYOND 2020 PBA/FS/16/02 and this publication has emanated from research supported in part by a Grant from Science Foundation Ireland under Grant number [SFI 20/SPP/3705].

Conflict of Interest

The authors declare that they have no conflict of interest.

References

1. Fabricius K, De'ath G, McCook L, Turak E, Williams DMB (2005) Changes in algal, coral and fish assemblages along water quality gradients on the inshore Great Barrier Reef. *Mar Pollut Bull* 51(1–4):384–398

2. Neal C, Jarvie HP, Wade AJ, Whitehead PG (2002) Water quality functioning of lowland permeable catchments: Inferences from an intensive study of the River Kennet and upper River Thames. *Sci Total Environ* 282–283:471–490
3. Sassolas-Serrayet T, Cattin R, Ferry M (2018) The shape of watersheds. *Nat Commun* 9(1):1–8
4. Plisnier PD, Nshombo M, Mgana H, Ntakimazi G (2018) Monitoring climate change and anthropogenic pressure at Lake Tanganyika. *J Great Lakes Res* 44(6):1194–1208
5. Carvalho L et al (2019) Protecting and restoring Europe's waters: an analysis of the future development needs of the water framework Directive. *Sci Total Environ* 658:1228–1238
6. Collins L, McGregor D, Allen S, Murray C, Metcalfe C (2017) Source water protection planning for Ontario first nations communities: case studies identifying challenges and outcomes. *Water (Switzerland)* 9(7):1–19
7. Papas M (2018) Supporting sustainable water management: Insights from Australia's reform journey and future directions for the Murray-Darling Basin. *Water (Switzerland)* 10(11)
8. Keiser D, Shapiro J (2018) Demand For Water Quality * The 1972 U . S . Clean Water Act sought “ to restore and main- tain the chemical , physical , and biological integrity of the Nation ’ s waters . ” This article quantifies changes in water pollution since before 1972 , studies th. *Quarterly J Econ* 1–48
9. Chapman DV et al (2016) Developments in water quality monitoring and management in large river catchments using the Danube River as an example. *Environ Sci Policy* 64:141–154
10. Bilotta GS, Brazier RE (2008) Understanding the influence of suspended solids on water quality and aquatic biota. *Water Res* 42(12):2849–2861
11. Amoatey P, Baawain MS (2019) Effects of pollution on freshwater aquatic organisms. *Water Environ Res* 91(10):1272–1287
12. Chacon-Hurtado JC, Alfonso L, Solomatine DP (2017) Rainfall and streamflow sensor network design: a review of applications, classification, and a proposed framework. *Hydrol Earth Syst Sci* 21(6):3071–3091
13. Jiang J, Tang S, Han D, Fu G, Solomatine D, Zheng Y (2020) A comprehensive review on the design and optimization of surface water quality monitoring networks. *Environ Model Softw* 132:104792
14. Nguyen TH, Helm B, Hettiarachchi H, Caucci S, Krebs P (2019) The selection of design methods for river water quality monitoring networks: a review. *Environ Earth Sci* 78(3):1–17
15. Randhawa S, Sandha SS, Srivastava B (2017) A multi-sensor process for in-situ monitoring of water pollution in rivers or lakes for high-resolution quantitative and qualitative water quality data. In: *Proceedings—19th IEEE international conference computer science engineering 14th IEEE international conference embedded ubiquitous computing 15th international symposium distributed computing applications to business, Engineering*, no. August, pp. 122–129, 2017.
16. Thiemann S, Kaufmann H (2002) Lake water quality monitoring using hyperspectral airborne data—a semiempirical multisensor and multitemporal approach for the Mecklenburg Lake District, Germany. *Remote Sens Environ* 81(2–3):228–237
17. Eichhorn M et al (2018) Modular AUV system with integrated real-time water quality analysis. *Sensors (Switzerland)* 18(6):1–17
18. Wong BP, Kerkez B (2016) Real-time environmental sensor data: an application to water quality using web services. *Environ Model Softw* 84:505–517
19. Toth C, Józków G (2016) Remote sensing platforms and sensors: a survey. *ISPRS J Photogramm Remote Sens* 115:22–36
20. Japitana MV, Demetillo AT, Burce MEC, Taboada EB (2019) Catchment characterization to support water monitoring and management decisions using remote sensing. *Sustain Environ Res* 29(1):1–10
21. Wang K, Franklin SE, Guo X, He Y, McDermid GJ (2009) Problems in remote sensing of landscapes and habitats. *Prog Phys Geogr* 33(6):747–768
22. Heery B et al (2016) ColiSense, today's sample today: a rapid on-site detection of β -D-Glucuronidase activity in surface water as a surrogate for *E. coli*. *Talanta* 148:75–83
23. Briciu-Burghina C, Heery B, Duffy G, Brabazon D, Regan F (2019) Demonstration of an optical biosensor for the detection of faecal indicator bacteria in freshwater and coastal bathing areas. *Anal Bioanal Chem* 411(29):7637–7643

24. Duff G, Regan F, Duffy G (2017) Recent developments in sensing methods for eutrophying nutrients with a focus on automation for environmental applications analyst critical review recent developments in sensing methods for eutrophying nutrients with a focus on automation for environmental. *Analyst* 142:4355
25. Burnet J-B, Dinh QT, Imbeault S, Servais P, Dorner S (2019) Autonomous online measurement of b-D-glucuronidase activity in surface water: is it suitable for rapid *E. coli* monitoring?
26. Maguire I et al (2018) Novel microfluidic analytical sensing platform for the simultaneous detection of three algal toxins in water. *ACS Omega* 3(6):6624–6634
27. Pellerin BA et al (2016) Emerging tools for continuous nutrient monitoring networks: sensors advancing science and water resources protection. *J Am Water Resour Assoc* 52(4):993–1008
28. Grand MM et al. (2017) A lab-on-chip phosphate analyzer for long-term In Situ monitoring at fixed observatories: optimization and performance evaluation in estuarine and oligotrophic coastal waters. *Front Mar Sci* 4:1–16
29. Monteiro-Silva F, Jorge PAS, Martins RC (2019) Optical sensing of nitrogen, phosphorus and potassium: A spectrophotometrical approach toward smart nutrient deployment. *Chemosensors* 7(4)
30. Kitchener BGB, Wainwright J, Parsons AJ (2017) A review of the principles of turbidity measurement. *Prog Phys Geogr* 41(5):620–642
31. Collins-camargo F, Associate E (2002) Turbidity and other sediment surrogates workshop, April 30–May 2, Reno, NV, vol 1. pp 2–4
32. Bleyen N, Albrecht A, De Cannière P, Wittebroodt C, Valcke E (2019) Non-destructive on-line and long-term monitoring of in situ nitrate and nitrite reactivity in a clay environment at increasing turbidity. *Appl Geochem* 100:131–142
33. Meyer AM, Klein C, Fünfroeken E, Kautenburger R, Beck HP (2019) Real-time monitoring of water quality to identify pollution pathways in small and middle scale rivers. *Sci Total Environ* 651:2323–2333
34. Whitt C et al (2020) Future vision for autonomous ocean observations. *Front Mar Sci* 7:697
35. Alilou H, Moghaddam Nia A, Saravi MM, Salajegheh A, Han D, Enayat BB (2019) A novel approach for selecting sampling points locations to river water quality monitoring in data-scarce regions
36. “Alliance for Coastal Technologies.” [Online]. Available: <https://www.act-us.info/>
37. Delgado A, Briciu-Burghina C, Regan F (2021) Antifouling strategies for sensors used in water monitoring: review and future perspectives. *Sensors (Switzerland)* 21(2):1–25
38. Bixler GD, Bhushan B (2012) Review article: biofouling: lessons from nature. *Philos Trans R Soc A Math Phys Eng Sci* 370(1967):2381–2417
39. Douglas RW, Menary W, Jordan P (2007) Phosphorus and sediment transfers in a grassland river catchment. *Nutr Cycl Agroecosyst* 77(3):199–212
40. Koponen S et al (2001) Analysis on the feasibility of multi-source remote sensing observations for chl-a monitoring in Finnish lakes. *Sci Total Environ* 268(1–3):95–106
41. Gomasasca MA et al (2019) Sentinel for applications in agriculture. *Int Arch Photogramm Remote Sens Spat Inf Sci—ISPRS Arch* 42(3/W6):91–98
42. Fu B, Merritt WS, Croke BFW, Weber TR, Jakeman AJ (2019) A review of catchment-scale water quality and erosion models and a synthesis of future prospects. *Environ Model Software*
43. Rocchini D (2013) Seeing the unseen by remote sensing: satellite imagery applied to species distribution modelling. *J Veg Sci* 24(2):209–210
44. O’Grady J, Zhang D, O’Connor N, Regan F (2020) A comprehensive review of catchment water quality monitoring using a tiered framework of integrated sensing technologies. *Sci Total Environ* 765:142766
45. Kim YH et al (2020) Application of satellite remote sensing in monitoring dissolved oxygen variabilities: a case study for coastal waters in Korea. *Environ Int* 134:105301
46. Li J, Menzel WP, Yang Z, Frey RA, Ackerman SA (2003) High-spatial-resolution surface and cloud-type classification from MODIS multispectral band measurements. *J Appl Meteorol* 42(2):204–226

47. Imen S, Chang NB, Yang YJ (2014) Spatiotemporal monitoring of TOC concentrations in lake mead with a near real-time multi-sensor network. In: Conference proceedings—IEEE international conference systems man cybernetics, January, vol 2014. pp 3407–3412
48. Dekker AG, Vos RJ, Peters SWM (2001) Comparison of remote sensing data, model results and in situ data for total suspended matter (TSM) in the southern Frisian lakes. *Sci Total Environ* 268(1–3):197–214
49. Liu X et al. (2019) Remote sensing of secchi depth in highly turbid lake waters and its application with MERIS data. *Remote Sens* 11(19)
50. Kratzer S, Brockmann C, Moore G (2008) Using MERIS full resolution data to monitor coastal waters—a case study from Himmerfjärden, a fjord-like bay in the northwestern Baltic Sea. *Remote Sens Environ* 112(5):2284–2300
51. Gürsoy A, Birdal C, Özyonar F, Kasaka E (2015) Determining and monitoring the water quality of Kizilirmak River of Turkey: first results. *Int Arch Photogramm Remote Sens Spat Inf Sci—ISPRS Arch* 40(7W3):1469–1474
52. Barnsley MJ, Settle JJ, Cutter MA, Lobb DR, Teston F (2004) The PROBA/CHRIS mission: a low-cost smallsat for hyperspectral multiangle observations of the earth surface and atmosphere. *IEEE Trans Geosci Remote Sens* 42(7):1512–1520
53. Kutser T (2012) The possibility of using the Landsat image archive for monitoring long time trends in coloured dissolved organic matter concentration in lake waters. *Remote Sens Environ* 123:334–338
54. Klemas V (2011) Remote sensing of sea surface salinity: an overview with case studies. *J Coast Res* 276(May):830–838
55. Goodberlet MA, Swift CT, Kiley KP, Miller JL, Zaitzeff JB (1997) Microwave remote sensing of coastal zone salinity. *J Coast Res* 13(2):363–372
56. Clark JM et al. (2017) Satellite monitoring of cyanobacterial harmful algal bloom frequency in recreational waters and drinking water sources. *Ecol Indic* 80:84–95
57. Park J, Kim KT, Lee WH (2020) Recent advances in information and communications technology (ICT) and sensor technology for monitoring water quality. *Water (Switzerland)* 12(2)
58. Roy PS, Behera MD, Srivastav SK (2017) Satellite remote sensing: sensors, applications and techniques. *Proc Natl Acad Sci India Sect A Phys Sci* 87
59. Anderson CR et al. (2019) Scaling up from regional case studies to a global harmful algal bloom observing system. *Front Mar Sci* 6
60. Hallegraeff GM (1993) A review of harmful algal blooms and their apparent global increase. *Phycologia* 32(2):79–99
61. Van Dolah FM (2000) Marine algal toxins: origins, health effects, and their increased occurrence. *Environ Health Perspect* 108(SUPPL. 1):133–141
62. Robbins IC, Kirkpatrick GJ, Blackwell SM, Hillier J, Knight CA, Moline MA (2006) Improved monitoring of HABs using autonomous underwater vehicles (AUV). *Harmful Algae* 5(6):749–761
63. Shen L, Xu H, Guo X (2012) Satellite remote sensing of harmful algal blooms (HABs) and a potential synthesized framework. *Sensors (Switzerland)* 12(6):7778–7803
64. Kirkpatrick GJ (2017) Monitoring *Karenia Brevis* blooms in the gulf of Mexico using satellite Ocean color imagery and other data monitoring *Karenia brevis* blooms in the Gulf of Mexico using satellite ocean color imagery and other data. 2:147–160
65. Lekki J et al. (2017) Airborne hyperspectral sensing of harmful algal blooms in the great lakes region: system calibration and validation from photons to algae information: the processes in-between, February 2017, pp 78
66. Davidson K et al (2016) Forecasting the risk of harmful algal blooms: preface to the asimuth special issue. *Harmful Algae* 5(6):1–7
67. Aleynik D, Dale AC, Porter M, Davidson K (2016) A high resolution hydrodynamic model system suitable for novel harmful algal bloom modelling in areas of complex coastline and topography. *Harmful Algae* 53:102–117

68. Wei GF, Tang DL, Wang S (2008) Distribution of chlorophyll and harmful algal blooms (HABs): a review on space based studies in the coastal environments of Chinese marginal seas. *Adv Sp Res* 41(1):12–19
69. Lee Z, Shang S, Qi L, Yan J, Lin G (2016) A semi-analytical scheme to estimate Secchi-disk depth from Landsat-8 measurements. *Remote Sens Environ* 177:101–106
70. Stauffer BA et al. (2019) Considerations in harmful algal bloom research and monitoring: perspectives from a consensus-building workshop and technology testing. *Front Mar Sci* 6:1–18
71. Blaen PJ, Khamis K, Lloyd CEM, Bradley C, Hannah D, Krause S (2016) Real-time monitoring of nutrients and dissolved organic matter in rivers: capturing event dynamics, technological opportunities and future directions. *Sci Total Environ* 569–570:647–660
72. Tundu C, Tumbare MJ, Onema JMK (2018) Sedimentation and its impacts/effects on river system and reservoir water quality: case study of Mazowe catchment, Zimbabwe. *Proc Int Assoc Hydrol Sci* 377:57–66
73. Yi Y, Wang Z, Zhang K, Yu G, Duan X (2008) Sediment pollution and its effect on fish through food chain in the Yangtze River. *Int J Sediment Res* 23(4):338–347
74. Calmano W, Förstner U, Series M (2004) Solid waste: assessment, monitoring and remediation comparative study of sediment and mussel aromatic compound content in European coastal environments. Relationship with specific biomarkers
75. Bell JE et al (2018) Changes in extreme events and the potential impacts on human health. *J Air Waste Manag Assoc* 68(4):265–287
76. Jentsch A, Beierkuhnlein C (2008) Research frontiers in climate change: effects of extreme meteorological events on ecosystems. *Comptes Rendus—Geosci* 340(9–10):621–628
77. Lo SW, Wu JH, Lin FP, Hsu CH (2015) Visual sensing for urban flood monitoring. *Sensors (Switzerland)* 15(8):20006–20029
78. Zhou Y, Shen D, Huang N, Guo Y, Zhang T, Zhang Y (2019) Urban flood risk assessment using storm characteristic parameters sensitive to catchment-specific drainage system. *Sci Total Environ* 659:1362–1369
79. Metcalfe P, Beven K, Hankin B, Lamb R (2017) A modelling framework for evaluation of the hydrological impacts of nature-based approaches to flood risk management, with application to in-channel interventions across a 29-km² scale catchment in the United Kingdom. *Hydrol Process* 31(9):1734–1748
80. Kim D, Chun JA, Aikins CM (2018) An hourly-scale scenario-neutral flood risk assessment in a mesoscale catchment under climate change. *Hydrol Process* 32(22):3416–3430
81. Braud I et al. (2016) Advances in flash floods understanding and modelling derived from the floodScale project in South-East France. In: E3S web conference, vol 7.
82. Castendyk D, Voorhis J, Kucera B (2020) A validated method for pit lake water sampling using aerial drones and sampling devices. *Mine Water Environ* 0123456789
83. Lally HT, O'Connor I, Jensen OP, Graham CT (2019) Can drones be used to conduct water sampling in aquatic environments? a review. *Sci Total Environ* 670:569–575
84. Giacomo R, David G (2017) Unmanned aerial systems (UAS) in agriculture: regulations and good practices
85. McGrane SJ, Hutchins MG, Miller JD, Bussi G, Kjeldsen TR, Loewenthal M (2017) During a winter of storms in a small UK catchment, hydrology and water quality responses follow a clear rural-urban gradient. *J Hydrol* 545:463–477
86. Dlamini S, Nhapi I, Gumindoga W, Nhwatiwa T, Dube T (2016) Assessing the feasibility of integrating remote sensing and in-situ measurements in monitoring water quality status of Lake Chivero, Zimbabwe. *Phys Chem Earth* 93:2–11
87. Muchini R, Gumindoga W, Togarepi S, Masarira TP, Dube T (2018) Near real time water quality monitoring of Chivero and Manyame lakes of Zimbabwe. *Proc Int Assoc Hydrol Sci* 378:85–92
88. Li J, Tian L, Song Q, Sun Z, Yu H, Xing Q (2018) Temporal variation of chlorophyll-a concentrations in highly dynamic waters from unattended sensors and remote sensing observations. *Sensors (Switzerland)*, 18(8)

89. Vander Woude A, Ruberg S, Johengen T, Miller R, Stuart D (2019) Spatial and temporal scales of variability of cyanobacteria harmful algal blooms from NOAA GLERL airborne hyperspectral imagery. *J Great Lakes Res* 45(3):536–546

Chapter 15

Spectral Induced Polarization (SIP) Imaging for the Characterization of Hydrocarbon Contaminant Plumes



Adrián Flores-Orozco and Matthias Bucker

Abstract We review the application of the Spectral Induced Polarization (SIP) imaging method to delineate the geometry of hydrocarbon contaminant plumes and monitor the effect of remediation measures. In the first two sections, we present a brief introduction into the SIP method and discuss the electrical properties of the rocks and soils. In the third section, we offer a detailed revision of the literature to illustrate the broad range of electrical properties of fresh and mature contaminant plumes. In the fourth and fifth section, we discuss challenges and good practices for collection, processing and interpretation of SIP imaging data, and illustrate these steps with a real-case example regarding the characterization of a benzene plume. Along this case study, we demonstrate how the occurrence of benzene in the dissolved plume and in free-phase changes the electrical conductivity and polarization properties of the contaminated subsurface materials. A second case study deals with SIP monitoring results obtained along the injection of zero-valent iron particles for the remediation of a TCE (Trichloroethylene) plume. This example illustrates the advantages of the SIP method to evidence changes in the pore-space, such as clogging and fracking, which may affect the effectivity of remediation measures.

15.1 Spectral Induced Polarization (SIP) Imaging

Induced polarization (IP) refers to a geophysical method, which quantifies the capacity of rocks and sediments to conduct electrical current and accumulate electrical charges. To carry out an IP measurement, a pair of electrodes (e.g., metallic bars) is used to inject an electrical current into the ground, while another pair of

A. Flores-Orozco (✉)

Research Unit of Geophysics—Department of Geodesy and Geoinformation, Technical University of Vienna (TU-Wien), Wiednerhauptstrasse 8—10, 1040 Vienna, Austria
e-mail: adrian.flores-orozco@geo.tuwien.ac.at

M. Bucker

Institute of Geophysics and Extraterrestrial Physics, Technische Universität Braunschweig, Mendelssohnstraße 3, 38106 Braunschweig, Germany
e-mail: m.buecker@tu-braunschweig.de

electrodes is used to measure the resulting voltage (Fig. 15.1a). IP measurements can be collected in time domain (TDIP) by measuring decaying voltages directly after a direct current is shut off (Fig. 15.1b); or in frequency domain (FDIP) by injecting a sinusoidal current and voltage readings, typically in the frequency range between 10 MHz and 10 kHz (Fig. 15.1c). TDIP data is commonly expressed in terms of the transfer resistance (R , given by the voltage-to-current ratio) and the integral chargeability (m , given by the integrated voltage decay). In FDIP, the measurements are expressed in terms of a complex-valued electrical impedance (Z), characterized by a magnitude ($|Z|$, corresponding to the voltage-to-current ratio, or transfer resistance $|Z| = R$) and the phase shift between the current and the voltage. The use of sinusoidal currents at different frequencies results in an impedance spectrum. This approach, which evaluates the frequency dependence of the electrical properties, is referred to as spectral induced polarization (SIP).

Under certain conditions, SIP data can be extracted from TDIP measurements (e.g., Fiandaca et al. [22]), especially if TDIP measurements are conducted with different pulse lengths (for current injection and the recording of the integral chargeability), this conversion yields good results. Based on this idea, the DAS-1 (from Multi-Phase Technologies, MPT) is a measuring device, which permits the collection of both TDIP and FDIP data. Other instruments, e.g., the latest Terrameter LS2 from ABEM, digitize the full voltage decay (also known as “full wave form”) at high sampling rates. If used in conjunction with suitable modeling algorithms, spectral parameters can be inverted directly from the full-waveform TDIP data. Although this approach has shown to yield good results under certain conditions, only the repetition of FDIP measurements at different frequencies or TDIP measurements with different pulse lengths enables a direct determination of the frequency-dependent electrical properties of the subsurface. A detailed comparison of TDIP and FDIP methods, with a particular emphasis on the spectral content can be found in the studies by Flores Orozco et al. [27], Maurya et al. [53], and Martin et al. [52]. For a comprehensive introduction into the SIP method we refer to Sumner [73] and Binley and Slater [7].

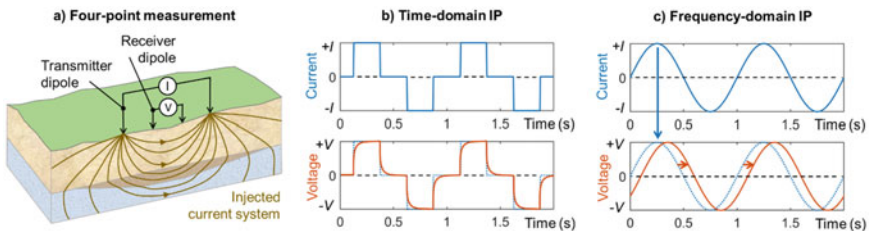


Fig. 15.1 Induced polarization (IP) measurement setup and wave forms. **a** Four-point measurement including a transmitter dipole for current injection, and a receiver dipole for voltage measurement. The distribution of the electrical current depends on the electrical resistivity of the subsurface materials. **b** For time-domain (TDIP) measurements, a square wave signal is injected into the ground; depending on the capacitive properties, the transient voltage signal is related to the charging and de-charging of the subsurface materials. **c** In frequency domain, (FDIP) these capacitive properties lead to a phase shift between alternating current and voltage signals

SIP imaging data are collected using tens to hundreds of electrodes and usually comprise hundreds to thousands of individual quadrupole (4-electrode) measurements. By varying the position of such quadrupoles along a line or surface, information on the lateral variation of electrical properties is gained. The total size of the electrode array, together with the electrical properties of the subsurface, control the depth of investigation of the measurement. In general, larger layouts gain information from deeper areas, while measurements with small separations between electrodes increase the resolution of near-surface data. However, conductive materials may channel the current flow limiting the sensitivity of the method to deeper areas. In order to reconstruct SIP images, measured transfer resistance and phase data are interpreted using inversion algorithms, which compute 2D sections—or 3D volumes—revealing the spatial variation of the electrical properties in the subsurface.

Here, we will limit ourselves to the discussion of results computed with smoothness-constraint inversion algorithms. This widely used inversion strategy favors the generation of electrical images with rather smooth transitions between regions of contrasting electrical properties. Kemna [44] and Binley and Slater [7] provide a revision on the inversion of TDIP and FDIP measurements. The open-source algorithms provided by Rücker et al. [63] and Johnson and Thomle [8] place well-established codes for the inversion of TDIP, FDIP and SIP datasets to the disposal of a broad audience. These algorithms have been used for the characterization of contaminated sites or the monitoring of groundwater remediation measures and permit using different inversion strategies, for instance, a frequency regularization to enhance the consistency of SIP imaging results at different frequencies [37, 41], a spatio-temporal regularization scheme for the inversion of monitoring data sets [21, 42, 46], or the use of a-priori information, such as structural constraints, to evaluate the performance of permeable reactive barriers of known geometry [70].

15.2 Electrical Properties of Natural Media

In the subsurface, electrical currents are mainly carried by the motion of ions through the electrolytic pore fluid. While most solid constituents of geologic materials can be considered electrically insulating (except for some metallic and other rare, conducting minerals), the mineral-electrolyte interface is covered by a conductive electrical double layer (EDL). The EDL (see Fig. 15.2a) forms due to the usually negative surface charge of the mineral and consists of two sections, (i) the Stern or fixed layer of counter-ions (cations) absorbed to the grain surface and (ii) the diffuse layer characterized by an increased concentration of counter-ions (cations) and a reduced concentration of co-ions (anions) compared to the undisturbed electrolyte. Driven by the electrical field imposed by the measuring device, ions in the electrolyte migrate along interconnected pathways in the water-filled pore space and ions in the EDL along interconnected surfaces (Fig. 15.2b). The amount of charges transported by these two conduction mechanisms known as electrolytic and surface conduction, respectively, controls the electrical conductivity (σ) of soils and rocks. In geophysics,

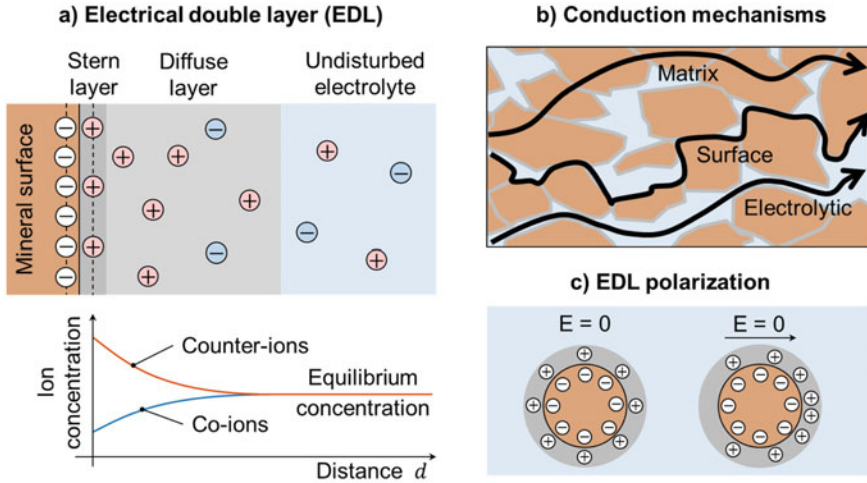


Fig. 15.2 Electrical properties of the mineral-electrolyte interface. **a** The usually negatively charged mineral surface is covered by an electrical double layer (EDL) consisting of the inner Stern and the outer diffuse layer. Across the diffuse layer, ion concentrations transition from their perturbed values at the mineral surface into the equilibrium concentration in the electrolyte. **b** Electrical conduction mechanisms including matrix conduction (often negligible), surface conduction, and electrolytic conduction. **c** Schematic sketch of the polarization of the EDL around a spherical grain: The application of an external electrical field leads to a redistribution of charges along the surface, the EDL polarizes

this property is often expressed in terms of the electrical resistivity $\rho = \sigma^{-1}$, the inverse of conductivity. Materials with highly charged surfaces and a large internal surface area, such as clay, often stand out with a high electrical conductivity (low resistivity). For further details we refer to Revil and Florsch [60], Kemna et al. [45], Bucker and Hördt [13], Bucker et al. [12].

Besides a considerable increase in conductivity, the EDL gives rise to the chargeability assessed by TDIP or the phase shift assessed by FDIP measurements. Driven by the external electrical field, the ions of the EDL accumulate on one side of the mineral grain and deplete at the other side. As soon as the external field is switched off (when the current injection is interrupted), diffusion forces redistribute the polarized charges within the EDL. This polarization and its relaxation result in the secondary voltage observed in TDIP or the phase shift in FDIP. As they do not only provide information about the conduction of current (i.e., migration of charges), but also information about the capacity of the subsurface to store charges (i.e., polarization of the EDL), IP methods offer additional complementary information compared to the resistivity method alone.

The bulk electrical conductivity of most natural media (except for metallic minerals or graphite) strongly depends on the conductivity of the pore fluid (σ_f). The porosity (θ , the ratio of pore volume to total volume) and the water saturation (S , the ratio of the water-saturated pore volume to the total pore volume) play

also an important role. Based on measurements on a large number of samples, [4] proposed an empirical model establishing a relation between these properties and the bulk conductivity of a material, which is widely used for hydrogeological and environmental investigations:

$$\sigma_{el} = \theta^m S^n \sigma_f$$

In this equation, also known as Archie's law, m and n are the cementation factor and the saturation exponent, respectively. The first is related to the connectivity between pores, while the second quantifies changes in the conductivity when replacing pore water by a non-conducting or fluid or gas. Both exponents are fitting parameters that need to be experimentally determined for each type of material. Since it has been established, many investigations have demonstrated the applicability of Archie's law to a wide range of rock and soil samples, as well as for different temperatures and chemical compositions of the pore water (see Glover [35]; and references therein). Nonetheless, in its original form, Archie's law does not hold for materials characterized by a large internal surface area and highly charged surfaces, such as clays, microbial cells, nanoparticles, organic matter, and in some cases contaminants. In these materials, surface conduction (σ_s) along the EDL plays a dominant role, which is not taken into account in Archie's law. Moreover, as discussed above, charges in the EDL polarize, which causes a frequency dependence of the electrical conductivity. To take both surface conduction and the associated polarization of charges into account, Archie's law can be expanded by adding a complex frequency-dependent surface conductivity $\sigma_s^*(\omega)$:

$$\sigma^*(\omega) = \theta^m S^n \sigma_f + \sigma_s^*(\omega)$$

Here, $\omega = 2\pi f$ is the angular frequency (in rad/s) associated to the frequency (f , in Hz) of the measurement. Complex-valued conductivities are convenient to calculate amplitude and phase of an alternating current together: The complex-valued surface conductivity σ_s^* , for instance, can be expressed in terms of its real component (σ_s'), which mostly describes Ohmic conduction or charge motion in-phase with the driving voltage, and its imaginary component (σ_s''), which quantifies the polarization properties or out-of-phase charge motion. By substituting $\sigma_s^* = \sigma_s' + i\sigma_s''$, where $i = \sqrt{-1}$, into the equation above, we can split the bulk conductivity of a material into a real part (σ') and an imaginary part (σ''):

$$\sigma^*(\omega) = \sigma' + i\sigma'' = [\sigma_{el} + \sigma_s'(\omega)] + i\sigma_s''(\omega),$$

Note that the real component contains contributions of electrolytic and surface conductivity, while the polarization is only related to the surface conductivity (σ_s'').

The SIP response of materials with one dominant polarization mechanism and a well-defined relaxation time scale (i.e., the time needed to establish the polarization of the material) is characterized by a well-pronounced peak in the phase (or imaginary conductivity) spectrum and an increase in the magnitude (or real conductivity). Such

a behavior can often be approximated by fitting relaxation models. One of the most widely used models for this purpose is the Cole–Cole model, which in terms of complex conductivity can be written as [57]:

$$\sigma^*(\omega) = \sigma_0 \left[1 + \frac{m(i\omega\tau)^c}{1 + (i\omega\tau)^c(1 - m)} \right] = \frac{1}{\rho^*(\omega)}$$

Here, σ_0 denotes the electrical conductivity at the low-frequency limit; m is the chargeability (between 0 and 1), which quantifies the amplitude of the polarization effect; $\tau = (2\pi f_c)^{-1}$ is the relaxation time, which is inversely proportional to the critical frequency (f_c), where the polarization peak is observed, and roughly proportional to the characteristic length scale of the polarization (e.g., the grain size or other important textural parameters); and c is a dispersion constant, which controls the broadness of the relaxation peak and roughly reflects the distribution of relevant relaxation times. The use of such relaxation models allows to reduce the rich information contained in highly resolved SIP data to a smaller number of relevant parameters. For further details, we refer the reader to Pelton et al. [57], Binley and Slater [7].

15.3 Electrical Properties of Contaminated Soil

Contaminants miscible in groundwater commonly tend to increase the real component of the electrical conductivity. Hence, geophysical electrical methods such as the electrical resistivity tomography (ERT), have been widely used in the last years for site characterization. For instance, conductive anomalies resolved through ERT have been used to image the leakage and migration of landfill leachates (e.g., De Carlo et al. [16]; Tsourlos et al. [74]; Soupios and Ntarlagiannis [71]; Nguyen et al. [55] and references therein). The accumulation of metallic ions or an increase in pH can also result in conductive anomalies; thus, ERT has been used to map heavy-metal contaminant plumes, acid mine drainage and other contaminants related to mine-tailings (e.g., Placencia-Gómez et al. [58]; Wang et al. [77]).

Hydrocarbon contaminants comprise a broad range of organic compounds such as chlorinated hydrocarbons (CHCs), polycyclic aromatic hydrocarbons (PAHs), aromatic hydrocarbons (e.g., the BTEX group: benzene, toluene, ethyl benzene and xylene), and phenols. These compounds are immiscible in water and represent some of the most important contaminants affecting soil and groundwater in Europe. Laboratory studies have demonstrated that fresh hydrocarbon contaminants effectively behave like electric insulators and that increasing their volumetric content in soils results in an increase of the electrical resistivity [17]. Hence, initial field studies demonstrated the applicability of the ERT method to delineate the geometry of fresh hydrocarbon-contaminant spills based on the detected resistive anomalies [6, 43, 64].

Like every indirect method, ERT methods suffer from the ambiguity in the interpretation of the resistivity values alone. IP or SIP methods for site characterization

respond to the necessity to gain further information and thereby reduce ambiguities in the interpretation. E.g., a conductive anomaly could either represent dissolved contaminants (e.g., landfill leachates) or simply reflect an elevated clay content in the host rock; resistive anomalies may indicate a fresh hydrocarbon spill or simply be related to unsaturated material or tight consolidated rock. By additionally analyzing the capacitive properties of the subsurface, or the induced polarization effect, the responses associated with the geology and those of the contaminants can often be discriminated better.

Especially in the case of hydrocarbon contaminants, various studies have revealed the sensitivity of SIP measurements to both chemical changes in the impacted groundwater and the geometry of the remaining water-filled pore space. The displacement of pore water by hydrocarbon contaminants modifies the geometry of the water-filled pore space and thus, the frequency dependence of the complex conductivity. These geometrical changes often result in a variation of the relaxation time (τ), which is known to be sensitive to the textural parameters of the material [45, 60]. Furthermore, hydrocarbons are organic compounds and as such may modify the chemical properties of the grain surfaces and thus the electrical properties of the EDL, which control the polarization response.

Olhoeft [56] carried out the first SIP measurements on soil samples impacted by organic waste and petroleum. His study revealed an increase in the conductivity phase (ϕ), which he attributed to interactions between the organic compounds and the surfaces of the solid constituent of the soil. This observation has prompted a large number of follow-up investigations over the last three decades, where the SIP response of a variety of organic compounds has been further evaluated in laboratory experiments. In summary, these investigations revealed that the polarity of the organic compounds as well as the hydrocarbon saturation mainly control the measured SIP response.

15.3.1 Hydrocarbons in Soils: Polar and Non-polar Compounds and Their SIP Response

Hydrocarbon contaminants are non-aqueous phase liquids (NAPL) that are—for practical reasons—classified into light NAPLs (or LNAPLs), which are less dense than water and float on the groundwater table, and dense NAPLs (DNAPLs), which are denser than water and sink down within the aquifer. In terms of electrical properties, the polarity of an organic contaminant, defined by its molecular electrostatic potential, is much more relevant than its density. “Non-polar” hydrocarbons form isolated droplets within the water filled pores because they lack ionic or polar groups to be attracted by the surrounding mineral surfaces (see Fig. 15.3a). They are also referred to as “non-wetting” hydrocarbons, considering that the pore water is in direct contact with the grain surface (i.e. water is the fluid wetting the grains). In contrast, “wetting” hydrocarbons do contain polar compounds and readily attach to the grain

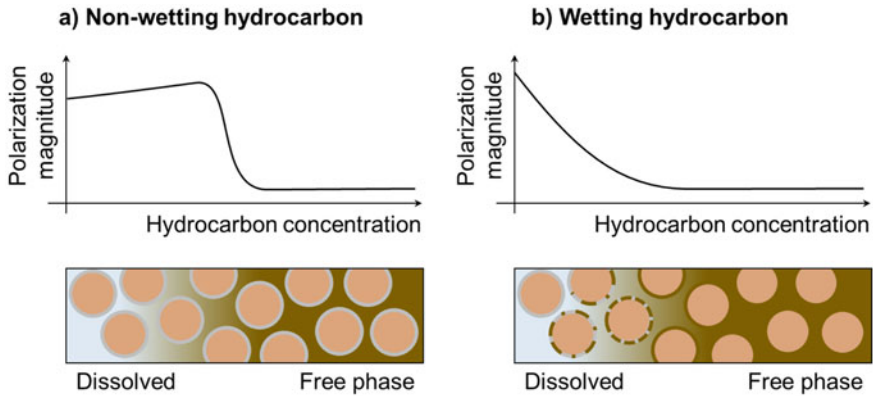


Fig. 15.3 Schematic sketch of the variation of the polarization magnitude with the contaminant concentration for **a** non-wetting and **b** wetting hydrocarbons

surfaces (see Fig. 15.3b), i.e., the liquid hydrocarbon is in direct contact with the grains. In this context, the wettability refers to the affinity of a specific NAPL for the soil surface [2].

In laboratory measurements, Schmutz et al. [65] observed a decrease of both real and imaginary conductivity (σ' and σ'') with increasing volumetric content of non-wetting hydrocarbon (see Fig. 15.3a). At the same time, the phase ($\phi \approx \sigma''/\sigma'$) increased with increasing volumetric content of non-wetting hydrocarbon. The critical frequency of the polarization (frequency at which the peak is observed) was found at low frequencies between 1 mHz and 1 Hz. In a similar study with non-wetting oils (e.g., paraffin and sunflower oil), Schmutz et al. [66] found contradictory trends, while Ustra et al. [75] also reported a negligible polarization in the low frequencies in columns experiments with toluene. Revil et al. [61] extended these experiments to investigate wetting oils and observed a decrease in ϕ as well as an increase in σ' with increasing oil volumetric content (see Fig. 15.3b). These results suggest that the introduction of a wetting oil, which—partly or entirely—covers the soil mineral surface, facilitates ion migration (increase of σ') rather than the accumulation and polarization of charges (decrease of ϕ). Schwartz et al. [67] and Schwartz and Furman [68] argue that the decrease in the polarization magnitude is a consequence of the adsorption of organic molecules to the mineral surface and the release of inorganic ions to the bulk electrolyte, resulting in an increase in σ' , and a decrease in both parameters expressing the polarization effect (ϕ and σ'').

Bucker et al. [10] recently proposed a mechanistic model to understand the SIP response of wetting and non-wetting hydrocarbon contaminants. Based on a membrane polarization model [13], they do not only take the hydrocarbon concentration into account, but also the surface charge at the hydrocarbon-water interface, as well as the geometrical configuration of water and hydrocarbon. They predict a decrease of σ' and ϕ with increasing hydrocarbon saturation irrespective of whether the hydrocarbon is wetting or non-wetting. Non-wetting hydrocarbons

with highly charged surfaces yield an increase of the conductivity magnitude with hydrocarbon saturation and a slight increase of the phase at intermediate hydrocarbon concentrations as sketched in Fig. 15.3a.

15.3.2 *Electrical Properties of Mature Hydrocarbon Plumes*

While pure hydrocarbons behave as electrical insulators, many studies on aged hydrocarbon-contaminated soil and rock materials have revealed high electrical conductivity values. This apparent contradiction has been resolved by attributing the increased conductivity to the effect of biotic and abiotic transformations of the contaminants and the accumulation of metabolic products in the pore water (e.g., Atekwana and Atekwana [5]; and references therein).

Hydrocarbons are electron donors and can be degraded by different bacterial strains [19, 33, 34]. This biodegradation depends on the adaptation of microorganisms to available electron acceptors and the respective energy yield. Differences in the energy efficiency of aerobic and anaerobic respiration and the successive depletion of electron acceptors leads to a sequence of redox reactions: After the oxygen is consumed by oxidizing bacteria (aerobic respiration), nitrate-reducing or denitrifying bacteria are responsible for the most effective anaerobic respiration, followed by manganese and iron reducing bacteria; and lastly sulfate-reducing microorganism. In absence of inorganic electron acceptors besides carbon dioxide (CO₂), methanogenesis, as a last step in the sequence of redox reaction, still permits the degradation of a variety of hydrocarbon contaminants [34, 47, 51]. Flores Orozco [32] and Flores Orozco et al. [31] have shown the sensitivity of the SIP imaging method to variations in the redox-status of the subsurface, thus, its potential to delineate redox zonation in contaminant plumes.

Besides the transformation of the hydrocarbon contaminant, the microbial activity results in the accumulation of metabolic products, such as carbonic acids, dissolved nitrate, iron or manganese in the surrounding groundwater, which in turn may result in the precipitation of minerals such as iron sulfides (e.g., Mewafy et al. [54]). Henceforth, the term “mature” plume refers to contaminant plumes undergoing such a biogeochemical transformation. The time required to reach such maturity depends on the availability of indigenous microorganisms and electron acceptors and varies largely between sites.

As stated above, the release of metabolic products often results in an increase of pore-water salinity around mature plumes and explains the conductive anomalies observed in ERT images (e.g., Atekwana and Atekwana [5]). An increasing pore-water salinity may also increase the polarization response (σ'') in SIP surveys, (e.g., Revil and Skold [62]; Hördt et al. [39]). However, laboratory studies indicate that this increase is only observed up to a certain salinity threshold and that σ'' values decrease at even higher ionic concentrations (e.g., Weller et al. [78]; Hördt et al. [39]). Based on their membrane polarization model, Hördt et al. [39] attribute this

maximum behavior to the salinity-dependent variation of the double-layer thickness at the mineral surface.

The stimulation of microbial activity by contaminants as carbon source also results in the accumulation of microbial cells and the formation of biofilms. Thus, the observed increase in both σ' and σ'' in mature plumes has also been attributed to the electrical properties of microbial cells, which have a surface area and a surface charge similar to clay minerals [3], or the weathering of grains, which is enhanced by the release of carbonic acids during microbially mediated reactions [1]. Recent studies suggest that the precipitation of electrically conducting minerals, such as iron-sulfides, following the activity of iron- and sulfate-reducing bacteria could explain the observed increase in both components of the complex conductivity σ^* [2, 54]. Electrical conductors permit the flow of current through electronic conduction (i.e., by the movement of electrons), which is often related to much higher conductivities than in the case of electrolytic and even surface conduction. Accordingly, the charges on the electrical conductor also polarize and increase the SIP response. For more details on this so-called electrode -polarization, see Bucker et al. [11, 14] and Revil et al. [59].

The vast number of laboratory data and accompanying modeling studies discussed above indicates a high sensitivity of the SIP method to both changes in the chemical composition of the pore water and changes in the pore-space geometry. Based on these findings, the SIP method appears to be a promising technique for site characterization and the monitoring of contaminant transformation. However, to date, only few studies investigate the SIP response at the field scale in detail. To fill this gap, in the following sections, we present SIP field data and show that the obtained imaging results clearly indicate the method's suitability for the characterization of a range of different hydrocarbon contaminants even under real-world field conditions.

15.4 Field Procedure and Data Processing

As noted above, laboratory studies indicate that hydrocarbon contaminants can cause significant contrasts with respect to electrical conductivity and polarization properties of the subsurface. However, to date only few studies have addressed the actual frequency dependence of the electrical response of hydrocarbon plumes in the field. The application of the SIP method at the field scale faces multiple challenges including instrumentation and survey design, data processing and inversion, as well as the interpretation of the imaging results.

In order to illustrate these challenges, we present exemplary raw data and imaging results of a SIP survey conducted on the grounds of a former hydrogenation plant, where groundwater is impacted by high concentrations of benzene. Benzene is a non-polar and non-wetting hydrocarbon with a saturation concentration of 1.79 g/L (at 15 °C). The lithology at the study site consists of three layers (from top to bottom): (1) backfill material with a thickness of approx. 2 m, (2) a sandy to gravelly unit with a thickness of approx. 9 m hosting the aquifer, and (3) a layer of clay and lignite, which

limits the aquifer downwards. During the survey, the groundwater table was located at a depth of -8 m. The SIP profile was centered at the zone, where high benzene concentrations > 2.2 g/L in groundwater indicated free-phase benzene. Contaminant concentrations decreased towards both ends of the profile.

To minimize the distortion of readings by anthropogenic noise due to pipes, storage tanks, power lines, or other subsurface installations, the SIP survey was conducted on the bottom of a trench, after the removal of the backfill material. 37 stainless steel electrodes were installed with a unit electrode spacing of 2.5 m (resulting in a total profile length of 90 m). The electrical impedance measurements were collected with a SIP256C (from Radic Research), using an actual sinusoidal waveform at 15 logarithmically equidistant frequencies between 0.07 and 1,000 Hz. The electrode configuration was a dipole–dipole “skip-3”, which means that the separated current and potential dipoles had a length of 4 times the unit electrode spacing (3 electrodes skipped between the poles).

One of the challenges regarding spatially resolved SIP field measurements is related to the adverse effect of polarized electrodes: The circulation of a current flow through a grounded electrode results in redox reactions at the surface of the metallic bar that might result in a remnant polarization affecting the quality of subsequent voltage readings [18, 48, 79]. Here, this issue was resolved by designing the dipole–dipole measuring protocol in such way that voltage measurements with electrodes, which have previously been used for current injection, were excluded. In other words, the voltage measurements were always collected with electrodes ahead of the current dipole.

Figure 15.4 shows the frequency dependence of the SIP raw data in terms of apparent conductivity magnitude (σ_{app}) and phase (ϕ_{app}). The apparent conductivity magnitude is computed from the measured impedance magnitude as $\sigma_{app} = (|Z|k)^{-1}$, where the geometrical factor k accounts for the geometrical configuration of the electrode layout; ϕ_{app} is equal to the measured phase. These apparent quantities do not represent a true image of the spatial variation of the electrical conductivity in the subsurface, which can only be obtained after the inversion of the data. However, they do permit a first visualization and assessment of the overall response including the frequency dependence of the electrical properties. The frequency dependence of the apparent conductivity of selected quadrupoles along the SIP profile in Fig. 15.4 (last row) shows different behaviors, which can roughly be attributed to three units: (1) the unsaturated soils on the top assessed by shallow measurements (center of the profile, short separation between current and potential dipole); (2) the free-phase contaminant or source zone (center of the profile, intermediate dipole separation); and (3) the plume of dissolved contaminants (first and last dipoles of the profile, intermediate dipole separations).

The steep increase of the phase values at frequencies > 100 Hz evidences another challenge of SIP data acquisition in the field: In small-scale (i.e., cm to dm range) laboratory data, a similar increase is often related to Maxwell–Wagner polarization processes (e.g., Revil et al. [61]), which reflect the polarization of interfaces between two or more materials of varying conductivity but may not be confused with polarization processes in the EDL, which are observed at lower frequencies. In contrast,

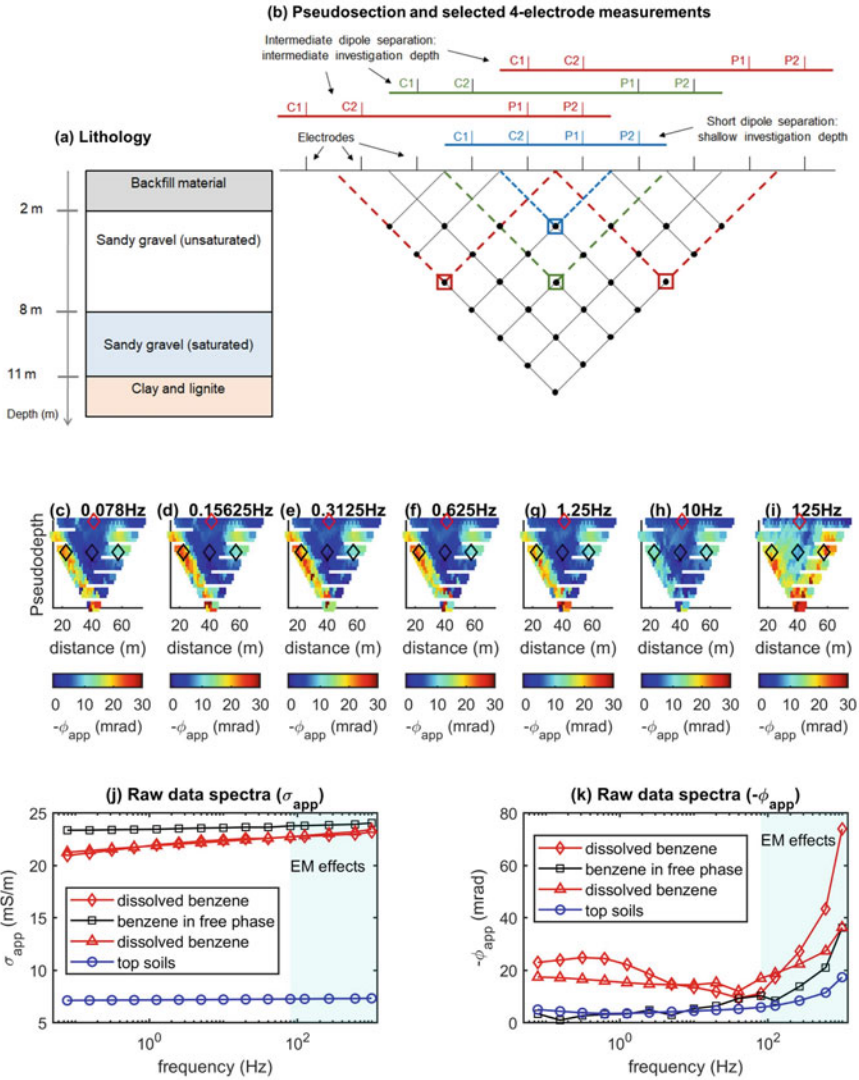


Fig. 15.4 SIP raw data collected over a benzene plume. **a** Lithology of the study area and **b** Schematic representation of a pseudo section including the selected pixels for the analysis of the raw data spectra. **c** to **i** pseudo sections representing the measured impedance phase values (ϕ_{app}), with the diamonds indicating the selected quadrupoles for the analysis of the raw data spectra. Raw data spectra for the selected quadrupoles expressed in terms of **j** the magnitude of the apparent conductivity (σ_{app}) and **k** the apparent phase (ϕ_{app}). The steep increase of ϕ_{app} at high frequencies indicates electromagnetic (EM) coupling effects.

high-frequency SIP measurements collected with large electrode layouts as usually used in the field (10 to 100 s of meters) are mainly affected by electromagnetic (EM) coupling, which comprises both inductive and capacitive effects along the cables connecting the measuring instrument with the electrodes. Phase readings affected by inductive EM-coupling increase linearly with acquisition frequency, ground conductivity and the square of the cable length [23, 24]. Hence, inductive coupling likely becomes important in the case of mature plumes, due to the expected increase in the bulk electrical conductivity, as discussed above.

Sometimes, EM-coupling is argued to be negligible at frequencies < 10 Hz (e.g., Kemna et al. [45]). However, unshielded multicore cables, such as those typically used for resistivity surveys, may provoke significant EM coupling in SIP data even at frequencies as low as 1 Hz. Therefore, Flores Orozco et al. [23] recently recommended the use of shielded cables to minimize inductive coupling due to cross talking between cables, and to improve the overall quality of SIP readings. The SIP256C measurement device used in this field-data example follows an alternative approach: Voltage readings are digitized directly at the electrode, which largely reduces cross talking between cables (e.g., Martin et al. [52]). Even though, the steep increase of ϕ_{app} at frequencies > 100 Hz (Fig. 15.4k) is a clear indication of a significant EM coupling. Besides adjustments to the instrumentation, different techniques have been suggested for the de-coupling of the data during processing (e.g., Pelton et al. [57]). Because their applicability is limited and taking into account that laboratory experiments have mainly revealed a significant frequency dependence in hydrocarbon-impacted sediments below 10 Hz, we hereafter only discuss the results collected at frequencies < 200 Hz.

The pseudo sections in Fig. 15.4 are constructed by plotting the values of ϕ_{app} below the midpoint of the respective quadrupoles and at “pseudo” depths, which are proportional to the total quadrupole length (or dipole separation). Considering that subsequent quadrupole readings along the profile measure overlapping volumes of the subsurface, pseudo sections are expected to vary gradually in both lateral and vertical direction. Thus, abrupt changes between neighboring points of the pseudo section indicate outliers or erroneous measurements (see Flores Orozco et al. [23]). Such outliers and erroneous measurements need to be removed before the inversion, otherwise structures in the resulting images may be generated that are only related to noise in the data and not to subsurface properties (also referred to as inversion artifacts). The pseudo sections in Fig. 15.4 vary smoothly at all frequencies. A slightly increased variability in the values is observed at large pseudo depths, corresponding to readings with large separations between current and potential dipole, which are affected by a poor signal-to-noise (S/N) ratio.

The above analysis of the pseudo-section visualizations permits a qualitative identification of outliers and erroneous measurements, but strongly depends on the experience of the user. A more quantitative approach is based on the analysis of the difference between normal and reciprocal readings. Here, reciprocal readings refer to measurements of the same quadrupole but with interchanged current and voltage dipoles. Initially proposed for ERT measurements by LaBrecque et al. [49], this method is based on the principle of reciprocity, which states that (theoretically)

normal and reciprocal measurements should be identical. Thus, a statistical analysis of the normal-reciprocal misfit can be used to quantify random error in the data. The occurrence of large misfits between normal and reciprocal readings is also useful to identify outliers or systematic sources of error, which might e.g. be related to a poor galvanic contact of the electrodes with the ground. The applicability of the normal-reciprocal analysis to FDIP and TDIP data has been documented in various studies (e.g., Slater and Binley [70]; Flores Orozco et al. [24, 28]). However, the collection of reciprocals at all frequencies of a SIP survey would be challenging considering that measurements at frequencies <5 Hz are related to long acquisition times. Hence, we recommend to collect reciprocals down to at least at 1 Hz and use the analysis of normal-reciprocal misfits to establish thresholds values (for injected current, voltage, and ϕ_{app}) that permits filtering of the low-frequency data, in case that the collection of reciprocals is not possible due to time constraints. The collection of reciprocals at high frequencies is also recommended to discriminate between EM coupling and other sources of error.

In the present case, the analysis of the normal–reciprocal misfit was conducted at all frequencies individually resulting in relative and absolute errors of 5% and 1 Ω , respectively, for the impedance magnitude and a constant absolute error of 5 mrad for the impedance phase. Independent inversions of single-frequency data converged to a weighted root mean square error (RMSE) of 1.0 ± 0.05 , meaning that the obtained model explains the data within these error bounds.

Independently from the chosen approach, the use of a consistent (and ideally quantitative) methodology for the processing of the data is critical to warrant the comparability of inversion results for data collected at different frequencies (e.g., Flores Orozco et al. [24, 31]). Furthermore, poor processing might lead to the creation of inversion artifacts. Accordingly, an inadequate identification of erroneous measurements and outliers might have a large influence in the inverted imaging results; thus, leading to an inadequate site characterization and hindering a more detailed analysis of the frequency dependence.

Instead of carefully processing the raw data, the consistency between inversion results obtained at different frequencies can also be enforced during the inversion. The use of spatial and frequency regularization schemes (e.g., Günther and Martin [37]) permits to impose an expected spectral response, such as a Cole–Cole relaxation, during the simultaneous inversion of data collected at different frequencies. However, an adequate processing of the raw data has been demonstrated to minimize the impacts of cultural noise in IP monitoring results [26] as well as to provide better results than the use of (multiple) regularizations (e.g., Lesparre et al. [50]).

15.5 Interpretation of Field-Scale SIP Imaging Results

The inversion results of SIP data collected along one measurement line consist of 2D sections revealing both lateral and vertical changes in the electrical properties of the subsurface. If data was collected along several parallel lines or with electrodes

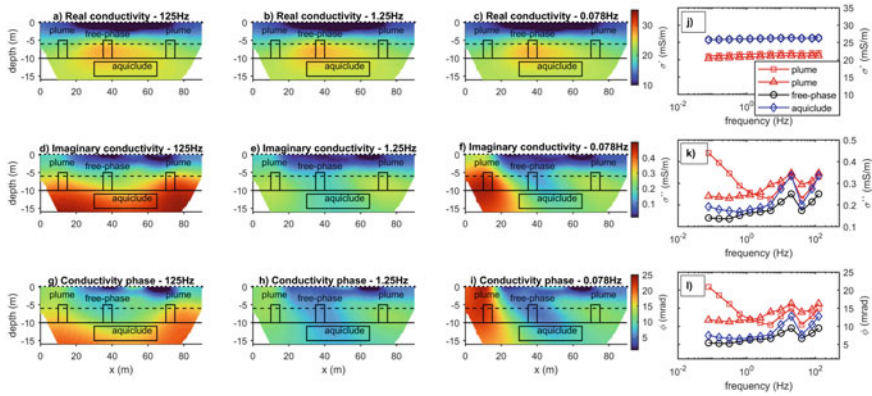


Fig. 15.5 SIP imaging results expressed in terms of the real (*a, b, c*) and imaginary (*d, e, f*) component of the complex conductivity (σ^*), as well as their ratio expressed by the phase ($\phi \approx \sigma''/\sigma'$) for data collected at two different frequencies (*g, h, i*). The spectral response of the electrical parameters (*j, k, l*) for selected areas, which are indicated by black boxes in the electrical images. The position of the electrodes along the surface (black circles), the groundwater level (dashed line), and the limit of the aquifer (solid line) are indicated, too

distributed over a grid, a 3D inversion can be carried out to obtain a 3D model of the subsurface. The results are usually expressed in terms of the complex resistivity (ρ^*) or its inverse, the electric conductivity (σ^*). In either case, the complex quantity can be visualized in terms of real and imaginary components, or as magnitude and phase. In Fig. 15.5, we present the imaging results of the data collected at the benzene-contaminated site in terms of real (σ') and imaginary (σ'') conductivity as well as conductivity phase (ϕ) at low (0.078 Hz) and high (125 Hz) frequencies, respectively. Because $\sigma' \gg \sigma''$ and thus $|\sigma^*| \approx \sigma'$, the magnitude image is practically equal to the real part image and not shown here for brevity.

The real part of electrical conductivity (σ') reveals two main units (Fig. 15.5a–c): (i) an uppermost layer with low conductivities (< 10 mS/m) associated with the unsaturated soils and (ii) a second, more conductive layer, which extends from 7.5 m downward and corresponds to the saturated sediments of the aquifer. A highly conductive anomaly (up to 25 mS/m) is located at the position of the benzene in free phase, i.e. the source zone, and corresponds with the expected signature of a mature plume undergoing degradation. The known lithological contact with the clay-rich formation at 11 m depth is not easily identified at both ends of the geoelectrical section, but may be inferred from the maximum depth of the conductive anomaly at its center. As expected from the flat frequency response of the σ_{app} raw data, no significant differences exist between low and high frequency σ' images. As discussed above, the high values in σ' are likely related to the accumulation of metabolic products, which increase the salinity and thus the electrolytic conductivity of the pore water.

The polarization properties of the subsurface are expressed in terms of both the imaginary conductivity σ'' (Fig. 15.5d–f) and the conductivity phase ϕ (Fig. 15.5g–i) to permit a direct comparison with laboratory results (e.g., Schmutz et al. [61]; Revil

et al. [65]). The σ'' and ϕ images clearly reveal contrasts between unsaturated and saturated materials as well as between the benzene in the dissolved plume and in free phase. The lowest polarization response is observed at the center of the section within the saturated zone, where high contaminant concentrations indicate the presence of free-phase benzene. At the same time, σ'' and ϕ values in the plume first increase with the distance to the source area and then slightly decrease towards both ends of the profile.

Similar observations, i.e., a slight increase of the polarization response with increasing contaminant concentration in the plume and a largely reduced polarization within the source area, have been reported earlier by Flores Orozco et al. [27] from a BTEX-contaminated site. Bucker et al. [10] attributed this behavior to the geometrical configuration of the contaminant within the pore space. In their model, the polarization response of non-wetting hydrocarbons increases with increasing concentration but strongly decreases as soon as the contaminant droplets of neighboring pores become continuous across the connecting pore throats.

Besides the clear response of free-phase benzene and the associated plume at intermediate depths, there are two more features of the polarization images (i.e., σ'' and ϕ), which are worth mentioning. Firstly, the uppermost layer (first 2 m) shows large heterogeneities with respect to both σ'' and ϕ , which are likely related to anthropogenic structures still in place after the removal of the backfill material. Secondly, the high-frequency images show a strong increase below 5–10 m depth, which most likely reflects the strong polarization response of the clayey formation confining the aquifer at depth, due to polarization of the Stern layer or membrane polarization mechanisms (e.g., Revil and Florsch [60]; Bucker et al. [26]).

As expected from the flat frequency response of the σ_{app} raw data, the spectral variation of σ' is weak within all three zones of interest (see Fig. 15.5j). At the same time, the spectral variation of σ'' and ϕ (see Fig. 15.5k and l) of free-phase benzene (source zone), plume and aquiclude are readily distinguished: Particularly the increase of both parameters at low frequencies (<1 Hz) seems to be characteristic for the plume of dissolved benzene, while the response is much lower and eventually flattens out in the source zone and aquiclude. It is worth mentioning that a similar behavior, i.e. an increase in the polarization with increasing benzene concentrations has also been observed in laboratory measurements on non-polar hydrocarbon compounds (e.g., Schmutz et al. [66, 65, 67]; Deceuster and Kaufman [20]; Shefer et al. [69]; Blondel et al. [9])

At intermediate frequencies (at 2 Hz) a phase peak appears in all four spectra (Fig. 15.5k and l), which we therefore interpret as the characteristic response of the background material. Most probably, this peak is related to the fine-grained fraction as it is most pronounced within the clayey aquiclude and weaker within the sandy to gravely aquifer. At higher frequencies, the response is increasingly affected by EM coupling, which makes the interpretation difficult.

A comparison of the apparent electrical conductivity in Fig. 15.4 with the inverted complex conductivity image in Fig. 15.5 reveals that the general trends regarding the frequency dependence of the electrical parameters are visible in both data and inverted model parameters. This is particularly important, as in the approach chosen here, the

inversions are carried out independently for each frequency and no regularization is used to enforce spectral consistency of the inverted models.

While the results presented here are based on a multi-frequency measurement, recent investigations propose to retrieve the spectral variation of $\sigma^*(\omega)$ from full-wave form TDIP data (e.g., Fiandaca et al. [22]). This approach also improves the investigation of contaminated sites compared to a pure ERT survey or the use of integral chargeability values [40, 53]. However, the TDIP data is fitted to a relaxation model, the selection of which strongly predetermines the possible frequency dependencies of $\sigma^*(\omega)$. As the present case study illustrates, properties such as chemical composition of groundwater (here, contaminant concentration and fluid conductivity), biogeochemical processes as well as the pore-space geometry have a large and likely site-specific influence on the electrical response. In particular, the complex interplay of these properties may result in spectral responses consisting of multiple relaxations, the recovery of which might be challenging for full-wave form inversion approaches. Therefore, we stress that the collection of SIP data in the frequency domain is the most direct way to evaluate the frequency dependence of the electrical properties of subsurface materials.

Flores Orozco et al. [25] demonstrated the use of coaxial cables to collect high quality SIP data in a site impacted by a jet fuel spill. The results in that study are consistent to those presented in Fig. 15.5. In their study, Flores Orozco et al. [25] also reveal variation in the frequency dependence of the complex conductivity in imaging data sets collected in clean sediments, the plume of dissolved contaminants and close to the source zone, where free-phase oil is trapped within the pore space. The interpretation of SIP results was confirmed through laser induced fluorescence (LIF) loggings. Clearly the analysis of the frequency-dependence in the polarization response provides an improved site characterization than those investigations conducted solely with DC-resistivity methods, or single-frequency IP.

15.6 Monitoring of Nanoparticles Injections for Groundwater Remediation

To illustrate the applicability of the IP method as a monitoring tool, e.g., to accompany the application of remediation measures, we present here imaging results obtained along the injection of micro-scale iron particles. The measurements were collected inside an industrial area, where groundwater is impacted by chlorinated aliphatic hydrocarbons (CAHs), especially TCE (chlorinated ethane) released during the production of solvent-based paints. TCE is polar hydrocarbon, which is denser than water (DNAPL). The injection of reactive nano- and micro-scale particles into the subsurface is a promising approach for the in-situ degradation of pollutants as it reduces remediation times and can be applied to areas not accessible by common remediation techniques (e.g., Grieger et al. [36] and references therein). A variety of techniques has been proposed for the remediation of CAH plumes, yet, it is beyond the

scope of this chapter to discuss these techniques and the accompanying changes in the electrical properties in detail. Nonetheless, the following case study demonstrates the sensitivity of the complex resistivity to different chemical processes as needed for an improved delineation of subsurface processes compared to the resistivity magnitude alone.

The study area can be described by three main units (from top to bottom): (1) a shallow aquifer comprised of gravel and sand with a thickness of ca. 4.5 m, (2) an aquiclude composed by clay-rich sediments (between 4.5 and 8 m depth), and (3) a deep aquifer composed of coarse sand and gravels. A schematic representation of the site is presented in Fig. 15.6a. The remediation targeted the deep aquifer, where guar-gum coated micro-scale zero-valent iron particles (GG-mZVI) [76] were injected between 10.5 and 8.5 m depth in 0.5 m steps, starting at the deepest position (see Fig. 15.6a). Each injection step had a duration of 15 min and aimed at delivering 20 kg mZVI at low pressures. During the injections it took another 15 min to relocate the pump and collect IP data.

IP measurements were collected during the relocation of the pump at a single frequency (1 Hz) using 24 stainless steel electrodes with a separation of 1 m. The profile was centered at the position of the injection well. For further details, we refer to Flores Orozco et al. [30]. Baseline imaging results obtained from data collected one day before the GG-mZVI injection reflect the known three-layered geology (Fig. 15.6a). A noticeable anomaly characterized by high σ^* values corresponds to

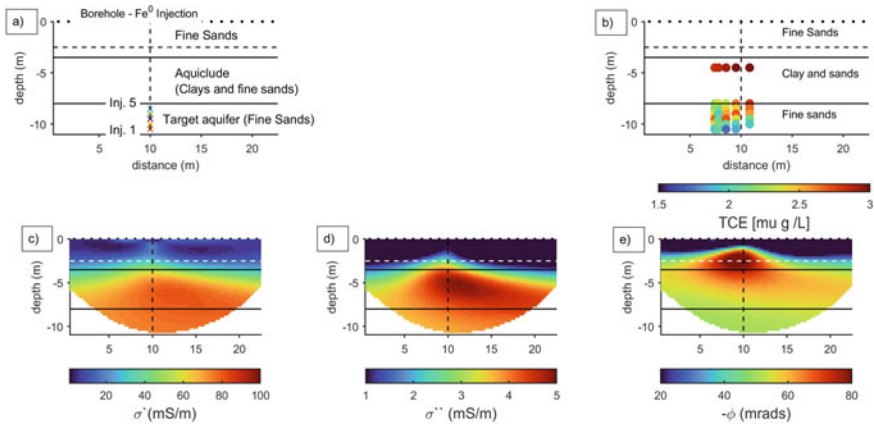


Fig. 15.6 Contaminant concentrations and imaging results for baseline measurements collected at a TCE-impacted site prior to the injection of guar-gum coated micro-scale zero-valent iron (GG-mZVI). **a** schematic representation of the lithological units at the site and the protocol used for the injection (Inj.) of the GG-mZVI, and **b** reported concentrations of TCE in groundwater samples collected before subsurface amendment. Complex conductivity imaging results expressed in terms of the real **c** and imaginary **d** components as well as the conductivity phase **e**. The horizontal solid lines indicate the position of the aquiclude, the dashed line indicates the depth of the groundwater table during the IP survey, and the black dots along the surface the electrode positions. Figure modified from [30]

the plume of dissolved TCE observed e.g., in Fig. 15.6b (concentrations in groundwater – 1 mg/L). The lack of information about TCE concentrations within the clay-sand aquitard is due to the practical limitations of direct site-investigation methods, for instance based on the extraction of groundwater samples, which cannot be carried out in low permeable formations. The increase in conductivity observed in Fig. 15.6c may again reflect the maturity of the organic contaminant. Besides, as a polar hydrocarbon, TCE might also result in highly charged surfaces of the hydrocarbon phase as modelled by Bückner et al. [10], explaining the increase in the polarization response. Similar responses have also been observed in TDIP investigations on other CAHs contaminated materials [15, 38, 40, 72].

The monitoring results presented in Fig. 15.7 reflect the absolute change between the baseline image and the images obtained after each injection step. Both conductivity magnitude and phase reveal an increase in the deep aquifer as the injection proceeds. This is the expected effect of the amendment of GG-mZVI, as the stabilizing solution is more conductive than the local groundwater and the coated iron particles are expected to cause a strong electrode-polarization response. Beside the changes in the deep aquifer, even larger changes (>50%) can be observed within the shallow sediments, a few meters above the injection points. These unexpected changes indicate the migration of particles along vertical flow paths. Such preferential flow paths are due to fractures created during the injection that resulted in an off-target delivery of the particles. Geochemical data obtained from the analysis of cores recovered after the injection confirmed the migration of particles and stabilizing solution to shallow areas through fractures. Additionally, properly delivered particles in the deep aquifer can be related to the positive changes in both IP images between 8 and 10 m depth. Likely due to the enzymatic consumption of the guar-gum coating upon the arrival in the targeted aquifer, the bare metallic particle develops a strong electrode polarization response. On the contrary, the particles delivered off-target in

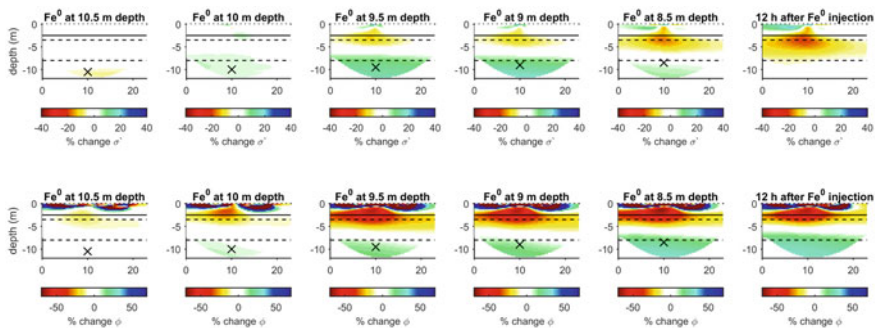


Fig. 15.7 Absolute temporal changes in the IP imaging results computed as the differences between baseline and time-lapse data after each particle injection. IP parameters are expressed in terms of conductivity magnitude (top) and phase (bottom). Spatial variations in the IP response are related to the accumulation of: bare particles in the deep aquifer close to the injection points (indicated by “x”) and coated GG-mZVI delivered off-target into the unsaturated zone. The dashed horizontal lines represent lithological contacts and the solid line the groundwater table

the unsaturated zone and shallow aquifer are still coated by the guar-gum; thus, the metallic surfaces are not in direct contact with the electrolyte, hindering the development of electrode polarization. A more detailed discussion can be found in Flores Orozco et al. [30]. Additionally, monitoring results obtained along the injection of nano-scale Goethite particles by Flores Orozco et al. [29] demonstrates the abilities of electrical monitoring to delineate clogging of the pore space following the injection of nano-Goethite particles, which in turn resulted in fracking and daylighting, i.e., particles flowing to the surface.

15.7 Summary and Conclusions

The two case studies illustrate that using the SIP method improves the characterization of contaminated sites compared to resistivity methods alone. While the conductivity magnitude (i.e., resistivity) is mainly sensitive to lithological changes and variations in the fluid conductivity, the polarization properties assessed by the SIP method are sensitive to the presence of immiscible fluids, such as hydrocarbon contaminants, to the resulting changes in the pore-space geometry, and the accumulation of metabolic products accompanying the natural transformation of organic contaminants. The polarization effect can be expressed in terms of both the imaginary component and the phase of the complex conductivity. Moreover, an analysis of the frequency dependence of these polarization properties can provide further information for the interpretation of the imaging results. In particular, we highlighted the possibility to measure comparable responses not only under well-controlled conditions in the laboratory but also in field-scale investigations. Even though the obtained results are promising, further field investigations are needed to fully understand the electrical response of contaminated subsurface materials. Despite the lack of a universal law linking contaminant concentration and electrical parameters, the SIP method can already be considered a practice-proven technique to delineate changes in the subsurface accompanying remediation techniques with a spatial and temporal resolution much higher than obtained with conventional sampling-based methods.

References

1. Aal GZA, Slater LD, Atekwana EA (2006) Induced-polarization measurements on unconsolidated sediments from a site of active hydrocarbon biodegradation. *Geophysics* 71(2):H13–H24
2. Abdel Aal GZ, Atekwana EA (2014) Spectral induced polarization (SIP) response of biodegraded oil in porous media. *Geophys J Int* 196(2):804–817
3. Abdel Aal GZ, Atekwana EA, Slater LD, Atekwana EA (2004) Effects of microbial processes on electrolytic and interfacial electrical properties of unconsolidated sediments. *Geophys Res Lett* 31(12)
4. Archie GE (1942) The electrical resistivity log as an aid in determining some reservoir characteristics. *Trans AIME* 146(01):54–62

5. Atekwana EA, Atekwana EA (2010) Geophysical signatures of microbial activity at hydrocarbon contaminated sites: a review. *Surv Geophys* 31:247–283
6. Benson AK, Payne KL, Stubben MA (1997) Mapping groundwater contamination using dc resistivity and VLF geophysical methods—a case study. *Geophysics* 62(1):80–86
7. Binley A, Slater L (2020) Resistivity and induced polarization: theory and applications to the near-surface earth. Cambridge University Press
8. Blanchy G, Saneiyani S, Boyd J, McLachlan P, Binley A (2020) ResIPy, an intuitive open source software for complex geoelectrical inversion/modeling. *Comput Geosci* 137:104423
9. Blondel A, Schmutz M, Franceschi M, Tichané F, Carles M (2014) Temporal evolution of the geoelectrical response on a hydrocarbon contaminated site. *J Appl Geophys* 103:161–171
10. Bucker M, Flores Orozco A, Hördt A, Kemna A (2017) An analytical membrane-polarization model to predict the complex conductivity signature of immiscible liquid hydrocarbon contaminants. *Near Surf Geophys* 15(6):547–562
11. Bucker M, Flores Orozco A, Kemna A (2018) Electrochemical polarization around metallic particles—Part 1: the role of diffuse-layer and volume-diffusion relaxation. *Geophysics* 83(4):E203–E217
12. Bucker M, Flores Orozco A, Undorf S, Kemna A (2019) On the role of stern-and diffuse-layer polarization mechanisms in porous media. *J Geophys Res: Solid Earth* 124(6):5656–5677
13. Bucker M, Hördt A (2013) Analytical modelling of membrane polarization with explicit parametrization of pore radii and the electrical double layer. *Geophys J Int* 194(2):804–813
14. Bucker M, Undorf S, Flores Orozco A, Kemna A (2019) Electrochemical polarization around metallic particles—Part 2: the role of diffuse surface charge. *Geophysics* 84(2):E57–E73
15. Cardarelli E, Di Filippo G (2009) Electrical resistivity and induced polarization tomography in identifying the plume of chlorinated hydrocarbons in sedimentary formation: a case study in Rho (Milan—Italy). *Waste Manage Res* 27(6):595–602
16. De Carlo L, Perri MT, Caputo MC, Deiana R, Vurro M, Cassiani G (2013) Characterization of a dismissed landfill via electrical resistivity tomography and mise-à-la-masse method. *J Appl Geophys* 98:1–10. <https://doi.org/10.1016/j.jappgeo.2013.07.010>
17. Cassiani G, Kemna A, Villa A, Zimmermann E (2009) Spectral induced polarization for the characterization of free-phase hydrocarbon contamination of sediments with low clay content. *Near Surf Geophys* 7(5–6):547–562
18. Dahlin T, Leroux V, Nissen J (2002) Measuring techniques in induced polarisation imaging. *J Appl Geophys* 50(3):279–298
19. Das N, Chandran P (2011) Microbial degradation of petroleum hydrocarbon contaminants: an overview. *Biotechnol Res Int*
20. Deceuster J, Kaufmann O (2012) Improving the delineation of hydrocarbon-impacted soils and water through induced polarization (IP) tomographies: a field study at an industrial waste land. *J Contam Hydrol* 136:25–42
21. Doetsch J, Ingeman-Nielsen T, Christiansen AV, Fiandaca G, Auken E, Elberling B (2015) Direct current (DC) resistivity and induced polarization (IP) monitoring of active layer dynamics at high temporal resolution. *Cold Reg Sci Technol* 119:16–28
22. Fiandaca G, Auken E, Christiansen AV, Gazoty A (2012) Full waveform modelling of time domain induced polarization. *Geophysics* 71:G43–G51
23. Flores Orozco A, Aigner L, Gallistl J (2021) Investigation of cable effects in spectral induced polarization imaging at the field scale using multicore and coaxial cables. *Geophysics* 86(1):E59–E75
24. Flores Orozco A, Bucker M, Steiner M, Malet JP (2018) Complex-conductivity imaging for the understanding of landslide architecture. *Eng Geol* 243:241–252
25. Flores Orozco A, Ciampi P, Katona T, Censini M, Papini MP, Deidda GP, Cassiani G (2021) Delineation of hydrocarbon contaminants with multi-frequency complex conductivity imaging. *Sci Total Environ* 768:144997
26. Flores Orozco A, Kemna A, Binley A, Cassiani G (2019) Analysis of time-lapse data error in complex conductivity imaging to alleviate anthropogenic noise for site characterization. *Geophysics* 84(2):B181–B193

27. Flores Orozco A, Kemna A, Oberdörster C, Zschornack L, Leven C, Dietrich P, Weiss H (2012) Delineation of subsurface hydrocarbon contamination at a former hydrogenation plant using spectral induced polarization imaging. *J Contam Hydrol* 136:131–144
28. Flores Orozco A, Kemna A, Zimmermann E (2012) Data error quantification in spectral induced polarization imaging. *Geophysics* 77(3):E227–E237
29. Flores Orozco A, Micić V, Bucker M, Gallistl J, Hofmann T, Nguyen F (2019) Complex-conductivity monitoring to delineate aquifer pore clogging during nanoparticles injection. *Geophys J Int* 218(3):1838–1852
30. Flores Orozco A, Velimirovic M, Tosco T, Kemna A, Sapion H, Klaas N, Sethi R, Bastiaens L (2015) Monitoring the injection of microscale zerovalent iron particles for groundwater remediation by means of complex electrical conductivity imaging. *Environ Sci Technol* 49(9):5593–5600
31. Flores Orozco A, Williams KH, Kemna A (2013) Time-lapse spectral induced polarization imaging of stimulated uranium bioremediation. *Near Surf Geophys* 11(5):531–544
32. Flores Orozco A, Williams KH, Long PE, Hubbard SS, Kemna A (2011) Using complex resistivity imaging to infer biogeochemical processes associated with bioremediation of an uranium-contaminated aquifer. *J Geophys Res Biogeosci* 116(G3)
33. Fritsche W, Hofrichter M (2000) Aerobic degradation by microorganisms. In: Klein J (ed) *Environmental processes—soil decontamination*. Wiley-VCH, Weinheim, Germany, pp 146–155
34. Ghattas AK, Fischer F, Wick A, Ternes TA (2017) Anaerobic biodegradation of (emerging) organic contaminants in the aquatic environment. *Water Res* 116:268–295
35. Glover PWJ (2015) 11.04—geophysical properties of the near surface earth: electrical properties. *Treatise Geophys* 89–137
36. Grieger KD, Fjordbøge A, Hartmann NB, Eriksson E, Bjerg PL, Baun A (2010) Environmental benefits and risks of zero-valent iron nanoparticles (nZVI) for in situ remediation: risk mitigation or trade-off? *J Contam Hydrol* 118(3–4):165–183
37. Günther T, Martin T (2016) Spectral two-dimensional inversion of frequency-domain induced polarization data from a mining slag heap. *J Appl Geophys* 135:436–448
38. Hort RD, Revil A, Munakata-Marr J, Mao D (2015) Evaluating the potential for quantitative monitoring of in situ chemical oxidation of aqueous-phase TCE using in-phase and quadrature electrical conductivity. *Water Resour Res* 51(7):5239–5259
39. Hördt A, Bairlein K, Bielefeld A, Bucker M, Kuhn E, Nordsiek S, Stebner H (2016) The dependence of induced polarization on fluid salinity and pH, studied with an extended model of membrane polarization. *J Appl Geophys* 135:408–417
40. Johansson S, Fiandaca G, Dahlin T (2015) Influence of non-aqueous phase liquid configuration on induced polarization parameters: conceptual models applied to a time-domain field case study. *J Appl Geophys* 123:295–309
41. Johnson TC, Thomle J (2018) 3-D decoupled inversion of complex conductivity data in the real number domain. *Geophys J Int* 212(1):284–296
42. Karaoulis M, Revil A, Tsourlos P, Werkema DD, Minsley BJ (2013) IP4DI: a software for time-lapse 2D/3D DC-resistivity and induced polarization tomography. *Comput Geosci* 54:164–170
43. Kaufmann O, Deceuster J (2007) A 3D resistivity tomography study of a LNAPL plume near a gas station at Brugelette (Belgium). *J Environ Eng Geophys* 12(2):207–219
44. Kemna A (2000) Tomographic inversion of complex resistivity—theory and application. Ruhr-University of Bochum, Ph.D.
45. Kemna A, Binley A, Cassiani G, Niederleithinger E, Revil A, Slater L, Williams KH, Flores Orozco A, Haegel FH, Hördt A, Kruschwitz S (2012) An overview of the spectral induced polarization method for near-surface applications. *Near Surf Geophys* 10(6):453–468
46. Kim B, Nam MJ, Kim HJ (2018) Inversion of time-domain induced polarization data based on time-lapse concept. *J Appl Geophys* 152:26–37
47. Klonowski MR, Breedveld GD, Aagaard P (2008) Spatial and temporal changes of jet fuel contamination in an unconfined sandy aquifer. *Water Air Soil Pollut* 188(1–4):9–30

48. LaBrecque D, Daily W (2008) Assessment of measurement errors for galvanic-resistivity electrodes of different composition. *Geophysics* 73(2):F55–F64
49. LaBrecque DJ, Miletto M, Daily W, Ramirez A, Owen E (1996) The effects of noise on Occam's inversion of resistivity tomography data. *Geophysics* 61(2):538–548
50. Lesparre N, Robert T, Nguyen F, Boyle A, Hermans T (2019) 4D electrical resistivity tomography (ERT) for aquifer thermal energy storage monitoring. *Geothermics* 77:368–382
51. Löser C, Seidel H, Zehnsdorf A, Stottmeister U (1998) Microbial degradation of hydrocarbons in soil during aerobic/anaerobic changes and under purely aerobic conditions. *Appl Microbiol Biotechnol* 49(5):631–636
52. Martin T, Günther T, Flores Orozco A, Dahlin T (2020) Evaluation of spectral induced polarization field measurements in time and frequency domain. *J Appl Geophys* 180:104141
53. Maurya PK, Fiandaca G, Christiansen AV, Auken E (2018) Field-scale comparison of frequency-and time-domain spectral induced polarization. *Geophys J Int* 214(2):1441–1466
54. Mewafy FM, Werkema DD Jr, Atekwana EA, Slater LD, Aal GA, Revil A, Ntarlagiannis D (2013) Evidence that bio-metallic mineral precipitation enhances the complex conductivity response at a hydrocarbon contaminated site. *J Appl Geophys* 98:113–123
55. Nguyen F, Ghose R, Isunza Manrique I, Robert T, Dumont G (2018) Managing past landfills for future site development: a review of the contribution of geophysical methods. In: *Proceedings of the 4th international symposium on enhanced landfill mining*, pp 27–36
56. Olhoeft GR (1985) Low-frequency electrical properties. *Geophysics* 50(12):2492–2503
57. Pelton WH, Ward SH, Hallof PG, Sill WR, Nelson PH (1978) Mineral discrimination and removal of inductive coupling with multifrequency IP. *Geophysics* 43(3):588–609
58. Placencia-Gómez E, Parviainen A, Hokkanen T, Loukola-Ruskeeniemi K (2010) Integrated geophysical and geochemical study on AMD generation at the Haveri Au–Cu mine tailings, SW Finland. *Environ Earth Sci* 61(7):1435–1447
59. Revil A, Coperey A, Mao D, Abdulsamad F, Ghorbani A, Rossi M, Gasquet D (2018) Induced polarization response of porous media with metallic particles—Part 8: influence of temperature and salinity. *Geophysics* 83(6):E435–E456
60. Revil A, Florsch N (2010) Determination of permeability from spectral induced polarization in granular media. *Geophys J Int* 181(3):1480–1498
61. Revil A, Schmutz M, Batzle ML (2011) Influence of oil wettability upon spectral induced polarization of oil-bearing sands. *Geophysics* 76(5):A31–A36
62. Revil A, Skold M (2011) Salinity dependence of spectral induced polarization in sands and sandstones. *Geophys J Int* 187(2):813–824
63. Rücker C, Günther T, Wagner FM (2017) pyGIMLi: an open-source library for modelling and inversion in geophysics. *Comput Geosci* 109:106–123
64. Sauck WA (2000) A model for the resistivity structure of LNAPL plumes and their environs in sandy sediments. *J Appl Geophys* 44(2–3):151–165
65. Schmutz M, Revil A, Vaudelet P, Batzle M, Viñao PF, Werkema DD (2010) Influence of oil saturation upon spectral induced polarization of oil-bearing sands. *Geophys J Int* 183(1):211–224
66. Schmutz M, Blondel A, Revil A (2012) Saturation dependence of the quadrature conductivity of oil-bearing sands. *Geophys Res Lett* 39(3)
67. Schwartz N, Huisman JA, Furman A (2012) The effect of NAPL on the electrical properties of unsaturated porous media. *Geophys J Int* 188(3):1007–1011
68. Schwartz N, Furman A (2012) Spectral induced polarization signature of soil contaminated by organic pollutant: experiment and modeling. *J Geophys Res Solid Earth* 117(B10)
69. Shefer I, Schwartz N, Furman A (2013) The effect of free-phase NAPL on the spectral induced polarization signature of variably saturated soil. *Water Resour Res* 49(10):6229–6237
70. Slater L, Binley A (2006) Synthetic and field-based electrical imaging of a zerovalent iron barrier: implications for monitoring long-term barrier performance. *Geophysics* 71(5):B129–B137
71. Soupios P, Ntarlagiannis D (2017) Characterization and monitoring of solid waste disposal sites using geophysical methods: current applications and novel trends. In: *Modelling trends*

- in solid and hazardous waste management. Springer, Singapore, pp 75–103. https://doi.org/10.1007/978-981-10-2410-8_5
72. Sparrenbom CJ, Åkesson S, Johansson S, Hagerberg D, Dahlin T (2017) Investigation of chlorinated solvent pollution with resistivity and induced polarization. *Sci Total Environ* 575:767–778
 73. Sumner JS (1976) Principles of induced polarization for geophysical prospecting. Elsevier, Amsterdam
 74. Tsourlos P, Vargemezis GN, Fikos I, Tsokas GN (2014) DC geoelectrical methods applied to landfill investigation: case studies from Greece. *First Break* 32(8):81–89
 75. Ustra A, Slater L, Ntarlagiannis D, Elis V (2012) Spectral induced polarization (SIP) signatures of clayey soils containing toluene. *Near Surf Geophys* 10(6):503–515
 76. Velimirovic M, Tosco T, Uyttebroek M, Luna M, Gastone F, De Boer C, Klaas N, Sapion H, Eisenmann H, Larsson PO, Braun J (2014) Field assessment of guar gum stabilized microscale zerovalent iron particles for in-situ remediation of 1, 1, 1-trichloroethane. *Journal Contam Hydrol* 164:88–99
 77. Wang TP, Chen CC, Tong LT, Chang PY, Chen YC, Dong TH, Liu HC, Lin CP, Yang KH, Ho CJ, Cheng SN (2015) Applying FDEM, ERT and GPR at a site with soil contamination: a case study. *J Appl Geophys* 121:21–30
 78. Weller A, Zhang Z, Slater L (2015) High-salinity polarization of sandstones. *Geophysics* 80(3):D309–D318
 79. Yang C, Liu S, Feng Y, Yang H (2018) Influence of electrode polarization on the potential of DC electrical exploration. *J Appl Geophys* 149:63–76

Chapter 16

Direct Current Electrical Methods for Hydrogeological Purposes



Enzo Rizzo and Valeria Giampaolo

Abstract The climate change has dramatically decreased the useful freshwater resources so raising the probability of severe droughts. Near-surface geophysics uses the investigational methods of geophysics leading to their massive use in all scientific sectors (geology, hydrogeology, engineering, archaeology, environmental problems). Moreover, the increasing challenge of quantifying extractable, economically viable, potable water supplies has led to the definition of a new subdiscipline of hydrology known as hydrogeophysics. Direct current (DC) electrical methods are probably the most widely used near surface geophysical techniques for environmental investigations. DC methods are increasingly used in different approaches to cover a larger field of applications. In hydrogeological applications, the electrical resistivity distribution can provide important information that allows to characterize the heterogeneity of the aquifers and soil, to reconstruct the geometry of the aquifers and/or waterproof, to study the relationships between freshwater and seawater, or from groundwater different salinity.

Keywords DC · Electrical resistivity · Conductivity · Hydrogeological

16.1 Introduction

In the last decades rapid increase in population and climate change related phenomena have dramatically increased the exploitation of freshwater resources so raising the probability of severe droughts. Nowadays, the need for clean groundwater resources is driving improvements of methods able to provide quantitative information on groundwater quantity and quality.

Near-surface geophysics is largely exploited to study the subsoil and all the phenomena connected with it, such as the hydrogeological aspects. In the last years,

E. Rizzo (✉)

Dipartimento di Fisica e Scienze della Terra, University of Ferrara, Ferrara, Italy
e-mail: enzo.rizzo@unife.it

E. Rizzo · V. Giampaolo

National Research Council (CNR-IMAA), Marsico Nuovo, Italy

near-surface geophysical techniques have had significant technological advances, by eliminating the gap between data quality/quantity and resolution and leading to their massive use in all scientific sectors (geology, hydrogeology, engineering, archaeology, environmental problems).

Groundwater geophysics is a common topic in the last 30 years and it is connected to the use of near-surface geophysical techniques to support groundwater investigation. The ever-increasing need for groundwater detection and characterization has translated into using subsurface imaging to meet the demand. Many of the earlier approaches were concentrated on using geophysics to define lithological boundaries and other subsurface structures. These interpretations were mainly qualitative, but many attempts are now made to gain quantitative information about the subsurface.

The increasing challenge of quantifying extractable groundwater resources is a major factor driving this growth and has led to the definition of a new subdiscipline of hydrology known as hydrogeophysics [14, 73].

Direct current (DC) electrical methods are probably the most widely near-surface geophysical techniques used for environmental investigations. This is due to different factors: (1) subsurface electrical properties are often well correlated to physical and chemical properties of fluids within the pore space (e.g., saturation and salinity) and lithologic properties (e.g., porosity and clay content) [40]; (2) the theoretical concepts are relatively straightforward; (3) field measurement techniques are highly scalable, allowing investigations to depths from tens of centimeters to hundreds of meters; (4) instrumentation is relatively low cost and straightforward to operate; and (5) data analysis techniques have matured—robust data inversion tools, for example, are widely available [11].

DC resistivity methods have been developed in the early 1900s, however, only in the late 1970s, the arising of new modelling tools [32, 33, 55] led to the development of modern electrical resistivity tomography (ERT).

Nowadays, ERTs have been used to study 3D and even 4D systems. Moreover, time-lapse methods have been increasingly employed as a means of studying dynamic processes (e.g., tracer tests, groundwater clean-up, saline intrusion in the coastal zone, etc.).

In the 1980s, multi-electrode measurement systems were introduced, further, by the mid-to the late 1990s, the use of multi-measurement channel hardware have allowed to reduced survey time.

Nowadays, DC methods are increasingly used in different approaches to cover a larger field of applications: from samples measurements in the lab (e.g., [18, 85]), to measurements in one or between several boreholes (e.g., [27]), across water bodies [36], and 3D or 4D monitoring with time-lapse imaging or with permanent surveys (e.g., [58, 91]).

DC methods enable the estimation of the spatial distribution of the electrical resistivity of the subsurface as a weighted average of the electrical properties of its mineral grains, liquid, and air. In hydrogeological applications, the electrical resistivity distribution can provide important information for characterizing the heterogeneity of the aquifers and soil, to reconstruct the geometry of the aquifers and/or waterproof,

Table 16.1 Effect of physicochemical properties of subsoil on the measured electrical resistivity parameter

Factors	Effect on electrical resistivity
Water saturation increase	Decrease
Electrolyte salinity increase	Decrease
Porosity increase (water-filled voids)	Decrease
Fractures number increase (water-filled)	Decrease
Electrolyte temperature increase	Decrease
Porosity (air, gas, and oil-filled voids)	Increase
Fractures number increase (air, gas, and oil-filled)	Increase

to study the relationships between freshwater and seawater, or from groundwater different salinity.

As summed in Table 16.1, electrical resistivity is sensitive to porosity, hydraulic conductivity, fluid content, and salinity [13, 15, 25, 27, 48, 81]. Because these physicochemical properties can be modified by the presence of contaminants and biodegradation activity, electrical resistivity variations can provide information about the contamination state of subsoil [3].

16.2 Definition and Hydrogeological Context

Direct current (DC) electrical methods are probably the oldest and most used techniques for non-invasive geophysical investigations. These methods are essentially based on the measurement of an electric field, artificially created in the ground, by means of suitable electrodes devices aimed to determine the subsoil spatial electrical resistivity distribution (ρ , Ωm) or its reciprocal, electrical conductivity (σ , Sm^{-1}).

The physical basis of the method is Ohm's Law, which states that that in an electrical circuit, the current I (A) passing through a conductor between two points is directly proportional to the difference in electric potential V (V) and inversely proportional to the resistance of the material R (Ω) between the two points:

$$V = IR. \quad (16.1)$$

The resistance R depends on the path length l (m) of the current flow, the cross-sectional area A (m^2) that the current flows through and the resistivity ρ (Ωm) of the material:

$$R = \rho \frac{l}{A}. \quad (16.2)$$

The resistivity describes only the intrinsic resistive properties of the material to the flow of charge carriers and is not affected by the geometry of the sample. It corresponds to the resistance of a sample 1 m long with a constant cross-sectional area for current flow that is 1 m².

In heterogeneous grounds, current flows toward regions with high conductivity however, at room temperature, the subsoil behaves as insulator, while, electric charge is nearly always carried by ions, dissolved in water, which can be found almost everywhere in the ground. The higher the water content inside interconnected pores of the rock, the higher the ion content of the water and the more conducting the rock.

In the 1942, Gustavus E. Archie published the first study concerning the integration of the electrical resistivity and hydrogeological characteristics of the subsoil. According to Archie's law [1], there is a quantitative relationship between the electrical resistivity of the bulk formation (ρ_b), the electrical resistivity of pore water (ρ_w), the effective porosity (ϕ), and the degree of saturation (S_w):

$$\rho_b = \rho_w \phi^{-m} S_w^{-n} \quad (16.3)$$

where m and n are material constants and empirically derived [66, 79]. Archie establishes that the exponent m (cementation index) ranged from 1.3 for unconsolidated sands to approximately 2.0 for consolidated sandstones. The saturation index n is usually larger than the cementation index, because as saturation decreases, the water films surrounding the grains become thinner and the conducting paths become more tortuous. The term ϕ^{-m} is called formation factor (F). It represents an intrinsic measure of material microgeometry, and it is often assumed to be an indicator of the hydraulic tortuosity.

Archie's formula is considered valid for medium- to coarse-grained sediments, where the grain surface conductivity (reciprocal of resistivity) can be considered negligible. Equation 16.3 is frequently used to estimate hydrocarbon saturation in 'clean' sandstones and other relatively permeable reservoir rocks in the oil industry.

On the contrary, the contribution of grain surface conductivity becomes important when small grain sizes dominate the lithology and/or when clay minerals are present. In this case, it is necessary to modify Archie's law to include the electrical resistivity contribution due to grain surface (ρ_s) [92]:

$$\rho_b = a \rho_w \phi^{-m} S_w^{-n} + \rho_s. \quad (16.4)$$

Starting from this relationship, the DC electrical resistivity methods have received a great attention on the possibility to define the correlations with the hydraulic properties, such as the water content (θ), hydraulic conductivity (K), and transmissivity (T). In general, hydraulic conductivity was estimated by using empirical relationship site specific or Kozeny's equation [49] in combination with Archie's law.

The validity of Archie's equation was verified in many papers [1, 2, 39, 50]. However, in the case of carbonate rocks characterized by primary, secondary (fractures and faults), and conduit porosity, the validity of Archie's law has been questioned [96]. Moreover, the used ρ - K relationships were unable to fully capture the substantial heterogeneity present in the carbonate aquifers where hydraulic conductivity depends on fracture intensity, offset and spacing, fracture network connectivity, and aperture distributions [47, 72].

16.3 Measurement Setting

The basic principle of DC electrical method is to inject a current (I , A) into the subsoil by using two current electrodes A (or C1) and B (or C2) and after to measure the potential difference ΔV (mV) through two other electrodes M (or P1) and N (or P2) on the ground surface. In this way it is possible to measure the subsoil electrical resistivity by:

$$\Delta V_{MN} = I_{AB} R \quad (16.5)$$

where, ΔV_{MN} (Volt) is the measured voltage between electrodes M and N, I_{AB} (A) is the injected current between electrodes A and B, and R (Ω) is the resistance of the material through which the current flows.

As the potential between M and N, the current introduced through A and B, and the electrode configuration are known, the resistivity of the ground can be determined; this is referred to as the "apparent resistivity" (Ωm):

$$\rho_a = K_g \frac{V_{MN}}{I_{AB}}. \quad (16.6)$$

For a homogenous, flat earth, the apparent resistivity represents the true resistivity of the subsurface, while, for inhomogeneous and anisotropic media, ρ_a is defined as the ratio between the measured value of the parameter in question and its theoretical value in a homogeneous and isotropic medium of unit resistivity [52].

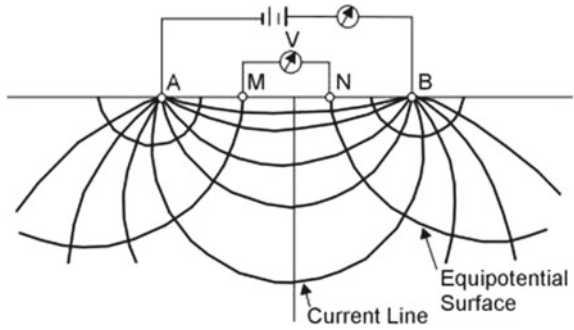
Therefore, in real cases, inverse methods must be applied to turn from the apparent resistivity to the true spatial distribution of the resistivity.

K_g (m) is called geometric factor; it depends on electrodes geometry (array) and can be calculated from the different electrode spacing (Fig. 16.1) by

$$K_g = 2\pi \left[\left(\frac{1}{AM} - \frac{1}{BM} - \frac{1}{AN} + \frac{1}{BN} \right) \right]^{-1}. \quad (16.7)$$

There are different electrode configurations (Szalai and Szarka 2008): they have advantages and disadvantages, therefore the choice is based upon the sensitivity of the

Fig. 16.1 The injection electrodes (AB) and the potential ones (MN) and the equipotential line distribution



device, the vertical and horizontal variations in resistivity, the depth of investigation, the data horizontal coverage, and the signal strength (Fig. 16.2; Table 16.2).

Due to the fact that the electrical resistivity method is sensitive to both electrolyte and solid-fluid interface chemistry, its application has recently increased for geoenvironmental investigations, including the hydrogeological purposes. Earlier explorations made use of 1D (VES) method [7, 46], nowadays the VES method has been replaced by Electrical Resistivity Tomography (ERT) with 2D and 3D data interpretations [4, 54, 77].

In general, DC resistivity surveys can be performed in a wide range of configurations (Table 16.3), whose choice will depend mainly upon the objectives of the survey and site access and instruments constraints [11].

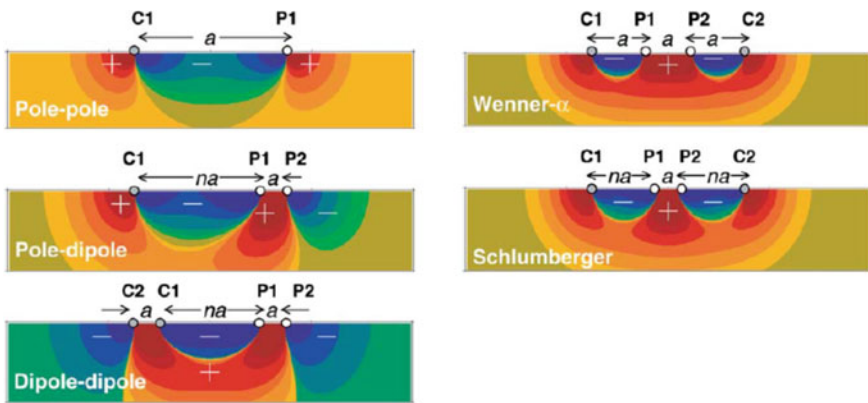


Fig. 16.2 Most common electrode arrays and their sensitivity patterns for 2D resistivity surveys. C1 and C2: current electrodes, P1 and P2: potential electrodes. In Pole-Pole, C2 and P2 must be placed at a distance that is more than 20 times the C1-P1 maximum separation. In Pole-Dipole, C2 must be placed at a distance that is more than 5 times C1-P1 maximum separation. Letters a and n control the electrodes spacing and dipoles maximum separation, respectively. Modified from Dahlin and Zhou [28]

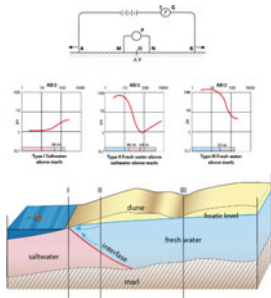
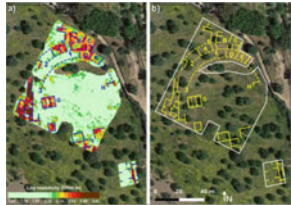
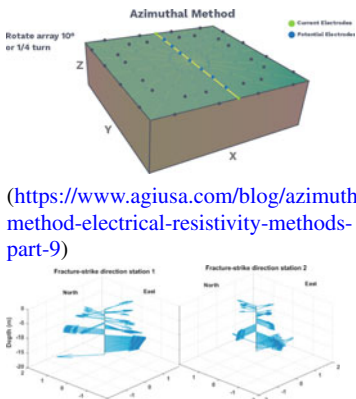
Table 16.2 Comparison of the most common electrode arrays for 2D surface-based surveys

Array	Geometric factor	Vertical and horizontal variations	Depth of investigation	Horizontal coverage	Signal strength
Pole-Pole	$K_g = 2\pi a$	Poorly sensitive to both horizontal and vertical structures	0.867a	++++	+
Pole-Dipole	$K_g = 4\pi a$	More sensitive to horizontal changes (i.e. vertical structures)	0.519a (n = 1) 3.247 (n = 8)	++	++
Dipole-Dipole	$K_g = \pi n(n + 1)(n + 2)a$	Very sensitive to horizontal changes (i.e., narrow vertical structures)	0.416a (n = 1) 2.236 (n = 8)	+++	++
Wenner α	$K_g = 2\pi a$	Good in resolving vertical changes (i.e., horizontal structures)	0.519a	+	++++
Schlumberger	$K_g = \pi n(n + 1)a$	Moderately sensitive to horizontal (at low "n" values) and vertical structures (at high "n" values)	0.519a (n = 1) 3.247 (n = 8)	++	+++
Multigradient	$K_g = f(XA, XB, XM, XN)$	A non-conventional array with a good sensitive to vertical and horizontal changes. It is a mix between Schlumberger and Dipole-Dipole	0.529a (n = 1) 3.8 (n = 9)	+++	++

16.3.1 Unconventional DC Field Configuration

Nowadays, the availability of generalized modelling tools permits full flexibility in electrode configuration, not just using surface-based electrodes. The main need is providing higher informative data at depth.

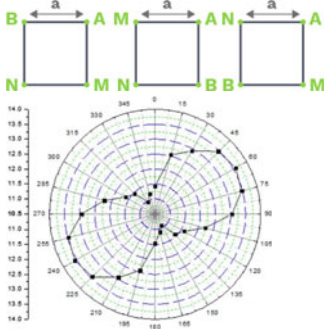
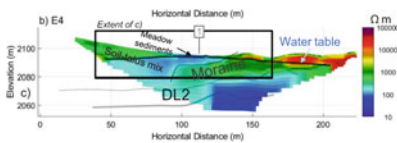
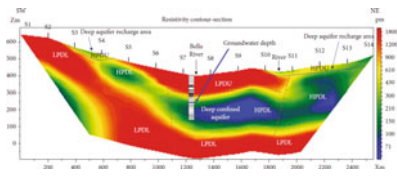
Table 16.3 Conventional ground surface geoelectrical configuration

Configuration	Description	Use	Image
VES	Determination of 1-D resistivity variation along a vertical profile (no lateral variations)	Water table	 <p>(https://geofisicaargentina.com/vertical-electrical-sounding.html)</p>
Map	Determination of 2-D resistivity lateral variations at a predetermined depth of investigation	Archaeology	 <p>[24]</p>
Azimuth	Four-electrode measurements (typically Wenner or Schlumberger) made at different orientations, centered on a single point	Jointed and faulted systems	 <p>(https://www.agiusa.com/blog/azimuthal-method-electrical-resistivity-methods-part-9)</p> <p>[60]</p>

(continued)

In the **Mise-à-la-masse** method a current electrode (A) is placed in a borehole at depth, while the other current electrode (B) is placed at a great distance (ideally, infinite). The potential distribution is measured by receiving dipoles (M and N) positioned at different points on the soil surface. Usually, the Pole–Pole configuration is preferred; this explains its early popularity. However, the interpretation of results can

Table 16.3 (continued)

Configuration	Description	Use	Image
Square array	Four electrodes (two potential and two current injection) define a square which is turned 15 degrees around its center point for each measurement	Preferential flow paths in fractures	 <p>(Hydrogeosite Laboratory data, CNR-IMAA)</p>
TOMO 2D/3D	Determination of lateral and vertical resistivity variations	Groundwater characterization and monitoring	 <p>[21]</p>
DERT	It is generally used to increase resolution for deeper target (investigation depth > 200 m)	Deep groundwater resources	 <p>[69]</p>

be challenging without suitable modeling tools and when sensitivity to geoelectrical contrasts is limited. Examples of *mise-a-la-masse* application areas include mineral exploration (e.g., [9, 56]), geothermal application (e.g., [6]), and hydrogeological applications [8, 58, 63].

Borehole electrical resistivity tomography (Fig. 16.3b–e) consists of apparent resistivity measurements using plate or cylindrical electrodes in one, two or more boreholes, placed in contact with the host soils/rocks or with the formation fluid. First applications were described by Shima [78] and Zhou and Greenhalgh [].

Geological setting of the study area and logistical aspects, such as ensure the electrical contact between electrodes and the surrounding media, influence the ways of installing electrodes into the subsurface. In dry holes, for example, mud, sand, or concrete grout may be used to backfill the boreholes and completely cover the electrodes; if groundwater is close to the surface, a watertight electrical cable can be simply lowered into the measurement boreholes verifying that the electrodes lies entirely below the water table [62].

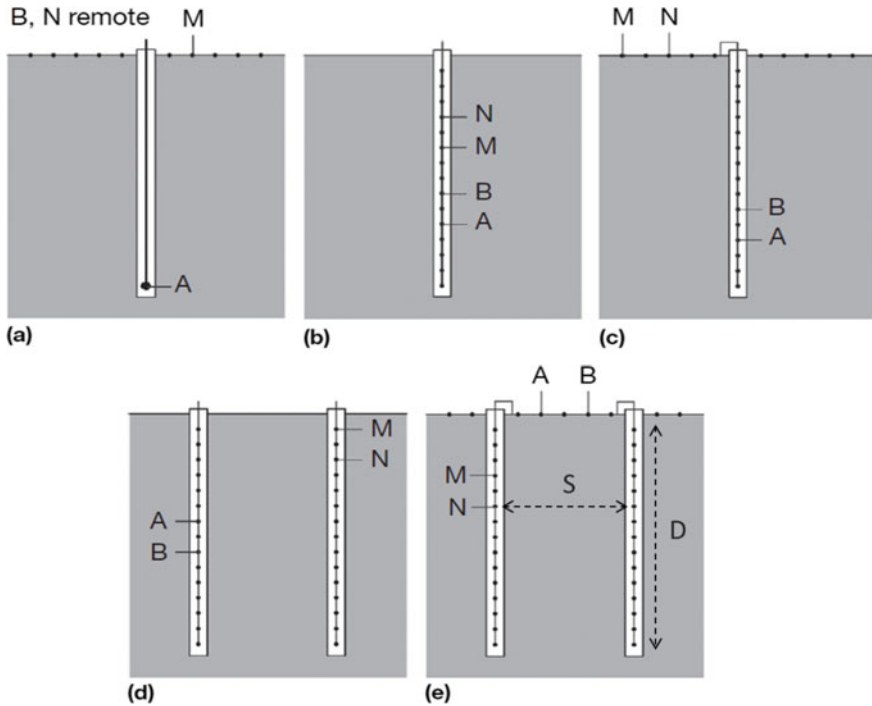


Fig. 16.3 Schematic of possible uses of boreholes for electrical imaging. **a** The mise-a-la-masse, **b** single borehole, **c** borehole-to-surface, **d** cross borehole, and **e** cross borehole with surface. A, B, M, and N are electrodes, D is borehole depth, S is borehole separation. $D/S > 1.5$. Modified from Binley [11]

Single-borehole electrode arrays (Fig. 16.3b) are generally rarer [57, 87]. In order to improve the sensitivity pattern, surface electrode arrays can be used. Borehole-to-surface surveys (Fig. 16.3c) could be advantageous when used with varying surface azimuthal arrays to assess anisotropy, for example, in fractured environments.

A cross-borehole electrical resistivity tomography (Fig. 16.3d) allows to identify lateral and vertical resistivity variations in the area between two or more boreholes.

Cross-hole ERT is characterized by higher resolution at depth compared to the one associated to the surface surveying [15]. However, the costs of the survey are larger if new boreholes are required and the ratio between boreholes depth and separation should be >1.5 otherwise sensitivity is reduced (Fig. 16.3e).

Moreover, uncertainties in the electrodes positions and the contrast existing between the resistivity of the soil/rock formation and that of the boreholes backfill material or fluid must be carefully considered in order to avoid images strongly contaminated by artefacts [62, 93]. Finally, the electrode shape itself becomes important if the electrode spacings are of comparable magnitude, i.e., $\text{length}/\text{spacing} > 0.2$ [74].

Nowadays, the cross-hole ERT has become very common in environmental investigations for the study of the vadose zone, to quantify the hydraulic conductivity spatial distribution, and to obtain information on the spatial variability of solute transport processes [13, 19, 26, 27, 41, 45, 65, 80, 81, 94]. Moreover, cross-hole measurement techniques allow to more readily detect anisotropy compared to surface measurements.

A less common cross-borehole approach is the use electrodes installed along horizontal boreholes, or along mine/tunnel for surface to tunnel and tunnel to tunnel imaging [29, 51, 76, 89].

Recently, Rizzo et al. [70] and Guerriero et al. [42] demonstrated the usefulness of 3D surface to tunnel ERT methodology with electrodes located on surface and along underground natural tunnel (karts cave), to increase electrical resistivity imaging resolution between the underground structure and the topographic surface (see Sect. 5.2). This method is potentially well-suited for imaging fracture zones and therefore it can be used for monitoring groundwater flow and geochemistry directly inside karst aquifers.

16.4 Modelling and Inversion

Data from 2-D imaging surveys are normally presented as a pseudo-section of apparent resistivity (Fig. 16.4). Measurements with larger electrode separations sample deeper portions of the earth, lines at 45° angles are drawn from the mid-points of the current and potential electrode pairs and the datum is plotted at the intersection of these lines. In case of pole transmitter or receiver, the 45° lines are drawn directly from the electrode location. The pseudo-section does not provide an accurate image of the subsurface distribution of resistivity, it just allows to visualize plotted measured data.

The translation of geoelectrical measurements to geoelectrical properties requires the use of inversion tools. The data processing software handles importing,

Fig. 16.4 Surface 2-D electrical imaging pseudo-section for Dipole-Dipole array. Each survey level corresponds to a different dipole separation (n). From Tucker et al. [88]

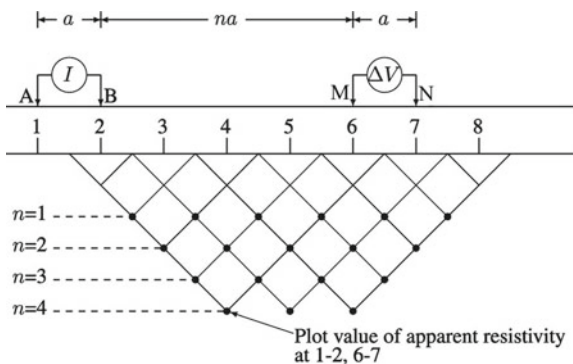


Table 16.4 Most common commercial and open- source available software for electrical resistivity data inversion

Commercial software	Link
Res2DInv, Res3DInv	www.geotomosoft.com
ERTLab	www.geostudiastier.it
ZondRes2d	www.zond-geo.com
EarthImager 2D and 3D	www.agiusa.com
Open-source software	Link
pyGIMLi	www.pygimli.org
R2, R3t and the python GUI ResIPy	www.es.lancs.ac.uk/people/amb/Freeware/Freeware.htm
SimPEG	www.simpeg.xyz
E4D	www.e4d.pnnl.gov/Pages/Home.aspx

filtering, error modelling of geoelectrical data and makes use of the codes for modelling/inversion of data, including time-lapse data analysis.

Generally, modelling/inversion codes are finite element based and admit the incorporation of complex topography and modelling of bounded regions [11]. They allow full flexibility of electrode allocation, helpful, for example, in borehole electrode-based surveys.

Nowadays, there is an increasing availability of open-source codes which are able to provide both users and developers access to comment and advance codes, allowing contributions from multiple developers (Table 16.4).

The inversion procedure typically involves five steps:

- the check of data quality;
- the generation of computational meshes;
- the exploitation of a priori information;
- the prediction of measurement responses on a given model (forward step);
- the correction of the model to achieve a better fit (inversion step).

Forward modelling is used to compute the apparent resistivity response for a given geoelectrical structure of the subsurface. Typically, the measurements are composed of a set of resistances (or apparent resistivities) from a given electrode configuration.

Although technically a low-frequency alternating current is used and inductive and capacitive effects are typically ignored, the governing equation is:

$$\nabla \cdot (-\sigma \nabla V) = \mathbf{I} \cdot (\delta(\mathbf{r} - r_A) - \delta(\mathbf{r} - r_B)). \quad (16.8)$$

Here, ∇V represents the electric potential, σ is the subsurface electrical conductivity, and $\mathbf{I} \cdot (\delta(\mathbf{r} - r_A) - \delta(\mathbf{r} - r_M))$ are point current sources from the electrodes located at positions r_A and r_M (one electrode acts as current source, and the other as current sink).

To formulate the inverse problem, the considered distribution of electrical properties is discretized into elements or cells. Then, the inverse problem involves finding a model m which, using the forward calculation according to Eq. 16.8, reproduces data d to the specified level of uncertainty.

Many inverse problems in geophysics can be solved by minimizing an objective function containing data weighting (W_d), model relative smallness (λ), and smoothness or flatness (W_m). In 2D, this is described by:

$$\tilde{m} = \min_m \left\{ (F(m) - d)^T W_d (F(m) - d) + \lambda (m - m_0)^T W_m (m - m_0) \right\} \quad (16.9)$$

where $F(m)$ are some particular forward models F depending on parameters m , m_0 is a reference model to which we believe the physical property distribution should be close. Often m_0 is chosen to be a constant average value. Parameter λ controls the balance between fitting the data and satisfying model smallness in the solution. W_d is a data weight matrix; applying such weights permits the differential weighting of poor and good data, while W_m is a matrix containing information about prior criteria (relative smallness, flatness, Smoothness, etc.).

Solving Eq. (16.9) can be done using a variety of approaches: gradient descent; Newton's method; quasi-Newton method; Levenberg-Marquardt algorithm; Occam's method. Each of them has its advantages and drawbacks depending on the problem size, degree of non-linearity, speed of forward model computations, etc.

Key to any of these methods are a starting model, m_{init} , where begin our iterations and progress downhill to the local minimum and the Jacobian or sensitivity matrix, $J = J(m)$, where:

$$J_{i,j} = \frac{\partial d_i}{\partial m_j}. \quad (16.10)$$

For more details about the inverse methods, see among others Friedel [35], Binley and Kemna [15], Binley [11], Cardarelli and De Donno [17], Binley and Slater [16].

16.5 Field Applications

In this paragraph, we describe the hydrogeological field application of some ground surface and borehole electrical resistivity survey. In Sect. 5.1, a multi-temporal cross-borehole electrical resistivity survey was carried out during a tracer test experiment. Moreover, two unconventional applications are shown: (1) cave-surface electrical resistivity survey for karst aquifer assessment in Sect. 5.2; (2) deep electrical resistivity tomography survey for deep groundwater studies in Sect. 5.3. For the three examples, the whole geoelectric processing, i.e., data analysis, inversion using different inversion softwares, and appraisals, is shown.

16.5.1 Cross-Hole Electrical Resistivity Tomography for High Resolution Image of a Confined Aquifer

Sustainable management of groundwater resources required detailed information on subsurface conditions. Several work have shown the capability of cross-hole electrical resistivity method for providing high-resolution images of hydrogeological structures at depth and detailed assessment of dynamic processes in the subsurface environment, such as fluids migration [22, 34, 61, 86]. This is particularly true if electrical resistivity imaging method is applied in an automated, time-lapse manner, using modern data acquisition systems and processing techniques.

In this case study, a saline tracer injection experiment was monitored using multi-temporal cross-hole electrical resistivity tomography (CHERT) measurements. The Montalto Uffugo test site (Calabria, Italy) represents a valley of recent formation with alluvial, conglomeratic, and sandy deposits [37, 67, 71, 84]. In particular, the site is characterized by the presence of a main confined aquifer while a shallow perched aquifer is present during part of the year. The main aquifer hydraulic conductivity is in the order of 10^{-6} m/s [37, 84].

In 2009, to obtain a higher resolution image of the test site through cross-hole ERT measurements, two new piezometers (P1 and P2) were drilled, reaching a depth of 55 m, and instrumented. The distance between the holes is approximately 10 m (Fig. 16.5).

In order to carry out cross-hole ERT, a cheap geoelectrical system was realized ad-hoc, comprising two series of 24 plate steel electrodes (5 cm high and 2 m spacing) connected to multichannel cables.

The installation phase consisted of attaching electrodes and cables to the PVC casing. Then, the instrumented casing was lowered smoothly into the ground. At a final stage, the space between the electrodes and the walls of the hole was filled by a gravel grout. Electrodes were connected to Syscal pro resistivity meter which, in turn, was connected to a PC, allowing to acquire electrical resistivity data and to control them in real time.

In 2011, At Montalto Uffugo test site, 400 L of saltwater solution (100 g/l of NaCl) were injected into the confined aquifer through the B1, while 1 l/s of water was pumping in the B9, in order to create a water flux longitudinal compared to boreholes P1-B5-P2 (Fig. 16.6a).

The first cross-hole electrical resistivity survey was performed in natural flow conditions. A total of 1836 measurements were taken with reciprocal (swapped current and potential electrodes) measurements. Prior to the experiment, the piezometric levels and the water electrical conductivity were also measured directly in P1, B5, and P2 down to -40 m (Fig. 16.6b, c). The mean electrical conductivity of water was $798 \mu\text{S}/\text{cm}$. During the first 7 days of tracer injection, geoelectrical measurements were made every 4 h, while in the following period (up to 1 month after tracer injection) cross-hole ERT data were collected twice daily.

Reciprocal measurements allowed the estimation of measurements errors. Then, the apparent resistivity values have been inverted using the R2 code [10] based on



Fig. 16.5 Phases of installation of borehole electrodes for geoelectrical measurements at test site

the widely used Occam's approach of deGroot Hedlin and Constable [31]. The area under investigation was parameterized using a 2D quadrilateral mesh made by 30×66 elements, covering a region of $128 \text{ m} \times 221 \text{ m}$ to account for current flow towards infinite boundaries. Within the 2D mesh, element sizes in the x-directions increase away from the boreholes, in the (vertical) z-direction, element sizes increase with depth below the bottom of the boreholes. The resistivity image obtained, compared with test site stratigraphy, is shown in Fig. 16.7a. The RMS error was lower than 2.7%.

Time-lapse electrical resistivity imaging (Fig. 16.7b) allows to delineate plume evolution showing evidence for a prevalent horizontal transport pathway under 35 m depth. Figure 16.7 highlights that the salt plume follows a complex pattern influenced by the hydraulic conductivity and dispersivity parameters of the area. In particular, the electrical imaging indicates tracer transport through the deepest portion of aquifer B in an area characterized by resistivity values between 60 and $130 \Omega\text{m}$ (saturated sands), while the most resistivity portion of the aquifer is interested with a certain

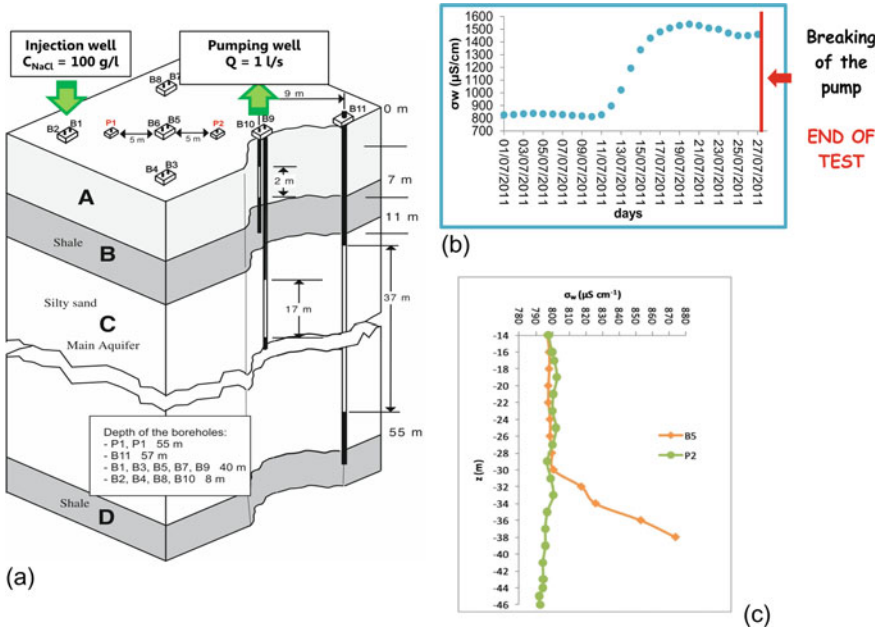


Fig. 16.6 a Tracer test experiment at Montalto Uffugo test site. (A) Shallow aquifer, heterogeneous gravels in a silty sand matrix; (B) shale; (C) main aquifer, silty sands alternated to conglomerate and clay lenses; (D) shale. B1-11 are boreholes. P1-2 are piezometers for cross-hole ERT. **b** Water electrical conductivity (normalized at 20 °C) monitored in P1, at 30 m depth. **c** Water electrical conductivity logs (normalized at 20 °C), measured 15 days after the salt injection (14/07/2011), in boreholes B5 and P2. Modified from Giampaolo et al. [37]

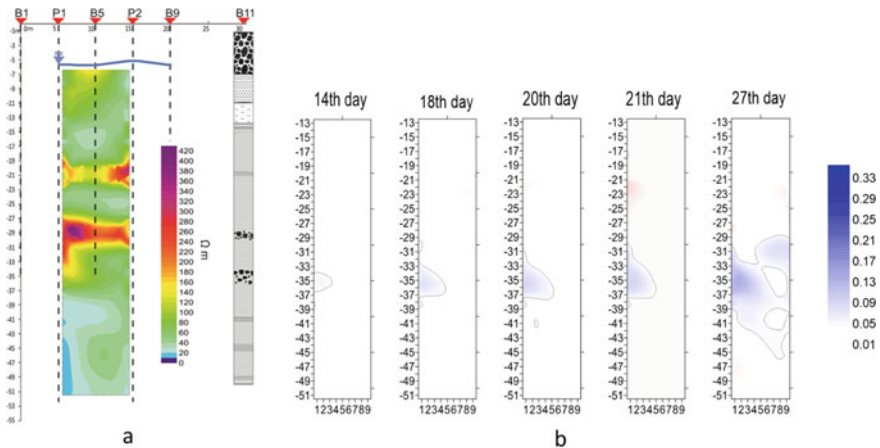


Fig. 16.7 a Cross-hole electrical resistivity tomography acquired at test site in natural flow conditions. **b** Images of resistivity change relative to a pre-tracer condition in term of $\rho_r = 1 - (\rho_t/\rho_0)$

delay. This may be associated to the presence of a clayey matrix that surrounds the resistive crystalline fragments, characterized by lower hydraulic conductivity values.

16.5.2 Cave-Surface Electrical Resistivity Tomography for Karst Aquifer Assessment

Karst landscapes are valuable sources of clean water for potable use, irrigation, and power generation due to the exceptional water quality and quantity. At the same time, karst areas are very vulnerable and dynamic environments therefore, there is the need of innovative methodologies application for their investigation.

Nowadays, karst areas are very difficult environment for any geophysical exploration; selection of the best-suited geophysical method is not always easy due to the highly variable and unpredictable target characteristics. In so complex karst systems, geophysical methods from the surface can only give partial information due to a low resolution for deeper target.

In order to overcome this problem, this case study introduces a new 3D geoelectrical approach for karst system study, i.e., “cave-surface” electrical resistivity tomography (ERT), which allows an improvement of the deep resolution compared to surface ERT. The application of this new methodology in the Castel di Lepre underground laboratory (CNR-IMAA, municipality of Marsico Nuovo, Basilicata region, Italy) is described, where a natural cave was used as horizontal well for performing surface-cave ERTs [42, 70]. This approach permitted speleologists to install inside the karstic cave some still electrodes (n.24) connected to multichannel cables. The remaining part of the electrode lines (24 electrodes) was installed on the karst mountain, in order to have a cross disposition between the cave and the top of the mountain.

Castel di Lepre underground laboratory (Fig. 16.8a) is constituted by Castel di Lepre cave and an abandoned railway tunnel built in the early twentieth century, active until the 1960. The railway tunnel has a total length of 1229 m. The carbonate rock covers over the tunnel ranges in thickness from 0 to 240 m depending on the topography (Fig. 16.8d). Castel di Lepre cave has a total length of 1848 m and a depth of 146 m from the entrance. Furthermore, ponds and waterfalls are present (Fig. 16.8c). In the cave, a small river is well detected, and a tracer test was performed in the cave to study where the water feeds the spring in the valley. The tracers were detected in the Monaco Santino spring (Paterno village) after 16 h.

From a geological point of view, Castel di Lepre is a carbonate massif (Maddalena Mt.) characterized by the outcrops of stratified and fractured carbonate rocks [30]. Large karstic conduits characterized only a small portion while, based on the hydrodynamic and geochemical data collected at the sources, water flows mainly through a series of smaller fractures in less karstified areas. Therefore, faults and fractures networks represent the main water circulation routes (Fig. 16.8b). As a result, the cave and the tunnel intersect some flow paths in the karst unsaturated zone [70].

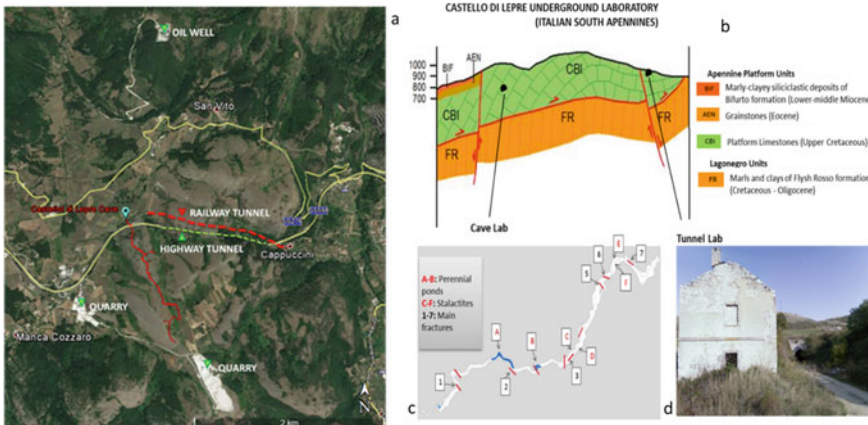


Fig. 16.8 **a** Google Map image of the Castel di Lepre karst area, **b** geological section cross the karst cave, **c** the main underground features along the karst cave, **d** the entrance of the underground karst laboratory along an old railway tunnel [42]

The characterization of this karst system is not simple; therefore, it is important to develop new technological strategies that can improve the subsurface information in such karst context. The geophysical techniques are good candidates as they require a non-invasive approach, high resolution, and good depth of penetration. In this case study, the presence of a tunnel and a cave offers an advantageous perspective to monitor a karst aquifer, from the inside, improving the knowledge of the fluid circulation in a carbonate rock formation.

In order to obtain the distribution of high-resolution electrical resistivity between the cave and the surface topography, a 3D cave-surface ERT was acquired using 24 electrodes installed along the underground natural cave in the cave and three surface lines with 24 electrodes on the Castel di Lepre mountain (Fig. 16.9a). To ensure the electric contact between electrodes and the cave rock, 24 little holes were drilled, and a bentonite mud was used (Fig. 16.9b). The electrode spacing was 20 m. A 96 channel Syscal pro resistivity meter and a battery were placed near the cave entrance, in order to inject the current and to measure the drop of potential. GPS technology was used to derive the 3D position of each electrode on the ground surface. Three 2D ERTs of the cave-surface type were acquired using an ad-hoc array. In total, 7900 apparent resistivity data were measured (Fig. 16.9c).

The first elaboration step consisted of processing the apparent resistivity data considering measurements errors and topographic correction.

To obtain a 3D resistivity distribution of the karst area over Castel di Lepre cave, cave-surface apparent resistivity data measured were inverted using ERTLab (Geostudi Astier srl and Multi-Phase Technologies LLC). ERTLab is an inversion software that provides full three-dimensional resistivity modelling and inversion. A mesh with 30.000 tetrahedral cells, a mixed boundary condition (Dirichlet and Neumann), and a starting homogeneous apparent resistivity of 200 Ωm were used.

Both a core and a boundary mesh were generated to accommodate boundary conditions (16.9d). A 5% standard deviation estimate for noise was assumed to invert electrical resistivity data sets with a robust inversion.

Figure 16.10a shows the final 3D resistivity model of the subsoil between the cave and the ground surface that obtained the best error (<5%). Electrical resistivity ranges from 1 to about 10,000 Ωm . It can be observed that, in correspondence of the electrodes placed in the cave, there is a strongly resistive layer (>600 Ωm) consistent with the cave itself filled by air. The central portion is characterized by relatively low resistivity values (<500 Ωm), while, in the upper part, a higher resistive layer is found again (>600 Ωm).

A 3D images of resistivity can more simply be visualized by 3D contouring of iso-resistivity volumes [70]. In Fig. 16.10b, the resistivity data set is displayed with iso-resistivity volumes using the threshold value $\rho < 150 \Omega\text{m}$.

In this representation, the transparency function is defined by electrical resistivity threshold values, ρ_1 ($\rho < \rho_1$). In the range $\rho > \rho_1$, data are rendered as transparent, while only the data in the interval $\rho < \rho_1$ are shown. The choose of a valuable threshold calibration is a very delicate task because by lowering the threshold value, not only the visibility of the main anomaly is raised, but also that of the smaller objects and noise increases. On the other hand, this kind of visualization allows the resistivity anomalies to be better emphasized and correlated with the geological, structural, and hydrogeological features of the investigated area. It is hypothesized that the volume with $\rho < 150 \Omega\text{m}$ could be associated to the saturated carbonate rock,

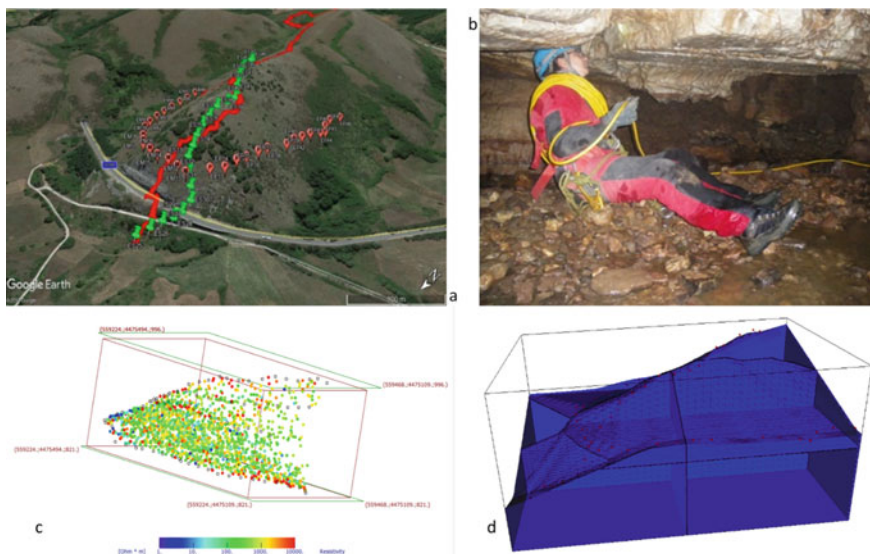


Fig. 16.9 **a** Electrodes layout on the ground surface with respect to the trace of the cave (red line), **b** electrodes and cable installation inside the cave by Castel di Lepre speleological group, **c** 3D electrical resistivity data measured, and **d** mesh for electrical resistivity data inversion [70]

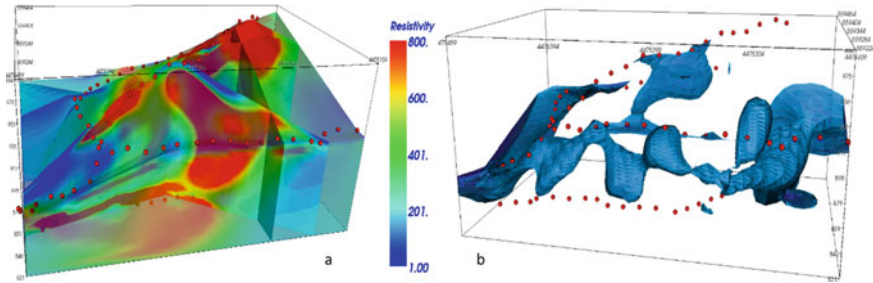


Fig. 16.10 **a** 3D electrical resistivity distribution, **b** iso-resistivity volumes using the threshold value $\rho < 150 \Omega\text{m}$ [70]

where a more intense rock fracturing state allows the water circulation. However, it is possible to observe sub-vertical surfaces in the contact areas of the different volumes that could be associated with the presence of tectonic structures like faults, which can be correlated with the main ones located inside the cave.

16.5.3 *Electrical Resistivity Tomography for Deep Groundwater Studies*

The electrical resistivity tomography (ERT) is mostly applied for shallow application to solve environmental, engineering and geological problems. Recent technological improvements in data acquisition and processing let this method to reach deeper investigation depths down to 4 km depth [5, 38, 64, 83].

As introduced by Hallof [43], the basic principle of the Deep Electrical Resistivity Tomography (DERT) method is the use of physically separated systems for current injection and the voltage measurements.

Nowadays, even if the Deep Electrical Resistivity Tomography (DERT) method is considered a proper geophysical approach for deep hydrogeological targets (>200 m), it is not a common system for deep groundwater studies as demonstrated by the presence of few examples reported in the literature [69, 75, 82].

This case study describes the challenging activity carried out by Hydrogeosite laboratory research team, where deep electrical resistivity tomographies (DERT) were used for hydrological purposes in the Agri Valley basin in the Basilicata region, Italy (Fig. 16.11). This basin is characterized by higher seismic hazard and it is the most important area in Europe for onshore oil production. In recent times, the area was characterized by dense urbanization causing an exponential increasing of water demand for agriculture and farming practices.

The main goal of deep geoelectrical investigation was to improve the reconstruction of the complex geometry of the basin by delineating the deep boundary between the quaternary alluvial deposits (thickness > 500 m) and the pre-quaternary basin,

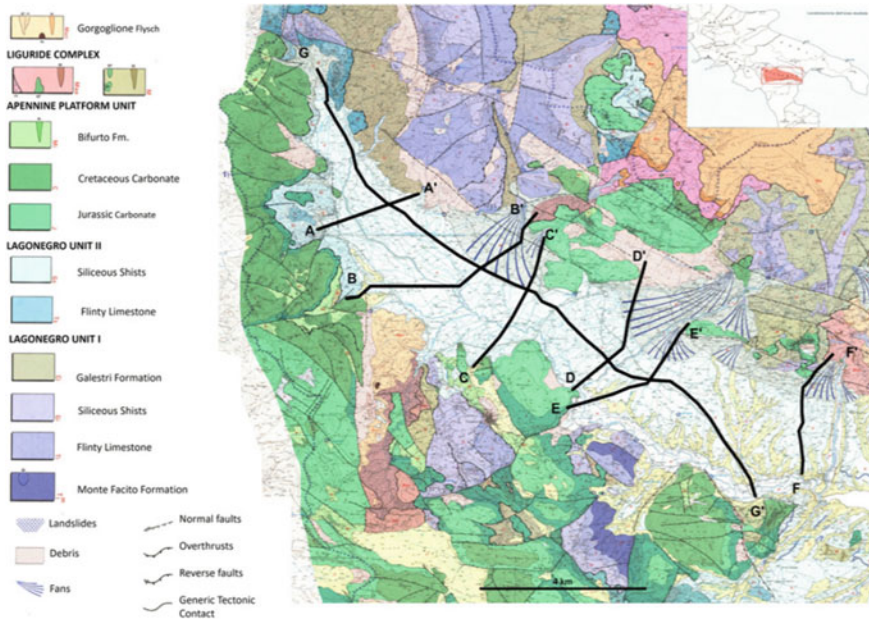


Fig. 16.11 Agri Valley geological map with the location of deep electrical resistivity surveys [68]

the Mesozoic-Tertiary carbonates, where deep groundwater resources are present (Fig. 16.11).

DERTs were acquired through a new deep multichannel system designed and built at the Hydrogeosite Laboratory of the CNR-IMAA (Fig. 16.12). In detail, long stainless-steel current electrodes (AB) are connected by a long monopolar electric cable to a transmitting station constituted by a transmitter, a voltage regulator, and an external power system. This energizing system can inject into the ground a time-domain (50% duty cycle) square-waveforms current signal, with a maximum energizing current of 20 A (Fig. 16.12b). Furthermore, the voltage measuring system consists of potential electrodes (MN) connected to a multichannel receiver system composed by remote multichannel datalogger and a GPS antenna, radios connected to a personal computer, which can simultaneously record several generated voltage signals (mV), timing, and geographic position (Fig. 16.12a).

The elements of innovation of this device consist in the possibility of expanding and adapting the system to the most varied logistical conditions and recording a greater amount of data in less time, to significantly reduce the survey times.

In detail, 6 DERTs (A-F), 2 km long and 1 km depth, were acquired along transversal sections of the Agri Valley basin [23, 67, 71]. Moreover, a DERT profile of about 21 km and an investigation depth of about 1 km was acquired along the longitudinal section of the Agri Valley basin (G-G'). This last geoelectrical survey lasted about 1 month [68]. As a technical advice, this kind of acquisition needs a



Fig. 16.12 New DERT device system. Receiver (a) and transmitter (b) units are physically separated. Current and potential signal measured in real-time (c)

group of 5/6 people distributed among dataloggers for voltage recordings and the energizing system.

Current and potential electrodes were arranged with dipole–dipole (DD) electrode configuration so that the distance between the measuring electrodes and the current ones can be limited only by the sensitivity of the instruments and the background noise. This is the reason why it is more suitable for deep investigations (>200 m) that cannot be reached with other quadripolar configuration.

Considering the great distances between current and potential dipoles, the success of the methodology is related to a good amplitude of the current signal (3–20 A) and the duration of voltage recordings for the extraction of useful signal from the noise.

Therefore, the first step of measured data analysis (Fig. 16.13) consists in comparing the acquired current signals (A) and the drop of potential data (mV), to define the same timing. The following steps consist of spike removing, de-trending analysis (to remove the natural trend that enveloped the data, see Fig. 16.13b), FFT analysis to convert the voltage signal from its original time domain to a representation in the frequency domain. In particular, the amplitude of voltage signal in the frequency domain defines the amount of the drop of potential at current transmission frequency (Fig. 16.13d).

Then, the inversion of resistance values, calculated using Eq. 16.5, were carried out using ZondRes2D software (Zond geophysical software), for the DERT longitudinal profile (335 data) to the valley. Moreover, the complete dataset (882 data) was inverted by 3D ERTLab software.

3D inversion used a mesh with more than 300,000 tetrahedral cells ($200 \times 200 \times 50 \text{ m}^3$), a mixed boundary condition (Dirichlet and Neumann), and a starting homogeneous apparent resistivity of $100 \Omega\text{m}$. A 2% standard deviation estimate for noise was assumed to invert the data. The inversion time lasted about 1 h.

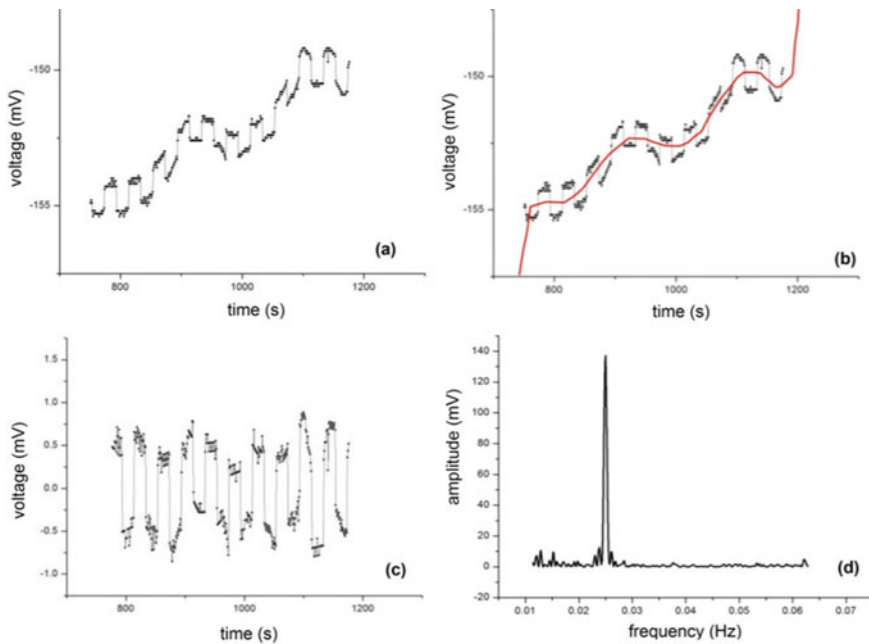


Fig. 16.13 Data analysis: **a** an example of the original potential difference (mV) data set; **b** polynomial type trend that was removed; **c** application of Fourier analysis to an example of signal recording with a good signal-to-noise ratio; **d** the peak at the energization frequency. Modified from Rizzo and Giampaolo [68]

Figure 16.14 shows the result of the 3D and 2D DERT, in both cases the investigation reached a depth > 1000 m below ground level. It is possible to observe a large, relatively conductive area (<100 Ωm) distributed along the whole valley. Higher resistivity zones (>300 Ωm) are observed alternating with relatively conductive areas.

Alluvial deposits and the pre-quatertiary substrate are characterized by a strong resistivity contrast allowing to highlight the complex geometry of the basin. The new data highlights that the thickness of the sedimentary filling varies considerably, both in the transverse and longitudinal directions, reaching thicknesses of over 1 km.

16.6 Conclusions

The demand for better information on groundwater quality and quantity developments and how best to equitably manage them is increasing worldwide. This should force enhancements in methods to gather data on groundwater use and quality [53].

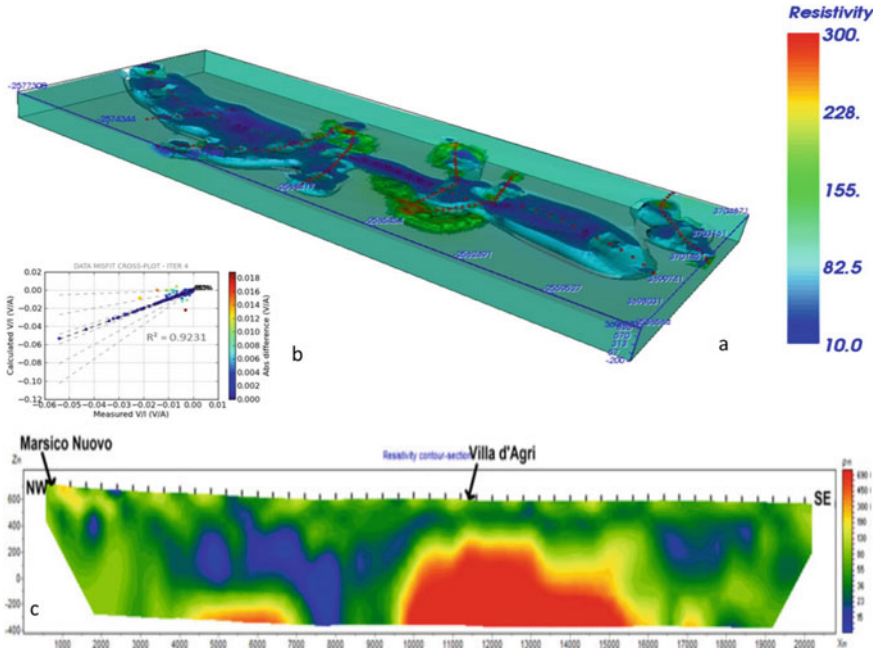


Fig. 16.14 **a** The 3D electrical resistivity image of Agri Valley obtained by ERTLab inversion software. **b** The misfit graph of the last interactions (n.4). **c** 2D DERT longitudinal image of Agri valley. From Rizzo and Giampaolo [68]

Although modelling is indispensable to understanding past and present conditions of groundwater, the relative inaccessibility of aquifers and the complexity of subsurface processes also makes the integration of geological, geochemical, hydraulic, and near surface geophysical data indispensable.

Among other near surface geophysical techniques, direct current (DC) electrical methods are widely used for hydrogeological investigations because the subsoil electrical resistivity distribution is sensitive to textural properties, temperature, porosity, hydraulic conductivity, water content, and solute concentrations (see Sect. 16.2).

Published studies have underlined the objectives where DC electrical methods are more adapt: (1) hydrogeological mapping, (2) hydrogeological parameter estimation, and (3) monitoring of hydrological processes [12].

DC electrical methods can be applied at a wide range of laboratory and field scales, and surveys may be made in arbitrary geometrical configurations (for example, on the soil surface and down boreholes, see Sect. 16.3). ER surveys can be performed from the Earth surface, in 2D mode using co-linear electrode arrays or in 3D mode, using areal distributions of electrodes. Cross-hole DC electrical imaging, with electrodes installed in two or more horizontal or vertical boreholes, is also widely applied.

Nowadays, a wide choice of codes (paid and open source) and solving approaches are available for data inversion. Each of them has its advantages and drawbacks

depending on the problem size, mesh settings, and speed of computations (see Sect. 16.4).

DC electrical methods have been demonstrated for:

- investigation of pore aquifers,
- mapping of fracture zone and karst aquifers,
- determination of groundwater quality (saltwater intrusions),
- assessment of hydraulic properties of soils and aquifers (porosity, hydraulic conductivity, water content),
- determination of aquifer vulnerability,
- mapping of contaminated sites, contaminant plume identification, both vertical and horizontal distribution including monitoring changes over time.

In particular, the hydrogeological interpretation of a controlled tracer test described in the first case study (Sect. 5.3.1) identifies the potential value of electrical imaging in groundwater studies: in fact, the proposed cross-hole electrical resistivity method results to be capable to track, in real time and with high resolution, deep plumes phenomena (contaminants or salt intrusions). Quantification of transport parameters at a study site may be possible by integrated geophysical a relatively small number of direct measurements samples.

Geophysical techniques can be considered as important methodologies for the characterization of karst environments. Section 5.3.2 describes a new way to use geoelectrical technique for karstic environments, exploiting the concept of cross-hole in horizontal wells (cave-surface), the only way allowing us to have an excellent spatial resolution in the karst critical zone. The results obtained are very good, highlighting that the new experimentation was successful; in fact, the electrical resistivity data acquired with this new technique show a 3D model with high spatial resolution and optimal data quality. The success achieved during this experimental phase certainly represents the beginning of an analysis to be carried out in the same area, also exploiting an old railway tunnel for a 3D electrical resistivity study of Castel di Lepre karst area.

Moreover, the possibility to easily export this methodology in other countries represents an added value. In fact, worldwide abandoned railway tunnels could be an important point of observation to monitor karst aquifers, where important groundwater resources are sited.

Finally, the filed application in Sect. 5.3.3 shows a useful case study for identifying possible deep aquifers using Deep Electrical Resistivity Tomography (DERT).

The individuation of deep groundwater source is not an easy task. Deep wells are expensive therefore information are generally sparse, usually available at distances ranging from hundreds to thousands of meters. In this case study, 3D DERT allows us to individuate low resistivity zones corresponding to alluvial deposits where shallower aquifers are present. On the contrary, deep high resistive areas are linked to carbonates where deep groundwater resources may be presents.

Despite the benefits extensive electrical resistivity datasets can provide to aquifer characterization efforts, at now, some limitations still exist. Uncertainty related to

field data collection and inversion, can be associated with uncorrect interpretation/analysis of ERT results. For example, choosing a particular collection array and settings instead of another may yield different outcomes. Moreover, 2D imaging is still preferred to 3D one because of its simplicity in fieldwork and lower modelling effort [44]. The use of different inversion software and algorithms can produce different outputs. Interpretation is also an inherently critical component of ERT data analysis, therefore the integration with other geophysical observations methods should be considered [20, 90].

References

1. Archie GE (1942) The electrical resistivity log as an aid in determining some reservoir characteristics. *Trans AIME* 146:54–62
2. Archie GE (1952) Classification of carbonate reservoir rocks and petro-physical considerations. *AAPG Bull* 36(2):278–298
3. Atekwana EA, Atekwana EA (2010) Geophysical signatures of microbial activity at hydrocarbon contaminated sites: a review. *Surv Geophys* 31(2):247–283
4. Ayolabi EA, Folorunso AF, Idem SS (2012) Application of electrical resistivity tomography in mapping subsurface hydrocarbon contamination. *Earth Sci Res* 2:93–103
5. Balasco M, Galli P, Giocoli A, Gueguen E, Lapenna V, Perrone A, Piscitelli S, Rizzo E, Romano G, Siniscalchi A et al (2011) Deep geophysical electromagnetic section across the Middle Aterno Valley (Central Italy): preliminary results after the April 6, 2009 L'Aquila earthquake. *Boll di Geofis Teorica ed Appl* 52(3):443–455
6. Beasley C, Ward S (1986) Three-dimensional mise-a-la-masse modeling applied to mapping fracture zones. *Geophysics* 51(1):98–113
7. Benson AK, Payne KL, Stubben MA (1997) Mapping groundwater contamination using DC resistivity and VLF geophysical methods—a case study. *Geophysics* 62:80–86
8. Bevc D, Morrison HF (1991) Borehole-to-surface electrical resistivity monitoring of a salt water injection experiment. *Geophysics* 56(6):769–777
9. Bhattacharya B, Gupta D, Banerjee B, Shalivahan (2001) Mise-a-la-masse survey for an auriferous sulfide deposit. *Geophysics* 66(1):70–77
10. Binley A (2007) R2: summary. Lancaster University, Lancaster, UK
11. Binley A (2015) Tools and techniques: electrical methods. In: Schubert G (ed) *Treatise on geophysics*. Elsevier, pp 233–259 (11.08.2015).
12. Binley A, Cassiani G, Deiana R (2010) Hydrogeophysics: opportunities and challenges. *Boll di Geofis Teorica ed Appl* 51(4):267–284
13. Binley A, Cassiani G, Middleton R, Winship P (2002) Vadose zone flow model parameterisation using cross-borehole radar and resistivity imaging. *J Hydrol* 267:147–159
14. Binley A, Hubbard SS, Huisman JA, Revil A, Robinson DA, Singha K, Slater LD (2015) The emergence of hydrogeophysics for improved understanding of subsurface processes over multiple scales. *Water Resour Res* 51:3837–3866
15. Binley A, Kemna A (2005) Electrical methods. In: Rubin Y, Hubbard SS (eds) *Hydrogeophysics*. Springer, pp. 129–156
16. Binley A, Slater L (2020) Resistivity and induced polarization. Theory and applications to the near-surface. Cambridge University Press
17. Cardarelli E, De Donno G (2019) Advances in electric resistivity tomography: theory and case studies. In: Persico R, Piro S, Linford N (eds) *Innovation in near-surface geophysics*. Elsevier, pp 23–57

18. Caselle C, Bonetto S, Comina C (2019) Comparison of laboratory and field electrical resistivity measurements of a gypsum rock for mining prospectation applications. *Int J Min Sci Technol* 29(6):841–849
19. Chambers JE, Wilkinson PB, Weller AL, Meldrum PI, Ogilvy RD, Caunt S (2007) Mineshaft imaging using surface and crosshole 3D electrical resistivity tomography: a case history from the East Pennine Coalfield, UK. *J Appl Geophys* 62:324–337
20. Cheng Q, Chen X, Tao M, Binley A (2019) Characterization of karst structures using quasi-3D electrical resistivity tomography. *Environ Earth Sci* 78:285
21. Christensen CW, Hayashi M, Bentley LR (2020) Hydrogeological characterization of an alpine aquifer system in the Canadian Rocky Mountains. *Hydrogeol J* 28:1871–1890
22. Clément R, Moreau S, Henine H, Guérin A, Chaumont C, Tournebize J (2014) On the value of combining surface and cross-borehole ERT measurements to study artificial tile drainage processes. *Near Surf Geophys* 12:763–775
23. Colella A, Lapenna V, Rizzo E (2004) High-resolution imaging of the High Agri Valley basin (Southern Italy) with electrical resistivity tomography. *Tectonophysics* 386(1–2):29–40
24. Cozzolino M, Calì LM, Gentile V, Mauriello P, Di Meo A (2020) The discovery of the theater of Akragas (Valley of Temples, Agrigento, Italy): an archaeological confirmation of the supposed buried structures from a geophysical survey. *Geosciences* 10:161
25. Dam D, Christensen S (2003) Including geophysical data in groundwater model inverse calibration. *Ground Water* 41:178–189
26. Daily W, Ramirez A (2000) Electrical imaging of engineered hydraulic barriers. *Geophysics* 65:83–94
27. Daily W, Ramirez A, Labrecque D, Nitao J (1992) Electrical-resistivity tomography of vadose water-movement. *Water Resour Res* 28:1429–1442
28. Dahlin T, Zhou B (2004) A numerical comparison of 2D resistivity imaging with 10 electrode arrays. *Geophys Prospect* 52:379–398
29. Danielsen BE, Dahlin T (2010) Numerical modelling of resolution and sensitivity of ERT in horizontal boreholes. *J Appl Geophys* 70(3):245–254
30. De Martino G, Capozzoli L, Giampaolo V, Rizzo E (2020) Geophysical measurements in an abandoned old railway tunnel (Marsico Nuovo, Italy). *EGU2020-7448*. <https://doi.org/10.5194/egusphere-egu2020-7448>
31. de Groot-Hedlin C, Constable S (1990) Occam's inversion to generate smooth, two-dimensional models from magnetotelluric data. *Geophysics* 55:1613–1624
32. Dey A, Morrison HF (1979) Resistivity modelling for arbitrarily shaped two dimensional structures. *Geophys Prosp* 27:106–136
33. Dey A, Morrison HF (1979) Resistivity modelling for arbitrarily shaped three dimensional structures. *Geophysics* 44:753–780
34. Folch A, del Val L, Luquot L, Martínez-Pérez L, Bellmunt F, Le Lay H, Rodellas V, Ferrer N, Palacios A, Fernández S, Marazuela MA, Diego-Feliu M, Pool M, Goyetche T, Ledo J, Pezard P, Bour O, Queralt P, Marcuello A, Garcia-Orellana J, Saaltink MW, Vázquez-Suñé E, Carrera J (2020) Combining fiber optic DTS, cross-hole ERT and time-lapse induction logging to characterize and monitor a coastal aquifer. *J Hydrol* 588:125050
35. Friedel S (2003) Resolution, stability and efficiency of resistivity tomography estimated from a generalized inverse approach. *Geophys J Int* 153(2):305–316
36. Giampaolo V, Capozzoli L, Grimaldi S, Rizzo E (2016) Sinkhole risk assessment by ERT: the case study of Sirino Lake (Basilicata, Italy). *Geomorphology* 253:1–9
37. Giampaolo V, Rizzo E, Straface S, Votta M (2011) Hydrogeophysics techniques for the characterization of a heterogeneous aquifer. *Boll di Geofis Teorica ed Appl* 52(4):595–606
38. Giocoli A, Magri C, Piscitelli S, Rizzo E, Siniscalchi A, Burrato P, Vannoli P, Basso C, Di Nocera S (2008) Electrical resistivity tomography investigations in the Ufita Valley (Southern Italy). *Ann Geophys* 51:213–223
39. Glover P (2009) What is the cementation exponent? A new interpretation. *Lead Edge* 28(1):82–85

40. Glover PWJ (2015) Geophysical properties of the near surface earth: electrical properties. In: Schubert G (ed) *Treatise on geophysics*, 2nd edn. Elsevier, pp 89–137 (11.04.2015)
41. Goes BJM, Meekes JAC (2004) An effective electrode configuration for the detection of DNAPLs with electrical resistivity tomography. *J Environ Eng Geophys* 9:127–141
42. Guerriero M, Capozzoli L, De Martino G, Giampaolo V, Rizzo E, Canora F, Sdao F (2019) Geophysical techniques for monitoring carbonate karstic rocks. *Ital J Eng Geol Environ.* <https://doi.org/10.4408/IJEGE.2019-01.S-10> Project: Landslide Risk Assessment along roads (LaRIS), Special Issue 1 (2019) Sapienza Università Editrice
43. Hallof PG (1957) On the interpretation of resistivity and induced polarization measurements, Ph.D. thesis, MIT, Cambridge
44. Hung Y-C, Lin C-P, Lee C-T, Weng K-W (2019) 3D and boundary effects on 2D electrical resistivity tomography. *Appl Sci* 2019(9):2963
45. Irving J, Singha K (2010) Stochastic inversion of tracer test and electrical geophysical data to estimate hydraulic conductivities. *Water Resour Res* 46:W11514
46. Kelly WE (1976) Geoelectric sounding for delineating ground-water contamination. *Ground-water* 14(1):6–10
47. Kirkby A, Heinson G, Krieger L (2016) Relating permeability and electrical resistivity in fractures using random resistor network models. *J Geophys Res Solid Earth* 121(3):1546–1564
48. Kosinski WK, Kelly EW (1981) Geoelectric sounding for predicting aquifer properties. *Ground Water* 19:163–171
49. Kozeny J (1953) *Hydraulik*. Springer, Wien, p 588
50. Kozlov B, Schneider MH, Montaron B, Lagues M, Tabeling P (2012) Archie's law in microsystems. *Transp Porous Media* 95(1):1–20
51. Kruschwitz S, Yaramanci U (2004) Detection and characterisation of the disturbed rock zone in claystone with the complex resistivity method. *J Appl Geophys* 57:63–79
52. Kunetz G (1966) Principles of direct current resistivity prospecting. In: *Geoexploration monographs, series 1, no 1*. Schweizerbart Science Publishers, Stuttgart, Germany, 103 p
53. Lall U, Jossel L, Russo T (2020) A snapshot of the world's groundwater challenges. *Annu Rev Environ Resour* 45:7.1–7.24
54. Loke M, Barker R (1996) Rapid least-squares inversion of apparent resistivity pseudosection by a quasi-Newton method. *Geophys Prospect* 44:131–152
55. Lytle RJ, Dines KA (1978) An impedance camera: a system for determining the spatial variation of electrical conductivity. Lawrence Livermore National Laboratory UCRL-52413
56. Mansinha L, Mwenifumbo C (1983) A mise-a-la-masse study of the Cavendish geophysical test site. *Geophysics* 48(9):1252–1257
57. Marescot L, Palma Lopes S, Lagabrielle R, Chapellier D (2002) Designing surface to borehole electrical resistivity tomography surveys using the Frechet derivative. In: *Proceedings of 8th meeting of the environmental and engineering geophysical society—European section*, pp 289–292
58. Mary B, Peruzzo L, Boaga J, Cenni N, Schmutz M, Wu Y, Hubbard SS, Cassiani G (2020) Time-lapse monitoring of root water uptake using electrical resistivity tomography and mise-à-la-masse: a vineyard infiltration experiment. *Soil* 6(95–114):2020
59. Mohamed A, Paleologos E (2017) Groundwater. In: *Fundamentals of geoenvironmental engineering: understanding soil, water, and pollutant interaction and transport*. Butterworth-Heinemann
60. Ogunbo JN, Mamukuyomi EA, Wahab SA, Harrison A, Olamide A, Chukwuebuka RU (2018) Panoramic azimuthal Schlumberger vertical electrical sounding for fracture orientation and anisotropy quantification. *Heliyon* 4(12):e00998
61. Palacios A, Ledo JJ, Linde N, Luquot L, Bellmunt F, Folch A, Marcuello A, Queralt P, Pezard PA, Martínez L, del Val L, Bosch D, Carrera J (2020) Time-lapse cross-hole electrical resistivity tomography (CHERT) for monitoring seawater intrusion dynamics in a Mediterranean aquifer. *Hydrol Earth Syst Sci* 24:2121–2139
62. Perri MT, Barone I, Cassiani G, Deiana R, Binley A (2020) Borehole effect causing artefacts in cross-borehole electrical resistivity tomography: a hydraulic fracturing case study. *Near Surf Geophys* 18(4):445–462

63. Perri MT, De Vita P, Masciale R, Portoghese I, Chirico GB, Cassiani G (2018) Time-lapse *mise-à-la-masse* measurements and modeling for tracer test monitoring in a shallow aquifer. *J Hydrol* 561:461–477
64. Pucci S, Civico R, Villani F, Ricci T, Delcher E, Finizola A, Sapia V, De Martini PM, Pantosti D, Barde-Cabusson S et al (2016) Deep electrical resistivity tomography along the tectonically active Middle Aterno Valley (2009 L'Aquila earthquake area, central Italy). *Geophys J Int* 207(2):967–982
65. Ramirez A, Daily W, Binley A, LaBrecque D, Roelant D (1996) Detection of leaks in underground storage tanks using electrical resistance methods. *J Environ Eng Geophys* 1:189–203
66. Riedel M, Collett TS, Hyndman RD (2005) Gas hydrate concentration estimates from chlorinity, electrical resistivity, and seismic velocity. *Geol Surv Can Open-File Rep* 4934
67. Rizzo E, Colella A, Lapenna V, Piscitelli S (2004) High-resolution images of the fault controlled High Agri Valley basin (Southern Italy) with deep and shallow electrical resistivity tomographies. *Phys Chem Earth* 29:321–327
68. Rizzo E, Giampaolo V (2019) New deep electrical resistivity tomography in the High Agri Valley basin (Basilicata, Southern Italy). *Geomat Nat Haz Risk* 10(1):197–218
69. Rizzo E, Giampaolo V, Capozzoli L, Grimaldi S (2019) Deep electrical resistivity tomography for the hydrogeological setting of Muro Lucano Mounts Aquifer (Basilicata, Southern Italy). *Geofluids* 2019b(Article ID 6594983): 11 p
70. Rizzo E, Guerriero M, Gueguen E, Capozzoli L, De Martino G, Perciante F (2017) Cave-surface electrical resistivity tomography in “Castello di Lepre” karst system (Marsico Nuovo, Southern Italy). In: *Monitoring and characterization of the shallow subsurface I, EAGE 2017*. <https://doi.org/10.3997/2214-4609.201702078>
71. Rizzo E, Suski B, Revil A, Straface S, Troisi S (2004) Self-potential signals associated with pumping-test experiments. *J Geophys Res* 109:1–14
72. Roubinet D, Irving J, Pezard P (2018) Relating topological and electrical properties of fractured porous media: insights into the characterization of rock fracturing. *Minerals* 8(1):1–14
73. Rubin Y, Hubbard SS (2005) *Hydrogeophysics*, 523 pp. Springer, NY
74. Rücker C, Günther T (2011) The simulation of finite ERT electrodes using the complete electrode model. *Geophysics* 76:F227–F238
75. Santilano A, Godio A, Manzella A, Menghini A, Rizzo E, Romano G (2015) Electromagnetic and DC methods for geothermal exploration in Italy, state-of-the-art, case studies and future developments. *First Break* 33(8):81–86
76. Sasaki Y, Matsuo K (1993) Surface-to-tunnel resistivity tomography at the Kamaishi mine. *Batsuri-Tansa* 46:128–133
77. Shevnin V, Delgado-Rodríguez O, Mousatov A, Ryjov A (2006) Estimation of hydraulic conductivity on clay content in soil determined from resistivity data. *Geofis Internacional* 45:195–207
78. Shima H (1992) 2D and 3D resistivity image reconstruction using crosshole data. *Geophysics* 57:1270–1281
79. Schön JH (2004) *Physical properties of rocks: fundamentals and principles of petrophysics*. Elsevier, Amsterdam, 600 pp
80. Slater L, Binley A (2003) Evaluation of permeable reactive barrier (PRB) integrity using electrical imaging methods. *Geophysics* 68:911–921
81. Slater LD, Binley A, Brown D (1997) Electrical imaging of fractures using groundwater salinity change. *Ground Water* 35:436–442
82. Tamburriello G, Balasco M, Rizzo E, Harabaglia P, Lapenna V, Siniscalchi A (2008) Deep electrical resistivity tomography and geothermal analysis of Bradano foredeep deposits in Venosa area (Southern Italy): preliminary results. *Ann Geophys* 51(1)
83. Troiano A, Isaia R, Di Giuseppe MG, Tramparulo FDA, Vitale S (2019) Deep electrical resistivity tomography for a 3D picture of the most active sector of Campi Flegrei caldera. *Sci Rep* 9:15124

84. Troisi S, Fallico C, Straface S, Migliari E (2000) Application of kriging with external drift to estimate hydraulic conductivity from electrical resistivity data in unconsolidated deposits near Montalto Uffugo, Italy. *Hydrogeol J* 4:356–367
85. Tschofen (2014) Geoelectrical monitoring of rock permafrost in the laboratory, thesis
86. Tso CM, Johnson TC, Song X, Chen X, Kuras O, Wilkinson P, Uhlemann S, Chambers J, Binley A (2020) Integrated hydrogeophysical modelling and data assimilation for geoelectrical leak detection. *J Contam Hydrol* 234:103679
87. Tsourlos P, Ogilvy RD, Papazachos C, Meldrum PI (2011) Measurement and inversion schemes for single borehole-to-surface electrical resistivity tomography surveys. *J Geophys Eng* 8:487–497
88. Tucker SE, Briaud J, Hurlebaus S, Everett ME, Arjwech R (2015) Electrical resistivity and induced polarization imaging for unknown bridge foundations. *J Geotech Geoenviron Eng* 141(5):04015008
89. Van Schoor M, Binley A (2010) In-mine (tunnel-to-tunnel) electrical resistance tomography in South African platinum mines. *Near Surface Geophys* 8:563–574
90. Vogelgesang JA, Holt N, Schilling KE, Gannon M, Tassier-Surine S (2020) Using high-resolution electrical resistivity to estimate hydraulic conductivity and improve characterization of alluvial aquifers. *J Hydrol* 580:123992
91. Watlet A, Kaufmann O, Triantafyllou A, Poulain A, Chambers JE, Meldrum PI, Wilkinson PB, Hallet V, Quinif Y, Van Ruymbeke M, Van Camp M (2018) Imaging groundwater infiltration dynamics in the karst vadose zone with long-term ERT monitoring. *Hydrol Earth Syst Sci* 22:1563–1592
92. Waxman MH, Smits LJM (1968) Electrical conductivities in oil-bearing Shaly sands. *Soc Petrol Eng J* 8:107–122
93. Wilkinson PB, Chambers JE, Lelliott M, Wealthall GP, Ogilvy RD (2008) Extreme sensitivity of crosshole electrical resistivity tomography measurements to geometric errors. *Geophys J Int* 173(1):49–62
94. Wilkinson PB, Chambers JE, Meldrum PI, Ogilvy RD, Caunt S (2006) Optimization of array configurations and panel combinations for the detection and imaging of abandoned mineshafts using 3D cross-hole electrical resistivity tomography. *J Environ Eng Geophys* 11:213–221
95. Wu W, Lo M, Wada Y, Famiglietti JS, Reager JT, Yeh PJ-F, Ducharme A, Yang Z (2020) Divergent effects of climate change on future groundwater availability in key mid-latitude aquifers. *Nat Commun* 11:3710
96. Yue WZ, Tao G (2013) A new non-Archie model for pore structure: numerical experiments using digital rock models. *Geophys J Int* 195(1):282–291

Chapter 17

Digital Soil Mapping Using Drone-Borne Ground-Penetrating Radar



Kaijun Wu and Sébastien Lambot

Abstract A drone-based ground-penetrating radar (GPR) is introduced for digital soil mapping in this chapter. The radar system is lightweight and consists of a hand-held vector analyzer (VNA), a computer stick, and a differential GPS for positioning. A power bank is used to provide electricity for the whole radar system. A smartphone or tablet controls the radar and GPS measurements remotely. Full-wave inversion is used to retrieve the soil dielectric permittivity from the soil surface reflection, hereby to estimate volumetric soil water content through a petrophysical relation. The radar works in the frequency domain, and data processing is carried out in the time domain to focus on the surface reflection only. A look-up table (LUT) is pre-calculated to reduce the processing time during inversion, formulated as a least-squares problem. Soil moisture maps are generated by kriging interpolation. We present several examples of soil moisture maps produced in agricultural fields in Belgium.

Keywords Ground-penetrating radar · GPR · Drone · Full-wave inversion · Soil moisture mapping

17.1 Introduction

Soil qualities affect daily life of human-being indirectly or directly. Characterization of the shallow subsurface is essential for agriculture, hydrology, meteorology, environment science etc. Generally, soil carries and circulates nutrients and water for crops, and serves as a reservoir of biodiversity [1–3]. Infiltration and runoff of rainfall depend largely on soil properties [4], and it is helpful to forecast some natural disasters like floods, landslides and droughts etc. Climate change regulating can be

K. Wu (✉) · S. Lambot
Université Catholique de Louvain, Earth and Life Institute, Croix du Sud 2, Box L7.05.02, 1348 Louvain-la-Neuve, Belgium
e-mail: kaijun.wu@uclouvain.be

S. Lambot
e-mail: sebastien.lambot@uclouvain.be

© The Author(s), under exclusive license to Springer Nature Switzerland AG 2022
A. Di Mauro et al. (eds.), *Instrumentation and Measurement Technologies for Water Cycle Management*, Springer Water, https://doi.org/10.1007/978-3-031-08262-7_17

417

conducted by soil due to its carbon cycle function, and soil affects climate patterns by sequestering carbon or greenhouse gases [5, 6]. Besides providing with a large amount of food and necessities, soil is capable of restricting pests and diseases for humans, animals and plants, and monitoring the epidemic risk [4, 7]. In addition, field-scale soil water content information like soil moisture maps provides guided reference for irrigation which helps to save water resources.

From the perspective of geophysics, time-domain reflectometry (TDR), electrical resistivity tomography (ERT), electromagnetic induction (EMI) and ground-penetrating radar (GPR) have been the most widely used sensors for soil properties characterization. EMI operates in much lower frequencies (e.g., 0.3–30 kHz) than GPR (10 MHz to 10 GHz). TDR measures dielectric constant by inserting electrode probe into the medium and observing the reflected waveform, but it suits for small-scale characterization. ERT determines subsurface resistivity from multiple measurements of electrical resistance using electrodes with varying locations and spacing. EMI and GPR equipments can be contactless and, therefore, fixed on vehicles for fast, high-resolution and large-scale soil properties characterization and mapping [8–11]. GPR has demonstrated to be a useful technique not only for soil surveys, but also for road inspection [12–15], tree trunk imaging [16–18], buried objects detection [19, 20], etc.

Soil moisture is usually related to the dielectric permittivity through petrophysical relationships like Topp's [21], Ledieu's [22] models, etc. For GPR with medium/air-coupled antenna(s), the dielectric permittivity can be generally obtained from (1) electromagnetic (EM) wave propagation velocity in the medium, and (2) surface reflection amplitude. Borehole GPR, fixed-offset or multi-offset measurements like common midpoint (CMP) and wide angle reflection and refraction (WARR) provide EM wave velocity information [23–27]. More details about multi-offset GPR can be found in a review of Forte and Pipan [28]. Average envelope amplitude (AEA) method or early-time signal analysis focus on changes of the first arrival signals in terms of amplitude, shape and duration, resulting from variations soil properties like dielectric permittivity and conductivity [29–33]. Both the surface reflection method and full-wave inversion can be conducted using off-ground GPR systems with a single antenna acting as transmitter and receiver at the same time, which makes the radar system and measurement configuration much simpler. Lambot et al. [34] and Lambot and André [35] introduced a full-wave radar equation that is especially valid for wave propagation in three-dimensional planar layered media. This radar equation accounts for the radar source and antenna effects, including antenna-medium interactions. So it importantly permits to get rid of the antenna internal reflections and transmissions, hereby to retrieve dielectric permittivity accurately through full-wave inversion. One practical advantage of full-wave inversion compared with the surface reflection method is that a priori knowledge of antenna height is not required [36].

The application of electromagnetic methods for underground exploration using aerial platforms like airplanes and helicopters have been proven to be very useful [37–41]. Nowadays, the booming of unmanned aerial vehicles (UAVs) or drones provides an enjoyable lifestyle for human and numerous possibilities of development for various fields thanks to their features such as low-cost, easy-controlled, lightweight,

high-effective and so on [42–44]. Considering the loading capacity of drones, radar systems to be used have to be as light as possible. Though there are still some technical challenges, using GPR on drone has been drawing more and more attention in recent years, and an increasing number of relevant researches and their results are presented in literature and scientific conferences. When it flies at a relatively low altitude of 0.5 m, a GPR system composed by two antennas (transmitter and receiver) and a Software Defined Radio technology has been used on drone to find out 0.2 m depth underground landmine-shaped objects containing enough content of metallic material, and could even distinguish true and false targets [45]. Ludeno et al. [46, 47] proved the potential of radar imaging through drone technologies. Experiments and results of Garcia et al. show that a vehicle-drone bistatic GPR configuration using synthetic aperture radar algorithm provides a high resolution subsurface images for the purpose of landmines and Improvised Explosive Devices detection [48, 49]. Sipos and Gleich [50] propose a compact Stepped Frequency Continuous Wave GPR radar with two Vivaldi-horn antennas for landmine detection. Noviello et al. [51] achieved a high resolution radar imaging for targets with different geometric shapes and properties. However, few research in publications is about drone-GPR for soil properties characterization. The drone requires a lightweight radar system and air-coupled measurement, but lots of commercial GPR radars are either too heavy or not well adapted for drone applications. To this concern we need to have small system or devices. For data processing, a full-wave inversion proposed by Lambot et al. permits to model radar signal and filter antenna effect out from raw data through a radar equation [34, 35], hereby to retrieve medium properties. This method is fast, and requires only a simple measurement configuration. More importantly, as the forward model is full-wave, it is theoretically optimal in terms of accuracy and processing automation, and it has been used for soil permittivity characterization and mapping successfully [8, 9, 52, 53]. With full-wave inversion, Wu et al. [54] proposed a lightweight frequency-domain GPR and used it for soil moisture mapping, thereby demonstrating the concept that it is possible to combine the drone and GPR technology for fast and high-resolution mapping of soil properties. On the whole, the drone-borne GPR and full-wave inversion are capable of making soil moisture mapping fast and precise, thanks to (1) the application of drones, (2) the radar equation accounting for the antenna and 3D propagation in planar layered media so that inversion is accurate, and (3) a LUT being used to greatly reduce processing time and to make minimization robust. In this chapter, we describe our drone-borne GPR system and processing, and we show several soil moisture mapping examples performed in agricultural fields in Belgium.

17.2 Methodology

The method we use for soil properties characterization with drone-GPR is full-wave inversion. For this application, full-wave inversion is conducted simpler in the following measurement conditions, on which drones manage to be applied: (1) zero-

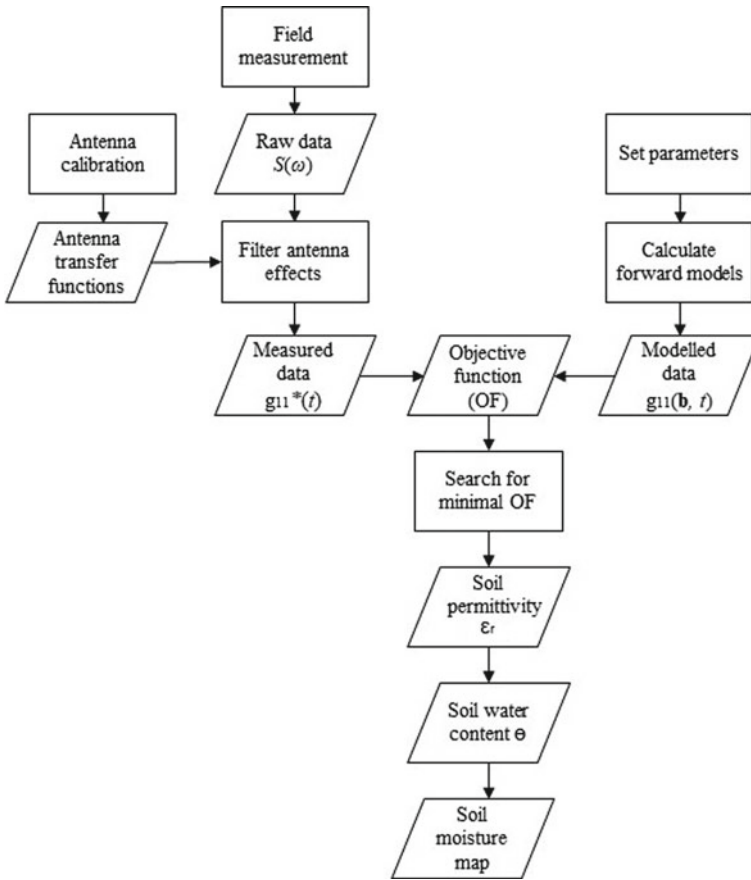


Fig. 17.1 Inversion flowchart of drone-borne GPR for soil moisture mapping. ω denotes the angular frequency, indicating that the radar measures in the frequency domain, t is the time indicating that data being processed in the time domain. \mathbf{b} is the parameter vector, depending on the parameters being set for forward models. Topp’s model [21] is used to obtain the volumetric water content θ from the relative dielectric permittivity ϵ_r . The soil moisture map is generated by kriging interpolation

offset configuration. Namely, there is only one antenna to be used as transmitter and receiver at the same time, which greatly lighten the whole GPR system. (2) air-coupled measurements. With the radar equation proposed by Lambot et al. [34], antenna effects are filtered out of the recorded signals and inversion is performed on the Green function.

On the whole, the data processing procedure is shown in Fig. 17.1. \mathbf{b} is the parameter vector. Modeled data is pre-computed and stored in a LUT for fast and robust inversion. Topp’s model [21] is used to obtain the volumetric soil water content θ from the relative dielectric permittivity ϵ_r . Other relationships can also be used [55]. More detail is given in the following sections.

17.2.1 Radar Equation

The radar equation of Lambot et al. is used for antenna calibration by calculating antenna transfer functions (i.e., calculating $\mathbf{g}_{i1}^*(t)$ from raw data $S(\omega)$ in Fig. 17.1) [34, 35]. In radar antennas, there are variations of impedance between the radar reference plane where the field is measured and the antenna aperture. These variations lead to infinite multiple reflections and transmissions inside the radar-antenna system. These reflections also make the antenna free-space response different from zero. In addition, they cause multiple reflections between the antenna and the medium, which are particularly significant in near-field conditions (antenna-medium coupling). These phenomena produce unwanted signals appearing in the recorded radar data. Radar measurements can be described with the radar equation of Lambot et al. [34] and Lambot and André [35]. The generalized antenna model relies on solution of the 3-D Maxwell's equations, and it in particular accounts for the interactions between the antenna and planar layered medium. The radar equation can be therefore used (1) to filter out antenna effect and (2) to evaluate antenna performances with antenna characteristic functions.

In general, the model can be depicted using a block diagram as represented in Fig. 17.2. It assumes that there are a set of infinitesimal electric dipoles acting as the source, and the receiver consists of an equivalent set of points. This assumption is resulting the fact that the scattered field distribution over the antenna aperture is not always uniform but depends on the antenna-medium distance and medium properties. Complex and frequency-dependent global reflection and transmission coefficients are used to describe the wave propagation between the radar reference plane and these source/field points. The general form of the radar equation is expressed in the frequency domain as Eq. (17.1) as [35].

$$S(\omega) = \frac{b(\omega)}{a(\omega)} = R_i(\omega) + \mathbf{T}_s (\mathbf{I}_N - \mathbf{G}^0 \mathbf{R}_s)^{-1} \mathbf{G} \mathbf{T}_i \quad (17.1)$$

with

$$\mathbf{T}_i = [T_{i,1}(\omega) \ T_{i,2}(\omega) \ \cdots \ T_{i,N}(\omega)]^T \quad (17.2)$$

$$\mathbf{T}_s = [T_{s,1}(\omega) \ T_{s,2}(\omega) \ \cdots \ T_{s,N}(\omega)] \quad (17.3)$$

$$\mathbf{R}_s = \text{diag}([R_{s,1}(\omega) \ R_{s,2}(\omega) \ \cdots \ R_{s,N}(\omega)]) \quad (17.4)$$

$$\mathbf{G} = \begin{bmatrix} G_{11}(\omega) & G_{12}(\omega) & \cdots & G_{1N}(\omega) \\ G_{21}(\omega) & G_{22}(\omega) & \cdots & G_{2N}(\omega) \\ \vdots & \vdots & & \vdots \\ G_{N1}(\omega) & G_{N2}(\omega) & \cdots & G_{NN}(\omega) \end{bmatrix} \quad (17.5)$$

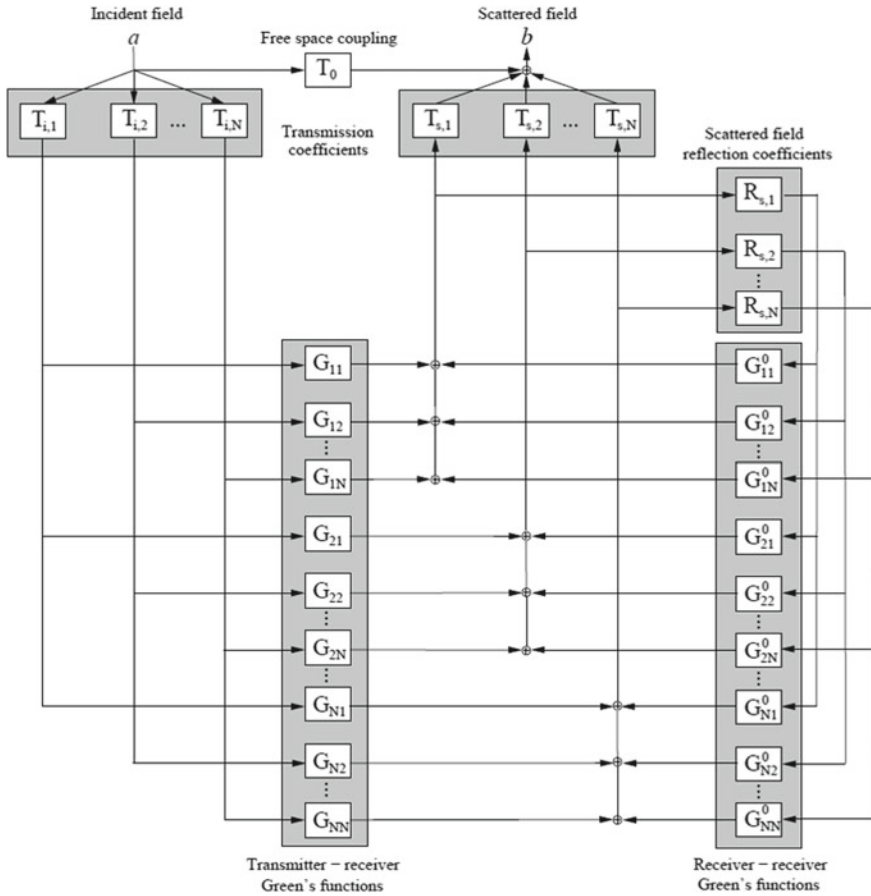


Fig. 17.2 Linear block diagram for near-field antenna-multilayered system, representing the transmitting and receiving antenna model. It permits to describe wave propagation between the radar reference plane, point sources, and field points [35]

and

$$\mathbf{G}^0 = \begin{bmatrix} G_{11}^0(\omega) & G_{12}^0(\omega) & \cdots & G_{1N}^0(\omega) \\ G_{21}^0(\omega) & G_{22}^0(\omega) & \cdots & G_{2N}^0(\omega) \\ \vdots & \vdots & \ddots & \vdots \\ G_{N1}^0(\omega) & G_{N2}^0(\omega) & \cdots & G_{NN}^0(\omega) \end{bmatrix} \tag{17.6}$$

$S(\omega)$ is the radar signal measured by a VNA. The incident and scattered field $a(\omega)$ and $b(\omega)$ are, respectively, the received and emitted signals at the VNA reference plane. The global reflection coefficient $R_i(\omega)$, also being called the return loss, corresponds to the antenna free-space response. $T_{i,\cdot}(\omega)$ and $T_{s,\cdot}(\omega)$ are the global transmission coefficients for fields incident from, respectively, the radar reference plane onto the

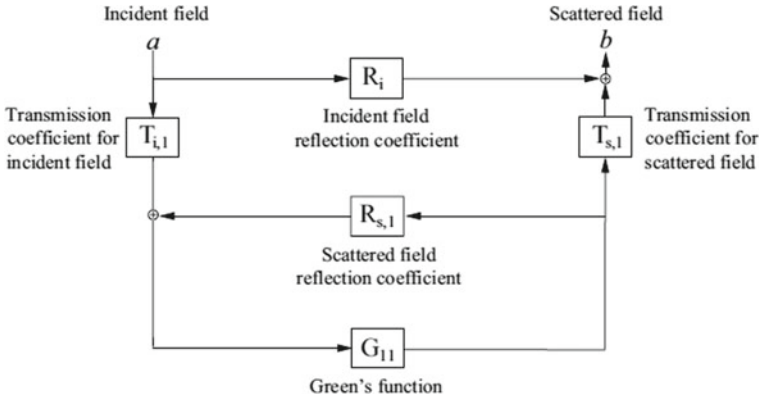


Fig. 17.3 Linear block diagram for far-field antenna-multilayered medium system, representing the far-field antenna model, and it describes wave propagation between the radar reference plane and the source or field points [34]

source point and the field point onto the radar reference plane. $R_{s, \cdot}(\omega)$ is the global reflection coefficient for fields incident from the layered medium onto the field point, and it accounts for infinite wave reflections between the antenna and medium. $G_{\cdot, \cdot}(\omega)$ and $G_{\cdot, \cdot}^0(\omega)$ denote the layered medium Green’s functions. \mathbf{I}_N is the N -order identity matrix, so N is also the number of source and field points under consideration. The number of source and field points to be used somehow depends on the distance between antenna aperture and medium, while at this moment, there is not a specific rule to define this number, except for the so-called far-field conditions. Usually, $N = 8$ performs well in most near-field conditions.

When $N = 1$, it becomes a far-field model depicted as in Fig. 17.3, and expressed as Eq. (17.7), in which we define $T(\omega) = T_{s,1}(\omega)T_{i,1}(\omega)$ as the transmitting-receiving response function. Generally, if the distance between the antenna and the medium is over 1.2 times of the maximum dimension of antenna aperture, it is considered as a far-field model [56]. A geometrical sketch is shown in Fig. 17.4. In far-field conditions, it is assumed that the field is homogeneous over the antenna aperture, which results in $N = 1$ in Eq. (17.1). Only its amplitude and phase change with frequency and the layered medium of interest. Hence, Eq. (17.1) reduces to:

$$S(\omega) = \frac{b(\omega)}{a(\omega)} = R_i(\omega) + \frac{T_s(\omega)G_{11}(\omega)T_i(\omega)}{1 - G_{11}(\omega)R_s(\omega)} \tag{17.7}$$

From the radar measurements $S(\omega)$, the Green’s function can be analytically calculated as:

$$G_{11}(\omega) = \frac{S(\omega) - R_i(\omega)}{T(\omega) + S(\omega)R_s(\omega) - R_i(\omega)R_s(\omega)} \tag{17.8}$$

In addition, it is worth to note that there are two ways to get the transfer function $R_i(\omega)$, (1) conducting a set of radar measurements above a flat surface with known

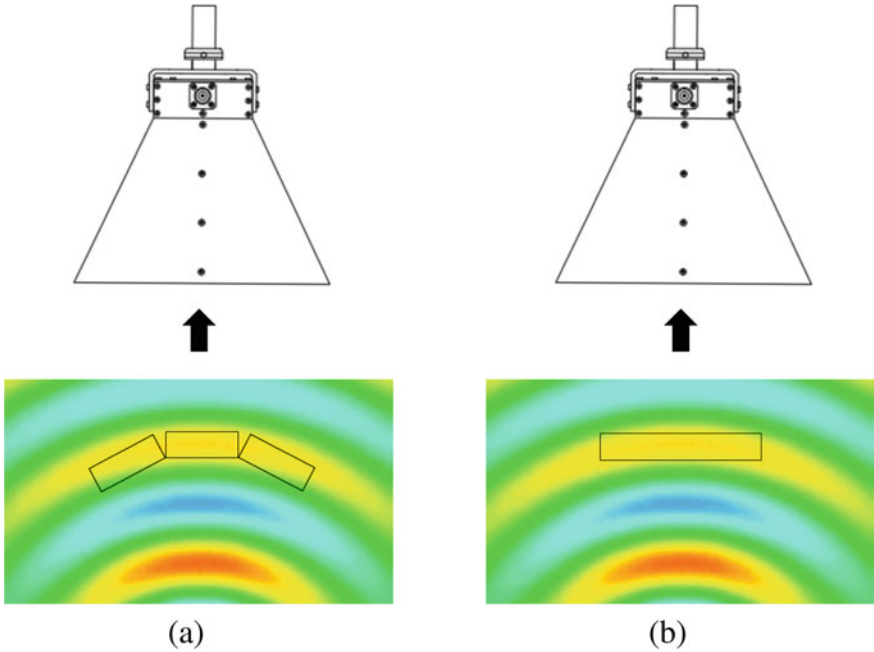


Fig. 17.4 Geometrical sketches of **a** near- and **b** far-field conditions. The determination of near- or far-field depends on the antenna dimension and the distance between the antenna aperture and the layered medium

properties like a large metal sheet or water surface, and then solving a linear system of equations with these data, or (2) measuring in free space conditions, so that when $G_{11} = 0$, $R_i(\omega)$ is equal to $S(\omega)$. The measurement in free space is easy to be done with a drone-radar by flying sufficiently high, so that the soil reflection amplitude becomes lower than the noise level. These two $R_i(\omega)$ results could be a further checking for antenna calibration.

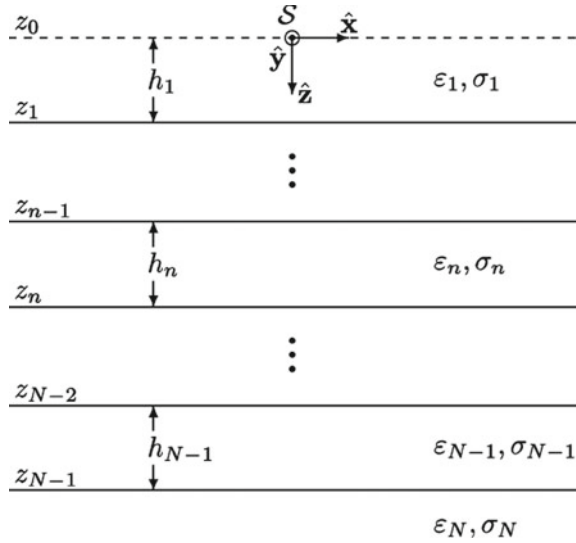
17.2.2 Green's Function

We use the Green function to calculate forward models (i.e., $\mathbf{g}_{11}(\mathbf{b}, t)$ in Fig. 17.1). The Green's function is a solution of Maxwell's equations for EM waves propagation in multilayered media [57]. The model configuration is shown in Fig. 17.5.

The spatial-domain Green's function is define as:

$$\mathbf{G}_{..} = \frac{1}{8\pi} \int_0^{+\infty} \tilde{\mathbf{G}}_{..}(k_\rho) k_\rho dk_\rho \tag{17.9}$$

Fig. 17.5 Model configuration of the three-dimensional N -layered medium. S is the source [34]



where $\tilde{\mathbf{G}}(k_\rho)$ is the spectral Green's function, and computed as:

$$\tilde{\mathbf{G}}_{..}(k_\rho) = [J_0(k_\rho \rho) \left(\frac{\Gamma_0 R_0^{TM}}{\sigma_0 + j\omega \epsilon_0} - \frac{j\omega \mu_0 R_0^{TE}}{\Gamma_0} \right) - J_2(k_\rho \rho) \cos(2\theta) \left(\frac{\Gamma_0 R_0^{TM}}{\sigma_0 + j\omega \epsilon_0} + \frac{j\omega \mu_0 R_0^{TE}}{\Gamma_0} \right)] e^{-2\Gamma_0 h_0} \quad (17.10)$$

where ω is the angular frequency and $j = \sqrt{-1}$. J_0 is the first kind zero-order Bessel's functions, and J_2 is the second. ρ and θ are the distance and angle in the xy -plane between the field and source points. h_0 is the distance between the source/receiver points and the first medium interface. σ_0, ϵ_0 and μ_0 are, respectively, the electrical conductivity, the dielectric permittivity and the magnetic permeability of the upper half-space layer (free-space in our case). $\Gamma_0 = \sqrt{k_\rho^2 - k^2}$ denotes the vertical wavenumber, in which $k^2 = \omega^2 \mu (\epsilon - (j\sigma/\omega))$. R_n^{TM} and R_n^{TE} are the global TM-mode and TE-mode reflection coefficients at interface n ($n = 0, \dots, N - 1$), and defined as Eqs. (17.11) and (17.12).

$$R_n^{TM} = \frac{r_n^{TM} + R_{n+1}^{TM} e^{-2\Gamma_{n+1} h_{n+1}}}{1 + r_n^{TM} R_{n+1}^{TM} e^{-2\Gamma_{n+1} h_{n+1}}} \quad (17.11)$$

$$R_n^{TE} = \frac{r_n^{TE} + R_{n+1}^{TE} e^{-2\Gamma_{n+1} h_{n+1}}}{1 + r_n^{TE} R_{n+1}^{TE} e^{-2\Gamma_{n+1} h_{n+1}}} \quad (17.12)$$

$$r_n^{TM} = \frac{(\sigma_{n+1} + j\omega\varepsilon_{n+1})\Gamma_n - (\sigma_n + j\omega\varepsilon_n)\Gamma_{n+1}}{(\sigma_{n+1} + j\omega\varepsilon_{n+1})\Gamma_n + (\sigma_n + j\omega\varepsilon_n)\Gamma_{n+1}} \quad (17.13)$$

$$r_n^{TE} = \frac{\mu_{n+1}\Gamma_n - \mu_n\Gamma_{n+1}}{\mu_{n+1}\Gamma_n + \mu_n\Gamma_{n+1}} \quad (17.14)$$

r_n^{TM} and r_n^{TE} denote the local plane wave TM and TE mode reflection coefficients. Therefore when $n = 0$, R_0^{TM} and R_0^{TE} are the transverse magnetic (TM) and transverse electric (TE) global reflection coefficients of all reflections and multiples from all multilayered interfaces.

17.2.3 Full-Wave Inversion

The inverse Fourier transform is used to obtain $\mathbf{g}_{11}(t)$ for both modeled and measured data:

$$\mathbf{g}_{11}(t) = F^{-1}\{\mathbf{G}_{11}(\omega)\} = \frac{1}{2\pi} \int_{-\infty}^{\infty} e^{i\omega t} \mathbf{G}_{11}(\omega) d\omega \quad (17.15)$$

The inverse problem is defined with the least-squares formulation, and the objective function is defined as:

$$\phi(\mathbf{b}) = \left(\mathbf{g}_{11}^{\uparrow*}(t) - \mathbf{g}_{11}^{\uparrow}(\mathbf{b}, t) \right)^T \left(\mathbf{g}_{11}^{\uparrow*}(t) - \mathbf{g}_{11}^{\uparrow}(\mathbf{b}, t) \right) \quad (17.16)$$

where $\mathbf{g}_{11}^{\uparrow*}(t)$ is the measured Green's function vector in the time domain with variable t being time. $\mathbf{g}_{11}^{\uparrow}(\mathbf{b}, t)$ including the parameter vector \mathbf{b} is the modeled Green's function. The up arrows indicates that those are the upward electric fields. Parameter vector $\mathbf{b} = [h_0, \varepsilon_r]$, where h_0 is the distance between antenna phase centre and soil surface, and ε_r is the relative dielectric permittivity of the half-space medium (soil in this case). In the forward modeling, besides these two variables, magnetic permeability μ_m for each layer is constant as in free space, and electrical conductivity σ can be neglected according to the operating frequency range [36]. The modeled GPR signals $\mathbf{g}_{11}^{\uparrow}$ are pre-computed and stored in a LUT, and the two variables lead to a 2D LUT in this study. The benefit of performing inversion in the time domain is that inversion can focus on the surface reflection only, by defining a maximum time for the considered waveform. The petrophysical relation of Topp et al. is used to estimate the volumetric soil water content based on the relative dielectric permittivity ε_r as Eq. (17.17) [21]. Finally, soil moisture map is generated by kriging interpolation.

$$\theta = -5.3 \times 10^{-2} + 2.92 \times 10^{-2} \varepsilon_r - 5.5 \times 10^{-4} \varepsilon_r^2 + 4.3 \times 10^{-6} \varepsilon_r^3 \quad (17.17)$$

17.3 Surface Soil Moisture Mapping in Agricultural Fields

The drone we used is an X8 model from RCTakeOff (Overijssel, Belgium). It has 4 arms with 8 motors and propellers. It can lift a charge up to 5 kg for a flight time of about 20 min, depending on the flying conditions. The radar consists of a microcomputer with homemade control application packages written in C++ and Javascript, a smartphone for remote control, a differential GPS for positioning, a handheld VNA, a half-wave dipole with an aperture of 50 cm operating in the 235–334 MHz frequency range, and a power bank for providing electricity to the whole radar system. The microcomputer connects to a wifi hotspot made by the smartphone, so users can control radar measurement remotely through the user interface, and preset measurement parameters like operating frequency range and steps, and project information. Measured data is stored on an SD card and data are subsequently processed on another computer. The drone-GPR is shown in Fig. 17.6.



Fig. 17.6 Half-wave dipole antenna and radar mounted on the drone

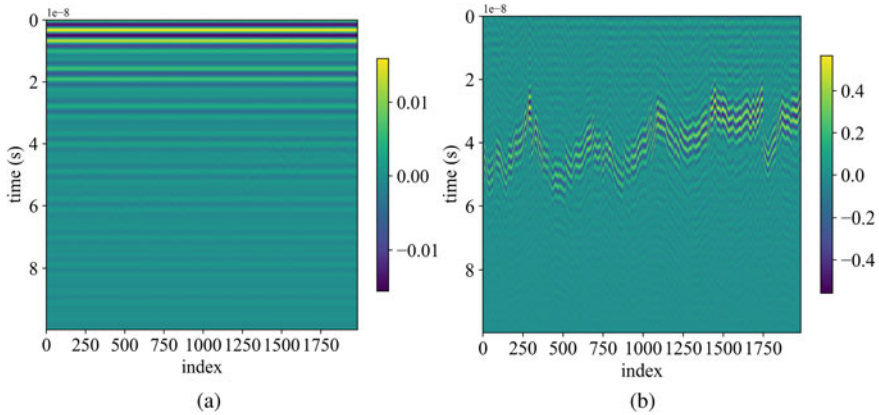


Fig. 17.7 Time-domain representation of radar measurements in a bare agricultural field. **a** Measured signal s_{11} (raw data). **b** Filtered signal g_{11}

The measurements were conducted over a bare agricultural field in Walloon Region, Belgium. The antenna transfer functions were determined from radar measurements performed at different heights over a lake as reference medium. For the measurements, the operating and processing frequency range were fixed as 235–334 MHz with a step of 1 MHz, and about 4–5 measurements were acquired per second. Flying height is around 4–8 m above the soil. For the electromagnetic model, soil roughness can be neglected within these low frequencies as roughness amplitude was relatively small compared to the wavelength following Rayleigh’s criterion. Parameters are fixed as:

$$\mathbf{h}_0 = [3.00 \ 3.01 \ 3.02 \ \dots \ 11.99 \ 12.00]^T \text{ m}$$

$$\boldsymbol{\epsilon}_r = [3.0 \ 3.5 \ 4.0 \ \dots \ 24.5 \ 25.0]^T$$

leading to a 2-D LUT of size 901×45 .

Figure 17.7 represents an example of the application of the radar equation Eq. (17.7) to filter out antenna effects from drone-borne GPR data acquired over the ground surface. s_{11} is raw data measured by VNA, and it contains a lot of reflection within antenna itself with large amplitude at early time, which overwhelms the surface reflection. Whereas in the filtered signal g_{11} , only the soil surface reflection is visible. Figure 17.8 shows the calibrated and measured R_i , in which the measured curve is obtained in free space conditions (drone flight at relatively high altitude). The calibrated and measured R_i correspond well within the frequency range of 235–334 MHz, R_i is less than 0.5, corresponding to a voltage standing wave ratio (VSWR) less than 3.

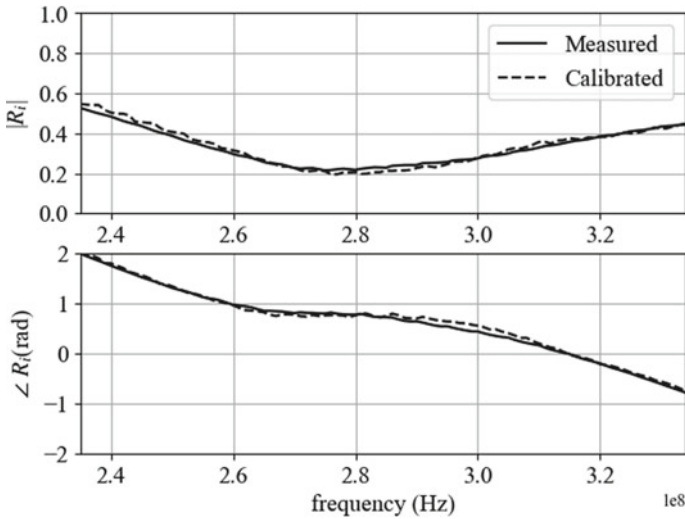


Fig. 17.8 Magnitude and phase of calibrated and measured feedback loss R_i

Figure 17.9 gives examples of objective functions and corresponding optimal fits with two different flying heights. From both examples, it is observed that the radar signal is more sensitive to h_0 than to ϵ_r . In addition, in the fitting example in Fig. 17.9b of the data from lower height, the measured and modeled signals agree better than in Fig. 17.9d. This is due to the damping of the soil surface reflection amplitude with increasing height in relation to the limited signal-to-noise ratio related to the low-power radar system (effective dynamic range of about 70 dB). Hence, flying height should be as small as possible. In particular, higher is the frequency, lower should be the flying height for a given signal-to-noise ratio.

The result is presented in Fig. 17.10, including the corresponding elevation map and soil orthophotography. We used the DJI Phantom 4 Pro for the elevation and orthophotography acquisition. The flying height is 90 m, and the resolution of the surface model is about 5 m. The elevation map was obtained from aerial drone photographs using photogrammetry, and was processed using Agisoft Metashape software. Figure 17.11 shows the soil water content distribution and its semivariogram. The soil moisture values fall well within the possible values of soil moisture, and the spatial correlation of soil moisture reaches about 25 m.

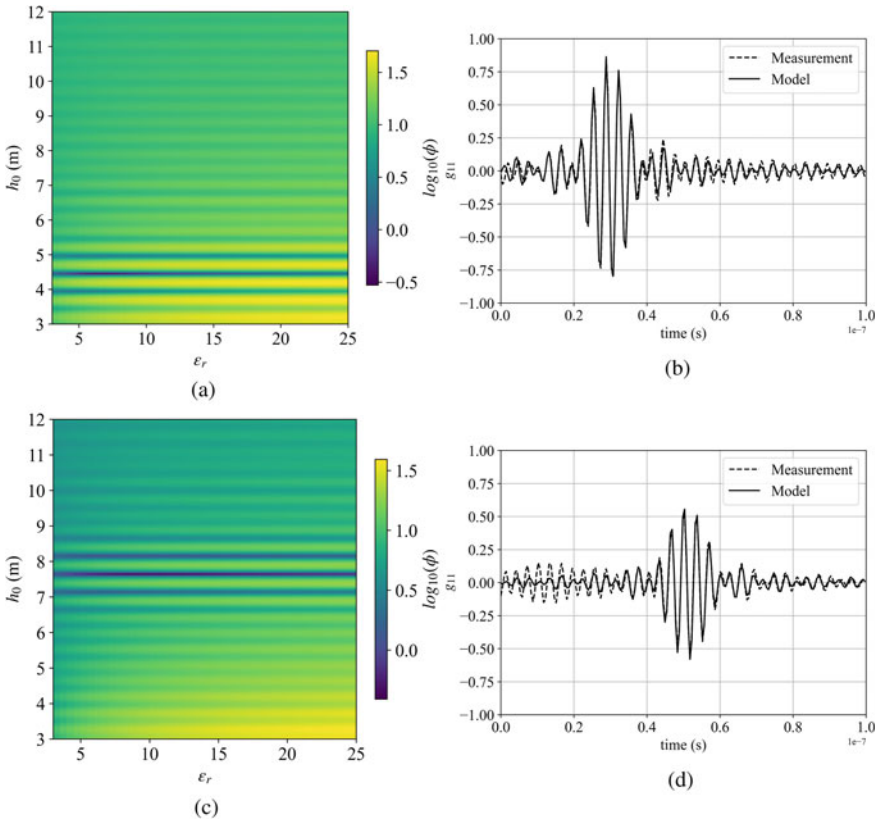
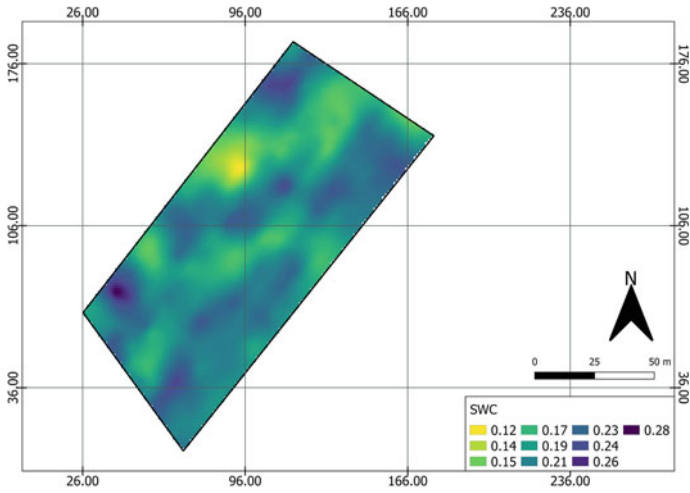


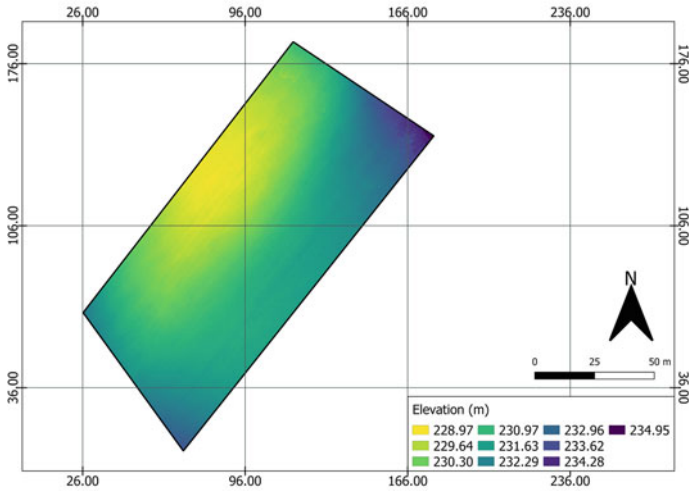
Fig. 17.9 Objective functions and fitting examples of full-wave inversion with different measuring heights (4.5 m for (a, b), 7.6 m for (c, d))

17.4 Summary and Perspectives

We have developed a new drone-GPR technology for fast and high-resolution digital soil mapping is achieved. The GPR system is lightweight, and the measurements can be controlled remotely. Full-wave inversion focused on the surface reflection in the time domain is applied to retrieve soil dielectric permittivity, hereby to get the soil water content. Besides these satisfying results, there are still some challenges to be addressed. A automatic drone flying mode is needed, in which the drone should fly following the field terrain, to make the distance between antenna and soil surface minimal for optimal signal-to-noise ratio. The incidence angle might affect inversion results due to the inherently non-uniform radiation pattern of the antenna. This research opens promising applications in precision agriculture, e.g., for optimizing irrigation.



(a)



(b)

Fig. 17.10 The agriculture field result: **a** soil moisture map, **b** digital elevation map, and **c** soil orthophotography. Coordinates are in WGS72/UTM zone 31N (m)

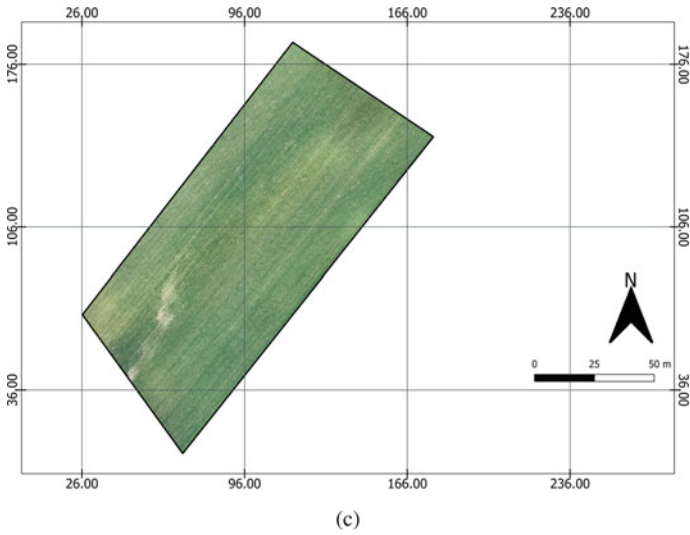


Fig. 17.10 (continued)

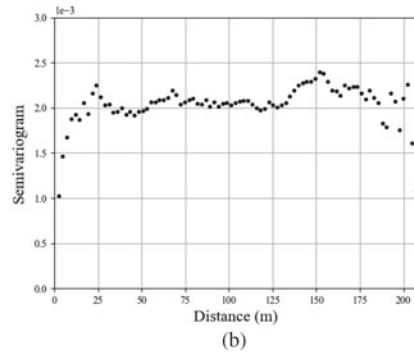
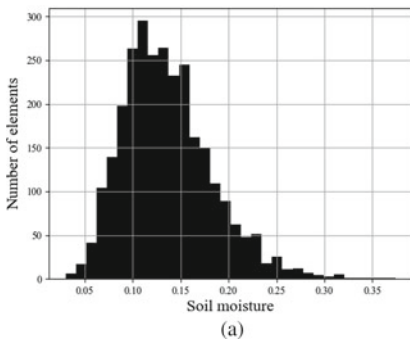


Fig. 17.11 The agriculture field: a soil moisture distribution, and b corresponding semivariogram

References

1. Dominati E, Patterson M, Mackay A (2010) A framework for classifying and quantifying the natural capital and ecosystem services of soils. *Ecol Econ* 69(9):1858–1868. <https://doi.org/10.1016/j.ecolecon.2010.05.002>
2. Corradini C (2014) Soil moisture in the development of hydrological processes and its determination at different spatial scales. *J Hydrol* 516:1–5. <https://doi.org/10.1016/j.jhydrol.2014.02.051>
3. Faticchi S, Or D, Walko R, Vereecken H, Young MH, Ghezzehei TA, Hengl T, Kollet S, Agam N, Avissar R (2020) Soil structure is an important omission in earth system models. *Nat Commun* 11(1):522. <https://doi.org/10.1038/s41467-020-14411-z>
4. Brocca L, Ciabatta L, Massari C, Camici S, Tarpanelli A (2017) Soil moisture for hydrological applications: open questions and new opportunities. *Water* 9(2). <https://doi.org/10.3390/w9020140>
5. Vereecken H, Huisman JA, Bogena H, Vanderborght J, Vrugt JA, Hopmans JW (2010) On the value of soil moisture measurements in vadose zone hydrology: a review. *Water Resour Res* 46(4). <https://doi.org/10.1029/2008WR006829>
6. Vereecken H, Aitkenhead M, Allison S, Assouline S, Baveye P, Berli M, Brüggemann N, Finke P, Flury M, Gaiser T, Govers G, Schnepf A, Ghezzehei T, Hallett P, Hendricks Franssen H, Heppell J, Horn R, Huisman J, Jacques D, Jonard F, Kollet S, Lafolie F, Hopmans J, Lamorski K, Leitner D, McBratney A, Minasny B, Montzka C, Nowak W, Pachepsky Y, Padarian J, Romano N, Roth K, Javaux M, Rothfuss Y, Rowe E, Schwen A, Šimunek J, Tiktak A, Van Dam J, van der Zee S, Vogel H, Vrugt J, Wöhling T, Or D, Young I, Roose T, Vanderborght J, Young M, Amelung W (2016) Modeling soil processes: review, key challenges, and new perspectives. *Vadose Zone J* 15(5). <https://doi.org/10.2136/vzj2015.09.0131>
7. Brevik EC, Cerdá A, Mataix-Solera J, Pereg L, Quinton JN, Six J, Van Oost K (2015) The interdisciplinary nature of soil. *Soil* 1(1):117–129. <https://doi.org/10.5194/soil-1-117-2015>
8. Minet J, Bogaert P, Vanclooster M, Lambot S (2012) Validation of ground penetrating radar full-waveform inversion for field scale soil moisture mapping. *J Hydrol* 424–425:112–123. <https://doi.org/10.1016/j.jhydrol.2011.12.034>
9. André F, van Leeuwen C, Saussez S, Van Durmen R, Bogaert P, Moghadas D, de Ressaéguier L, Delvaux B, Vereecken H, Lambot S (2012) High-resolution imaging of a vineyard in south of France using ground-penetrating radar, electromagnetic induction and electrical resistivity tomography. *J Appl Geophys* 78:113–122. <https://doi.org/10.1016/j.jappgeo.2011.08.002>
10. Doolittle J, Brevik E (2014) The use of electromagnetic induction techniques in soil studies. *Geoderma* s223–225:33–45. <https://doi.org/10.1016/j.geoderma.2014.01.027>
11. Brogi C, Huisman JA, Pätzold S, von Hebel C, Weihermüller L, Kaufmann MS, van der Kruk J, Vereecken H (2019) Large-scale soil mapping using multi-configuration EMI and supervised image classification. *Geoderma* 335:133–148. <https://doi.org/10.1016/j.geoderma.2018.08.001>
12. Loizos A, Plati C (2007) Accuracy of pavement thicknesses estimation using different ground penetrating radar analysis approaches. *NDT E Int* 40(2):147–157. <https://doi.org/10.1016/j.ndteint.2006.09.001>
13. Morcoux G, Erdogmus E (2010) Accuracy of ground-penetrating radar for concrete pavement thickness measurement. *J Perform Constr Facil* 24(6):610–621. [https://doi.org/10.1061/\(ASCE\)CF.1943-5509.0000123](https://doi.org/10.1061/(ASCE)CF.1943-5509.0000123)
14. Leng Z, Al-Qadi IL (2014) An innovative method for measuring pavement dielectric constant using the extended CMP method with two air-coupled GPR systems. *NDT E Int* 66:90–98. <https://doi.org/10.1016/j.ndteint.2014.05.002>
15. De Coster A, Van der Wielen A, Grégoire C, Lambot S (2018) Evaluation of pavement layer thicknesses using GPR: a comparison between full-wave inversion and the straight-ray method. *Constr Build Mater* 168:91–104. <https://doi.org/10.1016/j.conbuildmat.2018.02.100>

16. Jezova J, Mertens L, Lambot S (2016) Ground-penetrating radar for observing tree trunks and other cylindrical objects. *Constr Build Mater* 123:214–225. <https://doi.org/10.1016/j.conbuildmat.2016.07.005>
17. Ježová J, Lambot S (2019) A dielectric horn antenna and lightweight radar system for material inspection. *J Appl Geophys* 103822. <https://doi.org/10.1016/j.jappgeo.2019.103822>
18. Giannakis I, Tosti F, Lantini L, Alani A (2019) Health monitoring of tree trunks using ground penetrating radar. *IEEE Trans Geosci Remote Sens* 1–10. <https://doi.org/10.1109/TGRS.2019.2920224>
19. Daniels D (2006) A review of GPR for landmine detection. *Sens Imaging* 7:90–123. <https://doi.org/10.1007/s11220-006-0024-5>
20. Lopera O, Slob EC, Milisavljević N, Lambot S (2007) Filtering soil surface and antenna effects from GPR data to enhance landmine detection. *IEEE Trans Geosci Remote Sens* 45(3):707–717. <https://doi.org/10.1109/TGRS.2006.888136>
21. Topp GC, Davis JL, Annan AP (1980) Electromagnetic determination of soil water content: measurements in coaxial transmission lines. *Water Resour Res* 16(3):574–582. <https://doi.org/10.1029/WR016i003p00574>
22. Ledieu J, De Ridder P, De Clerck P, Dautrebande S (1986) A method of measuring soil moisture by time-domain reflectometry. *J Hydrol* 88(3):319–328. [https://doi.org/10.1016/0022-1694\(86\)90097-1](https://doi.org/10.1016/0022-1694(86)90097-1)
23. Huisman JA, Sperl C, Bouten W, Verstraten JM (2001) Soil water content measurements at different scales: accuracy of time domain reflectometry and ground-penetrating radar. *J Hydrol* 245(1–4):48–58. [https://doi.org/10.1016/S0022-1694\(01\)00336-5](https://doi.org/10.1016/S0022-1694(01)00336-5)
24. Binley A, Winship P, Middleton R, Pokar M, West J (2001) High-resolution characterization of vadose zone dynamics using cross-borehole radar. *Water Resour Res* 37(11):2639–2652. <https://doi.org/10.1029/2000WR000089>
25. Huisman JA, Snepvangers JJJ, Bouten W, Heuvelink GBM (2002) Mapping spatial variation in surface soil water content: comparison of ground-penetrating radar and time domain reflectometry. *J Hydrol* 269(3):194–207. [https://doi.org/10.1016/S0022-1694\(02\)00239-1](https://doi.org/10.1016/S0022-1694(02)00239-1)
26. Buursink M, Clement W, Knoll M (2002) Use of vertical-radar profiling to estimate porosity at two new England sites and comparison with neutron log porosity. <https://doi.org/10.4133/1.2927127>
27. Galagedara L, Parkin GW, Redman JD, von Bertoldi A, Endres A (2005) Field studies of the GPR ground wave method for estimating soil water content during irrigation and drainage. *J Hydrol* 301:182–197. <https://doi.org/10.1016/j.jhydrol.2004.06.031>
28. Forte E, Pipan M (2017) Review of multi-offset GPR applications: data acquisition, processing and analysis. *Sign Process* 132:210–220. <https://doi.org/10.1016/j.sigpro.2016.04.011>
29. Pettinelli E, Vannaroni G, Pasquo B, Mattei E, Di Matteo A, De Santis A, Annan P (2007) Correlation between near-surface electromagnetic soil parameters and early-time GPR signals: an experimental study. *Geophysics* 72. <https://doi.org/10.1190/1.2435171>
30. Matteo AD, Pettinelli E, Slob E (2013) Early-time GPR signal attributes to estimate soil dielectric permittivity: a theoretical study. *IEEE Trans Geosci Remote Sens* 51(3):1643–1654. <https://doi.org/10.1109/TGRS.2012.2206817>
31. Pettinelli E, Di Matteo A, Beaubien SE, Mattei E, Lauro SE, Galli A, Vannaroni G (2014) A controlled experiment to investigate the correlation between early-time signal attributes of ground-coupled radar and soil dielectric properties. *J Appl Geophys* 101:68–76. <https://doi.org/10.1016/j.jappgeo.2013.11.012>
32. Algeo J, Van Dam R, Slater L (2016) Early-time GPR: a method to monitor spatial variations in soil water content during irrigation in clay soils. *Vadose Zone J* 15. <https://doi.org/10.2136/vzj2016.03.0026>
33. Comite D, Galli A, Lauro SE, Mattei E, Pettinelli E (2016) Analysis of GPR early-time signal features for the evaluation of soil permittivity through numerical and experimental surveys. *IEEE J Sel Top Appl Earth Obs Remote Sens* 9(1):178–187. <https://doi.org/10.1109/JSTARS.2015.2466174>

34. Lambot S, Slob EC, Van Bosch ID, Stockbroeckx B, Vanclooster M (2004) Modeling of ground-penetrating radar for accurate characterization of subsurface electric properties. *IEEE Trans Geosci Remote Sens* 42(11):2555–2568. <https://doi.org/10.1109/TGRS.2004.834800>
35. Lambot S, André F (2014) Full-wave modeling of near-field radar data for planar layered media reconstruction. *IEEE Trans Geosci Remote Sens* 52(5):2295–2303. <https://doi.org/10.1109/TGRS.2013.2259243>
36. Lambot S, Weihenmüller L, Huisman JA, Vereecken H, Vanclooster M, Slob EC (2006) Analysis of air-launched ground-penetrating radar techniques to measure the soil surface water content. *Water Resour Res* 42(11). <https://doi.org/10.1029/2006WR005097>
37. Sen MK, Stoffa PL, Seifoullaev RK, Fokkema JT (2003) Numerical and field investigations of GPR: toward an airborne GPR. *Subsurface Sens Technol Appl* 4(1):41–60. <https://doi.org/10.1023/a:1023011413969>
38. Machguth H, Eisen O, Paul F, Hoelzle M (2006) Strong spatial variability of snow accumulation observed with helicopter-borne GPR on two adjacent alpine glaciers. *Geophys Res Lett* 33(13). <https://doi.org/10.1029/2006GL026576>
39. Siemon B, Christiansen A, Auken E (2009) A review of helicopter-borne electromagnetic method for groundwater exploration. *Near Surface Geophys* 7:629–646. <https://doi.org/10.3997/1873-0604.2009043>
40. Catapano I, Crocco L, Krellmann Y, Trilitzsch G, Soldovieri F (2012) A tomographic approach for helicopter-borne ground penetrating radar imaging. *IEEE Geosci Remote Sens Lett* 9(3):378–382. <https://doi.org/10.1109/LGRS.2011.2169390>
41. Siemon B, Seht M, Steuer A, Deus N, Wiederhold H (2020) Airborne electromagnetic, magnetic, and radiometric surveys at the German North Sea coast applied to groundwater and soil investigations. *Remote Sens* 12:1629. <https://doi.org/10.3390/rs12101629>
42. Floreano D, Wood RJ (2015) Science, technology and the future of small autonomous drones. *Nature* 521(7553):460–466. <https://doi.org/10.1038/nature14542>
43. Kardasz P, Doskocz J (2016) Drones and possibilities of their using. *J Civ Environ Eng* 6. <https://doi.org/10.4172/2165-784X.1000233>
44. Coops N, Goodbody T, Cao L (2019) Four steps to extend drone use in research. *Nature* 572:433–435. <https://doi.org/10.1038/d41586-019-02474-y>
45. Colorado J, Perez M, Mondragon I, Mendez D, Parra C, Devia C, Martinez-Moritz J, Neira L (2017) An integrated aerial system for landmine detection: SDR-based ground penetrating radar onboard an autonomous drone. *Adv Robot* 31(15):791–808. <https://doi.org/10.1080/01691864.2017.1351393>
46. Ludeno G, Catapano I, Gennarelli G, Soldovieri F, Vetrella AR, Renga A, Fasano G (2017) A micro-UAV-borne system for radar imaging: a feasibility study. In: 2017 9th International workshop on advanced ground penetrating radar, IWAGPR 2017—Proceedings. <https://doi.org/10.1109/IWAGPR.2017.7996034>
47. Ludeno G, Catapano I, Renga A, Vetrella AR, Fasano G, Soldovieri F (2018) Assessment of a micro-UAV system for microwave tomography radar imaging. *Remote Sens Environ* 212:90–102. <https://doi.org/10.1016/j.rse.2018.04.040>
48. Garcia-Fernandez M, Morgenthaler A, Alvarez-Lopez Y, Las Heras F, Rappaport C (2019) Bistatic landmine and IED detection combining vehicle and drone mounted GPR sensors. *Remote Sens* 11(19). <https://doi.org/10.3390/rs11192299>
49. Garcia-Fernandez M, Alvarez-Lopez Y, Heras FL, Morgenthaler A, Rappaport C (2019) Analysis of multistatic vehicle-drone ground penetrating radar configurations for mine detection. In: 2019 IEEE International symposium on antennas and propagation and USNC-URSI radio science meeting, pp 1637–1638. <https://doi.org/10.1109/APUSNCURSINRSM.2019.8888340>
50. Sipos D, Gleich D (2020) A lightweight and low-power UAV-borne ground penetrating radar design for landmine detection. *Sensors* 20:2234. <https://doi.org/10.3390/s20082234>
51. Noviello C, Esposito G, Fasano G, Renga A, Soldovieri F, Catapano I (2020) Small-UAV radar imaging system performance with GPS and CDGPS based motion compensation. *Remote Sens* 12(20). <https://doi.org/10.3390/rs12203463>

52. Lambot S, Slob E, Chavarro D, Lubczynski M, Vereecken H (2008) Measuring soil surface water content in irrigated areas of southern Tunisia using full-waveform inversion of proximal GPR data. *Near Surface Geophys* 6(6):403–410. <https://doi.org/10.3997/1873-0604.2008028>
53. Minet J, Lambot S, Slob EC, Vanclooster M (2010) Soil surface water content estimation by full-waveform GPR signal inversion in the presence of thin layers. *IEEE Trans Geosci Remote Sens* 48(3):1138–1150. <https://doi.org/10.1109/TGRS.2009.2031907>
54. Wu K, Rodriguez GA, Zajc M, Jacquemin E, Clément M, De Coster A, Lambot S (2019) A new drone-borne GPR for soil moisture mapping. *Remote Sens Environ* 235:111456. <https://doi.org/10.1016/j.rse.2019.111456>
55. Klotzsche A, Jonard F, Looms M, Kruk J, Huisman J (2018) Measuring soil water content with ground penetrating radar: a decade of progress. *Vadose Zone J* 17. <https://doi.org/10.2136/vzj2018.03.0052>
56. Tran AP, Andre F, Craeye C, Lambot S (2013) Near-field or far-field full-wave ground penetrating radar modeling as a function of the antenna height above a planar layered medium. *Prog Electromagnet Res* 141:415–430. <https://doi.org/10.2528/PIER13053106>
57. Michalski KA, Mosig JR (1997) Multilayered media green's functions in integral equation formulations. *IEEE Trans Antennas Propag* 45(3):508–519. <https://doi.org/10.1109/8.558666>

Chapter 18

Seismic Methods for Aquifer Analysis: The Basso Livenza Case Study



Umberta Tinivella, Michela Giustiniani, Stefano Picotti, and Flavio Accaino

Abstract In the last decades, many efforts have been dedicated to improve direct and indirect methodologies to study and monitor the aquifers. In particular, seismic method was successfully applied for this purpose. In this work a case study in the North East of Italy is described, for which seismic data were acquired and analyzed to characterize an aquifer system. All the phases of the experiment are illustrated, from the choice of the acquisition parameters to the final interpretation. Both 2D and 3D data were acquired in different seasons in order to define any possible seasonal variation. In order to obtain detailed petrophysical information, amplitude preserving processing, advanced tomographic imaging and Amplitude Versus Offset procedures were used. This analysis enabled to estimate the petro-physical properties of the subsoil and to locate a deeper aquifer not yet identified, as confirmed by a subsequent new well. The discovered aquifer, at 480 m depth, has been proved to be suitable for capturing for domestic purposes.

18.1 Introduction

Indiscriminate use of water and poor protection of resources pose dangers to future generations even in areas where water is plentiful. The combined challenges of population growth, pollution and climatic changes add urgency to this problem.

In the last decades, the scientific community has spent many efforts to improve direct and indirect methodologies applied in engineering and environmental investigations and, in particular, to study and monitor the aquifers (i.e., [57]). The use of the seismic method has become more frequent due to its cost-effectiveness and suitability in near-surface investigations [28, 50]. In particular, by recording both P- and S-wave data, it is very efficient in determining the properties of subsurface [25–27, 34, 36, 50, 65, 66]. The seismic method has been used in several geological contexts, such as on Quaternary deposits and on various hydrogeological studies of

U. Tinivella · M. Giustiniani (✉) · S. Picotti · F. Accaino
National Institute of Oceanography and Applied Geophysics—OGS, Borgo Grotta Gigante 42C,
34010 Trieste, Italy
e-mail: mgiustiniani@ogs.it

tunnel valley aquifers in USA and Canada (i.e., [4, 45, 46, 50, 63]) and Northern Europe [33, 35, 42] as well as in esker characterization in Canada [8, 19, 20, 50, 51, 56], in Finland [5, 14, 41] and in the Alpine range [15]. In addition, the seismic method has been applied in urban environments [13, 25–27, 36] and in the shallow subsurface imaging of transport routes [40, 48]. In particular, the seismic reflection technique did not become technically or economically viable in the field of shallow hydrogeology until the 1980s. In the next decades, this technique has been applied to many hydrogeological problems with varying results. Bachrach and Nur [7] have clearly shown the relation between the water table and its seismic image, as well as the seismic response of the subsurface under different wetting and draining situations. Cardimona et al. [16] and Whiteley et al. [69] have shown good examples of seismic surveys to map shallow aquifers. Bradford and Sawyer [12] and Giustiniani et al. [25, 26] have illustrated that pre-stack depth migration can significantly improve quality and accuracy of the seismic image for hydrogeologic purposes. The relationship between lithological properties and body wave velocity has been explored, for many years, as a means of indirectly characterizing porous aquifers (i.e. [61]). In existing literature, different approaches have been proposed: in some cases the water table level is attributed to specific compressional wave velocity (VP) values [30, 31, 53, 72], in others, the hypothetical aquifer layer is identified by the ration between VP and shear wave velocity (VS; [18, 43, 59, 61]), Poisson's ratio [26, 37] or water seismic index that is theoretically derived from the propagation of VP in 2D or 3D models of water table surfaces in unsaturated–saturated interfaces [29]. In addition, more complex theory-based approaches exist, which derive from the principles of the elastic wave propagation within saturated and unsaturated porous media [22]. These approaches require a preliminary and detailed knowledge of the lithological sequences of the site under investigation.

The high resolution seismic reflection method provides important information about the variations in bedrock topography and about continuities and thicknesses of sedimentary units, which control groundwater formation and flow patterns. Seismic interpretation of the sedimentary sequences can be used to estimate the continuity of different units and extrapolate them outside the seismic profiles.

In this context, the European Commission supported several projects in order to define a protocol to characterize aquifers by using integrated methodologies. The “Water-bearing characterization with integrated methodologies—CAMI” project (LIFE04 ENV/IT/000500), based in the Torrate di Chions area of north-east Italy (Fig. 18.1), was designed to support the Water Framework EU Directive by using a new integrated approach to assess and manage a water-basin area. It aimed to become a model to be transferred to other river basin areas. The project developed and tested a method of combining works across a range of different scientific disciplines to identify ways to achieve better sustainability in water resources exploitation. This purpose entails detailed investigation into the characteristics of the hydro-geological district and then an evaluation of the impact of human activity.

The CAMI project was designed mainly to (i) assist planning of water resources for different uses (civil, agricultural, industrial), (ii) provide evaluation methods for the impact of new industrial and civil settlements on water resources, (iii) model ways of

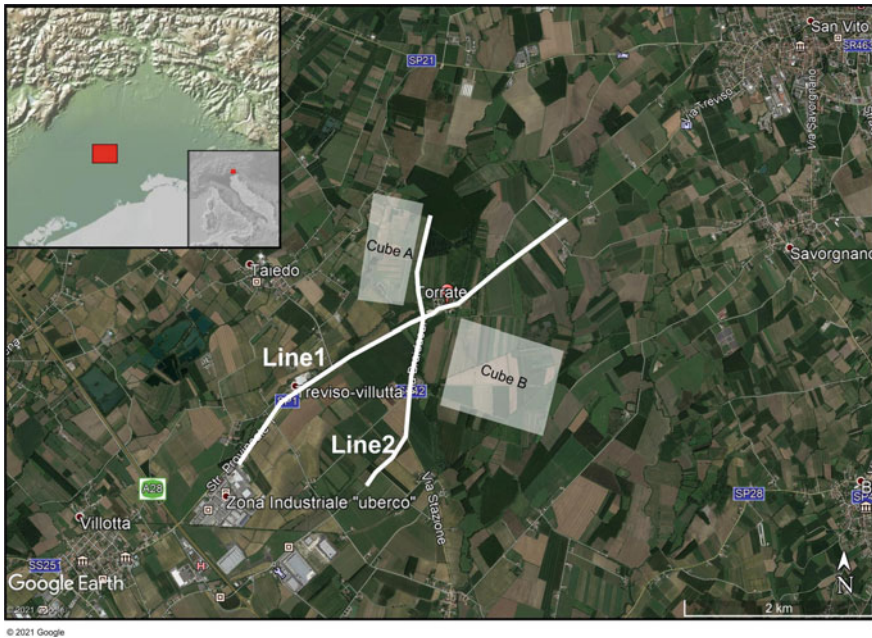


Fig. 18.1 Location Map of the 2D and 3D seismic data acquired in the frame of the CAMI project

quantifying groundwater, and (iv) provide data for research into management of water ecosystems. The experience of the CAMI project is very useful to future analysis of aquifers. Here, we reported the results obtained from the application of seismic methodology to characterise aquifers, underlining advantages and disadvantages of the method.

18.2 Seismic Acquisition

The cost of a water catchment systems for aquifers exploitation can be significant, especially for the high drilling costs. In order to reduce these costs, it is useful to carry out geophysical surveys to define the geometry of the aquifer system in depth and to extract the petrophysical characteristics of the subsoil. This approach allows to define the best location for extraction wells, avoiding poorly productive wells.

The first step of defining a seismic acquisition for an aquifer study is to collect all the information already existing on the investigated area, such as geology, petrophysical characteristics of the sediments, and typology and depth of the aquifer. On the basis of this information, geophysical investigations will be planned and carried out to obtain all the missing information for defining the aquifer and to determine the characteristics of the catchment well. The available information can be used to build

an initial 3D geophysical model to simulate a seismic acquisition. The modeling is necessary to optimize the seismic acquisition configuration in order to have the appropriate characteristics, i.e. a sufficient resolution and coverage, in particular to detect the shallower aquifer, and adequate offset to correctly define the seismic velocities in depth. The same approach should be adopted to simulate both P- and S-wave data acquisition.

In the frame of the CAMI project, this procedure was successfully applied (i.e., [27]). An initial 3D geophysical model was built and used to simulate a seismic data acquisition and to create a synthetic shot gather, as shown in Fig. 18.2. In this case the initial geophysical model was built by using the stratigraphy of several water catchment wells present in the study area and the information from some seismic sections acquired in the frame of the Italian CROsta Profonda (CROP) Project (i.e., [44, 55]). Information not available in this area, such as S-wave velocity, density and quality factors of both P and S waves, were defined either using values present in the literature for similar geological formations or by using empirical equations [10, 49, 54]. The model included alternating water-saturated gravel layers and clay impermeable layers, where the latter are characterized by lower velocities as proved by laboratory measurements [10].

After the modeling and the analysis of the synthetic data, a field test to confirm the goodness of the acquisition parameters is indispensable. The field test allows also to define the source characteristics, such as the best sweep, if the Vibroseis is used as source, and to investigate the random and the coherent noise (ground roll). If the adopted source is dynamite, it is indispensable to define the amount of explosive to

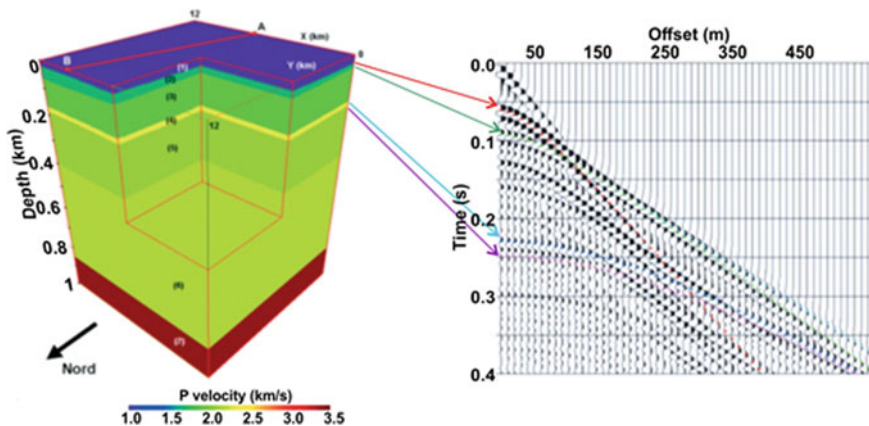


Fig. 18.2 Left: The synthetic 3D seismic model of the aquifer system. The seismic simulation was carried out along the line AB. Right: The simulated seismogram of a shot ensemble recorded at 80 Hz. The events of interest are the reflections from the second layer (red and green) and from the fourth layer (blue and purple), and the refraction related to the second layer (sky-blue). Modified after Giustiniani et al. [27]

obtain an adequate resolution and investigation depth. The shot depth has also to be carefully defined in order to avoid a strong ground roll.

The main recording parameters that must be defined are: acquisition cable length, inter-trace interval, time sampling and record length. The adopted acquisition parameters for the 2D data acquisition are summarized in Table 18.1.

In this case study, an asymmetric pattern configuration was adopted, with a maximum offset of 300 m and 1000 m to the left and to the right of the shot, respectively. Shot and receiver intervals have been chosen in order to obtain an adequate coverage for both the shallower and deeper aquifers. This choice was made in order to obtain information about the velocity of the shallower structures. For this purpose we have used refracted events which, in order to obtain reliable results, require conjugated profiles. An offset of 300 m allows for investigating 100 m in depth.

After the definition of the acquisition parameters it is essential to plan the acquisition from the time point of view. In this case, it is necessary to acquire the same dataset in two different seasons, in order to identify the variations of the seismic parameters as a function of the seasonal variations of the aquifer. Another factor that should be considered is the complexity of the investigated area from a geological and petro-physical point of view. This evaluation is important to choose if 2D lines are enough or if it is necessary to carry out a 3D survey. In the case of a 3D survey, a modeling to define the distance between in-line, cross-line and shot distance should be performed to obtain a homogeneous coverage inside the investigated area.

In this case study, two 3D seismic acquisitions in two different areas were done (Fig. 18.1). The first one of about 0.4 km² and the second one of 0.6 km². In each area, two surveys in two different seasons, in spring (March) and in summer (July), were carried out. The geometry acquisition of the two cubes is characterized by a line spacing (in-line) and receiver interval of 18 m. The source interval and the shot line spacing (cross-line) are of 18 m and 36 m respectively. In order to obtain adequate binning coverage a bin size of 9 m × 9 m was adopted [27]. Unfortunately, despite this, the two cubes are characterized by differences in the coverage due to environmental problems that strongly influenced the seismic acquisition.

18.3 Seismic Analysis

18.3.1 *Traveltime Reflection Tomography and Modeling in Depth*

Two sets of parameters usually characterize a seismic earth model in depth: the interval seismic velocities and the interfaces geometry. The estimation of these parameters with high accuracy represents a challenging task for seismic exploration. The subsurface seismic imaging is finally realised by the pre-stack depth migration, which migrates, using the final velocity field, the seismic data into a depth section. More reliable is the velocity field supplied to the migration algorithm, more realistic

will be the depth imaging. Seismic tomography represents a versatile tool for estimating the interval velocity field and the depth of the interpreted horizons. Compared to the conventional velocity analysis, it allows a better definition of the vertical and lateral velocity variations, which is considerably important for a reliable reconstruction of the real subsurface structures. In this case study, we employed two methods to build the velocity-depth aquifer model, schematized in Fig. 18.3: the traveltime reflection tomography for the two 2D profiles (panel a), and the modeling in depth technique for the 3D cubes (panel b).

The first method reconstructs the velocity-depth structures by performing a tomographic inversion of reflected arrival traveltimes picked on the pre-stack seismic data. Several algorithms are available; here, the adopted tomographic algorithm, the CAT-3D software [68], is based on a procedure involving the simultaneous iterative reconstruction algorithm [58, 64] and the minimum-time ray tracing [9]. The algorithm estimates the velocity field and the reflector structure in sequence, from the shallowest to the deepest horizon. The model consists of voxels, in which the velocity is assumed vertically constant, and whose base and top define the interfaces. For each horizon an iterative procedure is used, starting from a constant velocity within the layers and horizontally flat interface (Fig. 18.3a). At each iteration, the picked travel times of the reflected events are first inverted in order to update the velocity model. Then, the new interfaces are estimated, following the principle of minimum dispersion of the reflected points [17]. The travel time residuals associated to each reflected event is then converted to depth by using the velocity field updated in the first step of any iteration. The inversion proceeds by simultaneous iterative adjustments of the velocity field and the depth of the interfaces. The loop ends when the variations of the resulting model with respect to that of the previous step are sufficiently small. This occurs when the dispersion of the estimated reflection points reaches a minimum, so that the reconstructed interface geometry does not vary considerably anymore. At

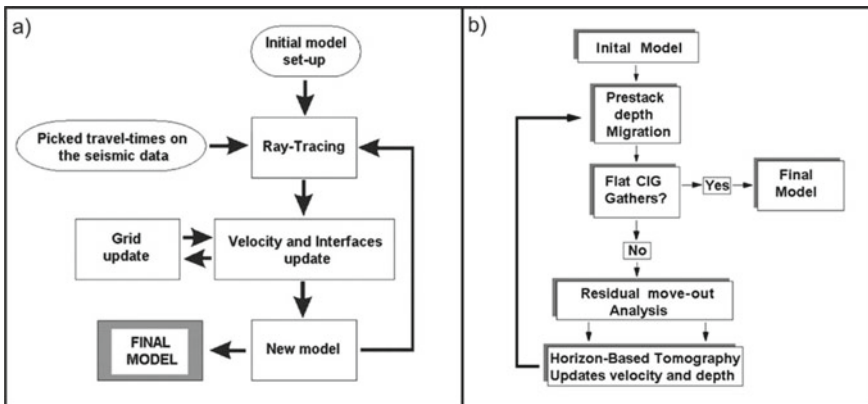


Fig. 18.3 Flow-chart of the traveltime reflection tomography **a** and modeling in depth **b** procedures. After Giustiniani et al. [26, 27]

the end of the inversion, a chi-squared test to the picked and computed traveltimes is applied, to evaluate the reliability of the tomographic model [71].

The second method consists in an iterative updating procedure for refining and improving an initial model in depth, involving pre-stack depth migration, residual move-out analysis and seismic reflection tomography. The software adopted in this work is the Paradigm® GeoDepth® package, and the applied modelling flow-chart is shown in Fig. 18.3b. The initial model generally consists in an horizontally layered structure with laterally invariant velocities, or in a partially refined model obtained from other techniques and information. Residual move-out analysis uses semblance sections computed vertically or along interpreted horizons on a depth migrated section, to find the residual errors in the computed interval velocity field. If the velocity field has been estimated with sufficient accuracy, then the common image gathers (CIGs) derived from the pre-stack depth migration using this model should exhibit a flat sequence of events (i.e., [62]). Any error in interval velocities and/or reflector geometries should give rise to a residual move-out along the distribution of events on the CIGs (i.e., [39]). The degree of no-flatness of the reflection events on the CIGs is a measurement of the error in the model, and residual move-out analysis identifies the correction required to flatten the reflection events (i.e., [67]). Tomography is then performed, following the grid- and/or horizon-based approach, to refine the velocity-depth model. It uses residuals as input and attempts to obtain a better model by minimizing the errors in the velocity field and horizon geometry. According to the flow-chart in Fig. 18.3b, a new pre-stack depth migration is performed using the velocity field derived from the tomographic inversion.

At each iteration, both velocity and reflector geometries are updated, until the two sets of parameters reach a good degree of stability. Generally, stability is achieved when the CIGs exhibit a flat sequence of events, and the velocity-depth model is consistent with the depth image. Therefore, the result of modelling updating needs to be verified for consistency with the seismic data (i.e., the final imaging section) and examined for any remaining residual move-outs to decide whether or not to continue with the iterations of tomographic update (i.e., [70]). The main consistency checks are the following:

1. Overlay the depth horizons from the updated model onto the image section derived from pre-stack depth migration and note if they coincide with the reflectors associated with the layer boundaries included in the model.
2. Compute the residual move-out semblance spectra from the CIGs at selected locations after the model update and compare them with those before the update.

Consistency may be achieved with only a few iterations when the initial residual move-outs are small.

18.3.2 2D Seismic Data

The analysis of seismic data for aquifer characterisation is finalised to extract geometrical and petrophysical information. To better explain the procedure for aquifer characterisation, we report here the experience gained in the frame of the CAMI project (i.e., [25–27, 47]).

As already mentioned 2D seismic data was acquired to optimise a later 4D survey (i.e., 3D survey repeated in time) with the purpose of monitoring the changes occurring in the aquifers between different seasons. The 2D raw seismic data quality was satisfactory, despite the ground-roll. The reflections related to the presence of the aquifers are evident from 0.03 to about 1.1 s, while the refractions are not always detectable because of velocity inversions caused by the alternance of permeable and impermeable layers [10]. The processing was focused to enhance the signal-to-noise ratio and to increase the vertical resolution; the ‘true-amplitude’ approach was adopted in order to preserve the relative amplitudes of the reflected energy [70], essential to perform amplitude versus offset (AVO) analysis [38, 60]. After editing the traces showing a persistent level of noise, a band-pass filter was applied to attenuate the low and high frequency noise and a 50 Hz notch filter to suppress the power line noise. After a spherical divergence correction, the data were deconvolved using a 200 ms length predictive deconvolution operator with a gap of 8 ms and a white noise level of 1%. To attenuate the ground-roll, a trimmed mean dynamic dip filter was applied on the shot ensembles [32, 70]. The ground-roll removal greatly facilitate the picking of the reflected events used for the tomographic inversion. Then, a surface consistent residual static correction, using the tomographic velocity field, was calculated and applied to attenuate the effects due to strong shallow lateral velocity variations, due to the presence of soft plough, harder untilled land and roads. This correction improves the results of the tomographic technique, which is based on the ray theory. Explained in the previous paragraph, seismic tomography is more reliable than the standard stacking velocity analysis methods [11, 12].

Hence, the tomographic velocity fields, converted from interval to root-mean square (RMS) velocity, were used to stack the data, after the application of an external mute function to remove the stretched direct arrivals. During the processing, the amplitude spectrum should be checked in order to prevent any possible modifications, as required by the AVO analysis. A time-variant filter and F-X deconvolution were applied to the post-stack data to further increase the signal-to-noise ratio and the lateral continuity of the signal [70]. The final 2D stacked sections are reported in Fig. 18.4, showing the good correlations between the main reflections at the intersection of the seismic lines. The seismic sections show the presence of two principal aquifers at about 30 and 180 m depth, respectively.

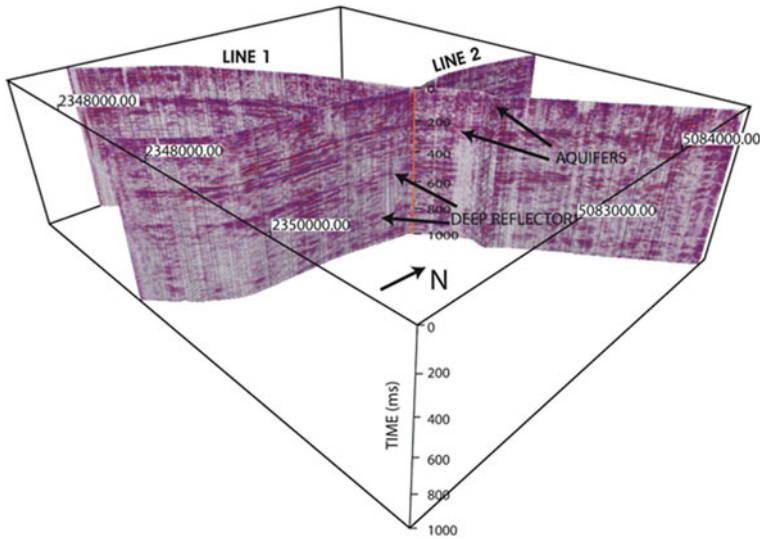


Fig. 18.4 The correlation between the 2D acquired seismic lines. After Giustiniani et al. [26]

18.3.3 3D Seismic Cubes

The quality of the 3D raw data was satisfactory, despite the ground-roll. Similarly to the 2D dataset, the reflections of interest are evident from 0.1 s to about 1 s, while the refractions are not always detectable because of velocity inversions caused by the alternation of impermeable and water filled permeable layers [10]. The processing was focused to enhance the signal-to-noise ratio and to increase the vertical resolution for the AVO analysis, as already explained for the 2D seismic data. After editing the traces showing a persistent level of noise, we applied a 20–160 Hz band-pass filter to remove the low- and high-frequency noise. After applying a spherical divergence correction using the seismic velocity field obtained from the imaging procedure, a predictive deconvolution was applied with a 120 ms operator length and a lag of 5 ms. A white noise level of 1% was added to stabilize the procedure. In the study area, the lateral variation of lithological composition in the shallow subsurface layers causes strong shallow lateral velocity variations. Thus, we performed a surface consistent residual static correction using the velocity field obtained from the iterative updating procedure, as described in the previous section. The obtained velocity fields, converted from interval to RMS velocity, were used to stack the data, after the application of a muting function to remove the stretched direct arrivals. A time-variant filter and F-X deconvolution was then applied to the post-stack data to further increase the signal-to-noise ratio and the lateral continuity of the signals of the different interfaces.

18.3.4 AVO Analysis

The pre-stack data analysis underlines the presence of AVO effects associated with lithologic changes and/or the presence of fluids at high pressure [61]. In fact, P-wave velocity depends on both fluid and solid properties and the S-wave velocity depends mainly on the solid properties. To obtain the sections showing the normalized change in P- and S-wave velocities, we linearized Zoeppritz's equations using the Aki-Richards method [6]. This approach considers the linearization of the equations with respect to the P-wave velocity reflectivity (mainly influenced by the near offsets; R_{VP}), the S-wave velocity reflectivity (mainly influenced by the medium-large offsets; R_{VS}) and the density reflectivity (related to the very large offsets; R_ρ). Although in theory the solution for all three reflectivities is attainable, in practice, because of numerical reasons (e.g., matrix stability, limited aperture, noise and incomplete amplitude recovery), R_ρ estimation is unstable. Therefore, the density is represented empirically in terms of P-wave velocity by using the Gardner formula [24] and AVO is solved for the R_{VP} and the R_{VS} parameters only. Then, the AVO inversion process calculates the elastic earth variables, obtaining two sections in the time domain that show the normalized change in P- and S-wave velocities. Recalling that the P-wave velocity depends on both fluid and solid properties and the S-wave velocity depends mainly on the solid properties, the joint analysis of the AVO sections provides information about the nature of the main reflections (i.e., [38, 60]). If a reflection is present in both sections, it is mainly caused by a change of the solid properties at the interface, i.e., by a lithologic change. On the contrary, if a reflection is identified only in the P-wave reflectivity section, the contrast of P-wave velocity without any change of the S-wave velocity can be justified assuming fluid content changes at the interface (i.e., [1, 2]).

18.4 Results

18.4.1 2D Depth Models

The final tomographic P-wave velocity model of Line 2 (Fig. 18.1), obtained using the traveltimes reflection tomography (Fig. 18.3a), is reported in Fig. 18.5b as an example of seismic results. The high resolution of the acquired seismic data allowed the recovery of the thickness of the two aquifers (layers 2 and 4). The dominant frequency of the first 400 ms is about 80 Hz that implies an average picking error of ± 6 ms. This error is equivalent to about half wavelet cycle, and causes a mean deviation in the velocities inside the two aquifers of about ± 15 m/s. The tomographic velocity model (Fig. 18.5b) evidences the presence of a velocity inversion between the fourth (second aquifer) and fifth layer. Moreover, the two shallow aquifers are nearly flat and show noticeable lateral velocity variations with a maximum excursion of about 600 m/s, whereas the structures of the deeper reflectors are more irregular.

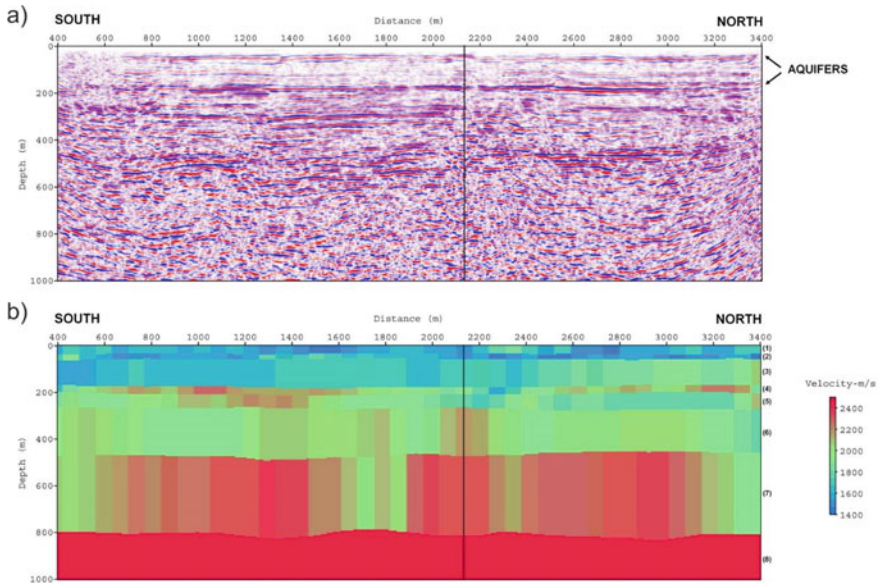


Fig. 18.5 Prestack depth migration **a** and final tomographic P-wave velocity model **b** of the Line 2. The vertical solid line indicates the intersection between Line 1 and Line 2. Modified after Giustiniani et al. [25]

For these reasons and in order to improve the quality of the depth seismic imaging, a pre-stack depth migration is necessary. The horizons of the final depth migrated profile show a good lateral continuity (Fig. 18.5a). Comparing the migrated sections and the velocity models of the two lines at their intersection, a good correlation both for the depth of the reflectors and layer velocities has been found [25, 26].

18.4.2 3D Depth Models

The results of the 2D seismic analysis was indispensable to define a preliminary subsurface geometry [25, 26], to analyse the seismic response of the aquifers and to plan and optimise a subsequent 4D survey [47]. As already mentioned, two different areas called A (about 0.4 km²) and B (about 0.6 km²) were investigated (Fig. 18.1). In each area, we carried out two surveys: the first one in March 2006 acquiring two cubes called CubeA-spring and CubeB-spring, respectively, and the second in July 2006 obtaining the CubeA-summer and CubeB-summer. The 2D velocity models of analysed lines obtained by using tomographic inversion were interpolated to build a 3D velocity model, adopted as an initial model for depth modelling of 3D seismic data.

The final tomographic P-wave velocity models of Cube A and Cube B, acquired in the spring season and obtained using the modeling in depth procedure (Fig. 18.3b), are represented in Fig. 18.6b,d. In this case, as already mentioned, the initial model was the 3D interpolated velocity field obtained from the tomographic inversions of the 2D seismic lines (Fig. 18.5; Giustiniani et al. [27]). We refined the model and performed the 3D pre-stack depth migrations using the commercial package Paradigm® GeoDepth®, as described above. During each iteration, we carried out a residual move-out analysis, for all the identified horizons, by picking the coherences on the semblance profiles, and a tomographic update was performed. After the third

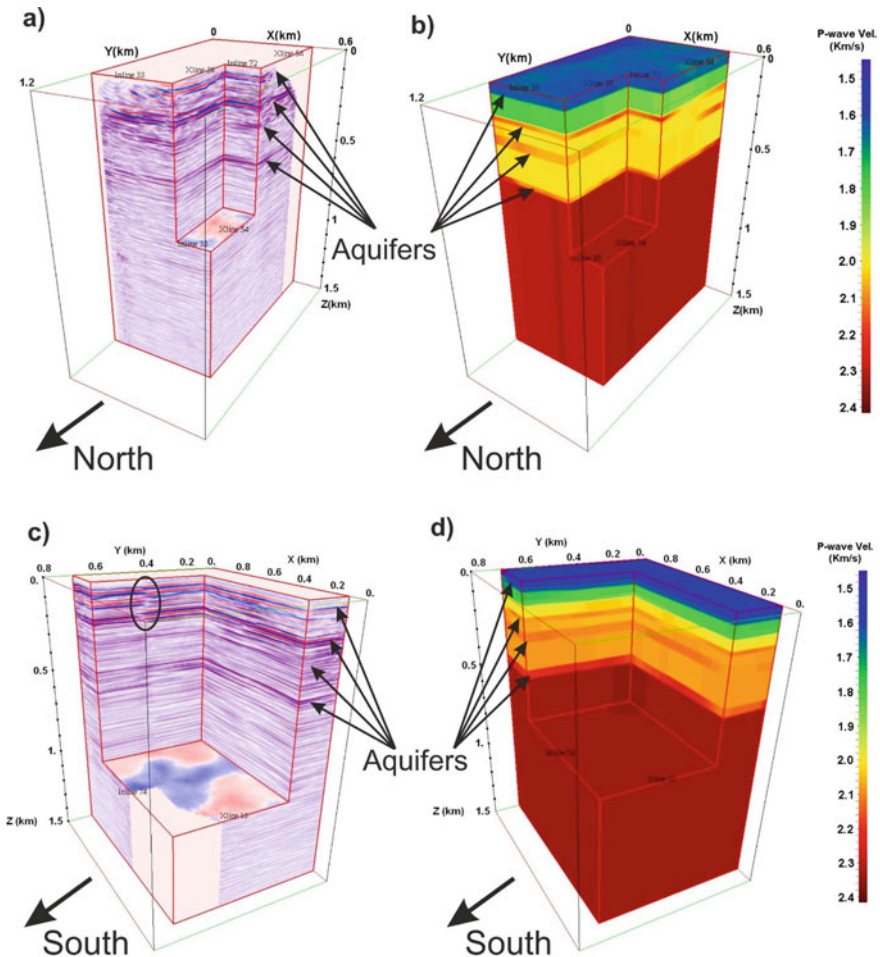


Fig. 18.6 3D prestack depth migrations of the Cube A **a** and the Cube B **b** using the corresponding final tomographic velocity models **c** and **d**, respectively. All the cubes correspond to the spring season. Modified after Giustiniani et al. [27]

iteration, the model reached a good accuracy, because the events on the CIGs were nearly flat and the depth horizons showed a good consistency with the corresponding reflectors on the image section. Figure 18.6a,c shows the resulting 3D pre-stack depth migrations of Cube A and Cube B, respectively. The vertical resolution is satisfactory and we notice that two high velocity layers are evident at about 270 m and 460 m, respectively, which could be associated with deeper aquifers. The cubes are sectioned to show the good lateral continuity of the reflectors. Only the spring cubes are shown, because the summer cubes are very similar [27]. The difference in the P-wave velocity values between the spring and summer velocity models is less than the estimated velocity error. Assuming for the first two aquifers an average picking error of about ± 6 ms, the resulting average velocity deviation inside the two aquifers is about 2%. For the deeper aquifers, the velocity error increases and it could be estimated to be about 5% for this inversion algorithm. The resolution and lateral continuity of Cube B is better, because of the higher coverage. For this reason, other two layers were identified and picked between the two shallow aquifers. In the chaircut of the migrated Cube B (Fig. 18.6c) a lateral amplitude inversion in the shallow layers is evidenced (with a circle). This feature may be due to lateral changes in the lithology or to a fault.

18.4.3 AVO Inversions

The inputs of the amplitude inversion are: (1) the data processed following a true-amplitude scheme, (2) the acquisition geometry used to apply a correction for source and receiver directivities, and (3) the velocity model obtained by the tomographic inversion (i.e., [60]). The velocity model allows calculating the ray path and converting the offsets to angles of incidence. We analysed the amplitude variations versus angle of incidence and obtained sections of both P- and S-wave velocity reflectivities. The ratios between the P- and S-wave reflectivities are related to the Poisson's ratio and, consequently, to the fluid content (i.e., [3]). After a qualitative comparison of the reflectivity sections, a quantitative method was applied to interpret the AVO results. We evaluated the ratio between P and S reflectivity, as shown in Fig. 18.7a. The two main aquifers are identified by the strong Poisson ratio variation. We blanked the area where the AVO inversion is not reliable, i.e., the areas where the curve fitting is suspect, due to noise or insufficient aperture. Note also the high contrast at about 500 m depth, related to a lithologic change and interpreted as an unknown aquifer, as discussed in the next section. Finally, we evaluated the cross-plots of P and S velocity versus reflectivity (Fig. 18.7b), to verify if different petrophysical characteristics versus depth can be detected along the seismic profiles. To this end, we selected two areas where the coverage is high enough to guarantee a reliable AVO inversion, i.e., between common depth points 200–400 and 800–1000 (Fig. 18.7a). To detect different trends, we considered the following depth intervals (Fig. 18.7a: (1) shallow part (between 0 and 16 m; black colour); (2) first aquifer (between 16 and 40 m; red colour); (3) layer between the two main aquifers (between 60 and 140 m);

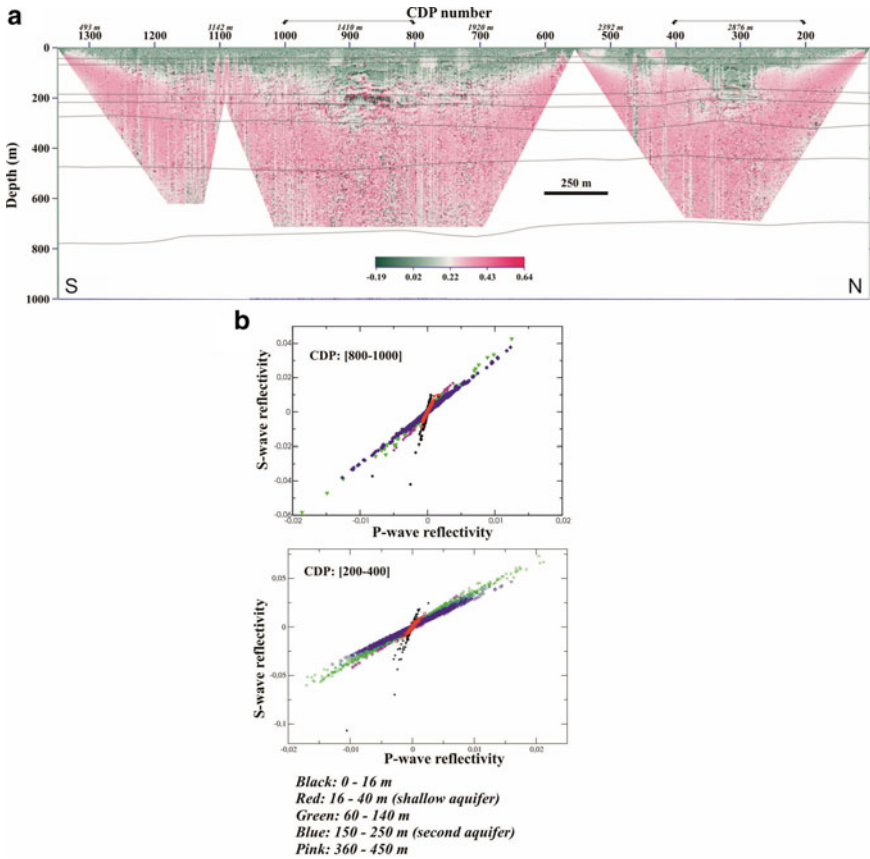


Fig. 18.7 a P to S wave velocity reflectivity section; b P- versus S-wave velocity reflectivities at selected common depth point (CDP) intervals selected in panel A. Black colour: between 0 and 16 m. Red colour: between 16 and 40 m. Green colour: between 60 and 140 m. Blue colour: between 150 and 250 m. Magenta colour: between 360 and 450 m. After Tinivella et al. [61]

green colour; (4) second aquifer (between 150 and 250 m; blue colour); (5) depth greater than 250 m (between 360 and 450 m; magenta colour). In the crossplot, two main trends have been identified: one between 0 and 40 m depth and a second one until 500 m. In both of these depth intervals, the two main aquifers can be recognized because of anomalous trends.

The AVO analysis was applied on the 3D seismic dataset by using the procedure already explained for the 2D seismic data. The reliability of the result depends on the seismic data quality and on the coverage. As well as travel-time tomography, also AVO analysis is not able to detect any seismic response difference between the two seasons. As already observed in the analysis of 2D seismic data (Giustiniani et al. 2008), the comparison between P- and S-wave reflectivities confirms that the top of

each aquifer is well evident, confirming that the seismic interface is mainly generated by lithological changes, with a minor contribution from the fluid condition changes.

18.4.4 Petrophysical Properties

The 2D and 3D velocity models were interpolated in order to obtain a complete 3D model of the study area by using a commercial software. We assumed a cell size of $20(x) \times 20(y) \times 25(z)$ m and a number of cells equal to 198, 211, and 23 along the three directions, respectively. The data were interpolated by using the inverse distance algorithm [21, 23]. The inverse distance method is a weighted average interpolator that can be either an exact or a smoothing interpolation. We applied the interpolator module to all data sets obtaining velocity, density and porosity distribution.

In order to extract petrophysical characteristics of the subsurface, the 3D interpolated velocity model was translated in terms of density, by using the Gardner relationship [24], and porosity, supposing the density of the matrix equal to 2600 kg/m^3 and that one of the water equal to 1000 kg/m^3 [61].

The analysis of 3D interpolated velocity models shows that the shallowest confined aquifer is characterized by a density of about 1900 kg/m^3 and a porosity of about 36–40%. The second aquifer, located at about 180 m depth, is well imaged because it shows a higher porosity (equal to about 32%) with respect to the upper layer, which is characterized by a porosity of about 28%. Note that the deeper aquifer presents a porosity of about 33%. Regarding the density, the deep aquifers are characterized by a density of about 2100 kg/m^3 . The results are reported in Figs. 18.8, 18.9 and 18.10, where the depth ranges from 0 to 550 m. The 3D models indicate that the

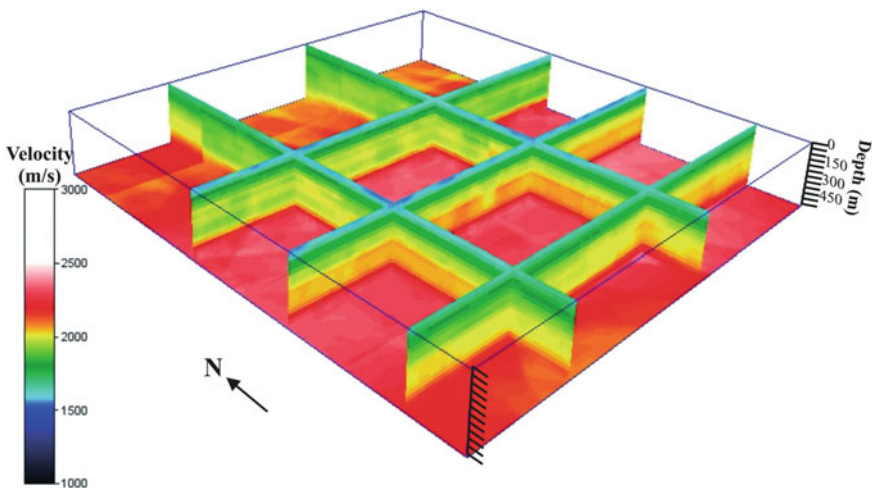


Fig. 18.8 3D velocity (m/s) models after the interpolation. After Tinivella et al. [61]

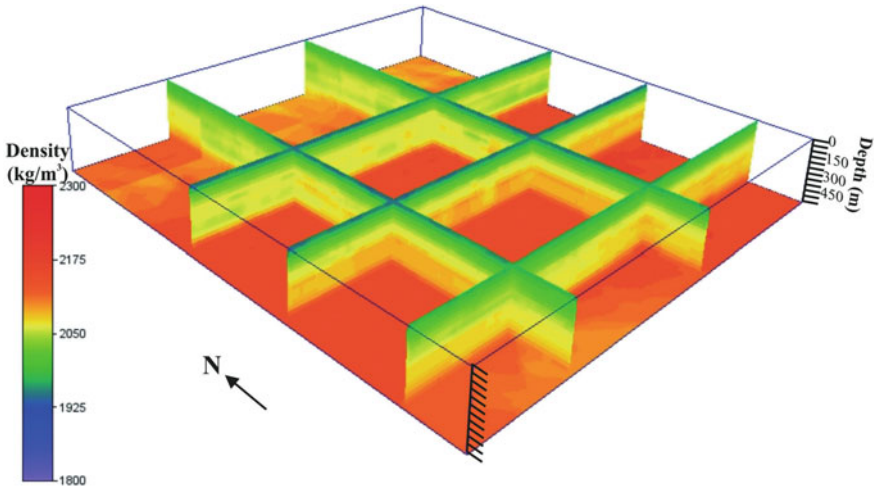


Fig. 18.9 3D density (kg/m^3) model after the interpolation. After Tinivella et al. [61]

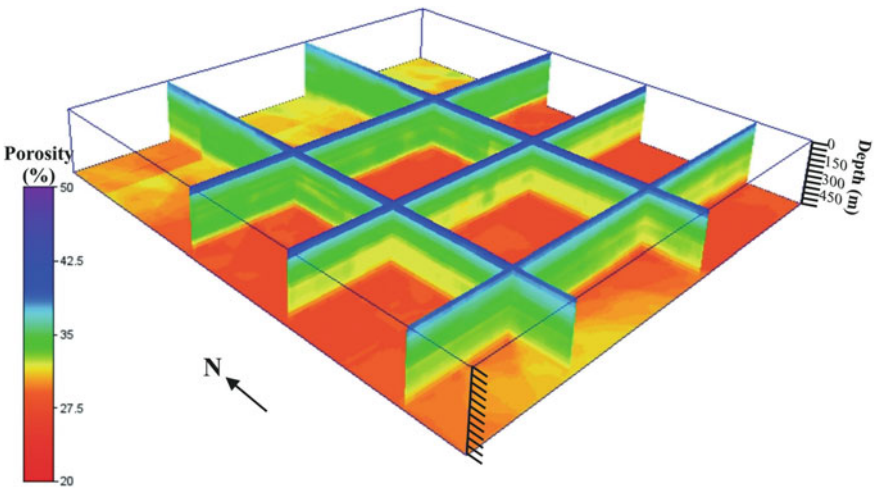


Fig. 18.10 3D porosity (%) model after the interpolation. After Tinivella et al. [61]

area has variable characteristics, with strong lateral velocity variations that suggest changes in the interface geometry and the aquifer system thickness. The analyses of these data indicate an increase of porosity and the thickness of aquifers northwards.

18.5 Discussion

The results obtained from the analysis of the seismic data show that the seismic method is a very useful tool to identify the lithological changes and the geometry of a multilayered aquifer system. In the case study here presented, the seismic acquisition was optimised by using numerical wave simulations of synthetic seismograms, based on the seismic parameters obtained from well information. The 2D and 3D seismic imaging identify four aquifers at different depths. In addition, the 3D velocity cubes, obtained from the tomographic inversion and from the analysis of the CIGs, showed that the seasonal variations are minimal and within the error of the tomographic inversion procedure. This highlights that the investigated aquifers have a fairly constant flow throughout the year, especially the deeper ones.

A reflector was identified at about 480 m depth and interpreted as the top of an unknown aquifer, in accordance with high resistivity values detected by the time domain electromagnetic method [52]. In light of this evidence, a drilling was subsequently carried out up to the depth where, from the analysis of the geophysical data, the presence of an aquifer was assumed. Therefore, from the point of view of identifying new aquifers, the result obtained from the project can be defined as excellent. The comparison between the stratigraphy identified during drilling and the seismic imaging has also shown that the aquifers are well identifiable on the seismic data. Furthermore, this comparison has also highlighted the goodness of the interpretation, derived from the various analyses carried out on the seismic data (AVO and tomographic analyses).

The results obtained from the AVO analysis confirm the presence of the shallow aquifer (at about 30 m) and the deeper one (at about 180 m). In particular, the cross-plots of the P-versus S-wave velocity reflectivities show different trends, which are related to fluid contents and lithologic changes.

The 3D velocity models, obtained from the interpolation of 2D velocity models and 3D velocity cube, suggest that the second aquifer could be characterized by strong lateral variations [47]. The thinning in the southern part is in agreement with the hydrogeological data. In fact, a water well, drilled about 20 years ago, showed the absence of the deeper aquifer in the southern part.

On the basis of the seismic data results, a 510 m deep well was drilled, which verified the real consistency of our 3D models. Figure 18.11 shows a transversal depth section of the Cube A, overlapped to the corresponding interval velocity section, together with the well stratigraphy and the down-hole velocity log. There is an excellent correspondence between the horizons picked on the migrated section and the main discontinuities reported in the well stratigraphy, except for some slight discrepancies, which could be due to the distance between the well and the survey area (about 200 m). The two high velocity layers at about 270 and 480 m correspond in the well stratigraphy to two deep aquifers. Those aquifers were unknown because the catching wells are limited to depths of about 200 m. Moreover, Fig. 18.11 shows the good correlation between the down-hole velocity log and the interval velocity section for aquifers 2 and 3. The four aquifers indicated on the well stratigraphy correspond

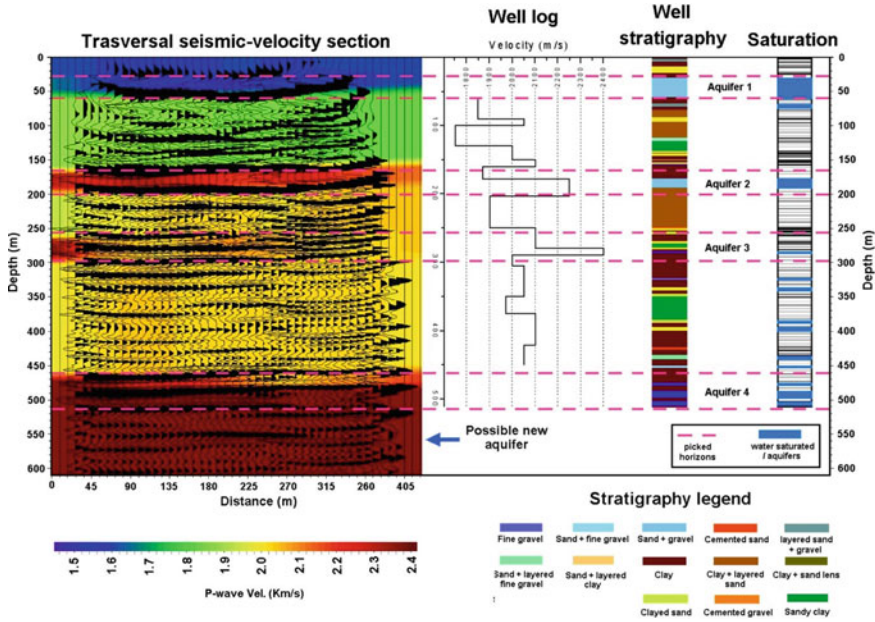


Fig. 18.11 Correlation of the well stratigraphy with a transversal section of Cube A. The velocity section is overlapped to the seismic migrated section. The dashed violet lines identify the picked horizons on the depth seismic section. Giustiniani et al. [27] Modified from

to high interval velocity values, which are mainly related to the lithological variation. In fact, the velocity is affected mainly by three factors: (1) the matrix, (2) the pore fluid and (3) the pore pressure. In our case, as shown in Fig. 18.11, aquifer layers are composed of sand and gravel, while the adjacent layers are mainly composed of water saturated sandy clays. Note that, because of compaction effects, clay velocity increases with depth. It is well known that, for unconsolidated sediments, sandstones are characterized by higher velocities than shales [54]. Moreover, the pore fluid in overpressure conditions, slightly reduces the seismic velocity [61]. So, the combined effect is the increase of the seismic velocity in correspondence of the aquifers.

18.6 Summary

The application of 2D and 3D seismic methods is a useful tool to define aquifers geometry and petrophysical characteristics, enabling to identify lateral variations in underground bodies and to extend information obtained from the well stratigraphy, when available. Unconventional analysis of seismic data, including “true amplitude processing”, is essential for the geometrical and petrophysical characterization of shallow and deep aquifers that allow to obtain very useful information regarding the

Table 18.1 2D acquisition parameters and source characteristics.

Source	MiniVib IVI T2500-linear sweep 10–150 Hz-length sweep 12 s
Receiver	10 Hz geophones—receiver interval: 5 m
Shot interval	10 m
Record length	3 s—after cross-correlation of acquired data with pilot trace
Time sampling	1 ms

presence of fluids and lithological changes. A detailed velocity model is fundamental to obtain the geometry of the underground bodies by using the pre-stack migration in depth that improves the image of the subsoil. However, it should be noticed that the seismic data cannot detect the overpressure seasonal variations in confined aquifers. On the other hand, simultaneous analysis of P- and S-wave data is an excellent tool for the petrophysical characterization of the subsoil, but it requires specific conditions to achieve these purposes, such as adequate planning and accurate data acquisition. In conclusion, the seismic methodology is a useful tool for aquifer characterization.

Acknowledgements We acknowledge the European Community that has supported the CAMI project (LIFEProject Number—LIFE04 ENV/IT/000500). We used the following software: Paradigm® Epos®, VISTA Desktop Seismic Data Processing Software and Seismic Unix, to process the data, and Tesser Technologies Inc., to perform modelling.

References

1. Accaino F, Tinivella U, Rossi G, Nicolich R (2005) Imaging of CROP 18 deep seismic crustal data. *BSGI* 3:195–204
2. Accaino F, Tinivella U, Rossi G, Nicolich R (2005) Geofluid evidences from analysis of seismic data from Southern Tuscany (Italy). *JVGR* 148:46–59
3. Accaino F, Nicolich R, Tinivella U (2006) Highlighting the crustal structure of southern Tuscany by the reprocessing of the CROP03 NVR profile. *Bollettino di Geofisica Teorica ed Applicata* 47:425–445
4. Ahmad J, Schmitt DR, Rokosh CD, Pawlowicz JG (2009) High-resolution seismic and resistivity profiling of a buried Quaternary subglacial valley: Northern Alberta, Canada. *Geol Soc Am Bull* 121:1570–1583. <https://doi.org/10.1130/B26305.1>
5. Ahokangas E, Mäkinena J, Artimo A, Pasanen A, Vanhala H (2020) Interlobate esker aquifer characterization by high resolution seismic reflection method with landstreamer in SW Finland. *J Appl Geophys* 177:104014
6. Aki K, Richards PG (1980) *Quantitative seismology: theory and methods*. W.H. Freeman, San Francisco
7. Bachrach R, Nur A (1998) High-resolution shallow-seismic experiments in sand, Part I: water table, fluid flow and saturation. *Geophysics* 63:1225–1233
8. Barnett PJ, Sharpe DR, Russell HAJ, Brennand TA, Gorrell G, Kenny FM, Pugin AJ-M (1998) On the origin of the Oak Ridges Moraine. *Can J Earth Sci* 35:1152–1167. <https://doi.org/10.1139/cjes-35-10-1152>

9. Böhm G, Vesnaver AL (1999) In quest of the grid. *Geophysics* 64:1116–1125
10. Bourbié T, Coussy O, Zinzner B (1987) *Acoustics of porous media*. Gulf Publishing, Houston
11. Bradford JH (1998) Characterizing shallow aquifers with seismic reflection, Part II—prestack depth migration and field examples. *Geophysics* 67:98–109
12. Bradford JH, Sawyer DS (2002) Characterizing shallow aquifers with seismic reflection, Part II—prestack depth migration and field examples. *Geophysics* 67:98–109
13. Brodic B, Malehmir A, Juhlin C, Dynesius L, Bastani M, Palm H (2015) Multicomponent broadband digital-based seismic landstreamer for near-surface applications. *J Appl Geophys* 123:227–241. <https://doi.org/10.1016/j.jappgeo.2015.10.009>
14. Brodic B, Malehmir A, Pugin AJ-M, Maries G (2018) Three-component seismic land streamer study of an esker architecture through S- and surface-wave imaging. *Geophysics* 83:1–16. <https://doi.org/10.1190/geo2017-0747.1>
15. Burschil T, Buness H, Tanner DC, Wielandt-Schuster U, Ellwanger D, Gabriel G (2018) High-resolution reflection seismics reveal the structure and the evolution of the Quaternary glacial Tannwald Basin. *Near S Geophys* 16:593–610. <https://doi.org/10.1002/nsg.12011>
16. Cardimona SJ, Clement WP, Kadinsky-Cade K (1998) Seismic reflection and ground-penetrating radar imaging of a shallow aquifer. *Geophysics* 63:1310–1317
17. Carrion P, Böhm G, Marchetti A, Pettenati F, Vesnaver A (1993) Reconstruction of lateral gradients from reflection tomography. *J Seism Explor* 2:55–67
18. Castagna JP, Bazle ML, Eastwood RL (1985) Relationship between compressional-wave and shear-wave velocities in elastic silicate rocks. *Geophysics* 50(571):581
19. Cummings DI, Russell HAJ (2007). The Vars-Winchester Esker Aquifer, South Nation River Watershed, Ontario. CANQUA Field Trip, June 6th 2007, Geological Survey of Canada, Open File 5624, p 74
20. Cummings DI, Gorrell G, Guilbault JP, Hunter JA, Logan C, Ponomarenko D, Pugin AJ-M, Pullan SE, Russell AJ, Sharpe DR (2011) Sequence stratigraphy of a glaciated till basin fill, with a focus on esker sedimentation. *Geol Soc Am Bull* 127:1478–1496. <https://doi.org/10.1130/B30273.1>
21. Davis JC (1986) *Statistics and data analysis in geology*. Wiley, New York, NY, p 646
22. Foti S, Lai CG, Lancellotta R (2002) Porosity of fluid-saturated porous media from measured seismic wave velocities. *Geotechnique* 52(5):359–373
23. Franke R (1982) Scattered data interpolation: tests of some methods. *Math Comput* 38:181–200
24. Gardner GHF, Gardner LW, Gregory AR (1974) Formation velocity and density—the diagnostic basics for stratigraphic traps. *Geophysics* 39:770–780
25. Giustiniani M, Accaino F, Del Negro E, Picotti S, Tinivella U (2008) Characterisation of shallow aquifers by 2d high-resolution seismic data analysis. In: Nieto D, Santarato D (eds) *BGTA*. vol 50(1), pp 29–38
26. Giustiniani M, Accaino F, Picotti S, Tinivella U (2008) Characterisation of shallow aquifers by high-resolution seismic data. *Geophys Prospect* 56(5):655–666. <https://doi.org/10.1111/j.1365-2478.2008.00705.x>
27. Giustiniani M, Accaino F, Picotti S, Tinivella U (2009) 3D seismic data for shallow aquifers characterization. *J Appl Geophys* 68(3):394–403. <https://doi.org/10.1016/j.jappgeo.2009.03.005>
28. Giustiniani M, Tinivella U, Accaino F (2010) P and S reflection and P refraction: an integration for characterising shallow subsurface. *J Appl Geophys* 71:149–215
29. Grelle G, Guadagno FM (2009) Seismic refraction methodology for groundwater level determination: “Water seismic index.” *J Appl Geophys* 68:301–320
30. Haeni FP (1986) Application of seismic refraction methods in groundwater modelling studies in New England. *Geophysics* 51(2):236–249
31. Hasselstrom B (1996) Water prospecting and rock-investigation by the seismic refraction method. *Geoexploration* 7(2):213
32. Holcombe HT, Wojslaw RS (1992) Spatially weighted trim stacking: a technique for pre-stack noise suppression. In: *Proceedings society of exploration geophysicists, 62nd SEG Annual Meeting, New Orleans, USA*, pp 1157–1160

33. Huuse M, Piotrowski JA, Lykke-Andersen H (2003) Geophysical investigations of buried Quaternary valleys in the formerly glaciated NW European lowland: significance for groundwater exploration. *J Appl Geophys* 53:153–157. [https://doi.org/10.1016/S0926-9851\(03\)00115-0](https://doi.org/10.1016/S0926-9851(03)00115-0)
34. Inazaki T (2004) High-resolution seismic reflection surveying at paved areas using an Swave type Land Streamer. *Explr Geophys* 35:1–16. <https://doi.org/10.1071/EG04001>
35. Kirsch R, Rumpel HM, Scheer W, Wiederhold H (2006). Groundwater resources in buried valleys—a challenge for geosciences. Leibniz Institute for Applied Geosciences (GGA-Institut), Hannover, Germany, p 303
36. Krawczyk CM, Polom U, Trabs S, Dahm T (2012) Sinkholes in the city of Hamburg—new urban shear-wave reflection seismic system enables high-resolution imaging of subsurface structures. *J Appl Geophys* 78:133–143. <https://doi.org/10.1016/j.jappgeo.2011.02.003>
37. Lees JM, Wu H (2000) Poisson's ratio and porosity at Coso geothermal area, California. *J Volcanol Geoth Res* 95:157–173
38. Loreto MF, Tinivella U, Ranero CR (2007) Evidence for fluid circulation, overpressure and tectonic style along the Southern Chilean margin. *Tectonophysics* 429:183–200
39. Loreto MF, Tinivella U, Accaino F, Giustiniani M (2011) Gas hydrate reservoir characterization by geophysical data analysis (Offshore Antarctic Peninsula). *Energies* 4(1):39–56. <https://doi.org/10.3390/en4010039>
40. Malehmir A, Lindén O, Friberg B, Brodic B, Möller H, Svensson M (2018) Unravelling contaminant pathways through a detailed seismic investigation, Varberg-Southwest Sweden. In: EAGE 24th European meeting of environmental and engineering geophysics. Investigations—high-resolution engineering seismic studies I. <https://doi.org/10.3997/2214-4609.201802610>
41. Maries G, Ahokangas E, Mäkinen J, Pasanen A, Malehmir A (2017) Interlobate esker architecture and related hydrogeological features derived from a combination of high-resolution reflection seismics and refraction tomography, Virttaankangas, SWFinland. *Hydrogeol J* 25:829–845. <https://doi.org/10.1007/s10040-016-1513-9>
42. Martinez K, Ploug C, Pugin A, Mendoza JA (2010) New three-component landstreamer system developed for groundwater and engineering applications. In: Extended abstract. Near surface 2010—16th European meeting of environmental and engineering geophysics, P29. Zurich, Switzerland, 6–8 September 2010
43. Nicholson C, Simposon DW (1985) Changes in VP/Vs with depth: implication for appropriate velocity models, improved earthquake locations, and material properties of the upper crust. *Bull Seismol Soc Am* 75:1105–1124
44. Nicolich R, Della Vedova B, Giustiniani M, Fantoni R (2004) Carta del sottosuolo della Friulana. Litografia Cartografica, Firenze
45. Oldenborger GA, Pugin AJ-M, Pullan SE (2013) Airborne time-domain electromagnetics, electrical resistivity and seismic reflection for regional three-dimensional mapping and characterization of the Spiritwood Valley Aquifer, Manitoba, Canada. *Near Surf Geophys* 11:63–74. <https://doi.org/10.3997/1873-0604.2012023>
46. Oldenborger GA, Logan CE, Hinton MJ, Pugin AJ-M, Sapia V, Sharpe DR, Russell HAJ (2016) Bedrock mapping of buried valley networks using seismic reflection and airborne electromagnetic data. *J Appl Geophys* 128:191–201. <https://doi.org/10.1016/j.jappgeo.2016.03.006>
47. Picotti S, Giustiniani M, Accaino F, Tinivella U (2008) Depth modelling and imaging of the 4D seismic survey of Basso Livenza (CAMI project). In: Nieto D, Santarato G (eds) BGTA, vol 50(1), pp 71–82
48. Pilecki Z, Isakow Z, Czarny R, Pilecka E, Harba P, Barnaś M (2017) Capabilities of seismic and georadar 2D/3D imaging of shallow subsurface of transport route using the Seismobile system. *J Appl Geophys* 143:31–41. <https://doi.org/10.1016/j.jappgeo.2017.05.016>
49. Prasad A, Meissner G (1992) Attenuation mechanism in sands: laboratory versus theoretical (Biot) data. *Geophysics* 57:710–719

50. Pugin AJ-M, Oldenborger GA, Cummings DI, Russell HAJ, Sharpe DR (2014) Architecture of buried valleys in glaciated Canadian Prairie regions based on high resolution geophysical data. *Qua Sci Rev* 86:13–23
51. Pullan SE, Pugin AJ-M, Hunter J (2007) Shallow seismic reflection methods for the delineation and hydrogeological characterization of buried eskers in eastern Ontario: Denver, Colorado. In: 20th annual symposium on the application of geophysics to environmental and engineering problems (SAGEEP) meeting, 1–5 April 2007
52. Rapti-Caputo D, Bratus A, Santarato G (2007). Deep multiaquifer system: hydrogeological exploration integrated with geophysical data. IUGG XXIV General Assembly, Perugia
53. Sander JE (1978) The blind zone in seismic ground-water exploration. *Ground Water* 165:394–395
54. Schon S (1996) Physical properties of rocks-fundamentals and principles of petrophysics. In: *Handbook of geophysical exploration: seismic exploration*, vol 18. Pergamon, Oxford/Tarrytown
55. Scrocca D, Doglioni C, Innocenti F, Manetti P, Mazzotti A, Bertelli L et al (eds) (2003) CROP ATLAS—seismic reflection profiles of the Italian crust. *Memorie Descrittive Carta Geologica d'Italia* 62
56. Sharpe DR, Pullan SE, Warman TA (1992) A basin analysis of the Wabigoon Area of Lake Agassiz, a Quaternary Clay Basin in Northwestern Ontario. *Geogr Phys Quat* 46:295–309. <https://doi.org/10.7202/032916ar>
57. Steeples DW, Miller RD (1990) Seismic-reflection methods applied to engineering, environmental, and ground-water problems. In: Ward S (ed) *Geotechnical and environmental geophysics*, 1, review and tutorial, investigations in geophysics No. 5. Society of Exploration Geophysicists, pp 1–30
58. Stewart RR (1991) *Exploration seismic tomography: fundamentals*. Society of Exploration Geophysicists, Course Note Ser., 3
59. Stümpel H, Kähler S, Meissner R, Milkereit B (1984) The use of seismic shear waves and compressional waves for lithological problems of shallow sediments. *Geophys Prospect* 32:662–675
60. Tinivella U, Accaino F, Rossi G, Nicolich R (2005) Petrophysical analysis of CROP 18 crustal seismic data. *BSGI* 3:205–211
61. Tinivella U, Accaino F, Giustiniani M, Picotti S (2008) Petro-physical characterization of shallow aquifers by using AVO and theoretical approaches. In: Nieto D, Santarato G (eds) *BGTA*, vol 50(1), pp 59–69
62. Tinivella U, Loreto MF, Accaino F (2009). Regional versus detailed velocity analysis to quantify hydrate and free gas in marine sediments: the South Shetland Margin case study. In: Long D, Lovell MA, Rees JG, Rochelle CA (eds) *Sediment-hosted gas hydrates: new insights on natural and synthetic systems*, vol 319. The Geological Society, London, Special Publications, pp 103–119
63. Tremblay T, Hunter J, Lamontagne C, Nastev M (2010) High resolution seismic survey in a contaminated Esker Area, Chateauguay River Watershed, Quebec. *Can Water Resour J* 35:417–432. <https://doi.org/10.4296/cwrj3504417>
64. Van der Sluis A, Van der Vorst HA (1987) Numerical solutions of large, sparse linear systems arising from tomographic problems. In: Nolet G (ed) *Seismic tomography*. D. Reidel Pub., Dordrecht, Holland, pp 49–84
65. Van der Veen M, Spitzer R, Green AG, Wild P (2001) Design and application of a towed landstreamer for cost-effective 2D and pseudo-3D shallow seismic data acquisition. *Geophysics* 66:482–500. <https://doi.org/10.1190/1.1444939>
66. Vangkilde-Pedersen T, Dahl FJ, Ringgaard J (2006) Five years of experience with landstreamer vibroseis and comparison with conventional seismic data acquisition. In: *Proceedings of the symposium on the application of geophysics to engineering and environmental problems (SAGEEP'06)*, Seattle, Washington, USA, 2–6 April 2006, pp 1086–1093. <https://doi.org/10.4133/1.2923567>

67. Vargas-Cordero IC, Tinivella U, Villar-Munoz L, Giustiniani M (2016) Gas hydrate and free gas estimation from seismic analysis offshore Chiloé island (Chile). *Andean Geol* 43(3):263–274
68. Vesnaver A, Böhm G, Madrussani G, Petersen S, Rossi G (1999) Tomographic imaging by reflected and refracted arrivals at the North Sea. *Geophysics* 64:1852–1862
69. Whiteley RJ, Hunter JA, Pullan SE, Nutalaya P (1998) “Optimum offset” seismic reflection mapping of shallow aquifers near Bangkok, Thailand. *Geophysics* 63:1385–1394
70. Yilmaz O (2001) *Seismic data analysis: processing, inversion and interpretation of seismic data*. In: SEG series: investigation in geophysics. Tulsa
71. Zelt CA, Smith RB (1992) Seismic travelttime inversion for 2-D crustal velocity structure. *Geophys J Int* 108:16–34
72. Zohdy AAR, Eaton GP, Mabey DR (1974) Application of surface geophysics to groundwater investigation. U.S. Geol. Surv. *Techniques of Water-Resource Investigations*, book 2, chapter D1

Chapter 19

Multi-geophysical Field Measurements to Characterize Lithological and Hydraulic Properties of a Multi-scale Karstic and Fractured Limestone Vadose Zone: Beauce Aquifer (O-ZNS)



Céline Mallet, Clara Jodry, Arnaud Isch, Gautier Laurent, Jacques Deparis, and Mohamed Azaroual

Abstract The deciphering of the coupled processes that govern the transfers of mass and heat within the vadose zone is recognized as a complex issue. In this context, an observatory of transfers in the vadose zone (O-ZNS) has been implemented near Orléans (France). By combining multiscale laboratory and field experiments using various monitoring techniques, this observatory will improve our knowledge regarding water flow and contaminant transport throughout the 15–19 m highly heterogeneous vadose zone. To image the lithological and hydraulic properties of its heterogeneous facies, we adopted a multi-geophysical monitoring strategy in order to overcome the limitations of each individual geophysical method. This approach includes surface, borehole, and well multi-geophysical measurements. Preliminary investigations undertaken since 2017 leads to an effective and complete characterization of the vadose zone including (i) a lithological description of the geological facies, (ii) the identification of local heterogeneities (karsts, fractures, silicified

C. Mallet (✉) · A. Isch · G. Laurent · M. Azaroual
University Orléans, CNRS, BRGM, ISTO, UMR 7327, 45071 Orléans, France
e-mail: celine.mallet@univ-orleans.fr

A. Isch
e-mail: arnaud.isch@terrainnova.fr

G. Laurent
e-mail: gautier.laurent@univ-orleans.fr

M. Azaroual
e-mail: m.azaroual@brgm.fr

C. Jodry
Institut Terre Et Environnement de Strasbourg, Université de Strasbourg/EOST/ENGEES, CNRS
UMR 7063, 5 rue Descartes, 67084 Strasbourg, France
e-mail: cjodry@unistra.fr

J. Deparis
BRGM, French Geological Survey, 45060 Orléans, France
e-mail: j.deparis@brgm.fr

layers) whose density increases with depth, and (iii) an estimation of the water content variations within the vadose zone. This whole set of results constitutes a first base to ongoing joint inversion that should lead to a refined characterization of the petrophysical and transport properties of the vadose zone column.

19.1 O-ZNS Project

19.1.1 Generalities

The Vadose Zone (VZ) extends between the soil surface and the water table and is of critical importance for the preservation and management of groundwater resources because of its control on transfers of water and contaminants down to the aquifer i.e. saturated zone [1, 2]. Developing novel strategies for the characterization and monitoring of coupled processes at stake in the VZ is thus crucial to improving our knowledge of mass and heat transfers. However, the complexity of the heterogeneous lithologies and multi-scale structure of the VZ leaves a lot of unknowns leading to difficulties for interpreting their hydraulic and transport properties.

In this context, an Observatory of transfers in the VZ (O-ZNS) is under development within an agricultural field at the heart of the Beauce region, in Villamblain (Centre-Val de Loire, France—Fig. 19.1 and described in Chap. II.2. by Abbar et al. [3]. O-ZNS offers a unique support for observing and quantifying the mass and heat transfers throughout the VZ of a vulnerable limestone aquifer. This observatory is developed thanks to an exceptional well (20 m-deep and 4 m-diameter—black circle in Fig. 19.1) and surrounding boreholes (blue and red dots in Fig. 19.1). This configuration makes it possible to combine observations over a wide range of spatial and



Fig. 19.1 Localization of the O-ZNS site and its organization with the well (black circle) and the six boreholes (in red for the ones from 2017 and blue for the most recent ones from 2020) used for this study

temporal scales. Measurements combine focused hydrogeological and biogeochemical monitoring techniques together with geophysical imaging. The main objectives, the localization, borehole details, and the instrumentation strategy of the O-ZNS platform are presented in a companion chapter [3]. For this study, we mainly consider three cored boreholes (B1–B3 in red in Fig. 19.1) drilled in spring 2017. Newer boreholes, drilled in spring 2020 and denoted B5–B7 (displayed in blue in Fig. 19.1), are also shown and used for direct log imagery.

19.1.2 HydroGeophysical Approach for Subsoil Characterization

Geophysical methods have been developed for characterizing underground microstructural, petrophysical, and transport properties, including karst properties, within the VZ [4]. Considered individually, these methods have specific limitations in terms of resolution and depth of observation but they also have their specific interest. For example, surface-based seismic methods are adapted to detecting horizontal objects [5], electrical method to characterizing fluid saturation and behavior [6], electromagnetic methods for identifying karst and fractures, and inferring water content [7, 8], microgravimetric methods to detect deeper heterogeneities that could be hydrogeological anomalies and to estimating water storage [9].

Coupled geophysical approaches and joint inversion have been developed to broaden physical description, range of resolution, and depth of observation [10–12]. For example, fracture density characterization is enhanced by coupling seismic and electric methods [13]; aquifer storages are better monitored when crossing gravimetric and electromagnetism [14]; seismic characterization of shear zone is much more accurate when coupled to electromagnetism [15]. More recent approaches couple geomechanical, geological, and geophysical data to improve models and recover meaningful hydrological and reservoir properties at various scales [16–19]. However, these methods, while based on model development, are still needing experimental laboratory and field validations [13, 20, 21]. Improvements are still underway to balance the uncertainties between each field and those related to the petrophysical relationships linking geophysical and hydrological quantities [22–25].

There are recent large-scale field hydro-thermo-geophysical experiments that tested coupling models and push forward our knowledge on subsoil characterization and on fluid flow within the VZ [26–30]. These studies, performed under more or less controlled conditions and more or less blind soil structure, highlighted the importance of being able to couple field hydraulic experiments to geophysical field and laboratory characterization. It is in this lineage that O-ZNS takes place. Indeed, the challenge posed by the characterization of the hydraulic and transport properties of the VZ calls for a coupled multi-geophysical approach. It will provide a multi-scale characterization of the VZ facies in the context of highly heterogeneous lithological and hydraulic properties [31]. In addition, it is expected to provide exceptional study

outlooks with time monitoring, coupled measurements and joined interpretations and inversions. The full and specific O-ZNS geophysical strategy based on the state-of-the-art applied to a VZ of a limestone aquifer is presented in Sect. 19.2, following the lithology and structure description.

19.1.3 Overall Lithology

In this section and the following, a description of the VZ facies and the site heterogeneities are presented giving a general view of the geological structure. The lithological description of the Beauce limestone aquifer is displayed on Fig. 19.2. It has been depicted from direct core observations taken from B1-3 [31] and complemented

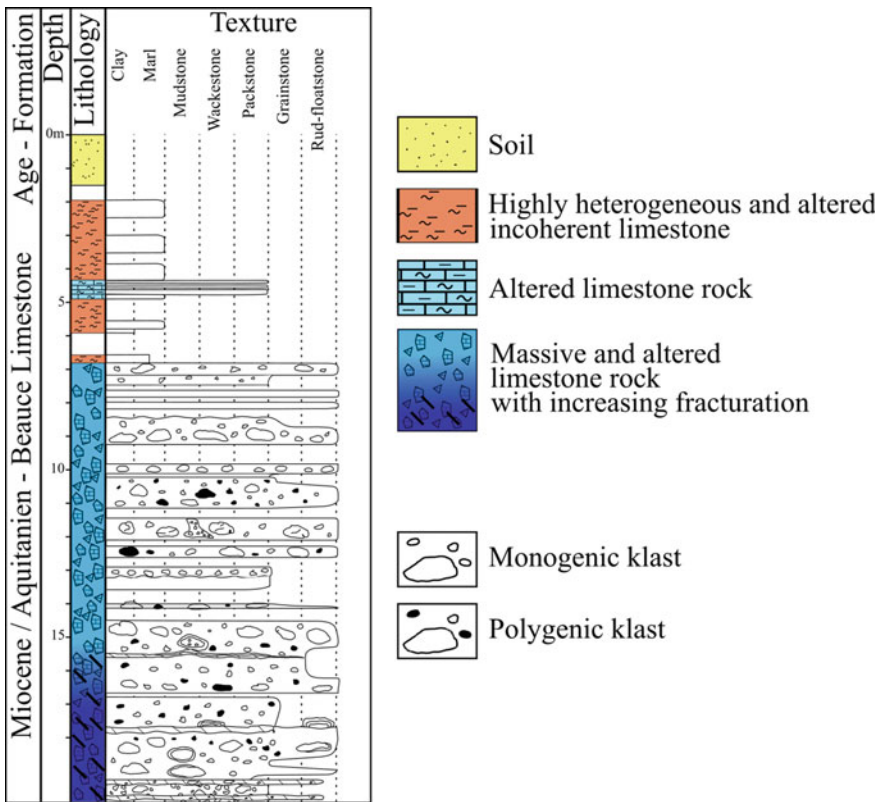


Fig. 19.2 Lithology of the VZ interpreted from direct core observations and log imagery in six boreholes (B1-3 and B5-7)

with log imagery from B5-7 boreholes. The global formation presents a heterogeneous altered/karstified limestone facies, with a macro- and micro-porosity, cracks and fractures.

From the surface down to 25 m deep, the following facies identified as part of the Pithiviers limestone formation were observed:

- 0–1.5 m: silt loam soil typical of the Beauce region [32].
- 1.5–7 m: highly heterogeneous incoherent limestone presenting intense alteration (i.e., fractures, weathering, oxidations), powdery limestones, clay lenses, calcareous sand interbeds, and few thin massive, but still altered and karstified, limestone facies (the blue altered limestone rock displayed on the log in Fig. 19.2).
- 7–20 m: massive and altered limestone rock presenting heterogeneous fracture density (especially after 15 m deep).
- 20–25 m: interbeds of silicified limestone and pluri-centimetric silica cherts. Some rare silicified zones are observed in the previous layers (below 18 m deep) but not recurrently thus not appearing in the log.

The whole column is developed on a semi-permeable layer of white clay that was identified as part of the “*Molasses du Gâtinais*”. *The bottom of this layer has not been reached by the boreholes* but its thickness regionally ranges from 1 to 2 m.

The water table level is not depicted on the lithological log. It usually varies between 18 and 20 m deep, with historical variations from 14.5 to 22.5 m deep [31, 33]. For each of the result presented in this paper, the depth of the water table was measured from the O-ZNS boreholes and is presented in the corresponding section.

19.1.4 Geological Structures Characterization

Optical log imaging (May 2020, B5 to 7, Fig. 19.3) provide a clear view of the largest heterogeneities (dm to m scale) that can be found along the VZ of the O-ZNS experimental site. Different types of porosity (cracks, pores, fractures, karsts) are observed in the limestone rock facies with an increasing occurrence of karstification and fracturation with depth.

Drill core pictures (Fig. 4a) and 3D reconstruction by photogrammetry of a core sample (Fig. 4b) illustrate the complex and multi-scale (mm to cm) smaller heterogeneities such as macro-pores, clasts, and cracks. Figure 4a also illustrates the facies described in Sect. 19.1.2 with first, the soil, followed by the highly heterogeneous incoherent limestone (with a thin layer of massive limestone) and the limestone rock, more or less altered and fractured.

At a lower scale, Fig. 5a presents optical microscopic views of massive limestone rock taken between 11 and 14 m deep. We observe mechanical and chemical micro-heterogeneities as cracks developing inside grains (intragranular cracks), oxidation and dissolution-recrystallisation of the calcite [26]. The lowest scale of scanning electron microscopy (SEM) highlights the micro porosities (Fig. 5b).

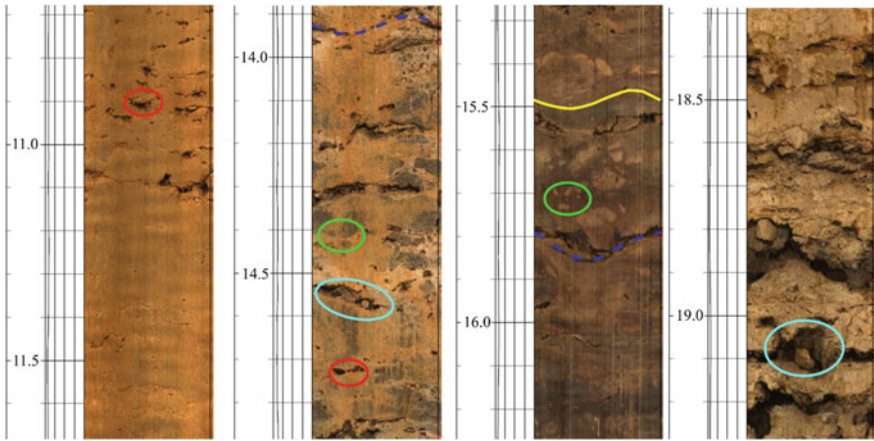


Fig. 19.3 Imagery of B5 at different depths highlighting the variety of heterogeneities (macropores in red, clasts in green, macro-cracks/fractures in dark blue, karsts in light blue, lithological interfaces in yellow)

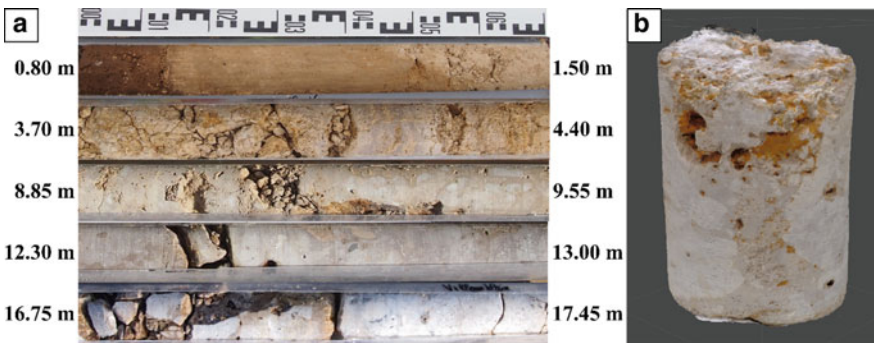


Fig. 19.4 **a** Pictures of cores from B1 (70 cm each) taken in the four facies presented in Fig. 19.2. **b** 3D reconstruction of a core sample taken from B7 at 11 m deep

To summarize the multi-heterogeneities, Table 19.1 gives their ranges of length and aperture measured following a vectorization method [35, 36] and observed on these figures and in the whole work of Aldana [34]. Note that for the fractures the upper size is yet unknown and will be determined with future field imagery investigations.

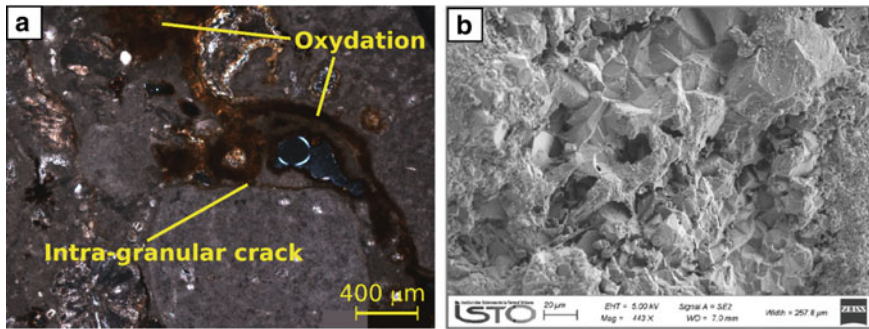


Fig. 19.5 **a** SEM observation of micro-porosity in limestone rock from B2 at 9.7 m deep. **b** Polarized microscopic observation of calcareous matrix showing oxidation and intra-granular crack, from B2 at 11.1 m deep. Modified from [34]

Table 19.1 Classification of heterogeneities observed on log imageries, core samples (as in Fig. 19.4) and microscopic observations (Fig. 19.5 and [37])

	Length		Aperture	
	min	max	min	max
Spherical pore or clast	5 μm	60 mm		
Crack	1 mm	10 cm	1 μm	6 mm
Fracture	10 cm	Unknown	>cm	Unknown
Karst	5 cm	30 cm	1 cm	5 cm

19.2 O-ZNS Geophysical Strategy

19.2.1 Interest of a Multi-geophysical Approach

As introduced in Sect. 19.1.2, coupling geophysical methods broadens the physical description, the range of resolution and depth of observations, as suggested by Fig. 19.6 which presents all methods used during O-ZNS preliminary investigations.

Specific advantages and drawbacks of the four methods used for this study are detailed below:

- Nuclear Magnetic Resonance (NMR) monitors the electromagnetic signal produced by water bodies in response to oscillating magnetic perturbations [40, 41]. As this method directly relates to the water content, it is primarily used to estimate hydraulic properties of the VZ [40]. NMR also provides different scales of observation with surface (SNMR or MRS [7]), borehole, and recently, surface-to-borehole measurements [41, 42]. Development of multi-channel instruments has also allowed to access from 1 to 2D and 3D measurements [43]. Although the poor signal to noise ratio limits this method [42], it has proven its efficiency for limestone VZ and karstic aquifer characterization [7, 44, 45].

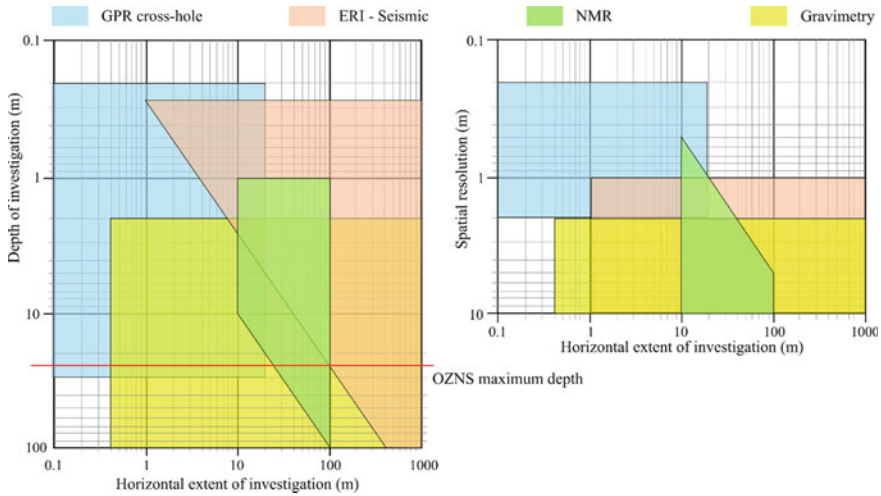


Fig. 19.6 Comparison of depth of investigation and spatial resolution of geophysical methods: GPR, ERI, Seismic, NMR, and Gravimetry. Adapted from Fan et al. [38], authors' experiences and other synthesized data (e.g. [39])

- Seismic refraction methods [46–48] are best applied to the characterization of tabular objects such as soil layers or horizontal cracks [5]. They also provide insights into water saturation for groundwater modeling [46] or into deep formations [39]. Seismic interpretation can be complex, even unsolvable when crossing blind zone (i.e. velocity decrease in function of depth) [47]. However, as saturation increases P and S-wave anisotropy [48], it may allow to better characterize the presence of fluid.
- Electromagnetic methods [6, 49] such as DC Electrical Resistivity Imaging (ERI) [50] and Ground Penetrating Radar (GPR) [49, 51, 52] depend on many factors, including salinity, water content, cation exchange capacity and porosity of the material [53, 54]. Although these methods can be applied to the monitoring of the water content, for example in agriculture [55] and the VZ of calcareous environments [56], the interpretation of direct current resistivity data alone is particularly complex because it is often impossible to separate the so-called volume contribution from that of the phase interfaces (conduction of electrical double layer) [57]. While GPR gives high resolution, in conductive environment, it presents a small penetration depth [58]. Since these two methods (ERI and GPR) have complementary resolution, they are often coupled together [59].

19.2.2 Overview of the Measurements Made on O-ZNS Experimental Site

Surface measurements

The area around the O-ZNS experimental field has been historically studied with early observation conducted by INRAE and BRGM since the 1990s [7, 32, 55] and more recently by ISTO as part of several projects. From that time, electrical map and electrical resistivity tomography have been made together with SNMR measurements (monitoring 1999–2000 and 2017) on a field located in close proximity (1 km south) of O-ZNS experimental site [7].

Since the beginning of O-ZNS project surface investigations have been conducted including:

- 1D and 2D SNMR in January 2019.
- 2D ERI in 2017, 2018 and 3D in April 2019.
- 2D seismic in October 2018.

Finally, in August 2020 a multi-geophysical monitoring campaign has been carried out that included 2D seismic surface, 3D ERI, 3D SNMR and gravimetry mapping. These full data sets, coupled to the borehole measurements performed at the same time (Table 19.2) will be joined in a global inversion for future contribution and will complement the initial characterization of the VZ functioning undertaken since 2017.

Borehole measurements

In addition to surface measurements, the same methods have been employed in boreholes when applicable (Table 19.2). Note that due to wave attenuation (i.e. high conductive subsurface zone), GPR measurements are only feasible in borehole and cross-hole fashion.

Future equipment and measurements

The instrumentation strategy of the O-ZNS project is briefly detailed in the Chap. II.2. by Abbar et al. [3] with the description of few hydrogeological monitoring solutions under consideration and the installation of fiber optic sensors. Indeed, continuous measurements are planned for monitoring purposes, including three distributed fiber optic sensors (temperature-DTS), strain-DSS and acoustic-DAS) installed in a continuous and permanent loop along B5, 6 and 7 boreholes. In addition, in the same boreholes, seismic and GPR monitoring are planned as well as the implementation of vertical electrical resistivity devices to continuously monitor the conductivity of the VZ materials.

Further geophysical equipment are expected once the well is in place: seismic measurements, composed by 60 triple geophones with a natural frequency of 100 Hz and a seismic well source; GPR antennas placed on the inside on the well to communicate with the surrounding boreholes; gravimetry and muon measurements from inside the well. From the wall of the well itself, lateral slanted boreholes will be

Table 19.2 Borehole measurements on O-ZNS experimental site. B4 and 8–9 are presented in Abbar et al. [3] (Chap. II.2.)

Method	Borehole	Date	Made with	
Log	B1–4	03–2017	Iduna-Soleo	Diameter, electric conductivity, γ - γ
Log	B1–4	03–2017	Iduna-Soleo	Diameter, trajectory, imaging (low resolution), γ -ray
Log	B1–4	05–2017	Iduna-Soleo	Neutron-neutron
GPR	B1–3	01–2019	BRGM-EOST	Cross-hole: 3 panels
Log	B5–9	05–2020	Semm Logging	Diameter, electric conductivity, trajectory, imaging, γ - γ , neutron-neutron, γ -ray
GPR	B5–8	08–2020	BRGM	Borehole and cross-hole (6 panels)
Log	B6–7	09–2020	Semm Logging	γ - γ , neutron-neutron (cased hole)
Log	B5–8	09–2020	NMRSA	NMR
Log	B5–8	09–2020	Geosciences Montpellier	γ -ray, magnetic susceptibility, electric conductivity, physico-chemical parameters (pT, Eh, pH), PS in a single borehole
Seismic	B5–8	10–2020	BRGM	Cross-hole (P and S-wave)

drilled at various depths containing further geophysical equipment such as Time Domain Reflectivity (TDR) probes (communicating with surface probes and GPR antenna fixed in the lateral wall) to measure permittivity, polarizable and unpolarizable electrodes for DC electrical resistivity and spontaneous potential measurements respectively.

19.2.3 *Protocols of the Measurements Presented in This Study*

Even though all scales of NMR survey are applied at O-ZNS site, this chapter focusses on a **Surface Nuclear Magnetic Resonance (SNMR) survey**, performed in January 2019, which consisted in four soundings aligned in half-overlapping square loops along a North-West profile using coincident transmitter and receiver loops (Fig. 7a). The loops are of 20×20 m side with two turns to concentrate our investigation on the superficial part of the aquifer. Thanks to the multi-channel NMR system NumisPoly[®], a synchronous reference loop was placed nearby to mitigate the noise. Indeed, this loop was placed far enough to avoid the NMR signal and close enough to register the same ambient electromagnetic field as the measure loop. Note that a

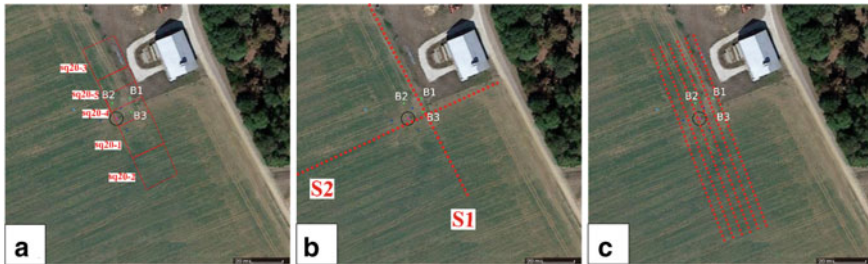


Fig. 19.7 Surface field measurements presented in this study. **a** NMR loops of Jan. 2019. **b** Seismic lines of Oct. 2018. **c** Electric lines of Apr. 2019

preliminary measurement using a pair of eight-shape loops [60] proved the O-ZNS site to have low level of noise.

The pulse frequency was 2034 Hz according to the Larmor Frequency, which is the precession of the magnetic moment, in Central France at the date of measurements (January 2019). Each sample contains 200 records (commonly called stacks) of 24 ms length sampled at 19.2 kHz and include a band-pass (16 Hz) and Notch filter. The measurements comprised 10 pulses with a maximum pulse moment of 3.500 A-ms.

The post-processing is based on previous analyses defining ambient noise between 100 and 200 nV [61]. The NMR inversion has been done thanks to SAMOVAR[®] software based on the Tikhonov regularization method [40] and resistivity of the subsurface obtained by the ERI inversions (see below).

Surface seismic measurements performed in October 2018, consisted in two lines (S1 and S2) measuring P-wave velocity and crossing the O-ZNS site (Fig. 7b). The two perpendicular lines of 144 m were equipped by Z-component geophones (with natural frequency of 14 Hz) spaced by 1 m. According to the profile length, this spacing ensures a depth of observation up to the limestone rock located at 20 m deep. The shots were made by a 5 kg hammer every 4 geophones starting at 0.5 m after the first geophone, for both lines. The first arrival times were inversed using RAYFRACT[®] software [62, 63] in order to obtain 2D spatial variations of P-wave velocity. During inversion process, the Eikonal equation is solved numerically by a finite difference method approach [64, 65].

Electrical Resistivity Imaging (ERI) performed in April 2019 consisted in a direct 3D acquisition of 288 electrodes. Specifically, it is composed by six linked 3D profiles made of 48 electrodes with an electrode spacing of 2.5 m and an inter-line spacing of 5 m thus covering a total area of 117.5×25 m. Acquisition was carried out with a Syscal Pro[®] using two configurations. The first one has 7574 quadrupoles of dipole–dipole type. The second configuration is composed of 5130 gradient-type quadrupoles. Both include $\times 1$ quadrupoles for each line and $\times 2$ inter-line quadrupoles. The measurement sequences include electrical resistivity as well as induced polarization. The same parameters have been applied to each configuration and comprise an injection time of 2000 ms, semi-log chargeability sampling

(not shown here), a standard deviation of 5% on 3–10 stacks and requested injection and reception voltage of 50 mV–800 mV respectively. Finally, both datasets were merged and processed (filter on reception voltage) to obtain a number of 9295 inverted measurements. Inversion of apparent resistivity values used BERT software [66] with a lambda regularization equal to 20, a L-curve optimization and with L1 norm (robust inversion). The model grids contain 83,866 cells and inverse model contain 44,510 cells. After 6 iterations, the Chi^2 value is equal to 1.50 and 1.46 and the Root Mean Square (RMS) is equal to 5.46% and 0.21% respectively for Resistivity and IP measurements.

The **Ground Penetrating Radar (GPR)** was performed in January 2019, and acquired with a ProEx GPR system (Malå Geosciences). We used Malå 100 MHz borehole antennae, with a sampling frequency of 1000 MHz and time-window of 240 ns. All measurements were stacked 128 times. Acquisition consists in 3 Zero Offset Profile (ZOP) between B1-2; B2-3; and B3-1. The ZOP profiles can be thoroughly investigated as providing a 1D log view as depth between each borehole. ZOP profiles consist in simultaneously descending the transmitting antenna and the receiving antenna in two different boreholes. The measurement step is equal to 50 cm. The data were processed using a zero phase 40–180 MHz band-pass filter with an Automatic Gain Control (AGC) time equalization. It is used only for picking first arrival. A final stage consists in picking of the first arrivals. Knowing the distance between two boreholes, the picking of the first arrival was transformed in apparent relative permittivity (ϵ_r) [67].

19.3 O-ZNS Preliminary Characterization

19.3.1 Surface Results

Figure 8a presents resistivity issued from the 3D electrical survey at 5 m deep. Resistivity map highlights two different anomalies with lower (A1) and higher (A2) resistivity than background. Considering that at 5 m deep, we are in the strongly altered limestone layer, the A1 anomaly is considered here as an incoherent limestone with high content of clay while A2 anomaly is assimilated to calcareous sand or altered limestone rock with low content of clay. Initially, O-ZNS main well was supposed to be located on the A1 heterogeneity (cf., grey circle on Fig. 8a). Following this first characterization, the well has been moved to the black circle in order to include this area in the monitoring as well as the representative background area.

Note that due to resolution limitations of the method, we are not sensitive to the apparition of the water table. Indeed, in the presence of water, resistivity should decrease. The fact that a decrease in resistivity value was not observed is due to our field protocol and inversion process that put forward the first ten meters instead of deepest points. The idea of this first characterization is indeed to accurately describe the spatial variations between the surface and 10 m-deep.

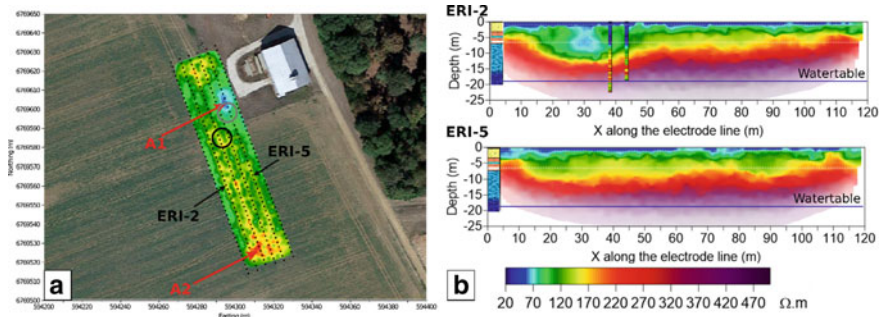


Fig. 19.8 **a** Electric resistivity observed on the 2D surface at 5 m-deep. Black and grey circles are the O-ZNS well localization and the initially planned one, respectively. **b** ERI-2 and ERI-5 profiles. On ERI-2 profile, B3 and B4 (a pressiometric borehole, located in the middle of B1, 2, 3 and presented in Abbar et al. [3]—Chap. II.2.) are shown [68]. Resistivity scale is for both figures. The water table level is indicated from our piezometric data at the date of the ERI measurement

19.3.2 2D Profiles

ERI-2 and ERI-5 profiles depicted on Fig. 8a, also taken from the 3D ERI, are shown on Fig. 8b. ERI-2 profile further illustrate A1 heterogeneity. Indeed, it goes from the sub-surface (around 1–2 m deep) to 12 m deep. Both profiles recover the three main geological facies identified on the core samples during the lithological description, at a lower resolution but at a larger scale. The first layer of soil (0–1.5 m deep) presents an electric resistivity of 20 Ω m. It is followed by the heterogeneous altered limestone facies, from 2 to 7 m deep, with an electric resistivity around 120 Ω m apart from A1 patch. Under this depth, the electric resistivity increases up to 500 Ω m down to 25 m deep. Chargeability is not shown here, but locally, the A1 heterogeneity goes up to almost 6 mV/V [68]. Due to this higher chargeability, we confirm that this layer and the A1 anomaly are filled by clayed materials.

Figure 19.9 introduces S1 and S2 profiles (Fig. 7b) and their respective P-waves velocities obtained in October 2018. Again, these surface measurements confirm the three facies succession with values under 500 m/s for the silt loam soil, from 500 to 1200 m/s for the altered limestone facies between 1.5 and 7 m deep, and an increasing velocity up to 3500 m/s for the massive and altered limestone rock. Apart from that, this investigation was not able to detect any other feature. Note that raw data showed high discrepancy and anisotropy for the altered limestone facies that have been smoothed out here by the inversion process.

19.3.3 Electrical, GPR, and NMR Profiles

The electric borehole sounding performed in March 2017 (Figs. 8b and 10a) shows an almost constant resistivity value from 1.5 to 7.0 m deep ranging from 40 to 60 Ω m with a slight increase to 100 Ω m at 2 m deep. Below this layer, the log gives

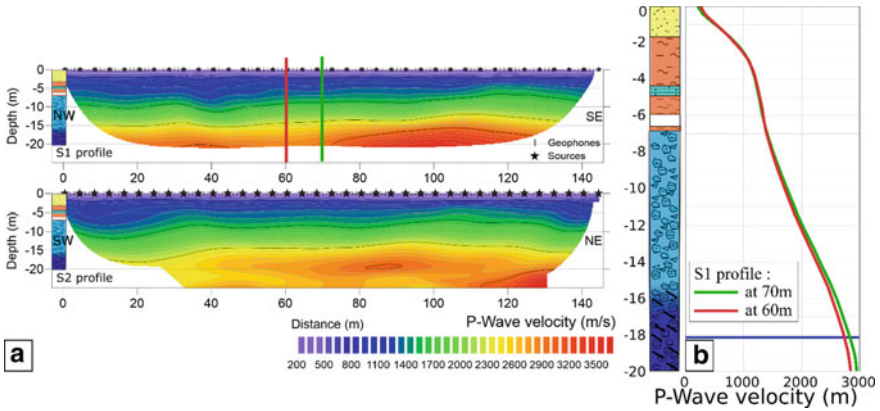


Fig. 19.9 **a** P-wave velocities obtained on both seismic profiles made in October 2018. **b** Two vertical velocity log extracted from S1 profile (lithologic log are recalled along depth)

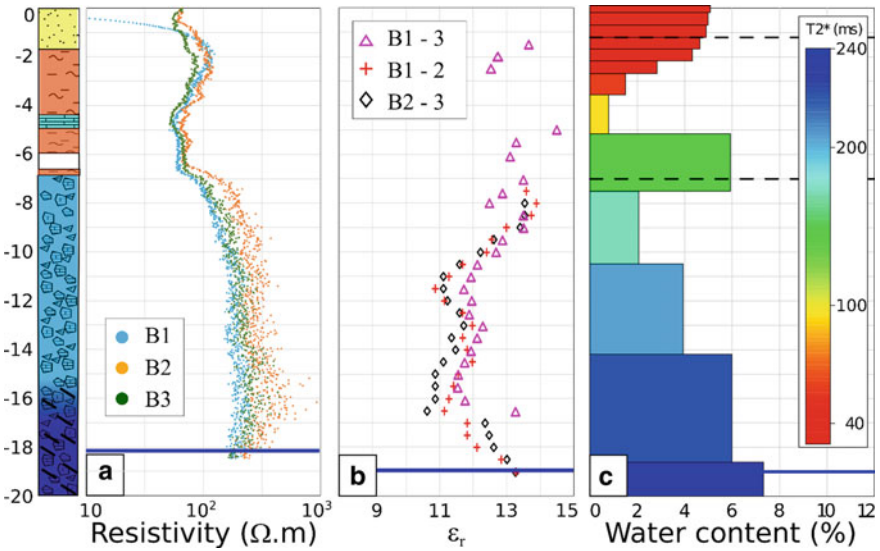


Fig. 19.10 Geophysical profiles with respect to depth: **a** electrical resistivity. **b** cross-hole profile from GPR measurements. **c** NMR water content and $T2^*$ (as defined by [41]) obtained from the NMR sounding [68]. On every figure the water table level is indicated by a blue line. On the left part a simplified lithological log is added (from Fig. 19.2) with the soil formation followed by the incoherent limestone and the massive rock facies with an increase of fracturation from 15 m deep

an important accuracy about the distribution of the electric resistivity compared to the ERI with a high resistive layer ranging mostly from 100 to 300 Ω m with some values going up all the way to 900 Ω m between 15 and 17 m deep.

Radar profiles of the GPR monitoring campaign conducted on January 2019 are presented on Fig. 10b. In our range of possible observations, we represent the results with ZOP cross-hole profiles between B1, 2 and 3. It appears that from 1 to 7 m deep, and due to significant wave attenuation (i.e. low resistive area), the GPR results are almost constant with a permittivity of 13.5. It decreases up to a permittivity of 11.5 at 11 m-deep and stay almost constant. We finally observe at 17 m-deep a jump of permittivity that could be due to the influence of the water table revealing a capillary fringe. However, it cannot be assessed without further studies coupled to fracturation and macro-permeability measurements.

NMR 1D profile with T2* [40] is shown on Fig. 10c for the loop sq20-4 (Fig. 7a) with significant NMR water content variations. Between the surface and 5 m deep, NMR water content shows a decreasing trend from 5 to 1% with highest content observed for the soil. Between 5 and 8 m deep, water content increases rather abruptly from 1 up to 6%. Then, between 8 and 20 m deep, the NMR water content uniformly increases from 2% up to the water table where it reaches a value of 7%.

19.4 Discussion

19.4.1 Geophysics for Microstructure and Lithology

We compared here two different scales of observation for electrical and seismic measurements, to specify the O-ZNS lithology (laboratory scale of seismic data can be found in [37]).

Both ERI and seismic data, and lithological observations agree, highlighting three main layers including a silt loam soil, a heterogeneous incoherent and altered limestone, and a massive and altered/fractured limestone rock. Facies by facies we can add some specifications to these lithology and microstructures:

- **In the first two facies (from 0 to 1.5 and from 1.5 to 7.0 m deep)**, the almost constant borehole resistivity is interpreted in terms of interleaved materials with high content of clay and silt. This result is in good agreement with the direct core observations (Sect. 19.1.4). The transition at 1.5 m-deep between soil and incoherent limestone is not accurate between electric and seismic measurements showing the importance of coupling these data. Indeed, as seen on the seismic log extracted between B1 and 3 (Fig. 9b orange curve), the transition is observed at 3 m deep. Although, this transition is highlighted by a slight ERI increase, but observed at 2 m-deep. The locally more important chargeability in A1 anomaly (<1.5 mV/V in the overall layer and up to 3 mV/V in A1 [68]) confirms the presence of clay in these overall facies. We also noted a slight decrease of electric resistivity in the lower part of this unit showing its higher clay content compared

to the upper part. Here again we show the importance of comparing seismic data to any other as this anomaly is not observed on the seismic log extracted at this location (Fig. 9b green curve)

- In the same layer, lithological log shown a thin layer of altered limestone rock around 4.5 m deep (Fig. 19.2). It should imply a local increase of electric resistivity and seismic velocities that are, however, not observed. This could be due to the layer that is too thin or thus too diffuse to be seen or, for the electrical data, to the method itself that is controlled by the less resistive surrounding material (A1 anomaly) that “hides” high resistive small inclusion [69].
- In the massive and altered limestone rock facies, from 7 to 20 m deep, a huge discrepancy (increasing after 15 m) was observed on the electrical log. This discrepancy is consistent with the variations observed on laboratory seismic measurements and during geomechanical tests [35]. It highlights an important degree of fracturation, becoming even more important after 15 m deep. In a companion laboratory study [39], the microcrack density has been estimated at around 0.3, with some local maximum up to 0.5 above 15 m deep. This is in good correlation with the observed fracturation on the core samples (Fig. 19.4) and the lithological log (Fig. 19.2). This increasing fracturation shown a limitation of the field seismic method. Indeed, it should be linked to a wave velocity decrease that cannot be observed by refraction methods. However, we still observe a slow-down of velocity increase with depth. On the other hand, we can see that electric resistivity data taken alone couldn't see this fracturation increase (except from its discrepancy). Indeed, the resistivity values are almost constant with no particular variations around 15–17 m-deep.
- Finally, for both ERI and seismic surface measurements, an increase was observed particularly between 17 and 20 m deep where silicified limestone rocks have been identified on direct core observations. However, due to the low resolution of these methods at that depth from surface investigations, no conclusion can be given regarding the extent of this silicified layer.

As a summary, 3D ERI and seismic surface methods have a lower resolution at greater depth but give an overview of the different lithological facies and spatial heterogeneities that brought us to revise the location of the well. The log measurements give us a better resolve of depth resistivity that match the direct core observations. Finally, we highlight the importance of coupling these two methods to depict both clay anomalies and fracturation increase that could be seen with a single method.

19.4.2 Hydrogeophysics: A Powerful Solution for Monitoring the Water Content in the Vadose Zone

As part of the first characterizations carried out within the framework of the O-ZNS project, recent studies have focused on the simulation of water flow along the heterogeneous VZ of the Beauce limestone aquifer [33]. Ten undisturbed cored samples

representative of the VZ facies (2–20 m deep) were extracted from B1 to 3. The hydraulic properties (water retention and hydraulic conductivity) of these samples were determined in the laboratory [31]. A 23 m deep VZ profile composed of thirteen layers was reconstituted in HYDRUS-1D software [70] for B2. The hydrodynamic parameters of each layer were obtained using the RetC software [71] and by fitting the experimental hydraulic properties with the van Genuchten’s expression (water retention curve) [72] and a statistical pore connection model (hydraulic conductivity curve) [73]. The simulation of water flow within the VZ profile was performed over a 54 years period (1966–2019) considering the meteorological and water level data. It allows us to compare our field geophysical measurements and interpretations to the water content values simulated at the same date (Fig. 19.11).

Looking at the extreme water content variations between the minimum ($WTL_{MIN} = -22.45$ m on 26/08/1992) and maximum ($WTL_{MAX} = -14.84$ m on 18/05/2001)

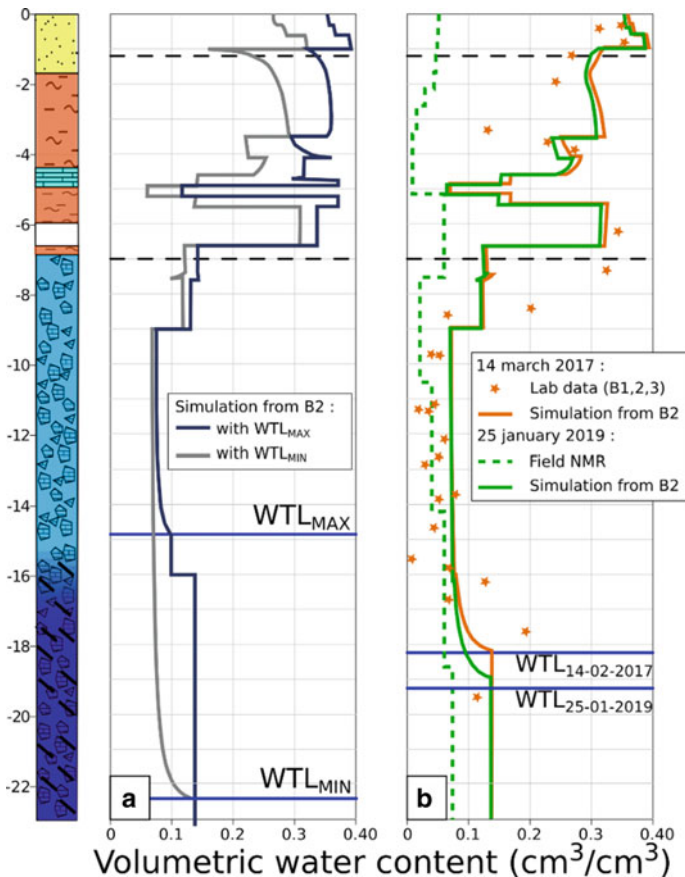


Fig. 19.11 Volumetric water content values: **a** Simulated at the dates corresponding to the minimum and maximum water table levels. **b** Field NMR data compared to simulations at the same date

water table level, we observe that the water content of the deepest part of the VZ is relatively stable. Indeed, the most significant changes between the two profiles were observed between 0 and 7 m deep ($>0.10 \text{ cm}^3/\text{cm}^3$ and up to $0.23 \text{ cm}^3/\text{cm}^3$). Inversely, the least significant changes between the two profiles ($<0.05 \text{ cm}^3/\text{cm}^3$) were observed below 7 m (Fig. 11a). This first observation assesses the average geological interpretations highlighting the soil and the incoherent limestone facies above 7 m deep followed by the massive and altered limestone rock facies down to the water table.

On Fig. 11b, experimental water content measured on core samples in the laboratory were compared to simulations made at the same date [31]. This figure also compared the experimental NMR water content profile obtained from the surface NMR sounding sq20-4 made on 25/01/2019 (from Fig. 10c) and water content simulated by HYDRUS-1D (based on hydraulic properties measured in the laboratory) at the same. At this stage of O-ZNS first characterization, we do not have the means to define petrophysical relations and thus link quantitatively ERI and GPR to the water content (but it is currently under process). Still, we use the data presented in Fig. 19.10 A and B to qualitatively improve our discussion, knowing that we have to stay careful because these data were not measured at the same date as the SNMR.

Between 0 and 7 m deep, the NMR results displayed much less water storage than the simulated profile. Although it has been shown that the model slightly overestimated laboratory experimental water content (Fig. 11b orange results) [31], this difference is still important. It can be explained by the weak capability of NMR to detect water in materials with high proportions of clay and/or silt [7] that is largely present at these depths. Indeed, in this layer GPR data is not often measurable (Fig. 10b) due to the low resistive area representative of a clayed zone. This is coherent with preliminary studies made within the framework of the O-ZNS project that have shown that the majority of the VZ materials located from 0 to 5 m deep had high proportions of clay and silt, ranging from 13 to 26% and from 32 to 53%, respectively [31].

In the thin sub-layer around 5 m deep, NMR results are slightly closer to those obtained with HYDRUS-1D. As highlighted by the visual examination of the undisturbed cored samples [31], this could be attributed to the calcareous sand intervals observed between 5 and 6 m deep and/or to the altered limestone rock observed at around 5 m deep in the VZ profile (Fig. 19.2). Indeed, these geological facies displayed much lower clay and silt proportions than the other VZ materials allowing the NMR to detect more precisely their water content [6]. Note that, NMR results of the other loops demonstrated the same global variations of the water content along the VZ profile. It seems coherent with the ERI variations (Fig. 10a) highlighting here a decrease in the resistivity (even so this comparison has to be considered carefully because these two measurements haven't been made at the same date). This observation could indicate the presence of a more clayey facies, but also the presence of a calcareous layer with low values of water content. The second option is in good agreement with the simulated values of water content (Fig. 11b orange results) and NMR results. Thus, our interpretation for this thin layer is the presence of a massive

calcareous zone presenting a high porosity due to fracturation and alteration with low water content at the date of the measurements.

Between 8 and 23 m deep, NMR water content measured in the massive and altered limestone rock facies ranged from 0.020 to 0.085 cm³/cm³. These results were consistent with those obtained by Legchenko et al. [7] during surface NMR sounding conducted between 26/04/1999 and 15/03/2000 at a few hundred meters from O-ZNS study site. The simulated values were also relatively close, although always higher, than the experimental water content and SNMR results (Fig. 11b). As observed by Legchenko et al. [7], and with this field data, it is worth noting that the NMR sounding did not allow to detect precisely the water table level (measured at -18.92 m on 25/01/2019) because of the limited resolution of the method or maybe because of the presence of a potential capillary fringe as seen by the GPR data.

19.5 Conclusion

Throughout this chapter, we proposed a multi-geophysical monitoring approach in order to characterize the lithological and petrophysical properties of a highly heterogeneous vadose zone of a vulnerable limestone aquifer.

Taken individually, electric, electromagnetic or seismic measurements are not able to fully describe the various sizes and scales of fractures and karsts present at different depths. Therefore, O-ZNS geophysical strategy relies on coupled methods. Altogether, geophysical imaging, made from the surface as well as in boreholes, makes it possible to obtain valuable information on lithology as well as about the variations of the water content within the VZ. Especially, SNMR preliminary results illustrates the impact of the presence of facies with low proportions of clay and silt on the variations in water content along the VZ. GPR highlights the possible presence of a capillary fringe and the water table level, with the increasing of permittivity observed from 17 m deep. ERI draws attention to the presence of layers with high proportions of clay and high water content identified between 4 and 7 m deep. Seismic measurement describes variation in the lithology with depth and also gives an estimation of the crack density at the laboratory scale.

With our first crossed interpretations, we have clearly shown that the results obtained with geophysical soundings can be coupled to laboratory hydraulic properties measurements and numerical simulations, and lithological description made on undisturbed core samples. This comprehensive set of results lead to a significantly enhancement of possible interpretations.

However, further studies are still needed for quantitatively linking the measured geophysical parameters to petrophysical and transport properties of the vadose zone. Ongoing work is focused on the joint inversion of data obtained through multiple surface and borehole geophysical soundings (NMR, GPR, ERI, Seismic, and Gravimetry) conducted in August 2020. In addition, it is planned to carry out

laboratory investigations to accurately apply Topp and Archie's laws to quantitatively describe the water content from the already presented GPR and electric data [74–76]. Then, added to fracture and connected karst imagery from the seismic data, it is finally expected to obtain the overall in-situ permeability. Furthermore, larger scale investigations based on the O-ZNS well and surrounding boreholes will ensure complementary scales of observation and couplings of methods to reduce uncertainties and better image the VZ heterogeneities. To do so, it is planned to compare the surface well imagery (acquired during the well digging) to our multi-geophysical methods. The comparison of this whole set of data between them and with the hydrogeological measurements conducted in parallel should improve the estimation of the variations of the water content through the whole porosity (matrix and fractures) of the VZ. This will help for the characterization of the transport properties of its highly heterogeneous facies by building on 3D multiphase reactive transport models.

Acknowledgements This research work was conducted within the framework of the O-ZNS project which is part of PIVOTS project. We gratefully acknowledge the financial support provided by the Région Centre-Val de Loire (ARD 2020 program and CPER 2015–2020) and the French Ministry of Higher Education and Research (CPER 2015–2020 and public service to BRGM). This is also co-funded by European Union with the European Regional Development Fund (FEDER). Finally, this research work is co-funded by the Labex VOLTAIRE (ANR-10-LABX-100-01).

Authors are also thankful for the help of K. Moreau and B. Brigaud from Université Paris Saclay, S. Andrieu and E. Husson from the BRGM for the characterization of rock facies, L. Bodet, R. Guérin and CRITEX for the seismic acquisition, A. Bitri from the BRGM for the seismic inversion, J.-M. Baltassat and S. Ammor from the BRGM for the NMR acquisition and inversion, T. Jouen (ISTO) and J.-C. Gourry (BRGM) for the ERT acquisition and inversion, SEMM Logging for the geophysical logs, IRIS Instrument, Geosciences Montpellier and NMR Services Australia for the equipment loan.

References

1. Stephens D (1995) *Vadose zone hydrology*. CRC press
2. Arora B, Dwivedi D, Faybishenko B, Jana RB, Wainwright M (2019) Understanding and predicting vadose zone processes. *React Transp Nat Eng Syst* 85:303–328
3. Abbar B, Isch A, Michel K, Vincent H, Abbasimaedeh P, Azaroual M Fiber optic sensors for environmental monitoring: state of the art and application in heterogeneous karstic limestone vadose zone of an agricultural field—Beauce Aquifer (O-ZNS), Orleans, France. *Instrum Measure Technol Water Cycle Manage Chapter II.2*
4. Chalikakis K, Plagnes V, Guerin R, Valois R, Bosch F (2011) Contribution of geophysical methods to karst-system exploration: an overview. *Hydrogeol J* 19(6):1169
5. Lamb PB, Londhe DR (2012) Seismic behaviour of soft first storey. *IOSR J Mech Civil Eng* 2278–1684
6. Falzone S, Robinson J, Slater L (2019) Characterization and monitoring of porous media with electrical imaging: a review. *Transp Porous Media* 130(1):251–276
7. Legchenko AV, Baltassat J-M, Duwig C, Boucher M, Girard J-F, Soruco A, Beauce A, Mathieu F, Legout C, Descloitres M, Patricia FAG (2020) Time-lapse magnetic resonance sounding measurements for numerical modeling of water flow in variably saturated media. *J Appl Geophys* 175:103984

8. Keskinen J, Klotzche A, Looms MC, Moreau J, van der Kruk J, Holliger K, Stemmerik L, Nielsen L (2017) Full-waveform inversion of crosshole GPR data: Implications for porosity estimation in chalk. *J Appl Geophys* 140:102–116
9. Champollion C, Deville S, Chéry J, Doerflinger E, Le Moigne N, Bayer R, Vernant P, Mazzilli N (2018) Estimating epikarst water storage by time-lapse surface-to-depth gravity measurements. *Hydrol Earth Syst Sci* 22(7):3825–3839
10. Vozoff K, Jupp DLB (1975) Joint inversion of geophysical data. *Geophys J Roy Astron Soc* 42:977–991
11. Linde N, Doetsch J (2016) Joint inversion in hydrogeophysics and near surface geophysics. In: *Integrated imaging of the earth: theory and applications*. John Wiley & Sons, pp 119–135
12. Gallardao LA, Fontes SL, Meju MA, Buonora MP, de Lugao PP (2012) Robust geophysical integration through structure-coupled joint inversion and multispectral fusion of seismic reflection, magnetotelluric, magnetic, and gravity images: example from Santos Basin, offshore Brazil. *Geophysics* 77(5):B237–B251
13. Carcione J, Ursin B, Nordskog J (2007) Cross-property relations between electrical conductivity and the seismic velocity of rocks. *Geophysics* 72(5):193–204
14. Davis K, Li Y, Batzle M (2008) Time-lapse gravity monitoring: A systematic 4D approach with application to aquifer storage and recovery. *Geophysics* 73(6):WA61–WA69
15. Doetsch J, Krietsch H, Schmelzbach C, Jalali M, Gischig V, Villiger L, Amann F, Maurer H (2020) Characterizing a decametre-scale granitic reservoir using ground-penetrating radar and seismic methods. *Solid Earth* 11(4):1441–1455
16. Lochbühler T, Doetsch J, Brauchler R, Linde N (2013) Structure-coupled joint inversion of geophysical and hydrological data. *Geophysics* 78(3):ID1–ID14
17. Cassidy R, Comte J-C, Nitsche J, Wilson C, Flynn R, Ofterdinger U (2014) Combining multi-scale geophysical techniques for robust hydro-structural characterisation in catchments underlain by hard rock in post-glacial regions. *J Hydrol* 517:715–731
18. Linde N, Renard P, Mukerji T, Caers J (2015) Geological realism in hydrogeological and geophysical inverse modeling: a review. *Adv Water Resour* 86:86–101
19. Grana D (2018) Joint facies and reservoir properties inversion Dario. *Geophysics* 83(3):M15–M24
20. Linde N, Binley A, Tryggvason A, Pedersen L, Revil A (2006) Improved hydrogeophysical characterization using joint inversion of cross-hole electrical resistance and ground-penetrating radar traveltimes. *Water Resour Res* 42(12)
21. Shahin A, Myers M, Hathon L (2020) Global optimization to retrieve borehole-derived petrophysical properties of carbonates. *Geophysics* 85(3):D75–D82
22. Heincke B, Jegen M, Moorkamp M, Hobbs RW, Chen J (2017) An adaptive coupling strategy for joint inversions that use petrophysical information as constraints. *J Appl Geophys* 136:279–297
23. Colombo D, Rovetta D (2018) Coupling strategies in multiparameter geophysical joint inversion. *Geophys J Int* 215(2):1171–1184
24. Miotti F, Zerilli A, Menezes PTL, Crepaldi JLS, Viana AR (2018) A new petrophysical joint inversion workflow: advancing on reservoir’s characterization challenges. *Interpretation* 6(3):SG33–SG39
25. Jordi C, Doetsch J, Günther T, Schmelzbach C, Maurer H, Robertsson JOA (2020) Structural joint inversion on irregular meshes. *Geophys J Int* 220(3):1995–2008
26. Monaghan AA, Dochartaigh BO, Fordyce F, Loveless S, Entwisle D, Quinn M, Smith K, Ellen R, Arkley S, Kearsey T, Campbell SDG, Fellgett M, Mosca I (2017) UKGEOS: glasgow geothermal energy research field site (GGERFS): initial summary of the geological platform
27. Bogena HR, Montzka C, Huisman JA, Graf A, Schmidt M, Stockinger M, Von Hebel C, Hendricks-Franssen HJ, Van Der Kruk J, Tappe W, Lücke A, Baatz R, Bol R, Groh J, Pütz T, Jakobi J, Kunkel R, Sorg J, Vereecken H (2018) The TERENO-Rur hydrological observatory: a multiscale multi-compartment research platform for the advancement of hydrological science. *Vadose Zone J* 17(1):1–22
28. Liu S, Li X, Xu Z, Che T, Xiao Q, Ma M, Qinhuo L, Rui J, Jianwen G, Liangxu W, Weizhen W, Yuan Q, Hongyi L, Tongren X, Youhua R, Xiaoli H, Shengjin S, Zhongli Z, Junlei T, Yang

- Z, Zhiguo R (2018) The Heihe integrated observatory network: a basin-scale land surface processes observatory in China. *Vadose Zone J* 17(1):1–21
29. Bogen HR, White T, Bour O, Li X, Jensen KH (2019) Toward better understanding of terrestrial processes through long-term hydrological observatories. *Vadose Zone J* 17(1)
 30. Blazevic LA, Bodet L, Pasquet S, Linde N, Jougnot D, Longuevergne L (2020) Time-lapse seismic and electrical monitoring of the vadose zone during a controlled infiltration experiment at the Plomeur hydrological observatory, France. *Water* 12(5):1230
 31. Aldana C, Isch A, Bruand A, Azaroual M, Coquet Y (2021) Relationship between hydraulic properties and material features in a heterogeneous vadose zone of a vulnerable limestone aquifer. *Vadose Zone J* e20127
 32. Ould Mohamed S, Bruand A, Bruckler L, Bertuzzi P, Guillet B, Raison L (1997) Estimating long-term drainage at a regional scale using a deterministic model. *Soil Sci Soc Am J* 61(5):1473–1482
 33. Isch A, Coquet Y, Abbar B, Aldana C, Abbas M, Bruand A, Azaroual M (2022). A comprehensive experimental and numerical analysis of water flow and travel time in a highly heterogeneous vadose zone. *J Hydrol*, 610: 127875
 34. Aldana C (2019) Etudes des propriétés de transfert de la zone non saturée. Application aux calcaires aquitainiens de l'aquifère de Beauce. PhD thesis, Orleans'University
 35. Mallet C, Fortin J, Guéguen Y, Bouyer F (2013) Effective elastic properties of cracked solids: an experimental investigation. *Int J Fract* 182(2):275–282
 36. Mallet C, Fortin J, Guéguen Y, Bouyer F (2014) Evolution of the crack network in glass samples submitted to brittle creep conditions. *Int J Fract* 190(1–2):111–124
 37. Mallet C, Isch A, Azaroual M (2022) Heterogeneity and fracturation characterization of the carbonate O-ZNS site through uniaxial and triaxial tests. *Int J Rock Mech Mining Sci*, 153:105050
 38. Fan B, Liu X, Zhu Q, Qin G, Li J, Guo L (2020) Exploring the interplay between infiltration dynamics and critical zone structures with multiscale geophysical imaging: a review. *Geoderma* 374:114431
 39. Binley A, Hubbard SS, Huisman JA, Revil A, Robinson DA, Singha K, Slater LD (2015) The emergence of hydrogeophysics for improved understanding of subsurface processes over multiple scales. *Water Resour Res* 51(6):3837–3866
 40. Legchenko AV (2013) *Magnetic resonance imaging for groundwater*. John Wiley & Sons
 41. Behroozmand A, Keating K, Auken E (2015) A review of the principles and applications of the NMR technique for near-surface characterization. *Surv Geophys* 36(1):27–85
 42. Müller-Petke M, Yaramanci U (2008) Resolution studies for magnetic resonance sounding (MRS) using the singular value decomposition. *J Appl Geophys* 66:165–175
 43. Kremer T, Müller-Petke M, Michel H, Dlugosch R, Irons T, Hermans T, Nguyen F (2020) Improving the accuracy of 1D surface nuclear magnetic resonance surveys using the multi-central-loop configuration. *J Appl Geophys* 177:104042
 44. Mazzilli N, Boucher M, Chalikakis K, Legchenko AV, Jourde H, Champollion C (2016) Contribution of magnetic resonance soundings for characterizing water storage in the unsaturated zone of karst aquifers. *Geophysics* 81(4):WB49–WB61
 45. Mazzilli N, Chalikakis K, Carrière SD, Legchenko AV (2020) Surface nuclear magnetic resonance monitoring reveals karst unsaturated zone recharge dynamics during a rain event. *Water* 12:3183
 46. Gregory A (1976) Fluid saturation effects on dynamic elastic properties of sedimentary rocks. *Geophysics* 41(5):896–921
 47. Haeni F (1986) Application of seismic refraction methods in groundwater modeling studies in New England. *Geophysics* 51(2):236–249
 48. Pasquet S, Bodet L, Bergamo P, Camerlynck C, Dhemaied A, Flipo N, Guérin R, Rejiba F (2015) Contribution of seismic methods to hydrogeophysics. In: *Near surface geoscience 2015–21st European meeting of environmental and engineering geophysics*, vol 1, pp 1–5
 49. Révil A, Karaoulis MC, Johnson TC, Kemna A (2012) Review: some low-frequency electrical methods for subsurface characterization and monitoring in hydrogeology. *Hydrogeol J* 20(4):617–658

50. Loke MH, Chambers JE, Rucker DF, Kuras O, Wilkinson PB (2013) Recent developments in the direct-current geoelectrical imaging method. *J Appl Geophys* 95:135–156
51. Catarina P, Alcalá FJ, Carvalho JM, Ribeiro L (2017) Current uses of ground penetrating radar in groundwater-dependent ecosystems research. *Sci Total Environ* 595:868–885
52. Liu X, Chen J, Cui X, Liu Q, Cao X, Chen X (2019) Measurement of soil water content using ground-penetrating radar: a review of current methods. *Int J Digital Earth* 12(1):95–118
53. Revil A, Cathles L, Losh S, Nunn J (1998) Electrical conductivity in shaly sands with geophysical applications. *J Geophys Res* 103(B10):23925–23936
54. Jougnot D, Revil A (2010) Thermal conductivity of unsaturated clay-rocks. *Hydrol Earth Syst Sci* 14:91–98
55. Michot D, Benderiter Y, Dorigny A, Nicoullaud B, King D, Tabbagh A (2003) Spatial and temporal monitoring of soil water content with an irrigated corn crop cover using surface electrical resistivity tomography. *Water resource Research* 39(5)
56. Watlet A, Kaufmann O, Triantafyllou A, Poulain A, Chambers JE, Ledrum PI, Wilkinson PB, Hallet V, Quinif Y, Van Ruymbeke M, Van Camp M (2018) Imaging groundwater infiltration dynamics in the karst vadose zone with long-term ERT monitoring. *Hydrol Earth Syst Sci* 22:1563–1592
57. Leroy P, Li S, Jougnot D, Revil A, Wu Y (2017) Modeling the evolution of complex conductivity during calcite precipitation on glass beads. *Geophys J Int* 209(1):123–140
58. Deparis J, Fricout B, Jongmans D, Villemin T, Effendiantz L, Mathy A (2008) Combined use of geophysical methods and remote techniques for characterizing the fracture network of a potentially unstable cliff site (the “Roche du Midi”, Vecors massif, France). *J Geophys Eng* 5(2):147–157
59. Carrière SD, Chalikakis K, Sénéchal G, Danquigny C, Emblanch C (2013) Combining electrical resistivity tomography and ground penetrating radar to study geological structuring of karst unsaturated zone. *J Appl Geophys* 94:31–41
60. Girard J-F, Jodry C, Matthey P-D (2019) On-site characterization of the spatio-temporal structure of the noise for MRS measurements using a pair of eight-shape loops. *J Appl Geophys* 178:104075
61. Lubczynski M, Roy J (2004) Magnetic resonance sounding: new method for ground water assessment. *Groundwater* 42(2):291–303
62. Schuster GT, Quintus-Bosz A (1993) Wavepath eikonal travelttime inversion: theory. *Geophysics* 58(9):1314–1323
63. Rohdewald SR (2011) Interpretation of first-arrival travel times with wavepath eikonal travelttime inversion and wavefront refraction method. In: *Symposium on the application of geophysics to engineering and environmental problems*, pp 31–38
64. Lin FC, Ritzwoller MH, Snieder R (2009) Eikonal tomography: surface wave tomography by phase front tracking across a regional broad-band seismic array. *Geophys J Int* 177(3):1091–1110
65. Hubral P, Tygel M, Schleicher J (1996) Seismic image waves. *Geophys J Int* 125(2):431–442
66. Team GD (2020) pyGIMLi tutorials. https://www.pygimli.org/_tutorials_auto/index.html. Accessed 2020
67. Giroux B, Gloaguen E, Chouteau M (2007) bh_tomo—a matlab borehole georadar 2D tomography package. *Comput Geosci* 33(1):126–137
68. Jodry C, Jouen T, Isch A, Baltassat J-M, Deparis J, Laurent G, Mallet C, Azaroual M (2019) Geophysical imaging for the petrophysical properties characterization of a limestone heterogeneous vadose zone—beauce aquifer (france). In: *AGU Fall Meeting, San Fransisco, USA, Dec 2019*
69. Telford WM, Geldart LP, Sheriff RE (1990) *Applied geophysics*. Cambridge university press
70. Šimůnek J, van Genuchten MT, Šejna M (2016) Recent developments and applications of the HYDRUS computer software packages. *Vadose Zone J* 7(15):25
71. van Genuchten M, Leif F, Yates S (1991) The RETC code for quantifying hydraulic functions of unsaturated soils. USEPA, Washington, DC

72. van Genuchten M (1980) A closed-form equation for predicting the hydraulic conductivity of unsaturated soils. *Soil Sci Soc Am J* 44(5):892–898
73. Mualem Y (1976) A new model for predicting the hydraulic conductivity of unsaturated porous media. *Water Resour Res* 12(3):513–522
74. Archie GE (1942) The electrical resistivity log as an aid in determining some reservoir characteristics. *Trans AIME* 146(01):54–62
75. Topp GC, Davis JL, Annan AP (1980) Electromagnetic determination of soil water content: measurements in coaxial transmission lines. *Water Resour Res* 16(3):574–582
76. Glover PWJ (2011) Geophysical properties of the near surface Earth: electrical properties. *Treatise Geophys* 11:89–137

Chapter 20

Measuring the Dielectric Properties of Soil: A Review and Some Innovative Proposals



Iman Farhat, Lourdes Farrugia, Julian Bonello, Charles Sammut, and Raffaele Persico

Abstract In this contribution the main electromagnetic techniques exploited for the measurement of the dielectric permittivity of a material under test (MUT) are resumed, with particular emphasis on the technique of the Time Domain Reflectometry (TDR). In this framework, we propose also an innovative multilength TDR strategy, in order to achieve more information on the MUT, even at single frequency. This can help for the measure of the dispersion law of the materials, that can be a sort of signature of that material with respect to its moisture content and possibly with respect to the inclusion of some polluting substance melted in it.

Keywords Dielectric permittivity · TDR

20.1 Introduction

Soil water content (SWC) is an important parameter in relation to phenological and biophysical processes, as e.g. seed germination, healthy plant growth and of course in order to optimise crop yield. SWC also affects water infiltration and the spreading of possible polluting substances. For these reasons, accurate and reliable quantification of SWC is necessary for several applications in agriculture, and in particular for an optimal irrigation that limits as much as possible the waste of water.

I. Farhat · L. Farrugia · J. Bonello · C. Sammut
Department of Physics, University of Malta, Msida, Malta
e-mail: iman.farhat@um.edu.mt

L. Farrugia
e-mail: lourdes.farrugia@um.edu.mt

J. Bonello
e-mail: julian.bonello@um.edu.mt

C. Sammut
e-mail: charles.sammuto@um.edu.mt

R. Persico (✉)
Department of Environmental Engineering (DIAM), University of Calabria, Rende, Italy
e-mail: raffaele.persico@unical.it

Time domain reflectometry (TDR) is a technique that allows an indirect measure of the water content in the soil because it is sensitive to the dielectric permittivity which is affected by the water content in the soil. There are semi-empirical relationships between dielectric permittivity and water content in the literature, the most famous of which is the polynomial relation introduced by Topp et al. [1]. Indeed, establishing the physico-chemical relationship can enable a calibration of the relationship for the soil at hand, thus extracting a reliable correspondence with SWC.

In this contribution we will focus on measurements of the electromagnetic characteristics of the soil (namely the complex permittivity, also accounting for the electrical conductivity). In particular, we will expose the main techniques based on guided waves and eventually focus on TDR measurements, because a TDR device can be deployed in the field more easily than other methodologies.

Soil might also present some magnetic permeability. We will not focus on this because it is a relatively rare occurrence, but it is worth outlining that a TDR technique can also be able to reveal possible magnetic properties of soil [2]. Customarily, these are not much related to the water content but rather to the presence of iron minerals, such as magnetite or maghemite [3], or possibly to some polluting substances containing iron (it is thought that varnishes of some fertilizers might create magnetic anomalies but at this stage we have not found any published works specifically devoted to testing or disproving this hypothesis).

TDR probes are mainly used in the time domain [4] but processing in the frequency domain is possible through the Fourier transformation of the measured data. Moreover, the analysis that is proposed in this chapter will be based on the reflection coefficient, which is not always the quantity directly measured. However, this quantity can be retrieved by separating, in time domain, the incident and reflected contributions to the electromagnetic signal and then consider the ratio of their spectra in the frequency domain.

That said, the innovative proposal that is discussed in this contribution makes use of multi-length TDR probe measurements where, at each frequency, information is gathered by means of multiple TDR probes of different lengths. In this way, the dispersion law of the material can be retrieved (or at least tested if some a-priori hypothesis is assumed) and consequently more information can be deduced about the water content that, for a given type of soil, should correspond to a given dispersive behaviour. In other words, after calibrating a given type of soil, an anomalous dispersion could be correlated to the presence of some unforeseen substance present in the soil, apart from water.

20.2 Technologies for the Measurement of Dielectric (and Possibly Magnetic) Properties of Soil

Several methods can be exploited for retrieving the dielectric permittivity of the soil based on a TDR signal. We will make use of a numerical modelling to retrieve the

dielectric characteristics of a material under test (MUT) versus frequency. The molecular structure of the MUT meaningfully influences its permittivity. Consequently, any discontinuity present in the volume interested by the electromagnetic radiation will have an effect on its measured permittivity. For this reason, a TDR equipment can provide an indirect measurement of electromagnetic characteristics of the MUT. The latter are correlated to its molecular structure. Therefore, TDR can present an alternative method if the characteristics of interest are not easily evaluated directly. In particular, TDR can be exploited to evaluate SWC. TDR is a cheap and qualitatively good method for the measurement of the dielectric permittivity and SWC of the MUT and offers the valuable possibility to perform the measurements in the field instead of in a laboratory setting. This is a meaningful advantage with respect to other methods requiring transportation of MUT in order to measure moisture as well as dielectric and/or magnetic properties [5]. Moreover, TDR measurements in the field makes it possible to achieve a continuous and non-destructive evaluation versus time of the moisture in the soil. Further studies are somehow recommended in order to enhance the accuracy of TDR spectroscopy and related signal processing in the optimal frequency range, exploiting in particular TDR as a tool for the evaluation of SWC in presence of spurious affecting factors. The next section proposes an overview of the most common strategies for characterizing a MUT with respect to its electromagnetic properties [6]. Afterwards, a new TDR technique for the measurement of the dielectric and magnetic properties of a MUT for a wide range of applications will be proposed [7].

20.2.1 Electromagnetic Methods of Measuring Permittivity

This section discusses widely used methods for measuring the permittivity and permeability of low conductivity materials. According to microwave theory, material characterisation methods are classified broadly as either non-resonant or resonant. These methods are often used in parallel as non-resonant techniques provide electromagnetic properties data over a frequency range whilst resonant methods are often used to obtain accurate dielectric properties of a material at a single frequency or at several discrete frequencies. Therefore, initiating both methods together enables precise knowledge of material properties over a wide frequency range. This can be implemented by modifying the general knowledge of the properties over the frequency band retrieved from non-resonant methods while accurately ‘pinning’ the results at several discrete frequencies obtained from resonant procedures. In the following, an overview of transmission/reflection-based measurement methods for the electromagnetic characterisation of materials is discussed.

20.2.2 Resonant Methods

Resonant techniques (involving resonators or resonant-perturbation methods) are more accurate in comparison to non-resonant techniques and are particularly suitable when the losses are low or negligible.

The method of the resonator (also called the method of the dielectric resonator) is quite common for the measure of high dielectric permittivities (Cohn and Kelly 1966) in non-magnetic ($\mu = \mu_0 = 1.2566 \times 10^{-6} \text{ H m}^{-1}$) and low-loss media (Krupka et al. 1994), as well as in anisotropic MUTs (Geyer and Krupka 1995). Moreover, the dielectric resonator method can also be exploited for measuring both the permittivity of dielectric materials and the surface resistance of conducting materials. In this kind of measurements, the MUT plays the role of a resonator within a microwave circuit. Both dielectric permittivity and loss tangent of the MUT are retrieved from the frequency of resonance and the quality factor of the resonator (Kobayashi and Tanaka 1980). In particular, a configuration for this kind of measurements is shown in Fig. 20.1, where the MUT is inserted between two metallic plates.

The resonant properties are worked out from the properties of the dielectric cylinder, assuming knowledge of the properties of the metallic plates. The technique is based on the TE_{011} propagation mode in the structure with no transverse component of the electric field with the MUT. Consequently, a small gap between the MUT and the plates will not affect the results significantly.

On the other hand, resonant-perturbation methods rely on a sample of MUT inserted into a resonator. This influences the resonant frequency and quality factor of the resonator, and thus, the electromagnetic properties of the MUT can be retrieved from these changes. Three main kinds of resonant perturbation technique exist,

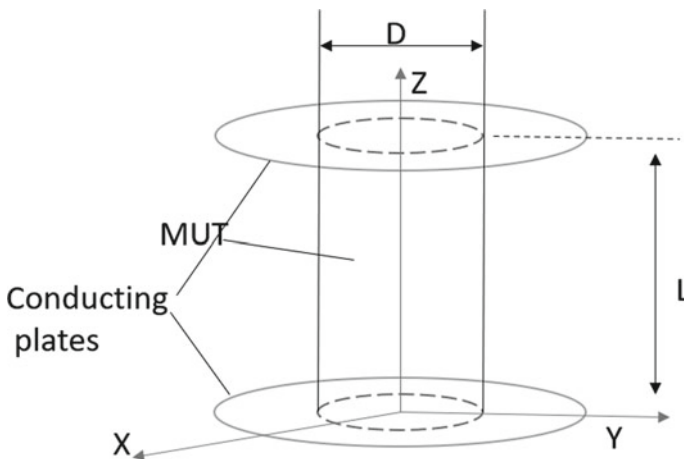
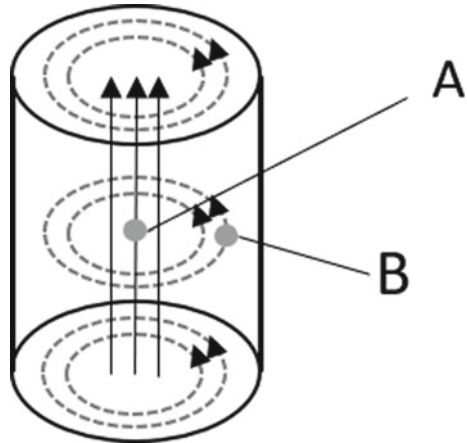


Fig. 20.1 Schematic of a cylindrical dielectric sandwiched between two conducting plates as used in the resonator technique

Fig. 20.2 Cylindrical cavity (TM_{010} mode) for measurement of material properties using the resonant-perturbation method



respectively labelled as cavity shape perturbation, wall-loss perturbation, and material perturbation. Customarily, cavity shape perturbation is exploited to adjust the resonant frequency of a cavity, whereas material perturbation (also referred as cavity-perturbation method) is employed for measurements in low-loss materials. The wall-loss perturbation method, instead, is more often exploited to measure the surface resistance of conductors. In this method, the cavity walls are partially replaced by the MUT.

Depending on the focus of the measure on dielectric or rather magnetic characteristics of the MUT, in the framework of the cavity perturbation method, the MUT might be inserted either into an antinode of the electric field or into an antinode of the magnetic field. Figure 20.2 shows the situation when the MUT is placed at a point (A), where the electric field is maximum and the magnetic field is minimum. In this case, the focus of the measure is on the dielectric characteristics of the MUT. Instead, if the sample of MUT is placed at B (a point of minimum for the electric field and a point of maximum for the magnetic field) the measure is focused on the magnetic properties of the MUT.

To sum up, the two physical phenomena at the basis of the material characterization in the microwave frequency range are the propagation (for non-resonant methods) and the resonance (for resonant methods). The application of these methods is based either on *field approach* or on a *line approach*. The field approach involves the analysis of the distributions of the electric and magnetic fields, whereas the line approach makes use of equivalent microwave circuits.

20.2.3 Non-resonant Methods

The non-resonant methods deduce the properties of materials relying on the characteristics of travelling electromagnetic wave velocities in the material and their

impedance. According to electromagnetic wave propagation theory, when propagating from one medium to another, the characteristic (intrinsic) wave impedance and the wave velocity change, resulting in a partial reflection of the electromagnetic wave from the interface between the two media. Hence, measurements of the reflection and transmission coefficients from and through such an interface provide information related to permittivity and permeability and consequently these can be correlated to other properties of MUT. Non-resonant techniques are subdivided into reflection and transmission/reflection methods. Reflection methods retrieve the properties of the material based on the calculations of the reflection coefficient from the sample and, in a transmission/reflection procedure the coefficients are calculated based on reflection from and transmission through the sample. In principle, non-resonant methods are designed so as to direct the electromagnetic energy towards a material and then sample the reflected waves from, and/or transmitted through, the material. All types of transmission lines can be used for implementing this technique, the most popular being coaxial lines, hollow metal waveguides, dielectric waveguides, planar transmission lines, and free space (although not a transmission line) [6].

20.2.3.1 Reflection Methods

In these methods, the properties of the MUT are retrieved from the reflection coefficient at a defined reference plane where the electromagnetic waves are incident. There are two types of reflection methods for material property characterization: open-circuit reflection, referred to as the open-reflection method and short-circuit reflection (shorted reflection method). In principle, a reflection method can only retrieve one parameter, either permittivity or permeability. Coaxial lines are often used to conduct measurements with the reflection method over broad frequency bands.

For the open-reflection method, the outer conductor at the open end often terminates into a flange to provide suitable capacitance and ensure repeatability of sample loading [8]. This measurement fixture is referred to as the coaxial dielectric probe and is illustrated in Fig. 20.3. It is based on the assumptions: (a) that MUT is nonmagnetic, (b) that the electromagnetic field does not stray beyond the non-contacting boundaries (the flange) of the probe, (c) that the thickness of the sample is much larger than the aperture diameter of the open-ended coaxial probe, and consequently, (d) that the material is sufficiently lossy [6].

For the shorted reflection method which involves a shortcircuit terminating one of the probe ends, the MUT is usually electrically short and it is often used to measure magnetic permeability [9, 10]. In this method the permittivity of the sample is not sensitive to the measurement and in the calculation of magnetic permeability, the permittivity is often assumed to be that of free space $\epsilon_0 = 8.854 \times 10^{-12} \text{ F m}^{-1}$. Figure 20.4 illustrates the coaxial short circuit reflection for two scenarios (i) and (ii), where the MUT is inserted into or at the end of the coaxial line.

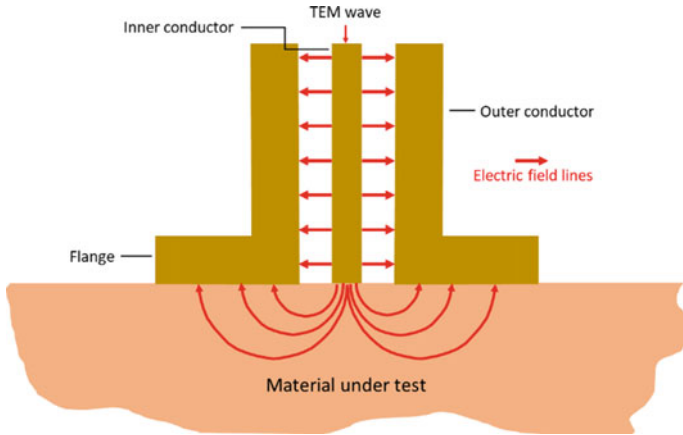


Fig. 20.3 Coaxial open-circuit reflection method, showing the electric field penetrating the MUT

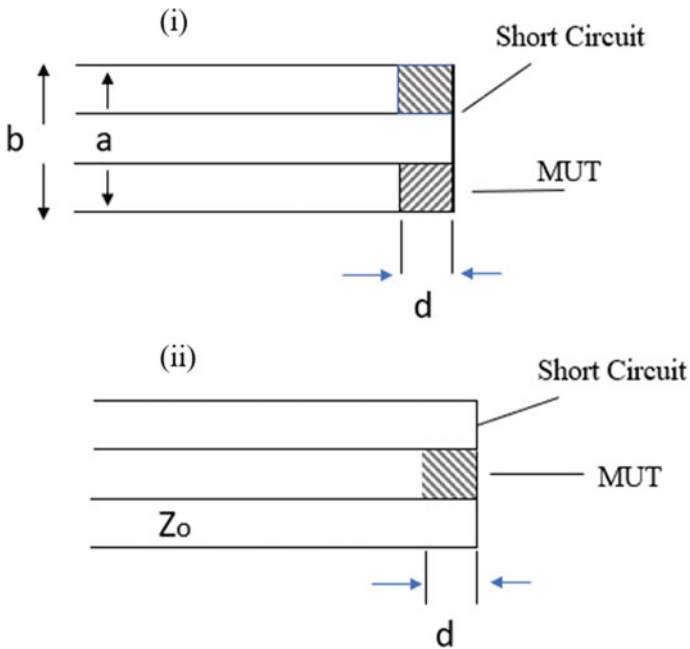
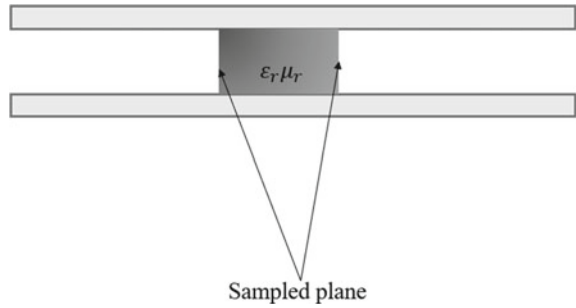


Fig. 20.4 Coaxial short circuit reflection methods

In particular, the MUT in the transmission line method is inserted inside the line as depicted in Fig. 20.5. It is based on the variation in the characteristic impedance of the transmission line section loaded with the sample from that of the line without the sample. This difference results in special transmission and reflection properties

Fig. 20.5 A material sample fitted inside a transmission line



at the interfaces which can allow extraction of the permittivity and permeability from the sample-loaded cell [11, 12]. This method is widely used in measurement of the permittivity and permeability of low conductivity materials and can also be used in the measurement of the surface impedance of high-conductivity materials [13].

Techniques for measuring dielectric properties involve a combination of precise instruments, test fixture to hold the MUT, software to retrieve complex permittivity and permeability parameters and display the results. The instruments used for dielectric measurement depend on the frequency band of interest and include vector network analysers, impedance analysers and LCR meters that can provide accurate results over frequencies ranging from a few Hz up to 1.5 THz. The methods that apply non-resonant techniques, such as coaxial probe, parallel plate, coaxial/waveguide transmission lines, are shown in Fig. 20.6.

In the transmission-line theory, the line approach is used in the analysis of transmission structures by means of equivalent circuits, and the propagation of equivalent voltage and current along transmission structures [6].

On the basis of transmission line theory, the values of the real part, ϵ' , and of the imaginary part, ϵ'' , of the relative dielectric permittivity can be determined by measuring the phase and amplitude of reflected microwave signal from a sample which could be composed of either a solid or a liquid material (unlike resonant-perturbation methods, which apply only to solid samples). The validity of this method

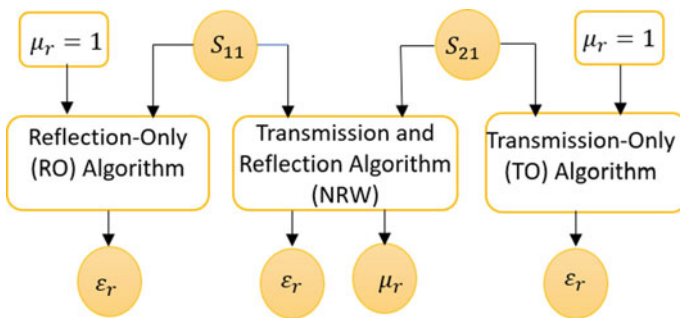


Fig. 20.6 Summary of non-resonant material measurement methods

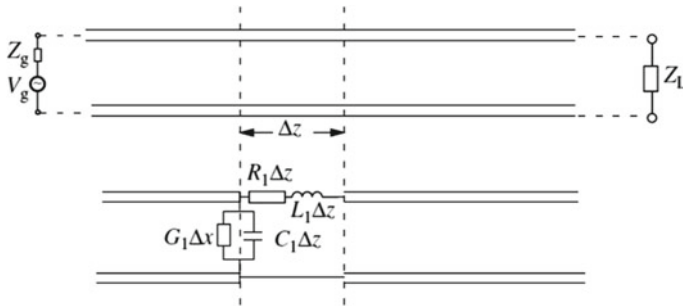


Fig. 20.7 Model of the transmission line showing one element consisting of series impedance $\Delta Z = R_1 \Delta z + j\omega L_1 \Delta z$ and shunt admittance $\Delta Y = G_1 \Delta z + j\omega C_1 \Delta z$

relies on the measurements obtained from detectors and this necessitates calibration of the line using materials of known dielectric constant.

20.2.4 Transmission Line Method

In transmission line theory, the line is represented by a cascade of distributed elements of length $\Delta z \ll \lambda$, each consisting of an L - C network with series inductance (L) and resistance (R) per unit length, and capacitance (C) and shunt conductance (G) per unit length (Fig. 20.7).

Transverse electric and magnetic (TEM) waves require a guiding structure of at least two separate conductors [14]. Transverse electric (TE) waves, without an electric field component in the propagation direction, and transverse magnetic (TM) waves, without a magnetic field component in the propagation direction can propagate along single-conductor hollow waveguides [6].

The most well-known methods to determine the permittivity and permeability of a material sample are the Nicolson-Ross-Weir (NRW) (Nicolson and Ross 1974) and the Baker-Jarvis (BJ) iterative method [15]. Both methods are based on the measurement of the reflection and transmission coefficients in a transmission line or a waveguide embedded in or filled with the MUT. Different methods have been developed to convert the measured reflection coefficient to permittivity [16, 17]. However, this process is generally done automatically by software embedded in the VNA [18].

20.2.4.1 Open-Ended Coaxial Probe

The open-ended Coaxial Probe technique is a method that employs a coaxial line equipped with a tip that senses the signal reflected from the investigated material (see Fig. 20.3). The permittivity and dielectric loss are calculated from the phase and

amplitude of the signal reflected from the end of the open-ended coaxial line inserted into the sample. This technique is valid for materials with loss factor greater than 1 across frequencies from 400 MHz to over 100 GHz, depending on the probe in-use. It is widely used for broadband permittivity measurements of liquids. However, MUT inhomogeneity and bubbles formed between the end of the coaxial probe and the sample can cause errors. The open-ended coaxial probe measurement set-up is shown in Fig. 20.8 while the probe cross-section is shown schematically in Fig. 20.1. This measurement method involves an open-ended coaxial probe (truncated section of a transmission line) being immersed in a liquid or put in contact with the surface of a semi-solid material. This is connected to a vector network analyser (VNA), which is controlled by a computer. The VNA emits an EM field which propagates through the coaxial probe. The VNA inputs an RF signal over a selected frequency range and the reflected signal is sampled and compared with the incident signal to obtain the complex reflection coefficient, from which the complex permittivity of the MUT is extracted. The fields emanating from the tip of the probe are referred to as fringing fields and are considered to reside in a half-infinite plane. For this reason, the MUT should completely encompass the region defined by the fringing fields.

Two distinct techniques are mainly used to retrieve the corresponding MUT permittivity from the measured S_{11} ; lumped-element equivalent circuit models and full wave formulation techniques. The latter are known to provide more accurate permittivity values but are more computationally demanding. The equivalent circuit method is more computationally efficient, however, it is only accurate for a limited range of frequencies and permittivity values. In this method, the discontinuity at the coaxial probe/material interface is modelled as a lumped-element equivalent circuit [19]. Various conversion algorithms have been developed over the years, such those outlined in Fig. 20.9. These models use knowledge of both the reflection coefficient and the permittivity of different known materials to first solve the system admittance and then the permittivity of other unknown materials. A typical antenna used for these measurements is presented in Fig. 20.9c, manufactured by Keysight.

The first method for examining the open-ended coaxial probe was proposed by Marsland and Evans and dealt with the coax as an antenna in transmission mode [20]. This drove to a 5th order equation in the permittivity ϵ_m . The same two authors proposed a simplified solution by neglecting the radiation conductance. This requires

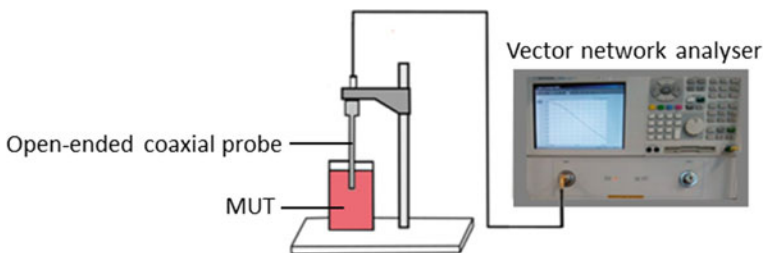


Fig. 20.8 Open-ended coaxial probe technique experimental setup

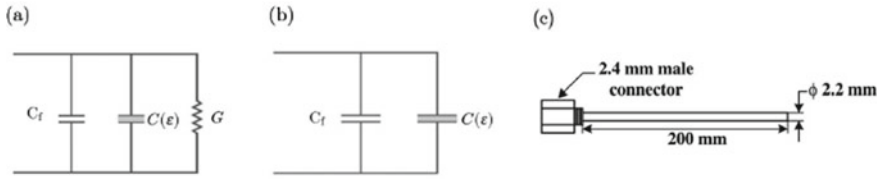


Fig. 20.9 The slim form probe with its **a** radiating antenna equivalent circuit model, **b** capacitive equivalent circuit model, and **c** dimensions (Keysight slim form probe)

just 3 calibrations (open, short, load—distilled water) and drives toward a 1st order relationship in the permittivity ϵ_m to be looked for.

A second method was published by Stuchly and Stuchly [21]. Essentially, it consists of a simplified version of the previous model of Marsland and Evans, achieved by neglecting the radiating conductance.

Such an approximation was licit due to the fact that the radiating conductance can be assumed quite smaller than the impedance associated to the capacity if the radius of the inner conductor is a small fraction of the wavelength. According to the model of Stuchly and Stuchly, a calibration procedure can be done exploiting an open, short and a liquid load. The latter usually being distilled water.

20.2.4.2 Mathematical Reflection Model

In this section we describe the case of a transmission line composed of perfect electric conductors and embedded in (in the case of a multi-filar line) or filled up with (in the case of a coax) a MUT, possibly lossy. In particular, we made use of the reflection coefficient recorded for 3 kinds of loads according to Farhat et al. [7]. In particular, we solved the problem through a least square matching between a transmission line model and full wave data. The data referred to a coaxial probe partially filled up with the MUT, and the 3 loads were a short open and a matched load. The reference plane for the calculation of the reflection coefficient is placed just before the MUT, as shown in the schematic of Fig. 20.10.

The schematic of the three terminations with the MUT filling a coaxial line section of length L whose relative complex permittivity, relative complex permeability, and characteristic impedance are ϵ_r , μ_r , and Z_{l2} , respectively, is now described. The reflection coefficient (S_{11}) at a reference plane $x = -L$, and the termination point is at $x = 0$. The characteristic impedance within the region $-L \leq x \leq 0$ which is filled with the MUT is $Z_{l2} = \sqrt{\frac{\mu_r}{\epsilon_r}} Z_{0l2}$, where μ_r and/or ϵ_r are complex if the medium is lossy and are real if the medium is lossless. The reflection coefficient of a wave incident at $x = -L$ from the air-filled side is given by

$$\Gamma = \frac{Z_{-L} - Z_{0l1}}{Z_{-L} + Z_{0l1}}, \tag{20.1}$$

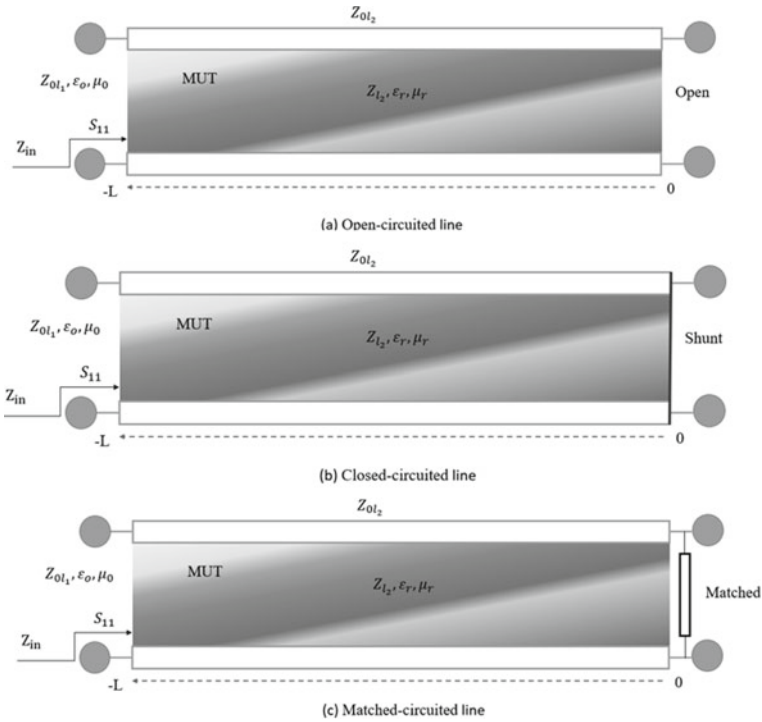


Fig. 20.10 Schematic of the S_{11} -parameter and the input impedance of the sample-loaded transmission line, energised from the left

where Z_{0i1} is the characteristic impedance of the air-filled transmission line before the section, which is to contain the MUT, and Z_{-L} is the impedance of the termination at $x = 0$ transformed through the MUT to the reference plane at $x = -L$. Thus, for the short-circuited transmission line, the input impedance is given by

$$Z_{-L} = j Z_{0i2} \frac{\mu_r}{\epsilon_r} \tan(k_0 \sqrt{\mu_r \epsilon_r} L), \tag{20.2}$$

where k_0 is the wavenumber in free space.

For the transmission line terminated with an open circuit, the input impedance at $x = -L$ is

$$Z_{-L} = -j Z_{0i2} \frac{\mu_r}{\epsilon_r} \cot(k_0 \sqrt{\mu_r \epsilon_r} L). \tag{20.3}$$

Finally, the impedance at $x = -L$ when the transmission line is terminated with a matched load is

$$Z_{-L} = \sqrt{\frac{\mu_r}{\varepsilon_r}} Z_{0l_2} \frac{1 + j\sqrt{\frac{\mu_r}{\varepsilon_r}} \tan(k_0\sqrt{\mu_r\varepsilon_r}L)}{\sqrt{\frac{\mu_r}{\varepsilon_r}} + \tan(k_0\sqrt{\mu_r\varepsilon_r}L)}. \quad (20.4)$$

The reflection coefficient at $x = -L$ reference plane when the line is terminated with a short circuit can be reformulated using Eqs. (20.1) and (20.2):

$$Z_{-L} = \sqrt{\frac{\mu_r}{\varepsilon_r}} Z_{0l_2} \frac{1 + j\sqrt{\frac{\mu_r}{\varepsilon_r}} \tan(k_0\sqrt{\mu_r\varepsilon_r}L)}{\sqrt{\frac{\mu_r}{\varepsilon_r}} + \tan(k_0\sqrt{\mu_r\varepsilon_r}L)}; \quad (20.5)$$

$$\Gamma_{\text{short}}(-L) = \frac{\left(Z_{0l_2}\sqrt{\frac{\mu_r}{\varepsilon_r}} - Z_{0l_1}\right) + \exp\left(-2j\frac{2\pi fL}{C_0}\sqrt{\mu_r\varepsilon_r}\right)\left(Z_{0l_2}\sqrt{\frac{\mu_r}{\varepsilon_r}} + Z_{0l_1}\right)}{\left(Z_{0l_2}\sqrt{\frac{\mu_r}{\varepsilon_r}} + Z_{0l_1}\right) - \exp\left(-2j\frac{2\pi fL}{C_0}\sqrt{\mu_r\varepsilon_r}\right)\left(Z_{0l_2}\sqrt{\frac{\mu_r}{\varepsilon_r}} - Z_{0l_1}\right)}. \quad (20.6)$$

Similarly, the reflection coefficient of the transmission line when terminated with an open circuit, can be obtained from Eq. (20.6) by substituting from Eqs. (20.3) and (20.1):

$$\Gamma_{\text{open}}(-L) = \frac{\left(Z_{0l_2}\sqrt{\frac{\mu_r}{\varepsilon_r}} - Z_{0l_1}\right) - \exp\left(-2j\frac{2\pi fL}{C_0}\sqrt{\mu_r\varepsilon_r}\right)\left(Z_{0l_2}\sqrt{\frac{\mu_r}{\varepsilon_r}} + Z_{0l_1}\right)}{\left(Z_{0l_2}\sqrt{\frac{\mu_r}{\varepsilon_r}} + Z_{0l_1}\right) - \exp\left(-2j\frac{2\pi fL}{C_0}\sqrt{\mu_r\varepsilon_r}\right)\left(Z_{0l_2}\sqrt{\frac{\mu_r}{\varepsilon_r}} - Z_{0l_1}\right)}. \quad (20.7)$$

The reflection coefficient when the line is terminated by a matched load is determined by substituting Eq. (20.4) in (20.1), giving:

$$\Gamma_{\text{Load}}(-L) = \frac{\left(\sqrt{\frac{\mu_r}{\varepsilon_r}} + 1\right)\left(Z_{0l_2}\sqrt{\frac{\mu_r}{\varepsilon_r}} - Z_{0l_1}\right) - \exp\left(-2j\frac{2\pi fL}{C_0}\sqrt{\mu_r\varepsilon_r}\right)\left(Z_{0l_2}\sqrt{\frac{\mu_r}{\varepsilon_r}} + Z_{0l_1}\right)}{\left(\sqrt{\frac{\mu_r}{\varepsilon_r}} + 1\right)\left(Z_{0l_2}\sqrt{\frac{\mu_r}{\varepsilon_r}} + Z_{0l_1}\right) - \exp\left(-2j\frac{2\pi fL}{C_0}\sqrt{\mu_r\varepsilon_r}\right)\left(Z_{0l_2}\sqrt{\frac{\mu_r}{\varepsilon_r}} - Z_{0l_1}\right)}. \quad (20.8)$$

where Z_{0l_2} is the characteristic impedance of the transmission line in the case of void before inserting the MUT. Z_{0l_1} is the intrinsic impedance of the transmission line in the part preceding the MUT. The permittivity and permeability in propagation media are different from those in free space, and they are usually expressed respectively as products $\varepsilon_r\varepsilon_0$ and $\mu_r\mu_0$, where ε_r and μ_r represent the dimensionless relative permittivity and relative permeability, respectively. In lossy isotropic media, ε_r is complex and can be expressed as

$$\varepsilon_r = \varepsilon' - j\varepsilon'', \quad (20.9)$$

where ε' and ε'' are positive and in general frequency dependent. Similarly, for media with magnetic losses, μ_r is complex, and can be expressed as

$$\mu_r = \mu' - j\mu'', \tag{20.10}$$

where μ' and μ'' are positive and in general, frequency dependent.

20.2.4.3 Coaxial and Bifilar Lines, S-parameters and the TEM Mode

The coaxial line has a centre conductor concentric with an outer conductor. The outer radius of the inner conductor is here denoted by a and the inner radius of the outer conductor by b , as shown in Fig. 20.11. Apart from the propagation factor, if a TEM wave propagates into an infinite coaxial cable, the electric and magnetic fields are given (in cylindrical coordinates) by

$$E_r = \frac{V \exp(-jkz)}{r \ln \frac{b}{a}}; \tag{20.11}$$

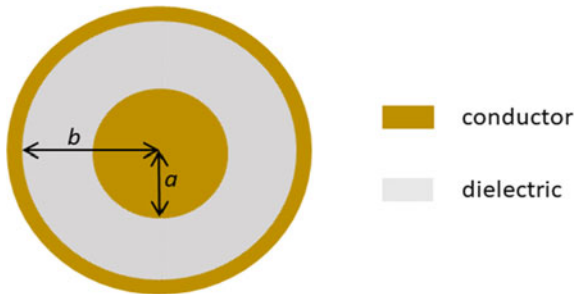
$$H_\phi = \frac{I \exp(-jkz)}{2\pi r}. \tag{20.12}$$

The exponential $\exp(-jkz)$ is the propagation factor and k is the wavenumber. The other components of the electric and the magnetic fields are zero in the fundamental mode.

The ratio between the transverse components of the electric and magnetic fields is the wave impedance and is equal to $\sqrt{\frac{\mu}{\epsilon}}$, where μ and ϵ are respectively the magnetic permeability and the dielectric permittivity of the medium through which the wave propagates. In free space, this quantity is equal to $\zeta_o = \sqrt{\frac{\mu_o}{\epsilon_o}} = 377 \Omega$. In any other homogeneous medium, this quantity can be expressed as $\sqrt{\frac{\mu}{\epsilon}} = \zeta_o \sqrt{\frac{\mu_r}{\epsilon_r}}$, making use of the dimensionless complex relative dielectric permittivity and magnetic permeability of the medium. So, dividing Eq. (20.10) by (20.11),

$$\frac{E_r \exp(-jkz)}{H_\phi \exp(-jkz)} = \zeta_o \sqrt{\frac{\mu_r}{\epsilon_r}} = \frac{V}{I} \frac{2\pi}{\ln \frac{b}{a}}, \tag{20.13}$$

Fig. 20.11 Geometry of the cross-section of a coaxial cable, where a and b are respectively the inner and outer conductor diameters



The ratio V/I at any point along an infinitely long or a matched transmission line is the characteristic impedance of the line since there are no reflections and the wave propagates in one direction. So, Eq. (20.13) gives the intrinsic impedance of a coaxial cable as

$$Z_{\text{coax}} = \zeta_o \sqrt{\frac{\mu_r}{\epsilon_r}} \frac{\ln \frac{b}{a}}{2\pi}. \tag{20.14}$$

The factor $\zeta_o \frac{1}{2\pi}$ in Eq. (20.14) is a constant equal to about 60Ω . In this contribution we will focus on non-magnetic media, so that (20.14) reduces to

$$Z_{\text{coax}} = \frac{\zeta_o}{\sqrt{\epsilon_r}} \frac{\ln \frac{b}{a}}{2\pi}. \tag{20.15}$$

In the case of a bifilar line, and again in the case of non-magnetic media, the intrinsic impedance is instead given by

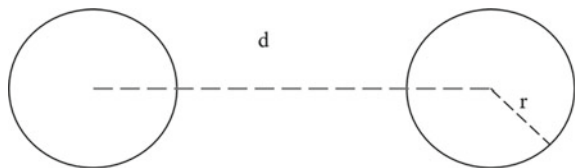
$$Z_{\text{bif_line}} = \frac{\zeta_o}{\sqrt{\epsilon_r}} \frac{\ln \frac{d}{r}}{\pi}, \tag{20.16}$$

where, according to Fig. 20.12, d is the distance between the centres of the two rods of the transmission line and r is the radius of the rods (assumed equal).

As shown, the impedance depends on the characteristics of the medium through which the wave propagates, which constitutes the basis for retrieving the electromagnetic characteristics of the medium itself. However, the direct measurement of the intrinsic impedance is not practical because a matched load would be needed and this is difficult to obtain inside the medium. The quantities more easily measurable are the S-parameters, related to the impedance along the line away from the termination, as well described in [14]. The S-parameters are measured over a particular frequency range using a network analyser and usually mathematical techniques like de-embedding are applied to extract the S-parameters that characterize the material properties. The point at which the calibration is performed is called the calibration plane. Figure 20.12 shows the incident and reflected waves that contribute to the S-parameters.

As electromagnetic waves, swept over a specified frequency, range pass from Port 1 to Port 2 (Fig. 20.13), they encounter the test material surface, where part of the energy is reflected with the reflection coefficient Γ_{12} and the rest of the energy

Fig. 20.12 Geometry of the cross-section of a bifilar transmission line



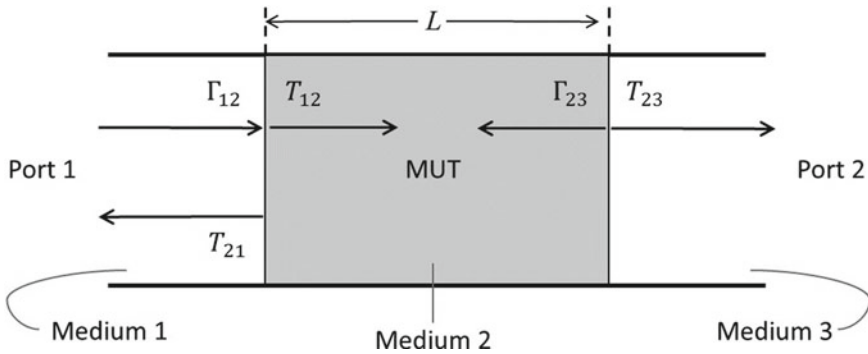


Fig. 20.13 Schematic representation of incident, reflected and transmitted waves resulting from RF input at port 1. The reflection and transmission coefficient subscripts indicate the order in which the boundaries between the two media are traversed by the wave

is transmitted with the transmission coefficient T_{12} into the sample of MUT. The transmitted wave travels for a distance L inside the material to encounter the second boundary, where it is partly reflected back into medium 2 (the MUT) with reflection coefficient Γ_{23} while the remaining energy is transmitted with coefficient T_{23} , and so on. Considering only the first internal reflection on the right-hand boundary (Fig. 20.11), the S-parameters for reflection and transmission can be expressed as follows:

$$S_{11} = \Gamma_{12} + T_{12}T\Gamma_{23}TT_{21} + T_{12}T\Gamma_{23}T\Gamma_{21}TT_{23}TT_{21}, \tag{20.17}$$

where $T = e^{-jkL}$ and k is the propagation constant in the material under test (MUT) [14] and L is the length of the sample of MUT. Similarly, S_{21} can be written as

$$S_{21} = T_{12}TT_{23} + T_{12}T\Gamma_{23}T\Gamma_{21}TT_{23} + T_{12}T\Gamma_{23}T\Gamma_{21}TT_{23}. \tag{20.18}$$

The wave experiences a change in characteristic impedance as it encounters different media along its path.

The problem is in general one of retrieving the complex dielectric permittivity and magnetic permeability from the S-parameters. A finite electrical conductivity of the MUT is accounted for within the imaginary part of the permittivity. One method to retrieve the characteristics of the MUT is to extend the ports on either side in order to include the walls of the MUT directly and measure the S-parameters. However, this approach is prone to error as extending ports to very small lengths might not yield accurate results. Combining both port extension and a de-embedding technique usually leads to more accurate results.

For materials with and without losses, the relationship between the material characteristics and S-parameters (in particular, for the TEM propagation mode) is provided by:

$$kL = \cosh^{-1}\left(\frac{1 - S_{11}^2 + S_{21}^2}{2S_{21}}\right). \quad (20.19)$$

In the case of a TDR probe, often we do not have the possibility to measure all the S-parameters because we have physical access only to one port. In these cases, what can be measured is the reflection coefficient Γ , related to the S-parameters by the following relationship:

$$\Gamma = \frac{S_{11}}{1 - S_{21}T}. \quad (20.20)$$

However, in this situation we cannot measure S_{21} . The reflection coefficient has to be calculated with reference to the composition of the line beyond the MUT which constitutes the termination of the probe. For a line shunted just at the end of the sample of MUT (it is often the case of a coaxial TDR probe), the expression is

$$\Gamma(-L) = \gamma(\varepsilon_r; f) = \frac{\left(\frac{Z_{l01}}{\sqrt{\varepsilon_r}} - Z_{l2}\right) - \left(\frac{Z_{l01}}{\sqrt{\varepsilon_r}} + Z_{l2}\right)\exp\left(-j\frac{4\pi f}{c_0}\sqrt{\varepsilon_r}L\right)}{\left(\frac{Z_{l01}}{\sqrt{\varepsilon_r}} + Z_{l2}\right) - \left(\frac{Z_{l01}}{\sqrt{\varepsilon_r}} - Z_{l2}\right)\exp\left(-j\frac{4\pi f}{c_0}\sqrt{\varepsilon_r}L\right)}. \quad (20.21)$$

In Eq. (20.21), Z_{l01} is the intrinsic impedance of the empty line that is to host the MUT [see Eqs. (20.15) and (20.16)] with unit relative permittivity. Z_{l2} is the intrinsic impedance of the line before the reference plane at $z < -L$, and $c_0 = \frac{1}{\sqrt{\varepsilon_0\mu_0}} = 2.9979 \times 10^8 \text{ ms}^{-1}$ is the propagation velocity of electromagnetic waves in free space.

Similarly, if the line is truncated just at the end of the sample of MUT (it is customarily the case in a bifilar or a three-filar TDR probe), the reflection coefficient is provided by

$$\Gamma(-L) = \gamma(\varepsilon_r; f) = \frac{\left(\frac{Z_{l01}}{\sqrt{\varepsilon_r}} - Z_{l2}\right) + \left(\frac{Z_{l01}}{\sqrt{\varepsilon_r}} + Z_{l2}\right)\exp\left(-j\frac{4\pi f}{c_0}\sqrt{\varepsilon_r}L\right)}{\left(\frac{Z_{l01}}{\sqrt{\varepsilon_r}} + Z_{l2}\right) + \left(\frac{Z_{l01}}{\sqrt{\varepsilon_r}} - Z_{l2}\right)\exp\left(-j\frac{4\pi f}{c_0}\sqrt{\varepsilon_r}L\right)}. \quad (20.22)$$

Whatever the case, the relative permittivity $\varepsilon_r = \varepsilon'_r - j\varepsilon''_r$ is retrieved with a least-squares minimisation of a cost function provided by the square norm of the measured reflection coefficient data minus the modelled data [2, 7].

The diversity needed to provide the sufficient amount of information is practically often provided by data gathered at several frequencies. However, the use of multi-frequency data implicitly assumes that the MUT is not dispersive or follows a pre-assigned dispersion law. In fact, permittivity is in general a function of frequency and therefore, additional data at different frequencies increases the number of unknowns. Alternatively, a multi-length probe approach was proposed (Persico et al. 2018), where at each frequency the information is provided by the reflection coefficient

measured with different lengths L of the MUT sample. The underlying assumption here is that the different samples of MUT have the same dielectric properties.

20.3 Results

In this section, some results with simulated data will be presented. The data were first simulated according to a transmission line model terminating with an open circuit, then full wave data in free space were considered as a preliminary case. The data refer to a bifilar line, so that the multi-length data correspond to varying rod lengths. Here, we consider the case of five lengths, as a simplified example of previous work (Persico et al. 2018), where 21 lengths had been considered.

The considered TDR system is a bifilar line open at the end. In Fig. 20.14 shows a simulation of the real and imaginary parts of the reflection coefficient. The data refers to a lossless case with $Z_{l01} = 250 \Omega$ (this might correspond e.g. to $r = 3 \text{ mm}$ and $d = 24.13 \text{ mm}$ (Fig. 20.12), that are realistic values). The relative permittivity of the medium is set as a constant equal to 6, and the rods of the probe are 40 cm long. The considered frequency band ranges from 200 to 1000 MHz, and the intrinsic impedance of the line before the MUT is frequency independent and equal to $Z_{l2} = 100 \Omega$. As can be expected and confirmed in Fig. 20.14, the real and imaginary parts of the reflection coefficient vary periodically with frequency [see Eqs. (20.21)–(20.22)]. These results are analogous to those achieved with a shorted coaxial cable, where comparisons with full wave simulated and experimental data have been reported previously [7]. The reflection coefficient magnitude is equal to 1 all over the band because the line is terminated with an open circuit and is lossless.

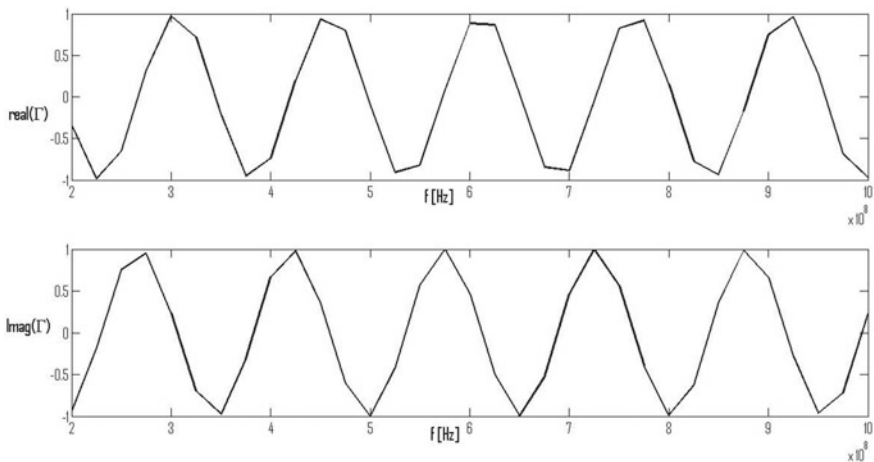


Fig. 20.14 Real (upper panel) and imaginary (lower panel) parts of the reflection coefficient versus frequency

At this point, let us show the case of an inversion of a dispersive medium with model data. Similar to the previous example, the intrinsic impedance of the line in free space is equal to 250Ω , the impedance of the generator is 100Ω , and the frequency band ranges from 200 to 1000 MHz (sampled at 25 MHz intervals). The medium follows a Deybe dispersion model according to Eq. (20.23), with low frequency limit $\epsilon_c = 7$, high frequency limit $\epsilon_\infty = 3$ and relaxation time $\tau = 3.183 \times 10^{-10}$ seconds,

$$\epsilon_r(\omega) = \epsilon_\infty + \frac{\epsilon_c - \epsilon_\infty}{1 + j\omega\tau}. \tag{20.23}$$

Five lengths are exploited at each frequency, ranging from 37 to 43 cm in steps of 1.5 cm. In Fig. 20.15, the extracted permittivity is shown as a function of frequency for noiseless data, in Fig. 20.16 the analogous result is shown with a Gaussian white noise (SNR = 40 dB) added to the data, and finally Fig. 20.17 presents similar results with the SNR decreased to 20 dB.

The discrepancy between the achieved result and the actual behaviour of the real part of the relative permittivity as a function of frequency was then calculated as:

$$\text{err} = 100 \frac{\|\text{real}(\epsilon_{ra} - \epsilon_{re})\|}{\sqrt{\|\text{real}(\epsilon_{re})\| \|\text{real}(\epsilon_{ra})\|}} \%, \tag{20.24}$$

where ϵ_{ra} is the *actual* real part of the relative permittivity and ϵ_{re} is the *estimated* real part of the relative permittivity. An analogous error function was used for the imaginary part of the relative permittivity. Table 20.1 reports the percentage errors for decreasing value of the SNR.

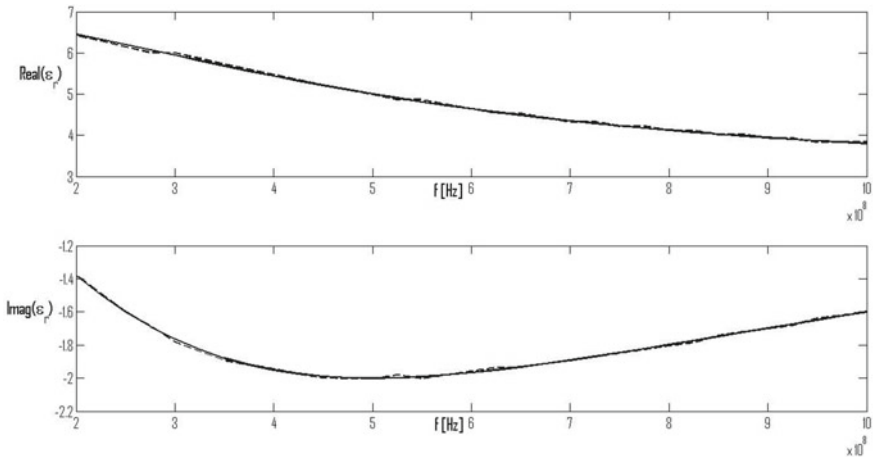


Fig. 20.15 Reconstructed (dashed line) and actual (solid line) relative permittivity. Upper panel: real part; lower panel: imaginary part. Noiseless data

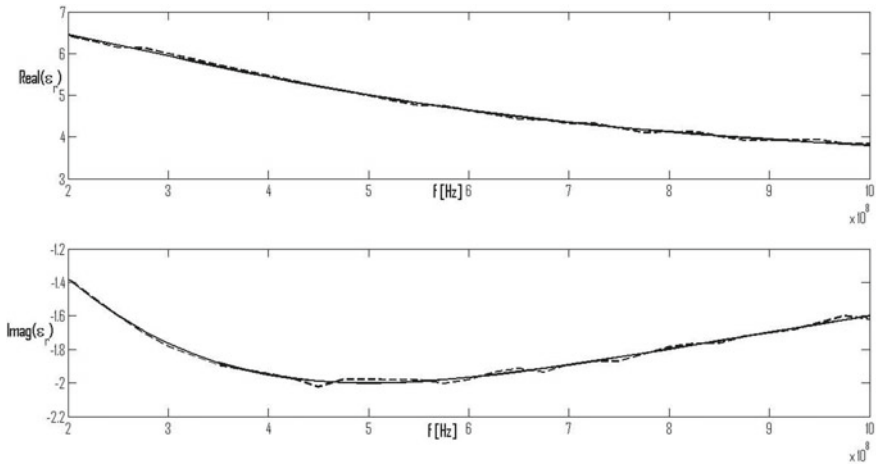


Fig. 20.16 Reconstructed (dashed line) and actual (solid line) relative permittivity. Upper panel: real part; lower panel: imaginary part. Noisy data with SNR = 40 dB

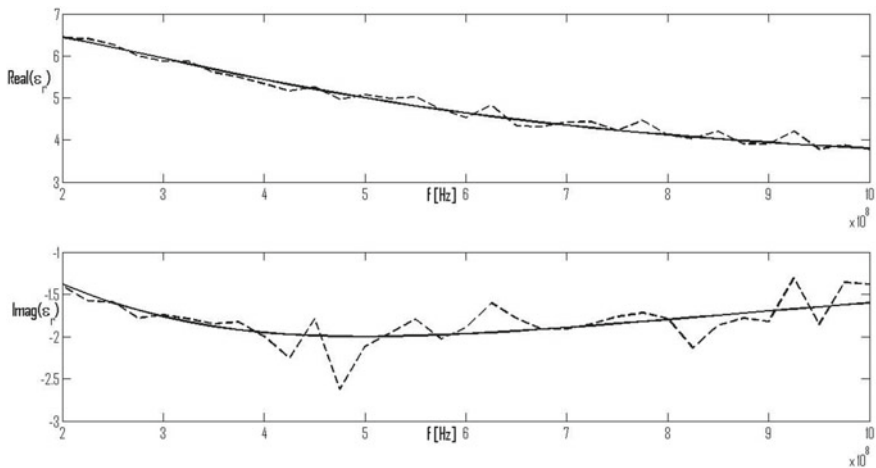


Fig. 20.17 Reconstructed (dashed line) and actual (solid line) relative permittivity. Upper panel: real part; lower panel: imaginary part. Noisy data with SNR = 20 dB

Table 20.1 Errors of the achieved results

	Error of the real part of the relative permittivity (%)	Error of the imaginary part of the relative permittivity (%)
SNR = ∞ (noiseless)	0.71	0.42
SNR = 40 dB	0.79	0.80
SNR = 20 dB	2.54	10.54

From Figs. 20.15, 20.16 and 20.17 and from Table 20.1 it can be noted that a good signal to noise ratio higher than 20 dB is required to achieve acceptable results, especially for the imaginary part of the relative permittivity.

In this case it has been assumed that no a-priori knowledge is known about the dispersion law of the MUT. If a-priori information is known or can be deduced from measurements, then it is possible to minimize the variance between the extracted parameters ϵ_o , ϵ_∞ and τ , and those obtained from a Deybe dispersion model. This minimization was performed here and the results are shown in Table 20.2.

In Fig. 20.18, the behaviour of the retrieved Deybe dispersion together with the actual Deybe dispersion law is reported in the case with SNR = 20 dB. In the other two considered cases (noiseless or with SNR = 40 dB) the two curves were indistinguishable from each other.

It can be noted that even with SNR = 20 dB the agreement between the actual and reconstructed relative permittivity values is good. This is because knowledge of the

Table 20.2 Retrieved parameters assuming the Deybe dispersion law for the MUT and the resulting relative errors with respect to the actual values

	ϵ_o	ϵ_∞	τ (s)
SNR = ∞	7 (err = 0)	2.998 (err = 0.07%)	3.178×10^{-10} (err = 0.16%)
SNR = 40 dB	7 (err = 0)	3.004 (err = 0.13%)	3.178×10^{-10} (err = 0.16%)
SNR = 20 dB	7.08 (err = 1.14%)	3.088 (err = 2.89%)	3.304×10^{-10} (err = 3.75%)

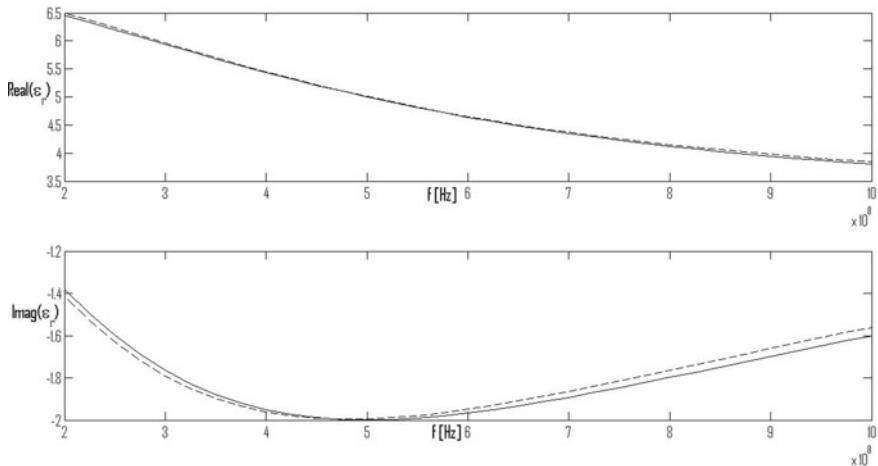


Fig. 20.18 Actual (solid line) and reconstructed (dashed line) relative permittivity when assuming a Deybe dispersion model for the MUT. Upper panel: real part; lower panel: imaginary part. Noisy data with SNR = 20 dB

MUT's dispersion law was considered in the inversion process which, in this case, only searches for three real quantities ($\epsilon_0, \epsilon_\infty$ and τ).

Considering the full wave FDTD field simulations obtained with CST Microwave Studio software, where the bifilar probe was embedded in a cylindrical medium that simulates the material under test enclosed by absorbing boundary conditions. The diameter of the rods considered 3 mm and their centre-to-centre separation was 3 cm. Initially, the probe was analysed in free space.

The intrinsic impedance of the generator was 50Ω and the analysis was carried out between 200 and 1000 MHz with five lengths: 36, 38, 40, 42 and 44 cm. Figures 20.19 and 20.20 show the real and imaginary parts of the reflection coefficient (S_{11}) for rod length of 40 cm. As can be seen, the simulated full wave trace is shifted with respect to that obtained from the transmission line model. This is probably due to the effect of

Fig. 20.19 Real part of the reflection coefficient versus frequency. Blue line: Transmission line model; red line: full wave simulation

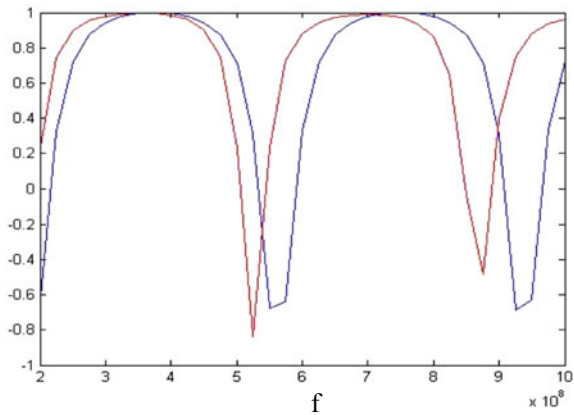
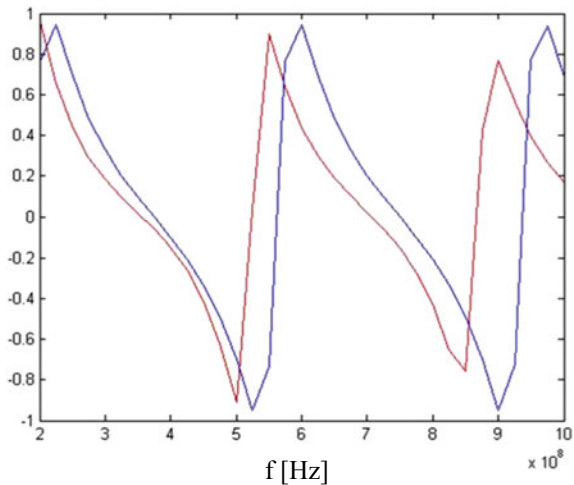


Fig. 20.20 Imaginary part of the reflection coefficient versus frequency. Blue line: Transmission line model; red line: full wave simulation



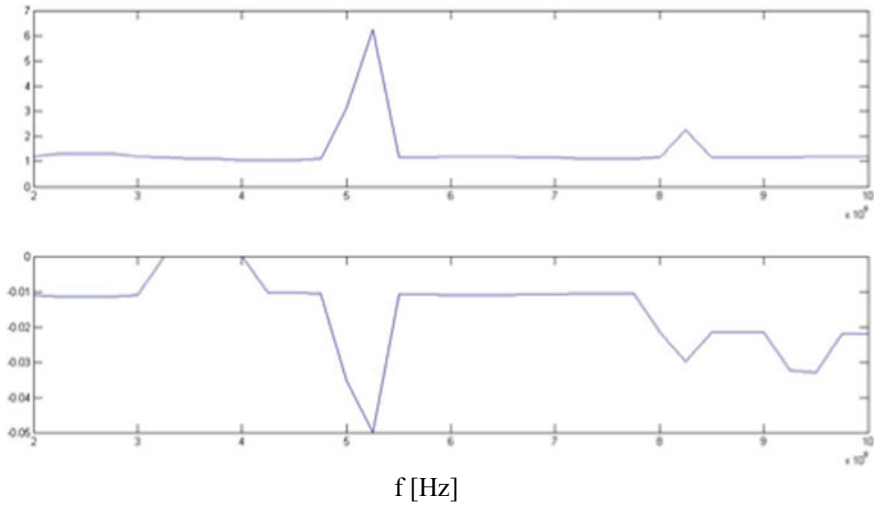


Fig. 20.21 Multi-length reconstruction achieved from full wave data. Upper panel: real part of the relative permittivity. Lower part: Imaginary part of the relative permittivity

the fringing fields at the end of the probe (Collin 2020), where the TEM symmetries of the cross section are interrupted. Future developments will be devoted to including the fringe field in the model, and we will first look for a reactance that replaces the open end in the equivalent transmission line model, so that this matches better the full wave data. After matching the model in free space, a general line termination will be determined to better represent the MUT.

Figure 20.21 shows the results of the inversion carried out to obtain the relative permittivity from the simulated reflection coefficient with the probe in free space ($\epsilon_r = 1 - 0j$). The extracted relative permittivity is in good agreement with that of free space over most of the frequency range. However, over some frequencies, there is significant disagreement which could be attributed to the fringe fields at the end of the line. Further studies are required to refine the model.

20.4 Conclusions

In this contribution, the main techniques for the measurement of the electromagnetic parameters of soil with specific reference to the measurement of the effects of water content on soil permittivity are outlined. In particular, preliminary results obtained with a multi-length TDR probe technique are presented. Further work is needed in order to achieve satisfactory results. In particular, the fringing field has to be correctly simulated and accounted for a bifilar or tri-filar TDR probe. The same problem does not occur with a shunt-terminated coaxial TDR probe, where the real field resembles

quite well a short-circuited ideal transmission line model, which was previously verified with full wave simulations.

In conclusion, it has been shown that the multi-length TDR probe technique with a relatively small number of probe lengths can provide enough information to retrieve the electromagnetic properties of the MUT. This is relevant because multi-length measurements are intrinsically less practical than multifrequency measurements for field applications. However, it can be anticipated that the same probe could be used at different penetration depths into the soil under test.

Acknowledgements The authors have developed the present study within the European Cooperation in Science and Technology framework, COST Action CA 17115 “MyWave” and adapted it for different applications through the support of the project ‘WetSoil’, funded by the Energy and Water Agency, Malta, through grant EWA 110/20/2/004-SE.

References

1. Topp GC, Davis JL, Annan AP (1980) Electromagnetic determination of soil water content: measurements in coaxial transmission lines. *Water Resour Res* 16(3):574–582
2. Persico R, Pieraccini M (2018) Measurement of dielectric and magnetic properties of materials by means of a TDR probe. *Near Surf Geophys* 16:1–9. <https://doi.org/10.3997/1873-0604.2017046>
3. Nabighian M (1897) Electromagnetic methods in applied geophysics-theory. In: Society of exploration geophysics, 1
4. Cataldo A, De Benedetto E, Cannazza G (2011) Broadband reflectometry for enhanced diagnostics and monitoring applications. Springer Verlag. Retrieved from ISBN 978-3-642-20232-2
5. Tan X, Wu J, Huang J, Wu M, Zeng W (2008) Design of a new TDR probe to measure water content and electrical conductivity in highly saline soils. *J Soils Sediments* 10(10):1–13. <https://doi.org/10.1007/s11368-017-1838-6>
6. Chen LF, Ong CK, Neo CP, Varadan VV, Varadan VK (2004) Microwave theory and techniques for materials characterization. In: *Microwave electronics: measurement and materials characterization* (1st ed, pp 37–140). Wiley. ISBN:978-0-470-84492-2
7. Farhat I, Farrugia L, Persico R, D’Amico S, Sammut C (2020) Preliminary experimental measurements of the dielectric and magnetic properties of a material with a coaxial TDR probe in reflection mode. *Prog Electromagnet Res M* 91:111–121. <https://doi.org/10.2528/PIE-RM19111904>
8. Li CC, Chen KM (1995) Determination of electromagnetic properties of materials using flanged open-ended coaxial probe-full wave analysis. *IEEE Trans Instrum Meas* 44:19–27
9. Fannis PC, Relihan T, Charles SW (1995) Investigation of ferromagnetic resonance in magnetic fluids by means of the short-circuited line techniques. *J Phys D Appl Phys* 28:2002–2006
10. Guillon P (1995) Microwave techniques for measuring complex permittivity and permeability of materials. In: *Materials and processes for wireless communication*, pp 65–71
11. Nicolson AM, Ross GF (1974) Measurement of the intrinsic properties of materials by time domain techniques. *IEEE Trans Instrum Meas* 19(4):377–382
12. Weir WB (1974) Automatic measurement of complex dielectric constant and permeability at microwave frequencies. *Proc IEEE* 62(1):33–36
13. Kim J, Kang J, Park J, Kang T (2014) A new method for the determination of the reflection and transmission characteristics of dielectric materials. In: *A new method for the determination of the reflection and transmission 83rd ARFTG microwave measurement conference*, pp 1–4. <https://doi.org/10.1109/ARFTG.2014.6899536>

14. Collin R (2000) Foundation for microwave engineering. IEEE Press
15. Baker-Jarvis J, Janezic MD, Jr Grosvenor JH, Geyer RG (1993) Transmission/reflection and short-circuit line method for measuring permittivity and permeability. National institute of Standards and technology Technical Note, 1355-R
16. Athey TW, Stuchly MA, Stuchly SS (1982) Measurement of radio frequency permittivity of biological tissues with an open-ended coaxial line. Part I. IEEE Trans Microw 30:82–86
17. Misra DKA (1987) Quasi-static analysis of open-ended coaxial lines. IEEE Trans Microw Theory Tech 35:925–928
18. Technologies K (2015) Keysight E5063A ENA series network analyser. Keysight Technologies, Santa Clara
19. Farina L, Ruvio G, Pinto R, Vannucci L, Cavagnaro M, Lopresto V (2017) Development of a portable setup suitable for in vivo measurement of the dielectric properties of biological tissues. In: 11th European conference on antennas and propagation (EUCAP), pp 2732–2736. <https://doi.org/10.23919/EuCAP.2017.7928435>
20. Marsland PT, Evans S (1987) Dielectric measurements with an open-ended coaxial probe. IEE Proc H (Microw Antennas Propag) 134:341–349(8)
21. Stuchly MA, Stuchly SS (1980) Coaxial line reflection methods for measuring dielectric properties of biological substances at radio and microwave frequencies-a review. IEEE Trans Instrum Meas 29(3):176–183. <https://doi.org/10.1109/TIM.1980.4314902>

Chapter 21

GPR Water Pipe Monitoring and Leaks Characterization: A Differential Microwave Tomography Approach



Ilaria Catapano, Roberta Palmeri, Francesco Soldovieri,
and Lorenzo Crocco

Abstract Water is an essential natural resource for assuring life and its effective usage and distribution is a key issue made more and more relevant by climate changes. This framework supports the development and employment of technological solutions devoted to improve water management through a growth of the efficiency of the network and distribution systems. In this frame, Ground Penetrating Radar (GPR) deserves attention being a portable, low-cost, non-invasive and high reliability technology suitable for water pipe monitoring and leak detection. Accordingly, the chapter reviews advantages and limits featuring GPR. Moreover, it proposes a data processing approach to improve GPR imaging and provides a proof of concepts assessing its reconstruction capability preliminarily.

21.1 Introduction

Nowadays, the development of smart solutions to increase resilience and improve the usage of natural resources deserves huge attention. In this framework, water pipeline monitoring and detection of possible leaks represent an important unmet challenge, which demands for the development of ad hoc innovative technological solutions and effective diagnostic protocols. Water is, indeed, a precious natural resource and, unfortunately, a large amount of it is lost during the distribution. The World Bank database report states that, each year around the world, a percentage ranging from 20 to 50% of water is lost due to physical leaks in water distribution systems. In addition, water leaks, beyond inconvenience due to service interruption and road closure, determine material corrosions and void formation thus increasing the hazard of structural collapses, which represent risks for people security and safety [1].

According to the above, it is evident that the monitoring of water pipes and the detection of leaks are relevant for both economic and social reasons related to the

I. Catapano (✉) · R. Palmeri · F. Soldovieri · L. Crocco
Institute for Electromagnetic Sensing of the Environment—National Research Council of Italy,
Napoli, Italy
e-mail: catapano.i@irea.cnr.it

present public attention towards a responsible, sustainable and efficient use of natural resources as well as safety improvement and risk mitigation.

Due to the importance of the topic, several technological solutions have been developed to assess the conditions of water distribution mains [2, 3] and pipe monitoring [4]. These methods can be classified into direct and indirect methods [3]. Direct methods aim at gathering indications about the pipe conditions and include automated/manual visual inspection, pipe sampling and nondestructive testing; these latter involve electromagnetic, acoustic and ultrasound methods. Conversely, indirect methods generate inferential indicators and involve water audit, flow testing and measurements of soil parameters to determine the risk of deterioration.

Among nondestructive testing technologies, this chapter focuses on Ground Penetrating Radar (GPR), which is an electromagnetic (EM) device allowing the “remote” characterization of pipeline status, i.e. without excavating, whilst being low-cost and efficient from the measurement point of view. In detail, the chapter provides general concepts regarding the GPR working principle and its configuration for pipe surveys. Moreover, it summarizes advantages and limits concerning the use of GPR for the application at hand. Then, a differential microwave tomographic approach for GPR data processing is presented and preliminarily assessed with simulated data.

21.2 The Ground Penetrating Radar (GPR)

The GPR is a non-invasive technology for the detection and location of buried and hidden objects, which exploits electromagnetic waves in the microwave frequency range by relying on their ability to penetrate non-metallic materials [5, 6].

Nowadays, GPR is widespread used in geology, archaeology and civil engineering; moreover, it is considered for the characterization of motorway pavement or railway tracks and for detecting anti-personnel mines or unexploded ordnances [5, 7].

21.2.1 Working Principle

The GPR working principle is very simple and is based on the scattering phenomenon of EM waves that occurs due to EM discontinuities present in the medium under test [5, 6].

Figure 21.1 shows a simplified model of the working principle of a GPR. Specifically, the GPR transmitting antenna emits a microwave signal that propagates into the probed medium. When an EM discontinuity is encountered, a reflected signal arises and it is collected by the GPR receiving antenna. Therefore, a GPR system is made by a transmitting antenna, whose task is the radiation of the EM field within the medium to be investigated, by a receiving antenna that records the backscattered

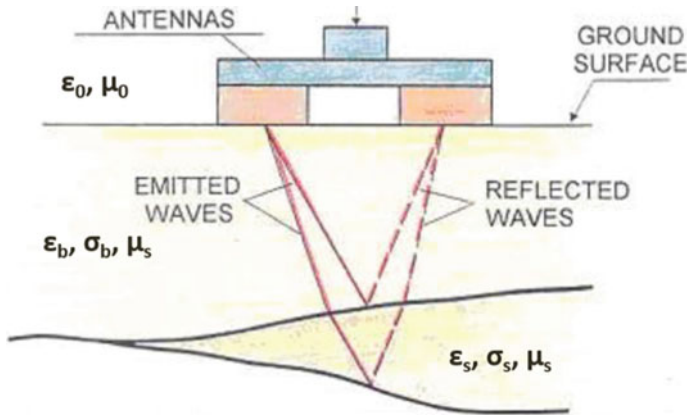


Fig. 21.1 GPR working principle

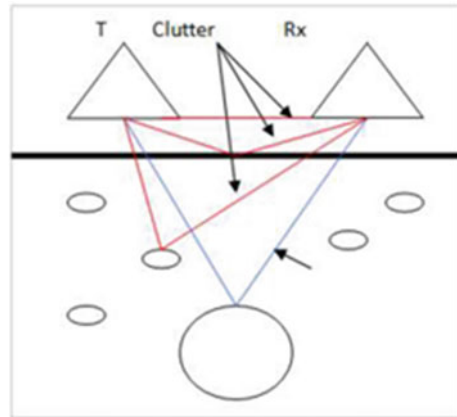
field and by an electronic unit, which controls the generation and collection of the signals.

Transmitting and receiving antennas usually move along a straight path. The data recorded at each measurement point along this path is referred to as ‘A-scans’, while a set of A-scans gives rise to the radargram, also referred to as ‘B-scan’. Commonly, GPR systems work in time domain. This means that the antenna transmits an impulse signal and the signal backscattered by the encountered discontinuity is recorded as a function of the two-way travel time, i.e., the time taken by the wave to propagate along the transmitter–anomaly–receiver path. Accordingly, if the phase velocity of the EM wave, which depends on the electromagnetic characteristics of the underground layers, is known, it is possible to estimate the depth d_n at which the discontinuity is located.

It is worth pointing out that, by representing the collected data as a function of the transmitting and receiving antenna system position and the two-way travel time, an image, referred to as radargram, is obtained. Within the radargram, a localized anomaly typically appears as a hyperbola, while a material interface as a continuous signal. Therefore, the GPR provides a ‘coded’ representation of the surveyed scenario and proper data processing approaches are necessary to obtain an easy interpretable image allowing the visualization of occurring details [7].

In this respect, one has to consider that the signal reflected by the EM anomaly, from now on named “target”, may be weak as compared to clutter signals. These latter are due to the direct coupling between transmitting and receiving antennas, the reflection from the air–ground interface and any other object in the scene different from those of interest. Figure 21.2 shows a sketch of the sources of clutter in a typical GPR scenario. This figure shows that the signal received by the GPR system is affected not only by the useful signal arising from the target (blue line) but also by the direct coupling between the antennas, the reflection from the air–soil interface and

Fig. 21.2 Sources of clutter (red lines) in a typical GPR scenario



those coming from spurious anomalies present in the scenario (which are represented by the red lines).

21.2.2 GPR Configuration for Water Pipe Monitoring

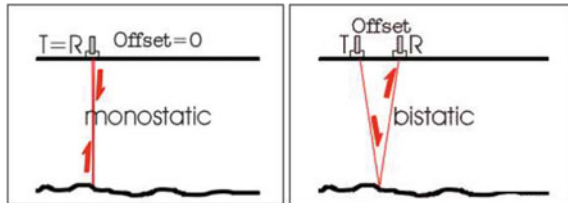
The definition of the GPR specifics must take into account various aspects related to the specific application at hand. In the case, herein of interest, of water pipe inspection, the main features to account for are the type of soil, the presence of stratifications and the depth to be reached. These factors affect the choice of the appropriate operating frequency band, the measurement configuration and the type of antenna. In the following, practical rules on how to choose them are given.

- Operating frequency:** the choice of the working central frequency depends on the electromagnetic features of the media wherein wave propagation occurs, mainly their dielectric permittivity and electric conductivity. Moreover, the choice of the working frequency is related to two important parameters, i.e., the image resolution and the penetration depth. The resolution increases as the frequency increases, while the penetration depth decreases due to the higher rate of attenuation of the EM waves. Therefore, the choice of the working frequency results as trade-off between the counteracting needs of the resolution limits and the achievable penetration depth. Generally, the best GPR results are obtained in low attenuation soils and high penetration depths are reachable in soils whose conductivity is very low, while the GPR survey is constrained to a shallow region in moist soils with high conductivity. Table 21.1 reports typical values of signal attenuation per unit length for different types of materials [5].

Table 21.1 Attenuation value of the electromagnetic signal for different materials encountered in subsoil inspections

Material	Attenuation (dB/m)
Sand	10
Wet soil	10–500
Clay	50–300
Salt water	10,000
Ice	1–10
Dry concrete	5–20

Fig. 21.3 GPR data acquisition modalities



- Measurement configuration:** among the various existing techniques for acquiring GPR data, the most common are the monostatic and the bistatic configurations. Figure 21.3 shows a scheme of the two operation modalities. In the monostatic configuration, the GPR uses a single antenna that first transmits and then is enabled to receive, or two antennas located at a distance negligible with respect to the probing wavelength. In the bistatic configuration, instead, the transmitting and receiving antennas are separated one from each other and their relative distance can be modified, in order to have a diversity in data collection.
- Type of antenna:** the choice of the type of antenna must take into account very important aspects, also linked to the other involved specifications. In particular, the penetration of the signal into the soil is the aspect that enforces the most important constraints in this choice. The main requirements are that the antenna is broadband, well adapted to allow good coupling with the air-ground interface, suitably polarized on the basis of the features of the target to be identified and small in size in order to facilitate portability. However, the above requirements often conflict with each other, so a compromise must be found.

Taking into account the information relating to the characteristics of the typical encountered scenarios of interest in this paper, i.e., the soil type, presence of stratifications and any containment structures, the useful frequency band is the one centred around 200 MHz. This choice also considers the extension of the area affected by the leak, which is commonly higher than 10 cm, and the distance of the pipe from the surface, which is assumed lower than 2 m.

Regarding the measurement configuration, the most suitable one is the multi-monostatic configuration, in which a pulsed system operating in the frequency band

centred around 200 MHz is moved along a scan line extending between 1.5 and 3 m. This choice allows for the achievement of the required depth (between 0.5 m and 2 m) for different types of soils and guarantees the flexibility of use, which is necessary due to the heterogeneity of the encountered scenarios. The scan should be carried out in the direction orthogonal to that of the pipeline and repeated along its extent for the section of interest with a spacing between 0.5 and 1 m.

As for the antennas, the geometry of the scenario under test, in which there is a known target with a predominant dimension (that is the pipeline), makes it appropriate the use of antennas with linear polarization, suitably oriented parallel to the pipeline itself in order to maximize the useful signal.

21.3 GPR and Water Pipe Monitoring: State of Art and Open Issues

GPR is a widely exploited technology for subsurface imaging and it has been also considered among possible non-destructive approaches to be used to cope with leaks detection and monitoring [3, 8].

GPR is potentially able to detect leaks in buried water pipes either by detecting underground voids created by the leaking water or by detecting anomalies in the depth of the pipe as well as changes of the velocity of radar signal propagation due to soil saturation with leaking water [9]. Moreover, compared to acoustic correlation techniques [10] and infrared imaging [11], GPR is non-sensitive to pipe material, pipe shape and acoustic noise. In addition, GPR is efficient for operational uses, because it does not require direct contact with the pipe or even the ground and it allows for 3D images of the subsurface useful to discriminate underground structures [12].

Accordingly, several GPR based approaches have been proposed and their performance have been tested in well-controlled conditions [12–18].

It is worth pointing out that the most usual strategy aims at detecting leaks by comparing visually radargrams acquired at different states of the leak evolution [19–21]. A leak, indeed, determines a growth of the water content characterizing the soil surrounding the pipe and this implies an increase of the soil relative permittivity. Since a growth of the relative permittivity of the material where the propagation occurs implies a reduction of the wave velocity, the presence of a leak is inferred by estimating the signal velocity. In this regard, different velocity estimation approaches have been proposed, see [22] and the references herein cited.

However, the characterization of the leak, i.e. the estimation of its extent and its origin, is very hard if not impossible without applying adequate data processing techniques. The backscattered signal due to the leak is indeed masked by geometrical spreading and predominant surface reflections, among which the signal due to the pipe [23]. Therefore, the use of GPR for the application at hand is not trivial and the fact that the leak appears as a weak perturbation, especially at its early stage, complicates further the GPR employment. Actually, the radargrams referred to scenarios

with and without the leakage look like similar each other. Consequently, the leak imaging depends strongly on the approaches used to process the data as well as on the user's expertise.

21.4 Microwave Imaging

21.4.1 Review of the Main Concepts

In order to improve the interpretability of the results achieved from a GPR survey, several data processing procedures have been developed over the years, including model-based approaches [7, 24, 25]. These approaches exploit mathematical models capable of describing the various physical phenomena underlying the signal-matter interaction, such as propagation, reflection, transmission, diffraction, and address imaging as an inverse problem of electromagnetic scattering. Model-based approaches are characterized by a high degree of flexibility, as they do not place any constraint on the measurement configuration and can be used to treat both canonical reference scenarios, such as homogeneous media, half-spaces and stratified structures, as well as non-canonical scenarios as long as they are at least approximately known [7, 25].

Among the different model-based approaches proposed in the literature for describing the functional link between the data and the unknown of the imaging problem [7], an approach successfully applied in many applications is the one based on Born-approximation and commonly referred to as linear microwave tomography [26]. Such an approach works in the frequency domain, hence it requires that the time domain GPR data are transformed by means of the Fourier Transform. In particular, the samples of the measured backscattered field are preliminarily filtered by means of time domain procedures, in order to reduce the contribution due to the direct coupling between the antennas and the air-medium interface as well as unwanted signals, such as noise and clutter. Then, the Fourier Transform is applied.

In the Born-approximation-based approach [26], the unknown is the contrast function, which accounts for the variations between of the actual permittivity occurring in the spatial domain under test and that assumed to describe the reference scenario. The contrast function is defined as:

$$\chi(r) = \frac{\varepsilon_x(r)}{\varepsilon_b(r)} - 1 \quad (21.1)$$

In Eq. (21.1), $\varepsilon_x(r)$ is the unknown dielectric permittivity, while, $\varepsilon_b(r)$ is the dielectric permittivity of the reference scenario and it is supposed to be known.

In addition, the relationship between the measured data and the unknown contrast is expressed by means of a linear integral equation. The kernel of this equation is the product of the Green function, i.e. the field irradiated on the measurement

surface by an elementary source placed in the considered reference scenario, and the incident field, that is the field radiated by the transmitting antenna in the scenario under examination if no target would be present. Specifically, by denoting with Ω the spatial region under investigation, at each angular working frequency ω , the back-scattered field E_s , measured at the measuring point r_m when the source is at the point r_s , is expressed by the following integral equation:

$$E_s(r_m, r_s, \omega) = k_b^2 \int_{\Omega} G(r_m, r, \omega) E_{inc}(r, r_s, \omega) \chi(r) dr \quad (21.2)$$

where k_b is the wavenumber of the medium where the signal propagation occurs, while G and E_{inc} represent the Green function and the incident field relative to the considered reference scenario, respectively.

By using the Method of Moments to discretize the integral relationship given in Eq. (21.2), the imaging problem is formulated as the solution of a matrix equation:

$$\mathbf{E}_s = \mathbf{L}[\boldsymbol{\chi}] \quad (21.3)$$

In Eq. (21.3), \mathbf{E}_s is the $(M \times F)$ dimensional vector, M and F denoting the number of measurement points and frequencies, respectively; \mathbf{L} is the $(M \times F) \times N$ dimensional matrix representing the discretized version of the integral operator in Eq. (21.2), N being the number of pixel partitioning Ω ; $\boldsymbol{\chi}$ is the N -dimensional vector representing the unknown contrast function.

Due to the smoothing properties of the kernel of the integral Eq. (21.2), the underlying problem belongs to the class of ill-posed inverse problems [27]. Accordingly, the matrix \mathbf{L} is ill-conditioned, so that the solution of (21.3) cannot be pursued by means of a straightforward matrix inversion.

To provide a stable, though approximate, solution, the linear system in Eq. (21.3) is solved in a regularized way by exploiting the Truncated Singular Value Decomposition (TSVD) of \mathbf{L} [27]. Therefore, an approximate expression of the contrast vector is given by:

$$\tilde{\boldsymbol{\chi}} = \sum_{i=1}^T \frac{1}{\sigma_n} \mathbf{E}_s \mathbf{u}_n \mathbf{v}_n \quad (21.4)$$

where σ_n denotes the n -th singular value of the matrix \mathbf{L} , \mathbf{v}_n and \mathbf{u}_n are its n -th singular left and right vectors, \langle, \rangle indicates the scalar product in the functional data space. Finally, the threshold $T \leq \{(M \times F), N\}$ is chosen in order to ensure a good compromise between the accuracy and stability of the result.

Finally, starting from the contrast retrieved through (21.4), a tomographic image is obtained. Typically, this latter shows the modulus of the contrast function as defined in Eq. (21.4) and normalized to its maximum value within the survey domain.

21.4.2 A Model-Based Differential Tomographic Approach for Leak Monitoring

The adoption of model-based tomographic approaches has proven to be effective in a number of cases as a means to provide enhanced GPR results. Such an approach can be conveniently exploited in the case at hand, wherein the peculiar aspects of the problem can be exploited to further enhance the GPR imaging capabilities. In particular, a differential linear Microwave Tomography approach, which takes advantage of the a priori information available on the investigated scenario, can be devised. Actually, it is reasonable to assume that the pipe diameter and its location are known as well as the electromagnetic properties of the pipe and the surrounding medium. Accordingly, it is possible to exploit these pieces of information to define a reference scenario and face the imaging of the leakage as the problem of retrieving a (possibly weak) perturbation of it. More in detail, let us assume as investigated scenario the one given in Fig. 21.4 and, as previously, let Ω the spatial domain under test. We assume as known parameters:

- the coordinate of the pipe center with respect to the reference system introduced in Fig. 21.4;
- the pipe diameter d_p ;
- the dielectric permittivity of the pipe, ϵ_p , that of the liquid inside it, ϵ_w , and that of the hosting medium, which is also referred as background, ϵ_b .

Moreover, all materials are not magnetic, i.e., their magnetic permeability is $\mu_0 = 4\pi \cdot 10^{-7}$ H/m, while their electric conductivity is neglected, when the imaging problem is faced.

Based on these hypotheses, we introduce the reference scenario depicted in Fig. 21.5, that is the same of that in Fig. 21.4 with the leak removed, and look for this

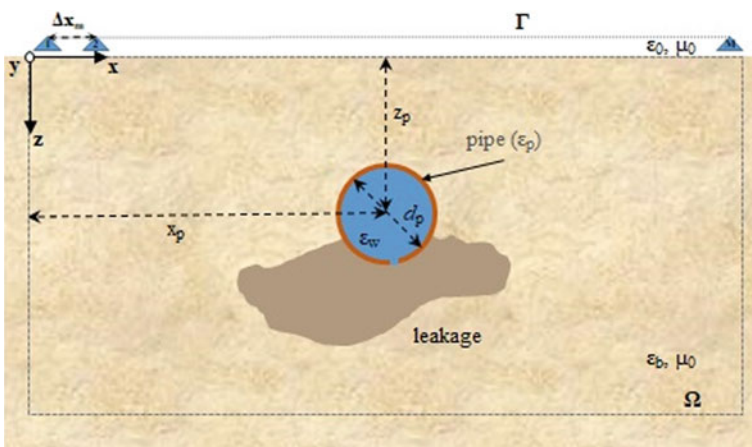


Fig. 21.4 Investigated scenario

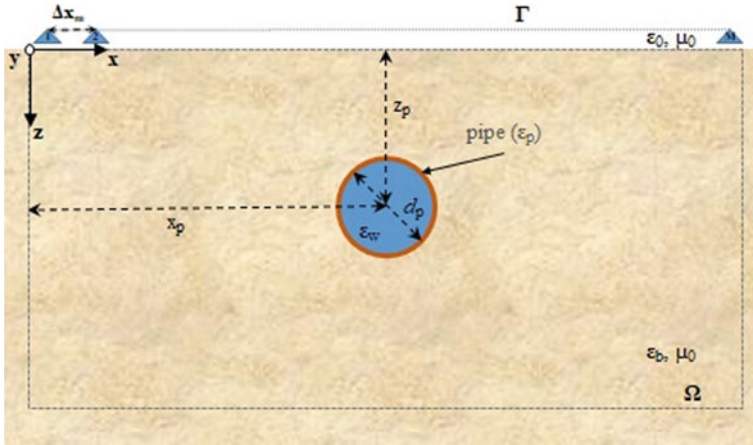


Fig. 21.5 Reference scenario

latter as a weak perturbation of the reference scenario. Therefore, by denoting with E_s the scattered field due to the investigated scenario, i.e., the scenario in Fig. 21.4, and with E_s^{ref} the scattered field due to the reference scenario, i.e. the scenario in Fig. 21.5, the scattered field due to the leakage is $E_s^l = E_s - E_s^{ref}$. We are pointing out that E_s is measured by the GPR system, while E_s^{ref} is numerically computed by means of an EM software able to simulate the reference scenario.

According to the Born Approximation [26], the leakage scattered field, E_s^l , is given by:

$$E_s^l(r_m, \omega) \approx \int_{\Omega} G^{ref}(r_m, r, \omega) E_{inc}^l(r, r_m, \omega) \chi^l(r) dr \tag{21.5}$$

where G^{ref} denotes the Green function related to the reference scenario depicted in Fig. 21.5 and E_{inc}^l is the incident field in Ω without the leakage, i.e. the total field referred to the reference scenario in Fig. 21.5. Both the quantities G^{ref} and E_{inc}^l are computed numerically; specifically, thanks to the reciprocity theorem [26] they are equal to each other. In Eq. (21.5), $\chi^l(r)$ is the contrast function accounting for the changes in terms of dielectric permittivity introduced by the leakage with respect to the reference scenario:

$$\chi^l(r) = \frac{\varepsilon^l(r)}{\varepsilon^{ref}(r)} - 1 \tag{21.6}$$

$\varepsilon^{ref}(r)$ being the space variable function denoting the relative dielectric permittivity of the reference scenario, i.e. the relative dielectric permittivity characterizing the scenario in Fig. 21.5.

21.5 Preliminary Validation Analysis

The tomographic approach introduced and discussed in the previous section is herein validated by considering the scenario depicted in Fig. 21.6a, wherein a buried water filled plastic pipe is present, as the better reference scenario. Such a scenario is the expected one for a water supply system in right conditions, i.e. a water-filled pipe without leakage. Conversely, Fig. 21.6b shows the case of a damaged pipe; hence, it is a perturbed case of that in Fig. 21.6a due to the presence of a leakage, which turns

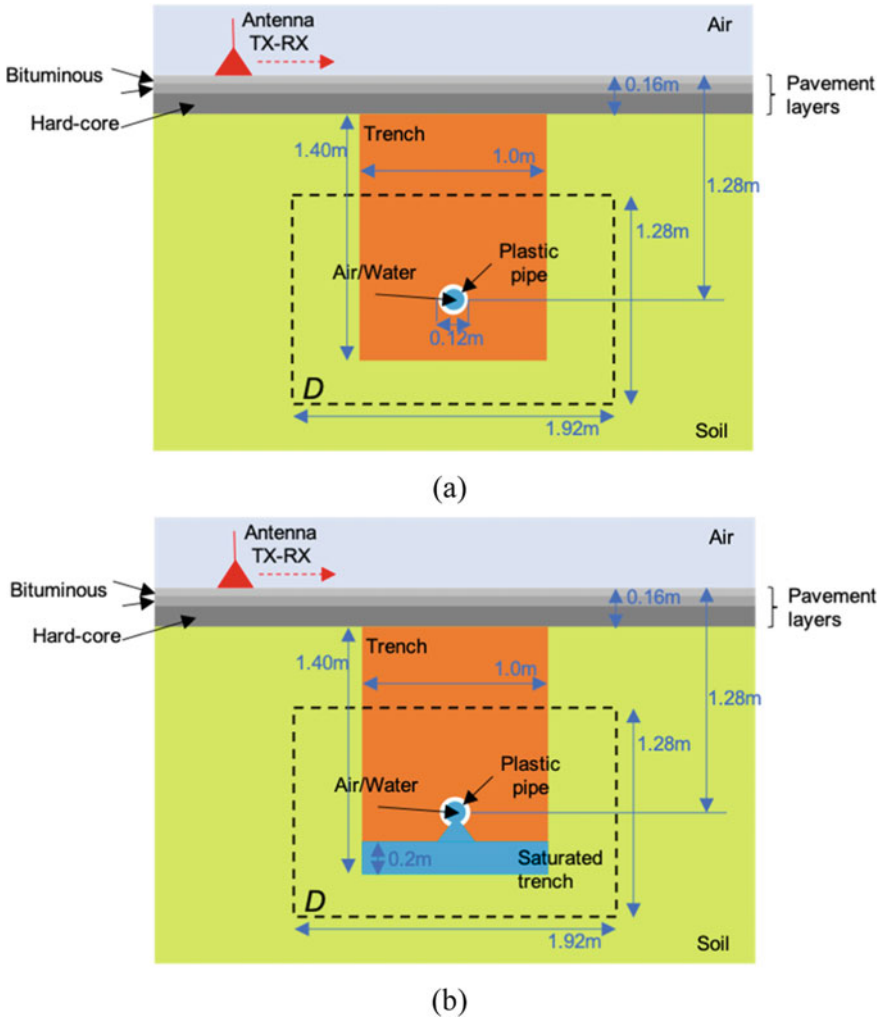


Fig. 21.6 Simulated scenarios: **a** Reference scenario; **b** Investigated scenario, i.e. leakage perturbed scenario

Table 21.2 Dispersive parameters for the materials in the scenario under test

Material	ε_{rs}	$\varepsilon_{r\infty}$	σ_s (mS/m)	τ_E (ps)	τ_σ (ps)
Air	1	1	0	0	0
Wearing coarse (bituminous)	4	4	0.1	0	0
Base layer (bituminous)	5	5	0.1	0	0
Hard-core	6	6	0.1	0	0
Sandy soil	15	13.1	10	70	0
Trench	7	6.1	1	70	0
Plastic pipe	4.5	1	0.1	0	0
Water	81	5.1	1	0.6	0
Saturated trench	14	12.3	5	70	0

into a change of the electromagnetic parameters of the soil surrounding the pipe. The scenario in Fig. 21.6b represents the actual investigated scenario.

Both the scenarios have been simulated by accounting for the material dispersive behavior. Specifically, the Debye model [28] is used for the relative permittivity:

$$\varepsilon(\omega) = \varepsilon_{r\infty} + (\varepsilon_{rs} - \varepsilon_{r\infty}) / (1 + j\omega\tau_E) \quad (21.7)$$

while, the Kelvin-Voigt model [29] is considered for the electric conductivity:

$$\sigma(\omega) = \sigma_s + (1 + j\omega\tau_\sigma) \quad (21.8)$$

The parameters appearing in Eqs. (21.7), (21.8) and referred to the involved materials are summarized in Table 21.2.

Multimonostatic-multifrequency data have been simulated by using the RF module of the electromagnetic software COMSOL Multiphysics [30]. Specifically, the antenna system has been moved in $M = 21$ measurement points, evenly spaced along a 2 m long straight line. At each measurement point, data have been simulated at $F = 15$ frequencies evenly spaced in the range [100–310] MHz.

Since the the Green's function G^{ref} and the incident field E_{inc}^l appearing in Eq. (21.5) depend on the considered reference scenario, in order to assess how the choice of this latter affects the capabilities of the imaging approach, beyond the reference scenario in Fig. 21.6a, further a-priori known unperturbed scenarios have been considered. These other reference scenarios are depicted in Fig. 21.7, while the corresponding tomographic images are given in the left column of Fig. 21.8 for noiseless data and in the right column of Fig. 21.8 for data corrupted by white Gaussian noise (SNR = 15 dB).

Figure 21.8a left panel shows the imaging result achieved by accounting for the reference scenario in Fig. 21.6a and noiseless data and it states clearly the ability to detect the leak and provide a satisfactory estimation of its extent along the x-axis, i.e. in the direction parallel to the measurement line. The leak is still detectable in

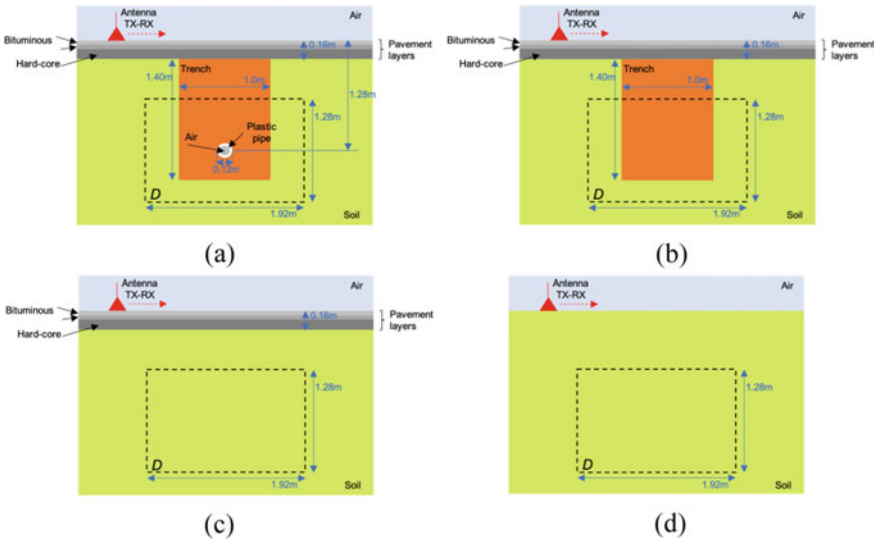


Fig. 21.7 Further reference scenarios considered for testing the tomographic imaging: **a** scenario similar to that in Fig. 21.6a but for an air-filled, instead of water-filled, pipe; **b** scenario accounting for the right characterization of soil but without the pipe; **c** scenario accounting for a homogeneous soil with pavement layers at interface; **d** scenario accounting for a homogeneous soil with pavement layers neglected

the case of noisy data, see the reconstruction in Fig. 21.8a right panel, and when less accurate reference scenarios are exploited, see Fig. 21.8b, c left and right panels. These latter have been achieved by considering noiseless and noisy data and the reference scenarios in Fig. 21.7a, b, respectively.

Figure 21.8b, c show that a reduction of the a-priori information exploited to define the reference scenario implies an increased de-focused image of the pipe, whose location is retrieved in a less accurate way, progressively.

The quality of the reconstruction decreases furtherly by accounting for the reference scenarios in Fig. 21.7d,e. The corresponding tomographic images are, indeed, more affected by artifacts, do not provide an accurate localization of the pipe and just allow for the detection of the bottom of the leak, see Fig. 21.8d, e.

In all the considered cases, the presence of noise on data slightly reduces the imaging capability and this corroborates the robustness of the tomographic imaging against noise.

The results in Fig. 21.8 have been obtained by setting the TSVD threshold in such a way to filter out all the singular values whose amplitude is lower than 25 dB for Fig. 21.8a, 20 dB for Fig. 21.8b–d, 15 dB for Fig. 21.8e, with respect to the maximum amplitude.

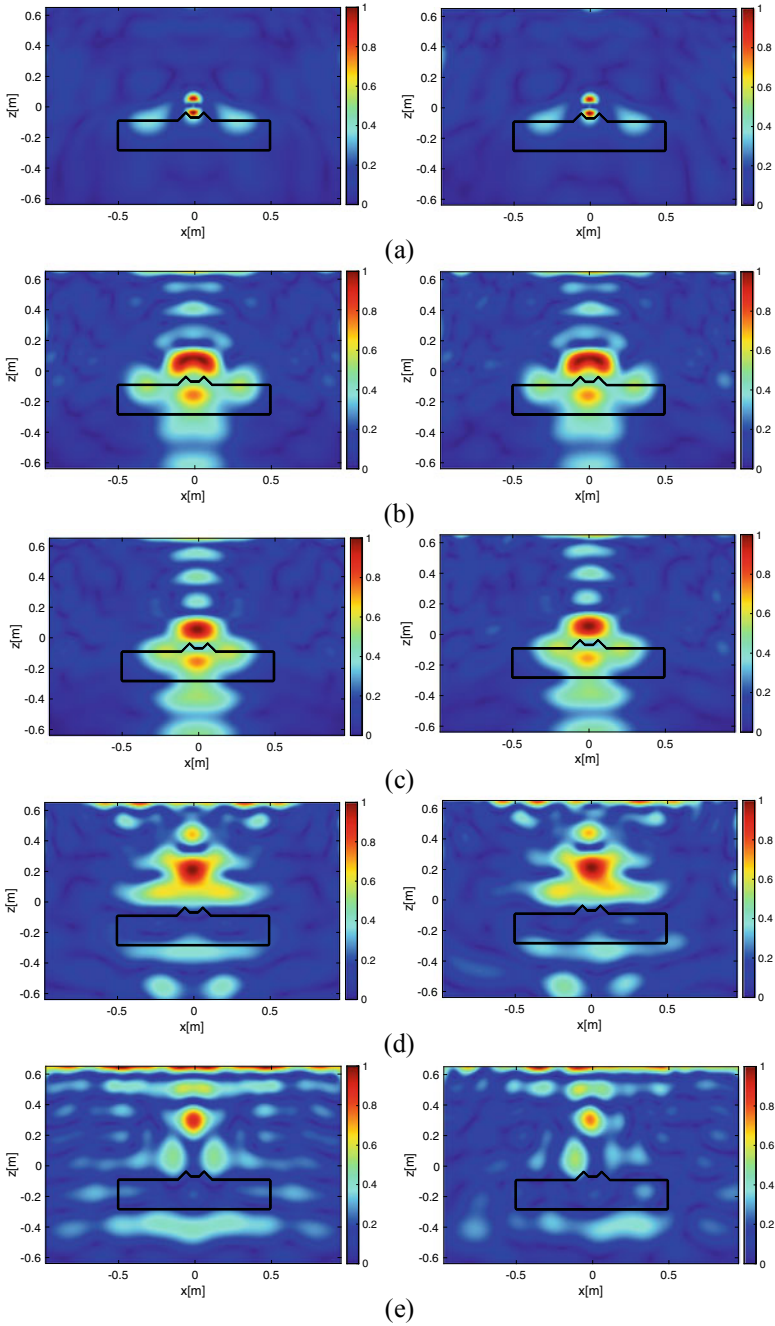


Fig. 21.8 Imaging results by adopting: **a** the better reference scenario, see Fig. 21.6a; **b** the reference scenario of Fig. 21.7a; **c** the reference scenario of Fig. 21.7b; **d** the reference scenario of Fig. 21.7c; **e** the reference scenario of Fig. 21.7d. Left column: noiseless data. Right column: noisy data (SNR = 15 dB). The black line indicates the actual extension of the leakage

21.6 Conclusions

This chapter has discussed the potentialities and limits of the GPR as a technology for imaging water leaks and outlined the interest towards the GPR engagement in the design of monitoring protocols devoted to improve the usage of natural resources. GPR is, indeed, a non-invasive diagnostic tool capable of providing a high-resolution image of the subsurface scenario under test.

The standard method of approaching GPR data, especially in monitoring applications as that herein of interest, consists in the direct observation by the operator of the so-called radargrams, i.e. images that report radar echoes as a function of time and the position of the radar. However, due to the complexity of the subsurface scenario, the interpretation of the radargrams is not simple and the extrapolation of the information depends on the operator's experience and it is inevitably influenced by his/her judgment.

To overcome this drawback and obtain "objective" images of the investigated scenario, model-based data processing approaches have been considered and a novel model-based differential tomographic approach has been proposed. This approach incorporates the information available on the investigated scenario, i.e., the expected position of the pipeline, its size, any presence of multiple pipes, the type of soil in which the pipeline is buried, and allow for obtaining images with the greatest possible spatial detail from which the operator can infer the information of interest. The reconstruction capabilities of the approach have been assessed preliminarily against simulated data and the presented results are encouraging and support an ongoing research activity regarding the experimental validation first in laboratory-controlled conditions and then on the field.

Acknowledgements The research activity described in this chapter has been partially supported by Italian Ministry of Research in the framework of call for Industrial research projects for Smart cities and communities and Social Innovation action under the contract SCN_00489 "WATERTECH—Smart Community for the Development and Application of Innovative Technologies for Monitoring of Distribution Networks for drinking, agricultural and industrial waters".

References

1. Desilva D, Burn S, Tjandraatmadja G, Moglia M, Davis P, Wolf L, Held I, Vollertsen J, Williams W, Hafskjold L (2005) Sustainable management of leakage from wastewater pipelines. *Water Sci Technol* 52:189–198
2. Hunaidi O (2006) Condition assessment of water pipes. In: *Proceedings of EPA workshop on innovation and research for water infrastructure in the 21st century*, Arlington, Virginia, USA, pp 1–6
3. Liu Z, Kleiner Y (2013) State of the art review of inspection technologies for condition assessment of water pipes. *Measurement* 46(1):1–15
4. Liu Z, Kleiner Y (2012) State of the art review of technologies for pipe structural health monitoring. *IEEE Sens J* 12(6):1987–1992

5. Daniels DJ (2004) Ground-penetrating radar, IET
6. Persico R (2014) Introduction to ground penetrating radar: inverse scattering and data processing. Wiley
7. Webster JG, Catapano I, Gennarelli G, Ludeno G, Soldovieri F, Persico R (2019) Ground-penetrating radar: operation principle and data processing. In: Webster JG (ed) Wiley encyclopedia of electrical and electronics engineering
8. Rizzo P (2010) Water and wastewater pipe nondestructive evaluation and health monitoring: a Review. *Adv Civil Eng* 1–13
9. Hunaidi O, Giamou P (1998) Ground-penetrating radar for detection of leaks in buried plastic water distribution pipes. In: Proceedings of 7th international conference on ground-penetrating radar, Lawrence, Kansas, USA
10. Brennan MJ, Joseph PF, Muggleton JM, Gao Y (2008) Some recent research results on the use of acoustic methods to detect water leaks in buried plastic water pipes
11. Fahmy M, Moselhi O (2010) Automated detection and location of leaks in water mains using infrared photography. *J Perform Constructed Facilit* 24(3)
12. De Coster A, Medina JP, Nottebaere M, Alkhalifeh K, Neyt X, Vanderdonck J, Lambot S (2019) Towards an improvement of GPR-based detection of pipes and leaks in water distribution networks. *J Appl Geophys* 162:138–151
13. Atef A, Zayed T, Hawari A, Khader M, Moselhi O (2016) Multi-tier method using infrared photography and GPR to detect and locate water leaks. *Autom Constr* 61:162–170
14. Jan Bimpas M, Amditis A, Uzunoglu N (2010) Detection of water leaks in supply pipes using continuous wave sensor operating at 2.45 GHz. *J Appl Geophys* 70(3):226–236
15. Dong L, Carnalla S, Shinozuka M (2012) GPR survey for pipe leakage detection: experimental and analytical study. SPIE proceedings, nondestructive characterization for composite materials, aerospace engineering, civil infrastructure, and homeland security, vol 8347, San Diego, USA, pp 1–7
16. Glaser D, Werkema D, Versteeg R, Henderson R, Rucker D (2012) Temporal GPR imaging of an ethanol release within a laboratory-scaled sand tank. *J Appl Geophys* 86:133–145
17. Lai W, Chang R, Sham J, Pang K (2016) Perturbation mapping of water leak in buried water pipes via laboratory validation experiments with high-frequency ground penetrating radar (GPR). *Tunn Undergr Space Technol* 52:157–167
18. Crocco L, Prisco G, Soldovieri F, Cassidy NJ (2009) Early-stage leaking pipes GPR monitoring via microwave tomographic inversion. *J Appl Geophys* 67(4):270–277
19. Amran TST, Ismail MP, Ahmad MR, Amin MSM, Ismail MA, Sani S, Masenwat NA, Basri NSM (2018) Monitoring underground water leakage pattern by ground penetrating radar (GPR) using 800 MHz antenna frequency. In: IOP conference series: materials science and engineering, vol 298, no 1. IOP Publishing, p 012002
20. Ayala-Cabrera D, Izquierdo J, Pérez-García R, Herrera M (2011) Location of buried plastic pipes using multi-agent support based on GPR images. *J Appl Geophys* 75(4):679–686
21. Hyun S, Oh H, Jo Y, Kim S, Kim Y (2007) The laboratory scaled-down model of a ground-penetrating radar for leak detection of water pipes. *Meas Sci Technol* 18(9):2791–2799
22. Cheung BWY, Lai WWL (2019) Field validation of water-pipe leakage detection through spatial and time-lapse analysis of GPR wave velocity. *Near Surface Geophysics*, 17(3-GPR in Civil and Environmental Engineering: Recent Methodological Advances), pp 231–246
23. Cataldo A, Persico R, Leucci G, De Benedetto E, Cannazza G, Matera L, De Giorgi L (2014) Time domain reflectometry, ground penetrating radar and electrical resistivity tomography: a comparative analysis of alternative approaches for leak detection in underground pipes. *NDT & E Int* 62:14–28
24. Turk AS (2011) Subsurface sensing, Chapter 5. Wiley, Hoboken, New Jersey, p 227
25. Catapano I, Gennarelli G, Ludeno G, Noviello C, Esposito G, Soldovieri F (2021) Contactless ground penetrating radar imaging: state of the art, challenges, and microwave tomography-based data processing. In: IEEE geoscience and remote sensing magazine. <https://doi.org/10.1109/MGRS.2021.3082170>

26. Chew WC (1995) *Waves and fields in inhomogeneous media*. Piscataway, NJ, 419 IEEE Press, USA
27. Bertero M, Boccacci P (1998) *Introduction to inverse problems in imaging*. CRC Press
28. Mantas PQ (1999) Dielectric response of materials: extension to the Debye model. *J Eur Ceram* 19(12):2079–2086
29. Bergman T, Robertsson JOA, Holliger K (1998) Finite-difference modeling of electromagnetic wave propagation in dispersive and attenuating media. *Geophysics* 63(3):856–867
30. <https://www.comsol.com/rf-module>

Chapter 22

Hydrogeophysical Methods for Water Resources Protection and Management



Giorgio Cassiani, Matteo Censini, Ilaria Barone, Maria Teresa Perri, Jacopo Boaga, and Rita Deiana

Abstract In this chapter we present a brief description of hydrogeophysical methods and their history over the past twenty years, with specific reference to their application for water resources protection and management. This generally requires that geophysical methods, and electrical/electromagnetic methods in particular, are used in time-lapse mode, thus allowing us to monitor hydrological changes in the subsurface. These data, in turn, can be used for calibration of hydrological models or for a better conceptualization of the subsurface hydrological processes. This can be done at a large variety of scales, even though here we present cases relevant to the small to intermediate scale. Examples concerning soil, vadose zone, hillslope and hydrogeological processes are shown and discussed.

22.1 Introduction

Hydrogeophysics was born in the early 1990s (see e.g. [1]) with the specific aim of providing data with unprecedented time/space resolution for the characterization of hydrological processes in the subsurface. Ever since, the number of publications in peer-reviewed journals, having “hydrogeophysics” in the title or keywords has steadily increased, and after three decades the term has become of general use and is widely accepted in the hydrology community. Nowadays, between 5 and 10% of hydrological papers describe some “hydrogeophysical” applications.

Together with this success, the wider use of geophysical techniques in hydrology has, however, also led to frequent misunderstandings and misuses. The main goal of

G. Cassiani (✉) · I. Barone · M. T. Perri · J. Boaga
Dipartimento di Geoscienze, Università degli Studi di Padova, Padua, Italy
e-mail: giorgio.cassiani@unipd.it

M. Censini · R. Deiana
CIBA, Università degli Studi di Padova, Padua, Italy

R. Deiana
DBC, Università degli Studi di Padova, Padua, Italy

this chapter is to cast some light on the meaning of hydrogeophysics and on its most useful and promising applications.

The use of geophysical techniques for hydrological purposes, and particularly for hydrogeological investigations dates back many decades (e.g. [2]) and originally the goal was (as it often still is) to provide information about the subsoil structure, especially in terms of sedimentary and hydrogeological units such as aquifers, aquitards, aquicludes. In this respect, geophysics plays in hydrology the same role it has for any other classical subsurface exploration, and specifically that of providing information about the geometries of geological bodies. While this application is often useful, it would be misleading to call this “hydrogeophysics” in a proper sense, as the hydrological purpose plays here the same role as would petroleum exploration, geothermal investigations, or solid mineral prospecting. In a nutshell, the link of geophysics with its goal is in this case very general, and not at all specific to hydrological processes.

The original idea behind hydrogeophysics has been since the early 1990 to attach hydrological meaning to the geophysical results. Indeed, this was not a new idea as, for instance, many efforts had been expended in the attempt, e.g., to link electrical resistivity as derived from geophysical data to estimates of hydraulic conductivity (e.g. [3]). hands, where prone to attain limited success (e.g. [4, 5]) as the underlying physical processes linking the motion of water in porous media to the motion of electrical charges are inherently very weak.

In spite of the difficulties, the great advantage that geophysics can provide, namely large spatial coverage and good resolution, potentially in 3D, called for renewed efforts to help hydrological characterization of the subsurface. As in many other cases, only a clear understanding of the processes to be characterized and monitored could lead to finding the right approach. Thus, the new wave came from researchers having primarily a hydrological background, who came to acquire a solid understanding of geophysical methods. The underlying idea is that both hydrology and geophysics are disciplines based upon physical laws, albeit in some cases based on experimental evidence only. Thus, the heart of the “new” approach to using geophysics for hydrology started from petrophysical consideration rather than from ad-hoc site-specific very weak correlations.

This “Copernican revolution” was based on three key ideas:

1. Any use of geophysics for hydrology should take into consideration the physical processes underlying both disciplines; in this manner the geophysics is not only an “imaging” technique, but goes back to its physical nature.
2. Geophysics can highlight not only subsoil structure, but also hydrological processes, i.e. the motion of water and dissolved substances in the system (let alone other relevant contamination issues such as presence of oily substances or of heavy metals). This, as apparent, requires repeated measurements, i.e. adding the 4th dimension: time.
3. Given the two points above, geophysics can provide (albeit indirect) measurements of the hydrological state variables of interest (e.g. moisture content, water salinity) that can be used to calibrate hydrological models: thus at the heart of

hydrogeophysics lies the ultimate idea of blending in measurements and models, or in other terms, conduct to data assimilation.

It is interesting to note that this line of thinking is totally analogous to the one that has led to time-lapse monitoring in the petroleum industry, where the tool of choice is (unlike in hydrogeophysics) 4D seismics, where 4 stands for space and time monitoring [6]. There too, geophysics is conducted in time-lapse, and differences over time are linked to the motion of fluids, with saturation mapped in time and space, to be then potentially used for multi-phase flow model calibration, and a much better management of fossil fuel resources. Note that similar approaches can, and should, be used also for the exploitation of renewable energy sources such as geothermics. Thus, geophysics moves from a pure characterization method to a monitoring tool.

Many extensive reviews of the development of hydrogeophysics can be found in the literature, both in terms of books [7, 8] and review papers [1, 9]. Recent applications of hydrogeophysics are numerous. Hydrogeophysical techniques can be applied at a large variety of spatial scales, spanning from a few meters with decimetric resolution, to hundreds of meters with meter to decameter resolution. In this chapter, we present several examples of different application scales.

In the sequel of this chapter we will sketch the basics of the adopted methods in hydrogeophysics, and present cases relevant to soil water dynamics (Sect. 22.3), deep vadose zone (Sect. 22.4), hillslope hydrology (Sect. 22.5), aquifer characterization (Sect. 22.6), before drawing conclusions and delineate ways forward (Sect. 22.7). The case studies have been chosen as examples where, to a different degree of complexity, measurements and modelling are integrated in the best spirit of hydrogeophysics.

22.2 Methodology

According to the three key ideas described in the introduction, the general hydrogeophysical approach is based on three fundamental steps:

1. Constitutive relationships
2. Time-lapse (high resolution) geophysical acquisition
3. Hydrological model calibration against geophysical data

The geophysical techniques more frequently used in hydrogeophysical applications are the ones that measure electro-magnetic properties, and particularly electrical conductivity/resistivity (Electrical Resistivity Tomography—ERT—and Electromagnetic Induction—EMI—Methods) and electrical permittivity (Ground-Penetrating Radar—GPR). For detailed reviews of these methods, and particularly in the hydrogeophysics contexts see e.g. [10–12].

Hydrogeophysics has potentially a large number of potential applications. Figure 22.1 shows a few, with the relevant sections of this chapter where some information can be retrieved for each case—the only exception not discussed in this chapter relates to contamination, which would require a specific discussion well

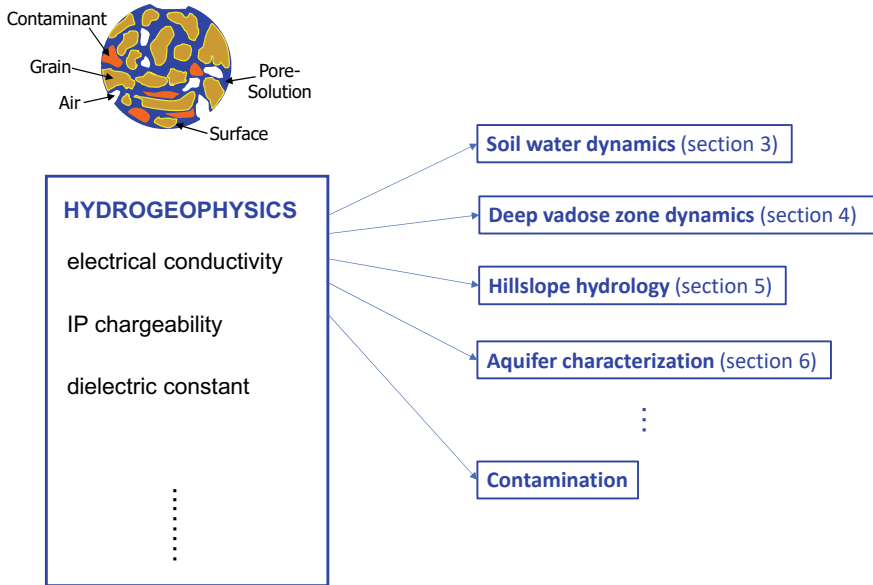


Fig. 22.1 The most important fields of application of hydrogeophysics, and the relevant sections of this chapter

beyond the scope of this chapter: some elements can be found e.g. in the book by [13] and in the paper by [14]. Table 22.1 conversely lists the references to which we direct the reader for more complete information on each field of application.

Table 22.1 References contained in this chapter with the method used and the relevant field of application

References	Methods	Application
[15–17] [18–23]	ERT, MALM, GPR	Monitoring of soil water dynamics with particular reference to the effects of root water uptake
[24–30]	ERT, GPR (both in cross-hole mode)	Monitoring of deep vadose zone water dynamics
[31–33]	ERT, gravimetry	Monitoring of hillslope hydrological states
[34–40]	ERT, MALM	Aquifer characterization and monitoring
[13, 14]	ERT, GPR, EMI	Contamination

22.2.1 *Constitutive Relationships*

At the heart of the hydrogeophysical approach lie the links between the physical parameters ultimately measured by geophysical methods (e.g. electrical resistivity, electrical permittivity, etc.) and the state variables that define the hydrological state of the system (e.g. soil moisture content, or soil water salinity, or others). Note that this is a fundamental difference with respect to older approaches, where a direct link was sought between parameters estimated from geophysics (e.g. electrical resistivity) and governing parameters of hydrological processes (especially hydraulic conductivity), and the corresponding correlations were found to be extremely weak [3] to the point of being of no practical use. The new approach has one obvious advantage, even though it requires much more effort in order to produce practical results. The advantage is that:

1. the correlation between some geophysical parameters and hydrological state variables is extremely good;
The disadvantage, that must necessarily be faced, is that:
2. as from geophysical data we can only infer estimates of the hydrological state variables, that thus describe the system state at one time, we must: (i) acquire data in time-lapse, and (ii) use the data to calibrate hydrological models in order to tune the hydraulic parameters and their distribution that is responsible for the system's behavior.

The most widely used constitutive relationships in the context of hydrogeophysics are those involving electromagnetic properties of soils and rocks. This is natural, as water has peculiar electrical characteristics, and its presence in porous media changes dramatically the electromagnetic response of the medium as measured by geophysical methods. In particular, two electromagnetic parameters are strongly affected by the presence of water: electrical conductivity, or its reciprocal electrical resistivity, and electrical permittivity. The most classical relationship linking (bulk) electrical resistivity ρ of the porous medium (as measured from electrical methods), water saturation S and water electrical resistivity ρ_w is Archie's law [41]. The key assumption underlying Archie's law is that current is conveyed solely through the conductive aqueous solution, while the solid matrix is a perfect insulator. As this assumption is not always satisfied, extensions and modifications have been proposed in order to account for the contribution of the solid phase (e.g. [8]) still largely dependent on empirical parameters to be calibrated.

Electrical permittivity of porous media, on the other hand, is also strongly linked to the presence of water per se, as the dielectric properties of water easily overwhelm those of air and solid grains. The relationship between electrical permittivity of the medium and its volumetric moisture content is therefore monotonically increasing, albeit non-linear. The most widely used relationships for this purpose are the so-called "universal" relationship by [42] and the Complex Refractive Index Model (CRIM—[43, 44]). Some attempts have also been made to merge into a single conceptual framework both electrical conductivity and electrical permittivity of a porous medium

in presence of water (e.g. [45]). For a fairly comprehensive view of the constitutive relationships used in hydrogeophysics see e.g. [46].

22.2.2 Time-Lapse Geophysical Acquisition

The second key component of the procedure is the acquisition of geophysical data capable of imaging hydrological processes in their time–space evolution. Space extent and resolution are inherently achievable via traditional geophysical investigations. The necessary novel aspect lies in the acquisition of repeated geophysical surveys over time, using the same spatial configuration. A large number of papers have appeared in the literature over the past couple of decades showing the power of time-lapse geophysical acquisition in highlighting changes in hydrological state variables such as soil moisture content (in the unsaturated zone—e.g. [16, 26, 27, 47]) or water electrical conductivity (in the saturated zone—e.g. [34, 36, 39, 40, 48, 49]). Some specific care must be taken when acquiring geophysical data in time-lapse, and specifically:

1. take care of the precise repeatability of measurements, in order to highlight the effect of changes over time that is often subtler than the signal coming from time-invariant structure;
2. invert data using strategies that enhance the effect of changes over time by taking into consideration two or more acquisitions taken at different times using the same configuration. In this respect typical solutions, e.g. for electrical methods, are ratio [28] or difference [50] inversions approaches.

22.2.3 Hydrological Model Calibration Against Geophysical Data

The availability of spatially and temporally dense data concerning the state variables of hydrological processes, albeit indirectly measured via geophysical methods, triggers the need for a comparison of the experimental results with the prediction of hydrological models. This comparison can be conducted in a variety of ways, from simple calibration in terms of key indicators (e.g. [24]) to full data assimilation (e.g. [17, 51–54]) in a variety of different fashions ([55–61]). Irrespective of how sophisticated the data assimilation/model calibration approach is, the key purpose of this approach is to extract from the geophysically-derived space–time data the information concerning the hydraulic behavior of the system, essentially condensed in terms of geometry and parameters spatial distribution of a hydrological model. While data assimilation approaches can provide more detailed estimates of hydraulic parameters, often in their spatial variability, and with the relevant uncertainty estimation, simpler calibration approaches have the advantage of being easier to manage and allow the user to have a more direct control on the calibration process. This often

leads to a better grasp of the parameters controlling the hydrological system, and a more educated understanding of the system's behavior. Note, in any case, that simpler and more sophisticated approaches are not alternative to each other but may be well used in sequence for a more effective estimation of hydraulic parameters and system's structure.

22.3 Soil Water Dynamics

As mentioned above, hydrogeophysical techniques can be applied at a variety of scales. The scale depends on the applied method, as well as on the acquisition geometry. The most flexible technique is, in this respect, ERT. As DC electrical methods are based upon a diffusive process that has no intrinsic scale (as opposed to wave-based methods, where the wavelength is a natural scale of the method), the method resolution depends on the acquisition geometry in terms of electrode spacing and spatial setup. This allows the user to scale the measurements down at will, and in particular it is possible to achieve the resolution necessary to image the dynamics of soil processes at a very small scale (e.g. [62]). This has led to a number of applications mostly related to the monitoring of soil moisture content as a response, also, to plant root activity (e.g. [15, 19–23]).

An example of this type of small scale time-lapse ERT applications, is provided by the case study by [18], concerning controlled infiltration experiments in an apple orchard. The work was conducted using time-lapse minimal-invasive 3D micro-electrical tomography (ERT) in order to monitor rhizosphere eco-hydrological processes in an apple orchard in the Trentino region, Northern Italy (Fig. 22.2). In particular, the work aimed at gaining a better understanding of the soil–vegetation water exchanges in the shallow critical zone, as part of a coordinated effort towards predicting climate-induced changes on the hydrology of Mediterranean basins (EU FP7 CLIMB project). The adopted strategy relied upon the installation of a 3D electrical tomography apparatus consisting of four mini-boreholes carrying 12 electrodes each plus 24 mini-electrodes on the ground surface (Fig. 22.2), arranged in order to image roughly a cubic meter of soil surrounding a single apple tree (Fig. 22.3). The monitoring program was initially tested with repeated measurements over about one year. Subsequently, three controlled irrigation tests were performed under different conditions, in order to evaluate the water redistribution under variable root activities and climatic conditions. Laboratory calibration on soil samples helped translate electrical resistivity variations into moisture content changes, supported also by in-situ TDR measurements.

The plant root suction activity was effectively imaged using time-lapse ERT and ratio inversion. The increase in resistivity with respect to the initial (early morning) condition show the location of the region at depth dried by root suction in the early afternoon (see e.g. Figure 22.4), providing a clear image of the 3D distribution of active roots as conditioned by the presence and efficiency of the drip irrigation system

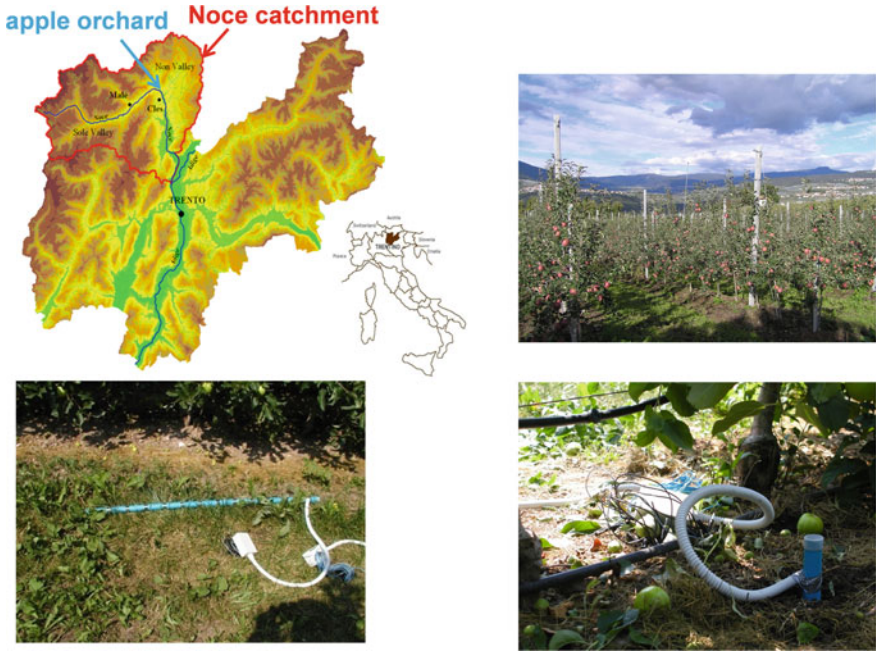


Fig. 22.2 The Maso Majano apple orchard in the Trentino Region (NE Italy): in clockwise order: geographical location, orchard landscape, installation around the apple tree, and single borehole setup before installation

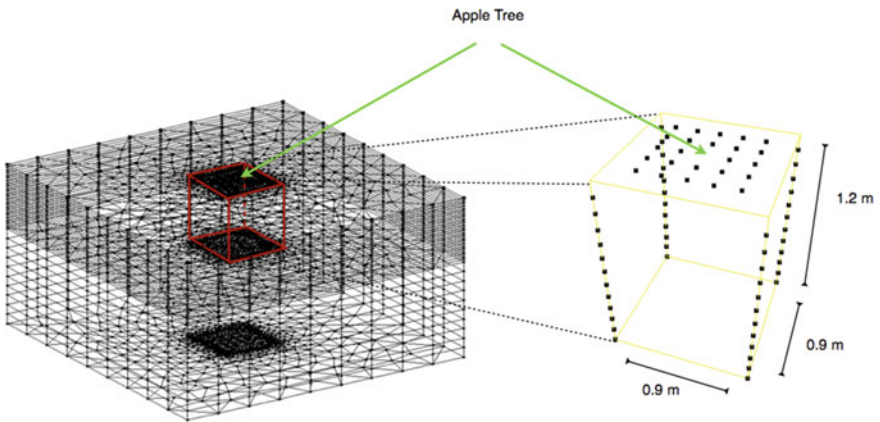


Fig. 22.3 ERT electrodes configuration around the monitored apple tree (right) and the corresponding finite element mesh (left) used in the ERT inversion code (R2—[64])

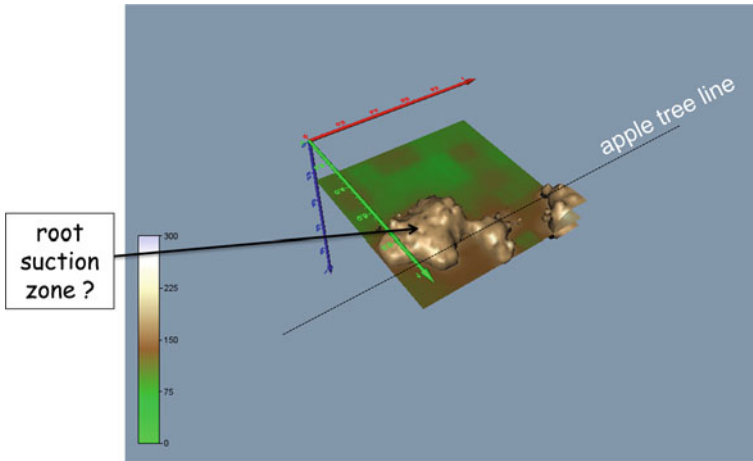


Fig. 22.4 May 2012 experiment: resistivity ratio with respect to background at 30 cm depth and at 8.5 h after start of irrigation

(thus leading to very localized water supply and corresponding root development and suction.

In the spirit of hydrogeophysics, Richards' equation modeling was used also to explain the monitoring evidence. In particular, the authors adopted CATHY (CATchment HYdrology) model (e.g. [63]), a physically-based 3D distributed model which uses Richards' equation to describe variably saturated flow in porous media. The infiltration model was also coupled with a particle-tracking algorithm in order to compute the simulated water travel time from the surface to depth.

The most informative result of this simulation (Fig. 22.5) was that at time 2.5 h the "new" irrigated water had indeed reached the depth where the deeper increase in resistivity is observed, i.e. around 80 cm from the ground surface, in both the May and November infiltration experiments, and has not gone any deeper. This information is particularly strong in corroborating the interpretation of the deeper electrical resistivity increase peak, to be linked to the displacement of "old" (i.e. resident) more saline water with "new" fresher water (with electrical conductivity in the range of $240 \mu\text{S}/\text{cm}$) irrigated at the surface.

The experiment and modelling results clearly identified the effect of root water uptake and the corresponding subsoil region where active roots are present, but also identified the need to consider the effects of different water salinity in the water infiltration process.

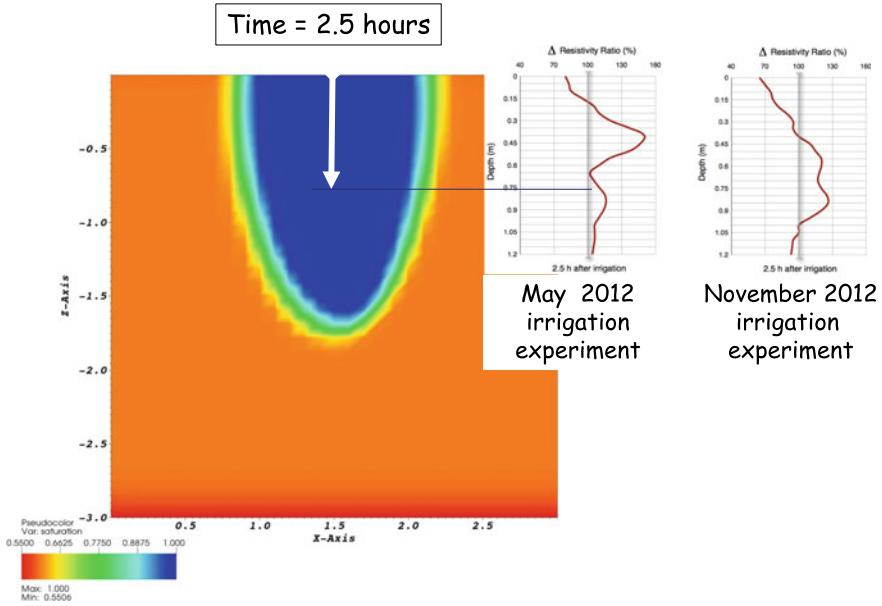


Fig. 22.5 Vertical sections cut across the 3D soil volume simulated using CATHY, and comparison with the location of the maximum resistivity increase in both May and November 2012 irrigation experiments

22.4 Deep Vadose Zone Dynamics and Groundwater Protection

The investigation of the vadose zone by means of non-invasive or minimally-invasive geophysical techniques can be easily extended to the deeper zone. ERT is by itself easily scalable to depths of tens of meters or more, being the placement of electrodes at depth only a logistical issue, easy to tackle. In addition, as the measurement volume increases, it becomes possible also to use GPR whose resolution depends on the natural scale of its wavelength: for GPR frequencies of 100 MHz or 200 MHz, typical of subsurface relatively deep investigations, the corresponding wavelength are in the 1–0.5 m range. Thus when the vadose zone characterization needs to be extended to ten meters or more, the joint use of ERT and cross-hole GPR is a viable and powerful option (e.g. [24, 25]).

Deiana et al. [29, 30] described in detail the results of two water infiltration experiments in the vadose zone of a gravel aquifer in the Po Plain, Northern Italy. The authors conducted both experiments by means of a fairly large infiltration trench (2.5 m × 0.5 m, 2 m deep). The site is characterized by Quaternary sand and gravel sediments that house an extensive unconfined aquifer. ERT and GPR were used in two-dimensional cross-hole configuration and time-lapse mode during a period of several days preceding and following the water injection experiments. Hereafter we

will present some results of the second infiltration experiment, which involved the injection of about 20 m³ of fresh water in the purposely excavated trench. The calibration of a three-dimensional infiltration model on the basis of the geophysical data was expected to provide useful estimates of saturated hydraulic conductivity, with a procedure similar to the one first introduced by Binley et al. [24]: a 3D unsaturated flow infiltration model is calibrated against field data, and in particular against moisture content changes, estimated indirectly from ERT and GPR measurements through the relevant constitutive relationships. The approach first proposed and implemented by Binley et al. [24] is based on condensing the entire information in terms of the depth migration of the center of mass of injected water. The approach is simple, easy to implement: the evidence by Binley et al. [24] shows that in this manner it is possible to obtain accurate estimates of hydraulic conductivity within a range of no more than a factor of 2.

The study involved both ERT and cross-hole GPR measurements, in time-lapse mode. A complex of 4 boreholes, 20 m deep, were drilled with the configuration shown in Fig. 6a. The three boreholes at the corners of the triangle were equipped with ERT electrodes spaced 0.8 m, for a total of 24 electrodes per borehole (Fig. 6b). As the boreholes are PVC-cased, it was also possible to acquire cross-hole GPR data between neighboring holes. An example of time-lapse results, showing ZOP profiles converted into volumetric moisture content as a function of depth, as shown in Fig. 6c: the evolution of moisture content during the seasonal decline of water table is clearly visible. A volume of 20 m³ of fresh water was injected in a 2 m deep trench placed between boreholes A and B (see Fig. 6a). Figure 22.7 shows the results of time-lapse monitoring of the resulting infiltration process using ERT and ZOP GPR. The center of mass of the infiltrating water bulb is marked in the ZOP GPR profiles. Primarily, this information was used to calibrate a 3D finite element infiltration model based on Richards' equation. The results of this calibration relevant to models assuming an isotropic hydraulic conductivity (Ks) field are shown in Fig. 8a. Note how it is possible to calibrate the model using a single homogeneous value of Ks equal to 5 m/d, with the same precision obtained in similar experiments by Binley et al. [24]. Another evidence is that the use of laboratory measured Ks values on material retrieved from the core of borehole D (Fig. 22.6) leads to a substantial underestimation of the infiltration speed, caused by the invasion of fine material coming from the shallow soil layer during coring: this confirms the need for in situ measurements that avoid issues related to sample disturbance.

However, a qualitative analysis of the shape of the infiltrating bulb (see Fig. 22.9) as imaged by both ERT and GPR tomography, suggests that the system might be hydraulically anisotropic, with a horizontal Ks larger than the vertical one. Indeed, if a ratio of horizontal vs vertical hydraulic conductivity is adopted equal to 3, practically all large values of Ks are suitable to fit the vertical movement of the water bulb, reaching values much larger than the 5 m/d estimated using an isotropic model. Indeed the larger the horizontal Ks, the slower the vertical migration of the water bulb, as water is dispersed laterally: thus to match the movement of the center of mass a larger vertical Ks is needed. In order to discriminate between the possible scenarios, we have to resort to a complementary piece of information. This is provided by the

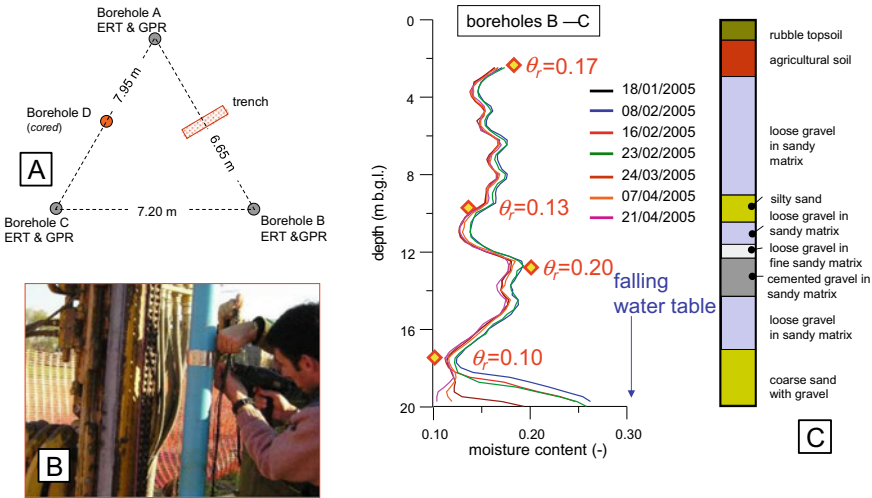


Fig. 22.6 Plan view of the borehole/trench setup at the Gorgonzola test site (a), along each ERT borehole 24 electrodes were placed with 0.8 vertical spacing (b), the same boreholes were used also for zero-offset cross-hole GPR acquisitions: the monitoring of the natural processes leads to concluding that the system is not very dynamic, a feature somehow expected in the deep vadose zone (c)

average moisture content change with respect to background as identified by the ZOP GPR: as the GPR wave propagation samples a finite volume that can be estimated from simple considerations based on the Fresnel’s Zone (e.g. [65]), it is reasonable to assume that the change in soil moisture content measured by ZOP GPR at each depth is the average value within the Fresnel Zone, whose size can be computed on the basis of elementary considerations. Thus a comparison can be made between this excess water volume in the measured data and in the simulations.

The results are shown in Fig. 22.10, where it is apparent how only with values of vertical Ks about 20 times larger than estimated using isotropic simulations it is possible to match both the movement of the center of mass and the amount of water in the infiltrating bulb. This relatively complex case study demonstrates on one side the power of hydro-geophysical data, on the other the need to squeeze out from them their information content entirely.

22.5 Hillslope Hydrology

Another area of application of hydrogeophysics is hillslope hydrology. Indeed, this sector suffers generally from lack of data concerning the subsurface behavior, partly caused by the logistics of operating along sometimes steep slopes. In general data are

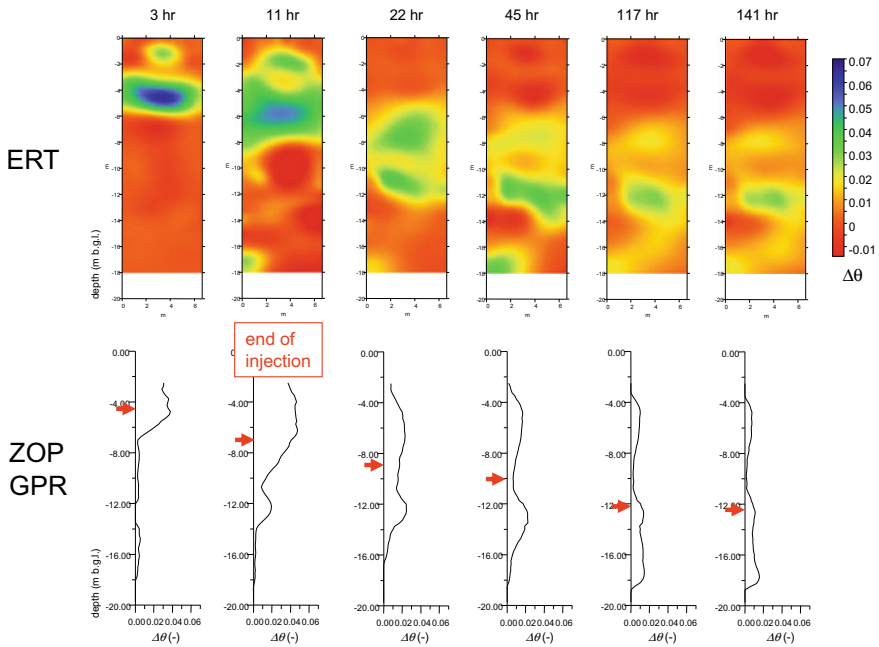


Fig. 22.7 Time-lapse images of soil moisture changes following a 20 m³ water infiltration experiment at the Gorgonzola test site: 2D reconstruction is provided by cross-hole ERT (top) and 1D vertical profiles are estimated from zero-offset (ZOP) cross-hole GPR (bottom), both measurements being conducted between boreholes A and B (see Fig. 22.6). In the GPR profiles the depth of the center of mass of the excess water with respect to background is marked by a red arrow

available concerning the shallow subsurface (the soil cover) and much less regarding the deeper slope structures.

The use of non-invasive techniques along hillslopes is indeed not very common yet, even though successful examples exist in the recent literature, showing the potential of time-lapse acquisitions both using electrical methods (e.g. [32]) and micro-gravimetry (e.g. [33]), the latter being particularly suitable at the larger scale, potentially involving an entire catchment.

In this section we present the results of a small scale experiment conducted along a very steep mountain catchment [31] in the North-Western Italian Alps. The experiment was conducted with the goal of understanding the partitioning of rainfall into surface runoff, shallow interflow in the soil cover, and deep infiltration into the fractured bedrock (Fig. 22.11). The latter component is particularly important, as it contributes to the storage of “old water” with all relevant implications in terms of potential flash floods and contaminant transport (e.g. [67]). At this catchment, located in the Montemezzo area (Como Lake), the bedrock is composed of schists with sub-vertical foliation that is likely to help water infiltration.

The experiment consisted of an irrigation experiment corresponding to about 2200 mm of artificial rainfall on a 4 m² surface equipped with a runoff box, capable

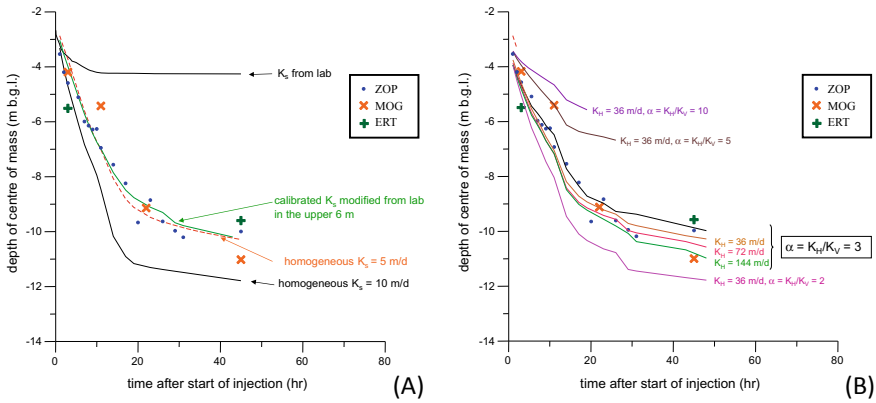


Fig. 22.8 Calibration of a 3D infiltration model against the data concerning the vertical location of the center of mass of the injected water, Gorgonzola test site. A model using isotropic values of hydraulic conductivity (left panel) indicates that the homogeneous value of hydraulic conductivity that best matches the data is equal to 5 m/d. However, if the isotropy assumption is released, it becomes apparent that models having a horizontal/vertical anisotropy ratio equal to 3 can all match the observed motion of the center of mass: however at the progressive increase of the mean hydraulic conductivity, while the center of mass fitting is always good, the total mass estimated in the Fresnel zone becomes progressively better matched (see Fig. 22.9)

of measuring the amount of water flowing downhill along the surface. Within the runoff box a 3D ERT setup was installed, composed of six 2-m deep boreholes having 12 electrodes each and 24 surface electrodes (Fig. 22.12). In practice only 4 boreholes were used for monitoring, adopting a 72-channel skip-zero dipole–dipole configuration and complete reciprocal acquisition to estimate data errors. In addition to the local 3D ERT setup, a 2D ERT line was also acquired from the ground surface extending for 35.5 m along the maximum slope line, thus reaching a depth of investigation sufficient to image well into the bedrock. The soil cover was ascertained to be no thicker than about 1 m.

The infiltration experiment produced some unexpected results, the most notable being that only about 7% of the irrigated water was captured by the runoff box. Considering the exceeding large artificial rainfall rate (2200 mm in 18 h), the large slope (about 40°) and the grass cover, this was a total surprise. The next question was what happened to the 93% of the irrigated water. The time-lapse measurements conducted from the 2D ERT line (Fig. 22.13) showed that practically no shallow subsurface interflow occurred, with all changes in electrical resistivity taking place below the runoff box where irrigation was occurring. This information is of course at a relatively large scale, and required confirmation from the 3D ERT data around the runoff box.

The 3D time-lapse ERT results confirmed the pattern already identified at the larger scale (Fig. 22.14). In a matter of a couple of hours, the bulk of the infiltrating water already reached the interface between soil and bedrock, placed at about 1 m, and penetrated deep into the rock fractures. The pattern visible at 2.4 h remains stable

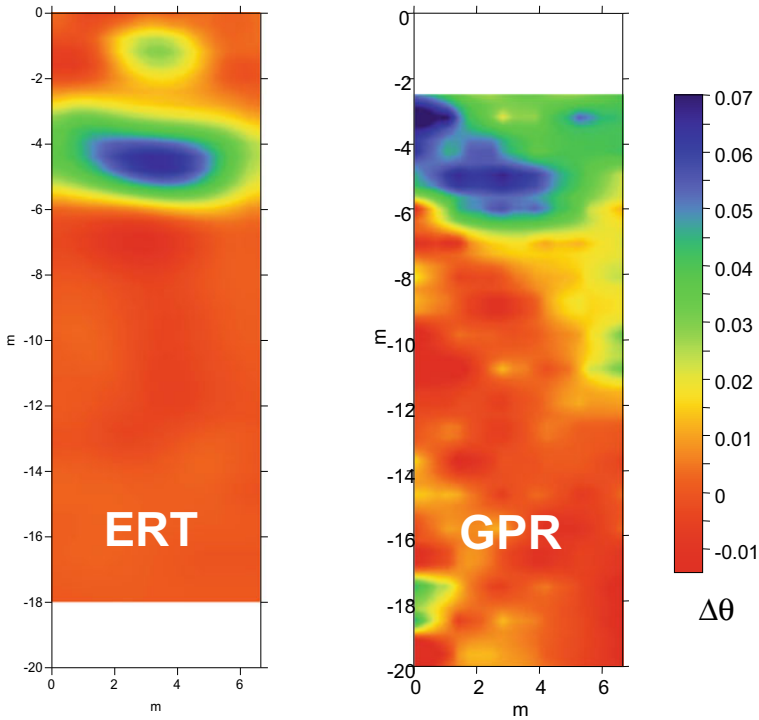


Fig. 22.9 Time-lapse images of soil moisture content changes with respect to background estimated from ERT and GPR tomography, at 3 h from the start of the water injection. Note the excellent agreement between the two images, and the evident development of a water bulb elongated horizontally, thus being a symptom of hydraulic anisotropy

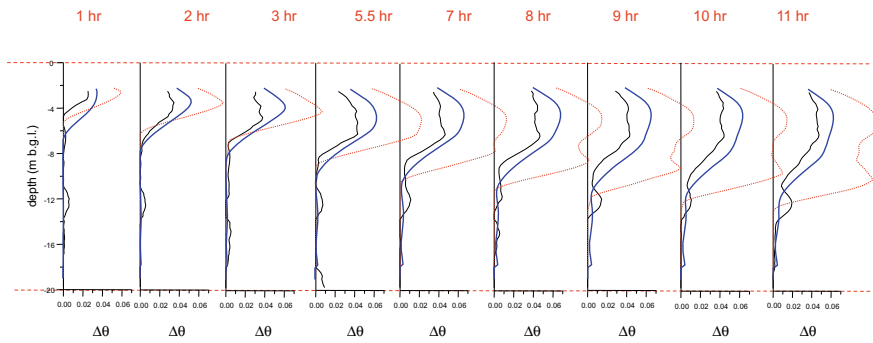


Fig. 22.10 Mass balance matching between measured soil moisture content vertical profile and simulated profiles simulated using the isotropic model with $K_s = 5$ m/d (red line) and the anisotropic model with horizontal conductivity equal to about 300 m/d, vertical conductivity of about 100 m/d (blue line)

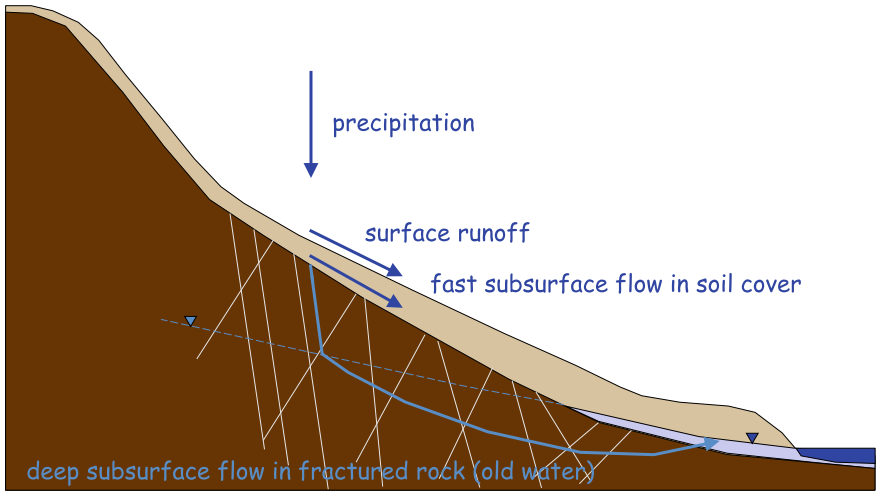


Fig. 22.11 Scheme of the Montemezzo site with the expected rainfall separation processes

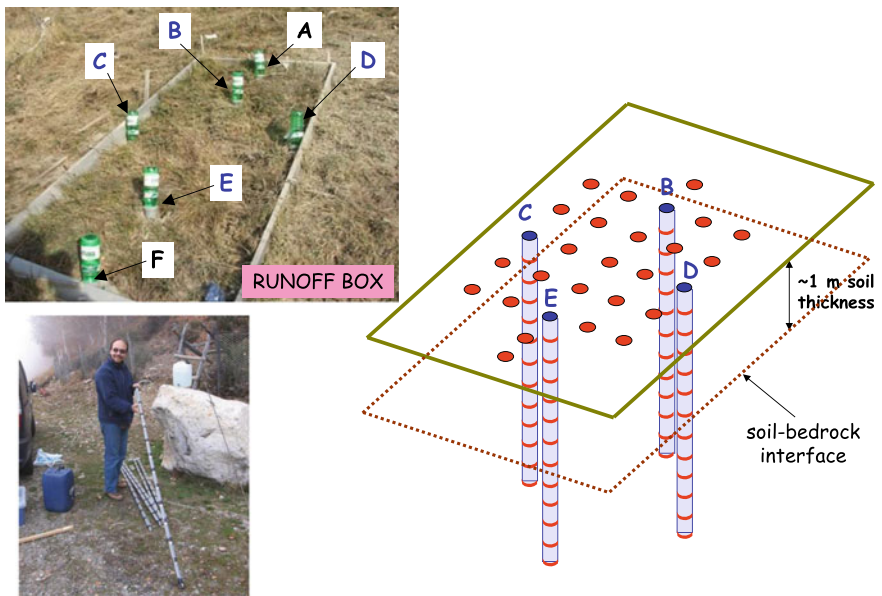


Fig. 22.12 3D ERT setup at the Montemezzo site: runoff box with installed boreholes, borehole image, and scheme of the adopted configuration for time-lapse monitoring during the irrigation experiment

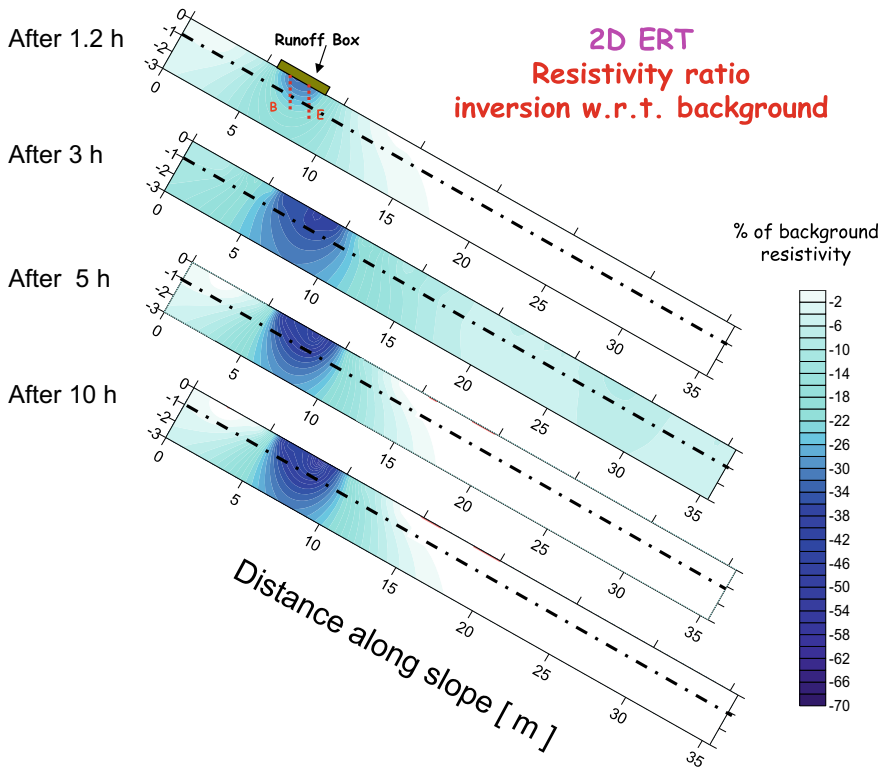


Fig. 22.13 2D ERT time-lapse monitoring at the Montemezzo site during the irrigation experiment

until the irrigation is active, with a fast drainage of the fractures once the feeding from irrigation is stopped at 18 h. The results fully confirmed that fast infiltration occurs into the deep structure of the hillslope, and is likely to have caused the past flash floods of the nearby creek, with deadly outcomes in the 1950s.

22.6 Aquifer Characterization

The use of geophysical methods for hydrogeology has a long history, as described in the introduction. In this section we describe, possibly, the most interesting hydrogeophysical application in this context. As the use of saline tracers is widespread in hydrogeology, and as geo-electrical methods are, of course, sensitive to changes in electrical conductivity of groundwater, combining the two methods using geoelectrics in time lapse-mode is an approach bound to give fruitful results. Indeed, twenty years of successful applications have been reported in the literature (e.g. [34,

dark blue = 30% of background

light blue = 70% of background

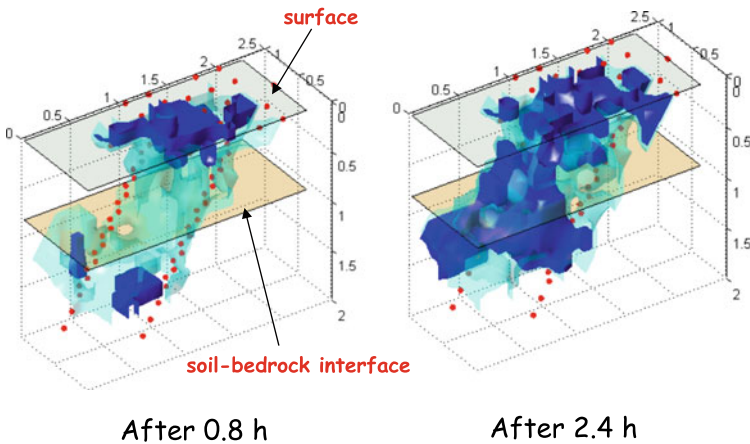


Fig. 22.14 3D ERT time-lapse monitoring at the Montemezzo site during the beginning of the irrigation experiment. Dark blue indicates 30% of resistivity value before irrigation, light blue indicates 70% of resistivity value before irrigation

36, 37, 39, 40]). Applications involving, vice versa, the injection of fresh or deionized water into saline groundwater have also been reported as successful (e.g., [35]). In some cases traditional methods such as *Mise-à-la-masse* (MALM) can also be applied to monitoring saline tracer migration in the saturated zone (e.g. [38]).

In this section we present an example of time-lapse ERT monitoring of a saline tracer injection in an aquifer of interest for water resources (for details, see [49]). The site is the foothills of the North-Eastern Italian Pre-Alps, in the riparian zone of the Piave river—Veneto Region—in the Valdobbiadene municipality. The riparian zone houses a number of water wells producing drinking water for civil and industrial use. A saline tracer test was performed in order to compute groundwater travel time and thus the extent of groundwater protection zones according to the Italian regulations. The setup is shown in Fig. 22.15, where injection and monitoring boreholes are shown, together with the main water works pumping well. The injection and monitoring boreholes were purposely drilled to a depth of 30 m below ground, and equipped with a fully slotted casing in order to allow continuous access to the surrounding saturated unconfined aquifer. Cross-hole ERT was performed using submerged cables with graphite electrodes that ensured electrical contact with groundwater with no need for permanent installation (as opposed to what is needed in the unsaturated zone—see above).

The results of the time-lapse monitoring (Fig. 22.16) clearly show how ERT allows for a complete visualization of the tracer arrival, as opposed to what is possible using only, e.g., electrical conductivity meters in boreholes. Specifically, in the case at

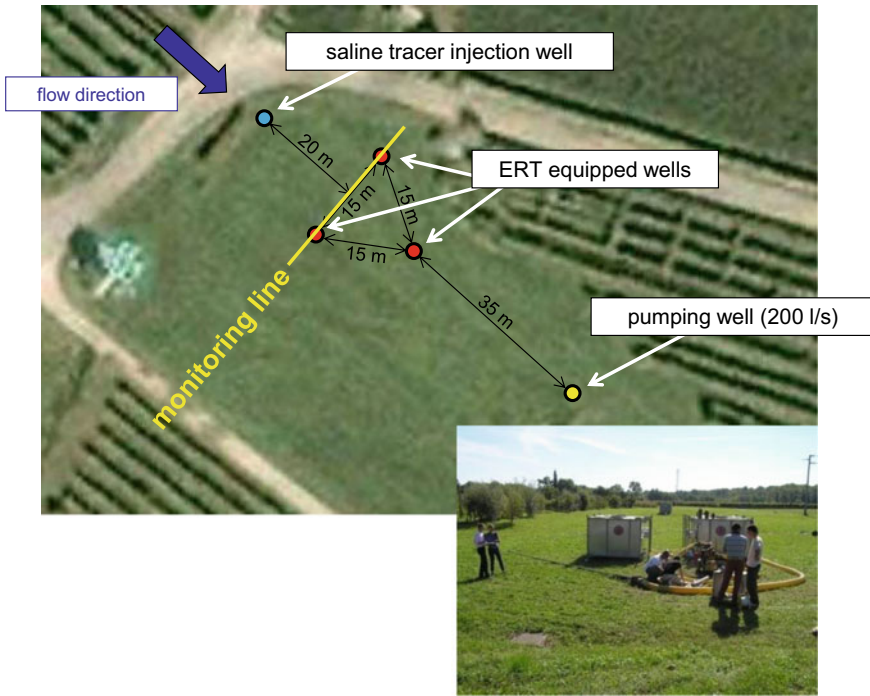


Fig. 22.15 Map showing the locations of wells in the Valdobbadiene test site, with the relevant information. The inset show a view of the test site during the injection experiment

hand, a deep fast arrival is visible at about three hours from the tracer injection 20 m upstream, corresponding to a very fast pathway. Note that this deep arrival may be difficult to detect, e.g., also from surface ERT acquisitions. A shallower, separate arrival is detected in a shallower zone some 6 h from the tracer injection. Overall time-lapse ERT monitoring provides a detailed picture of tracer migration not attainable using tradition hydrogeophysical approaches.

22.7 Conclusions

In this chapter we present a number of hydrogeophysical applications at different scales and concerning different hydrological processes, all relevant to water resources protection and management. The vast panorama of possible applications is warranted by the capability of geophysical methods to image the subsurface, in time lapse mode, with different penetration and resolution. The strongest point of the general methodology lies in its capability to be linked to predictive hydrological models that can be calibrated against the available, geophysically derived, data. A future of increasingly sophisticated used of such methodology is envisaged, benefitting from the more

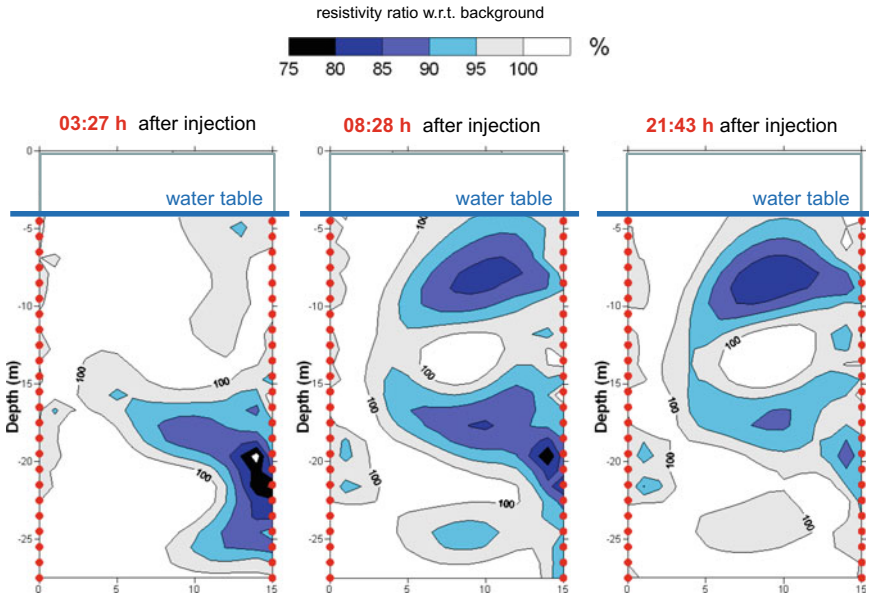


Fig. 22.16 Time-lapse ERT results of the Valdobbiadene saline tracer test experiment, showing 2D ERT inversion along the 2-borehole monitoring line shown in Fig. 22.15. Changes of electrical resistivity with respect to initial conditions are shown, depicting two tracer arrivals at different times

widespread availability of cheap and efficient equipment for quasi-continuous time-space field monitoring on one side, and from the increasingly popular use of data assimilation techniques on the other side.

In order to make this future possible, some limitations of today's approaches shall be overcome. In particular, even though the technology exists, nowadays it is uncommon that permanent installations with continuous monitoring are put in place. This would change the paradigm of hydrogeophysical monitoring, adding the necessary time sampling to the power of the method, that lies primarily in the dense spatial sampling.

Some techniques, that are only mentioned in this chapter, need substantial theoretical and practical advances in order to become state of the art tools in hydrogeophysical monitoring: these are specifically MALM, Induced Polarization—IP—and Spectral Induced Polarization—SIP—and Spontaneous Potential (SP) methods. Nuclear Magnetic Resonance (NMR) can also have a future role in hydrogeophysics, given the strong link of NMR response to the presence of “free” water in porous media.

References

1. Binley A, Hubbard SS, Huisman JA, Revil A, Robinson DA, Singha K, Slater LD (2015)

- The emergence of hydrogeophysics for improved understanding of subsurface processes over multiple scales. *Water Resour Res* 51(6):3837–3866
2. Kemna A, Vanderborght J, Kulesa B, Vereecken H (2002) Imaging and characterisation of subsurface solute transport using electrical resistivity tomography (ERT) and equivalent transport models. *J Hydrol* 267(2002):125–146
 3. McDonnell JJ, Bonell M, Stewart MK, Pearce AJ (1990) Deuterium variations in storm rainfall: Implications for stream hydrograph separation. *Water Resour Res* 26(3):455–458. <https://doi.org/10.1029/WR026i003p00455>
 4. Cassiani G, Medina MA (1997) Incorporating geophysical auxiliary data into groundwater flow parameter estimation. *Ground Water* 35:79–91
 5. Cassiani G, Boehm G, Vesnaver A, Nicolich R (1998) A geostatistical framework for incorporating seismic tomography auxiliary data into hydraulic conductivity estimation. *J Hydrol* 206(1–2):58–74
 6. Sheriff RE (1996) Understanding the fresnel zone, search and discovery. AAPG 40014
 7. Sambo C, Chimezie Iferobia C, Abbas Babasafari A, Rezaei S, Akanni OA (2020) The role of time Lapse(4D) seismic technology as reservoir monitoring and surveillance tool: a comprehensive review. *J Nat Gas Sci Eng* 80(2020):103312. <https://doi.org/10.1016/j.jngse.2020.103312>
 8. Waxman MH, Smits LJM (1968) Electrical conductivities in oil-bearing shaly sands. *Soc Petr Eng J* 8:107–122
 9. Binley AM, Cassiani G, Deiana R (2010) Hydrogeophysics—opportunities and challenges. *Bollettino di Geofisica Teorica ed Applicata* 51(4):267–284
 10. Binley A, Kemna A (2005) DC resistivity and induced polarization methods. In: Rubin Y, Hubbard SS (eds) *Hydrogeophysics*. Springer, Netherlands, p 523
 11. Visentini AF, Linde N, Le Borgne T, Dentz M (2020) Inferring geostatistical properties of hydraulic conductivity fields from saline tracer tests and equivalent electrical conductivity time-series. *Adv Water Resour* 146:103758
 12. Annan AP (2005) GPR methods for hydrogeological studies. In: Rubin Y, Hubbard SS (eds) *Hydrogeophysics*. Springer, Netherlands, p 523
 13. Kang X, Kokkinaki A, Kitanidis PK, Shi X, Revil A, Lee J, Soueid Ahmed A, Wu J (2020) Improved characterization of DNAPL source zones via sequential hydrogeophysical inversion of hydraulic-head, self-potential and partitioning tracer data. *Water Resour Res* 56(8). <https://doi.org/10.1029/2020WR027627>
 14. Cassiani G, Binley A, Kemna A, Wehrer M, Flores Orozco A, Deiana R, Boaga J, Rossi M, Dietrich P, Werban U, Zschornack L, Godio A, JafarGamdomi A, Deidda GP (2014) Non-invasive characterization of the Trecate (Italy) crude-oil contaminated site: links between contamination and geophysical signals. *Environ Sci Pollut Res*, Special Issue on "New approaches for low-invasive contaminated site characterization, monitoring and modelling" 21(15):8914–8931. <https://doi.org/10.1007/s11356-014-2494-7>
 15. Boaga J, D'Alpaos A, Cassiani G, Marani M, Putti M (2014) Plant-soil interactions in salt-marsh environments: experimental evidence from electrical resistivity tomography (ERT) in the Venice lagoon. *Geophys Res Lett* 41:6160–6166. <https://doi.org/10.1002/2014GL060983>
 16. Cassiani G, Ferraris S, Giustiniani M, Deiana R, Strobbia C (2009) Time-lapse surface-to-surface GPR measurements to monitor a controlled infiltration experiment. *Bollettino di Geofisica Teorica ed Applicata* 50(Marzo):209–226
 17. Roth K, Schulin R, Fluhler H, Attinger W (1990) Calibration of time domain reflectometry for water content measurement using a composite dielectric approach. *Water Resour Res* 26(10):2267–2273. <https://doi.org/10.1029/90WR01238>
 18. Cassiani G, Boaga J, Rossi M, Fadda G, Putti M, Majone B, Bellin A (2016) Soil-plant interaction monitoring: small scale example of an apple orchard in Trentino North-Eastern Italy. *Sci Total Environ* 543(Pt B):851–861. <https://doi.org/10.1016/j.scitotenv.2015.03.113>
 19. Crestani E, Camporese M, Salandin P (2015) Assessment of hydraulic conductivity distributions through assimilation of travel time data from ERT-monitored tracer tests. *Adv Water Resour* 84:23–36

20. Mary B, Vanella D, Consoli S, Cassiani G (2019) Assessing the extent of citrus trees root apparatus under deficit irrigation via multi-method geo-electrical imaging. *Sci Rep* 9:9913. <https://doi.org/10.1038/s41598-019-46107-w>
21. Mary B, Peruzzo L, Boaga J, Schmutz M, Wu Y, Hubbard SS, Cassiani G (2018) Small scale characterization of vine plant root water uptake via 3D electrical resistivity tomography and Mise-à-la-Masse method. *Hydrol Earth Syst Sci*. <https://doi.org/10.5194/hess-22-5427-2018>
22. Mazáč O, Kelly WE, Landa I (1985) A hydrogeophysical model for relations between electrical and hydraulic properties of aquifers. *J Hydrol* 79(1–2):1–19
23. Vereecken H, Binley A, Cassiani G, Kharkhordin I, Revil A, Titov K (eds) (2006) Applied hydrogeophysics. Springer-Verlag, Berlin
24. Binley A, Cassiani G, Middleton R, Winship P (2002) Vadose zone flow model parameterisation using cross-borehole radar and resistivity imaging. *J Hydrol* 267(3–4):147–159
25. Cassiani G, Binley A (2005) Modeling unsaturated flow in a layered formation under quasi-steady state conditions using geophysical data constraints. *Adv Water Resour* 28(5):467–477
26. Cassiani G, Strobbia C, Gallotti L (2004) Vertical radar profiles for the characterization of deep vadose zones. *Vadose Zone J* 3:1093–1115
27. Cassiani G, Fusi N, Susanni D, Deiana R (2008) Vertical radar profiles for the assessment of landfill capping effectiveness. *Near Surf Geophys* 6:133–142. <https://doi.org/10.3997/1873-0604.2008010>
28. Deiana R, Cassiani G, Villa A, Bagliani A, Bruno V (2008) Calibration of a vadose zone model using water injection monitored by GPR and electrical resistance tomography. *Vadose Zone J* (Feb 25):215–226 <https://doi.org/10.2136/vzj2006.0137>
29. Deiana R, Cassiani G, Kemna A, Villa A, Bruno V, Bagliani A (2007) An experiment of non invasive characterization of the vadose zone via water injection and cross-hole time-lapse geophysical monitoring. *Near Surf Geophys* 5(3 June):183–194. <https://doi.org/10.3997/1873-0604.2006030>
30. Everett ME, Meju MA (2005) Near-surface controlled-source electromagnetic induction: background and recent advances. In: Rubin Y, Hubbard SS (eds) *Hydrogeophysics*. Springer, Netherlands, p 523
31. Cassiani G, Godio A, Stocco S, Villa A, Deiana R, Frattini P, Rossi M (2009b) Monitoring the hydrologic behaviour of steep slopes via time-lapse electrical resistivity tomography. *Near Surf Geophys*, special issue on Hydrogeophysics—Methods Process 475–486. <https://doi.org/10.3997/1873-0604.2009013>
32. Perri MT, Cassiani G, Gervasio I, Deiana R, Binley AM (2012) A saline tracer test monitored via both surface and cross-borehole electrical resistivity tomography: comparison of time-lapse results. *J Appl Geophys* 79:6–16. <https://doi.org/10.1016/j.jappgeo.2011.12.011>
33. Pollock D, Cirpka OA (2012) Fully coupled hydrogeophysical inversion of a laboratory salt tracer experiment monitored by electrical resistivity tomography. *Water Resour Res* 48(1):W01505
34. Cassiani G, Bruno V, Villa A, Fusi N, Binley AM (2006) A saline tracer test monitored via time-lapse surface electrical resistivity tomography. *J Appl Geophys* 59:244–259. <https://doi.org/10.1016/j.jappgeo.2005.10.007>
35. Kaestner M, Braeckvelt M, Doberl G, Cassiani G, Petrangeli Papini M, Leven-Pfister C, Van Ree D (2012) Model-driven soil probing, site assessment and evaluation: guidance on technologies. University of Rome La Sapienza Press, Rome, Italy
36. LaBrecque, D.J., Yang, X., 2000. Difference inversion of ERT data: a fast inversion method for 3-D in-situ monitoring. *Proc Symp Appl Geophys Eng Environ Problems*, Environ Eng Geophys Soc 723–732
37. Nasta P, Boaga J, Deiana R, Cassiani G, Romano N (2019) Comparing ERT- and scaling-based approaches to parameterize soil hydraulic properties for spatially distributed model applications. *Adv Water Resour* 126(13):155–167. <https://doi.org/10.1016/j.advwatres.2019.02.014>
38. Perri MT, Barone I, Cassiani G, Deiana R, Binley A (2020) Borehole effect causing artefacts in cross-borehole electrical resistivity tomography: a hydraulic fracturing case study. *Near Surf Geophys Spec Issue: Geoelectr Monit* 18:445–462. <https://doi.org/10.1002/nsg/12111>

39. Piccolroaz S, Majone B, Palmieri F, Cassiani G, Bellin A (2015) On the use of spatially distributed, time-lapse micro-gravity surveys to inform hydrological modeling. *Water Resour Res* 51(9):7270–7288. <https://doi.org/10.1002/2015WR016994>
40. Topp GC, Davis JL, Annan AP (1980) Electromagnetic determination of soil water content: measurements in coaxial transmission lines. *Water Resour Res* 16(3):574–582. <https://doi.org/10.1029/WR016i003p00574>
41. Archie GE (1942) The electrical resistivity log as an aid in determining some reservoir characteristics. *Trans AIME* 146:54–62
42. Tran AP, Dafflon B, Hubbard SS, Kowalsky MB, Long P, Tokunaga TK, Williams KH (2016) Quantifying shallow subsurface water and heat dynamics using coupled hydrological-thermal-geophysical inversion. *Hydrol Earth Syst Sci* 20(9):3477–3491
43. Brovelli A, Cassiani G (2008) Effective permittivity of porous media: a critical analysis of the complex refractive index model. *Geophys Prospect* 56(5):715–727
44. Rubin Y, Hubbard SS (eds) (2005) *Hydrogeophysics*. Springer, Water Science and Technology Library
45. Brovelli A, Cassiani G (2011) Combined estimation of effective electrical conductivity and permittivity for soil monitoring. *Water Resour Res* 47:W08510. <https://doi.org/10.1029/2011WR010487>
46. Manoli G, Rossi M, Pasetto D, Deiana R, Ferraris S, Cassiani G, Putti M (2015) An iterative particle filter approach for coupled hydro-geophysical modeling and inversion of a controlled infiltration experiment. *J Comput Phys* 37–51. <https://doi.org/10.1016/j.jcp.2014.11.035>
47. Rossi M, Manoli G, Pasetto D, Deiana R, Ferraris S, Strobbia C, Putti M, Cassiani G (2015) Coupled inverse modeling of a controlled irrigation experiment using multiple hydro-geophysical data. *Adv Water Resour* 82:150–165. <https://doi.org/10.1016/j.advwatres.2015.03.008>
48. Busato L, Boaga J, Perri MT, Majone B, Bellin A, Cassiani G (2019) Hydrogeophysical characterization and monitoring of the hyporheic and riparian zones: the Vermigliana Creek case study. *Sci Total Environ* 648(2019):1105–1120. <https://doi.org/10.1016/j.scitotenv.2018.08.179>
49. Perri MT, De Vita P, Masciale R, Portoghesi I, Chirico GB, Cassiani G (2018) Time-lapse *Mise-à-la-Masse* measurements and modelling for tracer test monitoring in a shallow aquifer. *J Hydrol* 561:461–477. <https://doi.org/10.1016/j.jhydrol.2017.11.013>
50. Lesmes D, Friedman S (2005) Electrical and hydrogeological properties. In: Rubin Y, Hubbard SS (eds) *Hydrogeophysics*. Springer, Netherlands, p 523
51. Camporese M, Cassiani G, Deiana R, Salandin P (2011) Assessment of local hydraulic properties from electrical resistivity tomography monitoring of a three-dimensional synthetic tracer test experiment. *Water Resour Res* 47:W12508. <https://doi.org/10.1029/2011WR010528>
52. Camporese M, Cassiani G, Deiana R, Salandin P, Binley A (2015) Coupled and uncoupled hydrogeophysical inversions using ensemble Kalman filter assimilation of ERT-monitored tracer test data. *Water Resour Res* 51(5):3277–3291. <https://doi.org/10.1002/2014WR016017>
53. Daily W, Ramirez A, LaBrecque D, Nitao J (1992) Electrical resistivity tomography of vadose water movement. *Water Resour Res* 28:1429–1442
54. Mary B, Peruzzo L, Boaga J, Cenni N, Schmutz M, Wu Y, Hubbard SS, Cassiani G (2020) Time-lapse monitoring of root water uptake using electrical resistivity tomography and *Mise-à-la-Masse*: a vineyard infiltration experiment. *SOIL* 6:95–114. <https://doi.org/10.5194/soil-6-95-2020>
55. Bouzaglou V, Crestani E, Salandin P, Gloaguen E, Camporese M (2018) Ensemble Kalman filter assimilation of ERT data for numerical modeling of seawater intrusion in a laboratory experiment. *Water (Switz)* 10(4):397
56. Commer M, Pride SR, Vasco DW, Finsterle S, Kowalsky MB (2020) Imaging of a fluid injection process using geophysical data—a didactic example. *Geophysics* 85(2):W1–W16
57. Haaken K, Deidda GP, Cassiani G, Kemna A, Deiana R, Putti M, Paniconi C (2017) Flow dynamics in hyper-saline aquifers: hydro-geophysical monitoring and modelling. *Hydrol Earth Syst Sci* 21(3):1439–1454. <https://doi.org/10.5194/hess-21-1439-2017>

58. Kelly WE, Mareš S (1993) Applied geophysics in hydrogeological and engineering practice. *Dev Water Sci* 44:288
59. Preti F, Guastini E, Penna D, Dani A, Cassiani G, Boaga J, Deiana R, Romano N, Nasta P, Palladino M, Errico A, Giambastiani Y, Trucchi P, Tarolli P (2018) Conceptualization of water flow pathways in agricultural terraced landscapes. *Land Degrad Dev* 29(3):651–662. <https://doi.org/10.1002/ldr.2764>
60. Tso C-HM, Johnson TC, Song X, Chen X, Kuras O, Wilkinson P, Uhlemann S, Chambers J, Binley A (2020) Integrated hydrogeophysical modelling and data assimilation for geoelectrical leak detection. *J Contam Hydrol* 234:103679
61. Vanella D, Cassiani G, Busato L, Boaga J, Barbagallo S, Binley A, Consoli S (2018) Use of small scale electrical resistivity tomography to identify soil-root interactions during deficit irrigation. *J Hydrol* 556:310–324. <https://doi.org/10.1016/j.jhydrol.2017.11.025>
62. Binley A, Henry-Poulter S, Shaw B (1996) Examination of solute transport in an undisturbed soil column using electrical resistance tomography. *Water Resour Res* 32(4):763–769
63. Camporese M, Paniconi C, Putti M, Orlandini S (2010) Surface-subsurface flow modeling with path-based runoff routing, boundary condition-based coupling, and assimilation of multisource observation data. *Water Resour Res* 46:W02512
64. Binley A (2011). <http://www.es.lancs.ac.uk/people/amb/Freeware/freeware.htm>
65. Slater L, Versteeg R, Binley A, Cassiani G, Birken R, Sandberg S (2002) A 3D ERT study of solute transport in a large experimental tank. *J Appl Geophys* 49:211–229
66. Consoli S, Stagno F, Vanella D, Boaga J, Cassiani G, Rocuzzo G (2017) Partial root-drying irrigation in orange orchards: effects on water use and crop production characteristics. *Euro J Agron* 82:190–202. <https://doi.org/10.1016/j.eja.2016.11.001>
67. Monego M, Cassiani G, Deiana R, Putti M, Passadore G, Altissimo L (2010) A tracer test in a shallow heterogeneous aquifer monitored via time-lapse surface electrical resistivity tomography. *Geophysics* 75(4)

Chapter 23

Advanced Combined Geophysical-Geological Mapping of the Sea of Galilee and Its Vicinity



L. Eppelbaum, Y. Katz, and Z. Ben-Avraham

Abstract The Sea of Galilee (Lake Kinneret) is located in northern Israel in a complex tectonic setting where the Dead Sea Transform crosscuts other fault systems. The practical absence of boreholes in the sea hinders geological-geophysical data interpretation. For the first time, gravity, magnetic, paleomagnetic, radiometric, and seismological data were analyzed together. An integrated analysis of gravity and seismological data made it possible to clarify some tectonic parameters. The total magnetic field map shows an intricate pattern caused by a combined influence of the basalt flows of various ages and magnetization in and around the sea. Calculated statistical-probabilistic parameters of the magnetic field indicate some essential peculiarities of the medium. The recognized magnetic anomalies were analyzed using methods of quantitative interpretation especially developed for the complex physical-geological environments. 3D magnetic field modeling allowed to reveal the following important features: thick basaltic plate occurrence in the southernmost sea basin, presence of the reversely magnetized basalts near the sea's eastern boundary, and possible subsidence of basaltic bodies in the center of the pull-apart basin. The paleomagnetic stratigraphy of basalt associations around the Sea of Galilee basin proved to be correlated with the paleomagnetic zones and anomalies in the sea. The paleomagnetic characteristics of traps are linked with the development of the Dead Sea Transform. The previously constructed magnetic-paleomagnetic scheme with predominantly K–Ar dating has been significantly elaborated on the basis of newly arriving data. It is stated that a characteristic feature of the study area is the turns of tectonic blocks, mainly counterclockwise. The revised structural map of the Cover Basalts is intended to coordinate various geological and environmental investigations in this area.

L. Eppelbaum (✉) · Z. Ben-Avraham
Porter School of the Environment and Earth Sciences, Faculty of Exact Sciences, Tel Aviv
University, Ramat Aviv, 6997801 Tel Aviv, Israel
e-mail: levap@tauex.tau.ac.il

L. Eppelbaum
Azerbaijan State Oil and Industry University, Azadlig Avenue 20, Baku AZ1010, Azerbaijan

Y. Katz
Steinhardt Museum of Natural History and National Research Center, Faculty of Life Sciences,
Tel Aviv University, Ramat Aviv, 6997801 Tel Aviv, Israel

Keywords Magnetic anomalies · Quantitative analysis · Paleomagnetic mapping · Radiometric data · Gravity · Seismology · Integrated geophysical mapping

23.1 Introduction

The Sea of Galilee (Lake Kinneret) is Israel’s primary source of freshwater. It is located in northern Israel in a complex tectonic setting where the Dead Sea Transform (DST) (Fig. 23.1a) crosscuts other fault systems. This transform is more than 1000 km long and is a plate boundary separating the Sinai and Arabian plates [3, 40]. This small sea (lake) has an average surface of 166 km² and an average volume of 4.6 × 10⁹ m³. Maximal depths of the sea (about 50 m) are located in the northeast part of the basin. This sea is located with a larger basin which is a part of a series of rhomb-shaped grabens (pull-apart basins) along with the DST [38]. The present configuration of the Sea of Galilee formed about 24,000 years ago [44]. Geological studies indicate rock outcrops in this area, and rock samples discovered in boreholes surrounding this lake range from Jurassic to Quaternary.

The sea and the plains south of it (Kinnarot Valley) (Fig. 23.1b) are located in a depression bounded on east and west by active fault scarps with steep gradients. Within the lake, a few bathymetric scarps were identified [8]. West and east of the

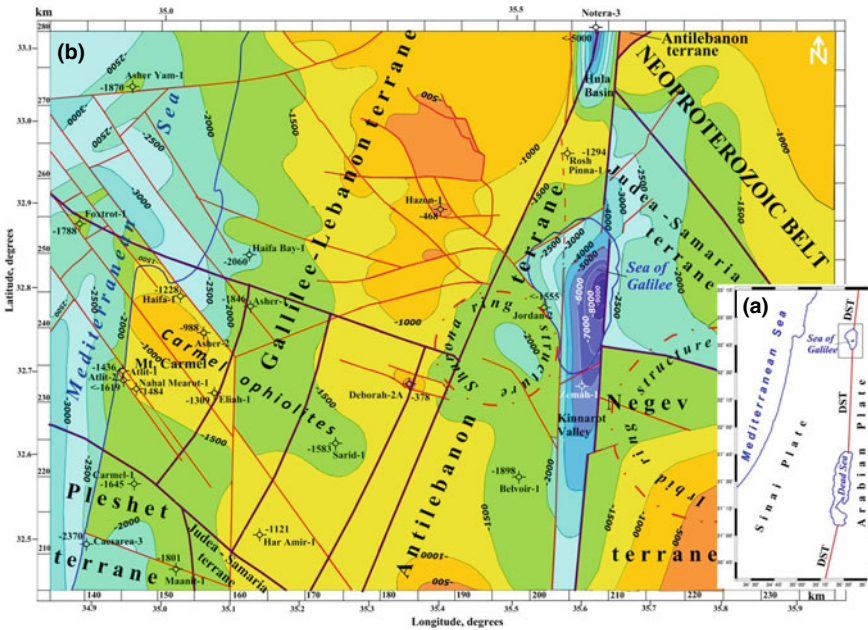


Fig. 23.1 a Areal map of the Easternmost Mediterranean (the rectangle at the top of the map represents the study area), b structural-tectonic map of the Galilee region and its vicinity (after Eppelbaum and Katz [31], with modifications). DST, Dead Sea Transform

lake fault systems of NW–SE and NE–SW directions, respectively, exist (e.g., [43]). Two phases of major basaltic volcanism—Miocene and Pliocene–Quaternary—are outcropped in the Lake Kinneret region [47, 71]. The basaltic formations make up the western part of the northern continuation of the Harrat Ash Shaam volcanic field, covering a total area of about 40,000 km² [77]. Under the Kinneret basin, the basalts are covered by terrigenous Pliocene–Quaternary formations. These basalts are underlain by thick series of Miocene salts [57]. Superposition of vertical displacements perpendicular or oblique to the transform makes structural interpretation of the investigated basin [10] quite difficult. Only combined geophysical mapping accompanied by the tectonic-structural analysis can help identify this complex area's key features.

In this study for a first time was performed an integrated analysis of gravity (e.g., [10, 22]), magnetic (e.g., [9, 24–26, 42]), paleomagnetic (e.g., [1, 17, 24–26, 31, 45–47, 59, 62, 63, 65, 71]), radiometric (e.g., [17, 45, 47, 59, 60, 69, 71]) and seismological (e.g., [16, 41, 43, 51, 54, 72–74]) data. Some seismic reference data were also attracted to this study (e.g., [8, 11, 49, 50, 64, 66, 67, 78]).

23.2 Brief Geological-Geophysical Background

In geological-geophysical terms, the region of the Sea of Galilee represents one of the most complex structures of the Earth's crust in the Eastern Mediterranean. Various types of morphological elements, tectonic structures, and complexes of sedimentary and igneous rocks are developed here. The recently obtained data indicate that this complexity of this area can be partially caused by its location above the zone of the arched apical part of the deep mantle uplift [27]. Another factor is associated with the development of intricate geodynamic processes in the so-called Arabian “syntaxis” zone, which covered the tectonic-geophysical junction of the Northern Gondwana, the Tethyan mobile belt, and Southwest Eurasia.

After the closure of the Neotethys Ocean in recent geological time, several lithospheric plates arose in this area. The most important are the Nubian, Sinai, Aegean-Anatolian, and Arabian plates [5]. Among these plates, the most active and diverse in the structure, physical properties, petrological-sedimentation, and paleogeographic content are the Sinai and Arabian plates separated by a complex-structured Dead Sea Transform (DST). Just in the northern zone of this transform, the Sea of Galilee is located (Fig. 23.1a). The following main tectonic elements surround the sea: the Alpine Cenozoic belt, the Levantine oceanic depression (e.g., [3]), the Neoproterozoic fold-metamorphic belt [76], and the Mesozoic Terrane Belt [30]. In this region, the last belt includes the Galilee-Lebanon, Pleshet, Negev, Judea-Samaria, and Antilebanon terranes. Some of these terranes are partially ruptured and displaced along the DST left shear motion for about 105 km [39] (Fig. 23.1a).

The area of the sea basin is characterized by the high intensity of both vertical and horizontal earth's crust movements. It follows, first of all, from a comprehensive analysis of geomorphological, neotectonic, and structural data in this area. The amplitude of the modern movements of the sea basin can be estimated by comparing

the hypsometry of the sea bottom surface (about -260 m), the highest elevations of the southern part of the Golan Plateau (700–900 m), and the hilly plateau of the northern Galilee (up to 1208 m at the top of Mt. Meron). The difference in amplitude of 1100–1500 m for the modern elevations in this area seems to be a maximum in the northern part of the DST (Fig. 23.1b).

This area's most crucial tectonic feature is the amplitude of the newest movements, which can be revealed by comparing the maps of neotectonic zonation [29, 31] constructed based on the surface deformation data of the Jurassic top leveling. Within the sea basin, the roof of the Jurassic deposits is lowered to a depth of about $-9,000$ m (Fig. 23.1b). To the north and northeast on 100–150 km (in the Mt. Hermon area), the roof is raised to a height of 1,600–2,500 m. Thus, when the DST began to develop, the total amplitude of the neotectonic uplifts in Neogene is averagely estimated for its northern branch to be about 11,500 m.

This area's second distinctive geodynamic feature is the pronounced asymmetry of the western and eastern parts of the sea basin, lying on both sides of the DST. In the west, from the Galilee region to the Mediterranean shelf, a complex system of diagonal and sublatitudinal fault dislocations is developed. This complex fault pattern has been associated with counterclockwise rotations (e.g., [10]). Here is necessary to note that this effect may be caused by the discovered counterclockwise rotation of the deep giant mantle structure below the Eastern Mediterranean [28]. This influence may have a local fragmentary effect on the overlying layers, not necessarily repeating its projection to the Earth's surface.

The third significant feature of the sea basin structure is the wide development of volcano-tectonic structures associated with the existence of the marginal zone of the Harrat Ash Shaam—the largest trap field in the Arabian Plate [77]. Here can be distinguished several circular depressions (e.g., Sharona) and a few uplifts (e.g., Irbid) outlined by the conical dikes (see Fig. 23.1b). To the northeast of the area, on the northern edge of the Golan Plateau, chains of the Quaternary volcanic cones are developed. The structures mentioned above outline the western wing of the Neoproterozoic belt, border the Mesozoic Terrane Belt [30], and are displaced northward along with the DST.

23.3 Gravity Field and Seismological Data

A general decrease of regional gravity field intensity from the west to east (Fig. 23.2) corresponds to the essential increase of the Moho boundary depth [35, 68]. Substantial negative gravity anomaly over the center of the sea reflects a combined effect of the thick sedimentary strata and salt layers. A combined 3D gravity-magnetic model computed along a profile constructed in the W–E direction through the sea indicates that the depth of the DST consists here more than 13 km [22] that agrees with the models computed in Ben-Avraham et al. [10].

In the study area, the isoline of '0 mGal' practically coincides with the western boundary of the DST zone (Fig. 23.2). The largest values of the positive anomalies

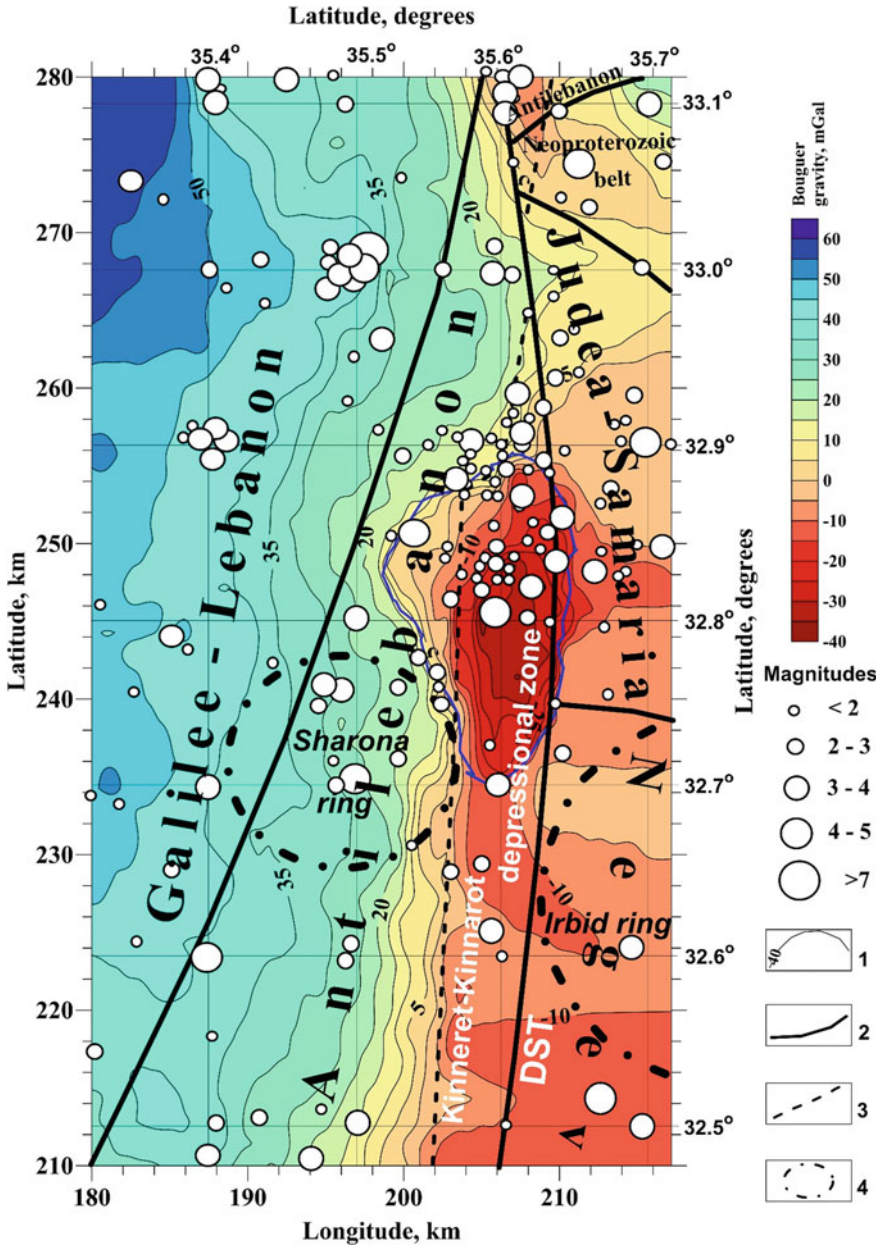


Fig. 23.2 Regional gravity map over the Sea of Galilee and its vicinity accompanied by tectonic elements and epicenters of the main earthquakes [with the magnitude of 4–7 (for the period of 1850–2020)], and recent events (with the magnitude of <math>< 2</math>, 2–3). (1) Bouguer gravity field isolines, (2) main faults, (3) boundaries of the depression zones within the DST, (4) ring structures

generally correspond to the Mt. Meron brachyanticlinal uplift, and the minimum gravity values are confined to the eastern part of the Sea of Galilee, where the pull-apart basin is mostly developed [10].

Structural peculiarities of the area under study manifested in the gravity field distribution and well supplemented by materials of the current seismic activity [16, 41, 43, 54, 72, 73] (Fig. 23.2). It is visible that most of the geodynamic events are concentrated in the northern part of the Sea of Galilee.

Three outlined regularities join here the structural and geodynamic features of this area: (1) the most extended seismicity zone corresponds to the regional Late Cenozoic disjunctive structure—DST, (2) the distinct but less sustained feature is the relation of the seismic events to the boundary faults of the Mesozoic terranes, and (3) the regional seismicity maximum corresponds to the northern part of the sea and the southern part of the Korazim uplift (Fig. 23.2). Apparently, the third regularity was firstly reported in Ben-Avraham et al. [7].

The nature of the seismicity manifestations in the region under study can be generally estimated based on the regional data involvement. They show three main features: (1) the presence of seismicity zones of the maximum appearance, (2) the development of seismicity zones concordant to the boundaries of the regional structures, and (3) the development of the elongated seismic zones intersecting the tectonic structures across the strike. Some thickening of the seismicity centers corresponds to the boundaries between the terranes that was earlier established in Eppelbaum and Katz [29]. Seismicity in this area also relates to the fault separating the Galilee-Lebanon and Antilebanon terranes (see Fig. 23.2).

Figure 23.2 testifies the SE-NW diagonal strike of the seismic event distribution, which is more clearly traced on the regional maps [29, 48, 72, 74]. A similar geodynamic phenomenon was previously inexplicable from the standpoint of inconsistency with the structural zonation, and distribution of the GPS vectors, which indicate the counterclockwise rotation of the Earth's crust blocks in the region. This phenomenon has been substantiated through the comprehensive, integrated geological-geophysical analysis of many independent factors [27].

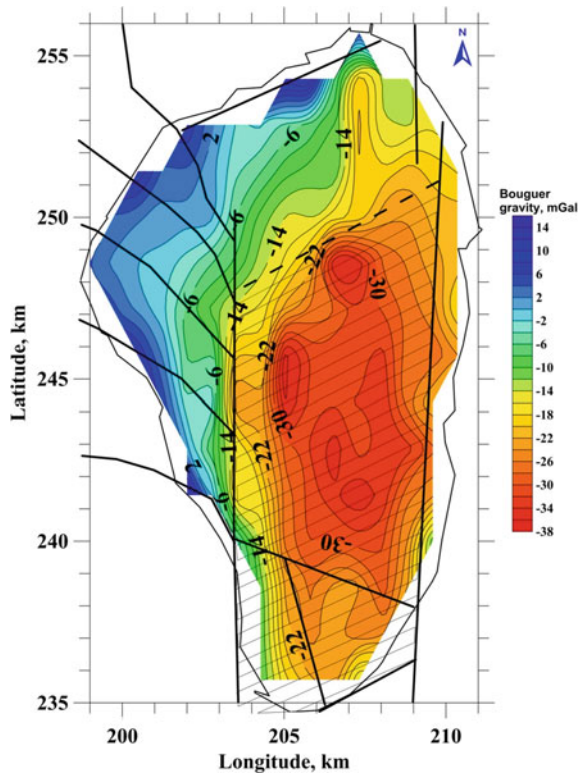
The maximum seismicity is mainly related to the regional faults outlining the Sinai plate [29] in the zone of their junction with the Arabian, Nubian, and Aegean-Anatolian plates. In this case, the most frequent seismicity is manifested in the DST zone [72], to which the region of the Sea of Galilee belongs. In the most submerged part of the sea pull-apart basin and further to the south, in the Kinnarot trough, the frequency of seismic events is comparatively low. This discrepancy between the structural and geodynamic plan suggests that the diagonal plan of distribution of the magmatic features and geodynamic events [27, 32] is due to the turn of active zones of the latest geodynamic events counterclockwise caused by the development of a vast rotating subcircular uplift in a lower mantle. Hereby, can be explained and connection between two hitherto incomprehensible seismic “nodes”—the northern sea basin and the area of Tsfat town ($32^{\circ} 96' N$, $35^{\circ} 50' E$) where the maximum magnitude (about 7) of the modern seismic activity is observed (Fig. 23.2). By the way, to the north of the diagonal line of the Sea of Galilee—Tsfat, the Miocene-Early

Pliocene traps are replaced by the younger Late Pliocene–Quaternary traps among which the volcanic cones are often developed.

The detailed Bouguer gravity anomalies within the coastline of the sea were compared with the data of our previous studies [24–26] involving the structural-tectonic zoning of sediments underlying the water area. The coincidence of the Bouguer gravity map and the data of structural mapping (see Fig. 23.3) confirms the general structural plan of the sea basin and the peculiarities of block tectonics and geodynamics.

First of all, it was revealed that the pull-apart basin contour is outlined by a zone of negative gravity anomalies with the steps corresponding to a rhomb-shaped graben. Analysis of gravity field also confirms an uplift zone of the southern part of the rhomboid graben revealed earlier by the acoustic reflectivity analysis [8] and an asymmetry of the graben established in the more extensive subsidence of its eastern part.

Fig. 23.3 Bouguer gravity map over the Sea of Galilee with the main tectonic elements



23.4 Magnetic Field Analysis

23.4.1 *Magnetic Map Compilation*

The magnetic map of the Sea of Galilee (Fig. 23.4) displays an intricate and, at the same time, informative pattern of the magnetic field distribution. This complex pattern is due to the integrated effect of the basalts surrounding the sea and the basalts occurring in the sea. Both positive and negative magnetic anomalies have been identified in the basin. However, further analysis is problematic without the magnetostratigraphic and chronostratigraphic justification of basalts in the study area. The desired scales are presented in Fig. 23.5 (after Eppelbaum et al. [24], with modifications).

We previously showed that the sources of the negative magnetic anomalies in the sea basin are the reversely magnetized basalts [25]. The marine magnetic map (mostly from Ben-Avraham et al. [9] with the addition of more late surveys) was merged with the surface magnetic observations in the Kinnarot Valley (mainly from Ginzburg and Ben-Avraham [42]). Figure 23.6 displays the generalized magnetic map joined with the simplified Cover Basalt structural map. The map indicates that some magnetic anomalies are associated with the magmatic sources of another age (for example, in the Kinnarot Valley and the areas of the Cover Basalt erosion outside the sea).

23.4.2 *Magnetic Field Transformations*

A variety of known transformations are potent tools to reveal some hidden peculiarities of the potential geophysical fields [23]. Various filtering algorithms were applied to transform the magnetic field observed in the sea. Results of one transformation procedure, “*Sign Classification*” (presented in Nikitin [61]) (Fig. 23.7b), shows that there is a nicely visible correlation with the map of the iron distribution in the sea bottom sediments (Fig. 23.7a). This circumstance testifies the migration of basaltic particles from the depth to the subsurface. The calculated maps of the total magnetic gradient (Fig. 23.8a) and entropy (Fig. 23.8b) indicate that the most part of the significant magnetic targets are located close to the sea margins. In the figures mentioned above, the transformation data are accompanied by the faults and outlines of the sea pull-apart basin. In addition, Fig. 23.1b evidently indicates the accordance of entropy zones to the areas of the Cover Basalts of the direct and reverse magnetization underlying the sea basin. These zones were identified within the sea based on the examining magnetic maps (Figs. 23.4 and 23.6) and their transformations (Figs. 23.7 and 23.8). In the land, these zones were indexed using the examination of the paleomagnetic and radiometric measurements of the trap complexes. Thus, it made it possible to perform a similar correlation of the magnetic anomalies and paleomagnetic features (identified and studied in the sea basin and beyond it) and the entropy zones.

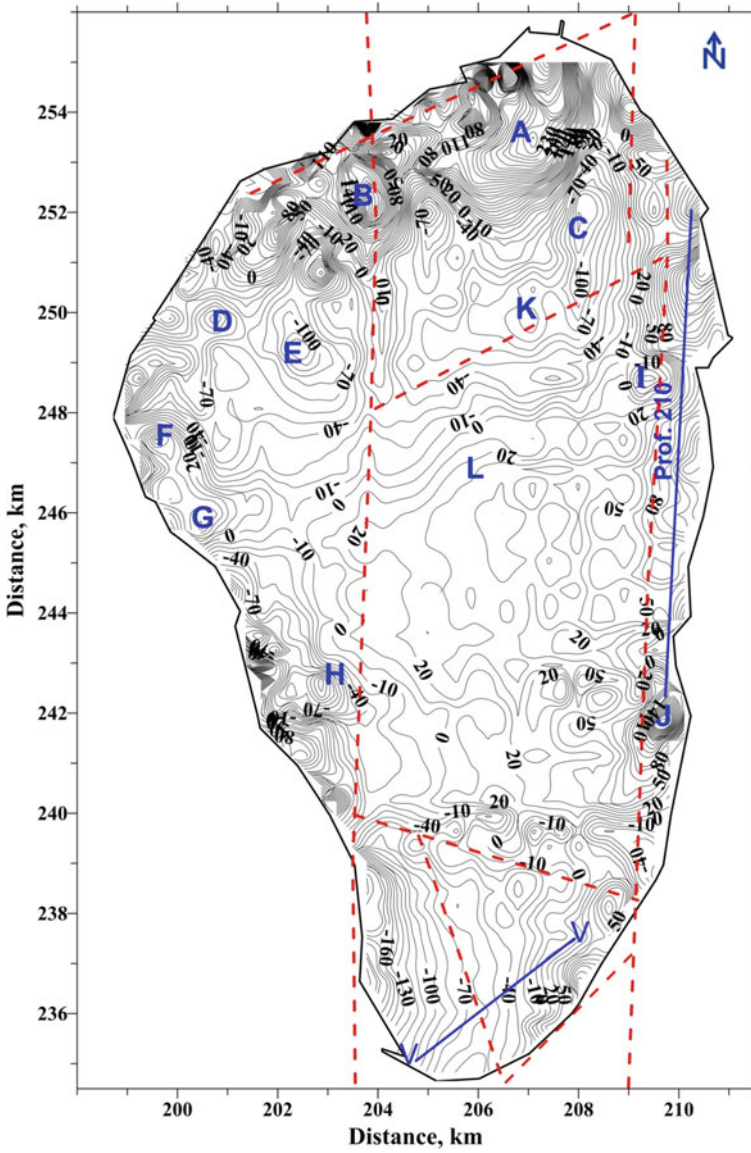


Fig. 23.4 The magnetic field of the Sea of Galilee with the location of interpreted anomalies (uppercase blue letters) and 3D modeling profiles (blue lines) as well as main faults (red dash lines)

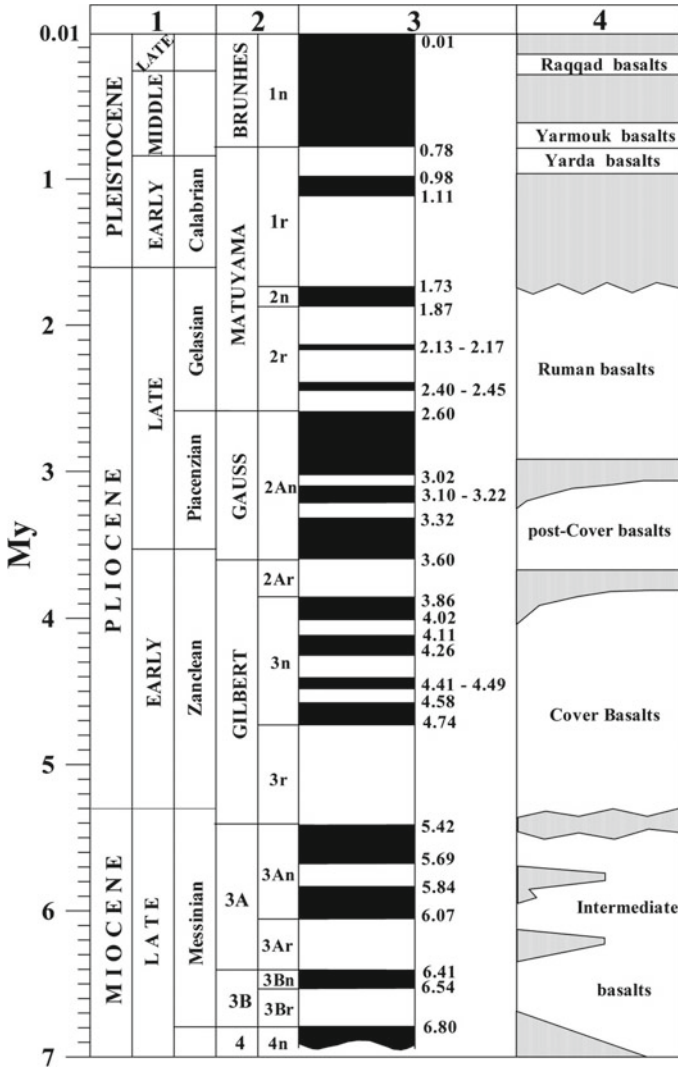


Fig. 23.5 Sea of Galilee: simplified chronostratigraphic and magnetostratigraphic scales of Late Cenozoic basaltic formations. (1) General stratigraphic scale (after Berggren et al. [12], Krijgsman et al. [53]), (2) paleomagnetic epochs and zones (after Cande and Kent [14]), (3) paleomagnetic scale and its radiometric boundaries (after Cande and Kent [14], Cornee et al. [15]), (4) sequence of basaltic formations (after Heimann [45], Heimann et al. [47], Marcus and Slager [57], Reznikov et al. [64], Shaliv [71])

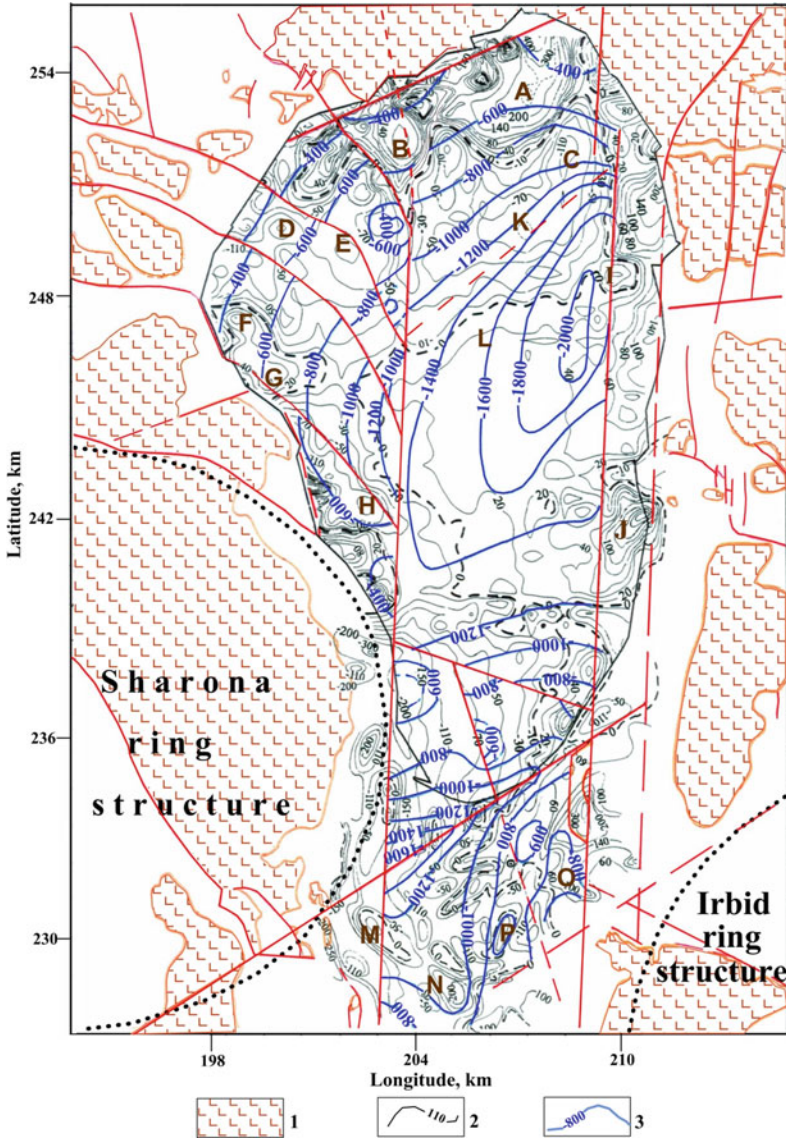


Fig. 23.6 Simplified joined magnetic map for the Sea of Galilee and Kinnarot Valley accompanied by the Cover Basalts occurrence. (1) Cover Basalts occurring at the earth's surface (based on Sneh et al. [75]), (2) isolines of the total magnetic field (simplified) (magnetic data for the Sea of Galilee after Ben-Avraham et al. [9], magnetic data for Kinnarot Valley after Ginzburg and Ben-Avraham [42]), (3) isolines of the Cover Basalt surface at a depth (after Eppelbaum et al. [25]) constructed on the basis of seismic data [11, 64, 66, 78], and magnetic data analysis. The red lines designate the location of faults

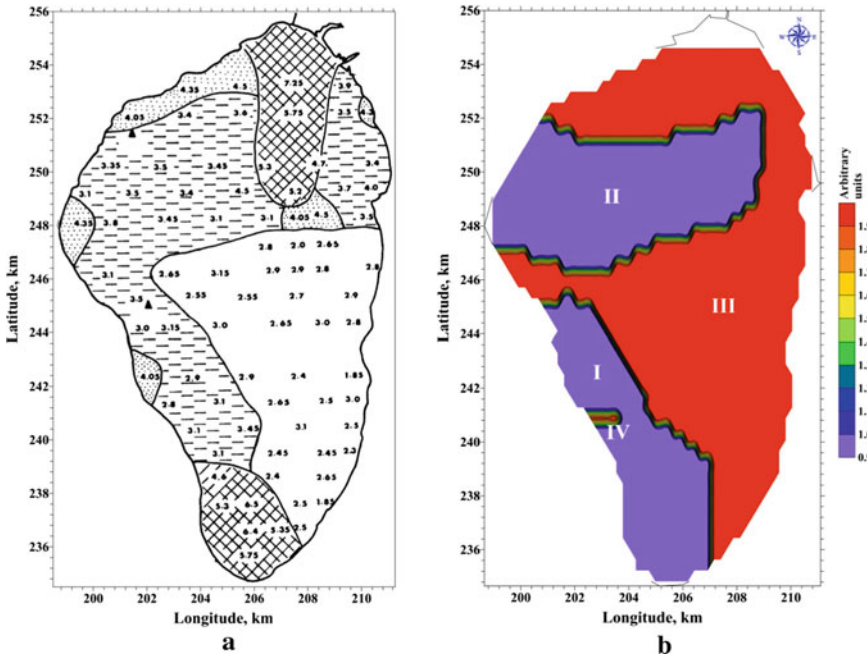


Fig. 23.7 **a** Distribution of iron in the surface sediments in the Sea of Galilee (in the percentage of dry weight) after Serruya [70]. **b** Magnetic map of the Sea of Galilee transformed by ‘Sign Classification’

23.4.3 Advanced Quantitative Interpretation

Most of the interpretation methods known in magnetic prospecting are anticipated for vertical magnetization cases and comparatively simple physical-geological conditions. For the conditions of oblique magnetization (in northern Israel, the magnetic inclination is 46° – 48°) and complex geological environments, these methods can cause substantial errors. Unlike the methods mentioned above, our interpretation involves the application of methods developed especially for quantitative analysis of magnetic anomalies observed in complex environments (oblique (inclined) magnetization, uneven topography, and superposition of different sources) [19, 21, 36, 37, 52]. We applied improved modifications of the *tangent*, *characteristic point*, and *areal* methods, with the employment of the most commonly used geometric models: (1) thin bed (*TB*), (2) thick bed (*THB*), (3) thin horizontal plate (*THP*), (4) horizontal circular cylinder (*HCC*) or *sphere*, and (5) intermediate models between the *THB* and *THP*.

These interpretation methods were verified on the Zemah magnetic anomaly (designated as “O” in Fig. 23.6). The “Zemah 1” borehole was drilled [57] at a point some 2 km south of the sea basin (see Fig. 23.1b). The obtained results of the

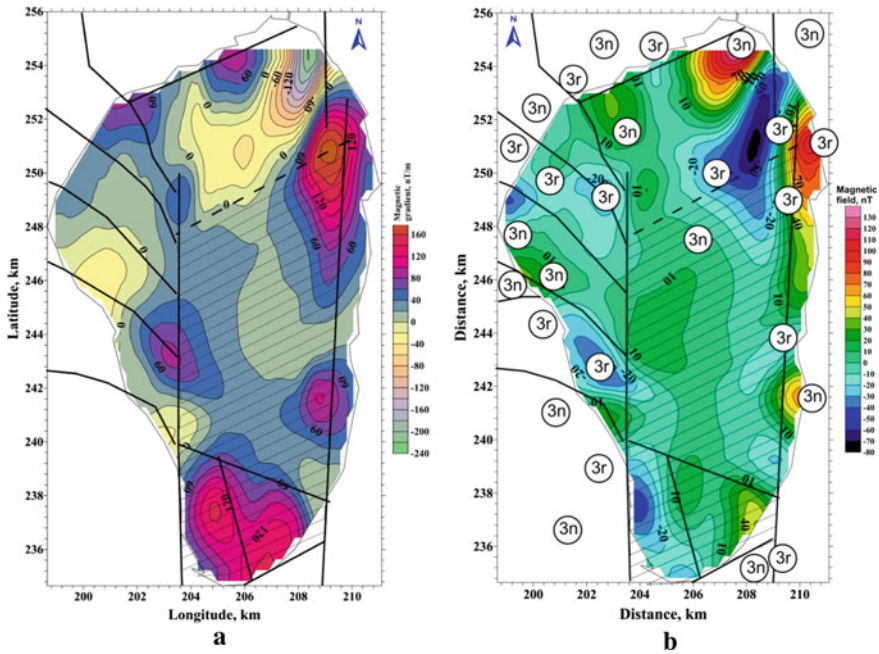


Fig. 23.8 **a** Map of the total magnetic field gradient with the tectonic elements. **b** Map of entropy filtering with the tectonic elements and paleomagnetic zone indexes (3r and 3n)

quantitative analysis (the upper edge of the magnetic body was determined at 515 m) are in good agreement with the drilling data (489 m) [25].

Altogether sixteen magnetic anomalies in the Sea of Galilee and Kinnarot Valley were examined. Results of the quantitative interpretation of anomalies A, B, and C in the sea basin using the aforementioned nonconventional methods are shown in Fig. 23.9. The determined depths of the magnetic sources range between -1500 m (below the level of the Sea of Galilee) for the *HCC* center (for anomaly L) and -300 m for the *TB* upper edge (for anomaly M). The obtained values of target magnetization range between the 0.009 and 0.06 **SI** units are in accordance with the physical measurements of basaltic samples in the vicinity of the sea basin (e.g., [18, 62]). The results of the performed quantitative interpretation of magnetic anomalies are compiled in Table 23.1.

23.4.4 3D Magnetic Field Modeling

3-D modeling of the magnetic field in this study was realized using GSFC (Geological Space Field Calculation) software. The main algorithm of this program provides the calculation of 3-D magnetic and gravity effects for a horizontal polygonal prism

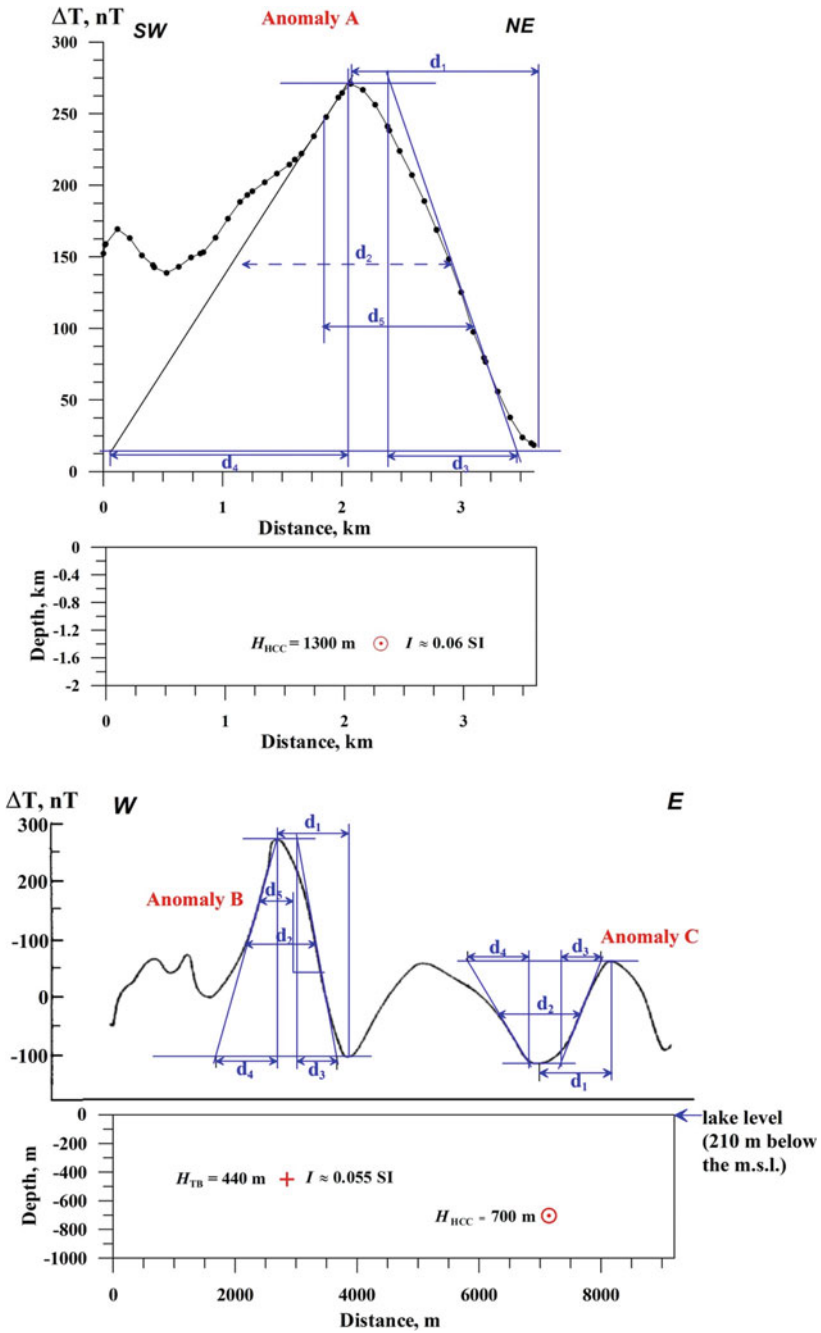


Fig. 23.9 Quantitative analysis of magnetic anomalies A, B, and C in the Sea of Galilee (location of these anomalies is shown in Figs. 23.4 and 23.6)

Table 23.1 Generalized results of quantitative analysis of magnetic anomalies in the Sea of Galilee and Kinnarot Valley

Anomaly	Sea of Galilee	Kinnarot Valley	Interpreting model	Depth of the TB, THB and THP upper edge (center of HCC or sphere), m	Magnetization (SI unit)	Direction of magnetization
A	+	–	(1) <i>HCC</i> (2) <i>THB</i>	1300 1100	0.06 0.05	Direct Direct
B	+	–	<i>TB</i>	440	0.055	Direct
C	+	–	<i>HCC</i>	700	0.017	Reverse
D	+	–	<i>TB</i>	525	0.04	Reverse
E	+	–	<i>TB</i>	460	0.05	Reverse
F	+	–	<i>TB</i>	510	0.016	Direct
G	+	–	<i>HCC</i>	700	0.017	Direct
H	+	–	<i>HCC</i>	670	0.015	Reverse
I	+	–	<i>HCC</i>	520	0.025	Reverse
J	+	–	<i>TB</i>	300	0.009	Direct
K	+	–	<i>HCC</i>	1030	0.020	Reverse
L	+	–	<i>HCC</i>	1500	0.03	Direct
M	–	+	<i>TB</i>	420	0.012	Direct
N	–	+	<i>TB</i>	430	0.013	Reverse
O	–	+	<i>TB</i>	515 (real value is 489)	0.01	Direct
P	–	+	<i>TB</i>	425	0.012	Direct
Profile 100	+		<i>THP</i>	0–10	0.04	Reverse
Profile V–V	+		<i>THP</i>	≈1000	0.032	Combined

Designations: *TB*, thin bed, *THB*, thick bed, *HCC*, horizontal circular cylinder, *THP*, thin horizontal plate

limited in the strike direction under physical-geological conditions of any complexity [36, 52].

Review of paleomagnetic investigations [1, 45, 47, 59] testifies in the areas surrounding the sea basin a diversity of the reversely magnetized basaltic samples (see also magnetostratigraphic scale in Fig. 23.5). An essential effect was found along profile 210 located in the eastern part of the basin (see Fig. 23.4): a clear inverse correlation between the magnetic field ΔT and the highs of the bottom relief in the eastern part of the sea. We interpreted this effect as the reversely magnetized

rock anomalies occurring at the bottom of the sea (or near the sea) [25]. As an initial approximation, the model of a thin horizontal plate occurring in the subsurface was employed here. 3-D iterative magnetic field modeling was applied to estimate the value of magnetization and the location of the magnetization vector of this thin plate with the uneven upper edge: 3300 mA/m and -125° , respectively. Analysis of the ages and magnetic polarities of the basalts occurring around the sea suggested that this reversely magnetized basaltic thin plate is of the Early Pliocene.

The post-basalt sedimentary basin fill explains the absence of essential magnetic anomalies in the central part of the basin [25]. The magnetic field 3-D modeling results indicate an occurrence of separate magnetic bodies at a depth of 1.2–1.3 km (see anomaly L in Fig. 23.4).

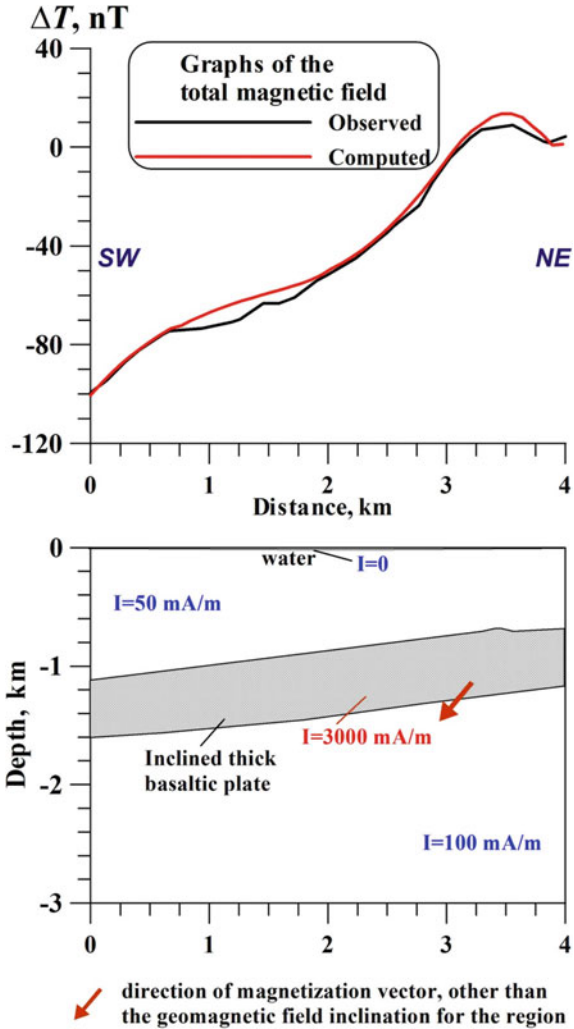
The outline of the magnetic field in the southern part of the sea noticeably contrasts with the magnetic field design in the central and northern parts of the basin. Remarkably, earlier Ben-Avraham et al. [4] have shown that the morphology of the bottom relief in the southern part of the sea also shows the substantial difference from other parts of the basin. Conducted 3-D modeling of the magnetic field along with profile V–V (see the location of the profile in Fig. 23.4) unambiguously indicates that this anomaly is caused by a thick hidden basaltic plate (with the magnetization of 3000 mA/m and the location of the magnetization vector of 135°) with a dip of about 12° from NE to SW (Fig. 23.10). The constructed SW–NE paleomagnetic profile along with the Zemah 1 well (Fig. 23.11) and results of seismic profiling [11, 67] clearly show that this dipping relates to the SW flank of the Zemah anticline. The location of the paleomagnetic profile (shown in Fig. 23.12) does not precisely coincide with the location of the profile V–V (see Fig. 23.5), but the general tendency is similar: the total thickness of this basaltic layer and its dipping from the northeast to southwest. Obviously, the integrated effect from the basalts of 3n (normal magnetization) and 3r (reverse magnetization) provides the mutual magnetic vector direction of 135° (see Fig. 23.10).

23.5 Paleomagnetic Reconstructions

Paleomagnetic mapping is an effective method for studying the structure and geodynamics of areas involved in transition zones from ocean to continent [32–34], to which the region of the Sea of Galilee belongs. Firstly the methodology of integrated paleomagnetic mapping was realized in Eppelbaum et al. [24, 26, 31]. Newly arriving geological-geophysical data enabled us the development of an enhanced combined paleomagnetic map of the Sea of Galilee and surrounding areas (Fig. 23.12). This area can be a successful example of the paleomagnetic mapping of tectonically complex regions to a certain extent. Therefore, in this work, we have expanded the range of studies both by (1) attracting new data and (2) methodological approaches and evaluating the recent developments in the deep geodynamic analysis [33].

The significant peculiarity of the presented paleomagnetic map of the Sea of Galilee and its vicinity (Fig. 23.12) is that the presented strata with paleomagnetic

Fig. 23.10 3D modeling of the magnetic field along with profile V–V in the southern part of the Sea of Galilee (location of this profile is shown in Fig. 23.4). The symbol “I” designates magnetization of the anomalous target and surrounding media



zones regularly replace each other both in the meridional and latitudinal directions (see also Fig. 23.5). This is caused by an intricate tectonic-geophysical zonation of this DST fragment. In the latitudinal direction (from west to east), block systems of the DST left shear are replaced, and in the meridional direction (from north to south), a complex tectonic pattern of the earth’s crust subsidence is developed. The pattern forms a pull-apart basin of the Sea of Galilee, which appears to be more complex than those other basins situated along with the DST [10]. In addition, the paleomagnetic zonation reflects the development of the Hula Basin [located to the north of the area of investigation (see Fig. 23.1b)] and the peculiarities of the Ash Shaam trap field [77], most paleomagnetic zones of which are located to the east of the study area.

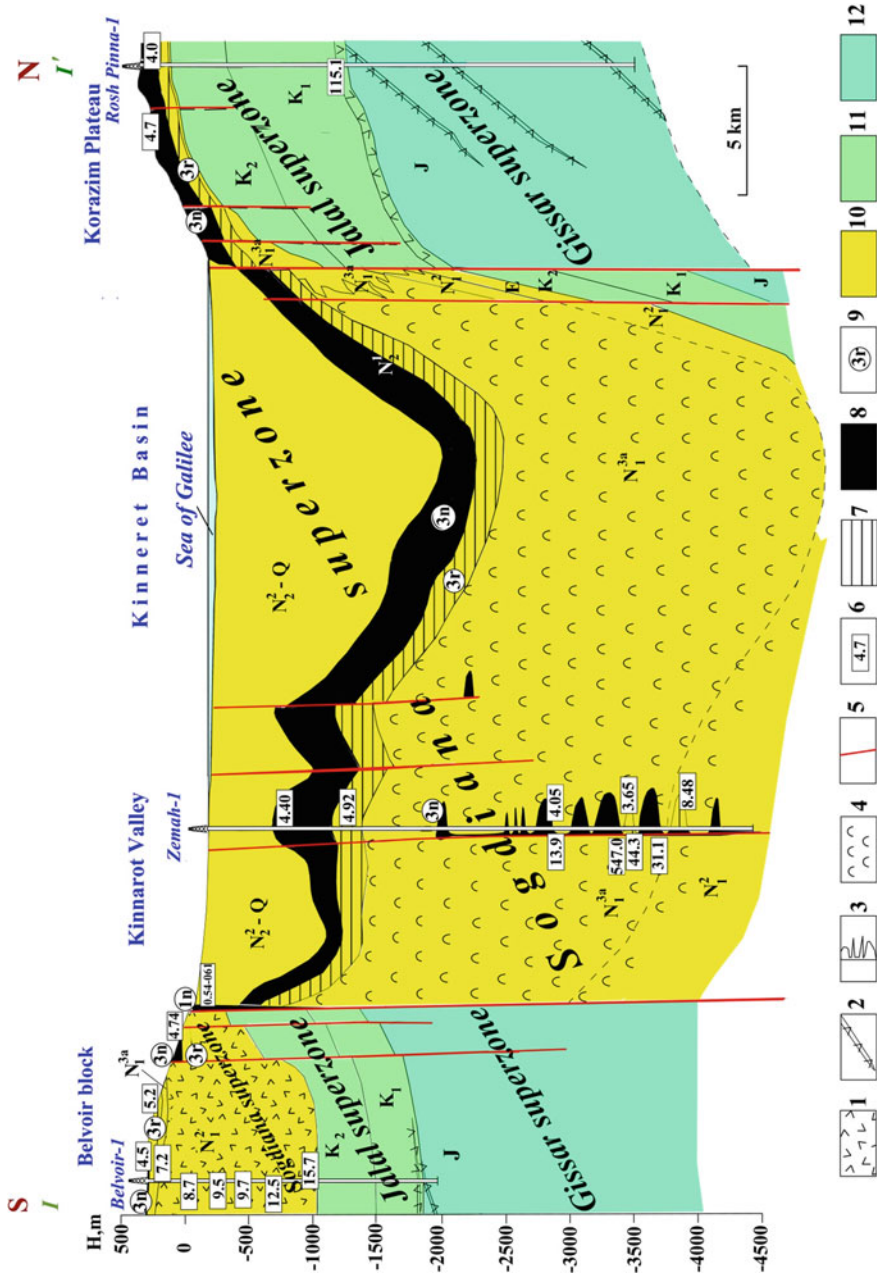
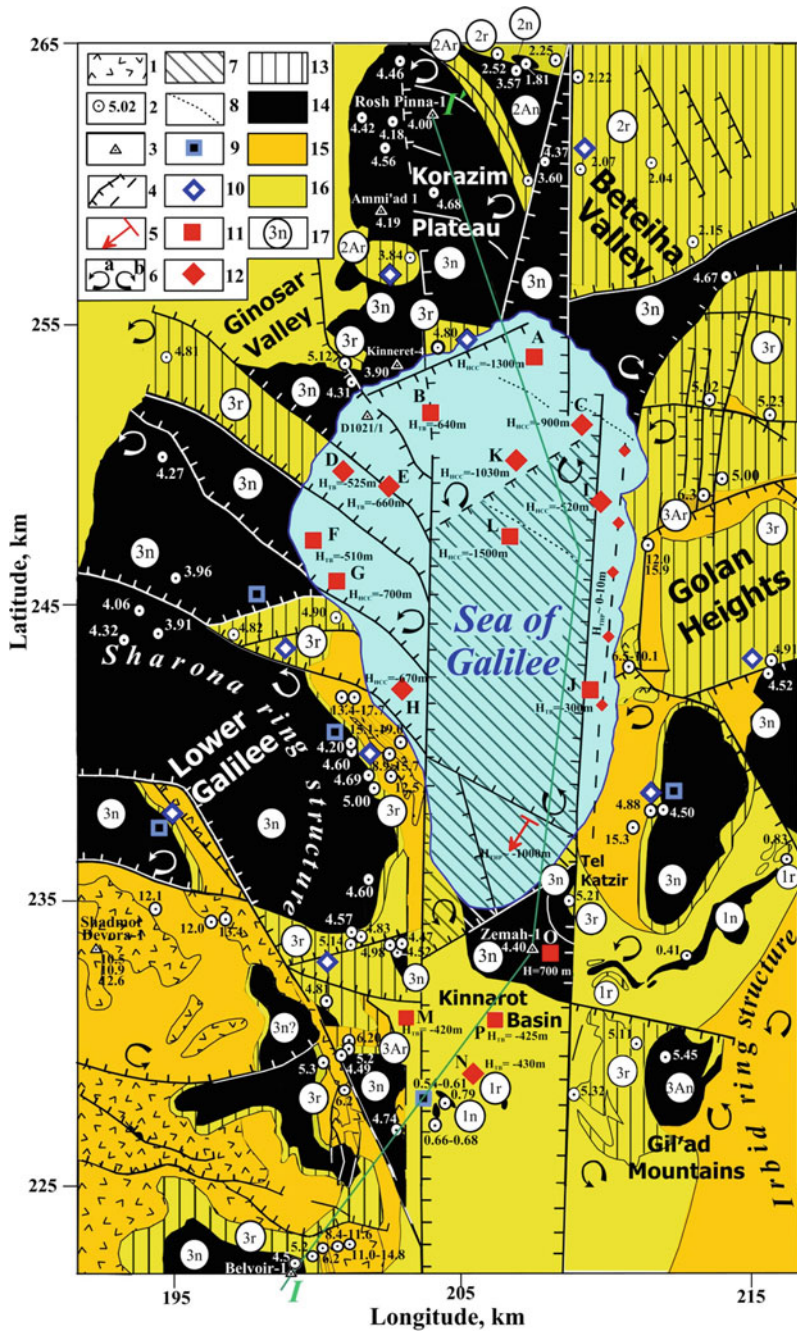


Fig. 23.11 Paleomagnetic profile *I-I'* through the Sea of Galilee (location of this profile is shown in Fig. 23.12). (1) Traps, (2) dykes, (3) diabase sills, (4) salts, (5) faults, (6) data of radiometric ages, geomagnetic polarities: (7) reversal, (8) normal, (9) index of paleomagnetic age, (10) Sogdiana superzone, (11) Jalal superzone, (12) Gissar superzone



◀**Fig. 23.12** Integrated tectonic-paleomagnetic scheme of the Sea of Galilee and adjoining areas. (1) outcropped Cenozoic basalts, (2) points with the radiometric age of basalts (in Ma), (3) boreholes, (4) faults, (5) general direction of the proposed buried basaltic plate dipping in the southern part of the Sea of Galilee, (6) counterclockwise (a) and clockwise (b) of faults and tectonic blocks, (7) pull-apart basin of the Sea of Galilee, (8) suggested boundaries of the paleomagnetic zones in the sea, data of land paleomagnetic measurements: (9 and 10) (9) reverse magnetization, (10) normal magnetization, (11 and 12) results of magnetic anomalies analysis: (11) normal magnetization, (12) reverse magnetization, (13) reversely magnetized basalt fields, (14) normal magnetized basalt fields, (15) Miocene basalts and sediments with complicated paleomagnetic characteristics, (16) Pliocene–Pleistocene basalts and sediments with complicated paleomagnetic characteristics, (17) index of paleomagnetic zonation. Tectonic setting after Ben-Avraham et al. [10], Heimann [45], Hurwitz et al. [49], Sneh et al. [75]. 1n, 2n, 3n, 1Ar, 2Ar, and 3Ar are the indexes of paleomagnetic zones (see Fig. 23.5). Radiometric data (K–Ar and Ar–Ar) after Heimann [45], Heimann and Braun [46], Heimann et al. [47], Segev [69], Shaliv [71]. Paleomagnetic data after [1, 17, 45–47, 59, 62, 63, 65, 71]. H_{TB} and H_{HCC} designate calculated depths of basaltic bodies in the basin: H_{TB} is the upper edge for the model of the thin bed, H_{THP} is the upper edge for the model of the thin horizontal plate, and H_{HCC} is the center for the model of the horizontal circular cylinder. The light green line shows the location of the paleomagnetic profile $I-I'$

Flood basalts are exposed in a series of fault-bounded blocks surrounding the Sea of Galilee (Fig. 23.12). More than 80% of the basalts around the basin belong to the Pliocene Cover Basalt formation, which consists of a 150–200 m thick sequence outside the rift valley, but reaches about 700 m in the Zemah 1 well—inside the Kinnarot Valley [57]. Altogether, 25 sites of zones with normal and reversed magnetic polarity in the basin and surrounding areas have been identified (Fig. 23.12).

This map also contains the results of the quantitative analysis of magnetic anomalies in the sea and outside it: altogether 16 anomalies were interpreted [they were approximated by the models of thin bed, thick bed, thin horizontal plate, and horizontal circular cylinder (sphere)].

The age of the Late Cenozoic basalts at the central part of the DST is based on over 300 radiometric dates [17, 45, 47, 71]. In the studied area, the radiometric age of the basalts was measured at more than 100 points (Middle Miocene–Pleistocene). From these data, 58 points (mainly belonging to the Cover Basalts and partially—of the uppermost Late Miocene, Late Pliocene, and Late Pleistocene) were selected for the paleomagnetic map construction (see Fig. 23.12).

In the south, predominantly paleomagnetic zones of the Miocene are developed, the older of which (age from 17.7 to 6.8 Ma) correspond to the Middle Miocene traps of the Lower Basalts. The younger Miocene basalts aged 6.8–5.42 Ma correspond to the Intermediate Basalts of the Upper Miocene (Messinian) and are subdivided into stages 3B and 3A (Fig. 23.5). The Early Pliocene (Zanclean) Cover Basalts, corresponding to the Gilbert paleomagnetic epoch (zones 3r-2Ar), are less developed in the same zone. From the eastern edge of the described part of the map in a diagonal direction, marked by the Yarmouk River fault, from the outskirts of the Golan Plateau to the southern part of the water basin, the youngest associations are developed: Pleistocene Yarmouk and Yarda basalts aged 0.41–0.83 Ma and corresponding to the Brunhes and upper Matuyama zones (Figs. 23.5, 23.11 and 23.12).

The age of these complexes is justified by the radiometric, paleomagnetic, magnetic and seismic data [1, 11, 17, 24, 26, 45–47, 49, 59, 60, 64].

In the central latitudinal zone of the region, the Early Pliocene Cover Basalts formations dominate, while in the Lower Galilee and below the water area, zone 3n traps dominate, and in the Golan Heights—reverse magnetized traps of zone 3r dominate. They are underlain by a sedimentary Miocene sequence with interlayers of effusive rocks belonging to both the Lower Basalts and Intermediate Basalts. North of the latitude of the Sea of Galilee, the Early Pliocene Cover Basalts (zones 3r-2Ar) and the Late Pliocene post-Cover and Ruman Basalts (zones 2An-2n) of the Gauss and Matuyama epochs are developed on Plateau Korazim and in the Beteiha Valley.

In the sublatitudinal direction (see Figs. 23.11 and 23.12), the directly and reversely magnetized Late Cenozoic rocks of the Sogdiana superzone are mostly submerged in the area of the Sea of Galilee—to the depths of more than 5 km. Here, thick Early Messinian-Late Tortonian salts, Early Pliocene basalts, and gabbroids of the Gilbert paleomagnetic zone are developed. In the latter, xenoliths aged from 13.9 to 547.0 Ma are developed [45, 47, 69].

23.6 Discussions and Conclusions

It is well known that an integrated examination increases the amount and reliability of geophysical-geological information sharply (e.g., [52]). Firstly a combined paleomagnetic-radiometric-geological mapping was successfully applied to investigate complex lava succession in the western Island [58]. Theoretically, if a set of geophysical methods is focused on investigating independent indicators of equal value, the anomaly detection reliability γ can be described by an error function (probability integral) [20] as:

$$\gamma = F\left(\frac{\sqrt{\sum_i v_i}}{2}\right),$$

where v is the ratio of the anomaly squared to the noise dispersion for each i th geophysical field, and F is the probability integral.

Let us assume that three points indicate the geophysical anomaly and that the mean square of the anomaly for each field is equal to the noise dispersion. For a single geophysical method, the reliability of the detection of an anomaly of a known form and intensity can be calculated by Kotelnikov's criterion (e.g., [13]). Hence the reliability for individual methods is 0.61 and 0.77 and 0.87 for a set of two or three methods, respectively. It means that the q value (risk of an erroneous solution) when integrating two or three methods decreases by factors of 1.7 and 3.0, respectively [20].

Thus, geophysical method integration significantly decreases the risk of an erroneous solution. Here we attempt to integrate the magnetic, paleomagnetic, radiometric, gravity, and seismological (and partially—seismic) data, which should significantly reduce uncertainty in constructing physical-geological models in complex geological-environmental conditions of the region under study.

Integrated analysis of the gravity map (Fig. 23.3), results of the 3D magnetic field modeling (Fig. 23.10), and the constructed paleomagnetic profile (Fig. 23.11) leads to the following conclusions. The basaltic layers (3n and 3r) (see Fig. 23.11) come closest to the water surface in the southernmost part of the lake. The positive density contrast between the basalts and surrounding rocks consists of a minimum of $500\text{--}600\text{ kg/m}^3$. However, the positive gravity effect produced by the basaltic plate is several times smaller than the negative gravitational anomalies from a few kilometer sedimentary-salt strata occurring below the Sea of Galilee. Therefore, in the southernmost part of the sea, the slight positive gravity anomaly is only weakly delineated (see Fig. 23.3).

The results of magnetic and paleomagnetic data analysis with the utilization of the seismic [11, 49, 66, 67] and tectonic [2, 4, 7, 10, 45–47, 71, 75] data were applied for compilation of a modified structural map of the Cover Basalt of the Sea of Galilee and its vicinity (Fig. 23.13). This map has been compiled outside the sea based on the Geological Map of Israel [75]. It should be underlined that the map (Fig. 23.13) clearly indicates the margins of a rhomb-shaped graben in the sea. It is in line with the results of detailed bathymetrical mapping of the sea [4]. The southern part of the rhomb-shaped graben is bordered by the diagonal (ESE–WNW) tectonic fault (Fig. 23.4), which was revealed for the first time by the acoustic reflectivity analysis [8]. The identified western boundary of the rhomb-shaped graben (Fig. 23.13) nicely correlates with the magnetic data interpretation (Table 23.1, Fig. 23.12), gravity field analysis (Fig. 23.3), results of magnetic field transformations (Fig. 23.8a, b), and integrated paleomagnetic reconstructions (Fig. 23.12).

The N–S paleomagnetic profile along the western part of the sea (see Fig. 23.11) shows that there are two topographic rises—in the south (Lower Galilee) and in the north (Korazim plateau), and depression in the center of the profile, which corresponds to the shallow-water part of the sea. Such a pattern indicates that the western part of the Sea of Galilee depression is probably an inversion trough formed along with the Pliocene uplift in the eastern part of Galilee.

Analysis of the structural map of Cover Basalt (Fig. 23.13) designates that displacement of basaltic units of the same age suggests the uplift rates of $\approx 0.005\text{ cm/yr}$ around the sea and subsidence rate of the seafloor of $\approx 0.05\text{ cm/yr}$. Heightened geotectonic activity in the sea basin is also confirmed by the relatively high thermal flow— 94 mW/m^2 [6], results of the seismic data analysis [8, 11, 50, 64] and the earthquake-induced surface ruptures observed in the vicinity of the sea [51, 55, 56].

The influence of the recently recognized quasi-ring rotating deep mantle structure [27, 28] on the near-surface geology for the northern continuation of the DST is reflected in: (1) rotating of the tectonic blocks mainly counterclockwise, (2) occurring

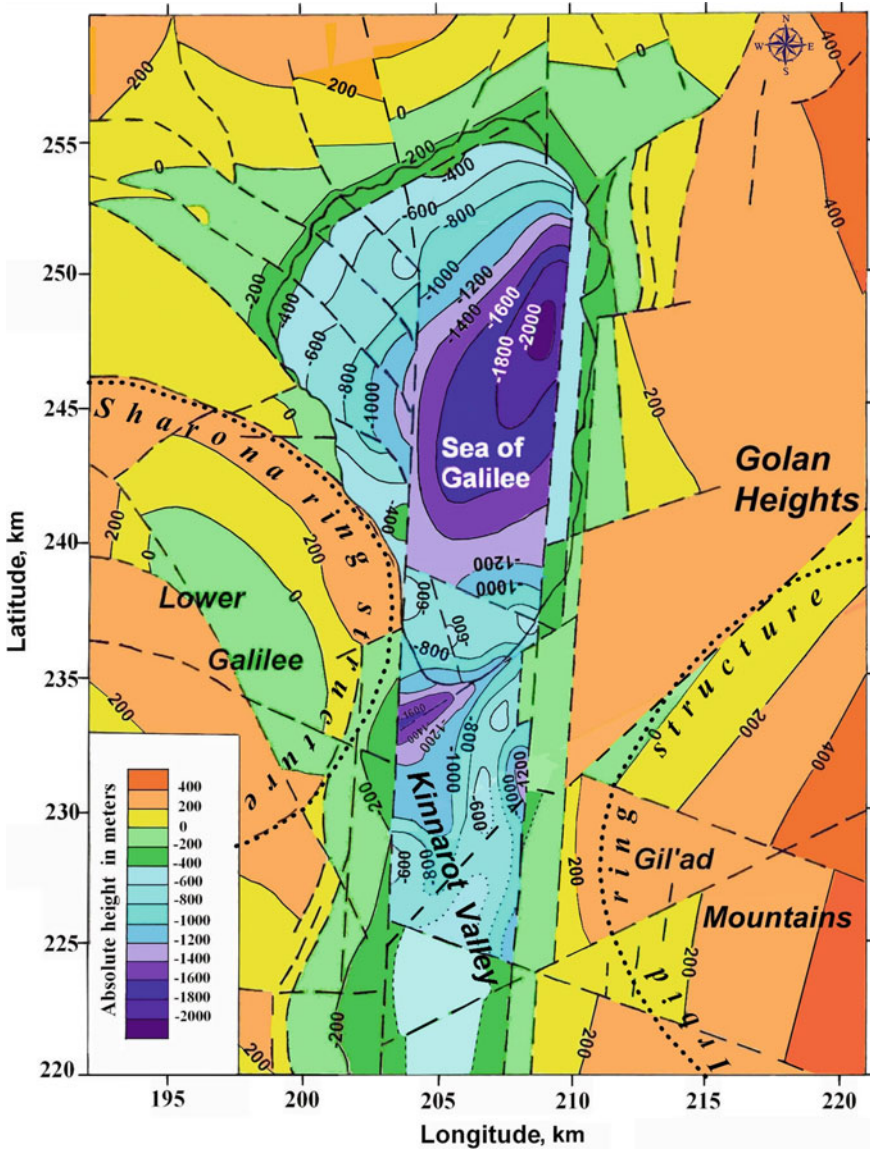


Fig. 23.13 Structural map of the Cover Basalts for the Sea of Galilee and its vicinity (after Eppelbaum et al. [26], with modifications)

the seismic event manifestations predominantly along the lines deviating counter-clockwise, and (3) arcuate tectonic faults mainly stretching from the southeast to northwest.

Thus, an integrated tectonic-geophysical analysis of the complex tectonic setting of the Sea of Galilee and its vicinity significantly increases the interpretation reliability and facilitates the creation of non-trivial physical-geological models reflecting the essential features of the media.

The undertaken studies based on the employment of a wide range of various geological-geophysical methods enabled the following: 1. to make significant changes in the understanding of the structural plan and typology of geological units of various types and genesis, 2. to identify a variety of sources, mechanisms, and types of the geodynamic features (both deep and subsurface), 3. to clarify the formation history of this unique region, which is essential for geocology, assessment of the water resources, geodynamic forecast, and monitoring of natural and engineering environmental factors.

Acknowledgements The authors would like to thank anonymous reviewers, who thoroughly reviewed the manuscript, and their critical comments and valuable suggestions were very helpful in preparing this paper. We are also grateful to the editors of the book, Anna Di Mauro, Francesco Soldovieri, and Andrea Scozzari, for their painstaking work in analyzing the submitted manuscripts.

References

1. Behar N, Shaar R, Tauxe L, Asefaw H, Ebert Y, Heimann A, Koppers AAP, Ron H (2019) Paleomagnetism and paleosecular variations from the Plio-Pleistocene Golan Heights volcanic plateau, Israel. *Geochem Geophys Geosyst* 20:4319–4335
2. Belitzky S, Ben-Avraham Z (2004) The morphotectonic pattern of Lake Kinneret. *Israel J Earth Sci* 53(3):121–130
3. Ben-Avraham Z (1978) The structure and tectonic setting of the Levant continental margin Eastern Mediterranean. *Tectonophysics* 46:3130331
4. Ben-Avraham Z, Amit G, Golan A, Begin ZB (1990) The bathymetry of Lake Kinneret and its structural significance. *Israel J Earth Sci* 39:77–84
5. Ben-Avraham Z, Ginzburg A, Makris J, Eppelbaum L (2002) Crustal structure of the Levant basin, Eastern Mediterranean. *Tectonophysics* 346:23–43
6. Ben-Avraham Z, Hänel R, Villinger H (1978) Heat flow through the Dead Sea rift. *Mar Geol* 28:253–269
7. Ben-Avraham Z, Rozenthal M, Tibor T, Navon H, Wust-Bloch H, Hofstetter R, Rybakov M (2014) Structure and tectonic development of the Kinneret Basin. In: Zohary T et al (eds) *Lake Kinneret, ecology and management*. Aquatic ecology series 6. Springer, Dordrecht, pp 19–38
8. Ben-Avraham Z, Shaliv G, Nur A (1986) Acoustic reflectivity and shallow sedimentary structure in the Sea of Galilee—Jordan Valley. *Mar Geol* 70:175–189
9. Ben-Avraham Z, Shosham Y, Klein E, Michelson H, Serruya C (1980) Magnetic survey of Lake Kinneret-central Jordan Valley Israel. *Marine Geophys Res* 4:257–276
10. Ben-Avraham Z, ten-Brink U, Bell R, Reznikov M (1996) Gravity field over the Sea of Galilee: evidence for a composite basin along a transform fault. *J Geophys Res* 101:533–544
11. Ben-Gai Y (2011) Subsurface geology of the southern Lake Kinneret (Sea of Galilee), Dead Sea transform—evidence from seismic reflection data. *Israel J Earth Sci* 58:163–175

12. Berggren WA, Hilgen FJ, Langereis CG, Kent DV, Obradovich JD, Raffi I, Raymo ME, Shackleton NJ (1995) Late Neogene chronology: new perspectives in high resolution stratigraphy. *GSA Bull* 107(11):1272–1287
13. Borda M (2011) *Fundamentals in information theory and coding*. Springer
14. Cande SC, Kent DV (1995) Revisited calibration of the geomagnetic polarity timescale for the Late Cretaceous and Cenozoic. *J Geophys Res* 100(4):6095–6095
15. Cornee JJ, Roger S, Munch P, Saint Martin JP, Feraud G, Conesa G, Pestrea-Sain Martin S (2002) Messinian events: new constrains from sedimentological investigations and new $^{40}\text{Ar}/^{39}\text{Ar}$ ages in the Melilla-Nador Basin (Morocco). *Sed Geol* 151:127–147
16. Curzon I, Nof RN, Laporte M, Lutzky H, Polozov A, Zakovsky D, Shulman H, Goldenberg A, Tatham B, Hamiel Y (2020) The “TRUAA” seismic network: upgrading the Israel seismic network—toward national earthquake early warning system. *Seismol Res Lett* 91(6):3236–3255
17. Dembo N, Hamiel Y, Granot R (2015) Intraplate rotational deformation induced by faults: Carmel-Gilboa fault system as a case study. *Geol Surv Isr. Report No. GSI/19/2015*, Jerusalem, 32p
18. Domzalski W (1967) Aeromagnetic survey of Israel. *Israel Inst Pet Res Geophys. Rep. SMA/482/67*, 63p
19. Eppelbaum LV (2011) Study of magnetic anomalies over archaeological targets in urban conditions. *Phys Chem Earth* 36(16):1318–1330
20. Eppelbaum LV (2014) Four color theorem and applied geophysics. *Appl Math* 5:358–366
21. Eppelbaum LV (2015) Quantitative interpretation of magnetic anomalies from bodies approximated by thick bed models in complex environments. *Environ Earth Sci* 74:5971–5988
22. Eppelbaum LV (2015) Comparison of 3D integrated geophysical modeling in the South Caucasian and Eastern Mediterranean segments of the Alpine-Himalayan tectonic belt. *Izvestiya Acad Sci Azerb Rep Ser: Earth Sci* 3:25–45
23. Eppelbaum LV (2019) *Geophysical potential fields: geological and environmental applications*. Elsevier, Amsterdam, N.Y
24. Eppelbaum L, Ben-Avraham Z, Katz Y (2004) Integrated analysis of magnetic, paleomagnetic and K–Ar data in a tectonic complex region: an example from the Sea of Galilee. *Geophys Res Lett* 31(19), L19602:1–4
25. Eppelbaum L, Ben-Avraham Z, Katz Y, Marco S (2004) Sea of Galilee: comprehensive analysis of magnetic anomalies. *Israel J Earth Sci* 53(3):151–171
26. Eppelbaum LV, Ben-Avraham Z, Katz YI (2007) Structure of the Sea of Galilee and Kinarot Valley derived from combined geological-geophysical analysis. *First Break* 25(1):21–28
27. Eppelbaum LV, Ben-Avraham Z, Katz Y, Cloetingh S, Kaban M (2020) Combined multifactor evidence of a giant lower-mantle ring structure below the Eastern Mediterranean. *Positioning* 11:11–32
28. Eppelbaum LV, Ben-Avraham Z, Katz Y, Cloetingh S, Kaban M (2021) Giant quasi-ring mantle structure in the African-Arabian junction: results derived from the geological-geophysical data integration. *Geotectonics (Springer)* 55(1):67–93
29. Eppelbaum LV, Katz YI (2012) Key features of seismo-neotectonic pattern of the Eastern Mediterranean. *Izvestiya Acad Sci Azerb Rep Ser: Earth Sci* 3:29–40
30. Eppelbaum LV, Katz YI (2015) Eastern Mediterranean: combined geological-geophysical zonation and paleogeodynamics of the Mesozoic and Cenozoic structural-sedimentation stages. *Mar Pet Geol* 65:198–216
31. Eppelbaum LV, Katz YI (2015) Paleomagnetic mapping in various areas of the Easternmost Mediterranean based on an integrated geological-geophysical analysis. In: Eppelbaum L (ed) *New developments in paleomagnetism research. Earth sciences in the 21st Century*, Nova Science Publisher, NY, pp 15–52
32. Eppelbaum LV, Katz YI (2020) Significant tectono-geophysical features of the African-Arabian tectonic region: an overview. *Geotectonics (Springer)* 54(2):266–283
33. Eppelbaum LV, Katz, YI (2022). Paleomagnetic-geodynamic mapping of the transition zone from ocean to the continent: A review. *Applied Sciences* 12, Spec. Issue: *Advances in Applied Geophysics*: 1–20

34. Eppelbaum L, Katz Y (2022) Combined zonation of the African-Levantine-Caucasian areal of ancient Hominin: review and integrated analysis of paleogeographical stratigraphic and geophysical-geodynamical data. *Geosciences (Switzerland)* 27(1):1–23
35. Eppelbaum LV, Katz YI, Ben-Avraham Z (2012) Israel—petroleum geology and prospective provinces. *AAPG Eur Newslett* 4:4–9
36. Eppelbaum LV, Khesin BE, Itkis SE (2001) Prompt magnetic investigations of archaeological remains in areas of infrastructure development: Israeli experience. *Archaeol Prospect* 8(3):163–185
37. Eppelbaum LV, Mishne AR (2011) Unmanned airborne magnetic and VLF investigations: effective geophysical methodology of the near future. *Positioning* 2(3):112–133
38. Freund R, Garfunkel Z, Zak I, Goldberg M, Weissbrod T, Derin B (1970) The shear along the Dead Sea Rift. *Philos Trans R Soc Lond Ser A* 267:69–85
39. Garfunkel Z (1981) Internal structure of the Dead Sea leaky transform (rift) in relation to plate kinematics. *Tectonophysics* 80:80–108
40. Garfunkel Z, Zak I, Freund R (1981) Active faulting in the Dead Sea Rift. *Tectonophysics* 80:1–26
41. Gasperini L, Lazar M, Mazzini A, Lupi M, Haddad A, Hensen C, Schmidt M, Caracausi A, Ligi M, Polonia A (2020) Neotectonics of the Sea of Galilee (northeast Israel): implication for geodynamics and seismicity along the Dead Sea Fault system. *Sci Rep* 10(11932):1–17
42. Ginzburg A, Ben-Avraham Z (1986) Structure of the Sea of Galilee Graben, Israel, from magnetic measurements. *Tectonophysics* 126:153–164
43. Haddad A, Alcanie M, Zahradník J, Lazar M, Antunes V, Gasperini L, Polonia A, Mazzini A, Lupi M (2020) Tectonics of the Dead Sea fault driving the July 2018 seismic swarm in the Sea of Galilee (Lake Kinneret), Israel. *J Geophys Res: Solid Earth* 125:1–14 e2019JB018963
44. Hazan N, Stein M, Agnon A, Marco S, Nadel D, Negendank JFW, Schwab MJ, Neev D (2005) The late quaternary history of Lake Kinneret (Sea of Galilee), Israel. *Quatern Res* 63:60–77
45. Heimann A (1990) The development of the Dead Sea Rift and its margins in northern Israel during the Pliocene and Pleistocene. PhD thesis, Hebrew University, Jerusalem, 114p. (in Hebrew, summary in English)
46. Heimann A, Braun D (2000) Quaternary stratigraphy of the Kinarot Basin, Dead Sea Transform, northeastern Israel. *Israel J Earth Sci* 49:31–44
47. Heimann A, Steinitz G, Mor D, Shaliv G (1996) The Cover Basalt formation, its age and its regional and tectonic setting: implications from K-Ar and $^{40}\text{Ar}/^{39}\text{Ar}$ geochronology. *Israel J Earth Sci* 45:55–71
48. Hofstetter A, van Eck T, Shapira A (1996) Seismic activity along fault branches of the Dead Sea-Jordan transform system: the Carmel-Tirtza fault system. *Tectonophysics* 267:317–330
49. Hurwitz S, Garfunkel Z, Ben-Gai Y, Reznikov M, Rotstein Y, Gvirtzman H (2002) The tectonic framework of a complex pull-apart basin: seismic reflection observations in the Sea of Galilee, Dead Sea transform. *Tectonophysics* 359:289–306
50. Kashai EL, Croker PF (1987) Structural geometry and evolution of the Dead Sea-Jordan rift system as deduced from new subsurface data. *Tectonophysics* 141:33–60
51. Katz O, Amit R, Yagoda-Biran G, Hatzor YH, Porat N, Medvedev B (2011) Quaternary earthquakes and landslides in the Sea of Galilee area, the Dead Sea Transform: paleoseismic analysis and implication to the current hazard. *Israel J Earth Sci* 58:275–294
52. Khesin BE, Alexeyev VV, Eppelbaum LV (1996) Interpretation of geophysical fields in complicated environments. *Modern approaches in geophysics*. Kluwer Academic Publishers, Dordrecht
53. Krijgsman W, Hilgen FG, Langereis CG, Santarelli A, Zachariasse WJ (1995) Late Miocene magnetostratigraphy, biostratigraphy and cyclostratigraphy in the Mediterranean. *Earth and Plan Sci Lett* 136:475–494
54. Lutzky H, Lyakhovskiy V, Kurzon I, Shalev E (2020) Hydrological response to the Sea of Galilee 2018 seismic swarm. *J Hydrol* 582:1–7
55. Marco S, Agnon A, Ellenblum R, Eidelman A, Basson U, Boas A (1997) 817 year old walls offset sinistrally 2.1m by the Dead Sea Transform, Israel. *J Geodyn* 24(1–4):11–20

56. Marco S, Hartal M, Hazan N, Lev L, Stein M (2003) Archaeology, history, and geology of the A.D. 749 earthquake, Dead Sea transform. *Geology* 31(8):665–668
57. Marcus E, Slager J (1985) The sedimentary-magmatic sequence of the Zemah-1 well (Jordan-Dead Sea rift, Israel) and its emplacement in time and space. *Israel J Earth Sci* 34:1–10
58. McDougall I, Saemundsson K, Johannesson H, Watkins ND, Kristjansson L (1977) Extension of the geomagnetic polarity time scale to 6.5 m.y.: K-Ar dating, geological and paleomagnetic study of a 3500-m lava succession in western Iceland. *Geological Soc Am Bull* 88:1–15
59. Mor (1993) A time-table for the Levant Volcanic Province, according to K-Ar dating in the Golan Heights, Israel. *J Afr Earth Sci* 16(3):223–234
60. Mor D, Steinitz G (1982) K-Ar age of the cover basalts surrounding the Sea of Galilee. *Geol Surv Israel. Rep., Jerusalem, Me/6/82*, 14p
61. Nikitin AA (1993) Statistical processing of geophysical data. Series of advanced geophysics, Russian experience, no 22, Electromagnetic Research Centre, Moscow (in Russian)
62. Nur A, Helsey CF (1971) Palaeomagnetism of tertiary and recent lavas of Israel. *Earth Planet Sci Lett* 10:375–379
63. Nur A, Ron H, Scott O (1989) Mechanics of distributed fault and block rotation. In: Kissel C, Laj C (eds) *Paleomagnetic rotations and continental deformation*. NATO ASI Series: mathematical and physical sciences, Kluwer Academy Publishers, Dordrecht, pp 209–228
64. Reznikov M, Ben-Avraham Z, Garfunkel Z, Gvirtzman H, Roitstein Y (2004) Structural and stratigraphic framework of Lake Kinneret. *Israel J Earth Sci* 53(3):131–149
65. Ron H, Freund R, Garfunkel Z, Nur A (1984) Block rotation by strike-slip faulting: structural and paleomagnetic evidence. *J Geophys Res* 89P:6256–6270
66. Rotstein Y, Bartov Y (1989) Seismic reflection across a continental transform: an example from a convergent segment of the Dead Sea rift. *J Geophys Res* 94:2902–2912
67. Rotstein Y, Bartov Y, Freislander U (1992) Evidence for local shifting of the main fault and changes in the structural setting, Kinarot basin, Dead Sea transform. *Geology* 20:251–254
68. Rosenthal M, Ben-Avraham Z, Schattner U (2019) Almost a sharp cut—a case study of the cross point between a continental transform and a rift, based on 3D gravity modeling. *Tectonophysics* 761:46–64
69. Segev A (2017) Zemah-1, a unique deep oil well on the Dead Sea fault zone, northern Israel: a new stratigraphic amendment. *Geol Surv Isr. Report GSI/21/2017*, Jerusalem, pp 1–27
70. Serruya C (1971) Lake Kinneret: the nutrient chemistry of sediments. *Limn Oceanog* 16:510–521
71. Shaliv G (1991) Stages in the tectonics and volcanic history of the Neogene basin in the Lower Galilee and the valleys. PhD thesis, Hebrew University, Jerusalem (in Hebrew, summary in English)
72. Shapira A (1988) Magnitude scales for regional earthquakes monitored in Israel. *Israel J Earth Sci* 37:17–22
73. Shapira A, Hofstetter A (1993) Source parameters and scaling relationship of earthquakes in Israel. *Tectonophysics* 217:217–226
74. Sharon M, Sagy A, Kurzon I, Marco S, Rosensaft M (2020) Assessment of seismic sources and capable faults through hierarchic tectonic criteria: implications for seismic hazard in the Levant. *Nat Hazards Earth Syst Sci* 20:125–148
75. Sneh A, Bartov Y, Rosenshaft M (1998) Geological map of Israel, scale 1:200,000. *Geol Surv Isr*
76. Stern RJ, Johnson P (2010) Continental lithosphere of the Arabian Plate: a geologic, petrologic, and geophysical synthesis. *Earth Sci Rev* 101:29–67
77. Weinstein Y, Navon O, Altherr R, Stein M (2006) The role of lithospheric mantle heterogeneity in the generation of Plio-Pleistocene alkali basalts suites from NW Harrat Ash Shaam (Israel). *J Petrol* 47(5):1017–1050
78. Zurieli A (2002) Structure and neotectonics in Kinarot Valley based on high-resolution seismic reflection. MSc Thesis, Tel Aviv University (in Hebrew, sum. in English), 92pp

Chapter 24

Modelling a Polluted Aquifer with Reconstructed Heterogeneity Using the Composite Medium Indicator Kriging



Francesco Chidichimo, Michele De Biase, and Salvatore Straface

Abstract Stochastic hydrology can be a powerful instrument to quantify uncertainty in complicated geological structures, since numerical models must accommodate high levels of material heterogeneity. The possibility to provide for the behavior of groundwater systems under specific conditions, thanks to a realistic representation of the hydraulic properties and geometries in a mathematical model, is the basis for a conscious management of engineering, economic, social and political problems which are typical of remediation actions. The composite media theory which allows the estimation of the spatial distribution of multiple materials, even when the medium is highly heterogeneous, is presented. The probabilistic reconstruction of boundaries between geologic facies is applied to the mathematical model of the contaminated aquifer involved by the industrial site of the city of Naples. Sedimentologic information led to the identification of different types of geomaterials, whose spatial variability is analyzed through the indexed variables approach. The hydraulic conductivity distribution is then estimated through a geostatistical analysis, and the values are calibrated as a function of the observed hydraulic heads. The realistic reconstruction of the morphology and the hydrodynamic characteristics of a polluted site within a modeling tool, gives a fundamental help to design efficient remediation processes, without causing unacceptable perturbation of the natural conditions of the sites and excessive costs.

Keywords Groundwater hydrology · Inverse modeling · Site characterization · Brownfield remediation · Geostatistics

F. Chidichimo · M. De Biase · S. Straface (✉)
Department of Environmental Engineering (DIAM), University of Calabria, 87036 Rende, Italy
e-mail: straface@unical.it

F. Chidichimo
e-mail: francesco.chidichimo@unical.it

M. De Biase
e-mail: michele.debiase@unical.it

24.1 Introduction

Sites characterization is often marked by the inadequate parameterization of the investigated porous media, which represents one of the main obstacles for an efficient and reliable description of flow and transport processes occurring in heterogeneous groundwater bodies. The enhancement in computational power and the numerical methods led to the implementation of increasingly larger modeling domains with millions of degrees of freedom. This means that the quantification of the values of hydrodynamic and hydrodispersive parameters, together with the associated uncertainties, to the nodes of a mesh where data are not available is becoming a key task. Another element that makes things even more difficult is represented by the gap between the scale of data acquisition and that for which they are subsequently used in numerical models [41]. A powerful tool, helping for parameter estimate and uncertainty quantification in groundwater flow and transport modeling, comes in the form of stochastic methods. Stochastic hydrogeology or Geostatistics was firstly developed for mining estimates by Matheron [51, 52], and then applied to hydrogeology by Delhomme [25–27], Freeze [38], Gelhar [39] and Smith and Freeze [63]. Geostatistics stated the new concept that heterogeneity can be described by a structure through the definition of the variogram of the permeability distribution. This results in the principle that the spatial distribution of the heterogeneous values derives from patterns imposed by the geological processes on the medium. The inference of this structure, defined by the spatial covariance (or variogram) of the observed data, is the first step of a Geostatistical analysis [19], or [29]. The Kriging approach, relying on a set of measured values, provides the estimate of the spatial distribution of the parameter values in the cells of a model. This method offers the minimum variance of the estimation error to assign permeability values to a model mesh with respect to zoning or arbitrary interpolation [19, 29]. Kriging extensions such as co-Kriging, or Kriging with external drift were developed to deal with data coming from different techniques in order to estimate permeability using well-test results and additional measurements like self-potential signals, or electric resistivity tomographies (e.g., [1–4, 64]). Kriging can incorporate data that are representative of different observation scales (e.g., slug test and well test data) and return estimates that are representative of averages over the precise area of a mesh, [19, 60, 61]. Kriged distribution of permeability can produce almost calibrated models that do not need important adjustments [59]. Nevertheless, calibration procedure can benefit from the constraint provided by Geostatistics to estimate the spatial distribution of parameter values and this set the basis for inverse approaches such as that of the Pilot Points method [9, 18, 28, 30, 48, 49, 58]. In the wake of geostatistical methods dealing with heterogeneity as a continuous process, MonteCarlo simulations, where the parameters are conditional realizations of their spatial distribution, provide an estimate of the resulting uncertainty on the flow and transport models [27, 48, 58, 72]. Most of these approaches are, however, limited to mildly heterogeneous porous media and this requirement is essential to guarantee the accuracy of closure approximations for analytical methods (moment equations) or to keep the number of realizations

manageable for purely numerical methods (MonteCarlo simulations). Conditioned simulations driven by stochastic methods dealing with high degrees of heterogeneity are all the more reliable, the greater the number of data at play in the process [40]. The question is how to make the best use of scarce datasets within the stochastic framework and still get a good description of the porous medium heterogeneity. The introduction of discontinuous Geostatistical models for the probabilistic reconstruction of geologic facies led to development of the Indicator Kriging approach, where an indicator, based on whether a point in space belongs to a given facies or not, may have the value one or zero [24, 34, 44–47, 53, 54, 62, 69, 70]. Guadagnini et al. [41] and Straface et al. [65] used the available data (e.g., stratigraphic measurements) to significantly increase the information content in order to estimate the statistics of facies geometry and to obtain the parameters distribution within each facies. This approach offers the opportunity to use the geologic information, that is in general available, or that could be collected at little additional cost. When the facies distribution is defined, it is necessary to assign properties (permeability, porosity, etc.) to each of them that is. the model has to be calibrated. This can be done by keeping the geometry of the facies, and change the values of the parameters within the facies. De Marsily et al. [31] state that natural heterogeneity is much more complex than any model can account for, so what brings out a specific model among others depends on how close it describes the reality and therefore provides better predictions.

We present, in this chapter, the mathematical model of the coastal aquifer, involved by the Industrial area of Naples (Italy). The Site of National Interest (SNI) called “Napoli Orientale”, has been established by the Ministry of the Environment with the Law No. 426 in December 9th 1998. It is, nowadays, the subject of studies for the definition of safety measures and remediation interventions. The territory is seriously compromised by the presence of numerous contaminants polluting the soil and the aquifer below. The situation, which is complex in itself, presents additional difficulties due to the urban context in which the site is located. The selection and the design of the operation for the environmental restoration, have been so supported by a modeling approach, which became propaedeutic for its real implementation. The use of hydrological data referred to both large (the lowland on the east of Naples) and local (SNI) scale, has been of great importance. Several hydrogeological studies carried out on the lowland area [5–8, 10, 13–17, 20, 22, 35, 67, 68], allowed the identification of sectors with different hydrogeological behavior. The aquifer in the plain, whose final delivery is represented by the sea, is characterized by a high heterogeneity because of the frequent change in lithology, grain size and thickness of the different overlapped aquifers which constitute the overall groundwater system. The estimation of the spatial distribution of the hydraulic conductivity, assumes an important role in a context like the one described before. The characterization of the aquifer, which flows under the SNI area, was developed by means of two different models: (1) A regional scale two-dimensional model (2) and a three-dimensional model at a local scale. The implementation of the regional scale model was necessary for the identification of the boundary conditions of the more complex and detailed local one. The local model, which has the function to guide the design of the remediation procedure by simulating the flow and transport phenomena at a smaller scale, was

reconstructed according to the Composite Medium approach [41]. Accurate sedimentologic information acquired in the site have led to the identification of different types of geomaterials, whose spatial variability have been analyzed by means of an indexed variables approach. The hydraulic conductivity distribution was then estimated through a geostatistical analysis. Finally, an estimation procedure of the hydraulic conductivity values, as a function of the observed hydraulic heads, has been performed.

24.2 Composite Medium Approach

The main goal of the method is the reconstruction of geologic facies boundaries from small scale data, and the estimation of the corresponding properties, which are considered as a constant in each facies, by means of inverse modeling.

Let us define n_a as the number of attributes $Y^{(a)}$ ($a = 1; \dots; n_a$) measured at points $p_i^{(a)}$ ($i = 1; \dots; n_m^{(a)}$). For the sake of simplicity, we assume that a medium consists of only two geologic facies, G_1 and G_2 . The procedure consists of the following tasks.

First task

Let n_0 be the number of points where more than one attribute is observed. All the points, hence, have at least one measurement so that the total of $n = \sum_{j=1}^{n_a} n_m^{(j)} - \sum_{j=1}^{n_0} n_m^{(j)} + n_0$. An indicator function is assigned to each of these points, p_i ($i = 1; \dots; n$);

$$I(p) = \begin{cases} 1 & p \in G_1 \\ 0 & p \in G_2 \end{cases} \quad (24.1)$$

If a datum falls within the interval $Y_1^- \leq Y_i^{(a)} \leq Y_1^+$, the measurement point $p_i \in G_1$, and $I(p_i) = 1$. Otherwise, the point $p_i \in G_2$, and $I(p_i) = 0$. The bond Y_1^- and Y_1^+ are derived from the analysis of corresponding bimodal distributions.

Second task

The relative volumes V_1 and V_2 respectively pertaining to the geologic facies G_1 and G_2 are evaluated through the global de-clustered mean of the indicator function. The irregular distribution of the measurement points introduces systematic bias that requires de-clustering (Issaks and Srivastava 1989).

Third task

A sample variogram is used to compute the correlation structure of the indicator function $I(p_i)$, and an Ordinary Kriging is performed to compute its variance $\sigma_I^2(p)$ and ensemble mean $\langle I(p) \rangle$. This latter provides the probability $P[p \in G_1] = \langle I(p) \rangle$

of finding the facies G_1 at a point p , and represents an estimate of the local volumetric fraction of the facies G_1 .

Fourth task

The probability distribution of the indicator function is calculated at each estimation point by assuming that $I(p)$ is a truncated Gaussian field. therefore, the mean and variance computed by the point Kriging uniquely specifies a single-point probability density function $pdf(I; p)$.

Fifth task

To preserve the relative volumetric fractions of each geologic facies, the mean boundary between the materials is assumed to be defined by points p , where $P[p \in G_1] = V_1$ (Ritzi et al. 1994). Then the isolines defining the boundaries between the geologic facies can be computed for any spatial discretization Δ as:

$$L(p) = \int_{V_1-\Delta/2}^{V_1+\Delta/2} pdf(I; p)dI \quad (24.2)$$

The isolines, defining boundaries B_i between the facies G_1 and G_2 , correspond to probabilistic weights W_i with which the statistics of the system (i.e.: mean hydraulic heads $\langle h \rangle$), are readily approximated by:

$$\langle h \rangle = \sum_i W_i \langle h \rangle_{B_i} \quad (24.3)$$

For practical purpose, the system is assumed to be composed by a number of disjoint blocks, each hosting a different geo-material type. Hydraulic conductivity of each facies is considered as a constant, to be determined by inverse modeling once the boundaries between materials, defining the internal architecture of the system have been identified. Identification of the boundaries is performed according to the steps detailed in the following.

1. Stratigraphic and sedimentological information are analyzed and grouped into n main classes. Each one of these identifies a material type. An indicator-based approach is adopted to classify the identified facies.
2. Three-dimensional sample indicator variograms are constructed for each class. These are interpreted by different theoretical models (Spherical, Exponential, Gaussian) and key geostatistical parameters (sill, range, nugget, anisotropy pattern) are identified for each class. Formal model discrimination criteria (e.g., AIC, AICc, BIC, KIC) are employed to select amongst a set of alternative variogram models.
3. Three-dimensional multi-indicator Kriging is performed.
4. Demarcation of the volumetric fraction of the system occupied by each category is performed by means of an extension of the method proposed by Guadagnini

et al. [41]. One starts upon assigning a value of the indicator, $I = 1$, to samples where material G_1 is observed, while assigning $I = 0$ to locations where other samples are available. Indicator Kriging is performed and the method of Guadagnini et al. [41] is adopted to demarcate the geometry of the boundaries between G_1 and all other geo-materials.

5. The procedure is repeated in sequence for all remaining material types, within the remaining portions of the system. This leads to a reconstruction of the facies distribution, which preserves the relative volumetric proportions of the materials assessed on the basis of the available sedimentological information.

24.3 Application to the Brownfield of “Napoli Orientale” (Italy)

The area enclosed by the SNI, is part of the plain located in the east of Naples which is characterized by a wide structural depression, on the regional tectonic extension, occurred during the late Pliocene. This depression was filled, during the Quaternary, by Vesuvian and Phlegraean deposits, as well as by alluvial and marine sediments (Fig. 24.1).

The lithostratigraphy of the deposits in the plain is very complex and significantly affects the groundwater flow. The aquifer is characterized, from a hydrodynamic point of view, by a high heterogeneity, because of the frequent change in lithology, grain size and thickness of the different overlapped aquifers which constitute the overall



Fig. 24.1 Aerial photogrammetry of the city of Naples. Perimeter of the Site of National Interest called “Napoli Orientale” (red line). View of the crater of the Vesuvius volcano at the right bottom side of the image (Image taken from Google Earth)

groundwater system. The transmissivity of the aquifer, defined by the interpretation of pumping tests [7], is variable and comprised in a range between 1.26×10^{-2} – 5.10×10^{-5} m²/s [8, 10–13, 22, 23, 36, 50, 57, 66, 68].

The stratigraphical articulation of the aquifer give rise, at local scale, to a layered groundwater flow which occurs in the coarse-grained deposits of alluvial-pyroclastic stones and in the fissured lava layers. The groundwater flow observed at the basin scale can be, however, considered as unitary, because of the interconnection between the different overlapped aquifers. This interconnection is caused by the presence of interruptions in the semipermeable layers [10, 68] by the draining fluxes occurring through the less permeable layers and by the presence of a large number of wrongly manufactured wells, which allow the direct interaction between the different aquifers. The groundwater flow is mainly oriented from NE to SW and it converges toward the center of the plain and the depression of the Volla river, where, in the past [37], several springs came to the surface (Volla, Cozzone, Sanseverino). The final delivery of the groundwater is the sea.

24.3.1 Regional Scale Bi-Dimensional Model

The hydrogeology of the groundwater basin has been reconstructed by considering the historical data, in particular the water table acquired in 1978–79 [13], and the one monitored in 2002 [55]. Figure 24.2 shows the piezometry adopted to derive the aquifer domain for the implementation of the large-scale mathematical model.

The aquifer extends over an area of about 21,700 hectares, while the superficial basin covers a territory with an area of approximately 9500 hectares. The area involved by the aquifer is almost half urbanized, while the other half is characterized by agricultural territories, forests and rural areas. The superficial basin is, instead, intensively urbanized by the city of Naples. It's important to underline that the area enclosed by the SNI, is located in the sea delivery zone of both the groundwater and superficial basins. The general hydrodynamic characteristics of the aquifer have been defined according to experimental values of the transmissivity of singular points and the hydrological forcing drawn from a study of Paoletti [56]. The permeability zones have been identified on the basis of the geological reconstruction of Corniello and Ducci [21]. The hydraulic conductivity values have been calibrated using PEst algorithm (Parameter ESTimation model—Doherty [33], to obtain a water table trend closer to that observed in the mentioned studies. The flow rate entering the inward flux boundaries have been considered equal to 0.8 m³/s for the contribution coming from the side of the Avella mountains and equal to 0.2 m³/s for the contribution of the Vesuvius [12]. The bottom of the model has been assumed horizontal for the whole extension of the domain, and placed at 20 m below the mean sea level, being this the most active zone of groundwater circulation. The ground surface has been obtained by the interpolation of the Digital Elevation Model (DEM) data. The water

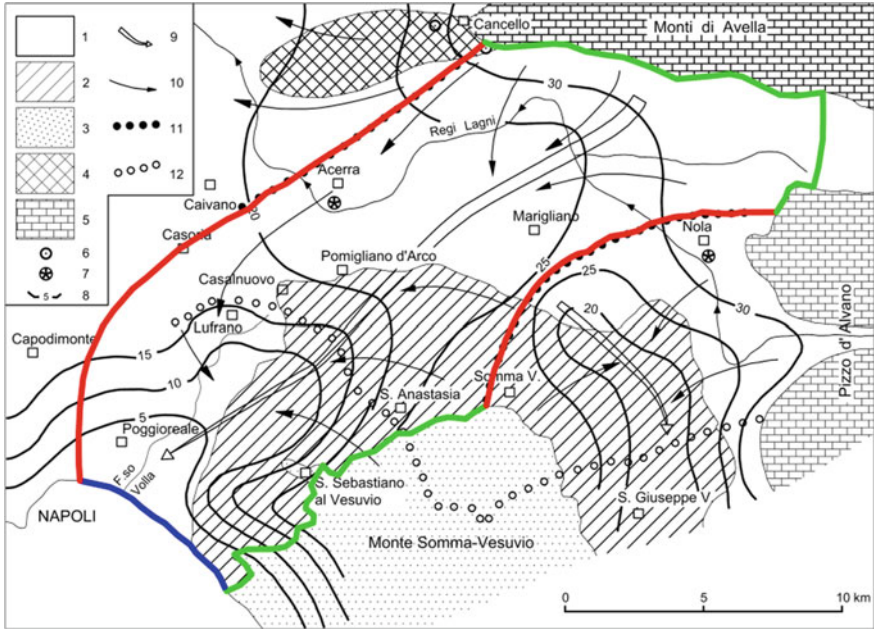


Fig. 24.2 Equipotential contour map of the plain to the east of Naples, with the delimitation of the hydrogeological basin, used for the construction of the regional scale model (red line: no flow boundary, green line: inward flux boundary, blue line: constant head boundary). Legend: (1) alluvial-pyroclastic deposits; (2) lavas and pyroclastic deposits; (3) lavas; (4) travertine deposits; (5) carbonate rocks; (6) major springs; (7) water levels monitoring stations; (8) equipotential curves; (9) preferential drainage axis; (10) main directions of groundwater flow; (11) groundwater watershed; (12) shallow watershed. (Image edited from Celico [13])

table in stationary conditions is showed in Fig. 24.3 as the result of the model implementation (ModFlow, Hill et al. [42]); it will provide detailed information to obtain the boundary conditions for the local scale model.

24.3.2 Local Scale Three-Dimensional Model

The regional scale study performed on the area to the East of Naples, allowed the determination of the boundary conditions for the local scale three-dimensional model, which otherwise would have been free of any hydrological reference. The calibration of the regional scale model, allowed the knowledge of the hydraulic head distribution of the entire basin, which is necessary to design the local scale model, affecting a limited part of the aquifer (the one involved by the SNI), with a higher spatial resolution. This model has been implemented assuming the aquifer to be phreatic, three-dimensional, heterogeneous and isotropic.

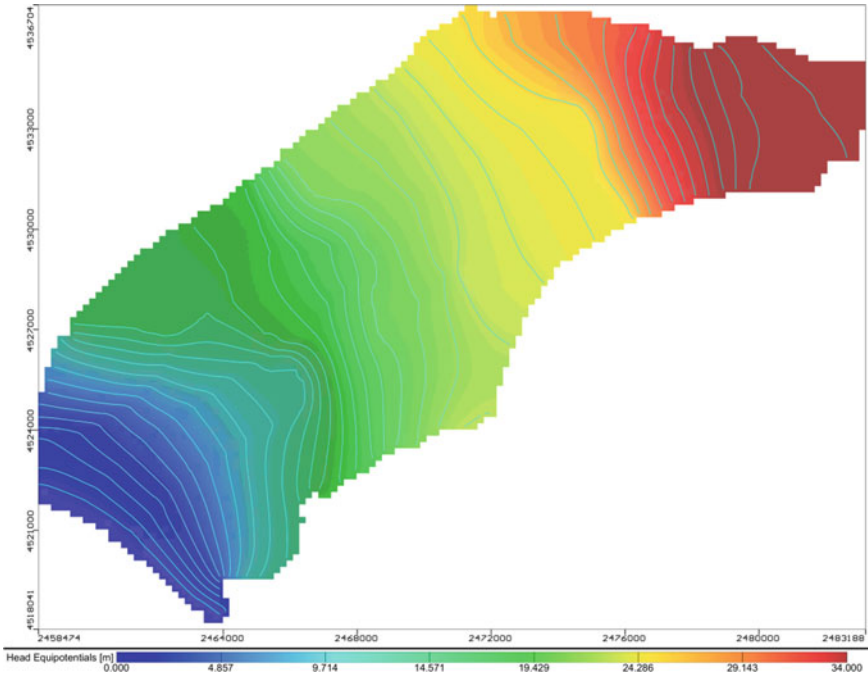


Fig. 24.3 Water table of the regional scale domain during stationary conditions

The local scale model, which has the task to guide the remediation project by simulating the groundwater flow and transport in a more detailed scale, has been implemented according to a composite medium approach [41]. The accurate analysis of sedimentological information of the system, has led to the identification of different geo-materials, whose spatial variability has been analyzed by means of an indexed variables procedure [65]. More than 250 coring, with known stratigraphic sequence, have been examined, allowing the identification of 6 lithofacies, each of which corresponding to a particular category of soil (Table 24.1).

As any geostatistical approach, the first step to perform a Composite Medium scheme to a given lithostratigraphy, is the structural or variographical analysis. The

Table 24.1 Assigning categories to the identified stratigraphy

Category	Lithology
1	Filling soils and sandy gravels
2	Silts and clay
3	Sand
4	Tuff
5	Pyroclastic deposits
6	Peat

experimental variograms of the identified categories, have been analyzed using the stratigraphic data obtained from the cores. This analysis showed the presence of a geometric and a zonal anisotropy because the sill and range values in the horizontal and vertical directions are different. The implementation of the experimental variograms has been realized using the GSLIB libraries [32]. The experimental variograms have been interpolated with the spherical and exponential model. The estimation of the parameters of the variograms has been conducted using the PEST optimization code [33]. The selection of the theoretical variograms was made considering appropriate criteria for model distinction (Model Validation Criteria), in particular the selection was performed based on KIC parameter [43]: the model that presents the lowest value of KIC is the one that best reproduces the experimental data. Figure 24.4 shows some experimental variograms and their corresponding interpretative models adopted for horizontal and vertical directions.

It's then possible to apply the procedure suggested by Guadagnini et al. [41], which follows the Composite Medium scheme, to derive the final geomaterials distribution field according to the sampling percentages, and to obtain the following quantities (Table 24.2).

Figures 24.5 shows the horizontal spatial distribution of the lithotypes identified in the area concerned by the mathematical model. Figure 24.6 shows two different cross sections of the lithostratigraphical reconstruction.

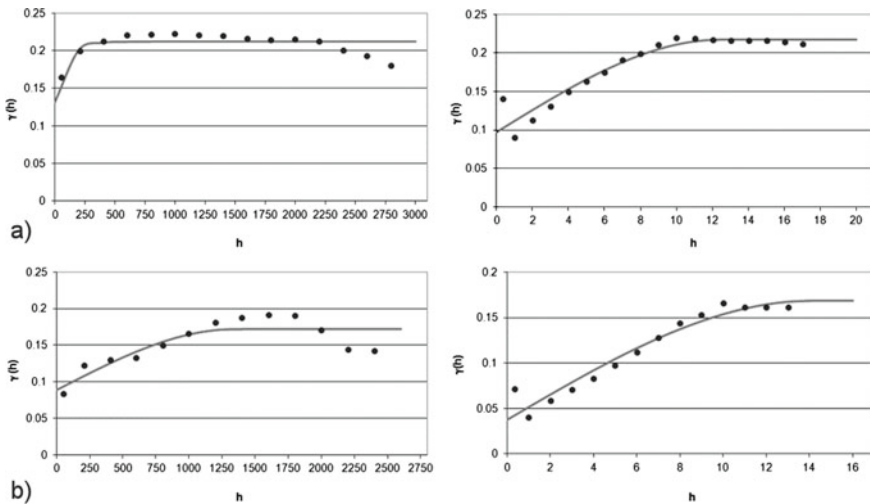


Fig. 24.4 Horizontal and vertical variograms for categories a 2 and b 3

Table 24.2 Sampling percentage of the lithotypes of the aquifer

Category	Lithology	Percentage (%)
1	Filling soils and sandy gravels	13.99
2	Silts and clay	23.64
3	Sand	46.77
4	Tuff	2.25
5	Pyroclastic deposits	8.64
6	Peat	4.71

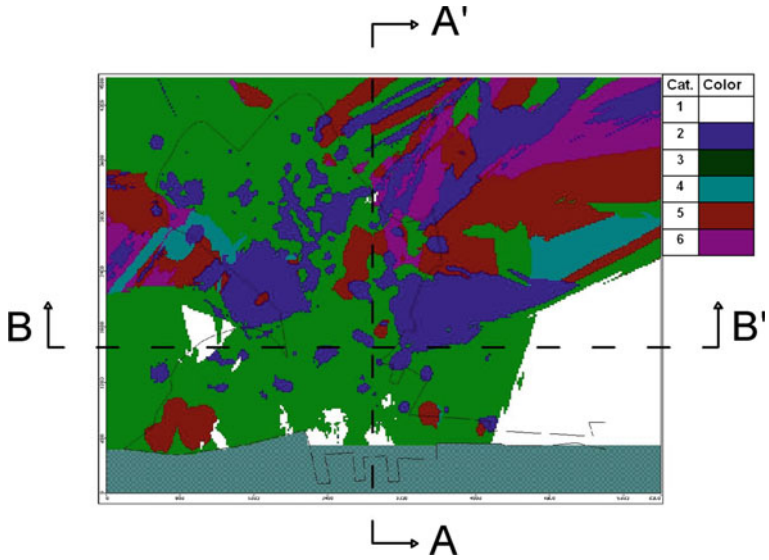


Fig. 24.5 Stratigraphic reconstruction of the aquifer at $Z = 0.5$ m (above sea level)

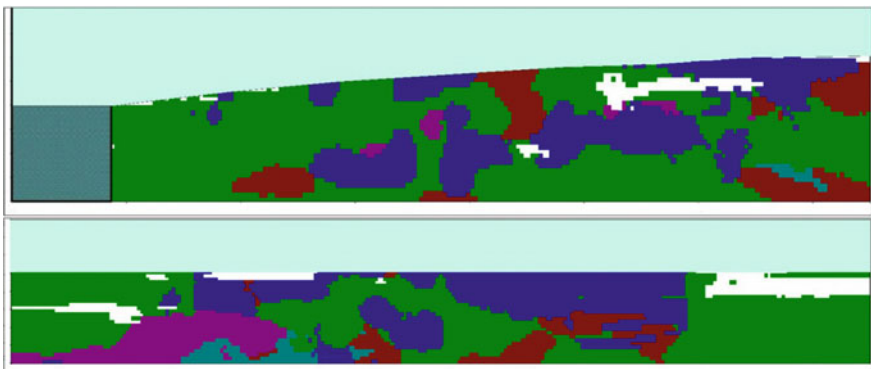


Fig. 24.6 Cross sections A-A' and B-B'

24.3.2.1 Flow Model for the Local Scale Domain

Once the aquifer lithostratigraphy has been reconstructed, it's necessary to assign a hydraulic conductivity value to all categories. The permeability of each category has been determined through a calibration procedure of the flow model using ModFlow simulation software [42]. The hydrological forcings are those obtained from the regional scale model, in which we considered the presence of the wells field of Lufrano (an area to the North with respect the SNI position), from which a flow rate of 400 l/s is withdrawn for irrigational purpose. The estimation of the hydraulic conductivities has been performed, once again, with the aid of the PEST optimization code [33]. The local scale model calibration has been reached using the hydraulic head measurements taken in 257 observing points, as shown in Fig. 24.7a. The estimation process reliability has been evaluated through the scatterplot between observed and calculated hydraulic head values in the 257 available wells. The scatterplot shows a correlation coefficient of 0.74 (Fig. 24.7b).

The estimated permeability values, associated to each category, are shown in Table 24.3.

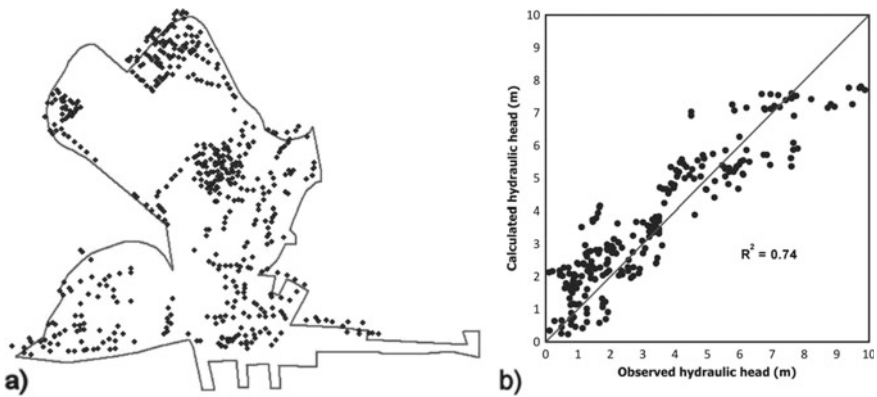


Fig. 24.7 a Observation points used for the calibration of the local three-dimensional model and b Scatterplot between observed and calculated hydraulic head values

Table 24.3 Estimated permeability values

Category	Lithology	Permeability (m/s)
1	Filling soils and sandy gravels	1.59×10^{-2}
2	Silts and clay	9.05×10^{-5}
3	Sand	1.60×10^{-3}
4	Tuff	1.63×10^{-4}
5	Pyroclastic deposits	2.50×10^{-3}
6	Peat	9.86×10^{-3}

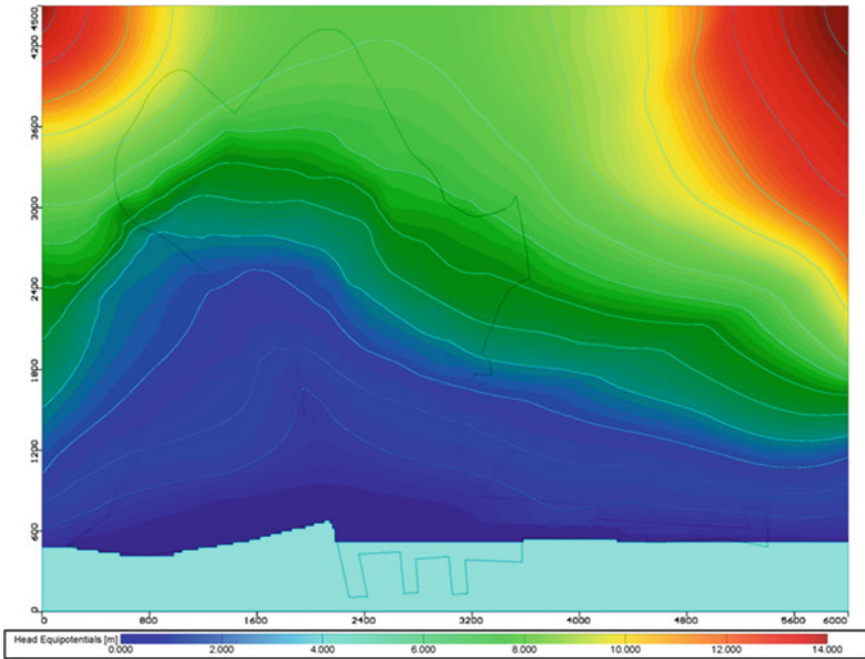


Fig. 24.8 Steady state hydraulic head distribution at the end of the calibration process

It was then possible to simulate the groundwater flow, to evaluate the water table in undisturbed conditions, and to quantify the amount of water arriving on the water-front (Fig. 24.8). The last parameter is essential for the design of the remediation works. The groundwater flow has been modeled by considering two different kinds of boundary conditions: (1) a Dirichlet or Constant Head condition on the East and West boundaries of the model, and along the waterfront; (2) a Cauchy or General Head condition on the North boundary. This boundary condition ensures a greater adaptability of the mathematical model with respect to the external forcings influencing the model itself.

24.3.2.2 Transport Model for the Local Scale Domain

The contamination affecting the Site of National Interest (SNI) is particularly complex. The industrial area is contaminated by a high concentration of heavy metals, aromatic organic compounds (phenols, chlorophenols, PCB), aliphatic organic compounds (most of them carcinogenic), inorganic compounds. The propagation of contaminants in the aquifer has been numerically calculated by coupling the groundwater flow model, previously implemented and described, with the solute transport model MT3D [71] based on the classical convective–dispersive transport

equation. The following boundary conditions have been adopted: (a) Dirichlet conditions at the sea boundary, where the pollutants concentration is set to zero, due to infinite dilution capacity of the sea, (b) Neumann conditions on the other boundaries, where the solute mass flux has been taken equal to zero. The initial pollutants concentrations have been considered uniformly equal to zero in the full domain, and the contamination sources have been considered punctual with constant assigned concentration. This choice was made considering that the contamination sources are still active, and that the overall mass of contaminants involving the system is unknown. The knowledge of the hydro-dispersive parameters is required in order to simulate the contaminant transport. Between those parameters the most important, and very difficult to determine, is the longitudinal dispersivity coefficient α_L . This is usually determined by means of in situ or laboratory tracer tests. Any tracer test was unfortunately performed for the case under examination, so that a homogeneous dispersivity coefficient has been evaluated through a calibration process of the transport model on the basis of the measured concentration data. The spatial and temporal distributions of each single contaminant has been inserted into the model domain and superimposed to the streamline derived by the flow simulation. In such a way, every point of known contaminant concentration could assume a role of contaminant source, or could be linked in a specific way to a contaminant source. More precisely, sampling points located along the streamlines with decreasing concentration both in time and space (from upstream to downstream), have been considered as contaminant sources connected by the propagation mechanism. This analysis, made for all the contaminant, allowed us to adjust the hydrodispersive parameters of the aquifer, by starting from literature values, and to derive the value of the longitudinal dispersivity coefficient α_L , which has been found equal to 60 m. The transversal dispersivity coefficient has been fixed equal to 6 m, as suggested in literature. Figure 24.9, for example, shows the results obtained for arsenic concentration after a simulation of twenty years. It can be noted how the points with the highest concentration become propagation sources spreading the contaminant in the aquifer and delivering it into the sea. The model therefore provides important information on the extent and the fate of the contamination, indicating where to carry out remediation operations and what priority should be given to each of them.

24.4 Conclusions

Dealing with heterogeneity in hydrogeology depends largely on a conscious decision to better characterize, describe and model the geology of the sites of interest. Homogenization or averaging approach that has been commonly used so far in hydrogeology has shown its limits in many instances. The probabilistic reconstruction of geologic facies presents some advantages: different information collected from pumping and tracer tests, well-logs, and geophysical techniques can be assimilated in a similar manner; the uncertainties in the estimate of the geologic texture and the hydraulic (and transport) parameters can be quantified. The methodology still leaves room for

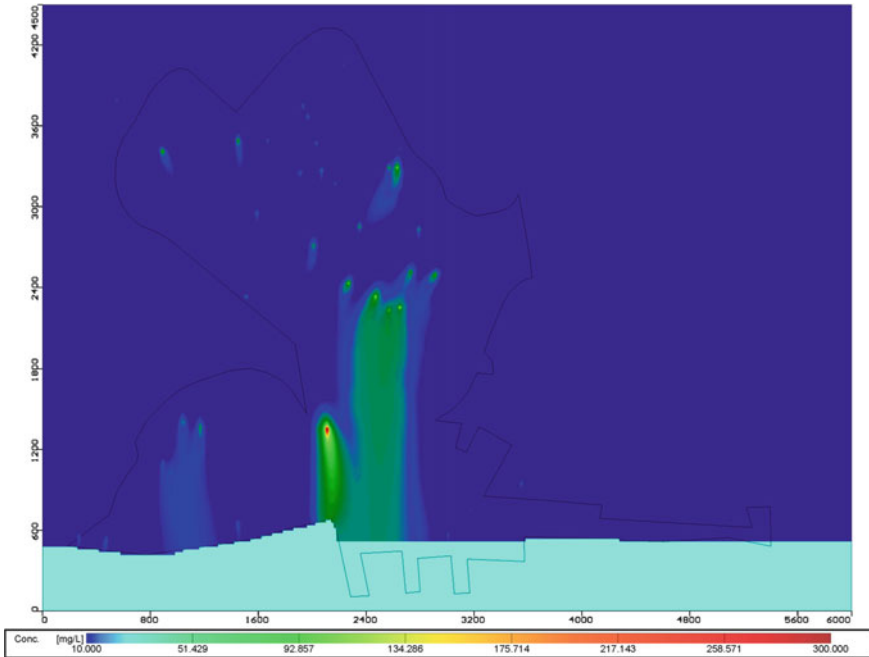


Fig. 24.9 Arsenic contamination plume

improvement. The reconstruction of the morphology and the hydrodynamic characteristics of a polluted site within a modeling tool, represents an effective system to describe the real behavior of the system and to understand the origin of the contamination and the effects of remediation. Numerical modeling gives a fundamental help to design efficient remediation processes, without causing unacceptable perturbation of the natural conditions of the sites and excessive costs. The importance of modeling becomes even more evident when the sites are located in strongly urbanized areas, and have a delicate hydrologic equilibrium.

24.5 Recommendations

Brownfield characterization should be guided by the outcomes of a well defined conceptual model. The overall monitoring system consisting in geological boreholes, piezometers and sampling stations should be planned by taking into consideration several aspects like their homogeneous spatial and temporal distribution across the site, the acquifer preferential flow direction, the possibility of deriving information about the system boundary conditions, etc. This approach would be helpful for modelers that often have a hard time fighting with redundant or useless data. These problems occur for a specific reason. Contaminated sites are usually located

within industrial areas hosting different companies, so when groundwater pollution phenomena are reported, each company is independently responsible for the installation and the management of the monitoring system. This results in a suboptimal spatial distribution of the monitoring points (very dense areas alternating with completely lacking ones), and in a non-homogeneous time collection of the samples. It would be appropriate to have a global management in the care of a main control unit taking care of the aforementioned aspects.

Acknowledgement The study has been performed in the framework of a research agreement with the Ministry of the Environment, Land and Sea Protection and SOGESID. The authors thank the late prof. Celico P. for his support on the recognition of the geological data of Naples aquifer, and the anonymous reviewer for his/her fruitful and constructive comments.

References

1. Aboufiras M, Marino MA (1984) Cokriging of aquifer transmissivities from field measurements of transmissivity and specific capacity. *J Int Assoc Math Geol* 16(1):19–35
2. Ahmed S, de Marsily G (1987) Comparison of geostatistical methods for estimating transmissivity using data on transmissivity and specific capacity. *Water Resour Res* 23(9):1717–1737
3. Ahmed S, de Marsily G (1988) Combined use of hydraulic and electrical properties of an aquifer in a geostatistical estimation of transmissivity. *Ground Water* 26(1):78–86
4. Ahmed S, de Marsily G (1993) Co-kriged estimation of aquifer transmissivity as an indirect solution of inverse problem: a practical approach. *Water Resour Res* 29(2):521–530
5. Allocca V, Celico P (2004) Risorse termali e minerali della provincia di Napoli. Assessorato Industria, Energia, Miniere e Risorse Geotermiche, Provincia di Napoli
6. Allocca V, Celico P (2004) Carta idrogeologica della provincia di Napoli (scala 1: 50.000). Assessorato Industria, Energia, Miniere e Risorse Geotermiche, Provincia di Napoli
7. Allocca V, Celico P (2008) Scenari idrodinamici nella piana ad Oriente di Napoli (Italia), nell'ultimo secolo: cause e problematiche idrogeologiche connesse. *Giornale di Geologia applicata* 9(2):175–198
8. Bellucci F, Corniello A, de Riso R, Russo D (1990) Idrogeologia della piana a N-E di Napoli. *Mem Soc Geol It* 45:339–349
9. Carrera J, Alcolea A, Medina A, Hidalgo J, Slooten LJ (2005) Inverse problem in hydrogeology. *Hydrogeol J* 13:206–222
10. Celico F, Celico P, Esposito L, Guadagno FM, Habetswallner F and Mele R (1995) Sull'evoluzione idrogeologica dell'area del Sebeto (Campania). In: Proceedings of the 1st national conference of applied geology, Taormina (Italy), Vol. 30
11. Celico F, Esposito L, Mancuso M (2001) Complessità idrodinamica e idrochimica dell'area urbana di Napoli: scenari interpretativi. *Geologia Tecnica & Ambientale* 2
12. Celico F, Petrella E, Celico P (2006) Hydrogeological behavior of some fault zones in a carbonate aquifer of Southern Italy: an experimentally-based model. *Terra Nova* 18:308–313
13. Celico P (1983) Idrogeologia dei massicci carbonatici, delle piane quaternarie e delle aree vulcaniche dell'Italia centro-meridionale (Marche e Lazio meridionali, Abruzzo, Molise e Campania). *Quaderni della Cassa per il Mezzogiorno* 4(2):1–225
14. Celico P (1990) Brevi considerazioni sulle possibili cause dell'aumento del tenore in nitrati, ferro e manganese nella falda di Lufrano. *L'Appennino Meridionale*, Napoli
15. Celico P, De Paola P (1992) La falda dell'area napoletana: ipotesi sui meccanismi naturali di protezione e sulle modalità di inquinamento - Studi e Ricerche. *Atti Giorn. di Studio: "Acque per uso potabile"*. Proposta per la tutela ed il controllo della qualità, 387C-412C

16. Celico P, Esposito L, De Gennaro A, Mastrangelo E (1994) La falda ad Oriente della città di Napoli: idrodinamica e qualità delle acque. *Geologica Romana*, Vol. 30, 653–660
17. Celico P, Esposito L, Guadagno GM (1997) Sulla qualità delle acque sotterranee nell’acquifero del settore orientale della Piana Campana. *Geologia Tecnica e Ambientale*, 4/97
18. Certes C, de Marsily G (1991) Application of the pilot point method to the identification of aquifer transmissivity. *Adv Water Resour* 14(5):284–300
19. Chiles JP, Delfiner P (1999) *Geostatistics: modeling spatial uncertainty*. Wiley, New York, p 695
20. Civita M, de Medici GB, de Riso R, Nicotera P and d’Elogio EN (1973) Carta idrogeologica della Campania Nord-Occidentale - Memoria descrittiva. In: *Proceedings of the II groundwater international conference, Palermo (Italy)*, I.A.H.
21. Corniello A, Ducci D (2002) Hazardous piezometric levels rising in Naples urban area (Italy) as a consequence of overexploitation reduction. In: *Proceedings of the SINEX, symposium of intensive use of groundwater, Valencia (Spain), December, 1–10*
22. Corniello A, de Riso R, Ducci D (1990) *Idrogeologia e idrogeochimica della Piana Campana*. *Mem Soc Geol It* 45
23. Corniello A, Ducci D, Catapano O, Monti GM (2003) Variazioni piezometriche nella zona orientale della città di Napoli. *Quaderni di Geologia Applicata* 10(2):43–57
24. Delbari M, Amiri M, Motlagh MB (2014) Assessing groundwater quality for irrigation using indicator kriging method. *Appl Water Sci* 9. <https://doi.org/10.1007/s13201-014-0230-6>
25. Delhomme JP (1976) *Application de la théorie des variables régionalisées dans les sciences de l’eau [Application of the theory of regionalized variables to water sciences]*. Doctoral thesis, University Paris VI
26. Delhomme JP (1978) Kriging in hydrosciences. *Adv Water Resour* 1(5):251–266
27. Delhomme JP (1979) Spatial variability and uncertainty in groundwater flow parameters: a geostatistical approach. *Water Resour Res* 15(2):269–280
28. de Marsily G (1978) *De l’identification des systèmes hydrologiques [On the calibration of hydrologic systems]*. Doctoral thesis, University Paris VI
29. de Marsily G (1986) *Quantitative hydrogeology*. In: *Groundwater hydrology for engineers*. Academic, New York, pp 440
30. de Marsily G, Delhomme JP, Coudrain-Ribstein A, Lavenue AM (2000) Four decades of inverse problems in hydrogeology. In: Zhang D, Winter CL (eds) *Theory, modeling, and field investigation in hydrogeology*. *Geol Soc America Special Paper* 348:1–17
31. de Marsily G, Delay F, Gonçalves J, Renard P, Teles V, Violette S (2005) Dealing with spatial heterogeneity. *Hydrogeol J* 13:161–183
32. Deutsch CV, Journel AG (1998) *GSLIB*. Oxford, Oxford University Press, *Geostatistical Software Library and User’s Guide*
33. Doherty J (2006) *PEST Model-Independent Parameter Estimation, V10.1*, Bethesda, Papadopoulos. S. S., Inc., Md., (Available at <http://www.sspa.com/pest/>)
34. Ducci D, Condeso de Melo MT, Preziosi E, Sellerino M, Parrone D, Ribeiro L (2016) Combining natural background levels (NBLs) assessment with indicator kriging analysis to improve groundwater quality data interpretation and management. *Sci Total Environ* 569–570:569–584
35. Esposito L (1998) Nuove conoscenze sulle caratteristiche idrogeochimiche della falda ad Oriente della città di Napoli (Campania). *Quaderni di Geologia Applicata*, Pitagora Editrice, 5-1/98
36. Esposito L, Piscopo V (1997) Groundwater flow evolution in the circumVesuvian plain, Italy. *British Committée XXVII Congress*. Nottingham, 21–27 September. In “*Groundwater in the Urban Environment*, Vol. I, Nottingham, IAH, Edited by John Chilton
37. Fiorelli T (1926) Cenni sull’andamento della falda acquifera nel sottosuolo della zona tra Napoli e Somigliano d’ Arco in relazione alla costituzione geologica e la topografia e idrologia superficiale del territorio medesimo. *Annali del genio Civile*, VII
38. Freeze RA (1975) A stochastic-conceptual analysis of one-dimensional groundwater flow in non-uniform homogeneous media. *Water Resour Res* 11(5):725–741

39. Gelhar LW (1976) Effects of hydraulic conductivity variation on groundwater flow. In: Second international symposium on stochastic hydraulics, International Association for Hydraulic Research, Lund, Sweden
40. Guadagnini A, Neuman SP (1999) Nonlocal and localized analyses of conditional mean steady state flow in bounded, randomly nonuniform domains. 1 Computational examples. *Water Resources Res* 35:3019–3040
41. Guadagnini L, Guadagnini A, Tartakovsky DM (2004) Probabilistic reconstruction of geologic facies. *J Hydrol* 294:57–67
42. Hill MC, Banta ER, Harbaugh AW, Anderman ER (2000) MODFLOW-2000, the U.S. Geological Survey modular groundwater model—User guide to the observation, sensitivity, and parameter estimation processes and three post-processing programs. U.S. Geol. Surv. Open File Rep., 00–184, pp 209
43. Kashyap RL (1982) Optimal choice of AR and MA parts in autoregressive moving average models. *IEEE Trans Pattern Anal Mach Intel* 4(2):99–104
44. Journel AG (1983) Nonparametric estimation of spatial distribution. *Math Geol* 15(3):445–468
45. Journel AG, Alabert FG (1990) New method for reservoir mapping. *J Pet Technol* February 42(2):212–218
46. Journel AG, Gomez-Hernandez J (1993) Stochastic imaging of the Wilmington clastic sequence. *Soc Pet Eng Form Eval* March 8(1):33–40
47. Journel AG, Isaaks EK (1984) Conditional indicator simulation: application to a Saskatchewan uranium deposit. *Math Geol* 16(7):685–718
48. Lavenue AM, Ramarao BS, de Marsily G, Marietta MG (1995) Pilot point methodology for automated calibration of an ensemble of conditionally simulated transmissivity fields: part 2: application. *Water Resour Res* 31(3):495–516
49. Lavenue MA, de Marsily G (2001) Three-dimensional interference test interpretation in a fractured/unfractured aquifer using the pilot point inverse method. *Water Resour Res* 37(11):2659–2675
50. Marzano V (2001) Applicazione e confronto dei metodi SINTACS e TOT per la valutazione della vulnerabilità all'inquinamento dell'acquifero piroclastico nel settore sud-orientale della Piana Campana. Experimental thesis, Università degli Studi di Napoli Federico II
51. Matheron G (1963) Principles of geostatistics. *Econ Geol* 58:1246–1266
52. Matheron G (1965) Les variables régionalisées et leur estimation [Regionalized variables and their estimation]. Masson, Paris, p 185
53. Medina-Ortega P, Morales-Casique E, Hernández-Espriú A (2019) Sequential indicator simulation for a three-dimensional distribution of hydrofacies in a volcano-sedimentary aquifer in Mexico City. *Hydrogeol J* 27:2581–2593
54. Mohammadpour M, Bahroudi A, Abedi M, Rahimpour G, Jozanikohan G, Khalifani FM (2019) Geochemical distribution mapping by combining number-size multifractal model and multiple indicator kriging. *J Geochem Explor* 200:13–26
55. North-Western Basin Authority of the Campania Region (2004) Il contributo al Piano di Tutela delle Acque della Regione Campania. Voll. 1, 2, 3, Naples
56. Paoletti (2009) Il bilancio idrologico, studio di fattibilità per la realizzazione degli interventi di messa in sicurezza di emergenza della falda acquifera, Ministero dell'Ambiente della Tutela del Territorio e del Mare, SOGESID
57. Piscopo V, Baiocchi A, Fantucci R, Lotti F (2005) La risposta al pompaggio di acquiferi vulcanici: alcuni esempi delle aree napoletane e viterbese. *Italian J Eng Geol Environ* 1:21–35
58. Ramarao BS, Lavenue AM, de Marsily G, Marietta MG (1995) Pilot point methodology for automated calibration of an ensemble of conditionally simulated transmissivity fields: part 1—theory and computational experiments. *Water Resour Res* 31:3475–3493
59. Raoult Y (1999) La nappe de l'Albien dans le bassin de Paris: de nouvelles idées pour de vieilles eaux [The Albian aquifer in the Paris basin: new ideas for old waters]. Doctoral thesis, University Pierre et Marie Curie, Paris VI, pp 170
60. Rivoirard J (2000) Cours de géostatistique multivariée [Lecture notes for multivariate geostatistics]. Note C-172, Ecole des Mines de Paris, Centre de Géostatistique, Fontainebleau

61. Roth C, Chilés JP, de Fouquet C (1998) Combining geostatistics and flow simulators to identify transmissivity. *Adv Water Resour* 21:555–565
62. Sakata Y, Katsura T, Nagano K (2020) Estimation of ground thermal conductivity through indicator kriging: nation-scale application and vertical profile analysis in Japan. *Geothermics* 88:101881
63. Smith L, Freeze RA (1979) Stochastic analysis of steady state groundwater flow in a bounded domain. 1. One-dimensional simulations. 2. Two-dimensional simulations. *Water Resour Res* 15(3):521–528 and 15(6):1543–1559
64. Straface S, Rizzo E, Chidichimo F (2010) Estimation of water table map and hydraulic conductivity in a large-scale model by means of the SP method. *J Geophys Res* 115. <https://doi.org/10.1029/2009JB007053>
65. Straface S, Chidichimo F, Rizzo E, Riva M, Barrash W, Revil A, Cardiff M, Guadagnini A (2011) Joint inversion of steady-state hydrologic and self-potential data for 3D hydraulic conductivity distribution at the Boise hydrogeophysical research site. *J Hydrol* 407:115–128
66. Tedeschi C (1974) Ravvenamento di pozzi artesiani e nuova trivellazione profonda per la Centrale Termoelettrica di Napoli Levante. *Rivista Italiana di Geotecnica* 8(4):221–231
67. Viparelli C (1967) Le acque sotterranee. In: *Proceedings of the VIII Convegno di Geotecnica*, Cagliari, ESI- Edizione Scientifiche Italiane
68. Viparelli M (1978) Le acque sotterranee ad oriente di Napoli. *Fondazione Politecnica per il Mezzogiorno d'Italia*, Napoli, p 111
69. Winter CL, Tartakovsky DM (2000) Mean flow in composite porous media. *Geophys Res Lett* 27:1759–1762
70. Winter CL, Tartakovsky DM (2002) Groundwater flow in heterogeneous composite aquifers. *Water Resources Res* 38(8). <https://doi.org/10.1029/2001WR000450>
71. Zheng C (1990) MT3D, A modular three-dimensional transport model for simulation of advection, dispersion and chemical reactions of contaminants in groundwater systems. Report, Rockville, Maryland: S.S. Papadopoulos & Associates
72. Zimmerman DA, de Marsily G, Gotaway CA, Marietta MG, Axness CL, Beauheim R, Bras R, Carrera J, Dagan G, Davies PB, Gallegos D, Galli A, Gomez-Hernandez J, Grindrod P, Gutjahr AL, Kitanidis P, Lavenue AM, McLaughlin D, Neuman SP, Ramarao BS, Ravenne C, Rubin Y (1998) A comparison of seven geostatistically-based inverse approaches to estimate transmissivities for modeling advective transport by groundwater flow. *Water Resour Res* 34(6):1373–1414